GSI

GSI Report 2012-1
May 2012

SCIENTIFIC REPORT 2011

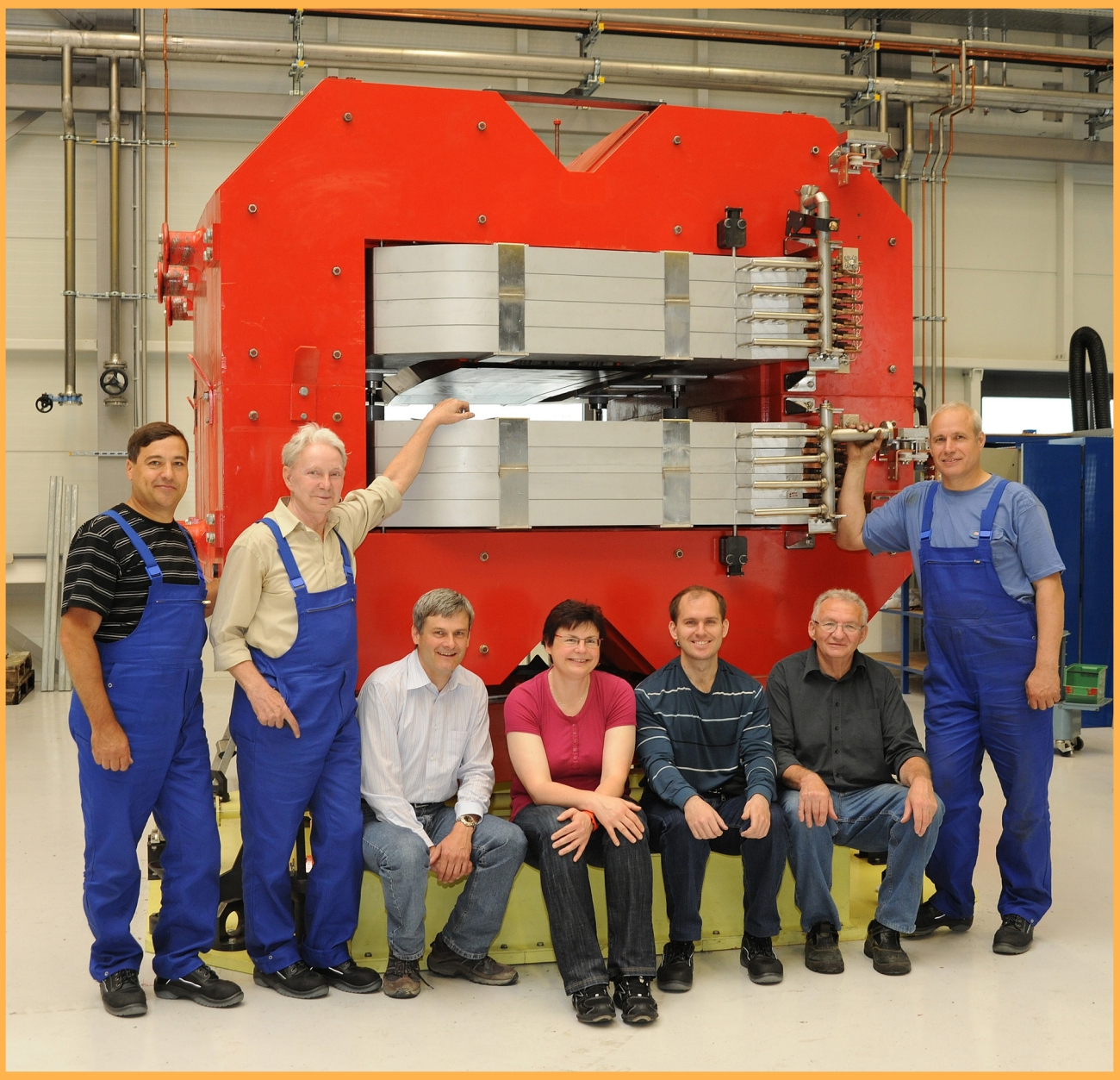

GSI Helmholtzzentrum für Schwerionenforschung GmbH
Member of the Helmholtz Association

The first dipole magnet for the Super-FRS (FRagment Separator) was built in close collaboration with the Budker Institute for Nuclear Research in Novosibirsk. It is approx. 3m x 3m x 3m in size and weighs 95 tons. Originally to be thought as a prototype it will be used within the Super-FRS as it fulfils the specification completely.
The magnet needs to be radiation resistant as it will be used in the vicinity of the Super-FRS target. It was built without any organic material to guarantee a life time of 20 years. The design allows a remote controlled assembly of the magnet as well as remote controlled alignment.
After delivery the magnet was assembled by a mixed german-russian team in the so-called testing hall. There it is awaiting the latest tests and will be used to train the special assembly and alignment procedures.

Successful collaboration - staff of GSI and Budker Institute assembled the dipole. From left to right: Victor Shardrin (Budker Institute), Yuriy Kolokolnikov (Budker Institute), Carsten Mühle (GSI), Christina Will (GSI), Denis Gurov (Budker Institute), Claus-Herbert Mühle (GSI) und Alexander Zhigaleev (Budker Institute).

GSI Scientific Report 2011

GSI Report 2012-1
<http://www.gsi.de/library/GSI-Report-2012-1/>

ISSN: 0174-0814
and GSI Report 2012-1

Publisher: GSI Helmholtzzentrum für Schwerionenforschung GmbH,
Planckstr. 1, 64291 Darmstadt, Germany, <http://www.gsi.de>
GSI is a member of the Helmholtz association of national research centres <http://www.helmholtz.de>.
E-only-edition: <http://www.gsi.de/library/GSI-Report-2012-1/>

Editor: Katrin Große,
Contact: gsilibrary@gsi.de, phone: +496159 712610, fax: +496159 713049.
Cover photograph: Gabi Otto.
Publication Date: May 2012
Technical Team at GSI: T. Badura, K. Große, V. Schaa and K. Schiebel.

For the production of this report templates and scripts of the JACoW collaboration (Joint Accelerator Conferences on Web <http://www.jacow.org>) were used.

Foreword

FAIR is on its way! During the past year GSI, and its national and international partners, have achieved important milestones on the path of the construction towards the Facility of Antiproton and Ion Research, Europe's next-generation flagship in basic research. Fittingly on December 6 - Santa Clause day - GSI received a sizable gift: Dr. Helge Braun, Germany's Parliamentarian Undersecretary for Education and Research, brought the first cheque for 50 Million Euros, which has been used in the meantime to order the first magnets for the new SIS100 accelerator for FAIR. Also the outer appearance of GSI has changed: road works have started, trees have been cut and sediment tests have been performed. Since February 2011 GSI greets visitors with a new office building which hosts the scientists of the ALICE and Hades collaborations and of the theory department. Furthermore the new building is home to the Helmholtz Alliance EMMI and to the FAIR directorate and administration. Furthermore the ground floor boosts an auditorium and a foyer which can be used to further strengthen the ties between GSI and FAIR scientists and the public; a partnership, which, for example, has been very successfully demonstrated when EMMI hosted the international exhibition about the 'world machine' and GSI invited the public for its summer open house.

Partnership - a word which has strong tradition in GSI's history and which becomes even more relevant when we look towards our future. Of course, FAIR is a truly international facility with more than 2500 scientists and engineers from institutions from more than 40 countries being involved in designing, constructing and, later, using the worldwide unique new accelerator and experimental infrastructures. Besides this impressive international and also nationwide participation, a crucial role is clearly played by our partner universities in Darmstadt, Frankfurt, Giessen, Heidelberg, Jena and Mainz, and the Frankfurt Institute of Advanced Studies FIAS. Here a strongly intertwined network of collaborations and synergies has been built to optimally incorporate the expertise present at the partner institutions into our challenging project. The heart of the network is the Helmholtz International Center for FAIR funded within the excellence initiative Loewe of the Hessian state. Originally proposed by the universities of Darmstadt, Frankfurt and Giessen together with FIAS and GSI, this think-tank has the goal to develop novel methods and models for the accelerators and experiments at FAIR. In 2011 an international expert committee evaluated HIC for FAIR

and stressed its impressive success and importance which is also reflected in the fact that the other universities in Hessen and the Hochschule Darmstadt have joined as associated partners. An extremely positive evaluation was also given to the Helmholtz Alliance EMMI which has clearly established itself as an international institution bringing together researchers from particle, nuclear, atomic, plasma and astrophysics to perform interdisciplinary research on strongly correlated systems.

The third pillar connecting GSI with its partner universities is the Helmholtz Graduate School (HGS) "Hire for FAIR". Supported with funds from the Helmholtz Association a structured education for graduate students has been developed and, now in its third year, the school comprises nearly 300 students doing FAIR-related research under the supervision of about 80 professors at the 6 partner universities. HGS "Hire for FAIR" draws strong international attention: applications are coming in worldwide and talks have started to connect the school with partners abroad, making it even more attractive for our own students, but also allowing students from foreign universities to participate in the unique opportunities offered with FAIR at the horizon.

EMMI, HIC for FAIR and, not the least the graduate school "Hire for FAIR" are backbones for the coming years, when GSI will focus its efforts towards the construction of FAIR. During this period of reduced GSI beamtimes and associated research activities they guarantee the continuation and conservation of the unique research expertise present in the GSI environment and so much needed once FAIR will be operational. The same role, of course, is played by the two Helmholtz Institutes in Jena and Mainz. Both Institutes foster the synergy to the university, on which campus they are established, and bring in strong expertise on FAIR-related topics, focusing mainly on hadron and nuclear physics as well as on accelerator development in Mainz and on atomic and plasma physics in Jena.

We have also gladly witnessed our network growing and adding new partners during last year. NAVI - the Nuclear Astrophysics Virtual Institute newly established with the help of funds from the Helmholtz Association - brings in researchers from the University of Würzburg who, together with colleagues from GSI and several other national and international institutions want to perform interdisciplinary research in observational astronomy, astrophysics and experimental and theoretical nuclear physics, preparing for the new era in nuclear astrophysics offered by FAIR. Finally GSI was proud to see three young female researchers succeed in the competition for the prestigious

Helmholtz Young Investigator Awards.

2011 was also a year of many research highlights, several of them due to the unique synergy and collaboration between scientists from the accelerator and research departments. Due to progress on the path advancing the current GSI accelerator facility to meet the goals needed for FAIR, the intensity and time-structure of the uranium beams at the highest energies have been improved to new world-leading levels. This, in turn, allowed the production of about 40 new isotopes strengthening the position of GSI as the premier laboratory for the discovery of new isotopes in the world for the last two decades. The close collaboration of the ion source group, accelerator scientists, the target laboratory and members of the TASCA collaboration led to the development of the first high-intensity and long-time stable ^{50}Ti beam in the world, thus - hopefully - opening the door to the discovery of the new elements in the periodic table with charge numbers Z=119 and 120. Further highlights of the NuSTAR activities include the successful completion of the PRESPEC in-flight gamma-spectroscopy equipment at the fragment separator FRS, an important milestone towards the first AGATA campaign in 2012/13. Another step towards the future has been witnessed in June 2011 when the first magnet for the SuperFRS arrived at GSI. The 95-tons magnet has been designed, constructed and tested by our Russian partners from the Budker Institute in Novosibirsk. Although originally anticipated as a prototype, it meets all specifications and can thus be used in the SFRS.

In biophysics, a new treatment of tumors has been proposed which is based on the radiation with 4.5 GeV protons and promises highest precision and cures with higher doses than possible with carbon therapy. In another branch of the APPA pillar, atomic physicists, with strong GSI participation, succeeded to observe the spin-flip of a single proton in an electromagnetic trap deducing in this way its magnetic moment. The novel trap device has been designed for protons and antiprotons alike. Hence the present experiment, although an important achievement in its own rights, is a major milestone towards the goal to determine the magnetic properties of the antiproton with many orders better accuracy than is currently possible. These high-precision tests of the matter-antimatter symmetry is a cornerstone of the physics program at FLAIR.

GSI plays an important role in the physics program of the ALICE detector at the CERN Large Hadron Collider. Here the unprecedentedly high Pb-Pb interaction rates, achieved at the current world machine for ultra-relativistic heavy-ion collisions, allowed an exciting new view on the properties of nuclear

matter showing, that at even the highest transverse momenta of 50 GeV/c achievable today nuclear matter is not yet transparent in head-on collisions.

The present Scientific Report gives again proof of the widespread and high-quality research activities performed at GSI. I wish you much pleasure at reading about achieved scientific milestones, but also about the plans and progress which brings us closer to our ultimate goal - to construct FAIR (the next 'world machine') and to exploit its unprecedented research opportunities.

Karlheinz Langanke
GSI Director of Research

Contents

The ExtreMe Matter Institute EMMI

P. Braun-Munzinger[1,2,3] *and C. Ewerz*[1,4]

[1]ExtreMe Matter Institute EMMI, GSI, Darmstadt, Germany; [2]Research Division, GSI, Darmstadt, Germany; [3]TU Darmstadt, Germany; [4]University of Heidelberg, Germany

Since 2008 the Helmholtz Alliance 'Cosmic Matter in the Laboratory' is funded in the framework of the Alliance program of the Helmholtz Association. The aim of the Alliance program is to strategically enhance the profiles of the participating Helmholtz Centres and to transfer successful developments into one of the Helmholtz Association's research programs. The research performed within the Helmholtz Alliances is collaborative and brings together universities, Helmholtz Centres and other non-university research institutions. In the case of the alliance 'Cosmic Matter in the Laboratory' the funding contribution from the Helmholtz Association amounts to 18.745 Mio. Euro for six years.

A key step in the strategic positioning of the Helmholtz Alliance 'Cosmic matter in the Laboratory' was to establish a new, world-leading institute for research on matter at the extremes of density and temperature: the ExtreMe Matter Institute EMMI hosted by GSI. It was founded simultaneously with the start of the Alliance in April 2008.

The scientific aim of the ExtreMe Matter Institute is to perform forefront research in the area of matter under extreme conditions. This comprises in particular four key areas of the research field 'Structure of Matter' of the Helmholtz Association:

- quark-gluon plasma and the phase structure of strongly interacting matter
- neutron matter
- electromagnetic plasmas of high energy density
- cold quantum gases and extreme states in atomic physics.

The relevant science themes range from the quark-gluon plasma as it existed shortly after the Big Bang to ultracold quantum gases created in laboratory experiments, to the quantum dynamics of extreme fields, and from hot and highly compressed classical bulk plasmas and to the astrophysically relevant dense medium of nucleons and neutrons that governs the properties of the evolution of supernovae and neutron stars. It hence comprises the study of the coldest, of the hottest, and of the densest known forms of matter in the Universe. The key idea is to conduct this research in an interdisciplinary framework, based upon common underlying concepts for the theoretical and phenomenological understanding of the physical phenomena in the four areas.

Under the lead management of the GSI Helmholtz Centre for Heavy Ion Research the Alliance links 13 German and international research centers and universities as partner institutions:

- GSI Helmholtzzentrum für Schwerionenforschung, Darmstadt, Germany
- Forschungszentrum Jülich, Germany
- Ruprecht-Karls-Universität Heidelberg, Germany
- Goethe Universität Frankfurt, Germany
- FIAS Frankfurt Institute for Advanced Studies, Germany
- Technische Universität Darmstadt, Germany
- Universität Münster, Germany
- Université VI, Paris, France
- Max-Planck-Institut für Kernphysik, Heidelberg, Germany
- Lawrence Berkeley National Laboratory, Berkeley, USA
- Joint Institute for Nuclear Astrophysics (JINA), USA
- RIKEN, Saitama, Japan
- University of Tokyo, Japan.

In addition, the Alliance benefits from the expertise of internationally renowned scientist who are closely linked to it as Associated Partners. Currently, the Alliance has 31 Associated Partners, among them two Nobel laureates.

The partner institutions have committed themselves to creating 18 senior positions, including full professorships and equivalent tenure-track and tenured positions, in the framework of the Alliance. By the end of 2011, 15 of these 18 positions are filled. Among these positions are four EMMI Fellow positions in experimental physics at GSI, one for each of the main research areas of EMMI. The EMMI fellows lead their own research groups and organize joint activities.

EMMI is strongly committed to fostering the education and training of young researchers through a postdoctoral research program and training of graduate students. Structured PhD education for students within the Alliance is offered in close collaboration with the various Graduate Schools at the partner institutions, for example with the Helmholtz Graduate School for Hadron and Ion Research (HGS-HIRe), the Heidelberg Graduate School of Fundamental Physics (HGSFP) and the Helmholtz Research School Quark Matter Studies (H-QM). Many of the students in the Alliance have participated in various events (lecture weeks of HGS-HIRe, H-QM and HGSFP, graduate days of the HGSFP etc.) of these Graduate Schools in 2011.

An important activity of the ExtreMe Matter Institute EMMI is to organize and to host workshops and research programs on topical and interdisciplinary subjects in the area of matter under extreme conditions. 8 EMMI Workshops and one three-week EMMI Program with strong international participation took place in 2011. In November 2011, the EMMI Physics Days were organized at GSI in which 120 EMMI members participated. In December

2011, the first EMMI Rapid Reaction Task Force was organized and addressed the problem of thermalization in heavy ion collisions. The Rapid Reaction Task Forces are a new instrument which allows EMMI to gather a group of 15 to 20 world experts in order to address a particular scientific question in intense discussion. These meetings can be organized on a short timescale in order to react quickly to current and emerging questions.

Several renowned experts have visited EMMI partner institutions for extended periods in 2010 as EMMI Visiting Professor, and have made progress in their collaborations with EMMI members.

In March 2011 EMMI has moved to the new office building at GSI. The building offers a lecture hall and four seminar rooms and provides a unique infrastructure for the activities of EMMI, in particular for workshops and programs.

In March 2011, as the first event organized in the new building, the Midterm Review of the ExtreMe Matter Institute and of the Helmholtz Alliance 'Cosmic Matter in the Laboratory' took place. It was conducted by a high-profile review committee in collaboration with the Helmholtz Association. More than 200 EMMI scientists from all participating institutions were present during the review. The review committee gave a very positive evaluation and strongly recommended to continue the activities of EMMI on a long-term basis.

For two weeks in August and September 2011, EMMI hosted the LHC exhibition 'Weltmaschine' in the new building. The exhibition explained to the general public, with the help of genuine samples, how physicists investigate the fundamental questions about the Universe at the LHC. Pictures and displays showed the construction and functionality of the LHC. Physicists working at the LHC were present during the exhibition and answered the many questions raised by the visitors. Public lectures on the weekends informed the visitors about the current questions in elementary particle physics and cosmology. In total, the exhibition had more than 4500 visitors.

On November 23, 2011, EMMI participated in the nationwide 'Tag der Weltmaschine', marking two years of particle collisions at the LHC. EMMI offered a public evening lecture and a video transmission of an interview with the CERN Director General, followed by ample opportunity to ask questions.

In 2011 the research within EMMI resulted in more than 250 publications in refereed journals. Many important results are described in various contributions to the GSI Scientific Report 2011.

Excellent year for HIC for FAIR

B. Bäuchle[*]*, M. Bleicher, and G. Meyer*
Helmholtz International Center for FAIR, Max-von-Laue-Straße 1, 60438 Frankfurt am Main, Germany

After a successful evaluation in March 2011, the Helmholtz International Center for FAIR (HIC for FAIR) has been granted prolongation of the center for another three years. Thus, the ambitious research activities for FAIR conducted at the Universities of Frankfurt, Darmstadt and Gießen, the Frankfurt Institute for Advanced Studies (FIAS) together with the partners GSI, and the Helmholtz Association continue. Total support by the LOEWE program initiated by the state of Hesse amounts to 19.4 million Euro for the second funding period.

Ground-breaking research for FAIR

HIC for FAIR has been founded in 2008 in the first call of the Hessian LOEWE initiative (Landes-Offensive zur Entwicklung Wissenschaftlich-ökonomischer Exzellenz). The Universities of Frankfurt, Darmstadt and Gießen, the Frankfurt Institute for Advanced Studies (FIAS), GSI, and the Helmholtz Association have bundled their resources and research activities to foster FAIR-related research in Hesse. HIC for FAIR covers all four research pillars of FAIR including especially PANDA, CBM, nuclear astrophysics (NuSTAR), APPA and accelerator physics. Expertise and funding is provided for the development of the various experiments, theoretical investigations and large-scale computing via LOEWE-CSC (Center for Scientific Computing).

[*] baeuchle@fias.uni-frankfurt.de

LOEWE professorships, Helmholtz Young Investigators and young scientists

The hiring of faculty members at the HIC for FAIR partner institutions is nearly completed: 13 W2/Fellow- and seven W3-positions out of 26 have been filled. HIC for FAIR is actively promoting young scientists. Out of nine W1/Junior Fellow positions, five have been filled. In addition, three Helmholtz Young Investigator (HYI) groups have succeeded in a competitive selection procedure of the Helmholtz Association and will join HIC for FAIR in 2012.

In 2011, the number of doctoral students working in HIC for FAIR has increased to nearly 200 young scientists coming from 30 different nations.

International visibility

More than 30 international conferences and workshops have been (co-)funded and organized by HIC for FAIR scientists. More than 150 visiting scientists from all over the world have contributed to the scientific program at HIC for FAIR.

Acknowledgements

HIC for FAIR thanks all its partners for continuing support and a lively and fruitful collaboration. HIC for FAIR is supported by the Hessisches Ministerium für Wissenschaft und Kunst, EMMI, F+E, GSI and the Helmholtz Association.

Figure: Prof. Kester (on the right, HIC for FAIR, Univ. Frankfurt, head of the accelerator division at GSI) discussing with the reviewers sitting in the front row (left: Prof. Harris, Yale Univ.; right: Prof. Lippert, Jülich). MC in the left background: Prof. Bleicher. Photo: © Uwe Dettmar, Frankfurt am Main.

HGS-HIRe and H-QM*

H. Büsching[1], G. Burau[2], and S. Vogel[2]

[1]IKF, Goethe-Universität Frankfurt am Main, Germany; [2]FIAS, Frankfurt am Main, Germany

The Helmholtz Graduate School for Hadron and Ion Research (HGS-HIRe for FAIR), established in October 2008 as a joint endeavor of the GSI Helmholtzzentrum für Schwerionenforschung and the universities at Darmstadt, Frankfurt, Giessen, Heidelberg and Mainz together with FIAS, looks back on a successful third year of operation. Established to provide a common platform for structured doctoral education in the scientific fields of hadron and ion research, HGS-HIRe is attracting an increasing number of participating students who perform their research projects in these fields at GSI and the other partner institutions. More than 270 doctoral students are participating in the program of HGS-HIRe by the end of 2011. Nearly 30% of the participants have an international background. 19 participants of HGS-HIRe graduated in 2011.

The increasing number of participants in 2011 allowed for a consequent strengthening of the education program. In addition the Helmholtz Research School for Quark Matter Studies (H-QM) is more and more integrated in the structure of HGS-HIRe. H-QM is a joint project of the GSI Helmholtzzentrum, Goethe-Universität Frankfurt and FIAS to specially support a selected group of outstanding students performing research in the field of theoretical and experimental heavy-ion physics. Both, H-QM and HGS-HIRe are supported by the Initiative and Networking Fund of the Helmholtz Association.

Within the education program of HGS-HIRe and H-QM, numerous events on various topics have been organized in 2011: Scientific skills have been addressed by five lecture weeks (hot and dense nuclear matter studies, nuclear structure, accelerator physics, atomic physics) and three power weeks (data analysis methods, statistics, AdS/CFT). In particular the lecture weeks on nuclear structure and atomic physics have been strongly supported by scientists from GSI who were actively involved as lecturers. A total of ten soft skill seminars have been devoted to the training of the students in transferable skills. With the latter HGS-HIRe is breaking new ground and has developed, together with experienced trainers from the UK, an integrated series of three courses focusing on various transferable skills, combining different aspects of professional and personal development. Additionally, the HGS-HIRe Perspectives events were introduced to facilitate the career planning of the students after finishing the PhD. Offered in 2011 on a regular basis, these events have been established as integral part of the program.

Last but not least three special events have been organized by HGS-HIRe in 2011:
The first joint Helmholtz-Rosatom School took place in Hirschegg (Austria) in February 2011. Participants of HGS-HIRe as well as scientist from GSI/FAIR (among others Prof. Stöcker and Prof. Sharkov) and fellows of the FAIR Russia Research Centre in Moscow came together to discuss and learn about various aspects of the new FAIR accelerator complex.
During the summer months of 2011 HGS-HIRe and GSI organized an international Summer Student Program which is offered to undergraduate students in physics or related natural science disciplines. 41 students from 14 countries, mostly from Europe but also from GSI/FAIR partner countries in Asia and South America took part in this year's program. Each participant joined one of the GSI research groups and worked on a small project during the program. In addition a dedicated lecture series - given by GSI scientists and complemented by an introductory HGS-HIRe soft skill program - was held introducing the various research fields at GSI.
The second HGS-HIRe Graduate Days were held in Königstein/Taunus in October 2011. Nearly 200 participants and members of HGS-HIRe - many of them associated to GSI - joined this central event. Over the course of two days participants reported on their projects, experienced researchers gave overview talks and the HGS-HIRe Excellence Awards 2011 have been granted to Matthias Lochmann (Mainz) and Niels Strodthoff (Darmstadt).

Other pillars of the HGS-HIRe program were further strengthened. The individual PhD committees, which meet every six month to discuss the current status and future plans of the doctoral project, have been integrated further. The HGS-HIRe Scientific Travel Program for participants with the optional inclusion of long term stays at institutes abroad, i.e. the HGS-HIRe Abroad program, has been further developed. Within this program participants can file a research proposal for a research stay abroad for a period of one to three months to facilitate their thesis project. A limited number of HGS-HIRe Abroad grants has been awarded in a competitive process several times per year.

In addition, HGS-HIRe and H-QM have been involved in a couple of public outreach activities:
The first International Masterclass at GSI was conducted in cooperation with scientists from GSI and doctoral students of HGS-HIRe. International Masterclasses are organized in the framework of the European Particle Physics Outreach Group and the Initiative 'Netzwerk-Teilchenphysik' of the German BMBF.

* supported by the Helmholtz Association
#info@hgs-hire.de

Furthermore, HGS-HIRe is actively involved in an outreach program for elementary school kids with HGS-HIRe participants visiting elementary schools to talk about what it is like 'to be a scientist' (organized in cooperation with 'Polytechnische Gesellschaft' in Frankfurt).
Last but not least the 'Tag der Weltmaschine' - an event including presentations at the partner institutions of HGS-HIRe and a small exhibition for the general public at Goethe-Universität Frankfurt featuring the physics, the experiments and the technological challenges of the Large Hadron Collider LHC at CERN - has been organized in cooperation with scientists from GSI, EMMI and HIC for FAIR in November 2011.

The second year of physics and data taking with the ALICE experiment at the LHC

*The ALICE Collaboration**

The activities of the GSI/EMMI ALICE group in 2011 were mainly focussed on two issues. One is the analysis of the first data from Pb–Pb collisions at $\sqrt{s_{NN}} = 2.76$ TeV which were taken at the end of 2010 at the CERN LHC accelerator. The second is the preparation for the second Pb–Pb run which took place in November/December 2011 and the analysis of the data that were taken during this run. In addition, the analysis of pp data taken at $\sqrt{s} = 7$ TeV in 2010 and 2011 as well as at $\sqrt{s} = 2.76$ TeV in 2011 was continued, with interesting physics results and, in particular, also providing a reference for the Pb–Pb physics. The GSI/EMMI ALICE group, together with colleagues at surrounding universities, played a crucial role in the operation and calibration of the TPC as well as of TRD data.

A number of important physics topics were addressed, with particular emphasis on the following measurements:

1. nuclear modification factor of unidentified charged particles in Pb–Pb collisions, extending the reach in transverse momentum to 50 GeV/c.
2. higher harmonics in the anisotropic flow of charged particles in Pb–Pb collisions.
3. J/ψ production cross section and its dependence on multiplicity in pp collisions; the nuclear modification factor of J/ψ production in Pb–Pb collisions.
4. production of antinuclei and hypernuclei in Pb–Pb collisions.
5. Hanbury Brown Twiss (Bose-Einstein) correlations in Pb–Pb collisions.
6. identified charged particle transverse momentum spectra in pp and Pb–Pb collisions.
7. π^0- and η-meson production in pp and Pb-Pb collisions via conversion electron measurements.
8. open charm production in pp and Pb–Pb collisions via the measurement of hadronic decays.
9. open charm and open beauty production in pp and Pb–Pb collisions via the measurement of semi-electronic decays.
10. low mass electron-positron continuum and low mass vector mesons in pp and Pb–Pb collisions.

*Work supported by GSI, BMBF, and the Helmholtz Alliance HA216/EMMI. The list of ALICE members and institutions is available at `http://aliweb.cern.ch/General/Members/List_Institutes.html`

Final results from most of these analyses have been published in refereed journals or are in the process of beeing published. Preliminary results have been presented at conferences and published as proceedings. A selection of results can be found in separate contributions to this report.

The preparation of the 2011 Pb–Pb run with ALICE at the LHC was of particular importance. The Pb–Pb luminosity delivered by the LHC improved drastically from 2010 to 2011, *i.e.* the hadronic collision rate was increased from 150-200 Hz in 2010 to 3-4 kHz in the 2011 run. In order to cope with the resulting increase in data rate ALICE had to be operated in a different mode in 2011 compared to 2010. First, a complex trigger scheme had to be put in place. Second, the data delivered by the TPC had to be compressed online in the ALICE HLT compute cluster. The GSI/EMMI group played a crucial role in the validation of this approach in which a compression factor of four was achieved. The number of most central Pb-Pb collisions could be increased from $\sim$ 2 million recorded in 2010 to $\sim$ 30 million in the 2011 run.

In addition to the tasks related to the operation of the experiment, calibration of detectors, data reconstruction and physics analysis, the GSI/EMMI ALICE group, together with GSI-IT, is responsible for the operation of the ALICE Tier2/3 computing center at GSI, where an analysis platform is provided to all ALICE members in Germany.

In the following, the performance of the TPC and TRD detectors is illustrated with a few selected results.

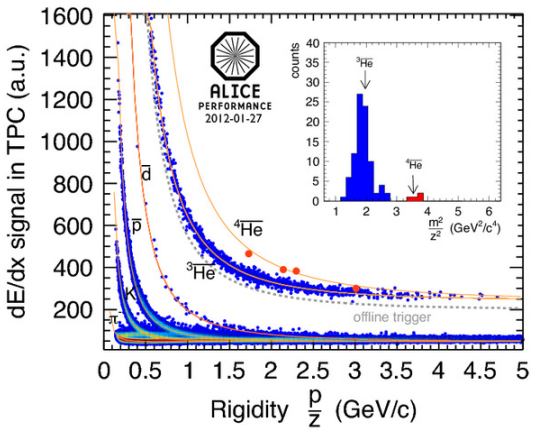

Figure 1: TPC signal vs. rigidity for Pb-Pb events with at least one particle with charge $|z| \geq 2$. Only negatively charged particles are shown.

The unique TPC particle identification capability is il-

lustrated in Fig. 1, where we show the energy loss of negatively charged particles in the TPC, dE/dx, vs. rigidity for all Pb-Pb events with at least one track with charge $|z| \geq 2$. The four anti-α candidates found in 16 million Pb-Pb events are indicated in red. The insert shows the combined mass measurement with the TOF system which is in particular needed to separate the $\bar{\alpha}$ candidate with the largest momentum from the $^3\bar{H}e$ particles. The power of the TPC particle identification, alongside that of other ALICE subsystems, is crucial for the study of several observables, like the nuclear modification factor and flow for identified particles, while (anti-)matter and exotic light (anti-)nuclei production in Pb-Pb collisions at the LHC remains as well in our focus.

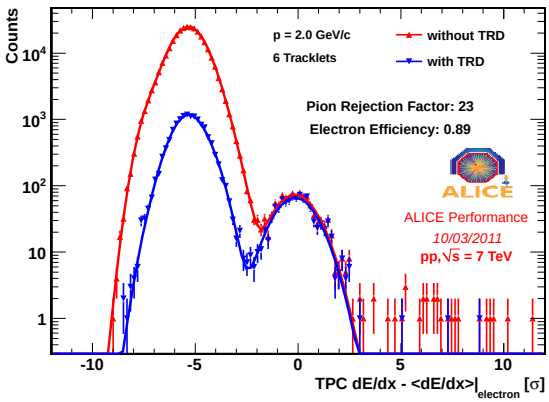

Figure 2: TPC dE/dx signal (in units of resolution) relative to the electron Bethe-Bloch line, with and without electron tagging in the TRD.

In Fig. 2 we show the distribution of the TPC signal relative to the electron Bethe-Bloch line for 2 GeV/c tracks, with and without electron tagging in the TRD. Obtained for pp collisions at 7 TeV, this result demonstrates, for tracks with 6 TRD tracklets, a TRD pion rejection factor of 23 for 90% electron efficiency, obtained with a likelihood method employing the integral charge deposit in a TRD chamber. Ongoing studies show that a bidimensional likelihood exploiting the position information in the TRD via computing the detector signal in 2 spatial regions leads to the design rejection factor of 100. The present TRD electron identification capability is already instrumental in physics results. For instance, in the measurement of electrons from the decay of hadrons carrying charm or beauty quarks in pp collisions the TRD allows to extend the transverse momentum range up to 10 GeV/c (while the combination of TPC and TOF would allow for a clean electron identification only up to $\sim$4 GeV/c).

Another demonstration of the crucial role the TRD plays for electron identification, this time in central (0-40%) Pb-Pb collisions, is given in Fig. 3. We show the invariant mass of electron-positron pairs selected using either the TPC alone or, in addition, the TRD to identify electrons and

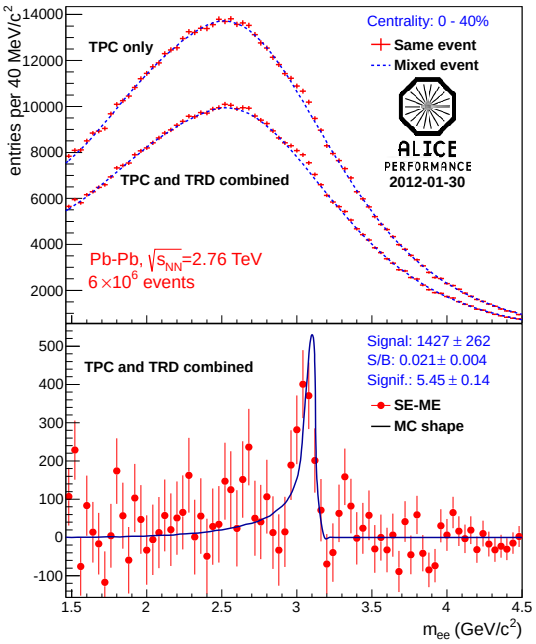

Figure 3: Invariant mass of electron-positron pairs selected with TPC and TRD for central Pb-Pb collisions.

positrons. While, thanks to the good TPC electron identification, the J/ψ signal is already visible without the TRD, it is improved when employing the TRD to suppress hadrons. Only 7 out of 18 TRD supermodules were installed in year 2010 when the data shown in Fig. 3 were taken, but with the 10 supermodules available in 2011 (and another 3 which have just been installed) the efficiency of TRD is sizably improved. Employing the TRD for triggering is a major goal for the upcoming data taking in the year 2012.

The second year of physics with ALICE at the LHC has produced many exciting new results. Publications in refereed journals are listed below for reference.

References

[1] K. Aamodt *et al.* (ALICE Collaboration), Phys. Lett. B 696 (2011) 30.

[2] K. Aamodt *et al.* (ALICE Collaboration), Phys. Rev. Lett. 106 (2011) 032301.

[3] K. Aamodt *et al.* (ALICE Collaboration), Eur. Phys. Jour. C 71 (2010) 1594.

[4] K. Aamodt *et al.* (ALICE Collaboration), Phys. Lett. B 696 (2011) 328.

[5] K. Aamodt *et al.* (ALICE Collaboration), Eur. Phys. Jour. C 71 (2010) 1655.

[6] K. Aamodt *et al.* (ALICE Collaboration), Phys. Lett. B 704 (2011) 442.

Suppression of High Transverse Momentum Particles in Pb–Pb Collisions at $\sqrt{s_{NN}}$ = 2.76 TeV in ALICE

P. Lüttig[1], *H. Appelshäuser*[1], *H. Büsching*[1], *M. Ivanov*[2], *M. Knichel*[2], *J. Otwinowski*[2]
for the ALICE Collaboration
[1]Institut für Kernphysik, Goethe University, Frankfurt; [2]GSI, Darmstadt

In 2010, the ALICE experiment at the CERN-LHC has measured the first heavy ion collisions at a center-of-mass energy of $\sqrt{s_{NN}} = 2.76$ TeV, an energy which has never been measured before. Here we report on the production of charged particles as a function of the transverse momentum (p_T). The particle yield in nucleus-nucleus collisions is compared to the scaled particle yield in nucleon-nucleon (pp) collisions in terms of the nuclear modification factor R_{AA}:

$$R_{AA}(p_T) = \frac{\left(1/N_{evt}^{AA}\right) d^2N_{ch}^{AA}/d\eta dp_T}{\langle N_{coll}\rangle \left(1/N_{evt}^{pp}\right) d^2N_{ch}^{pp}/d\eta dp_T} \quad (1)$$

where $\langle N_{coll}\rangle$ denotes the average number of superpositioned independent nucleus-nucleus collisions. In the absence of nuclear modification R_{AA} will reach unity at high p_T.
Details of the analysis as well as the determination of the centrality of the collisions have been published in [1] [2].

For the determination of R_{AA} a well described pp baseline at the same center-of-mass energy is needed. A total of 50.5 $\cdot 10^6$ minimum-bias nucleon-nucleon collisions at $\sqrt{s} = 2.76$ TeV has been recorded and analyzed in 2011 and is used to construct a reference.
The pp yield has been parametrized with a so-called Hagedorn function to extrapolate it to hight p_T ($p_T = 50$ GeV/c):

$$\frac{1}{2\pi p_T}\frac{d^2N_{\rm ch}}{d\eta dp_T} = A\frac{p_T}{m_T}\left(1+\frac{p_T}{p_{T,0}}\right)^{-n} \quad (2)$$

m_T denotes the transverse mass $m_T = \sqrt{m_\pi^2 + p_T^2}$, where the pion mass has been assumed for all tracks.
The final reference is constructed from the measured data points up to $p_T = 5$ GeV/c and the extrapolation from the parametrization.
To check the quality of the reference it can be compared to references constructed using alternative methods.
A p_T spectrum simulated with Pythia8 agrees well with our reference for $p_T > 1$ GeV/c, while the reference constructed by the CMS collaboration agrees only for $p_T > 15$ GeV/c.

Figure 1 shows the nuclear modification factor for three different centrality selections, the most central collisions (0 - 5%), a semi-central class (20 - 40%) and a semi-peripheral (40 - 80%) class. The suppression is highest for the most central collisions and reaches a factor seven for $p_T = 6 - 7$ GeV/c. It decreases for more peripheral collisions. A strong p_T dependence for the most central collisions is observed, which seems to flatten out for more peripheral collisions and for $p_T > 30$ GeV/c. The boxes at unity show the systematic uncertainty on the determination of the average number of collisions $\langle N_{coll}\rangle$.

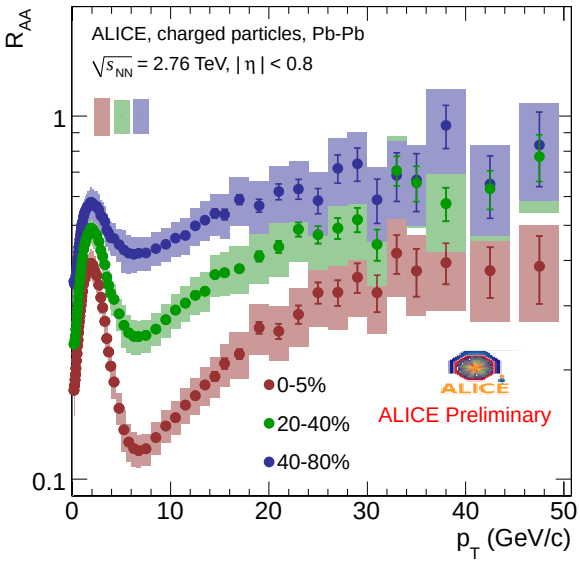

Figure 1: R_{AA} of charged particles measured with ALICE in central Pb−Pb collisions in three centrality intervals.

A suppression of high p_T particles has been observed by the RHIC experiments in Au–Au collisions at $\sqrt{s_{NN}} = 200$ GeV before. A similar p_T dependence has been measured, but the suppression is less strong at RHIC and a rise with p_T was not evident.
The Pb–Pb collisions measured in fall 2011 will increase the transverse momentum range and ongoing studies of the detectors involved will increase the momentum resolution at high p_T.

Work supported by H-QM, HGS-HIRe, GSI, BMBF, and Helmholtz Alliance HA216/EMMI.

References

[1] K. Aamodt [ALICE Collaboration], Phys. Rev. Lett. 105 (2010) 252301, Phys. Rev. Lett. 106, (2011) 032301.

[2] K. Aamodt [ALICE Collaboration], Phys. Lett. B 696, (2011) 30.

High p_{T} suppression of Λ and $\mathrm{K}^0_{\mathrm{s}}$ in Pb–Pb collisions at $\sqrt{s_{\mathrm{NN}}} = 2.76$ TeV with ALICE*

S. Schuchmann and the ALICE collaboration[1]

[1]Goethe-University Frankfurt, Institut für Kernphysik, Germany

The investigation of transverse momentum spectra of identified particles is not only important for the studies of hadro-chemistry, i.e. particle ratios at freeze-out, but also for the examination of parton energy loss in the medium. In particular, identified baryon and meson spectra at high p_{T} may allow to disentangle differences between the energy loss of quarks and gluons. This energy loss before hadronization is believed to lead to a suppression of high transverse momentum (p_{T}) hadrons in AA collisions relative to pp. The nuclear modification of particle production is commonly expressed in terms of the so-called nuclear modification factor R_{AA}[1]:

$$R_{\mathrm{AA}} = \frac{1}{\langle N_{\mathrm{bin}} \rangle} \cdot \frac{(\mathrm{d}N/\mathrm{d}p_{\mathrm{T}})_{\mathrm{AA}}}{(\mathrm{d}N/\mathrm{d}p_{\mathrm{T}})_{\mathrm{pp}}} \qquad (1)$$

$\langle N_{\mathrm{bin}} \rangle$: number of binary NN collisions in AA collisions. In this article, we address the question if the Λ baryon and the $\mathrm{K}^0_{\mathrm{s}}$ meson show different modification patterns at high p_{T} which may help to shed light on the underlying energy loss mechanism.

The Λ and $\mathrm{K}^0_{\mathrm{s}}$ are reconstructed employing a topological secondary vertex finder using tracking information from the Time Projection Chamber and the Inner Tracking System of the ALICE experiment. Further details about the analysis and the corrections can be found in [2]. The following results are extracted from two centrality classes in Pb–Pb collisions (0 – 5%, 60 – 80%) at $\sqrt{s_{\mathrm{NN}}} = 2.76$ TeV and from the corresponding pp reference data at $\sqrt{s} = 2.76$ TeV.

In figure 1 the R_{AA} of Λ and $\mathrm{K}^0_{\mathrm{s}}$ are shown together with the R_{AA} of charged particles [3] in peripheral and central collisions, respectively. As seen with the charged particles above $p_{\mathrm{T}} = 7$ GeV/c, the suppression of $\mathrm{K}^0_{\mathrm{s}}$ in peripheral events with respect to pp collisions (upper panel) is similar. While the $\mathrm{K}^0_{\mathrm{s}}$ R_{AA} remains rather constant with p_{T} at a moderate suppression of $R_{\mathrm{AA}} \approx 0.6$, the Λ shows little nuclear modification at $p_{\mathrm{T}} = 2 - 5$ GeV/c, $R_{\mathrm{AA}} \approx 1$, which is decreasing with p_{T} and finally approaching the suppression level of $\mathrm{K}^0_{\mathrm{s}}$ as well as that of the charged particles at high p_{T}. In the lower panel in figure 1 the Λ- and $\mathrm{K}^0_{\mathrm{s}}$-$R_{\mathrm{AA}}$ for central events reveal a strong suppression at high p_{T} for both hadrons which again is similar to the modification of charged particles. This particle-type independence of the nuclear modification suggests that the ernergy loss happens on a partonic level and that the difference between light quarks and gluons is small. Regarding the low-to-intermediate p_{T} region, we observe an enhancement of Λ-

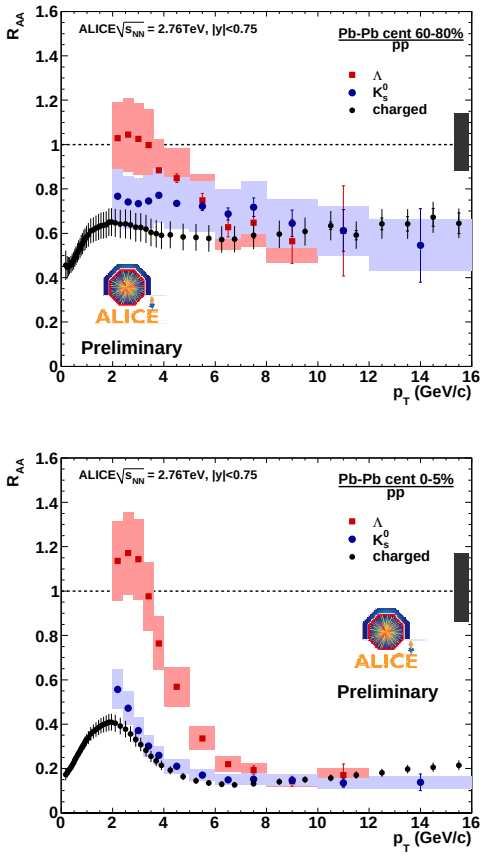

Figure 1: R_{AA} of $\mathrm{K}^0_{\mathrm{s}}$ and Λ for peripheral (upper panel) and for central (lower panel) collisions. The boxes around the data points and the vertical error bars of the charged particles R_{AA} [3] show the systematic uncertainties.

R_{AA} over the $\mathrm{K}^0_{\mathrm{s}}$-$R_{\mathrm{AA}}$ which can be interpreted in terms of a baryon-to-meson anomaly [4]. The impact of these results will be further investigated and compared to model calculations.

References

[1] Majumder A and Van Leeuwen M 2010 *Preprint* arXiv:hep-ph/1002.2206.

[2] S. Schuchmann [ALICE Collaboration], J. Phys. G: Nucl. Part. Phys. 38 (2011) 124080.

[3] J. Otwinowski [ALICE Collaboration], J. Phys. G: Nucl. Part. Phys. 38 (2011) 124112.

[4] I. Belikov [ALICE Collaboration], J. Phys. G: Nucl. Part. Phys. 38 (2011) 124078.

* Work supported by BMBF, Helmholtz Association and GSI

A study of jet fragmentation properties in proton-proton collisions at $\sqrt{s}$ = 7 TeV with ALICE at the LHC*

H. León Vargas[1], *C. Blume*[1], *and C. Klein-Bösing*[2] *for the ALICE Collaboration*

[1]IKF, University of Frankfurt, Germany; [2]Institut für Kernphysik Münster, Germany

Introduction

In this report we present the preliminary results of a study of charged jet properties as a function of the associated event multiplicity. The data used to produce the figures of this report is from Pythia6 and Phojet, including the full detector simulation of the ALICE experiment. Charged jets are those found by the jet finding algorithms using as input charged tracks. The multiplicity estimator was developed such that it quantifies the global soft event characteristics. The observable used to characterize the charged jets is *NT90*, which was introduced in a previous report [1].

Multiplicity estimator

The multiplicity estimator is based on the track multiplicity measured in the ALICE TPC. In order to minimize the influence of the jet fragmentation in the multiplicity estimator the event geometry is separated into two regions in the $\eta - \phi$ space ($\eta = -\ln[\tan(\theta/2)]$). One region contains mainly the jet activity and is defined by the jet finder output. The region that contains the jet activity is extended such that the di-jet activity is also taken into account. The region of the acceptance that remains after subtracting from the total acceptance these regions is used to estimate the associated event multiplicity.

In order to further separate the jet properties from the multiplicity estimator, a transverse momentum gap between the tracks used in the observable measurement ($p_{\mathrm{T}}^{\mathrm{Track}} > 1$ GeV/c) and the tracks used for the multiplicity estimation (150 MeV/c $< p_{\mathrm{T}}^{\mathrm{Track}} <$ 900 MeV/c) is introduced.

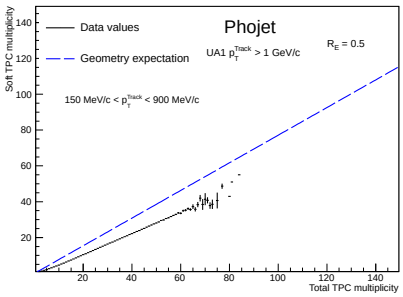

Figure 1: Distribution of the mean values of the associated event multiplicity as a function of the total multiplicity.

Figure 1 shows the distribution of the mean values of the multiplicity measured in the region without jet activity (soft TPC multiplicity) as a function of the total number of charged tracks within the range 150 MeV/c $< p_{\mathrm{T}}^{\mathrm{Track}} <$ 900 MeV/c measured in the whole acceptance. The dashed line in plot shows the result that would be expected in the case that the exclusion regions produce a trivial decrease in the multiplicity due to geometrical exclusion.

Results

Figure 2 shows the distribution of *NT90* as a function of the normalized soft TPC multiplicity. The soft TPC multiplicity was separated into 6 multiplicity ranges (1-5, 5-10, 10-15, 15-20, 20-30 and $\geq$ 30 tracks). The mean value in each multiplicity range $\langle \mathrm{TPC}_{\mathrm{Soft}}^{\mathrm{Bin}} \rangle$ was normalized to the global mean multiplicity $\langle \mathrm{TPC}_{\mathrm{Soft}}^{\mathrm{Total}} \rangle$ of each data sample. The data points were parametrized using the function $\langle NT90 \rangle = m \ln \frac{\langle \mathrm{V0}_{\mathrm{Soft}}^{\mathrm{Bin}} \rangle}{\langle \mathrm{V0}_{\mathrm{Soft}}^{\mathrm{Total}} \rangle} + b$.

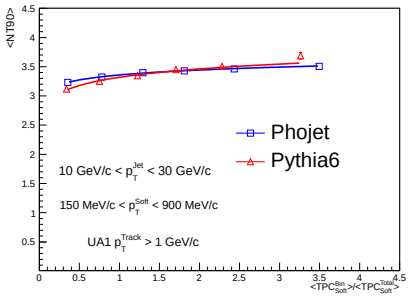

Figure 2: Experimental results and the predictions from Pythia6 and Phojet for $\langle NT90 \rangle$ as a function of the normalized soft TPC multiplicity.

The parametrization of the dependency of $\langle NT90 \rangle$ on the normalized multiplicity shows that Phojet and Pythia6 predict a different dependence of the observable on the normalized soft TPC multiplicity. The value of the slope for Phojet is $m = 0.123 \pm 0.004$ and for Pythia $m = 0.205 \pm 0.007$. Both Monte Carlo models show a dependence of the observable on the associated soft TPC multiplicity. This could be related to the fact that the underlying event model used by both Phojet [2] and Pythia6 [3] is based on multiple parton interactions.

References

[1] H. León Vargas, C. Blume and C. Klein-Bösing, *GSI SCIENTIFIC REPORT PHN-NQM-ALICE-04* (2010).

[2] The ALICE Collaboration, *arXiv:1112.2082v2 [hep-ex]* (2011).

[3] CDF Collaboration, *Phys. Rev. D* **65** (2002) 092002.

* Supported by HGS-HIRe, H-QM, GSI, BMBF, and Helmholtz Alliance HA216/EMMI.

Sources of Event Background Fluctuations for Jet Reconstruction in Pb-Pb Collisions at the LHC *

C. Klein-Bösing[†1,2], *J. Anielski*[1], *B. Bathen*[1], *O. Busch*[3], *L. Cunqueiro*[4], *T. Dietel*[1], *D. Emschermann*[1], *L. Feldkamp*[1], *M. Heide*[1], *A. Passfeld*[1], *H. Poppenborg*[1], *E. Sicking*[1], *M. Wilde*[1], *J. P. Wessels*[1], *M. Verweij*[5], *U. Westerhoff*[1], *and M. Zimmermann*[1] *for the ALICE Collaboration*

[1]Institut für Kernphysik, University of Münster, Germany; [2]ExtreMe Matter Institute EMMI, GSI Darmstadt, Germany; [3]Physikalisches Institut, University of Heidelberg, Germany; [4]INFN, Frascati, Italy; [5]Institute for Subatomic Physics, Utrecht University, Netherlands

The reconstruction of jets in elementary pp-collisions provides the most direct access to the properties of hard scattered (large momentum transfer Q^2) partons. In heavy-ion collisions the initial hard parton scattering, occurs before the formation of a thermalized medium ($t \approx 1/Q \ll 1\,\mathrm{fm}/c$) and the modification of the jet fragmentation process compared to the QCD vacuum potentially allows to map out the properties of the QCD-medium. However, in heavy-ion collisions the reconstruction of full jets is complicated by the background from the underlying event and its fluctuations not associated with the hard scattering.

For data collected by the ALICE-experiment during the first Pb–Pb run of the LHC, jets have been reconstructed based on charged particle tracks measured with the central barrel Inner Tracking System and Time Projection Chamber. For jets in the 10% most central collisions with distance parameter of $R = 0.4$ and momentum cut-off $p_{\mathrm{t}}^{\mathrm{min}} = 0.15\,\mathrm{GeV}/c$ the typical background contribution to the reconstructed transverse momentum is about 70 GeV/c. In practice the jet p_{t} is corrected for the background p_{t}-density ρ in each event using the jet area $A^{\mathrm{jet,rec}}$ with $p_{\mathrm{t}}^{\mathrm{jet}} = p_{\mathrm{t}}^{\mathrm{jet,rec}} - \rho \cdot A^{\mathrm{jet,rec}}$ [1]. After this correction region-to-region background fluctuations are the main source of jet momentum uncertainty. They can have a large impact on jet structure observable and will e.g. distort the measured jet energy balance even in the absence of medium effects [2].

To study different sources of background fluctuations in an unbiased fashion a single cone with radius $R = 0.4$ is placed in each reconstructed event at random ϕ and η. The background fluctuations are characterized by calculating the difference of the scalar sum of all track p_{t} in the cone and the expected background: $\delta p_{\mathrm{t}} = \sum_i p_{\mathrm{t,i}} - A \cdot \rho$, where $A = \pi R^2$. The resulting distributions are centered at zero with standard deviation $\sigma(\delta p_{\mathrm{t}})$ shown in Fig. 1 for three variations of the random cone method: (i) sampling of measured Pb–Pb events, (ii) sampling of measured Pb–Pb events, but requiring a distance $D = 1.0$ to the axis of the leading jet, and (iii) sampling of Pb–Pb events in which the (η,ϕ) direction of the tracks has been randomized within the acceptance, which destroys all correlations in the event. The width of the δp_{t} distribution due to purely random fluctuations can be estimated from the expected number of tracks in the cone area N_A and the measured single particle spectrum via its average p_{t} and standard deviation $\sigma(p_{\mathrm{t}})$. Local variations of the average multiplicity, $\langle p_{\mathrm{t}} \rangle$, or $\sigma(p_{\mathrm{t}})$, lead to additional fluctuations. These region-to-region variations can be induced e.g. by (mini-)jets, where the particle p_{t} spectrum is considerably harder than for the global event average, and by collective flow. Uncorrelated non-Poissonian (NP) fluctuations can be added knowing their standard deviation, e.g. for additional region-to-region variation of the average multiplicity:

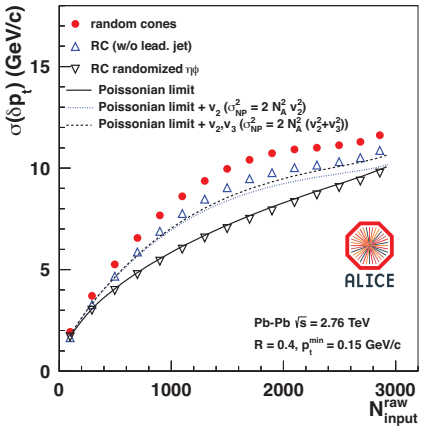

Figure 1: Multiplicity dependence of charged particle background fluctuations in Pb–Pb collisions.

$$\sigma(\delta p_{\mathrm{t}}) = \sqrt{N_{\mathrm{A}} \cdot \sigma^2(p_{\mathrm{t}}) + (N_{\mathrm{A}} + \sigma^2_{\mathrm{NP}}(N_{\mathrm{A}})) \cdot \langle p_{\mathrm{t}} \rangle^2}. \quad (1)$$

The multiplicity dependence of purely statistical fluctuations well describes the randomized events in Fig. 1, while the inclusion of elliptic and triangular flow induced multiplicity fluctuations accounts for the deviation from the $\sqrt{N}$ increase. Using Eq. 1 the background induced fluctuations for jet reconstruction can be estimated based on few experimental observables.

References

[1] Cacciari and G. P. Salam. *Phys. Lett.*, B659:119–126, 2008.

[2] M. Cacciari, G. P. Salam, and G. Soyez. *Eur. Phys. J.*, C71:1692, 2011.

*Work supported by GSI, BMBF, and Helmholtz Alliance HA216/EMMI.

† Christian.Klein-Boesing@uni-muenster.de

Three-Particle Correlations With an Intermediate or High-p_T Trigger Particle*

J.G. Ulery† *for the ALICE Collaboration*
Institut für Kernphysik, Goethe Universität, Frankfurt, Germany

Introduction

The Large Hadron Collider has collided lead ions at energies up to 2.76 TeV per nucleon pair in the ALICE detectors. These collisions produce a hot and dense matter, which may be a deconfined state of quarks and gluons called a Quark Gluon Plasma. This matter can be studied by examining correlations of particles with an intermediate or high-p_T trigger particle, which likely come from jets. These correlations can be used to study how the jet and medium produced in these collisions interact. Three-particle correlations provide us with different insights and systematics than two-particle correlations.

Analysis

This analysis has a complicated background structure and the background subtraction technique has been improved in the past year. One change is that the additional background that arises from the third flow harmonic has been incorporated and now the analysis subtracts contributions from the second, third and fourth harmonics. There has also been a change in how the two-particle correlations are subtracted from the three-particle correlations. This change has resulted in greatly reduced systematics in the flow measurements, which is essential due to the increased uncertainty from the additional flow harmonic.

The three-particle correlation before background subtraction contains two-particle correlations from jets and flow which are subtracted using a two-particle correlation and a normalized mixed event. Mixed event backgrounds are normalized assuming the background subtracted signal is zero at its minimum to correct for trigger bias. The three-particle flow correlation was calculated for this analysis and was subtracted using flow values measured by the ALICE flow group. Additionally a jet flow cross term, where two particles are jet-like correlated and the third particle is correlated from flow, is estimated and subtracted.

Results

A three-particle correlation is shown in Fig. 1 as a function of the azimuthal angle of the associated particles relative to the trigger particle. A near-side peak can be seen at (0,0) while the away-side displays predominately a four peak structure with peaks at $(\pi \pm 1.5, \pi \pm 1.5)$. This type of structure is what is expected from conical emission in three-particle correlations[1],[2] which could come from a Mach Cone shock wave[3] or Čerenkov emission of gluons[4].

A projection of the away-side along the $\delta\phi_1 + \delta\phi_2 = \pi$ axis is also shown. The systematic errors are shown by the grey band. The central peak should come from jet particles that do not deviate significantly in angle when passing through the medium. The two side peaks which are consistent with conical emission are systematically significant though the error band is large. There has been extensive study into the systematic errors in this analysis over the year. The dominant contributions to the systematic error are from different methods used to measure the flow and from the estimation of the flow correlation of two-particle jet-like correlated particles.

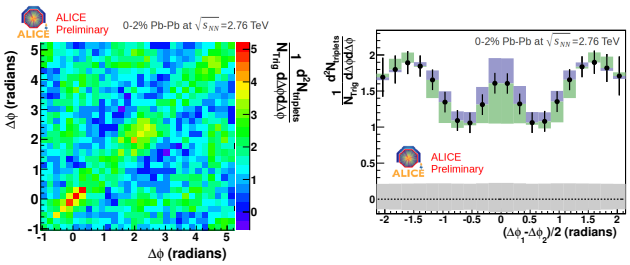

Figure 1: Three-particle correlation for $2.5 < p_T^{Trig} < 4$ GeV/c and $1 < p_T^{Assoc} < 2$ GeV/c in 0-2% most central Pb-Pb collisions at $\sqrt{s_{NN}} = 2.76$ TeV. Left panel shows the away-side projection along the $\Delta\phi_1 + \Delta\phi_2 = 2\pi$ axis.

Summary

In conclusion, a significant signal consistent with conical emission is seen in this analysis in Pb-Pb collisions at $\sqrt{s_{NN}} = 2.76$ TeV. Additional simulations and systematic checks still need to be completed. However, this analysis will soon be finalized.

References

[1] J.G. Ulery and F. Wang, *Analysis Method for Jet-Like Three-Particle Azimuthal Correlations*, *NIM* **A595** 502 (2008).

[2] T. Renk and J. Ruppert, *Mach Cones in an Evolving Medium*, *Phys. Rev.* **C73** 011901 (2006).

[3] J. Hofmann, H. Stöcker, U. Heinz, W. Scheid, and W. Greiner, *Possibility of Detecting Density Isomers in High Density Nuclear MACH Shock Waves*, *Phys. Rev. Lett.* **36** 88 (1976).

[4] I.M. Dremin, *Ring-like events: Cerenkov Gluons or Mach Waves?*, *Nucl. Phys.* **A767** 233 (2006).

* Supported by GSI, BMBF, and Helmholtz Alliance HA216/EMMI.
† ulery@ikf.uni-frankfurt.de

Measurement of J/ψ Production as a Function of Charged-Particle Multiplicity in $\sqrt{s} = 7$ TeV pp Collisions*

F. Kramer[1], *A. Andronic*[2], *I. Arsene*[2], *C. Blume*[1], *and the ALICE Collaboration*
[1]Goethe University, Frankfurt, Germany; [2]GSI, Darmstadt, Germany

The understanding of hadronic production mechanisms of quarkonia is subject of ongoing work (for a review see e.g. [1]) and still a challenge. So far models treat the corresponding hard process independently from the underlying event and disregard a possible effect of multiple partonic interactions [2]. Especially at LHC energies, there might be a correlation between the two [3]. Therefore, ALICE [4] investigated the dependence of J/ψ production on the charged-particle multiplicity for the first time [5].

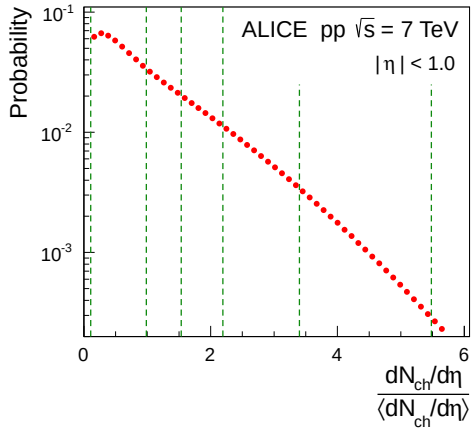

Figure 1: The distribution of the relative charged-particle density $(\mathrm{d}N_{\mathrm{ch}}/\mathrm{d}\eta)/\langle \mathrm{d}N_{\mathrm{ch}}/\mathrm{d}\eta \rangle$.

A total of $3.0 \cdot 10^8$ minimum bias pp events at $\sqrt{s} = 7$ TeV have been analyzed from the 2010 LHC running period. The number of tracklets in the SPD N_{trk} measured within the pseudorapidity range of $|\eta| < 1.0$, is used for the determination of the charged-particle multiplicity. Assuming a linear dependence of N_{ch} on N_{trk}, one can thus obtain the relative density of primary charged particles around mid-rapidity: $(\mathrm{d}N_{\mathrm{ch}}/\mathrm{d}\eta)/\langle \mathrm{d}N_{\mathrm{ch}}/\mathrm{d}\eta \rangle$. The distribution of the relative charged-particle density is shown in Fig. 1. Monte Carlo studies have been performed to verify that N_{trk} is proportional to $\mathrm{d}N_{\mathrm{ch}}/\mathrm{d}\eta$.

For the J/$\psi \rightarrow e^+e^-$ analysis, the same track selection criteria have been used as in [6]. Electrons are measured in $|\eta| < 0.9$. J/ψ are reconstructed in $|y| < 0.9$ down to $p_{\mathrm{t}} = 0$. The total sample of events has been divided in five multiplicity intervals, their boundaries are indicated by the vertical lines in Fig. 1. A separate invariant mass analysis has been performed in each interval.

Figure 2 shows the result of this analysis (red circles),

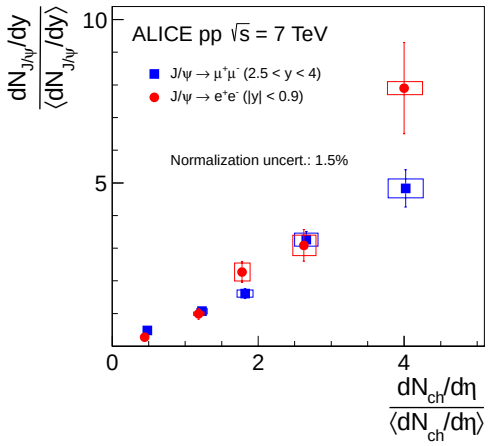

Figure 2: Relative yield as a function of the relative charged-particle multiplicity.

expressed as the relative yield:

$$\frac{Y^{\mathrm{i}}_{\mathrm{J}/\psi}}{Y^{\mathrm{pp}_{inel}}_{\mathrm{J}/\psi}} = \frac{\mathrm{d}N_{\mathrm{J}/\psi}/\mathrm{d}y}{\langle \mathrm{d}N_{\mathrm{J}/\psi}/\mathrm{d}y \rangle}, \qquad (1)$$

where the J/ψ yield in each multiplicity interval i is normalized to the total J/ψ yield in all inelastic pp collisions. On both axes relative numbers are given to facilitate comparisons to other experiments and theoretical models and to minimize systematic uncertainties. An approximately linear increase of the relative yield with the multiplicity is found. A corresponding analysis has been performed in the muon spectrometer at forward rapidities (blue triangles), showing a very similar trend [7]. This result calls for theoretical interpretations. Studies with different event generators are ongoing. In [8] it has been conjectured that the observed dependence could be due to gluon density fluctuations and the transverse structure of the proton.

References

[1] N. Brambilla et al., Eur. Phys. J. C71 (2011) 1534.
[2] T. Sjöstrand and M. van Zijl, Phys. Rev. D36, 2019 (1987).
[3] S. Porteboeuf et al., Nucl. Phys. Proc. Suppl. 214 (2011) 181.
[4] K. Aamodt et al. (ALICE), J. Inst. 3 (2008) S08002.
[5] B. Abelev et al. (ALICE), arXiv:1202.2816 (Submitted to Phys. Lett. B)
[6] K. Aamodt et al. (ALICE), Phys. Lett. B704 (2011) 442.
[7] M. Lenhardt, QM2011 Poster, Board 78
[8] M. Strikman, Phys. Rev. D84 (2011) 011501(R).

* Work supported by GSI, BMBF, Helmholtz Alliance HA216/EMMI, HQM, and HGS-HIRe

Elliptic flow of heavy-flavor electrons in Pb-Pb collisions at 2.76 TeV with ALICE*

R. Bailhache†[1] *and T. Rascanu for the ALICE Collaboration*[1]

[1]IKF, Frankfurt

In ultra-relativistic heavy-ion collisions, heavy quarks, i.e charm and beauty, are produced in the early stage of the reaction. Therefore, they are uniquely suited to probe the Quark-Gluon-Plasma (QGP), which is formed in such reactions. The properties of the QGP can be studied via the azimuthal anisotropy of the heavy-quark emission in the transverse plane. Anisotropic flow can be quantified by the elliptic flow, i.e. the second moment of the Fourier expansion of the particle azimuthal distribution. Experimentally, the heavy-quark anisotropy can be measured indirectly via the semi-leptonic decays of heavy-flavor hadrons to electrons.

Minimum bias Pb-Pb collisions at $\sqrt{s_{NN}}$=2.76 TeV were recorded by the ALICE experiment during the 2010 LHC heavy-ion run. The centrality of the collision is estimated with the signal amplitude in two scintillator arrays, i.e. VZERO detectors, placed on both side of the interaction point[1]. Electrons are tracked in the ALICE central barrel ($|\eta|$<0.8). To minimize the contribution from electrons coming from photon conversions in the detector material, the tracks were required to have a hit in the first silicon pixel layer, situated at a radius of 3.9 cm from the beam line. The energy loss in the Time Projection Chamber (TPC) and the particle velocity measured with the Time-Of-Flight (TOF) detector are used to identify electrons in the momentum range 1.5<p_t<6 GeV/c. Fig.1 shows the TPC dE/dx of tracks with a Time-Of-Flight within 3 sigma of the electron expectation in central Pb-Pb collisions. The upper half of the electron dE/dx distribution is selected for the analysis. Below 1.5 GeV/c, remaining proton and kaon contamination are present. The hadron contamination reaches about 10 % at 6 GeV/c in central Pb-Pb collisions. The elliptic flow analysis is performed with methods based on two-particle correlations, i.e. the event plane method $v_2\{EP\}$ and second order cumulant $v_2\{2\}$, as well as four-particle correlations, i.e; fourth order cumulant $v_2\{4\}$.

The inclusive electron spectrum consists of electrons from heavy-flavor hadron decays, Dalitz decays of light mesons, photon conversions in the material, and dielectron decays of vector mesons. Photon conversions and π^0 Dalitz decays represent the largest background contributions. At high p_t, the heavy-flavour hadron decays become dominant. In order to measure the anisotropic flow of heavy-flavor electrons, the contribution to the inclusive electron v_2 from the other electron sources must be subtracted. Therefore a fast simulation is being implemented to calculate the background electron v_2. The measured v_2 of the background sources (π^0...) is parametrized and the decay kinematics is applied to estimate the resulting v_2 of the decay electrons. Fig.2 shows the elliptic flow of π^0, simulated with preliminary p_t and v_2 distributions of $\pi^{\pm}$ measured by ALICE in 30-40 % central Pb-Pb collisions at 2.76 TeV[2], and the elliptic flow of the corresponding Dalitz electrons. Due to the decay kinematics, the v_2 of the electrons is shifted in p_t in comparison to the pion v_2.

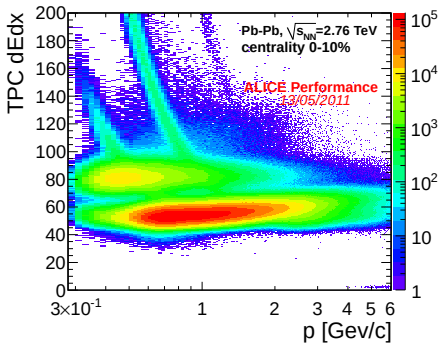

Figure 1: TPC dEdx distribution of tracks with a Time-Of-Flight measurement within 3 sigma of the electron expectation in 0-10% central Pb-Pb collisions.

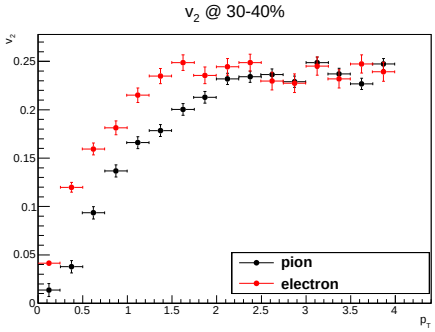

Figure 2: Elliptic flow of π^0, simulated with preliminary measured p_t and v_2 distributions in 30-40 % central Pb-Pb collisions[2], and v_2 of the Dalitz decay electrons.

References

[1] K. Aamodt et al., ALICE Collaboration, Phys. Rev. Lett. 106, 032301 (2011)

[2] M. Krzewicki for the ALICE Collaboration, arXiv:1107.0080v1, QM 2011 conference proceedings

* Work supported by GSI, BMBF, Helmholtz Alliance HA216/EMMI, and HQM.

† rbailhache@ikf.uni-frankfurt.de

Measurement of low-mass dielectrons with ALICE*

C. Baumann[1], *M.K. Köhler*[†2], *and the ALICE collaboration*
[1]IKF, Goethe-Universität Frankfurt, Germany; [2]GSI, Darmstadt, Germany

Low-mass dielectrons are a powerful tool to investigate the different stages of heavy-ion collisions since they do not interact strongly. One result in the search for the quark-gluon plasma is the observation of an enhancement over the expected hadronic sources in the mass region $m_{ee} \approx 0.5$ GeV$/c^2$, observed in heavy-ion collisions. In pp collisions, which can be seen as a medium-free reference for the possible modifications from medium effects in heavy-ion collisions, this enhancement is not seen [1].

Another interesting measurement is the search for an enhanced production of direct photons. These contribute via virtual photons to the dielectron channel. An enhanced production in central Au+Au collisions with respect to the pp-baseline has been observed at low momenta [2]. Among the four large experiments at LHC, the ALICE detector system [3] provides unique capabilities for the tracking and identification of low-momentum particles. It separates into the central barrel around mid-rapidity and detectors at forward rapidity. Electrons can be identified in the central barrel at $|\eta| \leq 0.9$ due to their specific energy-loss in the Inner Tracking System (ITS) and the Time Projection Chamber (TPC), with the Time-Of-Flight detector (TOF) and with the Transition Radiation Detector (TRD).

Besides the challenge of identifying electrons with a high purity at low momenta, another main issue in the analysis of low-mass dielectrons is the precise description of the combinatorial background. Since the origin of an electron or a positron is not known, every combination of electrons and positrons has to be taken into account in one event. As a consequence, a background from uncorrelated pairs arises, which can be described and then subtracted by the like-sign method: $N_{+-}^{\mathrm{CB}} = 2 \times \sqrt{N_{++} N_{--}}$, where N_{+-}^{CB} is the combinatorial background of the measured mass spectrum and N_{++} and N_{--} are the invariant mass spectra from combinations with the same sign.

The resulting mass spectrum after the subtraction of the combinatorial background for pp collisions at $\sqrt{s} = 7$ TeV is shown in Figure 1. The resonances up to the J/ψ are visible as well as a continuum which can at least be partially attributed to semi-leptonic decays of heavy flavor particles.

The measurement of pp collisions are an important baseline: We can test our models describing the vacuum decay of hadrons and use it as a baseline for the analysis of Pb–Pb collisions.

The search for a possible thermal enhancement in the production of virtual photons is a strong focus of the ongoing analyses. In Figure 2 the signal extracted in the invariant mass region relevant for such a photon signal from pp collisions is compared to a cocktail-simulation containing the known contributions from hadronic decays.

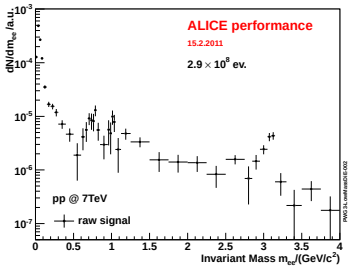

Figure 1: Raw dielectron invariant mass spectrum of proton-proton collisions at a collision energy of $\sqrt{s} = 7$ TeV.

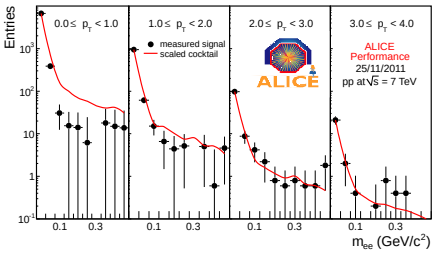

Figure 2: Raw dielectron invariant mass spectrum from pp collisions at a collision energy of $\sqrt{s} = 7$ TeV compared to a simulation of the signal expected from hadronic decays.

In summary, we have presented first results from the ongoing analyses of the dielectron signal in pp collisions measured with ALICE, which provide the baseline for the ongoing analysis of the Pb–Pb data. Besides studies of the efficiency and different methods for the description of the combinatorial background, a focus of the ongoing work is the development of new strategies for reducing the combinatorial background and also evaluate possible improvements by the ALICE upgrade.

References

[1] CERES Collaboration, Phys. Rev. Lett. **75** (1995) 1272.
[2] PHENIX Collaboration, Phys. Rev. Lett. **104** (2010) 132301
[3] ALICE Collaboration, *JINST 3 S08002* 2008.

*Work supported by GSI, BMBF, and Helmholtz Alliance HA216/EMMI.
† Additional support received from HQM and HGS-HIRe

Simulations for the Measurement of Electron-Positron Pairs with Reduced Magnetic Field in the Central Barrel of ALICE*

O. Hinrichs[1], *P. Reichelt*[1], *and the ALICE collaboration*
[1]IKF, Goethe-Universität Frankfurt, Germany

The measurement of electron-positron pairs in the low mass region ($m_{\rm ee} < 2$ GeV/c^2) gives access to the production and modification of light vector mesons during the evolution of a collision [1]. In ALICE, electrons are identified using TPC dE/dx information, supported by TOF for momenta $p > 400$ MeV/c [2]. We present an efficiency study of this combined PID method for two settings of the magnetic field in the ALICE central barrel. The simulations have been performed within the AliRoot framework. Detecting soft electrons ($p < 150$ MeV/c) with the ITS helps reducing the combinatorial background. The influence of the magnetic field is discussed.

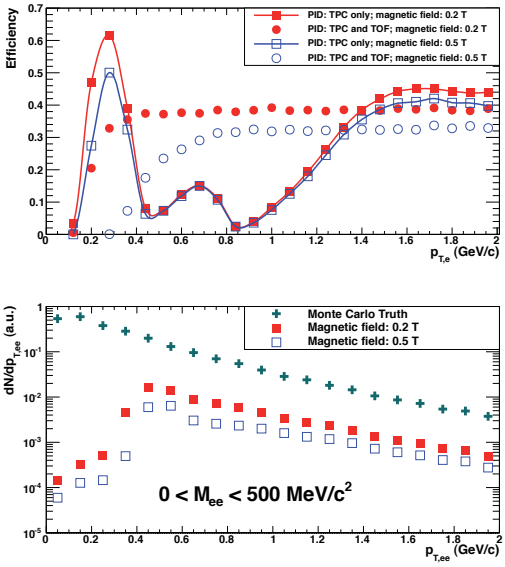

Figure 1: Reconstruction efficiency for electrons (top) and light vector mesons decaying to electrons (bottom).

After track reconstruction, electrons are identified using their energy loss in the TPC. The electron sample is cleaned either by excluding 3σ bands around the expected energy loss values of pions, kaons and protons in the TPC ("TPC only" PID), or by a 3σ cut around the expected electron signal in the TOF ("TPC and TOF" PID). Figure 1, upper panel, shows the single track efficiencies[1] for "TPC only" with squares and "TPC and TOF" with circles, for the nominal field of $B = 0.5$ T with open markers and for a reduced field of $B = 0.2$ T with closed markers.
The electron efficiency is optimized by switching from the "TPC only" to the "TPC and TOF" PID at $p = 400$ MeV/c, where the "TPC only" efficiency drops due to the cuts on the hadrons. At full field a clearly reduced efficiency is seen at $p_{\rm T} \approx 400 - 700$ MeV/c, while at reduced field the TOF efficiency has already saturated in this region. In total, an improvement over the full $p_{\rm T}$ range is seen.
The reconstruction efficiency of light vector mesons decaying to electron-positron pairs was simulated based on the single track efficiencies described above. The lower panel of Figure 1 shows the pair $p_{\rm T}$ spectra for both magnetic fields and the Monte Carlo truth. Comparing the integrated yields for both fields shows a ratio of 3.5. This indicates the potential improvement of the dielectron signal when reducing the magnetic field from 0.5 T to 0.2 T.

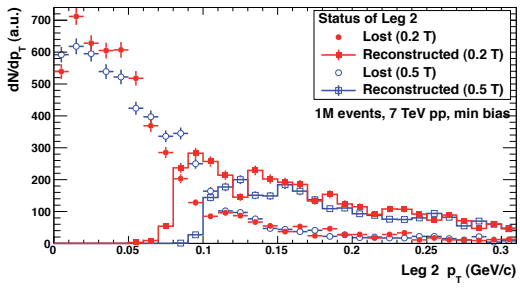

Figure 2: $p_{\rm T}$ distribution of second leg from π^0 Dalitz decays for which first leg is reconstructed as a global track.

For an invariant mass analysis, the rejection of electron-positron pairs from photon conversions and π^0 Dalitz decays is essential to reduce the combinatorial background. For that, both tracks have to be found. Figure 2 shows, for global electron tracks from π^0 Dalitz decays, the $p_{\rm T}$ distribution of the partner track. Circles are lost tracks, squares reconstructed ones. At nominal field (open markers), the ITS reconstructs tracks down to $p_{\rm T} \approx 100$ MeV/c. With $B = 0.2$ T (closed markers), 30 % more tracks are found with the currently implemented tracking, which is optimized for $B = 0.5$ T and does not fully exploit the kinematically possible low-$p_{\rm T}$ reach. The rejection efficiency of found π^0 Dalitz electron pairs is > 99 %, using an invariant mass cut of $m_{\rm ee} = 150$ MeV/c^2. This roughly doubles the significance ($\frac{S^2}{2B}$) of light vector meson signals compared to the 0.5 T magnetic field.

References

[1] I. Tserruya, arXiv:0903.0415v3 [nucl-ex] (2010).
[2] ALICE Collaboration, *ALICE Experiment at the CERN LHC*, CERN, ALICE Technical Paper I, (2008).

* Work supported by BMBF, GSI and the Helmholtz Association
[1]Fraction of all tracks within geometrical acceptance that is measured.

Photons, Neutral Pions, and Eta Mesons via External Conversions in ALICE*

K. Aamodt[1], *F. Bock*[2], *P. Braun-Munzinger*[3], *T. Dietel*[4], *P. Gonzalez*[5], *M. Heide*[4], *M. Ivanov*[3], *K. Koch*[2], *P. Ladrón de Guevara*[6], *S. Lindal*[5], *D. Lohner*[2], *A. Marín*[3], *K. Reygers*[2], *D. Röhrich*[1], *R. Rusanov*[2], *E. Serradilla*[6], *J. Stachel*[2], *T.S. Tveter*[5], *J.P. Wessels*[4], *M. Wilde*[4], *and the ALICE Collaboration*

[1]Department of Physics, University of Oslo, Oslo, Norway; [2]Physikalisches Institut, Ruprecht-Karls-Universität Heidelberg, Heidelberg, Germany; [3]ExtreMe Matter Institute EMMI, GSI Helmholtzzemtrum für Schwerionenforschung, Darmstadt, Germany; [4]Institut für Kernphysik, Westfälische Wilhems-Universität Münster, Münster, Germany; [5]Department of Physics, University of Oslo, Oslo, Norway; [6]Centro de Investigaciones Energeticas, Medioambientales y Tecnológicas (CIEMAT), Madrid, Spain

With the ALICE detector at the LHC photons can be measured with electromagnetic calorimeters (PHOS, EMCAL) and by reconstructing e^+e^- track pairs from photon conversions in the inner detectors with the Time Projection Chamber (TPC). The photon conversion probability in the relevant detector material is about 8.5 %. In conjunction with the track reconstruction efficiency in the TPC this leads to a reconstruction efficiency for the two-photon decay of π^0's and η's of only 0.34 % at maximum. However, a unique feature of the conversion method compared to calorimetric measurements is the excellent photon momentum resolution at low p_T ($p_T < 6$ GeV/c). Thus, the conversion method is well-suited for photon measurements in a range where in Pb+Pb collisions thermal photons from the quark-gluon plasma are expected to contribute significantly. Moreover, owing to the large acceptance of the TPC, the photon statistics at larger p_T is sufficient to study particle production in the hard scattering regime.

The motivation for photon, π^0, and η measurements in p+p collisions is to characterize particle production in a new, unexplored energy regime. In particular, one can test perturbative QCD at the highest available energies and constrain the $g \to \pi^0$,η fragmentation function as most π^0's and η's in the covered p_T range originate from gluons. In Pb+Pb collisions one can in addition study hadron suppression due to jet-quenching and thermal photon production. Moreover, the reconstruction of converted photons provides a detailed measurement of the material budget which is important for many analyses.

The measured π^0 spectra (Figure 1) exhibit a power law shape above $p_T > 1-2$ GeV/c as expected from perturbative QCD. A detailed comparison reveals that for a standard range of scales ($\mu = 0.5p_T, p_T, 2p_T$) the π^0 and η spectra at $\sqrt{s} = 2.76$ and 7 TeV are not well described by NLO QCD calculations employing gluons fragmentation functions which provide a good description of RHIC data [1]. In Pb+Pb collisions at $\sqrt{s_{NN}} = 2.76$ TeV it was found that the maximum suppression ($R_{AA} \approx 0.1$ at $p_T \approx 6$ GeV/c) is slightly stronger than the suppression observed in central Au+Au collisions at RHIC (Figure 2) [2].

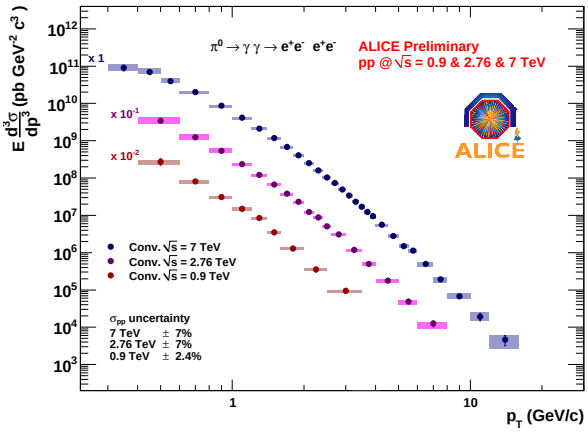

Figure 1: Inv. π^0 cross sections in p+p at $\sqrt{s} = 0.9$, 2.76, and 7 TeV measured with the conversion method.

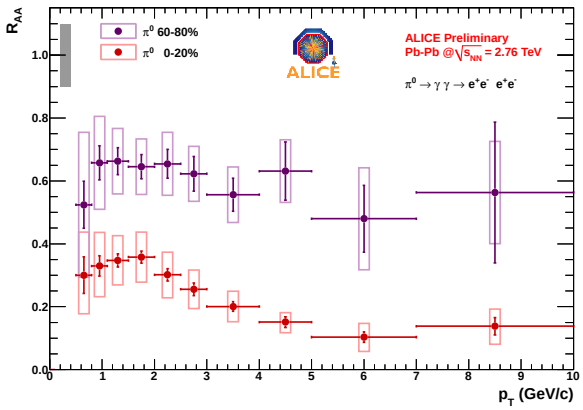

Figure 2: Nuclear modification factor $R_{AA} = dN/dp_T|_{\mathrm{Pb+Pb}}/(N_{\mathrm{coll}} \times dN/dp_T|_{\mathrm{p+p}})$ for Pb+Pb collisions at $\sqrt{s_{NN}} = 2.76$ TeV (2010 data) for neutral pions reconstructed with the conversion method.

References

[1] K. Reygers [ALICE Collaboration], J. Phys. G **38** (2011) 124076 [arXiv:1106.5932 [hep-ex]].

[2] G. Conesa Balbastre [ALICE Collaboration], J. Phys. G **38** (2011) 124117 [arXiv:1109.4929 [hep-ex]].

* Work supported by GSI, BMBF, HGS-HIRe, and Helmholtz Alliance HA216/EMMI.

Event-by-event mean p_{T} fluctuations in pp and Pb–Pb collisions measured by the ALICE experiment at the LHC

S. Heckel[1], *H. Appelshäuser*[1], *H. Büsching*[1], *and the ALICE collaboration*

[1]Institut für Kernphysik, Goethe-Universität, Frankfurt/Main, Germany

Event-by-event fluctuations of mean transverse momentum $\langle p_{\mathrm{T}} \rangle$ contain information on the dynamics and correlations in pp and heavy-ion collisions. Measurements in pp serve as a baseline. In heavy-ion collisions, fluctuations may be related to critical behaviour of the system in the vicinity of a phase boundary [1] or the occurrence of thermalization and collectivity [2].

In this analysis, non-statistical event-by-event fluctuations of $\langle p_{\mathrm{T}} \rangle$ of charged particles are studied using the ALICE detector at the LHC [3]. The analysis is performed in $0.15 < p_{\mathrm{T}} < 2$ GeV/c and $|\eta| < 0.8$. Multiplicity dependent results are obtained for pp collisions at $\sqrt{s}$ = 0.9, 2.76 and 7 TeV and Pb–Pb collisions at $\sqrt{s_{\mathrm{NN}}}$ = 2.76 TeV.

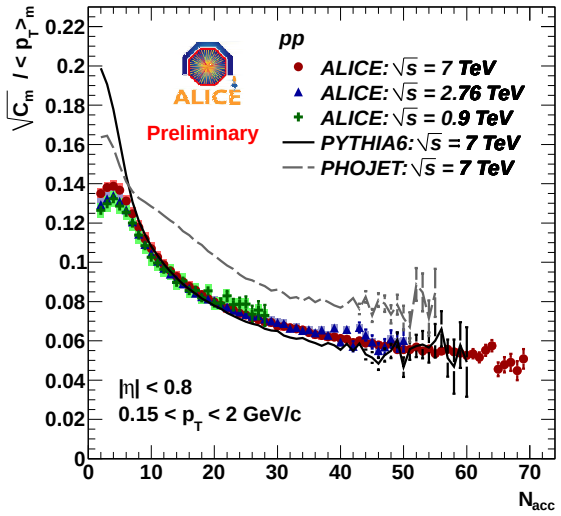

Figure 1: $\sqrt{C_m}/\langle p_{\mathrm{T}} \rangle_m$ as a function of N_{acc} in pp collisions at different energies and comparison to event generators: PYTHIA6 (solid line) and PHOJET (dashed line).

The two-particle correlator $C = \langle \Delta p_{\mathrm{T},i}, \Delta p_{\mathrm{T},j} \rangle$ is a measure of the dynamical fluctuations [4]. It is defined as

$$C = \frac{1}{\sum_{k=1}^{n_{\mathrm{ev}}} N_k^{\mathrm{ps}}} \sum_{k=1}^{n_{\mathrm{ev}}} \sum_{i=1}^{N_k} \sum_{j=i+1}^{N_k} (p_{\mathrm{T},i} - \langle p_{\mathrm{T}} \rangle)(p_{\mathrm{T},j} - \langle p_{\mathrm{T}} \rangle),$$

where n_{ev} is the number of events, N_k is the number of particles and $N_k^{\mathrm{ps}} = 0.5 \cdot N_k \cdot (N_k - 1)$ the number of particle pairs in event k. By construction, $C = 0$ in the presence of only statistical fluctuations. The correlator is calculated in bins of the event multiplicity N_{acc}, where N_{acc} is the number of tracks accepted by the analysis cuts.

Supported by GSI, BMBF, and Helmholtz Alliance HA216/EMMI.

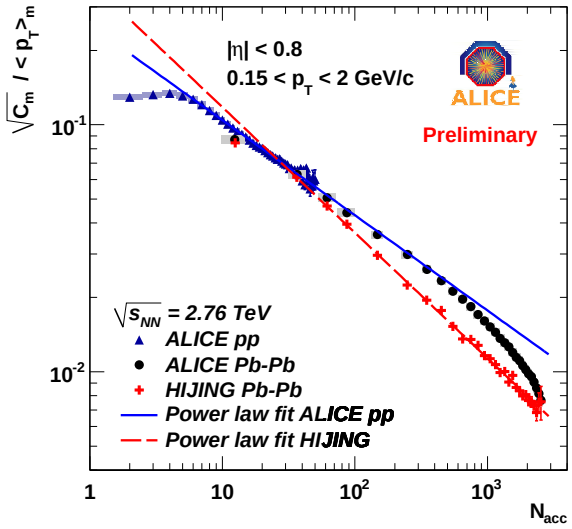

Figure 2: $\sqrt{C_m}/\langle p_{\mathrm{T}} \rangle_m$ as a function of N_{acc} in pp and Pb–Pb collisions at $\sqrt{s_{\mathrm{NN}}}$ = 2.76 TeV and comparison to the HIJING event generator. Power law fits for the pp data (solid line) and for HIJING (dashed line) are also shown.

The results are presented in terms of the relative fluctuations $\sqrt{C_m}/\langle p_{\mathrm{T}} \rangle_m$, where m indicates the given multiplicity class. Figure 1 shows the results for pp collisions together with Monte Carlo simulations using PYTHIA6 (Perugia0 tune) and PHOJET. Significant non-statistical fluctuations are observed, demonstrating a dilution with increasing multiplicity. In this relative representation the data look universal at LHC energies.

Pb–Pb collisions also show significant non-statistical fluctuations and dilution with increasing multiplicity as is presented in figure 2 together with pp data and a comparison to the HIJING event generator. The pp data are fitted with a power law. The Pb–Pb data agree well with this pp baseline up to $N_{\mathrm{acc}} \approx 600$. Central Pb–Pb collisions show a significant additional reduction of the fluctuations. Further studies are needed to identify possible mechanisms leading to this non-trivial reduction.

References

[1] M.A. Stephanov *et al* 1999 *Phys. Rev.* D **60** 114028

[2] S. Gavin 2004 *Phys. Rev. Lett.* **92** 162301

[3] K. Aamodt *et al* [ALICE] 2008 *JINST* **3** S08002

[4] S.A. Voloshin *et al* 1999 *Phys. Rev.* C **60** 024901

Upgrade of the ALICE experiment at the LHC

The ALICE Collaboration[*]

The Large Hadron Collider (LHC) at CERN dedicates the last period of operation of each year (roughly 4 weeks between November and December) to the collisions of lead beams, for the moment at the energy of $\sqrt{s_{NN}} = 2.76$ TeV. In 2011, the LHC reached and even exceeded the design heavy-ion interaction rate (hitting the record of 7 kHz). For the near future, after the long shutdown in 2012-2013, the expectation is to have Pb–Pb collision rates of about 10 kHz at full LHC energy, namely $\sqrt{s_{NN}} = 5.5$ TeV.

In 2010 and 2011, during the first two Pb–Pb runs, ALICE recorded an integrated luminosity of $\approx 10\mu\text{b}^{-1}$ and $\approx 100\mu\text{b}^{-1}$, respectively. In 2012, ALICE will record p–Pb collisions, which are crucial to understand initial state modifications in nuclei, such as shadowing or a non-linear QCD evolution.

The present ALICE detector is well suited to cope with the expected rates over the following few years. By collecting a few hundred μb^{-1} per year, at full energy, by 2017 ALICE will reach a data sample of the order of ≈ 1 nb^{-1}.

After the second long shutdown in 2018, the LHC plans to deliver Pb beams colliding at an interaction rate of about 50 kHz, i.e. instantaneous luminosities up to $6{\cdot}10^{27}$ cm^{-2}s^{-1}. In order to cope with these higher rates, to be able to inspect a major fraction of the collisions, and, therefore, offer an unprecedented physics reach, the ALICE detector requires several modifications [1].

With the perspective to accumulate of the order of 10 nb^{-1} in Pb–Pb collisions, the physics plans focus on rare probes both at low and high transverse momenta, which will allow a much more precise determination and a deeper understanding of the properties of the Quark-Gluon Plasma (QGP) produced in heavy-ion collisions. Here, we mention a few topics of interest.

The present results on the nuclear modification factor for charged particles in central collisions question the applicability of perturbative methods to describe the regime in the dense QGP. The hot fireball is so dense and strongly interacting that the concept of quasi-particles might cease to exist, and the perturbative QCD regime is not reached even for asymptotic transverse momenta above 100 GeV/c. To better characterize such strongly coupled matter, our understanding of parton energy loss needs a significant improvement. Precision data, both at intermediate and very high transverse momenta, are necessary, for example in jet-jet and photon-jet measurements, and with particle identification (which is one of the distinctive capabilities of ALICE).

In the area of heavy quarks and quarkonia, it will be important to make a precision measurement of the open charm and beauty cross section in Pb–Pb collisions. Charmed hadrons have to be studied at low momenta where they can provide stringent tests of models of the bulk medium, as their large mass and small cross sections make them more sensitive to details of equilibration. We want to further investigate the possible hydrodynamic flow of c and b quarks to see to what extent heavy quarks participate in the collective expansion of the medium. Ground states as well as excited $\mathrm{c\bar{c}}$ and $\mathrm{b\bar{b}}$ states could be studied in detail at mid-rapidity, down to low transverse momenta. This will further test models of suppression and generation of quarkonia in the medium.

A more detailed study of thermal photons and low-mass lepton pairs emitted from the hot fireball can shed light on the initial temperature and degrees of freedom of the QGP, as well as to offer means to study the nature of the chiral phase transition.

Finally, another area where ALICE measurements are unique is the search for exotic objects produced in heavy-ion collisions, e.g. multi-Λ hypernuclei, bound states of $\Lambda\Lambda$, or black holes.

We concentrate the attention on the upgrade of the ALICE central barrel, to be able to make full use of the much increased luminosity. This includes a new, high resolution, low material silicon tracking system based on active pixel sensors, and in conjunction a topological trigger for the selection of rare events; upgrades to improve the rate capability of the TPC, TRD, and TOF detectors; extension of the current electromagnetic calorimeter in coverage and trigger capabilities; new concept for the data acquisition system and the high level trigger.

In particular, the least biased investigation of the high rates could be achieved with a dead-time free readout of the ALICE Time Projection Chamber (TPC). This would be possible by equipping the TPC readout chambers with the GEM technology. This option will be investigated.

Driven by the fascinating extension of the physics which will become accessible, the GSI/EMMI group expresses interest and offers competences in the areas of the TPC, TRD, and HLT upgrades, as well as for the development of online selection algorithms, in synergy with applications in the experiments at FAIR.

References

[1] P. Braun-Munzinger, L. Musa, P. Vande Vyvre, "Upgrade strategy for the ALICE central barrel", ALICE Internal Note

[*] Work supported by GSI, BMBF, and the Helmholtz Alliance HA216/EMMI. The list of ALICE members and institutions is available at `http://aliweb.cern.ch/General/Members/List_Institutes.html`

The CBM Experiment at SIS100*

P. Senger[1] *and the CBM Collaboration*
[1]GSI, Darmstadt, Germany

Introduction

The mission of high-energy nucleus-nucleus collision experiments worldwide is to investigate the properties of strongly interacting matter under extreme conditions. At very high collision energies as available at RHIC and LHC, the measurements concentrate on the study of the properties of deconfined QCD matter at very high temperatures and almost zero net baryon densities. The goal of the Compressed Baryonic Matter (CBM) experiment at the FAIR SIS100/300 accelerator system is to explore the QCD phase diagram in the region of very high baryon densities. In particular, the experiments will focus on the search for the phase transition between hadronic and quark-gluon matter, the QCD critical endpoint, new forms of strange matter, in-medium modifications of hadrons and the onset of chiral symmetry restoration. A detailed discussion of the physics of compressed baryonic matter can be found in the CBM Physics Book [1].

The research on compressed baryonic matter will start already with beams from the SIS-100 accelerator as an integral part of the physics programme of the FAIR modularized start version as presented in the FAIR Green Paper [2]. In the SIS-100 energy range, the physics topics of dilepton and strangeness production will be addressed by two collaborations, HADES and CBM, sharing the same experimental area. The layouts and acceptances of both experiments are optimized for different beam energy regimes but provide sufficient overlap in beam energy to ensure two independent evaluations of these challenging measurements and to allow experimental crosschecks for the lighter collision systems. The investigation of dilepton-, strangeness-, and charm production over the full range of beam nuclei and energies will be conducted with a basis version of the CBM setup. The various observables and the corresponding experimental requirements will be discussed in the following.

The CBM research programme at SIS100

The SIS-100 accelerator will deliver beams of heavy ions (Au) up to $11A$ GeV ($\sqrt{s_{NN}} = 4.7$ GeV), light ions (e.g. Ca) up to $14A$ GeV ($\sqrt{s_{NN}} = 5.3$ GeV) and protons up to 29 GeV ($\sqrt{s_{NN}} = 7.5$ GeV). The research programme based on these beams will address the following fundamental questions:

- What is the equation of state of nuclear matter at neutron star densities (up to 6 times saturation density ρ_0), and what are the relevant degrees of freedom at these densities? Are there new phases of QCD matter like quarkyonic matter?
- How far can we extend the chart of nuclei towards the third (strange) dimension by producing single and double hypernuclei? Does strange matter exist in the form of heavy multi-strange objects?
- To what extent are the properties of hadrons modified in dense baryonic matter, and are there signatures for chiral symmetry restoration?
- How is charm produced at threshold beam energies, how does charm propagate in nuclear matter, and what are the in-medium properties of charmed particles?

Experimental setup

The measurement of bulk hadrons, multi-strange hyperons, hypernuclei, lepton pairs and charmed particles in nuclear collisions at SIS-100 energies requires a large-acceptance, high-rate detector system. The Compressed Baryonic Matter (CBM) experimental setup is being designed to fulfill these requirements (see figure 1 and Table 1). The setup comprises:

- A spectrometer with a silicon tracking system (STS) inside a superconducting magnet with large aperture (polar angle acceptance $2.5^\circ - 25^\circ$ for all azimuth angles). The STS will measure the trajectories of the produced particles in the magnetic dipole field, determine their momenta and reconstruct hyperons by their decay topology.
- A micro-vertex detector (MVD) for the high-precision measurement of the decay vertices of charmed hadrons.
- A large-area time-of-flight detector (TOF) consisting of multi-gap resistive plate chambers for the time-of-flight measurement.
- A RICH detector for the identification of electron-positron pairs from the decay of low-mass vector mesons.
- An intermediate tracking detector with three to four TRD layers allowing to match tracks reconstructed in the STS to the TOF measurement. This TRD constitutes the start version of the full TRD to be used at SIS-300, which will consist of about ten detector layers for the identification of high-momentum electrons.

*Supported by the Hessian LOEWE initiative through the Helmholtz International Center for FAIR (HIC for FAIR), BMBF Verbundforschung, GSI F&E, and by EU/FP7 Hadronphysics2

- A muon detection system (MUCH) for the measurement of charmonium via its decay into muon pairs. This MUCH start version, consisting of two detector triplets, will be upgraded to the full system with seven triplets for deployment at SIS-300. Both the MUCH and the RICH detectors will be movable in order to be used alternatively for muon or electron measurements.

- An electromagnetic calorimeter (ECAL) for the measurement of photons from light vector meson decays.

- A forward calorimeter (PSD) for the determination of the collision centrality and the reaction plane by the measurement of projectile spectators.

- An ultra-fast data acquisition (DAQ) and first level event selection (FLES) performed on a computer farm consisting of many-core CPUs accelerated with graphics cards.

In conclusion, the combination of the HADES detector with the basis version of the CBM set-up is very well suited to start an internationally competitive nuclear-matter research programme with a substantial discovery potential using beams from SIS-100. A world-wide unique experimental search for quark-gluon matter at ultra-high baryon densities will become possible with the full version of the CBM detector system using high-energy and high-intensity beams from SIS-300.

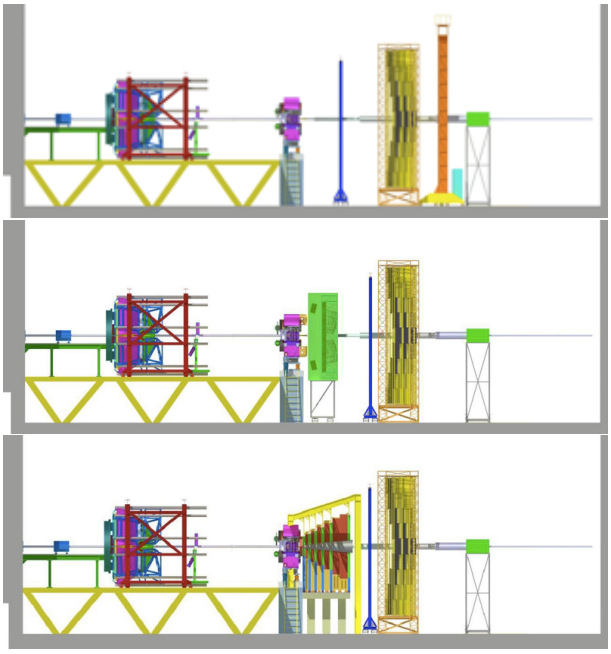

Figure 1: Three flavours of the CBM basis version with the HADES detector in front. Upper panel: CBM setup for the measurements of bulk hadrons, multi-strange hyperons and open charm consisting of the magnet, MVD (open charm only), STS, one TRD station as tracker, TOF, ECAL, PSD, and DAQ/FLES. Centre panel: CBM setup for the measurements of di-electrons with an additional RICH detector. Bottom panel: CBM setup for measurements of charmonium with a MUCH start version replacing the RICH.

Table 1: Observables and detector combinations at SIS100

Observables	Collisions systems	Detectors
Hadrons, hyperons e^+e^- from low-mass vector mesons	up to Ni+Ni at 8A GeV	HADES
Hadrons, hyperons, hypernuclei	up to Au+Au at 11A GeV	Magnet, STS, TRD, TOF, PSD, DAQ/FLES
e^+e^- from low-mass vector mesons	up to Au+Au at 11A GeV	Magnet, MVD, STS, RICH, TRD, TOF, PSD, DAQ/FLES
D mesons	p+A up to 30 GeV Ca+Ca up at 14A GeV	Magnet, MVD, STS, TRD, TOF, PSD, DAQ/FLES
Charmonium	p+A up to 30 GeV Ca+Ca up to 14A GeV Au+Au up to 11A GeV	Magnet, MVD, STS, MUCH, TRD, TOF, PSD, DAQ/FLES
Photons	Au+Au up to 11A GeV	Magnet, STS, ECAL, PSD, DAQ/FLES

References

[1] The CBM Physiks Book, Eds. B. Friman et al., Springer Series: Lecture Notes in Physics, Vol. 814, 2011, ISBN: 978-3-642-13292-6, Electronic authors version: `http://www.gsi.de/documents/DOC-2009-Sep-120-1.pdf`

[2] FAIR Green Paper - The Modularized Start Version, Darmstadt 2009, `http://www.gsi.de/documents/DOC-2009-Nov-124-1.pdf`

Development of high precision pixel sensors for the CBM vertex detector

M. Winter, for the IPHC team[1]

[1]IPHC, 23 rue du loess, BP 28, 67037 Strasbourg Cedex 2, France

CMOS Pixel Sensors (CPS) are developped since many years for the Micro-Vertex Detector (MVD) of the CBM experiment. While the sensor requirements governing the vertexing precision present no difficulty per se, those imposed by the running conditions are much more demanding because of the high particle rate foreseen.

The intrinsic potential of the CPS technology should, in principle, allow matching all the MVD requirements. However, commercially available technologies tend to feature fabrication parametres (e.g. sensitive volume characteristics, feature size, number of metal layers) which are relatively far from being optimal for charged particle detection. Over the last couple of years, however, several CMOS fabricant have started to offer manufacturing processes for imaging applications, which are based on a high-resistivity (typically 1 $k\Omega \cdot cm$), about 15μm thick, epitaxial layer. The development of CPS in the last few years was based on such a, 0.35μm feature size, CMOS process. It resulted in the fabrication of the MIMOSA-28 sensor for the vertex detector of the STAR experiment, constructed within the framework of its inner tracker upgrade [1].

This outcome is a major step in the development of the sensor needed for the MVD, but the 0.35 μm technology used is not adequate, in particular because of its limited ionising radiation tolerance. In 2011, a 0.18μm process recently made available was addressed, which seems to offer much more favourable parametres. Besides improving intrinsically the ionising radiation tolerance, the procees also allows using 6-7 metal layers and features deep p-wells in which PMOS transistors can be implemented without generating parasitic charge collection. Moreover, the process is also of interest for other projects, including the upgrade of the ALICE Inner Tracking System (ITS), which makes the development benefit from combined resources.

The first step of the development consists in exploring the technology characteristics impacting most the sensor detection performances. It is the goal of the chip called MIMOSA-32, fabricated end of 2011. It is composed of two main sub-arrays (see fig. 1) and peripheral test structures. One of the sub-arrays is composed of pixels with various dimensions and different amplification designs, some of them with PMOS transistors implemented in deep p-wells, with and without enclosed layout designs. The other sub-array is made of 128 columns of pixels, each column being ended with a discriminator. One of the test structures is a matrix of about 1000 elongated, 20×80 μm^2 large, pixels, each equipped with an integrated, low power, discriminator adapted to a rolling shutter read-out.

The sensor tests, scheduled for Spring and Summer 2012, will determine the radiation tolerance of the technology. Meanwhile, the next step of the development is being prepared. It consists in realising two complementary chips, one prototyping the upstream part of the final sensor architecture, while the other addresses its downstream part.

The upstream prototype, called MIMOSA-22THR, features 128 columns of 576 (22×22 μm^2) pixels. Each column is ended with a discriminator. It will essentially reproduce the MIMOSA-22 prototype [2], fabricated in 2008 in the 0.35 μm technology used up to now. Two smaller, more advanced, versions will also be fabricated. One of them features a more advantageous row sequencer implementation, while the other will allow reading two rows at once, with two discriminators ending each column. The latter design is intended to double the read-out speed.

The downstream prototype contains the zero-suppression micro-circuits. Called SUZE-02, it is an evolved version of the zero-suppression micro-circuit SUZE-01 fabricated in 2007 in the 0.35 μm technology mentioned earlier [3]. It differs from it in three aspects: a larger number of hits to process per frame, a 4 times faster frame read-out and the possibility to rely on an external trigger signal to activate the zero-suppression circuitry. This latter modification aims at reducing the power consumption and the data stream delivered by the sensor.

All these prototypes are foreseen for fabrication in Summer 2012. Assuming satisfactory test results, the two architectures will be merged in a sensor containing the full chain and featuring a sensitive area of 1 cm^2. Its manufacturing is foreseen in Summer 2013. It will act as a forerunner of the prototype suited to the MVD, to be fabricated in 2014/15.

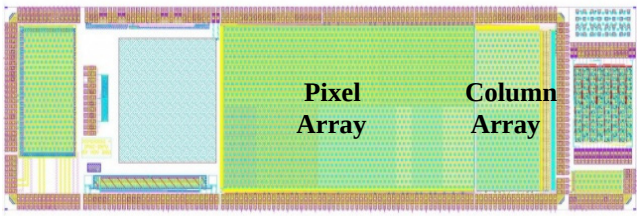

Figure 1: MIMOSA-32 layout and its main sub-sarrays.

References

[1] A.Dorokhov et al., *High resistivity CMOS pixel sensors and their application to the STAR PXL detector*, NIM A 650 (2011) 174-177

[2] M.Gelin et al., *Intermediate Digital Monolithic Pixel Sensor for the EUDET High Resolution Beam Telescope*, IEEE TNS 56-3 (2009) 1677-1684

[3] A.Himmi et al., *A Zero Suppression Micro-Circuit for Binary Readout CMOS Pixel Sensors*, proc. of TWEPP-09, Paris (21-25 sept. 2009)

Radiation tolerance studies on a CMOS Monolithic Active Pixel Sensor with high resistivity epitaxial layer*

D. Doering[1], *M. Deveaux*[1], *M. Domachowski*[1], *I. Fröhlich*[1], *M. Koziel*[1], *C. Müntz*[1], *P. Scharrer*[1], *and J. Stroth*[1]

[1]Goethe University Frankfurt/M, Max-von-Laue-Str. 1, 60438 Frankfurt/M, Germany

Nowadays CMOS active pixel sensors (MAPS) match the requirements of CBM in terms of spatial resolution and material budget. For several years, their radiation tolerance is being adapted to the needs of this experiment. Manufacturing MAPS in a CMOS process with a high resistivity epitaxial layer improved their tolerance to non-ionizing radiation by more than one order of magnitude[1, 2]. A novel sensor, MIMOSA-18AHR was hoped to provide further improvement.

MIMOSA-18AHR was designed by the PICSEL group of the IPHC Strasbourg and manufactured in a 0.35 μm CMOS technology featuring a 15 μm thick epitaxial layer with 400 $\Omega \cdot$ cm resistivity. It hosts pixels with a pitch of $10, 12.5$ and 25 μm. Some samples were irradiated with $3 \cdot 10^{14}$ n_{eq}/cm^2 reactor neutrons and tested with ^{55}Fe- and ^{106}Ru-sources. They were operated at $T = -35°C$ chip temperature to suppress their (shot-) noise to $\sim$ 16e ENC ($\sim$ 9e ENC before irradiation).

Figure 1 shows the amplitude spectrum of the 10 μm pixels of a non-irradiated and an irradiated sensor, which were illuminated with the 5.9 keV X-rays of a ^{55}Fe source. Its x-axis represents the charge collection efficiency (CCE) of a certain sub-volume of the active volume and the y-axis the relative size of this sub-volume. The unusually large depleted part of the pixel records the K_α and K_β-line of the source and defines our 100% CCE. The peak marked with an arrow represents the average CCE of the undepleted part of the active volume. Other than known from conventional chips, the CCE (35%) of this volume is not modified by radiation damage. However, the irradiated chip senses $\sim$ 15% less photons, which hints to a loss of active volume. Loosing active volume may cause blind spots in the pixels, which were feared to deteriorate the detection efficiency of the sensor for MIPs. This was however not observed when testing the sensors with the ^{106}Ru-source: The number of β-particles recorded by the irradiated sensor remains at $\gtrsim$ 99% of the initial value (see Figure 2). The most probable signal charge is reduced by $\sim$ 15% after irradiation. This coincides with the loss of active volume indicated by the ^{55}Fe-measurements. Both effects may be explained with a shrinking of the effective thickness of the active volume. In this case, the signal charge created by the β-rays is reduced due to shorter trajectories in the active volume.

The remaining S/N=31 (S/N =70 before irradiation) corresponds to the numbers known from non-irradiated MAPS with standard epitaxial layer. The study provides therefore a strong evidence that MIMOSA-18AHR can withstand a non-ionizing dose of $\gtrsim 10^{14}$ n_{eq}/cm^2, which goes substantially beyond the CBM requirements. However, this conclusion remains to be confirmed by a beam test scheduled for late 2012.

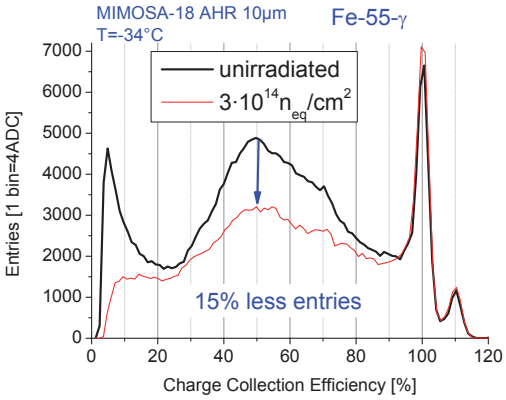

Figure 1: Response of MIMOSA-18AHR to X-rays from an ^{55}Fe source. See text.

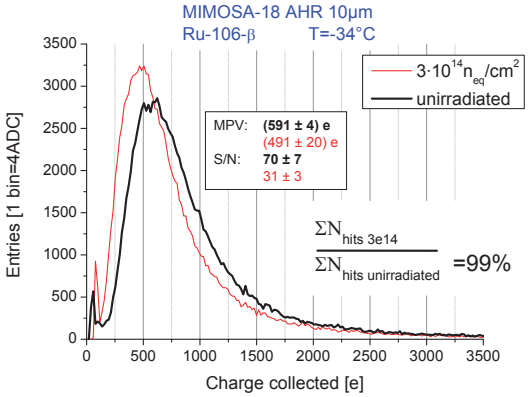

Figure 2: Response of MIMOSA-18AHR to β-rays of a ^{106}Ru-source.

References

[1] A. Dorokhov et al. Improved radiation tolerance of MAPS using a depleted epitaxial layer. *Nucl. Instr. and Meth. A* , 624(2):432–436, 2010.

[2] M. Deveaux et al. Radiation tolerance of a column parallel cmos sensor with partially depleted sensitive volume. *Nucl. Instr. and Meth. A*, 583(1):134 – 138, 2010.

*This work has been supported by the BMBF (06FY9099I), HIC for FAIR and GSI.

Status of the CBM-MVD prototype readout*

C. Schrader, S. Amar-Youcef, N. Bialas, M. Deveaux, M. Koziel, J. Michel, B. Milanovic, C. Müntz, B. Neumann, S. Schreiber, T. Tischler, M. Wiebusch, and J. Stroth for the CBM-MVD Collaboration

Institut für Kernphysik, Goethe-Universität, Frankfurt am Main

The readout system of the prototype of the CBM-MVD is intended to provide the bandwidth (of several GByte/s [1]) and scalability needed in the final MVD for SIS-100. It has been developed based on the state of the art prototype sensor MIMOSA-26 [2].

The concept of the readout system of the MVD-Prototype is shown in figure 1. Two sensors are bonded on a single layer flex-print cable (FPC) which transfers the data to a full passive radiation tolerant front-end board (FEB). The current FPC is based on copper traces and has an material budget of 0.08 % X_0 assuming 100 % fill factor (0.03 % X_0 for aluminum traces).

Additional single layer FPCs arrange the FEBs in a queue for JTAG boundary scan, which allows accessing to the internal register of the individual sensors. An FPGA based sensor slow control board writes the registers and reports errors to a user interface via the slow control channel of the HADES TrbNet protocol. The operation frequency of the JTAG interface (TTL signals) can be adjusted between 100 kHz and 10 MHz. Hence, the sensors of the MVD for SIS-100 can be programmed within $<$ 0.5 s (300 μs per sensor), optionally during one beam spill break. To operate the JTAG chain error-free the signal behavior, signal shape and the crosstalk between the lines of the single layer FPC was extensive studied and simulated. Currently the crosstalk is reduced to 150 mV, due to a moderate signal rise time and serial signal termination [3].

In order to characterize the internal digital-to-analog-converters of the MIMOSA-26 sensor needed for threshold setting, a highly integrated voltage measurement instrument has been developed. This device directly monitors the reference voltage outputs of the sensor and can be read out via a serial interface. A complete integration into the existing FPGA based MVD slow control is under development. The slow control provides also latch-up handling, on-line temperature and current monitoring.

In the current set-up the digital data stream of the sensors are transferred via LVDS cables to a converter board. However, to read-out the successor MAPS sensor (MIMOSIS-1 with up to 0.8 Gbps data output) an optical high speed read-out system is needed. A challenge is to realize the optical interface without any switchable logic to reduce the bit error rate due to radiation influences. To test several versions of optical high speed interfaces an optical demonstrator converter board has been developed based on a standalone transceiver TLK3101 (1.5 Gbps to 2.5 Gbps) and TLK6002 (0.47 Gbps to 6.25 Gbps). The transceiver provides the data for one optical link with 8bit/10bit encoding. Hence, one optical link will be used to transfer the data from one sensor module to the Read-Out-Controller (ROC). Such a sensor module comprises up to five MIMOSIS-1 sensors needed for the first and second station of the MVD of SIS-100.

The read-out protocol of the ROC is a modified version of the HADES-experiment readout network scheduled for the required triggerless data acquisition of the MVD prototype. The TrbNet protocol is highly scalable and provides a secure data acquisition, monitoring and slow-control [4]. The actual lab set-up is able to handle several Gbit/s and consists of three ROCs. An arbiter is responsible to synchronize the sensors and the data stream within few nanoseconds. The data are multiplexed via TrbNet hubs and transported to the PC via Ethernet. Each hub can handle 100 MByte/s. The first verified Gbytes data of four sensors are stored on the PC for analyzing.

A dedicated ROOT-based offline analysis software is used to evaluate the data. The software is designed to allow using major functionalities of CbmRoot including reconstruction and analysis.

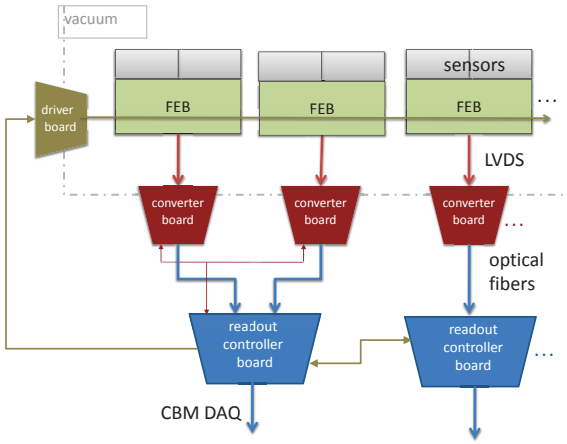

Figure 1: The current prototype read-out chain. The LVDS readout cables will be replaced by optical fibres in the next prototype iteration.

References

[1] S. Seddiki, Data rates of the CBM-MVD expected at SIS-100, CBM coll. meeting Romania, Oct. 2010

[2] C. Hu-Guo, Nim A 623,1 P480-482

[3] B.Neumann, Frequency dependent transmission in flex-print-cables, MVD internal note, Sept. 2011

[4] B. Milanovic, The CBM-MVD Prototype Readout Network - Version 1, GSI Report 2011

* Work supported by GSI, BMBF (06FY9099I), ULISI (EU-FP7), HIC for FAIR.

The CBM-MVD Prototype Readout Network*

B. Milanovic, M. Deveaux, I. Fröhlich, J. Michel, B. Neumann, J. Stroth, and C. Schrader for the CBM-MVD Collaboration

IKF, Goethe University Frankfurt, Germany

Currently, the prototype of the CBM Micro Vertex Detector is under development. In order to be prepared for the upcoming in-beam studies and to elaborate a first approach on the DAQ, a flexible readout network has been implemented.

The Micro Vertex Detector (MVD) for the CBM experiment is based on Monolithic Active Pixel Sensors (MAPS) built in silicon CMOS technology. Here, MIMOSA26 (Mi26) has been chosen as the sensor version used for the MVD-prototype. This chip digitizes the analogue signal directly on the chip and simplifies hearby readout and analysis. The resulting pattern is read out row-wise and encoded on-the-fly into a continuous data stream with a constant readout cycle time ("frames").

The aim of the readout network presented in this work is to support the control and readout of Mi26 and also of all following MAPS families (e.g. MIMOSIS-1). The data stream of the sensors is read out using Readout Controllers (ROCs), where one ROC is connected to multiple MAPS. The data is either extracted directly on the ROC or over network hubs to the nearby PC farm. As mentioned above, the cycle time of the sensors is constant, but in order to combine the individual frames into "Masterframes" which have the same time stamp, the network has to maintain the synchronization of all MAPS during runtime. The optimal solution for this task makes use of one centralized controller for clock distribution, synchronization and control named Central Control Unit (CCU). Moreover, the network must have a large throughput of several GByte/s, and should allow to connect the JTAG interface of the sensors for programming [1].

For the first version presented in this paper, the HADES TrbNet [2] has been chosen as a framework for the network. One of the main reasons for the decision towards TrbNet was the large toolset already present from the HADES Experiment. For instance, the EPICS input-output controller, DAQ scripts and various monitoring features are already tested and fully operational. The current ROC implementation uses the HADES-TRBv2 [3] with a MAPS-specific addon board [4]. Moreover, the CCU has been implemented on the FPGA of the TRBv2 board from the HADES experiment. The CCU distributes ROC controlling messages over three prioritized channels, multiplexed with prioritized Round Robin on one optical fibre. Clock distribution and network synchronization is performed using designated, equally long LVDS lines. In order to maintain the synchronization of all Front-Ends, the CCU transmitts deterministic SYNC pulses to all ROCs over the LVDS cables. After the SYNC, a frame request is sent to acquire the frame simultaniously on all ROCs. Therefore, if one sensor runs out-of-sync or experiences a major error, the problem is immediately recognized and the frame can be discarded from the ROCs keeping the data consistent.

Current configuration supports up to 4 Mi26 sensors per Trbv2. A setup consisting of 2 ROCs, each connected to 2 Mi26 is currently being tested (see picture below). The network operates fully synchronous without any measurable deviations. The CCU performs well and the data is extracted via TrbNet Hubs with up to 50 MByte/s to the PC. This setup can be further extended. The network is highly scalable and will be further improved with newer ROC versions, using for instance the recently developed TRBv3 board. With appropriate addon boards, such ROC could handle up to 40 Mi26 sensors. This new setup is planned to be tested under in-beam conditions soon.

In the final version of the MVD, the data format will be kept, and parts of the TrbNet protocol, namely the monitoring and slow-control can be incorporated into CBM-Net.

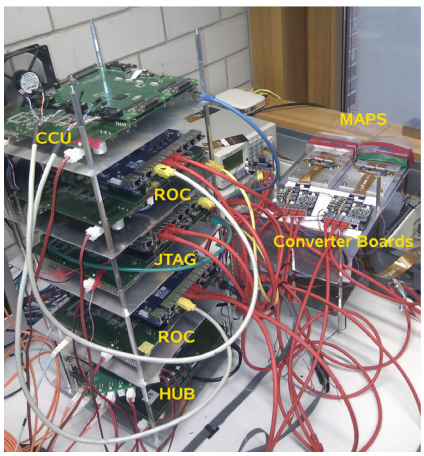

Figure 1: The tested MVD Prototype Readout chain.

References

[1] C.Schrader et al., Status of the CBM-MVD prototype readout, GSI Report 2011

[2] J. Michel et al., The upgraded HADES trigger and data acquisition system, TWEPP 2011 Vienna

[3] I. Fröhlich et al., A General Purpose Trigger and Readout Board for HADES and FAIR-Experiments, IEEE Trans.Nucl.Sci. 55 (2008)

[4] C. Schrader et al., A demonstrator for the Micro-Vertex-Detector of the CBM experiment, PoS 2010 Bormio

* Work supported by GSI, BMBF contract No. 06FY9099I, HIC for FAIR.

A latch-up protected power supply for the CBM-MVD*

M. Koziel, N. Bialas, C. Schrader, S. Schreiber, and J. Stroth for the CBM-MVD collaboration
IKF Frankfurt am Main, Germany, February 10, 2012

This report will summarize the implementation of a latch-up protected power supply for the CBM Micro Vertex Detector.

Introduction

At the CBM experiment CMOS sensors will equip the Micro Vertex Detector (MVD) and they will be constantly exposed to high flux of variety of particles. Latch-up will occur regularly, and therefore protection system is needed. Latch-up is a term used to describe a particular type of short circuit related to creation of a low-impedance path between the power supply rails of a MOSFET circuit. This path is created due to parasitic PNPN thyristor structures formed by nearby NMOS and PMOS transistor. During normal operation the parasitic thyristor is off. Spikes of the bias voltages or the charge carrier injections caused by impinging particles may switch-on and latch the thyristor. If so, the structure can start to conduct high currents which can lead to permanent damage of devices.

Latch-up detection system - requirements and implementation

Since the latch-up can be cured with power cycling, an option to handle it is to bias the sensors with a dedicated and protected low-voltage power supply. This power supply should detect the over-current caused by latch-up states, quickly switch-off the power after detecting the latch-up, and bias the device again when latch-up state is over.

The latch-up detection is realized by the means of so called "shunt resistor" (R_{SHUNT}). During normal operation, sensor consumes the current of around 150 mA for stated before 3.3 V bias. This leads to the voltage drop on the R_{SHUNT} of 0.6 V. During the latch-up/overcurrent state, this voltage drop increase, reflecting an increase of the current consumption. The voltage from the shunt resistor is compared with the reference one by the mean of the LT1711 comparator. If the voltage across the R_{SHUNT} is higher than the reference, the switches S1 and S2 are opened and the linear regulators become disconnected from power lines. Consequently, the sensor is switched off. The measured switch-off time, between the over current state and 0 A consumption is 2 µs for the capacitive load of 1.2 µF. After the time set by the timer, the power supply is switched on again.

Figure 1 depicts the simplified schematic view of the latch-up protection system for the CBM-MVD sensors. The analog (VDA) and digital power (VDD) supply channels are covered. The main elements used are:

- A shunt resistor $R_{SHUNT} = 4\Omega$. It is located before the voltage regulator in order to allow using larger resistances and determining a larger voltage drop of 0.6V across this resistor. Such a high V_{SHUNT} reduces the sensitivity of the latch-up detection system to pick-up noise and allows using this voltage without amplification for a comparison with the reference one.
- A fast comparator (4ns propagation time) with output latch - LT1711
- A CMOS linear regulator. It features 3.3V/500mA fixed output voltage, 5.5V input voltage and a low quiescent current. The sense input of this device is used to compensate for voltage drop along cables and to achieve the 3.3 V at the destination point. The regulator features a ramping output voltage (Vout arises to nominal value within 500 µs) which allows reducing the current consumption during switching the sensors on. Consequently, lower threshold values for the over current states may be applied.
- A timer LTC6993-1
- A fast MOS switch IRF7410 (S1 and S2)

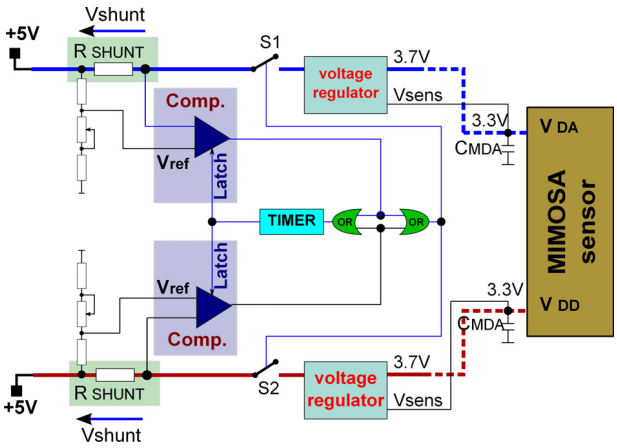

Figure 1: *Schematic view on latch-up protected power supply for the CBM-MVD sensors.*

Summary

The latch-up detection system discussed above was implemented in the Front End Board for the CBM-MVD readout system. It allows to detect over-current states and react to them by switching the sensors off within 2 µs.

* Work supported by GSI, BMBF (06FY9099I), ULISI (EU-FP7), and HIC for FAIR.

A simulation model for irradiated and partially depleted Monolithic Active Pixel Sensors*

M. Domachowski[1], *M. Deveaux*[1], *D. Doering*[1], *C. Dritsa*[1,2], *C. Müntz*[1], *C. Trageser*[1], *and J. Stroth*[1,3]

[1]Goethe-Universität, Frankfurt am Main; [2]Justus-Liebig-Universität, Giessen; [3]GSI Helmholtzzentrum für Schwerionenforschung, Darmstadt

The radiation tolerance of Monolithic Active Pixel Sensors (MAPS) has been significantly improved during the last few years. This was achieved by using a dedicated high resistivity epitaxial layer, which allows for a partial depletion of this active volume. The resulting acceleration of the charge collection counteracts the lower lifetime of charge carriers, which is found in silicon with radiation induced bulk damage. Moreover, the signal charge is concentrated in the central pixels of the hit clusters, which turns into smaller clusters and a higher S/N.

In the simulation framework of the CBM-experiment (CBMRoot), the response of MAPS is simulated with a dedicated Digitizer [1]. This response model is based on a parametrization of data obtained from MAPS with a standard epitaxial layer. We tested whether the existing Digitizer can be adopted to the response of the novel sensor generation.

The study was based on experimental data taken from MIMOSA-18AHR prototypes [2] delivered by the PICSEL group of IPHC Strasbourg. MIMOSA-18AHR is based on a $0.35\ \mu\mathrm{m}$ CMOS process and hosts four types of pixels with a pitch of 10 μm, 12.5 μm and 25 μm. The epitaxial layer of the chip has a resistivity of 400 $\Omega\ \mathrm{cm}$ and a thickness of 15 μm. First, the sensors were irradiated with up to $3{\cdot}10^{14}\ \mathrm{n_{eq}/cm^2}$. In a second step they were evaluated with β-rays of a $^{106}\mathrm{Ru}$ source. The data obtained was used to measure the pulse hight of the pixels in hit clusters, which provided the necessary input for tuning the Digitizer.

The accuracy of the simulation model is benchmarked with the so-called "'accumulated charge plot"' shown in Figure 1. This plot is provided by ordering the signals of the 25 pixels of a hit cluster according to their S/N. In a next step, the charge for the $(1 \leq \mathrm{N} \leq 25)$ pixels with highest S/N is summed up for the individual clusters. Afterwards, the sum is filled into the $\mathrm{N^{th}}$ of 25 histograms and the procedure is repeated for the next cluster. The 25 histograms obtained exhibit a Landau distribution which is fitted subsequently. The "'accumulated charge plot"' shows the most probable value (MPV) of the charge obtained from the fit of the $\mathrm{N^{th}}$ histogram as function of N.

The plot illustrates information about the distribution of the charge over the pixels of the cluster. For instance, the figure shown provides the information that roughly 45 % of the cluster charge is collected by the seed pixel $(\mathrm{N} = 1)$ while a group of 3 pixels already collect almost the total charge of the cluster. Decreasing charge $(\mathrm{N} > 15)$ is an artifact due to noise and the ordering with regard to S/N.

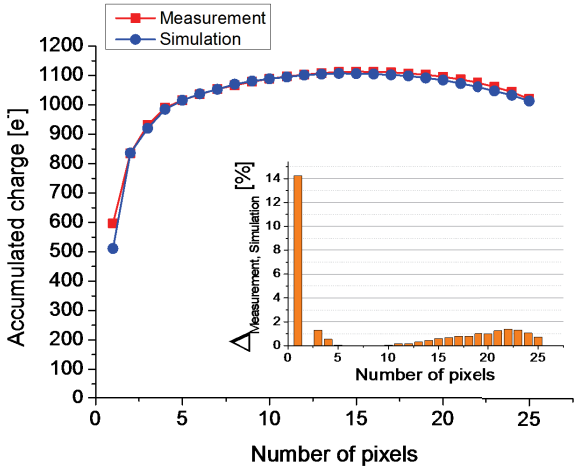

Figure 1: "'Accumulated charge plot"' (see text) for the 10 μm pixels of a MIMOSA 18-AHR irradiated with $10^{13}\ \mathrm{n_{eq}/cm^2}$. The measured and the simulated sensor response is compared.

The plot was generated with measured and simulated data after tuning the model parameters of the Digitizer. A representative example for a pixel irradiated with $10^{13}\ \mathrm{n_{eq}/cm^2}$ and with 10 μm pixel pitch is shown in Figure 1. One observes that all pixels except of the seed pixel are accurately described. For the seed pixel, the simulation underestimates the signal charge by $\sim 14\%$. This effect remains to be understood in detail. However, it is not expected to show a significant impact on potential simulation results.

We conclude that the Digitizer is suited for describing sensors with high resistivity epitaxial layer. This applies for unirradiated sensors as well as for sensors irradiated with non-ionizing doses.

The updated sensor models will be part of the upcoming novel version of the MVD-Digitizer software.

References

[1] Christina Dritsa, A detector response model for CMOS Monolithic Active Pixel Sensors, Proceedings of Science, 2010

[2] IPHC, Strasbourg University, http://www.iphc.cnrs.fr/List-of-MIMOSA-chips.html

*Work supported by GSI Helmholtzzentrum für Schwerionenforschung, BMBF (06FY9099I), HIC for FAIR

Simulation of the material budget of the CBM-MVD for SIS-100*

T. Tischler, S. Amar-Youcef, M. Deveaux, M. Koziel, C. Müntz, C. Schrader, and J. Stroth for the CBM-MVD Collaboration

Institut für Kernphysik, Goethe-Universität, Frankfurt

For the CBM Micro Vertex Detector (MVD) to be installed at SIS-100, improved geometries of the detector have been studied within the CbmRoot framework. To do so, a simplified model of the MVD including sensors (MAPS [1]), their support in the active area (CVD diamond) and copper heat sinks has been worked out [2]. To allow for using the CAD-model within the CbmRoot framework, it has been transformed into a Root-geometry by a customized converter provided by the Panda Collaboration [3].

Simulation of the material budget

Taking advantage of existing FairRoot classes, a new MVD-specific class has been written to estimate the material budget. The test-particles, e.g. neutrinos, are transported through the detector geometry. If they cross a given detector component, the position and the material of this component is stored in order to estimate the total material budget. The material budget is described by the percentage of the radiation length for a given polar angle θ in a given ϕ-range.

Results

The estimation of the material budget is currently performed for two cases: the prototype of the MVD, and for the MVD for SIS-100, see figures 1 and 2, respectively.

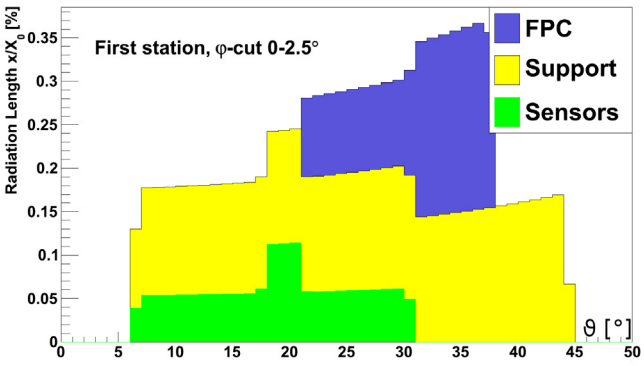

Figure 1: Material budget of the MVD prototype including sensors (50μm thin MIMOSA-26, double sided arrangement), sensor support (150μm thin CVD diamond) and a dedicated FlexPrint-Cable (FPC, $0.0861\%X_0$, [4]) for the sensor readout (one FPC in the active area only).

*Work supported by the GSI Helmholtzzentrum für Schwerionenforschung, BMBF (06FY9099I), ULISI (EU-FP7), HIC for FAIR, H-QM Helmholtz Research School.

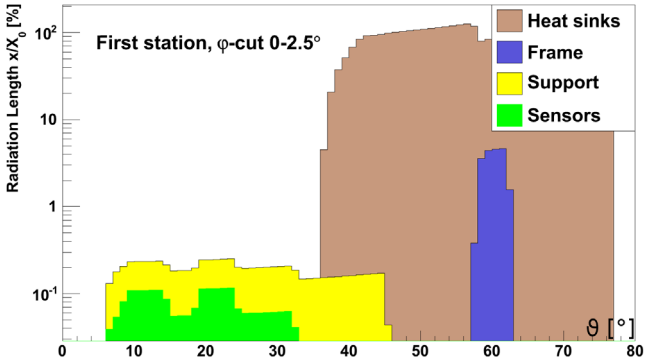

Figure 2: Material budget of the MVD for SIS-100 including sensors (50μm thin MIMOSIS-1, double sided arrangement), sensor support (150μm thin CVD diamond), an aluminum frame and heat sinks.

The MIMOSIS-1 sensors are currently under development. Nevertheless a first implementation has been done in order to test the compatibility of the preliminary geometrical layout of this sensor with respect to the acceptance coverage required by the CBM experiment. The heat sinks, which are placed outside of the acceptance, are made out of copper (to be replaced by aluminum). The aluminum frame is needed to mount the heat sinks for the sensors and to support the read-out electronics.

Conclusion

A successful implementation of the MVD prototype as well as SIS-100 geometry in CbmRoot is presented, starting from realistic CAD models. This allows estimating the material budget by considering the main detector building blocks based on realistic geometries and sensor integration. It has been shown that the material budget of few $0.1\%X_0$, required by the CBM experiment, is within reach.

References

[1] MIMOSA-26, DOI: 10.1016/j.nima.2010.03.043.

[2] T. Tischler et. al , GSI Scientific Report 2010, PHN-NQM-CBM-06.

[3] Panda CAD-Converter, panda-wiki.gsi.de.

[4] C. Schrader, 18th CBM Collaboration Meeting, 2011, Beijing, China.

Studies on the tracking efficiency of the CBM Micro-Vertex-Detector (MVD) *

Christian Trageser[1], *Michael Deveaux*[1], *Christina Dritsa*[1,2], *and Joachim Stroth*[1]
[1]Goethe - Universität, Frankfurt; [2]Justus-Liebig Universität, Gießen

The CBM MVD is to provide good sensitivity together with reasonably low device complexity and costs. To find a good compromise, we studied the STS to MVD track matching for different design options.

The cost efficient standard geometry of the MVD for SIS-300 bases on two stations located 5 cm and 10 cm downstream the target. Tracks found in the Silicon Tracking System (STS) of CBM are extrapolated and extended to this MVD. This is complicated by the large gap (20 cm) between both detectors and the high hit density (up to few $10/\mathrm{mm}^2$) caused by a pile-up of several collisions in the MVD. Mismatches in tracking, as caused by a wrongly attached hits, were feared to deteriorate impact parameter (IP) resolution of the MVD and to generate false decay vertex indications.

We studied the MVD geometries listed in Table 1 with 25 AGeV Au-Au collisions (+ δ electrons). The collision rates scaled from $\sim 3 \times 10^4$ /s (pile-up=0) to $\sim 3 \times 10^5$ /s (pile up = 10). The default STS geometry and the L1 tracking package of the CBMRoot Release April 2011 were used "as is". They might show better performances after parameter tuning. Only "long", primary tracks with >4 hits in the STS were considered and defined as "good" ("bad") if all related MVD-hits were correctly (falsely) assigned. Sub-classes account for hits missing due to the limited geometrical acceptance or inefficiencies of the MVD (see Table 2).

Most background tracks in the open charm reconstruction are emitted by the fireball of the Au-Au collision (PV), which turns into $IP = 0$. True signal tracks originate from a secondary decay vertex (SV) and their true IP is > 0. If the uncertainty of the IP-measurement is smaller than the width of the IP distribution of the signal, rejecting tracks with small IP forms a powerful cut. However, this accuracy is observed for tracks classified as "Good-1" and "Good-2" only. Cutting on IP/σ_{IP} may compensate but σ_{IP} is regularly underestimated for tracks with wrong hits.

Figure 1 shows the background rejection capability of the major single track cuts used in open charm analysis. We required $p > 1$ GeV/c, $p_t > 0.3$ GeV/c and $IP/\sigma_{IP} > 6$. The number of accepted background tracks per frame (or event) are shown as function of MVD geometry and collision pile-up. The color represents the classification of the tracks. The background is formed almost exclusively by tracks with missing or falsely attached hits and gets more pronounced with increasing pile-up. It is substantially reduced by adding one or two stations to the MVD-2.

Our results suggest that one needs an almost perfect track finding to exploit the sensitivity of the MVD. Accounting for this fact, one has to make sure that the detector provides a reliable and sufficient input for the tracking algorithms. Adding one or two tracking stations between MVD and STS might help to match this requirement.

Station nmb.:	1	2	3	4
Distance to target [cm]	5	10	15	20
Inner radius [mm]	5.5	5.5	8.3	11
Outer radius [mm]	25	50	75	100
Thickness [μm]	300	500	500	600
MVD2	X	X		
MVD3	X	X	X	
MVD4	X	X	X	X

Table 1: MVD geometries studied.

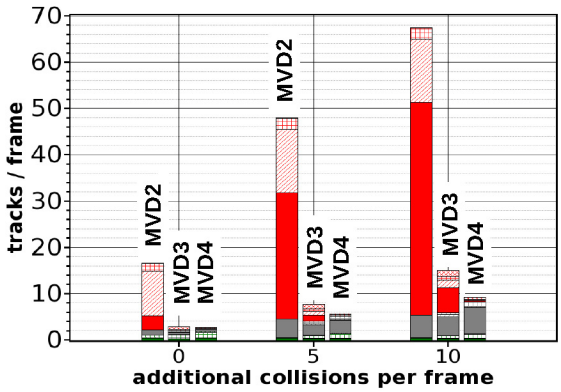

Figure 1: Falsely accepted background tracks per central Au-Au collision. Color code see Table 2.

name	case	○	×	□	■	Colorcode
Good Tracks	1	X				
	2	X		X		
	3	X			X	
	4	X		X	X	
Mixed Tracks	1	X	X			
	2	X	X	X		
	3	X	X		X	
	4	X	X	X	X	
Ghost Tracks	1		X			
	2		X	X		
	3		X		X	
	4		X	X	X	

Table 2: Definition of track classes - Hits correctly (○), falsely (×) assigned, not accepted (□), not detected (■).

* This work has been supported by the BMBF (06FY9099I), HIC for FAIR and GSI

Performance simulations of the CBM Silicon Tracking System*

A. Kotynia[1] *and J.M. Heuser*[2]
[1]Goethe University, Frankfurt, Germany; [2]GSI, Darmstadt, Germany

The layout of the Silicon Tracking System (STS) has been the object of extensive studies during the last years: the optimization of its performance has driven several choices concerning soft geometry parameters, such as detector pitch, number of tracking stations and their placement within the magnet volume. The STS performance studies presented in this report show the progress made with optimization of the stations and sensors layout, based on the increasing knowledge of the hardware involved in the detector. Relevant parameters such as the hit and the track reconstruction efficiencies and track parameters were monitored.

Detector layout

The STS consists of eight tracking layers located 30, 40, 50, 60, 70, 80, 90, 100 cm downstream of the target. Each layer is an array of vertical modules containing 300 μm thick double-sided strip sensors. The strip pitch is 58 μm on both sides. Two variations of sensor arrangement in a ladder have been studied (Fig. 1):

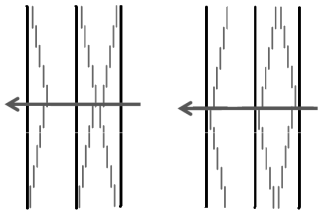

Figure 1: Side view of two neighboring STS ladders: left corresponds to description number 1, right to description number 2.

1. The outer sensors on top and on the bottom are mounted as closest to the support ladder. This creates a gap of approximately 2 cm along the beam in the inner part of station (close to beam pipe).
2. The inner most sensors in ladder are mounted closer to the support structure. In such setup, the gap between neighboring ladder is on the top and on the bottom of the station.

Both setups have been tested, and there was no significant difference with the yield of reconstructed K_s and Λ (Table 1). Also a possibility of different strip orientation in sensors has been investigated. Due to difficulties with the production of double-metalization on double-sided sensors, it was proposed to decrease the stereo angle from 15° with double-metalization [1] to 8° without double-metalization in order to decrease the size of the inactive corners in each sensor. The results from STS tracking performance as well as from K_s and Λ reconstruction for the two stereo angles have been summarized in Table 2.

Table 1: Results with different sensors arrangements on the STS ladder.

Sensor arrangement	Tracking efficiency	K_s S/B	Λ S/B	K_s/ev	Λ/ev
1	75.6%	0.40	1.17	2.54	2.95
2	75.4%	0.39	0.93	2.41	3.01

Table 2: Results with different stereo angle in STS sensors.

Front side	Back side	Tracking efficiency	Fake/Real hits	K_s S/B	Λ S/B
-7.5°	$+7.5^\circ$	0.40	4.11	0.40	1.17
-8.0°	0°	0.39	2.53	0.42	1.26

Performance studies

The layout presented above was used to implement the STS in the CBM simulation framework. This implementation includes the complete chain of physical processes caused by a charged particle traversing the detector, from charge creation in the silicon to the digital output signals. Signal sharing between strips together with charge collection inefficiency and Lorentz shift due to the presence of the magnetic field, channel dead time, and single-channel inefficiency are present in the simulations. Applications of realistic detector response functions together with a Cellular Automaton for track finding and a Kalman Filter for track fitting results in a track finding efficiency of 97% for fast primary tracks and 75% for secondary tracks, with a momentum resolution of 1.2%.

Next steps

In order to compare the simulation results with those obtained from in-beam experiments, a special geometry was prepared and implemented in simulation framework with the possibility of changing detector response parameters. However, such parameters are not yet defined or measured and consequently the full comparison of simulation with experimental data will be the subject of studies in the near future.

References

[1] R. Karabowicz, A. Kotynia, J.M. Heuser "Progress with layout studies of the CBM Silicon Tracking System", CBM Progress Report 2008

*Supported by EU/FP7 HadronPhysics2 and Helmholtz International Center for FAIR

Radiation environment of the CBM Silicon Tracking System

V. Friese
GSI, Darmstadt, Germany

Among the detector systems of the CBM experiment, the Silicon Tracking System (STS), being located in close proximity to the target, will have to face the harshest environment in terms of both ionising and non-ionising radiation. Of particular importance is the latter, causing damage effects in the bulk material which lead to an increased leakage current and, consequently, to an increase of the power dissipation of the sensors.

The standard tool to calculate the non-ionising irradiation is the FLUKA package, which is believed to provide the best physics description in particular for low-energy neutrons. Such calculations, however, are quite expensive in terms of CPU time and require expert knowledge of the FLUKA program. In this report, we present results derived from transport simulations with the standard CBM software `cbmroot`, using the GEANT3 transport engine with the GEISHA model for hadronic interactions, with an energy threshold of 1 keV for neutron production. The calculations were performed for the CBM setup comprising the STS and the muon system, i. e. with a heavy absorber directly behind the last STS station. Input events are minimum bias Au+Au collisions at 25A GeV generated with UrQMD. The results are scaled to $5 \cdot 10^{13}$ collisions, corresponding to a typical CBM run year of two effective months at 10 MHz interaction rate.

The non-ionising dose was calculated by counting the particles traversing the sensitive area of the silicon stations, giving each particle a weight (NIEL factor) according to its type and energy. The relative damage functions for neutrons, protons, pions and electrons were taken from the tabulations in [1]; the effect of other particle types was neglected. Figure 1 shows the results of this calculation for the first and last station, respectively. The maximal fluence is seen closest to the beam; it ranges from $4.5 \cdot 10^{13}\,\mathrm{n_{eq}/cm^2}$ (station 1) to $1.8 \cdot 10^{13}\,\mathrm{n_{eq}/cm^2}$ (station 8). In these inner parts, pions are the dominating source in the first stations, while the relative neutron contribution increases with distance from the target and reaches that of pions for the last station. In all stations, the radial profile of the neutron fluence is less steep than that of the charged hadrons; consequently, they dominate the total radiation at the periphery of the stations.

The leakage current is directly proportional to the non-ionising fluence [2]: $I_{leak} = \alpha V \Phi$, with the damage constant $\alpha = 4.73 \cdot 10^{-4}$ eV/K at room temperature. Since it is a strong function of the temperature [3], the STS will be operated in a thermal enclosure. Here, we assume an operating temperature of $-10\,^{\circ}$C, at which the leakage current is reduced to 6.3% of its value at room temperature. Under this assumption, we obtain a maximal current of $3.4\,\mu\mathrm{A/cm^2}$ for station 1 and $1.4\,\mu\mathrm{A/cm^2}$ for station 8. Assuming further an operating voltage of 120 V, corresponding to twice the full depletion voltage for non-irradiated sensors, the maximal power dissipation on the sensor is $4.1\,\mathrm{mW/cm^2}$ for station 1 and $1.6\,\mathrm{mW/cm^2}$ for station 8.

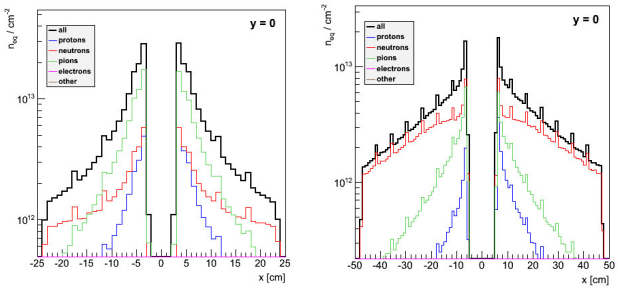

Figure 1: Non-ionising fluence in the bending plane for station 1 (left) and station 8 (right). The spikes are an artefact of the calculation, resulting from overlapping sensors.

The ionising dose was calculated by summing up the energy losses of the charged particles traversing the sensitive area as delivered by the GEANT calculation. We obtain maximal values of 23.7 kGy for station 1 and 7.2 kGy for station 8, respectively (see Fig. 2). It should be noted that these values need not coincide with the energy deposited in the material, since secondary electrons might leave the sensitive volume in particular when created close to the surface. Thus, the values presented here can be regarded as upper limits.

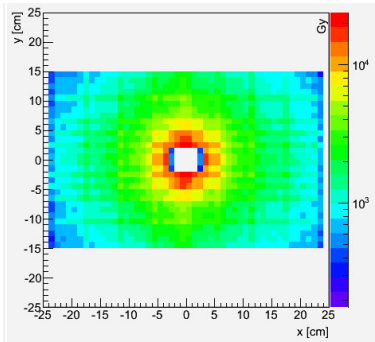

Figure 2: Total ionising dose for station 1

References

[1] A. Vasilescu and G. Lindstroem, *Displacement damage in silicon*, on-line compilation [http://sesam.desy.de/members/gunnar/Si-dfuncs.html]

[2] M. Moll *et al.*, Nucl. Instr. Meth. Phys. Res. **A 426** (1999) 87

[3] H. J. Ziock *et al.*, IEEE Trans. Nucl. Sci. **40** (1993) 344

Radiation damage modelling for the development of microstrip detectors for the CBM Silicon Tracking System*

S. Chatterji[1], *M. Singla*[2], *A. Lymanets*[2,3], *M. Merkin*[4], *and J.M. Heuser*[1]

[1]GSI, Darmstadt, Germany; [2]University of Frankfurt, Germany; [3]KINR, Kiev, Ukraine; [4]Moscow State Univ., Russia

The Silicon Tracking System (STS) of the CBM experiment requires radiation hard microstrip detectors standing neutron fluence up to 1×10^{14} $n_{eq}cm^{-2}$. We have implemented a radiation damage model (Perugia trap model) [1] into the SYNOPSYS TCAD simulation package and compared the results for double sided silicon strip detectors (DSSDs) with measurements of irradiated prototypes. This validated the applicability of the simulation tool towards optimizing the design and operating scenario of forthcoming full-size prototype detectors.

Synopsys [2], a finite element semiconductor simulation package, was used to determine the electrical behaviour of these devices. The effective doping concentration (N_{eff}) is parameterized using the Hamburg model while the minority carrier lifetime τ has been changed in our simulation package using the definition of Kraner's as follows:

$$1/\tau = 1/\tau_0 + \beta\,\phi_{eq}$$

where τ_0 is the minority carrier lifetime of the initial wafer, ϕ_{eq} is the integrated fluence, and β is the trapping time. The value of τ_0 have been set to 1 ms for electrons and 0.3 ms for holes as is expected for detector grade silicon.

Some of the CBM02 prototype DSSDs were irradiated at KRI cyclotron facility in St. Petersburg, Russia. These detectors were measured just after irradiation without any periods of annealing. The variation of leakage current and interstrip resistance with neutron fluence has been measured. The TCAD simulation is able to reproduce the measured observations as can be seen from Figures 1 and 2. The full depletion voltage (V_{fd}) indicates that the type inversion occurs at around 11.2×10^{12} $n_{eq}cm^{-2}$. In order to investigate the life time of DSSDs, it is imperative to extract the charge collection efficiency as a function of fluence. For this one has to understand strip isolation in particular on the ohmic side. The strip isolation in turn can be understood by studying interstrip resistance (R_{int}). It has been found that for the fluences up to type inversion, R_{int} is very low below full depletion and it increases steeply at full depletion and continues to increase slightly thereafter. However for type-inverted sensors, interstrip resistance is of the order of tens of MΩ even below full depletion and saturates at around 100 MΩ after the operating voltage is reached. One can observe that the operating voltage is much higher than V_{fd} especially in case of high fluences.

Figure 3 shows the variation of collected charge and cross talk versus V_{bias} for the same fluences as used for irradiation. The charge collection follows the same variation as the measured R_{int} does with V_{bias}. The crosstalk

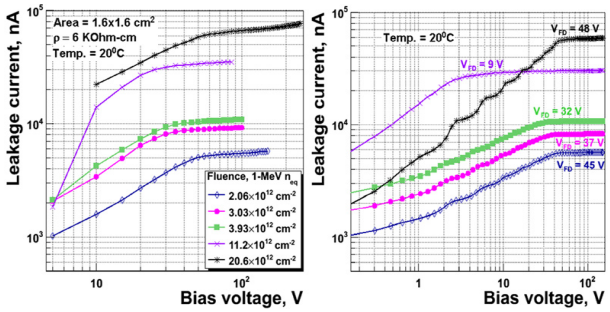

Figure 1: Comparision of measured vs. simulated leakage current for irradiated DSSDs.

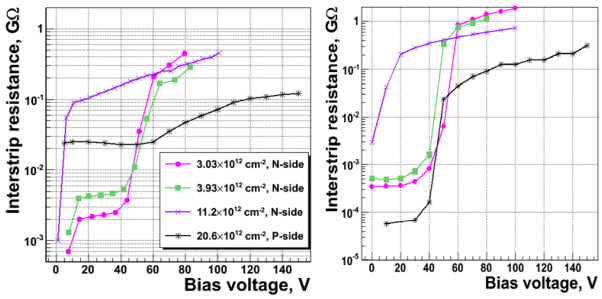

Figure 2: Comparision of measured vs. simulated interstrip resistance for irradiated DSSDs.

initially increases till V_{fd} is reached since the charge sharing between neighbouring strips increases. After V_{fd} is reached, the cross talk decreases since the bias also improves the drift velocity, which tends to reduce charge sharing. The *AC* interstrip capacitance has also been measured and simulated since it is the dominant contributor to the capacitive noise. Its value has been found to be around 2.09 pF/cm on the ohmic side and 1.6 pF/cm on the junction side. Also we have noted that C_{int} does not change appreciably with irradiation.

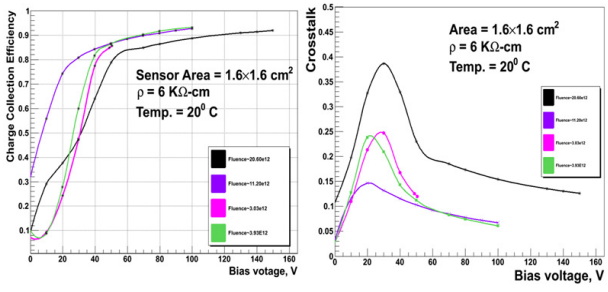

Figure 3: Expected charge collection efficiency and cross talk for the irradiated DSSDs as a function of V_{bias}.

References

[1] IEEE Trans. Nucl. Sci. NS-53 (5) (2006) 2971

[2] http://www.synopsys.com

* Supported by EU-FP7 HadronPhysics2 and HICforFAIR

Optimization of microstrip detectors for the CBM Silicon Tracking System *

J. M. Heuser[1], S. Chatterji[1], C. J. Schmidt[1], V. Kleipa[1], C. Simons[1], W. Niebur[1], J. Eschke[1], T. Balog[1,2], L. Long[3], H. G. Ortlepp[3], O. Brodersen[3], A. Lymanets[4,5], I. Sorokin[4,5], H. Malygina[4,5], M. Singla[4], P. Ghosh[4], Y. Bansal[6], N. Joshi[6], N. Sharma[6], and N. Tiwari[6]

[1]GSI, Darmstadt, Germany; [2]Comenius University, Bratislava, Slovakia; [3]CiS Forschungsinstitut für Mikrosensorik und Photovoltaik GmbH, Erfurt, Germany; [4]Goethe University, Frankfurt, Germany; [5]Kiev Institute for Nuclear Research, Kiev, Ukraine; [6]Mody Institute of Technology and Science, Lakshmangarh, India

A novel radiation tolerant structure that is expected to improve the application of double-sided silicon microstrip detector in harsh radiation environments as with the CBM experiment has been developed by CiS [1]. A sample of small prototype detectors produced at CiS has been exposed to several neutron fluences and subsequently characterized at GSI. The structure could be integraded in a forthcoming full-size prototype detector for the CBM Silicon Tracking System. Meanwhile the third prototype of a full-size microstrip detector for the CBM Silicon Tracking Detector System is being designed in cooperation of GSI and CiS. Based on the evaluation of the second prototype [2] several design optimizations are being applied and processing variations explored.

Radiation tolerant prototype FSD-CBM04

A new radiation tolerant structure ("Shottky barrier") has been designed by CiS in a BMWI supported project and produced on small double-sided microstrip detector prototypes of 256 by 256 orthogonal strips of 50 μm pitch. The Shottky barriers are expected to increase the charge collection on the ohmic sides of double-sided strip detectors after irradiation. GSI is research partner of CiS for the evaluation of the detectors in in-beam experiments with multi-channel front-end electronics. The detectors were checked in the GSI detector laboratory for the quality of their integrated *AC* coupling capacitors, the bulk currents and bulk capacitances as a function of the bias voltage applied. With some of the detectors, comprising a suitable biassing structure, the interstrip resistances and capacitances were directly measured. Precision equipment like a semi-automatic wafer probe station, source-measure units and LCR meters have been utilized and custom-specific programs for their automated control and readout developed. Out of the available 45 detectors a sub-set of 20 was selected and grouped into 4 irradiation samples. They were sent to Institute Jozef Stefan, Lubljana, Slowenia, and exposed to 1 MeV equivalent neutron fluences of 1×10^{12}, 1×10^{13}, 3×10^{13} and 1×10^{14} cm^{-2} within the EU-FP7 Project AIDA. An additional sample without radiation exposure is available for reference. The irradiated detectors were kept at temperatures of around -20° C. During testing they were handled at room temperature. The temperatures are logged to take into account annealing effects. The detectors are finally installed into circuit boards and complemented with front-end electronics. They will be operated in a beam test with 2.4 GeV protons scheduled for January 2012 at COSY, Research Center Jülich, Germany. A tracking telescope will be set up consisting of three stations of silicon microstrip detectors read out with self-triggering front-end electronics based on the *n-XYTER* chip. Two stations were already operated there in 2010 [3]. The third station will comprise the FSD-CBM04 detectors under test. The measurement programme aims at the determination of the charge collection efficiency and charge distribution onto neighbouring strips as a function of the detectors' neutron exposure and operating conditions.

Full-size prototype CBM05

In preparation of the next full-size prototype microstrip detector CBM05 we have investigated the short circuits in the *AC* coupling layer of the current full-size prototype CBM03 [2]. The thin oxide layer was identifed to be shorted in certain areas. This may be due to the quite complex structure of the detector. The processing steps for 19 masks, including the two metal layers per side, may have introduced stress there. A more sturdy layout including a slightly increased thickness of some of the layers has been proposed for the next prototype. Several technological tests are in preparation, reusing the masks of layout CBM03 for the production of a single-sided prototype CBM03'. After having evaluated this intermediate prototype in the beginning of 2012 we will launch the production of a batch of the next double-sided full-size prototype CBM05. Like the previous prototype it comprises 2×1024 strips of 58 μm pitch arranged under a stereo angle of $\pm 7.5^\circ$ on an area of 62 mm by 62 mm. The detector is laid out for readout connections at its top and bottom edge, involving double-metal interconnections of the corner strips so that sectors of daisy-chained detectors can be built and arranged on the Silicon Tracker's ladders.

References

[1] http://www.cismst.de

[2] GSI Scientific Reports 2009 70 and 2010 21

[3] GSI Scientific Report 2009 26

*Work supported by EU-FP7 HadronPhysics2, EU-FP7 AIDA, Helmholtz International Center for FAIR and Bundesministerium für Wirtschaft und Technologie INNO-KOM-Ost.

Performance of prototype Silicon Tracking Detectors for the CBM experiment*

H. Shang[1], *I. Sorokin*[2,3], *J. M. Heuser*[4], *and T. Balog*[4,5]

[1]Tsinghua University, Beijing, China; [2]FIAS, Goethe University Frankfurt, Frankfurt a. M., Germany; [3]KINR, Kiev, Ukraine; [4]GSI, Darmstadt, Germany; [5]Comenius University, Bratislava, Slovakia

Four demonstrator boards (named *2b-4 N001 ... N004*) were produced by SE SRTIIE in Kharkiv, Ukraine. Each of the boards integrated a double-sided CBM02-SPID detector with 256 strips on each side. The demonstrators were intended to be used in the upcoming beamtimes as reference tracking detectors and were tested in the laboratory therefore.

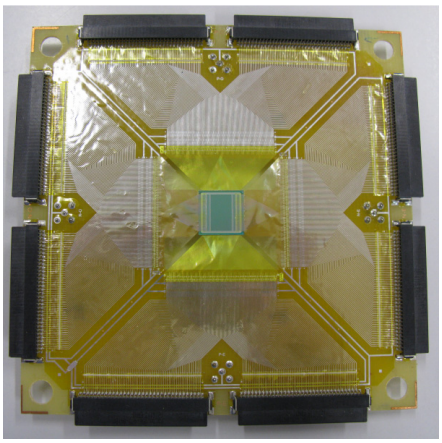

Figure 1: Demonstrator board *2b-4 N001*, n-side view.

First, the detectors were checked for defects in the DC-decoupling capacitors. Only one stip with a defect was found amoung the four boards.

Then current-voltage characteristics were measured. The full depletion kink, when observed, appeared around 80 V, as expected. The leackage current did not exceed 1 μA at 100 V (the operating voltage), which is normal.

One of the boards, the *2b-4 N003*, was installed into a detector station with n-XYTER-based [1] readout and tested with a β-source (^{90}Sr). After subtracting the slow shaper DC offsets (i.e. pedestals), clusters of various sizes (1 to 5) were reconstructed and the total signal amplitude was determined. The recent n-XYTER calibration [2] was applied. The measurement was repeated for a range of bias voltages (Fig. 3).

The signal amplitude after full depletion is compatible with the expected value of about 21.7 ke$^-$ (assuming 0.95 charge collection efficiency). The operating voltage of 100 V is proven to be a suitable value. The noise level in the assembled system was below 150 e$^-$ in most of the channels, which is way better than required.

* Supported by EU FP7 HadronPhysics2, HICforFAIR, HGS-HIRe for FAIR, and H-QM Helmholz Research School

The prepared detector system is going to be used as a reference tracking station in the upcoming beam tests.

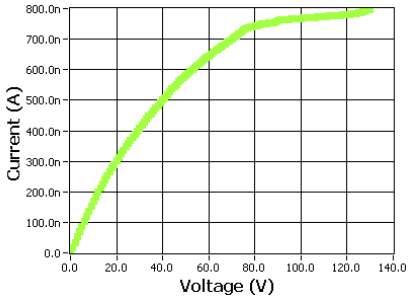

Figure 2: Current-voltage characteristic of *2b-4 N003*.

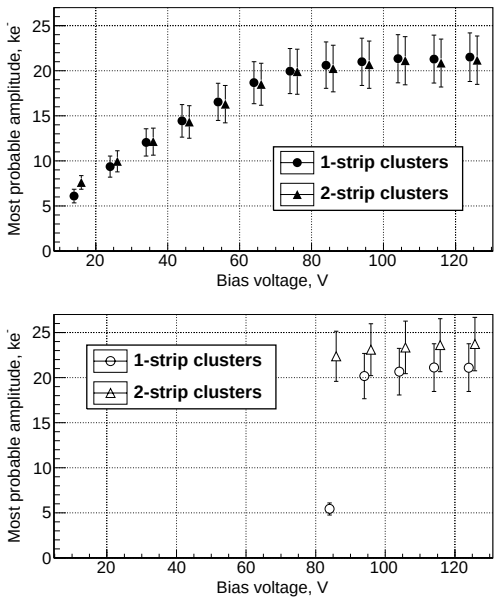

Figure 3: Signal amplitude vs. bias voltage on p- (top) and n-side (bottom) of demonstrator 2b-4 N003. Points are shifted by ± 1 V from original positions (15, 25, ... 125) for readability. Only the calibration uncertainty is shown.

References

[1] A.S. Brogna et al., Nucl. Instrum. Methods A 568 (2006) 301308

[2] T. Balog, A. Lymanets, *Calibration of n-XYTER front-end chip*, this report.

3D simulations of low-mass, low-noise analog readout cables for the CBM Silicon Tracking System *

M. Singla[1], *S. Chatterji*[2], *W.F.J. Mueller*[2], *V. Kleipa*[2], *and J.M. Heuser*[2]
[1]Goethe University, Frankfurt; [2]GSI, Darmstadt, Germany

In the CBM Silicon Tracking System kapton cables are used to transfer signal from sensors to front end electronics which is mounted outside the fiducial region. Simulations of these kapton cables have been performed with Raphael, a subpackage of Synopsys TCAD. The purpose of these simulations is to optimize the cables so as to reduce the capacitive and resistive load from these cables on front end electronics. For the validation of Raphael, kapton cables from the D0 experiment have been simulated and compared with ANSYS simulations reported in [1]. Table 1 shows an agreement between those simulations. For the equivalent noise charge (ENC) calculations [2], it is important to determine the contribution of the cables since their lengths could reach up to 50 cm for the inner modules of the CBM tracking system. Keeping various factors in mind including low radiation length, we explored several designs with aluminum and copper traces. An optimum is with copper traces having a cross-section of 16 μm $\times$ 8 μm. As marked in Fig. 1, and also shown in Table 2, the ENC of the optimized design is about 25% better than the current prototype, while maintaining the same material budget.

Spacer ϵ_r	Capacitance (pF/cm)		Relative Difference
	Ansys	Raphael	
1	0.328	0.337	2.27%
2	0.449	0.440	2.21%
3	0.566	0.531	6.19%

Table 1: Total Capacitance of D0 cables simulated with Ansys and Raphael.

Trace Dimesion μm x μm	Trace Material	Cap. (pF/cm)	Radiation length $\%X_0$	ENC e^-
16x8	Copper	0.60	0.11	1442
46x14	Aluminum	0.95	0.11	1831

Table 2: Comparison of various parameters for the present and the optimized designs.

A SPICE model has been implemented in TCAD package Sentaurus Device to study the transmission losses in the cable. Figure 2 shows the input/output pulses at 81 MHz and 320 MHz. For higher frequencies, the signal amplitude decreases and the pulse broadens at the input of the front end electronics which may lead to charge loss depending on the RC time constant of the shaper. Figure 3 (left panel) shows the schematics of the cable transmission line connected to the silicon detector and (right panel) the transmission losses versus frequency in the optimized design of a copper cable. The signal amplitude losses in the expected frequency range of CBM front end electronics (20 ns shaping time, 25 MHz) would result in $\approx$ 85% transmission.

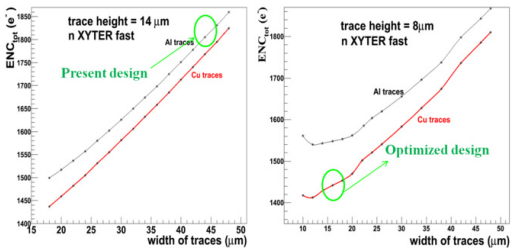

Figure 1: Total ENC vs. trace width for the CBM kapton cables having trace height of 14 μm and 8 μm.

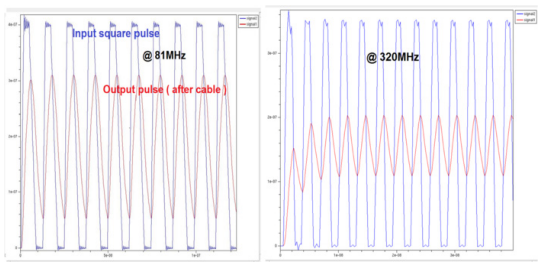

Figure 2: Transmission losses in cable at the frequency of 81 MHz and 320 MHz.

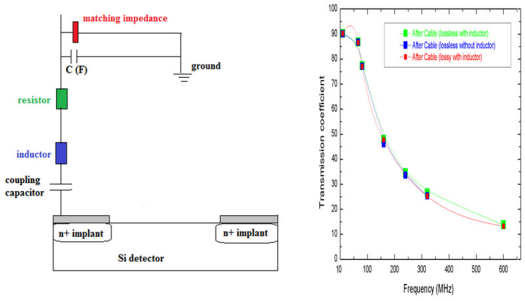

Figure 3: Schematics of cable transmission line and transmission in the optimized cable design with Cu traces.

References

[1] NIM A511 (2003) 121-123
[2] http://pdg.lbl.gov/2010/reviews/rpp2010-rev-particle-detectors-accel.pdf

* Supported by EU-FP7 HadronPhysics3 and HICforFAIR

Calibration of the n-XYTER front-end chip*

T. Balog[1,2] *and A. Lymanets*[3,4]

[1]GSI, Darmstadt, Germany; [2]Comenius University, Bratislava, Slovakia; [3]Goethe University, Frankfurt, Germany; [4]Kiev Institute for Nuclear Research, Kiev, Ukraine

The self-triggering n-XYTER chip has been developed for neutron physics experiments and is used also for early prototyping of several CBM detectors [1].

For a detailed understanding of the performance of the detectors, a calibration of the charge conversion is needed. In the following we describe a calibration with external pulsed signals as a general means of characterizing the behaviour of the front-end electronics.

Measurements

Charge injected into the front-end electronics can be realized through a known voltage step over a known capacitance. The input charge is then according to equation (1).

$$\Delta Q = C \cdot \Delta V \tag{1}$$

As a pulse generator model Philips PM 5786 has been used. This has allowed us to create input pulses with rise time 10 ns and duration 1 μs, as expected from silicon microstrip detectors. In the electronics a short rise time is needed to create a signal that can be easily measured by the fast shaper of each channel, having a shaping time of 19 ns. The pulse length is needed for the measurement of the proper signal amplitude in the slow shaper of each channel, with a shaping time of approx. 200 ns.

The output voltage of the generator can be adjusted between 128 mV and 5 V. Attenuators habe been used to reduce the signal amplitude into the dynamic range of the chip. Different combinations of 20dB and 10dB attenuators allowed us to reduce the signal amplitude by factors of 105, 330 and 1090, respectively.

For the voltage-to-charge conversion a capacitance of 1 pF has been used. This value is not the effective one, since one has to consider also parasitic capacitances. The total capacitance has been determined with an LCR meter as C = (2.3 $\pm$ 0.2) pF.

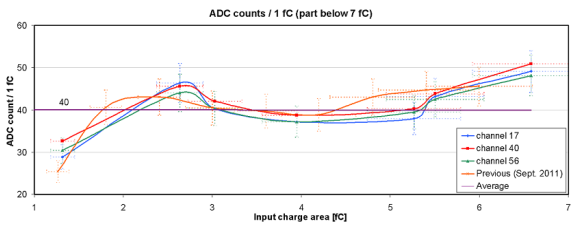

Figure 1: Energy calibration - ADC counts per 1 fC.

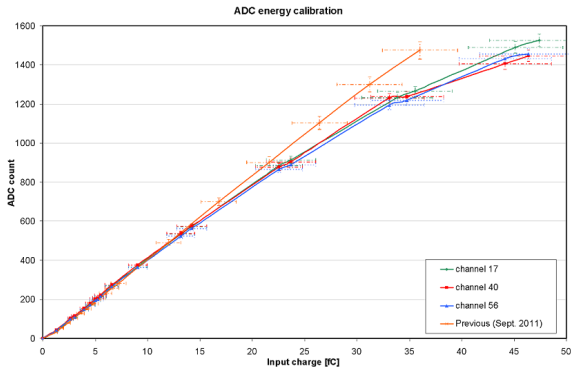

Figure 2: Energy calibration - ADC counts vs. charge.

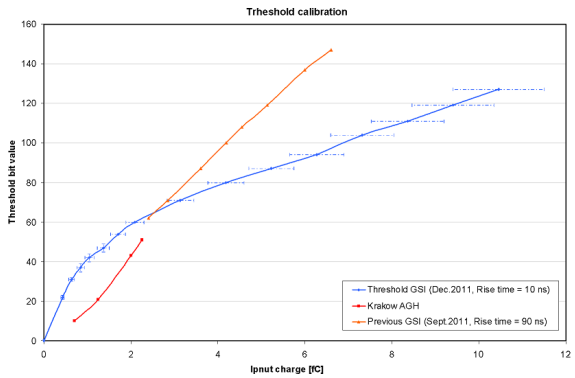

Figure 3: n-XYTER chip - threshold calibration.

We performed the calibration in September 2011 and in December 2011 for different n-XYTER front-end boards. There has not been any significant change for all measurements. The ADC energy calibration is shown in Figs. 1 and 2, and the threshold calibration is shown in Fig. 3.

Results

For one minimum ionizing particle (charge equal to 3.8 fC) the average ADC value 145 has been observed. Applied to the data from double-sided silicon microstrip detectors of the beam test of December 2010 [2] this leads to a charge collection efficiency of approximately 95%.

References

[1] GSI Scientific Report 2009 71

[2] GSI Scientific Report 2010 26

* Work supported by EU-FP7 HadronPhysics2, Helmholtz International Center for FAIR and EU-FP7 MC-PAD.

Performance of the n-XYTER-chip with external triggering*

J. Heuser[1], *V. Kyva*[2], *H. Malygina*[2,3], *V. Militsiya*[2], *Y. Panasenko*[2], *V. Pugatch*[2], *and I. Sorokin*[2,3]
[1]GSI, Darmstadt, Germany; [2]KINR, Kyiv, Ukraine; [3]Goethe University, Frankfurt, Germany

A double-sided prototype microstrip detector *CBM02-B2* and the n-XYTER-chip were used for the study. The n-XYTER [1] is a front-end detector readout ASIC that integrates 128 channels, each of them consists of low noise preamplifier and two shapers: 19 ns fast shaper and 139 ns slow shaper. The n-XYTER has two operational modes: self-triggering mode and external triggering mode.

MIPs simulation

We used a radioactive β-source ^{90}Sr-^{90}Y, which has a continuous spectrum up to 2.2 MeV. After passing through the thin Si-sensor the electrons were registered by a plastic scintillator. Then the scintillator triggered the n-XYTER processing of the signal from the Si-sensor. In the given experimental setup we had a trigger time delay less than 50 ns, excluding the ROC (Read-Out-Controller) delay. The scheme allowed us simulating the detection of minimum ionizing particles (MIPs) by selecting only high-energy electrons with $E \geqslant 1$ MeV. Since the peaking time of the n-XYTER's slow shaper is 139 ns, a 50 ns delay (Fig. 1, filled histogram) is appropriate for the external trigger. In this case a Landau-like spectrum is obtained from the MIPs. However, when the delay time is increased to 133 ns, no distinct-shape spectrum can be seen (Fig. 1, black histogram). Further increase up to 200 ns leads to the noise spectrum (Fig. 1, dashed histogram).

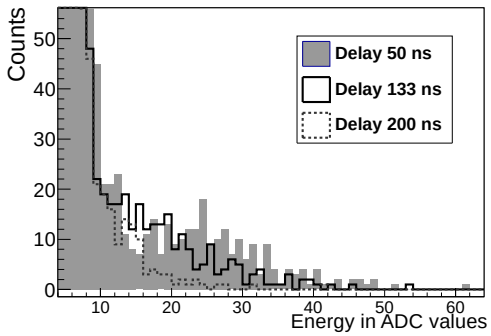

Figure 1: Energy spectrum of electrons with $E \geqslant 1$ MeV from one of the detector strips for different delays.

Even in the case of 50 ns delay the spectrum is not a pure Landau-distribution. This is because each MIP deposits the charge onto more than one strip. Thus, one needs to search for the distributed charge among several adjacent strips — a cluster. However, it is difficult to define clusters correctly. This is due to the fact that in our test set-up every second readout channel has higher noise than its neighbours channels. Such an unexpected noise behaviour concealed in the design of the microcable [2], that connects the Si-sensor with the n-XYTER. The cable has specific two-layer structure, which leads thereafter to the higher noise in the half of the strips and complicates clusters finding. This was corrected in a later design.

Amplitude vs delay

We investigated the dependence of the signal amplitude on the trigger delay time. A pulser generated both a square signal (near 200 mV) and a trigger signal (1.5 V) simultaneously. The square signal was then transferred through the attenuator to one of the channels of the n-XYTER. For the trigger signal we were able to change its delay time. For each new value of this delay we measured the amplitude of the measured resulting signal delivered by the n-XYTER chip. To achieve zero trigger delay we used an additional delay of square signal with effectively no trailing edge. As it can be clearly seen from Fig. 2, 10 ns trigger delay does not affect the resulting signal amplitude.

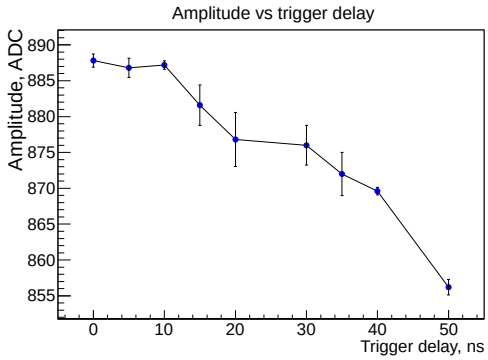

Figure 2: The resulting signal amplitude vs trigger delay (without the delay inside the read-out controller). The displayed errors are statistical errors.

References

[1] A.S. Bronga et al., Nucl. Instrum. Methods A568, 301 (2006).

[2] V.M. Borshchov et al., CBM Progress Report 2009, p. 15.

* Supported by EU FP7 HadronPhysics2, HICforFAIR, HGS-HIRe for FAIR, and H-QM Helmholz Research School

Rice formula applicability for noise rate estimation in the CBM and other experiments with self-triggered electronics: comparing the calculation to a measurement on example of the n-XYTER chip*

I. Sorokin[1,2], *W. F. J. Müller*[3], *and C. J. Schmidt*[3]

[1]Goethe University Frankfurt, Frankfurt, Germany; [2]KINR, Kiev, Ukraine; [3]GSI, Darmstadt, Germany

Self-trggered electronics is a natural solution for high-rate experiments with Poisson-like distributed events. One of the problems which arise when using self-triggered electronics is fake hits due to noise.

Self-triggered vs. triggered.

In a self-triggered system a noise hit is generated as soon as the instanteneous noise amplitude exceeds the threshold. This is in contrast to the conventional triggered systems, where a noise hit is generated only when a noise fluctuation conincides in time with the trigger. A triggered system is therefore inherently protected against fake hits.

Noise rate in a self-triggered system

When designing a self-triggered system the expected noise rate has to be estimated and taken into account. Underestimating the noise rate may result in overloading the data acquisition system and excessive background, whereas overestimating it may lower the efficiency.

Assuming a Gaussian noise with dispersion σ, the noise rate can be estimated with the Rice formula: [1]

$$f_t = \frac{f_0}{2} exp(-\frac{{\nu_t}^2}{2\sigma^2}) \quad (1)$$

where ν_t is the threshold; f_t is the threshold crossing rate, which the noise rate equals to provided the dead time is small; f_0 is the zero crossing rate, which depends on the system bandwidth. For a simple CR-$(RC)^3$ shaper with rise time τ, the zero crossing rate is given by: [1]

$$f_0 = \frac{1}{\pi\tau} \quad (2)$$

Applicability to n-XYTER

The Rice formula applicability to real systems was tested on example of the n-XYTER chip [2]. A large and stable in time noise was induced on a single n-XYTER channel by loading the input with 10 pF capacitance in series with 15.4 kOhm resistance. The noise rate was measured as a function of the `vth` threshold register. In order to compare the measurement to the Rice formula, the induced noise needed to be known in units of `vth`, and it was measured in the following way: the n-XYTER internal test pulse generator was enabled and the pulse detection efficiency was measured as a function of `vth`; the dependence was fitted with an error function, and the *sigma* paramter of the error function was taken as noise. Also the thresold offset (i.e. physical threshold in `vth` units at `vth=0`) had to be determined. For this the latter procedure was repeated with various pulse ampliutdes A, but now we extracted the *mean* parameter of the error function, which is the pulse amplitude A_{vth} in `vth` units. The theshold offset was evaluated by extrapolating the $A_{vth}(A)$ to $A = 0$. For a rough estimate of the f_0 parameter the formula (2) was applied (even though n-XYTER fast shaper is in fact CR-RC type; rise time $\tau_{fast} = 19$ ns): $f_0 = 16.8$ MHz.

Taking into account the simplicity of the model and the fact that no model parameters were fit to the measurement, the observed agreement over 6 orders of magnitude in rate is considered to be surprisingly good. We conclude the Rice formula can be used for noise rate estimates in designing self-triggered readout systems for future experiments.

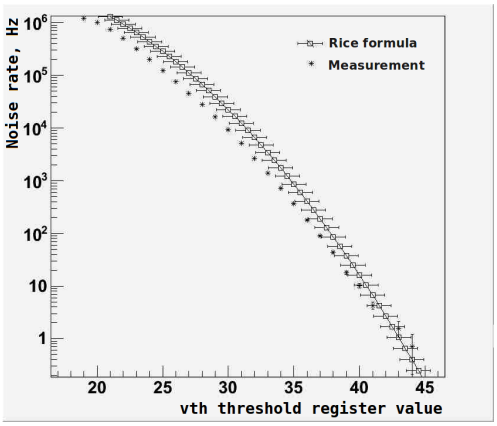

Figure 1: Comparison of the Rice formula calculation to the measurement.

References

[1] Dabrowski et.al., "Notes on requirements on noise level and threshold matching for the DETNI ASIC and on design validation".

[2] A.S. Brogna et al., Nucl. Instrum. Methods A 568 (2006) 301308

* Supported by EU FP7 HadronPhysics2, HICforFAIR, HGS-HIRe for FAIR, and H-QM Helmholz Research School

Development of a 512-channel front-end board with 4 n-XYTER2 chips *

O. Torheim[1], *V. Kleipa*[1], *C.J. Schmidt*[1], *and J. Heuser*[1]
[1]GSI, Darmstadt, Germany

Towards obtaining a sufficiently compact layout for the front end boards (FEB) of the CBM Silicon Tracking System, a prototype FEB with 512 input channels equipped with 4 n-XYTER2 readout chips has been developed.

Design constraints

The goal of the FEB development effort is to arrive with a design suitable for placing 1024 readout channels, contained in 8 forthcoming CBM-STS readout chips, on a board of about 6 cm width and a similar, minimum height, respecting reasonable constraints on manufacturing (cable and chip bonding), power consumption and data transmission. Compared to existing n-XYTER chips, the CBM-STS chips will be an improvement in terms of reduced power consumption and more compact bonding area. With the CBM-STS chip still to be designed, the current work with compacting the FEBs is based on the last n-XYTER chip, the n-XYTER2, and with conventional PCB design constraints (0.1 mm minimum pitch and micro vias of 0.1 mm diameter).

Cable attachment

The planned FEB interfaces the STS with a microcable of 120 μ pitch. To arrive with bonding at a much more relaxed pitch, a contact scheme has been developed where the cable attaches the PCB in a slanted manner. As a first step of proofing the principle, the cable bonding is to be separately tested. The test board comprises 128 signal lines that in the receiving end interfaces the microcable and in the transmitting end uses conventional connectors of small foot print to interface to already existing n-XYTER FEBs to enable the signal integrity test. The microcable connects to a CBM02 prototype microstrip detector.

Routing from cable landing pads to the chip

On the FEB, the n-XYTER chips are mounted into a hole to profit from wire bonding towards two PCB layers, thus realizing a dense layout. We adopt to this scheme also on the test board by routing the first cable layer directly to the first wire row at the PCB top layer, while the second layer of the cable is taken down to the second PCB layer using microvias, and then routed to the second row of landing pads. This is illustrated in Fig. 1.

Our PCB layout software allows routing through scripting. With footprint arrangement and routing performed through C++ generated scripts, one has full freedom to experiment with compactifying the layout and optimizing width and spacing to preferred design rules.

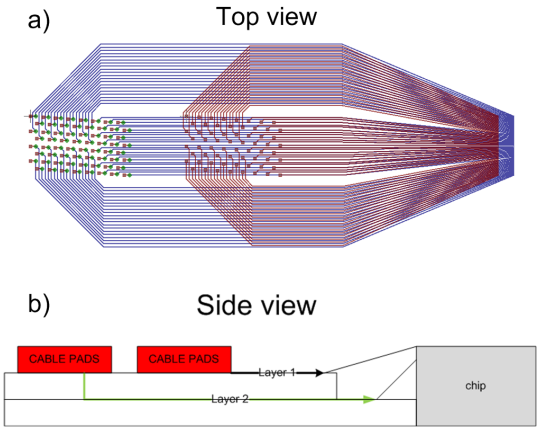

Figure 1: Routing from cable landing pads to chip pads.

Floorplan results

The new n-XYTER2 based FEBs interface the data acquisition system through two VHDCI connectors. The height of two stacked VHDCI connectors was assumed as a board height constraint for the new 4-chip board. Using this constraint, the layout was fullfilled with excellent margins. See Fig. 2.

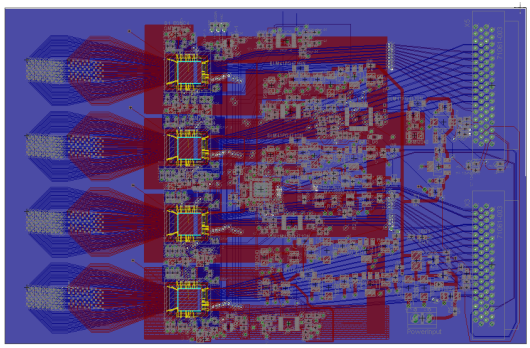

Figure 2: Board layout.

The analog power supply splits into separate domains for the ADC and each of the n-XYTER chips, minimizing noise and crosstalk, while a common power supply is used for digital signals. The digital power enters the chip with separate fingers which at the same time separates the analog plane shapes from each others. Hence, only two layers are used for power and ground distribution.

An Atmel AVR microcontroller controls and configures the four n-XYTER2 chips and other auxiliar units through I^2C and SPI interfaces. For the conversion of the sampled data the four N-XYTER chips share one common ADC.

* Supported by EU FP7 HadronPhysics2

Comparision of SPADIC and n-XYTER self-triggered front-end chips*

T. Balog[1,2], *W. F. J. Mueller*[1], *and C. J. Schmidt*[1]
[1]GSI, Darmstadt, Germany; [2]Comenius University, Bratislava, Slovakia

For detectors of the CBM experiment, high-rate, low-power and low-noise readout ASICs are needed. Since the Poisson distributed collisions between the nuclei are not correlated to a global trigger signal, the readout ASICs for both detectors as well as the data acquisition system itself must be self-triggered.

The n-XYTER chip was developed for neutron experiments and nowadays it is also used for early prototyping of the CBM detectors [1]. The performance of such a self-triggered front-end electronics has been studied last year [2]. The SPADIC chip [3] has been designed for the readout of the CBM transition radiation detectors.

n-XYTER and SPADIC chips

Their main difference is in the data storing and ordering mechanism. The n-XYTER chip applies a Token Ring while the SPADIC chip uses an ordering FIFO to aggregate data from all channels into a single output. The Token Ring loops over all channels and if there is any data in a channel FIFO the it reads it in and continues in the next period from next channel. Data do not come out time ordered and time re-sorting is needed at a later stage. This disadvantage is supposed to be eliminated by an ordering FIFO in the SPADIC chip. When a channel carries a signal it is (if possible) stored in the channel FIFO and at the same moment there is an input information sent to the ordering FIFO. The FIFO is checked at each time period and the channels are read-out according to the information from this particular FIFO. Such a reading can lead to unexpected higher losses in the SPADIC chip and its performance has to be simulated therefore.

Simulation

The study has been done in the SystemC description language which is built on the C++ standard. Both the n-XYTER and the SPADIC chips were simulated with the same amount of channels and the same channel FIFO depth (in this case 7), with the same clock. The proper size of the ordering FIFO and the comparision of the performance of both chips under the same conditions has been studied. Results are shown in Figs. 1 and 2.

Results

For a proper performance of SPADIC chip even at low data input frequencies the size of ordering FIFO has to be at least 80% of all cells in all channel FIFOs.

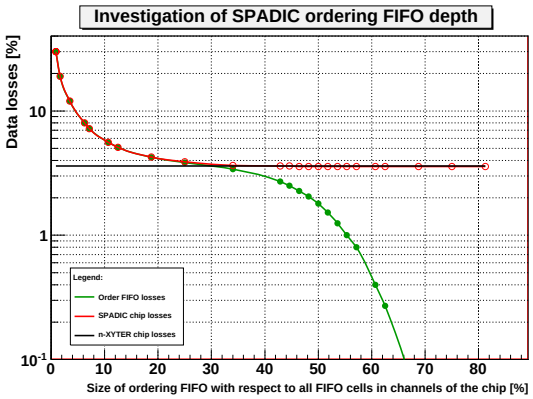

Figure 1: Comparision of SPADIC and n-XYTER data loss for a data input to output frequency ratio of 1.032 (to obtain data loss). The n-XYTER losses are taken as reference.

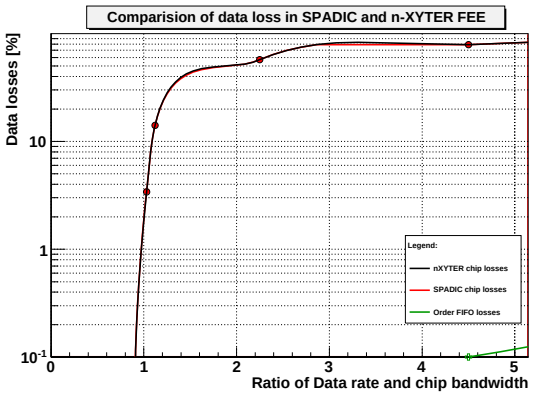

Figure 2: Comparision of SPADIC and n-XYTER data loss at different input frequencies. The SPADIC's Ordering FIFO is 80% size.

The ordering FIFO and Token Ring reading mechanisms do not show any significant change in performance at different frequencies. The key advantage of the ordering FIFO approach is that data is send time ordered by the front-end chip, which eliminates the need for resorting in later DAQ stages.

References

[1] GSI Scientific Report 2009 63

[2] GSI Scientific Report 2010 24

[3] T. Armbruster, P. Fischer, I. Peric: SPADIC-A Self-Triggered Pulse Amplification and Digitization ASIC, NSS Conference Record, 2010 IEEE, Knoxville, USA, November 2010, p. 1358-1362

* Work supported by EU-FP7 HadronPhysics2 and EU-FP7 MC-PAD.

Database development for the CBM Silicon Tracking System *

R. Nath[1], *S. Chatterji*[2], *and J.M. Heuser*[2]
[1]Mody Institute of Technology and Sciences, Lakshmangarh,India; [2]GSI,Darmstadt,Germany

The purpose of the project is to develop a client-server application for storing quality assurance data from the production of silicon microstrip detectors for the CBM Silicon Tracking System. For the Client side, *php* has been used and for the server side *MySQL* has been deployed to design the database. To create the user interface, some forms have been designed in *php* and a connection of the forms has been established to the databse. In this way, the users just have to choose from a given list of options and their choice sends a request to the server which in turn searches the database for the most appropriate result to be sent back to the user through the client. This application is also authenticated and the user has to login or register to get access. Figure 1 shows the welcome page and the registration form. MySQL server has been used to create the database.

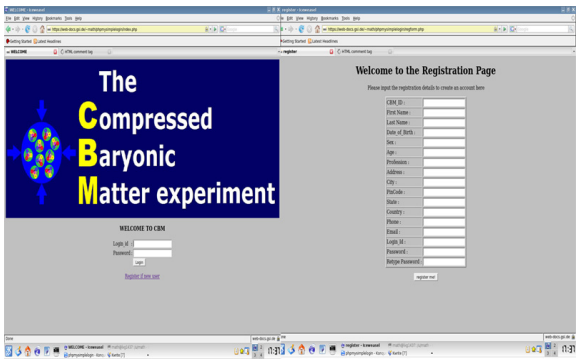

Figure 1: Welcome/Login page of the CBM STS Database.

It is a relational database management system (RDBMS) that runs as a server providing multi-user access to a number of databases. All the data is stored in tables and there are different tables for different types of data. Figure 2 shows such a table written in *MySQL*.

One can notice there are tables for many parameters like Current-Voltage (I-V), Capacitance-Voltage (C-V), Full Depletion, User details and so on. In the bottom of this figure, one can see how the details of the User are entered in *MySQL*. On the client side *php* has been used for designing the user interface. The interface is then connected to the *MySQL* database. Hence, the users can not see the database directly. They have to request data from the client side, which in this case is the interface designed using *php*. Figure 3 shows how the measured I-V and C-V data can be stored by the user on the client side. One can also extract the stored data from the database and can put some

```
mysql> show tables;
+----------------+
| Tables_in_CBM |
+----------------+
| CV             |
| FDP            |
| IV             |
| n_cint_v       |
| n_noise        |
| n_rint_v       |
| p_cint_v       |
| p_noise        |
| p_rint_v       |
| user           |
| vp             |
+----------------+
11 rows in set (0.00 sec)

mysql> desc user;
+-------------+-------------+------+-----+---------+-------+
| Field       | Type        | Null | Key | Default | Extra |
+-------------+-------------+------+-----+---------+-------+
| cbm_id      | varchar(20) | YES  |     | NULL    |       |
| fname       | char(20)    | YES  |     | NULL    |       |
| lname       | char(20)    | YES  |     | NULL    |       |
| DOB         | date        | YES  |     | NULL    |       |
| sex         | char(10)    | YES  |     | NULL    |       |
| age         | int(11)     | YES  |     | NULL    |       |
| profession  | char(20)    | YES  |     | NULL    |       |
| address     | varchar(40) | YES  |     | NULL    |       |
| city        | varchar(20) | YES  |     | NULL    |       |
| pincode     | double      | YES  |     | NULL    |       |
| state       | varchar(20) | YES  |     | NULL    |       |
| country     | varchar(30) | YES  |     | NULL    |       |
| phone_no    | varchar(20) | YES  |     | NULL    |       |
| email       | varchar(40) | YES  |     | NULL    |       |
| login_id    | varchar(30) | YES  |     | NULL    |       |
| password    | varchar(30) | YES  |     | NULL    |       |
+-------------+-------------+------+-----+---------+-------+
```

Figure 2: A sample *MySQL* table on the server.

search criterion. For example, Figure 4 shows how a user can search for stored I-V measured data for measurements done at temperature exceeding 10^0 C. The output displays the details of the sensors measured above 10^0 C along with other details like full depletion voltage, humidity, date of measurement, fluence and file path where data is stored. For collaborative access to the database, a user friendly web interface has been created.

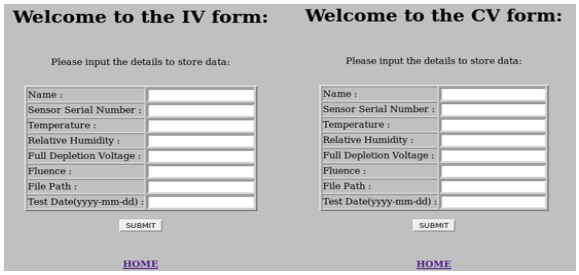

Figure 3: I-V and C-V forms for storing the data of leakage current and backplane capacitance.

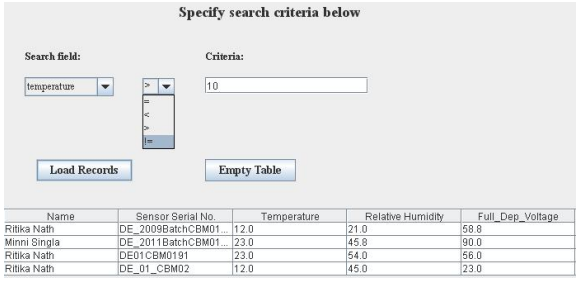

Figure 4: A sample search option in the STS database.

* Supported by EU-FP7 HadronPhysics2 and GSI Summer Students Programme

Common CBM beam test of the RICH, TRD and TOF subsystems at the CERN PS T9 beam line *

C. Bergmann[1], *A. Andronic*[1], *D. Emschermann*[1], *D. Vernekohl*[1], *J. P. Wessels*[1], *C. Pauly*[2], *M. Petriş*[3], *M. Petrovici*[3], *J. Adamczewski-Musch*[4], *S. Linev*[4], *W. F. J. Müller*[4], *A. Arend*[5], *and M. Hartig*[5]

[1]Institut für Kernphysik, Münster, Germany; [2]Bergische Universität Wuppertal, Germany; [3]NIPNE, Bucharest, Romania; [4]GSI, Darmstadt, Germany; [5]Institut für Kernphysik, Frankfurt/M, Germany

A common beam test of the CBM Ring Imaging CHerenkov (RICH), Time Of Flight (TOF) and various Transition Radiation Detector (TRD) prototypes was performed at the CERN Proton Synchrotron (PS) accelerator in October 2011. The measurements were carried out at the T9 beam line in a mixed beam of electrons and pions with momenta from 2 to 10 GeV/c. In addition to the above mentioned subsystems, the setup consisted of: a fiber-hodoscope, beam trigger scintillators, two Cherenkov detectors and a Pb-glass calorimeter for e/π identification (shown in Fig. 2). Upstream, at the beginning of the setup the fiber-hodoscope was mounted, followed by a large volume RICH prototype [1], 12 TRD prototypes from the four laboratories in Bucharest, Münster [2], Dubna and Frankfurt [3] and finally the TOF detector, see Figure 1.

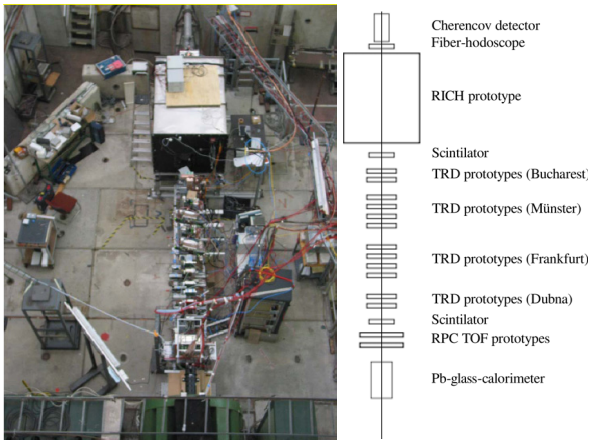

Figure 1: Setup of the PS/T9 beam line for CBM in 2011.

The RICH was based on a mirror focusing setup with CO_2 gas as radiator and 16 Hamamatsu MAPMTs, arranged in a 4×4 array. The readout of the RICH subsystem was based on the triggerless nXYTER [4] front-end. For the TRD, various MWPC geometries with and without a small drift section and with various wire/pad geometries were under test. Complementary approaches for the signal processing were investigated: The TRDs from Münster and Frankfurt were readout with the custom Self-triggered Pulse Amplification and Digitization asIC (SPADIC) [5], a sampling ADC, while the detectors from Bucharest and Dubna used the Fast Analog Signal Processor (FASP) ASIC or the MADC32, a VME-based peak sensing ADC. Part of the TRD test program were systematic high voltage scans, operation with different gas mixtures Ar(80%)+CO_2(20%) and Xe(80%)+CO_2(20%), variation of the incident beam angle and beam momentum, and tests of different radiator prototypes. Two RPC TOF prototypes from Bucharest were tested using a $C_2F_4H_2$(90%)+SF_6(5%)+C_4H_{10}(5%) gas mixture.

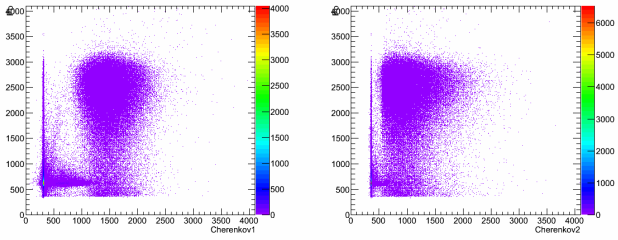

Figure 2: Pb-glass vs. Cherenkov 1 (left) and Pb-glass vs. Cherenkov 2 (right) at 4 GeV/c particle momentum.

A hybrid data acquisition based on the DABC/MBS system was prepared, to read the beam monitoring detectors and all triggered and self-triggered prototypes in a common system. The Go4 framework [6] was configured to provide a detailed online monitoring, including information from part of the slow control system [7], which helped to fine-tune and monitor the detectors during data taking.

* Work supported by BMBF and the HadronPhysics2 project financed by EU-FP7.

References

[1] J. Kopfer et al., “In-beam test of a real-size CBM-RICH prototype at CERN PS”, this report

[2] C. Bergmann et al., “Test of Münster CBM TRD prototypes at the CERN PS/T9 beam line”, this report

[3] A. Arend et al. , “In beam test of the Frankfurt TRD prototypes for the CBM experiment”, this report

[4] C. J. Schmidt et. al., “Development of the n-XYTER front end board FEB-D for CBM”, GSI Scientific Report 2010, p.227

[5] T. Armbruster et. al.,“CBM-TRD readout with the SPADIC amplifier / digitizer chip”, CBM Progress Report 2010, p.45

[6] J.Adamczewski-Musch, S.Linev, “A Go4-based online-analysis framework for CBM testbeams”, this report

[7] D. Emschermann et al. “Development of an EPICS controlled, MPOD based, mixed HV and LV system for the Münster CBM TRD prototypes”, this report

In-beam test of a real-size CBM-RICH prototype at CERN PS *

J. Kopfer[1], *V. Dobyrn*[5], *C. Dritsa*[4], *M. Dürr*[3], *J. Eschke*[2], *I. Galm*[3], *C. Höhne*[4], *K.-H. Kampert*[1], *L. Kochenda*[5], *P. Kravtsov*[5], *S. Lebedev*[4], *E. Lebedeva*[2], *T. Mahmoud*[4], *C. Pauly*[1], *J. Pouryamout*[1], *J. Rautenberg*[1], *S. Reinecke*[1], *E. Roshchin*[5], *V. Samsonov*[5], *J. Song*[6], *E. Vznuzdaev*[5], *M. Vznuzdaev*[5], *J. Yi*[6], *and I.-K. Yoo*[6]

[1]Bergische Universität Wuppertal; [2]GSI Helmholtzzentrum für Schwerionenforschung; [3]Hochschule Esslingen; [4]Justus-Liebig-Universität Gießen; [5]Petersburg Nuclear Physics Institute; [6]Pusan National University

A CBM-RICH prototype, real size in beam-direction, has been constructed and was tested in a common beam time together with other CBM groups using a mixed electron and pion beam at CERN PS T9 in October 2011 [1]. Cherenkov rings from electrons, pions, and muons could be seen and valuable data for the evaluation of the gas-, mirror-, and photo-detector-system could be collected. The prototype design and first beamtime results will be presented.

As intended for the final CBM-RICH detector, the prototype consists of a gaseous CO_2 radiator volume, VUV mirrors, and a photo-detector built from Hamamatsu H8500 multianode photomultiplier tubes (MAPMTs). Figure 1 shows a sketch of the detector box. The radiator length is 1.7 m. A computer-controlled gas system keeps the volume of 3.5 m^3 CO_2 clean and dry. During the beamtime O_2 and H_2O could be kept at 50 ppm and 200 ppm respectively. The detector was operated at 2 mbar over normal pressure resulting in a pion threshold of 4.65 GeV/c. The four spherical mirrors consist of an Al+MgF_2 coating on a 6 mm thick glass substrate. They have a size 40 x 40 cm^2 each and radii of 3 m. Every mirror is mounted on three actuators which can be adjusted for alignment. All together they are fixed on a remote-controlled rotatable frame allowing the ring image to be moved to different parts of the photo-detector. The photo-detector itself consists of 16 H8500 MAPMTs of different type with 1024 channels covering 20 x 20 cm^2 (Fig. 2). The size of the MAPMTs is such that one Cherenkov ring fits on four MAPMTs. Four MAPMTs are covered by a wavelength shifting film (WLS) which absorbs deep UV photons and shifts them to longer wavelengths where the transparency of the MAPMT window and the quantum efficiency of the photocathode is higher. The photo-detector is read out via attenuator boards by eight nXYTER [2] Frontend Boards (FEBs). Online monitoring and online ring fitting is done using the GSI Objected Oriented Online Offline system (Go4) [3].

During two weeks of beamtime, parameters like particle momentum, position of the ring on the photo-detector, position of the Cherenkov cone on the mirrors, gas parameters, and settings of thresholds and HV have been varied. From these measurements important quantities regarding the detector performance can be deduced.
Figure 3 displays ring images from electrons, muons, and pions accumulated over many runs as well as a typical single event. The rings are very clear due to a very low noise rate of the order of 10 kHz for the whole photo-detector, i.e. 10 Hz per channel. In order to quantify the ring size, a ring and ellipse finding alorithm based on a Hough Transform and a ring and ellipse fitting algorithm are applied [5].

In a RICH detector the number of registered photons per Cherenkov ring (hit multiplicity) is important for the effi-

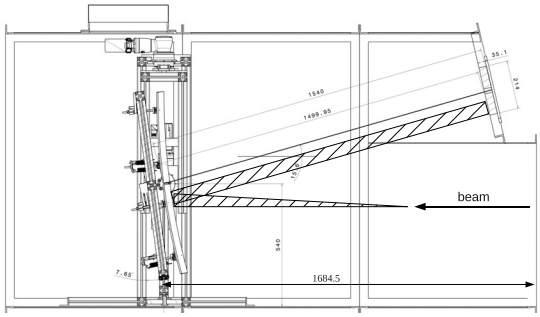

Figure 1: Sketch of the CBM-RICH prototype box with mirrors on rotable frame. The photo-detector is mounted on the upper right. The hatched area visualizes the Cherenkov cone and its reflection onto the photo-detector. The gas-system is assembled in a separate rack.

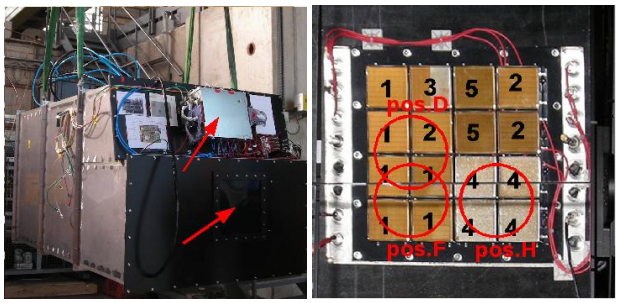

Figure 2: CBM-RICH prototype from the front. The quadratic beam entrance window and the photo-detector housing are marked with arrows (left). Photo-detector with 16 MAPMTs (right). The numbers refer to five different types of MAPMTs: 1. H8500-03 D no WLS, 2. H8500-03 C no WLS, 3. H8500-03 C 1/2 WLS, 4. H8500-03 D with WLS, 5. H10966, 8 stage, SBA. The WLS film can be recognized by its frosted surface which is seen like this only in the photograph.

*supported in part by GSI project WKAMPE1012, BMBF grant 06WU9195I, and by the LOEWE center HIC for FAIR

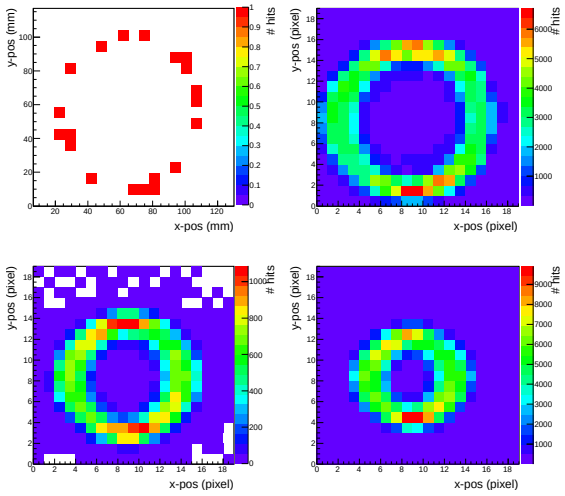

Figure 3: Single event display of a Cherenkov ring from one electron and accumulated rings from several thousand electrons, muons, and pions at 6 GeV/c (from top left to bottom right).

ciency of ring finding and the quality of ring fitting. By simply counting the hits per ring one gets hit multiplicities between 19 and 22 photoelectrons per electron ring depending on the quantum efficiency of the MAPMTs (see Fig. 4, pos.F and pos.D). This is compatible with the expected number of 21 photoelectrons from GEANT simulation [6]. Additional hits in neighbouring pixel due to crosstalk have to be substracted from the measured numbers. According to an analysis of all 16 MAPMTs with a different data set, $\approx$ 12 % of the hits are caused by crosstalk. Hence, the crosstalk corrected hit multiplicities vary between 16.7 and 19.4.

The WLS coated MAPMTs show enhanced hit multiplicities (Fig. 4, pos.H) when compared to the reference MAPMTs (pos.F). Other MAPMTs with same characteristics as the reference, however, also show a higher hit multiplicity (pos.D). In order to quantify the effect of the WLS film the efficiency of every MAPMT will be measured and considered in the analysis.

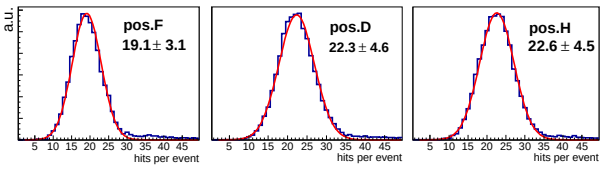

Figure 4: Hit multiplicity for different positions of the ring on the photo-detector (cf. Fig. 2).

The momentum of electrons and pions has been varied between 2 and 10 GeV/c in steps of 1 GeV/c. Figure 5 shows the simulated and measured ring radius for electrons and pions as function of particle momentum. One can see a very good agreement between simulation and data. Below pion threshold only electron rings can be seen. As electrons are ultrarelativistic over the whole momentum range the electron ring radius is constant with a value of $\approx$ 45.5 mm. Small variations are caused by fluctuations of the refractive index of the radiator due to temperature and pressure variation during the measurement. The data for different momenta was collected over a period of several days and nights. Projecting on the radius one can see that for

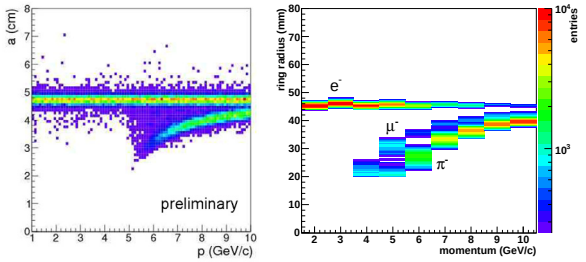

Figure 5: Ring radius for electrons and pions as function of momentum in simulation (left) [4] and data (right). In the data also some muons are visible.

particles with momenta of 8 GeV/c the separation of electrons and pions is $> 7\ \sigma_\pi$ (Fig. 6).

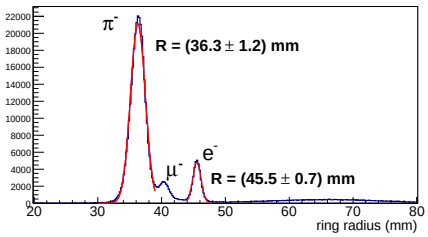

Figure 6: Fitted ring radius for electrons and pions at 8 GeV/c.

The authors would like to thank Jörn Adamczewski-Musch and Sergey Linev for setup and operation of the impeccably working DAQ system, Thomas Wasem and Wolfgang Niebur for technical support, Tanya Torres de Heidenreich and Burkhard Kolb for support with the mirror control system and slow control, Volker Kleipa for help with electronics.

References

[1] C. Bergmann et al., Common CBM beam test of the RICH, TRD and TOF subsystems at the CERN PS T9 beamline, this report

[2] A.S. Brogna et al., Nucl. Instr. and Meth. A 568 (2006) 301

[3] J. Adamczewski-Musch, S. Linev, A Go4-based online-analysis framework for CBM testbeams, this report

[4] D. Kresan, C. Höhne, Design studies for a CBM-RICH prototype, CBM Progress Report 2010

[5] S. Lebedev et al., J. Phys. Conf. Ser. 219 (2010) 032015

[6] C. Höhne et al., Nucl. Instr. Meth. A 639 (2011) 294-297

Single sided TRD prototype *

M. Petriş[1], *M. Târzilă*[1], *M. Petrovici*[1], *V. Simion*[1], *D. Bartoş*[1], *I. Berceanu*[1], *G. Caragheorgheopol*[1], *V. Cătănescu*[1], *F. Constantin*[1], *L. Rădulescu*[1], *C. Bergmann*[2], *D. Emschermann*[2], *S. Linev*[3], *W. F. J. Müller*[3], *and J. P. Wessels*[2]

[1]NIPNE, Bucharest, Romania; [2]University of Münster, Germany; [3]GSI, Darmstadt, Germany

Although unbeatable in terms of e/π discrimination in high counting rate environment, the size of a double sided TRD is limitted by the topology of the signal extraction. In order to overcome this problem we propose a standard TRD architecture of 2x4 mm amplification region coupled with a 4 mm drift zone with a gas thickness identical with 4x3 mm double sided prototype [1]. The drift zone size was chosen such to minimize the drift time ($<$ 250 nsec for 80%Xe+20%CO_2 gas mixture, 2000 V anode voltage and 500 V drift voltage [2]), while keeping the TR conversion efficiency as large as possible. Details on this architecture are presented in Fig.1. The detector is closed on one side by the drift electrode made from an aluminized kapton foil of 25 μm thickness streched on a 8 mm Rohacell plate and on the other side by the readout electrode made from a 300 μm thickness PCB. The anode wire plane made from Au plated W wires of 20 μm diameter (3 mm pitch) is situated in the middle of the amplification region. The cathode

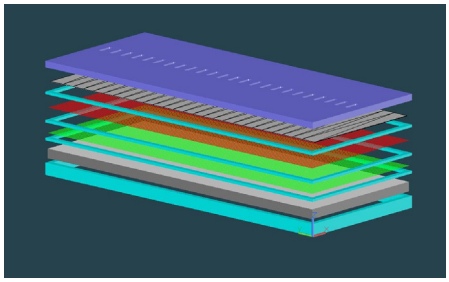

Figure 1: Sketch of the chamber configuration

wire plane made from 75 μm diameter Cu/Be alloy (1.5 mm pitch) separates the amplification region from the drift zone. Rectangular pads (10 x 80 mm^2) split on diagonal define a triangular shape for readout cell, each triangle being readout separetely. The pad signals were processed using 8 channel FASP front-end electronics [3].

The detector was flushed with an 80%Ar+20%CO_2 gas mixture and tested with the 5.9 keV X-ray ^{55}Fe source measuring both anode and pad signals. The obtained energy resolutions were of 8% for the anode signal and 9.7 % for the pad signals.

The in-beam tests were performed at PS accelerator of CERN [4]. It was operated with a 80%Xe+20%CO_2 gas mixture, 1900 V anode voltage, 400 V drift voltage and a regular radiator of 20/500/120 (20 μm foil thickness, 500 μm gap, 120 foils).

From the correlation of the signals from a Cherenkov detector and a lead-glass calorimeter, the pulse height distributions for electrons and pions at 2 GeV/c momentum were obtained (Fig. 2). Using the pulse height distributions as

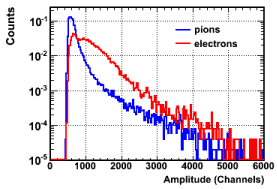

Figure 2: Pulse height distributions for pions (blue line) and electrons (red line)

input in a Monte Carlo simulation an electron misidentification probability of 1.1% is reached for a 6 layer configuration, as can be seen in Fig.3. .

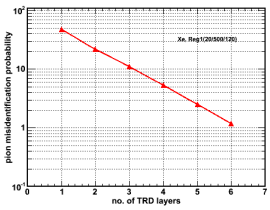

Figure 3: Misidentification probability as a function of number of layers

The position reconstruction and position resolution determination in both coordinates that defines the plane of the readout electrode were obtained following the procedure described in [1]. Position resolutions of about 320 μm

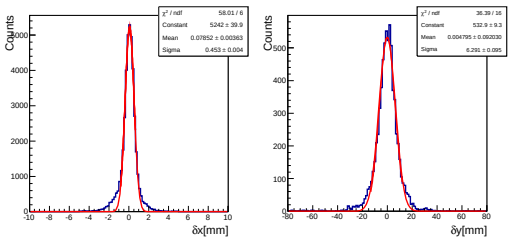

Figure 4: Distribution of the difference between the reconstructed position of the SSTRD and DSTRD-V1 [1]: left-side, x coordinate, right-side, y coordinate

across the pads (Fig. 4, left-side) and of 6.3 mm along the pads (Fig. 4, right-side) were obtained.

References

[1] M. Petriş et al.,"e/π identification and position resolution of double sided TRDs", this report

[2] M. Petrovici et al., CBM Collab. Meeting, Beijing, 2011

[3] A.Caragheorgheopol et al., GSI Report 2011-1, p. 35

[4] D. Emschermann et al., GSI Report 2011-1, p. 34

* Work supported by EU-FP7/HP2-WP18 Grant No 227431 and Romanian NASR/CAPACITATI-Modul III contract nr. 42 and NASR/NUCLEU Project

Test of Münster CBM TRD prototypes at the CERN PS/T9 beam line *

C. Bergmann [1], *A. Andronic* [1], *D. Emschermann* [1], *and J. P. Wessels* [1]

[1]Institut für Kernphysik, Münster, Germany

The Münster CBM TRD prototypes are derived from the design of the ALICE TRD modules. An amplification region of 3+3 mm or 4+4 mm is combined with a short drift section to obtain an active gas volume thickness of 12 mm, referred to as MS336 and MS444 respectively. Signals are induced on rectangular pads of 5 mm or 8 mm width, respectively, to allow for charge collection on 3 adjacent pads. This design is scalable to $1m^2$-size, required for the final CBM TRD modules.

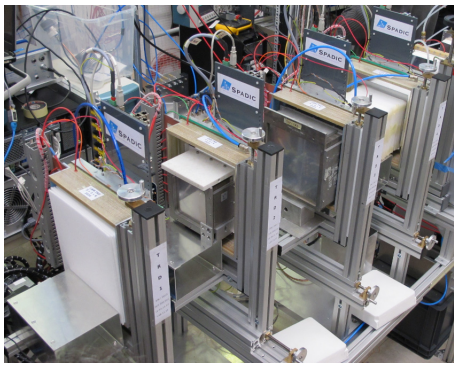

Figure 1: Münster TRD protoypes in the CBM beam test.

Various radiator types were investigated on the four Münster prototypes (Fig. 1) during the common CBM beam test [1] in October 2011. The read-out was performed with the SPADIC/Susibo front-end [2]. The setup was entirely EPICS controlled, allowing for online monitoring of the HV settings and inclusion of these values in the DAQ stream, as described in [3]. First results of the ongoing analysis are shown in Figures 2 and 3.

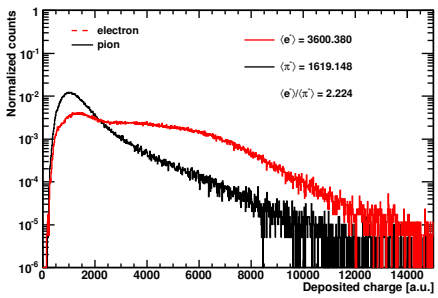

Figure 2: Integrated ADC spectra for electrons (red) and pions (black) on one of the MS336 prototypes operated with Xe/CO_2 (80:20) gas in combination with 30 cm polyethylene-foam radiator (H) at p=3 GeV/c.

* Work supported by BMBF and the HadronPhysics2 project financed by EU-FP7.

One important aspect of radiator choice is to match of the TR-emission spectrum with respect to the absorption spectrum of the detector. For a detailed investigation, we have built different radiator types: regular foil (B, C, D, E, F) and irregular foam (H and H++), fiber (G) and sandwiches (A, I(p) and I(u)). Ideally, a radiator should yield an optimal TR-performance while keeping the material budget as low as possible. While this consideration favors regular foil radiators, they usually require a significant external support frame to keep the foils streched and in position.

First results (Fig. 3) using self-supporting, irregular foam materials are promising (H and H++). Owing to space constraints during the test beam, foam radiators could only be tested on the upstream TRD prototype. Results from this detector are labelled MS336/10 in Fig. 3. They represent only upper limits, because of intermittent problems with the readout.

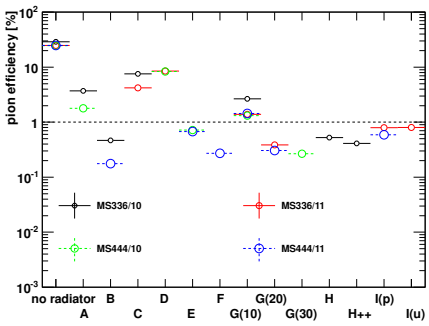

Figure 3: Extrapolated pion efficiency for a TRD consisting of 10 layers for different radiator types studied on the 4 different TRD prototypes. The dashed line indicates the design goal of 1% pion efficiency, at 90% electron efficiency, achieved by radiators below this line.

Further tests with foam radiators are planned for 2012. In addition, a self-supporting, micro-structured foil radiator with negligible frame material is currently under development.

References

[1] C. Bergmann et al., “Common CBM beam test of the RICH, TRD and TOF subsystems at the CERN PS T9 beamline”, this report

[2] T. Armbruster et. al.,“CBM-TRD readout with the SPADIC amplifier / digitizer chip”, CBM Progress Report 2010, p.45

[3] D. Emschermann et al. “Development of an EPICS controlled, MPOD based, mixed HV and LV system for the Münster CBM TRD prototypes”, this report

Test of the Frankfurt CBM TRD prototypes at the CERN-PS*

A. Arend, H. Appelshäuser, T. Bel, P. Dillenseger, and M. Hartig
Institut für Kernphysik, Goethe-University, Frankfurt am Main, Germany

The Transition Radiation Detector (TRD) for the Compressed Baryonic Matter (CBM) experiment aims to provide charged particle tracking and e/π separation in an environment of unprecedented high particle flux. To achieve the physics goal of CBM, a hadron misidentification probability of less than 1% (e.g. "pion efficiency") is required at 90% detection efficiency for electrons. Based on simulations [1] and results of previous test beams [2], thin MultiWire Proportional Chambers (MWPC) without additional drift region are considered to fulfill this requirement. Symmetric MWPCs with equal distances between entrance window, anode wires and read out plane resulting in a total thickness of 8 mm, 10 mm and 12 mm have been built. The anode wires have a diameter of 20 μm and a pitch of 2.5 mm. Three different types of TR-radiators have been attached to these MWPCs: a fiber radiator as used in the ALICE TRD, a polypropylene foam radiator, and regular radiators made of 20 μ m thick polypropylene foils. The foil radiators have been constructed in modules of 50 foils each with a spacing of 0.5 mm. The different configurations attached to one MWPC consisted of altogether 150, 200, and 350 layers of foil. The SPADIC chip [3] has been used for data read out. The prototypes have been tested during the common test beam time at the CERN-PS in October 2011 together with other CBM subsystems including the TRD prototypes from Münster, Bucharest and Dubna [4]. In the experimental area T9 a mixed e/π-beam with momenta of 2 to 10 GeV/c has been provided. The combined signals of two Cherenkov detectors and a lead glass calorimeter have been used as reference for particle identification.

Figure 1 shows the distribution of the integrated ADC signal for electrons and pions with a momentum of 3 GeV/c measured with the 8 mm thick MWPC using the foil radiator with 350 layers and a Xe/CO_2 (80:20) gas mixture. Based on these distributions, electron and pion efficiencies can be calculated using a likelihood method and extrapolated to multiple detector stations using a simple Monte Carlo. The remaining pion efficiencies are shown in Fig. 2 for the different radiator types for a required 90% electron efficiency. According to this preliminary result one can assume that a regular foil radiator as well as a foam radiator can fulfill and even significantly exceed the requirements in e/π separation for a detector setup with nine stations.

The present preliminary analysis of the test beam data will be further improved and extended. Based on the available results the developments in the Frankfurt CBM TRD group will be focused on the construction of regular foil radiators combined with the existing thin read out chamber geometry. These improvements will lead to a large scale prototype which will be tested in the upcoming beam times.

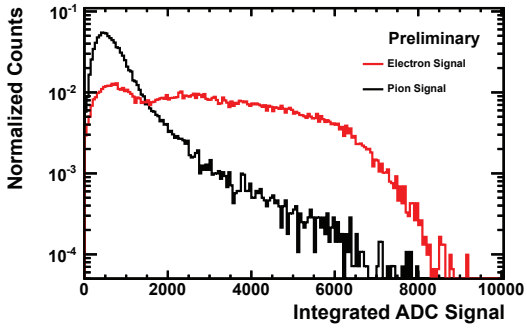

Figure 1: Integrated signal of electrons (red) and pions (black) for the 8 mm thick MWPC using the foil stack radiator with 350 layers.

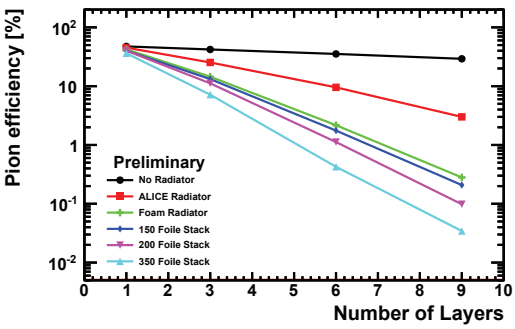

Figure 2: Extrapolated remaining pion efficiency at a beam momentum of 3 GeV/c for multiple layers of the 8 mm thick MWPC when applying 90% electron efficiency for the used radiators.

References

[1] P. Reichelt, et al., "Study on electron-pion discrimination with the CBM Transition Radiation Detector", CBM Progress Report 2010, Darmstadt 2011, p. 39.

[2] W. Yu, "First beam test of the Frankfurt prototypes for the CBM-TRD", CBM Progress Report 2010, Darmstadt 2011, p. 44.

[3] T. Armbruster, et al., "CBM-TRD readout with the SPADIC amplifier / digitizer chip", CBM Progress Report 2010, Darmstadt 2011, p. 45.

[4] C. Bergmann, D. Emschermann and J.P. Wessels, "Common CBM beam test of the RICH, TRD and TOF subsystems at the CERN PS", this report.

* Supported by BMBF and GSI-F&E

Free Running Mode Acquisition for High Counting Rate TRD *

F. Constantin[1], M. Petcu[1]

[1]"Horia Hulubei" National Institute for Physics and Nuclear Engineering, Romania

The in-beam test performed at PS-CERN in 2010 have shown high performance of double-sided [1] and standard single-sided [2] TRD prototypes in terms of e/π rejection and position resolution using dedicated FEE – FASP [3,4]. There still remains to be studied the dependence of this performance as a function of counting rate and high multiplicity environment. In order to perform such tests and taking into account the requirement of CBM experiment at FAIR in terms of DAQ, we developed an original Free Running Mode Acquisition Device for in-beam tests of our TRD prototypes.

The global architecture includes [5]:

- Two MAX1434 Evaluation kits [6]
- PIC32 Ethernet Starter Kit [7]
- A dedicated board
- Software for PIC32 acquisition, PIC32 data transfer through Ethernet to a PC and a visual user interface.

The MAX1434 a 10-bit analog-to-digital converter (ADC) features fully differential inputs, a pipelined architecture, and digital error correction incorporating a fully differential signal path. The MAX1434 offers a maximum sample rate of 50Msps. The MAX1434 evaluation kits (EV kits) are fully assembled and tested circuit boards that contain all the components necessary to evaluate the performance of this family of octal 10-/12-bit analog-to-digital converters (ADCs). These ADCs accept differential analog input signals. The EV kits digital outputs can be easily sampled with a user-provided high-speed logic analyser or data-acquisition system. The EV kits also feature an on-board deserialiser to simplify integration with standard logic analysis systems.

The PIC32 Ethernet Starter Kit provides the easiest and lowest cost method to experience 10/100 Ethernet development with PIC32. Combined with Microchip's free TCP/IP software, your project will be running in no time.

A dedicated board was designed and implemented in order to:

- provide the clock to the Maxim EV kit
- provide the different power supplies for each Maxim EV kits
- transfer data from EV kit to the Microchip micro controller
- provide the data transfer handshake

The two software applications were written in C++ for PIC32 and PC.

* Work supported by EU-FP7/HP2-WP18 Grant No 227431 and Romanian NASR/CAPACITATI-Modul III contract no. 42. and NASR/NUCLEU Project

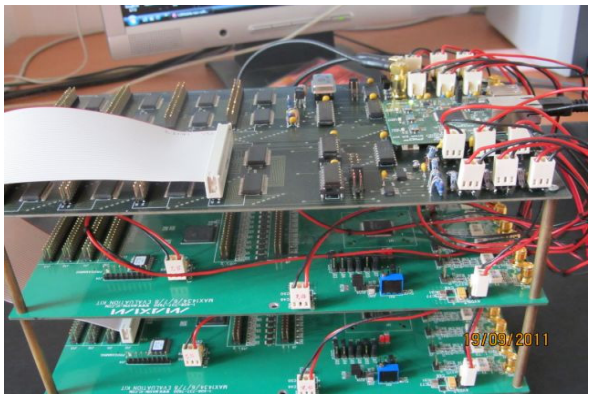

Figure 1. Free Running Mode Acquisition for High Counting Rate TRD Device

The hardware configuration is presented in Fig.1. Detailed tests using pulse generator and radioactive source are going on. Solutions for running such a configuration in conjunction with a standard CBM DABC DAQ system are being worked on.

References

[1]M. Petris et al., e/ π identification and position resolution of double sided TRDs, this report

[2] M. Petris et al., Single sided TRD prototype, this report

[3]V.Catanescu, CBM 10th Collaboration Meeting, Sept. 25-28,2007, Dresden

[4] V.Catanescu, et al., DPG,Bochum, March 18,2009

[5] F. Constantin CBM 17th Colaboration Meeting March, April 4-8, 2011, Dresden

[6]http://www.maxim-ic.com/datasheet/index.mvp/id/4906

[7]http://www.microchip.com/stellent/idcplg?IdcService=SS_GET_PAGE&nodeId=1406&dDocName=en545713

Development of an EPICS controlled, Mpod based, mixed HV and LV system for the Münster CBM TRD prototypes *

D. Emschermann [1], *J. Adamczewski-Musch* [2], *and B. W. Kolb* [2]
[1]Institut für Kernphysik, Münster, Germany; [2]GSI, Darmstadt, Germany

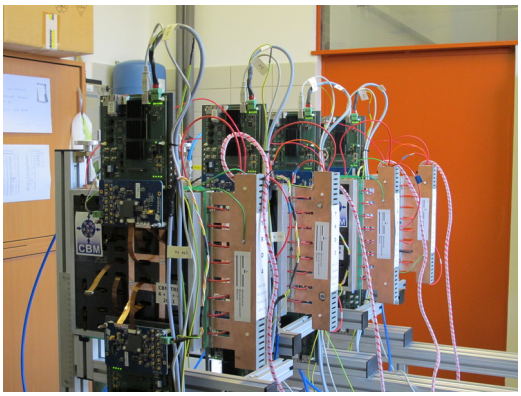

Figure 1: The four Münster CBM TRD prototypes 2011, equipped with eight SPADIC / Susibo front-end units.

A common CBM RICH / TRD / TOF beam test was performed at the CERN PS T9 beam line in October 2011 [1]. The low and high voltages of the Münster TRD prototypes [2] as well as the HV for the beam monitoring detectors and the high voltage of the RICH camera system [3] were managed by a slow control system based on the Experimental Physics and Industrial Control System (EPICS) [4]. The power for the Münster TRDs (Figure 1) was provided by a Mpod mini crate [5] equipped with the following list of modules [6]:

module	channels	function
EHQ 8630n	8 ch	beam monitor HV
EDS 20 025p	4 ch	TRD anode HV
EDS 20 025n	4 ch	TRD drift HV
MPV 8008LD	8 ch	TRD low voltage

The 8 SPADIC / Susibo front-end units on the TRDs were supplied by the MPV LV module. Only 8 HV channels of two polarities were required for the four TRDs. The communication between the controller in the Mpod crate and the EPICS IOC was handled through SNMP.

We made use of the EPICS data input to the Data Acquisition Backbone Core (DABC), as described in [7]. Using the Easy Channel Access (EZCA) extention [8], a set of slow control variables were transmitted to the DABC system every 5 seconds. As part of the DAQ stream, it was possible to visualise those EPICS variables in the attached Go4 [9] online monitoring analysis, which was helpful for the fine-tuning of the TRD detector settings during data taking.

* Work supported by BMBF and the HadronPhysics2 project financed by EU-FP7.

Figure 2: The TRD services infrastructure with the Mpod mini crate visible in the middle left part of the picture.

For 2012 we plan to test the behaviour of a large MPod crate, offering 10 slots, each equipped with a 32 channel EDS HV Module. Such a system with 320 HV channels per crate could be used as high voltage power source for the final CBM TRD. It remains to be tested under which conditions the crate controller can handle the data traffic generated by the EPICS IOC. The CBM TRD, consisting of some 700 modules, would require 1400 HV channels, which could be provided by 5 of the above crates.

References

[1] C. Bergmann et al., “Common CBM beam test of the RICH, TRD and TOF subsystems at the CERN PS T9 beamline”, this report

[2] C. Bergmann et al., “Test of Münster CBM TRD prototypes at the CERN PS/T9 beam line”, this report

[3] J. Kopfer et al., “In-beam test of a real-size CBM-RICH prototype at CERN PS”, this report

[4] EPICS, http://www.aps.anl.gov/epics/

[5] WIENER, Plein & Baus GmbH, http://www.wiener-d.com/

[6] ISEG Spezialelektronik GmbH, http://www.iseg-hv.com/

[7] J. Adamczewski-Musch et al., “DABC data acquisition input for slow control variables”, GSI Scientific Report 2010, PHN-NQM-CBM-30

[8] EZCA, http://www.aps.anl.gov/epics/extensions/ezca

[9] Go4, http://go4.gsi.de

e/π identification and position resolution of double sided TRDs *

M. Petriş[1], *M. Târzilă*[1], *M. Petrovici*[1], *V. Simion*[1], *D. Bartoş*[1], *I. Berceanu*[1], *G. Caragheorgheopol*[1], *V. Cătănescu*[1], *F. Constantin*[1], *C. Bergmann*[2], *D. Emschermann*[2], *S. Linev*[3], *W. F. J. Müller*[3], *and J. P. Wessels*[2]

[1]NIPNE, Bucharest, Romania; [2]University of Münster, Germany; [3]GSI, Darmstadt, Germany

Details on the architecture, energy resolution for ^{55}Fe X-ray source and preliminary results of in-beam tests of double sided TRD prototype with triangular read-out pads using FASP front-end electronics were already reported [1, 2]. Therefore, the present contribution is focused on the e/π identification and position resolution of the two versions with 3 mm (DSTRD-V1) and 4 mm (DSTRD-V2) anode-cathode distance, respectively. The in-beam tests were performed using a mixture of electrons and pions of 1-5 GeV/c momentum at T10 beam line of PS accelerator at CERN [3]. The electrons and pions were selected using the information from a Cherenkov and Pb glass calorimeter positioned in front and in the end of the beam line. The detectors were flushed with a 80%Xe+20%CO_2 gas mixture. The pulse height distributions of electrons and pions

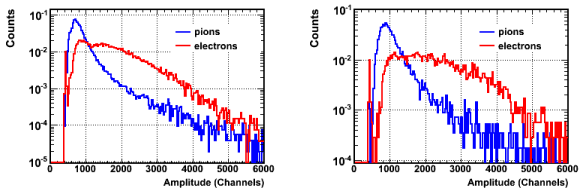

Figure 1: Pulse height distributions for pions (blue line) and electrons (red line):DSTRD-V1 (left-side) and DSTRD-V2 (right-side)

at 2 GeV/c are presented in Fig.1:left-side for DSTRD-V1 and right-side for DSTRD-V2.

DSTRD-V1 was operated at 1700 V with a regular radiator of 20/250/220 (20 μm foil thickness, 250 μm gap, 220 foils) while DSTRD-V2 was operated at 2000 V with a regular radiator of 20/500/120. These distributions were

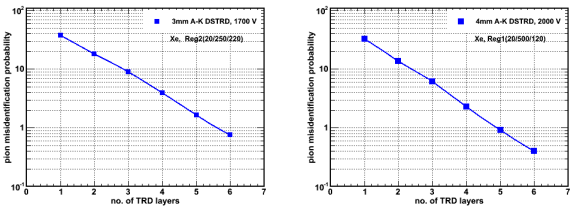

Figure 2: Misidentification probability as a function of number of layers: DSTRD-V1 (left-side), DSTRD-V2 (right-side)

used as input for a Monte Carlo simulation of the misidentification probability as a function of number of layers. The results are presented in Fig.2: an electron misidentification probability of 0.74% (left-side) for a 6 layer configuration based on DSTRD-V1 is obtained, while using 6 layers based on DSTRD-V2 configuration, the electron misidentification is improved by a factor of 2, i.e 0.38% (right-side).

In order to estimate the position resolution, we used the position information from both detectors. For the position reconstruction we used the following procedure/algorithm: across the split pads we reconstructed the x coordinate in a system of coordinates (x,y) parallel with the cathetus of the right triangle. For the position reconstruction along the

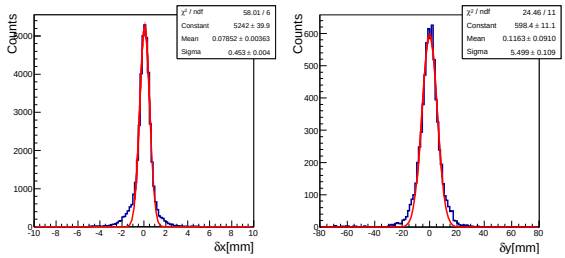

Figure 3: Distribution of the difference between the reconstructed position of the DSTRD-V1 and DSTRD-V2: x coordinate (left-side), y coordinate (right-side)

pads - y coordinate a second x$'$ reconstruction was made in a coordinate system (x$'$,y$'$) tilted with the hypotenuse angle. Taking a parallel to y and y$'$ axes for each case through the reconstructed x and x$'$ coordinates, we obtained from their crossing, the y coordinate of the event. The position resolution was obtained from the standard deviation of a Gaussian fitted to the difference between the reconstructed position with the two prototypes. With the assumption that the two prototypes have equal contribution, a position resolution across the pads of about 320 μm was obtained for both x (Fig. 3 - left side) and x$'$ coordinates. The 5.5 mm position resolution (Fig. 3 - right side) along the pads (y coordinate) was obtained using as reference the information from the DSTRD-V1 rotated by 90^0 relative to the DSTRD-V2.

These results combined with the ones obtained in previous tests of smaller size prototypes of similar architecture in high counting rate environment [4] show the high performance of such an architecture and associated FEE in terms of e/π discrimination and position resolution in counting rate environment up to 2 x 10^5 part.$\cdot$cm^{-2} $\cdot$s^{-1}.

References

[1] M.Petriş et al. GSI Report 2011-1, p. 38

[2] A.Caragheorgheopol et al., GSI Report 2011-1, p. 35

[3] D. Emschermann et al., GSI Report 2011-1, p. 34

[4] M. Petrovici et al, NIM. A 579, (2007), 961

* Work supported by EU-FP7/HP2-WP18 Grant No 227431 and Romanian NASR/CAPACITATI-Modul III contract nr. 42 and NASR/NUCLEU Project

Time and position resolution for high granularity, multigap, symmetric, differential readout - timing RPC *

M. Petriş[1], *M. Petrovici*[1], *V. Simion*[1], *D. Bartoş*[1], *G. Caragheorgheopol*[1], *F. Constantin*[1], *I.Deppner*[2], *N. Herrmann*[2], *P. Loizeau*[2], *K. Doroud*[3], *and M.C.S. Williams*[4]

[1]NIPNE, Bucharest, Romania; [2]Physikalisches Institut der Universität Heidelberg, Germany; [3]CERN, Geneva, Switzerland; [4]INFN, Bologna, Italy

As shown previously [1, 2], the differential strip read out together with the low resistivity glass keeps the good timing characteristics of the glass MRPCs at high rates (up to 1.6x10^4 part.$\cdot$s^{-1}cm^{-2}). In order to cope also with the high multiplicity environment of CBM experiment at low polar angles, a new high granularity design has been proposed. Details on the architecture and preliminary results from in-beam tests were already presented in [3].

Here we report on time and position resolution obtained in beam test performed at the T10 beam line of the CERN PS with 6 GeV/c pions.

Three MRPCs of similar design, have been tested; two of them are based on float glass resistive electrodes, with a 2 x 7 gaps (140 μm each) configuration. The third one was built with 2 x 5 gaps using a special low resistivity glass [4]. The counters were operated with a 95% $C_2F_4H_2$ + 5% SF_6 gas mixture and 2,086 V/gap high voltage.

The anode and cathode signals were transported via twisted pair cables to a differential FEE based on the NINO chip [4]. The LVDS NINO outputs were fed into a V1290A VME TDC. We recorded the time information at both ends of each strip (t_{left}, t_{right}). In order to eliminate the position dependence in the estimation of the time resolution, the mean t_{mean}=(t_{left}+t_{right})/2 was used.

The time distribution is the difference between t_{mean} measured by each chamber. The time resolution for different runs, after walk correction and quadratical subtraction of the electronic contribution (measured in a separate run using pulser signals injected at the level of NINO cards), can be followed in Fig.1. As could be seen, the intrinsic time resolution is at the level of σ = 50 ps.

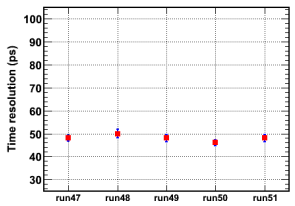

Figure 1: Time resolution for different runs

The position resolution along the strips is given by the standard deviation of the distribution of the time difference; i.e. t_{diff}=(t_{left}-t_{right}).

The position calibration was performed using the orthogonal position of the strips of one RPC relative to the strips of the other RPC. Selecting the tracks within a strip pitch in the reference counter, the position distribution along a given strip in the studied counter was obtained. The obtained position resolution ($\sim$ 4.5 mm) for two measured strips conditioned by 5 strips in the reference counter is represented in Fig. 2.

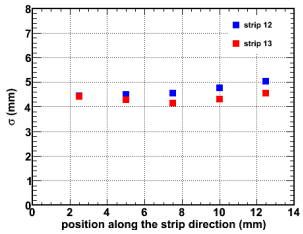

Figure 2: Position resolution along the strip

The position reconstruction across the strips was obtained using the center of gravity method based on time-over-threshold information. The reference was the track reconstructed using two of the three tested detectors. The position resolution across the strips ($\sim$ 170 μm) was extracted from the Gaussian fit of the distribution of residuals given by the difference between the reconstructed position in the third MRPC and the reference (Fig 3).

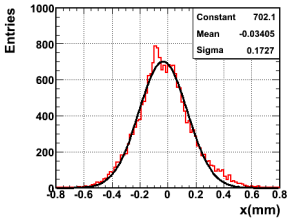

Figure 3: Distribution of the residuals with a Gaussian fit

Based on the results reported in this contribution and previous measurements with low resistivity glass [1], we strongly recommend such an architecture to be used for the most inner region of the CBM-TOF subdetector.

References

[1] D. Bartoş et al. 2008 NSS/MIC, Vols. 1-9 Book Series: IEEE Nuclear Science Symposium - Conf. Rec. Pg: 1933-1935.

[2] M.Petriş et al., Rom. Journ. Phys. 2011.

[3] M.Petriş et al., GSI Scientific Report 2011-1, p. 40

[4] Yi Wang et al., ,CBM Progress Report 2010, p. 50

[5] F. Anghinolfi et al., Nucl. Instr. And Meth. A 533(2004), 183

*Work supported by EU-FP7/HP2-WP18 Grant No 227431 and Romanian NASR/CAPACITATI-Modul III contract nr. 42. and NASR/NUCLEU Project

Performance of large area MMRPC prototype*

I. Deppner† [1], *N. Herrmann*[1], *P.-A. Loizeau*[1], *K. Wisniewski*[1], *C. Xiang*[1,2], *Y. Zhang*[1], *M. Ciobanu*[3], *J. Frühauf*[3], *M. Petriş*[4], *and M. Petrovici*[4]

[1]Physikalisches Institut Uni. Heidelberg, Heidelberg, Germany; [2]Institute of Particle Physics, Central China Normal University, China; [3]GSI, Darmstadt, Germany; [4]NIPNE, Bucharest, Romania

For the low rate region (< 1 kHz/cm^2) of the CBM Time-of-Flight wall the setup of Multi-strip Multi-gap Resistive Plate Chambers (MMRPC) equipped with thin standard float glass is considered to be a proper solution which allows to fulfill the PID capability requirements [1]. Making use of the knowledge gained from the previous prototype (see [2]) we developed a new fully differential large area MMRPC prototype at Physikalisches Institut in Heidelberg. Here we report on the design of this counter and present first results obtained during test experiments at GSI.

Figure 1: MMRPC mounted in a aluminum box. 16 out of 32 readout strips were equipped with FEE-boards directly on the counter

In order to approach a real size demonstrator we enlarged the active area of the new counter to 32 x 27 cm^2. Consequently the number of strips was increased to 32. For mechanical stiffness 6mm thick honeycomb structured layers were introduced. Fig. 1 illustrates the MMRPC embedded in the gas-tight aluminum box. The inner structure of the counter (gap size, number of gaps, strip width, glass thickness and glass type) is identical to the previous prototype [2]. Modifications were done on the signal pickup electrodes by improving the impedance matching to the front end electronics (FEE) which is now in the order of 93 Ω and in particular on the signal transition between strip and FEE. Alternatively it is possible now to connect the FEE-cards carrying the PADI-discriminator directly on the RPC pickup electrode. Therefore RPC signals which are in the order of 20 mV can be discriminated immediately without quality loss due to propagation in the cable. During the test beam time some of the strips were equipped with FEE-boards on the counter. Fig. 2 shows the obtained dependence of the efficiency on the applied RPC high voltage. The red squares symbolize the measured efficiency with the electronics attached directly on the RPC inside the box. The threshold of PADI which is applied after the amplification (Gain ≈ 8) of the analog signal was set remotely to 27 mV. The black data points are related to the results obtained with the electronics located outside the chamber. The threshold in this cases was set to 30 mV (square) and to 50 mV (diamond). This plot illustrate that the demanded

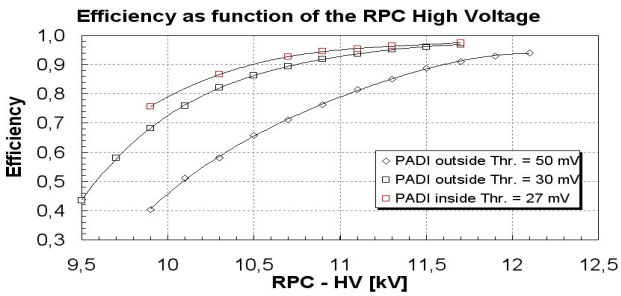

Figure 2: Efficiency vs. applied RPC high voltage for various thresholds.

efficiency of 95% is reachable for thresholds up to 30 mV at the nominal working voltage of about 11.3 kV. Efficiency measurements done with the electronics mounted inside show slightly better results even if one scales them to the same threshold. The best efficiency (above 97%) was achieved at a threshold of 23 mV. The mean cluster size which is defined as the average number of neighboring strips which fire simultaneously is strongly connected with RPC-HV and therefore with efficiency as well. At nominal working voltage it is in the order of 1.3 and is not reducible without efficiency loss. As a reference for time resolution measurements a high granularity MRPC prototype from Bucharest with electrodes made of low resistive glass [3] was used. Due to its good spatial resolution (below mm scale) edge effects of the Heidelberg counter could be studied as well. Including walk correction a full system time resolution of about 70 ps - 75 ps was achieved. Under the assumption that both RPCs have simular resolution a single counter time resolution between 50 ps and 55 ps including the contribution from its FEE is obtained.

References

[1] I. Deppner et al, Nucl. Instrum. and Methods A, Volume 661, Supplement 1, 2012, Pages S121 - S124

[2] I. Deppner et al, CBM Progress Report 2009

[3] M. Petriş et al, CBM Progress Report 2010

*Work supported by BMBF 06HD9121I and EU/FP7 I3 Hadron Physiks 2

† deppner@physi.uni-heidelberg.de

Rate Performance of low-resistive glass MRPCs

J. Wang, Y. Wang, H. Chen, and X. Fan

Department of Engineering Physics, Tsinghua University, Beijing, China

At present MRPCs are considered the best choice to fulfill the CBM-TOF requirements in terms of time resolution, rate capability and granularity [1]. In the current conceptual design, the whole TOF wall is arranged in four "rate regions". In the most inner region of the wall, pad readout MRPCs based on low-resistive glass can be efficiently used to cope with the high particle fluxes (above 20 kHz/cm^2), while strip-readout MRPCs represents a natural choice for the outer region. Here we report on the progress made during the last few years on counter based on the newly developed low-resistive doped glass.

A kind of low resistive silicate glass with bulk resistivity on the order of 10^{10} Ωcm was produced in Tsinghua University. Fig.1 shows a photo of the low resistivity doped glass. The thickness uniformity and the surface quality were obtained with precise devices, yielding excellent performances. The long term stability with time and high transported charge was tested for 34 days [2]. A summary of the parameters is shown in Table1.

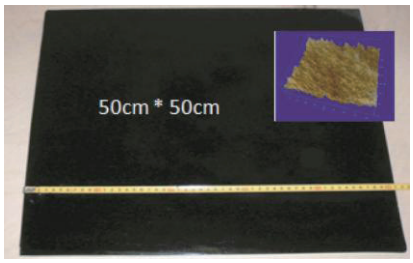

Figure 1: Photo of the low-resistive glass.

Maximal dimension	50 cm × 50 cm
Bulk resistivity	10^{10} Ωcm
Standard thickness	0.7mm, 1.5mm
Thickness uniformity	<20 μm (5μm typical)
Surface roughness	<10 nm
Dielectric constant	7.5 – 9.5
DC measurement	Ohmic behavior Stable up to 1C/cm2

Table 1: Specifications of the low-resistive doped glass.

The rate capability was evaluated in a first experiment in 2009 at GSI-Darmstadt under secondary particles scattering from 2.5 GeV proton collisions. A rate capability of 25 kHz/cm^2 can be estimated (for details, see Ref. [2]).

In order to confirm the rate capability, the electron beam (30MeV) of the ELBE facility [3] at HZDR was used in 2011. Real-size pad and strip modules were developed and tested. Fig.2 and Fig.3 show the compilation of the behaviour of the various counters tested as a function of the average particle flux. The rate capability of this type of MRPCs can reach up to the range of 25 - 35 kHz/cm^2.

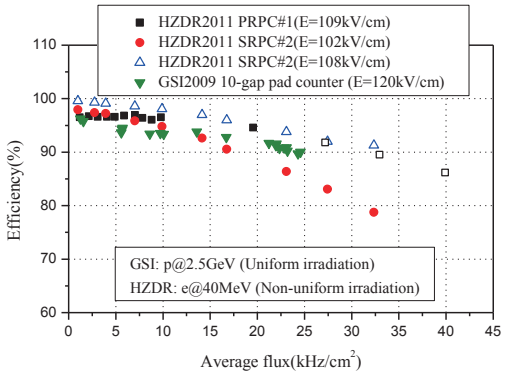

Figure 2: Efficiencies of the various counters tested as a function of the average flux. The open symbols indicate the extrapolated efficiencies (using DC model [4]).

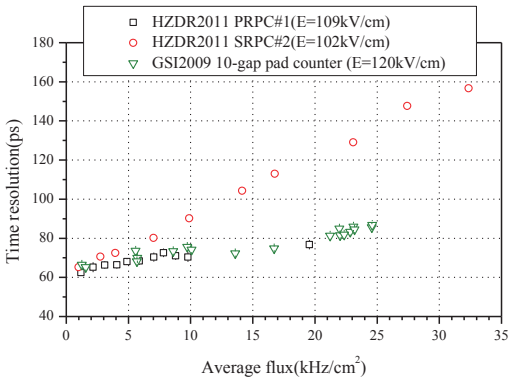

Figure 3: Time resolutions of the various counters tested as a function of the average flux

At GSI the proton beam was uniformly distributed, while at HZDR the electron beam profile was non-uniform. We have observed that the estimate of the average flux under the non-uniform irradiation condition is strongly connected with the definition of the effective area. In this report the average flux is obtained with the mathematical expectation of the beam profile. However, more detailed analysis should be done in future.

References

[1] I. Deppner, et al., Nucl. Instr. and Meth. A (2010), doi:10.1016/j.nima.2010.09.165

[2] J. Wang, et al., Nucl. Instr. and Meth. A 621 (2010) 151.

[3] L.Naumann, et al., Nucl.Instr. and Meth. A 635 (2011) 113.

[4] D. Gonzalez-Diaz et al., Nucl. Phys. B (Proc. Suppl.), 158(2006)111.

Aging Test of High Rate MRPC

*Yi Wang**, *Xingming Fan, Jingbo Wang, Huangshan Chen, Yuanjing Li, and Jianping Cheng*
Department of Engineering Physics, Tsinghua University, Beijing, 100084, China

The TOF wall of CBM, used for hadron identification, is proposed to be constructed with MRPCs[1]. In the center area, MRPCs have to be assembled with low resistivity glass to reach the high hadron flux rate up to $20kHz/cm^2$. A kind of low resistive silicate glass with bulk resistivity in the order of $10^{10}\Omega \cdot cm$ were produced in Tsinghua University[2]. Two kinds of MRPCs (Pad readout and strip readout) were developed with this low resistivity glass. The beam test results shows that the detectors have a very promising rate capability: time resolutions below $70ps$ and efficiencies larger than 90% were obtained for particle fluxes up to $30kHz/cm^2$. The low resistivity glass is a new material, The goal of the test is to know if the performance of the detector is deteriorated by the large irradiation dose expected in the experiment in several years of operation.

The experiment was operated with the pad MRPC[3] assembled with low resistivity glass. The dimension of readout pad is $2cm \times 2cm$. The detector consists of ten gaps and the width of gap is $220\mu m$. The working gas consists of 90% Freon, 5% isobutane and 5% SF6. The working voltage is $12kV$. An X ray machine is used to do the radiation experiment. In order to monitor the performance, two digital rate meter were used to record the current and signal rate per minute. This is shown in Fig.1.

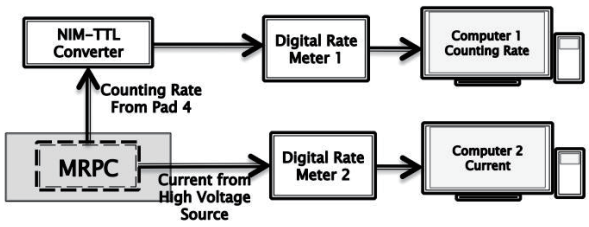

Figure 1: The schematic diagram of monitoring syetm.

The dose rate is about $2.16 \times 10^{-3}Gy/h$, which is equal to be irradiated with $30MeV$ electron with flux rate of $10kHz/cm^2$. The irradiation is separated into three phase and the total time is $300hours$. Fig.2 shows that the current and counting change with test time. It can be seen that the current is stayed at $200nA$ and the counting rate is about $35kHz/pad$. Both are very stable during the irradiation time. To protect the X ray supplier, the machine has to be switched off for $30minutes$ between every $8hours$ of irradiation. It can be seen from Fig.2 when the X ray is switched on or off, the current and counting change very fast. Fig.3 and 4 show the comparison between high rate MRPC and common glass MRPC. When the X ray supplier turn on, current takes a few seconds for high rate MRPC to reach stable state, but for common glass MRPC, this process will last about two hours.

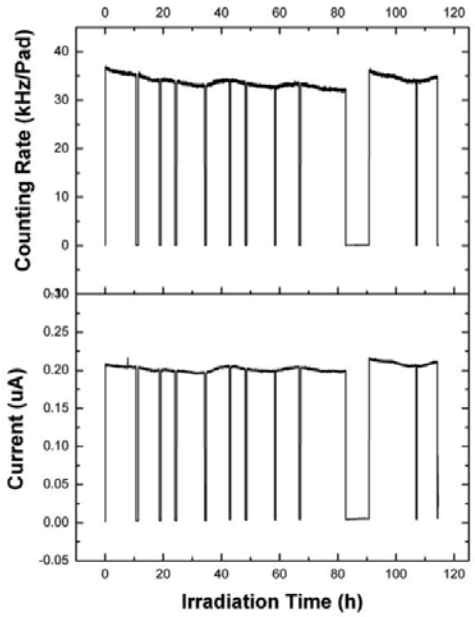

Figure 2: Current and counting rate change with test time.

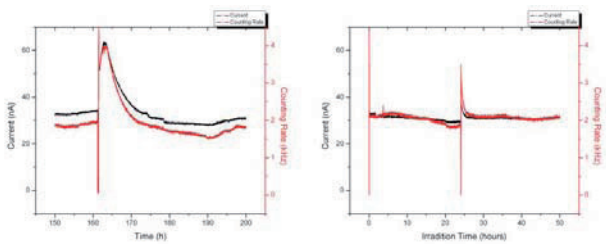

Figure 3: Current and counting rate change with test time.

Between each phase, the MRPC has to be test with cosmic ray. Efficiency, time resolution and other performance were tested. For example, the time resolution of the 4^{th} pad is $90ps$ before irradiation, it becomes $95ps$ after $100hour's$ irradiation and it is about $90ps$ after $300hour's$ irradiation. In conclusion, we do not observe any significant performance degradation .

References

[1] I.Deppner et al. Nucl. Instr. Meth. A 661 (2012) S121-S124
[2] Jingbo Wang et al. Nucl. Instr. Meth. A 621 (2010) 151-156
[3] Yi Wang et al. Nucl. Instr. Meth. A 661 (2012) S134-S136

* yiwang@mail.tsinghua.edu.cn

Development of ceramics RPC for high rate capability timing detector application *

B. Kämpfer[1], *M. Kaspar*[1], *R. Kotte*[1], *A. Laso Garcia*[1], *L. Naumann*[1], *R. Peschke*[1], *D. Stach*[1], *C. Wendisch*[1], *and J. Wüstenfeld*[1]

[1]Helmholtz-Zentrum Dresden-Rossendorf, Germany

The installation of timing Resistive Plate Chambers (RPC) is under consideration for the Compressed Baryonic Matter (CBM) experiment [1]. For that purpose prototype timing RPC have been developed at Helmholtz-Zentrum Dresden-Rossendorf (HZDR). Electrodes with a volume resistivity of about $10^9\,\Omega$cm [2, 3] are considered for detectors to cope with high rates of $\leq 2{\cdot}10^4\,\mathrm{s}^{-1}\mathrm{cm}^{-2}$. Special ceramics composites have been developed and processed.

Two new ceramic prototypes have been built and tested in 2011. One small ($10\times10\,\mathrm{cm}^2$) prototype with 300 μm gas gaps and one larger detector ($20\times20\,\mathrm{cm}^2$) with 250 μm gas gaps. Both detector are dual-two gap type, where the gaps are obtained by means of mylar separators in the small RPC and by fishing line in the large one.

These two detectors were exposed to 30 MeV electron at the electron accelerator ELBE@HZDR, and to 2.5 Gev/c protons at COSY, FZ-Jülich. With the electron beam, the beamspot amounts to 10-20 cm^2, while for the proton beam the beamspot was in the order of mm^2. In both tests, efficiency and time resolution have been measured at the most central part of the detectors (Figure 1 and 2), and the rate capabilities (defined as a 5 % efficiency drop) of these RPCs have been extracted from the data. Thus the larger detector has a rate capability of $\sim 8{\cdot}10^4\,\mathrm{cm}^{-2}\,\mathrm{s}^{-1}$ and the small detector of $\sim 10^5\,\mathrm{cm}^{-2}\,\mathrm{s}^{-1}$.

The efficiency is estimated as the number of hits in the RPC, with valid time signals, divided by the number of coincidence signals in the trigger scintillators. For the time of flight a gauss fit to the meantime spectra between both ends of the same strip is obtained. The contribution of the reference time is quadratically substracted. For the proton beam, due to the small size of the beamspot, only the strip with the most hits is taken into account for the time of flight estimation.

Due to the small charge corresponding to the signal collected by the detector no walk-correction was performed. Also the contribution of the electronics was not substracted.

All these values are obtained with high voltages such that the apparent field in the gas gap would amount to ≈100-115 kV/cm (Figure 3).

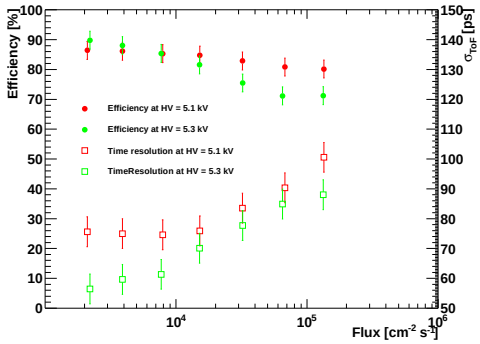

Figure 1: Efficiency and time resolution of the $20\times20\,\mathrm{cm}^2$ RPC as a function of the average electron flux.

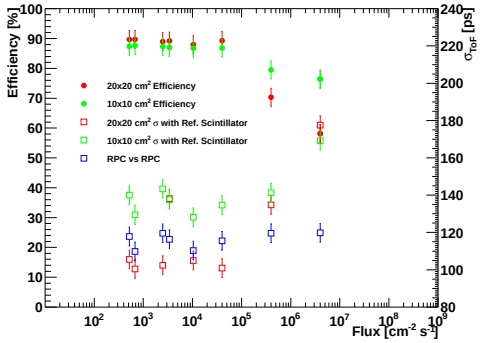

Figure 2: Efficiency and time resolution for both large and small detectors as a function of the average proton flux.

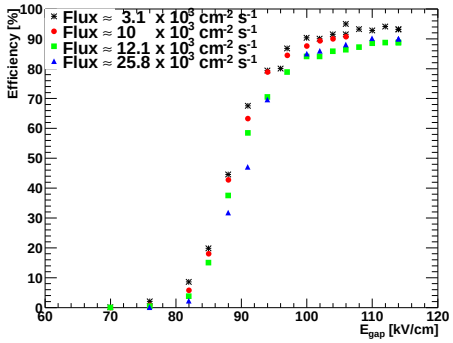

Figure 3: Working curves as a function of the electric field in the gap for the 20x20 cm^2 RPC.

References

[1] I. Deppner et al., Nucl. Instr. Meth. A 661 (2012) 121

[2] L. Naumann et al., Nucl. Instr. Meth. A 628 (2011) 138

[3] L. Naumann et al., Nucl. Instr. Meth. A 635 (2011) 113

* Work supported by BMBF 06DR9059D.

In beam test of CBM-TOF electronics chain*

P.-A. Loizeau[1], *N. Herrmann*[1], *I. Deppner*[1], *K. Wisniewski*[1], *C. Xiang*[1,2], *J. Adamczewski-Musch*[3], *M. Ciobanu*[3], *H. Deppe*[3], *H. Flemming*[3], *J. Frühauf*[3], *K. Koch*[3], *S. Linev*[3], *and S. Manz*[4]

[1]Physikalisches Institut, Universität Heidelberg, Germany; [2]Institute of Particle Physics, Huazhong Normal University, China; [3]GSI, Darmstadt, Germany; [4]Kirchhoff-Institut für Physik, Heidelberg, Germany

The data acquisition of the CBM experiment will be mostly free-streaming. We develop a prototype for the CBM-Time Of Flight wall electronic chain, specifically developped for Resistive Plate Chambers (RPC), and present here in-beam test results. The free-streaming data were acquired last November at COSY, Jülich, with an hybrid DAQ combining and synchronizing them with triggered data.

The self-triggered chain hardware was the same as last year test in COSY[1], while the RPC was the full size prototype tested this June at GSI with triggered electronics[2]. Modifications were done to the Readout Controller (ROC) and DABC DAQ to reset all GET4 chips automatically if their buffer get stuck. The signals used as time reference in this test are produced by 3 plastic scintillators, 2 in front of the setup and 1 in the back, equipped on both ends with Photomultipliers (PMT). We readout these signals in a triggered CAEN VME TDC board, to decouple the readout system test from the triggered detectors test. For this reason we need the hybrid system. The trigger was built from coincidences of 1 front and 1 back scintillator signals. Detector signals are measured with the GET4 free-streaming TDC.

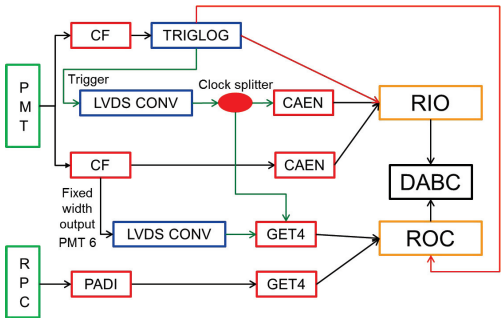

Figure 1: Synchronization in the hybrid system, Green lines are time synchronization signals and red ones are event synchronization. CF = Constant Fraction Discriminator.

The synchronization between the two systems proceed with two levels of accuracy: first at the event level, using already existing possibilities of the DABC DAQ and the TRIGLOG trigger board, then at the timing resolution level, using signals measured in both systems. The first one allows to match free-streaming hits with a defined triggered event. It is done by injecting in both the MBS event and all ROC data streams an event number generated by the TRIGLOG. This number is timestamped by each ROC on reception. The second one allow to have a common point for each event in both the free streaming time frame and the triggered TDC time frame. This is needed to compare the reference time to the detector time and evaluate the system performances, as they run on different clocks. It is performed by converting the NIM trigger signal from the triggered system to a LVDS signal accepted by both systems, splitting it with a low jitter clock splitter and reinjecting it in the input of the GET4 TDC and the CAEN TDC, see Fig.1. The PMT 6 signal is also measured in the GET4 system, allowing for an independent cross check of the time offset.

The time resolution is obtained from the width of the time difference distribution $\Delta t_{ref} = (t_{f1} + t_{f2})/2 - (t_{f3} + t_{f4})/2$ of the front scintillators. It amounts to $\sigma_{\Delta t_{ref}} = 45ps$. The contribution of the time synchronization part of the setup can be estimated by calculating the time difference between the PMT6 signal in the triggered system and its signal in the free-streaming system, re-aligned using the offset obtained with the trigger signal: $\Delta t_{PM6} = t_{PM6,CAEN} - t_{PM6,GET4} - Offset$ with $Offset = t_{trigger,CAEN} - t_{trigger,GET4}$. The contribution is given by the width of the difference between those two, as in Fig. 2, which gives $\sigma_{\Delta t_{PM6}} = 80ps$.

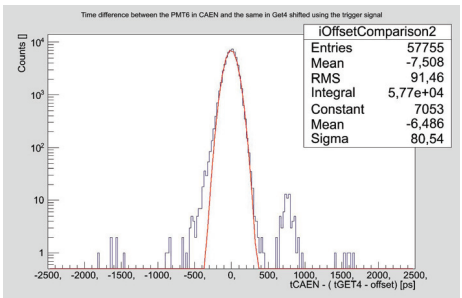

Figure 2: Difference between the real time of PMT6 in the triggered system and the same time in the free-streaming system corrected using the trigger signal

Next steps for the estimation of the free-streaming system performances are extracting both time resolution and efficiency for the RPC + electronic part and comparing to the triggered system to extract the electronics contribution. This comparison will be based on data with a maximum rate of around 100Hz, up to which the current free-streaming system run stably.

References

[1] P.-A. Loizeau et al., “CBM Progress report 2010”, Darmstadt 2011, p.55

[2] I. Deppner et al., “Performance of large area MMRPC prototype”, this report

* Work supported by EU/FP7 WP2 and BMBF 06HD9121I

FPGA based control and monitor for CBM-TOF - readout*

C. Xiang† [1,2], *N. Herrmann*[2], *I. Deppner*[2], *P.-A. Loizeau*[2], *K. Wisniewski*[2], *Y. Zhang*[2], *J. Frühauf*[3], *S. Linev*[3], *and S. Manz*[4]

[1]Institute of Particle Physics, Central China Normal University, China; [2]Physikalisches Institut, Universität Heidelberg, Germany; [3]GSI, Darmstadt, Germany; [4]Kirchhoff-Institut für Physik, Heidelberg, Germany

As the CBM experiment will apply a free streaming data acquisition system, the system will be exposed to a potentially very high data rate with like in the case of noisy channels. In order to suppress useless data as soon as possible to prevent bottle-necks in readout bandwidth, we design a data preprocessing module in the readout chain [1]. In order to control the proper functioning of the system one needs in addition a monitor module. A third task that could be integrated in the readout controller is a control module that could be used e.g. to automatically modify thresholds. The system is sketched in Fig. 1.

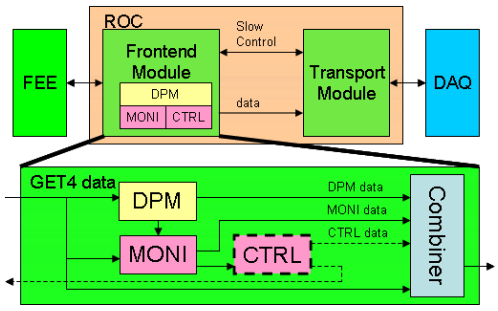

Figure 1: ROC firmware (Frontend module)

The data preprocessing module (DPM) reads in data from the GET4-ASIC [2], inspects the data and sends the results by the transport module to the DAQ system. Several functions are implemented in the DPM like time ordering, hit building and checking the validity of the time-over-threshold (TOT) determination. The main task of the monitor module is to assure the synchronization of the system. This is done by checking the validity of the epoch marks that are part of the GET4 data output stream. When any of these status goes wrong, a message will be sent to DAQ and possibly to the control module. After the control module gets these messages, it will decide what to do and send the control information to DAQ at same time. The monitor module also reads the PADI thresholds and the status of the DPM. To control the full TOF system different ways to implement a control tasks are possible ranging from manual control to fully automatic self-control. While the best control strategy is still under evaluation, for the test experiments, that are performed with prototype components, the manual control initialized by the user via the DAQ interface is fully sufficient.

* Work supported by China Scholarship Council, BMBF 06HD9121I and EU/FP7 I3 Hadron Physiks 2

† chxiang@physi.uni-heidelberg.de

As the logic resources in the FPGA of the ROC board are limited, the DPM only implemented from channel 0 to channel 7 out of 56 channels. The ROC firmware was tested at COSY with proton beam. The software for the offline analysis is under development at which first results are presented here. The left panel of Fig. 2 shows the examples of TOT spectrum registered in different channels. The red line is the TOT of channel 9. Comparing with other channels, it has larger number of hits than others, and the TOT spectrum extends to very large unphysical values. This is because of the threshold of channel 9 is too low, which requires an increase of the PADI discrimination threshold. After reconfiguring its threshold, another run was obtained. The right panel shows the total number of hits and the number of valid hit. The black line shows the number of valid hits obtained by the offline analysis, the red line the total number of hits obtained by the offline analysis, the green line the total number of hits obtained by the DPM in ROC, the blue line the number of valid hits obtained by the DPM in ROC. For the first 8 channel, only blue line can be seen, as the other three colored lines are over written. This shows that the DPM in ROC gives the same results as offline analysis. There is a large difference between the total number of hits and the number of valid hits registered on channel 13, the reason is its rising edges and leading edges were separated in two epochs. The only way to resolve this problem is to reset the GET4 chip.

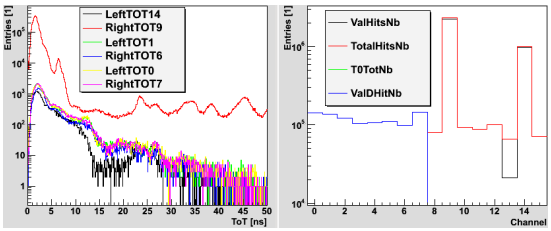

Figure 2: Left: Channel TOT spectrum; Right: the number of hits

The offline analysis result shows the DPM and the monitor module function properly. Next step is adding new features in the DPM, like cluster finding, and implementing self-control.

References

[1] S. Manz, GET4 Read-Out Development, CBM FEE/DAQ Workshop, February 22nd-23rd, 2010@GSI

[2] H. Flemming and H. Deppe, IEEE-NSS, Orlando (2009), 1082

FLUKA calculation for the beam dump of CBM at SIS300

A. Senger[1], G. Fehrenbacher[1], T. Radon [1]

[1]GSI, Darmstadt, Germany

The Compressed Baryonic Matter (CBM) experiment is one of four scientific pillars of the FAIR project. The CBM research program is focused on the investigation of dense nuclear matter as it exists in the core of neutron stars. Such conditions are generated in the collision zone of heavy ions at FAIR energies. Promising probes of the dense fireball are particles which contain strange or even charm quarks. These particles, however, are produced very rarely, and, therefore, the experiment requires the highest beam intensities. In order to avoid secondary collisions of the produced particles in the target the interaction probability of the beam with the target is only 1%, and almost the entire beam hat to be stopped in the beam dump. The highest dose rates and activation are expected for a 35 A GeV gold beam with the intensity of 10^9 ions/s, and for a 90 GeV proton beam with the intensity of 10^{11} p/s.

FLUKA [1, 2] calculations were carried out for the construction permission of the building G014 (CBM Cave). One of the most important components of the building G014 concerning radiation safety is the beam dump (Fig.1). It consists of about 3430 tons of steel and 5830 tons of concrete (the dimensions are shown in the Fig. 1). The FLUKA dose calculations were carried out for a 35 A GeV gold beam with the intensity of 10^9 ions/s, and for a 90 GeV proton beam with the intensity of 10^{11} p/s. Gold discs of 250 µm (for gold beam) or 3 mm of thickness (for proton beam) were used as a targets corresponding to an interaction rate of about 1% in each case.

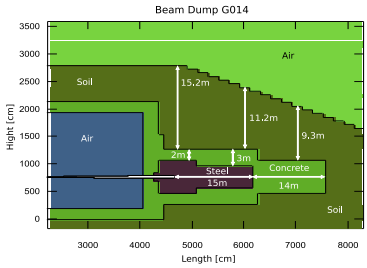

Figure 1. FLUKA geometry of the CBM beam dump

The Z projection of the dose rate in the beam dump around the beam (r =50 cm) is shown in figure 2. One can see that the dose rate at a distance of 15 m after the concrete wall exceeds the value of 10 µSv/h for the proton beam (blue extrapolation line), while the dose rate for the gold beam is less than 0.5 µSv/h (red extrapolation line).

Another parameter which was studied is the profile of the dose rate in different cut positions. The profile is different for proton and gold beams, but the dose level above soil stays below 0.5 µSv/h. According to [3] the concrete shielding should have a thickness of 1.2 m for proton-induced muons at 35 GeV and a beam intensity of 10^9 p/s, and a thickness of 2.4 m for 100 GeV protons and a beam intensity of 10^{11} p/s. According to the results of the FLUKA calculations these conditions are fulfilled by the design of CBM beam dump.

The FLUKA results demonstrate that the height of the CBM beam dump is sufficient to shield a 90 GeV proton beam with an intensity of 10^{11} p/s. However, the length of the beam dump is too short to shield the muons. The beam dump consists of about 15 m of steel and 14 m of concrete in beam direction. Corresponding to the FAIR ground plan the distance from the end of the beam dump up to the fence of GSI is approx. 80 m of soil. According to [4] the shielding performance of the CBM beam dump (15 m of steel, 14 m of concrete and 80 m of soil) corresponds to 40 m of iron. Using the formula from [4] one can estimate the dose rate after an iron shielding of 40 m thickness. The expected dose rate is about 0.01 µSv/h for a proton beam at 90 GeV with an intensity of 10^{11} p/s. This result was confirmed by FLUKA calculations of the dose rate in the soil after the beam dump for a proton beam at 90 GeV with an intensity of 10^{11} p/s. In conclusion, the shielding effect of the soil after the CBM beam dump is sufficient for 90 GeV proton beams with an intensity of 10^{11} p/s.

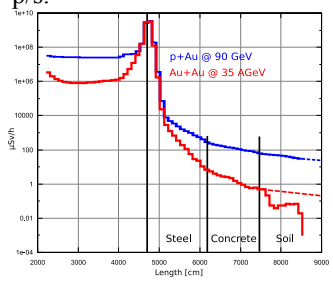

Figure 2. Dose rate in the beam dump for a proton beam at 90 GeV (blue line), and for a gold beam at 35 A GeV (red line)

References

[1] "The FLUKA code: Description and benchmarking", G. Battistoni, S. Muraro, P.R. Sala, F. Cerutti, A. Ferrari, S. Roesler, A. Fasso`, J. Ranft, Proceedings of the Hadronic Shower Simulation Workshop 2006, Fermilab 6-8 September 2006, M. Albrow, R. Raja eds., AIP Conference Proceeding 896, 31-49, (2007)

[2] "FLUKA: a multi-particle transport code", A. Fasso`, A. Ferrari, J. Ranft, and P.R. Sala, CERN-2005-10 (2005), INFN/TC_05/11, SLAC-R-773

[3] "Shielding against High Energy Radiation", Landolt-Börnstein, New Series Group 1, Volume 11, Springer Verlag

[4] "A guide to radiation and radioactivity levels near high-energy particle accelerators", A.H. Sullivan, Nuclear Technology Publishing 1992

SysCore3 — a new board for the Universal ROC*

N. Abel[1], *C. Garcia*[1], *J. Gebelein*[1], *S. Manz*[1], *and U. Kebschull*[1]

[1]Infrastructure and Computer Systems for Data Processing (IRI), Frankfurt University, Frankfurt/Main, Germany

Introduction

Since 2007 our contribution focused the Silicon Tracker's FEE (Front End Electronic). Since 2009 we are also designing and implementing readout logic for the GET4 chip. To keep the re-usability as high as possible, we split the ROC into two fully independent modules: the readout logic and the transport logic. This modularization of the ROC and the consequential separation of the control software into different layers, enabled us to provide a Universal ROC, which offers quick access to a long-run tested transport logic and allows us to easily add new readout logic for further FEE setups [1]. The Universal ROC is currently based on the SysCore2 board. In 2011 we focused on the further support of the GET4 chip, the development of a Feature-Extraction for TRD [2] and the design of the new SysCore3 board, which will become the new basis of the Universal ROC in 2012. The design of the SysCore3 board is the logical next step in the development of a platform which shall be as flexible as possible. Based on its flexibility SysCore3 is planned to be used as prototyping platform in a number of subsystems. Examples are the development of read-out ASICs using CBMnet interfaces, the development of read-out controllers for nXYTER and GET4, CBMnet HUB chip development and DPB development. Furthermore the SysCore3 will serve as fault tolerant read-out controller for ToF [3].

The SysCore3 board is based on a Spartan-6 LX150T (while SysCore2 is based on a Virtex-4). This change is motivated by the high difference in cost between the Virtex-Series and the Spartan-Series. It is enabled by the fact that, starting with Version 6, the Spartan-Series supports high speed optical links, high speed interfaces (like DDR3) and dynamic reconfiguration which is essential for fault tolerance [4].

CBMnet

If two or more boards are used to reconstruct a physical event, such as the motion of a particle, one of the most important features is time synchronization. The CBMnet provides a very flexible synchronization approach which does not depend on cable lengths [5]. If a board shall not only be able to receive an external clock via an optical port, but shall also be able to respond with a determined latency on the same port, it needs a special connection between the FPGA and this optical port. To put it in a nutshell, the optical port needs different reference clocks for its receiver and its sender part. The SysCore3 board implements this special connection on a particular port (called "uplink"). Furthermore it provides a jitter cleaner which takes the recovered clock from the FPGA, cleans the jitter and thus enables the usage of the recovered clock as reference clock for optical transceivers. This board-based feature is essential to be able to fully support the CBMnet functionality.

Fault Tolerance

The heart of most ROCs is an SRAM based FPGA, since these FPGAs provide the best combination of performance and long-term flexibility. However, there is a crucial problem regarding FPGAs: the radiation which is inevitable in high energy physics experiments can cause the FPGA's doped silicon to change its electrical properties. This physical separation of electron-hole pairs results in spontaneous Single Event Effects (SEE). This becomes extremely critical for flip-flops at clock signal setup/hold times, which can lead to erroneous data and in the worst case to a total system halt. Thus, the usability of FPGAs in radiation environments highly depends on the usage of mitigation technologies such as scrubbing (based on dynamic reconfiguration). This has a strong influence on the board design: the SysCore3 board provides an external FLASH memory and an additional radiation hard flash-based FPGA — both are essential to be able to realize scrubbing. In 2011, example designs have been practically tested under experimental conditions within different particle accelerator beams. Test boards have been directly placed into the center of the particle beam line to get comprehensible results at a maximum ionization impact. Current results are very encouraging and show that the usage of scrubbing in combination with double or triple module redundancy significantly reduces the number of radiation based functional interrupts [6].

References

[1] N. Abel et. al, "Design and Implementation of an Universal Read Out Controller", GSI Progress Report 2009, Darmstadt, Germany

[2] C. Garcia, "First steps towards feature extraction in TRD" CBM Collaboration Meeting 2011, Beijing, China

[3] W. Müller, "SysCore V3 - Hardware Concept and Use Cases" CBM Collaboration Meeting 2011, Beijing, China

[4] N. Abel, "SysCore V3 - Firmware Aspects" CBM Collaboration Meeting 2011, Beijing, China

[5] F. Lemke et. al, "A Unified Interconnection Network with Precise Time Synchronization for the CBM DAQ-System" RT-2009, Beijing, China

[6] J. Gebelein et. al, "FPGA fault tolerance in radiation susceptible environments" GSI Progress Report 2011, Darmstadt, Germany

* Work supported by BMBF (06HD9123I)

ALICE CRORC as CBM FLES Interface Board Prototype

H. Engel and U. Kebschull
Goethe University Frankfurt, Germany

The ALICE Common Read-Out Receiver Card (CRORC) is an FPGA based PCIe read-out card with high density parallel optic connectivity which is currently being developed at CERN. As the requirements for a CBM First Level Event Selector Interface Board (FLIB) prototype are similar to this card, FLIB-specific requirements have already been considered during the planning of the CRORC.

ALICE Background

The ALICE Experiment at CERN is using FPGA based Read-Out Receiver Cards (RORCs) at Data Acquisition (DAQ) and High-Level Trigger (HLT) as an interface between the optical Detector Data Link (DDL) and the host machines. The currently used RORCs at DAQ and HLT have similar functionality, but have been developed as independent projects. However, they are now facing the same problem: both cards implement PCI-X as interface to the host machine, which was a state of the art interface standard at the time these cards have been developed, but can now hardly be found in any recent PC mainboard. Furthermore, increased read-out data rates on the optical links are planned, but not possible with the current RORCs.

These facts lead to the development of the CRORC as a common project of DAQ and HLT with recent hardware and interface standards.

FLIB Prototype Requirements

The FLES Interface Board serves as an interface between Data Processing Boards and the First Level Event Selector. It is planned to be implemented as an FPGA-based PCI-Express plug-in card with optical interfaces at the FLES input nodes. Streaming data received on the optical interface from the front-end electronics via Read-Out Controllers and Data Processing Boards is received by the FLIB and written into the host machine with Direct Memory Access (DMA). A first prototype board is required as a test platform for FLES hardware and software development as well as a read-out device for testbeams or lab setups.

The full FLES cluster will be fully equipped at a very late stage but all detector components have to be connected at early stages so for the prototype a large number of links is more crucial than a high input rate per link. The FLIB read-out is planned as a two staged process with large on-board buffers to mitigate PCIe bottlenecks and enable partial or on-demand read-out. A FLIB prototype is therefore required to have plenty of DDR memory with a high bandwidth. A more detailed description of the FLES architecture can be found in [1].

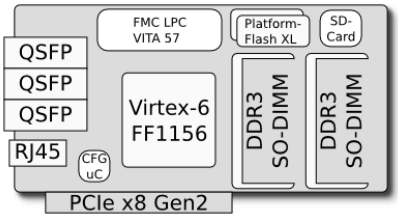

Figure 1: Schematic sketch of the CRORC

CRORC as FLIB Prototype

The CRORC currently developed for ALICE is a Virtex-6 FF1156 based board with twelve optical links, a PCIe interface and two DDR3 SO-DIMM sockets. A sketch of the board is shown in figure 1.

The FPGA-internal PCIe hard block is used as interface to the host machine which enables the use of up to eight PCIe Gen2 lanes with an overall bandwith of up to 32 Gbps. The twelve optical links are realized with three QSFP sockets connected to the Virtex-6 GTX transceivers. A configurable transceiver reference clocks allows link speeds over the whole range of the GTX capabilities of up to 6.5 Gbps per link.

The two DDR3 SO-DIMM sockets can be equipped with standard DDR3 memory modules and can be operated independently with up to 1066 Mbps per data line. The second socket has specifically been added for FLIB prototype purposes.

An FPGA Mezzanine Connector (FMC) allows the connection of custom interface modules or external transceiver reference clocks to the FPGA in order to run the CBMnet protocol.

The FPGA configurations can be stored in on-board flash memories for automatic configuration. Configuration management and monitoring can be done with the FPGA and a microcontroller. An SD-Card slot provides additional non-volatile memory and the RJ45 socket can be used for LVDS IO.

Status of the CRORC

The schematic design of the CRORC is completed and the PCB layout is mostly done. Component purchase and prototype production are currently being prepared. First prototypes are expected for 2012.

References

[1] J. de Cuveland et al., "CBM First-level Event Selector Dataflow Architecture and Microslice Concept" , This report

FPGA fault tolerance in radiation susceptible environments*

J. Gebelein[1] *and U. Kebschull*[1]

[1]Infrastructure and Computer Systems for Data Processing (IRI), Frankfurt University, Frankfurt/Main, Germany

Continuous research and development in the field of particle accelerator detector electronics focusing on Static Random Access Memory (SRAM) Field Programmable Gate Arrays (FPGA) confirmed that the use of fault tolerance techniques is inevitably required for safe operation in radiation susceptible environments [1, 2, 3]. (Not even ASICs are spared from it [4].) Therefore, several formerly presented research results dealt with the well-known partial configuration scrubbing, especially Blind Scrubbing, supported by a subset of such devices as well as the creation of standardized components to be used within a Programmable System-on-Chip (PSoC) [5]. Current approaches mainly address techniques on Register-Transfer-Level (RTL), for example the use of Hamming-based Finite State Machines (FSM) in combination with Global Triple Modular Redundancy (GTMR). Due to the fact that commercially available tools like Mentor Precision Rad-Tolerant Tool, BYU Partial TMR Tool (BLTmr), Xilinx XTMR Tool and STAR Tool, which apply GTMR to existing hardware designs, are quite expensive and are working on netlists only, manual Hamming FSM designs with surrounding TMR have been created and tested in GeV proton particle beam at the COSY accelerator in Juelich, Germany. Manual design of fault tolerance on RTL means in the first order to multiply existing resources and to teach synthesis tools to do not remove them when optimizing the circuitry in several stages. Code multiplication itself comprises mainly of signal duplication/triplication and the correspondent use in the entire design. For example, when a concurrent process statement is triplicated, each externally read and written signal within has to be triplicated. Furthermore, each of these new processes has to be adapted to use only one of the triplicated signals. In case of single connected external resources (e.g. I/O pins) are used within the process statement, new signals have to be added, which are provided with voters for output direction or splitters for input direction. Because this manual design is error-prone and mistakes may lead to an overall reduced fault tolerance of the entire design, an automated approach is currently going to be realized. This tool may be the first step for a designer to create a fault-tolerant design on RTL. Afterward, he can decide whether or not to use the provided mechanism or to reduce some parts to a less sensitive fault tolerance method. Some of these manually created fault-tolerant designs were tested in GeV proton particle beam as seen in figure 1. All of the designs implemented a 2048 states Hamming FSM with a minimum distance of 3 and used Blind Scrubbing to continuously restore static configuration memory. Whereas design C did not use any additional fault tolerance and hence showed the worst results, design E added GTMR and FSM dummy transitions and hence returned the fewest output errors. As seen, Scrubbing works perfectly in restoring configuration memory and even better when joined with fault tolerance techniques, but can still be improved by advancing from Blind Scrubbing to Selective Frame Scrubbing, which is going to be implemented within the next project phase. Looking forward to a detector providing maximum fault tolerance, the recommendation is to double/triple all signal paths, including I/O pins.

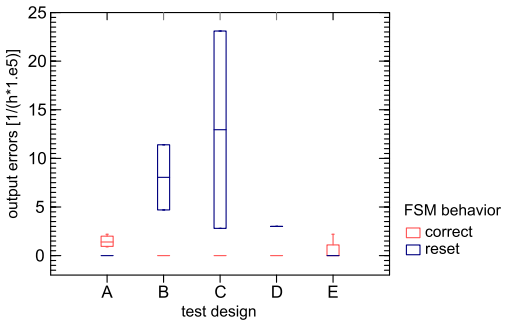

Figure 1: Boxplot (median and quartiles) of the obtained Hamming d=3 FSM beamtest results, normalized to 1/h, 100% chip size and 1.e5 p+. Test designs are using Blind Configuration Scrubbing as well as the following fault tolerance techniques: A: nearly GTMR with FSM dummy transitions, B: nearly GTMR, C: none, D: GTMR, E: GTMR with FSM dummy transitions. I/O pins as well as DCM are single-use in all designs.

References

[1] N. Battezzati, L. Sterpone, M. Violante, “Reconfigurable Field Programmable Gate Arrays for Mission-Critical Applications”, 1st Edition, 2011, Springer Verlag, ISBN 978-1-4419-7594-2

[2] M. Violante, L. Sterpone, “Reconfigurable FPGAs in radioactive environment”, CERN-talk, October 2011, http://indico.cern.ch/conferenceDisplay.py?confId=152527

[3] K. Røed, “Single Event Upsets in SRAM FPGA based readout electronics for the Time Projection Chamber in the ALICE experiment”, University of Bergen, PhD Thesis, 2009

[4] S. Bonacini, “Redundancy methods in ASICs”, CERN-talk, June 2011, http://indico.cern.ch/conferenceDisplay.py?confId=131762

[5] J. Gebelein, H. Engel, U. Kebschull, “FPGA fault tolerance in radiation susceptible environments”, Proceedings on Radiation Effects on Components and Systems (RADECS) 2010, September 2010

* Work supported by BMBF (06HD9123I)

CBM First-level Event Selector Dataflow Architecture and Microslice Concept*

J. de Cuveland[1], *D. Hutter*[1], *and V. Lindenstruth*[1]

[1]FIAS Frankfurt Institute for Advanced Studies, Goethe-Universität Frankfurt am Main, Germany

The First-level Event Selector (FLES) is the central system in the CBM experiment at which all measured data arrives and is analyzed in real time. The detector frontends operate self-triggered, creating a continuous, time-stamped data stream (Fig. 1). The selection of interesting events in the FLES requires sophisticated online analyses including a complete event reconstruction at an incoming data rate exceeding 1 TByte/s.

The FLES system consists of a scalable supercomputer with custom FPGA-based input interface cards and a fast event-building network (Fig. 2) [1]. It will be constructed largely from standard components. As a site for the FLES computer system, the new FAIR data center ("Green IT Cube") has been identified. This location provides an ideal infrastructure for efficient operation of the computer and offers the opportunity to exploit synergies with other FAIR computing systems installed there.

The input interface into the FLES is implemented by add-on cards in the FLES PCs. The FLES Interface Board (FLIB) requires high-speed optical inputs to receive the data from the CBM readout electronics, a high-performance interface to the host PC, and a large buffer memory. A specially developed FPGA-based card with a PCIe interface at the maximum achievable rate will be employed here. A prototype board, realized in cooperation with the ALICE experiment, is currently in an advanced stage of development. It is based on a Xilinx Virtex-6 FPGA and 8x PCIe, and it contains 12 optical links, each at up to 6.6 Gbit/s, and two DDR3 memory module sockets.

The FPGA design implements the DAQ protocol for receiving the data, merges the input links, manages the buffer memory, and controls the PCIe transfer. In addition, it analyzes the incoming time stamp information and builds index tables to facilitate a timestamp-based data access from the host PC.

As the high event rate of 10 MHz prevents a clear a priori assignment of measured particle tracks to events, fundamentally new techniques are necessary regarding the data flow in the system and the reconstruction of events. The employed selection algorithms need the data pertaining to an event of all detectors in a computing node. Instead of event building as in a triggered system, the FLES performs *timeslice building*. The data is first segmented into timeslices containing several events and then distributed appropriately through a network at the full input data rate of 1 TByte/s. The use of InfiniBand QDR for data transfer between the FLES nodes has proven practical.

In order not to require the full bandwidth in case of special selection scenarios and during the phased commissioning of the system, a two-stage selection process has been

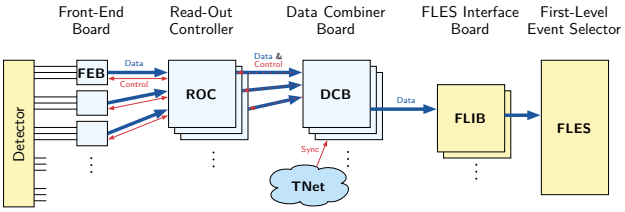

Figure 1: Data flow into the First-level Event Selector.

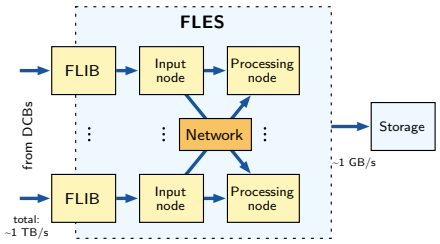

Figure 2: Architecture of the FLES.

developed. Data from detectors that do not contribute to the first selection stage is stored in the input nodes and transmitted only on request for selected events to the appropriate computing nodes.

The individual CBM detectors have very different time resolutions and data format requirements. In addition, the data messages sent by the detectors are usually only a few bytes in size. Therefore, the data format of each subsystem is optimized independently for efficient transmission and analysis. However, the FLES system has to collect the data of each timeslice, i. e., an interval of the continuous detector run-time, from all detectors and transmit it to a compute node. Therefore, it needs a way to divide the continuous data streams of the detectors without any loss of information, and it must be able to access the time information in the data stream in a global format. The new concept of *microslices* solves these problems by introducing a special global container format directly at the inputs of the system, where one container comprises the detector data of a globally defined, constant time interval (e. g., 1 µs). The lightweight container format generates an overhead of less than 2 percent.

After event selection, the data to be stored it is forwarded for archiving. The resulting data stream of at least 1 Gbyte/s is sent directly via the FLES network to the mass storage system.

References

[1] J de Cuveland *et al*, 2011 *J. Phys.: Conf. Ser.* **331** 022006

* Work supported by BMBF 06FY9125D and HIC for FAIR

Status of data acquisition software DABC

S. Linev[1], J. Adamczewski-Musch[1] , and P. Zumbruch[1]

[1]GSI, Darmstadt, Germany

Introduction

The Data Acquisition Backbone Core (DABC) has been established as DAQ and event building software for CBM test beams [1]. Development of the future version 2 of the DABC framework has been started within 2011. A prototype of DABC v2 was applied in fall 2011 for the test beams at CERN and COSY. For the first time DABC nodes were monitored and controlled by an EPICS-based operator GUI.

New DABC features

Several changes in the DABC core classes were done to increase thread safety of the system. A main problem in a multithreaded environment is that objects created and used by one thread can potentially be destroyed by another thread. To provide a convenient solution for the developers, the special *Reference* class was introduced to the framework, implementing a thread-safe pointer to any DABC object.

Another important change in the framework was the introduction of a *ConnectionManager* to establish and maintain the data connections between DABC nodes. Such component is crucial in multi-node setups where the probability of a single-node failure is increasing. The task of the *ConnectionManager* in such case is to renew all connections when a crashed node is restarted.

A new interface to the slow control system was introduced to DABC. In contrast to the first version, the control system is fully decoupled from the core functionality of the DABC framework. An implementation for the previous DIM based control protocol was done. The new interface allows to implement and use several control systems simultaneously.

EPICS control

Already DABC v1 had provided a monitoring and control interface by means of the DIM protocol. To integrate the DAQ to the EPICS slow control system [2] that is common for CBM experiment, a separate DIM-EPICS interface application has been used. During the testbeams, this was run as a component of the main EPICS IOC, together with the other detector control system modules. The DABC records as exported via DIM are subscribed by the EPICS IOC and converted to related EPICS process variables. Hence they can be observed and controlled by a regular EPICS GUI, such as the CSS/BOY environment [3]. Figure 1 shows the dedicated GUI as developed for the CERN testbeam in October 2011.

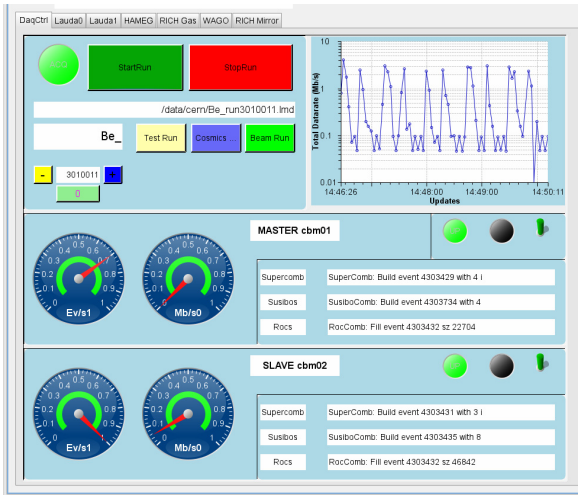

Figure 1: DABC operator GUI at CERN testbeam.

Application for CBM test beams

The version 2 prototype of the DABC framework has been used in production for different test setups of the CBM collaboration. A beamtime for TRD and RICH prototypes was performed at CERN/PS T9 in October 2011 [4]. Here a complex heterogeneous setup was implemented: two MBS systems in two VME crates; 12 Susibo/SPADICs boards; 5 ROC/nXYTERs; EPICS readout. Data from all these components were read out and combined together by three DABC nodes.

Another test beam for TOF/RPC components was done at COSY in November 2011. Here the ROC/GET4 frontend combination was read out via optical fibre connection and PCIe board. A special code in the DABC application was implemented to cope with some readout problems of the GET4 chip.

Status and outlook

Version 2 of DABC is under development and has already been used successfully at different detectors tests by the CBM collaboration. DABC version 2 will be released in 2012 and will provide new functionalities not only for CBM test beams, but also for InfiniBand performance tests.

References

[1] S.Linev, J.Adamczewski-Musch, and J.Frühauf, "DABC as data acquisition framework for CBM", *GSI Sci. Report 2010,* PHN-NQM-CBM-29, p 44.

[2] http://www.aps.anl.gov/epics

[3] http://cs-studio.sourceforge.net

[4] D.Emschermann et al., this report

A Go4-based online-analysis framework for CBM testbeams

J. Adamczewski-Musch[1], *and S. Linev*[1]

[1]Experiment-Electronics, GSI, Darmstadt, Germany

Introduction

The GSI analysis system *Go4* (http://go4.gsi.de) is a standard tool for online and offline analysis, based on the *ROOT* framework. Since 2008 the CBM collaboration has used *Go4* at several detector test beamtimes. To match the requirements for increasing complexity of such tests, the CBM online monitoring software was newly organized as a modular application framework on top of the *Go4* framework.

The software framework

The basic *Go4* framework allows to split subsequent stages of the analysis into "analysis steps", with each step producing intermediate data which is used by the following step. So the first analysis step would unpack the raw data from DAQ. The second analysis step would map such DAQ channels into a detector display and perform a specific analysis. Each analysis step is defined by an "event processor" class which produces an "event element" structure as resulting output.

However, to cover the use case of various readout systems for different test detectors, each of these analysis steps still needs to be divided up in structurally parallel processing entities and their resulting data structures. Hence the CBM beamtime framework introduces a "composite event processor" class that can register and run a number of regular *Go4* "event processors" together within each analysis step. Additionally, the resulting data structures of these software processors are aggregated as a common "*Go4* composite event", reflecting the hierarchy of the DAQ and detector set up. An advanced offline analysis could be implemented in a third analysis step, or could be based on the *Go4* output events stored to *ROOT TTree*s. Figure 1 illustrates the structure of a typical implementation.

By means of shared libraries, the analysis set up for a specific beam time can re-use existing classes of various standard readout components that are acquired and combined by the DAQ system *DABC* [1]. Their data is delivered to *Go4* in generic containers ("*MBS* events"): either via TCP sockets, or as listmode data file. So most components of the first *Go4* analysis step were just configured by macro scripts for the actual runtime setup.

The source code for each beamtime is also organized in a modular way: each detector subgroup can develop and run their individual code as standalone *Go4* analysis. The combination of several or all subgroup codes can run as advanced or full analysis.

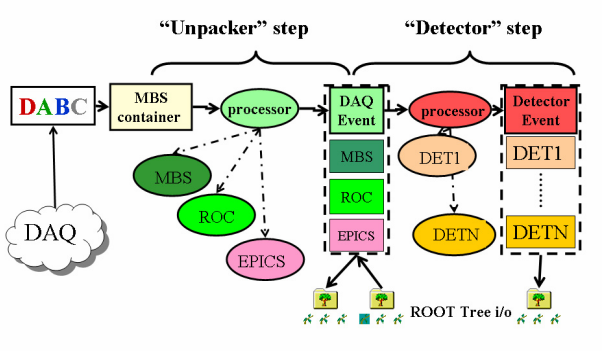

Figure 1: Composite Go4 analysis with two steps

Testbeams at CERN and COSY

In October 2011, a two week test of TRD and RICH detectors was done at CERN PS beam line T9 [2]. Online monitoring and initial offline analysis were implemented with the new *Go4* based framework. In the first analysis step, generic software modules were used, such as for the *ROC/nXYTER* readout, for the *SPADIC* readout [1], and for *EPICS* slow control variables [3]. The unpacking of two MBS crates' data was treated with specific classes.

The components of the second analysis step were developed by various institutes. It has different processor modules for beam monitoring scintillators (Uni Frankfurt, GSI), a fiber hodoscope (Uni Wuppertal), a RICH prototype (Uni Wuppertal, Uni Gießen, GSI), and several TRD stations (Uni Frankfurt, Uni Münster, NIPNE Bucharest, and JINR Dubna). The results of such subdetector analyses are combined in this step and can e.g. be used for particle identification.

For another beamtime at COSY in November 2011, the online monitoring was organized similarly. The first analysis step consisted of modules for a generic *ROC/Get4* and *ROC/NXYTERr* readout, the *MBS* system, and the *EPICS* input. The second analysis step contained code for different TOF/RPC prototypes (Uni Heidelberg, HZDR Rossendorf, NIPNE Bucharest), a diamond detector (GSI), and the fiber hodoscope.

References

[1] S.Linev, J.Adamczewski-Musch, and J.Frühauf, "DABC as data acquisition framework for CBM", *GSI Sci. Report 2010,* PHN-NQM-CBM-29, p 44.

[2] D.Emschermann et al.., this report

[3] J.Adamczewski-Musch, B.W. Kolb, and S.Linev , "DABC data acquisition input for slow control variables", *GSI Sci. Report 2010,* PHN-NQM-CBM-30, p 45.

Numerical Stability of the KF Track Fit in Single Precision*

I. Kisel[1,2], *I. Kulakov*[1,3], *and H. Pabst*[4]

[1]Uni-Frankfurt, Germany; [2]GSI, Darmstadt, Germany; [3]Uni-Kyiv, Ukraine; [4]Intel, Germany

The Kalman Filter (KF) track fit is the core of the event reconstruction in the CBM experiment, therefore its optimization with respect to speed and precision is crucial. The KF track fit has been implemented recently [1] in single precision in order to use the full power of modern many-core processors. However, the conventional KF algorithm becomes numerically unstable in single precision, opposite to the widely used double precision. In order to improve numerical stability an accurate initial approximation of the track parameters and stabilization of the covariance matrix computation at the measurement update step have been used [1].

Further improved numerical stability can be obtained using a square root KF approach [2]. It operates with a square root S of the covariance matrix $C = SS^T$. Logarithm of the condition number of the square root matrix is smaller by a factor of two, therefore the precision of calculations is doubled.

In the square root KF algorithm the track parameters are propagated and updated at each measurement. The propagation step has been implemented by constructing an orthogonal matrix T and a lower triangular matrix S_k^- such that:

$$\begin{aligned} \mathbf{r}_k^- &= F_k \mathbf{r}_{k-1}^+, \\ T \begin{bmatrix} (S_{k-1}^+)^T F_{k-1}^T \\ Q_{k-1}^{T/2} \end{bmatrix} &= \begin{bmatrix} (S_k^-)^T \\ 0 \end{bmatrix}, \end{aligned} \qquad (1)$$

here $\mathbf{r}_k^-$ and $\mathbf{r}_k^+$ are the track parameters vectors before and after the k-th measurement update, S_k^- and S_k^+ — correspondent square roots of the covariance matrix, F_k — a propagation matrix, $Q_k^{T/2}$ — a transported square root of a process noise matrix. The measurement update has been implemented according to the equations (2) assuming that the measurement m_k is a scalar.

$$\begin{aligned} \varphi &= S_k^- H_k^T, & S_k^+ &= S_k^-(I - a\gamma\varphi\varphi^T), \\ a &= \frac{1}{\varphi^T\varphi + V_k}, & K_k &= aS_k^-\varphi, \\ \gamma &= \frac{1}{1+\sqrt{aR_k}}, & \zeta_k &= m_k - H_k\mathbf{r}_k^-, \\ & & \mathbf{r}_k^+ &= \mathbf{r}_k^- + K_k\zeta_k, \\ & & \chi_k^2 &= \chi_{k-1}^2 + \zeta_k^T a \zeta_k, \end{aligned} \qquad (2)$$

here H_k is the model of measurement, V_k — the covariance of the k-th measurement, χ_k^2 — the total χ^2-deviation.

In the implementation we use for vectorization: headers with overloaded operators, Vector classes (Vc) [3] and Intel Array Building Blocks (ArBB) [4]. Intel Threading Building Blocks (ITBB) [4] and ArBB are used also for task level parallelization. Two methods for extrapolation are implemented: a 4-th order Runge-Kutta propagation and an analytic formula, which uses the Tailor expansion [1].

	Resolution (μm, mrad, %)			Pull			Time,
	x	t_x	p	x	t_x	q/p	μs
Header	43.0	0.30	0.94	1.1	1.2	1.3	0.93
Vc	43.0	0.30	0.94	1.1	1.2	1.3	0.92
ArBB	43.1	0.31	0.94	1.1	1.2	1.3	0.92

Table 1: Track fit quality (resolutions and pulls) and time per track per core of the square root KF approach.

Tests of the time and track fit quality have been performed on a computer lxir075 with 4 Xeon E7-4860 processors, which gives 80 logical cores in total. The results are shown in Table 1. Widths of resolutions and pulls distributions are similar to that ones obtained with the conventional KF approach in double precision. In Figure 1 the scalabilities using ITBB are shown. The figure shows a good linear scalabilities for both propagation methods.

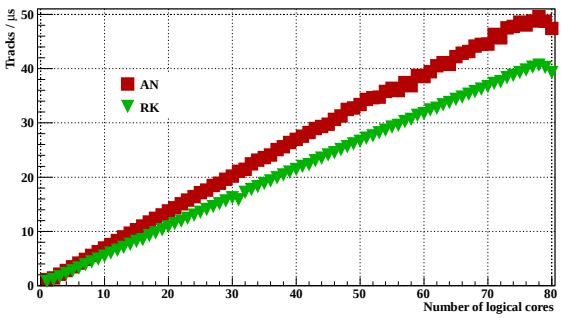

Figure 1: Scalability of the square root KF track fitter using headers with the 4-th order Runge-Kutta propagation (RK) and the analytic formula (AN).

Concluding, the square root KF approach shows good numerical stability, timing and many-core scalability.

References

[1] S. Gorbunov at al., Fast SIMDized Kalman filter based track fit, Comp. Phys. Comm. 178 (2008) 374-383.

[2] P.G. Kaminski, Discrete Square Root Filtering: A Survey of Current Techniques. IEEE Vol. AC-16, No. 6, December 1971.

[3] Vector Classes, `http://gitorious.org/vc`.

[4] Intel software, `http://www.intel.com`.

*This work was supported by the Hessian LOEWE initiative through the Helmholtz International Center for FAIR (HIC for FAIR), HGS-HIRe, GSI F&E, BMBF Verbundforschung and EU-FP7 HadronPhysics2. Das Projekt wird vom Hessischen Ministerium fuer Wissenschaft und Kunst gefoerdert.

Optimization of the CA Based Track Finder for CBM*

S. Jarp[1], *I. Kisel*[2,3], *I. Kulakov*[2,4], *J. Leduc*[1], *and M. Zyzak*[2,4]

[1]CERN, Geneva, Switzerland; [2]Uni-Frankfurt, Germany; [3]GSI, Darmstadt, Germany; [4]Uni-Kyiv, Ukraine

The main tracking challenges of the CBM experiment are: up to 10^7 collisions per second, about 1000 particles per central collision, non-homogeneous magnetic field, double-sided strip detectors. The Cellular Automaton (CA) algorithm is used for track reconstruction [1] in the Silicon Tracking System (STS). It is the most sophisticated and time consuming part of the event reconstruction, therefore it should be fast and should have a good scalability with respect to number of cores. The speed of the CA algorithm is especially important, since the full event reconstruction and selection are required at the First Level Event Selection (FLES) stage.

Reference primary set efficiency	97.7
Extra primary set efficiency	90.5
Reference secondary set efficiency	81.9
Extra secondary set efficiency	50.9
All set efficiency	88.9
Clone level	0.1
Ghost level	0.3
Number of reconstructed tracks per event	121
Time per event, ms	11

Table 1: Track reconstruction quality for minimum bias events: efficiencies (%) for different sets of tracks, clone and ghost levels (%) and time on a single core.

The CA algorithm creates short track segments (triplets) in each three neighboring stations, then links them into track-candidates and selects them according to the maximum length and minimum χ^2 criteria. The algorithm is already optimized with respect to time, fully implemented in single precision [2] and robust with respect to the detector geometry and inefficiency. The algorithm has been optimized further with respect to time: additional information (acceptance, χ^2) is taken into account, input data are resorted, computations are simplified, data copying and number of finding iteration are reduced. The speed up of 5 has been achieved with the same track reconstruction quality.

For tests 1000 minimum bias Au+Au UrQMD events at 25 AGeV with realistic STS setup have been simulated. Tests of the time and efficiency have been performed on a server lxir075 with 4 Xeon E7-4860 processors, which gives 80 logical cores in total. The results are given in Table 1 and in Figure 1. The efficiencies for reference tracks, which include tracks of particular physics interest, are high.

*This work was supported by the Hessian LOEWE initiative through the Helmholtz International Center for FAIR (HIC for FAIR), HGS-HIRe, GSI F&E, BMBF Verbundforschung and EU-FP7 HadronPhysics2. Das Projekt wird vom Hessischen Ministerium fuer Wissenschaft und Kunst gefoerdert.

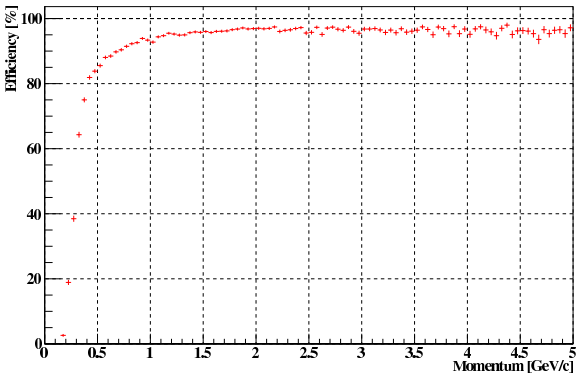

Figure 1: Track reconstruction efficiency versus momentum.

The efficiencies for extra and secondary tracks are lower, since such tracks are shorter and more complicated for reconstruction. Clone and ghost levels are negligible.

For scalability tests FIAS and CERN openlab servers have also been used. The Figure 2 shows a good linear scalability using Intel Threading Building Blocks [3] for all tested many-core systems.

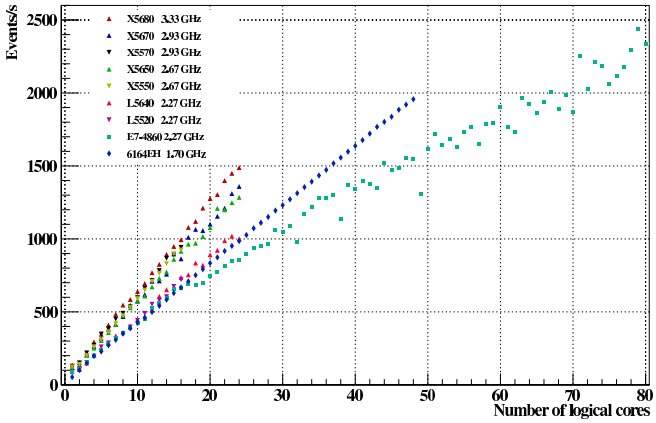

Figure 2: The scalability of the CA track finder on many-core systems at GSI, FIAS and CERN.

In conclusion, running on a computer with 80 cores the CA track finder demonstrates the maximum throughput of 2500 mbias events per second and track reconstruction efficiency of 97.7% for fast primary tracks. The scalability of the CA track finder is linear.

References

[1] I. Kisel, Event reconstruction in the CBM experiment, Nucl. Instr. and Meth. A566 (2006) 85-88.

[2] I. Kisel at al., Numerical Stability of the KF Track Fit in Single Precision, this report.

[3] Intel software, http://www.intel.com

Optimization and Scalability of the CA Based Track Finder for the STAR Experiment*

Y. Fisyak[1], *I. Kisel*[2,3], *I. Kulakov*[2,4], *J. Lauret*[1], *and M. Zyzak*[2,4]

[1]BNL, Brookhaven, USA; [2]Uni-Frankfurt, Germany; [3]GSI, Darmstadt, Germany; [4]Uni-Kyiv, Ukraine

STAR is an active collider heavy-ion experiment [1] at RHIC (BNL, USA). A Cellular Automaton (CA) algorithm [2] will be used for track reconstruction in the Time Projection Chamber (TPC) of the STAR experiment. Since the collision rate is increased up to 40 KHz for Au+Au 200 *A*GeV and up to 1 MHz for p+p 500 GeV and recording rate — up to 10 KHz, the speed of the track reconstruction is crucial.

The CA algorithm creates short triplets in each three neighboring pad rows, then connects overlapping triplets into track segments. The track segments are merged between sectors into global tracks. The final track parameters are estimated using the Kalman filter. The algorithm is highly parallelized on both data (using a SIMD instruction set) and task (using the Intel Threading Building Blocks technology [3]) levels. The memory usage in the algorithm is optimized. The algorithm itself has been optimized further with respect to time: additional selection of track segments is added, number of fits and track propagations is reduced, time consuming computations are reformulated, merger combinatorics is reduces by sorting track segments and dividing the procedure into several steps. The speed up of 3.5 has been achieved with the same track reconstruction efficiency.

Reference set efficiency	96.6
Extra set efficiency	87.4
All set efficiency	88.6
Clone level	10.6
Ghost level	12.6
Number of reconstructed tracks per event	659
Time per event, ms	48

Table 1: Track reconstruction quality for minimum bias events: efficiencies (%) for different sets of tracks, clone and ghost levels (%) and time on a single core.

For tests 100 minimum bias Au+Au events at 200 *A*GeV have been generated using the fast simulator. Tests of the time and efficiency have been performed on a server lxir039 with 2 Xeon X5550 processors. The results are given in Table 1. Track reconstruction efficiency is defined as the number of reconstructed tracks assigned to generated particles divided by the number of all reconstructible tracks. Reconstructible tracks are those, which have momentum greater than 0.05 GeV/c and intersect the sensitive regions of at least 10 consecutive stations. A reconstructed track is assigned to a particle, if at least 90% of its hits have been caused by this particle. A reference track should have a momentum greater than 1 GeV/c in addition. If a reconstructed track is not assigned to any particle it is called ghost. If the particle is reconstructed more then ones all additionally reconstructed tracks are called clones. The efficiency for reference tracks, which include tracks of particular physics interest, is high. The efficiency for extra tracks is lower, since such tracks are curved and more complicated for reconstruction.

For scalability tests a lxir075 server with 4 Xeon E7-4860 10-cores processors has been also used. Each physical core has two logical cores due to the hyper-threading technology, that gives 80 logical cores in total. The track finding has been run on various numbers of cores, processing 100 events on each logical core. The results given in Figure 1 show good linear scalability on the many-core servers.

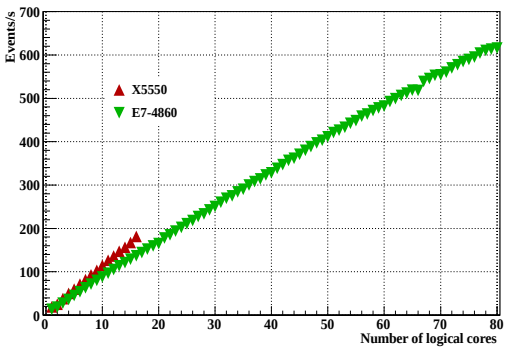

Figure 1: Scalability of the CA track finder for minimum bias events.

Concluding, the execution time of the STAR TPC CA track finder is 48 ms, which satisfies the STAR HLT requirements (50 ms). The scalability of the CA track finder is linear.

References

[1] STAR Collaboration, Conceptual Design Report for the Solenoid Tracker at RHIC, LBL PUB-5347, June 15, 1992.

[2] Y. Fisyak, I. Kisel, I. Kulakov, J. Lauret and M. Zyzak, Track Reconstruction in the STAR TPC with a Cellular Automaton Based Approach, CHEP-2010, Taipei, Taiwan, 2010.

[3] Intel software, `http://www.intel.com`.

* This work was supported by the Hessian LOEWE initiative through the Helmholtz International Center for FAIR (HIC for FAIR), HGS-HIRe, GSI F&E, BMBF Verbundforschung and EU-FP7 HadronPhysics2. Das Projekt wird vom Hessischen Ministerium fuer Wissenschaft und Kunst gefoerdert.

A SIMDized Particle Finder for the CBM Experiment*

I. Kisel[1,2], *I. Vassiliev*[1,2], *and M. Zyzak*[1,3]

[1]Uni-Frankfurt, Germany; [2]GSI, Darmstadt, Germany; [3]Uni-Kyiv, Ukraine

One of the most challenging tasks of the CBM experiment is a full event reconstruction with an event rate up to 10^7 collisions per second. For on-line selection purposes a fast and efficient reconstruction of short-lived particles is required. Since modern CPUs are many core systems and have SIMD units, parallelization and vectorization of the algorithms are necessary for utilization of the full power of the CPU. In order to achieve the maximal speed the particle finding procedure is being developed, that is based on the SIMDized algorithms for the track and particle fitting.

Our investigations have been started with a reconstruction of K^0_s, which decays into $\pi^+\pi^-$ with a branching ratio 69.2%, and Λ, which decays into $p\pi^-$ with a branching ratio 64%. Containing strangeness they are of an interest of the CBM experiment. These particles have been chosen as a first step because of simplicity of their reconstruction algorithm.

The particle finder is based on the Kalman filter track fitter [1] and the KFParticle package [2]. The whole reconstruction procedure is implemented in single precision and SIMDized. The reconstruction algorithm is similar to those, which is used in the off-line reconstruction of K^0_s and Λ.

The algorithm consists of few steps. First, a primary vertex of an event is reconstructed. Then secondary tracks are selected according to two criteria: the tracks should be well displaced from the primary vertex since $c\tau$ of K^0_s is 2.68 cm and 7.89 cm for Λ; parameters and covariance matrices of tracks should be well defined. In order to reject tracks originated from the primary vertex only tracks with $\chi_{\text{prim}} > 3$ are selected, where χ_{prim} is a distance between primary vertex and a track position at the target plane normalized on the total error of the track and the primary vertex. From selected secondary tracks particle-candidates for K^0_s and Λ are constructed assuming pion masses of the tracks. Tracks, which construct particle-candidates with a good quality (the parameters of the particle-candidate are well defined and its χ^2/NDF < 3), are selected for the further analysis. As a final step the particles are constructed from the tracks, which satisfy all cuts, assuming corresponding masses of the daughters: for K^0_s a pion mass is assumed for both daughters, for Λ a proton mass is assumed for a positive daughter and pion for negative.

The algorithm has been tested with 1000 central Au+Au UrQMD events at 25 AGeV. Only the STS detector has been used for these studies. The test has been performed on the lxir039 server with Xeon X5550 processors. The developed SIMDized K^0_s and Λ particles finder shows practically the same results as the off-line algorithm (see Figure 1 and Table 1). Efficiencies of the SIMDized particle finder normalized on all particles (in 4π) are 13.9% for K^0_s and 12.1% for Λ. Efficiencies normalized on particles, which have both daughters reconstructed, are 68% and 57.8% respectively. The execution time of the SIMDized particle finder per event is 0.7 s. The reconstruction of primary vertex takes 65.2%, selection of tracks — 26.2%, reconstruction of K^0_s — 4.3%, reconstruction of Λ — 4.3%.

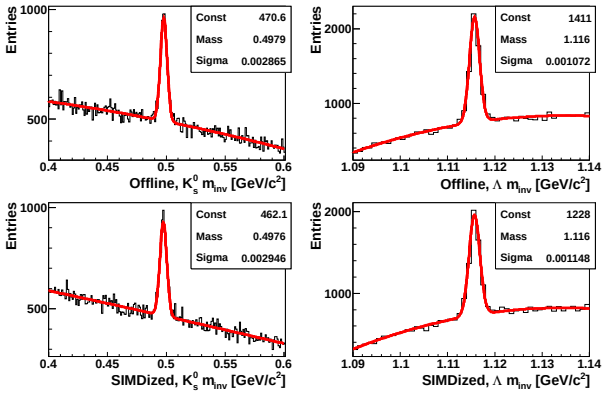

Figure 1: Mass spectras for the offline and SIMDized algorithms.

		S	S/B	M	σ_M
K^0_s	Offline	3225	0.57	497.9	2.9
	SIMDized	3258	0.60	497.6	2.9
Λ	Offline	3619	1.14	1115.7	1.1
	SIMDized	3373	1.01	1115.7	1.1

Table 1: Comparison of the off-line and SIMDized algorithms. Here S is a signal (a number of reconstructed particles), S/B is a signal to background ratio, M and σ_M — a reconstructed mass and its error in MeV/c^2.

As a next step more particles of the particular interest, such as D-mesons and strange hyperons, will be included to the particle finder and parallelization between cores will be investigated.

References

[1] S. Gorbunov, U. Kebschull, I. Kisel, V. Lindenstruth and W.F.J. Müller, Fast SIMDized Kalman filter based track fit, Comp. Phys. Comm. 178 (2008) 374-383.

[2] S. Gorbunov and I. Kisel, Reconstruction of decayed particles based on the Kalman filter. CBM-SOFT-note-2007-003, 7 May 2007.

*This work was supported by the Hessian LOEWE initiative through the Helmholtz International Center for FAIR (HIC for FAIR), HGS-HIRe, GSI F&E, BMBF Verbundforschung and EU-FP7 HadronPhysics2. Das Projekt wird vom Hessischen Ministerium fuer Wissenschaft und Kunst gefoerdert.

Status of event reconstruction for the RICH detector in the CBM experiment*

S. Lebedev[1,2], *C. Höhne*[1], *A. Lebedev*[2,3], *G. Ososkov*[2], *and I. Rostovtseva*[4]

[1]University Gießen, Germany; [2]LIT JINR, Dubna, Russia; [3]GSI, Darmstadt, Germany; [4]ITEP, Moscow, Russia

In this report the status of development regarding RICH detector simulation is presented.

Systematic studies of the ring finder [1] were done in order to improve ring reconstruction and understand losses in the efficiency. In the performed studies the algorithm was tested using events with one primary e^+ or $e-$, thus only one electron ring was registered in the RICH detector per event. For such ideal case the ring reconstruction efficiency was lower than 100% and it dropped down significantly for rings with less than 15 hits. The investigation of this efficiency losses was performed. Two main reasons of the losses were found. The first one is division of hits into two groups while performing hough transform [1]. In this case the peak in hough space was not high enough and, therefore, many rings were rejected at this step. The second reason is a very strong cuts in the ring finding algorithm in order to reject fake rings, as it was tuned for high ring multiplicity events. For events with one ring these cuts can be softer. After these modifications 99.4% of the ring reconstruction efficiency was obtained for events with a single ring with more than 7 hits and 100% efficiency for reference rings with 15 or more hits (see Fig. 1). The ring finder was also tested with different hit producer parameters. For example, noise hits and additional hit errors due to the mirror inhomogeneities were eliminated. It was found that these parameters do not influence the ring finding efficiency. It was observed that many 7 – 9 hit rings are not reconstructable as their hits are distributed non-uniformly but they are concentrated on a half of a ring. Most of such rings are located on the edges of photodetector or even on both photodetectors. They even can not be properly fitted. The remaining 0.7% of not reconstructed rings belong to this category and have to be eliminated from the RICH detector acceptance calculation.

The $CbmRichGeoTest$ class was significantly improved and many new features were implemented. It helps to get better understanding of the RICH detector performance. The detector acceptance vs. transverse momentum, rapidity, momentum and number of hits in ring are calculated. New RICH ring fitting visualization display was implemented which draws MC points, hits, fitted circles and ellipses.

As currently our simulation does not provide pure Monte-Carlo information about RICH ring parameters. The RICH Monte-Carlo points are fitted by the circle and ellipse fitters, obtained parameters are assumed to be Monte-Carlo RICH ring parameters. It was obtained that mean ring radius for circle fit using MC points is 4.88 cm and RMS equals to 0.29 cm, using hits circle fit gives about the same mean value (4.80 cm), but RMS is factor of 2 larger (0.59 cm).

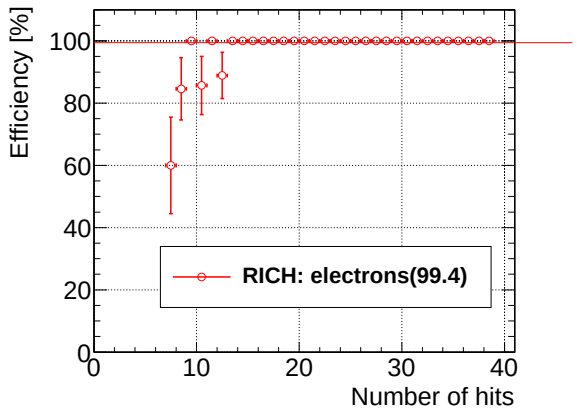

Figure 1: The ring reconstruction efficiency in dependence on the number of hits in ring for events with one ring.

The difference between MC point and hit fitting was assumed to be a ring parameter errors due to the digitization in the photodetector. These errors depend on the number of hits in ring, they are larger for the rings with smaller number of hits. The integrated RMS of the error for the circle fit: R – 0.13 cm, X_c – 0.13 cm, Y_c – 0.16 cm; for the ellipse fit: A – 0.19 cm, B – 0.17 cm, X_c – 0.15 cm, Y_c – 0.19 cm.

The fitting efficiency is the number of accepted rings divided by the number of correctly fitted rings. Correctly fitted ring is a ring with parameters in a range $\pm 3RMS$ around mean value. The mean integrated efficiency of circle fitting is 97.4% and it drops down to less than 60% for rings with 10 hits. The mean integrated efficiency of ellipse fitting is 92.6%, and it drops down to less than 60% for rings with 15 hits.

The parameter error calculation for the circle fit was implemented. In order to test fitting algorithms a toy model of the ring simulation was used. The residuals and pulls of circle fit were calculated. The RMS values of the pull distributions of all parameters are around one as it should be.

References

[1] S. Lebedev et al., CBM Progress Report 2008, Darmstadt 2009, p. 84

* Supported by the Hessian LOEWE initiative through the Helmholtz International Center for FAIR (HIC for FAIR), and by EU/FP7 Hadronphysics2

Status of global track reconstruction in the CBM experiment *

A. Lebedev[1,2], *S. Lebedev*[1,3], *and G. Ososkov*[2]

[1]GSI, Darmstadt, Germany; [2]LIT JINR, Dubna, Russia; [3]University Gießen, Germany

Global track reconstruction i.e. tracking in the TRD and MUCH, track merging between STS, TRD and MUCH, TOF hit merging and construction of global tracks are performed by the `littrack` package in the CBMROOT framework. In this report the status of developments in the `littrack` package is presented.

The structure of the package was significantly reorganized. For convenience and in order to decrease the dependencies between different parts of the `littrack` the package is decomposed into four main parts: 1) `cbm` - interface of the tracking software to CBMROOT, quality monitoring etc. 2) `std` - scalar implementation of the tracking using full magnetic field map and `TGeo` for geometry navigation. It depends on ROOT and does not depend on CBMROOT. 3) `parallel` - SIMDized and multithreaded implementation of the tracking. It depends only on the compiler and can be used in standalone mode for performance testing. 4) `cuda` - test implementation using CUDA.

The quality assurance routines for the track reconstruction were considerably improved.

In the performed studies the algorithms were tested using central Au+Au collisions at 25 AGeV beam energy from UrQMD. In addition, to check the reconstruction of signal tracks 5 J/Ψ decayed into $e+$ $e-$ pair in case of electron setup or $\mu+$ $\mu-$ pair in case of muon setup were embedded in each event. In this simulations a realistic detector description which was implemented in STS, TRD and MUCH detectors was used. It includes advanced digitization and clustering procedures.

Global tracking efficiency in dependence on momentum for electron setup is shown in Fig. 1. Global tracking efficiency for signal tracks ($e+$ $e-$ or $\mu+$ $\mu-$) for two alternative CBM setups: electron and muon is 76.1% and 92.1% respectively. The mean TRD track finding efficiency for all tracks is 94.5% and 89% for signal $e+$ $e-$. For electrons which lose most of their energy due to bremsstrahlung track reconstruction efficiency is lower. The mean tracking efficiency for MUCH detector is 95.1%.

A study was done in order to investigate STS tracking performance. It was shown that the observed STS tracking efficiency drop with increasing momentum is due to a weak acceptance of the new STS geometries (`v11a` and `v11b`) compared to the previous one (`v09a`).

A comparison of the STS and global tracking efficiencies for two new STS geometries (`v11a` and `v11b`) using different strip stereo angles ($\pm 7°$, $0° - 4°$, $0° - 6°$, $0° - 8°$) was performed. It was shown that the STS and global reconstruction efficiency stays the same for both STS geometries. The tracking efficiency starts to drop down and ghost rate increases starting with small stereo angles ($0° - 4°$).

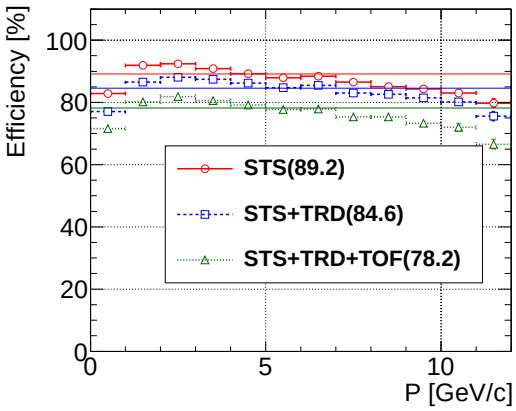

Figure 1: Global track finding efficiency in dependence on momentum for the electron CBM setup. Mean efficiency numbers in % are shown in brackets.

A fast parallel tracking algorithm was further investigated. To avoid the use of the main memory and to implement SIMDized algorithm we use a polynomial approximation of the magnetic field map. However, detailed studies of such an aproach showed that in stray magnetic field after the STS detector polynomial approximation is not accurate enough. A new algorithm for field approximation was implemented. It builds a grid, similar to that of field map, but only on a predefined xy slices perpendicular to z position. The drawback of such an approach is that access to the grid cannot be effectively SIMDized. But on the other hand the algorithm is as accurate as the field map, has low memory consumption and its fast. The algorithm was tested with track propagation and track fit. Its implementation into the tracking is ongoing.

Software documentation is an important part of the development process. Thus the documentation of the `littrack` package was improved. The documentation was implemented using Doxygen. The documentation can be accessed using the following link: `http://www-linux.gsi.de/~andrey/littrack-docs/html/`.

Global track reconstruction algorithms for the CBM experiment are well advanced now. The developed `littrack` package is the default global track reconstruction software in CBM. It provides good tracking efficiency for both, the electron and muon setup of CBM. It is suitable for detector optimization studies of different CBM setups.

* Supported by the Hessian LOEWE initiative through the Helmholtz International Center for FAIR (HIC for FAIR), and by EU/FP7 Hadronphysics2

Towards automatization of simulation quality monitoring in CBM*

A. Lebedev[1,2], *S. Lebedev*[2,3], *and G. Ososkov*[2]

[1]GSI, Darmstadt, Germany; [2]LIT JINR, Dubna, Russia; [3]University Gießen, Germany

Automatization of regularly performed tasks is an important component of a well organized software development process. One of such important tasks is a software testing. Good and automatized testing procedure can considerably improve the development process, since the developers can be sure that changes made in the code are correct and do not crash the program. It can also considerably reduce the development cycles.

In the development of the physics simulation software like CBMROOT it is important to have a reliable and unified tool which provides a set of quality assurance tests and gives a global picture of simulation results, namely, Monte-Carlo simulation, detector simulation, event reconstruction and physics analysis. In this report we discuss a prototype of simulation quality tool which is being developed for CBMROOT.

The main goal of this development is to run standard simulation, reconstruction and analysis chains automatically on a regular basis, check simulation results and publish them on a web site for common access. The tool consists of two main components. The first one is "performance calculator" which creates histograms and performs actual calculation of results. The second component is responsible for representation of results to a user: it extracts useful numbers from histograms, draws them and generates reports.

As a first step we started our developments with event reconstruction performance. Developed routines allow to calculate a set of important quality assurance numbers and histograms like detector acceptance, track and ring reconstruction, electron identification and pion suppression efficiencies etc. They calculate local reconstruction efficiencies for each detector (STS, RICH, TRD, MUCH, TOF) as well as for different combinations of detectors and normalizations (MC, STS-RICH, STS-TRD etc.). All efficiencies are evaluated in dependence on momentum, transverse momentum, rapidity and number of hits. For a specific detector this list can be extended.

For better and quicker understanding of the obtained simulation results it is important to have a good representation of it which contains main useful numbers, tables and figures in an east-to-read format. Report is generated in two steps. First, all necessary numbers are extracted from histograms and saved in JSON format. Figures are created and saved in PNG files. Second, report is generated out of JSON and image files in HTML, Latex or plain text format (for console output).

Automatic check of the simulation results on correctness was also implemented. It allows to inspect the results based on the predefined limits for each value. In the report each value can be marked with a certain color which indicates whether it is correct, not correct or not checked.

Combination of the described tools allowed to automatize event reconstruction quality monitoring. Nightly tests for electron and muon CBM setup are performed. The simulation and reconstruction are run using standard CBMROOT dashboard which is based on CDASH. Than the tracking performance is calculated. Simulation results are automatically checked. HTML report is generated and copied to the web server.

Simulation of the experiment requires to perform a lot of systematic and detector optimization studies in which many different simulations have to be compared. The interpretation and analysis of the results obtained in such studies are hard as a big verity of numbers has to be checked. In order to improve and speedup such studies a new feature was implemented which allows to produce an easy-to-read summary report out of many different simulations.

Developed QA routines allow to improve CBMROOT framework testing. It does not require any additional efforts from the developers since testing is done automatically.

The developed prototype of the event reconstruction quality monitoring can be found in the following link: `http://www-linux.gsi.de/~andrey/api/index.php`.

Further development will concentrate on extension of the test suit in order to get higher code coverage and improvements of the web site.

* Supported by the Hessian LOEWE initiative through the Helmholtz International Center for FAIR (HIC for FAIR), and by EU/FP7 Hadron-physics2

K^0_s, Λ and Ξ^- reconstruction in Au+Au collisions at NICA energy region*

I.Vassiliev[1,2] and V. Akishina[1,3]

[1]Goethe-Universität, Frankfurt am Main, Germany; [2]GSI, Darmstadt, Germany; [3]LIT, JINR, Dubna

The main goal of the CBM experiment is to study the behaviour of nuclear matter in the conditions of high baryonic density in which the transition to a deconfined quark gluon plasma phase is expected. One of the signatures of this new state is the enhanced production of strange particles; therefore hyperon reconstruction is essential for the understanding of the heavy ion collision dynamics. Hyperons will be measured in CBM by their decay into charged hadrons, which are detected in the Silicon Tracking System (STS).

To study the feasibility of Ξ^-, Λ and K^0_s reconstruction in the CBM experiment, a set of 10k central Au+Au UrQMD events at 4,85 AGeV were simulated. At 4,85 AGeV central Au+Au UrQMD event contains on average 5 K^0_s, 7 Λ and 0.029 Ξ^-. The Ξ^- decays to $\Lambda + \pi^-$ with branching ratio 99.9% and $c\tau$ = 4.91 cm. The STS geometry with 8 double-sided segmented strip detectors were used for tracking. No kaon, pion or proton identification is applied. In order to reconstruct the $\Lambda \rightarrow p\pi^-$ decay the proton mass was assumed for all positively charged tracks and pion mass for all negatively charged ones. K^0_s is reconstructed assuming pion mass for both tracks. The combination of single track cut ($\chi^2_{prim} > 3\sigma$) and geometrical vertex ($\chi^2_{geo} < 3\sigma$) cut allows to see clear signal. For K^0_s the invariant mass resolution is 1.2 MeV/c^2 and the signal-to-background ratio in 2 σ peak region is 2.44. For Λ the invariant mass resolution value is 2.7 MeV/c^2 and the signal-to-background ratio in 2 σ peak region is about 10.(see Fig. 1 and Fig. 2) . The Ξ^- event reconstruction includes several steps: fast

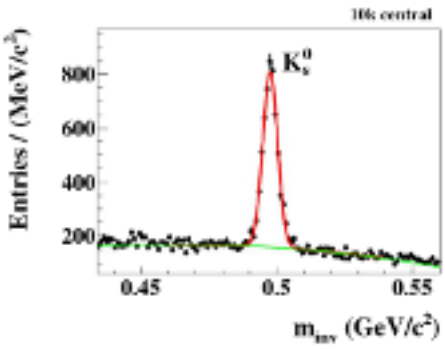

Figure 1: The $\pi^+\pi^-$ invariant mass spectrum. Red line is signal Gaussian fit, green line is polynomial background.

on-line tracks finding and fitting [1,2], where all tracks are found; tracks with $\chi^2_{prim} > 8$ and 5σ (positively and negatilely charged respectivly) are selected for a Λ search, where positevely charged tracks were combined with the π^--tracks to construct a Λ-KFParticle; good quality geometrical vertex ($\chi^2_{geo} < 3\sigma$) was required to suppress combinatorial background.

Particle:	K^0_S	Λ	Ξ^-
Multiplicity (HSD):	5	7,2	0,029
Decay chanel:	$\pi^+\pi^-$	π^-p	$\pi^+\pi^-$p
Branching ratio:	69,2 %	63.9 %	63.8 %
Rec. efficiency	8.5 %	13.9 %	2.8 %
Acceptance	24,9 %	28.9 %	20 %

The invariant mass of the reconstructed pair is compared with the Λ mass value; only pairs inside 1.116 $\pm 0.016(6\sigma)$ were accepted; primary Λ rejection, where only Λ with $\chi^2_{prim} > 5\sigma$ and z-vertex greater than 6 cm are chosen. Selected Λs were combined with the secondary π^- ($\chi^2_{prim} > 8\sigma$) tracks and Ξ^--KFParticle were created. The Ξ^--candidate was accepted if it has good quality geometrical and topological detached vertex: $((\chi^2_{geo} < 3\sigma), (\chi^2_{topo} < 3,5\sigma))$ and z-vertex greater than 2 cm downstream target.

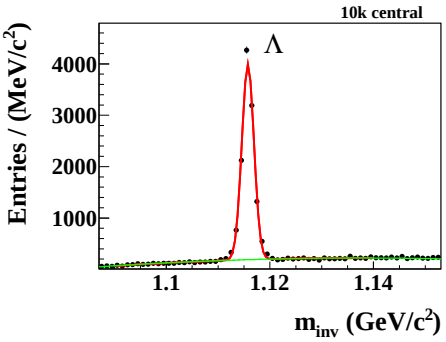

Figure 2: The proton π^- invariant mass spectrum. Red line is signal Gaussian fit, green line is polynomial background.

As a result of the invariant mass $\Lambda\pi^-$ candidates spectrum 8 Ξ^- were reconstructed with no background.The signal reconstruction efficiency is about 2.8%.

References

[1] I. Kisel, Event reconstruction in the CBM experiment, Nucl. Instr. and Meth. A566 (2006) 85-88.

[2] S. Gorbunov, U. Kebschull, I. Kisel, V. Lindenstruth and W.F.J. Müller, Fast SIMDized Kalman filter based track fit, Comp. Phys. Comm. 178 (2008) 374-383.

*Supported by the Hessian LOEWE initiative through the Helmholtz International Center for FAIR (HIC for FAIR), and by EU/FP7 Hadronphysics2

Radiation dose calculations for the CBM detectors with FLUKA

A. Senger[1]

[1]GSI, Darmstadt, Germany

Radiation dose calculations for the CBM detectors were carried out with the FLUKA code [1,2] for a gold beam with an energy of 35 A GeV and an intensity of 10^9 ions/s. The gold target had a thickness of 250 µm resulting in an interaction rate of about 1%. The calculations were performed for the two CBM detector setups with the MUCH detector and the RICH detector (see Figure 1).

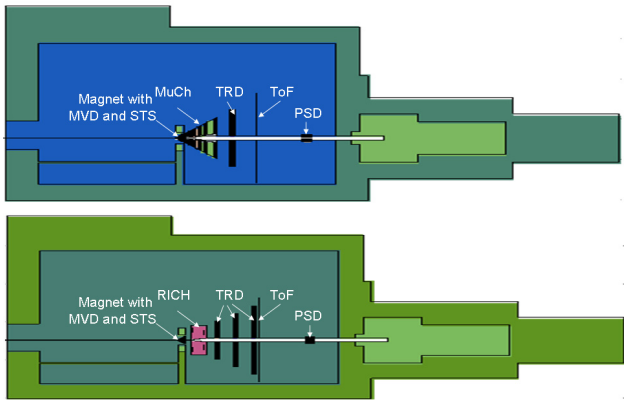

Figure 1. FLUKA geometry of CBM: top – muon setup with MuCh, bottom – electron-setup with RICH.

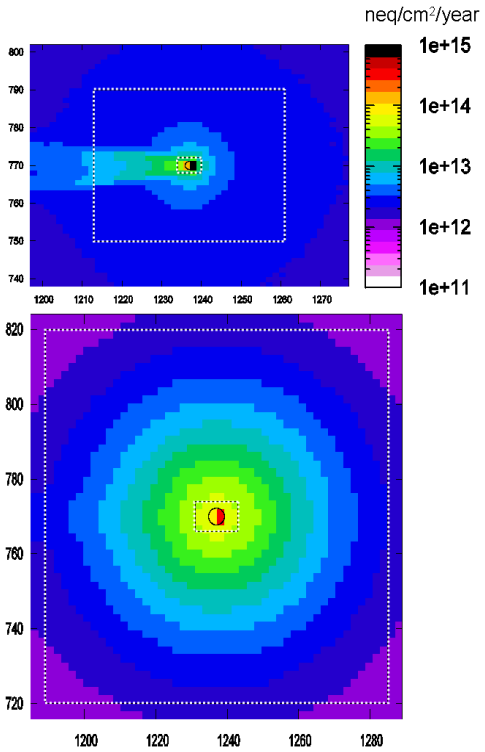

Figure 2. Non-ionising dose in first (top) and last (bottom) STS. The inner and outer dashed lines correspond to the detector acceptance.

The results of the calculations are shown in Figure 2 and in Table 1. Figure 1 depicts the non-ionising energy loss (NIEL) in units of 1 MeV neutrons per cm^2 and per year for the first (top) and the last (bottom) STS layer. In the first STS layer the effect of delta-electrons is clearly seen. The ionizing dose and the NIEL are listed in Table 1 for all CBM detector systems. The results refer to an integral number of $5{\cdot}10^{13}$ gold beam particles for the MVD, and to $5{\cdot}10^{15}$ gold beam particles for the other detector systems.

detector	Dose (Gy/year)		NIEL (n_{eq}/cm^2/year)	
	max	min	max	min
MVD				
5 cm	10^4	100	$2{\times}10^{13}$	$5{\times}10^{10}$
10 cm	$5{\times}10^3$	10	$7{\times}10^{12}$	$5{\times}10^{10}$
15 cm	10^3	5	$2{\times}10^{12}$	$5{\times}10^{10}$
STS				
30 cm	$8{\times}10^4$	200	$2{\times}10^{13}$	$5{\times}10^{12}$
40 cm	$3{\times}10^4$	50	$2{\times}10^{13}$	$5{\times}10^{12}$
50 cm	$3{\times}10^4$	50	10^{13}	$5{\times}10^{12}$
60 cm	10^4	50	10^{13}	$5{\times}10^{12}$
70 cm	$7{\times}10^3$	50	10^{13}	$5{\times}10^{12}$
80 cm	$7{\times}10^3$	50	10^{13}	$5{\times}10^{12}$
90 cm	$5{\times}10^3$	50	$4{\times}10^{13}$	$2{\times}10^{12}$
100 cm	$4{\times}10^3$	50	$6{\times}10^{13}$	10^{12}
MuCh				
1	10^3	50	$8{\times}10^{13}$	$5{\times}10^{12}$
2	100	5	$8{\times}10^{12}$	$5{\times}10^{11}$
3	80	1	10^{12}	10^{11}
RICH	1000	0.1	$2{\times}10^{12}$	$2{\times}10^{9}$
TRD	100	0.5	$5{\times}10^{11}$	$8{\times}10^{8}$
ToF	100	1	10^{11}	10^{10}
PSD	10^4	8	10^{14}	$5{\times}10^{12}$
electronics cave	0.2		$2{\times}10^{9}$	10^{8}

Table 1. Ionising dose and non-ionising energy loss in the CBM detector systems calculated for a 35 A GeV Au beam impinging on a 1 % interaction Au target. A "CBM year" corresponds to $5{\cdot}10^{13}$ beam ions for the MVD, and to $5{\cdot}10^{15}$ beam ions for the other detector systems. The STS results were obtained for the muon setup.

References

[1] "The FLUKA code: G. Battistoni et al., Proceedings of the Hadronic Shower Simulation Workshop 2006, Fermilab 6-8 September 2006, M. Albrow, R. Raja eds., AIP Conference Proceeding 896, 31-49, (2007)

[2] "FLUKA: a multi-particle transport code", A. Fasso`, A. Ferrari, J. Ranft, and P.R. Sala, CERN-2005-10 (2005), INFN/TC_05/11, SLAC-R-773

D^{*+} decay reconstruction in C+C collisions at 25AGeV in the CBM experiment*

I. Vassiliev[1,2], *I. Kisel*[1,2], *and V. Vovchenko*[2,3]

[1]IKF, Goethe University, Frankfurt, Germany; [2]GSI, Darmstadt, Germany; [3]T. Shevchenko National University, Kyiv, Ukraine

The nucleus-nucleus collision research program in the CBM experiment at FAIR is aimed at studying the QCD phase diagram at high baryon densities and moderate temperatures. One of the main observables are D-mesons or Λ_c which carry a charm quark and are expected to be created in the early stages of nucleus-nucleus collisions. The D-mesons can be detected via hadronic decay into charged pions and kaons. This task requires fast and efficient track reconstruction algorithms and high resolution secondary vertex determination. Particular difficulties in recognizing the displaced vertex of the rare Open Charm decays are caused by weak K^0_S and Λ decays which produce displaced vertices downstream the target, very low multiplicity of the Open Charm production, low branching ratios, multiple scattering in the beam pipe and detectors. To calculate multiplicity of different D mesons in C-C collisions at 25A GeV the Hadron String Dynamics (HSD) v2.5 microscopic model is used [1].

To study the feasibility of D^0 and D^{*+} decays reconstruction in the CBM experiment a set of 10^5 central C+C UrQMD events at 25 AGeV was simulated. D^{*+} decay to $\pi^+ + D^0$ was added to each event in order to simulate a signal in the environment of background hadrons. Realistic STS geometry with 2 MAPS at 5 cm (thickness 300 μm) and 10 cm (thickness 500 μm) and 8 double-sided (thickness 400 μm) segmented strip detectors was used. The primary vertex was reconstructed with high accuracy (6 μm in z direction, 1 μm in x and y) from about 450 tracks reconstructed in the STS in a non-homogeneous magnetic field by the SIMDized Kalman filter procedure described in [2].

The D^0 particle is reconstructed from its $K^+\pi^-$ daughter particles using the primary vertex as the production point. D^0 z-vertex resolutions is 52 μm. Because of originating from a displaced decay vertex, D^0 daughter tracks have a non-vanishing impact parameter at the target plane. Since the majority of the primary tracks have very small impact parameter, large part (99%) of the background tracks was rejected using a cut on their χ^2 distance to the primary vertex. The combinatorial background is suppressed mainly by the geometrical and topological vertex cuts. The shape of the background in the signal IM region has been estimated using the event mixing technique. The resulting background plus D^0 signal spectra calculated using HSD model are shown in Fig.1.

D^{*+} decays in primary vertex, the D^{*+} daughter tracks must originate from primary vertex. Therefore, in order

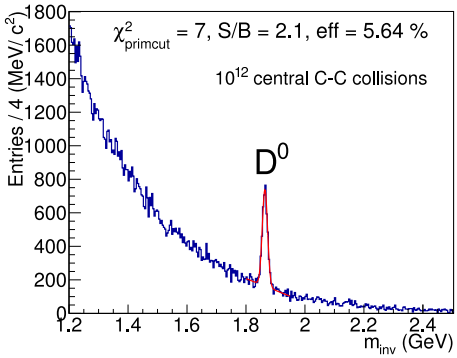

Figure 1: Reconstructed D^0-mesons in 10^{12} central C+C collision at 25 AGeV. Red line is D^0 signal, blue is combinatorial background.

to reconstruct D^{*+} one needs to combine all identied D^0 in the window $1.84 < m_{inv}(GeV/c^2) < 1.89$ with positive primary tracks. $\chi^2_{geo} < 3\sigma$ cut was used to insure that daughter tracks come close enough to each other to be considered as daughter products of D^{*+}. $\chi^2_{topo} < 3\sigma$ cut also was used for combinatoprial and direct D^0 background suppression. One can see in Fig.2 that the D^{*+} signal is clearly distinguishable and S/Bg ratio is relatively high. Total number of collected $D^{*+}$is about 740. Efficiency of D^{*+} reconstruction is 3.82%.

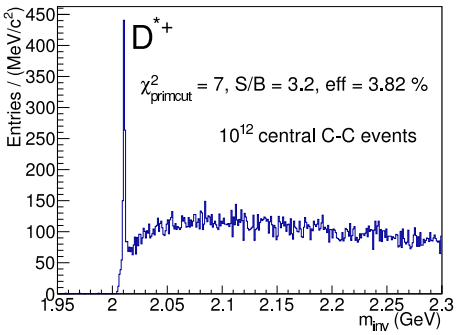

Figure 2: Reconstructed D^{*+}-mesons and combinatorial background in 10^{12} central C+C collision at 25 AGeV.

References

[1] W. Cassing, E.L. Bratkovskaya, Phys. Rep.308, 65 (1999).

[2] I. Kisel et al., Comp. Phys. Comm. 178 (2008) 374-383.

*Supported by the Hessian LOEWE initiative through the Helmholtz International Center for FAIR (HIC for FAIR), and by EU/FP7 Hadronphysics2

Status of low-mass di-electron simulations in the CBM experiment*

E. Lebedeva[1], *T. Galatyuk*[1], *C. Höhne*[2], *and J. Stroth*[1,3]

[1]Frankfurt University, Germany; [2]Gießen University, Germany; [3]GSI, Germany

Results of systematic studies of the reconstruction performance of low-mass di-electrons for different CBM detector setups are presented in this report. In this study 4 different simulation setups were compared, i.e. 100% and 70% magnetic field scales and setups with and without the MVD detector. In case of presence of the MVD detector simulations were performed including δ-electrons as well. The report thus presents the most realistic simulations performed so far.

The simulations were carried out for central Au+Au collisions at 25 GeV/u beam energy. Low mass vector mesons (ρ^0, ω, ϕ) were generated using the Pluto event generator. δ-electrons are produced in the target by all Au ions crossing the target. They are registered only by the MVD detector as it has comparably long readout time, for other detectors this effect can be neglected. According to the used 25 μm thick (0,1% nuclear interaction length) gold target, assuming 33 kHz interaction rate and 30 μs readout time of the MVD detector, 1000 Au ions are embedded for each UrQMD event. The mean number of hits in MVD per event is 1100. Including δ-electrons gives 3000 hits per event. Using the 70% B-field the number of MVD hits increases further by 30% up to 3900.

The reconstruction performance results for single $e^{\pm}$ from ρ^0 -mesons are shown in Table 1. The number of reconstructed global tracks per event is 580 – 680 depending on the setup. The detector acceptance of single $e^{\pm}$ from ρ^0 is 50% for 100% B-field, and 54% for 70% B-field. The global reconstruction efficiency in STS+RICH+TRD+TOF for single $e^{\pm}$ from ρ^0 is around 65%. The RICH, TRD and TOF detectors provide a momentum integrated (0-10 GeV/c) pion suppression factor of 7000 – 9200 at around 54% electron identification efficiency depending on the setup. The momentum resolution increased from 1.14% to 1.88% when using the MVD detector and 70% B-field.

Several background rejection cuts were used [1]: γ conversion cut, track topology cuts, transverse momentum cut. When the MVD detector is present in simulations an MVD cut is used: this is a two dimensional cut, the distance between the intersection point of an electron track in the MVD station to its nearest neighbor hit vs. electron track momentum.

The invariant mass spectrum of electron pairs including full event reconstruction and electron identification after applying background rejection cuts is shown in Fig. 1.

Six detector setups with the most realistic simulations being available so far were investigated. Results are comparable with previous results [1]. Efficiencies are the same, S/BG ratios are within factor 2. However, the fact that the S/BG ratio seems to drop if including the MVD detector is not understood yet and needs more investigations.

Table 1: Reconstruction: summary table of the reconstruction performance of single $e^{\pm}$ from ρ^0 for different simulation setups. Analysis: summary table of the analysis of ρ^0, ω and ϕ mesons after all cuts for different simulation setups. $S/B_{(0.2-0.6)}$ is S/B for $0.2 < M_{ee}/(GeV/c^2) < 0.6$.

	100% B-field scale			70% B-field scale		
MVD?	no	yes		no	yes	
δ-electrons?	—	no	yes	—	no	yes
Reconstruction of single $e^{\pm}$ from ρ^0 meson						
global tr./ev.	581	621	677	593	624	674
Acc/MC [%]	50.4	50.0	50.1	54.3	53.9	54.7
rec. eff. [%]	66.2	66.2	63.7	66.4	65.4	63.2
el. id. eff. [%]	55.7	55.6	53.3	55.0	53.9	51.8
pion supp.	7100	8550	6890	9190	9060	7010
dP/P$_{RMS}$ [%]	1.14	1.26	1.49	1.50	1.64	1.88
Analysis						
ω: eff. [%]	5.7	5.9	5.5	6.4	6.4	5.5
ω: S/BG	0.40	0.32	-	0.3	0.29	0.25
ρ^0: eff. [%]	4.4	4.5	4.0	4.8	4.8	3.9
ϕ: eff. [%]	7.5	8.9	8.2	8.6	9.5	8.4
ϕ: S/BG	0.49	0.24	-	0.31	0.18	0.17
$S/B_{(0.2-0.6)}$	0.012	0.01	0.006	0.03	0.02	0.02

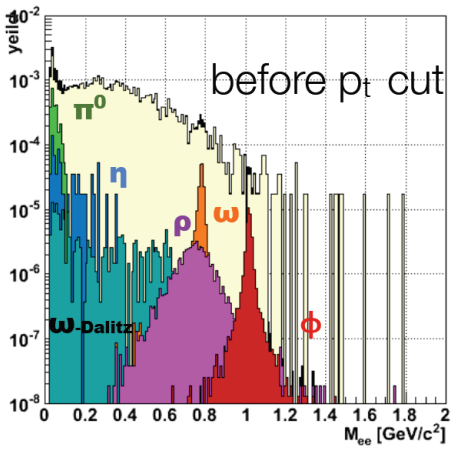

Figure 1: Invariant mass spectra after all cuts (except P_t). Setup: MVD, 70% field scale, no δ-electrons, 70k events.

References

[1] T. Galatyuk et al., CBM Progress Report 2009, Darmstadt 2010, p. 63

* Supported by the Hessian LOEWE initiative through the Helmholtz International Center for FAIR (HIC for FAIR), and by EU/FP7 Hadronphysics2

J/ψ detection in p + Au collisions at 30 GeV*

O. Yu. Derenovskaya[1] and I. O. Vassiliev[2,3]
e-mail: odenisova@jinr.ru, [1]Laboratory of Information Technologies, JINR, Dubna
[2]Goethe University, Frankfurt, Germany, [3]GSI, Darmstadt, Germany

The investigation of p + Au collisions at 30 GeV beam energy is considered as a part of the CBM research program and will be performed in the first phase of FAIR with a start version of the CBM detector at the SIS-100 accelerator. Here we present the results of $J/\psi \rightarrow$ (e+e-) reconstruction in p + Au collisions. Complete CBM track reconstruction chain includes current STS detector as a main tracker and RICH, TRD and TOF detectors are used for the particle identification.

The feasibility study of J/ψ detection is based on set of central (b = 0) proton-gold UrQMD events at 30 GeV. One J/ψ decay to *e+e-*, generated by PLUTO, was added to each event in order to simulate a signal in the environment of background tracks.

In order to reconstruct J/ψ we used full electron identification procedure including the RICH, TRD and TOF detectors. We use the elliptic ring fit in the RICH and apply ring quality cuts based on the neural network to separate electrons from pions.

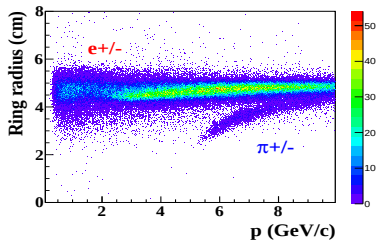

Figure 1: The radius of the reconstructed rings as a function of the particle momentum. Electrons and pions are clearly separated up to momentum 5.5 GeV/c.

Also the electrons are identified via their transition radiation measured with the TRD. Based on the individual and total energy loss (see Fig.2), we employed neural network to discriminate electrons from misidenified pions in the RICH. In addition to RICH and TRD, the information from TOF is also used to separate hadrons from electrons (see Fig. 3).

A momentum dependent cut on squared mass is used to reject hadrons pions from the identified electron sample.

With the combined information from all detectors, we achieve an efficiency of 68 %. The combined RICH and TRD identification suppressed pions to a level of about 24 thousand.

* Supported by the Hessian LOEWE initiative through the Helmholtz International Center for FAIR (HIC for FAIR), and by EU/FP7 Hadronphysics2

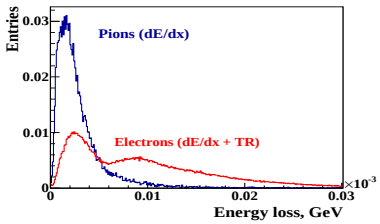

Figure 2: Distribution of electrons energy losses (dE/dx + TR) and pions (dE/dx) in the TRD.

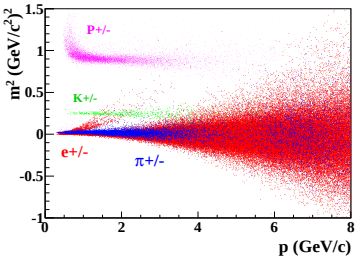

Figure 3: The squared mass of charged particles as a function of the particle momentum in the TOF for RICH identified electrons and misidentified pions.

The reconstructed invariant-mass spectra of J/ψ mesons in central p + Au collisions at 30 GeV beam energy are shown in Fig.4.

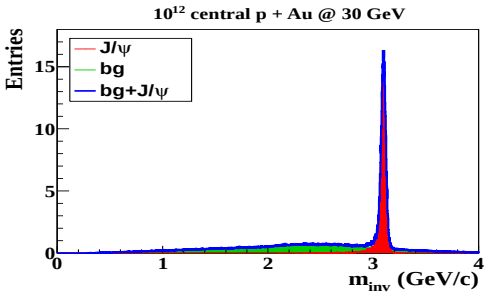

Figure 4: Reconstructed invariant mass spectra of J/ψ mesons for central p+Au collisions at 30 GeV.

The resulting invariant-mass spectrum in the charmonium mass region is displayed in Fig.4. The signal reconstruction efficiency is about 27 %. For the simulation we assume a multiplicity of 6 $\times 10^{-8}$ and a branching ratio of 6 %. The invariant mass resolution is 23 MeV, signal-to-background ratio in a 2σ region around the peak is 18.

J/ψ - e+e- reconstruction in Au+Au collision at SIS300 energies*

O. Yu. Derenovskaya[1] and I. O. Vassiliev[2,3]
e-mail: odenisova@jinr.ru, [1]Laboratory of Information Technologies, JINR, Dubna
[2]Goethe University, Frankfurt, Germany, [3]GSI, Darmstadt, Germany

The investigation of charmonium production is one of the key goals of the CBM experiment. The main difficulty lies in the extremely low multiplicity expected in Au+Au 25 AGeV collisions near J/ψ production threshold. That's why, the efficient event selection based on J/ψ signatures are necessary in order to reduce the data volume to the recordable rate. Here we present results of J/ψ meson reconstruction in its di-electron decay channel using KFParticle package with a complete reconstruction chain including current STS detector as a main tracker and RICH, TRD and TOF are the particle identification detectors.

To study the feasibility of J/ψ detection, background and signal events have been simulated. Decay electrons from J/ψ were simulated by PLUTO generator. The background was calculated with set of central Au+Au UrQMD events at 25 AGeV. Signal embedded into background was transported through the standard CBM detector setup. In the event reconstruction, particles are tracked by the silicon tracking sistem placed inside a magnetic field, providing the momentum of the tracks. Global tracking provides additional particle identification information using RICH, TRD and TOF subdetectors.

In order to reconstruct J/ψ we used full electron identification procedure including RICH, TRD and Time Of Flight detectors (see [1]).

The negatively charged tracks emerging from the target which was identified as electrons by the RICH, TRD and TOF detectors are combined with positively charged tracks (positrons) to construct a J/ψ candidate, using the KFParticle package [2]. In order to suppress the physical electron background a transverse momentum cut at 1 GeV/c was applied to the track candidates for J/ψ decays to di-electrons.

Figure 1 demonstrates z - vertex of reconstructed J/ψ. KFParticle package allows to reconstruct J/ψ z-vertex with a quite good (about 250 μm) presicion.

In order to study the signal-to-background ratio, the signal mass spectrum was generated from events with one J/ψ decay embedded into UrQMD background. The combinatorial background was obtained from the original central UrQMD events. To increase the statistics and got proper shape of the background, the event mixing technique was applied. The signal spectrum was added to the background after scaling, taking into account the assumed multiplicity (HSD transport code), J/ψ reconstruction efficiency and the decay branching ratio. The resulting invariant-mass spectrum in the charmonium mass region is displayed in Fig.2.

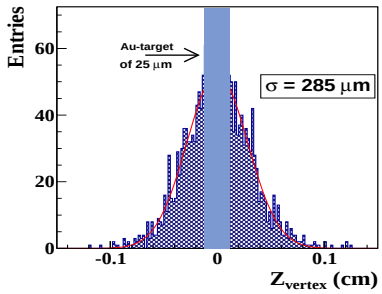

Figure 1: Distribution of z - vertex of constructed J/ψ, rectangle is target area.

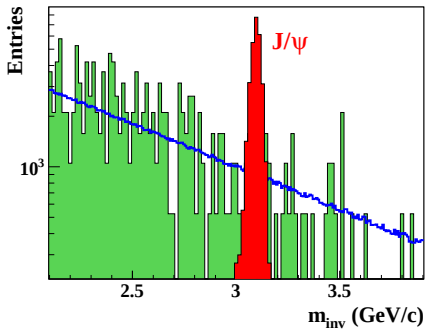

Figure 2: Invariant mass spectra of J/ψ and ψ' mesons for central Au+Au collisions at 25 AGeV.

	Mult.	Br.ratio	S/B	Eff.	σ
J/ψ	1.92×10^{-5}	0.06	2	0.19	24 MeV
ψ'	2.56×10^{-7}	0.0088	0.043	0.19	25 MeV

Table 1: Multiplicity, branching ratio, signal-to- background ratio, reocnstruction efciency and mass resolution for J/ψ and ψ' in central Au+Au collisions at 25 AGeV.

Obtained results shows CBM detector ability to measure J/ψ and even ψ' with high statistic in Au+Au collisions at SIS-300 energies.

References

[1] I. Vassiliev and O. Derenovskaya:, this report.
[2] S. Gorbunov and I. Kisel: *Reconstruction of Decayed Particles Based on the Kalman Filter*, CBM-SOFT-note-2007-003, http://www.gsi.de/documents/DOC-2007-May-14.html.
[3] O. Derenovskaya, Drezden, Germany, 2011, 17th CBM collaboration meeting.

* Supported by the Hessian LOEWE initiative through the Helmholtz International Center for FAIR (HIC for FAIR), and by EU/FP7 Hadronphysics2

Centrality dependence of sideward flow of K^+ mesons in Ni+Ni collisions at 1.91A GeV *

T. I. Kang †[1,2], *V. Zinyuk*[2], *N. Herrmann*[2], *R. Averbeck*[3], *K. D. Hildenbrand*[3], *B. Hong*[1], *M. Kiš*[3], *Y. Leifels*[3], *K. Piasecki*[2], *W. Reisdorf*[3], *A. Schüttauf*[3], *and the FOPI Collaboration*

[1]Korea University, Seoul, Korea; [2]Physikalisches Institut der Universität Heidelberg, Heidelberg, Germany; [3]GSI, Darmstadt, Germany

A restoration of chiral symmetry of QCD predicts substantial modifications of the kaon properties, i.e., the effective kaon mass shift, in dense nuclear matter [1]. This modification is described by a kaon-nucleus potential and manifests itself in azimuthal emission pattern of kaons in dense environment [2], as created, e.g., in the heavy-ion collision. The propagation pattern can be expressed by the first and second order Fourier coefficients, v_1 and v_2 [3].

The FOPI experiment recorded about 69×10^6 Ni+Ni collisions in S325(e) experiments, corresponding to the most central 60 % of the reaction cross section. In total, about 233,300 K^+ mesons were identified in the interval of $\pm 2\sigma$ around the K^+ nominal mass. The events were centrality selected by imposing conditions on the charged baryon multiplicity (Mul); peripheral events for $0 < Mul \leq 47$ and central events for $48 \leq Mul \leq 90$, which correspond to the impact parameter ranges of $3 < b_{geo} < 7$ fm and $b_{geo} < 3$ fm, respectively.

Fig. 1 shows v_1 of K^+ as a function of p_T in two impact ranges, $3 < b_{geo} < 7$ fm (peripheral) and $b_{geo} < 3$ fm (central), near target rapidity, $-1.3 < y_0 < -0.5$. Here $y_0 = y_{lab}/y_{cm} - 1$ is defined to be +1 at projectile and -1 at target rapidity. The systematic errors (boxes in Fig. 1) are estimated to be 0.024 and 0.012 for peripheral and central collisions, respectively. The data show a strong p_T dependence. At low transverse momentum, $p_T < 0.4$, v_1 of K^+ are positive and the magnitude of v_1 is decreasing with increasing p_T and at around $p_T = 0.4$ GeV/c the value of v_1 turns negative in both centrality selections. Near threshold beam energies, the produced kaons usually have small momenta, hence by rescattering with energetic nucleons, their momenta increase, as does their flow strength in the direction of nucleons [4] and therefore, v_1 of K^+ has negative values at higher transverse momenta, $p_T > 0.4$ GeV/c. Note that protons have been measured with a negative v_1 for the whole p_T range [5].

In order to evaluate the implications of the experimental data in terms of K^+ properties in the dense, hot nuclear medium, in Fig. 1 we utilized transport models; Hadron String Dynamics (HSD) [6] and Isospin Quantum Molecular Dynamics (IQMD) [7] with and without an in-medium potential. Earlier publications on v_1 of K^+ [5] and K^0_s [8] spectra could successfully be described by HSD with an in-medium potential of 20 ± 5 MeV, while the rapidity distribution of K^0 was described by IQMD with 40 MeV [9].

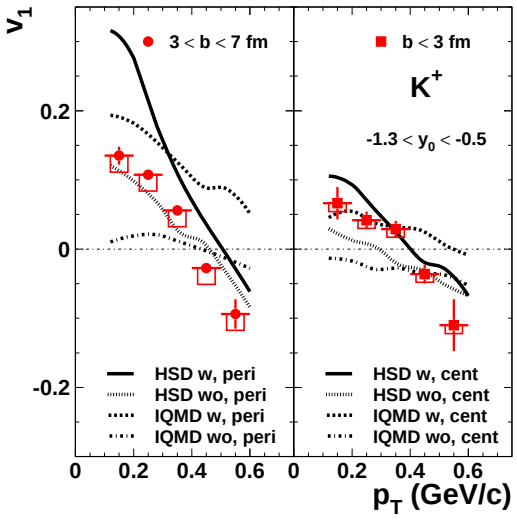

Figure 1: The p_T-differential v_1 of K^+ mesons in peripheral (right) and central (left) collisions. The various lines represent the HSD and IQMD calculations with ('w') and ('wo') an in-medium potential.

Therefore, in this comparison, the depth of the repulsive potential at normal nuclear matter density and zero momentum, was introduced as 20 and 40 MeV for HSD and IQMD, respectively.

Both models predict an enhanced "antiflow" [5] when turning on the kaon potentials. For peripheral collisions, however, the data are better described without the presence of a potential, while for central collisions the inclusion of the in-medium potential provides a better agreement with the data.

References

[1] C. Fuchs, Pro. Part. Nuclear Phys. **56**, 1 (2006).

[2] G. Q. Li *et al.*, Phys. Rev. Lett. **74**, 2 (1995).

[3] S. Voloshin and Y. Zhang, Z. Phys. C **70**, 665 (1996).

[4] G. Q. Li and G. E. Brown, Nucl. Phys. A **636**, 487 (1998).

[5] P. Crochet *et al.*, Phys. Lett. B **486** (2000) 6-12

[6] W. Cassing *et al.*, Phys. Rep. **308**, 65 (1999).

[7] C. Hartnack *et al.*, arXiv:nucl-th/1106.2083.

[8] M. L. Benabderrahmane *et al.*, Phys. Rev. Lett. **102**, 182501 (2009).

[9] G. Agakishiev *et al.*, Phys. Rev. C **82**, 044907 (2010).

* Work supported by DFG 446 KOR 113/2160/0-1, BMBF 06HD9121I and EU/FP7 HadronPhysics2.

† kang@physi.uni-heidelberg.de

Production of hyper-tritons in Ni+Ni collisions at 1.91A GeV *

Y.P.Zhang[†1], *N.Herrmann*[1], *K.Wisniewski*[1], *K.Piasecki*[1,2], *and FOPI collaboration*

[1]Physikalisches Institut, Universität Heidelberg, Germany; [2]Faculty of Physics, University of Warsaw, Poland

The production of hypernuclei in heavy-ion collisions have been first proposed almost two decades ago [1]. Recently, the STAR collaboration measured the production of (anti-)hyper-tritons at ultrarelativistic energies at RHIC [2]. In this contribution, we report about the production of hyper-tritons in Ni+Ni collisions at 1.91A GeV, carried out with the FOPI spectrometer [3] at SIS18 in GSI/Darmstadt.

In the FOPI experiment, hyper-tritons can be identified by reconstructing the invariant mass of their charged decay-products. In our previous contribution [4], the reconstruction method for the two-body decay channel, ${}^3_\Lambda H \rightarrow \pi^- + {}^3He$, was described in details. In the upper panel of Fig. 1, the invariant mass distribution of identified (π^-,^3He) pairs is shown. The improved result was obtained after the reconstruction and analysis algorithms were optimized in order to achieve the best description of the mixed-event background (dashed-blue line) in the control regions (depicted by the horizontal arrows). The signal obtained by subtracting the mixed-events background (shown in the lower panel of Fig. 1) is fitted with a gaussian function and integrated within the $3{\cdot}\sigma$ (13.8 MeV) range around the fitted mean (2.9926 GeV), which results in the total yield of 343 counts and the significance of about 5.2.

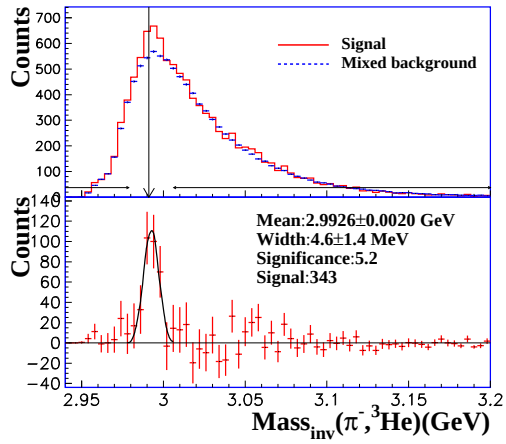

Figure 1: Upper panel: Invariant mass distribution of $\pi^- - He^3$ pairs (solid line) and mixed-event background (dashed line). The horizontal arrows depict the control regions in which the background is optimized. Lower panel: Invariant mass distribution after subtracting the optimized background distribution.

The reconstruction efficiency of ${}^3_\Lambda H$ was studied by means of MC simulations of the FOPI detector response, in which ^3He,Λ and ${}^3_\Lambda H$ embedded in appropriate QMD events were fully tracked through the analysis chain. Results of simulations with events that did not contain the source of ${}^3_\Lambda H$ helped to verify that the observed signal is not artificially generated by the reconstruction methods.

In order to extract the mean lifetime of ${}^3_\Lambda H$, the distribution of decay-time of the reconstructed ${}^3_\Lambda H$ candidates was evaluated: $t = r_s/(\beta{\cdot}\gamma)_t$, where r_s is the distance from the secondary vertex to the primary vertex in the transverse plane, $(\beta{\cdot}\gamma)_t = p_t/m_{{}^3_\Lambda H}$ is the transverse velocity, p_t is the transverse momentum and $m_{{}^3_\Lambda H}$ equals to 2.991 GeV. Open squares in Fig. 2 depict the decay-time distribution of ${}^3_\Lambda H$, after correcting it for the reconstruction efficiency. The exponential fit to the distribution gives rise to a 333±72 ps mean lifetime of ${}^3_\Lambda H$. This result can be directly compared to a 262.3±6.0 ps mean lifetime of the Λ hyperon, obtained by fitting the decay-time distribution of Λ, depicted by open circles in the Fig. 2.

The ongoing analysis concentrates on estimating the systematic errors and on optimizing MC simulations in order to obtain the best description of the detector response and the efficiencies of the reconstruction algorithms. The hyper-triton signal will be also searched for in the three-body decay channel: ${}_\Lambda t \rightarrow \pi^- + p + d$.

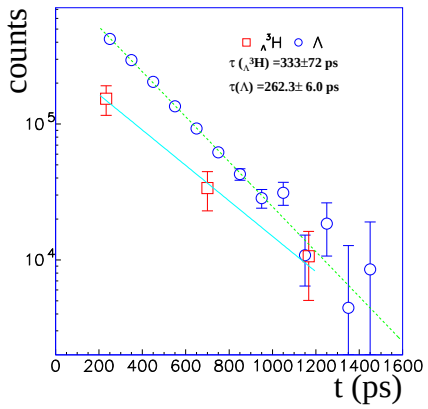

Figure 2: Decay-time distributions of ${}^3_\Lambda H$ (open squares) and Λ (open circles). Extracted mean lifetimes of ${}^3_\Lambda H$ and Λ are 333±72 ps and 262.3±6.0 ps respectively.

References

[1] A. K. Kermann, M. S.Weiss, Phys. Rev. C 8, 408 (1973)

[2] The STAR Collaboration, Science, 328, 58 (2010) and reference therein.

[3] M. Kiš, M. Ciobanu, et al,NIM A, 646, 27 (2011)

[4] Y. P. Zhang, N. Herrmann, et al. GSI Scientific Report 2010, P67

* This work was supported by BMBF 06HD9121I

† ypzhang@physi.uni-heidelberg.de

Status of the pkΛ Analysis in pp Collisions with the FOPI Spectrometer

R. Münzer[1], M. Berger[1], L. Fabbietti[1], and D. Pleiner[1] for the FOPI Collaboration
[1]TU München - Excellence Cluster Universe, 85748 Garching

The investigation of the kaon-nucleon interaction has been intensified in the last years due to new results on $\Lambda(1405)$ (1) and indications on the existence of the ppK^- bound state [1, 2]. The possible creation of the ppK^- has been investigated at the FOPI spectrometer at GSI in proton-proton-collisions at 3.1 GeV. According to some theoretical predictions, this reaction should favour the formation of the ppK^-[3].
Additionally to the FOPI spectrometer a silicon detector system placed close to the target has been constructed and employed to improve the vertex determination and used as an online trigger for the selection of Λ hyperons. This system consists of two layers of silcion detectors. The second layer is a double sided detetor, which reconstructs an additional trackpoint [4]. About $70 \cdot 10^6$ events have been collected after the second level trigger selection.
The hitpoint reconstructed with the tracker was used to

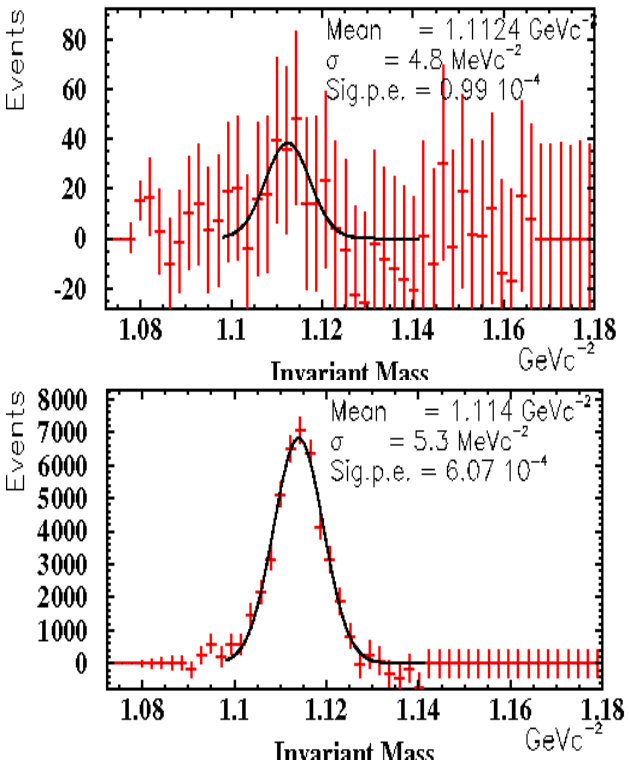

Figure 1: The pictures show the background substracted invariant mass of p and π^- for level one (upper) and level two trigger condition (lower). The black curve show a gaussian fit in the Λ region.

improve the secondary vertex information for the Λ reconstruction. The right panel of Figure 1 shows the invariant mass of a π^- and p. The π^- is reconstructed in the backward tracking system of FOPI (CDC, Barrel). The p is reconstruted in the forwards tracking system (Helitron drift chamber, Plastic Wall) combined with the hitpoint reconstruced with the tracker information. The required trigger condition for the used events is the second-level-trigger. In comparison the left panel of figure 1 shows the picture for the first-level-trigger condition.

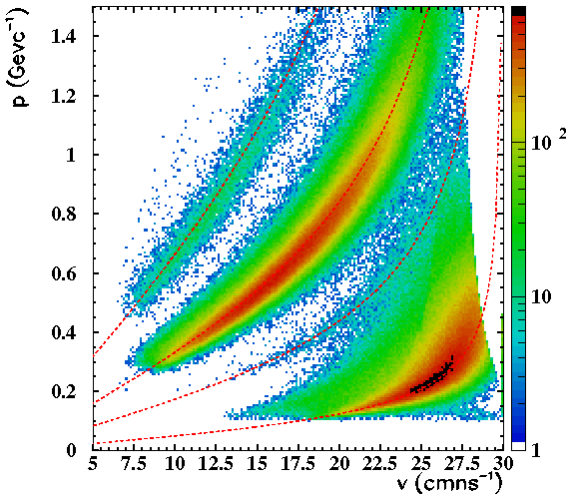

Figure 2: Momentum versus velocity of CDC-RPC Matched tracks. Additional cuts are applied to reduce the background of missidentified particles.

The number of reconstructed Λ are normalized to the total number of events of the corresponding trigger sample. From these numbers one can see, that the number of Λ particles per event could be enhanced by the Λ-Trigger by a factor of 6.
The K^+ are identified via measuring their momentum in the Central drift chamber and their velocitiy measured by the RPC barrel detector [5]. Figure 2 shows the momentum versus velocity correlation plot. A clear separation of Kaons from π^+ is visible up to 0.7 $GeVc^{-1}$ and 22.5 $cmns^{-1}$.

References

[1] J. Siebenson, L. Fabbietti / in press.
[2] M.Maggiora, Proceedings of the 'Hypernuclear and Strange Particle Physics' conference, Tokai, 2009
[3] Yamazaki and Akaishi, Phys.Rev.C 76(2007)045201
[4] "The ppK^- Experiment at GSI", GSI Jahresbericht 2009 "A Λ-Trigger for the FOPI Detector System", Jahresbericht 2007
[5] http://www.gsi.de/documents/DOC-2007-Mar-168-1.pdf

Development of a kinematical refit for the analysis of the reaction $pp \rightarrow pK\Lambda$ at 3.1 GeV with FOPI

D. Pleiner[1], *M. Berger*[1], *L. Fabbietti*[1], *R. Muenzer*[1], *and the FOPI Collaboration*
[1]Excellence Cluster "Universe", TU Munich, Garching, Germany

Introduction

In order to study the existence of the ppK^- kaonic bound state, the FOPI experiment took data with a 3.1 GeV proton beam hitting a LH_2 target in August 2009. The ppK^-, which might decay into a Λ and a proton [1], is searched for, applying the missing mass and invariant mass technique. The reaction of interest is $pp \rightarrow pK^+\Lambda$, where the Λ further decays into a proton and a π. In order to improve the mass resolution of the reconstructed Λ and the momentum resolution of the refitted particles, a kinematical refit was developed.

The refit imposes the knowledge of several physical processes on the trackfitting by introducing certain constraints on the reconstructed tracks of the final reaction $pp \rightarrow pK^+p\pi^-$ [2]. In addition to several non-vertex constraints (energy/momentum conservation, invariant mass), also constraints on the different vertex positions are implemented.

Test with simulations

The effect of the kinematical refit is tested with pp URQMD simulations at GEANT level and full scale level with the respective errors. Different signatures as e.g. χ^2 distributions and pull functions, which are sensitive to the correct error input and its systematical and statistical character, are used to set the fit parameters properly for different constraint combinations. The effect of the kinematical refit on the reconstructed Λ, where only energy and momentum conservation are set as constraints, is shown in Fig.1. The refit decreases the width of the $p\pi^-$ invariant mass distribution by 25% and the width of the pK^+ missing mass spectrum by 90%.

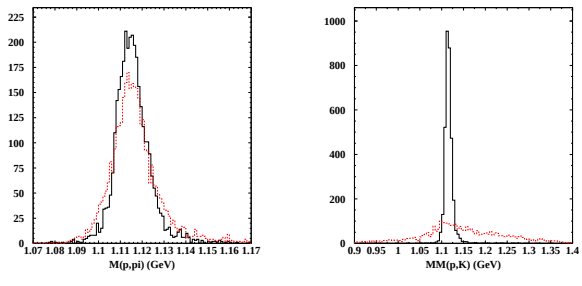

(a) Invariant Mass p + pi (b) Missing Mass p + K

Figure 1: Application of the kinematical refit to simulations: The dashed line corresponds to the unrefitted, the solid line to the refitted spectra

Elastic reactions

A nice tool to study the improvement of the momentum resolution by applying the kinematic fit is the pp elastic reaction. Due to the fixed kinematics, the momentum of the particles can be predicted theoretically by measuring it's polar angle [3]:

$$p_{th}(\Theta) = \frac{p_{beam}}{cos\Theta + \gamma_{CMS}^2 sin\Theta cos\Theta} \qquad (1)$$

Fig.2 shows the deviation of the theoretical momenta from the reconstructed ones for raw (dashed line) and refitted (solid line) tracks, where the two protons are measured with two different tracking detectors for small ($\Theta_1 < 27$) and large ($\Theta_2 > 27$) polar angles. The constraints for the kinematical refit were set such, that the two protons fulfill the energy and momentum conservation and intersect at a common spacepoint after the fit.

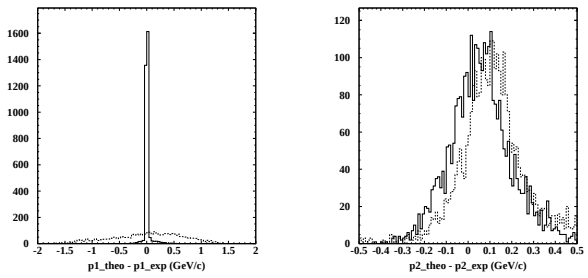

(a) Proton 1 (b) Proton 2

Figure 2: Resolution of the proton momenta with (solid line) and without (dashed line) Kinematic Refit

The refit drastically improves the proton momentum resolution in the forward direction and simultaneously shifts the mean value of the two distributions to zero.

References

[1] T. Yamazaki, Y. Akaishi, PRC 76, 045201 (2007)

[2] P. Avery. http://www.phys.ufl.edu/ avery/fitting.html, 1998

[3] Stefano Spataro, "Characterization of the HADES spectrometer in pp collisions at 2.2 GeV: Elastic scattering and exclusive eta reconstruction", Dissertation, University of Catania, 2005

π^- Induced Reactions with FOPI

O.N. Hartmann[1] *and the FOPI Collaboration*
[1]SMI, Vienna, Austria

The study of strangeness production in π^- induced reactions complements the physics program of FOPI [1]. In the 2011 experiment, a secondary beam of π^- of 1.7 GeV/c (which corresponds to $\sqrt{s} \simeq 2$ GeV in the $\pi^- N$-system) was hitting a nuclear target. The charged reaction products where measured by the FOPI detector. The goal is to study the production of K^+K^- as a function of the target mass number.

The π^- beam is produced by a primary $^{14}_{7}\mathrm{N}^{7+}$ beam impinging on the production target (a cylinder of Beryllium, with 4-6 mm diameter and 10-12 cm length). The π^- yield is mainly determined by the primary beam intensity onto the production target. In a dedicated test beam time and several days of setup at the beginning of the experiment, a good compromise in terms of SIS extraction energy, machine parameters and beam transport has been found. The extraction energy was set to 1.923 AGeV (18.0 Tm). Fig. 1 shows the comparison for the $\pi^\pm$ yields under forward angles for primary beam energies of 2 and 1.923 AGeV as simulated with FLUKA [3]. The decreasing π^- production for the lower energy could be compensated by a better SIS extraction efficiency. In the finally stable operation conditions, from $9 \cdot 10^{10}$ ions accelerated in the SIS, $5 - 6 \cdot 10^{10}$ have been measured in front of the production target ($\leq$ 77% extraction efficiency). Setting the secondary beamline to 5.67 Tm, the interesting pion momentum of 1.7 GeV/c could be selected. Pion yields for negative and positive polarity have been compared; in the latter case, the secondary beam contains protons and π^+ of the same momentum. From the FLUKA simulation, the $\frac{p}{\pi^+}$ ratio at 1.7 GeV/c has been estimated to $\simeq$ 130, in good agreement with the later measured π^- yield. At the FOPI target, 89 m upstream of the pion production target, $2.9 \cdot 10^4$ π^- per spill could be achieved.

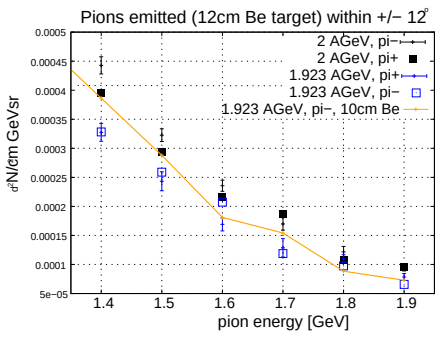

Figure 1: FLUKA simulation: charged pion yield as a function of the pion momentum for π^+ and π^- and different production reactions.

For the cycle time of 3.22 s this corresponds to a rate of 9000 π^-/s, which agrees with the estimate from the experiment proposal [4]. The intensity at the FOPI target is mainly limited by the the long flight path and the geometrical acceptance of the beamline.

Compared to its standard configuration, the FOPI detector has been complemented by two new subsystems. The prototype of a GEM-TPC (see [5]), successfully integrated and tested in 2010/2011, was placed in the inner hole of FOPI's Central Drift Chamber (CDC). Since the target was placed inside the GEM-TPC, a compact design of a VETO detector became necessary. This detector allows to discard (beam) particles outside the active target area. An arrangement of scintillators read out by SiPM was chosen [6].

In the production run of 17 days we had "beam on target" for ≈60% of the time. Three target nuclei (carbon, copper, lead) have been irradiated, and between 1.5 and 2.8 million good events could be recorded. The data calibration and analysis is ongoing. The data quality looks promising, the statistics of interesting events still has to be evaluated. Fig. 2 shows, as an example, a mass spectrum of K^+ mesons identified by the correlation of momentum (measured by the CDC) and time of flight (measured by the RPC TOF barrel) over the full measured momentum range.

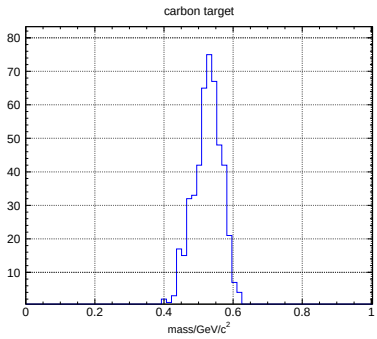

Figure 2: Mass spectrum (in GeV/c^2) of K^+ mesons identified by the momentum-velocity correlation.

References

[1] http://www-fopi.gsi.de/

[2] J. Diaz et al., NIM A 478 (2002) 511

[3] G. Battistoni et al., AIP Conf. Proc. 896 (2007) 31;
A. Ferrari et al., CERN-2005-10

[4] SIS experiment proposal S339 (2007)

[5] L. Fabbietti et al., NIM A 628 (2011) 204;
F. Cusanno et al., GSI Scientific Report 2011
M. Berger et al., GSI Scientific Report 2011

[6] G. Ahmed, GSI Scientific Report 2011

A Veto detector for the Pion Beam Experiment at FOPI

G. Ahmed[1,2], P. Bühler[1], O. Hartmann[1], K. Suzuki[1], J. Zmeskal,[1] and the FOPI collaboration

[1]Stefan Meyer Institute for Subatomic Physics of the Austrian Academy of Sciences, Vienna, Austria.
[2]Al-Azhar University, Faculty of Science, Physics Department, Cairo, Egypt.

The FOPI collaboration carried out a measurement to study the in medium properties of the K^+K^- system by using the π^- (1.7 GeV/c) + $A \rightarrow K^+K^-$ + X reaction [1]. The almost 4π geometrical acceptance and the excellent vertex reconstruction capability make the FOPI detector at GSI a suitable apparatus to perform this measurement [2]. A veto counter was installed in front of the target in order to tag the events in which the secondary beam went undesirably off axis. A difficulty arose with the newly installed GEM-TPC [3] that sets a spatial constraint for the beam tube (ø=80 mm), the target (45 x 45 mm^2) and the veto counter (ø=40 mm hole) to fit at the 50 cm depth in an inner hole with a diameter of 90 mm (see Fig. 1). The 0.6 T magnetic field from the FOPI solenoid magnet poses an additional constraint on the detector design.

The veto counter consists of a 5-mm-thick single layer doughnut-shaped scintillator and Silicon Photomultipliers (SiPMs). The outer diameter of the scintillator was maximized inside the beamtube. The outer surface was partly planed to accommodate a few mm of space for the photosensors (Hamamatsu MPPC S10985-100, 3 x 3 mm^2 sensitive area, 5.9 x 6.5 x 2 mm^3 outer dimension [4] with a preamplifier board ~ 8 x 25 mm^2). The photosensor is directly attached to the scintillator with an optical grease. The scintillator is divided into 4 pieces in order to monitor also a roughly the spatial distribution of the beam halo (left, right, up and down). Each scintillator covers an angle slightly larger than 90 deg and overlaps with the neighboring pieces in order to avoid insensitive gaps between two scintillators. 2 SiPMs are attached to one piece of scintillator, thus 8 SiPMs in total (Fig. 1, 2).

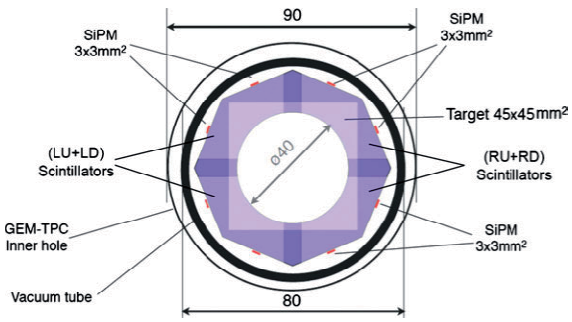

Figure 1: Schematic drawing of the veto detector based on a scintillator with SiPM readout. The inner diameter of the GEM-TPC, the beamtube and the target dimension are also indicated.

Figure 2: Photograph of the VETO setup, seen from downstream.

The most crucial parameter for the veto counter is the efficiency. The logical OR of the two sensors attached to the same scintillator is used as the veto signal. Comparing the scaler counts of the logical AND to the counts of the logical OR gives an estimate of the detection efficiency. The Hamamatsu SiPM is known to be very sensitive to temperature variations. Due to the space limitation we had no temperature regulation system of the SiPM. We experienced up to 20 °C temperature variation that caused the gain variation of the SiPM about a factor 2. The detector "efficiency" was monitored through the beamtime. Despite of that given condition, the efficiency stayed very stably at the satisfactory level of 99%.

Though the novel SiPM has started to replace the vacuum PMT in many photosensing applications, the SiPM has also drawbacks and requires often a tricky operation. An adoption of PMT was, however, nearly impossible in the reported case. The SiPM's unique features (compactness and insensitivity to magnetic fields) were fully exploited and worked very satisfactory even with the large temperature variations.

References

[1] Study of Pion-induced In-medium Production and Propagation of Strangeness., FOPI Proposal, March 2007.
[2] FOPI Collaboration. ″Technical Proposal GSI Report″, 88 - 03 (1988).
[3] L. Fabbietti et al., NIM A 628 (2011) 204
[4] Hamamatsu Photonics http://www.hamamatsu.com/

Silicon-strip beam-tracker for minimum-ionising particles

P. Koczoń[1] *and FOPI Collaboration*[2]
[1]GSI, Darmstadt, Germany

To improve the precision of primary vertex determination in FOPI experiments (particularly in a low track-density environment) a beam-tracker based on two double-sided silicon-strip detectors was build and tested with pions of 1.7 GeV/c in June 2011.

The two PF-128CD-128CD-32*32-500EB detectors (32x32mm x 500 μm, 128 strips each side) were manufactured by Canberra and bonded on individually designed PCB's. On site, the detectors were mounted on the beampipe with vacuum flanges, separated by certain distance, as planned for the real experiment. Special adapter boards had to be constructed in order to properly bias the detectors. Each side of the detector (128 signals) was connected to the self-triggered n-XYter chip followed by an ADC [1]. The digitized hits, containing time stamps as well as the ADC information, were read-out in a triggered mode by the Exploder board [2] newly developed by EE at GSI. The trigger was made out of the signal from a small scintillator (18x6 mm), placed behind the silicon detector. The readout system allows to select hits in a predefined time window placed around the trigger appearing time what allows for a significant noise reduction. The data acquisition based on the MBS system allowed simple integration with the existing DAQ of FOPI.

The setup was first tested with the electrons from the ^{90}Sr source, collimated to a 2mm wide profile. In Fig.1 the two dimensional distribution of hits registered by the silicon detector is shown. Besides the fake hits due to the noise (in the left-middle part) the signal is clearly visible. In Fig.2 a similar result is shown when the detector was placed in the beam of pions with momentum of 1.7 GeV/c. The registered pattern corresponds to the shape of the scintillator itself because in this case the beam profile was much wider than the trigger-scintillator. The histogram in Fig. 3 shows the charge-amplitude distribution of signals collected on one of the strips, when the detector was exposed to a 3 GeV proton beam. Charge-amplitude distribution measured in 100 ns wide time window around trigger is overlayed. Noise reduction of factor of 3 could be achieved.

Interest of other groups (e.g. HADES) as well as future FAIR experiments (e.g R3B) drives further developement of the beam-tracker system in order to adapt it for different silicon detectors and experimental conditions.

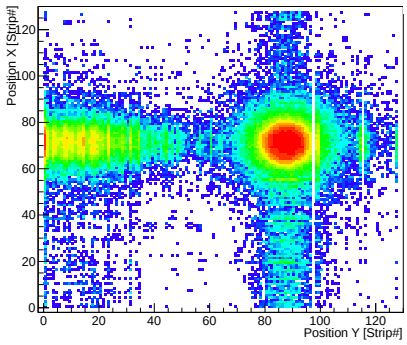

Figure 1: Collimated ^{90}Sr source of electrons.

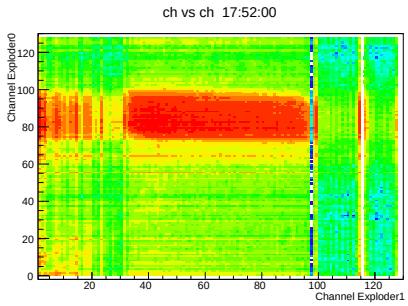

Figure 2: 18x6 mm scintillator-detector image taken using 1.7 GeV/C pions.

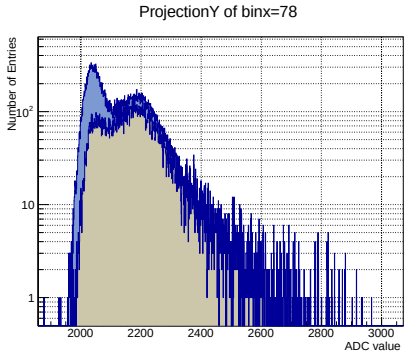

Figure 3: Charge amplitude distribution collected on one of the strips. Bright histogram - raw data, grey histogram - hits registered in a 100 ns wide time-window, correlated with the trigger signal.

References

[1] http://cbm-wiki.gsi.de/cgi-bin/view/Public/PublicNxyter.

[2] http://www.gsi.de/informationen/wti/ee/elekt_entwicklung /exploder_1.html.

GEM-TPC: Alignment and combined analysis with RPC in FOPI *

F. Cusanno for the GEM-TPC Collaboration[1,2,3,4,5,6]

[1]T. U. München, Excellence Cluster Universe, Garching b. München, Germany; [2]Technische Universität München, Garching b. München, Germany; [3]GSI Helmholtzzentrum für Schwerionenforschung GmbH, Darmstadt, Germany; [4]Helmholtz-Institut für Strahlen- und Kernphysik, Bonn, Germany; [5]Universität Heidelberg, Heidelberg, Germany; [6]Stefan Meyer Institut für Subatomare Physik, Wien, Austria

Introduction

A large GEM-TPC prototype [1] was tested with FOPI and used in a physics run. Tracks of TPC and CDC/RPC are matched, to improve the momentum calculation.

Alignment of the GEM-TPC in FOPI

In order to obtain software alignment of the GEM-TPC in the FOPI coordinate system, tracks fitted in CDC are used as reference, by extrapolation into the GEM-TPC volume. A minimization procedure (MINUIT) of the corresponding residuals of GEM-TPC clusters is employed in order to determine the three rotational and three translational parameters needed for alignment. Since the CDC resolution in Z is worse than in X, Y, the Z component of the residuals is not taken into account. Fig. 1 shows the improvement in the distribution of X component of the residuals after the alignment procedure. Statistical uncertainties in the positioning of the order of $10\ \mu$m are obtained. The systematic error is evaluated considering the maximal variation in the alignment parameters producing residual distributions of the same quality, and resulted to be $\sim 100\ \mu$m. Quality checks of the alignment parameters as function of time and precise determination of the systematics for FOPI experiment S339 are ongoing.

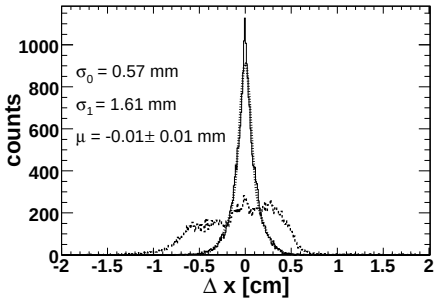

Figure 1: Distribution of X component (lab system) of the residuals of GEM-TPC clusters to CDC tracks before (dashed curve) and after (solid curve) the alignment, for a data sample of S339. Double-gaussian fit (dotted line) is superimposed to the final distribution.

Combined Analysis with the RPC

Once the alignment parameters are extracted, combined CDC/TPC tracks are reconstructed and fitted in order to calculate the corresponding momentum. The GENFIT toolkit [2] is employed for this purpose, using the CDC momentum as starting value. For tracks in the RPC acceptance, correlation plots of momentum versus particle velocity might provide measure of the improvement on momentum resolution of combined tracks with respect to standard CDC tracks only.

Preliminary comparison of those correlation plots is shown in Fig. 2 for a sample of π^- beam @ 1.7 GeV on Carbon target. The improvement in the momentum resolution is $\sim$ 20% for protons and $\sim$ 10% for pions.

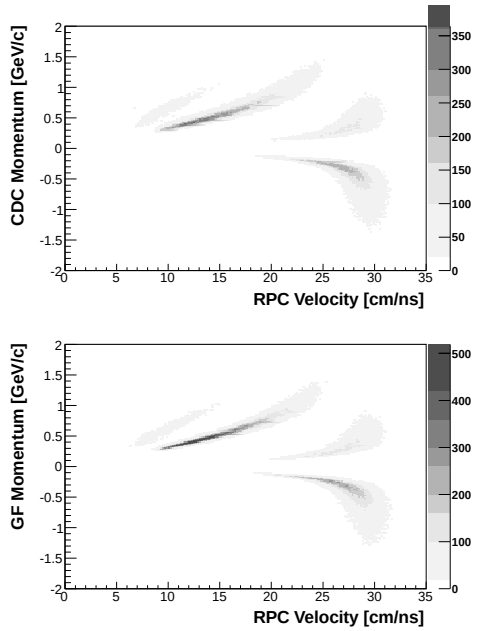

Figure 2: Correlation plot of CDC momentum vs RPC velocity (top panel) compared with the corresponding plot for combined tracks (bottom panel).

References

[1] GEM-TPC Collaboration, GSI SCIENTIFIC REPORT 2010, PHN-HSD-PANDA-09111-115. 204-208.

[2] C. Höppner, S. Neubert, B. Ketzer, S. Paul, Nucl Instr Meth A620 (2010) 518-525.

* Work supported by HGF and DFG-Excellence Cluster Universe.

Resolution studies with a GEM-TPC prototype

M. Berger[1] *for the GEM-TPC Collaboration*[1,2,3,4,5,6]

[1]T. U. München, Excellence Cluster Universe, Garching b. München, Germany; [2]Technische Universität München, Garching b. München, Germany; [3]GSI Helmholtzzentrum für Schwerionenforschung GmbH, Darmstadt, Germany; [4]Helmholtz-Institut für Strahlen- und Kernphysik, Bonn, Germany; [5]Universität Heidelberg, Heidelberg, Germany; [6]Stefan Meyer Institut für Subatomare Physik, Wien, Austria; [7]Excellence Cluster Origin and Structure of the Universe, Garching b. München, Germany

Introduction

A GEM-TPC detector was build as a prototype of the inner tracker for the future $\overline{\mathrm{P}}$ANDA experiment at FAIR and as an updgrade for the FOPI experiment at GSI. A GEM-TPC can exploit the intrinsic suppression of back drifting[1] ions from the amplification stage of the GEM foils to overcome the problem of drift-field distortions in a ungated operation. This prototype was designed to fit into the FOPI spectrometer, where the commissioning, tests with cosmic rays and beam tests were carried out[2].

Experimental setup

For the commissioning the prototype was installed inside the FOPI spectrometer which was set up for triggering on cosmic particles. FOPI is a fixed target spectrometer for heavy ion beams. It consists of an inner drift chamber which is surrounded by a scintillator and an RPC time-of-flight barrel. In forward direction is another drift chamber and a scintillator time-of-flight wall. The whole setup is surrounded by a superconducting 0.6 T solenoid magnet.

Results from cosmics tracks

Data with cosmic tracks were taken for several different detector parameters:

- Drift gases: Ar/CO_2 and Ne/CO_2, both in a 90/10 mixture
- Drift fields: 150, 200, 300 and 360 V/cm
- Different gains for the GEM stack for both gases

The track finding and noise suppression was done with a Riemann[3] pattern recognition after clustering. The found tracks were fitted with GENFIT[4], a generic fitting tool based on a Kalman[5] filter. The drift volume was divided into 6 slices along the drift direction and the residuals of the hit points to the fitted tracks were calculated for each slice. Fig.1 shows the residual distribution for the first slice which means the shortest drift length. The resolution one gets by fitting the distribution with three Gaussian functions is 274 µm. Fig.2 shows the obtained resolutions as function of the drift length while the squares indicate the resolution by only taking the most centered Gaussian into account and the circles show the weighted mean of all three fitted Gaussian functions. Both plots are from a measurement with Ne/CO_2 a drift field of 360 V/cm and a gain of 2000 and are in good agreement with simulations.

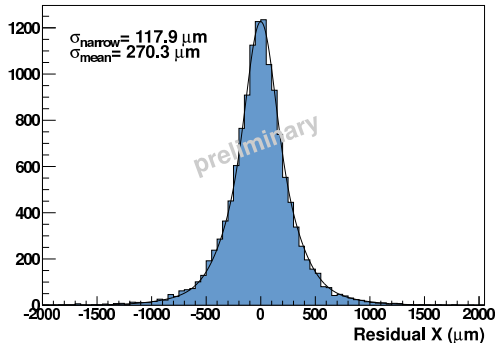

Figure 1: The residual distribution of the first slice along the drift direction.

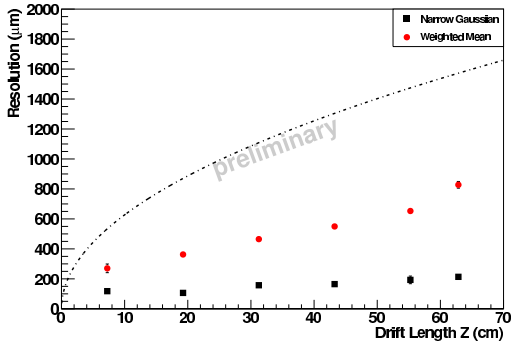

Figure 2: The obtained resolution for slices along the drift direction. The dash-dotted line shows the single-electron diffusion.

References

[1] A. Lyashenko et al., Nucl. Instr. Meth. A, 598 116 (2009)

[2] L. Fabbietti, Nucl. Instr. and Meth. A, 628 204-208 (2011)

[3] A. Strandlie et al., Comp. Phys. Comm. 131, 95 (2000).

[4] C. Höppner, S. Neubert, B. Ketzer, and S. Paul, Nucl. Instr. and Meth. A 620, 518 (2010)

[5] R. Frühwirth, Nucl. Instr. and Meth. A 262, 444 (1987)

High-Rate Event Mixing Studies for the PANDA TPC*

F. V. Böhmer[†1], *J. Rauch*[1], *and the GEM-TPC Collaboration*[1,2,3,4,5]

[1]Technische Universität München, Germany; [2]GSI Helmholtzzentrum für Schwerionenforschung GmbH, Darmstadt, Germany; [3]Helmholtz-Institut für Strahlen- und Kernphysik, Bonn, Germany; [4]Universität Heidelberg, Heidelberg, Germany; [5]Stefan Meyer Institut für Subatomare Physik, Wien, Austria

Continuously running GEM TPC

In past experiments, Time Projection Chambers (TPCs) have been equipped with a gating structure to prevent the migration of avalanche ions created during gas amplification – traditionally realized with Multi Wire Proportional Chambers (MWPCs) – in order to maintain drift field homogeneity. This, however, limited the application of TPCs to experiments with trigger rates smaller than $\mathcal{O}(10^3\,\mathrm{Hz})$.

To overcome this important limitation introduced by gating techniques, one has to find other means of ion suppression. We propose to exploit the intrinsic ion back-flow inhibition capabilities of Gas Electron Multiplier (GEM) [1] foils and have built a large prototype of such a GEM TPC [2, 3].

PANDA as a triggerless experiment

Within the PANDA physics environment, the inverse reaction rate is much smaller than the electron drift time ($\mathbf{u}^- \approx 50\,\mu\mathrm{s}$). As a consequence, a TPC would store the tracks of $\mathcal{O}(10^3)$ events in its active volume at any given time. With continuous readout, such a detector would constitute an *analog event pipeline*, providing a constant stream of 3-dimensional track data.

This new kind of data acquisition (DAQ) concept would very well fit PANDA's philosophy of a triggerless experiment, where data streams from different kinds of detectors will be scanned for interesting signatures by high-performance online algorithms. This scheme will mark an important step on the path away from the event paradigm defined on trigger level in particle physics experimental DAQ.

Event Deconvolution with the GEM TPC

In the online high level trigger scheme foreseen for PANDA as described above, the central tracking (CT) detector will play a crucial role. Its data will have to be unambiguously associable with the data provided by other detectors, and it will have to be able to contribute to the trigger decision itself for example in channels involving decays of neutral particles inside the CT volume.

Without the knowledge of an "event time" t_0 it has to be shown that it is possible to successfully find and associate

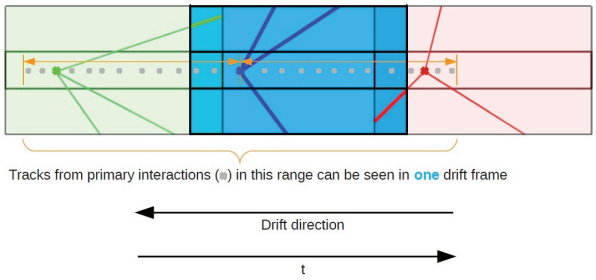

Figure 1: Overlapping of different events inside the GEM TPC. Tracks from different events can be found within a certain time window (e.g. one electron drift time, one *drift frame*) selected from the buffered data stream.

the convoluted tracks (c.f. Fig. 1) belonging to a given physics event, taking into account

- the full overlap (*"convolution"*) of events in the drift volume due to the high rate environment,
- distortion of tracks caused by remaining space charge effects, and
- the efficiency of realistic pattern recognition (PR) algorithms inside the high-rate environment when subjected to distortion effects.

The general strategy of *"event deconvolution"* inside the data stream of overlapped events with unknown event time provided by the GEM TPC is then the following:

1. Clean detection of distorted tracks *in the TPC alone* with efficient PR algorithm(s).
2. Estimate event time on the µs level by extrapolating the (distorted) track (or neutral track reconstructed via secondary vertex detection) to the beam axis within a certain *target cut* (c.f. Fig. 2).
3. Associate with information from other systems, e.g. the Micro Vertex Detector (MVD), Scitil, EMC.
4. Keep interesting signatures. Offline Analysis involves distortion corrections.

Results & Conclusion

In the course of the PANDA CT evaluation process, detailed simulation studies have been performed to answer these questions.

* Work supported by EU, BMBF
† felix.boehmer@tum.de

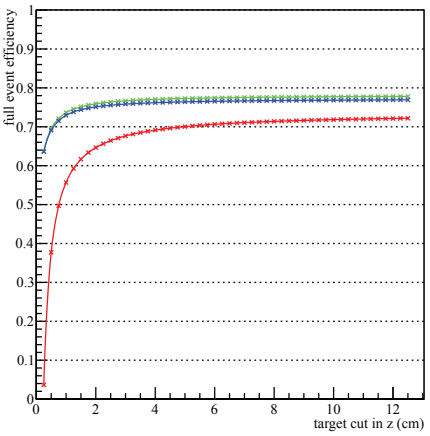

Figure 2: Event reconstruction study on the channel $\eta_c \rightarrow \phi\phi \rightarrow K^+K^-K^+K^-$ at full PANDA event rate. Shown is the efficiency of successfully detecting (more than 50% of the hits associated) all four Kaons with TPC Riemann pattern recognition only at full track density as a function of the target cut applied when extrapolating the distorted tracks back to the known Monte Carlo vertex. The green curve shows the situation at zero distortions, blue and red at distortions scaled to 20% and 100%, respectively.

Space charge effects have been simulated on microscopic level based on realistic particle generators for the PANDA $\bar{p}p$ physics [4], and we have developed a sophisticated pattern recognition algorithm based on the Riemann Transformation showing excellent performance and robustness against distortion effects [5].

With these tools we have simulated physics events and convoluted them with background events according to the full event rate foreseen for PANDA ($2 \cdot 10^7$ Hz), and evaluated the total efficiency of retaining all relevant tracks after pattern recognition in the full track density as a function of the target cut and for different magnitudes of drift distortions (Fig. 2).

In another study we have checked the reconstruction efficiency of $\Lambda \rightarrow p\pi^-$. This is an important benchmark for the CT, as a large part of these decays happen inside its volume and thus have to be detected by the CT *alone* in order to flag the signature inside the PANDA data stream. It also marks sort of a worst case scenario, as the decay products are strongly boosted in forward direction and will enter the CT at small angles.

We have shown [6] that with still very crude vertexing techniques we are able to successfully reconstruct Λ vertices at the correct mass with an efficiency of well above 30%.

These results show that already with the current version of our online reconstruction algorithms, the TPC would be able to detect and associate tracks in PANDA's high rate environment taking into account conservative simulations of the projected drift distortions inside the TPC volume without relying on any external information, and moreover be able to contribute to the "trigger decision" inside the ambitious DAQ scheme of PANDA as a *standalone detector*.

References

[1] F. Sauli, *"GEM: A new concept for electron amplification in gas detectors"*, Nucl. Instr. and Meth. A, 386 (1997), p. 531

[2] L. Fabbietti et al., *"The PANDA GEM-based TPC prototype"*, Nucl. Instr. and Meth. A, 628 (2011), pp. 204-208

[3] H. Angerer et al., *"First test of a prototype GEM-TPC for PANDA"*, GSI Scientific Report (2010)

[4] F. V. Böhmer et al., *"Simulations of a High-Rate TPC for PANDA"*, IEEE Nuclear Science Symposium Conference Record (2009), pp. 2273-2279

[5] J. Rauch, *"Tracking with a high-rate GEM-TPC"*, Diploma Thesis at Technische Universität München (2012)

[6] S. Dørheim, *"$\Lambda\bar{\Lambda}$ in the TPC"*, talk given at the PANDA collab. meeting, Sept. 8th, 2011

Elliptic Flow in Heavy-Ion Reactions: Status of Experiment S394 *

P. Russotto[1] *and the ASYEOS Collaboration*[2]

[1]INFN-LNS and Università, I-95123 Catania, Italy; [2]Bucharest, Catania, Daresbury, Darmstadt, GANIL, GSI, Kraków, Liverpool, Messina, Milano, MSU, München, Napoli, RIKEN, Riyadh, Santiago, TAMU, Warsaw, Zagreb

In May 2011, the data taking of experiment S394 has been completed. With beams of ^{197}Au, ^{96}Zr, and ^{96}Ru of 400 MeV/nucleon and with enriched ^{96}Zr and ^{96}Ru targets, the symmetric collision systems ^{197}Au+^{197}Au, ^{96}Zr+^{96}Zr, and ^{96}Ru+^{96}Ru have been studied. The Large Area Neutron Detector (LAND) and the Kraków triple-telescope array [1] were positioned at laboratory angles around 45° with respect to the beam direction with the aim to measure the directed and elliptic collective flows of neutrons and light charged particles from these reactions with high precision. The impact parameter and the orientation of the reaction plane were determined with eight rings of the CHIMERA multidetector [2], carrying 448 individual CsI(Tl) elements and covering the angular range $7^\circ \leq \theta_{\rm lab} \leq 20^\circ$, combined with a 1x1-m^2 section of the ALADIN Time-of-Flight Wall covering the solid angle up to $\theta_{\rm lab} \leq 7^\circ$. Fifty thin CsI(Tl) elements of the Washington-University μ-ball array [3], covering $60^\circ \leq \theta_{\rm lab} \leq 147^\circ$, surrounded the target for distinguishing reactions on heavy target nuclei from background reactions on non-target material.

The ratio of the parameters describing the elliptic-flow of neutrons with respect to that of protons or light charged particles in reactions at relativistic energies has recently been proposed as an observable sensitive to the strength of the symmetry term in the equation of state at supranormal densities [4, 5]. This was derived from the analysis of the existing FOPI/LAND data for ^{197}Au + ^{197}Au collisions at 400 MeV/nucleon in comparison with predictions of the UrQMD transport model [6] and more recently confirmed by calculations with the Tübingen version of the QMD transport model [7].

The new experiment S394 has been proposed and performed with the aim to confirm this result with new data of much higher statistical precision for the measured flow parameters and to extend the study to light fragments up to atomic number $Z = 4$ with special emphasis on the two pairs of mirror nuclei ^{3}H/^{3}He and ^{7}Li/^{7}Be.

The analysis of the collected data has been started with calibrations for the individual detector systems and with overall quality checks. An important parameter is the resolution achieved in measuring the azimuthal orientation of the reaction plane. It largely determines the uncertainty associated with the deduced flow parameters [8].

The analysis performed so far shows that the particle identification achieved with the CHIMERA detector modules is better than anticipated which will improve the reaction plane resolution beyond the estimated values. For the relative azimuthal orientation of two subevents generated with selected data of charged-particle multiplicity $M_c \geq 10$ at center-of-mass rapidity $y_{\rm c.m.} > 0.1$ (i.e. mid-rapidity excluded) collected with the CHIMERA rings in ^{197}Au+^{197}Au collisions, a distribution with a width $\Delta\phi \approx 60^\circ$ (rms) was obtained. As illustrated in Fig. 1, the corresponding resolution parameter $\chi = 1.2$ leads to a correction factor for elliptic flow of 0.48, meaning that the true v_2 is about twice the measured value [9]. It is to be expected that these values will improve considerably once the full information, including also the Time-of-Flight-Wall and μ-ball data, will be available for the analysis.

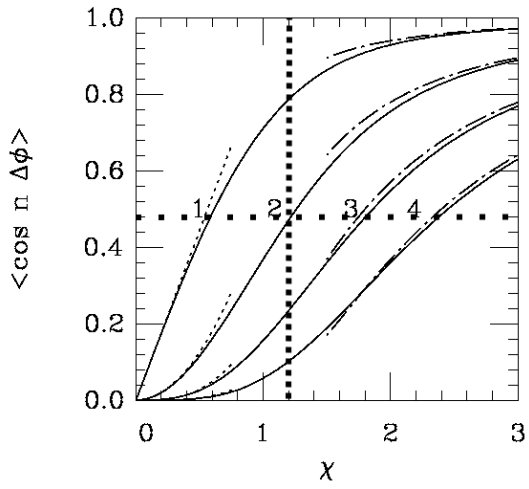

Figure 1: Correction curves for the first four harmonics v_n (n=1-4) as a function of the resolution parameter χ with their asymptotic forms given by the dotted and dash-dotted curves (from Ref. [9]). The obtained $\chi = 1.2$ (vertical dotted line) implies a correction factor $\langle\cos(2\Delta\phi)\rangle = 0.48$ for the elliptic flow parameter v_2 (horizontal dotted line).

References

[1] J. Łukasik et al., GSI Scientific Report 2010, p. 69, and contribution in this report.
[2] A. Pagano et al., Nucl. Phys. A 734 (2004) 504.
[3] D.G. Sarantites et al., Nucl. Instr. and Meth. 381 (1996) 418.
[4] P. Russotto et al., GSI Scientific Report 2010, p. 68.
[5] P. Russotto et al., Phys. Lett. B 697 (2011) 471.
[6] Q. Li et al., J. Phys. G 31 (2005) 1359; J. Phys. G 32 (2006) 151; J. Phys. G 32 (2006) 407.
[7] M.D. Cozma, Phys. Lett. B 700 (2011) 139.
[8] A. Andronic et al., Eur. Phys. J. A 30 (2008) 31.
[9] J.-Y. Ollitrault, preprint nucl-ex/9711003.

* Work supported by EU under contract No. FP7-227431 (Hadron-Physics2).

Performance of the Triple Telescope Array during the ASY-EOS experiment*

J. Łukasik[†1], *J. Brzychczyk*[2], *M. Adamczyk*[2], *A. Budzanowski*[‡1], *B. Czech*[1], *S. Kupny*[2], *P. Lasko*[2], *P. Pawłowski*[1], *I. Skwirczyńska*[1], *Z. Sosin*[2], *A. Wieloch*[2], *M. Kiš*[3], *Y. Leifels*[3], *and W. Trautmann*[3] *for the ASY-EOS Collaboration*

[1]IFJ-PAN, Kraków, Poland; [2]IF UJ, Kraków, Poland; [3]GSI, Darmstadt, Germany

A Triple Telescope Array, TTA, has been built to measure the energy, emission angles and isotopic composition of light charged reaction products (Z<7). It performed very well during the ASY-EOS experiment [1] conducted in May 2011 at GSI (S394). The experiment was aiming at pinning down the density dependence of the nuclear symmetry energy by measuring flows and isotopic composition of the reaction products, including neutrons. The neutrons were measured by the LAND detector and the orientation and magnitude of the impact vector were estimated using the CHIMERA and ALaDiN ToF-Wall detectors. The reactions of ^{197}Au+^{197}Au, ^{96}Ru+^{96}Ru and ^{96}Zr+^{96}Zr at the incident energy of 400 MeV/nucleon have been studied.

The 35 modules of TTA, arranged in a 7x5 array, were placed opposite to LAND at the distance of 40 cm from the target, and covered 160 msr of the solid angle (see Fig. 1).

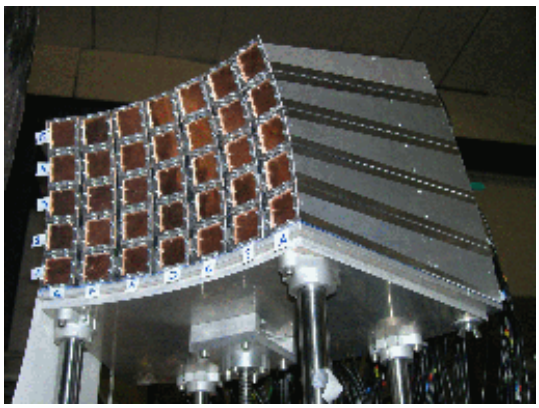

Figure 1: Triple telescope array.

The modules of TTA consist of two, optically decoupled, CsI(Tl) crystals (thickness of 2.5 and 12.5 cm) and three large area, 500 μm thick, PIN photodiodes. The first photodiode served as a Si ΔE detector and supplied the ionization signal alone. The second one worked in a "Single Chip Telescope" [2] configuration and provided both, the ionization signal and the light output from the thin crystal. The third photodiode read out the light from the thick crystal (see [3] for the details). The signals from the photodiodes were integrated by the custom-made low-noise charge preamplifiers and digitized with 100 MHz, CAEN V1724 digitizers.

Very good isotopic resolution has been obtained in the whole dynamic range [4]. Fig. 2 shows a measured count rate spectrum for all 35 modules. It can be viewed as a sequence of 5 "angular distributions", each one for a corresponding row of 7 telescopes, ranging from about 20 to 60 degrees of the laboratory polar angle.

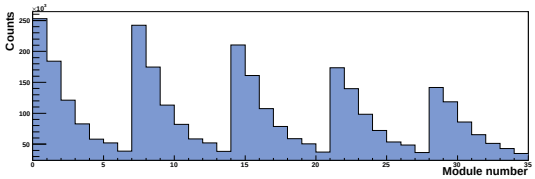

Figure 2: Count rates for all the modules.

Thickness of the photodiodes and CsI(Tl) crystals allowed to detect protons and alpha particles in the range from about 8 to 260 MeV/nucleon. However, the digital acquisition and the pulse shape analysis allowed to reduce the lower threshold to about 2 MeV/nucleon by enabling the identification of particles stopped in the first photodiode. Fig. 3 shows an identification spectrum of the amplitude of the signal vs the position of maximum (mode) of the current signal deduced from the charge waveform.

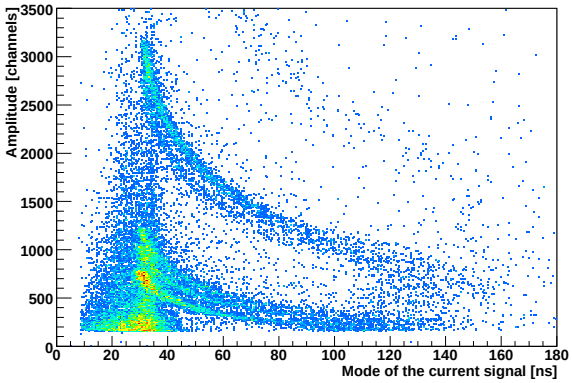

Figure 3: Identification map of particles stopped in the first photodiode. The ID-lines correspond to p,d,t, ^{3}He and α particles, from bottom to top, respectively.

Overall, the TTA array has met the expectations and fulfilled the design requirements.

References

[1] www.irb.hr/users/mkis, www.ct.infn.it/asyeos2010, P. Russotto et al., Phys. Lett. B 697 (2011) 471.

[2] G. Pasquali et al., NIM A 301(1991) 101.

[3] J. Łukasik et al., GSI Scientific Report 2010, p. 69.

[4] http://pro.ganil-spiral2.eu/events/cw/iwm/2011/presentations/lukasik-iwm2011.

* Work supported by Polish Ministry of Science and Higher Education under grant No. DPN/N108/GSI/2009

† jerzy.lukasik@ifj.edu.pl

‡ deceased

Thermalized or not thermalized? The SHM at SIS energies *

M. Lorenz[1], *R. Holzmann*[2], *and J. Stroth*[1,2] *for the HADES collaboration*
[1]Goethe-Universität, Frankfurt, Germany; [2]GSI Helmholtzzentrum für Schwerionenforschung, Darmstadt

With the HADES detector we have investigated in great detail the collision system Ar+KCl at 1.76 AGeV, thus reconstructing in one system the up to now most complete set of particle species in the 1-2A GeV energy regime. These results allow for a stringent test of various phenomenological models, in particular the statistical hadronization models (SHM). These models have been quite successful in explaining particle multiplicities in (ultra-)relativistic heavy-ion collisions by assuming a sudden freeze-out in chemical equillibrium [1, 2]. With the help of SHM fits it has been possible to systematically map out a unique chemical freeze-out line in the $T - \mu_b$ plane of the phase diagram of strongly interacting matter, with T denoting temperature and μ_b the baryochemical potential (see e.g. [3]). At high beam energies the chemical freeze-out line is believed to mark the boundary between the hadronic gas phase and the phase of free quarks and gluons, i.e. the QGP. Recently it was conjectured, that in the region of high baryo-chemical potential, this universal freeze-out curve might mark the boundary between a hadron gas and a new phase, called "quarkyonic matter" [4]. In this phase, chiral symmetry should be restored while the quarks would still be confined. At beam energies of a few GeV, however, the validity of the SHM models is not firmly established. Indeed, a mechanism providing fast enough equilibration has not yet been uniquely identified. The situation is further complicated by the need for strangeness suppression which is indeed handled differently in the various implementations of the SHM. As an extension of our work presented in [5] we have fitted thirteen particle yields obtained from the Ar+KCl run with a statistical hadronization model (see Fig. 1). We have chosen the SHM implemented in the freely available THERMUS code [6]. It uses the mixed canonical ensemble, which conserves strangeness explicitly while energy and baryon number are calculated grand-canonically, i.e. are conserved on average only. An additional free parameter, R_c, allows to restrict strangeness conservation to sub-volume only. All particle yields have been corrected for reconstruction efficiencies and have been extrapolated to full phase space. All yields are fitted simultaneously, except for the $\Sigma^{\pm}$ yield which has not been independently measured, but calculated from the multiplicities of all other particles containing strangeness by making use of a strangeness balance relation. The model takes the proper quantum statistics of each particle as well as the finite width of resonances into account. The charge chemical potential μ_Q is furthermore constrained by the ratio of the baryon and charge numbers of the collision system, leading in total to four free fit parameters: T_{chem}, μ_b, R_c and R. The fit results in a chemical freeze-out temperature of $T_{chem} = (73 \pm 3)$ MeV and at a baryo-chemical potential of $\mu_b = (785 \pm 21)$ MeV. The strangeness correlation radius comes out as $R_c = (2.5 \pm 0.5)$ fm, corresponding to about half the fitted radius $R = (4.7 \pm 0.7)$ fm of the whole fireball. A detailed comparison of the data with the statistical model fit is shown in the upper part of Fig. 1, while its lower part depicts the ratio of data and fit. All measured particle yields, except for the η [1] and the Ξ^-, are remarkably well described, considering the fact that semi-central collisions of a medium sized collision system are used as input. Note, however, that the Ξ^- yield shows a strong enhancement over thermal production.

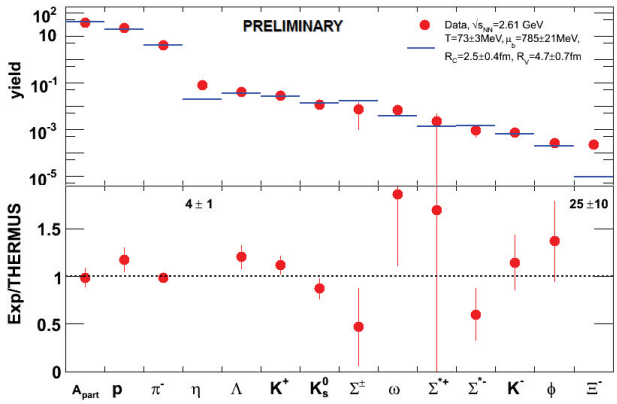

Figure 1: The upper plot shows the yields of hadrons in 1.76 AGeV Ar+KCl reactions (full red circles) and a THERMUS fit (blue bars). The lower plot shows the ratio of the experimental and SHM values. For the Ξ^- and the η the ratio is off-scale and its value is quoted instead.

References

[1] R. Averbeck, R. Holzmann, V. Metag and R. S. Simon, Phys. Rev. C **67**, 024903 (2003).

[2] F. Becattini, M. Gazdzicki, A. Keranen, J. Manninen and R. Stock, Phys. Rev. C **69**, 024905 (2004).

[3] J. Cleymans, H. Oeschler, K. Redlich and S. Wheaton, Phys. Rev. C **73**, 034905 (2006).

[4] A. Andronic *et al.*, Nucl. Phys. A **837** 65 (2010).

[5] G. Agakishiev *et al.* [HADES Collaboration], Eur. Phys. J. **A 47** 21 (2011).

[6] S. Wheaton and J. Cleymans, Comput. Phys. Commun. **180**, 84 (2009).

* Supported by BMBF (06 FY 9100 I), HIC for FAIR, EMMI and GSI.

[1]The yield of the η meson has been interpolated from TAPS measurements done at 1.5 and 2.0A GeV [1]; it was not included in the fit.

Production of Light Fragments in Ar+KCl at 1.756A GeV*

H. Schuldes[1], *M. Lorenz*[1], *C. Müntz*[1], *J. Markert*[1], *and J. Stroth*[1,2] *for the HADES collaboration*
[1]Goethe-Universität, Frankfurt; [2]GSI, Darmstadt, Germany

The heavy ion reaction Ar+KCl is the heaviest mass system measured with the High Acceptance Dielektron Spectrometer (HADES) [1] so far. The hadron analysis was focused on light particles with masses below 1 GeV/c^2. This study highlights the light fragments deuterons, tritons and ^{3}Helium detected with HADES.

Fragments are excellent probes to study radial flow, as the impact of a given particle species on this effect is proportional to its mass. One signature of radial flow is the mass dependent increase of the inverse slope parameter of the tranverse mass spectra.

The fragments have been identified by means of three independent informations detected in different sub-systems of the spectrometer. The first selection has been performed with cuts on the energy loss of the particles in the Multiwire Drift Chambers (MDC) and Time of Flight detectors (TOF and TOFino). To improve on the particle identification, the time of flight information and momentum reconstruction is used by cutting on mass windows of the selected particle species in different phasespace regions.

After background subtraction and corrections for acceptance and efficiency, one obtains the transverse mass spectra for different rapiditiy regions.

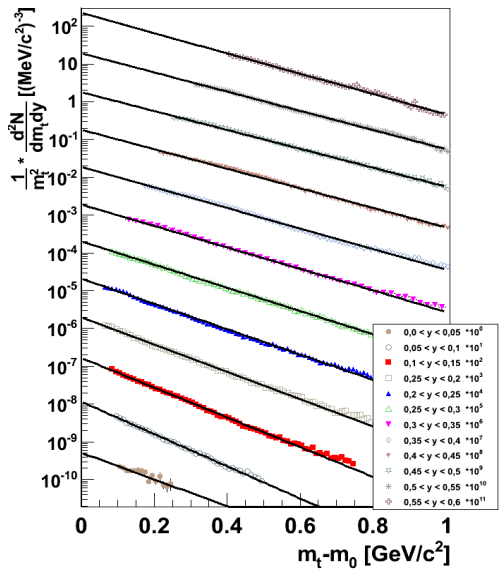

Figure 1: Preliminary for acceptance- and efficiency-corrected (m_t-m_0)-spectra of the deuterons in different rapidity regions ranging from 0.0-0.6 (scaled) in the TOF-region, fitted with Boltzmann-distributions.

* Work supported by BMBF (06 FY 9100 I), HIC for FAIR, EMMI and GSI

Figure 1 shows the resulting preliminary (m_t-m_0)-spectra for deuterons in the TOF-region ($45° \leq \Theta \leq 85°$) for different rapidities ($0.0 \leq y \leq 0.6$). By extracting the inverse slope parameter T_B for each measured rapidity region and after extrapolation to midrapidity (y_{CM}=0.86), one can estimate the effective temperature, which naively corresponds to the emission of particles from a thermalized system at midrapidity.

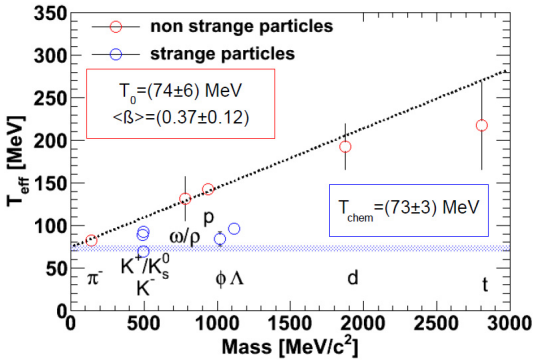

Figure 2: Inverse slope parameters at midrapidity (y_{CM}=0.86) for different particlespecies. The blue line shows the chemical freeze-out temperature estimated by statistical model calculations with the THERMUS code [4]

Figure 2 shows the resulting effective temperatures for deuterons and tritons compared to published data of lighter particles [2][3]. By making use of the simplified assumption:

$$T_{eff} = T_0 + \frac{1}{2} m < \beta_r >^2 \qquad (1)$$

we obtain the kinetical freeze-out temperature T_0=(74 ± 6) MeV and the radial flow velocity $< \beta_r >$=0.37 ± 0.12. The kinetical freeze-out temperature is in agreement with the chemical freeze-out temperature T_{Chem} = (73 ± 3) MeV estimated by statistical model calculations with the THERMUS code [4]. The radial flow velocity is in agreement with extrapolated values from the heavier system Au+Au at similar beam energies measured by the FOPI-collaboration [5].

References

[1] G. Agakishiev et al, Eur.Phys.J. 243-277 (2009)
[2] G. Agakishiev et al, Eur.Phys.J. A47 21 (2011)
[3] G. Agakishiev et al, Phys.Rev. C84 014902 (2011)
[4] S. Wheaton, J. Cleymans, M. Hauer, Comput.Phys.Commun. 180 84-106 (2009).
[5] W. Reisdorf et al, Nucl. Phys. A848 366-427 (2010)

Σ(1385) production in Ar+KCl reactions at 1.756A GeV*

L. Rehnisch[1], *T. Scheib*[1], *M. Lorenz*[1], *J. Markert*[2], *and J. Stroth*[1,2]
[1]Goethe-Universität Frankfurt am Main; [2]GSI, Darmstadt, Germany

A wide ranging study of produced strange particles in the Ar+KCl collision system at 1.756A GeV kinetic beam energy has already been accomplished [1]. To complete the picture of strangeness production and hence to get an in-depth understanding of strangeness production and propagation in the nuclear medium, also the resonances of the already investigated particles have to be measured. All of them are produced several hundred MeV below their NN threshold, which makes them good probes for the described issues.

Note that data on the first excited strange resonance states are rare at SIS energies. The only published data are reconstructed K^* mesons and Σ(1385) hyperons both in Al+Al collisions at 1.9A GeV published by the FOPI collaboration [2, 3].

The charged baryon resonance Σ(1385) has been reconstructed via its main decay channel $\Sigma(1385)^{\pm} \longrightarrow \Lambda + \pi^{\pm}$, where the Λ hyperon, which is also a short-lived particle, was reconstructed via its decay channel $\Lambda \longrightarrow p + \pi^-$. Since the latter is a weak decay, off-vertex cuts are used to significantly reduce the background. After a clear and for significance optimized Λ signal was extracted, a 2σ region around the peak was selected to be combined with pions of the respective charge. Since Σ(1385) decays under strong interaction, its lifetime is too short ($\sim$5fm/c) to distinguish between primary pions and Σ(1385) decay products, which leads to a high amount of combinatorial background.

Due to the small expected S/B ratios (0.01 in this case) a good knowledge of uncertainty causing effects in the background description are of eminent importance. Therefore special attention was payed to the calculation of the mixed event background. Stringent conditions have been set on combining only events with similar event vertices and multiplicity. Furthermore the effect of the normalization region on the signal has been carefully investigated. It turned out that both widths and signal of the $\Sigma(1385)^-$ show only minor dependence on the latter one. Finally a normalization on the left side of the signal is chosen in order to avoid distortions from higher lying resonances which might contribute in the higher invariant mass regions.

Subtraction of the normalized mixed event background leads to the signal shown in figure 1 for the $\Sigma(1385)^-$. Despite of this careful background estimation a structure on the left side of the peak remains, which might be due to correlated background or still problems in calculating the mixed event background with the needed precision which is on the per mill level. For the $\Sigma(1385)^+$ this effect is more pronounced hence further studies on systematics effects using simulated correlated and uncorrelated pions and

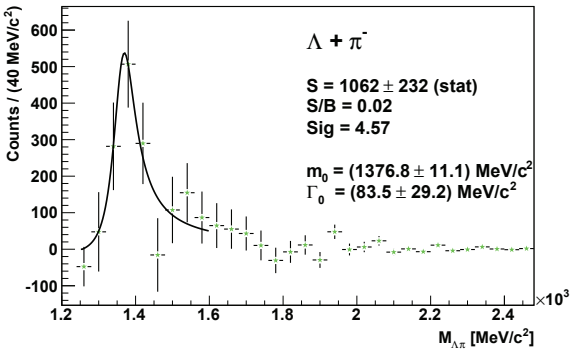

Figure 1: Spectrum after mixed-event background subtraction. The solid line represents a relativistic Breit-Wigner distribution adjusted to the data.

Λ hyperons are ongoing.

Neglecting the remaining structure the signal can be fitted using a relativistic p-wave Breit-Wigner functions with mass dependent width. Within the errors, the position $m_0 = 1376.8 \pm 11.1\ MeV/c^2$ is well in agreement with the value of $m_0 = 1387.2 \pm 0.5\ MeV/c^2$ provided by the PDG, whereas the width of $\Gamma = 83.5 \pm 29.2\ MeV/c^2$ is above the nominal value of $\Gamma = 39.4 \pm 2.1\ MeV/c^2$. This shift can not be explained by the expected broadening due to the detector resolution. Hence it is probably due to the not understood structure discussed before, which hopefully will be understood by the discussed ongoing investigations.

References

[1] G. Agakishiev et al. (HADES Collaboration), "Hyperon Production in ArKCl collisions at 1.76A GeV", Eur. Phys. J. A **47** (2011) 21.

[2] The FOPI Collaboration, "Sub-threshold production of Σ(1385) baryons in Al+Al collisions at 1.9 AGeV", Phys. Rev. C **76** (2007) 052203.

[3] X. Lopez *et al.* (FOPI Collaboration), Phys. Rev. C **81**, 061902 (2010).

* Supported by BMBF (06 FY 9100 I), HIC for FAIR, EMMI and GSI

Hypertriton reconstruction in Ar+KCl reactions at 1.756A GeV*

T. Scheib[1], *L. Rehnisch*[1], *H. Schuldes*[1], *M. Lorenz*[1], *R. Holzmann*[2], *J. Markert*[2], *and J. Stroth*[1,2]
[1]Goethe-Universität Frankfurt am Main; [2]GSI, Darmstadt, Germany

In September 2005 the collision system Ar+KCl at a kinetic beam energy of 1.756 GeV per nucleon was measured with HADES. Among other observables in particular several hadrons carrying strangeness have been reconstructed. Due to the conservation of the strangeness quantum number its production is a highly correlated process. The relative distribution of strange and anti-strange quarks among the hadrons in the final state, including excited states and resonances, can provide important insight into the production and propagation of quarks and thus information about the EOS of dense matter [1].

A strange particle not investigated so far by HADES is the hypertriton ${}^3_\Lambda H$, the lightest of the so called hypernuclei. In addition to the classical nucleons - the proton and the neutron - these nuclei contain at least one hyperon, which is in the explicit case of the hypertriton a $\Lambda-$hyperon.

Hypertritons are reconstructed through their bound decay into a negative pion and a ${}^3He$. The branching ratio for this decay is about 35% [2]. Hence, an important issue of the analysis is a good identification of the two final state particles π^- and ${}^3He$ via the Time-of-Flight information in the TOF and TOFino walls and the energy loss in the Multiwire Drift Chambers (MDC) and the TOF and TOFino walls. In particular the identification of the ${}^3He$ is a demanding task, since most of the produced helium nuclei are flying in the inner part of the detector and are therefore detected by the TOFino wall, which has low granularity. Hence, the probability for multi-hits in this subdetector corresponds to 65% in the Ar+KCl collision system [3]. As the Time-of-Flight signal of a particle is distorted by a second hit during the read-out time, this information is lost for both hits. Therefore both corresponding tracks are discarded in the analysis. The mass spectrum of the TOF region, which has a higher granularity than the TOFino detector, and the ${}^3He$ signal are shown in Figure 1 with and without applying cuts on the energy loss in MDC and TOF [4].

In order to reduce the background coming from uncorrelated pairs of negative pions and helium nuclei, secondary-vertex cuts are applied. The decay topology is comparable to $\Lambda \rightarrow \pi^- + p$ decay [5], but since the mass of ${}^3_\Lambda H$ is by a factor of about 2.5 higher than the one of Λ, its velocity and therewith the mean flight distance are significantly smaller. After subtracting the mixed-event spectrum of uncorrelated $\pi^- + {}^3He$ pairs from the invariant mass spectrum of the same event, no signal emerges above the background. For the optimization of the applied cuts the hypertriton is simulated in order to observe their effects on the significance of the signal. After simulating a thermally produced hypertriton with Pluto [6], the simulation package GEANT [7] delivers the detector response of HADES on the analyzed decay, which therefore had to be implemented in advance. The ideal signal is embedded in real data to get a realistic simulation of the uncorrelated background.
Subsequent steps of analysis are in progress.

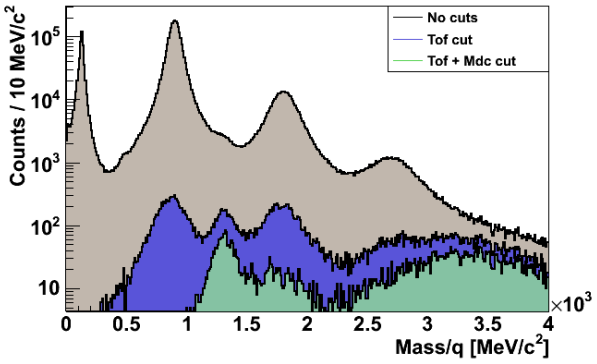

Figure 1: The mass spectrum in the TOF region with no additional conditions included (grey) and the ${}^3He$ signal after applying cuts on dE/dx information in the MDC and TOF walls (green).

References

[1] G. Agakishiev et al., "Hyperon Production in ArKCl collisions at 1.76A GeV", Eur. Phys. J. A **47** (2011) 21.

[2] H. Kamada, J. Golak, K. Miyagawa, H. Witala, W. Gloeckle, "Pi-mesonic decay of the hypertriton", arXiv:nucl-th/9709035v1

[3] A. Schmah. "Produktion von Seltsamkeit in Ar+KCl Reaktionen bei 1.756 AGeV", Dissertation, Fachbereich Physik, Technische Universität Darmstadt, Darmstadt, 2008.

[4] H. Schuldes, "Leichte Fragmente in Ar+KCl-Reaktionen bei 1.756A GeV", Masterarbeit, Institut für Kernphysik, Goethe-Universität Frankfurt, to be published 2012.

[5] L. Rehnisch, "Seltsame Resonanzen in Ar+KCl-Reaktionen bei 1.756A GeV", Masterarbeit, Institut für Kernphysik, Goethe-Universität Frankfurt, 2011.

[6] PLUTO, Pluto++, A Monte Carlo Simulation Tool for Hadronic Physics, 2004. http://wwwhades.gsi.de/computing/pluto/html/PlutoIndex.html.

[7] GEANT. Detector Description and Simulation Tool, 2004. http://cont.cern.ch/writeup/geant/, Online User Guide.

* Supported by BMBF (06 FY 9100 I), HIC for FAIR, EMMI and GSI

Inclusive dielectron production in the 2.2 GeV $p + p$ reaction*

R. Holzmann[1] *and M. Gumberidze*[2] *for the HADES collaboration*

[1]GSI, Darmstadt, Germany; [2]IPN, CNRS/IN2P3 – Université Paris Sud, Orsay, France

Inclusive e^+e^- production in $p + p$ reactions had formerly been studied in the range of 1 – 5 GeV by the DLS experiment at the Bevalac [1], and more recently by HADES at 1.25 GeV [2] and 3.5 GeV [3]. In particular, the comparison of the latter data sets with various models demonstrated a need for improved theoretical descriptions. We now supplement the available experimental results with data on e^+e^- production in the $p + p$ reaction at 2.2 GeV.

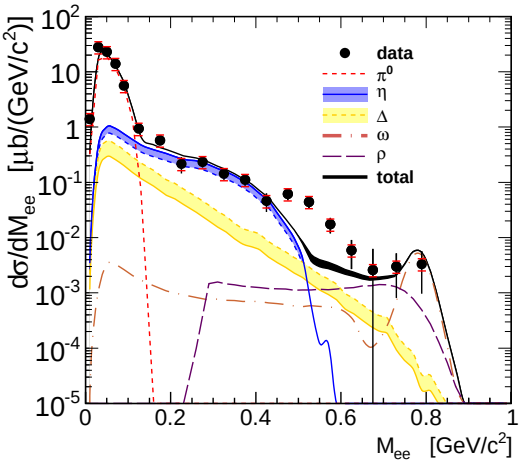

Figure 1: Pair cross section $d\sigma/dM_{ee}$ measured in 2.2 GeV $p + p$ reactions compared with a simulated e^+e^- cocktail.

The efficiency-corrected invariant-mass distribution obtained within the HADES acceptance and normalized to the known elastic scattering cross section is shown in Fig. 1. While the π^0 Dalitz peak dominates at low masses, the intermediate-mass yield is mainly from η and Δ Dalitz decays, and vector meson decays contribute mostly at high mass. To quantify the various contributions the spectrum is compared to an e^+e^- cocktail simulated with the Pluto event generator. At 2.2 GeV π^0 and η production proceeds via resonance excitation involving mostly 1-meson and 2-meson channels [5, 6, 7]. Whereas for ρ^0 and ω production we have assumed phase-space population. The following cross sections were used in Pluto: (1) 14 mb for inclusive π^0 production, (2) 0.26–0.35 mb for inclusive η production, (3) 0.01 mb each of ω and ρ^0 production [8], and (4) 10–21 mb of inclusive $\Delta^{0,+}(1232)$ excitation. The extremes of the cross section range used for Δ production correspond to the following two scenarios: (I) assumes that *all* pion production is mediated by single Δ excitation, resulting in 21 mb; scenario (II) sums explicitly the Δ contributions from one-pion and two-pion production channels [7].

The resulting e^+e^- cocktails, filtered with the HADES acceptance, are overlaid in Figs. 1 with the data. Up to masses of $\simeq 0.45$ GeV/c^2 the agreement is good, but above, the measured yield is not well reproduced. Inclusive η production, however, is constrained by our data within the range of assumed Δ contributions. Based on this, we propose for inclusive η production in 2.2 GeV $p + p$ reactions a cross section of 0.31 ± 0.09 mb.

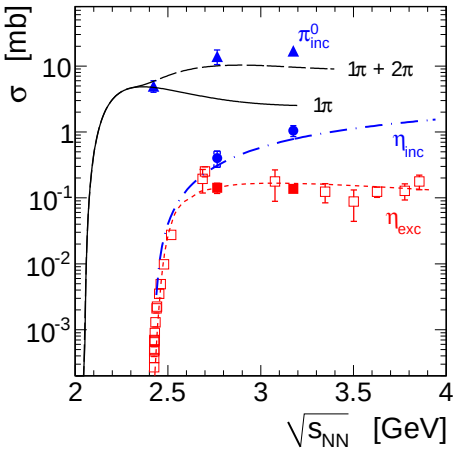

Figure 2: π^0 and η production cross sections in $p + p$ as function of c.m. energy. The HADES results are shown as full symbols. See text for meaning of curves.

Our inclusive π^0 and η cross sections are shown with other HADES measurements [2, 3] in Fig. 2 as function of $\sqrt{s_{NN}}$, together with exclusive data [4, 6] (open symbols) and various model curves. Fits to 1π and $1\pi + 2\pi$ cross sections [5] are shown as solid and long-dashed lines, respectively. The short-dashed line corresponds to the Teis *et al.* resonance model [9] and the dot-dashed line is a parametrization of inclusive η production from [10]. Our data constitute valuable input for the modeling of proton-nucleus and heavy-ion collisions in the few-GeV regime.

References

[1] Wilson *et al.*, Phys. Rev. C **57**, 1865 (1998).

[2] G. Agakishiev *et al.*, Phys. Lett. B **690**, 118 (2010).

[3] G. Agakishiev *et al.*, arXiv:1112.3607v1 [nucl-ex].

[4] G. Agakishiev *et al.*, submitted to Eur. Phys. J. A.

[5] J. Bystricky *et al.*, J. Physique **48**, 1901 (1987).

[6] P. Moskal *et al.*, Prog. Part. Nucl. Phys. **49**, 1 (2002).

[7] X. Cao *et al.*, Phys. Rev. C **81**, 065201 (2010).

[8] M. Abdel-Bary *et al.*, Phys. Lett. B **647**, 351 (2007).

[9] S. Teis *et al.*, Z. Phys. A **356**, 421 (1997).

[10] A. Sibirtsev *et al.*, Z. Phys. A **358**, 357 (1997).

*Work supported by EMMI and the IN2P3/CEA/GSI agreement

Baryon resonance production in proton-proton interactions at 3.5 GeV

A. Dybczak[1] *and P. Salabura*[1]
[1]SIP JUC, Cracow, Poland

In year 2007 $p+p$ reactions at 3.5 GeV were studied by HADES with the main goal to measure inclusive e^+e^- production. The measured e^+e^- invariant mass distribution was compared to the expected e^+e^- sources given by; the Dalitz decays of π^0, η, ω mesons and $\Delta(1232)$ and 2-body decays of the ρ/ω mesons [1]. The data can be fairly well described by the simulation assuming aforementioned components, but not in the mass region below vector meson pole ($M_{inv}^{e^+e^-} \in (0.5-0.7)[GeV/c^2]$). A possible reason can be omission of contributions of the Dalitz decays of heavier baryonic resonances (Δ and N^*) and/or mass dependency of the respective electromagnetic transition form-factors. In order to study contribution of higher lying baryonic resonances to e^+e^- production several exclusive channels ppe^+e^-, $pp\pi^0$, $pn\pi^+$, $pp\omega(\eta) \rightarrow \pi^+\pi^-\pi^0$ were analysed [3, 4]. The main idea is to constraint the resonance cross sections from their hadronic decays (i.e to the final states including one pion and the eta) and then compute the resulting e^+, e^- yield from model predictions [5, 6]. In this report we present results on the $pn\pi^+$ and $pp\pi^0$ final states. Distributions of the invariant mass and the centrum of mass polar angle of pion-nucleon system are presented and compared to Monte-Carlo calculations based on the resonance model [2] assuming incoherent sum of various resonances.

To select the final states with one pion production events with two positive tracks were analysed. Protons and positive pions were distinguished using conditions on the reconstructed track momentum and velocity, determined from the track time-of-flight and path length. The channels were selected via conditions on the missing mass of pion-nucleon and proton-proton systems. A clear peaks related to the mass of missing n and π^0 were visible. The signal yield was obtained as a number of counts in the peak above fitted continuous background. In the case of $pp\pi^0$ additional conditions on proton-proton angles (polar and azimuthal) were imposed to eliminate elastic scattering. Cross sections of various resonances, were estimated by simultaneous fits of the invariant masses ($M_{inv}^{p\pi^+}$, $M_{inv}^{n\pi^+}$, $M_{inv}^{p\pi^0}$ - see Fig.1 (up)) and angular distributions ($cos\theta_{CM}^{p\pi^+}$, $cos\theta_{CM}^{n\pi^+}$, $cos\theta_{CM}^{p\pi^0}$ - see Fig.1 (down)), in several bins of the $N-\pi$ invariant mass, inside HADES acceptance. Only 3^* or 4^* resonances, indicated in the figures legend, with the mass and width from the PDG were considered. Iterative procedure was applied: in the first step a flat angular distribution was assumed for the resonances production. Since experimental distributions show a clear forward-backward peaking, in the next step a modified distribution of the form $d\sigma/dt \sim A/t^\alpha$ was adjusted. The t, A, α are t-

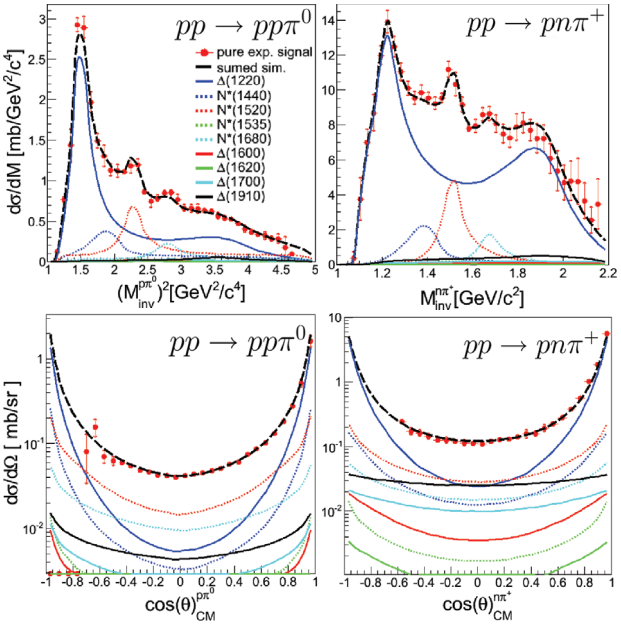

Figure 1: Invariant mass of the nucleon-pion (up) and angular distribution of the nucleon-pion system in the center of mass frame (down) spectra for both $pp\pi^0$ and $pn\pi^+$ final state compared to fit result assuming incoherent sum of various resonances (see legend).

Mandelstam variable and fit parameters depending on the resonance mass, respectively. Furthermore, the isospin relations between cross sections of various resonance were preserved in the fitting procedure.

The applied resonance model of baryon resonance production can fully describe production of pions in the two $pp\pi^0$ and $pn\pi^+$ channels. The derived cross section for $\Delta(1232)$ production as well as for the total π^0 and π^+ yields are in a good agreement with previous measurements [2, 7]. Obtained cross sections for the various resonances will be used to calculate dielectron yield and will be compared to the yields measured in the ppe^+e^- channel.

References

[1] A. Rustamov et al. , arXiv:1112.3607v1 [nucl-ex].
[2] S. Teis et al. , *Z. Phys. A*, **356**, 421-435, (1997).
[3] K. Theilab, PhD thesis (2011).
[4] A. Dybczak, PhD thesis.
[5] M. Zetenyi and G. Wolf, *Heavy Ion Phys.*, **17**, 27-39, (2003).
[6] M. I. Krivoruchenko and B. V. Martemyanov., *Annals Phys.*, **296**, 299-346, (2002).
[7] S. A. Bass, *Prog.Part.Nucl.Phys.*, **41**, 225-370, (1998).

Resonant production of η and ω mesons in proton-proton interactions at 3.5 GeV*

K. Teilab[1,3], *I. Fröhlich*[1], *H. Ströbele*[1], *and J. Stroth*[1,2]
[1]Goethe-University, Frankfurt, Germany; [2]GSI, Darmstadt, Germany; [3]EMMI, Darmstadt, Germany

Measurements of meson production in nucleon-nucleon interactions at low and intermediate energies reveal important information about the nature of the interaction and the mediating and contributing states. The HADES collaboration has measured the exclusive production of η and ω in proton-proton interaction at E_{kin} = 3.5 GeV. The determined distributions indicate a strong contribution of the $N(1535)$ resonance to η meson production while the resonant production of ω mesons is marginal.

Analysis

Events of the exclusive reaction $pp \longrightarrow pp\pi^+\pi^-\pi^0$ (I) were selected for further analysis. The momenta of the charged particles (p, π^+, π^-) are determined by measuring their deflection in the magnetic field using the HADES drift chambers [1]. Using the kinematic constraint on the mass of the missing particle, events in which a neutral pion was produced were selected and the identity of the positive particles was determined. In a second step, a kinematic fit was applied to the measured momenta to improve the resolution. Figure 1 shows the pp missing mass spectrum in events of reaction I after applying the kinematic fit. The two peaks at 548 and 783 MeV/c^2 correspond to the η and ω mesons respectively. The dotted dashed curves show the shapes of the signals as obtained by simulations while the continuous line shows a fit to the data points with the simulated peak shapes on top of a continuous background.

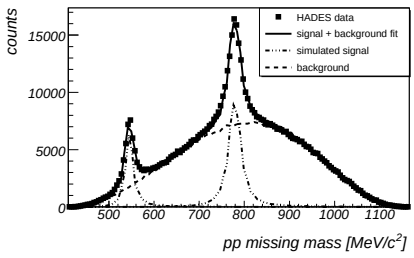

Figure 1: The proton-proton missing mass spectrum in reaction I.

Results

Figure 2 shows the distribution of the invariant mass squared of the η meson and one of the protons in the reaction $pp \longrightarrow pp\eta$ (II). The distribution is well reproduced by

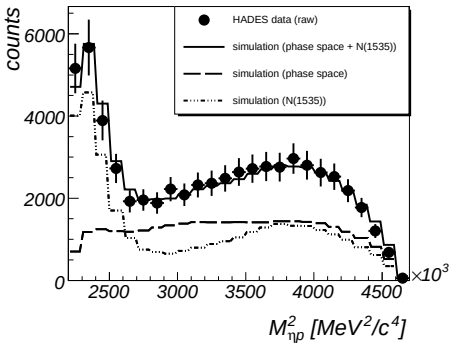

Figure 2: The proton-η invariant mass squared spectrum in reaction II.

simulations assuming about 47% of the produced η mesons to originate from the decay of the $N(1535)$ resonance (dotted dashed curve). The rest of the η mesons follow the distribution according to mere phase space (dashed curve).

On the other hand, figure 3 shows the distribution of the invariant mass squared of the ω meson and one of the protons in the reaction $pp \longrightarrow pp\omega$ (III). The distribution shows no significant peak along the measurable range. However, it shows a considerable deviation from the expected distribution as obtained from phase space simulations (dashed curve).

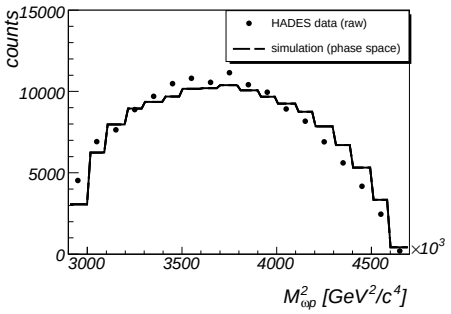

Figure 3: The proton-ω invariant mass squared spectrum in reaction III.

References

[1] G. Agakishiev *et al.* [HADES Collaboration], Eur. Phys. J. A **41** (2009) 243 [arXiv:0902.3478 [nucl-ex]].

* Supported by: BMBF (06FY9100I), HIC for FAIR, EMMI and GSI.

Production of Strange Baryonic Resonances in p+p collisions at 3.5 GeV

J. Siebenson[1] *and L. Fabbietti*[1] *for the HADES collaboration*

[1]Excellence Cluster "Universe", TU München, Boltzmannstr. 2, 85748 Garching, Germany

We have analyzed data on p+p reactions at a beam kinetic energy of 3.5 GeV measured with the HADES experiment. We have concentrated on the production of strange baryonic resonances close to the $\bar{K}$N threshold and achieved to reconstruct the hyperons $\Sigma(1385)^+$ and $\Lambda(1405)$ with considerable statistics. Although the $\Sigma(1385)^+$ is a well known 3-quark baryon with a nominal width of 35.8 MeV/c^2 and a nominal mass of 1382.8 MeV/c^2 [1], the data base on p+p reactions is rather scarce. The statistics we obtained with our measurement is sufficient to perform differential studies [2]. In this way angular distributions can be extracted, which can give important information on the different production mechanisms.

The $\Lambda(1405)$ is of special interest as this hyperon was already predicted by Dalitz to be a possible bound state of a kaon and a nucleon [3]. Nowadays this particle is described in a coupled channel approach based on chiral dynamics. In this ansatz the $\Lambda(1405)$ is generated dynamically as an interference of two states, a $\bar{K}$N quasi-bound state and a $\Sigma\pi$ resonance [4]. Therefore, the properties of the $\Lambda(1405)$, especially its line shape, can set important constraints on the kaon-nucleon dynamics below threshold.

The $\Sigma(1385)^+$ was reconstructed in the associated production together with a neutron and a K^+ followed by the decay into $\Lambda\pi^+$. For an exclusive analysis the Λ, the π^+ and the K^+ were measured directly with the HADES apparatus. The neutron was reconstructed via the missing mass technique.

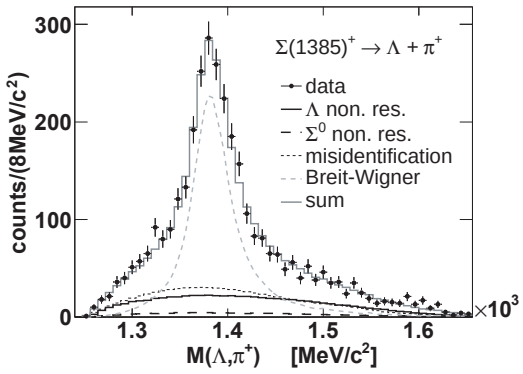

Figure 1: Invariant mass of Λ and π^+. The histograms show the different contributions to the experimental data.

Fig. 1 shows the final invariant mass spectrum of the Λ and the π^+ (M(Λ,π^+)) where a clear $\Sigma(1385)^+$ signal is overlaid by contributions of non-resonant $\Lambda\pi^+$ and $\Sigma^0\pi^+$ production, as well as background due to misidentified particles. The signal is well described by a relativistic Breit-Wigner function and yields a width of 39.2 MeV/c^2 and a mass of 1383 MeV/c^2. Differential studies have also been performed and show a highly anisotropic production of the $\Sigma(1385)^+$, indicating the peripheral character of the production mechanism.

In p+p reactions, the $\Lambda(1405)$ hyperon is mainly produced together with a K^+ and a proton and finally decays into $\Sigma\pi$ pairs. We have analyzed the two charged decay channels ($\Sigma^+\pi^-$ and $\Sigma^-\pi^+$). After identifying the final state particles, clear Σ^+ and Σ^- signals could be reconstructed. Extracting these signals, the missing mass of the proton and the K^+ (MM(p,K^+)) can be investigated where the $\Lambda(1405)$ should be visible. Fig. 2 shows the sum of both charged decay channels for this observable within the HADES acceptance. A good agreement between experimental data and simulations has been obtained. The simulations include the production of $\Lambda(1405)$, $\Sigma(1385)^0$, $\Lambda(1520)$ and non-resonant $\Sigma\pi$ production. The relative contribution of $\Lambda(1405)$ and $\Sigma(1385)^0$ is an external constraint obtained by the analysis in [5]. The $\Lambda(1405)$ has been simulated with a mass of 1385 MeV/c^2 and also in the experimental data the observed peak is located well below the nominal mass value of 1405 MeV/c^2. This result might set important constraints on the related kaon-nucleon dynamics.

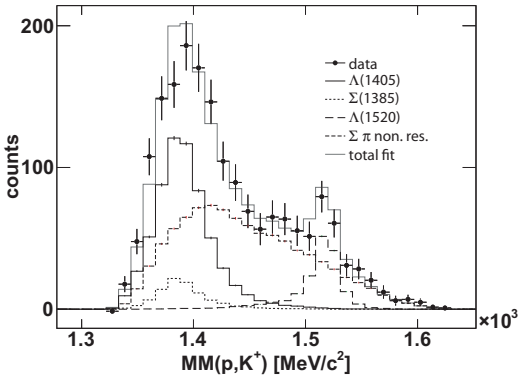

Figure 2: Missing mass of proton and K^+. Experimental data are compared to simulations.

References

[1] K. Nakamura et al., J. Phys. G **37**, 075021 (2010).

[2] G. Agakishiev, et al. (2011). arXiv:1109.6806 [nucl-ex].

[3] R. H. Dalitz et al., Phys. Rev. Lett. **2**, 425-428 (1959).

[4] T. Hyodo et al., Phys.Rev. C **77**, 035204 (2008).

[5] E. Epple et al., Int. J. Mod. Phys. A **26**, 616-618 (2011).

Neutral Kaon Production in p+p and p+^{93}Nb*

J. Berger-Chen[1], L. Fabbietti[1], and K. Lapidus[1] for the HADES collaboration
[1]Excellence Cluster 'Universe', TU Munich, Garching, Germany

The modification of kaon properties in dense and cold nuclear matter has been a subject of interest in related theoretical and experimental studies. In particular it is crucial to extract the kaon-nucleon/nucleus potential. Several experiments have studied this aspect at normal nuclear density in p+A [1] and π^-+A [2] reactions and in heavy ion collisions [3] all obtaining repulsive potentials. However, the determined strengths are not consistent with each other (U_0 = 20-40 MeV). Therefore we propose to analyse the K^0 production in p+p and p+^{93}Nb at a kinetic beam energy of 3.5 GeV with HADES. The good event statistics of low p_t-kaons ($p_t < 100$ MeV/c) ensure the sensitivity of our measurement to the nuclear matter effects. Finally a comparison of the K^0 differential yields may provide access to the in-medium kaon-nucleus potential at normal nuclear density.

K^0_S analysis

Similar analyses were carried out for both data sets. The K^0_S was reconstructed by its charged decay particles π^+ and π^- (BR = 69.20%), which were identified via graphical cuts on the energy loss versus momentum distribution. To increase the signal-to-background ratio, following secondary vertex cuts were applied: (1) distance between the two pion tracks ($d_{\pi^+-\pi^-} < 7$ mm), (2) distance between the primary reaction vertex and the secondary decay vertex ($d(K^0_S - V) > 25$ mm), (3) distance of closest approach to the primary vertex for the two pion tracks (DCA$_{\pi^+} > 7$ mm, DCA$_{\pi^-} > 7$ mm). These cuts were optimized to maximize the ratio S^2/B. A clear peak at the expected K^0_S mass is seen in the resulting $\pi^+\pi^-$ invariant mass spectra for both reactions over combinatorial background with $(\frac{S}{B})_{pp} = 0.41$ and $(\frac{S}{B})_{pNb} = 2.87$. Both spectra are described by a fit of the signal (two Gaussians) and the combinatorial background (Landau function and polynoms). High statistics allow differential yield analyses in rapidity ($\Delta y = 0.1$) and transverse momentum ($\Delta p_t = 75$ MeV/c). For acceptance and efficiency corrections of the p+p reaction the Pluto [4] event generator based on Monte Carlo was used. 13 K^0 production channels were simulated isotropic, while one ($p + p \rightarrow \Sigma^+ + p + K^0$) was weighted with an angular distribution according to [5]. Each channel was weighted with its corresponding cross section and processed through the full analysis chain. The cross sections from the Landolt-Börnstein database were recalculated with updated experimental cross sections using a phasespace fit from [6]. Three of the channels with the highest contributions are listed in table 1. In case of the p+^{93}Nb reaction UrQMD calculations [7] were used.

Reaction	$\sigma[\mu$b]
$p + p \rightarrow \Sigma^+ + p + K^0$	21.3
$p + p \rightarrow \Lambda + p + \pi^+ + K^0$	18.4
$p + p \rightarrow \Sigma^0 + p + \pi^+ + K^0$	12.4

Table 1: Three K^0 production channels with highest cross sections used as simulation input.

Preliminary results

To evaluate the Monte Carlo simulation for the p+p collisions, simulated p_t-spectra were compared to acceptance and efficiency corrected experimental data. The spectra were normalized using one scaling factor obtained at mid-rapidity. Overall an agreement within 10% deviation was observed. Moreover, the rapidity distributions were compared (fig. 1). To extract the yields the measured points in the p_t-spectra were summed up in the region where measurements are available. A Boltzmann function was fitted to the tail of the p_t-spectra to extrapolate the yield to the not measured region. Finally the goal will be to determine absolute normalized yields and the in-medium KN potential from the ratio $\sigma(pNb)/\sigma(pp)$.

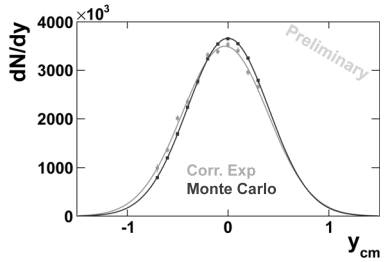

Figure 1: Comparison of the K^0_S rapidity distribution of corrected experimental data (p+p) and simulated data fitted with a Gaussian (μ_{exp} = -0.02 $\pm$ 0.01).

References

[1] M. Büscher et al., Eur. Phys. J. A 22, 301-317 (2004).
[2] M.L. Benabderrahmane et al., PRL 102, 182501 (2009).
[3] G. Agakishiev et al., Phys. Rev. C 82:044907 (2010).
[4] I. Fröhlich et al., arXiv:nucl-ex/0708.2382v2 (2007).
[5] M. Abdel-Bary et al., Eur. Phys. J. A 46, 27-44 (2010).
[6] A. Sibirtsev et al., arXiv:nucl-th/9802019 (1998).
[7] S.A. Bass et al., Prog. Part. Nucl. Phys. 41, 255-369 (1998).

* Work supported by BMBF and Excellence Cluster Universe.

The role of the ρ meson in the HADES dilepton mass spectra*

C. Behnke[1], *T. Galatyuk*[1,2], *J. Stroth*[1,3], *and the Hades Collaboration*

[1]Goethe-Universität, Frankfurt; [2]ExtreMe Matter Institute EMMI, Darmstadt; [3]GSI Helmholtzzentrum für Schwerionenforschung, Darmstadt

Photons and lepton pairs emerging from decays of virtual photons are the most promising probes of dense hadronic matter. In the energy domain of 1 - 2 GeV per nucleon, HADES has measured electron pairs in C+C and Ar+KCl collisions and will measure Ag+Ag and Au+Au collisions in the following years. An experimentally constrained N+N reference spectrum was established. Moreover, for the first time at this energy the inclusive production cross sections for light vector mesons were extracted. This result allows putting tight constraints on vector meson production in heavy-ion collisions at beam energies of a few GeV per nucleon. Theoretically the question of how the spectral function of the ρ meson changes in the medium is still under active discussion. Microscopic transport models are used to link experimental observables to the different phases and manifestations of hadronic matter. The HADES data was compared to predictions from UrQMD [1] microscopic transport model calculations. An approach which will allow to separate in a transparent way the generation of the event background from the emission pattern of a physics observable was introduced. To study the scaling of the e^+e^- pair yield with the system size collisions at the same beam energy, i.e. 1.25 GeV/u has been simulated.

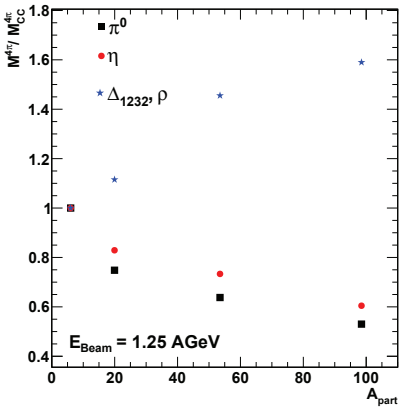

Figure 1: e^+e^- multiplicities extracted from heavy ion collisions at the same beam energy simulated with UrQMD

Figure 1 shows the multiplicities of the π^0 and η are found to be reduced when A_{part} increases. In case of the π^0 this might be explained by the time-integrated cross section for the Δ_{1232} reabsorption process (NΔ $\rightarrow$ NN), which in the Au+Au collisions is larger compared to C+C collisions. Consequently, the total number of π^0 observed in the final state is up to 50% less in Au+Au collisions. The η mesons multiplicities are decreasing by nearly 40%. In contrast, the excess pair yield i.e. e^+e^- pair yield above the η contribution in the mass range of $0.15 \leq M_{ee}GeV/c^2 \leq 0.55$, which is mainly represented by the Δ_{1232} and the ρ meson. It has been investigated that the e^+e^- pair yield comes from the emission density region which is a factor of 3 lager compared to the normal nuclear matter density. Since UrQMD uses only vacuum spectral functions the predictions for e^+e^- radiation from high density stages of the heavy ion collision can be refined.

The inverse-slope parameter of the mt spectra was extracted using a χ^2 minimization method[2]. The extracted

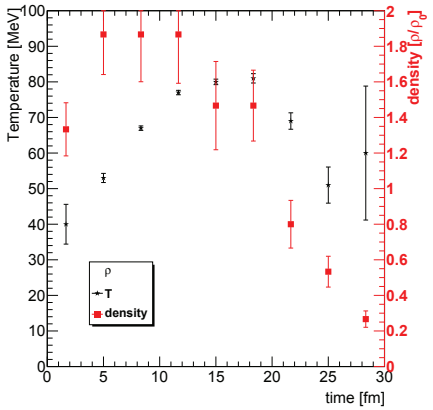

Figure 2: Emission temperature and emission density versus time from $\rho \rightarrow e^+e^-$ from Au+Au 1.25 GeV/u

temperatures are of the same order as measured slope parameters with the T_{eff} variation on the level of 10 to 15 MeV. The extracted temperatures and densities (see Fig. 2) can be used as an input to a thermal model. For each hadron the temperature and the density of the maximum decay probability of the dilepton sources for the given time step of the heavy ion collision is shown. Dileptons from $\rho \rightarrow e^+e^-$ decay originate from phases of high densities of the heavy ion collision. Here the density of 1.9 times normal nuclear matter density where ρ mesons decay to e^+e^- pairs is reached. They show a significant rise from 40 to 80 MeV at an early stage of the collision.

References

[1] Bass, S. A. and others, "Microscopic models for ultrarelativistic heavy ion collisions", Prog. Part. Nucl. Phys. 41 (1998) Pages: 255-369

[2] Behnke C., "Development of an event generator for dilepton production in heavy ion collisions in the SIS energy regime", Unpublished Master Thesis (2011) Pages: 43-48

* Work supported by BMBF (06 FY 9100 I), HIC for FAIR and EMMI

HADES Track Reconstruction in Au+Au collisions at E_{kin} = 1.24 GeV/u

V. Pechenov[1], *O. Pechenova*[2], *T. Galatyuk*[2], *and J. Markert*[2]
for the HADES collaboration
[1]GSI, Darmstadt, Germany; [2]Goethe Universität, Frankfurt

In order to ensure an efficient and accurate operation of the track reconstruction in HADES at a multiplicity up to 200 within the acceptance in Au+Au collisions, a new approach for the tracking has been developed.
The reconstruction of the particle trajectories is accomplished in several steps: First, the spatial correlation of fired drift cells in the multi-wire drift chambers (MDCs) is performed. The wire clusters are defined using only the geometrical positions of the fired drift cells. *Track candidates* are finally obtained through the matching of track segments in the inner and outer drift chambers within one sector. Second, the corresponding space positions of the *track candidates* are fitted by a model function taking into account the drift time information of the cells. For the inner drift chambers the projection is performed with respect to the centre of the target.

For the most central Au+Au collisions the occupancy in the MDCs is on the level of 20%. Due to by chance correlation of fired drift cells many ghost tracks can be created. Obviously, highly efficient rejection algorithms are needed to suppress those ghost candidates.

The reconstruction algorithms have been improved by the following features: (i) To increase the contrast between the real track candidates and the by chance correlated wires, the projection algorithm for the drift cell volumes has been changed to make use of the measured drift time; (ii) only the part of the drift cell volume defined by the radius around the sense wire according to the measured drift time is projected. Furthermore the resolution of the projection plane has been increased. The results in a better definition of correlated wires, but at the same time leads to an higher number of ghost tracks.
To allow for an even more tight correlation window the exact knowledge the of event vertex position is required. A new method has been developed to estimate the event vertex on the level of candidate search without involving any track fit. The method identifies the target segment where the collision took place with an efficiency of close to 100%. The event vertex is therefore known with a precision of 500 μm giving improved initial track parameters (see Fig. 1a).
To cope with the high probability ghost clusters in a high multiplicity environment an advanced procedure for ghost track suppression has been introduced. To avoid unnecessary combinatory with the outer drift chambers the ghost suppression starts in the inner MDCs before any extrapolation to the outer MDCs is performed.
The projection of the fired drift cells for the outer MDCs is carried out in the area of physical possible tracks, given by the curvature of tracks in the momentum range of interest. This procedure avoids needless combinatory and significantly speeds up the reconstruction.
The ghost track suppression algorithms keep the amount of ghost tracks in the highest track density below 10%. Further suppression can be archived by selecting on the track quality parameters.

In August 2011 Au+Au collisions at E_{kin} = 1.24 GeV/u have been investigated in an short run. The data have been reconstructed using the improved tracking software. The performance of the track reconstruction has been found to be comparable to simulation results (see Fig. 1b). This goal could be achieved due to a strong effort improving the calibration and alignment algorithms of the detectors.

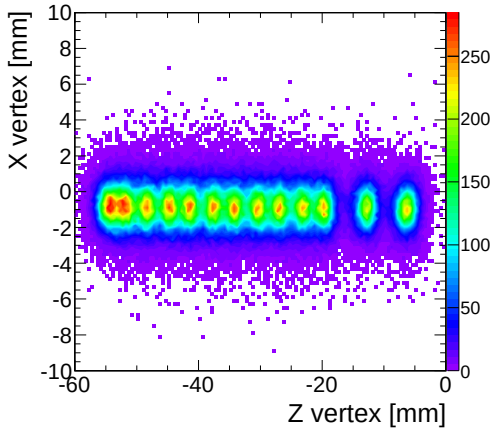

(a)

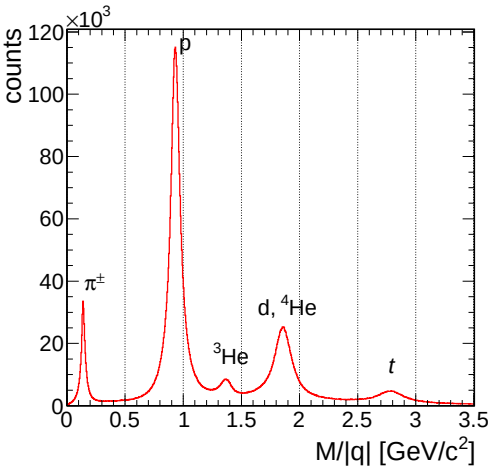

(b)

Figure 1: (a) Reconstructed event vertices, (b) mass of the reconstructed particles in the RPC detector.

Application of a Kalman and Deterministic Annealing Filter in HADES*

E. Krebs[1] *and J. Markert*[1] *for the HADES collaboration*
[1]Goethe-Universität, Frankfurt am Main

The Kalman filter [1] is a mathematical method to estimate the evolution of linear, dynamical systems and has become an established method for track reconstruction. A Kalman filter that takes multiple scattering and energy loss into account has been implemented for the track reconstruction in the HADES experiment. The filter uses position information obtained from track segments reconstructed with the standard algorithm and the results have been compared to a global track fit.

The Kalman filter has been tested with Geant simulations of Au+Au reactions at $1.25\,$AGeV and $1.5\,$AGeV. Figure 1 shows a comparison of the residuals in momentum obtained from the current tracking method with the Kalman filter for reconstructed positron tracks. The momentum resolution has improved from an RMS of around 3.7% down to 2.8% with the Kalman filter. Moreover, the asymmetry in the tails of the residuals that had been present so far for positrons and electrons could be reduced by taking energy loss and multiple scattering into account.

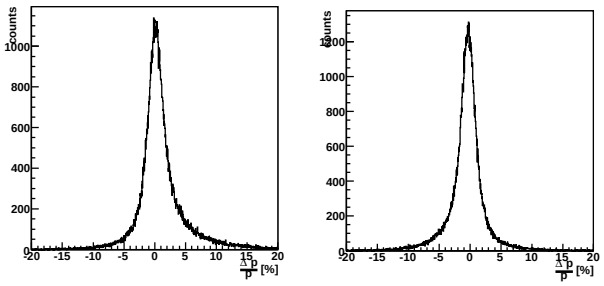

(a) Current Tracking. (b) Kalman Filter.

Figure 1: Residuals in momentum reconstructed with the current tracking method (a) and with the Kalman Filter (b). The Kalman filter has improved the residuals down to an RMS of 2.8% from 3.7% of the current tracking method.

To reduce systematic errors of the segment reconstruction for highly curved tracks the Kalman filter has been revised to work directly with the wire information of the drift chambers. Additionally, track candidates may include measurements from multiple tracks. For such an environment with ambigious and multiple measurements, an extension of the Kalman filter, called the Deterministic Annealing Filter [2], is used to discriminate measurements that do not belong to a track. Measurements are assigned weights and an annealing process is introduced to avoid local optima in the measurement assignments.

Overall, both the Kalman and the Deterministic Annealing Filter show a similar momentum resolution. However, as can be seen in fig. 2, the Deterministic Annealing Filter could enhance track reconstruction at the borders of the drift chambers compared to the Kalman filter.

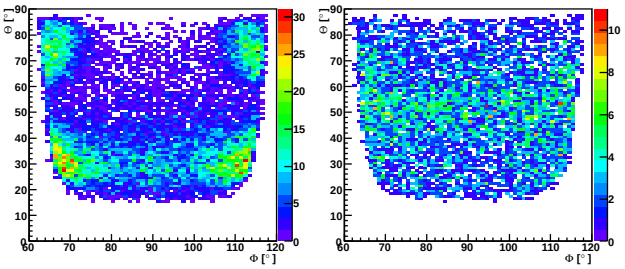

(a) Kalman Filter. (b) Deterministic Annealing Filter.

Figure 2: Distribution of simulated tracks that either could not be reconstructed or showed a high χ^2 value. The Kalman Filter (a) still shows clusters of such problematic tracks at the borders of the drift chambers where the magnetic coils are located. These patterns are gone with the Annealing Filter (b).

A Kalman filter and a Deterministic Annealing Filter have successfully been implemented in the HADES reconstruction software to cope with high multiplicity events. The Kalman filter is able to work with hit coordinates from the segement fitter as well as with the time information from the drift chambers. The algorithms take energy loss and multiple scattering into account. Performance studies with simulated data show good improvements. The average event reconstruction time could be reduced by further code optimizations. The upcoming Au+Au beam time in 2012 would present a good opportunity to test the new algorithms with real data.

References

[1] R. E. Kalman, “A new approach to linear filtering and prediction problems”, ASME Journal of Basic Engineering, 82, pp. 33-45, 1960

[2] R. Frühwirth and A. Strandlie, “Application of adaptive filters to track finding”, Nucl. Instr. and Meth. in Physics Research, A (559), pp.162-166, 2006

*This work is supported by BMBF (06 FY 9100 I), HIC for FAIR, EMMI and GSI F+E.

PID capability of the upgraded HADES spectrometer*

K. Gill[1], *T. Galatyuk*[1,2], *O. Pechenova*[1], *and V. Pechenov*[3]
for the HADES collaboration
[1]Goethe-Universität, Frankfurt; [2]ExtreMe Matter Institute EMMI, Darmstadt; [3]GSI, Darmstadt

The HADES detector is installed at the GSI Helmholtzzentrum für Schwerionenforschung in Darmstadt, Germany. It is a unique apparatus built to search for new states of matter using rare and penetrating probes. Ar+KCl is the heaviest system which has been measured by HADES so far. The combined measurement of di-electrons and strangeness has provided intriguing results and quests for a heavier collision system and higher statistics.

A major improvement of the spectrometer in terms of granularity and particle identification capability was achieved by replacing the TOFino detector by the new shielded timing Resistive Plate Chamber (RPC) time-of-flight detectors [1]. Results with in beam measurements show a RPC efficiency of 99 %, a time resolution of 73 ps together with an average multi-hit time resolution of about 83 ps and an average longitudinal position resolution of 7.7 mm [2]. Among the detector systems which have been replaced are all six chambers of the inner tracking plane. In addition, a completely new detector read-out and data-acquisition (DAQ) system has been implemented which greatly improved our data-taking rates. In scope of the DAQ upgrade all read-out controllers and trigger boards were replaced introducing a modular system integrating trigger distribution, data transfer and a slow control data traffic to the same optical link [3].

The commissioning beam time took place in August 2011. A gold beam of up to 2×10^6 ions per second was incident on the segmented gold target [4]. The new DAQ system run at event rates of more than 13 kHz. Within the 64 hours of beam on the target a total of $0.84 \cdot 10^9$ events with a total size of 17 TB were collected. This is, compared to the data volumes recorded in the previous beam times, an enormous gain of statistics.

The particle identification plays an important role for the overall performance of the experiment. In Fig. 1 and Fig. 2 we present results obtained from the online analysis of Au+Au collisions at 1.24 GeV/u with preliminary detector alignment and calibration. 1/8 of the total statistic has been analyzed up to now. An efficient and accurate event reconstruction is achieved with a new approach for the tracking in high track density environment [5]. Fig. 1 shows the measured velocity as a function of the particle momentum times polarity in the RPC detector. The different particle species are clearly visible in a wide momentum range. In Fig. 2 we present the M/|q| distribution of the reconstructed particles in the RPC detector. After applying a set of cuts the mass peak of K^+ is already visible. The challenge here would be to reconstruct a K^- signal.

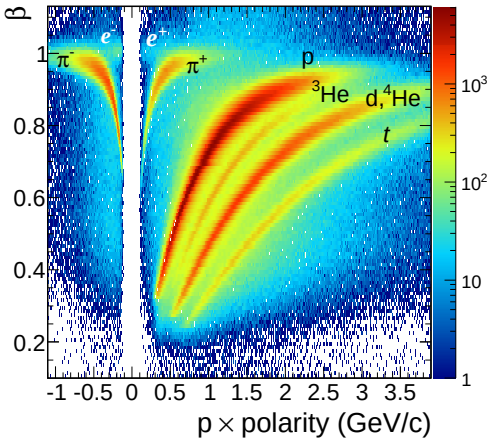

Figure 1: Velocity as a function of the particle momentum times polarity in the RPC detector

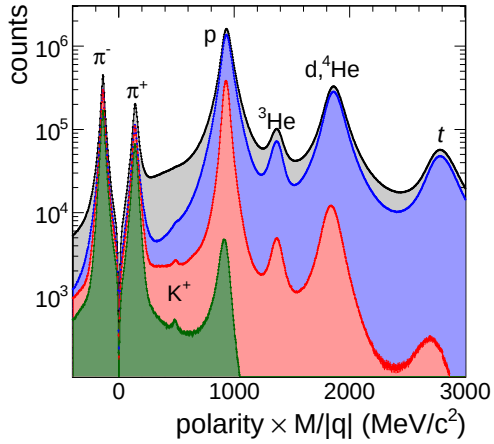

Figure 2: M/|q| of the reconstructed particles in the RPC detector after the track quality (blue curve), momentum (red curve) and energy loss of particles in the multi-wire drift chambers (green curve) cuts applied

References

[1] H. Alvarez-Pol *et al.*, Nucl. Instr. Meth. A **535**, 277 (2004).
[2] A. Blanco *et al.*, Nucl. Instr. Meth. A **602** (2009).
[3] J. Michel *et al.*, Journal of Instr., JINST 6 C12056 (2011).
[4] B. Kindler *et al.*, Nucl. Instr. Meth. A **655** (2011).
[5] V. Pechenov *et al.*, this report.

* Supported by BMBF (06FY9100I), HIC for FAIR, EMMI and GSI.

Development of a High Rate Tracker for secondary Pion Beams*

E. Epple[1], *L. Fabbietti*[1], *R. Lalik*[1], *and R. Münzer*[1] *for the HADES Collaboration*
[1]Excellence Cluster 'Universe', Garching, Germany

Field of application

After the successful upgrade of HADES and a planned extension with an electromagnetic calorimeter the set-up will be ready for data taking of pion induced reactions. A further important detector for the pion beam run is a beam tracking system called CERBEROS (**Ce**n**t**r**a**l **Be**am T**r**acker for Pi**o**n**s**), installed 15m in front of HADES. This detector system will be necessary to determine the momentum of the secondary produced pions. It will consist of two silicon detectors placed at the dispersive plane of the two quadrupole magnets that follow the pion production target. For an exhaustive description see [1] and Fig. 1.

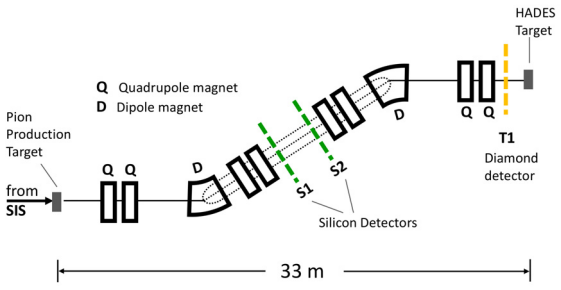

Figure 1: Beam line for the secondary Pion Beam

Silicon Detector

For the pion beam detection two double-sided silicon detectors with a thickness of 300μm and 2x128 channels will be installed inside the beam line. The large momentum spread of the pion beam ($\frac{\Delta p}{p}$ ≈10%) translates into a large position deviation at the dispersive plane where the two silicons are placed. As our aim is to cover the accepted momentum space completely the detectors have a large active area of 10x10 cm. Furthermore the detectors have to cope with large particle intensities up to 10 p/sec. This requires a rather high radiation hardness. The silicon detectors, delivered for this purpose by Micron Semiconductor, have already been tested in our lab (with α-particles) and the energy resolution is below 1%.

Readout

An n-XYTER-exploder [2] based readout, planned as front-end electronic for the silicon detectors, will be integrated into the HADES DAQ system. The readout was tested in a 3 GeV proton beam at the COSY facility in the FZ-Jülich. In this test the n-XYTERs [3] were connected to a smaller silicon detector (34.5x34.5 mm and 500μm thick). The p and n-side of the two detectors were read out each by one n-XYTER mounted on a FE-board. Between the detectors a 18x18 mm sized scintillator (2) was placed for triggering and another one (scintillator 1) was installed in front of the setup. The detector in front of the scintillator was read out by a SysCore-card and the one behind by an eXploder-card, see Fig. 2. A qualitative prove of the working principle is visible in Fig. 3. Here events which were time correlated with the scintillator 2 signal are shown as x-y hit distribution of the silicon detector which was read out by the eXploder setup. The shadow of the smaller scintillator is clearly visible. The analysis of the ADC spectra and the quantitative comparison with the data collected by the SysCore board is still ongoing.

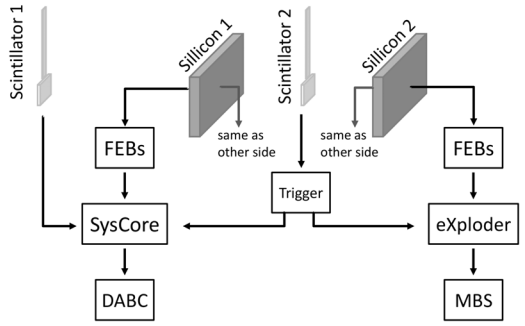

Figure 2: Read out scheme for the silicon detectors

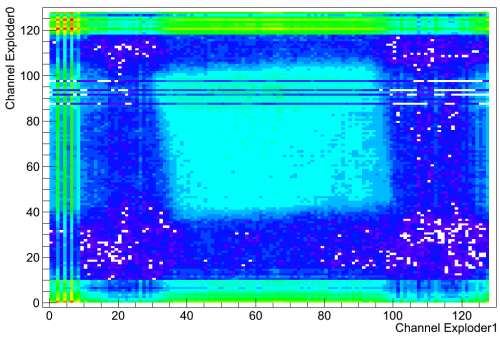

Figure 3: Hit distribution of trigger correlated events

References

[1] Daz, J. et al., Nucl. Instr. and Meth. A 478 (2002).
[2] P. Koczoń, GSI Jahresbericht (2011).
[3] A. Brogna et al. Nuc. Instr. and Meth. A 568 (2006).

* Work supported by F&E Project:TMFABI1012

Simulations of Strange Particles Measurements with Pion-Induced Reactions

K. Lapidus[*1], *O. Arnold*[1], *L. Fabbietti*[1], *and J. Siebenson*[1] *for the HADES collaboration*

[1]Excellence Cluster "Universe", TU München, Boltzmannstr. 2, 85748 Garching, Germany

Motivation

We investigated a possibility to measure production of strange particles in pion-proton reactions ($\pi^- p$) at a beam momentum of 1.75 GeV/c with the **H**igh **A**cceptance **D**ielectron **S**pectrometer (HADES) at the GSI Helmholtzzentrum. A number of strangeness production channels was studied with help of realistic full-scale simulations, taking into account all relevant background channels.

Measurements in pion-induced reactions are necessary for a better understanding of strangeness production in heavy-ion reactions. Moreover, pion-nucleus reactions offer a possibility to study in-medium properties of mesons with open and hidden strangeness, such as K^0, K^+ and ϕ at normal nuclear density.

Besides mesons, we investigate the reconstruction of strange baryons close to the $\bar{K}N$ threshold: $\Sigma(1385)$ and $\Lambda(1405)$. The latter particle is of particular interest, since the ambiguity in the current theoretical understanding of the $\Lambda(1405)$ resonance calls for new experimental efforts. It is predicted that the observed properties of the resonance (i.e. position of the pole and the lineshape) depend on both the production mechanism [1] (γ-, π-, kaon- or proton-induced reactions) and the decay mode ($\Sigma^{\pm}\pi^{\mp}$, $\Sigma^0\pi^0$).

Existing bubble-chamber measurements of the $\Lambda(1405)$ production in pion-induced reactions [2, 3, 4] have principal flaws. First of all, the neutral decay channel $\Lambda(1405) \rightarrow \Sigma^0\pi^0$ was never measured. Besides that, the $\Sigma(1385)^0$ contribution was not subtracted from the observed spectra.

$\Lambda(1405)$ reconstruction

In order to understand the properties and the production mechanisms of strange baryons such as $\Sigma(1385)$, $\Lambda(1405)$ a possibility to detect various decay modes, including decays into neutral particles, is important. Though in the present configuration the HADES setup is not capable of photon detection, an installation of an electromagnetic calorimeter is foreseen [5].

A detailed study of the $\Lambda(1405)$ reconstruction feasibility employing the standard HADES set-up plus the electromagnetic calorimeter was performed in the reaction channel

$$\pi^- + p \rightarrow \Lambda(1405) + K^0.$$

A number of analyses strategies was examined. The study showed that a semi-exclusive reconstruction requiring a single photon or a π^0 in the final state is the most promising with respect to background considerations.

As an example, in the decay chain $\Lambda(1405) \rightarrow \Sigma^+ + \pi^-$, $\Sigma^+ \rightarrow p + \pi^0$, $\pi^0 \rightarrow \gamma\gamma$ the final $p\pi^-\gamma\gamma$ state was reconstructed. After applying necessary selection cuts, an invariant mass spectra (Fig. 1) shows a clear signal of the $\Lambda(1405)$. In this way, about 800 $\Lambda(1405)$'s can be reconstructed in a 25 days beamtime, given a beam intensity of $1.2{\cdot}10^6$ pions/spill. The analysis of this decay mode will be compared with the $\Lambda(1405) \rightarrow \Sigma^- + \pi^+$ analysis, where only charged particle reconstruction is sufficient, in order to study isospin interference effects.

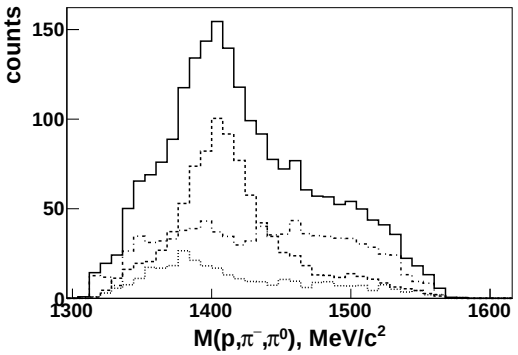

Figure 1: (Simulated) invariant mass spectra of p, π^-, π^0. Contributions are: $\Lambda(1405)$ (dashed curve) reconstructed in its $\Sigma^+\pi^-$ decay channel, $\Sigma(1385)$ (dotted curve) and the non-resonant production of the $\Sigma^+\pi^- K^0$ final state (dash-dotted curve). Sum of all contributions is shown by a solid curve. Counts on the y-axis correspond to the expected yield.

Realistic simulations have shown that the HADES experiment is well suited for the strange particles measurements in pion-induced reactions. Of particular interest is an exclusive reconstruction of the $\Lambda(1405)$ resonance in all of its decay channels.

References

[1] V. K. Magas *et al.*, Phys. Rev. Lett. **95** (2005) 052301.

[2] G. Alexander *et al.*, Phys. Rev. Lett. **8** (1962) 447.

[3] A. Engler *et al.*, Phys. Rev. Lett. **15** (1965) 224.

[4] D. W. Thomas *et al.*, Nucl. Phys. B **56** (1973) 15.

[5] W. Czyzycki *et al.*, arXiv:1109.5550 [nucl-ex].

[*] kirill.lapidus@ph.tum.de

Dense hypernuclear and color-superconducting quark matter and compact stars *

A. Sedrakian, L. Bonanno, and D. Hess

Institut für Theoretische Physik, J. W. Goethe-Universität Frankfurt am Main, Germany

It is now well-established that the emergence of new degrees of freedom of hadronic and quark matter softens the equation of state of dense matter. Such softening can be tested against the measurements of masses of compact stars in binaries. The recent observation of $2M_\odot$ mass neutron star (millisecond pulsar J1614-2230) is evidence that the ultra-dense matter in neutron stars cannot be soft, i.e., agents that will substantially soften the EOS are potentially excluded. One of the outstanding challenges in the theory of compact objects is to exploit fully the consequences of this recent observation and to provide new EOSs that are capable to produce compact objects as massive as the millisecond pulsar J1614-2230.

Our recent study based on relativistic hypernuclear Lagrangians predicts stiff hypernuclear equations of state above saturation density [1]. This equation of state was supplemented with the Nambu-Jona-Lasinio (NJL) based equation of state of quark matter featuring color-superconducting phases. The NJL Lagrangian was extended to include vector interactions, which have the effect of stiffening of the equation of state of quark matter. We have constructed stable configurations of compact stars with masses equal and above the measured 1.97 solar-mass star [1]. The resulting configuration have exotic matter in their interiors in the form of hyperons and quark matter, of which the quark matter is color-superconducting in the two-flavor 2SC and/or three-flavor CFL phases (see Fig. 1). Our models contain two tunable parameters: (1) the density of the transition from the baryonic to the quark matter; (2) the coupling constant G_V in the vector channel. The parameter range, where stable configuration exist was established. Our main conclusion is that the recent observations of massive compact stars do not exclude the possibility of the appearance of hyperonic and color-superconducting quark matter in dense matter in general and in compact stars in particular [1].

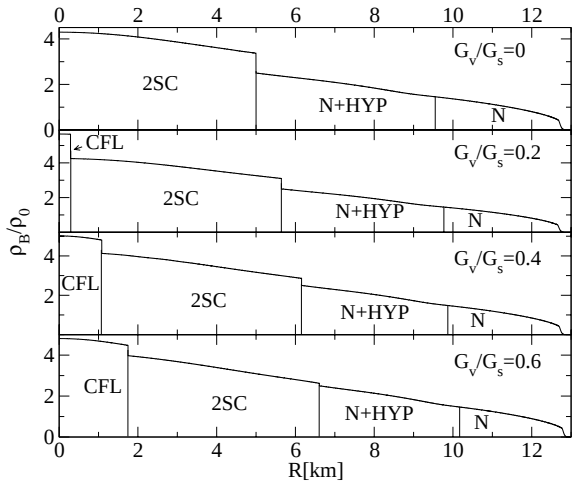

Figure 1: The density profiles of compact stars as a function of their inner radius for several values of the ratio of the vector G_V to scalar G_S coupling in the NJL Lagrangian.

The cooling of neutron stars provides another channel on the properties of dense matter, which is sensitive to the composition of matter and weak interactions therein. In Ref. [2] we examined the thermal evolution of a sequence of compact objects containing low-mass hadronic and high-mass quark-hadronic stars, which have masses above the observed 1.97 $M_\odot$ lower bound. The dependence of the cooling tracks in the temperature versus age plane is studied on the variations of two parameters: (1) the gaplessness parameter (the ratio of the pairing gap for red-green quarks to the electron chemical potential) and (2) the magnitude of blue quark gap. The pairing in the red-green channel is modeled assuming an inhomogeneous superconducting phase to avoid tachionic instabilities and anomalies in the specific heat; the blue colored condensate is modeled as a Bardeen-Cooper-Schrieffer-type color superconductor. We find in Ref. [2] that massive stars containing quark matter cool faster in the neutrino-cooling era if one of the colors (blue) is unpaired and/or the remaining colors (red-green) are paired in a inhomogeneous gapless superconducting state. The cooling curves show significant variations along the sequence, as the mass (or the central density) of the models is varied. This feature provides a handle for fine-tuning the models to fit the data on the surface temperatures of same-age neutron stars and to test theories of dense matter via astrophysical observations. The perspectives and future research plans are summarized in the contribution [3].

References

[1] L. Bonanno and A. Sedrakian, "Composition and stability of hybrid stars with hyperons and quark color-superconductivity," *accepted for publication in* Astronomy and Astrophysics, arXiv:1108.0559 [astro-ph.SR].

[2] D. Hess and A. Sedrakian, "Thermal evolution of massive compact objects with dense quark cores," Phys. Rev. D **84**, 063015 (2011) [arXiv:1104.1706 [astro-ph.HE]].

[3] A. Sedrakian, "Two solar-mass compact stars: structure, composition, and cooling," *accepted for publication in* Acta Phys. Polon. B, arXiv:1111.6929 [astro-ph.SR].

* Work supported by HIC for FAIR, GSI-GU R&D project, and HGS-HIRe.

Chiral thermodynamics of isospin-asymmetric nuclear matter*

S. Fiorilla, N. Kaiser, and W. Weise
Physik-Department, Technische Universität München, D-85747, Garching, Germany

In the framework of in-medium chiral effective field theory we investigate the dependence of the thermodynamic properties of nuclear matter on isospin-asymmetry and temperature T [1]. Calculations of the free energy density are performed to three loop order and systematically incorporate one- and two-pion exchange dynamics to this order. Effects from 2π-exchange with explicit Δ-isobar excitation are included, as well as three-body forces [1, 2].

Fig. 1 shows the evolution of the saturation point, defined as the minimum of the energy curve at $T = 0$, for increasing isospin-asymmetry (dashed line). The energy per particle $\bar{E}$ is plotted as a function of the nucleon density ρ. Starting from its minimum for symmetric nuclear matter, $\bar{E}_0 = -16$ MeV at the nuclear saturation density $\rho_0 = 0.157\,\mathrm{fm}^{-3}$, the binding energy per nucleon is reduced continuously with decreasing proton fraction $x_p = Z/A$ until it vanishes at $x_p = 0.12$. Beyond this point neutron-rich matter is always unbound for any temperature and density.

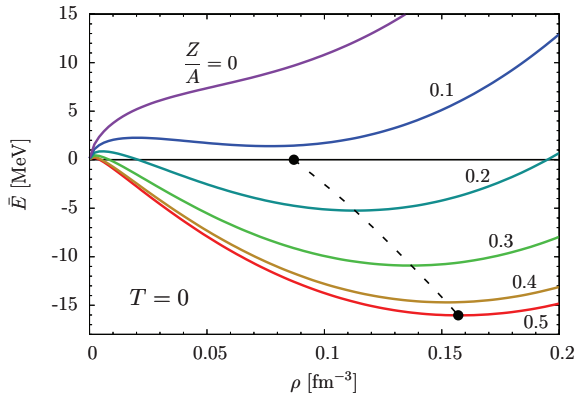

Figure 1: Dependence of energy per particle and saturation point of nuclear matter at T = 0 on isospin-asymmetry.

Fig. 2 shows the temperature vs nucleon chemical potential phase diagram for different values of the proton fraction, demonstrating how the matter evolves with increasing asymmetry. In the coexistence region of the liquid-gas phase transition, μ is constant for a given isotherm. The coexistence region shrinks to a line in the $T - \mu$ diagram. The dashed line shows the evolution of the critical point and its disappearance at $x_p = 0.053$. For $x_p < 0.053$ no liquid-gas phase transition occurs. Neutron-rich matter is realized as an interacting Fermi gas.

Recently we have studied selected four-body contributions to the equation of state of nuclear matter. A particularly simple class of four-loop in-medium diagrams (at T = 0) has been evaluated [1]. In distinction from the method of unitary transformations [3], we consider only diagrams related to "genuine" four-nucleon forces. The upper curve in Fig. 3 shows the four-body contribution as a function of ρ for isospin-symmetric nuclear matter, the lower curve shows the same contribution for neutron matter. One observes that up to $2\rho_0$, the effects from the genuine long-range (pion-induced) four-nucleon correlations stay below 0.1 MeV in magnitude, and thus are negligibly small. Induced four-body correlations involving virtual Δ-excitations are, however, more significant.

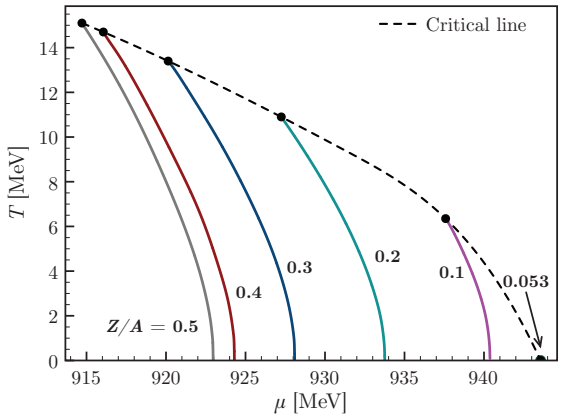

Figure 2: $T-\mu$ phase diagram of nuclear matter and evolution of the critical point for decreasing proton fraction x_p.

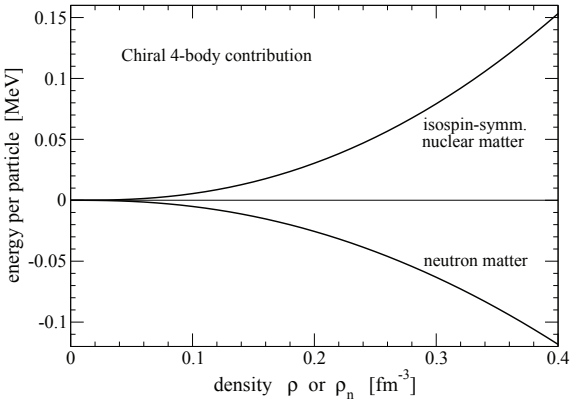

Figure 3: Contribution to the energy per particle at $T = 0$ arising from the long-range chiral four-nucleon interaction.

References

[1] S. Fiorilla, N. Kaiser, W. Weise, Nucl. Phys. **A** (2012) in print, [arXiv:nucl-th/1111.279].

[2] S. Fritsch, N. Kaiser, W. Weise, Nucl. Phys. **A750** (2005) 259.

[3] E. Epelbaum, Eur. Phys. J. A **34**, 197 (2007).

* Supported by GSI F+E.

Fluctuations as probe of QCD phase transition in heavy ion collisions*

B. Friman[1], *F. Karsch*[2], *K. Redlich*[3], *and V. Skokov*[1,2]

[1]GSI, Darmstadt, Germany; [2] BNL, Upton, USA; [3]University of Wroclaw, Poland

Unraveling the structure of QCD phase diagram poses a formidable challenge for theoretical and experimental physics.

On the theory side, first principle lattice QCD (LQCD) calculations provide a systematic approach to investigate nuclear matter at non-zero temperature. Presently, LQCD is, however, limited only to calculations of basic thermodynamic quantities at zero chemical potential. LQCD has demonstrated a very non-trivial fact, that thermodynamics of QCD is well approximated by the Hadron Resonance Gas (HRG) model up to the phase transition temperature T_{pc} at zero chemical potential.

On the experimental side, the QCD phase diagram has been studied in heavy-ion collision. Particle ratios, and particle yields measured in such experiments are in a good agreement with the HRG model fit. The fit parameters define the freeze-out conditions, i.e. the thermal parameters corresponding to the last interaction of the hadrons participating in the collective expansion and cooling of the matter formed in a heavy ion collision. In view of the discussion in the previous paragraph, it is not surprising that the HRG describes the measured multiplicities well.

Data obtained at small values of the baryon chemical potential suggest that the freeze-out curve is close to the expected QCD phase boundary. At larger values of $\mu_B = 3\mu_q$, however, there is a discrepancy between the slope of the freeze-out curve and current LQCD results on the curvature of the chiral phase transition line.

In a series of articles summarized in Refs. [1] and [2] we have shown to which extent a refined analysis of the freeze-out conditions can establish the existence of and proximity to the chiral phase transition. Here we highlight the main results of these papers.

The net-baryon and electric charge fluctuations are sensitive probes of the phase transition. At present, however, lattice calculations provide only limited information on cumulants up to eighth order. In particular, controlled predictions on their properties in the continuum limit are still lacking; their characteristic features are obtained on a qualitative level, but quantitative results are not yet available. Viable alternatives for discussing qualitative features of the net baryon number and electrich charge fluctuations is offered by O(4) scaling theory and by chiral models, like e.g. the Polyakov loop-extended quark-meson (PQM) model.

In Figs. 1 and 2 we show the crossover transition line and the region where the six order cumulant of net-baryon χ_6^B and electric charge χ_6^Q fluctuations computed in the PQM model are negative. At zero chemical potential, calculations suggest that the regime of negative sixth order cumulants starts below but close to the QCD crossover transition temperature. At non-zero baryon chemical potential, the temperature interval of negative χ_6^B and χ_6^Q shrinks and follows the crossover transition line down to the critical end point.

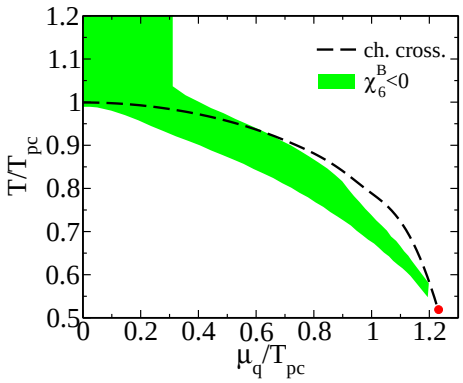

Figure 1: The shaded region shows the parameter range for which the sixth order cumulant of net-baryon number fluctuations is negative. The crossover transition is shown by the dashed line.

Thus if freeze-out occurs close to the chiral crossover temperature the sixth order cumulant of the net baryon number and electric charge fluctuations will be negative at LHC energies as well as at the top RHIC beam energies This is in contrast to hadron resonance gas model calculations which yield a positive sixth order cumulant.

References

[1] B. Friman et. al., Eur. Phys. J. C **71**, 1694 (2011).

[2] V. Skokov, B. Friman and K. Redlich, arXiv:1108.3231.

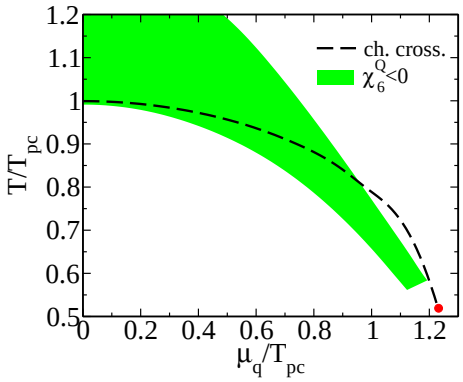

Figure 2: The same as in Fig. 1 but for electric charge fluctuations.

* Work supported by EMMI.

Role of mesonic fluctuations in the Polyakov loop extended quark-meson model at imaginary chemical potentiall*

K. Morita [1,2], *V. Skokov* [2,3], *B. Friman* [2], *and K. Redlich* [4]

[1]YITP, Kyoto, Japan; [2]GSI, Darmstadt, Germany; [3]BNL, NY, USA; [4]ITP, University of Wrocław, Poland

The imaginary chemical potential provides complementary information on the nature of the QCD phase transition. In particular, since there is no sign problem at imaginary μ, the corresponding phase diagram can be computed in lattice QCD. This provides constraints on effective models for real μ which are not directly accessible in lattice QCD. Consequently, studies of thermodynamics at imaginary μ are important for the exploration of the thermodynamics of QCD at finite density.

The Polyakov loop-extended quark-meson (PQM) model is a model that reproduces the essential features of the QCD thermodynamics already in the mean-field approximation at real and at imaginary μ. In this work, we consider the PQM model at imaginary μ and study its critical properties and phase diagram within the functional renormalization group (FRG) approach. We formulate and solve the suitably truncated FRG flow equation for fluctuations of the meson fields in the presence of the Polyakov loop which is treated as a background field on the mean-field level. Comparing with the mean-field results, we explore the influence of fluctuations on the chiral and deconfinement order parameters [1].

In the FRG approach, the thermodynamic potential for the quark and meson subsystems is obtained by solving the flow equation for the scale-dependent grand canonical potential density Ω_k at the leading order of the derivative expansion:

$$\partial_k \Omega_k = \frac{k^4}{12\pi^2}\left\{\frac{3}{E_\pi}[1+2n_B(E_\pi)]\frac{1}{E_\pi}[1+2n_B(E_\sigma)] - \frac{4N_cN_f}{E_q}[1-N(\Phi,\Phi^*)-\bar{N}(\Phi,\Phi^*)]\right\}, \qquad (1)$$

where n_B and $N(\bar{N})$ are the distribution functions for mesons (σ, π) and (anti)quarks, respectively. The full thermodynamic potential is then given by $\Omega(\Phi,\Phi^*;T,\theta) = \Omega_{k\to 0}(\Phi,\Phi^*;T,\theta) + \mathcal{U}(\Phi,\Phi^*;T)$, where $\theta = \mu_I/T$ and $\mathcal{U}$ denotes the Polyakov loop potential. The order parameters are determined by the stationarity conditions. Model parameters and initial conditions for the flow equation are chosen in a way as to reproduce the in-vacuum properties of σ and π mesons.

The upper panels of Fig. 1 show the chiral order parameter normalized by as a function of temperature scaled by the chiral crossover temperature at $\theta = 0$, T_{pc}, which was identified by the maximum of $-d\sigma/dT$. There is a clear change in the shape of σ with increasing θ from 0 to $\pi/3$, both in the mean-field case as well as in the FRG approach. However, the mesonic fluctuations included in the FRG scheme imply a strong smoothening of the chiral transition.

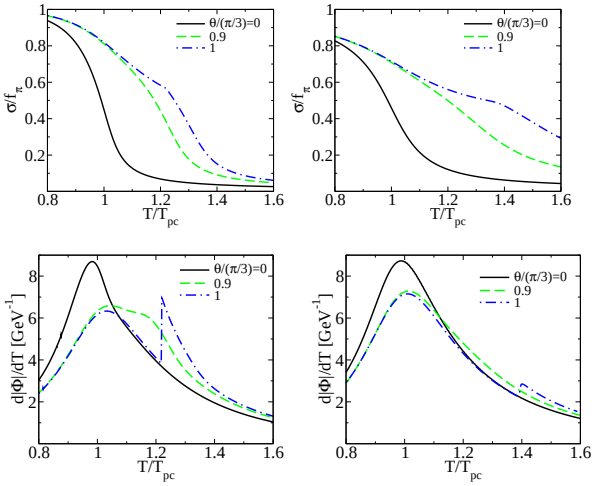

Figure 1: (Upper) The chiral order parameter normalized by f_π, as a function of temperature for different values of θ in the mean-field approximation (left panel) and in the FRG approach (right panel). Lower panels : $d|\Phi|$/dT as a function of temperature for different values of θ in the mean-field approximation (left panel) and in the FRG approach (right panel).

The effect of the fluctuations on the deconfinement transition is illustrated by the derivative of the Polyakov loop with respect to the temperature $d|\Phi|/dT$ shown in the lower panels. At small T this derivative has a unique peak, which is attributed to the location of the deconfinement transition. An additional peak induced by rapid change of the phase of the Polyakov loop appears near $\theta = \pi/3$. One sees two well-separated maxima and a discontinuity (Roberge-Weiss endpoint) both in the mean field and in the FRG calculations. However, the jump associated with the discontinuity is smaller in the FRG case owing to mesonic fluctuations. Consequently, the Polyakov loop variables are also influenced by mesonic fluctuation through the change of the chiral order parameter.

References

[1] K. Morita, V. Skokov, B. Friman, K. Redlich, Phys. Rev. D 84 (2011) 074020.

* Work supported by EMMI and YIPQS.

Interacting hadron resonance gas meets lattice QCD*

A. Andronic[1,2], *P. Braun-Munzinger*[1,3,4], *J. Stachel*[5], *and M. Winn*[5]

[1]GSI Helmholtzzentrum für Schwerionenforschung and EMMI, Darmstadt, Germany; [2]Institut für Kernphysik, Universität Münster, Germany; [3]Technical University Darmstadt, Germany; [4]Frankfurt Institute for Advanced Studies, J.W Goethe University, Germany; [5]Physikalisches Institut der Universität Heidelberg, Germany

We present, in the framework of the interacting hadron resonance gas (HRG), an evaluation of thermodynamical quantities. The interaction is modelled via a correction for the finite size of the hadrons [1]. Here we show results of our calculations for radii in the range of R=0.3±0.05 fm. Our calculations, with and without (R=0) excluded volume corrections, for thermodynamical quantities as energy and entropy densities and pressure are confronted with predictions using the lattice Quantum Chromodynamics (QCD) formalism.

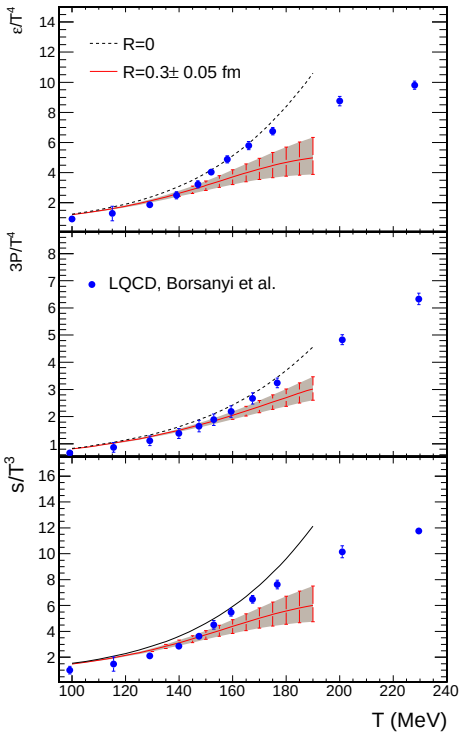

Figure 1: Temperature dependence of thermodynamical quantities. The calculations with the hadron gas model are compared to LQCD results of Borsányi et al. [3].

In Fig. 1 we show the temperature dependence of energy density, pressure, and entropy density, each normalized to appropriate powers of the temperature. The case without interactions (no excluded volume correction) has the expected strong dependence on temperature. As noted early on by Hagedorn [2], a limiting temperature, also called "Hagedorn temperature", of $T_H \simeq 200$ MeV arises for calculations of thermodynamical quantities within the HRG model. For the case of calculations employing finite hadron volume corrections the Hagedorn infinities are tamed. For temperatures below 120 MeV the HRG model results with and without excluded volume correction almost coincide, see Fig. 1. For larger temperatures, the HRG with interactions yields, in our view, a realistic description of the hadronic phase. The expectation is that, as soon as effects of deconfinement become important in the lattice QCD results, they should increasingly exceed the HRG values. In Fig. 1 the most recent predictions of lattice QCD are compared to the HRG results. Indeed, below T=150 MeV good agreement between results of lattice QCD [3] and the interacting HRG is found.

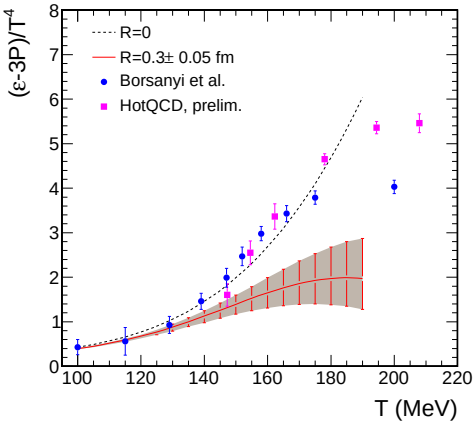

Figure 2: Temperature dependence of the trace anomaly. The calculations within the hadron gas model are compared to LQCD calculations of Borsányi et al. [3] and HotQCD collaboration [4] (preliminary results).

In Fig. 2 we compare our calculations for the trace anomaly $\varepsilon - 3P$ (normalized to T^4) to LQCD results [3, 4]. We see an agreement between LQCD data and our calculations for the interacting hadron gas only up to T=140 MeV, beyond which effects of deconfinement are apparent.

References

[1] A. Andronic, P. Braun-Munzinger, J. Stachel, M. Winn, arXiv:1201.0639.

[2] R. Hagedorn, CERN-TH-4100/85 (1985).

[3] S. Borsányi et al., JHEP **1011** (2010) 077 [arXiv:1007.2580].

[4] A. Bazavov, P. Petreczky (for the HotQCD collaboration), PoS **LATTICE2010** (2010) 169 [arXiv:1012.1257]; W. Soldner (for the HotQCD collaboration), PoS **LATTICE2010** (2010) 215 [arXiv:1012.4484].

* work supported by EMMI

Heavy quarkonium at finite temperature from QCD sum rules with the maximum entropy method*

P. Gubler[1], *K. Suzuki* [1], *K. Morita* [2,3], *and M. Oka*[1]

[1]Department of Physics, Tokyo Institute of Technology, Tokyo, Japan; [2]GSI, Darmstadt, Germany; [3]Yukawa Institute for Theoretical Physics, Kyoto, Japan

Properties of heavy quarkonia have been extensively studied since it was pointed out that they provide information on deconfinement transition of QCD. While expected suppressions of the quarkonia have been measured in heavy ion experi- ments, interpretation of these data is not so straightforward, because of not only the complexity of the collision processes but also the fact that spectral properties of the heavy quarkonia are not well understood yet. In this report, we focus on a novel approach to this problem utilizing QCD sum rules combined with the maximum entropy method (MEM) [1].

We start with the current correlation function for the vector current $j^\mu = \bar{Q}\gamma^\mu Q$ with heavy quark mass being m_Q,

$$\Pi(q^2) = \int d^4x e^{iq\cdot x}\langle T[j^\mu(x)j_\mu(0)]\rangle. \qquad (1)$$

Taking large negative q^2 enables us to compute $\tilde{\Pi}(q^2) = \Pi(q^2)/(3q^2)$ via operator product expansion (OPE) in which the dimension four gluon condensate takes into account the leading order non-perturbative contribution. Moreover, a large separation scale by virtue of the heavy quark mass gives better convergence property and allows us to impose all the medium effect on the condensate, unless the typical energy scale of the medium exceeds the separation scale. We apply the Borel transformation to improve the convergence of the OPE. Then the Borel-transformed correlator $\mathcal{M}(\nu)$ reads

$$\mathcal{M}(\nu) = e^{-\nu}A(\nu)[1 + \alpha_s(\nu)a(\nu) + b(\nu)\phi_b(T) + c(\nu)\phi_c(T) + d(\nu)\phi_d(T)] \qquad (2)$$

where $\nu = 4m_Q^2/M^2$ and M is the so-called Borel mass parameter. $\phi_i (i = b, c, d)$ denote the scalar, twist-2, and dimension six gluon condensates, respectively. The temperature dependence of the dimension four condensates have been extracted from lattice QCD while dimension six term is estimated by the instanton liquid model to check the convergence property of the OPE. See Refs. [2] and [1] for detail of the OPE.

The relation to the physical quarkonia, $q^2 = m^2_{\bar{Q}Q}$, is kept through the dispersion relation. After the Borel transformation, which also optimizes the dispersion relation such that the integral over the energy is dominated by the lowest resonance, the dispersion relation for the transformed correlator $\mathcal{M}(\nu)$ reads

$$\mathcal{M}(\nu) = \int dx^2 e^{-\nu x^2}\rho(2m_Q x, T) \qquad (3)$$

where $\nu = 4m_Q^2/M^2$ and M is the so-called Borel mass parameter. QCD sum rules gives a systematic framework to extract spectral properties from the OPE of the current correlation function, (2), via dispersion relation (3). Recently, Gubler and Oka proposed to apply MEM to QCD sum rules [3]. In this method, we do not have to assume a specific functional form on the spectral function. Futhermore, compared to lattice calculations using MEM, we can take as many points as possible and the dispersion relation does not have a temperature dependence other than the spectral function itself. Here we take into account the uncertainties of the values of m_Q, α_s, and the gluon condensates and evaluate the most probable form of the spectral function $\rho(\omega, T)$ via MEM. Figure 1 displays the results of

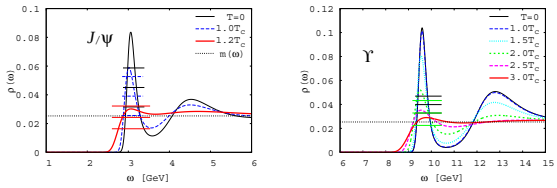

Figure 1: Spectral functions of J/ψ (left) and Υ (right) at various temperatures obtained by QCD sum rules with the maximum entropy method. $m(\omega)$ is the so-called default model which incorpolates the prior knowledge on the asympotic values of $\rho(\omega)$.

the QCD sum rule+MEM approach. Although resolution of the width in the lowest peak is not sufficient, one sees how the peak dissolves as temperature increases. The drastic change around T_c seen in the case of J/ψ is consistent with previous sum rule calculations [2] while Υ hardly reflects the phase transition but exhibits sizable modification above $2T_c$. Owing to the limited resolution, the peak seen in the Υ channel seems to contain contribution from excited states. Details will be discussed in a future publication [4].

References

[1] P. Gubler, K. Morita, M. Oka, Phys. Rev. Lett. 107 (2011) 092003.

[2] K. Morita, S. H. Lee, Phys. Rev. D 82 (2010) 054008.

[3] P. Gubler, M. Oka, Prog. Theor. Phys. 124 (2010) 995.

[4] P. Gubler, K. Suzuki, K. Morita, M. Oka, in preparation.

* Work supported in part by JSPS and YIPQS.

Net-charge probability in heavy ion collisions at chemical freeze-out*

P. Braun-Munzinger[1,2,3,4], *B. Friman*[1], *F. Karsch*[5,6], *K. Redlich*[7], *and V. Skokov*[1,5]

[1]GSI, Darmstadt, Germany; [2]EMMI, GSI, Darmstadt; [3]TU Darmstadt, Germany; [4]FIAS, Frankfurt; [5] BNL, Upton, USA; [6]Universität Bielefeld, Germany; [7]University of Wroclaw, Poland

The proximity of the freeze-out curve to the phase boundary suggests that the QCD phase transition and its related critical properties should be observable in heavy ion collisions. However, an experimental verification of a phase change in a medium created in such collisions requires sensitive probes. In this context, a particular role is attributed to fluctuations of conserved charges.

Recently, it was argued that, at high energies, the history of the system, in particular the path through the QCD cross-over transition from the deconfined and chirally symmetric phase to the hadronic one, may be reflected in fluctuations of conserved charges, specifically in their higher cumulants [1].

The characteristic signature of such a transition may thus be manifested in deviations of higher cumulants of the charge distributions from the Hadron Resonance Gas (HRG) results, if the freeze-out takes place near or at the QCD phase boundary. At vanishing chemical potential, the sixth and higher order cumulants can be negative, also in the hadronic phase, in contrast to the predictions of the HRG model, where only positive yields are obtained. It is therefore useful to consider the HRG model results on moments of charge fluctuations as a theoretical baseline; any deviation from this could be an indication for critical phenomena at the time of hadronization.

In Ref. [2], we computed the probability distribution for fluctuations of strangeness, electric charge and net-baryon number in the Boltzmann approximation. Here, we give only the probability distribution $P(N)$ for fluctuations of the net-baryon number N, which can be expressed in terms of the mean-number of baryons $\bar{N}_1$ and antibaryons $\bar{N}_{-1}$ by the Skellam distribution,

$$P(N) = \left(\frac{\bar{N}_1}{\bar{N}_{-1}}\right)^{\frac{N}{2}} I_N\left(2\sqrt{\bar{N}_1\bar{N}_{-1}}\right) \exp\left[\bar{N}_1 + \bar{N}_{-1}\right], \quad (1)$$

where $I_k(x)$ is a modified Bessel function.

The mean number of particles $\bar{N}_n$ and antiparticles $\bar{N}_{-n}$ obtained in experiment can, when available, be used directly in Eq. (1), where the volume and all thermodynamic parameters have been eliminated. Thus, predictions of the HRG model can be compared with data in an unambiguous way, avoiding further model assumptions.

Alternatively, in the HRG model the mean number of particles $\bar{N}_n$ and antiparticles $\bar{N}_{-n}$ entering $P(N)$ in Eq. (1) can be computed, given the thermal and volume parameters. In applications of the HRG model to heavy-ion phenomenology the thermal parameters are determined along the chemical freeze-out curve. The volume can then be fixed to reproduce the net charge number or particular particle yields.

In Fig. 1 using these approaches we show predictions on the probability distribution of net-proton number at different energies.

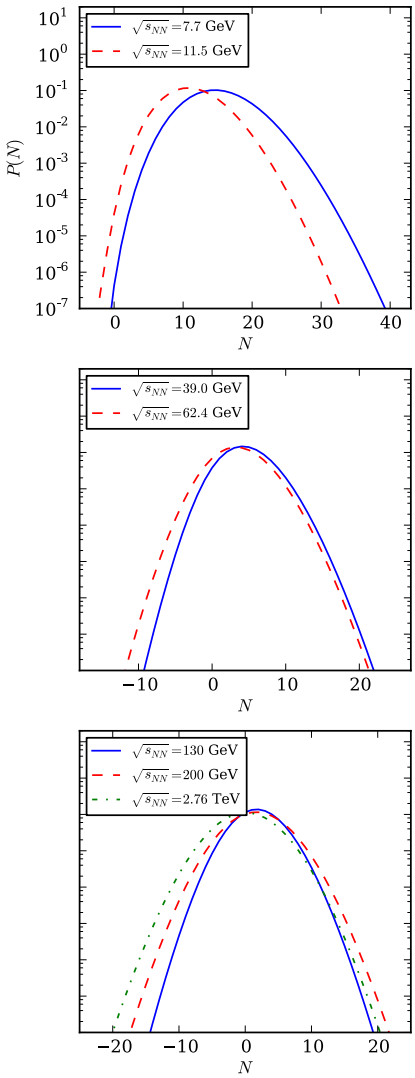

Figure 1: Predictions of the HRG model for the net proton probability distribution in central nucleus-nucleus collisions at different energies.

References

[1] B. Friman et. al., Eur. Phys. J. C **71** (2011) 1694.

[2] P. Braun-Munzinger et. al., arXiv:1111.5063; Phys. Rev **C84** (2011) 064911

* Work supported by EMMI.

The thermal model on the verge of the ultimate test: particle production in Pb-Pb collisions at the LHC*

A. Andronic[1,2], *P. Braun-Munzinger*[1,3,4], *K. Redlich*[5], *and J. Stachel*[6]

[1]GSI Helmholtzzentrum für Schwerionenforschung and EMMI, Darmstadt, Germany; [2]Institut für Kernphysik, Universität Münster, Germany; [3]Technical University Darmstadt, Germany; [4]Frankfurt Institute for Advanced Studies, J.W Goethe University, Germany; [5]Institute of Theoretical Physics, University of Wrocław, Poland; [6]Physikalisches Institut der Universität Heidelberg, Germany

We investigate the production of hadrons in nuclear collisions within the framework of the thermal (or statistical hadronization) model. We discuss both the ligh-quark hadrons as well as charmonium and provide predictions for the LHC energy [1].

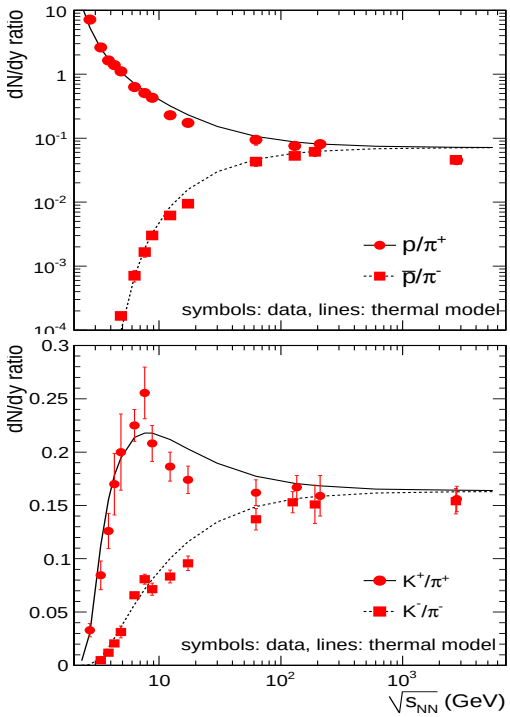

Figure 1: Energy dependence of the relative production ratios of protons ($\bar{p}$) and kaons (K^-) to pions (π^-).

The values of T and μ_b obtained from fits can be parametrized as a function of $\sqrt{s_{NN}}$ [2] and we employ these parametrizations to compare the model to data over a broad energy range. As an illustration, the production yields of protons and kaons relative to pions are shown in Fig. 1, demonstrating that the model describes the data well (although smaller p/π^+ and $\bar{p}/\pi^-$ ratios are measured by PHENIX and at SPS [2]). The trends seen in the p/π^+ and $\bar{p}/\pi^-$ ratios reflect both the strong increase followed by saturation for T and the strong decrease of μ_b as a function of $\sqrt{s_{NN}}$. Preliminary ALICE data [3] indicate lower p/π^+, $\bar{p}/\pi^-$ ratios compared to model predictions. While the K^-/π^- ratio shows a monotonic increase and saturation as a function of energy, the K^+/π^+ ratio shows a maximum at a beam energy of 30 AGeV. In the thermal model this maximum occurs naturally at as an effect of the steep rise and saturation of T and the strong monotonous decrease in μ_b [2].

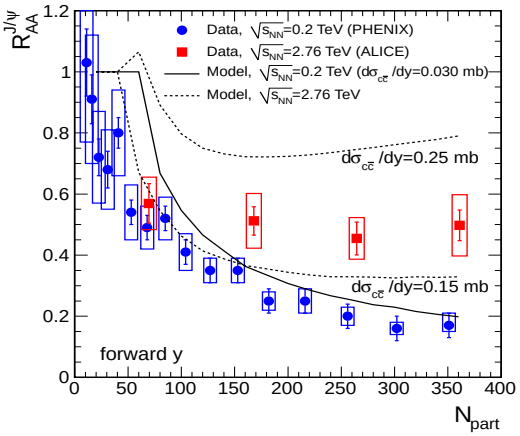

Figure 2: Centrality dependence of $R_{AA}^{J/\psi}$ for RHIC and LHC energies at forward rapidity. The two curves shown for the LHC energy correspond to a range of expected charm cross section.

The centrality dependence of the nuclear modification factor $R_{AA}^{J/\psi}$ is shown in Fig. 2. The model reproduces very well the decreasing trend versus centrality seen in the RHIC data [4]. At the much higher LHC energy the larger charm production cross section could lead to a different trend as a function of centrality, depending on the magnitude of shadowing in Pb-Pb collisions. A generic prediction of the model is that the $R_{AA}^{J/\psi}$ value at LHC is larger than at RHIC and this is confirmed by the preliminary ALICE data [5] measured at forward rapidity, which demonstrate, in our view, that charmonium is produced at LHC at the phase boundary (chemical freeze-out).

References

[1] A. Andronic et al., J. Phys. G **38** (2011) 124081.

[2] A. Andronic et al., Phys. Lett. B **673** (2009) 142.

[3] M. Floris (ALICE coll.), J. Phys. G **38** (2011) 124025

[4] A. Adare et al. (PHENIX coll.), arXiv:1103.6269.

[5] P. Pillot (ALICE coll.), J. Phys. G **38** (2011) 124111

* work supported by EMMI

Complex Transport Simulations

K. Gallmeister[1]

[1]Institut für Theoretische Physik, Johann Wolfgang Goethe - Universität Frankfurt, Max-von-Laue-Str. 1, D-60438 Frankfurt am Main, Germany

Introduction

In order to understand and analyze current and future experiments in modern nuclear and hadron physics, a number of very complex computer programs based on transport theoretical models have been developed in the last years.

One prominent example is the program "BAMPS"[1], which is a important tool for the understanding of the dynamics of the hot and dense quark gluon phase in high energetic heavy ion collisions. This description is primarily relevant for the understanding of RHIC and LHC experiments. Here quarks and gluons are the relevant degrees of freedom. On the other side, hadronic models try to describe the same topic in terms of hadronic degrees of freedom, as, e.g. "UrQMD"[2, 3] or "GiBUU"[4].

While "BAMPS" and "UrQMD" are mostly relevant for heavy ion experiments at SPS, RHIC and ALICE, "GiBUU" is at the moment more suitable to describe elementary collisions like $\gamma^{(*)}A$, πA, pA, νA or $\overline{p}A$. Here the neutrino induced and the anti-proton induced reactions are an unique feature of this model. Especially due to the inclusion of anti-protons, "GiBUU" is a very important tool for the understanding of experiments (PANDA) at FAIR.

Unfortunately, all these programs reside in different stages of programming techniques. The used programming languages range from Fortran 77 up to C++. Accordingly, the underlying program structures as modularity or object orientation differ drastically.

In addition, due to the different used languages, the use of standardized (and well tested) libraries is implemented in different levels. A very strong deficiency of these programs is the heterogeneous input/output strategy. It is not possible, to import immediately the results of one program into another in order to process them further.

Also the aspect of maintainability is diversified. A concept of version control is implemented at the moment only partially.

A very important aspect is the development of computer hardware during the last years. In order to cope with this, new programming techniques are necessary. Thus an adaption of the existing software and their development for multi and many-core architectures is very important.

Improvements

At the moment we are using the program "BAMPS" as a test field for possible improvements.

It has shown up, that some cleaning up of the code, including restructuring of some of its elements was necessary to enhance the readability and maintainability. A very important aspect for pooling the efforts of the different members of the group was the introduction of a version control for the source code in the framework of Subversion [5]. A web interface via Trac [6] including ticketing has proven to be very helpful.

The transport codes mentioned above have some underlying structure, which contradicts in general some (naive) parallelization. Thus we are currently working to use the modern hardware architectures in the framework of GPGPU programming. Here first steps have been done, to parallelize the calculation of complex particle-particle cross sections for the "BAMPS" simulation in the framework of OpenCL [7].

While already some essential improvements have been reached, we are still in a learning phase to really figure out, where and how we can put the different codes on some common footing.

Conclusions

To summarize we state, that it is very important to bring the computer programs used by physicists in order to understand modern experiments to a stage, that corresponds modern programming knowledge and eliminate old coding techniques and languages. This will facilitate the use of the programs and allow their direct use by the experimentalist as a tool for planning, understanding and analyzing their experiments. We have started this effort successfully for the transport theoretical programs "BAMPS", "UrQMD" and "GiBUU".

References

[1] Z. Xu and C. Greiner, Phys. Rev. C **71**, 064901 (2005) [hep-ph/0406278].

[2] S. A. Bass, M. Belkacem, M. Bleicher, M. Brandstetter, L. Bravina, C. Ernst, L. Gerland and M. Hofmann *et al.*, Prog. Part. Nucl. Phys. **41**, 255 (1998) [Prog. Part. Nucl. Phys. **41**, 225 (1998)] [nucl-th/9803035].

[3] H. Petersen, J. Steinheimer, G. Burau, M. Bleicher and H. Stocker, Phys. Rev. C **78**, 044901 (2008) [arXiv:0806.1695 [nucl-th]].

[4] O. Buss, T. Gaitanos, K. Gallmeister, H. van Hees, M. Kaskulov, O. Lalakulich, A. B. Larionov, T. Leitner, J. Weil and U. Mosel, arXiv:1106.1344 [hep-ph].

[5] http://subversion.tigris.org/

[6] http://trac.edgewall.org/

[7] http://www.khronos.org/opencl

Dilepton production at SIS energies with the GiBUU transport model*

J. Weil† *and U. Mosel*
Institut für Theoretische Physik, Universität Giessen, Germany

The HADES collaboration has recently measured dilepton spectra from pp, pA and AA reactions (see e.g. [1, 2, 3]) in order to investigate in-medium properties of vector mesons and solve the long-standing "DLS puzzle".

We simulate the corresponding reactions with the GiBUU transport model, which provides a unified framework for various types of elementary reactions on nuclei as well as heavy-ion collisions [4]. This model takes care of the correct transport-theoretical description of the hadronic degrees of freedom in nuclear reactions, including the propagation, collisions and decays of particles.

While a string-model approach may still be applicable at the highest HADES energies [5], a resonance-model description of the elementary NN collisions is surely more appropriate below $\sqrt{s} \approx 3\,\mathrm{GeV}$. We are currently extending the GiBUU resonance model, which is based on the Teis analysis [6], to higher energies, in order to have one consistent model for the whole energy regime probed by HADES.

Fig. 1 shows a comparison plot of a resonance model simulation to HADES data for p+p collisions at 3.5 GeV. The simulation results have been corrected for the HADES detector acceptance and resolution and reasonably reproduce the shape of the data over most of the spectrum. In the intermediate mass region, the spectrum is sensitive to 'baryonic' effects: As the green band in fig. 1 shows, the two-step production of ρ mesons via baryon resonances gives a great enhancement of low-mass ρ mesons over the direct ρ production in a string-model simulation. Furthermore, the transition form factor of the Δ Dalitz decay is experimentally undetermined up to now. The orange band in fig. 1 visualizes the effect of the form-factor model of Iachello et al. [7]. It seems that the $NN \to NR \to NN\rho$ process alone provides a reasonable description of the data in the intermediate mass range (and the corresponding p_T spectra), but minor contributions from the Δ Dalitz decay can not be excluded at present.

After fixing the cocktail contributions in the elementary reaction, one can investigate in-medium effects in p+Nb at the same energy. Fig. 2 shows GiBUU simulations with different in-medium scenarios for the vector-meson spectral functions, like collisional broadening (CB) or a pole-mass shift of 16% (for an overview of in-medium physics see e.g. [8]). However, it is not possible to draw any final conclusions at this point, since the data are still preliminary.

Even larger medium effects are expected in heavy-ion collisions like Ar+KCl [3], which we plan to investigate in the future.

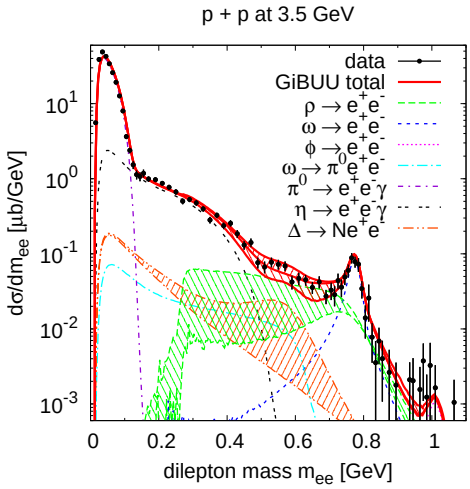

Figure 1: Dilepton spectrum for p+p@3.5GeV: GiBUU transport simulation compared to HADES data [1].

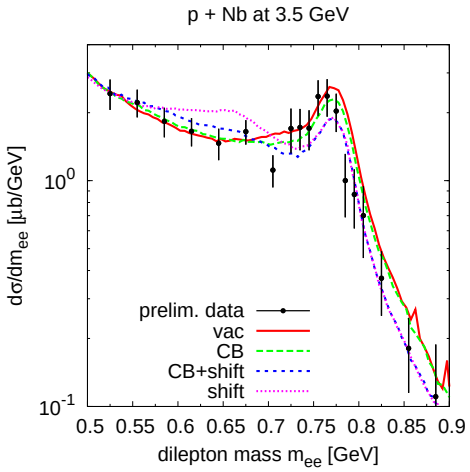

Figure 2: Dilepton spectrum for p+pNb@3.5GeV with different in-medium scenarios compared to preliminary data [2].

References

[1] G. Agakishiev et al., arXiv:1112.3607v1 [nucl-ex].
[2] M. Weber, Int. J. Mod. Phys. A 26 (2011) 737.
[3] G. Agakishiev et al., Phys. Rev. C 84 (2011) 014902.
[4] O. Buss et al., arXiv:1106.1344v1 [hep-ph].
[5] J. Weil et al., arXiv:1105.0314v1 [nucl-th].
[6] S. Teis et al., Z. Phys. A 356 (1997) 421.
[7] Q. Wan, F. Iachello, Int. J. Mod. Phys. A 20 (2005) 1846.
[8] S. Leupold, V. Metag, U. Mosel, Int. J. Mod. Phys. E 19 (2010) 147-224.

* Work supported by HGS-HIRe and BMBF.
† janus.weil@theo.physik.uni-giessen.de

Space-time evolution of the magnetic field in relativistic heavy-ion collisions

V. P. Konchakovski[1], *E. L. Bratkovskaya*[2,3], *W. Cassing*[1], *V. D. Toneev*[3,4], *and V. Voronyuk*[3,4]
[1]ITP, Uni-Giessen, Germany; [2]ITP, Uni-Frankfurt, Germany; [3]FIAS, Frankfurt, Germany; [4]JINR, Dubna, Russia

In dense QCD matter in the presence of an external magnetic field and/or topological defects, a spontaneous creation of axial currents may happen. The presence of a magnetic field also favors the formation of spatially inhomogeneous spiral-like quark condensate configurations at low temperatures and non-zero chemical potentials. The influence of a constant magnetic field on possible color-superconducting phases (the color Meissner effect) has also actively been discussed. A clarification of such phenomena by experimental observations requires e.g. the production of QCD matter in relativistic heavy-ion collisions where in non-central reactions strong electromagnetic fields are created by the charged four-current of the spectators.

We study the space-time evolution of electromagnetic fields formed in relativistic heavy-ion collisions. The Hadron String Dynamics (HSD) transport approach, which solves Kadanoff-Baym equations and treats the nuclear collisions in terms of quasiparticles with a finite width, is used as a basis of our considerations. In our approach the dynamical formation of the electromagnetic field, its evolution during a collision and influence on the quasiparticle dynamics as well as the interplay of the created electromagnetic field and back-reaction effects are included simultaneously. The set of transport equations is solved in a quasiparticle approximation by using the Monte-Carlo parallel ensemble method. To find the electromagnetic field, a space-time grid is used. The quasiparticle propagation in the retarded electromagnetic field is calculated as:

$$\frac{d\mathbf{p}}{dt} = e\mathbf{E} + \frac{e}{c}\mathbf{v}\times\mathbf{B}\,. \qquad (1)$$

The time evolution of $eB_y(x, y = 0, z)$ for Au+Au collisions for the colliding energy $\sqrt{s_{NN}}$ =200 GeV at the impact parameter $b = 10$ fm is shown in Fig. 1. If the impact parameter direction is taken as the x axis (as in the present calculations), then the magnetic field will be directed along the y-axis perpendicularly to the reaction plane $(z - x)$. The geometry of the colliding system at the moment considered is demonstrated by points in the $(z-x)$ plain where every point corresponds to a spectator nucleon. It is seen that the largest values of $eB_y \sim 5m_\pi^2$ are reached in the beginning of a collision for a very short time corresponding to the maximal overlap of the colliding ions. Note that this is an extremely high magnetic field, since $m_\pi^2 \approx 10^{18}$ gauss. The first panel in Fig. 1 is taken at a very early compression stage with $t = 0.01$ fm/c. The next panel shows configuration of the magnetic field at the time $t = 0.2$ fm/c. Then, the system expands (note the different z-scales in the different panels of Fig. 1) and the magnetic field decreases. For $b = 0$ the overlap time is maximal and roughly given by $2R/\gamma_c$ which for our case is about 0.15 fm/c. For peripheral collisions this time is even shorter.

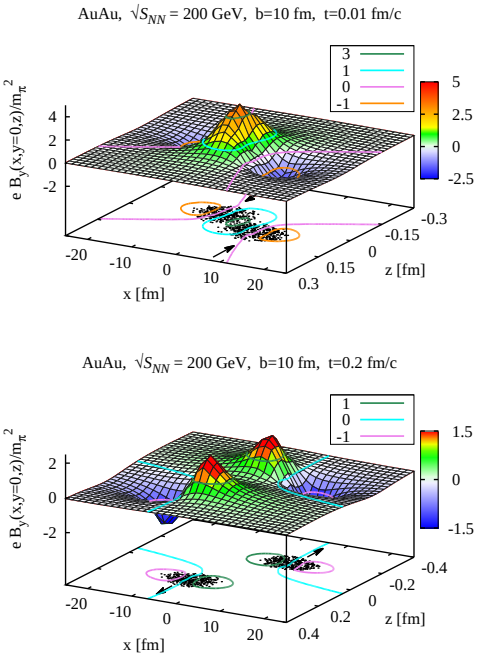

Figure 1: Time dependence of the spatial distribution of the magnetic field B_y at times t created in Au+Au ($\sqrt{s}$=200 GeV) collisions with the impact parameter b =10 fm. The location of spectator protons is shown by dots in the $(x-z)$-plane. The level $B_y = 0$ and the projection of its location on the $(x - z)$ plane is shown by the solid lines.

Globally, the spatial distribution of the magnetic field is evidently inhomogeneous and Lorentz-contracted along the z-axis. At the compression stage there is a single maximum which in the expansion stage is splitted into two parts associated with the spectators. In the transverse direction the bulk magnetic field is limited by two minima coming from the torqued structure of the single-charge field. See references [1, 2] for more details.

References

[1] V. Voronyuk, V. D. Toneev, W. Cassing, E. L. Bratkovskaya, V. P. Konchakovski and S. A. Voloshin, Phys. Rev. C **83**, 054911 (2011).

[2] V. D. Toneev, V. Voronyuk, E. L. Bratkovskaya, W. Cassing, V. P. Konchakovski and S. A. Voloshin, arXiv:1112.2595 [hep-ph].

Triggering of Ξ^- production in antiproton-nucleus collisions*

A.B. Larionov† [1,2] *and U. Mosel*[1]

[1]Institut für Theoretische Physik, Universität Giessen, D-35392 Giessen, Germany; [2]RRC "I.V. Kurchatov Institute", 123182 Moscow, Russia

One important part of the PANDA project is related to the double-Λ hypernuclei production by conversion of a stopped Ξ^- hyperon to 2Λ on a proton of the secondary target nucleus [1]. The Ξ^- hyperons will be produced in $\bar{p}$ interactions with the primary target nucleus. The proposed experimental scheme requires a triggering condition in order to tag the outgoing Ξ^-. The two possible triggers were proposed [1]: The first trigger is based on detection of a high-momentum $\bar{\Xi}^+$ in forward direction. The second trigger relies on the possibility that the $\bar{\Xi}^+$ hyperon will annihilate on a nucleon of the primary target producing a pair of positive kaons which will be detected. It is expected that the second ($2K^+$) trigger will provide significantly higher count rates than the first ($\bar{\Xi}^+$) trigger.

To analyse Ξ^--triggering, we have performed a GiBUU model [2] simulation of $\bar{p}$ interactions at $p_{\rm lab} = 3,\ 9$ and 15 GeV/c with gold nuclei. First, we studied the momentum spectra of Ξ^-'s under the two triggering conditions mentioned above as shown in Fig. 1. Indeed, we

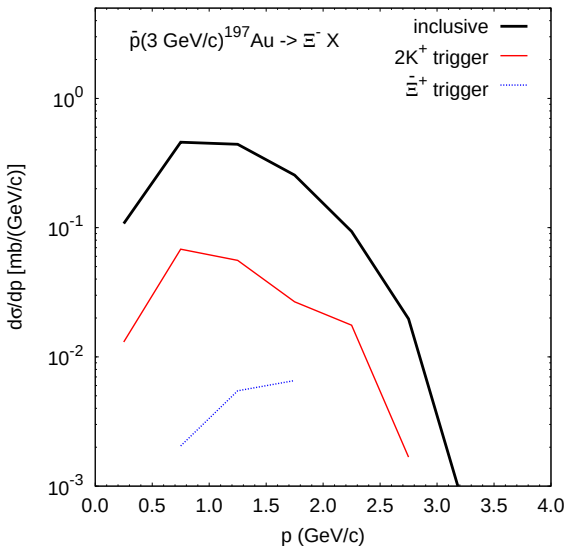

Figure 1: The Ξ^- momentum spectrum triggered by $2K^+$ (thin solid line) and by $\bar{\Xi}^+$ (dotted line) from $\bar{p}$+^{197}Au collisions at 3 GeV/c. The inclusive spectrum of Ξ^-'s is shown by thick solid line.

observe that the cross section of Ξ^- production in combination with two positive kaons is much larger than the one in combination with $\bar{\Xi}^+$. Moreover, the $2K^+$ trigger seems to favour the production of low-momentum Ξ^-'s, which is convenient for their further deceleration in the secondary target material [1]. However, the most crucial question is which trigger is more selective for Ξ^- production? Fig. 2 shows the ratios of cross sections for various final channels. The total $\bar{p}$ absorption cross sec-

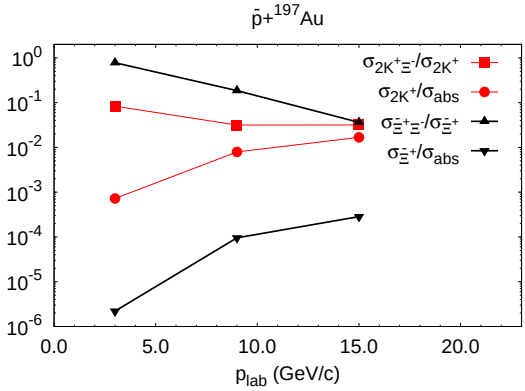

Figure 2: Beam momentum dependence of some selected cross section ratios.

tion is denoted as $\sigma_{\rm abs}$. The absorption is understood here in a Glauber sense, i.e. it means the removal of an antiproton from the beam and not only annihilation. Other notations $\sigma_{\bar{\Xi}^+}$, $\sigma_{\bar{\Xi}^+\Xi^-}$, σ_{2K^+} and $\sigma_{2K^+\Xi^-}$ correspond to the cross sections of the processes $A(\bar{p},\bar{\Xi}^+)X$, $A(\bar{p},\bar{\Xi}^+\Xi^-)X$, $A(\bar{p},2K^+)X$ and $A(\bar{p},2K^+\Xi^-)X$. The fraction of events containing $2K^+$ or $\bar{\Xi}^+$ among all $\bar{p}$ absorption events grows with beam momentum, as expected. The probability to produce $2K^+$ is two-three orders of magnitude larger than the probability to produce a $\bar{\Xi}^+$-antihyperon. However, the events containing $\bar{\Xi}^+$ are much more enriched by Ξ^-'s than events with $2K^+$. This is especially pronounced at lower beam momenta near the $\bar{\Xi}^+\Xi^-$ production threshold in $\bar{p}p$ collisions ($p_{\rm lab} = 2.6$ GeV/c). At 3 GeV/c, the probability that an event containing $\bar{\Xi}^+$ contains also Ξ^- is about 0.8, while the probability that an event with $2K^+$ includes also a Ξ^--hyperon is only 0.1. The reason is that many double-kaon events are caused by collisions of secondary mesons (mostly π, ω, see ref. [3] for details) with nucleons, $MN \to YK$. Thus, our analysis shows that, at least for heavy primary targets, only the $\bar{\Xi}^+$ trigger turns out to be effective. The similar analysis for the light primary targets remains to be done yet.

References

[1] J. Pochodzalla, Nucl. Phys. A **754**, 430 (2005).

[2] O. Buss et al., arXiv:1106.1344, accepted in Phys. Rept.

[3] A.B. Larionov, T. Gaitanos, U. Mosel, arXiv:1107.2326.

* Work supported by BMBF and HIC for FAIR.

† Alexei.Larionov@theo.physik.uni-giessen.de

High Intense Hydrogen Cluster-Jet Beams for PANDA*

E. Köhler†[1], *A.-K. Hergemöller*[1], *A. Täschner*[1], *D. Bonaventura*[1], *H.-W. Ortjohann*[1], *and A. Khoukaz*[1]

[1]Institut für Kernphysik, Westfälische Wilhelms-Universität Münster, Germany

A high density cluster-jet target will be one of two planned target stations of the PANDA experiment. The internal target for PANDA has to fulfil several challenging requirements. The target material has to be of high purity to avoid background reactions. In addition, the target thickness should be homogeneous and constant in time to prevent luminosity fluctuations. Depending on the experimental programme the target density, the target beam shape and its size have to be variable. Particularly the effective target beam size should be as small as possible for precise vertex reconstruction and low influences on the vacuum conditions at the storage ring. The most challenging requirement is the distance of $2.1\,\mathrm{m}$ between the target production point and the interaction point to allow for a nearly full 4π solid angle acceptance of the detection system. Furthermore, an area thickness above $10^{15}\,\mathrm{hydrogen\,atoms/cm^2}$ at the interaction point is required to fully exploit the antiproton production rate.

At the University of Münster a cluster-jet target prototype for PANDA has been built up and set successfully into operation in complete PANDA geometry. The used Laval type nozzle used for the cluster production has a diameter of $28\,\mu\mathrm{m}$ at the narrowest point and typically operates in a temperature range of 19 to $35\,\mathrm{K}$ and at pressures $> 18\,\mathrm{bar}$. Due to significant improvements the current setup achieves a target thickness ρ of more than $10^{15}\,\mathrm{atoms/cm^2}$.
The influence of the gas input temperature on the target beam density is shown in Fig. 1 for a constant gas input pressure of $17\,\mathrm{bar}$. As expected the target density increases with decreasing temperature down to $24\,\mathrm{K}$. The steeper rise at $35\,\mathrm{K}$ is caused by different phases at the cluster formation process.

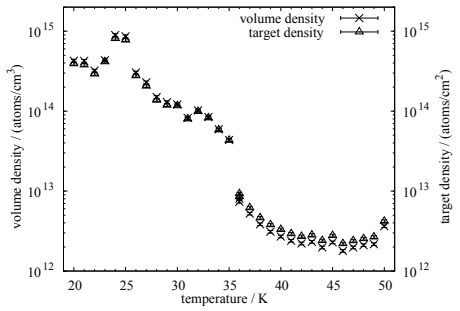

Figure 1: Volume density and target thickness at $17\,\mathrm{bar}$ in dependence of the hydrogen temperature at the nozzle inlet [1].

The decrease of the target density below $24\,\mathrm{K}$ is related to the jet beam structures observed in the skimmer chamber presented in Fig. 2. The cluster beam structures directly behind the nozzle (bright and less bright parts) depend on the temperature and pressure settings. To extract and measure the density of the bright and less bright areas of the cluster beam, a special tilting system was designed and installed. First tests with the tilting system lead to a significant improvement of the target thickness of $> 10^{15}\,\mathrm{atoms/cm^2}$ at $19\,\mathrm{K}$ and $18.5\,\mathrm{bar}$. These structures also explain the observed variations and the decrease of the target density in Fig 1. By means of the new tilting system, which can be adjusted during target operation, these density drops can be avoided and a stable operation with highest target thickness is possible.

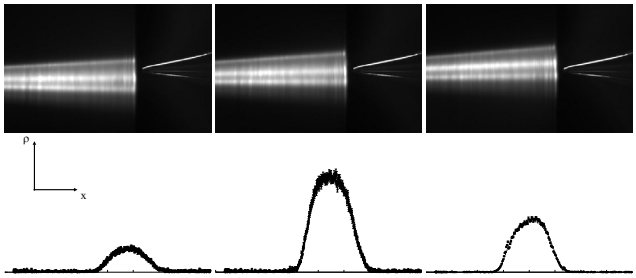

Figure 2: Top: Photographs of the cluster beam directly behind the nozzle (left) at constant hydrogen temperature and pressure settings of $19\,\mathrm{K}$ and $18.5\,\mathrm{bar}$. Bottom: Target beam profile at the scattering chamber and later PANDA interaction point. The use of the tilting system shows the change of the beam angle relative to the first skimmer and the variation of the target density at same pressure and temperature settings [2].

In the near future systematic studies on the temperature and pressure settings in combination with the tilting system are planned. Research on cluster mass and size are also intended as well as further tests with specially shaped collimators.

References

[1] A. Täschner et al., Nucl. Instr. and Meth. A 660 (2011) 22-30, doi:10.1016/j.nima.2011.09.024

[2] E. Köhler, Design and performance of the future cluster-jet target for PANDA at FAIR, in proceedings of STORI'11 conference, PoS (STORI11)063.

* Work supported by EU (FP6 and FP7), BMBF and GSI.

† e_koeh02@uni-muenster.de

Irradiation tests for the $\overline{\mathrm{P}}$ANDA MVD*

R. Schnell†[1], *K.-Th. Brinkmann*[1], *T. Quagli*[1,2], *J. Tummo*[1], *and H.-G. Zaunick*[1]

[1]Helmholtz-Institut für Strahlen- und Kernphysik, Universität Bonn, Germany; [2]I.N.F.N. Sezione di Torino, Torino, Italy

Introduction

The Micro-Vertex-Detector (MVD) for tracking and vertexing in PANDA will be the detector component closest to the interaction region. Therefore, all components must be radiation hard up to a level of 10 MRad of ionizing dose and up to $10^{14}\,\mathrm{n_{1MeV\,eq}\,cm^{-2}}$ of non-ionizing dose within the lifetime of the PANDA detector [1]. Besides silicon detectors such as pixel detectors and double-sided strip detectors also front-end electronics and services, e.g. cables, must be guaranteed to work reliable under such conditions. Hence, irradiation tests have to be conducted to verify components and their functionality.

Setup

Irradiations were carried out at the isochronous cyclotron facility in Bonn [2] using a 14 MeV proton beam. The device under test was placed inside a scattering chamber as depicted in figure 1. In order to apply a known dose to the device under test the size of the beam, the applied fluence and the energy loss in the target material must be known. The energy loss can be calculated using SRIM [3]. The fluence was measured with a Faraday cup and the beam size was determined using a fluorescent screen observed by a camera. Combining these measurements the applied dose can be estimated.

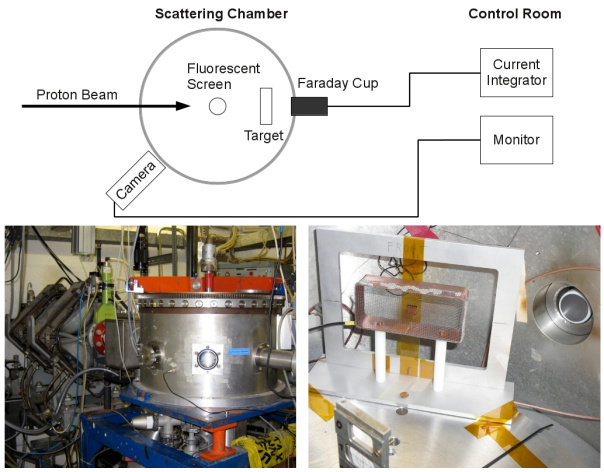

Figure 1: Top: Schematical overview of the setup. Lower left: Scattering chamber and beam line. Lower right: Probe fixture with silicon strip sensor, the fluorescent screen for beam size determination and the Faraday cup for charge measurement can be seen as well.

Results

Irradiation of low mass cables for the pixel detector [4] and prototype sensors for the strip detectors was performed. The low mass data cables were irradiated with a dose of approximately 16 MRad and yielded a performance within the predefined operation parameters.

The prototype sensor was irradiated with a total fluence of $2.2 \cdot 10^{13}\,\mathrm{cm^{-2}}$ corresponding to 10 MRad or $8.0 \cdot 10^{13}\,\mathrm{cm^{-2}}$ of 1 MeV neutron equivalent fluence via NIEL scaling. The obtained leakage current displayed in figure 2 can be compared with similar studies [5]. Several measurements were performed between annealing intervals showing the expected reduction of the leakage current.

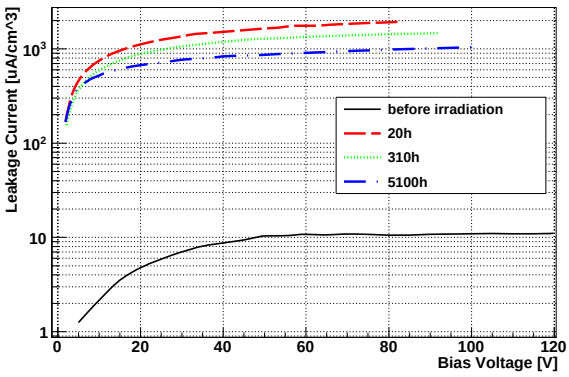

Figure 2: Annealing behavior of leakage current characteristics after irradiation of a PANDA prototype sensor with 14 MeV protons to a total dose of 10 MRad. The I-V-trends of the sensor were recorded after 20 hours (red-dashed), 310 hours (green-dotted) and 5100 hours (blue-dash-dotted) of annealing time normalised to 25 °C [1].

References

[1] PANDA Collaboration: Technical Design Report for the PANDA Micro Vertex Detector, to be published

[2] The Bonn isochronous cyclotron, http://www.zyklotron.hiskp.uni-bonn.de/zyklo/index.html

[3] J.F. Ziegler, J. Biersack, U. Littmark: The Stopping and Range of Ions in Matter, Pergamon Press, (1985)

[4] T. Quagli: New Aluminum Microstrips for Data Transmission in the PANDA Experiment, Master Thesis, Turin, (2011)

[5] M. Moll et al., Nucl. Instr. Meth. A **426** (1999), p. 87

* Work supported by BMBF [06BN9005I] and GSI [BNBRIN1012].

† schnell@hiskp.uni-bonn.de

The mechanical structures of the PANDA GEM-Tracker*

B. Voss[1,†], D. Auer[2], A. Ehret[2], C. Kaya, J. Kunkel, A. Neeb, A. Remers[2], J. Reuss[2], S. Schütz[2], Ed. Traut[2], El. Traut[2], E.T. Yamedji[2]

[1]GSI, Darmstadt, Germany; [2]Hochschule Darmstadt, Darmstadt, Germany;

Precise tracking in forward direction inside the PANDA target spectrometer requires accurate positioning of each of the detectors involved in the tracking process. Aiming for accuracy in the order of 100 µm requires e.g. pre-mounting the GEM-Disc [1] detectors of the PANDA GEM-Tracker system prior to installation as a complete system. This keeps the whole set in an adjusted position even during and after mounting (fig. 1.).

In order to maximize the geometrical acceptance and minimizing the adjustment effort, an outer skeleton made from 0.6 mm carbon-reinforced plastics has been developed in the framework of several (8) internships and (7) bachelor theses (fig. 2). The so called 'Riddle' is a rigid and light-weight (3.6 kg) multi-purpose support structure of multi-conical shape with the detector mounting-planes serving as stiffener for the support structure ('Matroschka' principle). The diameters are 902/1600/1482 mm; the overall length is 744 (1100) mm for the 3 (4) GEM-Disc option. The whole set is assumed to be fixed onto the downstream face surface of the solenoid vessel inside the target spectrometer of PANDA.

All required supplies like e.g. low- and high-voltage, sensors, transport of gas- and cooling fluids, optical fibers for readout have been integrated into the structure, making any loose connections inside the setup like e.g. long cables obsolete. Moreover, optimizing the internal structures of each connection type as well as by making use of their individual functionalities in a combined way allows a 30-50% reduction of the overall weight. An intermediate panel offering single-movement simultaneous connection of all media and signals is integral part of the setup.

For the fabrication of the Riddle shell, inner and outer molds with a sandwich structure based on Rohazell® and glass-fiber lining laminated on a wooden/aluminum support were built for the vacuum resin-injection process (fig. 3). The total weight of the re-usable installation is approximately 250 kg; the achieved accuracy of its roundness is 150 µm which is well within the specifications. A first hand-laminated specimen of the Riddle, made of glass-fiber fabric (GRP) for the present, has been casted (fig. 4) and tested for its shape stability. For estimated loads of 20, 30, 40 kg for GEM-Disc1, -2 and -3, respectively, and 50 kg for the supplies infrastructure the sag of 2 mm measured with dummy loads agrees well within the uncertainties of the calculation with the values determined by FEM simulations.

As next steps, the carbon version of the Riddle as well as a first version of the supplies conduit will be built and put into operation.

* Work supported by EU, 7th framework program
† Corresponding author: B.Voss@GSI.de

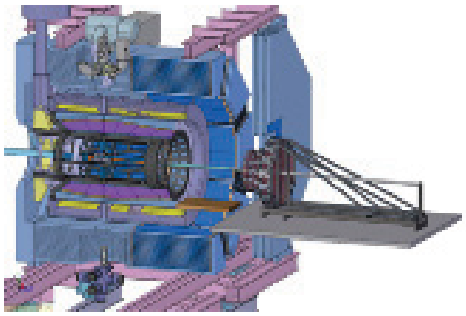

Figure 1: Mounting of the GEM-Tracker in PANDA.

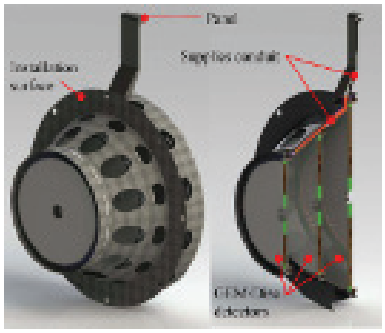

Figure 2: Design of the 3-GEM-Disc GEM-Tracker setup.

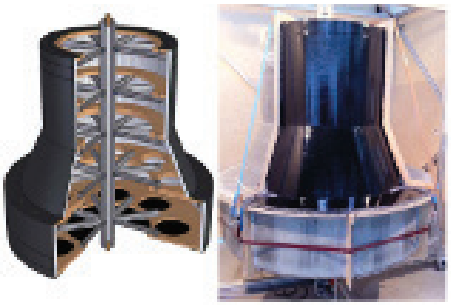

Figure 3: Mould design (left) and realization (right).

Figure 4: First GRP specimen of the 'Riddle'.

References

[1] B. Voss, J. Kunkel, R. Karabowicz, The GEM-Discs for the PANDA experiment; GSI scientific report 2010, GSI Report 2011-1, 2011, p.338.

Pattern Recognition in the GEM-TPC

J. Rauch[*1] *and the GEM-TPC Collaboration*[1,2,3,4,5]

[1]Technische Universität München, Germany; [2]GSI Helmholtzzentrum für Schwerionenforschung GmbH, Darmstadt, Germany; [3]Helmholtz-Institut für Strahlen- und Kernphysik, Bonn, Germany; [4]Universität Heidelberg, Heidelberg, Germany; [5]Stefan Meyer Institut für Subatomare Physik, Wien, Austria

The Riemann Pattern Recognition

The Riemann Pattern Recognition (PR) is a track following algorithm, that associates three-dimensional space points to track candidates by using different correlations between hits and tracks. Fast helix fits using a Riemann transformation are employed to estimate and update track parameters during the process.

Track Building

To begin with, the clusters (space points measured in the TPC) are presorted by z, radius or angle. Therefore the PR goes from areas of low track density, where tracks can easily be separated by their proximity in space, to areas of high track density. The very first *track* is built and contains only one hit at this time, then the algorithm loops through the presorted clusters. Each hit is checked against each existing track. The hit is then assigned to the best matching track, according to the following matching criteria (*"hit-track correlators"*):

- The *Proximity Correlator* checks proximity in space, by finding the nearest cluster in the track.
- The *Helix Correlator* calculates the distance of the cluster to the prefitted *helix* that defines the track.

If no track matches, a new track is made up from the hit.

Helix Prefit

When a track has more than a user definable minimum number of hits, a helix fit is performed in two steps [2]:

- A plane fit on the Riemann sphere.
- A straight line fit of the hit positions s along the track vs. the z-positions.

The Riemann transformation maps circles and straight lines on the (x, y)-plane to circles on the Riemann sphere, which again define planes in space. Accordingly, the non-linear task of circle-fitting is reduced to the linear task of plane-fitting [3]. Such a plane fit, projected back onto the pad-plane, delivers a circle. It is the projection of the true helical track onto the readout plane.

In a second step the dip of the helix is fitted: The position of each cluster along the helix can be defined by its angle. A straight line fit of the hit positions s on the track versus the z positions of the clusters is then performed, which delivers the dip ϑ of the track.

Track Merging

In the process of track building, the actual tracks might not be found as a whole. Therefore, a second level *tracklet merging* is performed. Similar to the track building process, the tracklets are presorted, and then compared to each other. Again, there are several *track-track correlators*:

- The *Proximity Correlator* compares the position of the first and last hits of the two tracks.
- The *Dip Correlator* compares the dip angles of the two tracks.
- Finally, the tracklets have to pass the *Helix Correlator*: A new track is created temporarily, containing the hits of both tracks. A helix fit is performed and a *helix-cut* on the RMS of the distance of the hits to the helix is applied.

Sectorization

In order to be performant for large numbers of hits and tracks, the TPC volume is sectorized. Track building and merging is done for each sector separately, and only then global merging is performed.

Multistep Approach

The PR efficiency for different track topologies depends strongly on the presorting of the clusters. Performance is best for tracks in sorting direction. Thus, it is advantageous to run the PR more than once, and use a different presorting in each step. Tracks that reach certain quality criteria (i.e. a minimum number of hits and an RMS of distances of the hits to the helix smaller than a certain cut) are kept, the remaining clusters are sorted again, and the procedure is repeated.

This approach yields high efficiencies for all kinds of track topologies and a high track resolution power.

References

[1] J. Rauch, "Tracking with a High-Rate GEM TPC", Diploma Thesis in preparation, 2012

[2] R. Frühwirth, A. Strandlie and W. Waltenberger, "Helix fitting by an extended Riemann fit", NIMA 490, 2002, p. 366 - 378

[3] A. Strandlie, J. Wroldsen, R. Frühwirth and B. Lillekjendlie, "Particle tracks fitted on the Riemann sphere", Computer Physics Communications 131, 2000, p. 95 - 108

[*] johannes.rauch@mytum.de

Track-Fitting and Vertex-Reconstruction with GENFIT

J. Rauch[*1], *C. Höppner*[1], *and the GEM-TPC Collaboration*[1,2,3,4,5]

[1]Technische Universität München, Germany; [2]GSI Helmholtzzentrum für Schwerionenforschung GmbH, Darmstadt, Germany; [3]Helmholtz-Institut für Strahlen- und Kernphysik, Bonn, Germany; [4]Universität Heidelberg, Heidelberg, Germany; [5]Stefan Meyer Institut für Subatomare Physik, Wien, Austria

Track-Fitting with GENFIT

After the pattern recognition tools have determined sets of detector hits which comprise particle trajectories, the best estimates for the track parameters, i.e. the particle positions and momenta with their covariances, have to be obtained. Space points measured by the TPC have to be fitted in combination with hits from other detectors with different geometries. This can be achieved with GENFIT [1], a generic toolkit for track fitting in complex detector systems. It is now the standard track fitting tool in PANDA as well as in the Belle-II project, and is now also used in the FOPI experiment.

Fitting Algorithms

The fact that GENFIT is applicable to a very wide range of experiments, independent of the specific event topology, detector setup, or magnetic field arrangement, is due to its completely modular design. Fitting algorithms are implemented as interchangeable modules. At present, the framework contains a validated Kalman filter [2] and a Deterministic Annealing Filter (DAF) [3]. The DAF is an iterated Kalman filter which has the virtue of being able to dynamically assign reduced weights to noise hits in planar detectors or to outlier hits in the TPC. Other algorithms like Gaussian Sum Filters [4] can be implemented easily in the GENFIT framework.

Track Representations

Track parameterizations and the routines required to extrapolate the track parameters and their covariance matrices through the experiment are also implemented as interchangeable modules. This allows the use of well established track extrapolation tools (e.g. GEANE [5]) as well as the development and evaluation of new track extrapolation tools. Different track parameterizations and extrapolation routines can be used simultaneously for fitting of the same physical tracks, which allows a direct comparison in terms of execution time, resolution, and efficiency.

Hit Representations

Representations of detector hits are the third modular ingredient to the framework. The hit dimensionality and orientation of planar tracking detectors are not restricted in any way. Tracking information from detectors which do not measure the passage of particles in a fixed physical detector plane, e.g. drift chambers or TPCs, is used without any simplification. This goal is achieved via the concept of virtual detector planes, which are calculated dynamically each time a hit is to be used in a track fit. This allows to maintain complete modularity of GENFIT because the fitting-algorithm modules treat all hits in the same manner. In the case of space point hits in the TPC, the virtual detector plane is defined to be perpendicular to the track and to contain the point of closest approach of the track to the hit. This allows the fitting algorithm to minimize the orthogonal distances of the track to the hits without projecting the hits onto predefined planes. The projection of hits onto planes defined by pad rows is common practice in TPC reconstruction.

GENFIT is implemented as a very light-weight C++ library, which is available as free software [6].

Vertex Reconstruction with GFRAVE

GENFIT has an interface to the vertex fitting framework RAVE [7]. RAVE is a detector-independent toolkit for vertex reconstruction, originally developed for CMS [8]. GFRAVE takes full advantage of the GENFIT material model, as well as of the sophisticated algorithms of RAVE, allowing for precise vertex reconstruction.

References

[1] C. Höppner, S. Neubert, B. Ketzer and S. Paul, “A Novel Generic Framework for Track Fitting in Complex Detector Systems”, NIMA 620, August 2010, p. 518 - 525

[2] R. Frühwirth, “Application of Kalman filtering to track and vertex fitting”, NIMA 262, 1987, p. 444 - 450

[3] R. Frühwirth and A. Strandlie, “Track fitting with ambiguities and noise: A study of elastic tracking and nonlinear filters”, Computer Physics Communications 120, 1999, p. 197 - 214

[4] G. Kitagawa, “The two-filter formula for smoothing and an implementation of the Gaussian-sum smoother”, Annals of the Institute of Statistical Mathematics 46, 1994, p. 605 - 623

[5] M. Innocente, V. Mairie and E. Nagy, “GEANE: average tracking and error propagation package”, CERN Program Library W5013-E, 1991

[6] C. Höppner and S. Neubert, “GENFIT”, http://sourceforge.net/projects/genfit/

[7] W. Waltenberger, “RAVE: A detector-independent toolkit to reconstruct vertices”, IEEE TNS 58, 2011, p. 434 - 4444

[8] CMS Collaboration, “The CMS experiment at the CERN LHC”, JINST 0803, 2008, p. S08004

* johannes.rauch@mytum.de

Lifetime of latest generation Microchannel Plate PMT's

A. Britting[1], *W. Eyrich*[1], *A. Lehmann*[†1], *F. Uhlig*[1], *and PANDA Cherenkov group*
[1]Physikalisches Institut IV, Universität Erlangen-Nürnberg, Erwin-Rommel-Str. 1, D-91058 Erlangen

Introduction

Multi-anode microchannel plate (MCP) PMTs have superior performance characteristics compared to standard dynode PMTs: they are very compact, they can be operated in magnetic field environments up to 2 Tesla, and they show an excellent time resolution of <50 ps. These are the main reasons why MCP-PMTs are the preferred option for both PANDA DIRCs.

Over the past few years our group has studied the characteristics of many of the commercially available types of MCP-PMTs. During this time their two main drawbacks, rate capability and lifetime, were improved step by step [1, 2]. Still, until recently the lifetime of these devices was not enough for the anticipated period of operation inside PANDA of 10 years. At the focal plane of the PANDA DIRCs photon rates up to 5 MHz/cm^2 are expected which may add up to an integrated anode charge of several C/cm^2/year. During 2010, new models of MCP-PMTs became available whose lifetimes are getting close to the requirement of 5 C/cm^2 for the barrel DIRC.

Techniques to Increase the Lifetime

A diminishing quantum efficiency (QE) of the photo cathode (PC) is the primary cause for the aging of MCP-PMTs. The 3 main manufacturers of MCP-PMTs apply different techniques to prolong the lifetime. Hamamatsu's approach for their R10754X is a very thin protection layer of aluminium oxide between the 1st and the 2nd channel plate to stop feedback ions from hitting the PC. BINP creates an improved vacuum inside the tube and the MCP surfaces are scrubbed with electrons. In addition the PC is treated in vapors of antimony and cesium which seems to significantly improve its hardness against feedback ions.

A quite different technique is applied in the latest MCP-PMT prototype (XP85112) of Photonis. To reduce the outgassing of the lead glass MCPs, these are coated with a thin layer of a secondary electron emissive material directly on the pores using an atomic layer deposition (ALD) technique. Currently this seems to be the most promising approach to increase the lifetime of MCP-PMTs.

Results

Our group is presently in the process of simultaneously measuring the lifetimes of several types of MCP-PMTs of the 3 manufacturers listed above. The illumination of all tubes is done in parallel with an intensity comparable to that expected inside PANDA. In time intervals of several days the quantum efficiencies are measured as a function of the wavelength; in addition, every several weeks a scan of the position dependence of the QE across the PC is done.

The current status is shown in Fig. 1, where the QE of all investigated MCP-PMTs is plotted as a function of the integrated anode charge. Obviously all of the latest models show a very significant improvement in the lifetime.

In Fig. 2 the same plots are shown for different wavelengths. At least for the XP85112 the QE behaves the same for all wavelengths still at 1 C/cm^2. This is different to former observations where aging caused the QE to drop faster for longer wavelengths than for shorter ones [3]. We see this as a positive sign that the tube will stand more charge.

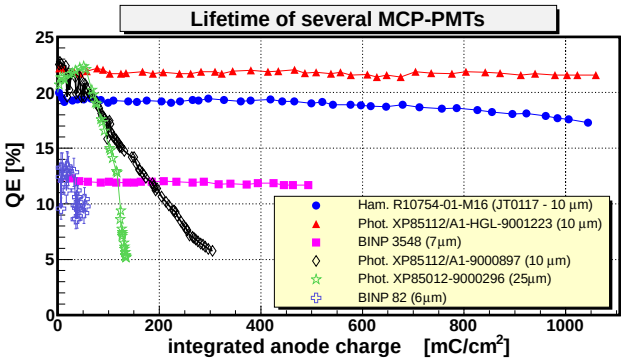

Figure 1: QE at 400 nm for old (open) and new generation (solid dots) MCP-PMTs as function of the anode charge.

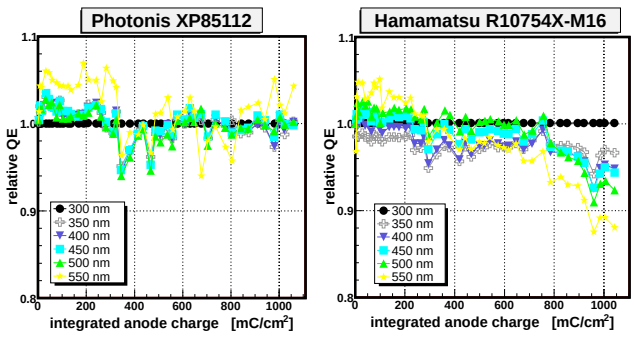

Figure 2: Relative QE for different wavelengths normalized to 300 nm for the XP85112 and R10754X MCP-PMTs.

References

[1] A. Lehmann et al., GSI Scientific Report 2010, p. 106.
[2] A. Lehmann et al., Nucl. Instr. and Meth. A639 (2011) 144.
[3] A. Lehmann et al., GSI Scientific Report 2009, p. 7.

Work supported by BMBF and GSI
† lehmann@physik.uni-erlangen.de

Optical Properties of Radiator Bar Prototypes for the PANDA Barrel DIRC*

R. Hohler[1,2], *G. Kalicy*[†1,2], *D. Lehmann*[1], *K. Peters*[1,2], *G. Schepers*[1], *C. Schwarz*[1], *and J. Schwiening*[1]
[1]GSI, Darmstadt, Germany; [2]Goethe Universität Frankfurt, Germany

One of the key requirements for the physics program of the PANDA experiment at FAIR is excellent charged particle identification (PID). The main system responsible for PID in the barrel part of the detector will be the Cherenkov counter DIRC (Detection of Internally Reflected Cherenkov light). In the PANDA Barrel DIRC [1] Cherenkov photons are generated by a charged particle traversing the synthetic fused silica radiator bar. A fraction of these photons are transmitted over long optical pathlengths with a large number of internal reflections before exiting the bar. An array of Micro-Channel Plate Photomultiplier Tubes measures the location and the arrival time of the Cherenkov photons.

The efficiency of the photon transport inside the radiator bar depends on the photon energy and the quality of the bar polish, in particular on the surface roughness, which can be determined from bulk attenuation and reflection coefficient measurements. A setup with motion-controlled elements, shown in Fig. 1, was designed and installed in a dark, temperature-stabilized clean room. The polarized laser beam enters the bar at Brewster angle to minimize the front surface loss and is internally reflected 15-50 times, depending on the bar orientation and length. Two photodiodes record the transmitted laser intensity T and correct for laser intensity fluctuations. The coefficient of total internal reflection ($\mathcal{R}$) can be calculated as:

$$T = \mathcal{R}^N \cdot \exp\left(-\frac{L}{\Lambda}\right),$$

where N is the number of internal reflection inside the quartz bar, Λ the attenuation length of fused silica (determined in a separate measurement in the same setup), and L the optical pathlength of the laser beam. The probability of the reflection loss $(1-\mathcal{R})$ for a single reflection is related to the roughness σ of the radiator by the scalar scattering theory [2]:

$$1-\mathcal{R} \approx \left(\frac{4\pi \cdot \sigma \cdot cos(\Theta) \cdot n}{\lambda}\right)^2 \quad \text{for} \quad \sigma \ll \lambda,$$

where n the refractive index, λ the wavelength, and Θ is the reflection angle within the radiator bar.

Previous measurements [3], performed in a more compact setup using lasers with three different wavelengths, demonstrated good agreement with the scalar scattering theory (see Figure 2). The new setup, completed in late 2011, is capable of measuring longer bars, up to 2.5 m length, as well as wider radiator plates. Furthermore, a UV-laser (266 nm) is added to increase the lever arm for the comparison between data and theory. The resulting measurement is expected to be more sensitive to bar imperfections, such as sub-surface damage, providing important information about the bar production process. New prototype DIRC bars and plates from several manufacturers, using different polishing techniques, will be measured in the setup in 2012.

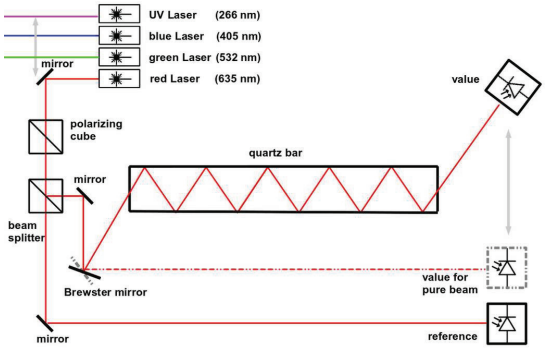

Figure 1: Schematic illustration of the optical setup used to measure the coefficient of total internal reflection of DIRC bars.

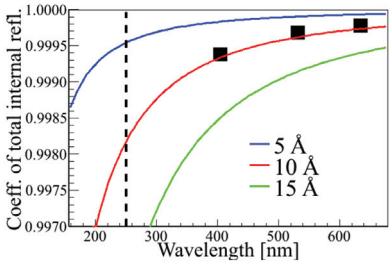

Figure 2: Coefficient of total internal reflection as function of the wavelength. Measured results [3] for a bar produced by Schott Lithotec are compared to predictions from scalar scattering theory for different surface roughness values. The dashed line indicates the wavelength of the new UV laser.

References

[1] J. Schwiening et al., Nucl. Instr. and Meth. Phys. Res. Sect. A 639 (2011) 315.

[2] P. Beckmann and A. Spizzichino, "The Scattering of Electromagnetic Waves from Rough Surfaces", Pergamon (1963) 1. Edition

[3] R. Hohler, "Prototyp-Radiatoren eines Barrel-DIRC für das PANDA-Experiment", Ph.D. thesis, GSI (2011).

* Work supported by HGS-HIRe, HIC for FAIR, EU FP6 grant, contract number 515873, DIRACsecondary-Beams, and EU FP7 grant, contract number 227431, HadronPhysics2.

† G.Kalicy@gsi.de

Beam Test of a PANDA Barrel DIRC Prototype*

A. Gerhardt[1], *K. Götzen*[1], *R. Hohler*[1,2], *G. Kalicy*[1,2], *D. Lehmann*[1], *M. Patsyuk*[1,2], *K. Peters*[1,2], *G. Schepers*[1], *C. Schwarz*[1], *J. Schwiening*[†1], *and M. Zühlsdorf*[1,2]

[1]GSI, Darmstadt, Germany; [2]Goethe Universität Frankfurt, Germany

Particle identification (PID) will play a crucial role in reaching the physics goals of the PANDA experiment at FAIR. The charged PID in the barrel region of the target spectrometer (polar angles between 22° and 140°) needs a thin detector operating in a 1-2 T magnetic field, capable of pion-kaon separation with more than three standard deviations for momenta between 0.5 and 3.5 GeV/c. A Ring Imaging Cherenkov detector using the DIRC (Detection of Internally Reflected Cherenkov light) principle is an excellent match to those requirements.

The PANDA Barrel DIRC design [1] is based on the successful *BABAR* DIRC [2] detector with several important improvements, such as focusing optics, fast timing, and a compact expansion region. Several key aspects of the current design were implemented in a prototype and tested in the summer of 2011 in hadronic particle beams at GSI and at CERN.

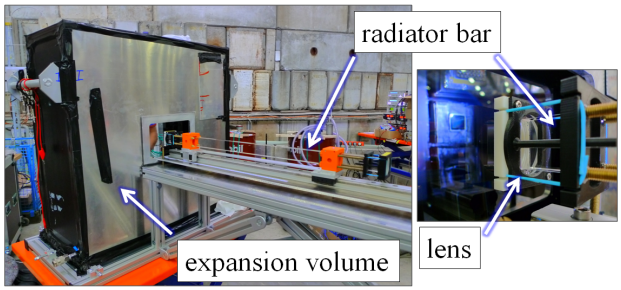

Figure 1: Views of the prototype in the T9 area at CERN.

The prototype is shown in Figure 1. A synthetic fused silica bar with the dimensions $17 \times 35 \times 800$ mm^3 with a spherical lens attached to one end and a front-coated mirror attached to the other end was placed into a light-tight container. An expansion volume with a depth of 30 cm, located about 1 cm from the lens, was filled with Marcol 82 mineral oil and an array of sensors, including Micro-Channel Plate Photomultiplier Tubes (MCP-PMTs) and Silicon Photomultipliers, was placed against the back window of the oil tank. The data acquisition[1] for 640 detector channels was performed using the HADES trigger and readout board (TRB) [3] with the TOF add-on, combining the NINO chip and CERN HPTDC to provide timing with a resolution of 98 ps per count and pulse height information from charge-to-width.

The setup was placed into a 1.7 GeV/c momentum pion beam at GSI and into a mixed hadron beam at the T9 area of the CERN PS with momenta adjustable between 1.5 and 10 GeV/c. The trigger was provided by two scintillator counters and the sensors were calibrated with a 405 nm Pi-Las laser diode providing light pulses with 25ps FWHM timing resolution. A total of about 130M triggers were recorded in several configurations. Lenses with and without anti-reflective coating were tested in combination with bars produced from different manufacturers. The angle between the particle beam and the bar was varied between -30° and +30° and the interception point between beam and bar was adjusted by some 30 cm along the long bar axis.

Figure 2 shows the distribution of hits per MCP-PMT pixel for a 19.5° incident angle between bar and hadron beam at CERN. Two ring segment images, symmetric around the radiator bar location, can be seen, consistent with the expected Cherenkov ring image for 10 GeV/c pions, calculated from simulation, shown as points. Detailed analysis of the 2011 data set, including the determination of the Cherenkov angle resolution for each prototype and beam configuration, is ongoing. The next test beam campaign is planned for 2012 to study additional design options. These include the use of wide radiator plates instead of narrow bars and of a solid fused silica expansion volume replacing the oil tank.

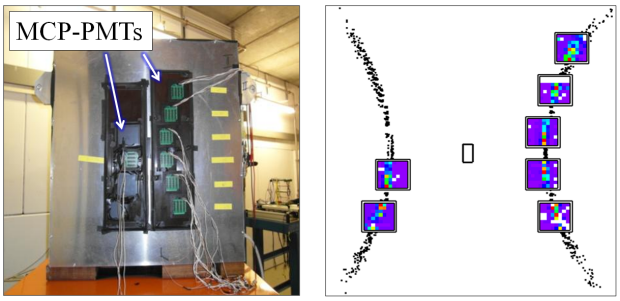

Figure 2: Back view of the imaging plane showing the MCP-PMT locations (left) and number of detected photoelectrons per MCP-PMT pixel (right). The observed occupancy is compared to the expected pattern from simulation.

References

[1] J. Schwiening et al., Nucl. Instr. and Meth. Phys. Res. Sect. A 639 (2011) 315.

[2] I. Adam et al., Nucl. Instr. and Meth. Phys. Res. Sect. A 538 (2005) 281.

[3] I. Fröhlich, et al., IEEE Trans. Nucl. Sci. 55 59 (2008).

*Work supported by HGS-HIRe, HIC for FAIR, EU FP6 grant, contract number 515873, DIRACsecondary-Beams, and EU FP7 grant, contract number 227431, HadronPhysics2.

† J.Schwiening@gsi.de

[1]We would like to thank M. Palka and M. Traxler for their help with the data acquisition system.

Simulation and Reconstruction of the PANDA Barrel DIRC*

K. Götzen[1], *G. Kalicy*[1,2], *M. Patsyuk*[†1,2], *K. Peters*[1,2], *C. Schwarz*[1], *J. Schwiening*[1], *and M. Zühlsdorf*[1,2]

[1]GSI, Darmstadt, Germany; [2]Goethe Universität Frankfurt, Germany

A compact ring imaging detector is being developed to meet the requirements for charged particle identification for the PANDA experiment at FAIR. It will cover the barrel region (polar angles between $22°$ and $140°$) of the PANDA multi-purpose detector, which will perform precise spectroscopy of hadronic states in order to gain deeper understanding of the nature of strong interaction. To distinguish between charged pions and kaons for momenta between $0.5 - 3.5$ GeV/c a detector using the DIRC (Detection of Internally Reflected Cherenkov light) principle [1] will be used, which was first successfully implemented in the *BABAR* DIRC [2]. The design of the PANDA Barrel DIRC is based on the *BABAR* DIRC with some important improvements, such as fast photon timing, focusing optics, and a compact expansion volume.

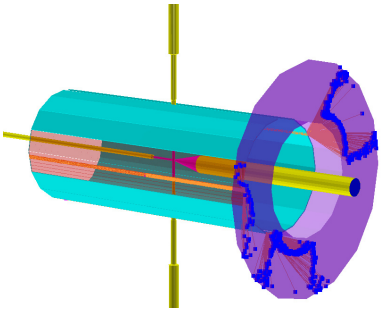

Figure 1: Display of a simulated event with three tracks in the PANDA Barrel DIRC detector.

The current PANDA Barrel DIRC design [3], shown in Fig. 1, uses 80 fused silica radiator bars (1.7 cm x 3.2 cm x 250 cm) placed in 16 bar boxes located at the radial distance of 47.6 cm around the beam pipe. Cherenkov photons, produced by a charged particle traversing the radiator bar, propagate inside the bar via total internal reflection. A mirror at the forward end of the bar reflects photons towards the readout end where they are focused through a lens on the backplane of a 30 cm-depth expansion volume filled with mineral oil. An array of Micro-Channel Plate Photomultiplier Tubes is placed in the focal plane to measure the photon arrival time with a precision of about 100 ps.

Simulation of the detector within Geant4 is an essential aspect of the R&D of the PANDA Barrel DIRC, which focuses on cost optimisation and performance improvement. Several design options were implemented in the simulation, so that they can be compared in terms of single photon Cherenkov angle resolution and photon yield per particle. The use of wide plates instead of bars offers possible production cost saving and a prism attached to the end of the bar could reduce the number of photon detectors and electronic channels. The thickness of the bar influences the resolution and photon yield as well as the performance of the calorimeter system surrounding the DIRC.

To estimate the detector performance, a reconstruction method was developed. It is based on a proven *BABAR* DIRC algorithm [2]. The photon direction vector for the combination of a given pixel and radiator bar is taken from a look-up table, determined from simulation, and combined with the direction of the charged particle to determine the Cherenkov angle.

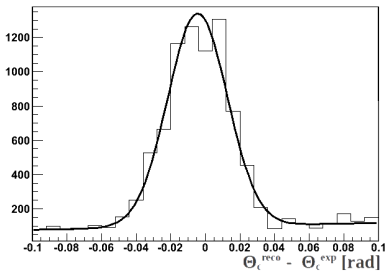

Figure 2: Difference between the reconstructed and expected Cherenkov angle per photon for a simplified DIRC geometry.

As a proof of principle the reconstruction was applied to a simplified DIRC geometry without a focusing system, where the fused silica bars were directly attached to the expansion volume. The reconstructed value of the single photon Cherenkov angle resolution, shown in Fig. 2, agrees with expectation. However, to be able to compare different design options a deeper study of the factors affecting the detector resolution, such as impact of ambiguities due to the photon reflections inside the bar or correlation between the track polar angle and the location of the photons hit pattern, is required.

References

[1] B.N. Ratcliff, SLAC-PUB-5946 (1992), SLAC-PUB-6047 (1993); P.Coyle et al., Nucl. Instr. and Meth. Phys. Res. Sect. A 343 (1994) 292.

[2] I. Adam et al., Nucl. Instr. and Meth. Phys. Res. Sect. A 538 (2005) 281.

[3] J. Schwiening, Nucl. Instr. and Meth. Phys. Res. Sect. A 639 (2011) 315.

* Work supported by HGS-HIRe, HIC for FAIR, EU FP6 grant, contract number 515873, DIRACsecondary-Beams, and EU FP7 grant, contract number 227431, HadronPhysics2.

† M.Patsyuk@gsi.de

Conceptual Design of a 3D Disc DIRC for the PANDA Experiment*

M. Düren[†1], *I. Brodski*[1], *K. Föhl*[1], *A. Hayrapetyan*[1], *P. Koch*[1], *K. Kreutzfeldt*[1], *B. Kröck*[1], *O. Merle*[1], *D. Mühlheim*[1], *J. Rieke*[1], *M. Sporleder* [1], *H. Stenzel*[1], *and M. Zühlsdorf*[1]

[1]II. Phys. Inst., Justus-Liebig-Universität, Heinrich-Buff-Ring 16, 35392 Giessen, Germany

A 3D Disc DIRC for PANDA

The scientific programme of PANDA, particularly the precision hadron spectroscopy in the charmonium region, requires high-performing particle identification (PID) in the entire detector phase space. A DIRC-type PID detector [1], allowing a very compact design, is proposed for the forward endcap region of the PANDA target spectrometer. Cherenkov light is internally reflected inside the disc-shaped radiator to the photon sensors at the disc rim. The 3D design combines the angle-to-time conversion of the time-of-propagation (TOP) technique [2] with the angle-to-position technique of the focussing light guide design [3].

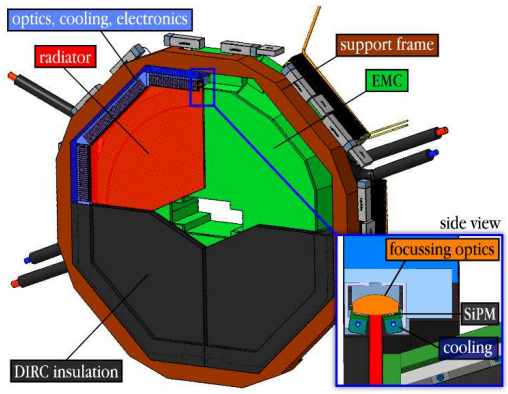

Figure 1: The disc DIRC consists of four independent quadrants. The 3D design uses small focussing light guides, attached to the rim of the plate, that focus the Cherenkov light onto fast photon detectors.

Prototyping a 3D-Disc-DIRC

A first 3D disc DIRC prototype has been tested in 2011 [4]. One-sided focussing light guides have been chosen in this test to match the shape of the available photon sensors. Figure 2 shows the radiator disc being set up for a testbeam experiment at DESY. It was equipped with five lightguides. Because of cost reasons the radiator was made of Borofloat glass and the light guides of acrylic glass. At PANDA, the optical elements will be made from fused silica because of the required radiation hardness.

A scan of the incident angle of the electron test beam that crosses the DIRC disc is shown in Fig. 3. The Cherenkov

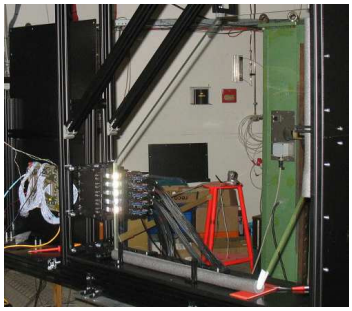

Figure 2: A quarter disc radiator is equipped with five small light guides on the rim.

cone is projected by the five light guides onto the photon sensors and shows up as a slightly curved line. The position of the line on the photon sensors is a function of the incident angle and will be used to determine the Cherenkov angle.

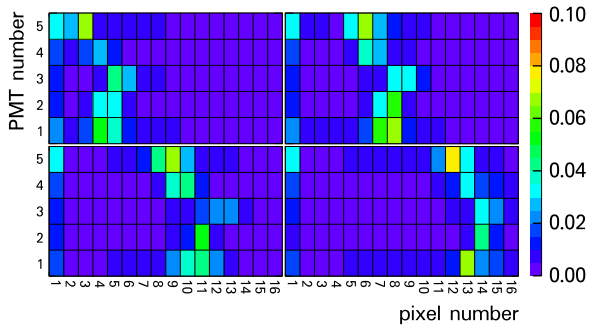

Figure 3: First preliminary results of the image of the Cherenkov cone that is projected onto the photon sensors by the light guides. The four panels show an angular scan where the image of the cone moves from left to right across the 1 mm wide pixels in four steps.

References

[1] The BaBar-DIRC Collaboration, I. Adam *et al.*, The DIRC Particle Identification System for the BABAR Experiment, Nucl. Instr. and Meth. A **538** (2005) 281

[2] M. Düren *et al.*, The Panda time-of-propagation Disc DIRC, 2009 JINST 4 P12013

[3] K. Föhl *et al.*, The focussing light guide disc DIRC design, 2009 JINST 4 P11026

[4] M. Düren *et al.*, The Panda 3D Disc DIRC, submitted for publication in JINST (2012)

* Work supported by GSI, BMBF and HIC for FAIR

† Michael.Dueren@uni-giessen.de

Scintillating Tiles as Timing Detector for PANDA*

C.Schwarz[1,#], S. Diehl[2], K. Goetzen[1], H. Orth[1], G. Schepers[1], L. Schmitt[1], and A. Wilms[1,3]

[1]GSI, Darmstadt, Germany; [2]JLU, Gießen, Germany, [3]GU, Frankfurt a.M., Germany

The PANDA experiment at FAIR uses in the target spectrometer a timing barrel for PID of slow charged particles, for detection of γ-conversion in front of the EMC, and for event timing. A new detector in place of the barrel time-of-flight detector is proposed [1]. The main criticism of previous concepts of barrel time-of-flight detectors is the material budget deteriorating the performance of the lead tungstate crystal calorimeter. The available space in radial direction is extremely tight so that some detector concepts have problems to fit in. The concept presented here takes the optimization of material and thickness to the extreme implementing a timing detector with less than 2% of a radiation length and less than 2 cm radial thickness including readout and mechanics. This detector is based on small scintillator tiles (SciTils) read out by silicon photomultipliers (SiPM). A time resolution of better than 100 ps should be achieved by the system to allow for good time-of-flight measurement and other timing applications. Due to the lack of a start detector relative timing will be used.

The new timing detector concept is based on small 28.5 x 28.5 x 5 mm^3 thin plastic scintillator tiles coupled directly to two SiPMs with excellent time resolution to read out the scintillation light. A minimum ionizing particle generates approximately 10000 photons across the tile thickness of which about 100 are directly measured by the SiPMs. This allows a threshold well above the intrinsic noise of the SiPMs.

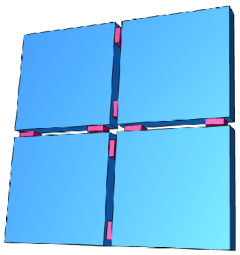

Figure 1: Quad module with four SciTils. Each tile is read out by two SiPM.

The tiles are arranged as quad tile module (Fig. 1) with a readout PCB containing one 8-channel readout ASIC and a data transfer chip. A super module contains 90 quad tiles and 16 super modules form a barrel (Fig. 2).

A prototype with a size of 20 x 20 x 5 mm^3 was studied with a ^{90}Sr-source. It was equipped with four

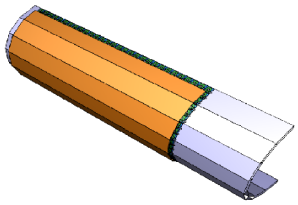

Figure 2: An entire SciTil half barrel composed of 8 super-modules.

SiPM from Hamamatsu [2] (2xS10931-050P, 2x S10362-33-050C). The signals were amplified by preamplifiers of PHOTONIQUE [3]. The achieved time resolution for the SiPMs with the fast Amp611 and the slow Amp604 preamplifiers is shown in Fig 3. The time jitter of the remaining electronics was subtracted and the timing was done with the first arriving photon. The best time resolutions are observed by the slower preamplifiers which have a significantly higher gain.

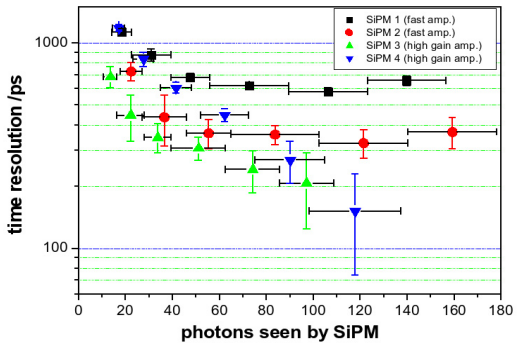

Fig. 3: Time resolutions for SiPMs read out by fast and slow preamplifiers as function of the observed photon number.

References

[1] K. Goetzen et al., Proposal for a Scintillator Tile Hodoscope for PANDA, http://panda-wiki.gsi.de/pub/Tof/SciTil/scitil.pdf

[2] Hamamatsu Photonics, http://www.hamamatsu.com

[3] Photonique SA, http://photonique.ch/

* Work supported EU FP6 grant, contract number 515873, DIRACsecondary-Beams, and EU FP7 grant, contract number 227431, HadronPhysics2.

#c.schwarz@gsi.de

Development of a prototype for the $\overline{\text{P}}$ANDA-EMC*

A. Aab[1], *M. Albrecht*[1], *J. Becker*[1], *A. Csapó*[1], *F. Feldbauer*[1], *M. Fink*[1], *P. Friedel*[1], *F.-H. Heinsius*[1], *T. Held*[1], *L. Klask*[1], *H. Koch*[1], *B. Kopf*[1], *S. Leiber*[1], *M. Leyhe*[1], *C. Motzko*[1], *M. Pelizäus*[1,2], *J. Pychy*[1], *B. Roth*[1], *T. Schröder*[1], *J. Schulze*[†1], *C. Sowa*[1], *M. Steinke*[1], *T. Triffterer*[1], *U. Wiedner*[1], *and J. Zhong*[1]

[1]Ruhr-Universität Bochum, Bochum, Germany; [2]University of Hawaii at Manoa, Honolulu, Hawaii, USA

The Proto192, a full-size prototype of the inner part of the forward endcap calorimeter [1] of the $\overline{\text{P}}$ANDA experiment (antiProton ANnihilation at DArmstadt), has been set up. It consists of 216 lead-tungstate crystals (6 % of the forward endcap calorimeter) read out by vacuum photo triodes, tetrodes and avalanche photo diodes. The custom-made mechanical parts were produced until March 2011, and the process of setting the Proto192 up began.

The aluminium backplate, which is the backbone of the Proto192, has been mounted rotatable, so that it is possible to switch between measuring cosmic muons (with the crystals in vertical position) or particle beams from accelerators when in horizontal position. To ensure a flexible handling of the supply lines, support beams had to be built to hold cables and electronics like the THMP (Temperature and Humidity Monitoring Board for $\overline{\text{P}}$ANDA) [2], the light pulser and the flow control system for dried gas flushing. To block the incoming heat through the support structure, the suspension material has be chosen as glass-fiber reinforced plastic, featuring high mechanical rigidity and low thermal conductivity.

The feed-through of signals, high/low voltage and sensors is achieved by using printed circuit boards (PCB) glued into adapter pieces which can be mounted to a frame behind the backplate to ensure vacuum tightness. This vacuum tightness is needed due to the problem of condensation on cold parts inside the Proto192. PCBs feature a high signal density and low thermal conductivity to reduce the heat flow from the warm outside into the cooled prototype.

The two cooling circuits, one in front and one at the backplate, have been engineered and mounted. This is important, because the Proto192 has to be cooled to -25 °C to boost the light yield of the lead tungstate scintillator by about a factor of 4. As an isolation against the ambient temperature, vacuum insulation panels are used to provide a stable environment. Vacuum insulation panels feature a very low thermal conductivity, being an order of magnitude lower than conventional isolation material consisting of rigid foam.

The development of thin temperature sensors consisting of a sandwich of platinum wire between two Kapton foils has been successfully pursued; about a hundred sensors have been produced, calibrated and built into the Proto192. The calibration method ensures a maxium measurement uncertainty of less than 0.05 °C and takes place for 15 sensors at the same time, taking less than 30 hours.

To test the Proto192, feasibility studies under realistic conditions have been performed using test beams at two facilities: positron and muon beams at CERN, Geneva, at the end of August 2011 and photons at ELSA, Bonn. The mechanical parts have proven to be feasible and temperature stability and control system tests are still ongoing in Bochum. First results show high spatial and temporal stability of the crystals' temperature.

On-going physics data analyses investigate the usability of different types of available photodetectors. Furthermore, analyses of energy and spatial resolution as well as rate dependencies of the photodetectors are studied in more detail while preparing for the next test beam at MAMI, Mainz.

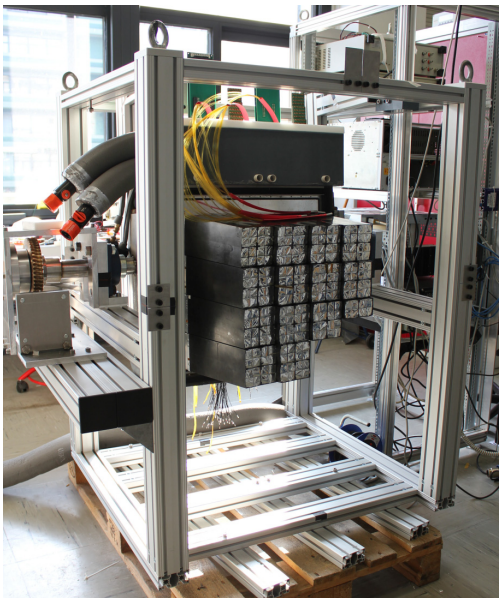

Figure 1: The prototype Proto192 before mounting the front hull

References

[1] PANDA-Collaboration, EMC Technical Design Report, 2008

[2] A. Aab et al., Development of the Slow Control for the PANDA-EMC, GSI Scientific Report, 2012

* Supported by GSI F+E and BMBF Contract 06BO9013

† e-mail: jansch@ep1.rub.de

Development of the Slow Control for the PANDA-EMC*

A. Aab[1], *M. Albrecht*[1], *J. Becker*[1], *F. Feldbauer*[†1], *M. Fink*[1], *P. Friedel*[1], *F.-H. Heinsius*[1], *T. Held*[1], *L. Klask*[1], *H. Koch*[1], *B. Kolb*[2], *B. Kopf*[1], *S. Leiber*[1], *M. Leyhe*[1], *C. Motzko*[1], *M. Peliz̈aus*[1,3], *D. Protopopescu*[4], *J. Pychy*[1], *B. Roth*[1], *T. Schröder*[1], *J. Schulze*[1], *C. Sowa*[1], *M. Steinke*[1], *T. Triffterer*[1], *U. Wiedner*[1], *J. Zhong*[1], *and P. Zumbruch*[2]

[1]Ruhr-Universität Bochum, Bochum, Germany; [2]GSI, Darmstadt, Germany; [3]University of Hawaii at Manoa, Honolulu, Hawaii, USA; [4]University of Glasgow, Glasgow, UK

Introduction

The Slow Control of the PANDA experiment will be based on EPICS (Experimental Physics and Industrial Control System). EPICS is a set of open source software tools, libraries and applications used worldwide to create distributed real-time control systems for scientific instruments and industrial applications [1].

For the PANDA-EMC the slow control will monitor the temperature, humidity and pressure inside the calorimeter as well as control the power supplies for the read out electronics, crates and the cooling system.

The Proto192 EMC Endcap Prototype

A full-size prototype of the inner part of the forward endcap of the PANDA-EMC, the Proto192, has been set up in Bochum and tested at CERN and ELSA this year [2]. Since EPICS control systems are freely scalable, the Proto192 can also be seen as a prototype for the slow control of the PANDA-EMC.

Three independent cooling circuits, one for front cooling, one for the main cooling at the backplate and one for dried air cooling, are used to achieve a temperature of $-25\,^{\circ}\mathrm{C}$.

For the temperature and humidity monitoring inside the prototype the THMP (Temperature and Humidity Monitoring Board for PANDA) was developed. The THMP is a modular read out system consisting of a mainboard and up to eight piggyback boards. There exist two kinds of piggyback boards: one for temperature sensors and one for humidity and pressure sensors. This design allows variable numbers of temperature and humidity/pressure sensors, respectively.

Inside the prototype 130 temperature and 8 humidity sensors are mounted. Also 56 HV channels are controlled and monitored by the slow control.

For the CAN communication the HadCon was used as a working station running an EPICS IOC. The HadCon is a general purpose I/O module for SlowControl and small DAQ-systems developed by the HADES collaboration [3].

* Work supported by BMBF and EU

† E-mail: florian@ep1.ruhr-uni-bochum.de

Further Development

For the PANDA Slow Control System it is planned to build a PANDA-specific version of Control System Studio (CSS), a toolkit based on Eclipse and Java [4], as user interface for the EPICS controll system. CSS provides a GUI editor, archiving and alarm handling tools.

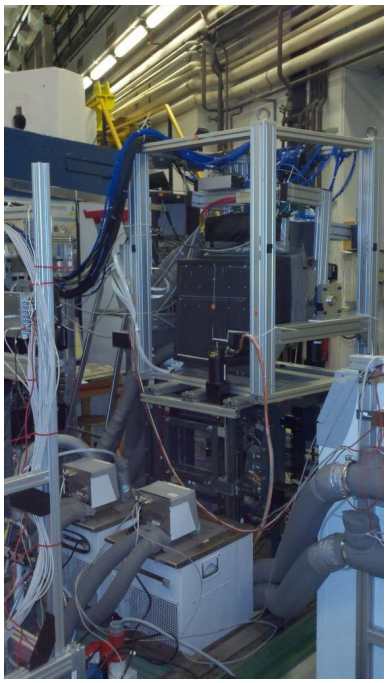

Figure 1: Proto192 at ELSA. The prototype is mounted on top of a x-y-table. In front of the table the two small chillers for the air and front cooling can be seen. At the lower right the chiller for the main cooling is located.

References

[1] D. Protopopescu et al., “The Slow Controls System of PANDA”, GSI Scientific Report 2010, p. 116

[2] A. Aab et al., “Development of a prototype for the PANDA-EMC”, GSI Scientific Report 2011

[3] HadCon wiki page, `http://wiki.gsi.de/Epics/HadCon`, Jan. 6, 2012

[4] CSS project page, `http://cs-studio.sourceforge.net`, Jan. 6, 2012

Online calibration of the PANDA EMC and Analysis of Crystal Barrel at LEAR data*

B. Roth†[1], *A. Aab*[1], *M. Albrecht*[1], *J. Becker*[1], *A. Csapó*[1], *F. Feldbauer*[1], *M. Fink*[1], *P. Friedel*[1], *F.-H. Heinsius*[1], *T. Held*[1], *L. Klask*[1], *H. Koch*[1], *B. Kopf*[1], *S. Leiber*[1], *M. Leyhe*[1], *C. Motzko*[1], *M. Pelizäus*[1], *J. Pychy*[1], *T. Schröder*[1], *J. Schulze*[1], *C. Sowa*[1], *M. Steinke*[1], *T. Triffterer*[1], *U. Wiedner*[1], *and J. Zhong*[1]

[1]Ruhr University, Bochum, Germany

Calibrating the EMC of PANDA

For the PANDA experiment [1, 2] we have developed an algorithm to calibrate the electromagnetic calorimeter. This algorithm is designed for a frequent online calibration at run time. Therefore performance is a very important issue.

The calibration itself is using the π^0 peak in an invariant $\gamma\gamma$ spectrum as reference signal. Such a spectrum is generated for each crystal in the electromagnetic calorimeter during run time of PANDA. Therefore for each crystal multi γ events, with hits in this crystal, are accumulated. In the next step the resulting distributions are fitted to extract the π^0 peak positions. Therefore we have implemented interfaces to the minimizers Minuit, Minuit2, and Geneva. Minuit2 and Geneva are both multithreaded, which is very important for an accurate performance.

Another issue considering the performance of the algorithm was I/O. As a $\gamma\gamma$ distribution with several hundred entries is needed for each crystal, an accurate handling of this large-scaled data set is essential. For this we have implemented a database connection as storage back end. We were able to demonstrate the successful usage of the minimizer and the database with very accurate performance, using a Monte Carlo generated data set.

For testing purposes we have started with porting this calibration algorithm to the older Crystal Barrel offline analysis software from LEAR [3]. After doing so, we will be able to verify this software on real data, with the aim to also improve the available calibration of this data.

Meson spectroscopy

Furthermore we studied several decay chains in Antiproton Proton annihilation with the intention to find exotic states in meson spectroscopy. The used data was taken from the Crystal Barrel experiment at the LEAR storage ring, which is available for beam momenta between 900 MeV/c up to 1800 MeV/c. The final states considered are two neutral chains ($8\,\gamma$, and $10\,\gamma$), and corresponding charged chains ($\pi^+\,\pi^-\,\eta$, and $\pi^+\,\pi^-\,2\pi^0\,\eta$). The main emphasis of this analysis is the $\eta(1405)$, a potential exotic state, decaying to $\eta\,\pi\,\pi$ (see fig. 1), but also the $\pi_1(1600)$, another potential exotic state, was taken into account.

Besides this analysis the final states $\eta\,\pi^+\,\pi^-$, with η decaying to $\gamma\,\gamma$ and $2\pi^0$, were also studied. Especially the first one with its high statistics and low signal to background ratio delivers an excellent opportunity for a complete partial wave analysis. The work on this is already in progress and will also deliver a chance for testing the PANDA PWA software, which is being developed in parallel.

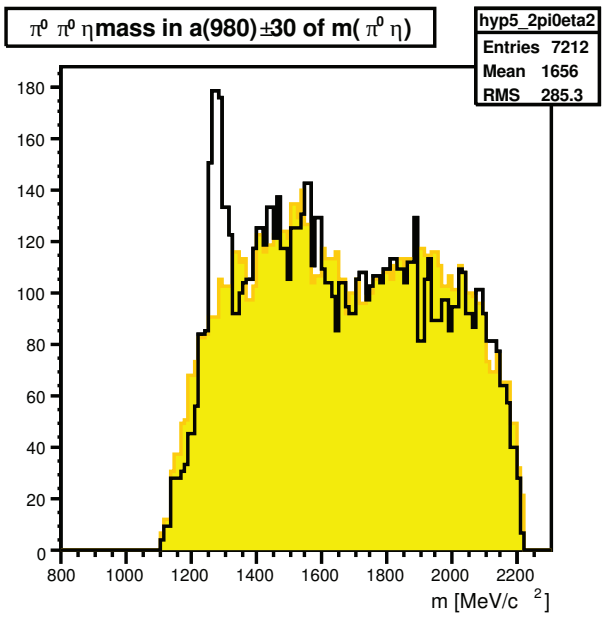

Figure 1: $\pi^0\,\pi^0\,\eta$ invariant mass of the $8\,\gamma$ final state in the $a(980)\;\rightarrow\;\pi^0\,\eta$ band at a $\bar{p}$ beam momentum of 1800 MeV/c . The acceptance is underlaid in shaded mode.

References

[1] M. F. M. Lutz *et al.* [PANDA Collaboration], "Technical Progress Report for PANDA", GSI Feb 2005

[2] M. F. M. Lutz *et al.* [PANDA Collaboration], "Physics Performance Report for PANDA: Strong Interaction Studies with Antiprotons", Mar 2009, arXiv:0903.3905 [hep-ex].

[3] E. Aker *et al.* [Crystal Barrel Collaboration], "The Crystal Barrel spectrometer at LEAR", Nucl. Instrum. Meth. A **321** (1992) 69.

* Work supported by EU, EURONS contract No. 506065.

† Email: bernhard@ep1.rub.de

Fast Monte Carlo simulations for physics processes involved in the HypHI project

C.Rappold[*1], *O. Borodina*[1,2], *V. Bozkurt*[1], *E. Kim*[1], *F. Maas*[1,2], *S. Minami*[1], *D. Nakajima*[1,4,5], *and T.R. Saito*[1,2]

[1]GSI, Darmstadt, Germany; [2]Mainz University, Mainz, Germany; [3]KEK, Tsukuba, Japan; [4]Tokyo University, Tokyo, Japan

The first experiment of the HypHI collaboration aimed to demonstrate the feasibility of the hypernuclear spectroscopy by means of heavy ion beam induced reactions [1]. With the on-going data analysis of phase 0 experiment, more physics simulations have been requested in order to reproduce experimental observations. A fast Monte Carlo simulation code has been employed to allow a fast feedback loop between the simulation and the experimental data analysis. The main goal of this simulation code was to estimate possible contribution from physics processes which can be involved in collisions of ^{6}Li beam nucleus at 2AGeV with a ^{12}C target nucleus. The processes of interest are mainly the 2-body or 3-body decay of hypernucleus which could be produced in those collisions ($^{3}_{\Lambda}$H, $^{4}_{\Lambda}$H, $^{4}_{\Lambda}$He, $^{5}_{\Lambda}$He, $^{6}_{\Lambda}$He) and could contribute into miss-recontruction of another hypernucleus. First of all, the probability density functions (pdf) of the kinematic observable, p_t, η, φ of produced hypernuclei from UrQMD and GiBUU collision simulations [1, 2] are used as input, in order to reproduce the shape of the phase space of the hypernuclei production. If the pdfs for a species was not available in the output of the UrQMD or BiGUU simulation, the pdfs from the closest species are used to obtain a rough estimation of its physical properties.

The simulation of a specific decay is then calculated via the phase space decay class available in ROOT [3]. Two-body, three-body decay and two-body decay chain have been used. After the phase space decay calculation, two options are then available : either this calculation output is used directly via event weighting, calculated from the geometrical acceptance and reconstruction efficiency, or it is propagated inside the geometry in order to obtained digitized hits on the detectors. Those digitized hits are obtained by smearing out the hit information with known position-, energy- and time resolutions of each detector. In the case of the three-body decay, theoretical evidences show that the 3-body mesonic weak decay would be a two-body decay chain, which would involve a first decay of a π^- and a excited state residue and the following decay of the residue into two smaller fragments. Thus two different processes are available for the study of three-body decay.

The event reconstruction has been investigated to show possible contributions of miss-reconstruction of different decay branches of hypernuclei mesonic weak decay. In the case of a three-body decay ($hyp_1 \rightarrow \pi^- + f_1 + f_2$), by missing one of the residual fragment (for example f_2) this decay branch might have a possible contribution into the background of the 2-body reconstruction ($hyp_2 \rightarrow \pi^- + f_1$). In the case of the 2-body decay ($hyp_1 \rightarrow \pi^- + f_1$), the miss particle identification of the fragment (f_1) into a fragment (f_2) might also have a contribution to the background of the reconstruction ($hyp_2 \rightarrow \pi^- + f_2$). All combination of those scenarios have been investigated. Table 1 summarizes the possible contribution of those scenarios in the 2-body reconstruction of $\Lambda \rightarrow$p+π^-, $^{3}_{\Lambda}$H $\rightarrow^{3}$He+π^- and $^{4}_{\Lambda}$H $\rightarrow^{4}$He+π^- respectively.

3-body decay	Λ (p+π^-)	$^{3}_{\Lambda}$H (^{3}He+π^-)	$^{4}_{\Lambda}$H (^{4}He+π^-)
$^{3}_{\Lambda}$H (p+d+π^-)	C	-	-
$^{4}_{\Lambda}$H (p+t+π^-)	C	-	-
$^{4}_{\Lambda}$H (^{3}He+n+π^-)	-	X	-
$^{4}_{\Lambda}$He (^{3}He+p+π^-)	-	X	-
$^{5}_{\Lambda}$He (^{4}He+p+π^-)	-	-	C
$^{6}_{\Lambda}$He (^{4}He+d+π^-)	-	-	X

Miss fragment PID	Λ (p+π^-)	$^{3}_{\Lambda}$H (^{3}He+π^-)	$^{4}_{\Lambda}$H (^{4}He+π^-)
Λ (p+π^-)	-	X	X
$^{3}_{\Lambda}$H (^{3}He+π^-)	X	-	X
$^{4}_{\Lambda}$H (^{4}He+π^-)	X	C	-

Table 1: Contribution of 3-body decay miss reconstruction and of 2-body decay miss fragment PID. (label C, X and - correspond to "may contribute", "do not contribute", "not related")

The full background signal estimation in the reconstruction of Λ, $^{3}_{\Lambda}$H, and $^{4}_{\Lambda}$H is on progress, using those possible sources of contribution in addition to the combinatorial background signal, evaluated by a mixing event procedure.

References

[1] Proposal of the HypHI Phase 0 experiment, the HypHI collaboration.

[2] T. Gaitanos, H. Lenske, and U. Mosel, Phys. Lett. B **675** (2009) 297.

[3] http://root.cern.ch/root/html/TGenPhaseSpace.html.

* c.rappold@gsi.de

Fine time calibration of the TOF+ detector

C.Rappold[*1], *O. Borodina*[1,2], *V. Bozkurt*[1], *E. Kim*[1], *F. Maas*[1,2], *D. Nakajima*[1,3,4], *and T.R. Saito*[1,2]

[1]GSI, Darmstadt, Germany; [2]Mainz University, Mainz, Germany; [3]KEK, Tsukuba, Japan; [4]Tokyo University, Tokyo, Japan

The data analysis of the first experiment of the HypHI collaboration aims to show the feasibility of the hypernuclear spectroscopy by means of heavy ion beam induced reactions. The phase 0 experiment was performed with a ^{6}Li beam at 2AGeV impinged on a stable ^{12}C target material. The main goal of the experiment was to produce, reconstruct and identify decay vertexes of Λ particle and ${}^{3}_{\Lambda}$H, ${}^{4}_{\Lambda}$H and ${}^{5}_{\Lambda}$He hypernuclei [1].

During the track reconstruction procedure, decoded detector hits are gathered into track candidates before the track fitting calculations based on Kalman Filter. The definitive particle identification is a important process after the track fitting in which potential decayed particles from hypernuclei have to be properly identified before the vertex and event reconstruction. A mis-determined particle identification would result in a wrong vertex reconstruction and so may participate for instance to the background signal of the invariant mass spectrum of the considered mother particle. The particle identification for positively charged particles uses both correlation between the estimated velocity β, the total energy deposit dE measured by the TOF+ detector and the momentum-over-charge ratio of particles. A precise enough correlation velocity-momentum is needed if a separation between proton, kaon and deuteron is wanted. The velocity of particle is estimated by time-of-light measurement between the recorded start time from TOF-start detector and the stop time provided by the scintillating bars of the TOF+ detector.

The time-of-flight measured via each TOF+ bar needs a fine time calibration in order to accumulate all the β-momentum correlation of each bar of the TOF+ detector. Moreover, it occurred that whether or not a cluster hit can be constructed over the hit measurement on the TOF+ detector, the calibration of time measurement of a bar does not have a same time offset. By considering all conditions of hit clusterization and all the bars, individual correlation velocity-momentum is possible for particle identification, however accumulating all of them can not be used without fine calibration.

The idea developed is to have an automatic procedure in order to estimate all the needed time offsets for a good accumulated velocity-momentum correlation. Two new observables are introduced to ease the procedure since the β-momentum curve are difficult to align automatically. For each bar and each clustering condition, the time-of-flight of a hypothetical kaon, proton and deuteron is calculated by assuming its mass $m_{k^+,p,d}$ in the formula $t_{k^+,p,d} = L/30 \cdot \sqrt{1 + m^2_{K^+,\,p,\,d}/P^2}$, in which P and L stand for the momentum and path length estimated in the track fitting process. Those hypothetical time-of-flights are then used to calculate the correlation $X = (t_d - t_{k^+})/2$ versus $Y = (t_d + 2 \cdot t_p + t_{k^+})/4 - \mathrm{TOF}_{\mathrm{measured}}$, in which $\mathrm{TOF}_{\mathrm{measured}}$ is the measured time-of-flight of particles. Thanks to this correlation the β-momentum curves of each particle species are transformed into 2D Guassian-like distributions.

For each distribution, corresponding to a well identified particle, the mean value of the projection over the Y variable are then deduced. A time offset δt are thus estimated over the $\mathrm{TOF}_{\mathrm{measured}}$ observable in order to align the obtained mean values of a identical bar. Fig. 1 shows those mean values of each particle of each bar id before (left panel) and after correction (right panel).

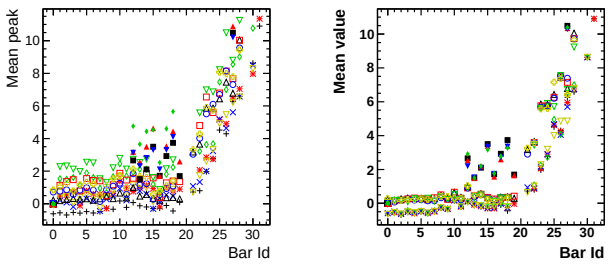

Figure 1: Mean value of Y-projected distribution of each type of clustering and each PID per bar id, before time correction (left panel) and after correction of the time-of-flight (right panel).

The method has been applied successfully to align all β-momentum correlations of each bar in order to identify possible K^+ mesons resulting from the strangeness production process like $NN \rightarrow N^{\star}N \rightarrow N\Lambda K$ induced by the nucleus-nucleus collision [2].

References

[1] Proposal of the HypHI Phase 0 experiment, the HypHI collaboration.

[2] Th. Gaitanos, H. Lenske, U. Mosel, Phys. Lett. B **675** (2009) 297.

* c.rappold@gsi.de

Improvements of the track reconstruction of the HypHI project with deterministic annealing filter

C.Rappold[*1], *O. Borodina*[1,2], *V. Bozkurt*[1], *E. Kim*[1], *F. Maas*[1,2], *D. Nakajima*[1,3,4], *and T.R. Saito*[1,2]

[1]GSI, Darmstadt, Germany; [2]Mainz University, Mainz, Germany; [3]KEK, Tsukuba, Japan; [4]Tokyo University, Tokyo, Japan

In the current data analysis code of phase 0 experiment, track reconstruction procedure is based on a Kalman Filter for fitting the track candidates [1]. Before the fitting procedure, track candidates are determined from a combinatorial track following method, distinct from the proposed Hough transform. It selects all hit combinations from the downstream and upstream parts of the setup which can fulfill several geometrical acceptance and tracking model considerations. It results in a mean value of 7.6 tracks candidates with a RMS value of 85.5 tracks. The distribution is shown in Fig.1 (left panel, highest values truncated). In some events, there are up to more than 1000 possible tracks. The fitting process of all of those track candidates takes a significant amount of cpu time to be completed.

The large number of the track candidates can be explained by the downstream pre-tracking, the combination of hits of the downstream part of the setup which involves 2 stations of fiber detectors and a drift chamber. The fiber detectors are made up of two bundles of scintillating fiber layers in order to measure precisely X- and Y-hit positions **??**. The drift chamber consists of 3 pair-plane layers providing hit measurement in stereo view **??**. The downstream pre-tracking then assembles 4 1D-layer measurement from the fiber detectors and maximum 6 1D-layer stereo measurement from the drift chamber. Several track candidates have a common Time-of-Flight wall (TOF+ or TFW detectors) hit measurement. Indeed, the pre-tracking can not achieve a proper selection between downstream tracks to connect to the real measurement obtained by the final TOF wall detectors.

The proposed idea to circumvent this drawback is to gather, into a new track, all track candidates which have those TOF wall hits in common. The associated hits of all those tracks would be then used to only fit the new track. The algorithm *"deterministic annealing filter"* (DAF) can be employed in this purpose [4, 5]. The DAF is a Kalman Filter in which observations are re-weighted. It consists of a propagation part similar to the standard Kalman Filter, with a competition between each hits of a same surface. On each detector surface, gathered hits from multiple track candidates constitute a proxy weighted mean hit calculated from the hit weights. Those hit weights are calculated and updated after each completed fit process and are based on the residual and covariance of considered hit. outliner hits can then be rejected when their associated weight are below a threshold. The weighting procedure includes alsoa annealing factor, because at the initial step weights can not be known. Annealing method avoids local minimum on the fitting process by an iterative procedure, giving a more robust fit. So the hits gathered from several track candidates can be used and the algorithm would sort out outliner hits which should not have been associated to the tracks. It thus reduces the inefficiency of the pre-tracking. Even though the DAF algorithm is slower in comparison to the classic Kalman Filter algorithm, the DAF fitting procedure is up to 8 times faster than current track fitting code on the full data set recorded during the phase 0 experiment. The drastic reduction of the track candidate is responsible for the decrease in the total processing time. The distribution of number of track candidates with this method is shown in Fig. 1 (right panel).

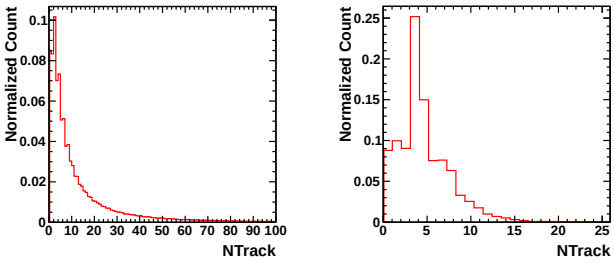

Figure 1: Distribution of the number of track candidates in the previous data analysis (left panel), and in the DAF procedure (right panel)

The full reconstruction including DAF is still in progress. It is also considered for the data analysis of the second data set from the experiment of March 2010 in which a ^{20}Ne beam was impinged on a ^{12}C target at an energy of 2 A GeV. Those ^{20}Ne+^{12}C collision produces a particle multiplicity much higher than ^{6}Li+^{12}C collision so the DAF algorithm will be needed in order to sustain the higher hit multiplicity and those track multiplicity.

References

[1] C.Rappold *et al*, Nucl. Instr. and Meth. A **662** (2010) 231.

[2] D. Nakajima *et al* Nucl. Instr. Meth. A **608** (2009) 287.

[3] T. Fukuda, *et al*, Nucl. Instr. Meth. A **361** (1995) 485.

[4] R. Frühwirth and A. Stradlie, Comp. Phys. Comm. **120** (1999) 197.

[5] A. Stradlie and R. Frühwirth, Nucl. Instr. and Meth. A **566** (2006) 157.

* c.rappold@gsi.de

Combined large-N_c and heavy-quark operator analysis of 2-body meson-baryon counterterms in the chiral Lagrangian with charmed mesons

M.F.M. Lutz[1], *D. Samart*[1,2], *and A. Semke*[1]
[1]GSI, Darmstadt, Germany; [2]SUT, Nakhon Ratchasima, Thailand

The main objective of the present study is to pave the way for systematic coupled-channel computations on open-charm baryon resonances. A first application of the chiral Lagrangian to s-wave baryon resonances considered the coupled-channel interaction of the Goldstone bosons with the ground-state baryons with open charm [1]. A rich spectrum of chiral excitations was obtained. The challenge of the open-charm sector is the possibility of charm-exchange reactions, where the charm of the baryon is transferred to the meson. A first phenomenological case study modeled the coupled-channel force by a t-channel exchange of vector mesons in the static limit [2, 3, 4]. Such a t-channel force recovers the leading order predictions of the chiral symmetry whenever Goldstone bosons are involved. It was shown in [2, 3, 5] that a rich spectrum of s- and d-wave baryon resonances is generated dynamically based on such a schematic ansatz. Two types of resonances are generated. The resonances of the first type are formed predominantly by the interaction of the Goldstone bosons with the open-charm baryon ground states, and the second type is a consequence of the coupled-channel interaction of the D mesons with the octet and decuplet baryons. For both types of resonances the exchange of the light vector mesons constitute the driving forces that generate the hadronic molecules. The exchange of charmed vector mesons leads to the typically small widths of the second type resonances.

While the interaction of the Goldstone bosons with any hadron is dictated by chiral symmetry, this is not true for the interaction of the D mesons with e.g. baryons. At leading order the D mesons interact with baryons via local counter terms that are undetermined by chiral symmetry. This resembles the situation encountered in chiral studies of the nucleon-nucleon force (for a review see e.g. [6]). Only the long-range part of the interaction is controlled by chiral interactions, the short range part needs to be parameterized in terms of a priori unknown contact terms. Needless to state that a reliable coupled-channel computation requires the consideration of both, the short-range and long-range forces.

The purpose of the present work is a systematic construction of the leading order contact terms for the interaction of the D mesons with the baryon octet and decuplet states. Though the chiral symmetry does not constraint such contact terms, there are significant correlations amongst the counter terms implied by the heavy-quark symmetry and the large-N_c limit of QCD. In the limit of a large charm quark mass the pseudoscalar and vector D mesons form a spin multiplet with degenerate properties [7]. Thus, a systematic coupled-channel computation in this limit requires the simultaneous consideration of pseudoscalar and vector D mesons. This leads necessarily to the presence of long-range t-channel forces. The transition of a vector D meson to a pseudoscalar D meson involves a Goldstone boson. Similarly, in the limit of a large number of colors in QCD the baryon octet and decuplet states form a super multiplet [8, 9]. This asks for the simultaneous consideration of the octet and decuplet baryons.

Following [10] we derived sum rules for the leading order two-body counter terms of the chiral Lagrangian as implied by a combined heavy-quark and large-N_c analysis. There are altogether 26 independent terms in the chiral Lagrangian with baryon octet and decuplet fields that contribute to the D and D^* meson baryon scattering process at chiral order Q^0.

At leading order in the heavy-quark expansion we find the relevance of 11 operators only. Additional sum rules were derived from the $1/N_c$ expansion. Combining both expansions, the number of unknown parameters is further reduced to 5. At present such sum rules can not be confronted directly with empirical information. They are useful constraints in establishing a systematic coupled-channel effective field theory for D meson baryon scattering beyond the threshold region.

References

[1] M.F.M. Lutz and E.E. Kolomeitsev, Nucl. Phys. **A 730** (2004) 110.

[2] J. Hofmann and M.F.M. Lutz, Nucl. Phys. **A 763** (2005) 90.

[3] J. Hofmann and M.F.M. Lutz, Nucl. Phys. **A 776** (2006) 17.

[4] L. Tolos, J. Schaffner-Bielich and A. Mishra, Phys. Rev. **C 70** (2004) 025203.

[5] C.E. Jimenez-Tejero, A. Ramos and I. Vidana, Phys. Rev. **C 80** (2009) 055206.

[6] E. Epelbaum, H.-W. Hammer and U.-G. Meiner, Rev. Mod. Phys. **81** (2009) 1773.

[7] H. Georgi, Phys.Lett. **B 240** (1990) 447.

[8] M.A. Luty and J. March-Russel, Nucl. Phys. **B 426** (1994) 71.

[9] R. F. Dashen, E. E. Jenkins and A. V. Manohar, Phys. Rev. **D 51**, (1995) 3697

[10] M.F.M. Lutz and A. Semke, Phys. Rev. **D 83** (2011) 034008.

[11] M.F.M. Lutz, D. Samart and A. Semke, Phys. Rev. **D 84** (2011) 096015.

On kinematical constraints in fermion-antifermion systems

S. Stoica[1], *M.F.M. Lutz*[2], *and O. Scholten*[3]
[1,3]KVI, Groningen, The Netherlands; [2]GSI, Darmstadt, Germany

We report on an important advance in the study of fermion-antifermion annihilation [1]. Though it is straight forward to introduce partial-wave scattering amplitudes in the helicity formalism of Jacob and Wick [2], it is a non-trivial task to derive transformations that lead to amplitudes that are kinematically unconstrained. Much work has gone in the derivation of kinematically unconstraint amplitudes for spin-$1/2$ scattering, see for example Ref. [3]. Such amplitudes have so far not been established for systems involving spin-$1/2$ and $3/2$ fermions. Kinematically unconstraint amplitudes are useful for partial-wave analysis or effective field theory approaches which consider the consequences of micro causality in terms of partial-wave dispersion-integral representations [4, 5, 6, 7]. Our results are relevant for the PANDA experiment at FAIR, where protons and antiprotons may be annihilated into systems of spin $3/2$ states.

In an initial step we decomposed the scattering amplitude into invariant functions. We considered all two-body reactions possible with spin-$1/2$ and $3/2$ fermions. For on-shell kinematics such a decomposition is not unique for systems involving particles with nonzero spin. We established bases of invariant functions that are free of kinematical constraints. Such amplitudes are expected to satisfy a Mandelstam dispersion-integral representation [9, 8].

In a second step we considered partial-wave projections of the scattering amplitude. We introduced partial-wave amplitudes with convenient analytic properties that justify the use of uncorrelated dispersion-integral relations. In particular we avoided cumbersome constraints relating different partial-wave amplitudes. Our starting point are the helicity partial-wave amplitudes. It is well known that different helicity partial-wave amplitudes are correlated at various kinematical conditions. This is readily seen if the helicity partial-wave amplitudes are expressed in terms of a basis of invariant functions. The kinematical constraints in the helicity partial-wave amplitudes were eliminated by means of nonunitary transformation matrices that map the initial, respectively final helicity sates to new covariant states. Since the mapping procedure is based on the exclusive use of on-shell matrix elements there is no model-dependent off-shell dependence in our considerations.

Furthermore we constructed a projector algebra that solves the two-body Bethe-Salpeter scattering equation in the limit of short range forces. It was pointed out that the existence and smoothness of such a projector basis is closely related to the existence of covariant partial-wave amplitudes. Explicit expressions for such projectors were presented for the two simplest reactions.

We established an efficient starting point for analyzing baryon-anti-baryon scattering in a covariant coupled-channel approach that takes into account the constraints set by micro-causality and coupled-channel unitarity.

References

[1] S. Stoica, M.F.M. Lutz and O. Scholten, Phys. Rev. **D 84**, 125001 (2011).

[2] M. Jacob and G. C. Wick, Ann. Phys. **7**, 404 (1959).

[3] G. Cohen-Tannoudji, A. Morel, and H. Navelet, Annals of Physics **46**, 239 (1968).

[4] G. F. Chew, M. L. Goldberger, F. E. Low, and Y. Nambu, Phys. Rev. **106**, 1345 (1957).

[5] N. Nakanishi, Phys. Rev. **126**, 1225 (1962).

[6] F. A. Berends, A. Donnachie, and D. L. Weaver, Nucl. Phys. **B4**, 1 (1967).

[7] A. Gasparyan and M. F. M. Lutz, Nucl. Phys. **A848**, 126 (2010), 1003.3426.

[8] J. S. Ball, Phys. Rev. **124**, 2014 (1961).

[9] S. Mandelstam, Phys. Rev. **112**, 1344 (1958).

Dynamical light vector mesons in low-energy scattering of Goldstone bosons

I.V. Danilkin[1,2], *L.I.R. Gil*[1], *and M.F.M. Lutz*[1]
[1]GSI, Darmstadt, Germany; [2]ITEP, Moscow, Russia

The study of Goldstone boson interactions is a time honored challenge in hadron physics. In the close-to-threshold region chiral perturbation theory (χPT) is applicable and leads to controlled results that are consistent with the empirical scattering data. Extensions of χPT, that implement coupled-channel unitarity by means of partial summation techniques, aim at a description of the scattering data at somewhat larger energies where meson resonances play an important role.

The purpose of our work is to explore the dynamic role of light vector mesons in a chiral Lagrangian and its implication for the two-body scattering of Goldstone bosons. The motivation for considering the light vector mesons as explicit degrees of freedom is twofold. First, we recall that the relevant counter terms of the chiral Lagrangian formulated in the absence of vector meson fields can be estimated by a resonance saturation mechanism where the light vector mesons appear to dominate [1]. Second, the light vector mesons play a particular role in the hadrogenesis conjecture [2]. Together with the Goldstone bosons, they are identified to be the relevant degrees of freedom that are expected to generate the meson spectrum of QCD with up, down and strange quarks.

The starting point of our study are partial-wave dispersion relations. Following [3] a generalized potential $U^J_{ab}(s)$ is constructed in the subthreshold region from the chiral Lagrangian and then analytically extrapolated to higher energies. We consider in particular the contribution of the exchange of the light vector mesons in the s-,t- and u-channel. The partial-wave scattering amplitudes $T^J_{ab}(s)$ are obtained as solutions of the non-linear integral equation

$$T^J_{ab}(s) = U^J_{ab}(s) + \sum_{c,d} \int_{\mu^2_{thr}}^{\infty} \frac{d\bar{s}}{\pi} \frac{s-\mu_M^2}{\bar{s}-\mu_M^2} \frac{T^J_{ac}(\bar{s})\,\rho^J_{cd}(\bar{s})\,T^{J*}_{db}(\bar{s})}{\bar{s}-s-i\epsilon},$$

which leads to a controlled realization of the causality and coupled-channel unitarity condition. Here $\rho^J_{cd}(s)$ is the phase-space matrix and μ_M is a matching scale which is identified with the smallest two-body threshold accessible in a sector with isospin and strangeness (I,S).

There are two relevant and known parameters only, the chiral limit value of the pion decay constant and a coupling constant characterizing the decay of the rho meson into a pair of pions. As was pointed out in [3], the generalized potential $U^J_{ab}(s)$ can be reconstructed unambiguously in terms of its derivatives at an expansion point that lies within its analyticity domain and where the results of χPT

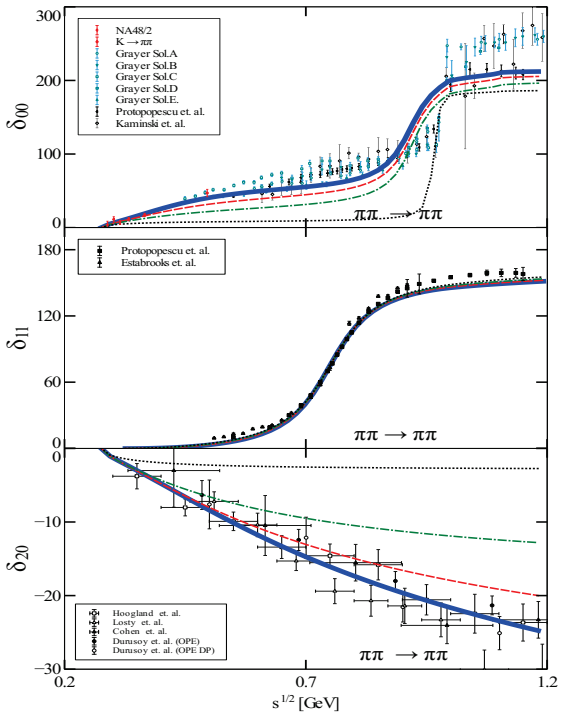

Figure 1: Results for $\pi\pi$ phase shifts δ_{IJ}. The dotted, dash-dotted, dashed and solid lines correspond to a truncation in the expansion (1) at order $0,\ 1,\ 2,\ 3$ respectively.

are reliable. It holds

$$U(s) = \sum_{k=0}^{n} c_k\, \xi^k(s), \qquad (1)$$

where the coefficients c_k are determined by the first k derivatives of $U(s)$ at the expansion point. The function $\xi(s)$ is a suitable conformal map constructed as to analytically continue the potential to larger energies.

Some selected results are shown in the Figure illustrating good agreement with the data set up to about 1.2 GeV. The sensitivity of our results on the truncation index n in (1) suggests the crucial importance of the light vector meson as active degrees of freedom.

References

[1] G. Ecker, J. Gasser, A. Pich and E. de Rafael, Nucl. Phys. B **321** (1989) 311.

[2] M. F. M. Lutz and E. E. Kolomeitsev, Nucl. Phys. A **730** (2004) 392 [nucl-th/0307039].

[3] A. Gasparyan and M. F. M. Lutz, Nucl. Phys. A **848**, 126 (2010) [arXiv:1003.3426 [hep-ph]].

[4] I. V. Danilkin, L. I. R. Gil and M. F. M. Lutz, Phys. Lett. B **703** (2011) 504 [arXiv:1106.2230 [hep-ph]].

Compton scattering from chiral dynamics with unitarity and causality

A. M. Gasparyan[1,2], *M.F.M. Lutz*[1], *and B. Pasquini*[3]

[1]GSI, Darmstadt, Germany; [2]ITEP, Moscow, Russia; [3]Universit'a degli Studi di Pavia and INFN, Pavia, Italy

Nucleon Compton scattering provides an important testing ground for Chiral Perturbation Theory (χPT). One of the reasons is that for such a process the leading order loop contributions do not depend on unknown parameters, when calculated in the heavy baryon formalism [1]. The same is true for some of the higher order terms [2]. The application of strict χPT is however limited to the near threshold region.

A method to extrapolate χPT results beyond the threshold region using analyticity and unitarity constraints was proposed recently in [3]. It is based on the chiral Lagrangian involving pion, nucleon and photon fields [4]. The terms relevant at the next-to-next-to leading order for pion elastic scattering, pion photoproduction and nucleon Compton scattering are taken into account. A strict chiral expansion of the various scattering amplitudes to this order includes tree-level graphs, loop diagrams, and counter terms. The latter are adjusted to the empirical data on πN elastic scattering and pion photoproduction. The Compton scattering involves no additional free parameters, providing an independent cross-check of the χPT predictions. The extrapolation of the amplitudes obtained within χPT is performed utilizing constraints imposed by basic principles of analyticity and unitarity.

We made predictions for the nucleon spin polarizabilities within this scheme [5]. The spin structure of the nucleon is described by the effective interaction of the third order

$$\begin{aligned} H_{\rm eff} = -2\pi \big[& \gamma_{E1E1} \vec\sigma \cdot (\vec E \times \dot{\vec E}) + \gamma_{M1M1}\, \vec\sigma \cdot (\vec H \times \dot{\vec H}) \\ & - \gamma_{M1E2} \left(\vec\nabla \cdot \vec\sigma\, E_i + \nabla_i \vec E \cdot \vec\sigma\right) H_i \\ & + \gamma_{E1M2} \left(\vec\nabla \cdot \vec\sigma\, H_i + \nabla_i \vec H \cdot \vec\sigma\right) E_i \big], \end{aligned}$$

where the four spin polarizabilities γ_{E1E1},γ_{M1M1}, γ_{M1E2}, γ_{E1M2} are related to the multipole expansion. The comparison of our results for the spin polarizabilities with other theoretical approaches is presented in Table 1. All four spin polarizabilities γ_{E1E1}, γ_{M1M1}, γ_{E1M2}, γ_{M1E2} are in a reasonable agreement with the calculations based on fixed-t dispersion relations [6]. While for the transition polarizabilities $\gamma_{E1M2}, \gamma_{M1E2}$ we recover the results of strict χPT, for the diagonal $\gamma_{E1E1}, \gamma_{M1M1}$ elements we find significant effects from analyticity and unitarity constraints.

	χPT [2]	DR [6]	this work
γ_{E1E1}	-5.93	-4.3	-3.68
γ_{M1M1}	-1.19	2.9	2.47
γ_{E1M2}	1.19	0.0	1.19
γ_{M1E2}	1.19	2.1	1.19
γ_0	4.74	-0.7	-1.16
γ_π	4.74	9.3	6.14

Table 1: Proton spin polarizabilities obtained from different sources in units of 10^{-4} fm^4.

At present there are empirical constraints on two combinations of the polarizabilities. The forward (γ_0) and backward (γ_π) polarizabilities are

$$\begin{aligned} \gamma_0 &= -\gamma_{E1E1} - \gamma_{M1M1} - \gamma_{E1M2} - \gamma_{M1E2} \\ &= (-1.01 \pm 0.08 \pm 0.13)\, 10^{-4}\text{fm}^4\,, \end{aligned}$$

$$\begin{aligned} \gamma_\pi &= -\gamma_{E1E1} + \gamma_{M1M1} - \gamma_{E1M2} + \gamma_{M1E2} \\ &= (8.0 \pm 1.8)\, 10^{-4}\text{fm}^4\,. \end{aligned}$$

Our results for the forward and backward spin polarizabilities are in agreement with experimental values within error bars.

We also studied several spin observables in nucleon Compton scattering from threshold up to $E_{lab} = 350$ MeV as it will be measured at MAMI [7]. Particularly we looked at the beam asymmetry Σ_3 for linearly polarized photon and unpolarized proton target, double polarization asymmetry Σ_{2x} for circularly polarized photon and target spin aligned transversely with respect to the photon momentum, and double polarization asymmetry Σ_{2z} for circularly polarized photon and target spin aligned longitudinally. Our results are close to the ones obtained from fixed-t DRs, although the two approaches are quite different in construction [5]. This illustrates the enormous predictive power of combining the unitarity and analyticity constraint in hadron physics. Furthermore, the comparison between the two calculations provides an important cross check and can be used to estimate the theoretical uncertainty in calculations of Compton scattering observables.

References

[1] V. Bernard, N. Kaiser and U. -G. Meissner, Int. J. Mod. Phys. E **4**, 193 (1995) [hep-ph/9501384].

[2] K. B. Vijaya Kumar, J. A. McGovern and M. C. Birse, Phys. Lett. B **479**, 167 (2000) [hep-ph/0002133].

[3] A. Gasparyan and M. F. M. Lutz, Nucl. Phys. A **848**, 126 (2010) [arXiv:1003.3426 [hep-ph]].

[4] V. Bernard, Prog. Part. Nucl. Phys. **60**, 82 (2008) [arXiv:0706.0312 [hep-ph]].

[5] A. M. Gasparyan, M. F. M. Lutz and B. Pasquini, Nucl. Phys. A **866**, 79 (2011) [arXiv:1102.3375 [hep-ph]].

[6] D. Drechsel, B. Pasquini and M. Vanderhaeghen, Phys. Rept. **378**, 99 (2003) [hep-ph/0212124].

[7] The A2 Collaboration, Exp.-Nr. A2-11/09.

Super-FRS Design Status Report

M. Winkler[1], K.-H. Behr[1], T. Blatz[1], A. Breidert[1], A. Brünle[1], F.Fuentes[2], H. Geissel[1,3], M. Gleim[1], C. Karagiannis[1], B. Kindler[1], K. Kopp[1], E. Kozlova[1], A. Kratz[1], H. Leibrock[1], B. Lommel[1], C. Mühle[1], G. Münzenberg[1], I. Mukha[1], C. Nociforo[1], S. Pietri[1], W.R. Plaß[3], A. Prochazka[1], C. Scheidenberger[1,3], C. Schlör[1], H. Simon[1], B. Sitar[4], M. Tomut[1,5], P. Vobly[6], H. Weick[1], C. Will[1], and J.S. Winfield[1]

[1]GSI, Darmstadt, Germany; [2]HIP Helsinki, Finland; [3]JLU Giessen, Germany; [4]CUB Bratislava, Slovakia; [5]NIMP, Bucharest, Romania, [6]BINP, Novosibirsk, Russia.

System and building design

The system design of the Super-FRS has been further detailed. The resulting requirements have been incorporated into the building design. In particular the focusing system in front of the production target which connects the High Energy Beam Transport (HEBT) to the Super-FRS was adapted to the technical requirements [1]. The approval planning for all NUSTAR buildings within the Modularized Start Version (MSV) was finished. The planning of media supply such as local cryogenics and cable trays was started and is still ongoing.

For the target building an alternative solution for the target shielding compared to that presented at [2] was developed. It is based on simple cubes with a weight of approximately 10 ton each. To start formwork planning the final shielding version will be chosen with respect to a possible technical realization as well as cost and time aspects.

In the separator tunnel it turned out that the niches at the focal plane areas became too small to house all required control units. It was necessary to change them to a service tunnel which is running parallel to the separator tunnel separated by a 1 m thick shielding wall. The detailed planning on placing the different racks and the connections to the components in the tunnel is still ongoing.

Also a re-planning for the service building of Super-FRS was necessary to avoid problems rising from ground water. In principle the building was lifted by approximately 3 m and only a ground water protected direct access to separator tunnel remained on the original level.

In parallel to the civil construction planning also the documents to apply for radiation protection construction permission were prepared.

Magnets

In May/June 2011 the first radiation resistant dipole magnet for the Super-FRS target area was transported from BINP Novosibirsk (Russia) to GSI. The yoke was dismounted into 6 parts each coming on a separate truck and an additional truck was delivering the coil and the support stand. Colleagues from BINP participated on reassembling the 90 ton magnet in the testing hall which was done within approximately 2 weeks. For 2012 it is foreseen to simulate the installation of this magnet in a 'tunnel-dummy' by means of remote handling.

GSI submitted in 2012 the proposal to deliver the superferric multiples for Super-FRS as a German in-kind contribution which was approved by the FAIR Boards. The specification documents for the multiplets are in preparation as well as the tendering documents and it is aimed to start the tendering procedure in spring 2012.

Figure 1: The first radiation resistant dipole magnet for Super-FRS after assembling in the testing hall.

Detector Development

The GEM TPC is considered as a next generation of current tracking TPC detector at Super-FRS. It will be based on digital strip readout and a signal amplification using the GEM foils. A prototype detector with delay-line readout and 2 different strips configurations was developed together with HIP Helsinki, Finland and CUB Bratislava, Slovakia. The next steps will be the integration of the NXYTER readout as well as beam time tests at FRS in 2012.

Figure 2: Assembled GEM-TPC: field cage integration (left) and mounting in a vacuum chamber (right).

References

[1] J. Winfield *et al.*, this report.
[2] M. Winkler *et al.*, GSI report (2010-1) 15

#m.winkler@gsi.de

Discovery and Cross-Section Measurement of Neutron-Rich Isotopes in the Element Range $61 \leq Z \leq 78$

F. Farinon[1], *J. Kurcewicz*[1], *H. Geissel*[1], *S. Pietri*[1], *C. Nociforo*[1], *A. Prochazka*[1], *H. Weick*[1], *J.S. Winfield*[1], *A. Estradé*[1], *A. Bail*[2], *G. Bélier*[2], *J. Benlliure*[3], *G. Benzoni*[4], *M. Bunce*[5], *M. Bowry*[5], *I.Dillmann*[1], *A. Evdokimov*[1], *J.Gerl*[1], *A. Gottardo*[6], *E. Gregor*[1], *R. Janik*[7], *A. Kelić-Heil*[1], *R. Knöbel*[1], *T. Kubo*[8], *Yu. A. Litvinov*[1], *E. Merchan*[1], *I. Mukha*[1], *F. Naqvi*[1], *M. Pfützner*[9], *M. Pomorski*[9], *Zs. Podolyák*[5], *P.H. Regan*[5], *B. Riese*[1], *M.V. Ricciardi*[1], *C. Scheidenberger*[1], *B. Sitar*[7], *P. Spiller*[1], *J. Stadlmann*[1], *P. Strmen*[7], *I. Szarka*[7], *J. Taïeb*[2], *S. Terashima*[1,8], *J.J. Valiente-Dobón*[6], *M. Winkler*[1], *and Ph. Woods*[10]

[1]GSI Helmholtzzentrum für Schwerionenforschung, Darmstadt, Germany; [2]CEA DAM DiF, Arpajon Cedex, France; [3]Universidad de Santiago de Compostela, Santiago de Compostella, Spain; [4]INFN sezione di Milano, Milano, Italy; [5]University of Surrey, Guildford, Surrey, UK; [6]INFN - Laboratori Nazionali di Legnaro, Legnaro, Italy; [7]Comenius University, Bratislava, Slovakia; [RIKEN]RIKEN Nishina Center, Saitama, Japan; [9]University of Warsaw, Warsaw, Poland; [10]University of Edinburgh, Edinburgh, UK

We report on the results of an experiment investigating heavy neutron-rich isotopes in the Dy and Os region, performed at the projectile fragment separator (FRS) [1] of GSI Darmstadt. With the detector setup described in [2] and the high-resolution performance of the fragment separator FRS at GSI we discovered 57 new isotopes in the atomic number range of $60 \leq Z \leq 78$. The new isotopes have been unambiguously identified in reactions with a ^{238}U beam impinging on a Be target at 1 GeV/u. The isotopic production cross-section for the new isotopes have been measured and compared with predictions of different model calculations. In general, the ABRABLA and COFRA models agree better than a factor of two with the new data, whereas the semiempirical EPAX model deviates much more. Projectile fragmentation is the dominant reaction creating the new isotopes, whereas fission contributes significantly only up to about the element holmium.

In the particle identification plot (Fig. 1), all isotopes covered in the magnetic field settings centered on ^{172}Dy and ^{194,198,202}Os are displayed with the full statistics and all the separation criteria applied. The red solid line indicates the border of the discovered new isotopes.

The first measured property of the discovered isotopes was the determination of the production cross sections. They are highly relevant to plan further studies with the discovered nuclei and contribute to the basic understanding of projectile fragmentation reactions. A comparison with theoretical model calculations show good agreement.

The results of the present experiment opens a new field for nuclear spectroscopy and also for nuclear astrophysics in the heavy nuclei range. The next steps in this experimental campaign will be half-life and precise mass measurements, as well as decay spectroscopy after implantation in silicon detectors.

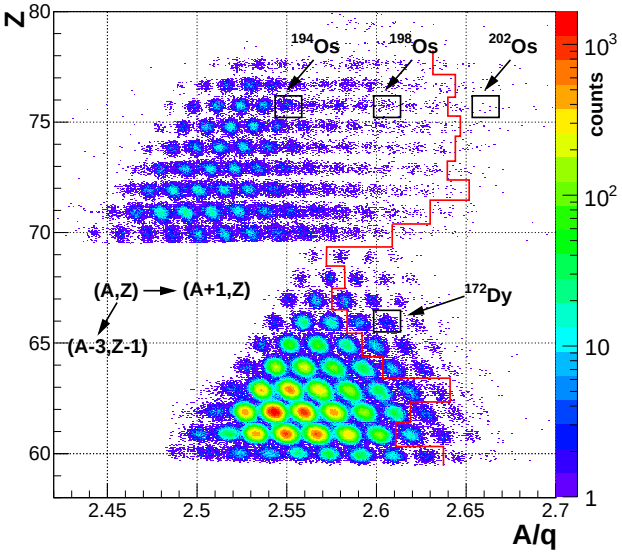

Figure 1: (TOP) Identified atomic number Z of the incoming ions as a function of their A/q ratio, at the final focal plane (F4). In the A/q ratio, the time-of-flight and magnetic rigidity analysis information is included. The plot shows the superimposed data acquired in all $B\rho$ settings measured (^{172}Dy, ^{194}Os, ^{198}Os and ^{202}Os). The solid line shows the border of hitherto unobserved isotopes, i.e., the discovered new isotopes are on the right hand side of the border line. The black rectangles show the group of ions corresponding to the $B\rho$ setting of the spectrometer.

References

[1] H. Geissel, et al., Nucl. Instrum. Methods Phys. Res. B 70 (1992) 286.

[2] J. Kurcewicz, et al., GSI Scientific Report 2010.

β-decay of very neutron-rich Rh, Pd, Ag nuclei

K. Smith[1,2], J. Agramunt-Ros[3], A. Algora[3], J. Benlliure[4], R. Caballero-Folch[5], D. Cano-Ott[6], T. Davidson[7], I. Dillmann[8,9], C. Domingo-Pardo[3], A. Estrade[8,10], A. Evdokimov[9], T. Faestermann[11], D. Galaviz-Redondo[12], A. García-Rios[6], H. Geissel[8,9], R. Gernhäuser[11], M.B. Gómez-Hornillos[5], M. Heil[8], C. Hinke[11], R. Knöbel[8], J. Kurcewicz[8], Y. Litvinov[8], G. Lorusso[13], L. Maier[11], J. Marganiec[8], M. Marta[8,9], F. Montes[2,14], I. Mukha[8], C. Nociforo[8], A. Parikh[5,15], G. Perdikakis[2,14], S. Pietri[8], A. Prochazka[8], S. Rice[16], B. Rubio[3], H. Schatz[2,14,17], C. Scheidenberger[8,9], K. Steiger[11], B. Sun[8], J.L. Taín[3], M. Takechi[8], H. Weick[8], J.S. Winfield[8], R. Wood[16], and P. Woods[7]

[1]Department of Physics, University of Notre Dame; [2]Joint Institute for Nuclear Astrophysics (JINA); [3]Instituto de Física Corpuscular, CSIC-Universitat de Valencia; [4]Universidad de Santiago de Compostela; [5]Departament de Física i Enginyeria Nuclear, Universitat Politecnica de Catalunya; [6]CIEMAT; [7]School of Physics and Astronomy, University of Edinburgh; [8]GSI Helmholtzzentrum für Schwerionenforschung GmbH; [9]II. Physikalisches Institut, Justus-Liebig Universität Giessen; [10]St. Mary's University; [11]Department of Physics E12, Technische Universität München; [12]Centro de Física Nuclear da Universidade de Lisboa; [13]RIKEN Nishina Center; [14]National Superconducting Cyclotron Laboratory, Michigan State University; [16]Institut d'Estudis Espacials de Catalunya; [17]Department of Physics, University of Surrey; [18]Department of Physics and Astronomy, Michigan State University

The astrophysical origin of about half of the elements heavier than iron have been attributed to the rapid neutron capture process (r-process). Reliable nuclear physics is needed to link theoretical models with astronomical observations. The region around $N = 82$ shell closure is of particular interest as it is responsible for the $A = 130$ peak in the solar abundance pattern. The peak is the result of the longer β-decay timescale compared to the neutron capture timescale when the r-process path reaches the shell closure [1] [2] [3].

An experiment to investigate half-lives and β-delayed neutron emission branching ratios of neutron-rich nuclei was recently performed at the GSI projectile fragment separator (FRS) [4]. A 900 MeV/u, ^{238}U beam delivered by the SIS-18 synchrotron impinged upon a 2480 mg/cm^2 thick beryllium target placed at the FRS entrance. The primary beam intensity was up to 2×10^9 ions/spill.

The FRS was used to separate fission reaction products of interest from unwanted contaminants. A 6 g/cm^2 aluminium degrader was used at the intermediate image (F2). The charge identification was obtained using two MUltiple Sampling Ionization Chambers (MUSIC) [5] at the FRS focal plane (F4). The time of flight was obtained by two plastic scintillators placed at F2 and F4. Time Projection Chamber (TPC) [6] detectors were used to provide isotope tracking information (position and angle) at F2 and F4. Following a variable thickness degrader, a third MUSIC was used to identify the unwanted isotopes that fragment in the variable degrader.

A stack of Si detectors consisting of two 300 µm single-sided silicon strip detectors (SSSDs), two 1000 µm SSSDs, three 60×40 mm^2, 700 µm double-sided silicon strip detectors (DSSDs) and two more 1000 µm SSSDs constituted the Silicon IMplantation detector and Beta Absorber (SIMBA) array [7]. The thickness of the variable degrader was selected such that nuclei of interest were implanted in the DSSDs. The high pixelation of the implantation detectors allowed for time correlation of the order of several seconds between implants and subsequent decay events.

A modified version of the BEta deLayEd Neutron detector (BELEN) [8] surrounded the SIMBA array. It consists of 30 ^{3}He gas proportional long counters arranged in two concentric rings embedded in a $80 \times 80 \times 100$ cm^3 polyethylene matrix. The emmited β-delayed neutrons were thermalized in the polyethylene. Thermalized neutrons have a higher probability of reacting with the ^{3}He in the proportional tubes. By comparing the ratio of β-decay events with and without neutrons, β-delayed neutron emission branching ratios were measured.

Several $B\rho$ settings of the FRS were used during the experiment to yield optimum secondary beam intensities of the ions of interest. Preliminary analysis has identified neutron-rich Rh, Pd, Ag, and Cd isotopes in the region close to the $N = 82$ shell closure. The determination of the implanted ion's half-lives and neutron branching ratios is currently underway.

References

[1] E. M. Burbidge, *et al.*, Rev. Mod. Phys. **29**, 547 (1957)

[2] J. J. Cowan, *et al.*, Phys. Rep. **208**, 267 (1991)

[3] M. Arnould, *et al.*, Phys. Rep. **450**, 97 (2007)

[4] H. Geissel, *et al.*, Nucl. Intr. and Meth. B, 70 (1992) 286

[5] G. Bauer, *et al.*, Nucl. Intr. and Meth. A, 386 (1997) 249

[6] R. Janik, *et al.*, Nucl. Intr. and Meth. A, 640 (2011) 54

[7] C. Hinke, PhD Dissertation, Technische Universität München (2010); GSI-Diss. 2010-15.

[8] M. B. Gómez-Hornillos, *et al.*, 2011 J. Phys.: Conf Ser. **312** 052008

Measurement of β-delayed neutrons around the third *r*-process peak

R. Caballero-Folch[1], *J. Agramunt*[2], *A. Algora*[2], *F. Ameil*[3], *Y. Ayyad*[4], *J. Benlliure*[4], *M. Bowry*[5], *F. Calviño*[1], *D. Cano-Ott*[6], *T. Davinson*[7], *I. Dillmann*[3,8], *C. Domingo-Pardo*[2], *A. Estrade*[3,9], *A. Evdokimov*[3,8], *T. Faestermann*[10], *F. Farinon*[3], *D. Galaviz*[11], *A. García-Rios*[6], *H. Geissel*[3,8], *W. Gelletly*[5], *R. Gernhäuser*[10], *M.B. Gómez-Hornillos*[1], *C. Guerrero*[12], *M. Heil*[3], *C. Hinke*[10], *R. Knöbel*[3], *I. Kojouharov*[3], *J. Kurcewicz*[3], *N. Kurz*[3], *Y. Litvinov*[3], *L. Maier*[10], *J. Marganiec*[13], *M. Marta*[3,8], *T. Martínez*[6], *F. Montes*[14,15], *I. Mukha*[3], *D.R. Napoli*[16], *Ch. Nociforo*[3], *C. Paradela*[4], *S. Pietri*[3], *Z. Podolyák*[5], *A. Prochazka*[3], *S. Rice*[5], *A. Riego*[1], *B. Rubio*[2], *H. Schaffner*[3], *Ch. Scheidenberger*[3,8], *K. Smith*[17,18], *E. Sokol*[19], *K. Steiger*[10], *B. Sun*[3], *J.L. Taín*[2], *M. Takechi*[3], *D. Testov*[19,20], *H. Weick*[3], *E. Wilson*[5], *J.S. Winfield*[3], *R. Wood*[5] *and P. Woods*[7]

[1]DFEN-UPC, Barcelona, Spain; [2]IFIC, CSIC-UV, València, Spain; [3]GSI, Darmstadt, Germany; [4]USC, Santiago de Compostela, Spain; [5]Department of Physics, University of Surrey, Guildford, UK; [6]CIEMAT, Madrid, Spain; [7]School of Physics and Astronomy, University of Edinburgh, UK; [8]II. Physikalisches Institut, Justus-Liebig Universität Giessen, Germany; [9]St. Mary's University, Halifax, Nova Scotia, Canada; [10]Department of Physics E12, TUM, München, Germany; [11]CFNUL, Lisboa, Portugal; [12]CERN, Geneva, Switzerland; [13]EMMI, GSI, Darmstadt, Germany; [14]NSCL, MSU, East Lansing, Michigan, USA; [15]JINA, MSU, East Lansing, Michigan, USA; [16]INFN, Legnaro, Italy; [17]Department of Physics, University of Notre Dame, South Bend, Indiana, USA; [18]JINA, University of Notre Dame, South Bend, Indiana, USA; [19]Flerov Laboratory, JINR, Dubna, Russia; [20]IPN Orsay, France

The aim of the S410 experiment was to measure the main decay properties (half-lives and β-delayed neutron emission probabilities) of neutron-rich nuclei in the mass region beyond A=200 and N=126, which corresponds to the third peak of the solar r-process abundance curve. Experimentally, this region is difficult to access due to the low production cross sections for the nuclei of interest and the large backgrounds induced by the fission fragments. Theoretical calculations[1] are difficult to validate on the basis only of the previous measurement available[2]. Clearly, more experimental data are needed in order to constrain better the theoretical models and to improve r-process calculations.

The experiment was carried out during 6 days in September 2011 at the final focal plane of the FRagment Separator (FRS)[3]. A primary beam of ^{238}U at 1 GeV/u impinged on a 1629 mg/cm^2 Be target with a 223 mg/cm^2 Nb stripper behind it. A 2500 mg/cm^2 aluminium degrader was placed at the first focal plane of the FRS in order to reduce the number of fission fragments arriving at S2 and S4. The FRS was operated in achromatic mode using a degrader at S2 of 3 g/cm^2 Al (Bρ - ΔE - Bρ method) for two different production settings, one centred on ^{215}Tl and another on ^{211}Hg.

Standard FRS tracking detectors, time projection chambers, organic scintillators and ionization chambers, were used for particle tracking and identification.

The fragments of interest were slowed down and implanted in a DSSD by adjusting the thickness of the S4 degrader for each setting. SIMBA (Silicon IMplantation detector and Beta Absorber)[4] was used for measuring both implants and β-decays. It also provided a redundant measurement of the ion position, which is of relevance for the accurate spatial correlation between implants and β-decays. A short run centred on ^{216}Po ($t_{1/2}$ = 145(2) ms) was carried out in order to validate the particle identification and the energy calibration of the SIMBA detector at high energy (E_α=6.778 MeV). Another run centred on ^{135}Sb (a well-known neutron-emitter) will allow us to examine in detail the systematics of β-neutron time correlations.

Neutrons were detected by the BEta deLayEd Neutron detector (BELEN)[5, 6] consisting of 30 ^{3}He proportional counters embedded in a polyethylene matrix placed around SIMBA. All detectors were read-out by means of conventional nuclear electronic modules (NIM and VME) and data were acquired using MBS[8]. In addition, BELEN data and some other relevant information were acquired using a Digital Data Acquisition System (DDAS)[7] coupled to MBS. The DDAS worked reliably and provided higher flexibility for time correlations in the offline data analysis.

The analysis of the data is in progress. So far, the most neutron-rich isotopes of Ir, Pt, Au, Hg, Tl, Pb and Bi in the region of interest have been identified for the first time.

References

[1] I. Borzov, Physics of Atomic Nuclei, 74 (2011) 1435-1444.

[2] T. Kurtukian-Nieto, PhD thesis, USC (2007).

[3] H. Geissel *et al.*, NIM B70 (1992) 286-297.

[4] Ch. Hinke, PhD thesis, TU München.

[5] M.B. Gómez-Hornillos *et al.*, J.Phys.: Conf. Ser. **312** 052008 (2011).

[6] M.B. Gómez-Hornillos *et al.*, to this Scientific Report.

[7] J. Agramunt *et al.*, to this Scientific Report.

[8] N. Kurz, GSI Data Acquisition System MBS Release Notes V5.0 (2006)

BELEN: A new BEta deLayEd Neutron detector

M.B. Gómez[1], *J. Agramunt*[2], *R. Caballero*[1], *I. Dillmann*[3,4], *M. Marta*[3], *A. Riego*[1], *and J.L. Taín*[2]
[1]UPC, Barcelona, Spain; [2]IFIC, Valencia, Spain; [3]GSI, Darmstadt, Germany; [4]Univ. of Giessen, Germany

The Beta Delayed Neutron detector [1], in its 30 counter version, (BELEN-30) has been used at GSI in the S323 and S410 experiments at the Fragment Separator in September 2011. The detector consists of 30 ^{3}He counters embedded in a polyethylene matrix. The detection of the neutron is based on the following reaction in the ^{3}He gas:

$$^3He + n \rightarrow ^3H + ^1H + 764\,keV$$

The polyethylene has the role of moderating the neutrons in order to increase the detection probability since the cross section of the detection reaction increases as the energy of the neutron decreases.

The design of the neutron detector has been performed using the Monte Carlo simulation code MCNPX. The aim was to obtain a detection efficiency as high and as constant as possible in the energy range of interest (from 1 keV to 1 MeV). In order to achieve this and accordingly to the results of the Monte Carlo simulation the ^{3}He counters were placed in two crowns, around the cylindrical hole of 23 cm-diametre, the first crown is at a radius of 14.5 cm and holds ten ^{3}He counters at a pressure of 10 atm; the second crown is at a radius of 18.5 cm and holds twenty ^{3}He counters at a pressure of 20 atm. The efficiency obtained with MC-

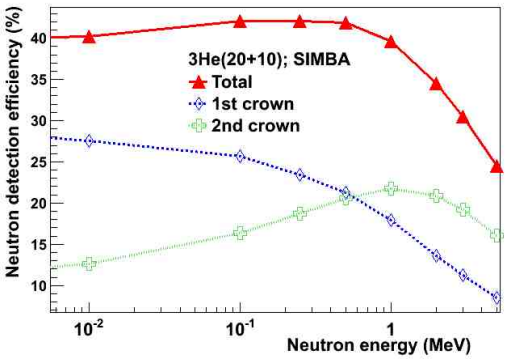

Figure 1: Efficiency of the BELEN-30 detector accordingly to MCNPX simulations.

NPX [2] for this arrangement of counters is shown in fig. 1, the inner crown detects the low energy neutrons since they require a shorter path in the polyethylene in order to be moderated; the higher energy neutrons are detected mainly in the outer ring. In addition, further polyethylene is added on the outer part, in order to shield the counters from background neutrons. The total dimensions of the polyethylene matrix are: 90 x 90 x 70 cm^3. It has a cylindrical hole with a radius of 11.5 cm that traverses the polyethylene matrix, where the implantation detector can be placed. The detector works with a self-triggered digital data acquisition system (DDAS) that is fully detailed in [3]. The system was also connected to a conventional analogue system. Both the analogue and the digital acquisitions were inserted into the MBS system. The typical signal from the ^{3}He counters is shown in fig. 2. The noise is below 150 keV, the neutron detection signal is from 150 to 850 keV where the plateau part corresponds to partial energy depositions due to the wall effect and the full energy peak is around 765 keV. There is also a pulser at 1050 keV in order to measure the live time of the system.

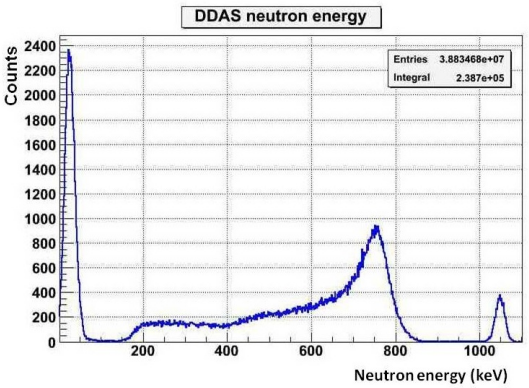

Figure 2: Spectrum from a ^{3}He neutron counter.

The neutron detection efficiency of BELEN-30 was measured with a ^{252}Cf neutron source that was placed in the centre of the beam hole. The efficiency obtained experimentally with the digital acquisition system was (35±1)%, whereas the value obtained from the analogue system was (25±1)%. The efficiency according to the MCNPX simulations was (34.5±0.5)%. The large difference between the experimental efficiency of the digital and analogue system was due to the high effective electronic threshold of the analogue system, which could not be reduced despite the efforts, whereas in the self-triggered digital acquisition it could be kept below the neutron signal. Both acquisition systems will be used in a complementary way during the data analysis.

References

[1] M. B. Gómez-Hornillos et al., J. Korean Phys.Soc. 59, 1573 (2011).

[2] http://mcnpx.lanl.gov/

[3] J. Agramunt et al., Nuclear Instrumentation and Methods. In preparation.

Development and test of an α-tagger detector at the FRS

F. Farinon[1], *S. Pietri*[1], *A. Brünle*[1], *H. Geissel*[1], *I. Kojouharov*[1], *and C. Nociforo*[1]
[1]GSI, Darmstadt, Germany

A novel α-tagger detector has been developed for secondary ions identification at the Fragment Separator facility (FRS) [1]. It consists of a Micron Semiconductor Ltd W(DS)-1000 5 cm $\times$ 5 cm double-sided silicon strip detectors (DSSD), of 1 mm thickness mounted inside a vacuum chamber. The thickness guaranteed a detection efficiency for α particles of $\sim$ 100%, since the range of an emitted α with an energy between 5 and 7 MeV varies between 20 and 25 μm in silicon. Inside the chamber, a removable α-source is used to perform the energy calibration. The vacuum chamber is placed at the final focal plane of the FRS and can be automatically removed from the beam-line. A variable homogeneous degrader is installed in front to slow down the fragments to match the range distribution to the DSSD thickness.

The DSSD is used to determine the energy, position and time for both the implanted secondary fragment and the α-particles following the subsequent radioactive decay and to perform event-by-event position and time correlations. The detector is divided in 16 front strips and 16 back strips, which provided the x and y coordinates, respectively. Combining the information from the front and the rear strips, it was possible to consider the detector made of 256 pixels, with a sensitive surface of 3.12 mm $\times$ 3.12 mm. In this way, implantations and decays can be spatially correlated within a given pixel. The absolute time of each event was measured with a time stamping system providing a resolution of 25 ns.

During the commissioning of the cryogenic stopping cell [2] (Fig. **??**), it performed a confirmation of the secondary particle identification for the first time. A primary $^{238}U^{92+}$ beam at an energy of 1000 MeV/u and a maximum intensity of $\sim$ 10^7 ions/s impinged on a 2.5 g/cm^2 Be target. The FRS was used in achromatic mode and optimized for the transmission of heaviest projectile fragments like ^{223}Th ions. The ions were slowed down and implanted into the 1 mm thick DSSD. The identification of the reaction products was performed using the standard time of flight and energy loss techniques [3] and the α-tagger. After the identification for each selected fragment the coordinates (strip x and strip y in the silicon detector) and time of the implanted ions were recorded. The α-decay spectrum in coincidence is obtained requiring the same spatial coordinates and a short delay in time. The results of this correlation method is a clean energy spectrum measured with the silicon detector (Fig. **??**. For comparison the corresponding α-decay spectra without any conditions are also shown in the same pictures. The kinetic energies of the emitted α particles are in excellent agreement with the well-known literature values. Thus this measurement provides another complete and independent identification pattern of the implanted α-emitters.

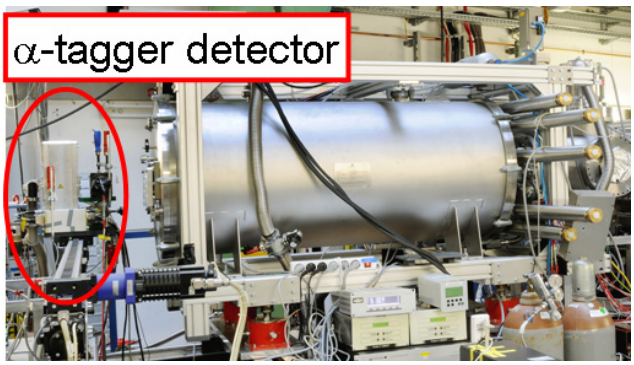

Figure 1: Photo of the α-tagger detector box in front of the Ion Catcher at the FRS final focal plane.

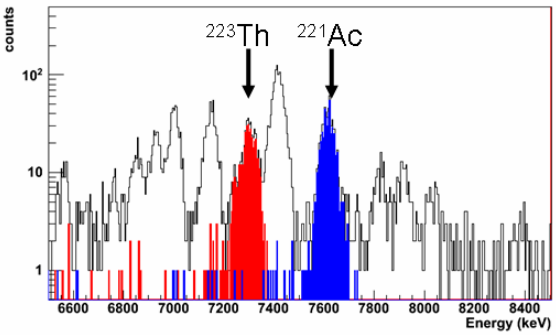

Figure 2: α-energy spectra measured during the FRS field setting for the separation of ^{223}Th. The black peaks represent the α-decays recorded without any additional identification condition. The red shaded spectrum (^{223}Th) and the blue one (^{221}Ac) were obtained under the condition of particle identification in-flight for ^{223}Th and ^{221}Ac, respectively, in coincidence with the implantation position in the silicon detector and excluding secondary reactions in the material at F4.

[1] H. Geissel et al., NIM B70, 286-297 (1992).
[2] T. Dickel et al., GSI Scientific Report 2011.
[3] B. Voss et al., Nucl. Inst. Meth. A364 (1995) 150.

The production and destruction rate of the radioactive isotope ^{60}Fe

T. Heftrich[*1], *E. Uberseder*[2], *T. Aumann*[4], *K. Boretzky*[3], *S. Haik*[3], *M. Heil*[3], *A. Kelic*[3], *R. Plag*[3], *R. Reifarth*[1], *V. Ricciardi*[3], *K. Sonnabend*[1], *H. Weick*[3], *M. Wiescher*[2], *and the s389 collaboration*

[1]Goethe-Universität Frankfurt, GER; [2]University of Notre Dame, USA; [3]GSI Darmstadt, GER; [4]TU Darmstadt, GER

One of the fundamental signatures for active nucleosynthesis in our galaxy is the observation of long-lived radioactive isotopes, for instance ^{22}Na, ^{26}Al, ^{44}Ti, and ^{60}Fe. Of particular importance are the isotopes ^{26}Al and ^{60}Fe in order to study stellar nucleosynthesis. Using high-resolution γ-ray observatories the ^{60}Fe/^{26}Al ratio was constrained by RHESSI (0.11 ± 0.03 [1]) and INTEGRAL (0.097 ± 0.039 [2]). While reactions of ^{26}Al have been studied extensively, very little is known about the reactions associated with the nucleosynthesis of ^{60}Fe. The interstellar ^{60}Fe abundance is mainly affected by the slow neutron (s) capture process in massive stars where high neutron densities and high temperatures are reached. ^{60}Fe is synthesized during the He shell burning in T-AGB stars where neutron densities of 10^{12} cm^{-3} and temperatures corresponding to kT = 30 keV are reached as well as during C/O shell burning in massive pre-supernova stars at neutron densities of 10^{12} cm^{-3} and temperatures of kT = 90 keV [3].

A measurement of the depletion ^{60}Fe(n,γ)^{61}Fe at temperatures of kT = 25 keV was performed directly by activation at the Van de Graaff accelerator in Karlsruhe, Germany. The Maxwellian average cross section was determined to $9.9\pm^{2.8(syst)}_{1.4(stat)}$ mbarn [4]. In addition, a measurement at kT = 25 meV was performed via activation at the TRIGA reactor in Mainz, Germany. Because of the short half life of ^{61}Fe ($t_{1/2}$ = 5.98 min), the experiments were performed in a sequence of cycles. The ^{60}Fe sample was produced at the PSI in Villigen, Switzerland. At FRANZ (Frankfurt Neutron Source), it will be possible to measure the depletion ^{60}Fe(n,γ)^{61}Fe at a temperature of kT = 90 keV which is in the temperature region of astrophysical interest.

Neutron capture on ^{59}Fe is very difficult to measure directly because of its short half-life ($t_{1/2}$ = 44.5 d). Therefore, the coulomb dissociation cross section of the inverse reaction ^{60}Fe(γ,n)^{59}Fe provides important information via the principle of detailed balance. In order to validate this method, the cross section extracted from applying this principle to the reaction ^{59}Fe(γ,n)^{58}Fe can be compared to previous direct measurements of ^{58}Fe(n,γ)^{59}Fe [5].

Coulomb dissociation measurements of ^{59}Fe and ^{60}Fe were performed at the R^{3}B/LAND setup at GSI. The unstable iron isotopes were produced by fragmentation of a 660 AMeV primary beam of ^{64}Ni on a 2511 mg/cm^2 Be target at FRS. The beam energy at the lead target was 535 AMeV. With intensities of 2-5·10^7 particles/s, the ^{60}Fe beam on a 515 mg/cm^2 lead target is exposed to a virtual photon spectrum with energies sufficient for (γ,n) reactions. The incoming particles were identified with scintillators via time-of-flight measurements. The fast outgoing neutrons were detected with LAND. The outgoing heavy fragments were measured with scintillator walls and fiber detectors. Figure 1 shows the masses of the outgoing fragments after tracking through the magnetic field of ALADIN and background subtraction. For that the identification and the momentum vector of each ion before and after the reaction is needed. In addition, the momentum vector of the emitted neutron is important to identify. Using position sensitive silicon strip detectors before ALADIN and position sensitive fiber detectors after ALADIN the particle trajectory is constrained. The ^{59}Fe and ^{60}Fe isotopes are separated by their different deflections in ALADIN based on their mass/charge ratio. An empty target run was used to subtract the background from the unreacted beam as well as break-up events in the setup. To determine the background resulting from nuclear interactions with the target, a carbon target run was performed.

Currently, the results from the successfully performed

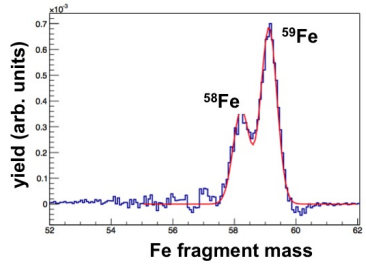

Figure 1: The outgoing tracked mass [6].

experiment are under analysis and the next steps will be the tracking of all reaction products and, eventually, the determination of energy-dependent information about the dissociation cross section ^{60}Fe(γ, n)^{59}Fe. Once the ^{59}Fe(n,γ)^{60}Fe is determined, nucleosynthesis simulations will be performed, leading to a better understanding of the evolution of massive stars within their late stages.

References

[1] D. Smith, arXiv:astro-ph/0404594v1.

[2] M. Harris et al., Astron. Astrophys. 433, L49 (2005).

[3] R. Reifarth, JPhCS.202a2022R (2010).

[4] E. Uberseder et al., PhRvL.102o1101U (2009).

[5] M. Heil et al., PhRvC..77a5808H (2008).

[6] E. Uberseder private communication (2010).

* supported by the HGF Young Investigator Project VH-NG-327.

Measurement of charge-changing cross sections of psd-shell nuclei

R. Kanungo[1], I. Tanihata[2], A. Estradé[1,3], F. Ameil[3], J. Atkinson[1], Y. Ayyad[4], D. Cortina-Gil[4], I. Dillman[3], A. Evdokimov[3], F. Farinon[3], H. Geissel[3], G. Guastalla[3], R. Janik[5], J. Kurcewicz[3], R. Knöbel[3], Y. Litvinov[3], M. Marta[3], M. Mostazo[4], I. Muhka[3], C. Nociforo[3], S. Pietri[3], A. Prochazka[3], C. Scheidenberger[3], B. Sitar[5], P. Strmen[5], H. J. Ong[2], M. Takechi[3], J. Tanaka[2], S. Terashima[6], Y. Vargas[4], H. Weick[3], and J. Winfield[3]

[1]Saint Mary's University, Halifax, Canada; [2]RCNP, Osaka University, Osaka, Japan; [3]GSI, Darmstadt, Germany; [4]Universidad de Santiago de Compostela, Santiago de Compostela, Spain; [5]Comenius University, Bratislava, Slovakia; [6]Beihang University, Beijing, China

We have performed an experiment to measure the charge-changing cross sections ($\sigma_{\rm cc}$) of neutron-rich Be, B, C, and O isotopes. The measured cross sections will be used to extract proton radii distribution through Glauber model analysis of the reaction, for example as in Ref. [1]. The measurement of charge-changing cross sections is a very sensitive technique, which coupled to the intense radioactive ion beams available at GSI can be used to measure the proton radii of very unstable isotopes.

The charge radius is a basic ground-state property of atomic nuclei. Our main motivation is the study of nuclear structure in light neutron-rich isotopes. Of particular interest are halo nuclei, where recent measurements by laser spectroscopy have shown significant changes of the charge radius due to the development of neutron halos (for example in ^{11}Li [2]). Measurements of proton distributions also provide a sensitive test for novel ab initio nuclear models, such as antisymmetrized molecular dynamics calculations [3]. Since the matter distribution in these isotopic chains has already been systematically measured up to very unstable isotopes [4, 5], we will also be able to study the evolution of the neutron skin thickness (difference between neutron and proton distributions).

The experiment was performed at the FRS fragment separator [6]. Primary beams of ^{22}Ne, and ^{40}Ar, at 1 GeV/u were used to produce secondary beams by fragmentation reactions in a beryllium target. The fragments of interest were selected in-flight by the $B\rho$–ΔE–$B\rho$ technique. The particle identification was performed by a simultaneous measurement of the time-of-flight, energy deposition, and magnetic rigidity (ToF–$B\rho$–ΔE technique), using the standard FRS detectors: plastic scintillators for timing, ionization chambers (MUSIC) for energy loss, and time-projection chambers (TPC) for beam tracking at dispersive positions of the FRS. Figure 1 shows the particle identification spectrum for the ^{17}B setting of the FRS.

The charge-changing cross section was measured, using a reaction target at the final focal point of the FRS (S4), by the transmission method:

$$\sigma_{\rm cc} = \frac{1}{t} \ln \frac{\gamma_0}{\gamma} \qquad (1)$$

where t is the number of target atoms per cm^2, $\gamma = N_{\rm sameZ}/N_{\rm inc.}$ is the ratio between the number of incident nucleus on the target ($N_{\rm inc.}$) and the number of out-going nuclei with the same atomic number Z ($N_{\rm sameZ}$), and γ_0 is the same ratio but measured without the reaction target. The reaction target was placed behind the standard FRS detectors, where the first MUSIC provided Z identification for the incoming fragments, and two TPC detectors provided beam tracking to determine the beam profile at the target position. In addition, a veto scintillator very close to the target was used to further constrain the beam position. A second MUSIC detector placed after the reaction target identified the Z of the outgoing ions. An additional TPC and a scintillator detector provided tracking for the outgoing beam. Reaction targets of C, CH_2, and Pb were used.

The data is currently under analysis.

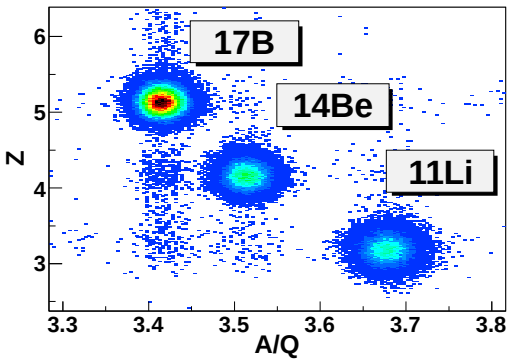

Figure 1: Particle identification plot for ^{17}B fragment setting.

References

[1] T. Yamaguchi et al, Phys. Rev. Lett. **107**, 032502 (2011).

[2] R. Sánchez et al, Phys. Rev. Lett. **96**, 033002 (2006).

[3] Y. Kanada-En'yo Phys. Rev. **C71**, 014310 (2005).

[4] A. Ozawa, T. Suzuki, and I. Tanihata, Nucl. Phys. **A693**, 32 (2001).

[5] R. Kanungo et al, Phys. Rev. C **84**, 061304(R) (2011).

[6] H. Geissel et al, NIM **B70**, 286 (1992).

Knockout from fast neutron-deficient carbon beams*

V. Volkov[1,#], T. Aumann[1,2], D. Cortina-Gil[3], J. Enders[1], F. Farinon[2], H. Geissel[2], M. Holl[1], N. Iwasa[4], R. Janik[5], R. Krücken[6], P. Maierbeck[6], C. Nociforo[2], A. Prochazka[2], C. Rodriguez-Tajes[3], H. Simon[2], E. C. Simpson[7], B. Sitar[5], P. Strmen[5], K. Sümmerer[2], J. A. Tostevin[7], H. Weick[2], J. Winfield[2]

[1]TU Darmstadt, Germany; [2]GSI, Darmstadt, Germany; [3]Universidad de Santiago de Compostela, Spain; [4]Tohoku University, Japan; [5]Univerzita Komenskeho, Bratislava, Slovakia; [6]TU München, Germany; [7]University of Surrey, UK.

Knockout of single nucleons from beams with intermediate to relativistic velocities is widely used to explore the single-particle structure of nuclei, in particular for rare isotopes, see Ref. [1]. It has been argued [3] that nucleon knockout reactions provide access to absolute spectroscopic factors. Measured spectroscopic factors C^2_{exp} are smaller than those predicted within a shell model calculation, C^2_{th}. The quenching factor $R_s = \sigma_{exp}/\sigma_{th} = C^2_{exp}/C^2_{th}$ from relativistic appears to approach unity for small binding energies of the knocked out nucleon, however for deeply bound nucleons significant quenching $R_s \ll 1$ is observed, see [6].

Experiment S341 studied, among others, the inclusive knockout reactions ^{9}Be(^{12}C,^{11}C)X, ^{9}Be(^{11}C,^{10}C)X, ^{9}Be(^{10}C,^{9}C)X, and ^{9}Be(^{9}C,^{8}B)X, covering a broad range of binding energy difference values. The reactions leading to the residues ^{9}C and ^{8}B are particularly simple to understand as the reaction residues have one bound state only, namely their ground state. Cross-sections for the reactions ^{9}Be(^{12}C,^{11}C)X and ^{9}Be(^{9}C,^{8}B)X have been measured before and can serve for benchmarking the experiment.

The experiment used an incident ^{12}C beam from the SIS at 1670MeV/nucl. incedent on a 4 g/cm^2 beryllium target at the FRS target position. At the intermediate F2 focus of the FRS, a 4.9 g/cm^2 ^{9}Be target served as secondary breakup target after charge identification in a preceding scintillator. The outgoing residues were tracked using time projection chambers (TPC). To maximize the optical transmission, reaction residues were detected at the FRS focus F3 using TPC tracking and scintillation counters for charge identification and time-of flight measurement.

The data analysis allowed us to extract the following inclusive one-nucleon removal cross sections: ^{9}Be(^{12}C,^{11}C)X: 55,9±2.6 mb; ^{9}Be(^{11}C,^{10}C)X: 24.9±1.9 mb; ^{9}Be(^{10}C,^{9}C)X; 21.4±1.7 mb; ^{9}Be(^{9}C,^{8}B)X: 37.2±2.4 mb. The experimental cross sections can be interpreted in the light of a Glauber-model description for the reaction and predictions for the spectroscopic factors from shell-model calculations using established empirical interactions fitted to data in the p-shell, in particular the WBT and WPT interactions [4]. The comparison between experimental and theoretical cross sections yields the following quenching factors: 0.57 for (^{12}C,^{11}C), 0.46 for (^{11}C,^{10}C), 0.53 for (^{10}C,^{9}C), and 0.81 for (^{9}C, ^{8}B). The results for (^{9}C, ^{8}B) and (^{12}C,^{11}C) are in agreement with previous experiments [2], and for (^{10}C,^{9}C) the group at Michigan State has reported a comparable result recently, as well [7].

Figure 1 shows the evolution of the quenching factor as a function of the difference between the binding energies of the removed nucleon and the unaffected nucleonic species. The dashed line indicates the average trend of the data compiled by Gade and co-workers [6]. The data points show our results that are consistent with previous experiments, but the quenching for removing deeply bound nucleons from carbon is less severe than for heavier systems. Hence, experimental results suggest that beyond the binding energy difference additional dependencies must play a role.

Part of the still significant quenching may be attributed to the lack of correlations included in the effective shell-model interaction. Using results of prediction of the Green's function Monte-Carlo method of Wiringa [7] one finds for the case of ^{9}Be(^{10}C,^{9}C)X a predicted spectroscopic factor of 1.04, compared to 1.77 (WPT). Hence the Green's function Monte-Carlo method may in part account for the quenching of spectroscopic strength, but cannot account for the full effect. Also, Timofeyuk [8] suggested that part of the quenching of spectroscopic strength may arise from the limited model space in shell-model calculations.

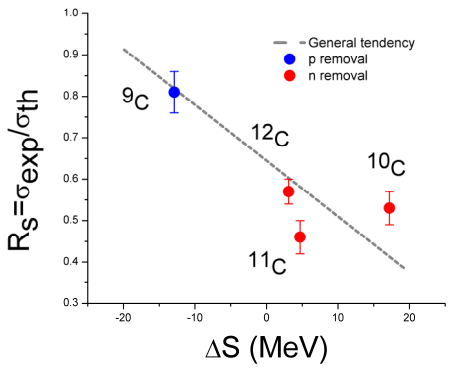

Figure 1: Reduction factors versus difference in nucleon separation energy.

References

[1] P. G. Hansen, J. A. Tostevin, Annu. Rev. Nucl. Part. Sci. 53, 219 (2003)
[2] J. Enders et al., PRC 67, 064301 (2003)
[3] B. A. Brown et al., Phys.Rev.C 65, 061601(R) (2002)
[4] E.C. Simpson, J.A, Tostevin Phys.Rev.C, *79 (2) 024616 (2009)*
[5] G.F. Grinyer et al., Phys.Rev.Lett. 106,(2011)
[6] A. Gade et al., Phys. Rev. C 77, 044306 (2008)
[7] I. Brida et al., Phys. Rev. C 84, 024319 (2011)
[8] N. K. Timofeyuk, Phys.Rev.Lett. 103, 242501 (2009)

* Work supported by BMBF, contract 06DA9040I, and through the state of Hesse (LOEWE center HIC for FAIR)

#v.volkov@gsi.de

Coulomb Excitation of ^{33}Ar – a test of isospin symmetry in the sd shell*

A. Wendt[1], P. Reiter[1], A. Algora[7], F. Ameil[2], M. Bentley[3], A. Blazhev[1], D. Bloor[3], N. Bondili[3], P. Boutachkov[2], M. Bowry[8], A. Bracco[5], N. Braun[1], F. Camera[5], J. Cederkall[4], F. Crespi[5], A. de la Salle[11], D. DiJulio[4], P. Doornenbal[9], K. Geibel[1], J. Gellanki[4], J. Gerl[2], P. Golubev[4], H. Grawe[2], J. Grebosz[10], G. Guastalla[2], T. Habermann[2], M. Hackstein[1], R. Hoischen[2], J. Jolie[1], A. Jungclaus[6], I. Kojouharov[2], N. Kurz[2], S. Lenzi[12], E. Merchan[2], B. Million[5], A. Morales[5], K. Moschner[1], S. Pietri[2], Z. Podolyak[8], D. Ralet[2], F. Recchia[12], D. Rudolph[4], H. Schaffner[2], L. Scruton[3], B. Siebeck[1], J. Taprogge[1,5], O. Wieland[5] and H.-J. Wollersheim[2]

[1]IKP, University of Cologne, Germany; [2]GSI, Darmstadt, Germany; [3]Department of Physics, University of York, UK; [4]Department of Physics, Lund University, Sweden; [5]INFN Milano, Italy; [6]CSIC Madrid, Spain; [7] IFIC, CSIC - Universidad de Valencia, Spain; [8] Department of Physics, University of Surrey, UK; [9]RIKEN, Japan; [10]Institute of Nuclear Physics PAN, Krakow, Poland; [11]Université de Nantes, France; [12]Università degli Studi di Padova, Italy

Very neutron deficient sd-shell nuclei may exhibit large distortions of the isospin symmetry. Differences in transition matrix elements between mirror nuclei provide access to changing collective behavior, expected by recent theoretical calculations. The matrix elements between the ground state and low lying excited states of the T=-3/2 isotope ^{33}Ar are subject of the relativistic Coulomb excitation experiment S377.

The ^{33}Ar ions were produced by fragmentation of a high-energy ^{36}Ar beam impinging on a secondary Au target with energy of ≈ 150 AMeV. The secondary beam was separated, identified and tracked by the FRS before the secondary target. After the target the newly developed "Lund-York-Cologne-CAlorimerter" LYCCA was employed for tracking and particle identification after nuclear reactions with secondary radioactive beams at the FRS final focal plane. The Time-of-Flight-ΔE-E telescope detector array will also be used by NUSTAR's future High-resolution In-flight SPECtroscopy (HISPEC) campaign [1,2].

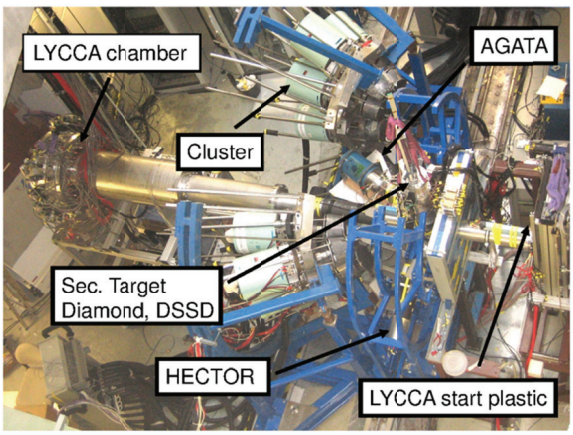

Figure 1: The PRESPEC setup in the FRS-S4 area

Gamma-rays were detected by the former Euroball germanium Cluster detectors of the PRESPEC setup and recorded together with particle information obtained with LYCCA. Figures 2 and 3 show preliminary γ–ray spectra from ^{33}Ar and ^{36}Ar gated by the various particle detector signals of FRS and LYCCA.

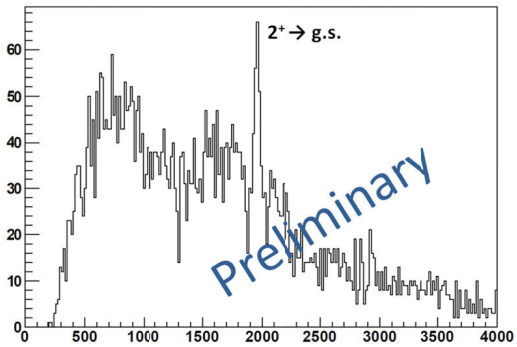

Figure 2: γ-spectra of ^{36}Ar (primary beam)

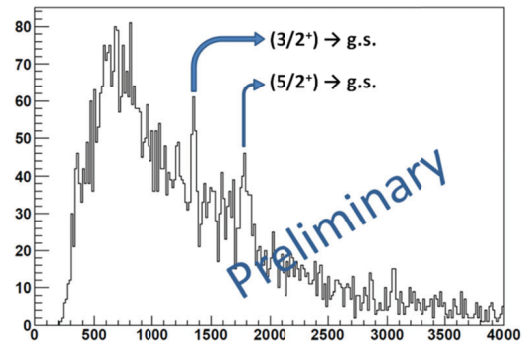

Figure 3: γ-spectra of ^{33}Ar

For ^{36}Ar the decay from the first excited state 2^+ and in the case of ^{33}Ar two transitions, which are coupling strong to the ground state, were detected. Spin and parity assignments are taken from the mirror nucleus ^{33}P. Thus the new B(E2) values for ^{33}Ar will be determined with respect to the known values of ^{36}Ar. Finally these values will be compared to theoretical results from large-scale shell model calculations employing modern effective nucleon-nucleon interactions.

References

[1] D. Rudolph et al. "LYCCA Technical design report" http://wwwnsg.nuclear.lu.se/lycca.

[2] R. Hoischen et al., submitted to Nucl. Instr. Meth. A.

* Supported by the German BMBF (06KY9136 TP1+TP7) and the "Helmholtz Graduate School for Hadron and Ion Research"

Relativistic Coulomb excitation of ^{88}Kr*

K. Moschner[1], A. Blazhev[1], N. Braun[1], M. Hackstein[1], J. Jolie[1], F. Naqvi[1,2], P. Reiter[1], M. Rudigier[1], J. Taprogge[1], T. Thomas[1], N. Warr[1], A. Wendt[1], F. Ameil[2], P. Boutachkov[2], J. Gerl[2], M. Górska[2], T. Habermann[2], I. Kojouharov[2], N. Kurz[2], E. Merchán[2], C. Nociforo[2], S. Pietri[2], A. Prochazka[2], H. Schaffner[2], H. Weick[2], H.-J. Wollersheim[2], M. Bentley[3], B. S. Nara Singh[3], L. Scruton[3], A. Algora[4], S. Brambilla[5], F. Camera[5], A. Corsi[5], A. Giaz[5], O. Wieland[5], J. Cederkäll[6], D. DiJulio[6], C. Fahlander[6], P. Golubev[6], R. Hoischen[6], D. Rudolph[6], M. Danchev[7], J. Grębosz[8], Z. Podolyàk[9], T. Möller[10], M. Reese[10], N. Mărginean[11], and T. Sava[11]

[1]IKP, University of Cologne, Germany; [2]GSI, Darmstadt, Germany; [3]Department of Physics, University of York, UK; [4]IFIC, CSIC - Universidad de Valencia, Spain; [5]INFN Milano, Italy; [6]Department of Physics, Lund University, Sweden; [7]Department of Physics, University of Sofia, Bulgaria; [8]Institute of Nuclear Physics PAN, Krakow, Poland; [9]Department of Physics, University of Surrey, UK; [10]IKP, TU Darmstadt, Germany; [11]HH-NIPNE, Bucharest, Romania

In autumn 2010, the first experiment of the fast-beam PreSPEC campaign was performed. We have studied the relativistic Coulomb excitation of ^{84,88}Kr with an energy of ∼120 MeV/u on a 0.4 g/cm^2 ^{197}Au secondary target.
The main goal was to study the strength and effects of proton-neutron interaction, which are manifested in particular in the existence and the properties of the so-called mixed symmetry (MS) states [1]. The N = 52 isotones close to the Z = 38, 40 sub-shell closures correspond to sufficiently small valence spaces for a practical description in terms of the nuclear shell model. This fact offers the unique possibility to compare interacting boson model (IBM-2) to shell-model calculations and to achieve a microscopic understanding of the building blocks of nuclear collectivity. Moreover, the evolution of MS states in N = 52 isotones can be tracked over different proton shells enabling us to investigate the variation of the proton-neutron interaction as a function of the nuclear valence space.
The Kr isotopes were produced by fission of a ^{238}U primary beam at 650 MeV/u on a 0.66 g/cm^2 ^{9}Be primary target and then selected by the FRS. To reduce the "background" caused by the Bremsstrahlung and Coulomb excitations of other nuclei, we have tried to optimize the purity of the secondary radioactive beams. Therefore, we had different FRS settings for the main nucleus of interest, ^{88}Kr, and for the ^{84}Kr isotope which has a known $B(E2)$ and was measured for normalization purposes. The FRS identification plot for the ^{88}Kr setting given in Fig. 1 shows the purity of the secondary beam. At the secondary target the PreSPEC Ge detector array in its fast-beam configuration was mounted. After the secondary target the newly developed Lund-York-Cologne-CAlorimeter (LYCCA) spectrometer for secondary fragment identification was successfully used in an experiment for the first time.
The multiple data branches, i.e. FRS, Ge, LYCCA, have to be well synchronized and require a proper trigger. As this was the first experiment of the fast-beam PreSPEC campaign some additional adjustments were needed. Nevertheless, Fig. 2 shows the observed relativistic Coulomb excitation of the 2_1^+ state in ^{88}Kr. Thus, the functionality of this complex setup was demonstrated. Information on Coulomb excitation of non-yrast 2^+ states could not be obtained from the data yet, but data analysis is still ongoing. For the reference setting on ^{84}Kr we were able to extract a similar spectrum to the one shown on Fig. 2.

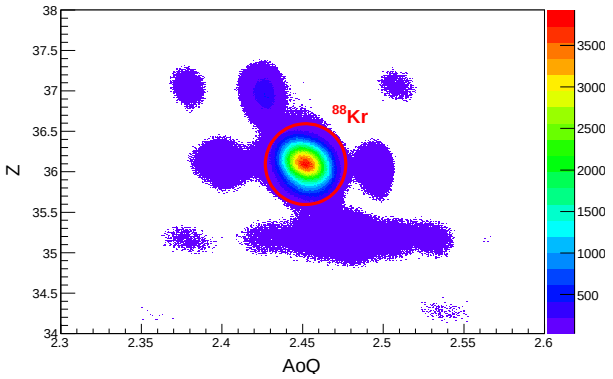

Figure 1: The FRS particle ID plot for the ^{88}Kr setting.

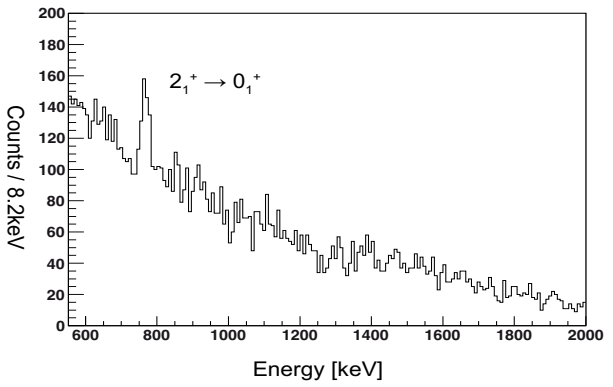

Figure 2: Observed relativistic Coulomb excitation of ^{88}Kr.

References

[1] N. Pietralla *et al.*, Prog.Part.Nucl.Phys. 60 (2008) 225

* Work supported by BMBF 06KY9136I

Development and Commissioning of a new Plunger Device for PRESPEC

M. Hackstein[1], C. Fransen[1], A. Dewald[1], A. Algora[6], F. Ameil[2], A. Blazhev[1], P. Boutachkov[2], N. Braun[1], T. Braunroth[1], A. Corsi[5], M. Doncel[7], A. Gadea[6], J. Gerl[2], J. Grebosz[2], G. Guastalla[2], T. Habermann[2], J. Jolie[1], N. Kurz[2], J. Litzinger[1], C. Louchart[5], E. Merchan[2], K. Moschner[1], C. Nociforo[2], A. Obertelli[5], P. Petkov[3], M. Pfeiffer[1], S. Pietri[2], D. Ralet[2], M. Reese[4], P. Reiter[1], W. Rother[1], B. Quitana[7], J. Taprogge[1], A. Wendt[1], H. Wollersheim[2], and K.O. Zell[1]

[1]IKP, Universität zu Köln, Germany; [2]KP II, GSI, Darmstadt, Germany; [3]INRNE, Sofia, Bulgaria; [4]IKP, TU Darmstadt, Germany; [5]CEA Saclay, France; [6]CSIC, University of Valencia, Spain; [7]Laboratorio de Radiaciones Ionizantes, Universidad de Salamanca, Spain

A new plunger device for radioactive ion beams for the PRESPEC setup at GSI is being devolopped at the University of Cologne. At first a basic fixed plunger (Fig. 1) has been constructed and tested in a commissioning experiment to test the feasibility of plunger measurements at RISING, e.g. with respect to the peak-to-background ratio. Here, fixed means that there was one fixed target - degrader distance. The known lifetime of the excited 2_1^+ state (835 keV) in stable ^{54}Cr has been measured by means of inverse relativistic Coulomb excitation.

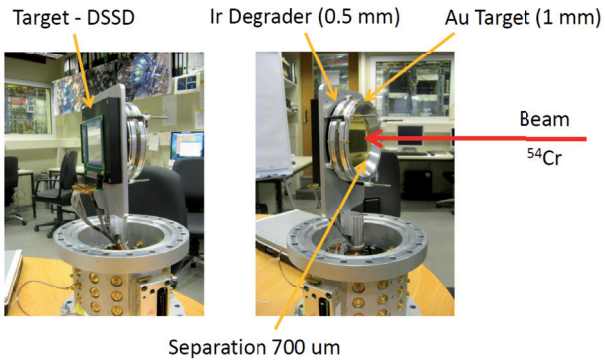

Figure 1: Fixed-plunger device seen from upstream (right) and downstream (left). The target gold foil and the target DSSD are visible.

A primary beam of ^{54}Cr at 393 MeV/u was directed onto a primary ^{9}Be target to degrade the beam and simulate realistic conditions for a radioactive ion beam experiment. The ^{54}Cr beam is tracked in the FRS before impinging onto a 1 mm thick ^{197}Au secondary target with an energy of 182 MeV/u. After the target, the Coulomb excited beam particles are slowed down in a 500 μm thick Iridium degrader, which is positioned 700 μm downstream, allowing for a sufficient energy separation of the detected Doppler shifted γ rays emitted from the decay of the 2_1^+ to the ground state in ^{54}Cr after the target and degrader, respectively. After the plunger the beam particles are detected in the LYCCA array, allowing for a good determination of the velocity and scattering angle of the beam. A total of about 10 h has been measured with six Ge clusters.

A preliminary γ spectrum is shown in Fig. 2. The two peaks originating from decays before and after the degrader, respectively, are visible. Although the analysis is still ongoing, the applicability of the technique at relativistic energies at GSI has been demonstrated.

This plunger device served to simulate and optimise the new plunger device for future experiments. For example, the amount of material close to target and degrader was chosen similar to that planned for final construction. Also the same target and degrader cones as well as the target DSSD of the LYCCA array that will be employed for the future plunger experiment at PRESPEC were used here. Fig. 1 shows the fixed plunger device as it was mounted in the target position.

Plunger experiments using intermediate beam energies (≈100 MeV/u) have been successfully performed in the past by our group at NSCL/MSU, e.g. [1]. With this new plunger device, also measurements at higher velocities will be possible, enabling access to lifetimes of excited states of a wider range of exotic nuclei.

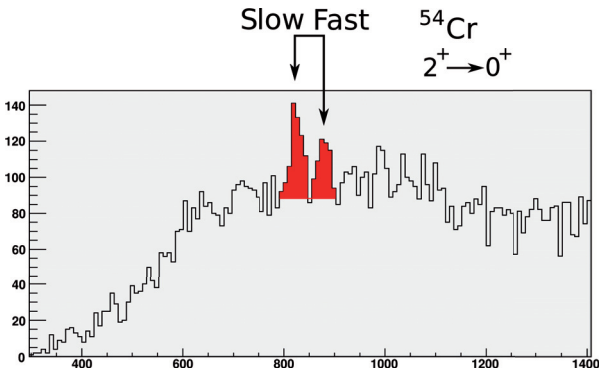

Figure 2: Doppler corrected γ ray spectrum. The two components from decays before (Fast) and after the degrader (Slow) are visible.

References

[1] W. Rother *et. al.*, Phys. Rev. Lett. 106, 022502 (2011)

In-beam validation of the PRESPEC LH_2 target

C. Louchart[1], J.M. Gheller[2], G. Authelet[2], P. Boutachkov[3,5], Ph. Chesny[1], A. Obertelli[1], S. Pietri[3], J.Y. Rousse[2], F. Ameil[3], L. Audirac[1], A. Corsi[1], Z. Dombradi[4], J. Gerl[3], A. Gillibert[1], E. Merchan[3,5], C. Nociforo[3], D. Ralet[3,5], M. Reese[5], V. Stepanov[2] and the PRESPEC collaboration

[1]CEA/IRFU/SPhN, *91191 Gif-sur-Yvette, France;* [2]CEA/IRFU/SACM, *91191 Gif-sur-Yvette, France;*
[3]*GSI, D-64291 Darmstadt, Germany;*[4]*ATOMKI, P.O. Box 51, H-4001 Debrecen, Hungary*;
[5]*IKP, TU Darmstadt, D-64289 Darmstadt, Germany.*

To exploit the most exotic nuclei through low-intensity radioactive beams at fragmentation facilities, the use of thick target is privileged to reach the necessary luminosity for in-beam gamma spectroscopy experiments.
The extraction of structure information from measured in-flight-emitted gamma rays requires a Doppler-effect correction necessitating the knowledge of the velocity of the recoil when it emits the photon and the photon's emission angle. The use of thick targets implies a significant energy loss in the target and the Doppler correction is therefore not well performed in case of a too thick target. A pure hydrogen target has the advantage of possessing a large number of scattering centers for a minimum energy loss in comparison with higher Z targets. A pure hydrogen target has also the advantage of avoiding background coming from reactions with other material.

In this context, a 20-mm thick target of liquid hydrogen has been developed at CEA Saclay/IRFU [1]. Liquid hydrogen is contained in a Mylar envelope whose shape is given by thermoforming. The entrance (exit) window is 100 µm (250 µm) thick (supporting a pressure of 8 bar).

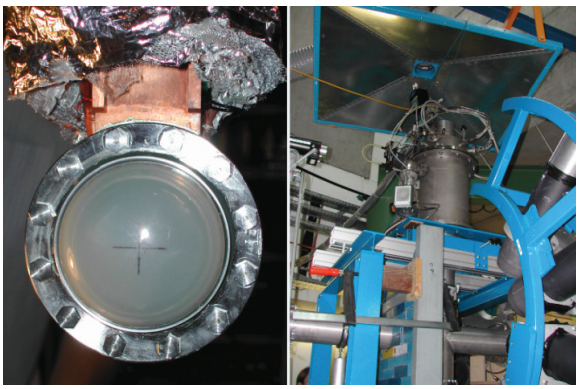

Figure 1: (left) exit window of the target; (right) Experimental FRS-S4 area where the LH2 target is positioned on the beam line.

The target built at CEA Saclay will be used in GSI for PRESPEC experiments with the AGATA array [2] and for future HISPEC campaigns at FAIR. The target could be of use to the R3B collaboration for some experiments. Thicknesses from 15 to 60-mm are available.
A first test of filling the envelope with liquid hydrogen was successfully completed at GSI. It was followed by an in-beam test in May 2011. The hydrogen target was inserted inside the RISING setup [3]. For this, a ^{54}Cr beam degraded to 130 MeV/nucleon was delivered to S4 at 400k/spill. Nucleon knockout and *(p,p')* inelastic scattering were measured.

The projectile-like were identified by LYCCA [4] and the γ-rays emitted in coincidence were measured by RISING composed of 12 clusters (84 HPGe crystals) placed at forward angles.
Downstream the target, reaction products were separated in Z and A with the Time of flight between the two LYCCA plastics (one placed before the target and another placed 3.4 m after), the energy loss in the DSSD and energy collected in CsI.

A preliminary gamma spectrum from the inelastic scattering of ^{54}Cr is given in Figure 2, where two peaks appear, one at 834 keV, corresponding to the transition $2^+ \rightarrow 0^+$, and the other around 1 MeV corresponding to a mixture of the $2^+ \rightarrow 0^+$ transition of ^{53}Cr and the $4^+ \rightarrow 2^+$ transition of ^{54}Cr. To obtain this spectrum, a selection on the prompt peak in the time distribution of RISING has been done. Furthermore a selection on the γ-rays emission angle was also used, excluding the closest detectors to the beam axis.

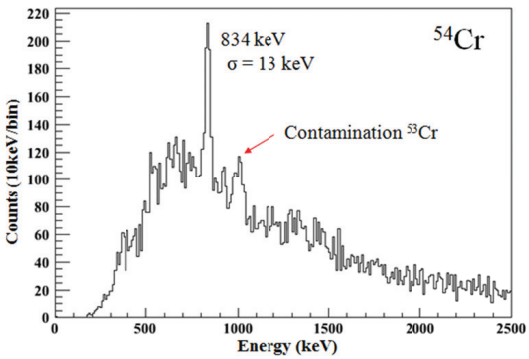

Figure 2 : Gamma spectrum from ^{54}Cr*(p,p')*^{54}Cr.

The Analysis is still ongoing to improve the spectra and to calculate the reaction cross sections for the elastic and knockout channels.

References

[1] A. Obertelli and T. Uesaka, EPJA **47**, 105 (2011).
[2] S. Akkoyun *et al.,* doi :10.1016/nima.2011.11.081
[3] H.J. Wollersheim *et al.,* NIMA **537**, 637 (2005).
[4] http://wwwnsg.nuclear.lu.se/lycca/

Measurement of α-decay half-life of bare and H-like ^{213}Fr ions

F. Farinon[1,2], C. Nociforo[1], A. Musumarra[3], K-H. Behr[1], F. Bosch[1], K. Blaum[1,2], C. Brandau[1], A. Brünle[1], R. B. Cakirli[1,2], C. Dimopoulou[1], A. Estrade[1], H. Geissel[1,2], P. Huelsmann[1], V. Ivanova[1], C. Karagiannis[1], R. Knöbel[1,2], C. Kozhuharov[1], J. Kurcewicz[1], N. Kuzminchuk[2], S. Litvinov[1], Y. A. Litvinov[1,4], I. Mukha[1], F. Nolden[2], P. Petri[1], S. Pietri[1], W. Plaß[1,2], A. Prochazka[1,2], M.W. Reed[5], B. Riese[1], M. S. Sanjari[1], C. Scheidenberger[1,2], D. Shubina[4], M. Steck[1], B. Sun[2], S. Terashima[1], P.M. Walker[5], H. Weick[1], J. S. Winfield[1], N. Winckler[1,4], and M. Winkler[1]

[1]GSI, Darmstadt, Germany; [2]Justus-Liebig Universität, Giessen, Germany; [3]INFN-LNS and University of Catania, Catania, Italy; [4]MPI-K, Heidelberg, Germany; [5]University of Surrey, Guildford, United Kingdom

We report on a pilot experiment of a measurement of the α-decay half-life of fully ionized and hydrogen-like (H-like) ^{213}Fr ions. The lifetime measurement of the corresponding neutral atoms was performed at the FRS by implanting the ions into an active Silicon stopper [1].

Radioactive ^{213}Fr ions have been produced via projectile fragmentation of $\sim 10^9$ $^{238}U^{73+}$ ions/spill, accelerated by the SIS-18 to 455 MeV/u. A 1.03 g/cm^2 thick Beryllium target has been used. The fully-ionized and H-like ^{213}Fr ions were separated in-flight by means of the Bρ-ΔE-Bρ method at the FRS and subsequently injected into the ESR. Stochastic and electron cooling were applied in both cases reducing the initial velocity spread to $\delta v/v \approx 5 \times 10^{-7}$ within 6-10 seconds. The identification of the cooled ions has been achieved exploiting the time-resolved Schottky Mass Spectrometry technique [2].

Several decay measurements of $^{213}Fr^{87+}$ and $^{213}Fr^{86+}$ have been performed using two different methods. The first one involves the change of the Schottky area under the frequency peak for many particles (many-particle method) and is described in [3]. The second one deals with very few stored particles and the decay is manifested by discrete jumps in the frequency intensity (single-particle method). This latter method has the advantage to be independent from the assumption of a strict proportionality of the Schottky area and the number of stored ions.

Applying the single-particle decay method [4] only a few ions were injected into the ESR, because the Schottky mass spectrometry is sensitive down to single stored ions. The steps of the decay could be identified only for 3-5 stored and cooled ions. In the Schottky spectra, the disappearance of the mother nuclei have detected and the decay time measured. The time resolution for the decay time assignment was about 100 ms.

In total 36 single-particle decays have been unambiguously identified and measured. The deduced time was inserted in a spectrum with a logarithmic time-scale. In this presentation the exponential decay is converted to a distribution with a universal shape independent of the half-life. The frequency distribution of the decay time can be written as a function of the logarithm of time $\theta = \log_e(t)$ as:

$$\frac{dn}{d\theta} = n\lambda e^{\theta} e^{-\lambda e^{\theta}}. \qquad (1)$$

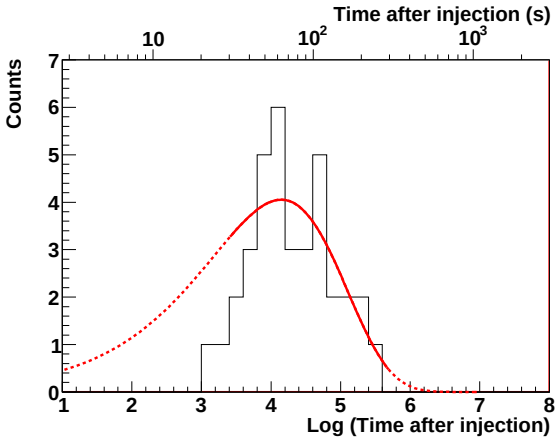

Figure 1: Spectrum of the time interval between the decays and the injection into the ESR. The horizontal axis represents the logarithm of the time after injection. For orientation the upper part of the horizontal axis shows the time after the injection in seconds. The solid line represents the best fit of the data with the function presented in equation (1). The fitting range was set from 20 to 300 seconds due to the cooling time. The dashed line is the extension of the fitting function outside the considered range.

Two free parameters, the number n of counts and the half-life $T_{1/2} = log(2)/\lambda$, determine the height and the position of the peak, respectively. The most probable value of this distribution is the logarithm of the life time ($\tau = 1/\lambda$). Figure 1 shows the spectrum of the time intervals between the decay and the injection into the ESR. The deduced half-life in the rest frame amounts to $T_{1/2}(^{213}Fr^{86+}) = 34 \pm 6$ s. The relatively big χ^2_r of 3.5 indicates the low statistics of this pilot experiment.

The results from our experiments with neutral and H-like ^{213}Fr demonstrate that both half-lives are in agreement within the error bars. This result is in good agreement with a more theoretical prediction [6].

[1] A. Musumarra et al., GSI Sci. Rep. 2008, p. 150.
[2] F. Nolden et al., GSI Sci. Rep. 2010.
[3] F. Farinon et al., GSI Sci. Rep. 2010.
[4] F. Bosch et al., Int. J. Mass Spectrom. 251, 212 (2006).
[5] Z. Patyk et al., Phys. Rev. C 78, 2008.

New Results on Mass Measurements of Neutron-Rich Nuclides at the FRS-ESR Facility

L. Chen[1,2], W. R. Plaß[1,2], H. Geissel[1,2], R. Knöbel[1], C. Kozhuharov[1], Yu. A. Litvinov[1], Z. Patyk[3], C. Scheidenberger[1,2], K. Siegień-Iwaniuk[3], B. Sun[1,4], H. Weick[1], K. Beckert[1], P. Beller[1], F. Bosch[1], D. Boutin[1], L. Caceres[1], J. J. Carroll[5], D. M. Cullen[6], I. J. Cullen[7], B. Franzke[1], J. Gerl[1], M. Górska[1], G. A. Jones[7], A. Kishada[6], J. Kurcewicz[1], S. A. Litvinov[1], Z. Liu[7], S. Mandal[1], F. Montes[8], G. Münzenberg[1], F. Nolden[1], T. Ohtsubo[9], Zs. Podolyák[7], R. Propri[5], S. Rigby[6], N. Saito[1], T. Saito[1], M. Shindo[10], M. Steck[1], P. M. Walker[7], S. Williams[7], M. Winkler[1], H.-J. Wollersheim[1], and T. Yamaguchi[11]

[1]GSI, Darmstadt, Germany; [2]JLU Gießen, Gießen, Germany; [3]National Centre for Nuclear Research, Warszawa, Poland; [4]Beihang University, Beijing, China; [5]Youngstown State University, Youngstown, USA; [6]University of Manchester, Manchester, UK; [7]University of Surrey, Guildford, UK; [8]MSU, East Lansing, USA; [9]Niigata University, Niigata, Japan; [10]University of Tokyo, Tokyo, Japan; [11]Saitama University, Saitama, Japan

At the FRS-ESR facility at GSI mass measurements on neutron-rich nuclei below uranium applied time-resolved Schottky Mass Spectrometry (SMS) [1] were performed. The exotic nuclei were produced in fragmentation processes of 670 MeV/u ^{238}U projectiles impinging on a Be-target placed at the entrance of the fragment separator FRS [2]. After being separated in-flight the fragments were injected into the storage-cooler ring ESR [3] where the revolution frequency of the ions were measured by the Schottky Mass Spectrometry method necessitating electron-cooling.

In an earlier evaluation a local calibration method was used to deduce the mass values [5]. Recently, the experimental data underwent a refined analysis. The here presented results were obtained by applying the correlation matrix method using a more sophisticated approach of preparing the input data. In addition, after our first evaluation we found a systematic deviation of our recalculated reference masses to the values given in the Atomic Mass Evaluation 2003 [6]. This observation led to the conclusion that the velocity dependent term in the frequency to mass-to-charge relation ($5 \cdot 10^{-7}$) cannot no longer be neglected as it was regarded in earlier analyses. Therefore, the radial velocity profile of the electron beam in the cooler had to be taken into account and was corrected for in the analysis. A comparison to the evaluation with the local calibration method shows an excellent agreement. Even more, it has led to a reduction of the systematical error by a factor of almost 3.

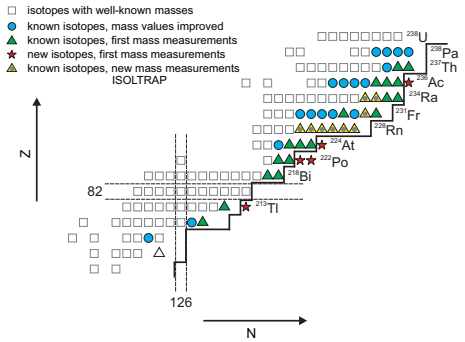

Figure 1: Nuclides covered in this experiment. The solid line indicates the boundary of known isotopes provided by the BNL-NNDC compilation [4] (status April 2011).

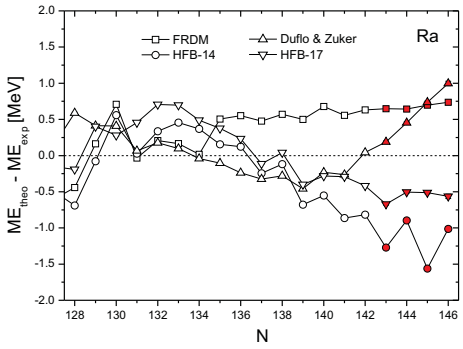

Figure 2: Comparison of experimental Mass Excess (ME) values for Ra isotopes with different theoretical models (experimental data: open symbols = AME03 [6], filled symbols = this work).

Among the more than 150 nuclides covered in this experiment new isotopes and isomers were discovered, see fig. 1. Accurate mass values of 33 neutron-rich nuclides have been obtained for the first time. A comparison of our results to theoretical predictions are shown in fig. 2 and clearly demonstrates the deficiency of the models towards more neutron-rich isotopes.

References

[1] Yu.A. Litvinov et al., Nucl. Phys. A 756 (2005) 3.

[2] H. Geissel et al., Nucl. Instr. Meth. B 70 (1992) 286.

[3] B. Franzke, Nucl. Instr. Meth. B 24-25 (1987) 18.

[4] http://www.nndc.bnl.gov/; http://www.nndc.bnl.gov/ensdf/

[5] L. Chen, doctoral thesis, JLU Gießen (2008).

[6] A. H. Wapstra et al., Nucl. Phy. A 729 (2003) 129.

Long-living ^{194}Re isomers observed in the ESR

M.W. Reed[1], P.M. Walker[1], I.J. Cullen[1], Yu.A. Litvinov[2,3], K. Blaum[2], F. Bosch[3], C. Brandau[3,4], J.J. Carroll[5,6], D.M. Cullen[7], A.Y. Deo[1], B. Detwiller[5], C. Dimopoulou[3], G.D. Dracoulis[8], F. Farinon[3], H. Geissel[3,9], E. Haettner[9], M. Heil[3], R.S. Kempley[1], R. Knöbel[3], C. Kozhuharov[3], J. Kurcewicz[3], N. Kuzminchuk[9], S. Litvinov[3], Z. Liu[10], R. Mao[11], C. Nociforo[3], F. Nolden[3], W.R. Plass[9], A. Prochazka[3], C. Scheidenberger[3,9], M. Steck[3], Th. Stöhlker[3,12], B. Sun[3], T.P.D. Swan[1], G. Trees[5], H. Weick[3], N. Winckler[2,3], M. Winkler[3], P.J. Woods[10], and T. Yamaguchi[13]

[1]Department of Physics, University of Surrey, Guildford, Surrey GU2 7XH, United Kingdom; [2]Max-Planck-Institut für Kernphysik, Saupfercheckweg 1, 69117 Heidelberg, Germany; [3]GSI Helmholtzzentrum für Schwerionenforschung, Planckstraße 1, 64291 Darmstadt, Germany; [4]ExtreMe Matter Institute EMMI, 64291 Darmstadt, Germany; [5]Youngstown State University, One University Plaza, Youngstown, Ohio 44555, USA; [6]US Army Research Laboratory, 2800 Powder Mill,Road, Adelphi MD, USA; [7]Schuster Laboratory, University of Manchester, Manchester M13 9PL, United Kingdom; [8]Department of Nuclear Physics, R.S.P.E., Australian National University, Canberra ACT 0200, Australia; [9]II Physikalisches Institut, Justus-Liebig-Universität Gießen, 35392 Gießen, Germany; [10]School of Physics and Astronomy, University of Edinburgh, Edinburgh EH9 3JZ, United Kingdom; [11]Institute of Modern Physics, Chinese Academy of Sciences, Lanzhou 730000, PR China; [12]Physikalisches Institut, Universität Heidelberg, Philosophenweg 12, 69120 Heidelberg, Germany; [13]Graduate School of Science and Engineering, Saitama University, Saitama 338-8570, Japan

Observation of long-living isomers presents a challenge experimentally. However, with the Experimental Storage Ring (ESR) it is possible to directly observe an isomer without requiring its decay [1]. The ESR enables observation of single ions, allowing measurements to be performed with low production cross sections [2]. Here we report on the use of projectile fragmentation of ^{197}Au with a ^{9}Be target. The reaction products were first passed through the FRagment Separator (FRS) [3] to select the isotopes of interest before being injected into the ESR. The ions were then cooled by electron and stochastic cooling, and observed by Schottky Mass Spectrometry (SMS) [4]. The experiment provided data for neutron-rich $71 \leq Z \leq 79$ isotopes. Results for hafnium ($Z = 72$) and tantalum ($Z = 73$) isomers have been published [5].

Further analysis has revealed a range of other isomers. We now present evidence for two isomers in ^{194}Re. From previous spectroscopic studies of the neutron-rich rhenium ($Z = 75$) isotopes with the RISING array coupled with the active stopper, three β-decaying states have been reported to feed different levels in ^{194}Os. These three states were observed to have three differing half-lives, $t_{1/2} = 5(1)$, 25(8) and 100(10) s, which feed 0^+, (11^-) and 6^+ states in ^{194}Os respectively [6]. In that study it was unclear as to which of these decaying states was the ground state and which were isomeric states. These three states have now been observed in the ESR (see Fig. 1) and excitation energies measured for one ground-state ion, one first-isomer ion and two second-isomer ions. The lower-energy isomer has been measured to have an energy of 285(40) keV whilst the higher-energy isomer has a energy of 833(33) keV. It has not been possible to connect the isomers to the associated measured lifetimes, as neither of the isomers decays during the ESR observation. However, the ground-state ion decays after a total observation time of 6 s. It is likely therefore that the fastest decay (5(1) s) observed in the spectroscopic study is from the ground state of ^{194}Re.

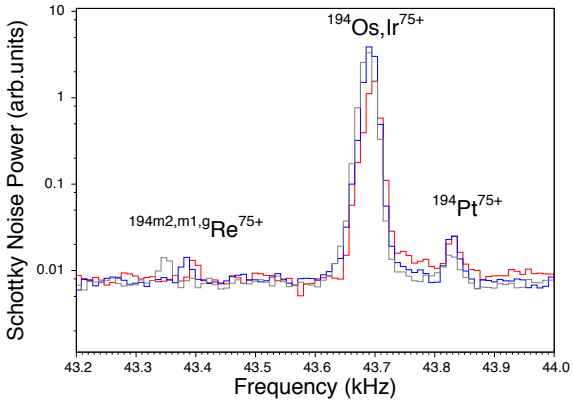

Figure 1: Schottky frequency spectra for three different injections in the ESR, showing the two isomers and the ground state of ^{194}Re. ^{194}Pt provides a frequency reference.

References

[1] B. Sun *et al.*, Eur. Phys. J. A **31**, 393 (2007).

[2] Yu.A. Litvinov, *et al.*, Nucl. Phys. A **756**, 3 (2005).

[3] H. Geissel *et al.*, Nucl. Inst. Meth. B **70**, 286 (1992).

[4] Yu.A. Litvinov & F. Bosch, Rep. Prog. Phys. **74**, 016301 (2011).

[5] M.W. Reed *et al.*, Phys. Rev. Lett **105**, 172501 (2010).

[6] N. Al-Dahan *et al.*, to be published.

Mass measurements of neutron-rich ^{197}Au projectile fragments at the ESR

D. Shubina[*1,2,3], *M.W. Reed*[4], *I.J. Cullen*[4], *P.M. Walker*[4], *K. Blaum*[1,2], *F. Bosch*[3], *C. Brandau*[3], *R.B. Cakirli*[1,5], *J.J. Carroll*[6,7], *R.F. Casten*[8], *D.M. Cullen*[9], *A.Y. Deo*[4], *B. Detwiler*[6], *C. Dimopoulou*[3], *F. Farinon*[3], *H. Geissel*[3,10], *E. Haettner*[10], *M. Heil*[3], *R.S. Kempley*[4], *R. Knöbel*[3], *C. Kozhuharov*[3], *J. Kurcewicz*[3], *N. Kuzminchuk*[3], *S.A. Litvinov*[3], *Yu.A. Litvinov*[1,3], *Z. Liu*[11], *R. Mao*[12], *C. Nociforo*[3], *F. Nolden*[3], *Z. Patyk*[13], *W.R. Plass*[10], *A. Prochazka*[3], *M.S. Sanjari*[3], *C. Scheidenberger*[3,10], *M. Steck*[3], *Th. Stöhlker*[2,3], *B. Sun*[3], *T.P.D. Swan*[4], *G. Trees*[6], *H. Weick*[3], *N. Winckler*[1,3], *M. Winkler*[3], *P.J. Woods*[11], *and T. Yamaguchi*[14]

[1]MPIK, Heidelberg; [2]Heidelberg University; [3]GSI, Darmstadt; [4]Surrey University; [5]Istanbul University; [6]YSU, Youngstown; [7]US Army Research Lab; [8]Yale University; [9]Manchester University; [10]Gießen University; [11]Edinburgh University; [12]IMP, Lanzhou; [13]SINS, Warsaw; [14]Saitama University

Heavy neutron-rich nuclei around tungsten ($Z = 74$) were investigated. For that purpose, ^{197}Au projectile fragments were studied by means of Schottky Mass Spectrometry (SMS). Those fragments were produced using an accelerated primary beam, which hit a beryllium target located before the fragment separator FRS. Nuclides of interest were separated in the FRS and stored in the storage ring ESR at an energy of a few hundred MeV/u. Sixty four stable or radioactive neutron-rich isotopes with $70 \leq Z \leq 79$ were identified.

The mass evaluation was performed in two different ways: using a well-established (see e.g. [1]) correlation matrix method (CMM) and a newly developed spline method. The comparison of the methods shows that 63% of obtained values agree within one σ and 98% of them agree within 2σ. The comparison with the AME03 table [2] shows that CMM generally understates the tabulated values, thus the distribution of deviations from the table shows a systematic shift. For this reason and the fact that the systematic error of the spline method is smaller, the latter was chosen for the final mass evaluation.

The result of the mass evaluation provided mass values of nine nuclides measured for the first time (^{181,183}Lu, ^{185,186}Hf, ^{187,188}Ta, ^{191}W and ^{192,193}Re) and also mass values for three nuclides (^{189,190}W and ^{195}Os), which were obtained with a higher accuracy than previously available.

Using the new measured values, two-nucleon separation energies and pairing gap energies $\Delta_{p,n}$ (additional energy of two-nucleon binding) were investigated. A comparison of the Δ_{p3} together with spectroscopic data for the same nuclides can be seen in Fig. 1.

The quantity $R_{42} = E(4^+)/E(2^+)$ is sensitive to structure, with values about 2.0 for spherical nuclei with surface vibrations and about 3.33 for deformed rotational nuclei [3]. As can be seen from Fig. 1, the R_{42} values decrease as one approaches the closed shells, pointing towards the spherical non-collective structures that result at $N = 82$ and $N = 126$.

We can compare the pairing gap energies with this ratio to find out whether the pairing gap energy is influenced by deformations. From the figure one can see that proton pairing gap decreases as the deformation grows. This could be an explanation for the dependence of pairing gap energies on neutron number N for Hf and W isotopes found in [4]. Furthermore, this behavior cannot be reproduced by any present mass model. At $N = 108$, Os and W proton pairing gaps as well as their R_{42} ratio have turning points, whereas for Hf neither proton pairing gap nor R_{42} ratio have one. This reflects the facts that (1) Hf remains in the region of the maximal deformation and (2) collective effects in the nuclear structure can be investigated by means of the pairing gap energy.

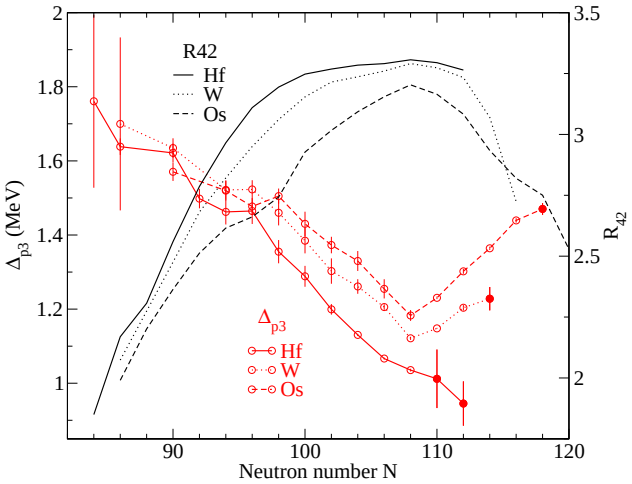

Figure 1: Δ_p and R_{42} as a functions of N for Os, W and Hf. New data are marked with filled symbols.

D.S. acknowledges support by the IMPRS-PTFS.

References

[1] T. Radon et al., Nucl. Phys. A677 (2000) 75.

[2] G. Audi, O. Bersillon, J. Blachot, and A. H. Wapstra, Nucl. Phys. A729, 3 (2003).

[3] P. Ring and P. Schuck, The Nuclear Many-Body Problem. Springer, 1980.

[4] Yu.A. Litvinov et al., PRL 95, 042501 (2005).

* D.Shubina@gsi.de

Orbital electron capture of stored highly charged ^{122}I ions

N. Winckler[1,2], *D. R. Atanasov* [1,3], *D. Balabanski*[4], *L. Batist*[5], *F. Bosch*[1], *D. Boutin*[1,7], *C. Brandau*[1,8], *C. Dimopoulou*[1], *H. G. Essel*[1], *T. Faestermann*[10], *H. Geissel*[1,9], *I. Hachiuma*[12], *S. Hess*[1], *T. Izumikawa*[13], *P. Kienle*[10,11], *R. Knöbel*[1], *C. Kozhuharov*[1], *J. Kurcewicz*[1], *N. Kuzminchuk*[9], *S. A. Litvinov*[1], *Yu. A. Litvinov*[1,2], *R. S. Mao*[14], *R. Märtin*[1,15], *M. Mazzocco*[1,16], *G. Münzenberg*[1,17], *K. Namihira*[12], *F. Nolden*[1], *T. Ohtsubo*[13], *Z. Patyk*[18], *R. Reuschl*[1,8], *M. S. Sanjari*[1,19], *C. Scheidenberger*[1,9], *D. Shubina*[1,2], *U. Spillmann*[1], *M. Steck*[1], *Th. Stöhlker*[1,6,15], *B. Sun*[9,20], *T. Suzuki*[12], *M. Trassinelli*[1,21], *I. I. Tupitsyn*[22], *H. Weick*[1], *M. Winkler*[1], *D. F. A. Winters*[1], *and T. Yamaguchi*[12]

[1]GSI, Darmstadt; [2]MPIK, Heidelberg; [3]Sofia University, Sofia; [4]INRNE, Sofia; [5]PNPI, Gatchina; [6]University, Heidelberg; [7]CEA-Saclay, Gif-Sur-Yvette; [8]EMMI, Darmstadt; [9]University, Gießen; [10]TU München, Garching; [11]SMI, Vienna; [12]University, Saitama; [13]University, Niigata; [14]IMP, Lanzhou; [15]Helmholtz-Institut, Jena; [16]INFN, Padova; [17]MAHE, Manipal; [18]SINS, Warsaw; [19]University, Frankfurt; [20]Beihang University, Beijing; [21]INSP, CNRS and University, Paris; [22]University, St. Petersburg

The β-decay studies of highly charged ions require experimental facilities such as GSI / Darmstadt or IMP / Lanzhou since the radioactive nuclei in high atomic charge states have to be produced, separated from contaminants and stored for extended periods of time. Previous experimental studies and theoretical considerations showed that the orbital electron capture (EC) decay rates of ions may be strongly dependant on the atomic charge state. This was measured in both ^{140}Pr and ^{142}Pm nuclides. Both parents decay by pure allowed Gamow-Teller transitions ($1^+ \rightarrow 0^+$) with more than 95% probability to the ground state of the corresponding bare daughter ions. It turned out that the measured ratio of hydrogen-like (H-like) to helium-like (He-like) EC-decay constant $\lambda_{\rm EC}^{\rm H-like}/\lambda_{\rm EC}^{\rm He-like} \approx 1.5$ [1, 2], which was not expected from the standard scaling of the density of the s-electrons at the nucleus. Studies showed that these experimental results could be explained by taking into account the conservation of both the total angular momentum and its projection of the nucleus plus leptons system [3, 4]. We have extended our experimental study to H-like ^{122}I [5]. As in the cases of ^{140}Pr and ^{142}Pm, the spin-parity of the ground state of ^{122}I atoms is 1^+. However, only about 82% of the decay strength goes to the ground state of the fully ionized daughter ^{122}Te ions ($1^+ \rightarrow 0^+$) while the remaining decay strength is distributed over several excited states in ^{122}Te nuclei. The transitions $(F_i = \frac{1}{2},\ I_i = 1^+) \rightarrow (F_f = \frac{1}{2},\ I_f = 0^+)$ conserve the total angular momentum. We expect that *allowed* Gamow-Teller transitions $(I_i = 1^+) \rightarrow (I_f = 2^+)$, become forbidden, since for this case it is impossible to form a final state $F_f = \frac{1}{2}$.

The experiment was performed using the FRS-ESR facility and employing the Schottky Mass Spectrometry (SMS) technique. In total, 5 measurements with bare ^{122}I^{53+} ions and 9 measurements with H-like ^{122}I^{52+} ions were performed. Due to a small production yield no successful measurement of He-like ions could be performed.

After production, the H-like ^{122}I ions could be in both hyperfine states with total angular momenta $F_i = 1/2$ or $F_i = 3/2$, respectively. Since the measured magnetic moment of ^{122}I is positive ($\mu = +0.94(3)\mu_{\rm N}$), the hyperfine ground state is $F_i = 1/2$. The hyperfine splitting energy has been estimated to $\Delta E_{hf} \approx 0.28$ eV, which corresponds to a relaxation half-life ($F_i = 3/2 \rightarrow F_i = 1/2$) of about $t_{1/2} = 1.95$ s. Therefore the beginning of the analysis was set to t_0 = 24 s after the injection into the ESR to ensure that all parent ions are in the hyperfine ground state.

All measurements showed consistent results. The measured EC-decay rate in H-like ^{122}I amounts to $\lambda_{\rm EC} = 7.4(3) \cdot 10^{-4}$ s^{-1} which equals within error bars the one measured in neutral ^{122}I atoms ($\lambda_{\rm EC}^{\rm neutral} = 7.0(5) \cdot 10^{-4}$ s^{-1}) although there are 52 additional bound electrons.

Theoretical estimations of the EC-decay rate in He-like ^{122}I have been performed in order to investigate the contributions of the $(I_i = 1^+) \rightarrow (I_f = 2^+)$ transitions which is expected to be first forbidden. However, the large error bars do not allow to take any conclusion on this latter hypothesis. Half-lives of more suitable nuclei should be measured to test such a hypothesis, like e.g. H-like ^{143}Sm, which decays with about 92 % by a single Gamow-Teller transition from its ground state ($F_i = 1$) to the ground state of ^{143}Pm ($F_f = 2$ or $F_f = 3$).

References

[1] Yu. A. Litvinov et al., Phys. Lett. B664 (2008) 162-168.

[2] N. Winckler *et al.*, Phys. Lett. B **679**, 36 (2009).

[3] Z. Patyk *et al.*, Phys. Rev. C **77**, 014306 (2008).

[4] A. N. Ivanov *et al.*, Phys. Rev. C **78**, 025503 (2008).

[5] D.Atanasov *et al. to be published*

Improved Timing Performance and Longer Ion Observation Times of a Time-of-Flight Detector for Isochronous Mass Spectrometry at the FRS-ESR Facility*

N. Kuzminchuk[1, 2], M. Diwisch[1], S. Ayet[1, 2], T. Dickel[1, 2], H. Geissel[1, 2], R. Knöbel[1, 2], W. R. Plaß[1, 2], C. Scheidenberger[1, 2], B. Sun[1], H. Weick[2], and the FRS-ESR Collaboration

[1]Justus-Liebig Universität, Gießen; [2]GSI, Darmstadt, Germany.

Isochronous Mass Spectrometry at the FRS-ESR facility can be used to determine the masses of exotic nuclei from precise revolution time measurements by a time-of-flight (TOF) detector. In the detector, ions passing a thin carbon foil release secondary electrons (SE), which are transported to microchannel plates (MCPs) by electric and magnetic fields. Significant instrumental improvements of the TOF detector were implemented, which increase the timing accuracy and the observation time. In addition, an on-line test with ^{238}U fission fragments was performed.

Timing Performance

Because of non-perfect electric fields in the detector, different points of emission of the SE from the foil as well as different initial velocities cause different electron transport times from the foil to the MCP detectors. In order to decrease the transport time spread, the TOF detector was modified to allow for higher electric and magnetic fields [1]. Simulations show (Figure 1) that by increasing the fields and hence the kinetic energy of the SE the time spread decreases. Off-line measurements with α-particles confirm this finding. By doubling the kinetic energy of the SE from the previously used value of 700 eV to 1400 eV, the measured time spread could be reduced from 44 ps to 33 ps. Using further optimizations of the detector, a minimum time spread of 26 ps could be achieved, almost doubling the timing accuracy of the detector [2].

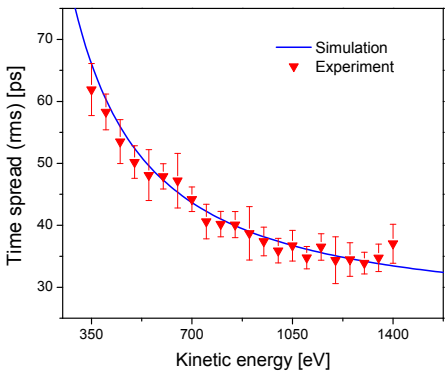

Figure 1: Simulated and measured time spread for a single branch detector as a function of the kinetic energy of the SE. Note that the values of the simulations have been increased to include an experimental constant that accounts for other limitations of the detector different than the electron transport time spread.

* Work supported by the BMBF under contract No. 06GI9115I

Ion Observation Time

The time period during which ions can be observed after injection into the ESR using the TOF detector is determined by the rate capability of the detector and by the energy loss of the ions in the foil. Previously it was shown in off-line measurements that MCPs with a pore size of 5 µm can accept a count rate that is about four times larger than that for MCPs with the same active diameter but with a commonly used pore size of 10 µm [3]. Further studies show that in order to reduce the energy loss of the ions in the foil, a foil with a thickness of about 10 µg/cm^2 should be used instead of the previously used foil of 17 µg/cm^2 with a coating of 10 µg/cm^2 CsI on both sides. These two effects were investigated in an on-line experiment using ^{238}U fission fragments. Figure 2 shows a comparison of the average number of the ions detected per turn in the present experiment, where a thin carbon foil (10 µg/cm^2) and MCPs with 5 µm pore size were used, and a previous experiment with thicker carbon foil (17 µg/cm^2) coated with 10 µg/cm^2 CsI on both sides and MCPs with 10 µm pore size. With the new setup, ions can be observed for a duration that is up to ten times longer than with the previous setup. This gain will increase mass measurement accuracy in future experiments.

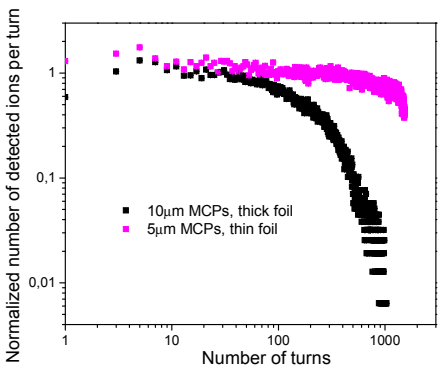

Figure 2: Average number of detected ions in the ring per turn for ^{238}U fission fragments for two different setups of the TOF detector. The data were normalized to 14 ions at turn number 10.

References

[1] M. Diwisch, Master thesis, Universität Gießen, 2011.
[2] N. Kuzminchuk, PhD thesis, Universität Gießen, 2011.
[3] N. Kuzminchuk et al., GSI Annual Report 2010 (2011), p.141.

Contributions to Network of Nuclear Structure and Decay Data*

B. Pfeiffer[1,2], *I. Dillmann*[1,2], *and C. Scheidenberger*[2,1]
[1]II. Physik. Inst., Universität Gießen, Germany; [2]GSI, Darmstadt, Germany

Introduction

In 2008, European nuclear physics research institutions instigated an effort to intensify their participation in the international task of establishing "Reference Data Libraries for Nuclear Applications" [1]. The II. Physikalisches Institut at Gießen and GSI are participating in the following topics:

NSDD

The participation at the task of evaluating nuclear structure data for the *Nuclear Data Sheets* (in 2009 the A=84 chain had been published [2]) was continued. The GSI represented Germany at the biannual meeting of the *INTERNATIONAL NETWORK OF NUCLEAR STRUCTURE AND DECAY DATA EVALUATORS* [3] at the IAEA headquarters in Vienna. These meetings serve to discuss the current status of the mass chain evaluations, evaluation responsibilities, and processing code needs, as well as ENSDF formats.

Masses

The systematic screening of the literature for experimental results on nuclear masses, half-lives, β-delayed proton and neutron emission probabilities, spins, parities and isomeric states has been continued. The collected values have been entered into data bases as the files underlying the *Intermediate Atomic Mass Evaluation 2011* [4] and the *NUBASE 2011* [5].

Beta-delayed neutron evaluation

The β-delayed neutron emission probabilities P_n and the energy spectra for fission products are important input data for the calculation of nuclear reactors, decay heat, and nuclear safeguard applications. For these applications, evaluated data are required. The latest compilations / evaluations date to around the year 2000 [7] and are limited to the fission product region.
With the advent of radioactive beam facilities, the production of very neutron-rich nuclei is now possible for a wider range of elements. The decay of these nuclei is studied at FRS applying a variety of detection methods. One technique detects the β-delayed neutrons emitted by very neutron-rich isotopes. Experiments in the A$\simeq$135 region had been performed with the Mainz 4π detector (see, e.g. [6]). Recently, the new neutron detector BELEN has been built [8] and first measurements have been performed at GSI in the lead region [9]. These measurements will be an important research program at the future SUPER-FRS.
During data treatment it got evident that a new evaluation encompassing **all** known delayed-neutron emitting isotopes has to be undertaken. Given the experience of the IAEA in Vienna with these evaluations, it was proposed to contact the Nuclear Data Group for establishing an IAEA coordinated research program. In October 2011 an *IAEA Consultant's Meeting on Beta-Delayed Neutron Emission Evaluation* [10] was held as a first step.
At GSI, also the emission of charged particles as protons have been observed following EC/β^+-decay. Beta-delayed nuclear fission is a decay mode which will be studied at FAIR. Therefore it would be desirable to extend the future evaluations also to these decay modes.

* Work supported by the Strategic Cooperation Contract between GSI and Justus-Liebig-Universität Gießen

References

[1] "Reference Data Libraries for Nuclear Applications – ENSDF"; Report of Technical Meeting of IAEA Nuclear Data Section INDC(NDS)-0543, November 2008, Vienna http://www-nds.iaea.org/publications/indc/indc-nds-0543.pdf

[2] D. Abriola, M. Bostan, S. Erturk, M. Fadil, M. Galan, S. Juutinen, T. Kibedi, F. Kondev, A. Luca, A. Negret, N. Nica, B. Pfeiffer, B. Singh, A. Sonzogni, J. Timar, J. Tuli, T. Venkova, K. Zuber, Nuclear Data Sheets 110 (2009) 2815.

[3] The 19^{th} Network meeting of the NUCLEAR STRUCTURE AND DECAY DATA EVALUATORS network, IAEA, Vienna, Austria, 4-8 April 2011 http://www-nds.iaea.org/nsdd/

[4] http://amdc.in2p3.fr/masstables/Ame2011int/file1.html

[5] http://amdc.in2p3.fr/nucleus/nucWxp2.exe

[6] K. Smith et al., 11^{th} Symposium on Nuclei in the Cosmos - NIC XI, Heidelberg, Germany, July 19 - 23, 2010 Proceedings of Science, PoS-NIC XII_283

[7] G. Rudstam et al., ADNDT 53, 1 (1993); B. Pfeiffer et al., Prog.Nucl.Energy 41, 39 (2002), and refrences therein.

[8] M.B. Gomez-Hornillos et al., Journal of Physics: Conference Series, Volume 312, 052008 (2011).

[9] C. Domingo Pardo et al., GSI-FRS Proposal S410 (2010)

[10] Summary report of *The IAEA Consultant's Meeting on Beta-Delayed Neutron Emission Evaluation*, IAEA, Vienna, Austria, 10-12 October 2011 IAEA Report INDC(NDS)-0599

A new resonator Schottky pick-up for short-lived nuclear investigations

B. Sun[1], R. Knöbel[1,2], N. Kuzminchuk[1], H. Weick[2], N. Winckler[2,3], S. Ayet[1], K. Blaum[3], F. Bosch[1], R.B. Cakirli[3,4], I. Dillmann[1,2], C. Dimopoulou[1], A. Estradé[2], F. Farinon[2], H. Geissel[1,2], P. Hülsmann[2], C. Jesch[1], C. Kozhuharov[2], J. Kurcewicz[2], S.A. Litvinov[2], Yu.A. Litvinov[2,3], I. Mukha[2], C. Nociforo[2], F. Nolden[2], P. Petri[2], S. Pietri[2], W.R. Plaß[1,2], A. Prochazka[2], M.W. Reed[5], B. Riese[2], M.S. Sanjari[2], D. Shubina[2,3], C. Scheidenberger[1,2], M. Steck[2], Th. Stöhlker[1], X. Tu[6], P.M. Walker[5], M. Winkler[2], and J.S. Winfield[2]

[1]JLU, Giessen; [2]GSI, Darmstadt; [3]MPIK, Heidelberg ; [4]Istanbul Uni.; [5]Uni. Surrey; [6]IMP, Lanzhou

A fast and sensitive resonant pick-up [1] was built into the ESR last year for the detection of heavy ion Schottky noise. In comparison with the standard Schottky pick-up used in previous experiments [2], the new probe has a significantly enhanced signal-to-noise ratio of Schottky spectra, which is critical for observation of fast changes such as short-lived nuclear decays or for more averaging to pursue a frequency spectrum with better quality. Here, we report the result from a pilot experiment on the application of this probe in short-lived nuclear investigation.

Shown in Fig. 1 is a measured revolution frequency spectrum of ^{238}U projectile fragments centered at ^{213}Fr, where the ESR is operated in the isochronous mode with the transition point γ_t being 1.4. The advantage of the new probe is clearly shown in the Schottky spectrum, where we are able to trace the fate of each circulating ion in the ring to the time accuracy of ms, e.g. 3.2 ms in the upper panel of Fig. 1, more than one order of magnitude reduced in comparison with previous storage ring experiments.

Especially for the isochronous mass measurement, it is even possible to reveal the dispersion of momentum $\delta p/p$ of each ion by the corresponding frequency spread $\delta f/f$ according to $\delta p/p = 1/\eta \cdot \delta f/f$, where η is the frequency dispersion function. This is demonstrated in Fig. 2, where the revolution frequency distribution of two species ^{213}Ra^{86+} and ^{213}Fr^{86+} is shown. Four ions are resolved by frequency lines for ^{213}Ra^{86+}.

For the 16 ms spectrum shown in the lower panel of Fig. 1, a frequency resolving power of 50, 000 is obtained. This value is comparable to that from the standard time-of-flight spectrum [2], where a TOF detector is used for the revolution frequency determination. Furthermore, a resolving power of 1.25×10^6 is obtained in the standard operational mode of the ESR with electron cooling.

In all, the new resonant Schottky pick-up opens a way towards precision measurements of short-lived nuclei with lifetimes down to a few tens of ms. For the isochronous mass measurement, however, studies show that Schottky band overlaps will occur, and a method for unambiguous identifications of the frequency spectra has to be developed. In addition, it needs to be verified if the noise power density of hot fragments obeys the same scaling law as that of the cooled fragments. Therefore, further experiments using well known long/short-lived nuclides need to be commissioned.

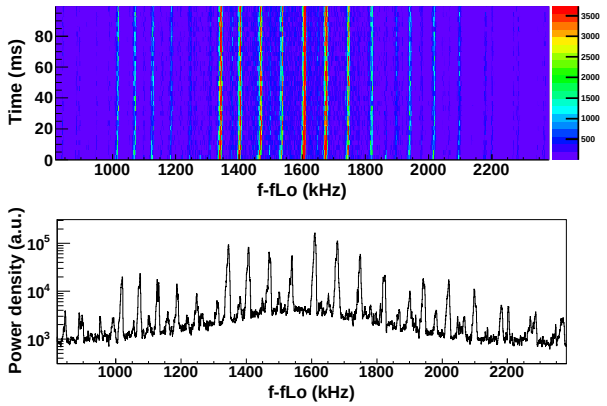

Figure 1: The time evolution of the Schottky revolution frequency spectrum (Upper panel) and the projection of the first 16 ms at the measurement (Lower panel). The raw spectrum is recorded by the new resonant Schottky pick-up. fLo is 244.9886 MHz.

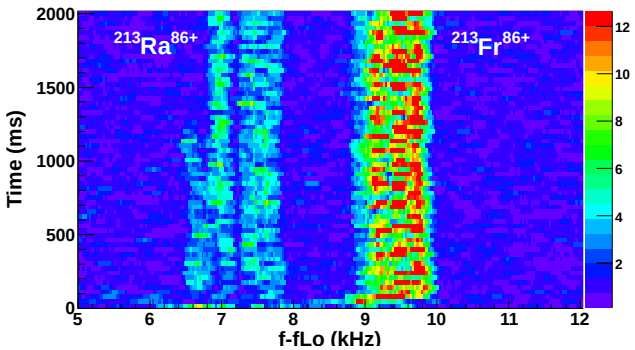

Figure 2: Frequency dispersion of two species ^{213}Ra^{86+} and ^{213}Fr^{86+}, which are injected into the ESR operated in isochronous mode. fLo here is 245.9245 MHz.

References

[1] F. Nolden, et al., Nucl. Instr. and Meth. A 659 (2011) 69.

[2] B. Franzke, H. Geissel, G. Münzenberg, Mass Spectrom. Rev. 27 (2008) 428.

Status of the focusing system in front of the Super-FRS target

J.S. Winfield[1,#], K.-H. Behr[1], H. Geissel[1,2], M. Gleim[1], H. Weick[1] and M. Winkler[1]

[1]GSI, Darmstadt, Germany, [2]Justus Liebig University, Giessen, Germany

The design and layout of the focusing system before the Super-FRS target has been refined and modified from the preliminary studies presented in Refs. [1,2]. First one should note that the split-unit design, using Super-FRS and SIS100 superconducting quadrupoles, has been adopted. Certain quadrupoles within a unit may be switched off, depending on the magnetic rigidity. The modifications to the lattice have resulted from the request to add two steerer magnets, one vertical and the other horizontal, and a diagnostic chamber. In addition, the desire to make the cryostats for the triplets and doublet+steerers the same length (5.6 m, including flanges), has resulted in a further adjustment. The new layout with respect to the building is shown in Fig. 1. In the figure, the beam from the coupling line from the synchrotron enters from the left. The focusing system starts with a doublet of SIS100-type 130-mm radius quadrupoles. Then follow a doublet and two triplets of Super-FRS-type quadrupoles. The wall in front of the doublet+steerers will be thinner and located further upstream than shown in Fig. 1.

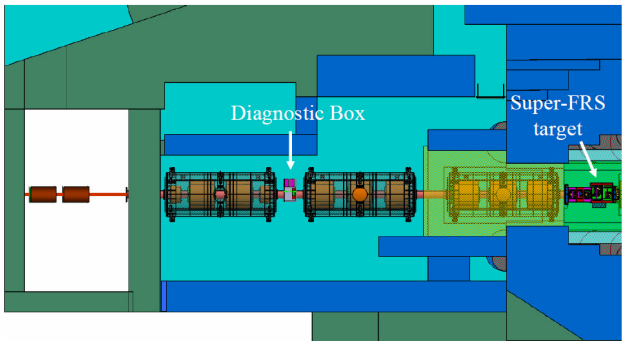

Figure 1: Plan view of the doublets and triplets of the focusing system with respect to the building walls and shielding. The cryostats for the Super-FRS type magnets are made transparent to show the magnets within.

The two superferric steerer magnets TFF1KH02 and TFF1KV02, coloured in purple in Fig. 2, are placed either side of the quadrupole doublet TFF1QS04-05. They are similar to the steerer magnets in the Super-FRS: 500-mm effective length, 380-mm by 240-mm usable aperture. The spacing between the quadrupoles and the steerers is arranged to fill a standard Super-FRS triplet cryostat.

The diagnostic chamber will be approximately 500 mm long and located as indicated in Fig. 1. It could be instrumented with, for example, a removable beam profiler and a viewing phosphor screen.

#j.winfield@gsi.de

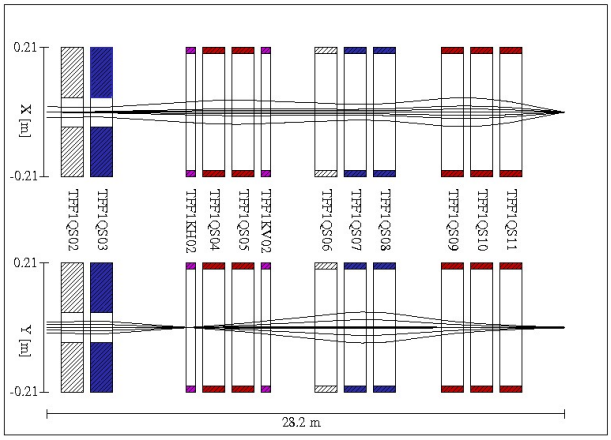

Figure 2: Example ion-optics of the focusing system ("8Q" mode). Upper part: horizontal plane; lower part: vertical. The two unused quadrupoles are uncoloured.

The 1st-order ion-optics, calculated by GICOSY [3], is shown in Fig. 2. The beam rigidity was 55 Tm and eight quadrupoles were used. The initial emittances for the SIS100 coupling beam-line (not shown in the figure) were ε_x = 12.75 mm mrad and ε_y = 4.6 mm mrad. The beam spot size at the Super-FRS target can be made as small as 1-mm by 2-mm for slow extraction experiments. Here the horizontal width is defined as

$$w_x = \sqrt{\beta_x \varepsilon_x} \,,$$

where β_x is the projection of the Twiss parameter. A similar definition holds for the y-width. The parameter corresponds roughly to the full-width at half maximum of the projection of the phase space along the respective axis. Fifth-order GICOSY calculations, without the use of any multipole correction-magnets, give a similar w_x but a w_y enlarged by about 50%. Note that the bend of the dipole magnets in the SIS100 coupling line are all in the vertical direction.

For fast extraction of the uranium beam, used for Ring Branch experiments, a larger beam spot size may be employed, in order to reduce the stress on the target by the high instantaneous power delivered [4].

References

[1] D. Boutin et al., EMIS07, Deauville, France, July 2007, Nucl. Instr. Meth.B 266 (2008) 4192.

[2] D. Boutin et al., GSI Scientific Report 2005, (GSI Report 2006-1) p. 49.

[3] H. Weick, GICOSY homepage, http//www-linux.gsi.de/~weick/Gicosy/.

[4] N. Tahir et al., J. Phys. D: Appl. Phys. 38 (2005) 1828.

Modifications of Graphite Material in the Super-FRS Beam Catchers*

M. Tomut[1,2], H. Weick[1,#], M. Avilov[3], M. Bender[1], M.Gleim[1], C. Karagiannis[1], I. Manika[4], J.Maniks[4], W. Mittig[5], F. Pellemoine[3], M. Schein[3], K. Schwartz[1], D. Severin[1], C. Trautmann[1,6], R. Zabels[4]

[1]GSI, Darmstadt, Germany; [2]NIMP, Bucharest, Romania; [3]FRIB, MSU, East Lansing, MI, USA; [4]Institute of Solid State Physics, University of Latvia, Riga, Latvia; [5]NSCL, MSU, East Lansing, MI, USA [6]TU Darmstadt, Germany

The beam catcher of the Super-FRS is a critical part in the design of the pre-separator. It has to absorb the full beam power of one fast extraction pulse, which leads to energy densities of up to 600 mJ/g in the peak [1]. Due to its low density and Young's modulus, graphite is the favourite material to reduce the magnitude of the resulting pressure waves. It has good thermal conductivity at room temperature, but less at high operating temperature. In addition, radiation damage may eventually severely reduce the thermal conductivities from 90 W/mK for pristine graphite at room temperature to values below 10 W/mK for irradiated graphite [2]. As a consequence the thermal conductivities of 90 W/mK for pristine graphite at room temperature can be reduced to values below 10 W/mK for irradiated graphite [2]. For the nominal operating conditions of the beam catcher, a power of up to 23 kW has to be transferred to a water cooled heat sink. For low thermal conductivities, this energy cannot be removed fast enough from the beam spot. Mechanical damage due to thermal stress and even sublimation of graphite may occur. Figure 1 shows the temperature distribution in the beam catcher calculated with ANSYS for the pristine material. Simulations show that this design would work for values of the thermal conductivity higher than 30 W/mK. For larger thermal conductivity degradation also the mouth-like opening design, aiming to increase the transverse surface area of the hot volume, cannot prevent the failure any longer.

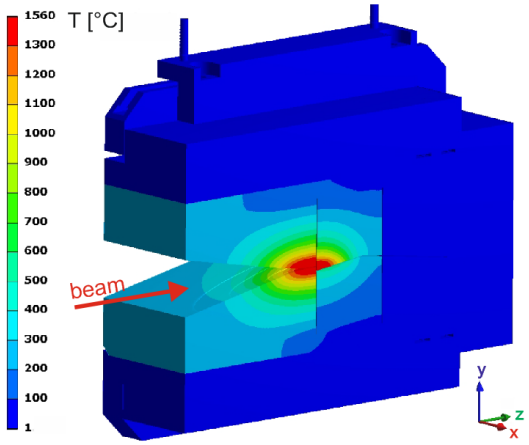

Figure 1: ANSYS FEM simulation of temperature distribution in equilibrium, for a beam of σ_x=2cm, σ_y=1cm, using parameters of pristine graphite (SGL R6650).

By operating the beam catcher at high temperatures, one expects to anneal significantly the radiation damage. If and how this works for ion-irradiated graphite is not known and it was the subject of recent studies performed at GSI in collaboration with FRIB. The goal is to investigate damage annealing in high-temperature ion-irradiated graphite, to infer the thermophysical and mechanical parameters necessary for simulations and find a mechanical design that takes advantage of the damage annealing. Thermal diffusivity measurements [3] show that operating the beam catcher at 1500 °C considerably reduces radiation-damage induced thermal conductivity degradation.

Radiation induced hardening of graphite reduces the capacity of shock absorption of the beam catcher. Indentation tests have been performed to follow the influence of the irradiation temperature on the degradation of mechanical properties of ion-irradiated high density, isotropic graphite. Our results show that irradiating at temperatures higher than 1000 °C, considerably reduces the heavy ion-induced hardening. Figure 2 shows measured values for the Young's modulus for graphite samples irradiated with 8.6 MeV/u Au ions at UNILAC, at temperatures of 445 °C (beam-induced heating), 1000 °C and 1600 °C (additional Joule heating), excluding the layer affected by sample roughness.

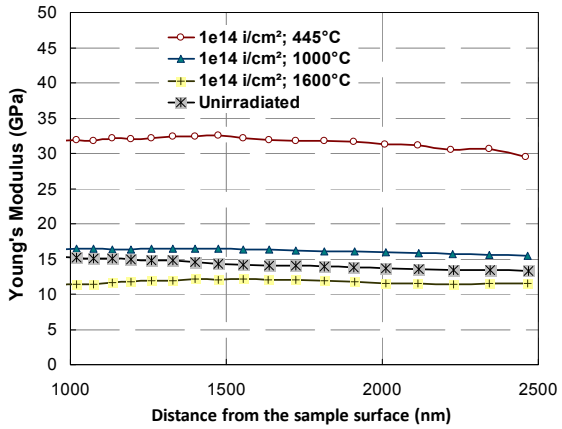

Figure 2: Evolution of graphite Young's modulus as function of depth after irradiation with 8.6 MeV/u ^{197}Au ions at different temperatures for a fluence of 10^{14} ions/cm^2.

Irradiation-induced increase of the Young's modulus increases the amplitudes of the beam-induced pressure waves in the fast-extraction regime. These recent results advocate operation temperatures above 1000 °C together with preheating of the target or beam catcher material.

[1] Super-FRS baseline Technical report (2008).
[2] T. Maruyama et al., J.Nucl.Mat. 195 (1992) 44.
[3] N. Horny et al., this GSI annual report.

* Work supported by EU, EuCARD contract No. 53102
#h.weick@gsi.de

First Operation of the Cryogenic Stopping Cell for the Super-FRS at the FRS Ion Catcher

T. Dickel[1,2], *S. Purushothaman*[2], *P. Dendooven*[3], *J. Ebert*[1], *A. Estrade*[2], *F. Farinon*[2], *H. Geissel*[1,2], *E. Haettner*[1], *C. Jesch*[1], *N. Kalantar-Nayestanaki*[3], *R. Knöbel*[1,2], *J. Kurcewicz*[2], *J. Lang*[1], *I. Moore*[4], *C. Nociforo*[2], *S. Pietri*[2], *W. Plaß*[1,2], *A. Prochazka*[2], *M. Ranjan*[3], *M.P. Reiter*[1], *S. Rinta-Antila*[4], *C. Scheidenberger*[1,2], *M. Takechi*[2], *J.S. Winfield*[2], *and H. Weick*[2]

[1]Justus-Liebig-Universität Gießen, Germany; [2]GSI, Darmstadt, Germany; [3]KVI, University of Groningen, Netherlands; [4]University of Jyväskylä, Finland

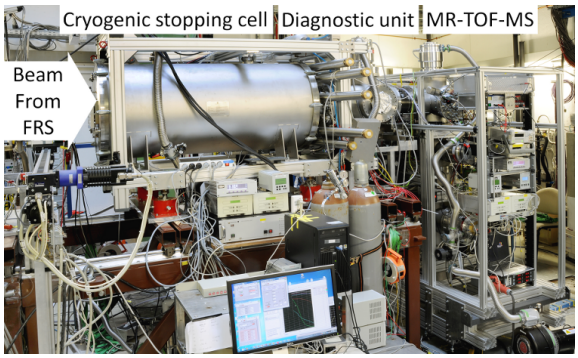

Figure 1: Photograph of the setup of the FRS Ion Catcher

A novel cryogenic stopping cell has been developed [1] for the Low Energy Branch (LEB) of the Super-FRS at FAIR. It will be used to stop and thermalize projectile and fission fragments, which have been produced, separated and range-bunched in the Super-FRS at relativistic energies, and to make them available for precision experiments with ions almost at rest. The cell has a stopping length of 100 cm, a diameter of 25 cm, and is designed to be operated with helium at temperatures of 60-90 K and pressures of up to 250 mbar, corresponding to densities up to 20 mg/cm^3.

For its commissioning, the cryogenic stopping cell was installed at the FRS Ion Catcher [2, 3] (Fig.1). The beam is made monoenergetic with a degrader in the mid-focal plane of the FRS. A homogenous degrader at the final focal plane is used to adjust the range of the ions such that they are stopped in the cell. A multiple-sampling ionization chambers and a silicon detector are used for ion identification and counting. Behind the stopping cell a low-energy radio-frequency quadrupole (RFQ) transport system, a diagnostics unit [4] and a multiple-reflection time-of-fligh mass spectrometer (MR-TOF-MS) [5] enables the detection, identification and quantification of the ions extracted from the cell. The diagnostics unit contains a silicon detector and channeltron detector, mounted on elevator stage, and can thus register both radioactive and stable ions.

The cryogenic stopping cell and the MR-TOF-MS were commissioned on-line with uranium projectile fragments, which were produced at 1 GeV/u and injected into the cell. In this experiment, the cell was operated at 100 mbar helium and 100 K, corresponding to an areal weight of 5 mg/cm^2 (He). The efficiency of the stopping cell was determined using the alpha emitter ^{223}Th. Fig. 2 shows a typical alpha spectrum measured with the silicon detector in the diagnostic unit behind the stopping cell. Preliminary analysis of the data yields an overall efficiency of about 8%, which includes the stopping, transport, and extraction from the cell. It can be divided into a stopping efficiency of 15% (determined by the range distribution of the ions and the areal weight of the stopping cell) and an ion survival and extraction efficiency of about 50%.

This experiment constitutes the first on-line operation of a gas-filled stopping cell at cryogenic temperatures. The helium density used in the experiment amounts to 0.05 mg/cm^3, which is about twice higher than the gas densities achieved in comparable room temperature stopping cells employing RF structures. The overall efficiency achieved for the stopping and extraction of relativistic projectile fragments is more by a factor of four larger than in a previous experiment [2] at FRS. In a forthcoming on-line experiment at the FRS Ion Catcher scheduled for spring 2012, further systematic studies of the cryogenic stopping cell as well as first test-measurements with the MRTOF-MS will be performed at the FRS Ion Catcher.

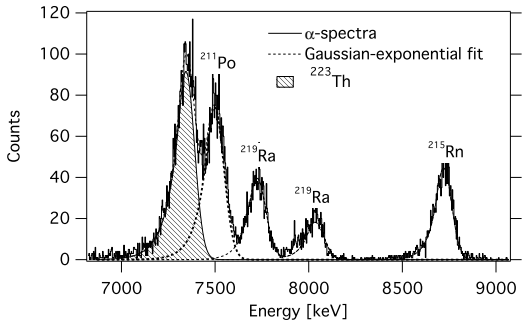

Figure 2: Typical alpha spectrum of ^{223}Th and its decay products obtained with the silicon detector behind the stopping cell

References

[1] M. Ranjan et al., Eur. Phys. Lett. 96 (2011) 52001.
[2] M. Petrick et al., Nucl. Instrum. Methods B 266 (2008) 4493.
[3] W.R. Plaß et al., GSI Scientific Report 2009 (2010), p. 137.
[4] M.P. Reiter, Master Thesis, JLU Gießen, 2011.
[5] T. Dickel, Doctoral Thesis, JLU Gießen, 2010.

RF Quadrupole Beam Lines for the Preparation and Manipulation of Beams of Exotic Nuclei: Instrumentation for SHIPTRAP and the FRS Ion Catcher*

E. Haettner[1,2], *M. P. Reiter*[1], *W. R. Plaß*[1,2], *T. Dickel*[1,2], *J. Ebert*[1], *H. Geissel*[1,2], *C. Jesch*[1], *M. Petrick*[1], *S. Purushothaman*[2], *and C. Scheidenberger*[1,2]

[1]Justus-Liebig-Universität Gießen, Germany; [2]GSI, Darmstadt, Germany

High precision experiments with exotic nuclei, such as spectroscopy or mass measurements, often require low-emittance ion beams with kinetic energies of only a few eV. These nuclei can be produced and separated in-flight, subsequently slowed down and thermalized in a gas-filled stopping cell and extracted as low-energy beams.

Conventional low-energy beam lines use a structure of electrostatic or magnetic fields for ion transport. In contrast, a novel concept employs continually radiofrequency quadrupole (RFQ) fields for ion transmission [1]. Depending on the RF and DC fields applied in the RFQs and the introduction of a buffer gas; ion cooling, identification, separation, bunching, and transport can be achieved. This diverse range of applications in addition to the compactness, easy optimization, the ability to operate at high residual gas pressures, and full transmission make RFQs ideal tools for the work with rare exotic nuclei, in particular in the vicinity of gas-filled stopping cells. This concept has been applied in developments for the FRS Ion Catcher [2], which serves as a test bench for the LEB of the Super-FRS at FAIR, and for SHIPTRAP.

For SHIPTRAP a triple RFQ system consisting of an RFQ cooler, RFQ mass filter and an RFQ buncher has been developed [3]. Maintaining nearly 100% transmission efficiency, the compact device with a total length of 1 m, allows for cooling, identification, mass selection and ion bunching. A mass resolving power (FWHM) of 240 has been demonstrated. Fig. 1 shows the energy spread of ions extracted from the RFQ buncher towards the Penning trap as a function of the temporal width of the ion bunch. The product of these two figures, the longitudinal emittance, is experimentally found to be 0.45(0.05) eVμs only and close to the theoretical limit determined by size of the storage volume and the temperature of the buffer gas. The emittance is an order of magnitude smaller than that of the present setup [4] and will enable a significantly improved broadband time-of-flight ion identification at SHIPTRAP.

The beam line at the the FRS Ion Catcher [2] consists of a sequence of RFQs. An RFQ diagnostics unit (Fig. 2) provides ion current measurement, detection and identification of radioactive ions and determination of the time structure of the ion population [5]. The unit contains three RFQ segments. The middle segment is mounted in an elevator structure, which in addition contains a silicon detector, a channeltron detector, and a Cs ion source for testing of instruments downstream of the diagnostics unit. By selection of the vertical position of the elevator, the respective functionality of the unit can be activated. Furthermore, the unit includes a gate valve to separate the stopping cell from the beam line. The unit has been constructed, commissioned and successfully used in the first online test of the cryogenic stopping cell at the FRS Ion Catcher [6]. Future development will include an electrically switchable RFQ beam switchyard. It will allow selective transmission of ions into one of six possible directions, e.g. to different experimental stations or for the introduction of reference ions.

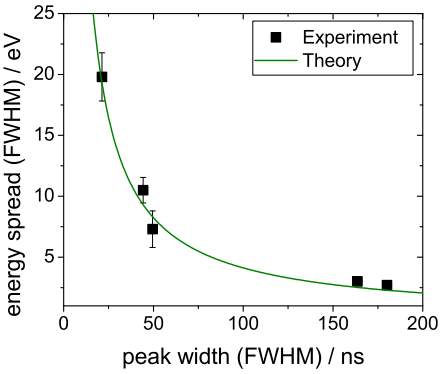

Figure 1: Energy spread versus the temporal width of ions extracted from the new RFQ system for SHIPTRAP [3].

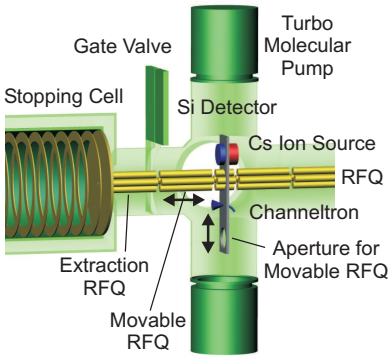

Figure 2: Schematic figure of the RFQ diagnostics unit [5].

References

[1] W. R. Plaß *et al.*, Eur. Phys. J. Special Topics **150** (2007) 367.

[2] W. R. Plaß *et al.*, GSI Scientific Report 2010 (2011) 137.

[3] E. Haettner, Doctoral thesis, University of Giessen, 2011.

[4] D. Rodríguez, Doctoral thesis, University of Valencia, 2003.

[5] M. P. Reiter, Master thesis, University of Giessen, 2011.

[6] T. Dickel *et al.*, this volume.

* Work supported by the BMBF under contract No. 06GI9114I

On-line Commissioning of the Multiple-Reflection Time-of-Flight Mass Spectrometer for the LEB at the FRS Ion Catcher*

J. Ebert[1], *T. Dickel*[1,2], *W. R. Plaß*[1,2], *S. Ayet*[2], *P. Dendooven*[3], *A. Estrade*[2], *F. Farinon*[2], *H. Geissel*[1,2], *E. Haettner*[1,2], *C. Jesch*[1], *N. Kalantar-Nayestanaki*[3], *R. Knöbel*[1,2], *J. Kurcewicz*[2], *J. Lang*[1], *I. Moore*[4], *C. Nociforo*[2], *S. Pietri*[2], *A. Prochazka*[2], *S. Purushothaman*[2], *M. Ranjan*[3], *M. P. Reiter*[1], *S. Rinta-Antila*[4], *C. Scheidenberger*[1,2], *M. Takechi*[2], *H. Weick*[2], *and M. I. Yavor*[5]

[1]Justus-Liebig-Universität, Gießen, Germany; [2]GSI, Darmstadt, Germany; [3]KVI, University of Groningen, Netherlands; [4]University of Jyväskylä and the Helsinki Institute of Physics, Finland; [5]Institute for Analytical Instrumentation of the Russian Academy of Sciences, St. Petersburg, Russia

At the Low Energy Branch (LEB) of the Super-FRS at FAIR, exotic nuclei produced by projectile fragmentation or fission will be slowed-down and thermalized in a cryogenic stopping cell [1], extracted and made available to experiments with ions almost at rest. A multiple-reflection time-of-flight mass spectrometer [2, 3] (MR-TOF-MS) positioned behind the stopping cell will provide isobar separation, broadband mass spectrometry for ion identification and diagnostic purposes, and allow for highly accurate mass measurement of very short-lived nuclei.

Recently, several improvements have been implemented in the MR-TOF-MS. It was modified to include a new moveable detector system, which consists of a time-of-flight SEM detector and a Bradbury-Nielsen-Gate (BNG) for mass separation. A silicon detector was mounted behind the BNG. The detector system can be driven by a vacuum-compatible stepper motor. A change between the detectors can be performed within half a minute and, thus, mass measurements and decay spectroscopy can be done quasi simultaneously. This opens new application areas of the MR-TOF-MS: (i) Decay spectroscopy and lifetime measurements of mass-separated ions. (ii) Identification of ions by the combination of a mass scan with the BNG and decay measurements in the silicon detector, which e.g. enables the detection of exotic nuclei in molecules. Further instrumental developments implemented in the MR-TOF-MS include improvements of the RFQ ion guide and injection trap system, increased vacuum separation between the individual stages of the MR-TOF-MS and the enhanced stability of the voltages of the time-of-flight analyzer [4].

The MR-TOF-MS was installed behind the cryogenic stopping cell at the FRS Ion Catcher [5, 6], which serves as test bench for the LEB, and in October 2011 it was commissioned with ^{238}U projectile fragments. Radioactive ions were extracted from the stopping cell and measured in the MR-TOF-MS. As a broadband and high resolution mass spectrometer, the MR-TOF-MS is the key device for the identification of ions extracted from the cryogenic stopping cell and hence for the performance characterization of the cell. The new detector system was tested with a ^{223}Ra ion source in the stopping cell, which provides decay products from ^{219}Rn to ^{207}Pb. Fig. 1 shows the mass and energy spectrum of the decay products. Following the recent on-line commissioning of the MR-TOF-MS, further systematic studies of the cryogenic stopping cell and first direct mass measurements will be performed with the MR-TOF-MS at the FRS Ion Catcher in 2012.

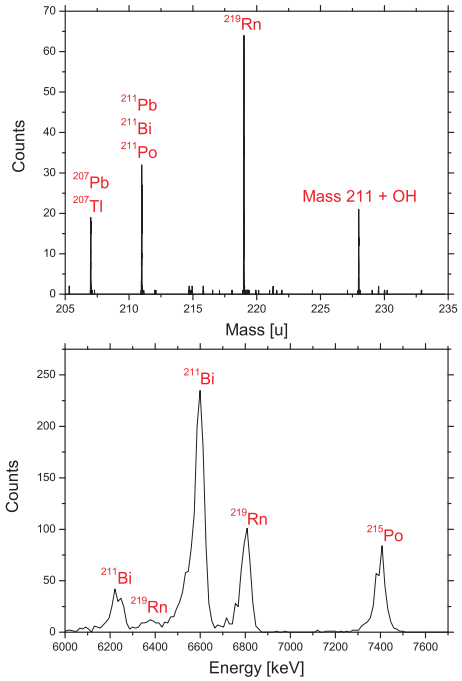

Figure 1: (a) Mass spectrum of the decay products of the ^{223}Ra ion source extracted from the cryogenic stopping cell. After a flight time of only 560 μs, the mass resolving power reaches 9000 (FWHM). (b) Alpha spectrum of the decay products of the ^{223}Ra ion source measured with the silicon detector [4].

References

[1] M. Ranjan et al., Eur. Phys. Lett. 96 (2011) 52001.
[2] W.R. Plaß et al., Nucl. Instrum. Methods B 266 (2008) 4560.
[3] T. Dickel, Doctoral Thesis, 2010, JLU Gießen.
[4] J. Ebert, Master Thesis, 2011, JLU Gießen.
[5] W.R. Plaß et al., GSI Scientific Report 2010 (2011), p. 137.
[6] T. Dickel et al., this volume.

* Work supported by the BMBF under contract No. 06GI9114I

Integration of A Self Triggered Digital Data Acquisition System into the FRS-MBS

J. Agramunt[1], N. Kurz[2], C. Nociforo[2], H. Schaffner[2], and J.L. Tain[1]

[1]IFIC, Valencia, Spain; [2]GSI, Darmstadt, Germany

A self-triggered Digital Data Acquisition System (DDAS) has been developed at IFIC-Valencia and integrated for the first time into the MBS system for the FRS experiments S323 and S410 carried out in September 2011 [1].

DDAS was originally developed as a stand-alone acquisition system [2] to solve some problems (see below) associated to the use of 4π neutron counters based in the combination of ^{3}He proportional tubes with hydrogenated neutron moderators. Such detectors are universally employed for the measurement of β-delayed neutrons and the determination of neutron emission probabilities P_n, a parameter of fundamental as well as practical relevance.

Due to the moderation process, a neutron needs considerable time (up to hundreds of microseconds) before it can be captured in ^{3}He to produce a distinctive breakup signal. On the other hand the most accurate determination of P_n is based in the comparison of beta-neutron coincidence rates with single beta rates. In a conventional DACQ it will be necessary to open long acquisition gates (typically 250 μs) after a beta trigger in order to register the coincidence. This introduces a considerable dead time in the system. Moreover in such a long period the possibility of having more than one neutron registration is not small. Multihit TDC modules with capacity of multiple time registration exist, but they do not offer the possibility to perform off-line noise discrimination by amplitude, which can introduce systematic errors.

As an alternative we use waveform digitizers with firmware resident digital processing filters. We have chosen the SIS3302 100 MHz 16 bit 8 channel modules from Struck Innovative Systeme [3] with Gamma Firmware. Individual ^{3}He tubes are connected to different input channels, each one operating in self-triggered mode. Every time a signal goes above the threshold the filters provide time (on 10 ns steps with a range of 48 bits) and amplitude information simultaneously. An external 100 MHz clock (SIS3820) provides the same time basis for all the modules connected. Each channel stores the time-amplitude data into a 64 MB memory. The memory space is divided into two data banks which are working in alternating mode: while one data bank is filled with the incoming data, the other one is being read-out through the VME bus. In this way a minimum system dead time is achieved, which is monitored with a fix-frequency pulse generator signal. Additionally this system provides complete freedom during the off-line analysis to select the length of the beta-neutron time correlation window, which can be made arbitrarily long. This feature is important to determine accurately the rate of random coincidences.

A side advantage of the use of the digitizers is an improved noise rejection capability. The signals from ^{3}He proportional tubes suffer from large electronic noise. We have found that the noise filtering capacity of the combination: preamplifier + amplifier + digitizer, allows setting a lower threshold than the conventional analogue scheme: preamplifier + timing filter amplifier + discriminator. In fact we found that in our noise conditions 25-30 % of good neutron signals were lost in the analogue branch.

The system was employed successfully in previous experiments with the BELEN detector [4] at the IGISOL online separator of JYFL (Finland) where the ancillary detectors, a single beta-detector and one HPGe detector, were read-out in the same way.

At the FRS the large number of ancillary detectors (including the SIMBA implantation detector [5] with a large number of channels) and the large expected rates would make impractical such an approach, which generates a very large volume of data. The solution adopted was to feed the thirty ^{3}He tube amplifier signals into a parallel DDAS (with a total of five SIS3302 modules) incorporated as an additional MBS branch to the standard FRS DACQ. The self-triggered neutron data accumulated in the module memory was read out with the general system trigger. The trigger itself was fed into one channel of DDAS to correlate the time as measured by DDAS with the MBS time stamp information. In order to limit the amount of data accumulated in the memory between readouts (and thus the volume of data transferred by MBS) a 100 Hz clock was added as a trigger to the system. In this way it was possible to ensure that DDAS was not determining the global system dead time.

DDAS was also used to register all the ions arriving at the end of the FRS and giving a signal in the first tracking detector (TPC). Most of these particles were not giving a trigger signal in the detectors behind the focal plane slits but were still producing neutrons at different material elements in between, which increased considerably the background rate in BELEN. The information provided by DDAS will be used to veto the unwanted neutron signals.

References

[1] M.B. Gomez et al., this Scientific Report

[2] J. Agramunt et al., "GasificTL: a self-triggered data acquisition system for decay experiments", in preparation.

[3] http://www.struck.de/

[4] M. Belen Gomez-Hornillos et al., J. Phys.: Conf. Ser. 312 (2011) 052008.

[5] Ch. Hinke, PhD Thesis, TUM, 2010.

Test and characterization of the VULOM with the *TRLO* firmware for the implementation of the Trigger Logic of the PRESPEC experiments

D. Ralet[1], *S. Pietri*[1], *H. T. Jahansson*[2], *J. Gerl*[1], *N. Pietralla*[3], *and the PRESPEC-AGATA collaboration*[1]

[1]GSI Helmoltzzentrum für schwerionenForschung GmbH, Darmstadt, Germany; [2]Chalmers University of Technology, Göteborg, Sweden; [3]Technische Universität, Darmstadt, Germany

Introduction

In April-May 2011, several experiments were performed at GSI, for the PRESPEC campaign. They had two objectives. The first one was to do nuclear structure physics and the second to prepare the AGATA campaign at GSI, which will start at the beginning of year 2012. A test for the trigger logic implementation was done during these experiments. It consisted in the feasibility study and the design of a new trigger logic tool which is more efficient and easier to use.

Overview of the electronic module

Dr. Hakan T. Johansson (University of Chalmers, Sweden) developed a firmware for the VULOM4 [2], a VME module including a FPGA. This firmware called the *TRLO* [3, 4] consists in a set of functions for the implementation of trigger logic. It makes use of the VULOM easy to use, and adaptable for different experiments. For the test performed in summer 2011, we have for example used two different logic, one for the FRS experiments (S410), and the other one for the PRESPEC experiments(S378).

Context of the test

During the experiments of May, tests of the *TRLO* were fulfilled in parallel to the main acquisition which uses a trigger logic based on NIM electronic modules. The inputs of the trigger logic of the main acquisition were duplicated and used as inputs for the module VULOM. This assure the same condition for the test.

The implementation of the PRESPEC trigger was done using most of the memory in order to reduce the global dead time of the acquisition. The one for the FRS experiment was easier because it used half of the tools available with the *TRLO* in order to generate the readout gates.

Results of the test

With these two acquisitions running in parallel , it was possible to compare the number of triggers generated by the VULOM and the one from the main acquisition. As shown on Fig. 1, the ratio between these two numbers was greater than 99%. Moreover, the time of the coincidence signal generated by the VULOM is shorter than the one from the NIM base trigger logic. These results were confirmed by a second test during an FRS experiment. This

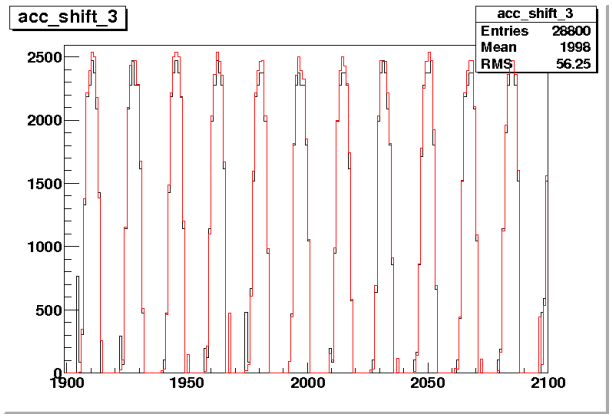

Figure 1: Numbers of accepted triggers as a function of time for the main acquisition and for the *TRLO*. The red curve corresponds to the scaler from the main acquisition and the black one to the scaler from the *TRLO*. The same reduction factors were used, and the same triggers were activated.

advantages will lead to the usage of the VULOM with the *TRLO* firmware for the next campaign: AGATA at GSI.

References

[1] VULOM4 documentation, "www.gsi.de/informationen/wti/ee/fertigung/module_datenpflege_e.html"

[2] Ana Isabel Martinho Henriques,A new trigger Logis system for the LAND/R3B setup, 2010

[3] Hakan T. Johansson, LAND TRLO II - trigger logics - in VULOM and TRIDI, TRLO Manual, 2010

Time of flight with a segmented plastic finger detector at high particle rate*

F. Ameil[1], M. Danchev[3], P. Boutachkov[2], J. Kurcewicz[1], S. Pietri[1], D. Ralet[2], J. Gerl[1], N. Pietralla[2] and the PRESPEC-AGATA collaboration

[1]GSI, Darmstadt, Germany; [2]TU Darmstadt, Germany; [3]University of Sofia, Bulgaria.

Improved SIS primary beam intensities and implementation of fast ramping time converts directly into higher yields of exotic nuclei. Improvements to the FRS [1] tracking detectors are necessary to allow for higher rates. This concerns in particular the rate at the intermediate focal plane S2 where tracking detectors allowing for rates higher than 10^6 s^{-1} are needed.

The segmented plastic finger detector consists of 15 strips of 14 mm width read out via 16 Hamamatsu R7400 fast subminiature photomultiplier tubes (see Fig. 1).

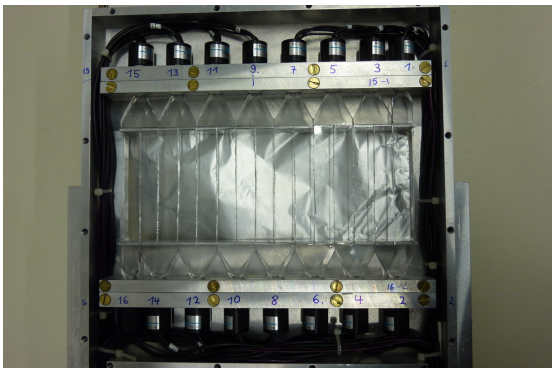

Figure 1: the finger detector.

This detector was refurbished and a performance test was performed with a pulsed LASER where an intrinsic time resolution of ~ 60 ps was achieved.

It was successfully commissioned in September 2010 and was used during several experiments at the FRS in 2010/2011 especially the PRESPEC campaign.

Fig. 2 shows the particle identification plot for a ^{104}Sn setting at a particle rate of ~ 10^6 s^{-1}, the ToF was determined using standard scintillators at the intermediate focal plane S2 and at the final focal plane S4, TPC's were used for the position correction. The same identification plot is shown in Fig. 3 using a ToF determination between the finger detector at S2 and the scintillator at S4, the finger detector was also used for the position correction.

At such high particle rate the mass resolution achieved with the finger is much better. At the same time the tracking efficiency was about 90%, while it went down to <10% for the standard S2 scintillator. At lower rate a better resolution was seen as well.

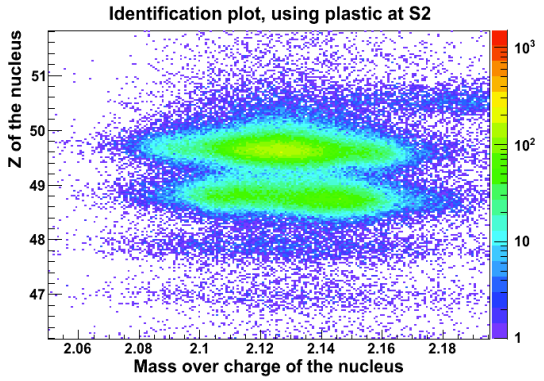

Figure 2: ^{104}Sn Identification plot taken from S372, using TPC's and standard plastic scintillators at S2, the rate was ~ 1 MHz

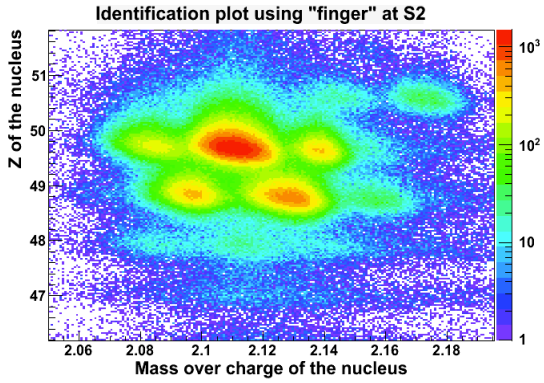

Figure 3: same as Figure 2 but using the segmented finger detector at S2

The on-going development of a new finger detector consisting on 60 strips of 4 mm width will allow a further increase of the maximal rate at S2.

References

[1] H. Geissel et al., Nucl. Instr. Meth. B 70 (1992) 286

* This work is partially supported by BgNSF (Grant No. DDVU 02/69)

Investigation of the spatial resolution of a large scale, emissive foil detector

M. Pfeiffer[*], *G. Pascovici, M. Cappellazzo, S. Thiel, N. Warr, and J. Jolie*
Institut für Kernphysik, Universität zu Köln, Germany

At the low energy branch of the Super-FRS at FAIR exotic isotopes far off the valley of stability will become available at the future HISPEC/DESPEC facility for high resolution nuclear spectroscopy. In order to open certain reaction channels at low energies ($\approx 5 - 10\mathrm{MeV/u}$), the fast extracted ions (up to several hundreds of MeV/u) have to be slowed down by a degrader close to the target. Such an additional spatial and time straggeling is introduced for most of the primary ions that will survive this process. A small fraction will end up in new spallation products. To give the experimenter a proper gate on the ions he is looking for, one has to place a tracking detector with a high timing resolution between the degrader and the target. The only choice left is to use an emmissive foil detector to not influence the degraded beam in a noteworthy way [1].

A prototype using the emitted secondary electrons by deflecting them out of the major beam axis on a MCP stack has been build and tested [2]. The timing resolution is in the order of $200\mathrm{ps}$ at an active area of $80 \cdot 100\mathrm{mm}^2$, which fits the desired needs. Opponent, the spatial resolution is varying a lot depending on the initial hit pattern on the foil, which has already been observed [3].

Especially the huge difference between the X and Y axis (as horizontal and vertical coordinate, in direction of beam) in each unit is of major concern. To further investigate this effect, we used several masks with multiple holes of known diameter. In a second step we simulated the ion optics to obtain the projected image at the conversion foil layer. This image was then used as reference to the measured image, taken with the double delay line readout of the detector.

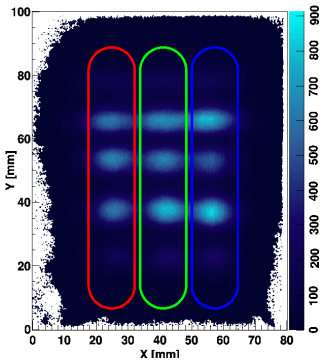

Figure 1: Image of a multi-hole mask, measured with unit one. The coloured areas correspond to graph 2.

Figure 1 shows the measured image of a 3×5 matrix of $6.5\mathrm{mm}$ diameter holes at $15\mathrm{mm}$ center to center pitch. The ideal FWHM value of the projection of a perfect parallel beam should be equal to the diameter of the holes. For each hole the FWHM values for the X and Y projection are corrected with the simulated reference. In figure 2 one can see that the X resolution tends to get worse with higher Y values, especially for the sides. On the contrary, the Y resolution is rather constant for the whole active area. This effect has already been predicted by Kozulin et al [4]. To proof the heliocentrical ground winding to be the source of this effect, we are currently building a new prototype with independend subunits (i.e. conversion foil, electrostatic mirror and detector head). Thus one can abandon the concept of a helical ground winding for the price of having more material obstructing the ion beam.

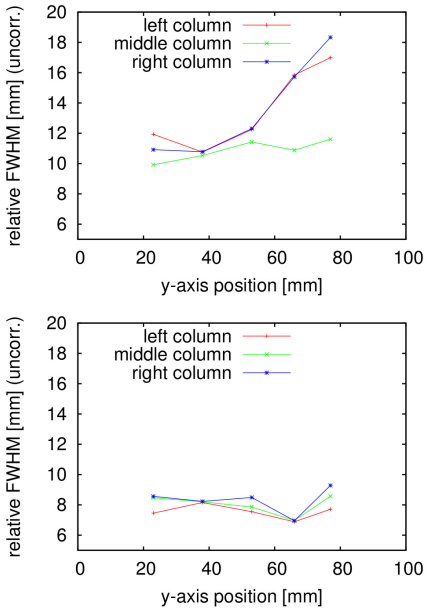

Figure 2: X and Y projected, relative FWHMs versus Y position, measured with unit 1. Note the difference in scale of both Y axis.

Work supported by F & E project KJOLIE and KJOLIE1012.

References

[1] F. Naqvi: Probing the collectivity in neutron-rich Cd isotopes via gamma-ray spectroscopy, PhD thesis (2011), Universität zu Köln

[2] M. Pfeiffer et al, GSI SciRep 2009 (2010), No. 1, p. 30

[3] M. Pfeiffer et al, GSI SciRep 2010 (2011), No. 1, p. 136

[4] E.M. Kozulin et al, Instr. and Exp. Tech. (2008), Vol. 56, No. 1, p. 44

[*] pfeiffer@ikp.uni-koeln.de

Status of the R^{3}B experiment *

H. Scheit[1] *and the R^{3}B Collaboration*

[1]Institut für Kernphysik, TU-Darmstadt, Germany

The experiment Reactions with Relativistic Radioactive Beams (R^{3}B) at the FAIR facility will be installed at the high-energy branch of the Super-FRS. It allows for the detection of all reaction products, resulting in kinematically complete nuclear reaction studies with short-lived radioactive ion beams in inverse kinematics, utilizing a wide beam energy range from about 100–1000 MeV/u covering the full mass range up to uranium. Experimental programs will address fundamental questions in nuclear structure and reaction physics, as well as nuclear astrophysics. The planned physics program requires a high resolution for all detection systems. This is reflected in the proposed experimental setup, which has been or will be designed and constructed by the R^{3}B collaboration based on many years of experience with the ALADIN/LAND setup at GSI.

Each part of the current setup has its improved counter part in the proposed R^{3}B setup, adapted (i) to overcome major limitation of the current setup, (ii) to reach much higher resolutions, (iii) to deal with the high-rigidity beams available at FAIR, and (iv) to deal with the large variety of reaction types to be studied. Recently, after a long research and development phase, important milestones toward the realization of the R^{3}B experiment have been reached: the technical design reports (TDR) for two core components of the R^{3}B setup, the NeuLAND high-resolution neutron time-of-flight spectrometer and the CALIFA Barrel detector, which serves as a γ-ray spectrometer, calorimeter and, together with the Si-tracker, as a target-recoil detector, have been finalized and submitted to FAIR for evaluation.

The NeuLAND detector is a next-generation neutron time-of-flight spectrometer featuring high detection efficiency, high resolution and an excellent multi-neutron hit resolving power. This is achieved by a high granularity—the detector consists of 3000 sub-modules with dimension of $5 \times 5 \times 250$ cm^3—and, in contrast to the current LAND detector, the full detector volume with a cross section of 2.5×2.5 m^2 and a depth of 3 m consists of plastic scintillator and is therefore a fully active detector with good calorimetric properties. At the high-acceptance position 15.5 m downstream from the target the detector face covers the full acceptance of the R^{3}B-GLAD magnet of 80 mrad, correspondoing to 100% acceptance for neutrons with a decay energy of up to 5 MeV for $E_{\rm beam} = 600$ MeV/u. The position and time resolutions of 1.5 cm and 150 ps, respectively, result in a decay energy resolution of 60 keV for a neutron with a decay energy of 1 MeV. At the furthest distance in the high-energy cave of FAIR the NeuLAND detector is 35 m downstream of the target. In this case the geometric acceptance is reduced to 35 mrad, but the decay energy resolution is less than 20 keV at 100 keV decay energy, which is important for the measurement of narrow resonances close to the threshold. Another major step forward is the improved multi-neutron hit recognition capability of the new fully active detector design. A reconstruction of the momentum vectors of several incident neutrons can be achieved, even for very low decay energies, where the neutrons are not well spatially separated. For instance, extensive simulations show that a 4 neutron hit can be identified as such with an efficiency of 60% and the decay energy resolution is still 42 keV for a decay energy of 100 keV.

The CALIFA calorimeter will surround the R^{3}B target position. The detector is sub-divided into a forward endcap and barrel section covering laboratory angles up to 43 $^\circ$ and 43–140°, respectively. Very high demands are placed on this detector by the planned physics program. It should not only detect γ-rays with energies from 100 keV up to several tens of MeV energy, but also highly energetic light charged particles, mainly protons, with energies reaching hundreds of MeV. The barrel section of the detector will consist of almost 2000 individual detector CsI crystals, which will be read out by avalanche photo diodes. The large number of individual detectors is needed to reduce the Doppler broadening due to the high beam velocities of more than 85% of the speed of light to a level comparable to the intrinsic resolution of the CsI crystals. For instance, an energy resolution of 5.5% and a full-energy peak efficiency of over 50% is achieved for 2 MeV photons emitted into the direction of the barrel section of CALIFA from a 700 MeV/u projectile.

Besides the completion and submission of the NeuLAND and CALIFA TDRs, the construction of another core component of the R^{3}B-setup, the superconducting large-acceptance large-gap dipole magnet R^{3}B-GLAD, is well underway with an expected delivery at GSI in the summer 2013. It will be used for the magnetic rigidity analysis of beam-rapidity charged fragments and bends them away from the direction toward the NeuLAND detector.

Furthermore, the design and construction of the R^{3}B Si-tracker, which is already fully funded, is also underway. Together with the CALIFA detector it will comprise the R^{3}B target recoil detector to accurately determine the momentum vectors of light charged particles after e.g. a (p,2p) reaction.

Concerning the future plans: first commissioning and physics experiments at GSI with R^{3}B-GLAD and 20%-versions of NeuLAND and the CALIFA Barrel will be carried out in 2014. Until 2016 the setup will be largely completed at GSI, used for commissioning and physics runs and moved to the new high-energy cave at FAIR in 2017/18.

* Work is supported by GSI F+E(Darmstadt) and HIC for FAIR.

NeuLAND@R^{3}B: A Fully-Active Detector for Time-of-Flight and Calorimetry of Fast Neutrons *

K. Boretzky[1], B. Agrawal[3], G.D. Alkhazov[11], V.A. Andreev[11], T. Aumann[2], P. Basu[3], D. Bemmerer[4], D. Bertini[1], P. Bhattacharya[3], S. Bhattacharya[3], A. Blanco[5], C. Caesar[2], S. Chakraborty[3], S. Chatterjee[3], M. Cherciu[6], L. Chulkov[12], M. Ciobanu[6], T. Cowan[4,10], U. Datta Pramanik[3], Z. Elekes[4], J. Endres[8], A.A. Fetisov[11], P. Fonte[5], D. Galaviz[7], V.L. Golotsov[11], M. Haiduc[6], J. Hehner[1], M. Heil[1], A. Heinz[13], A. Hennig[8], A. Ignatov[2], G. Ickert[1], E.A. Ivanov[11], M. Kempe[4], D. Kresan[2], A.G. Krivshich[11], P. Kumar Das[3], Y. Leifels[1], L. Lopez[5], J. Machado[7], V. Maroussov[8], J. Panja[3], M. Potlog[6], A. Rahaman[3], A. Ray[3], R. Reifarth[9], M. Röder[10], D. Rossi[1], J. Roy[3], H. Scheit[2], H. Simon[1], T. Sinha[3], M. Sobiella[4], D. Stach[4], E. Stan[6], P. Teubig[7], L.N. Uvarov[11], V.V. Vikhrov[11], M. Volknandt[9], S.S. Volkov[11], A. Wagner[4], J. Wüstenfeld[4], D. Yakorev[4], A.A. Zhdanov[11], A. Zilges[8], K. Zuber[10], and the R^{3}B collaboration

[1]GSI, Darmstadt, Germany; [2]TU Darmstadt, Germany; [3]SINP Kolkata, India; [4]HZDR, Dresden-Rossendorf, Germany; [5]LIP, Coimbra, Portugal; [6]ISS, Bucharest, Romania; [7]Univ. Lisbon, Portugal; [8]Univ. Cologne, Germany; [9]Univ. Frankfurt, Germany; [10]TU Dresden, Germany; [11]PNPI St. Petersburg, Russia; [12]Kurchatow Institute Moscow, Russia; [13]Chalmers Univ. of Technology, Göteborg, Sweden

NeuLAND (new Large-Area Neutron Detector) is the next-generation high-energy neutron detector (200 to 1000 MeV) designed for R^{3}B which meets all requirements defined by the ambitious physics program proposed for the R^{3}B facility. Within 2011 the layout of the detector was finalized and detailed in the Technical Design Report, submitted November, 1^{st}. NeuLAND features a high detection efficiency, a high resolution, and a large multi-neutron-hit resolving power. This is achieved by a highly granular design of plastic scintillators, omitting insensitive converter material. The detector will consist of 3000 individual submodules with a size of $5\times5\times250$ cm^3, arranged in 30 double planes with 100 submodules, each, providing an active face size of 250×250 cm^2 and a total depth of 3 m. NeuLAND can be divided into two detectors for special applications and can be placed at various distances from the target, in order to meet specific experimental demands. The design goals of NeuLAND comprise a one-neutron detection efficiency above 95% in a wide energy range and a full acceptance corresponding to an angular coverage of ±80 mrad at a distance of 12.5 m to the target. The desired resolutions for momenta and thus the excitation energies lead to the required spatial resolutions of $\sigma_{x,y,z} \leq 1.5$ cm and to a required time resolution of $\sigma_t \leq 150$ ps for the standard distance between detector and target of 15.5 m. When placed at a distance of 35 m, an excitation-energy resolution of less than 20 keV will be reached for an excitation energy of 100 keV above threshold at a beam energy of 600 AMeV. Apart from the excellent energy resolution, the enhanced multi-neutron recognition capability with an efficiency of up to 60% for a reconstructed four-neutron event will constitute a major step forward.

Different design concepts have been followed over the last years, including converter-based solutions, e.g., a detector based on steel converter plus charged-particle detection with resistive-plate chambers (RPC). The RPC concept has been ruled out mainly because of its much lower multi-neutron detection capability. A fully active detector with calorimetric properties has turned out to be the best solution. Submodules have been tested with proton and electron beams resulting in time resolutions of better than the required $\sigma_t \leq 150$ ps, even with inexpensive photomultipliers. In accordance with simulations, improved timing properties have been obtained with optimized light guides.

Extensive Monte-Carlo simulations have been performed leading to the final design. As a result, a fully-active detector design is required to provide the unambiguous identification of primary neutron interactions, the large efficiency at lower neutron energies and the high multi-neutron resolving power, the latter being due to its calorimetric properties. Details on the the final design simulations with respect to granularity and time-resolution are presented in a separate contribution to this report together with performance examples for several physics cases [1].

Several groups of the R^{3}B collaboration will contribute to the construction of the NeuLAND detector. The final assembly will take place at the GSI/FAIR site. We expect the beginning of construction in 2012, as soon as funding becomes available. The construction of the full detector will take about 3.5 years, allowing for first experiments with the complete detector in 2016. An important milestone will be met by using a 20% detector for physics experiments in the end of 2014 in Cave C at GSI, which will already profit from an improved resolution for neutron detection.

References

[1] D. Kresan et al., GSI Scientific Report 2011

* Supported by BMBF (06DR90581, 06KY9136I), by GSI F&E (Dresden, Darmstadt) and by the Helmholtz International Center for FAIR.

Recent Developments in NEULAND Simulations *

D. Kresan[1], T. Aumann[1], K. Boretzky[2], D. Bertini[2], M. Heil[2], D. Rossi[2], H. Simon[2], and the R3B Collaboration[2]

[1]TU, Darmstadt, Germany; [2]GSI, Darmstadt, Germany

The NEULAND will be used in R^{3}B for detection of fast neutrons, in particular for the classification of multi-neutron events ($\leq$ 6) with precise identification of a first interaction and determination of neutron momenta (in the range from 50 - 1000 MeV) by measurement of position and time of flight. For the summary on the detector concept of NEULAND see [1]. The aim of the work presented here was to achieve high performance of the reconstruction algorithm with respect to efficiency, purity and resolution of the identification of such physics observable as, e.g., the so-called tetra-neutron (4 neutrons with a narrow distribution in space and time).

The simulation package is implemented within the R3BRoot software [2], which is part of the FairRoot [3] framework, developed at GSI. Transport is performed using TGeant3 interface of Virtual Montecarlo (VMC) and GCalor as the engine for hadronic interactions. The geometry of NEULAND is introduced into the simulation on the level of single scintillator bars. A charged particle, crossing such a volume, looses energy which in turn creates light. This light signal is stored as the output of the simulation in the form of MCPoint with information about global position, time and energy loss, which is used as input for the reconstruction algorithm.

The reconstruction procedure implies two steps: first - hit producer (digitizer) and second - neutron tracking. The hit producer task is taking MCPoints as input and creating from them *digis*, applying light attenuation in the detector material and a light read-out from the two far ends of a scintillator bar by photomultipliers. The time resolution of a single photomultiplier is asumed to be 150 ps. The created digis serve as input for the second task of the reconstruction algorithm.

Before finding the first hits of incident neutrons, the decision on the event class (number of incident neutrons) has to be taken. It is done by applying a set of pre-calibrated 2-D cuts on the values of number of clusters (groups of digis representing track of a charged particle, which are created by analyzing digis pattern in an event with respect to position and time) and total energy deposit in the detector volume (see fig. 1). Simulation results in an anti-correlation between N_{cl} and E_{tot}, which allows to derive number of impact neutrons.

After the number of incident neutrons is determined as explained above, the tracking procedure starts. First of all, the cluster pattern of an event is analyzed with respect to elastic scattering of neutrons on hydrogen. The secondary hits of elastically scattered neutrons are eliminated from the further analysis. The remaining clusters are sorted according to the values of absolute deviation of potential neutron velocity from the beam velocity (smaller deviation has higher priority) and to the energy deposit in the cluster (higher energy deposit has higher priority). The first interactions of known number of incident neutrons are then taken from the list of sorted clusters.

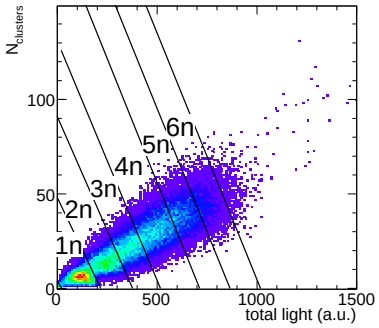

Figure 1: Simulated distribution of number of clusters versus total energy. Multi-neutron events separation is done based on this distribution by applying 2-D cuts.

The reconstruction algorithm is finalized by calculating the neutrons momenta and E_{rel}. Fig. 2 shows in this way reconstructed spectrum for the case of 4 incident neutrons.

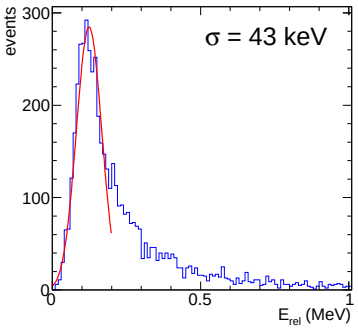

Figure 2: Relative energy spectrum for four neutron events at 600 MeV, simulated with relative energy of 100 keV with respect to projectile fragment. The tail towards higher values is caused by misidentification of first interactions.

References

[1] K. Boretzky et. al, GSI Scientific Report 2011

[2] J. Phys.: Conf. Ser. CHEP78R2

[3] J. Phys.: Conf. Ser. (2008) 119 032011

* Supported by the HIC for FAIR and GSI F+E(Darmstadt).

ToF simulations for the R3B experiment at FAIR

D. Bertini[1] *and E. Leistenschneider*[2]
[1]GSI, Darmstadt, Germany; [2] University of São Paulo

Introduction

R3B - Reactions with Relativistic Radioactive Beams [1] aims at constructing a versatile reaction setup with high efficiency, acceptance, and resolution for kinematically complete measurements of reactions with high-energy radioactive beams.

Time of Flight Detectors

The R3B experimental setup includes several detectors for beam tracking and particle identification. Two of them, so called Time-of-Flights Walls, consisting of plastic scintillator are designed to detect protons (ToF Wall) and heavy nuclear fragments (miniToF Wall). They are both a composition of horizontal and vertical paddle layers, which enables detector calibration and particle tracking. In figure 1 is shown a schema of the big ToF Wall

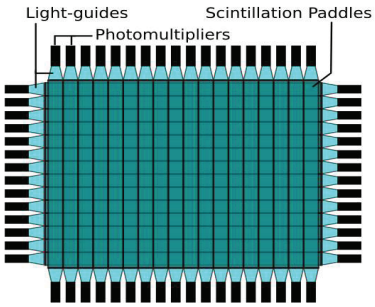

Figure 1: A schematical drawing of the ToF Wall for proton detection.

Digitization

The digitization modelizes the transport of scintillation photons through the paddles and light guides up to the PM's, where the light yield will be converted into charge signal and can be measured by the electronics.

The energy lost calculated with R3BRoot [2] is first converted to light equivalent L using the parametric Birk's law:

$$L = \frac{S\,E}{1 + C_1\,E + C_2\,E^2} \qquad (1)$$

where S is the scintillation efficiency and C_1 and C_2 are material related parameters

The light transportation is then implemented following a analytical approach schematically presented in fig. 2.

The time t_0 the particle reaches the detector is easily calculated considering the time signals (t_1 and t_2) that reaches both PMs. The scintillation point x can then be calculated

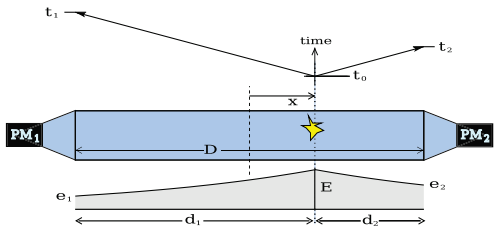

Figure 2: Light propagation in a paddle, showing the time and light yield signals that reach the two PMs.

as the difference of the two times. As the particle is supposed to cross the two paddle layers, it leaves signals in a vertical and a horizontal paddle. Knowing the physical properties of the BC408 platic [3] one can reconstruct the $x - y$ position for the cluster [4]

Conclusion and results

A segmented version of the ToF Walls have been included in the R3BRoot framework. The Figure 3 shows a example of the counts registered on the big ToF Wall paddles for a proton beam in a simulated experiment.

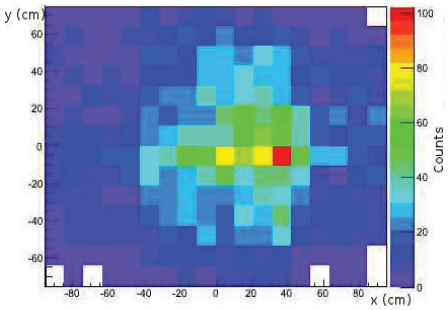

Figure 3: Proton counts on the big ToF Wall after a simulated experiment. The histogram bins correspond to the detector paddles.

References

[1] www.gsi.de/fair/experiments/NUSTAR/R3b

[2] D. Bertini, *R3BRoot, simulation and analysis framework for the R3B experiment at FAIR*, J. Phys.: Conf. Ser. 119 (2008)

[3] R. Perrino et al., *Timing measurements in long rods of BC408 scintillators with small cross-sectional sizes*, Nucl. Instr. and Meth. A 381 (1996).

[4] Y. Aksyutina, *Light Unbound Nuclear Systems beyond the Dripline*, Ph.D. Thesis, Frankfurt am Main (2009).

Technical design of the CALIFA/R^{3}B Barrel detector*

D. Cortina-Gil †[1], *H. Alvarez-Pol*[1], *T. Aumann*[13], *V. Avdeichikov*[4], *M. Bendel*[7], *J. Benlliure*[1], *D. Bertini*[5], *A. Bezbakh*[11], *T. Bloch*[13], *M. Böhmer*[7], *M.J.G. Borge*[2], *J.A. Briz*[2], *P. Cabanelas*[1], *E. Casarejos*[8], *M. Carmona Gallardo*[2], *J. Cederkäll*[4], *L. Chulkov*[12], *M. Dierigl*[7], *D. Di Julio*[4], *I. Durán*[1], *E. Fiori*[10], *A. Fomichev*[11], *D. Galaviz*[9], *M. Gascón*[1], *R. Gernhäuser*[7], *J. Gerl*[5], *P. Golubev*[4], *M. Golovkov*[11], *D. González*[1], *A. Gorshkov*[11], *A. Heinz*[3], *M. Heil*[5], *W. Henning*[7], *G. Ickert*[5], *A. Ignatov*[13], *B. Jakobsson*[4], *H.T. Johansson*[3], *Th. Kröll*[13], *R. Krücken* ‡[7], *S. Krupko*[11], *F. Kurz*[7], *T. Le Bleis*[7], *B. Löher*[10], *N. Montes*[1], *E. Nacher*[2], *T. Nilsson*[3], *C. Parrilla*[8], *A. Perea*[2], *N. Pietralla*[13], *B. Pietras*[1], *R. Reifarth*[6], *J. Sanchez del Rio*[2], *D. Savran*[10], *S. Sidorchuk*[11], *H. Simon*[5], *L. Schnorrenberger*[13], *O. Tengblad*[2], *P. Teubig*[9], *R Thies*[3], *J.A. Vilán*[8], *M. von Schmid*[13], *M.Winkel*[7], *S.Winkler*[7], *F. Wamers*[13], *and P. Yañez*[8]

[1]Universidad de Santiago de Compostela; [2]Instituto Estructura de la Materia, CSIC Madrid; [3]Chalmers University of Technology, Göteborg; [4]Lund University; [5]Helmholtzzentrum für Schwerionenforschung, Darmstadt; [6]Goethe University Frankfurt am Main; [7]Technische Universität München; [8]Universidad de Vigo; [9]Centro de Física Nuclear da Universidade de Lisboa; [10]Extreme Matter Institute and Research Division, GSI; [11]Joint Institute for Nuclear Research, Dubna; [12]Nuclear Reseach Center, Kurchatov Institute Moscow; [13]Technische Universität Darmstadt

The CALIFA (CALorimeter for the In Flight detection of γ rays and light charged pArticles) calorimeter surrounds the R^{3}B reaction target and is one of the key detectors of the R^{3}B experiment [1], accordingly optimised for the exacting requirements of the ambitious physics program proposed for the R^{3}B facility. CALIFA will be used in many of the physical cases of the R^{3}B experiments, even though the required functionality will vary greatly from one case to another. Three different working conditions for CALIFA can be considered:

It will be used as a high-resolution spectrometer, being responsible for the detection of relatively low-energy γ rays (0.1 to 2 MeV) with low multiplicity (2-3). The energy resolution will be in this case the most critical parameter of CALIFA. The goal has been set to ΔE/E < 6% (see Table 1) for a 1 MeV γ ray, which allows to distinguish most of the simple γ-ray cascades that come from the de-excitation of exotic nuclei. A typical example of reactions that could benefit from this operational mode are knock-out reactions employing radioactive beams.

Another physics case requirement is CALIFA's employment as a γ-ray calorimeter, required for the detection of very energetic excitations (up to 15 MeV) associated with high energetic γ-rays but also very fragmented decays (high-multiplicity events). In these cases the key parameters will be the total γ-ray absorption (intrinsic photopeak efficiency), γ-ray sum energy and γ-ray multiplicities. A typical reaction that will profit from this operational mode is the investigations of pygmy- (or giant-) resonance decays.

The most challenging scenario corresponds to the use of CALIFA as a hybrid detector that has to provide simultaneously good calorimetric properties together with high-resolution. A typical example of a reaction channel that might require this performance is that of quasi-free scattering (i.e (p,2p), (p,pn)...). In this case, the detection of highly energetic light charged particles (protons up to 320 MeV) has to be combined with the detection of the prompt γ ray de-excitation of the residual fragment, both processes measured with good energy resolution over a huge dynamic range.

The technical definition of the elements fulfilling these unprecedented requirements are summarised in Table 1.

CALIFA consists of two sections (see Fig. 1), a 'Forward EndCap', covering the region between beam pipe limit to 43.2° (polar angle) and concentrating 58.3% of the total γ rays emitted by a moving source at the nominal value of 0.82c[1], and a cylindrical 'Barrel' covering an angular range from 43.2 to 140.3° with 38.9% of γ rays emitted over this angular range. This report summarizes the technical details and the performance of the latter; the CALIFA Barrel, detailed in the Technical Design Report of this detector submitted to FAIR in November 2011 [2].

The CALIFA detector concept is based on an exhaustive R&D programme including detailed simulations of the typical experiments to be performed in R^{3}B. Here the interplay of intrinsic properties of the individual detector elements and the overall arrangement of the apparatus had to be optimised to individual requirements while maintaining sufficient flexibility for the versatile program of R^{3}B.

However, the basic characteristics of CALIFA are to a large extent determined by the particular kinematics of reactions at relativistic energies, notably the Doppler broadening and shift of γ rays emitted from excited projectile

* Work performed in the CALIFA/R^{3}B Working group and supported by the Helmholtz International Center for FAIR

† Convener of the CALIFA Working group

‡ Also affiliated to TRIUMF

[1]Nominal energy of the R^{3}B experiment

Intrinsic photopeak efficiency	40 % (at E_γ=15 MeV projectile frame)
γ-ray sum energy resolution $\Delta(E_{sum})/<E_{sum}>$	< 10% for 5 γ rays of 3 MeV
γ-ray Energy resolution	5-6 % ΔE/E for 1 MeV γ rays
Calorimeter for high energy light charged particles(LCP)	Up to 320 MeV in Lab system
LCP energy resolution	<1% $\Delta E_p/E_p$ $\frac{\sqrt{(100MeV)}}{\sqrt{E}}$
Proton-γ ray separation	For 1 to 30 MeV

Table 1: Nominal specifications of the R^3B calorimeter (β=0.82). These parameters are defined by the Physics programme stated in the R^3B Technical Proposal [1]

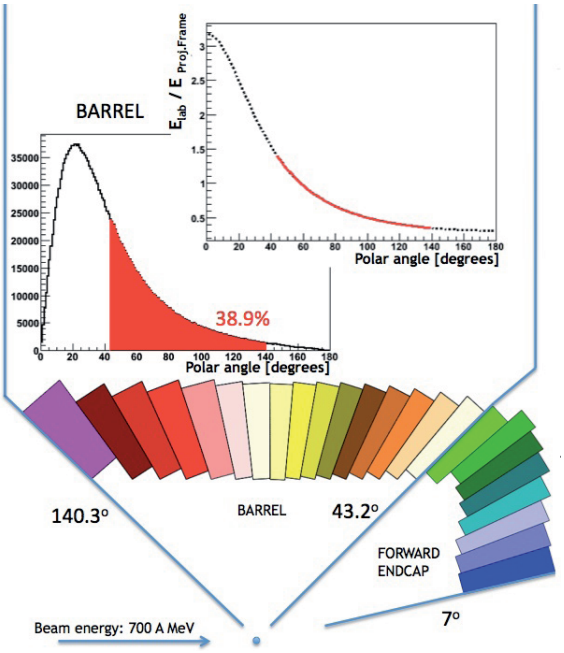

Figure 1: Schematic representation of the CALIFA detector profile. The portion of angular distribution of emitted γ rays covered by the CALIFA Barrel and the corresponding Doppler shift is highlighted in this figure.

remnants, and the high energies associated to light charged particles arising from the target. The key factors that have guided the calorimeter conceptual design are as follows [3]:

- the shape and length of the crystals; to ensure a high total absorption efficiency
- the detector granularity, which is crucial to provide the necessary angular resolution pertaining to the reconstruction of the gamma energies in the rest frame of the projectile.

The choice of the limit of approximately 43.2° between the Forward EndCap and Barrel section has been determined based on the following criteria: i) to preserve the angular region at approximately 25° where the γ-ray angular distribution is at its maximum, ii) allow the detection of one proton in each section in the case of (p,2p) reactions, and iii) avoid excessive tilting of the crystal position in the Barrel section with the intention of minimizing losses due to the non-detection of Compton events. These losses arise as a consequence of an increased displacement of crystal face alignment, causing a fraction of photons to scatter not into the adjacent crystal, but rather through the gap as a result of this displacement, which increases with increasing polar angle.

The election of about 140° in the backward angle coverage is justified by the γ-rays' angular distribution which has a tiny contribution of events above this angle and the aperture of the furthest backward angles facilitate detector cabling installation and access to the target area. It should be noted that although the percentage of γ rays emitted by the target is minimal at angles above 140°, some loss in efficiency for this region is due to the escape of pair-production photons from the EndCap.

The necessity to identify high-energy protons and γ rays with good geometrical efficiency limits first of all the minimum thickness of detectors in the beam direction. The degradation of the energy resolution (for γ rays) and the maximum acceptable loss of protons in inelastic reactions in the detector material condition the choice of the maximum detector length. At the same time, an increase in the crystal length will also translate in the γ ray case to a degradation of the energy resolution, as a consequence of the ratio between the entrance crystal area and the length; very far from the ideal 1:1. Those requirements have resulted in frustum-shaped crystals arranged in cylindrical symmetry around the beam line.

To overcome the Doppler broadening, the device will be highly segmented, with 1952 individual detection units in the Barrel and $\approx$ 3000 for the full CALIFA. Barrel crystals will have a unique shape and different angular aperture and length corresponding to different polar angle regions, comprising 11 different geometries in total.

A crucial point for the CALIFA performance is the selection of the most appropriate detector material and read-out

devices. The choice of Barrel detector scintillation material, CsI(Tl), is based on its high light output, rather good intrinsic resolution and capability of proton - γ-ray separation. Other important qualities are its simplicity to handle, low hygroscopy and relatively low price. The energy resolution requirement for CALIFA has driven the developement of CsI(Tl) with extremely low light output non linearities that demand a careful and individual treatment of the crystal surface [4]. Additionally, the absolute light output of CsI(Tl) is dependent on both the wrapping material and wrapping technique. The basic requirement of thin wrapping, while maintaining good reflectivity is fulfilled by the use of ESR - Enhanced Specular Reflector - produced by the 3M Company.

The best choice for the CALIFA Barrel photosensor has been found with the use of Avalanche Photodiodes, which exhibits a near perfect match to the CsI(Tl) spectral response. They are insensitive to the presence of magnetic fringe fields, and can cover large areas; providing an excellent physical coupling to the crystal surface exit. Therefore, APDs provide very good energy resolution for low energy γ rays [5]. Large Area APDs (LAAPD) with an active surface up to 10×20 mm^2 have been specifically designed for CALIFA. It is well known that APDs have high demands on temperature and voltage stability, thus CALIFA will be maintained at a constant temperature by a dedicate air cooling system. A further measure is proposed by fine gain voltage compensation, corresponding to a temperature precision below 0.1°C [2].

Modern techniques of digital data acquisition have proven to be a major advance in the next generation of detectors in nuclear physics. Certain advantages such as flexible trigger concepts, high rate capability and pile-up reduction, larger dynamic range and highly integrated concepts of data reduction processing in the frontends optimise the information stemming from the detector response [9].

The readout concept of the CALIFA Barrel is based on the technology of a fully digital readout divided into three independent layers.

The front-end electronics mounted directly at the detector is optimised for low noise and low power consumption to allow for a minimal cooling infrastructure and good mechanical access to the detector. To minimize the cabling effort and costs it houses individual channel high voltage control using a serial single line slow control bus with temperature compensation for gain variation of the Large Area Avalanche Photodiodes. This development was successfully performed in collaboration with a German company (Mesytec GmbH & Co. KG[3]) based on the existing preamplifier unit MPR-16.

Individual channel analogue differential signals are transported via standard 100 Ohms shielded twisted pair cables of 5 m in length to the digitiser modules located on the movable support structure of the detector.

These modules also perform full signal processing as described below and provide buffer memory for an asynchronous data collection. In the final layer the data collection uses only a few optical fibres and a trigger bus system connected to two computers, one for each side of the detector.

All prototypes of this modern digital DAQ electronics set-up are based on the Multi-Branch System (MBS) [6] and the GOSIP protocol [7][4], previously utilised in a number of CALIFA test experiments. This Digitizer module is based on the existing FEBEX 3 [8]. It features two 14-bit ADCs with 8 input channels each, operated at a 50 MHz conversion rate. The Lattice ECP3 150 FPGA with 149k LUTs provides sufficient logic and memory resources. A great feature of FEBEX 3 is the PCI express connector with which all front-end are assembled in a crate with a common optical fibre connection. For compatibility with the existing triggered R^{3}B DAQ and for all the ongoing developments, tests and experiments it is an essential advantage to use a system compatible with forthcoming developments from the FAIR DAQ group. In particular with regards to a future migration towards a more general timestamp based triggerless DAQ, a close collaboration with the NUSTAR DAQ group will provide a smooth transition and significant synergies for both sides.

A precise calibration of CALIFA is essential to the success of the project and has been forseen. It comprises of a combination of electronics and light pulsers, source measurements and reference experiments that will be performed with larger detector assemblies prior to its accommodation in the High Energy Branch cave and calibration procedures which will be regularly undertaken to monitor CALIFA during the experiments.

A complete simulation programme has been developed in order to accurately determine the capabilities of the present CALIFA design and its competence and effectiveness in the achievement of the requirements of the R^{3}B physics programme. The simulation is part of the R3BRoot common framework and includes an in-depth description of the detection process and signal digitization, data structures to account for the expected response of the calorimeter crystals, a detailed geometry description of the calorimeter crystals, support elements, and algorithms for the reconstruction and comparative evaluation of the detected signals. Appropriate event generators for the evaluation of CALIFA under realistic working conditions have been developed, including trivial gamma and charged particle distributions for a general performance evaluation, nuclear spectroscopy decay, giant and pygmy nuclear resonances and quasi-free scattering reactions. Event reconstruction algorithms conceived explicitly for the high granularity of the CALIFA detector have been developed and their parameters carefully tuned to enhance the complete energy detection in the addback procedure while preserving a high detection efficiency in events with higher multiplicity.

[2] Developement incorporated in the pre-amplification stage

[3] http://www.mesytec.com

[4] Both being developed by the FAIR DAQ group.

The response to γ rays and protons has been investigated for emission from fast, beam like sources: the energy resolution comprising of factors resulting from the combination of the intrinsic crystal resolution at low energies and the effect of the Doppler broadening at high energies. For γ rays the detection efficiency in the Barrel drops with increasing energy, from around 80% at lower energies to around 40% for those emitted in the projectile frame at the maximum energy of 15 MeV. Additionally, the efficiency for high multiplicity events has been optimised, being one of the compelling features of CALIFA. The response for protons has been also evaluated, demonstrating the importance of the wrapping for the detection efficiency. A particular effort has been devoted to the evaluation of the energy not deposited in the active crystal volume, determining the percentage of the energy deposited in passive elements, wrapping or escaping the detector.

A few selected physical cases which represent relevant center pieces of the experimental program of R^3B have been simulated, establishing the capability and potential of the CALIFA Barrel under realistic conditions. These detailed simulations had been the major input to constrain the layout and mechanical design of the full detector array.

The internal CALIFA Barrel radius has been determined according to the compromise of: i) allowing the installation of the R^3B target and Silicon Tracker System ii) approaching the CsI(Tl) crystal towards the target to maximise the solid angle covered by each individual CsI(Tl) crystal.

The individual CsI(Tl) crystals of the CALIFA Barrel with an approximate total weight of 1200 kg are supported via a carbon fibre alveolus structure. The challenge here lies in the suspension of such a weight with the required exact and stable positioning of all crystals, achieved through the use of a minimum of 'dead' material; in order to reduce as far as possible the detrimental effect of non-active material on detector performance. An additional factor to be accounted for is the support of the front-end electronic modules and the cooling system.

The proposed mechanical structure is built of three main layers: the inner, cover and external structures (see Fig. 2). The inner layer, consisting of an epoxy-carbon composite provides the support and positioning for all the crystals. It is segmented into separate compartments, termed 'alveoli', each of them holding 4 individually wrapped crystals. This inner layer is surrounded by a cylindrically shaped cover envelope comprised of equally sized 'tiles'. This structure acts as an interface between the inner layer and the external support. The cover holds both the 'tabs', pieces which support the internal epoxy-carbon composite structure, and the 'arms' employed to suspend the whole system from the mobile external structure. The cover also supports the front-end electronics (FEE) elements, with the corresponding connection passthroughs and the module support elements.

The humidity and temperature control of the active region is achieved via a continuous flow of dry nitrogen underneath the cover layer, and an air flow across the tiles;

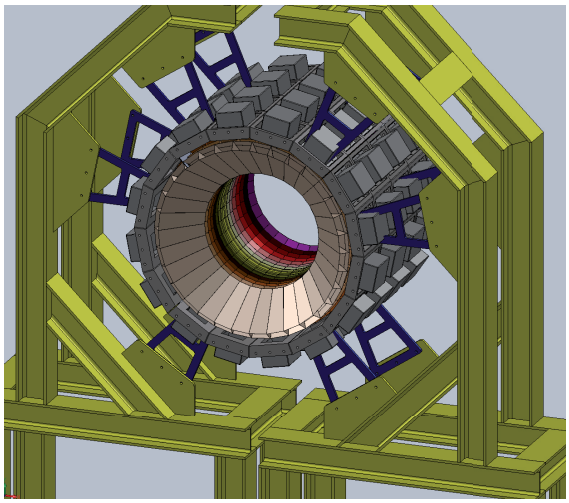

Figure 2: View of a section of the Barrel where the different structural components can be observed.

the necessary distribution pipes and passthroughs attached to the cover. The cover also guarantees the light- and gas-tightness of the system.

The project plan foresees start of construction for the Barrel section in 2012. An important milestone will be met with the operation of a 20% demonstrator detector for physics experiments in 2014 in Cave C at GSI, even at this stage profiting from the improved resolution for photon detection. The full detector is expected to be ready in the last quarter of 2015 and commissioned in 2016. The final detector will be moved after full commissioning and first production runs in Cave C to its final location at the High Energy Branch hall at the FAIR site in 2017, being fully operational for physics experiments in 2018 when the Super-FRS is expected to deliver its first beams at FAIR.

References

[1] T. Aumann et al., Technical Proposal for the design, construction, commissioning and operation of R^3B, A universal setup for kinematical complete measurements of Reactions with Relativistic Radioactive Beams (2005).

[2] T. Aumann et al., Techhical report for the Design, Construction and Commissioning of the CALIFA Barrel: The R^3B CALorimeter for In Flight detection of γ-rays and high energy charged particles (2011)

[3] H. Alvarez-Pol et al., Nucl. Inst. and Meth. in Phys. B 266 (2008) 4616

[4] V. Avdeichikov et al., private comunication

[5] M. Gascón et al., IEEE TRANSACTIONS ON NUCLEAR SCIENCE, VOL. 55 ,NO. 3, JUNE 2008

[6] J. Hoffmann et al., GSI SCIENTIFIC REPORT 2008

[7] H. Minami et al., IEEE TRANSACTIONS ON NUCLEAR SCIENCE, VOL. 58, NO. 4, AUGUST 2011

[8] J. Hoffmann et al., GSI SCIENTIFIC REPORT 2011

[9] M. Bendel et al., Particle-Gamma-Separation with CALIFA, GSI SCIENTIFIC REPORT 2010

Event reconstruction with the CALIFA calorimeter*

E. Fiori[1,2], P. Teubig[3], H. Alvarez Pol[4], B. Löher[1,2], D. Galaviz[3], D. Savran[1,2], and the R^{3}B Collaboration.

[1]ExtreMe Matter Institute EMMI and Research Division, GSI Helmholtzzentrum für Schwerionenforschung, Planckstraße 1, 64291 Darmstadt, Germany; [2]Frankfurt Institute for Advanced Studies FIAS, Ruth-Moufang-Str. 1, 60438 Frankfurt am Main, Germany; [3]University of Lisbon, Lisbon, Portugal; [4]Universidad de Santiago de Compostela, Santiago de Compostela, Spain

Introduction

The R^{3}B (Reactions with Relativistic Radioactive Beams) experiment at FAIR aims to "develop and construct a versatile reaction setup with high efficiency, acceptance, and resolution for kinematically complete measurements of reactions with high-energy radioactive beams" [1]. Surrounding the reaction target, the calorimeter CALIFA (CALorimeter for the In Flight detection of γ-rays and light charged pArticles) [1, 2] will detect protons and γ-rays.

Simulations

Depending on their energy, single γ-rays deposite energy in different parts of the calorimeter. Hence clustering algorithms that are able to reconstruct the initial energy of the γ-ray and its emission direction (for proper Doppler correction) are essential in the event reconstruction. These algorithms and the resulting performance of CALIFA have been investigated using GEANT4 simulations within the package R3BRoot, which allows for the generation and the analysis of the events.

At present, we focused on the add-back performances, measuring the algorithm's efficiency, calculated as the detected number of photons at the correct energy. The most basic approach to an algorithm for the reconstruction of the γ-ray energy consists in summing up the energy of all the crystals within a pre-defined angular region. Two different approaches were adopted when considering the angular region for add-back purposes: a circular window, with just one parameter $\Delta\vartheta$ defining the solid angle covered by the window; and a square one, with two parameters ($\Delta\theta$ and $\Delta\phi$) defining the angular region considered. The hit with the highest energy is taken as center for the angular region. The performances of the circular and square angular window were found to produce very similar results.

From events with only a single emitted γ-ray we observe that there is a certain angular window for which the efficiency presents a plateau, as shown in Fig. 1. In addition, this angular region shows a clear dependence on the energy of the photons, implying that the selection of a fixed angular parameter, not taking into account the energy of the hit, might not be the most efficient way to reconstruct the energy of the events.

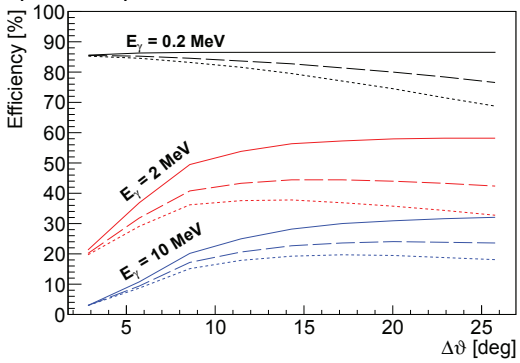

Figure 1: Dependence of the efficiency of the clustering algorithm on the solid angle for add-back for different energies (black 0.2 MeV, red 2 MeV, blue 10 MeV) and different event multiplicities (solid line - one, dashed line - three, dotted line - five). The photon source was at rest.

The performance of these algorithms has also been studied considering events with multiplicity larger than one. In this case the efficiency does not longer saturate for larger angular opening angles but it slowly decreases again. This effect can be explained with a mixing of crystal hits coming from different original γ-rays.

Results

Simulations clearly show that the photopeak efficiency of the clusterization algorithm presents a maximum which is function of both the energy and the multiplicity of the incoming γ-rays. A too small angular window is not able to collect all crystal hits stemming from a single γ-ray, while a large window leads to a mixing of crystal hits coming from different γ-rays. Both effects result in a lower-than-optimal photopeak efficiency. Overall, an adaptive angular window parameter that depends on both energy and event multiplicity is required to improve the performance of the reconstruction algorithm.

References

[1] "Technical design of the CALIFA/R^{3}B Barrel detector" in this GSI Annual Report 2011.

[2] T. Aumann *et al.*, Techhical report for the Design, Construction and Commissioning of the CALIFA Barrel: The R^{3}B CALorimeter for In Flight detection of γ-rays and high energy chArged particles (2011)

* This work was supported by the Alliance Program of the Helmholtz Association (HA216/EMMI).

[1] www.gsi.de/R3B/

Particle Identification using Clustering Algorithms*

R. Wirth[1,2], *E. Fiori*[1,2], *B. Löher*[1,2], *and D. Savran*[1,2]

[1]ExtreMe Matter Institute EMMI and Research Division, GSI Helmholtzzentrum für Schwerionenforschung, Planckstraße 1, 64291 Darmstadt, Germany; [2]Frankfurt Institute for Advanced Studies FIAS, Ruth-Moufang-Str. 1, 60438 Frankfurt am Main, Germany

Introduction

Particle identification (PID) is an important task for many experimental techniques. A well-known approach for PID in particle detection systems is based on pulse shape analysis (PSA), i.e. identification based on the difference in the detector pulse shape produced by different particle species. Most of these methods analyze specific features of the detector signals employing profound knowledge of the involved pulse shapes and usually need precise adjustment for each individual detector.

Clustering algorithms

A new approach to achieve PID using PSA is based on clustering algorithms without making any assumptions on the shape of detector pulses. The method is also self-adapting, i.e. no adjustment to a specific detector is necessary. This is achieved by interpreting the digitized detector pulses as points in n-dimensional space. Points representing similar pulse shapes will lie closely together in this space and grouping these points into clusters–one for each particle species–will yield the particle species that induced each individual pulse.

The clustering algorithm we used in this study is the fuzzy c-means algorithm which tries to find a cluster assignment for each point that minimizes the (euclidean) distance between points belonging to the same cluster. It is called fuzzy because these cluster assignments may be ambiguous, i.e. a single point may belong to multiple clusters with a certain probability. The fuzziness is controlled by a parameter m with $m = 1$ meaning no fuzziness, i.e. each point belongs to exactly one cluster (boolean logic), and $m \to \infty$ meaning each point being assigned an equal degree of membership for all clusters.

Principal pulse shapes

From the cluster assignments one can then derive principal pulse shapes by calculating the centroid of the cluster. Figure 1 shows the principal pulse shapes calculated from a set of proton- and γ-induced CsI(Tl) scintillator detector pulses recorded using a 60 MHz flash ADC with 12 bit resolution. These extracted principal pulse shapes can then be used to calculate discrimination amplitudes, i.e. integration weights for a much less computationally expensive method to discriminate between particle species. Figure 2 shows the discrimination value histogram of proton- and γ-induced pulses for two CsI(Tl) detectors with slightly different pulse shape characteristics. Despite these differences the discrimination value distributions are very similar: The particle species are represented by well-separated peak-like structures that have the same shape and position for both detectors. This allows for assignment of events to particle species using detector-independent candidate regions.

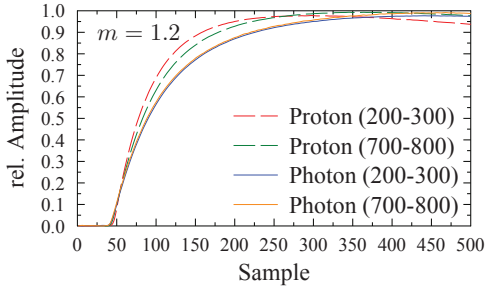

Figure 1: The principal pulse shapes for protons and photons as determined by the FCM algorithm for a CsI(Tl) scintillator detector. The pulses were shaped using a shaping amplifier prior to digitization. The proton principal pulse shape shows a strong energy dependency in contrast to the photon shape.

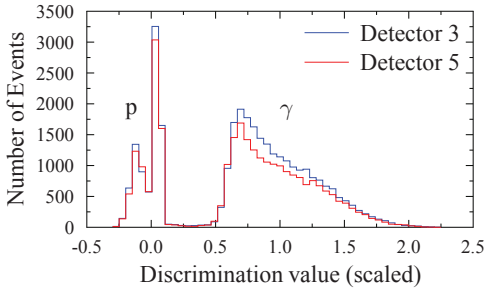

Figure 2: The histogram of discrimination values for two detectors, scaled so that the proton principal pulse shape has a discrimination value of 0 and the photon principal pulse shape is assigned a value of 1.

Results

The results show that PID based on clustering algorithms produces high-quality particle species assignments. The method's self-adapting property proves beneficial for setups with a large number of detectors as it reduces the amount of fine-tuning.

*This work was supported by the Alliance Program of the Helmholtz Association (HA216/EMMI).

Feasibility Studies for the EXL Project at FAIR*

K. Yue[1,2], S. Bagchi[3], S. Diebold[4], C. Dimopoulou[1], P. Egelhof[1], V. Eremin[5], S. Ilieva[6], N. Kalantar-Nayestanaki[3], O. Kiselev[1,6], T. Kröll[6], Yu.A. Litvinov[1], M. Mutterer[1], M.A. Najafi[3], N. Petridis[7], U. Popp[1], C. Rigollet[3], M. von Schmid[6], M. Steck[1], and B. Streicher[3]

[1]GSI, Darmstadt, Germany; [2]IMP, Lanzhou, China; [3]KVI, Groningen, The Netherlands; [4]Universität Tübingen, Germany; [5]PTI, St. Petersburg, Russia; [6] Technische Universität, Darmstadt, Germany; [7]Goethe Universität, Frankfurt a.M., Germany.

A feasibility study for the EXL [1] project was performed at the storage ring ESR. The aim of this test was to prove the possibility of deducing the elastic-scattering cross section by using silicon detectors in the UHV environment of the storage ring. In order to investigate the response of the EXL prototype DSSD to very low-energy protons, another detector test was performed at the 3 MeV Van-de-Graaff accelerator at Tübingen University.

Measurements at the ESR: ^{40}Ar(p, p)

For the feasibility experiment, an ^{40}Ar beam with an energy of 400 MeV/u was injected into the ESR, which interacted with an internal hydrogen gas-jet targe. An UHV compatible single-sided silicon detector was mounted in the target vacuum chamber to detect the target-like reaction products. It had 40 strips in total, read out in five groups of 8 strips each. The polar angle coverage of the recoil detector was from 73.4° to 89.5°.

The interaction profile was measured using a photomultiplier tube, detecting UV light produced by the interaction of the heavy ions with the hydrogen atoms. A target size of 5.1 mm (FWHM) was obtained. The beam size at high intensity was determined to be 3.3 mm (FWHM) after unfolding from the target size. The absolute luminosity was calculated measuring the beam intensity (by means of a current transformer) and the target density.

For the p-^{40}Ar interaction, the differential elastic-scattering cross section has been deduced as function of the four-momentum transfer squared $-t$, using data from the first sixteen Si-strips of the detector corresponding to c.m. angles close to 0°. Due to the limited angular resolution caused by the extended beam-target interaction zone, experimental values for $-t$ were determined only from the energy of recoils.

For the correction of punching-through events and inelastic-scattering events due to the first excited state in ^{40}Ar, Monte Carlo simulations were performed by implementing the detector, target and beam geometry in the Geant4 code. Inelastic scattering was calculated from theory using the Eikonal approximation [2]. The obtained differential cross section was analyzed within the Glauber multiple-scattering theory. Fig. 1 shows the experimental absolute differential cross section as a function of $-t$ without (circles) and with (squares) the correction for the punching-through events and inelastic-scattering events. The solid line represents the elastic-scattering cross section obtained from Glauber calculations for a point-like vertex. A matter radius R_{rms} = (3.30 ± 0.12) fm was determined. For a comparison the charge radius determined for ^{40}Ar is (3.423 ± 0.014) fm [3]. In order to compare both values the charge radius has to be unfolded from the proton radius which leads to the value (3.309 ± 0.016) fm, in good agreement with a present measurement.

* Work supported by BMBF (06DA9040I), HIC for FAIR and GSI F+E(Darmstadt). Work is part of HGS-HIRe.

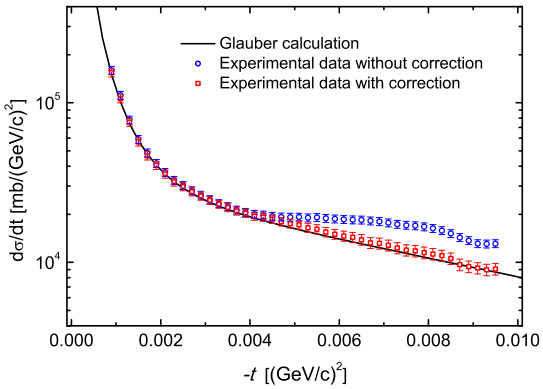

Figure 1: The experimental absolute differential cross section for p-^{40}Ar scattering at 400 MeV/u as a function of the four-momentum transfer squared $-t$.

Test of the prototype DSSD at low energy

A 16×16 strips EXL prototype DSSD was tested for its response to proton energies below 1.44 MeV at the Van-de-Graaff accelerator at Tübingen University. A beam of H_2 molecules was used to produce even lower energetic protons of about 400 keV. In addition, beam particles were scattered of from a carbon target to hit the detector, and further slowed down by a Mylar foil degrader. The energy resolution was 17.7 keV (FWHM) for 1.44 MeV protons and 20.0 keV (FWHM) for 74.7 keV protons, when energy straggling in the degrader was corrected for. This result fulfils the requirement of the EXL project.

References

[1] EXL Technical Proposal, <http://www.fair-center.de/fileadmin/fair/publications_FAIR/FAIR_BTR_1.pdf>
[2] G. Colò, private communication.
[3] C.R. Ottermann *et al*., Nuclear Physics A 379 (1982) 396-406.

The SOFIA/ANDES TwinMUSIC*

B. Voss✝ for the SOFIA / ANDES-collaboration

GSI, Darmstadt, Germany.

Experimental aim and set up

It is the aim of the SOFIA/ANDES collaboration to survey the structure effects at low excitation energies investigating electromagnetic-induced fission of ^{238}U and lighter short-lived actinides in the framework of the **S**tudies **O**n **FI**ssion with **A**ladin (SOFIA) experiment as well as performing spallation-fission of ^{208}Pb on ^{1}H in the framework of the **A**ccurate **N**uclear **D**ata for nuclear **E**nergy **S**ustainability (ANDES) [1] project studying the fission dynamics at high E*.

Both require the precise measurement of the fission fragments produced at CaveC at GSI and follow the ideas of former experiments [2]. In order to achieve this, it is necessary to determine the nuclear charge Z, mass A and kinetic energy Ekin of each fission fragment after prompt neutron emission in coincidence with the total neutron multiplicity prior to any β- decay on an event-by-event basis.

An overview of the experimental setup and conditions leading to the production of the secondary beams is given in [3,4] together with the design of the detector.

The Detector Design

The determination of the nuclear charge of the fragments will be performed by a **MU**lti-**S**ampling **I**onization **C**hamber with two identical active volumes (TwinMUSIC) symmetric to the vertical cathode plane. The detector features low mass in directions transversal to the beam in order to minimize secondary reactions produced by the primary beam particles also impinging on the central cathode of the detector.

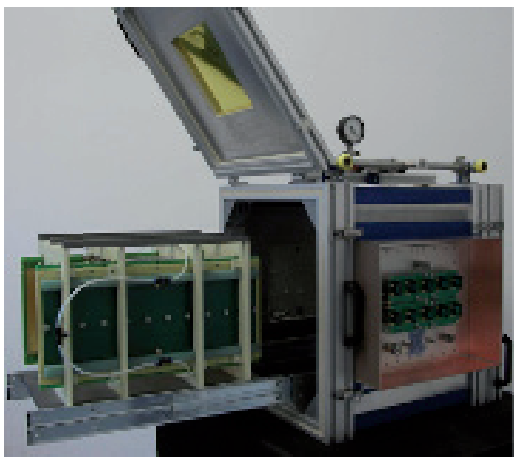

Figure 1: Photography of the TwinMUSIC with its functional unit pulled out of the housing.

* This work is supported by CEA DAM / IdF Bruyeres le Chatel and GSI

✝ Corresponding author: B.Voss@GSI.de

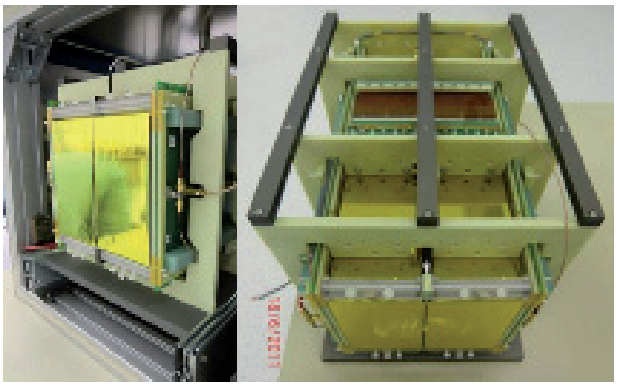

Figure 2: Photography of the functional detector unit. The main components and structures are visible.

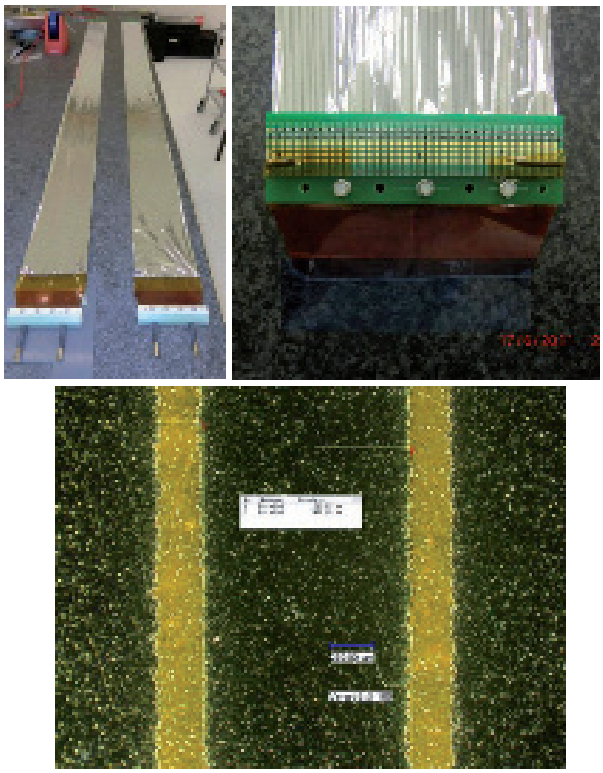

Figure 3: Photography of the strip-line field cage; the voltage divider (upper right) and magnified detail of the electro-etched strip lines (lower part) are shown.

The actual realization of the TwinMUSIC is shown in Figs. 1 and 2. The housing is made from standard industrial aluminium profiles and forms a faraday cage which may be evacuated slightly to support and fasten changes of the gas-composition. The frames of the outer skeleton of the detector unit serve for high-precision mounting of the various 'active' parts of the two sections which are formed by anodes with ten active electrodes of

(200 x 50) mm^2 each and two screening electrodes of (200 x 10) mm^2 surface each on PCB boards of 3.2 mm thickness. The adjustable distance to the adjacent Frisch-grids has been chosen to 5 mm. The wire layers are kept on ground potential with respect to the anodes at high voltage, generating a ≈800 V/cm electric field in order to reduce drift-time and -spread. A low-mass field-cage with a strip-line electrode design has been realized (Fig.3). The fields in the drift-region are adjusted to (400-500) V/cm.

A summary of requirements and features is listed in the table below:

Feature	Realization
Active volume	200 x 200 x 500 mm^3
Passive volume	Minimal in depth direction (z) according local conditions, ~200 l
Shape	Rectangular cross section (x,y)
Sectioning (x,y)	Twofold
Sectioning (z)	Rectangular, active: 10 sectors, each 200 x 50 mm^2 Screening: 2 sectors, each 200 x 10 mm^2
Environment	Ambient pressure and temperature
Thickness	Lowest possible, especially near the optical (beam) axis, no limitations otherwise
Detector gas low angular straggling fast drift 2 cm/µs	Ne (84-85Vol.-%) N_2 (0.3%) CH_4 (10-12%) CO_2 (4-3%)
Electric field	max. 500 V/cm (HV-stability)
Electronics	Customized pre-amps, flanged directly to the housing
Crucial observables	Energy-loss and Timing signal
Energy-loss resolution	2%
Horizontal position Resolution (Drift-time)	200 µm FWHM
Weight	~150 kg

For the 100 mm wide strip-line field-cage with an uncoiled length of ~1.8 m a self-made low-mass version of a Kapton® foil of 7.5 µm and 25 µm thickness, respectively, as well as an industrial fall-back version on a 50 µm foil were produced. The field-defining electrodes are made from Aluminium and Copper with thicknesses of ~200 nm and 12 µm, respectively. Both realize a staggered strip-line design of strips with 1 mm width and 0.5 mm gaps. As a first prototype a non-staggered specimen on the Aluminium coated version with a gap of 250 µm has been realized by electro-etching.

The cathode consists of an aluminized 7 µm thick Kapton® foil kept on 5 kV potential. In order to minimize the material on the beam axis its central region of 20 mm height is mechanically stabilized with Nylon® fishing lines of 300 µm diameter only.

Several options of the Frisch grid structures and materials are under investigation which are optimizing either for their electrical shielding properties and/or the electron transmission. Grids made from W-Re wires of 20 µm diameter and 2 mm spacing in a diagonal arrangement as well as meshes from stainless steel and/or Ni-coated PE have been built. The optical transparency of the meshes tested so far varies between 30 % and 70 %.

A gas regulation-system operating with pre-mixed gas keeping the near-atmospheric (over-)pressure and gas-flow constant to a level of (60-70)±0.1 mbar and (20-200)±0.1 l/h at the same time, has been set up and operated successfully. A SETRA 370 digital pressure gauge measures the gas pressure independent of the gas-regulation system. The pressure drop observed for an initial 70 mbar overpressure was 0.01 mbar/10 min. After flushing for 24 h with dry nitrogen at 200 l/h only low gas impurities were traced for the two 'main' and most crucial components O_2 (2 ppm) and H_20 (160 ppm). They were measured with an Orbisphere 3600-11.G sensor as well as with a Rapidox 3100 system (Cambridge Sensotec).

The detection system is read out using discrete pre-amplifiers with a sensitivity of 5 V/pC. Main spectroscopic (t_{shape}=500ns) and timing amplifier (t_{diff}=140ns, t_{int}=70ns) as well as CFD discriminator stages are realized in the combined VME Module MSCF-16F (MESYTEC). Energy and timing information were digitized by MADC-32 and V785 ADCs and V1290 TDCs (CAEN). The DAQ is based on the GSI Multi Branch System (MBS).

Experiment and Results

A detector setup consisting of prototype versions of the main detector systems have been deployed in parasitic test beam times at GSI. ^{238}U with 500 AMeV and primary rates of several 10^5 particles/second with spill duration of 1.2 s were impinging on 3 x 0.5 mg/cm^2 Pb foils in the active target. An example of the energy-loss spectrum at this place is shown in Fig. 4 for the center foil. Primary beam-particles as well as fission fragments emerging from various places are clearly separated.

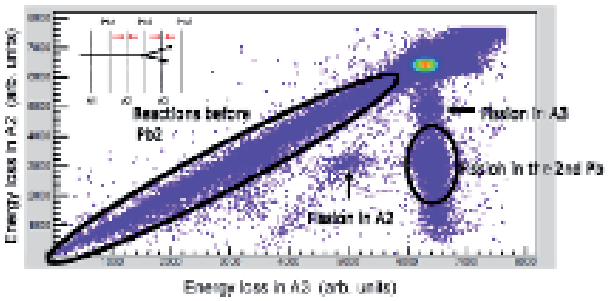

Figure 4: Energy-loss in two subsequent sections of the active target installed in front of the TwinMUSIC.

Preliminary results on the energy and timing resolution of the TwinMUSIC have been obtained. The respective spectrum for the left and right half-volume of the TwinMUSIC is shown in Fig. 5. The distribution on the right anodes, equipped with a less dense mesh shows a

favorable collection efficiency which is mainly due to its higher optical transparency of 37 % compared to 30 % installed on the left side.

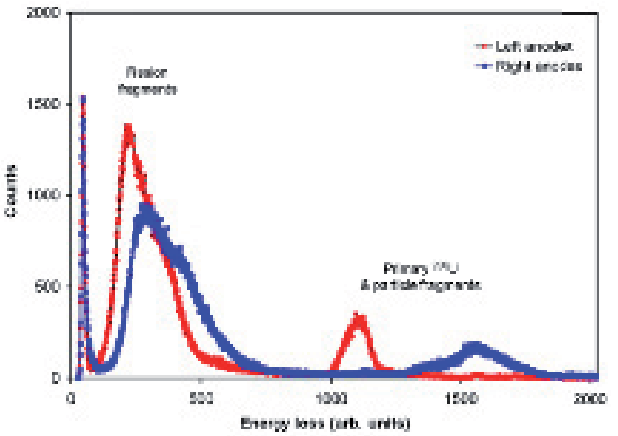

Figure 5: Energy-loss in the left (circles) and right (squares) half-volume of the TwinMUSIC.

An energy resolution of roughly 5 % for the primary particles is observed. A separation of the fission fragment by correlation with their time-of-flight values was not in the main focus of the test run. From the steep fall off of the drift-time distributions in the vicinity of the cathode surface one can deduce a horizontal-position resolution of 600 µm for a single anode (see Fig. 6). Taking into account all anodes 200 µm seem to be feasible to obtain.

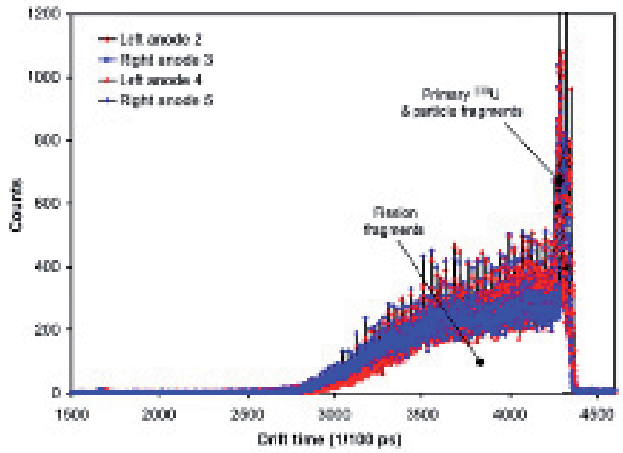

Figure 6: Drift times recorded in the left (circles) and right (squares) half-volume of the TwinMUSIC.

Outlook

The analysis of the data taken during the commissioning phase in 2011 is still ongoing. Small changes in the design and the final choice of the Frisch-grid option will be taken depending on the outcome. The TwinMUSIC prototype will be tested again early 2012 at CaveC/ALADIN@GSI. A first physics run is scheduled for May/June 2012 addressing questions from both, SOFIA and ANDES.

References

[1] http://www.andes-nd.eu
[2] K.-H. Schmidt et al., NPA 665 (2000) 221.
[3] B. Voss et al., GSI Scientific Report 2010, GSI Report 2011-1, 2010, p.223.
[4] Proceedings of the IEEE Nuclear Science Symposium, Medical Imaging Conference 2011, 2011, Valencia, Spain

Time resolution measurements with RPCs irradiated with ^{136}Xe at relativistic energies

Y. Ayyad[1], *J. Benlliure*[1], *E. Casarejos*[2], *I. Durán*[1], *N. Montes*[1], *C. Paradela*[1], *and J.R. Pereira*[1]
[1]USC, Santiago de Compostela, Spain; [2]UVi, Vigo, Spain

Timing Resistive Plate Chambers (tRPC) are proposed for the construction of the ion time-of-flight wall (iToF) for the R3B experiment at FAIR. This detector will provide high-accuracy time-of-flight measurements of the fragments produced in reactions using the inverse kinematic technique. Taking into account different flight paths, in order to identify nuclei with masses up to A=200 a demanding time resolution of about 30 ps (σ) is required for iToF. This could be reached with 4 detection planes with an intrinsic resolution each around 50 ps (σ) [1].

Prototypes of multistrip tRPCs adapted to the detection of relativistic heavy ions have been constructed (Fig. 1). These prototypes were built with two 400 mm x 200 mm, 1 mm thick float-glass plates defining one single 300 μm gap. To ensure its tightness, the perimeter of the gas volume was sealed with glue. Two metallic adapters were included to allow the gas circulation. This solution was adopted in order to minimize the amount of matter crossed by the ion beam.

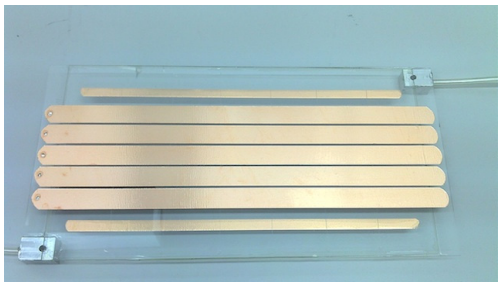

Figure 1: Single-gap self-supported multi-strip tRPC.

The active detection area consisted in five strips made of adhesive copper-tape, glued to the external faces of the glass plates. The HV was feeding the active strips of one face, while those strips on the other one served as ground reference. The signals were decoupled and picked-up from both ends of each strip.

In previous tests we investigated the detection efficiency of the RPCs with ions [2] and time resolution with electrons [3]. Those measurements shown detection efficiencies for heavy ions around 100% and time resolutions for 15 MeV electrons around 30 ps. In the present work, we used a beam of ^{136}Xe at 560 A MeV at GSI (Darmstadt). Two single-gap tRPC were placed between two fast scintillators of 25 mm x 80 mm, 1 mm thick, defining the external trigger. One event was defined by a ^{136}Xe ion detected in coincidence by both scintillators allowing the measurement of the efficiency of the RPC respect to the plastic scintillators. The time and charge of the signals coming from the central strip of the RPCs and from both sides of the scintillators were digitized using TACQUILA board [4]. The average measured rates of the ions were around 2-5 Hz/cm^2, with a beam spot of about 3 cm^2 and 5 s of spill duration. The iso-C_4H_{10} free gas mixture used was $C_2H_2F_4$ (90%) and SF_6 (10%). The in-beam current of the RPCs was around 40 nA and the HV was changed to find the proper working point of the RPCs and the efficiency plateau. At 2900 V the RPC reaches 99% of efficiency.

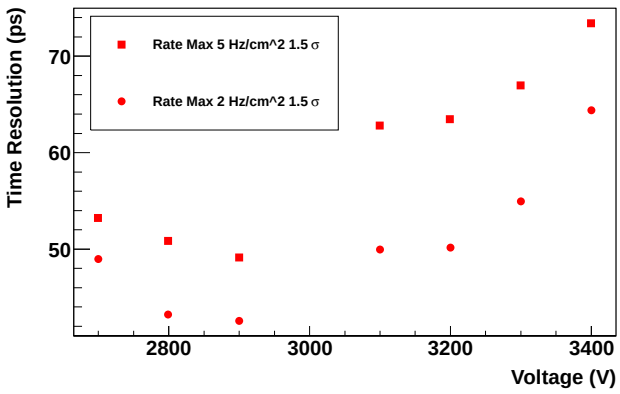

Figure 2: Time resolution as a function of the applied voltage at 2 and 5 Hz/cm^2.

The time resolution of an RPC detector as a function of the applied voltage at two ion rates is shown in Fig. 2. The working point can be found in the plateau between 2800 and 3100, where a time resolution of 40 ps was achieved at 2900 V. For the lowest ion rate, one can also observe a degradation of the time resolution for voltages above 3100 V, due to the increase of streamer signals. The average ion rate was found to have an important effect on the degradation of the time resolution. These results with ^{136}Xe beam confirms the excellent time resolution obtained with electrons and show the feasibility of RPC detectors for the construction of the iToF.

[1] E. Casarejos et al. Nucl. Instr. and Meth. A 661 (2012) 137-140
[2] E. Casarejos et al. Nucl. Instr. and Meth. A (accepted)
[3] Y. Ayyad et al. GSI Scientific report 2010, pag. 184
[4] K. Koch et al. IEEE Trans. Nucl. Sci. NS-52 (2005) 3

Angular-momentum content of momentum profile in one-neutron knockout from ^{14}Be*

Yu. Aksyutina[1,2], T. Aumann[3], K. Boretzky[3], M.J.G. Borge[4], A. Chatillon[3], L.V. Chulkov[1,5], D. Cortina-Gil[6], U. Datta Pramanik[7], H. Emling[3], H.O.U. Fynbo[8], H. Geissel[3], G. Ickert[3], H.T. Johansson[2], B. Jonson[2], R. Kulessa[9], C. Langer[3,10], M. Lantz[2], T. Le Bleis[3,10], K. Mahata[3], G. Münzenberg[3], T. Nilsson[2], G. Nyman[2], S. Paschalis[11], W. Prokopowicz[3], R. Reifarth[3,10], A. Richter[12], K. Riisager[8], G. Schrieder[12], H. Simon[3], K. Sümmerer[3], O. Tengblad[4], Y. Togano[1], H. Weick[3], and M. Zhukov[2]

[1]EMMI, Germany; [2]Chalmers University of Technology, Sweden; [3]GSI, Germany; [4]CSIC, Madrid, Spain; [5]RRC Kurchatov Institute, Moscow, Russia; [6]University of Santiago de Compostela, Spain; [7]SINP Kolkata, India; [8]Aarhus University, Denmark; [9]Jagellonian University, Krakow, Poland; [10]University of Frankfurt, Germany; [11]University of Liverpool, United Kingdom; [12]Technische Universität, Darmstadt, Germany

Recently, three data sets were published for ^{13}Be, all with different interpretations of its ground-state structure. From the data obtained at GANIL [1] it is a Breit-Wigner l=0 resonance, it is a virtual s-state populated in the one-neutron knockout from ^{14}Be at GSI [2], and finally it is interpreted as a l=1 resonance from data obtained at RIKEN [3].

In order to increase our ability to gain information on these very exotic nuclear systems we use a novel method for analysis based on a study of the root-mean-square (r.m.s) momentum of a fragment+n system after one-neutron knockout from a Borromean nucleus as a function of the relative energy between neutron and fragment (momentum profile, $\mathcal{P}(E_{nf})$).

The data analyzed here originate in an experiment performed at the ALADIN-LAND setup at GSI, where neutron-knockout reactions were studied with beams of ^{8}He (E=240 MeV/u), ^{11}Li (E=280 MeV/u) and ^{14}Be (E=304 MeV/u) impinging on a liquid hydrogen target. The selection of coincidences between a neutron of multiplicity one and the corresponding fragment gave the one-neutron knockout residues. The derived four momenta of neutrons and fragments were used to calculate fragment-n relative energy, E_{fn}, as well as $\mathcal{P}(E_{nf})$. $\mathcal{P}(E_{nf})$ was compared to model calculations using the eikonal approximation.

This is the first time the $\mathcal{P}(E_{nf})$ observable is used for analyzing experimental data. Therefore it is first put into analysis of two well-known nuclei, ^{7}He and ^{10}Li, to demonstrate its applicability. The conclusion is that the shape of $\mathcal{P}(E_{nf})$ in neutron knockout from ^{8}He and ^{11}Li allows a qualitative model-free analysis of the experimental data revealing contributions from different angular momenta. With this in mind the next step is to apply this method to ^{13}Be, a case where there are still many open questions in the understanding of its structure

$\mathcal{P}(E_{nf})$ for ^{12}Be+n system after one-neutron knockout from ^{14}Be is shown in Fig. 1(upper panel). The E_{fn} spectrum is given in the lower panel of Fig. 1. The solid line illuminates the bend in the spectrum at ≈ 0.3 Mev indicating a complex structure of the resonance peak. Four distinguishing characteristics were observed:

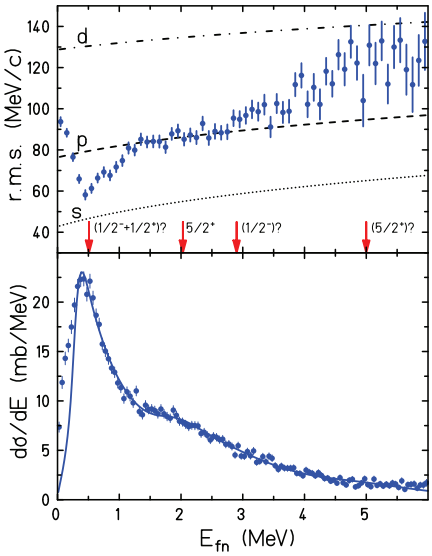

Figure 1: Upper panel: Momentum profile of ^{12}Be+n system. The model calculations are shown as a dotted line (s-wave), a dashed line (p-wave) and a dashed-dotted line (d-wave). Lower panel: Relative-energy spectrum.

- the decay of $5/2^+$ state at 2.0 MeV to ^{12}Be(2^+) via ^{12}Be$(2^+) \otimes (1s_{1/2})$ component is responsible for the large r.m.s. momentum at energies close to zero.
- the ^{12}Be$(1/2^+)$ state dominates at $E_{fn} \approx 0.5$ MeV.
- the $1/2^-$ state is situated at 2.9 MeV. An indication exists that it can be the second $1/2^-$ state.
- $\mathcal{P}(E_{nf})$ reveals a fingerprint of the second $5/2^+$ state, a result not observable by only analyzing the E_{fn} spectrum.

References

[1] J.L. Lecouey, Few-Body Systems, 34 (2004) 21.

[2] H. Simon et al., Nucl. Phys. A 791 (2007) 267.

[3] Y. Kondo et al., Phys. Lett. B 690 (2010) 245.

* This work was supported by the Alliance Program of the Helmholtz Association (HA216/EMMI)

Beyond the neutron drip-line - unbound oxygen

C. Caesar[1], T. Aumann[1], K. Boretzky[2], M. Heil[2], M. Heine[1], M. Holl[1], R. Plag[3], D. Rossi[2], H. Scheit[1], H. Simon[2], and the R^{3}B Collaboration

[1]IKP, TU Darmstadt, Germany; [2]GSI, Darmstadt, Germany; [3]Goethe Universität, Frankfurt a.M., Germany

The neutron-unbound ground state of ^{25}O was recently observed for the first time in a proton knock-out reaction from a ^{26}F beam on a beryllium target at the NSCL[1]. One single resonance was observed in the ^{24}O+n relative-energy spectrum.

The R3B-collaboration has studied the ^{26}F(p,2p)^{25}O reaction utilizing a kinematically complete measurement at relativistic beam energies with the R3B-LAND-setup [2]. This measurement provides improved data in several respects. The reaction was measured fully exclusive (including γ-ray detection) and with much larger acceptance. First results on the ^{26}F(p,2p)^{25}O channel will be presented in this report.

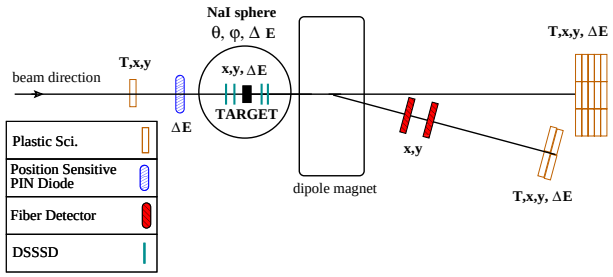

Figure 1: Sketch of the s393 setup in Cave C, only detectors used in the here presented analysis are shown.

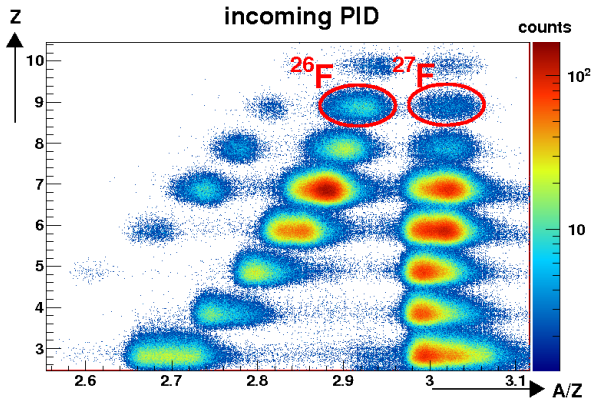

Figure 2: Incoming Particle Identification (PID). The secondary beam incident on the R3B target at Cave C was produced by fragmentation of ^{40}Ar. In the here shown setting the FRS was optimized for transport of ^{24}O.

A primary beam of ^{40}Ar and a thin degrader has been used to ensure transport of radioactive ions from Helium to Fluorine. Fig. 2 shows the beam composition for the most neutron-rich setting optimized for transport of isotopes with A/Z = 3.

The incoming ^{26}F ion beam has been identified via energy-loss and Time-of-Flight (ToF) measurements using a scintilator and a PIN diode infront of the reaction target, see Fig. 1. The charge of the fragments has been identified using two Si-strip detecors directly behind the traget and a scintilator based ToF wall at the end of the fragment branch. The mass of the fragments has been determined by tracking the flight path through the magnetic field of ALADIN using the already mentioned two Si-strip detecors in front of the magnet plus two scintillating fibre arrays behind it. The fragment mass distribution is shown in Fig. 3 The ToF as well as θ and φ of the neutrons have been measured using LAND.

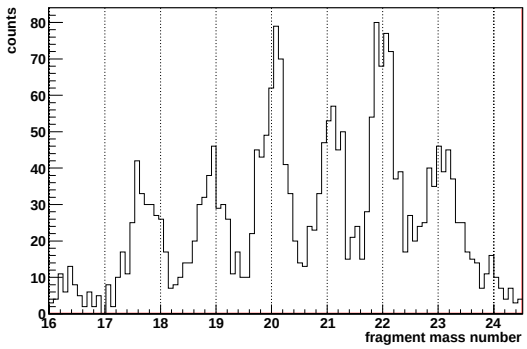

Figure 3: Fragment mass distribution for oxygen isotopes after proton knock-out from a ^{26}F beam incident on a 922 mg/cm^2 CH_2 target at 545 MeV/u.

The relative energy spectrum of fragment and neutron has been reconstructed and the preliminary result is in agreement with the NSCL measurement.

Acknowledgement

Supported by GSI F+E(Darmstadt). Work is part of HGS-HIRe.

References

[1] C.R. Hoffman et al. Phys.Rev.Lett 100 (2008) 152502

[2] 'Direct reactions of light exotic beams measured in complete kinematics at R3B', GSI Scientific Report, p.166, 2010

Coulomb break-up of ^{14,15}B for the astrophysical r-process

S.G. Altstadt[1,2] and the R^{3}B Collaboration[*2]
[1]Goethe University, Frankfurt; [2]GSI, Darmstadt, Germany

Introduction

Model calculations of r-process nucleosynthesis in a neutrino-driven wind scenario with a short dynamical timescale indicate that light, neutron-rich nuclei may have a crucial influence on final r-process abundances [1]. However, nuclear reaction rates of unstable nuclei far from stability are extremely difficult to determine and hence rarely known. Therefore, a kinematically complete measurement was performed with the R^{3}B/LAND setup. To determine the neutron capture cross sections of ^{13}B and ^{14}B, which are thought to be on the main flow path among the light elements with Z<10 [2], the time-reversed reactions ^{14}B(γ,n) and ^{15}B(γ,n) were measured via Coulomb dissociation.

Calibration & Analysis

The calibration of the detectors is at an advanced status. The incoming particle identification is shown in the figure below. The charge is determined from the measured energy loss in a position sensitive silicon pin diode, while the mass-to-charge ratio results from time-of-flight measurements. The isotopes of interest, ^{14}B and ^{15}B, can be cleary identified and were produced in sufficient numbers.

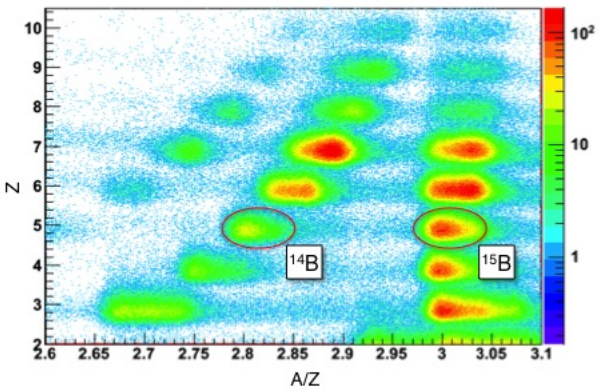

Figure 1: Incoming particle identification: ^{14}B and ^{15}B can be cleary identified and feature sufficient statistics.

The energy loss of the outgoing fragments was measured with a time-of-flight-wall (TFW). The different charges can be well separated as shown in figure 2. However, since the TFW can not provide any informations about the mass of a fragment, two fibre detectors were used to determine the different angles between different isotopes. The charged fragments are deflected in a dipol magnet and the mass-to-charge ratio is proportional to the deflecting angle. Hence the different boron isotopes can be disbanded and the reaction channels could be indentified.

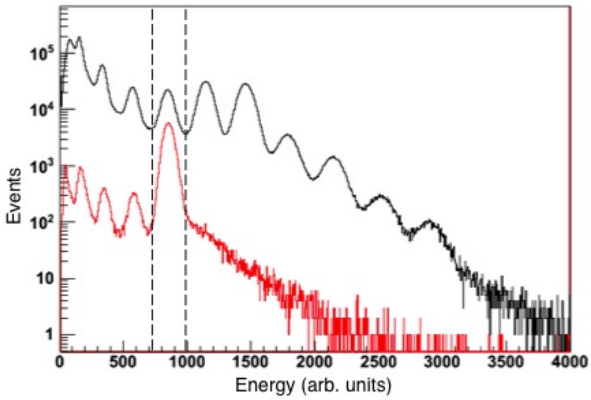

Figure 2: The different energies can be well distinguished to identify the charge of the questioned outgoing fragment. The range marks Z = 5 with incoming cut on ^{15}B (red) and without incoming cuts (black).

Outlook

The next step will be to finalize the calibration to begin outgoing particle tracking. After tracking of masses and angles the analysis will be able to provide the invariant mass to obtain the differential cross-sections and excitation spectra.

References

[1] M. Terasawa et. al, The Astrophysical Journal, 2001
[2] T. Sasaqui et. al, The Astrophysical Journal, 2005

*This project was supported by the Helmholtz International Center for FAIR, the Helmholtz Young Investigator Group VH-NG-327, GSI F+E(Frankfurt) and HGS-HIRe

Coulomb breakup of ^{18}C

M. Heine[1], T. Aumann[1], C. Caesar[1], M. Heil[2], R. Plag[2], D. Rossi[2], and the R^{3}B-collaboration
[1]IKP, TU Darmstadt, Germany; [2]GSI, Darmstadt, Germany

Recent research has shown that the (n,γ) cross-sections of light nuclei also have an influence on the neutron-balance during the r-process. Especially neutron rich carbon isotopes play an important role in r-process nucleosynthesis network calculations which include light nuclei, since these are aligned along major flow paths. In particular, ^{18}C is of interest, because it can be interpreted as a waiting point [1], due to it's comparably high neutron separation energy. The ^{17}C(n,γ)^{18}C rate could so far only be estimated theoretically and has an uncertainty of a factor of ten [2]. At the R^{3}B-CaveC setup, we have observed the inversed reaction, i.e. ^{18}C(γ,n)^{17}C, via Coulomb breakup of a ^{18}C beam. This was accomplished in a kinematically complete measurement by analyzing data on an event-by-event basis. The according (n,γ) cross-section can then be inferred via the detailed balance theorem.

The experiment has been performed by the R^{3}B-collaboration at Cave C in August 2010. Using an ^{40}Ar

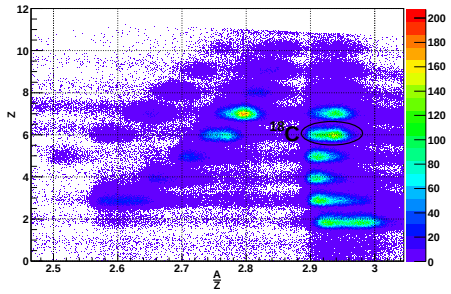

Figure 1: Secondary beam on the R^{3}B target at Cave C.

primary beam and a Be primary target, an exotic secondary beam comprising nearly all bound light nuclei was produced. The large A/Z range from 1.75 to 3 has been covered in several settings of the FRS and of the subsequent beamline to Cave C [3]. Figure 1 shows the ions contained in the most neutron rich setting.

The incoming particles were identified via Time-of-Flight (ToF) and energy-loss measurements, using plastic scintillators and a PIN diode in front of the Pb reaction target. Due to the relativistic beam energies the reaction products are strongly forward-boosted. The angle of the emitted neutrons and their energy was derived from ToF and positions measurements in the Large Area Neutron Detector (LAND). For the fragment identification, ToF and energy-loss measurements were performed.

The reaction channels were separated by means of the trajectories of the fragments, gained from position measurements with two fiber detectors, after passing the magnetic field of A LArge DIpole magNet (ALADIN). In Figure 2, the separation of the unreacted ^{18}C beam from several neutron-removal channels from Coulomb breakup is shown. In the case of a ^{17}C fragment a neutron is required.

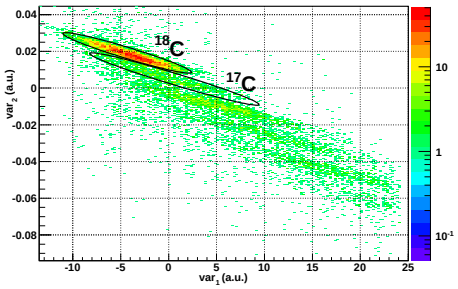

Figure 2: Separation of unreacted ^{18}C from reacted beam. In addition to incoming ^{18}C a neutron in the LAND is required.

The excitation energy of the (^{17}C+n) system was derived from the measured quantities according to Formula (1). For ^{18}C Coulomb breakup a preliminary excitation energy spectrum is shown in Figure 3. It starts at the ^{18}C neutron separation energy $S_n = 4.2$ MeV.

$$E^* = \sqrt{m_{^{17}\mathrm{C}} + m_\mathrm{n} + 2E_{^{17}\mathrm{C}}E_\mathrm{n}(1-\cos\vartheta_{(^{17}\mathrm{C-n})})} - m_{^{18}\mathrm{C}} \qquad (1)$$

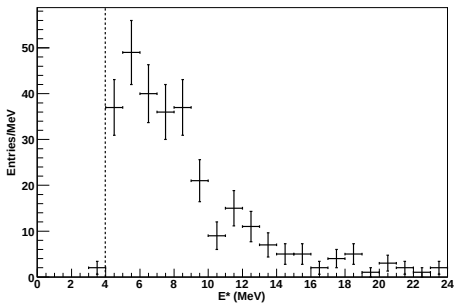

Figure 3: The distribution of excitation energies E* of ^{18}C measured in the (^{17}C+n) system. The ^{18}C separation energy is marked.

Supported by GSI F+E (Darmstadt). Work is part of HGS-HIRe.

References

[1] M. Terasawa et al., APJ 562 (2001) 470
[2] T. Sasaqui et al., APJ 634 (2005) 1173
[3] "PHN-NUSTAR-NR-04", GSI Scientific Report (2010) 166

Coulomb dissociation of ^{92,93,94,100}Mo *

O. Ershova[1,2], K. Göbel[1,2], T. Aumann[2,3], M. Heil[2], H. T. Johansson[4], T. Le Bleis[5], A. Movsesyan[2,3], S. Paschalis[6], R. Plag[1,2], R. Reifarth[1,2], D. Rossi[2], K. Sonnabend[1], and the s295 collaboration

[1]Goethe-Universität Frankfurt, Germany; [2]GSI, Darmstadt, Germany; [3]TU Darmstadt, Germany; [4]Chalmers Univ. of Technology, Sweden; [5]TU München, Germany; [6]LBNL, USA

Photodissociation reactions are important for the p-process nucleosynthesis in supernovae explosions. Theoretical calculations of isotopic abundances of the p-nuclei require a large reaction network linking thousands of isotopes, where most of the reaction rates must be derived from the statistical model. However, as many rates as possible need to be determined experimentally, in order to provide a reliable reference for the calculations. Measurements on Mo isotopes are highly demanded, since they contribute to the understanding of the significant underproduction of ^{92,94}Mo and ^{96,98}Ru in the models of p-process nucleosynthesis. An important aspect of the present project is to verify the validity of the employed experimental approach by comparing the results with the data of the experiments performed with real photons.

Experiment and results

At the LAND setup at GSI, Coulomb dissociation of Mo isotopes was studied in order to extract (γ,n) and (γ,2n) reaction cross sections. The primary beams of the stable ^{94,100}Mo were used. The secondary beams of ^{92}Mo and unstable ^{93}Mo were produced by fragmentation on a thick Be target and subsequent separation in the FRS fragment separator. At an energy of approximately 500 AMeV, the beam impinged on a secondary Pb target. In case of a peripheral collision, the interaction can be described as a reaction between the projectile and a virtual photon originating from a time-varying electromagnetic field of the target nucleus. Contributions of background reactions, such as those resulting from a nuclear interaction in the target or all kinds of reactions outside the target, are estimated by complementary measurements with a carbon target and without a target and subtracted from the Pb target measurement.

The LAND setup provides a possibility to detect all reaction products, thus delivering kinematically complete data. The incoming and all outgoing particles are identified with respect to their *A*, *Z* and four-momentum on an event-by-event basis. Although the setup allows to reconstruct the excitation energy spectrum via the invariant mass method, its application was hampered by the unexpectedly low efficiency of the CsI γ-detector. The overall response of the setup is very complex and does not allow a deconvolution. Alternative methods of data interpretation are currently investigated.

Integrated Coulomb excitation cross sections for the four reaction channels are presented in Table 1. The result on ^{93}Mo(γ,n) is especially important, since this isotope is unstable and the corresponding cross section has not been measured before. The reported errors include the contributions of both the statistical ($\leq$ 5%) and systematical (10-12%) errors.

Integrated cross sections of the ^{100}Mo(γ,n) and ^{100}Mo(γ,2n) reactions were compared directly to the data of Beil et al. [1] measured in Saclay by positron annihilation, and indirectly to a photoactivation measurement by Erhard et al. [2]. For the 1n-channel, the scaling factor between our result and Beil et al. data is consistent with the scaling factor reported by Erhard et al. between their data and Beil et al. data. Both results are in agreement with the scaling factor of 0.85 ± 0.03 recommended by Berman et al. [3] for the data measured at Saclay on nuclei in the respective mass region. A somewhat lower factor was observed for the 2n-channel. It can be explained under the assumption that the correction factor of 0.8 for the Saclay data stems from the wrongly estimated efficiency of one-neutron detection [3]. The efficiency of the two-neutron detection would then be wrong by a factor of 0.8^2=0.64, which is consistent with our result.

	$\sigma_{\mathrm{CE}}^{\mathrm{exp}}$ [mb]	$\frac{\sigma^{\mathrm{exp}}}{\sigma^{\mathrm{Beil}}}$	$\frac{\sigma^{\mathrm{Erhard}}}{\sigma^{\mathrm{Beil}}}$
^{92}Mo(γ,n)	369 ± 13		
^{93}Mo(γ,n)	728 ± 12		
^{100}Mo(γ,n)	799 ± 10	0.8 ± 0.1	0.89 ± 0.09
^{100}Mo(γ,2n)	220 ± 13	0.61 ± 0.09	

Table 1: Measured Coulomb excitation cross sections. The results for the ^{100}Mo are compared directly to the Beil et al. data [1]. A scaling factor reported by Erhard et al. [2] between their data and Beil et al. data is also presented.

Currently, the Coulomb excitation cross section for ^{94}Mo is under investigation. According to [4], ^{94}Mo is mainly synthesized via the (γ,n) photo disintegration chain starting from ^{98}Mo, for ^{92}Mo the most important production channel is ^{94}Mo(γ,n). The results of the analysis of ^{94}Mo(γ,n)^{93}Mo will also be compared to measurements with real photons. The data will thus complete the (γ,n) production chain of the p-isotopes of Mo.

References

[1] H. Beil et al., Nucl. Phys. A 227(3) (1974) 427.
[2] M. Erhard et al., Phys. Rev. C 81(3) (2010) 034319.
[3] B. L. Berman et al., Phys. Rev. C 36(4) (1987) 1286.
[4] C. Travaglio et al., The Astrophysical Journal, V. 739 (2011).

* Work is supported by GSI F+E(Frankfurt).

Coulomb Excitation of ^{32}Ar and ^{34}Ar *

O. Lepyoshkina[1], C. Langer[2], T. Aumann[3], K. Boretzky[4], R. Gernhäuser[1], R. Krücken[1], R. Plag[2], R. Reifarth[2], and the R^{3}B collaboration

[1]TU München, Germany; [2]Univ. Frankfurt, Germany; [3]TU Darmstadt, Germany; [4]GSI, Darmstadt, Germany

Motivation

Since experimental evidence for pygmy resonances in neutron-rich exotic nuclei was found a particular attention is paid to their analogues in proton-rich nuclei. Conceptually, RQRPA calculations predict the appearance of dipole strength for proton-rich nuclei like ^{32}Ar in the low-energy region between 8-10 MeV excitation energy [1, 2]. However, a significant drop of resonance strength is expected for ^{34}Ar. In contrast to neutron-rich nuclei for which the existence of the pygmy resonances was suggested by both theory and experiment, the proton-rich nuclei study lacking any experimental confirmation yet. At the same time a study of neutron-deficient nuclei in the Argon region is relevant for nuclei astrophysics [3]. The measurements of (γ, p) reactions are interesting for the calculation of reaction cross-section and radiative proton capture rates for the rp-process, e.g. the ^{31}Cl(γ, p) case.

Experiment

Using the Coulomb excitation method in inverse and complete kinematics at the LAND/R3B setup at GSI, an experiment using radioactive ^{32}Ar and ^{34}Ar beams has been performed. The isotopes were obtained via fragmentation of a 800 AMeV primary ^{36}Ar beam on a 6.347g/cm^2 Be-target situated at the entrance of the FRS. The produced proton-rich projectiles with a similar mass-to-charge ratio were separated in flight from the primary beam and from the other reaction products. The selected and identified proton rich isotopes were subsequently directed to a lead target of the LAND/R3B setup placed in Cave C. In order to determine the excitation energy after projectile excitation on the Pb target, all reaction products were identified (fragments, protons and gammas). The reconstruction of the excitation energy was derived from the particles momenta using the the invariant mass technique in an event-by-event mode, allowing for an investigation of dipole strength appearance. In order to distinguish electromagnetic and nuclear excitations in the Pb target, a measurements with a carbon target was performed to estimate the nuclear contribution. The background contribution is extracted from a measurement without target in addition.

Status of the Analysis

The fragment identification was completed (A,Z, P$_{frag}$) and the proton tracking allows the determination of momenta for 1p and 2p decays [4]. Figure 1 and 2 present the preliminary excitation energy spectra for ^{32}Ar(γ,p) and ^{32}Ar(γ,2p), respectively, from the measurement with the Pb target.

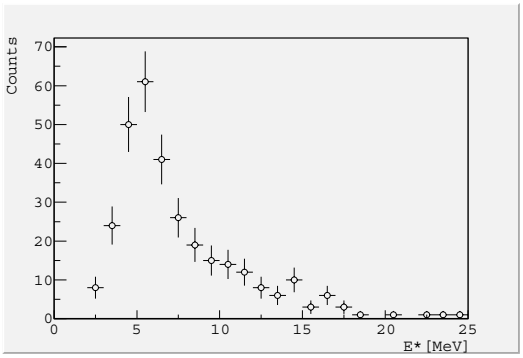

Figure 1: Excitation energy distribution for ^{32}Ar(γ,p)

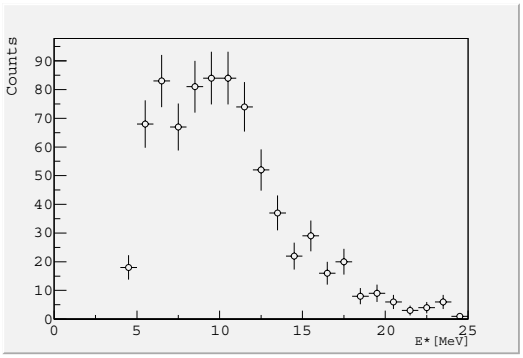

Figure 2: Excitation energy distribution for ^{32}Ar(γ,2p)

For an absolute measure of the Coulomb excitation cross section in a next step the measurements with different targets have to be normalized to separate the nuclear and background contribution. The analysis of the presented data will be finalized and complemented with a decay model allowing for an interpretation of the 1p- and 2p-decay data with respect to the appearance of low-lying strength.

References

[1] N. Paar et al., Phys.Rev.Letters 94, 182501 (2005)

[2] C. Barbieri et al., Phys.Rev.C.77, 024304 (2008)

[3] C. Langer, PhD thesis, Univ. Frankfurt, (2012)

[4] C. Langer et al., GSI Scientific Report, 170 (2010)

* Supported by EMMI.

Nuclear Breakup of ^{17}Ne and its Two-Proton Halo Structure *

F. Wamers[1], T. Aumann[1], C. Bertulani[2], L. Chulkov[3], M. Heil[3], J. Marganiec[4,5], R. Plag[3,6], H. Simon[3], and the R^{3}B Collaboration

[1]Institut für Kernphysik, TU Darmstadt, Darmstadt, Germany; [2]Texas A&M University-Commerce, Commerce, USA; [3]Kernreaktionen und Nukleare Astrophysik, GSI, Darmstadt, Germany; [4]ExtreMe Matter Institute, GSI, Darmstadt, Germany; [5]JINA, Notre Dame, USA; [6]Goethe Universität, Frankfurt, Germany

^{17}Ne is a proton-dripline nucleus that has raised special interest in nuclear-structure physics in recent years. As a Borromean 3-body system (^{15}O+2p), it is often considered to be a 2-proton-halo nucleus, yet lacking conclusive experimental and theoretical evidence about its structure. Therefore, in 2007 we have studied breakup reactions of ^{17}Ne secondary beams at 500 AMeV in inverse kinematics using the R^{3}B-LAND setup at GSI. As motivated and laid out in [1], one of the main goals in this experimental study is the determination of the s^2/d^2 configuration mixture of the two valence protons in the ^{17}Ne ground state. We have studied one-proton knockout reactions of ^{17}Ne projectiles on a carbon target, since the observables of these reactions, such as fragment-momentum distributions, are very sensitive to the angular-momentum value of the knocked-out proton. In such a reaction, a proton can be removed from the ^{17}Ne halo — assumed as being either in a $(2s_{1/2})^2$ or a $(1d_{5/2})^2$ configuration — as well as from $1p$-shell states in its ^{15}O core, so that lower or higher resonances in ^{16}F are populated, respectively (see Fig. 1 of [1]). By gating on events with a reconstructed ^{15}O+p relative energy below 2 MeV, we have been able to *exclusively* select knockout of a halo, that is valence, proton in ^{17}Ne (see Fig. 2 of [1]). In this report, we present a yet preliminary study of the ^{16}F transverse-momentum distributions, being observable after carbon-induced one-proton knockout from the halo states in ^{17}Ne. Fig. 1a and Fig. 1b show the x and y projections of the ^{16}F transverse-momentum distribution, comprising both experimental data (black crosses) and theoretical calculations (coloured lines). By employing the latest version of his Glauber-model based code [2], C. Bertulani has performed calculations of the ^{16}F transverse-momentum distributions that correspond to the knockout of either an s-wave proton (green-dashed line) or a d-wave proton (blue-dotted line) from the ^{17}Ne ground state. These distributions have been combined in a weighted superposition (red-solid line) to fit the experimental data. Taking a weighted average from the independent measurements in x and y, we determined a yet preliminary value for the $(2s_{1/2})^2$ weight in the halo of ^{17}Ne of 40.8±1.3(stat)±4.0(syst) %. The results suggests a moderately expressed two-proton halo of ^{17}Ne, and is in good agreement with a recent publication [3]. The ongoing work is focused on determining various aspects of the experimental response, such as efficiency and acceptance for detecting projectile-like protons, via the use of simulations. The aim here is to confirm and finalise the current picture, and to determine the $0p$-, $1p$-, and $2p$-knockout components of the measured two-proton-removal cross section on ^{17}Ne, which will, e.g., allow for extracting the spectroscopic factors of the ^{17}Ne halo protons.

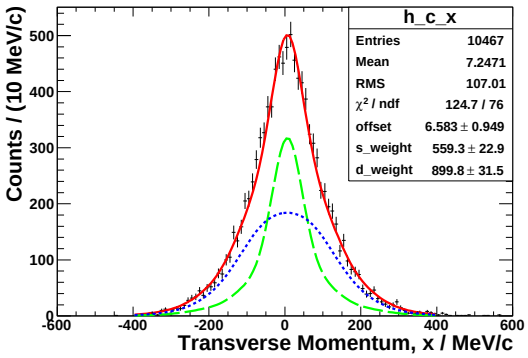

(a) ^{16}F $p_x^{\perp}$, ($E_{rel}(^{16}F) \leq 2$ MeV), C target.

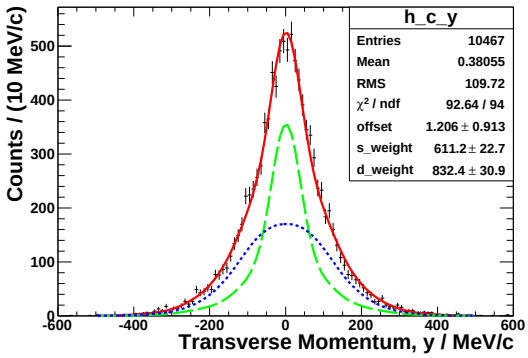

(b) ^{16}F $p_y^{\perp}$, ($E_{rel}(^{16}F) \leq 2$ MeV), C target.

Fig. 1: x (a) and y (b) components of the transverse-momentum distribution of ^{16}F, after one-proton knockout from halo states in ^{17}Ne on the C target. Experimental data (black crosses) is interpreted as a weighted superposition (red-solid line) of calculated distributions describing knockout of either an s-wave proton (green-dashed line) or a d-wave proton (blue-dotted line) from ^{17}Ne.

References

[1] Felix Wamers, GSI Scientific Report 2010.

[2] C. Bertulani and P. Hansen , Phys. Rev.C **70** (2004) 034609.

[3] W. Geithner et al., Phys. Rev. Lett. **101** (2008) 252502.

* Work was supported by EMMI and GSI F+E(Darmstadt). Work is part of HGS-HIRe.

Quasi-free knock-out reactions in inverse kinematics with ^{12}C at the R^{3}B/LAND-setup *

V. Panin[1,2], J. Taylor[3], T. Aumann[1,2], M. Chartier[3], L. Chulkov[1], R. Lemmon[4], R. Plag[1], F. Wamers[1,2], and the R^{3}B collaboration

[1]Kernreaktionen und Nukleare Astrophysik, GSI Darmstadt, Germany; [2]Institut für Kernphysik, TU Darmstadt, Germany; [3]Physics Department, University of Liverpool, UK; [4]STFC Daresbury Laboratory, UK

An important part of the physics programme at the future R^{3}B (Reactions with Relativistic Radioactive Beams) experiment at FAIR will be based on the study of proton-induced reactions in kinematically complete measurements at relativistic energies. These are in particular the Quasi-Free-Scattering (QFS) processes of the type (p,2p), (p,pn) etc. which will be used to investigate the single-particle and cluster structure of neutron-proton asymmetric nuclei. In order to establish the experimental technique of measuring in inverse kinematics, a benchmark experiment was performed in 2007 at R^{3}B/LAND-setup in Cave C. A ^{12}C beam at an energy of 400MeV/u has been chosen for this purpose since its structure is well studied and high-quality data from proton- as well as electron-induced knock-out reactions are available [1].

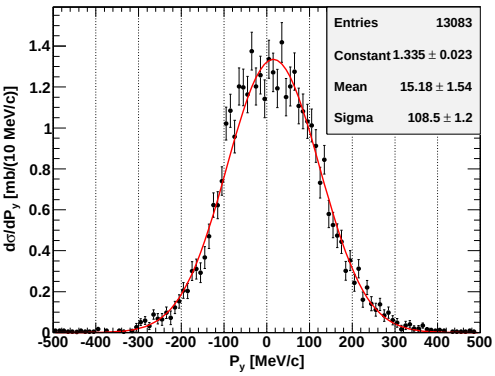

Figure 1: Transverse momentum distribution of the recoil ^{11}B from quasi-free proton knock-out from ^{12}C on the hydrogen (CH_2) target after subtracting carbon background

The setup was equipped with an array of 162 thick NaI scintilators (Crystal Ball) covering the full solid angle around the target for the detection and energy measurement of high-energy protons and gammas emerging in proton knock-out reactions. Additionally six Si micro-strip detectors (SSDs) covered the forward hemisphere for accurate tracking of the QFS protons in coincidence with residual heavy fragments [2].

The reactions of one-proton removal from a projectile-like ^{12}C were observed with carbon and hydrogen (CH_2) targets. The total cross-sections to observe ^{11}B in outgoing channels were measured to be 46.0 ± 4.4 mb and 18.4 ± 2.7 mb for carbon- and hydrogen-induced reactions respectively. The result for the carbon target is in good agreement with theoretical Glauber model calculations and with previous mesurements [3].

Figure 1 presents a preliminary transverse momentum distribution of the recoil ^{11}B from ^{12}C(p,2p)^{11}B QFS reaction. The distribution reflects the internal momentum of valence protons occupying p-shell in ^{12}C.

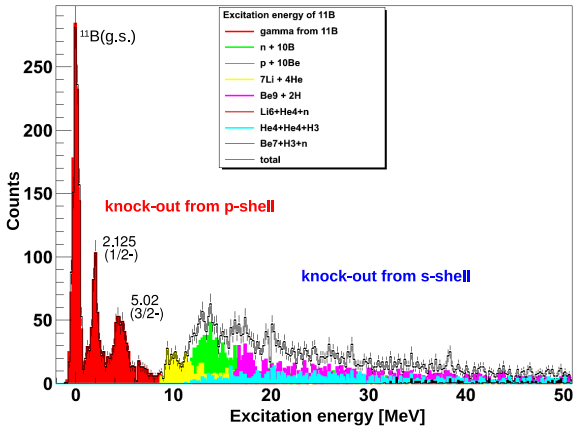

Figure 2: Preliminary excitation spectrum of ^{11}B from ^{12}C(p,2p)^{11}B reaction. The contribution of different decay channels is shown in colors. The ground-state peak is scaled down for a better representation. Only a qualitative interpretation can be made, since no acceptance and efficiency corrections are made.

An attempt was made to reconstruct the excitation spectrum of the residual ^{11}B from (p,2p) reaction combining the results of gamma-spectrometry and invariant-mass measurements of the breakup fragments. A preliminary result is shown in the figure 2. The contribution of the s-shell knock-out can be recognised.

The objective for the future analysis is to finalise the excitation spectrum of ^{11}B and to estimate exclusive (p,2p) cross-sections leading to different final states.

References

[1] G. Jacob and Th.A.J.Maris, Rev.Mod.Phys. 38 (1966) 121.

[2] V. Panin, T. Aumann, J. Taylor, GSI scentific report 2010, PHN-NUSTAR-NR-05, 167

[3] J.M Kidd *et all*. Phys.Rev.C 37 26132623 (1988) 6.

* Work is supported by GSI F+E(Darmstadt) and HIC for FAIR. Work is part of HGS-HIRe.

Quasi-Free Scattering of Relativistic Neutron-Deficient Carbon Isotopes*

M. Holl[1], *J. Enders*[1], *V. Panin*[1], *R. Plag*[2], *H. Simon*[2], *F. Wamers*[1], *and the R*^{3}*B Collaboration*

[1]Institut für Kernphysik, Technische Universität Darmstadt, Germany; [2]GSI Helmholtzzentrum für Schwerionenforschung, Darmstadt, Germany

Single-nucleon knockout reactions and quasi-free scattering are valuable tools to determine absolute spectroscopic factors. Quenching of these spectroscopic factors has been observed in nuclear knockout reactions [1]. This is in agreement with results from quasi-free electron scattering [2].

The R^{3}B-collaboration has conducted an experiment studying knockout and quasi-free scattering for light nuclei in a wide A/Q range in August 2010 [3]. Among others, the neutron-deficient carbon isotopes ^{10}C and ^{11}C were measured. A ^{40}Ar primary beam was incident on a production target, and the selected reaction residues were then transported through the fragment separator FRS to the R^{3}B-LAND setup in Cave C.

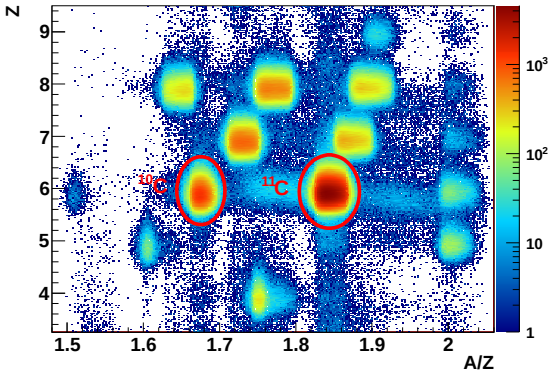

Figure 1: Identification plot of incoming particles. The charge of the nuclei is plotted against their A/Z ratio.

The incoming beam was identified using the time-of-flight between two scintillators, one at focus S8 of the FRS and one at the entrance of Cave C, and the energy loss in a PIN diode. The incoming angle of the beam was determined from the position on two silicon strip detectors in front of the target. Figure 1 shows a plot of the charge of the incoming particles versus the A/Z ratio derived from their time-of-flight.

The target area was surrounded by a NaI array used for γ and proton detection and a box consisting of four silicon strip detectors. After passing through the ALADIN magnet, the outgoing fragments were identified and tracked using the position and energy information given by two additional silicon strip detectors, two fiber detectors, and a time-of-flight wall.

Figure 2 shows the result of this tracking for an experimental run using a CH_2 target. Cuts on incoming ^{11}C and outgoing boron ($Z = 5$) have been applied. As one can see, it is possible to separate the different boron isotopes, ^{8}B and ^{10}B.

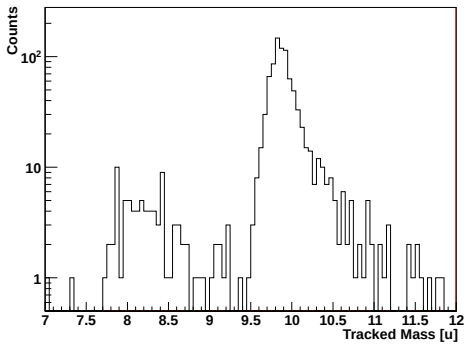

Figure 2: Tracked mass of outgoing boron fragments.

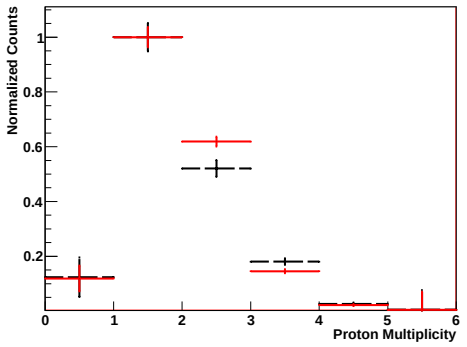

Figure 3: Comparison of the proton multiplicity measured by the NaI detector for a CH_2 (solid) and a carbon target (dashed).

In Figure 3 the proton multiplicity as measured by the NaI array is compared for the CH_2 and the C target. As expected, the detection of two coincident protons is enhanced for the CH_2 target due to the larger influence of quasi-free scattering. The analyis is in progress.

References

[1] A. Gade et al., Phys. Rev. C 77 (2008)

[2] G. J. Kramer, H.P. Blok, L. Lapikas, Nucl. Phys. A 679, 267 (2001)

[3] 'Direct Reactions of light exotic beams measured in complete kinematics at R3B', GSI Scientific Report 2010, p.166,

* Supported by the state of Hesse through the LOEWE center HIC for FAIR, and through the GSI-TU Darmstadt cooperation contract.

Systematic study of neutron-rich nuclei in island of inversion around N~20

U. Datta Pramanik[1,2], S. Chakraborty[1], A. Rahaman[1], T. Aumann[2], S. Beceiro[3], T. Le Bleis[4], K. Boretzky[2], D. Cortina-Gil[3], C. Caesar[2], M. Chartier[5], W. N. Catford[6], D. Gonzalez-Diaz[2], H. Emling[2], P. Diaz-Fernandez[3], I. Dillmann[2], Y. Dimitry[7], L. M. Fraile[8],G. De Angelis[9], O. Ershova[2], F. Farinon[2], H. Geissel[2], M. Heil[2], M. Heine[2], T. Heftrich[4], B. Jonson[10], A. Kelic[2], H. T. Johansson[10], R. Krucken[11], T. Kroll[4], J. Kurcewicz[2], C. Langer[2], Y. Leifels[2], G. Munzenberg[2], A. Movsesyan[2], J. Marganiec[15], C. Nociforo[2], M. A. Najafi[12], V. Panin[2], R. Plag[2], S.Pietri[2], H. A. Pol[3], S. Paschalis[13], A. Prochazka[2], R. Reifarth[2], V. M. Ricciardi[2], D. Rossi[2], J. Ray[1], G. Rastrepina[2], H. Simon[2], C. Scheidenberger[2], S. Terashima[2], S. Typel[2], J. Taylor[5], Y. Togano[14], E. Uberseder[2], V. Volkov[2], H. Weick[2], A.Wagner[7], F. Wamers[2], M. Weigand[2], J. Winfield[2], M. Zoric[2] for R[3]B collaboration*

[1]SINP, Kolkata, India; [2]GSI, Darmstadt, Germany; [3] Univ. of Santiago de Compostela, Spain; [4]TU, Dramstadt, Germany; [5] University of Liverpool, UK; [6]University of Surrey, UK; [7]HZDR Dresden-Rossendorf, Germany;[8]UCM, Madrid, Spain; [9]INFN, legnaro, Italy; [10] Chalmers University of Technology, Sweden; [11]TU, Munich, Germany; [12]KVI Groningen, Netherland; [13]LBNL, Berkeley, USA; [14]RIKEN, Japan; [15]EMMI, GSI, Darmstadt, Germany;

Magic numbers are considered as the backbone of nuclear structure since last sixty years, due to its applicability to explain properties of the nuclei near stability line. Through various experiments using Radioactive Ion Beam (RIB) facilities, it has been observed that those long cherished magic numbers are not valid anymore in neutron rich nuclei like ^{32}Mg etc. The possibility of breakdown of magic number was hinted in the late 1980's by Thibault et. al.[1] from the mass measurements in sodium nuclei (^{31,32}Na). Later, Motobayashi et. al.[2] showed large deformation in ^{32}Mg from BE(2) value measurements. A possible reason for this breakdown may be the occupation of valence nucleon(s) in *pf* shell rather than the expected *sd* shell in nuclei around N ~ 20. This leads to the concept of "Island of Inversion".

The exclusive set-up for kinematically complete measurement, the R^{3}B-LAND set-up, was used to study the properties of neutron rich nuclei around N~20, through electromagnetic excitation. Short-lived radioactive nuclei were populated by the fragmentation of ^{40}Ar beam (at 531 MeV/u) on a Be (8 gm/cm^2) target at fragment separator (FRS). A Secondary beam from the FRS, containing various isotopes (like ^{29,30}Na, $^{31-33}$Mg, ^{34,35}Al etc.) with A/Z between 2.55 to 2.85 (Fig. 1), was bombarded on target of Pb (for electromagnetic excitation) and CH_2 (for nuclear excitation). Empty target runs were taken for reaction in the detectors themselves.

Low-lying dipole strengths has already been observed in nuclei like ^{11}Be [3], ^{19}C [4], ^{15,17}C [5], $^{17-22}$O. For lighter neutron-rich nuclei the strength is mainly due to single particle excitation. Ground state configuration of these light neutron rich nuclei can be obtained by comparing experimental Coulomb breakup cross section with direct breakup model calculation [3-5]. Recent measurements regarding ground state spin of ^{33}Mg [6, 7] are in contradiction with that obtained from a beta-decay measurement [8]. The present experiment aims in validating the correct one. It is also our particular interest if the low lying dipole is pure single particle in nature or coupled with collective modes.

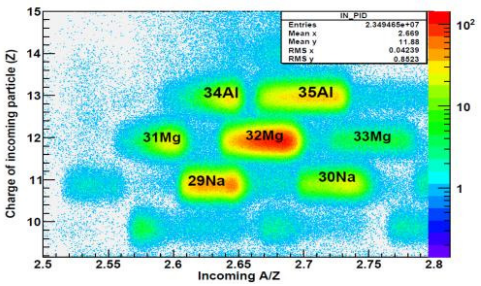

Fig. 1: Incoming ID plot.

Calibration of silicon strip detector (SST) and Time of Flight Wall (TFW) in the path of outgoing fragments have been performed. Fig. 2 shows a 2D plot of the charge of outgoing fragments from TFW and SST detectors before and after ALADIN, respectively.

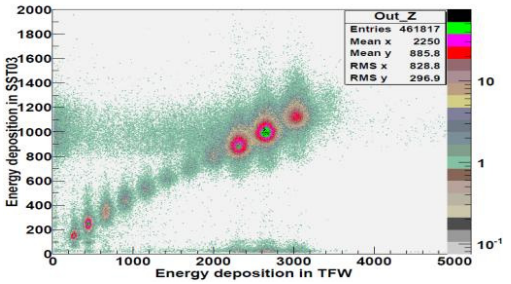

Fig 2: Outgoing fragment charge correlation (TFW:SST)

Through this experiment it will be possible to study experimentally the neutron-rich nuclei in the "island of inversion" region such as ^{29,30}Na, $^{31-33}$Mg, ^{34,35}Al etc. where lots of contradictory experimental and theoretical studies have already been done.

References

[1] C. Thibault et al., PRC 12 (1975) 644.
[2] T. Motobayashi et al., PLB 346 (1995) 9.
[3] R. Palit et. al., PRC 68 (2003) 034318.
[4] T. Nakamura et al. , PRL 83 (1999) 1112.
[5] U. DattaPramanik et al., PLB 551 (2003) 63.
[6] D. T. Yordanov et al. PRL 99 (2007) 212501.
[7] R. Kanungo et. al., PLB 685 (2010) 253.
[8] V. Tripathi et al . PRL 101 (2008) 142504.

*Supported by Alexander von Humboldt (AvH) foundation.

Measurements of (p,pX) neutron and proton knockout reactions on ^{57}Ni*

A. Movsesyan[1], *T. Aumann*[1,2], *S. Paschalis*[1], *D. Rossi*[2], *O. Ershova*[3], *and the s287 collaboration*[2]

[1]TU Darmstadt, Germany; [2]GSI, Darmstadt, Germany; [3]University of Frankfurt, Germany

One-nucleon-knockout reactions in inverse kinematics have been used to investigate the shell structure of short-lived nuclei. In the dedicated experiments, light targets such as Be or C are typically used, allowing for an analysis of only surface interactions (valence nucleons), and usually the heavy projectile-like fragments are detected. In this report, an exclusive experimental approach for investigating exotic nuclei using proton-induced knockout reactions is discussed. The experiment performed at the LAND-R^{3}B facility at GSI allowed for an analysis of (p,2p) as well as, for the first time, (p,pn) reactions in inverse kinematics from kinematically complete measurements of the incoming and outgoing channels. The structure of ^{57}Ni is addressed in the current work in proton and neutron knockout reactions populating states in ^{56}Ni and ^{56}Co, respectively.

A 500 AMeV secondary cocktail beam was directed into Cave C, on a 216 mg/cm^2 thick polyethylene (CH_2) target. The energy of the projectile was chosen such that the outgoing nucleons have energies in the minimum of the nucleon-nucleon cross-section, thus meeting "the quasi-free scattering" condition. Runs without a target and with a C target (187 mg/cm^2) were also taken, in order to determine the contribution of the background and of the reactions on the carbon component in CH_2. The incoming ^{57}Ni and outgoing heavy fragments were identified by ToF, ΔE and position measurements before and after the target.

A detailed analysis of the quasi-free-knockout reactions is performed with two particular detectors surrounding the target position. The CsI detector is an array of 144 individualy read-out CsI(Na) crystals of 12 different shapes, distributed in 12 segments surrounding the beam pipe (30° resolution in azimuthal angle). It is used for detection of prompt γ-rays, protons and neutrons. A detector consisting of 12 individually read-out plastic paddles (50x2.5x0.5 cm^3) was placed between the beam pipe and CsI, covering polar angles from $\sim$10° to 90°. Its purpose is to tag the protons that further hit the CsI volume. The quasi-free-knockout character of the reactions was identified event-wise by the reconstructed angular correlations of the scattered nucleons in these detectors. The two correlated nucleons are in the same plane ($\Delta\varphi \sim 180^\circ$) with an average opening angle of $\Delta\theta \sim 80^\circ$.

Inclusive cross sections of one-proton and one-neutron knockout from ^{57}Ni have been deduced and momentum distributions of the corresponding residual ^{56}Co and ^{56}Ni fragments have been reconstructed. The experimental setup is also capable to distinguish different reaction channels by observing the gamma decay of excited fragments. Comparison of the momentum distributions of ground and excited states with theoretical calculations will allow for the separation of the angular momentum states occupied by the knocked-out nucleon in the ^{57}Ni ground state. For example, knock-out of the neutron from the $p_{3/2}$ shell in ^{57}Ni will result in a ^{56}Ni residual in the g.s., whereas knocking out a neutron from the closed $f_{7/2}$ shell will lead to an excited ^{56}Ni, which will deexcite via gamma cascades.

Analysis of ^{56}Ni residues has been carried out within this work. An addback algorithm was used to reconstruct the protons, neutrons and gammas in the CsI detector. The deexitation from different excited states resulted in a spectrum with expressed transitions of 1.2 MeV, 1.7 MeV, 2.23 MeV and 2.7 MeV energies (Fig.1). The figure represents an example for the comparison of experimental data with a simulation of two final excited states (4935.5 keV and 5665.1 keV [1]) with a rough consideration of 50% probability for each. There is an overall agreement with the experiment and the inconsistency in the low energy region is being investigated. Analysis of proton and neutron responses is in process. Simulation of the corresponding reaction scenarios are in progress and will be used to extract differential cross sections for the reactions ^{57}Ni(p,pn)^{56}Ni(g.s.) and ^{57}Ni(p,pn)^{56}Ni(excited states). Comparison of these cross sections to single-particle model calculations will allow for the extraction of corresponding spectroscopic factors.

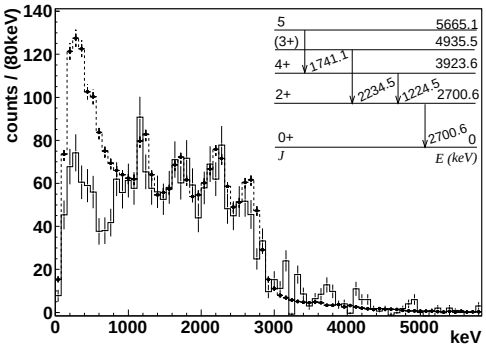

Figure 1: The energy spectrum of the highest energy gamma cluster reconstructed in each event. Solid line - experiment, dashed line - simulation of 5$\rightarrow$(3$^+$)$\rightarrow$2$^+\rightarrow$0$^+$ (50%) and 4$^+\rightarrow$2$^+\rightarrow$0$^+$ (50%) transitions.

References

[1] National Nuclear Data Center. http://www.nndc.bnl.gov/

* Work supported by HIC for FAIR, EMMI and GSI F+E(Darmstadt). Work is part of HGS-HIRe.

The ^{152}Sm(p,n) reaction and the LENA detector*

J. Glorius[1], *M. Pohl*[1], *and the s405 Collaboration*
[1]Institut für Angewandte Physik, Goethe Universität Frankfurt am Main, Germany

Under stellar conditions, low-lying excited states in nuclei are in thermal equlibrium with the ground state. If those excited states undergo β-decays with a higher rate than the ground state, the β-decay half-life of this nucleus is dominated by the excited state. The corresponding lifetimes are extremly difficult to measure directly on earth, since the excitation occurs mostly via internal transition.

If the β-decay occurs via the Gamow-Teller transition (ΔL = 0, ΔS = 0, Δ T$_z$ = $\pm$1), charge exchange reactions allow to investigate the decay strength. As shown in [1], there is a proportionality between the cross sections from (p,n) reactions at low momentum transfers (close to 0°) and Gamow-Teller strength distribution values (B(GT)):

$$\frac{d\sigma^{CE}}{d\Omega}(q=0) = \widehat{\sigma}(q=0)B(GT). \qquad (1)$$

In order to verify the method of measuring the B(GT) strength of unstable heavy nuclei via inverse kinematics, the reaction p(^{152}Sm,^{152}Eu)n was used as a test case. This measurement allows to set constraints on the temperature dependent electron capture of ^{152}Eu, which is an important s-process branching point.

The experimental task is to measure the cross section at small momentum transfers. In Fig. 1 the simulated reaction kinematics for a beam energy of 300 AMeV are plotted. The symbols show the energies of the emitted neutrons as a function of the angle relative to the incoming beam for different excitation energies.

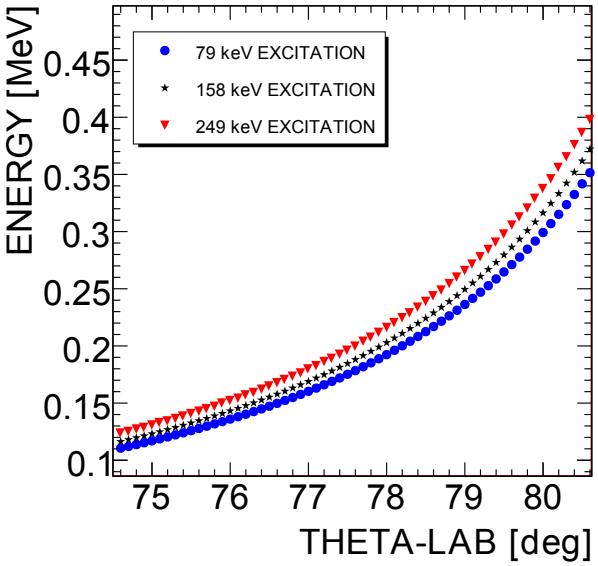

Figure 1: Simulation of the reaction kinematics for a ^{152}Sm(p,n) reaction with 300 AMeV beam energy. The kinematic energy of the recoil neutron is shown as function of the angle relative to the incoming beam. LENA was positioned to cover the area between 75 and 79 degrees, which corresponds to a center of mass angle of roughly 1.5 degrees and a neutron energy of about 120 to 220 keV.

LENA

A newly developed Low Energy Neutron detector Array (LENA) was used to measure the neutrons, which are emitted at large angles relative to the incoming beam. In the recent configuration it consits of 15 scintillating plastic bars with a size of 1x4.5x100 cm^3, splitted into three arrays of five bars each. Every bar is read out with one photomultiplier at each end, which not only allows to determine the detection time, but also the interaction point and the emission angle of the neutron. LENA was developed at ATOMKI Debrecen in cooperation with GSI [2]. During the experiment, the detector covered the region between 76 and 79 degrees relative to the incoming beam, which corresponds to a center of mass angle of roughly 1.5 degrees and a neutron energy of about 120-220 keV. Two of the arrays were placed vertically at the level of the beam line in a distance of about 1 meter, the third was placed horizontally 1 meter above the beam line.

The s405 experiment took place at the R^{3}B/LAND setup in cave C at GSI during october 2011. The results should serve as a proof of principle for the extraction of Gamow-Teller strength via inverse kinematics in case of heavy unstable isotopes, as already shown for isotopes in the iron region [3]. The method will allow to improve the description of electron capture rates on nuclei, important for modeling the nucleosynthesis processes in late evolution stars.

*This project was supported by the Helmholtz International Center for FAIR and the Helmholtz Young Investigator Group VH-NG-327, GSI F+E(Frankfurt) and HGS-Hire.

References

[1] T. Taddeucci et al., *The (p,n) reaction as a probe of beta decay strength*, Nucl. Phys. A469 (1987) 125

[2] C. Langer et al., *Development and tests of a new low-energy neutron detector for the R^{3}B-setup*, GSI Jahresbericht 2009

[3] M. Sasano et al., *Gamow-Teller Transition Strengths from ^{56}Ni*, Physical Review Letters 107, 202501(2011)

Measurements of proton-induced reactions on ruthenium-96 at the ESR*

G. Rastrepina[1,2], M. Heil[1], B. Mei[1,2], R. Plag[1,2], R. Reifarth[2], and the E062 collaboration[1]

[1]GSI Darmstadt, Germany; [2]University of Frankfurt, Germany

Introduction

The p-process nucleosynthesis is responsible for the production of the rare, proton-rich heavy isotopes (p-nuclei), which cannot be made by neutron capture. This process occurs in supernovae, where (p,γ) and (γ,n) occur on the seed s- and r- nuclei at high temperatures. The Experimental Storage Ring (ESR) at GSI provides the possibility to measure the cross sections for the (p,γ) reactions in inverse kinematics near the p-process Gamow window.

Measurements of ^{96}Ru(p,γ)^{97}Rh reaction

A pioneering experiment has been performed at ESR using a stable ^{96}Ru beam and a hydrogen gas target. The fully stripped ^{96}Ru ions were injected into ESR and slowed down to energies of 9, 10 and 11 AMeV. The thickness of the hydrogen target was 10^{13}/cm^2 [1]. The most important reactions of fully stripped ruthenium ions with hydrogen molecules are electron pick-up and proton-induced nuclear reactions like (p,γ), (p,n) and (p,α). The detection efficiency for (p,γ) events was close to 100%.

Monte-Carlo simulations with Geant4 code

In order to understand and subtract background from competing reactions, the most intense background sources were simulated using Geant4 [2]. The simulation comprises all beam pipes, quadrupole magnets and the dipole between the hydrogen target and the detector location as well as the DSSSD itself. Based on Geant4 simulations, a prediction of the distribution of the reaction products in the detector for different reactions was performed (see Fig.1).

Cross section determination

As the experiment was performed at energies of 9-11 AMeV, competing (p,n) and (p,α) reactions occurred too. These events have to be discriminated from the desired proton capture reactions based on the position on the Double Sided Silicon Strip Detectors (DSSSD), mounted in a pocket on the inside of ESR. The thickness about 25 μm of the pocket window restricted the beam energy to above 9 AMeV. An additional background component is the elastic scattering of ruthenium ions on protons. Multi-Wire Counters were installed on the outer side of the first dipole after the hydrogen target to detect products from electron pick-up. Germanium X-ray detectors were mounted close to the target at angles 35 and 90 degree to detect the emitted X-rays. The reaction cross section was measured relative to the electron pick-up cross section (^{96}Ru^{44+}+e$^-$ $\rightarrow$^{96}Ru^{43+}), thereby eliminating uncertainties from target thickness and number of primary ^{96}Ru ions. A rough estimate of the proton capture cross section of ^{96}Ru at 11 AMeV gives 1.5-3.5 mb, which is comparable to the predictions from the NON-SMOKER code [3].

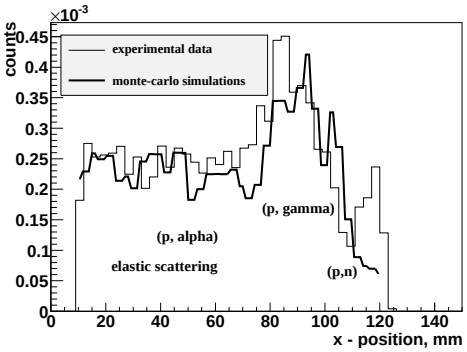

Figure 1: Position of reaction products on the Double Sided Silicon Strip Detectors.

Outlook

As subsequent experiments, the assessment of (α,γ) reactions and the measurement of the ^{112}Sn(p,γ)^{113}Sb cross section are planned. Because the dipoles deflect the products of (α,γ) reactions significantly stronger than the products of (p,γ) reactions, the detection of the (α,γ) products has to happen closer to the dipole. In the next experiment, the DSSSD will be installed at the end of the first dipole after the gas target to detect both, the products of (p,γ) reactions and the products of (α,γ) reactions. Besides, the DSSSD will be directly installed in the vacuum omitting the pocket window. Thus, the (p,γ) reactions can be investigated at lower energies of about 5 AMeV, near the Gamow window.

References

[1] Q.Zhong, T. Aumann, S.Bishop, K. Blaum, K. Boretzky, et al. *^{96}Ru(p,γ)^{97}Rh measurement at the GSI storage ring. Journal of Physics: conference Series* **202** (2010) 012011.

[2] S. Agostinelli, J. Allison, K. Amako, J. Apostolakis, H. Araujo, et al. *Nucl.Phys. A* **506**(2003)250.

[3] T. Rauscher, F.-K. Thielemann. *Astrophysical Reaction Rates From Statistical Model Calculations. Atomic Data Nucl.data Tables* **75**(2000)1.

*Work supported by the HGF Young Investigators Projects VH-NG-327 and VH-NG-331, the ERC grant no. 203175, HIC for FAIR and F&E Frankfurt/GSI.

Longitudinal momentum width in fragmentation reactions

M. V. Ricciardi[1], *A. Bacquias*[1], *A. Kelić-Heil*[1], *K.-H. Schmidt*[1]

[1]GSI, Darmstadt, Germany

The longitudinal momentum of fragmentation products separated and identified in ion-optical devices can be measured with great precision by their magnetic rigidity [1]. With this method, precise and absolute velocity values can be also used to disentangle binary-decay and fission fragments from evaporation residues and multifragmentation products. Recently, an analytical description of the standard deviation ($\sigma_{P||}$) of longitudinal momentum distributions of fragmentation and multifragmentation products has been established [2]. With respect to the previous works of Goldhaber [3] or Morrissey [4] limited to close-to-projectile fragments, the new study was extended to the entire production range, down to the lightest observed fragments. In this context, beside the contribution of abrasion, the effects of thermal break-up and sequential evaporation had to be included. The formula of Bacquias [2] is not empirical: it is based on a solid physical description of the physical processes behind the formation of the fragmentation products. On the other hand, in order to have a simple analytical formula useful for technical applications, some simplifying assumptions in the description of the different processes were done. The assumptions are justified for mid-peripheral collisions of relativistic heavy ions. In this work, we tested the predictive power of Bacquias' formula in two "extreme" conditions: at lower energy, and for lighter projectile nuclei.

In Figure 1, we present the results for the fragmentation of 140 A MeV ^{48}Ca on Be [5]. In this intermediate energy regime, higher than Fermi energy and lower that relativistic energy, longitudinal momentum distributions exhibit an asymmetry, which is attributed to the existence additional reaction mechanisms apart from the fragmentation component. Dissipative processes are responsible for the low-momentum tail, while neutron pick-up in the prefragment formation introduces a broadening. By means of a fitting procedure, Mocko evaluated the "pure" fragmentation component in the longitudinal momentum distributions, whose width is represented by the dots of Figure 1. The analytical formula of Bacquias (solid red line) reproduces satisfactorily the experimental data, demonstrating the validly of the physical description of the fragmentation process.

In Figure 2, the width of the longitudinal momentum distribution of the fragments produced by 2.1 *A* GeV ^{16}O on different targets [6] is shown. The very old experimental data are rather scattered, and leave much space to the possible theoretical predictions. Nonetheless, the comparison gives us some clear indications. First of all, the parameterisation of Morrissey is not well adapted to the description of light projectiles; here less than one third of the data can be reproduced by the Morrissey systematic. Secondly, multifragmentation is an important process, which should be modelled. This is evident when comparing the red (full Bacquias calculation) and green (Bacquias calculation without multifragmentation) curves.

To conclude, although the formula of Bacquias regards the fragmentation of relatively heavy projectiles at relativistic energies, it works satisfactorily also for lighter projectiles and at lower energies. This result could be interesting for technical applications in other laboratories, where these conditions are met.

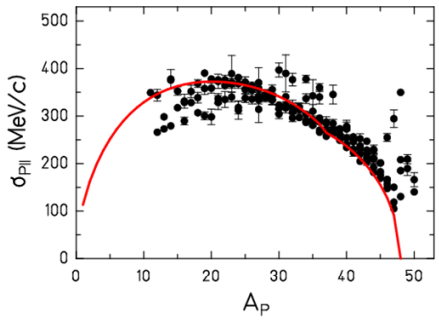

Figure 1: Dots: Experimental standard deviation of the longitudinal momentum distribution for fragmentation events in 140 *A* MeV ^{48}Ca on Be [5]. Line: prediction of Bacquias' analytical formula [2].

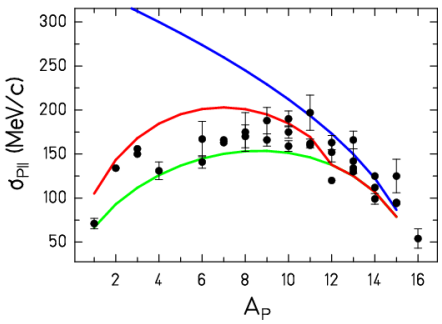

Figure 2: Dots: Experimental standard deviation of the longitudinal momentum for fragmentation products of 2.1 *A* GeV ^{16}O on different targets [6]. Lines: red: prediction of Bacquias' analytical formula [2]; green: prediction of Bacquias' analytical formula when multifragmentation is excluded; blue: Morrissey systematic [4]

References

[1] T. Enqvist et al., Nucl. Phys. A 658 (1999) 47
[2] A. Bacquias et al., Phys. Rev. C 85 (2012) 024904
[3] A. S. Goldhaber. Phys. Lett. B 53 (1974) 308
[4] D.J. Morrissey. Phys. Rev. C 39 (1989) 460.
[5] M. Mocko, PhD Thesis, Michigan State University, East Lansing, MI, USA, 2006.
[6] D. E. Greiner et al., Phys. Rev. Lett. 35 (1975) 152

Re-acceleration effect in the ^{124}Sn+^{124}Sn and ^{112}Sn+^{112}Sn reactions at 1 *A* GeV

V. Föhr[1,2], A. Kelić-Heil[1], M.V. Ricciardi[1] and K.-H. Schmidt[1]

[1]GSI, Darmstadt, Germany; [2]University of Jyväskylä, Finland.

The longitudinal re-acceleration phenomenon of the fragmentation residues, was observed originally in the projectile fragmentation of uranium [1,2] at the Fragment Separator (FRS), GSI Darmstadt. According to transport calculations [3], this phenomenon is related to the participants blast, and the longitudinal momenta of the surviving residues can give a direct access to the momentum-dependent properties of the nuclear mean field (MF), little affected by the uncertainties in nuclear incompressibility [3]. After this first experimental observation, a set of experiments was carried out at the FRS. The present work is devoted to a study of the importance of the isospin effects. To this purpose the fragmentation of two systems, ^{112}Sn+^{112}Sn and ^{124}Sn+^{124}Sn at 1000 *A* MeV, whose *N/Z* ratio is 1.24 and 1.48 respectively, was studied. If there are sensible effects of the momentum on the isospin dependence of the MF one could expect sensible differences [3] for the momentum transfer to the spectators, that would be visible in the mean longitudinal velocity of fragments from systems with different isospin content. The experimental set-up, data analysis and experimental results obtained in these two reactions have been published in ref. [4].

In the present contribution the BUU transport model is used to calculate the prefragment velocities. We consider some of the parameters of the model and their impact on the prefragment velocity in a similar manner that was performed in ref. [3], while expanding the studied range of impact parameters to include very peripheral collisions. In fact, the code was specifically tailored for these calculations in order to provide more accuracy on the velocities near the beam velocity [5].

In order to compare the BUU predictions with experimentally measured velocities, the code has been coupled with the GSI reaction model ABRABLA [5,6]. Details of this coupling are given in ref. [7]. BUU calculations have been made assuming the soft EOS; one set of the calculations corresponds to the momentum independent mean field and reduced in-medium nucleon-nucleon cross section (MI,IN-MED) while the second set to the momentum dependent mean field and free nucleon-nucleon cross-section (MD,FREE). The results for the mean value of the longitudinal velocity distributions obtained from these coupled calculations are shown in Fig. 1 together with the experimental results for both systems.

Fig. 1 verifies that the coupled calculation is able to produce the experimental data quantitatively very well for the heavier masses. The calculated ^{124}Sn projectile remnants shows slightly higher re-acceleration than the ones from ^{112}Sn which is in qualitative agreement with data. In mid-peripheral collisions, populating the final residues with mass losses <0.5, the simulations show that the rapidly expanding participant zone interacts with the spectator matter giving substantial enhancement on the longitudinal velocity. The comparison with measured data seems to favour the enhancement of the explosion of the fireball due to strong momentum dependence of the nuclear mean field and due to free NN cross section. However, even the strongest obtained forward velocity enhancement in the calculations fails to quantitatively reproduce the mean velocities in the lower final mass area. This discrepancy seen in this mass range was found to be about the same size as the enhancement obtained by changing the model parameters.

The observed difference in the re-acceleration part of the velocity mean value is merely due to mass difference between the two projectiles and not so much due to their different neutron-to-proton ratio.

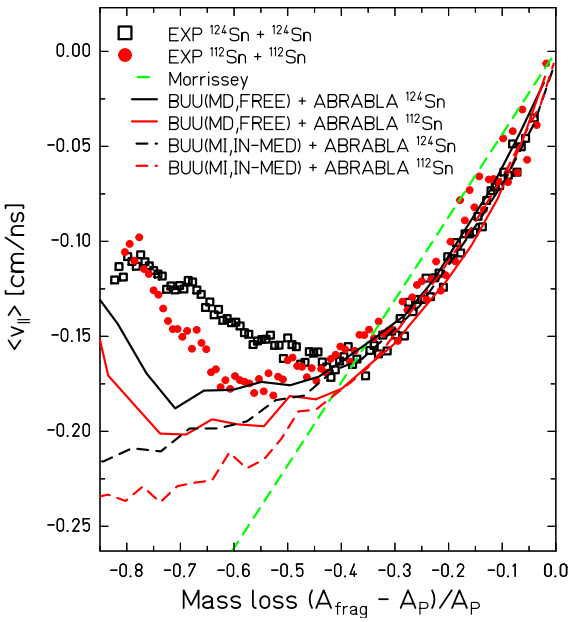

Figure 1: Mean values of the longitudinal velocity distributions of the final residues as measured in ^{112}Sn + ^{112}Sn in and in ^{124}Sn + ^{124}Sn at 1·A GeV together with the coupled calculations performed with BUU + ABRABLA. Experimental uncertainties are not plotted for clarity.

References

[1] T.Enqvist *et al.*, Nucl. Phys. A658 (1999) 47.
[2] M.V.Ricciardi *et al.*, Phys. Rev. Lett. 90 (2003) 212302.
[3] L.Shi *et al.*, Phys. Rev. C64 (2001) 034601.
[4] V. Föhr et al, Phys. Rev. C 84 (2011) 054605.
[5] J.-J. Gaimard and K.H. Scmidt, Nucl. Phys. A 531 (1991) 709.
[6] A. Kelić, M.V. Ricciardi and K.H. Schmidt, arXiv_nucl-th/0906.4193v1
[7] V. Föhr, PhD Thesis, Univ. of Jyväskylä, Finland.

s-process simulations in TP-AGB stars

A. Koloczek[1], R. Reifarth[1], M. Pignatari[2], C. Ritter[1], K. Sonnabend[1], and the NuGrid collaboration
[1]University of Frankfurt, Germany; [2]University of Basel, Switzerland

Introduction

After the big bang nucleosynthesis the universe consisted mainly of Hydrogen and Helium. This elemental composition was altered by stars through fusion. At some point fusion stops being efficient so that stars can only build up higher elements by neutron capture. One site for this to take place is in TP-AGB stars (Thermal Pulse Asymptotic Giant Branch Stars) during the s-process (slow neutron capture) [1]. The *main* s-process takes place in the He shell of low mass AGB stars in the period between thermal pulses. The driving neutron source during this period is the ^{13}C(α, n) reaction. This period is referred to as ^{13}C pocket.

In order to calculate the s-process abundance distribution in stars, one needs not only the stellar model but also a complete nuclear reaction network, which has to be fed with experimental data. The NUGRID collaboration developed a tool to post-process nucleosynthesis after the stellar model has been calculated. This way, the computing time can be reduced and different reaction networks can easily be used with the same stellar model.

Research activity

In 2011 we focused on setting up a computing grid at Goethe-Univerity Frankfurt am Main for the multizone post processeing software (mppnp) and performed sensitivity studies for a ^{13}C-Pocket in a 3 Solar Mass TP-AGB Star for the branching point ^{85}Kr in the uncertaintyrange of the KADONIS database [2]. Tools for the analysis of these studies are being developed at the moment.

An Example for the mass flow for the default rates in a ^{13}C pocket in the vicinity of ^{85}Kr is depicted in Fig. 1.

If one changes the rate within the recommended uncertainty for the reaction ^{85}Kr(n, γ) the branching ratio ^{86}Kr / ^{84}Kr changes significally.

Another emphasis was put on identifying a possible scenario for the LEPP (Light Element Primary Process). The idea is that nucleosyntheses with neutron densities around 10^{15} cm^{-3} occur in hydrogen combustion convective boundary mixings which were identified in hydrodynamic simulations of AGB stars [3]. For this scenario a two-zone model was developed to mix fresh Hydrogen shell material into the Helium intershell, but it turned out that two zones are not sufficient. At the moment a three zone model is being develloped, which should give the same results as the hydrodynamic simultations of convective boundary mixing, which can then be used to verify this scenario for the LEPP.

Conclusions and outlook

The sensitivity studies and analyses will be performed on other s-process branching points. This helps to identify crucial reaction rates which should be measured in future experiments. After completing the three-zone model, simulations of a wide variety of parameters will be performed in order to identify if the proposed process is a general one and can therefore be accounted as the main scenario for the LEPP.

References

[1] F. Kaeppeler et al. Rep. Prog. Phys. **52** (1989) 945-1013

[2] I. Dillmann et al. AIP Conf. Proc. **819** (2005) 123-127

[3] F. Herwig et al. (2011) ApJ **727** 89

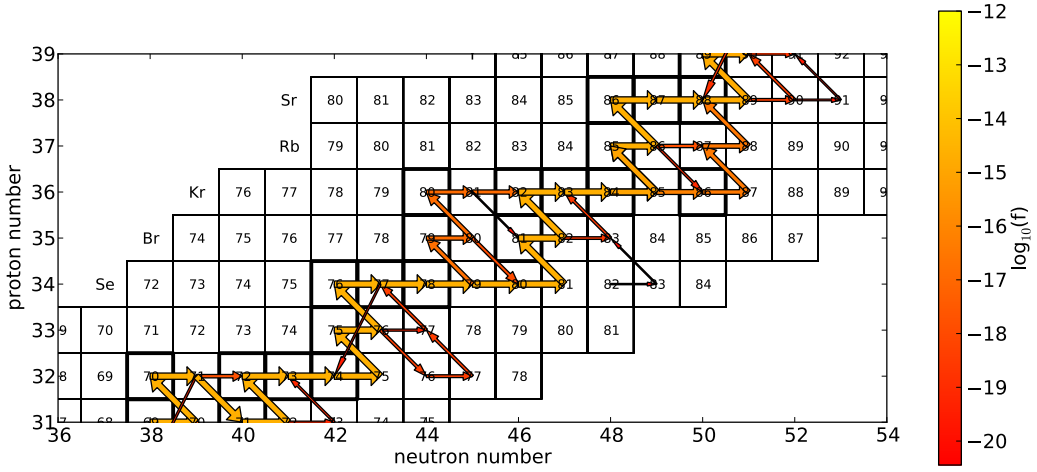

Figure 1: s-process path in the vicinity of the branching point ^{85}Kr. Stable isotopes are distuingished by bold frames. The integrated mass flow is plotted for 8 orders of magnitude.

Neutron capture on the s-process branch point nucleus ^{63}Ni

M. Weigand[1], T.A. Bredeweg[2], A. Couture[2], M. Jandel[2], F. Käppeler[4], G. Korschinek[3], J.M. O'Donnell[2], R. Reifarth[1], J.L. Ullmann[2], and A. Wallner[5]

[1]Goethe Universität, Frankfurt, Germany; [2]LANL, Los Alamos, USA; [3]TUM, Garching, Germany; [4]FZK, Karlsruhe, Germany; [5]Universität Wien, Austria

Introduction

One of the important questions in nuclear astrophysics is how the observed abundances of elements came to be. For this reason, it is important to know the rates of all relevant reactions under the different conditions found in the universe. Most of the elements heavier than iron have been and still are synthesized in neutron-induced reactions in stars of different stages. Nearly all of the observed abundances are either formed by the s- or the r-process in almost equal shares.

The precise s-process path depends on parameters like temperature, neutron density, cross sections (CS) and half-lifes in case of unstable isotopes. Such unstable isotopes on the s-process path play a special role. They act as branching points, creating different possible ways for the nucleosynthesis, neutron capture and β-decay compete. This branching and its ratio affects the isotopic abundancies of the heavier elements. Therefore it is important to know the capture CS for these isotopes. ^{63}Ni with $t_{1/2} \approx 100$ yrs is one of these branching points.

In order to determine the neutron capture cross section in the astrophysical energy region ($kT_{astro} \approx 1...100$ keV), an experiment at the Los Alamos National Laboratory has been performed using the calorimetric 4π-BaF_2 array DANCE.

The DANCE array at LANSCE

Driver of the experiments at LANSCE is a 800 MeV proton LINAC. High energety protons hit a tungsten spallation target to produce a neutron flux spectrum. The beam lines are arranged radially around the target. The DANCE detector at flightpath 14 consists of a spherical array of 160 4π-BaF_2 scintillators equipped with PMT's. Since almost the complete solid angle is covered, the sum energy of gamma cascades from single capture events can be measured. This allows to distinguish between neutron captures on different isotopes based on the Q-value of the reaction. The neutron energy is measured via the time-of-flight method. Additionally the event multiplicity (number of crystals fired) can be used to discriminate background.

Preliminary results

The sample was produced 20 years ago via neutron irradiation of an enriched ^{62}Ni sample. The total mass is 347 mg with only 11% of ^{63}Ni. But small amounts of other Ni isotopes are still present, along with ^{59}Ni, which was also produced in the reactor. Additionally, the decay of ^{63}Ni over this time lead to an amount of almost 6 mg of ^{63}Cu. A preliminary result of the ^{63}Ni experiment is shown in figure 1. The (n,γ) CS of ^{63}Ni has been determined relative to the known ^{62}Ni CS, which was also measured at Los Alamos in 2008 [1]. Various possible ^{63}Ni resonances have been identified via the Q-value. The contribution of other isotopes in the sample could be identified. Resonances from ^{59}Ni, ^{62}Ni and ^{63}Cu are visible, but most of it can be discriminated with a narrow cut on the Q-value of ^{63}Ni(n,γ) at 9.658 MeV. With this information the CS determination is possible in selected areas.

References

[1] A. M. Alpizar-Vicente, T. A. Bredeweg, E.-I. Esch, U. Greife, R. C. Haight, R. Hatarik, J. M. O'Donnell, R. Reifarth, R. S. Rundberg, J. L. Ullmann, D. J. Vieira, J. M. Wouters. *Neutron capture cross section of Ni62 at s-process energies*. **77**(1) 015806.

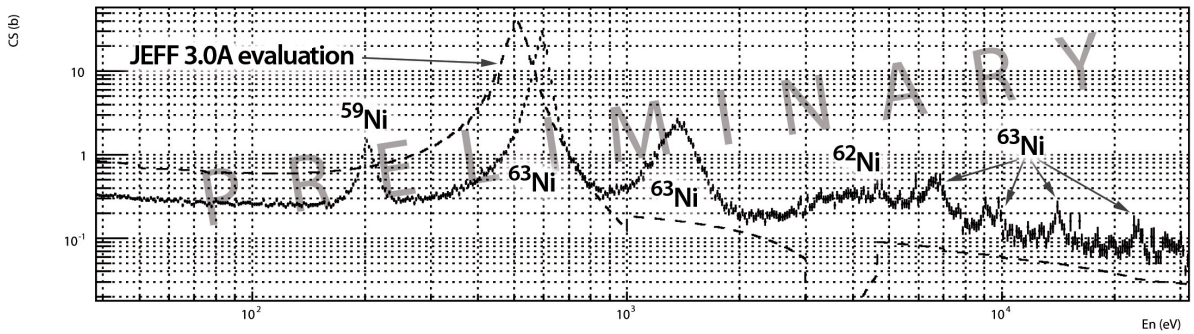

Figure 1: A preliminary cross section plot.

Attempts for the Synthesis of New Elements at SHIP

S. Hofmann[1,2], S. Heinz[1], D. Ackermann[1], S. Antalic[3], W. Barth[1], H.G. Burkhard[1], V.F. Comas[1], L. Dahl[1], K. Eberhardt[4], J. Gostic[5], R. Grzywacz[6,7], R.A. Henderson[5], J.A. Heredia[1], F.P. Heßberger[1,8], J.M. Kenneally[5], B. Kindler[1], I. Kojouharov[1], R. Lang[1], M. Leino[9], B. Lommel[1], R. Mann[1], J. Maurer[1], K. Miernik[6,10], D. Miller[7], K.J. Moody[5], G. Münzenberg[1], S.L. Nelson[5], K. Nishio[11], A.G. Popeko[12], J.B. Roberto[6], J. Runke[4], K.P. Rykaczewski[6], S. Saro[3], D.A. Shaughnessy[5], M.A. Stoyer[5], P. Thörle-Pospiech[4], K. Tinschert[1], N. Trautmann[4], J. Uusitalo[9], P.A. Wilk[5], and A.V. Yeremin[12]

[1]GSI, Darmstadt, Germany; [2]Goethe-Universität, Frankfurt, Germany; [3]Comenius University, Bratislava, Slovakia; [4]Johannes Gutenberg-Universität, Mainz, Germany; [5]LLNL, Livermore, USA; [6]ORNL, Oak Ridge, USA; [7]Univ. of Tennesee, Knoxville, USA; [8]HIM, Mainz, Germany; [9]Univ. of Jyväskylä, Jyväskylä, Finland; [10]Univ. of Warsaw, Warsaw, Poland; [11]JAEA, Tokai, Japan; [12]JINR-FLNR, Dubna, Russia

Calculations using the macroscopic-microscopic model (MM) resulted in two islands of increased stability in the region of the heaviest nuclei, one for deformed nuclei at Z=108 and N=162 and one for spherical superheavy nuclei (SHN) at Z=114 and N=184 [1]. Whereas the extension of the region of deformed nuclei is well explored using cold fusion reactions [2,3], the structure of the island of SHN is still unknown, although isotopes of elements up to Z=118 were synthesized in recent years [4].

Q_α values calculated in various models emphasize this uncertainty. In Fig. 1 we show calculated Q_α values over a wide range from Z=104 to 122 for an α-decay chain passing through ^{300}120 and ^{292}116. Two of the theoretical data shown are based on the MM model [5,6], one on the self-consistent mean field model using the Skyrme-Hartree-Fock-Bogoliubov (SHFB) method [7], one on the relativistic mean-field (RMF) model [8], and one on a semiempirical shell-model mass equation having Z=126 and N=184 as spherical proton and neutron shells [9].

Experimental data known for ^{288}114 and ^{292}116 [4,10] are also shown in Fig. 1. These data do not rule out one or the other model with respect to an extrapolation to heavier elements. However, the slope of the data reveals that a pronounced shell effect at Z=114 and N=174 as obtained in [6] is not observed. Similar conclusions can be drawn from a comparison of Q_α values passing through the decay chain of ^{298}120, where experimental data are known from the decay chain of the daughter ^{294}118 [4].

Decisive for determining the location of the SHN closed proton shell or subshells will be experimental Q_α values on nuclei of the elements 119 and 120. If the predictions of the MM models are correct, then the Q_α values of these nuclei will further increase so that nuclei of elements beyond Z=120 will have half-lives below 1 µs, which cannot be measured with present techniques.

For the synthesis of the new elements 119 and 120 only few reactions seem to have a realistic chance to be successful. For experiments at SHIP we proposed reactions based on the relatively unproblematic target material ^{248}Cm. The resulting reaction for element 119 is ^{51}V + ^{248}Cm → ^{299}119* and for element 120 it is ^{54}Cr + ^{248}Cm → ^{302}120*.

A first part of the Z=120 experiment was performed in April-May 2011. Priority during the 33 days of beam-on-target had the study of the target response at increasing beam intensity. Therefore, the beam intensity was limited to a maximum of 650 *p*nA, the mean value was 400 *p*nA. To facilitate a measurement of microsecond activities, the digital pulse processing complemented analogue data acquisition [11]. A cross-section limit of 0.56 pb was reached. We plan to continue the experiments using ^{248}Cm targets and higher beam intensities as soon as possible.

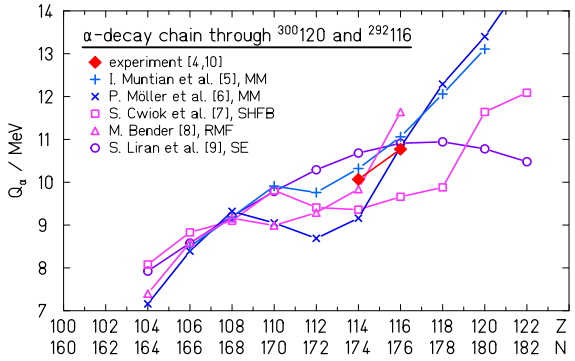

Figure 1: Comparison of measured and calculated Q_α values for nuclei of the decay chain passing through ^{300}120 and ^{292}116.

Supported by GSI F+E, HI Mainz, JINR Dubna, Slovak Research and Development Agency, and US Department of Energy.

References

[1] S.G. Nilsson et al., Nucl. Phys. A **131**, 1 (1969).
[2] S. Hofmann, G. Münzenberg, RMP **72**, 733 (2000).
[3] K. Morita et al., J. Phys. Soc. Jpn. **76**, 45001 (2007).
[4] Yu.Ts. Oganessian, J. Phys. G **34**, R165 (2007).
[5] I. Muntian et al., Phys. At. Nucl. **66**, 1015 (2003).
[6] P. Möller et al., ADNDT **66**, 131 (1997).
[7] S. Cwiok et al., Nature **433**, 705 (2005).
[8] M. Bender, Phys. Rev. C **61**, 31302 (2000).
[9] S. Liran et al., Phys. Rev. C **63**, 17302 (2000).
[10] S. Hofmann et al., GSI Report **2011-1**, 197 (2011).
[11] R. Grzywacz et al., NIM B **261**, 1103 (2007) and contribution to this report by D. Miller et al.

Upgrade of the Gas-filled Recoil Separator TASCA and First Search Experiment for the New Element 120 in the Reaction ^{50}Ti + ^{249}Cf

Ch.E. Düllmann[1,2,3], A. Yakushev[2], J. Khuyagbaatar[2,3], D. Rudolph[4], H. Nitsche[5], D. Ackermann[2], L.-L. Andersson[3,6], M. Block[2], D.M. Cox[6], J. Dvorak[3], K. Eberhardt[1], P.A. Ellison[5], N.E. Esker[5], J. Even[1,3], C. Fahlander[4], U. Forsberg[4], J.M. Gates[5], K.E. Gregorich[5], P. Golubev[4], O. Gothe[5], W. Hartmann[2], R.-D. Herzberg[6], F.P. Heßberger[2,3], J. Hoffmann[2], R. Hollinger[2], A. Hübner[2], E. Jäger[2], J. Jeppsson[4], B. Kindler[2], S. Klein[1], I. Kojouharov[2], J.V. Kratz[1], J. Krier[2], N. Kurz[2], S. Lahiri[7], B. Lommel[2], M. Maiti[7], R.R. Mändl[2,8], S. Minami[2], A. Mistry[6], C. Mokry[1], J.P. Omtvedt[9], G.K. Pang[5], I. Pysmenetska[2], D. Renisch[1], J. Runke[2], L.G. Sarmiento[10], M. Schädel[2,11], B. Schausten[2], A. Semchenkov[9], J. Steiner[2], P. Thörle-Pospiech[1], N. Trautmann[1], A. Türler[12], J. Uusitalo[13], D. Ward[4], N. Wiehl[1], M. Wegrzecki[14], V. Yakusheva[3]

[1]U. Mainz, Germany, [2]GSI, Darmstadt, Germany, [3]HIM, Mainz, Germany, [4]Lund U, Sweden, [5]LBNL+UC Berkeley, CA, USA, [6]U. Liverpool, UK, [7]SINP, Kolkata, India, [8]FH Frankfurt, [9]U. Oslo, Norway, [10]UNAL Bogotá, Colombia, [11]JAEA Tokai, Japan, [12]U. Bern+PSI Villigen, Switzerland [13]U. Jyväskylä, Finland, [14]ITE Warsaw, Poland

The heaviest elements were discovered in ^{48}Ca-induced fusion reactions with actinide targets [1]. The observation of the hitherto heaviest element 118 was claimed from irradiations of targets of ^{249}Cf, which is the highest-*Z* nucleus that is available in sufficient quantities. Hence, to search for elements beyond Z=118, reactions induced by projectiles with Z>20 are required. Previously, ^{64}Ni+^{238}U [2], ^{58}Fe+^{244}Pu [3], and recently ^{54}Cr+^{248}Cm [4] were studied, but element 120 is yet to be discovered. Theoretical predictions [5-8] agree on the ^{50}Ti+^{249}Cf reaction to have the highest cross section. Accordingly, the TASCA collaboration selected this reaction to search for element 120. Maximum predicted cross sections range from 0.04 pb [5] to 0.75 pb [6, 8]. For comparison, the ^{48}Ca+^{249}Cf → Z=118 experimental cross section is $0.5^{+1.6}_{-0.3}$ pb [9].

On the way to a first search experiment for element 120 at TASCA, upgrades of several key components were performed, compared to the setup as used for the ^{244}Pu(^{48}Ca,3-4n)^{288,289}114 reaction [10, 11]. These include the implementation of a larger-area target wheel with 100 mm diameter comprising four targets [12]. The heat of each 5-ms long UNILAC macropulse is now dissipated over a four times larger area (6 cm^2) than in the old system (1.4 cm^2) used for element 114.

The separation from unwanted nuclear reaction products was increased by a factor of ~10 [13] by (i) implementing a carbon stripper foil in front of the target to increase the beam charge state, (ii) a fixed scraper mounted in the center of the first quadrupole magnet, and (iii) a second, moveable scraper mounted behind the second quadrupole. Both scraper positions were chosen based on ion-optical simulations, which predicted significant background suppression without loss in EVR efficiency due to the scrapers. Measurements, e.g., of the ^{48}Ca+^{208}Pb reaction, confirmed the expectations (see also [14]). The efficiency of TASCA for element 120 produced in the reaction ^{50}Ti+^{249}Cf was calculated to be (62±6)%. Discrimination between various event types was enhanced by improving the multi-wire proportional counter veto detector efficiency compared to the element 114 experiment. Several predictions of decay properties of isotopes produced in the ^{50}Ti+^{249}Cf reaction suggest their half-lives, $T_{1/2}$, to be on the order of μs. This is shorter than the dead-time of the data acquisition (DAQ) system used in 2009 [11]. Therefore, a fast digital sampling pulse processing system was built and integrated into the DAQ system [15]. This allowed registering events with $T_{1/2}$ as short as 100 ns, as confirmed in a study of the reaction ^{50}Ti+^{176}Yb, which yields decay chains with very short-lived members [16].

Old ^{249}Cf samples were chemically reprocessed and electrodeposited on ~2.2-μm thick Ti backings by molecular plating [17], yielding ~0.5-mg/cm^2 thick targets.

In August-October 2011, a first experiment to search for element 120 was conducted. Intense beams (0.5-1.0 μA_{part}) were applied on the Cf targets during 39 days of beamtime. The data analysis is in progress.

Acknowledgments: We thank the ion source and accelerator staff for providing stable and intense ^{50}Ti beams, and the experimental electronics department for making the digital DAQ system available on a short time-scale. Work supported by the Helmholtz Institute Mainz.

References

[1] Y. Oganessian, Radiochim. Acta **99**, 429 (2011).
[2] S. Hofmann *et al.*, GSI Sci. Rep. 2008 (2009) p. 131.
[3] Yu.Ts. Oganessian *et al.*, Phys. Rev. C **79**, 024603 (2009).
[4] S. Hofmann *et al.*, this Scientific Report (2012).
[5] V. Zagrebaev *et al*., Phys. Rev. C **78**, 034610 (2008).
[6] G. G. Adamian *et al*., Eur. Phys. J. A **41**, 235 (2009).
[7] A. K. Nasirov *et al.*, Phys. Rev. C **84**, 044612 (2011).
[8] K. Siwek-Wilczynska *et al*., IJMPE **19**, 500 (2010).
[9] Yu.Ts. Oganessian *et al.*, Phys. Rev. C **74**, 044602 (2006).
[10] Ch.E. Düllmann *et al.*, Phys. Rev. Lett. **104**, 252701 (2010).
[11] J.M. Gates *et al.*, Phys. Rev. C **83**, 054618 (2011).
[12] T. Torres et al., GSI Sci. Rep. 2010 (2011) p. 236.
[13] J. M. Gates *et al.*, this Scientific Report (2012).
[14] U. Forsberg *et al.*, this Scientific Report (2012).
[15] N. Kurz *et al.*, this Scientific Report (2012).
[16] J. Khuyagbaatar *et al.*, this Scientific Report (2012).
[17] J. Runke *et al.*, this Scientific Report (2012).

Preparations towards X-Ray Fingerprinting of Element 115 Decay Chains*

U. Forsberg[1], P. Golubev[1], L. G. Sarmiento[2], J. Jeppsson[1], D. Rudolph[1], L.-L. Andersson[3,4], D. Ackermann[5], M. Asai[6], M. Block[5], K. Eberhardt[7], J. Even[4,7], Ch. E. Düllmann[4,5,7], J. Dvorak[4], J. M. Gates[8], K. E. Gregorich[8], R.-D. Herzberg[3], F. P. Heßberger[4,5], E. Jäger[5], J. Khuyagbaatar[4], I. Kojouharov[5], J. V. Kratz[7], J. Krier[5], N. Kurz[5], S. Lahiri[9], B. Lommel[5], M. Maiti[9], E. Merchán[5], J. P. Omtvedt[10], E. Parr[3], J. Runke[5], H. Schaffner[5], M. Schädel[5,6], and A. Yakushev[5]

[1]Lund University, Lund, Sweden; [2]Universidad Nacional de Colombia, Bogotá, Colombia; [3]University of Liverpool, Liverpool, United Kingdom; [4]Helmholtz Institute Mainz, Mainz, Germany; [5]GSI Helmholtzzentrum für Schwerionenforschung, Darmstadt, Germany; [6]Advanced Science Research Center, Japan Atomic Energy Agency, Tokai, Japan; [7]Johannes Gutenberg-Universität Mainz, Mainz, Germany; [8]Lawrence Berkeley National Laboratory, Berkeley, USA; [9]Saha Institute of Nuclear Physics, Kolkata, India; [10]University of Oslo, Oslo, Norway

In preparation for an approved experiment aiming at X-ray fingerprinting of element 115 decay chains to unambiguously determine the atomic number of the involved nuclei, a number of final tests were performed in June 2011. The main experiment is designed to measure the energies of characteristic X-rays emitted following de-excitation via internal conversion in coincidence with α decays into excited states. ^{287}115 will be produced in the ^{243}Am(^{48}Ca,4n) reaction, isolated in the gas-filled recoil separator TASCA [1], and guided to the TASISpec setup [2].

In this experiment we studied which of the two ion-optical modes of TASCA [1] is more beneficial to use together with TASISpec. Previously, TASISpec has been used with TASCA in the "Small image mode" (SIM) with good results. However, simulations and experiments [4] have shown that insertion of slits inside TASCA can decrease the background in "High transmission mode" (HTM) significantly. To investigate the performance of TASISpec with TASCA in HTM, the reaction ^{208}Pb(^{48}Ca,2n)^{254}No was used (for details, see [3]). First, the previously determined optimal TASCA SIM quadrupole magnet settings for TASISpec were confirmed to yield the maximum transmission. Secondly, a series of HTM tests using the nominal TASCA focal-plane detector confirmed that a strong background suppression can be achieved by inserting slits in TASCA. Thirdly, the HTM magnet settings were optimized to give the best transmission of ^{254}No into TASISpec. This optimization was guided by simulations [5] of the trajectories of ^{254}No through TASCA. Relative experimental transmissions were derived from the number of events recorded in the α peak from ^{254}No in the TASISpec implantation detector, normalized to the beam integral. The optimal settings were found within the range of magnet settings suggested by the simulations.

The spacial distribution of ^{254}No events over the TASISpec implantation detector with TASCA in HTM is illustrated in Fig. 1(b), showing data from a simulation of the experiment. The implantation profile is elongated in the horizontal direction, as expected in HTM. Since the ions have to pass a cylindrical tube on their way to TASISpec, the best use of the two focusing quadrupoles turned out to be when the horizontal focusing is somewhat stronger than the vertical one. The optimized settings established in this experiment can be used for determining how to tune the magnets in other experiments using TASISpec with HTM.

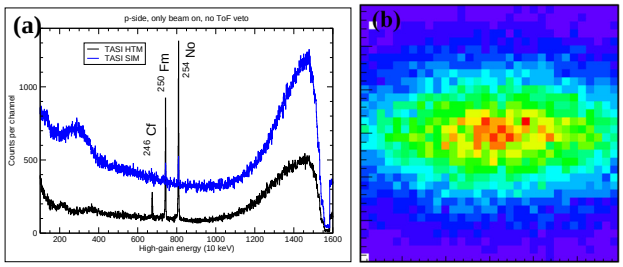

Figure 1: (a) Energy spectra accumulated using SIM (blue) and HTM (black). (b) Simulated distribution, in HTM, of ^{254}No in the TASISpec implantation detector [3].

The transmission to TASISpec with TASCA in HTM was ∼80% of the one achieved in SIM. The main advantage in HTM is the excellent background suppression. Fig. 1(a) shows beam-on energy spectra from SIM (blue) and HTM with slits inserted (black). The clean HTM spectrum implies that it is possible to search for α-X-ray coincidences in the beam-on periods as well as in the beam-off periods, even without using a veto detector, such as a MWPC, for implanted particles. In SIM, only beam-off data can be used when no MWPC is installed, due to too high background rates during beam-on periods. Since the beam-on data accounts for 25% of the events due to the duty cycle of the beam, the total amount of TASISpec data is comparable for HTM and SIM.

* This work was co-funded by the European Commission under the capacities program (Grant Agreement Number FP7-227867, ENSAR), and supported by the Helmholtz Institute Mainz. We also thank the Royal Physiographical Society in Lund for funding of equipment.

References

[1] A. Semchenkov *et al.*, Nucl. Instr. Meth. **B266**, 4153 (2008)
[2] L.-L. Andersson *et al.*, Nucl. Instr. Meth. **A622**, 164 (2010)
[3] U. Forsberg *et al.*, Acta Phys. Pol. B, in press
[4] J. M. Gates *et al.*, contribution to this report
[5] K. E. Gregorich *et al.*, GSI Scientific Report, 144 (2006)

Discovery of a K-Isomer in ^{266}Hs*

D. Ackermann[1], F.P. Heßberger[1,2], S. Antalic[3], M. Block[1,2], H.-G. Burkhard[1], V.F. Comas[1], P. Greenlees[4], S. Heinz[1], S. Hofmann[1], S. Ketelhut[4], J. Khuyagbaatar[1], B. Kindler[1], I. Kojouharov[1], M. Mazzocco[5], M. Leino[4], B. Lommel[1], R. Mann[1], J. Maurer[1], A.G. Popeko[6], J. Sorri[4], J. Uusitalo[4] and A.V. Yeremin[6]

[1]GSI, Darmstadt, Germany; [2]Helholtzinstitut Mainz, Germany, [3]Comenius University Bratislava, Bratislava, Slovakia; [4]JYFL, Jyväskylä, Finland; [5]University Padua, Padua, Italy, [6]FLNR, Dubna, Russia

In 2010 a second experiment on the investigation of ^{270}Ds and its decay products had been performed. Some of the results were reported last year [1], which are summarised in the decay scheme in Fig. 1.

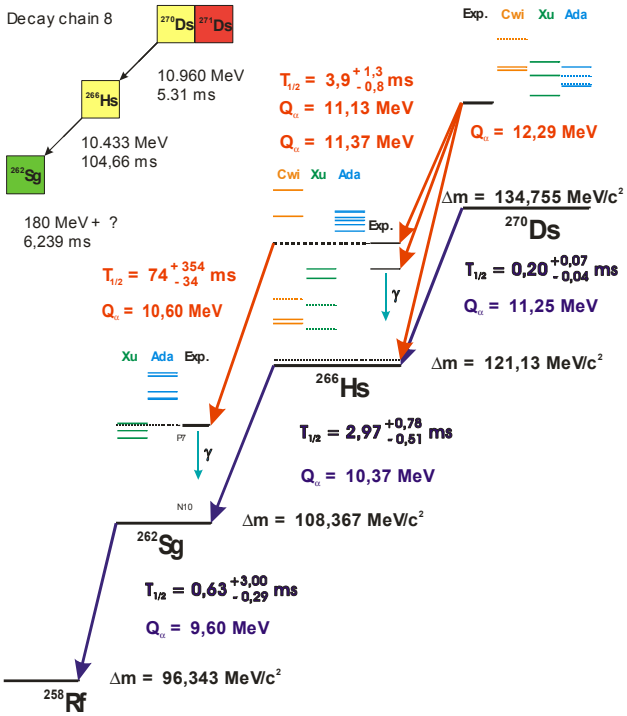

Figure 1: Decay scheme of ^{270}Ds and its decay products generated on the basis of observed α- and γ-decays. Transitions originating from isomeric states are shown by red arrows, ground state decays by blue arrows. The tentatively drawn experimental excited states are compared with HFB [2], configuration constrained PES [3] and TCSM calculations [4]. The insert shows decay chain #8 containing the ^{266}Hs K-isomer decay.

In addition to the g.s. to g.s. α-decay of ^{270}Ds, we observed decays from the K-isomer into excited states of the daughter ^{266}Hs. The α-spectra we obtained for both nuclei are shown in Fig. 2. For ^{270}Ds a fragmented group is visible at higher energies, which belongs to the isomer decay. Also the group around 11.202 MeV originates from it as well as some of the decays in the peak at 10.952 MeV, among those the decay in chain #8 (Fig. 1, insert). It populates the newly discovered K-isomer in the daughter ^{266}Hs, which we tentatively assign due to a more then one order of magnitude longer decay time of 105 ms and an approximately 200 keV higher α-decay energy, shown as the single count right from the main peak in Fig. 2, lower panel. In addition a γ-ray of 332 keV was observed in coincidence with this α-decay, proving that an excited state in ^{262}Sg was populated in this decay. In total we observed four α-γ coincidences, three of them for ^{270}Ds, which most likely originate from the isomeric state.

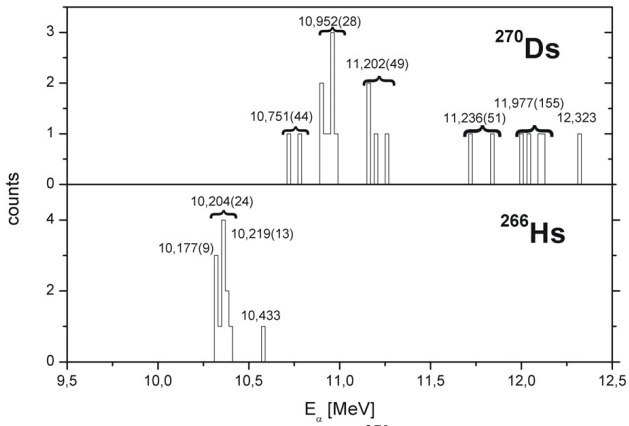

Figure 2: Alpha-decay spectra for ^{270}Ds (upper panel) and ^{266}Hs (lower panel). The values in brackets are the standard deviation which is given to compare possible structures with the detector resolution of ΔE >20 keV.

In Fig. 1 level energies, tentatively populated by the decay of the isomers, are compared with low lying nonyrast states predicted by several models. The experimental levels have been obtained by comparison of the experimental Q_α-values. They are due to finite detection efficiency for γ-rays lower limits for the respective state. The last decay step shown, including literature values, is connecting the decay chain to ^{254}No for which a precise mass value has been measured [5]. It therefore provides via the measured Q_α-values an experimental mass value for all members of the chain including ^{270}Ds (see Fig. 1).

References

[1] D. Ackermann et al., GSI Sci. Rep. 2010, (2011) 200.
[2] S. Hofmann et al., Eur. Phys. J. A **10**, (2001) 5.
[3] F.R. Xu, et al., Phys. Rev. Lett. **92**, (2004) 252501.
[4] G.G. Adamian et al., Phys. Rev. C **81**, (2010) 024320.
[5] M. Block et al., Nature **463**, (201 0) 785.

* Supported by HI Mainz

Decay Study of ^{259}Sg *

F.P. Heßberger[1,2], S. Antalic[3], D. Ackermann[1], S. Heinz[1], S. Hofmann[1,4], Z. Kalaninová[3], I. Kojouharov[1], J. Khuyagbaatar[1,2], B. Kindler[1], B. Lommel[1], R. Mann[1]

[1]GSI, Darmstadt, Germany; [2]HIM, Mainz, Germany, [3]Comenius University, Bratislava, Slovakia, [4]Goethe Universität, Frankfurt a. Main, Germany

Superheavy nuclei owe their stability against spontaneous fission solely to 'shell effects'. Therefore evalution of their shell structure is decisive for understanding their existence and also a stringent test for theoretical models describing nuclear properties. One strategy to do so is investigating systematic trends in low lying single particle levels (Nilsson levels) in deformed nuclei. Along the isotone (even-Z nuclei) or the isotope lines (odd-Z nuclei) the level sequence is known to remain similar as the unpaired nucleon essentially acts as a spectator when a pair of protons or neutrons is added to the nucleus.

In continuation of previous investigations of the N=153 isotones ^{253}Fm [1], ^{255}No [2], ^{257}Rf [3] a decay study of the next heavier one, ^{259}Sg, was performed. It was produced by the reaction ^{206}Pb(^{54}Cr,n)^{259}Sg with $\sigma_{max} \approx 1$ nb, separated from the primary beam by SHIP and implanted into the focal plane detector system, where its α-decay and possibly accompanying γ-rays were measured [4].

The α- and α-γ-coincidence spectra are shown in Fig. 1. Two groups of α decays are evident. One consists of a line at 9610 keV with a hindrance factor HF = 26, and a weaker one at 9035 keV (HF = 4), having half-lives around 400 ms. For the other one half-lives of 200−250 ms were measured. It consists of a strong line at 9545 keV, a broad distribution in the range 9100−9500 keV with an indicated peak at 9240 keV and a few events around 9710 keV. Thus the data clearly indicate α-decay from two different states in ^{259}Sg, that can be assumed as 1/2$^+$[620] and 11/2$^-$[725] as in ^{257}Rf [5]. But unlike ^{257}Rf the weak transition of 9710 keV (HF ≈ 4500) has the highest energy. As, on the other hand, the 11/2$^-$[725] decays into the 9/2$^-$[734] ground-state of ^{255}Rf (or the 11/2$^-$ member of the ground-state rotational band) it is unlikely that the 11/2$^-$[725] state is the isomeric one in ^{259}Sg. Due to the agreeing halflives we tentatively assign the line at 9710, 9545, and 9240 keV to the decay of the 1/2$^+$[620] level, which then must be isomeric based on the energy balance, and those at 9610, 9035 keV to the decay of the 11/2$^-$[725] state, tentatively assigned as the ground state. Due to its low hindrance factor the 9035 keV line is assigned as a favoured transition into the 11/2$^-$[725] state in the daughter nucleus ^{255}Rf. This assignment is supported by α-γ- coincidences shown in Fig. 1b (to enhance statistics data of a previous measurement [6] were added). Two γ events close in energy with a mean energy of 593.7±0.6 keV are found in coincidence with the 9035 keV α-decay. The Q-value ($Q = E_\alpha(1+m_\alpha/m_d) + E_\gamma = 9771$ keV) is comparable to that (9761 keV) of the 9610 keV line, so we conclude that both decays feed the same final state, supporting a high spin (>9/2) for the level emitting the γ's, as a lower spin state preferably would decay into 7/2$^+$[624] or 5/2$^+$[622] (or members of the rotational band built up on them), which are predicted at <500 keV in ^{255}Rf [7]. The tentative decay scheme is presented in Fig. 2.

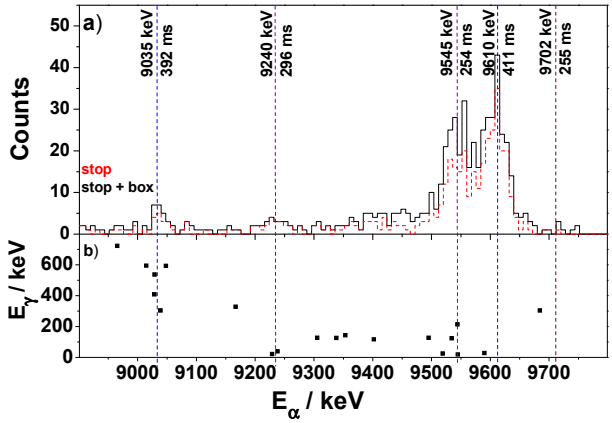

Figure 1: a) Spectrum of α-decays assigned to ^{259}Sg; dashe line: only stop detector; full line: stop+box - detector; b) α-γ- coincidence matrix.

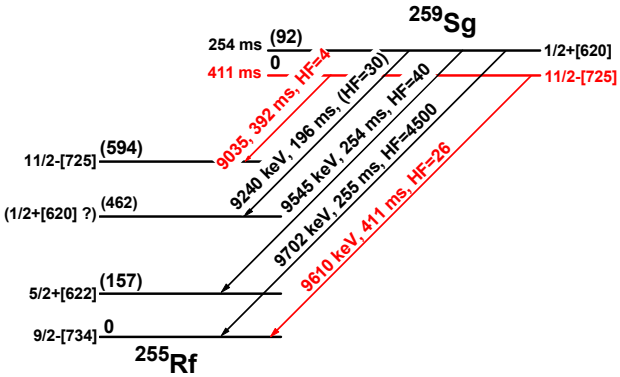

Figure 2: Tentative partial decay scheme of ^{259}Sg. α-transitions assigned to the decay of the ground-state are in red, those attributed to the isomer are in black.

References

[1] S.Antalic et al. EPJ A 47:62 (2011)
[2] F.P. Heßberger et al. EPJ A 29, 165 (2006)
[3] B. Streicher et al. EPJ A 45, 275 (2010)
[4] S. Hofmann et al. EPJ A 32, 251 (2007)
[5] F.P. Heßberger et al. Z. Phys. A 349, 415 (1997)
[6] F.P. Heßberger et al. EPJ A 41, 145 (2009)
[7] A. Parkhomenko et al. APP B36, 3115 (2005)

* supported by HI Mainz

Geant 4 simulations of ^{253}No α decay

Z. Kalaninová[*1], *S. Antalic*[1], *F.P. Heßberger*[2,3], *D. Ackermann*[2], *L.-L. Andersson*[3], *and Š. Šáro*[1]

[1]Comenius University, Bratislava, Slovakia; [2]GSI, Darmstadt, Germany; [3]Helmholtz Institut Mainz, Mainz, Germany

In SHIP experiments evaporation residues (ERs) are implanted into a Si-detector. The consequence of this method is possible energy summing of α particles and conversion electrons (CEs), when α decays of ERs populate excited states of daughter nuclei. Such summing causes (a) the occurence of additional lines in the α-energy spectrum or (b) a change in shape and relative intensities of α lines [1]. A typical example is the α-decay spectrum of ^{253}No.

^{253}No was produced at SHIP in the fusion-evaporation reaction ^{207}Pb(^{48}Ca, 2n)^{253}No. In the experiment plastic foils of different thicknesses were placed in front of the detector in order to achieve different implantation depths of ERs. It resulted in different probabilities for energy summing of α particle and CEs. As an example of this effect the different relative intensities of the 8004 keV peak and $\sim$ 8050 keV summing peak as a function of the implantation depth are shown in Fig. 1. In order to describe the shape of the spectra and to support the decay scheme of ^{253}No proposed in [3] we performed Monte Carlo simulations using Geant 4 [2].

The simulations included α particle emission followed by γ rays and/or emission of CEs, X-rays and Auger electrons. Simulated implantation depths and position distributions of decays followed a gaussian shape. Considered detector resolution was 30 keV (FWHM). Three possible decay paths were simulated (see Fig. 2):

- 7620 keV α particle (I$_{rel}$ = 0.0025) followed by the 669.5 keV E1 γ transition.
- 8075 keV α particle (I$_{rel}$ = 0.04) followed by the 209.3 keV M1 γ transition.
- 8004 keV α particle (I$_{rel}$ = 0.96) followed by one of the E1 γ transitions with energies of 279.5, 221.5 or 150.4 keV and subsequent E2 or M1 γ transitions.

After the emission of an α particle, the corresponding transitions were simulated either as γ rays or as CEs with the probabilities taken from [4]. When the internal conversion occurs on N-shell and higher, the binding energy of these electrons were neglected as it is smaller than 2 keV. Vacancies after CEs emission are filled by electrons from higher shells resulting in the emission of X-rays or Auger (or Coster-Kronig) electrons. Relative intensities of these electrons were taken from [5]. Propagating and filling of the vacancies was simulated up to the M-shell. All processes occuring in higher shells were simulated in one step as X-rays or electrons with energy corresponding to M-shell binding energy which is $\sim$ 6 keV.

It is always difficult to construct the decay scheme from experimental data in the case of complex decay patterns like ^{253}No. Geant 4 simulations are a valuable tool which can support our estimations and test hypotheses. The simulation described here reproduces the data well except of two energy regions: (a) surplus events around 8093 keV can be explained by the presence of ^{254}No in the data, (b) surplus events from 8200 to 8300 keV could indicate the weak transitions from the g.s. of ^{253}No either to ^{249}Fm g.s. or to its two lowest-lying rotational levels with the total relative intensity of ≈ 0.7 %.

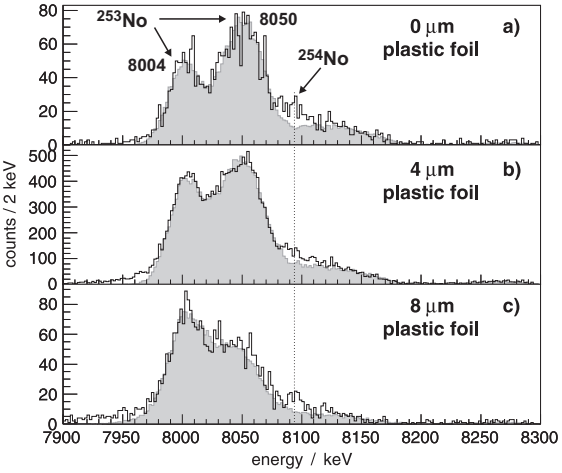

Figure 1: Simulated energy spectra (shaded region) compared to experimental data (black solid line) for 3 implantation depths of ERs: a) 7.0 μm, b) 3.6 μm, c) 1.0 μm.

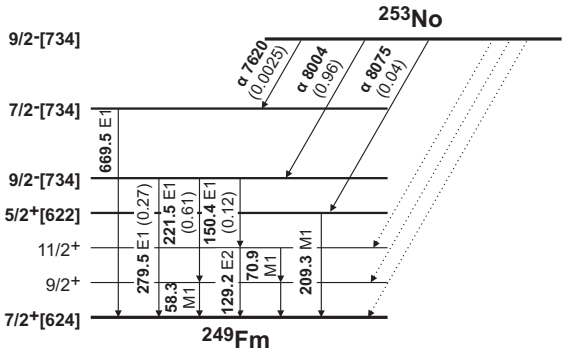

Figure 2: Decay scheme of ^{253}No [3]. Dashed lines represent decay either to g.s. or to its rotational levels.

References

[1] F.P. Heßberger *et al.*, NIM A **274**, 522 (1989).
[2] S. Agostinelli *et al.*, NIM A **506**, 250 (2003), geant4.cern.ch
[3] F.P. Heßberger *et al.*, submitted to EPJ A
[4] T. Kibédi *et al.*, NIM A **589**, 202 (2008).
[5] R.B. Firestone *et al.*, TOI, John Wiley & Sons, NY (1996).

* Zdenka.Kalaninova@fmph.uniba.sk

Mass Measurements of heavy actinides with SHIPTRAP*

E. Minaya Ramirez[1,2], *D. Ackermann*[2], *K. Blaum*[3,4], *M. Block*[2], *C. Droese*[5], *Ch. E. Düllmann*[1,2,6], *M. Dworschak*[2], *M. Eibach*[6], *S. Eliseev*[3], *E. Haettner*[2,7], *F. Herfurth*[2], *F.P. Heßberger*[1,2], *S. Hofmann*[2], *J. Ketelaer*[3], *J. Ketter*[3], *G. Marx*[5], *D. Nesterenko*[8], *Yu. Novikov*[8], *W.R. Plass*[2,7], *D. Rodríguez*[10], *C. Scheidenberger*[2,7], *L. Schweikhard*[5], *P.G. Thirolf*[11,*], *G.K. Vorobjev*[2,8], *and C. Weber*[11,*]

[1]Helmholtz-Institut Mainz; [2]GSI Helmholtzzentrum für Schwerionenforschung, Darmstadt; [3]Max-Planck-Institut für Kernphysik, Heidelberg; [4]Ruprecht-Karls-Universität Heidelberg; [5]Ernst-Moritz-Arndt-Universität, Greifswald; [6]Johannes Gutenberg-Universität Mainz; [7]Justus-Liebig-Universität Gießen; [8]PNPI RAS Gatchina, St. Petersburg; [10]Universidad de Granada; [11]Ludwig-Maximilians-Universität München

Masses in the region of the heaviest elements could previously only be derived indirectly by linking mass differences between nuclides and their decay products using measured α-decay energies. However this approach depends on the knowledge of nuclear level schemes. In contrast, direct mass measurements yield absolute mass values, binding energies and provide anchor points to pin down α-decay chains. This is especially important for odd-odd and odd-A nuclides, where the α decay typically populates excited states. In the absence of complete and quantitative information of the nuclear structure, no unambiguous mass determination is possible. Mass measurements of nuclides, e.g., around ^{254}No allow determining the masses of nuclides located in the superheavy element region.

Nuclides above fermium can only be produced at very low rates. Nonetheless, recently the first direct measurements on transuranium nuclides have been performed with SHIPTRAP [1]. The obtained accurate mass values provided anchor points to fix α-decay chains passing through the nobelium isotopes $^{252-254}$No [2]. The measurements have now been extended to further even more exotic nuclides, namely ^{255}No and $^{255-256}$Lr. The radionuclides were produced and separated from the primary beam by the velocity filter SHIP. Fusion-evaporation reactions of a ^{48}Ca beam with lead and bismuth targets were used to produce different nobelium and lawrencium isotopes with cross sections as low as about 50 nb. Evaporation residues were guided to SHIPTRAP. In a first step their energy was decreased from tens of MeV to a few eV using a buffer-gas filled stopping cell. Afterwards they were injected into a 7-Tesla double-Penning-trap system. The mass was determined by measuring the cyclotron frequency ν_c = qB/(2πm) of the ions using a time-of flight ion-cyclotron-resonance detection technique. An important development to substantially reduce long-term fluctuations of the magnetic field [3] allowed the recording of a single resonance over a period of 4 days in the case of ^{256}Lr. This measurement represents a significant breakthrough towards direct mass measurements of superheavy nuclides.

* Work supported by the BMBF (06ML236I, 06ML9148, 06GF9103I, RUS-07/015), Rosminnauki (2.2.1), GSI (Grant GFMARX1012), the Max-Planck Society, and the Research Center Elementary Forces, Mathematical Foundations and the Helmholtz Institute Mainz

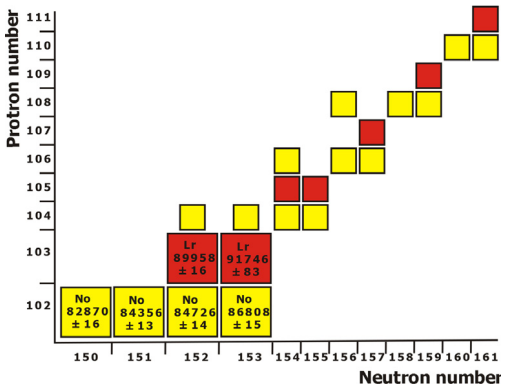

Figure 1: Decay chains linked to the direct mass measurements from this work. The mass excess is indicated in keV.

In the Atomic-Mass Evaluation 2003, the masses of the lawrencium isotopes ^{255,256}Lr were only estimated from systematic trends. The combination of our direct mass measurements with spectroscopic data allows determining the masses of superheavy nuclides (see Fig 1). The masses of α-decay chains starting with even-even nuclides, as for example ^{270}Ds (Z = 110), are now established with low uncertainties. For the first time we also provide anchor points for nuclides with an odd number of protons. Moreover, the new mass value from ^{255}No complement our previous results on the neutron-rich side of the N = 152 deformed shell. Thus our experimental binding energies provide precise values for the two-neutron separation energies S_{2n}. This allows mapping the deformed shell gap at N = 152, which is connected to the predicted spherical shell gap at N = 184 as it originates from the the same single-particle orbitals. Therefore the results obtained with SHIPTRAP enhance our knowledge of shell effects nearby the predicted island of stability.

References

[1] M. Block et al., Nature 463 (2010) 785.

[2] M. Dworschak et al., Phys. Rev. C 81 (2010) 064312.

[3] C. Droese et al., Nucl. Instrum. Meth. A 632 (2011) 157.

Search for short-lived uranium isotopes around N=126 *

J. Khuyagbaatar[1,2], Ch.M. Mrosek[3], A. Yakushev[1], D. Ackermann[1], L.-L. Andersson[2,4], M. Block[1], D.M. Cox[4], Ch.E. Düllmann[1,2,3],J. Dvorak[2], K. Eberhardt[3], P.A. Ellison[5], N.E. Esker[5], J. Even[2,3], C. Fahlander[6], U. Forsberg[6], J.M. Gates[5], K.E. Gregorich[5], P. Golubev[6], O. Gothe[5], W. Hartmann[1], R.-D. Herzberg[4], F.P. Heßberger[1,2], J. Hoffmann[1], R. Hollinger[1], A. Hübner[1], E. Jäger[1], J. Jeppsson[6], B. Kindler[1], S. Klein[3], I. Kojouharov[1], J.V. Kratz[3], J. Krier[1], N. Kurz[1], S. Lahiri[7], B. Lommel[1], M. Maiti[7], R.R. Mändl[1,8], S. Minami[1], A. Mistry[4], C. Mokry[3], H. Nitsche[5],J.P. Omtvedt[9], G.K. Pang[5], I. Pysmenetska[1], D. Renisch[3], D. Rudolph[6], J. Runke[1], L.G. Sarmiento[10], M. Schädel[1,11], B. Schausten[1], A. Semchenkov[9], J. Steiner[1], P. Thörle-Pospiech[3], N. Trautmann[3], A. Türler[11], J. Uusitalo[13], D. Ward[6], N. Wiehl[3], M. Wegrzecki[14], V. Yakusheva[2]

[1]GSI, Darmstadt, Germany, [2]HIM, Mainz, Germany, [3]U. Mainz, Germany, [4]U. Liverpool, UK, [5]LBNL+UC Berkeley, CA, USA, [6]Lund U. Sweden, [7]SINP, Kolkata, India, [8]FH Frankfurt, [9]U. Oslo, Norway, [10]UNAL Bogotá, Colombia, [11]JAEA Tokai, Japan, [12]U. Bern+PSI Villigen, Switzerland [13]U. Jyväskylä, Finland, [14]ITE Warsaw, Poland,

Production and decay of short-lived ^{221}U (previously unknown) and ^{222}U (only the half-life is known) were studied at the gas-filled separator TASCA. These two nuclei have only few neutrons more than the magic number N=126, which leads to high α decay Q-values and, therefore, to very short half-lives (< 10 μs). To explore this microsecond/sub-microsecond half-life region, digital electronics was implemented into a combined "ANalog" and "DIgital" (ANDI) data acquisition system [1].

A ^{50}Ti^{12+} beam was accelerated to energies E_{lab}=230 and 240 MeV and irradiated a rotating ^{176}Yb target wheel to produce ^{222}U and ^{221}U in 4n and 5n de-excitation channels of the complete fusion reaction, respectively.

The evaporation residues (ER) were separated from the primary beam by TASCA and implanted into the stop detector consisting of two double-sided silicon-strip detectors. Two signals, one from each side of the stop detector were processed in two different parts of the ANDI system with a common trigger and zero suppression [1]. The signals from 144 vertical front strips were processed by analog amplifiers connected to peak-sensing ADCs [2]. The preamplified signals from 48 horizontal back strips were processed by sampling ADC's (FEBEX2) with 60 MHz frequency. Traces with total length of 50 μs (7 μs before and 43 μs after) were recorded following an accepted trigger. The deadtime of the "analog" part was shorter than 43 μs. Therefore it was always ready to accept the next triggered event [1]. Further, both data were combined into single events by an event builder of MBS [1].

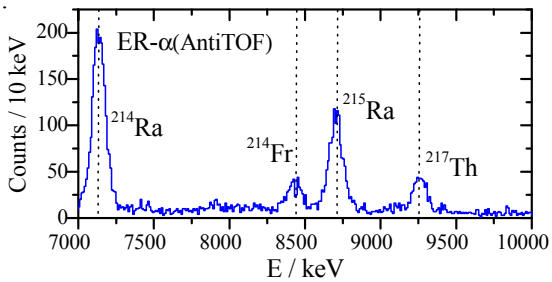

Fig 1: An energy spectrum of α-particles from the ER-α correlation up to 14 s, with both events occurring in the same pixel.

An ER-α correlation analysis was performed to find recoiling nuclei and identify the measured α lines (Fig. 1). Only α-particle events were considered without a signal from the time-of-flight detector. Alpha decays of ^{214}Ra, ^{215}Ra, ^{214}Fr, and ^{217}Th were identified. From further analyses the decay of ^{214}Fr was found as a member of ER-α(7-18MeV)-α(^{214}Fr) chains. The second member of this chain is typically a pile-up of two α decays. These events were investigated using the data from the "digital" part. Clearly two signals were found in traces of them and α decays of ^{222}Pa and ^{218}Ac were unambiguously determined (see Fig. 2a).

The traces of the ER's from ER-α(^{214}Ra) were investigated in order to find "missing" α decays of mother ^{218}Th and grandmother ^{222}U nuclei. In most cases only single signals were found, pointing to the implantation of ^{214}Ra. However, traces with two and three signals were also found (see Fig. 2b). These data allow us to unambiguously assign α decays of ^{218}Th and ^{222}U.

The traces of the ER's from ER-α(^{217}Th) were investigated to find the α decay of the new nucleus ^{221}U. In most cases a single ER signal was seen. However, traces with two signals, which include the α decay of the new nucleus ^{221}U, were also found (see Fig. 2c). More detailed information will be provided in [3].

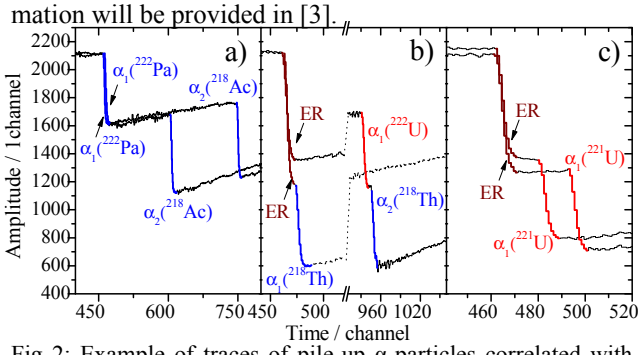

Fig 2: Example of traces of pile-up α-particles correlated with ^{214}Fr a), ER's correlated with ^{214}Ra b), and with ^{217}Th c).

* Work supported by HI Mainz

[1] N. Kurz et al., this Scientific Report (2012).
[2] J.M. Gates et al., Phys. Rev. C. 83 054618 (2011).
[3] J. Khuyagbaatar et al., to be published.

A study of the possibilities and limitations of the TRAPSpec setup*

L.-L. Andersson[†1], *M. Block*[2], *D. Rudolph*[3], *D. Ackermann*[2], *H.G. Burkhard*[2], *C. Droese*[4], *C. Fahlander*[3], *U. Forsberg*[3], *P. Golubev*[3], *F.P. Heßberger*[1,2], *J. Jeppsson*[3], *I. Kojouharov*[2], *M. Laatiaoui*[5], *R. Mändl*[6], *J. Maurer*[2], *E. Minaya Ramirez*[1,2], *L.G. Sarmiento*[7], *T. Schäfer*[4], *H. Schaffner*[2], *and M. Smirnov*[8]

[1]Helmholtz-Institut Mainz, Germany; [2]GSI Helmholtzzentrum für Schwerionenforschung, Germany; [3]Lund University, Sweden; [4]Universität Greifswald, Germany; [5]TU Darmstadt, Germany; [6]Fachhochschule Frankfurt am Main, Germany; [7]Universidad Nacional de Colombia, Colombia; [8]St. Petersburg State University, Russia

The TRAPSpec setup [1] was used for an experiment to study decay properties of several mass $A \approx$ 200-210 nuclides as well as to further explore its possibilities.

TRAPSpec consists of the TASISpec detector array [2] placed at the very end of SHIPTRAP. The latter is used as an additional separator for the studied nuclei, such that a selected nuclear quantum state is sent to the spectroscopy station. In this work only the purification trap in SHIPTRAP was used as its mass resolving power was sufficient to select the nuclides of interest. The nuclei were ejected from the Penning trap with a kinetic energy of ∼0.2 keV and guided via a focusing tube into the TASISpec detector chamber where they were "implanted" into a Si detector at a depth of only 24 Å. In the current experiment an upgraded version of TASISpec was used, consisting of a full set of five double sided silicon strip detectors (DSSSDs). The implantation detector consists of 32x32 strips, resulting in 1024 pixels, and the four Si box detectors were segmented into 16x16 strips, 256 pixels, each. All five wafers were 1.0 mm thick and utilised a reverse bias of -160 V. In addition, three composite Ge detectors were used, giving a total of 15 crystals positioned around the Si cube.

Several reactions were used during this experiment. The first reaction was ^{50}Ti + ^{160}Gd → ^{205}Rn + 5n. On average two impinging ^{205}Rn ions per second were measured in the detector before SHIPTRAP but no α particles of 6.26 MeV – belonging to the decay of ^{205}Rn – were observed in the TRAPSpec detectors. The reason is thought to lie in the fact that radon is a noble gas which, due to its filled valence electron shell, is not very likely to react with surrounding atoms. Thus, with a shallow implantation depth and a half-life of 2.83 m the ^{205}Rn nuclei will have plenty of time to diffuse out of the implantation detector or even the full detector cube before they decay. If the nuclei decay when being inside the Si cube, the α particles will be likely to be detected, but the unknown origin and hence direction of the emitted α particle makes it impossible to correct for the energy loss in the Si dead layer. The layer will account for up to several hundreds of keV in energy loss, thus making it impossible to separate the decay of ^{205}Rn from any of its daughter nuclei.

The ^{205}Rn nucleus was also studied via its mother nucleus, produced in the ^{50}Ti + ^{164}Dy → ^{209}Ra + 5n reaction. ^{209}Ra is then implanted into the Si detector and during the subsequent α decay the recoil energy of the mother will either implant the nucleus deeper into the detector or kick the nucleus out of the detector. When running this reaction with the TRAPSpec setup, α particles with the anticipated 6.26 MeV were registered in the detector. Further analysis of the decay of this nucleus will follow.

With the ^{50}Ti + ^{150}Sm reaction another feature of the detection setup was investigated. The ^{195}Po isotope was produced in the 5n reaction channel. Previous studies of this nucleus [3] show the population of two states with different decay properties. The short-lived state has a half life of $T_{1/2} = 1.9$ s and decays with an α particle of 6.70 MeV. The long lived state has a half life of $T_{1/2} = 4.6$ s and decays with an α particle of 6.60 MeV. In addition, each state can also decay via EC/β^+.

The purification trap normally runs with a trapping time of the ions of around 0.5 s. This time can however be prolonged, practically without any other losses than the decay of the nuclei, to last up to 6.4 s. This is useful when exploring the long-lived state in more detail. Such studies are beneficial to fully disentangle the decay properties of ^{195}Po, as it makes it possible to see mainly the decay following the long-lived state. The result from the selection can be seen in Fig. 1. The relative intensities of the 6.60 MeV and the 6.70 MeV α decay clearly show how the long trapping time can be used to suppress the short-lived state. A more detailed analysis is in preparation.

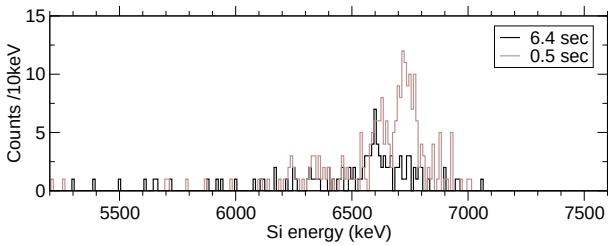

Figure 1: The gray curve illustrates α particles detected after a short trapping time and the black is the result following a longer trapping time. See text for details.

References

[1] D. Rudolph *et al.*, GSI Scientific Report 2009, p. 177, NUSTAR-SHE-08 (2010).

[2] L.-L. Andersson *et al.*, Nucl. Instr. Meth. A **622**, 164 (2010).

[3] V.R. Vanin *et al.*, Nucl. Data Sheets **108**, 2393 (2007).

* Supported by HI Mainz

† L.-L.Andersson@gsi.de

Search for a resonant enhancement of neutrinoless double electron capture with SHIPTRAP

S. Eliseev[1], K. Blaum[1,2], M. Block[3], C. Droese[4], M. Goncharov[1], F. Herfurth[3], E. Minaya Ramirez[5], D. Nesterenko[6], Yu.N. Novikov[3,6], C. Roux[1], L. Schweikhard[4], and K. Zuber[7]

[1] *MPIK Heidelberg,* [2] *Universität Heidelberg,* [3] *GSI Darmstadt,* [4] *Universität Greifswald,* [5] *Helmholtz-Institut Mainz,* [6] *PNPI, Gatchina, and* [7] *IKTP, Dresden*

The observation of neutrinoless double-electron capture $0\nu\epsilon\epsilon$ would unambiguously prove that neutrinos are massive Majorana particles. A measurement of its half-life would result in a determination of the effective Majorana neutrino mass $|m_{\epsilon\epsilon}|$. In general, this process is virtually unobservable due to its long half-life. However, some transitions can be resonantly enhanced if the initial and final states of the transitions are degenerate in energy [1]. This resonant enhancement is governed by a degeneracy parameter $\Delta = Q_{\epsilon\epsilon} - B_{2h} - E_\gamma$, where $Q_{\epsilon\epsilon}$ is the difference between the masses of the initial and final state, B_{2h} and E_γ are the binding energy of the atomic two-electron hole and the nuclear excitation energy of the daughter nuclide, respectively. Transitions with a degeneracy factor Δ close to the width of their final states Γ, *i.e.* a few tens eV, are maximally resonantly enhanced and of primary interest.

A search for such a resonantly enhanced transition has recently been initiated at SHIPTRAP. It is based on a determination of the $Q_{\epsilon\epsilon}$-values of the most promising transitions from direct high-precision Penning-trap measurements of cyclotron-frequency ratios of the singly charged ions of the parent and daughter nuclides. The ions were created from oxide or metallic samples of the respective element with a laser ablation ion source [2]. The purification trap was used to cool and center the ions of interest and to remove unwanted ions. The cyclotron frequencies $2\pi\nu_c = qB/M$ of the ions with the charge $q = e$ and mass M from each transition-pair were measured in the measurement trap in a magnetic field of strength B with the Time-of-Flight Ion-Cyclotron Resonance (ToF-ICR) technique. Two-pulse Ramsey rf field patterns were applied to measure the frequency ratios [3, 4].

The transitions between nuclear ground states are favored: they are all of type $0^+ \rightarrow 0^+$, have large values of the nuclear matrix element and the $2\nu\epsilon\epsilon$ mode is substantially suppressed. This makes them superior to all other types of $0\nu\epsilon\epsilon$-transitions. Based on these arguments ^{152}Gd, ^{164}Er and ^{180}W were identified as the most promising candidates. If the resonant condition for $0\nu\epsilon\epsilon$ in these nuclides is fulfilled, the de-excitation of the excited atomic states of the daughters will be a signature in the search for neutrinoless double-electron capture. Our measurement of the $Q_{\epsilon\epsilon}$-values has indeed discovered such a resonant enhancement of double-electron capture in ^{152}Gd resulting in an estimated half-life of a few $10^{26}/|m_{\epsilon\epsilon}|^2$ y, where the effective Majorana neutrino mass $|m_{\epsilon\epsilon}|$ is given in eV [5].

In contrast, neutrinoless double-electron-capture transitions to nuclear excited states are in general less probable. However, they possess a remarkable feature: several characteristic γ-rays may be emitted via a de-excitation of the nuclear excited state to the ground state of the daughter nucleus. These γ-rays provide a signature of the $0\nu\epsilon\epsilon$-transition. Furthermore, if the initial state of the transition is degenerate in energy with several excited states of the daughter atom, even a multiple resonant enhancement of the $0\nu\epsilon\epsilon$-probability can take place. With SHIPTRAP we have measured the $Q_{\epsilon\epsilon}$-values of the seven most promising transitions: ^{96}Ru, ^{162}Er, ^{168}Yb, ^{106}Cd, ^{102}Pd, ^{144}Sm and ^{156}Dy [6, 7, 8]. In ^{156}Dy we have discovered a unique phenomenon - a multiple resonant enhancement of $0\nu\epsilon\epsilon$ to four nuclear excited states resulting in an estimated half-life of $10^{28}/|m_{\epsilon\epsilon}|^2$ y. This phenomenon may allow an assessment of the realization of different mechanisms of neutrinoless double-electron capture. The five presently most probable transitions measured by Penning traps are presented in Table 1. All of them but ^{112}Sn have been measured with SHIPTRAP [5, 6, 9, 10, 11].

Table 1: Five most probable $0\nu\epsilon\epsilon$-transitions which $Q_{\epsilon\epsilon}$-values have been measured worldwide by Penning traps. Also given are their estimated half-lives normalized to the neutrino mass of 1 eV.

Transformation	$Q_{\epsilon\epsilon}$/keV	estimated half-life/ y
^{152}Gd$\rightarrow^{152}$Sm[5]	55.70(18)	1e26
^{180}W $\rightarrow^{180}$Hf[9]	143.20(27)	5e27
^{156}Dy $\rightarrow^{156}$Gd[8]	2005.95(10)	6e28
^{112}Sn$\rightarrow^{112}$Cd[11]	1919.82(16)	6e29
^{164}Er $\rightarrow^{164}$Dy[10]	25.07(12)	1e30

As can been seen, by far the most and, probably, the only suitable candidate for a search for neutrinoless double-electron capture is ^{152}Gd. There are four promising transitions remaining whose $Q_{\epsilon\epsilon}$-values are not known with sufficient precision. We are planning to measure their $Q_{\epsilon\epsilon}$-values in 2012.

References

[1] M. Krivoruchenko et al., Nucl. Phys. A **859** (2011) 140
[2] A. Chaudhuri et al., Eur. Phys. J. D. **45** (2007) 47
[3] M. Kretzschmar, Int. J. Mass. Spec. **264** (2007) 122
[4] S. George et al., Int. J. Mass. Spec. **264** (2007) 110
[5] S. Eliseev et al., Phys. Rev. Lett. **106** (2011) 052504
[6] S. Eliseev et al., Phys. Rev. C **83** (2011) 038501
[7] M. Goncharov et al., Phys. Rev. C. **84** (2011) 028501
[8] S. Eliseev et al., Phys. Rev. C **84** (2011) 012501
[9] Ch. Droese et al., Nucl. Phys. A, available online: http://dx.doi.org/10.1016/j.nuclphysa.2011.11.008
[10] S. Eliseev et al., Phys. Rev. Lett. **107** (2011) 152501
[11] S. Rahaman et al., Phys. Rev. Lett. **103** (2009) 042501

Nuclear Interaction Times Measured at SHIP

V. Comas[1,2], S. Heinz[1], S. Hofmann[1,3], D. Ackermann[1], J. A. Heredia[1,3], F.P. Heßberger[1], B. Kindler[1], B. Lommel[1], J. Maurer[1], and R. Mann[1]

[1]GSI, Darmstadt, Germany; [2]Justus Liebig Universität, Gießen, Germany; [3]Goethe Universität, Frankfurt, Germany

Experimentally, several methods have been applied in the past to determine nuclear interaction times which are in general strongly attached to different models. In particular, recent experiments using the mass-angle distributions (MAD) [1] and the crystal blocking method [2] in the reactions with ^{48}Ti, ^{58}Ni and ^{74}Ge projectiles with W targets, resulted in quite different values of the nuclear interaction times: $\leq 10^{-20}$ s (MAD) and 10^{-18} s (crystal blocking). The results of the crystal blocking method could not be interpreted as a decay from a compound nucleus (CN), and a very slow quasifission process was suggested to take place in the reactions.

We used the properties of the velocity filter SHIP to measure the nuclear interaction times in deep inelastic transfer reactions. SHIP allows the detection of the produced reaction products within a 2° cone with respect to the beam direction. Information on the reaction channel (fusion, transfer, dissipated energy) can be obtained from the velocity spectra of the reaction products [3]. In our experiment we used a comparable heavy system, ^{64}Ni + ^{207}Pb. Fig.1 shows the velocity distributions of the isotopes ^{212m}At, ^{213}Rn, ^{213}Fr and ^{215}Ra produced in deep inelastic transfer reactions at a beam energy of 5.92× A MeV, with large energy dissipation of ∼ 70 MeV. The velocity distributions show two peaks located symmetrically to the CN velocity (v_{CN}). The high-velocity component originates from a central collision where the target-like transfer product is emitted in forward direction. The low-velocity component is a direct consequence of the rotation of the di-nuclear system (DNS) by 180°. In this case the target-like products are emitted in backward direction in the center of mass system resulting in a reduced velocity in forward direction in the laboratory system (details in [3]). The nuclear interaction times can be deduced from the intensities of the low and high velocity components considering they originate from the decays of a rotating DNS at two different angles (0° and 180°).

Experimental values of the mean lifetime (τ) of the DNS are presented in the Table 1. They were deduced considering an average angular momentum of the DNS of $<L>=15.7\hbar$, estimated for an entrance channel quasifission barrier of B_{qf}=1 MeV. The values of τ increase with increasing number of transferred protons. This result is in accordance with the expected differences in the Coulomb repulsion of the exit channels, which is higher for more symmetric systems and leads to faster DNS decays compared to the more asymmetric ones. Theoretical values shown in the Table 1 were obtained considering the decay of the DNS as a one-dimensional Kramers rate [4, 5] using

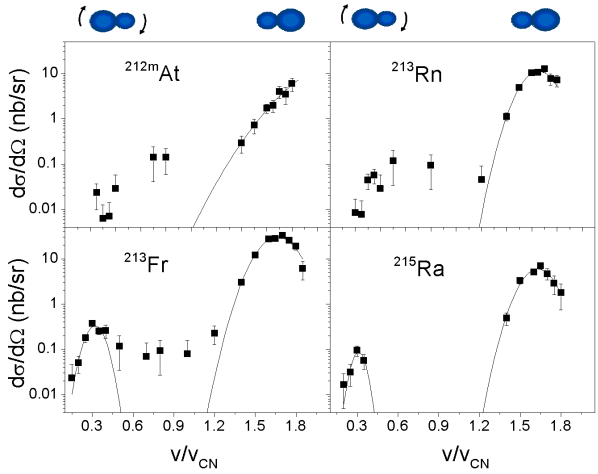

Figure 1: Velocity distributions of the reaction products ^{212m}At, ^{213}Rn, ^{213}Fr, ^{215}Ra produced in the reaction ^{64}Ni + ^{207}Pb.

Produced Isotopes	$\tau_{exp}\times10^{-20}$ s	$\tau_{theo}\times10^{-20}$ s
^{213}Rn	1.2	1.5
^{213}Fr	1.6	1.9
^{215}Ra	1.9	2.3

Table 1: ^{64}Ni + ^{207}Pb. Experimental and theoretical mean lifetimes of the isotopes: ^{213}Rn, ^{213}Fr and ^{215}Ra.

parameters from [6].

The theoretical values (τ_{theo}) are in agreement with the experimental results. The time scales of the order of 10^{-20}s are comparable with those obtained using the MAD method of $\leq 10^{-20}$s. The differences could be explained due to different Coulomb repulsions in the exit channels resulting from transfers occurring from the projectile to the target (our experiment) and from the target to the projectile (MAD) where more symmetric configurations produced result in a faster decaying DNS. The results are in contradiction with the crystal blocking method and the extremely slow quasifission picture used to explain the long times obtained of 10^{-18}s.

References

[1] R. du Rietz et al., Phys. Rev. Lett, **106**, 052701 (2011).

[2] J. U. Andersen et al., Phys. Rev. Lett, **99**, 162502 (2007).

[3] S. Heinz et al., Eur. Phys. J. A **8**, 227-232, (2008)

[4] H. A. Kramers, Physica **7**, 284 (1940).

[5] V. M. Strutinsky, Phys. Lett. B **47**, 121 (1973).

[6] G. G. Adamian, N. V. Antonenko and W. Scheid, Phys. Rev. C, **68**, 034601 (2033), and personal communication.

Metal carbonyl complexes – a new compound class accessible for transactinides

J. Even[1,2#], A. Yakushev[3], Ch.E. Düllmann[1,2,3], J. Dvorak[2], R. Eichler[4], O. Gothe[5], D.Hild[1], E. Jäger[3], J. Khuyagbaatar[2,3], J.V. Kratz[1], J Krier[3], L. Niewisch[1], H. Nitsche[5], I. Pysmenetska[1], M. Schädel[3,7], B. Schausten[3], A. Türler[4,6], N. Wiehl[1], D. Wittwer[4,6]

[1]University Mainz, Mainz, Germany; [2]HIM, Mainz, Germany; [3]GSI, Darmstadt, Germany; [4]PSI, Villigen, Switzerland, [5]LBNL, Berkeley, CA, USA; [6]University of Berne, Berne, Switzerland; [7]JAEA, Tokai, Japan

Gas-phase chemical studies of transactinide elements were so far restricted to simple, thermally stable, inorganic compounds. Metal-carbonyl complexes would provide a link to metal-organic chemistry. Binary, mononuclear, volatile carbonyl complexes are known for all lighter elements of group 6 and 8 of the periodic table. Seaborgium hexacarbonyl has been predicted to be stable [1]. Its experimental study would be interesting, because relativistic effects are predicted to influence the metal-CO bond.

We explored the method of rapid in-situ synthesis of transition-metal carbonyl complexes with short-lived isotopes. First tests were performed at the TRIGA Mainz reactor, using the ^{249}Cf(n,f) reaction. Recoiling fission products were thermalized either in pure N_2 or in a CO/N_2- mixture. All volatile compounds were transported in a gas stream to an activated charcoal trap, which was monitored with a γ-ray detector. Figure 1 shows a typical spectrum from the CO/N_2 measurements.

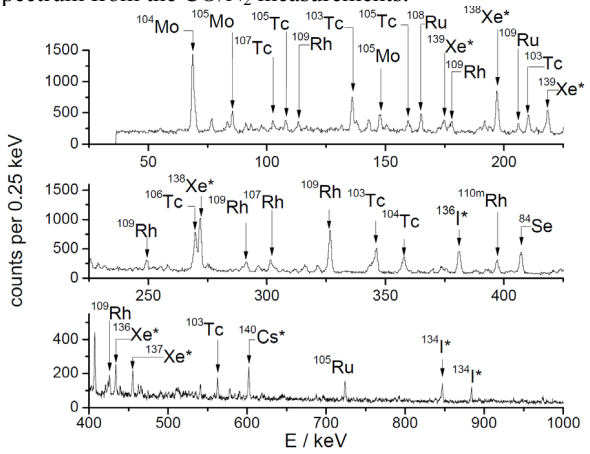

Figure 1: γ-ray spectrum of fission products transported in a CO/N_2 mixture collected for 2 min in a charcoal trap. Subsequently, the sample was measured for 2 min. γ-lines, which were also visible in spectra of pure N_2 experiments, are marked with *.

Short-lived isotopes of Se, Mo, Tc, Ru and Rh were only observed in the spectra when CO was added. These elements form volatile compound with the CO. Transport with cluster (aerosol) material can be excluded.

To test this method under experimental conditions relevant for transactinides, α-decaying ^{163}W, ^{164}W, ^{170}Os and ^{171}Os were produced in ^{144}Sm(^{24}Mg,4-5n) and ^{152}Gd(^{24}Mg,4-5n) reactions at the gas-filled recoil separator TASCA. Evaporation residues were separated from the primary beam and from unwanted transfer products within TASCA. They were thermalized in mixtures of He and CO in a Recoil Transfer Chamber (RTC) [2] at the TASCA focal plane. Volatile carbonyl complexes – most likely $Os(CO)_5$ and $W(CO)_6$ – were formed in the RTC and were transported with the gas stream to the thermochromatography detector COMPACT [3]. The COMPACT detector array is a chromatography channel consisting of SiO_2 covered PIN diodes, suitable to register α particles emitted from volatile species inside the channel. A negative temperature gradient was applied along the chromatography column. Figure 2 shows thermochromatograms of $Os(CO)_5$ and $W(CO)_6$. The measurements are compared to Monte Carlo Simulations. From the deposition patterns of W and Os, adsorption enthalpies of $W(CO)_6$ of (-46.5 ± 2.5) kJ/mol and $(-43\,^{+3.5}_{-2.5})$ kJ/mol for $Os(CO)_5$ were deduced. These values indicate physisorption of these carbonyl complexes on SiO_2.

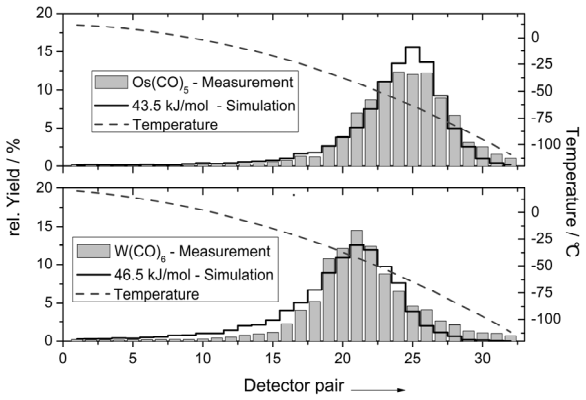

Figure 2: Upper graph: combined thermochromatogram of $^{170}Os(CO)_5$ and $^{171}Os(CO)_5$. Lower graph: combined thermochromatogram of $^{163}W(CO)_6$ and $^{164}W(CO)_6$.

Based on the results of our experiments, $Sg(CO)_6$ and $Hs(CO)_5$ are now within reach for transactinide chemistry. These compounds are suitable for chemical characterization by thermochromatography and appear highly promising for nuclear spectroscopy under low background conditions.

References

[1] C. S. Nash, B. E. Bursten, J. Am. Chem. Soc. **121** (1999) 10830.
[2] J. Even et al., Nucl. Instr. Meth. A. **638**, (2011) 157.
[3] J. Dvorak et al., Phys. Rev. Lett. **100** (2008) 132503.

* Work supported by the Helmholtz Institute Mainz, the Research Center Elementary Forces and Mathematical Foundations (EMG), the BMBF under contract No. 06MZ223I, and the Swiss National Science Foundation under contract No. 200020 126639 #evenj@uni-mainz.de

Preparation of ^{249}Cf targets from pre-used material

J. Runke[1], Ch.E. Düllmann[1,2,3], K. Eberhardt[2], P.A. Ellison[4,5], K.E. Gregorich[4], E. Jäger[1], B. Kindler[1], J. Krier[1], B. Lommel[1], C. Mokry[2], H. Nitsche[4,5], M. Schädel[6], P. Thörle-Pospiech[2], N. Trautmann[2], A. Yakushev[1]

[1]GSI Helmholtzzentrum für Schwerionenforschung GmbH, Darmstadt, Germany; [2]Johannes Gutenberg-Universität Mainz, Germany; [3]Helmholtz-Institut Mainz, Germany; [4]Lawrence Berkeley National Laboratory, Berkeley, CA, USA; [5]University of California, Berkeley, CA, USA;[6]Advanced Science Research Center, Japan Atomic Energy Agency, Tokai, Japan

For the synthesis of the new element with atomic number Z = 120, the fusion reaction of ^{50}Ti with ^{249}Cf was studied at the gas-filled recoil separator TASCA [1]. Pre-used ^{249}Cf, originating from the decay of ^{249}Bk, was provided by the Lawrence Berkeley National Laboratory to produce suitable targets.

The chemical form of the delivered ^{249}Cf was either the oxide, chloride or the nitrate. In a first step the material was dissolved in 8 M HCl. The ^{249}Cf solution contained Al, Fe, Pb and Ti as impurities. In a first purification step the anion-exchanger BioRad AG MP-1M was applied to remove Al and Fe from the solution. In the second step a cation exchange column with DOWEX 50WX8 was used for the removal of Pb and Ti. Over both purification steps the Cf recovery was almost 100 %.

A rotating target wheel assembly was used, which was previously tested to accept high beam intensities up to 2 µA (particle). Molecular plating (MP) [2] was employed for the preparation of ^{249}Cf layers on ~2.2-µm thick Ti backing foils produced by cold rolling at GSI.

The average foil thickness was determined by weighing, whereas the homogeneity of the foil thickness was checked by α-particle energy-loss measurements over 5 positions per foil. The standard deviation of the foil thickness varied between 0.03 and 0.14 µm.

The deposition parameters for Cf were optimized in experiments with Gd. This also included MP with ^{153}Gd-tracer to verify the homogeneity of the Gd layer using a commercial radiographic imager [3] (FLA 7000 from FUJIFILM Corp.).

The first step in the MP of Cf was the conversion of the Cf chloride into the nitrate by evaporation to dryness and re-dissolution in 8 M HNO_3. An aliquot of the Cf-solution with about 3 mg of ^{249}Cf (455 MBq) was evaporated to dryness in a Teflon™ beaker. The green residue was re-dissolved in a small volume (100 µl) of 0.1 M HNO_3. The solution was transferred into an electrochemical deposition cell (EDC) made of PEEK. The beaker was washed with 3 x 300 µl isopropanol, which was also transferred to the EDC. The EDC was filled up to a volume of 52 ml with isobutanol. For the mixing during the deposition process an ultrasonic stirrer was used [3]. For the MP of ^{249}Cf with a surface of 6 cm^2 a voltage of 200 – 600 V at a maximum current density of about 0.3 mA/cm^2 was applied. The deposition time was 4 – 5 hours. The deposition yield exceeded 90 %. Fig. 1 shows one of the produced target segments.

Figure 1: Cf target-segment

Prior to the production of ~0.5-mg/cm^2 thick ^{249}Cf targets, a thin ^{249}Cf target was prepared. With this target we tested the deposition parameters. Before the deposition, and in 1-h steps during the MP process, 10 µl aliquots of the ^{249}Cf-solution were evaporated to dryness for α-particle spectroscopy. With these measurements the decreasing Cf content in the solution during the deposition was determined as well as the deposition yield.

As a method for the yield determination, γ spectroscopy was used. For this, the thin ^{249}Cf target served as a reference sample. The distance from the target to the γ detector was about 3 m, the dead time was 5%. The data confirmed a thickness of ~0.5-mg/cm^2, and the final analysis of the thickness values, including measurements performed after the element 120 experiment [1], is in progress.

Acknowledgments: We would like to thank Robert F. Fairchild II, Naomi E. Reeves, John A. van Wart and LBNL's entire Radiation Protection Group of the Environmental Health and Safety Division for their leadership and active support with the preparation and execution of the ^{249}Cf shipment to Germany. This work was supported by the Helmholtz Institute Mainz.

References

[1] Ch.E. Düllmann et al., this scientific report (2012).
[2] K. Eberhardt et al., Nucl. Instrum. Meth. Phys. Res. A590, 134 (2008).
[3] A. Vascon et al., Nucl. Instrum. Meth. Phys. Res. A655, 72 (2011).

Background Reduction in TASCA

J.M Gates[1,#], K.E. Gregorich[1], L.-L. Andersson[2], Ch.E. Düllmann[3,4,5], J. Dvorak[5], J. Even[3,5], K. Eberhardt[3], U. Forsberg[6], D. Hild[3], E. Jäger[4], J. Jeppsson[6], J. Khuyagbaatar[4,5], J.V. Kratz[3], J. Krier[4], J.P. Omtvedt[7], I. Pysmenetska[4], D. Renisch[3], D. Rudolph[6], M. Schädel[4,8], A. Semchenkov[7], A. Vascon[3], N. Wiehl[3], A. Yakushev[4]

[1]LBNL, Berkeley, CA, U.S.A., [2]U. Liverpool, UK, [3]U. Mainz, Germany, [4]GSI, Darmstadt, Germany, [5]HIM, Mainz, Germany, [6]Lund U., Sweden, [7]U. Oslo, Norway, [8]JAEA Tokai, Japan

During the ^{244}Pu(^{48}Ca,3-4*n*)$^{289-288}$114 experiment, high background rates in TASCA were observed and attributed to (i) transfer reaction products (TRPs) that have a magnetic rigidity (Bρ) only ~15-30% less than the evaporation residues (EVRs) of interest and decay properties similar to the EVRs and (ii) primary beam passing through pinholes in the target and entering TASCA without charge-exchange or scattering reactions [1]. Both TRPs and primary beam are separated from the evaporation residues (EVRs) of interest in the dipole, but a small fraction are guided back to the focal plane detector by the horizontally focusing quadrupole. This is shown in Fig. 1 for primary beam as compared to EVRs.

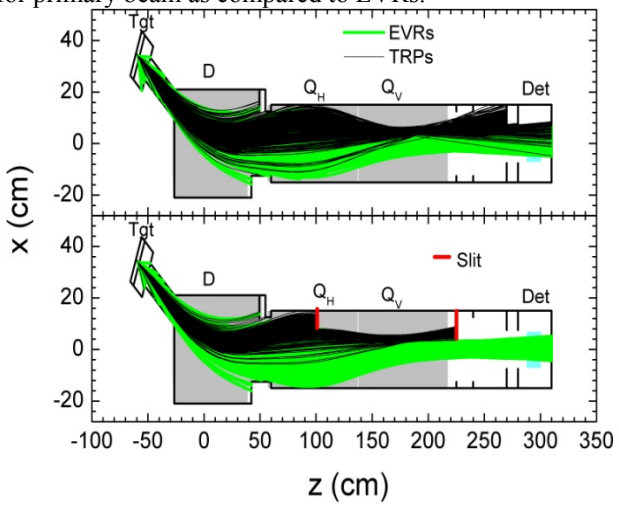

Fig. 1: Primary beam and EVR trajectories in TASCA.

Simulations [2] showed that separation between EVRs and background occurs at the center of the first quadrupole (Q1) and at the exit of TASCA. The use of strategic slits to reduce the acceptance of TASCA in these two areas was expected to result in significantly reduced background without large losses in EVR transmission efficiency as shown in the bottom of Fig. 1. Two solutions (hereafter referred to as M1 and M2) for reducing background in TASCA are:

M1. Introduction of a slit at the center of Q1 reaching from the low Bρ side of TASCA to 8 cm from center. This was expected to result in reductions of 4, 90 and 98% for EVRs, TRPs and primary beam.

M2. M1 plus a slit at the exit of TASCA reaching from the low Bρ side of TASCA to 3.5 cm from center. This was expected to result in reductions of 5, 97 and 99% for EVRs, TRPs and primary beam.

In April 2011, M1 and M2 were tested using the ^{208}Pb(^{40}Ar,x*n*) reaction, chosen to represent 'fast' recoils were the Bρ of the EVRs is approximately 15-30% higher than the Bρ of the TRPs or primary beam. This is similar to what would be expected in reactions such as those currently being investigated to produce elements 119 and 120: ^{249}Bk(^{50}Ti,x*n*) and ^{249}Cf(^{50}Ti,x*n*) and the TASISpec element 115 X-ray Fingerprinting experiment.

The high and low energy spectra during the macropulse and the low energy spectra outside of the macropulse for unmodified TASCA, and TASCA with M1 and M2 are shown in Fig. 2. Background reductions of 77 and 84% for TRPs and primary beam, respectively, were observed with M1. For M2, reductions of 93 and 96 were observed for TRPs and primary beam, respectively, in fair agreement with the simulations. Rates of all events in the macropulse were reduced 65 and 88% for M1 and M2, respectively, while the outside of macropulse event rate for M1 and M2 was reduced by 75 and 89%, respectively. The experimental change in EVR transmission efficiency could not be quantified due to the low ^{208}Pb(^{40}Ar,xn) cross section and interference from TRPs.

Without modification, the rate of events in the focal plane detector during the ^{208}Pb(^{40}Ar,x*n*) reaction was 2900 Hz during the macropulse and 40 Hz outside of the macropulse. With the addition of either M1 or M2, these rates were reduced to <200 Hz inside and <3 Hz outside of the macropulse.

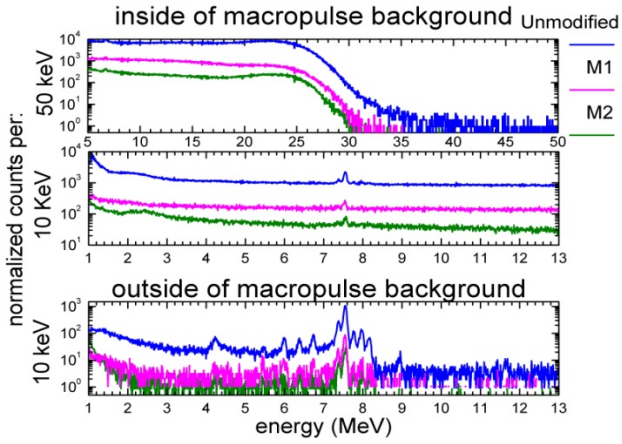

Fig. 2: Total energy spectra for TASCA unmodified and after M1-M2, normalized to the beam integral.

References:

[1] J.M. Gates *et al.*, Phys. Rev. C **83**, 054618 (2011)
[2] K.E. Gregorich *et al.*, Phys. Rev. C **71**, 014605 (2005)

Towards optical spectroscopy of nobelium*

M. Laatiaoui[1,2], *H. Backe*[3], *M. Block*[2], *F.P. Heßberger*[2], *P. Kunz*[4], *F. Lautenschläger*[1], *W. Lauth*[3], *and Th. Walther*[1]

[1]TU Darmstadt; [2]GSI, Darmstadt; [3]Universität Mainz; [4]TRIUMF, Vancouver, Canada

One of the most fascinating studies of the heaviest elements concerns the influence of relativistic effects on the valence electron configuration of atoms and its consequence on their chemical behavior. Deviations from the periodicity in the atomic shell structure, for instance, may be caused by such relativistic effects. A critical test of theoretically predicted relativistic effects would be to compare first ionization potentials and the atomic level schemes of the heaviest elements with modern Multi-Configuration-Dirac-Fock (MCDF) or Relativistic Coupled-Cluster (RCC) calculations. However, the experimental methods have to be sensitive enough to explore atomic properties of heavy elements artificially produced at very low rates, having short half-lives, and for which information on atomic level schemes is completely missing. In our experiments, we aim at the investigation of atomic properties of trans-fermium elements ($Z > 100$) which can be produced solely on-line at accelerator facilities. Our experimental method is based on the Radiation Detected Resonance Ionization Spectroscopy technique, which has been recently developed [1] to probe predicted atomic levels of the element nobelium ($Z = 102$). The latter can be produced at the UNILAC accelerator of the GSI with rates of approx. 17/s via the reaction ^{208}Pb(^{48}Ca, 2n)^{254}No. The reaction products are separated from the primary beam by the velocity filter SHIP and stopped inside a buffer gas cell in argon at a pressure of ca. 60 mbar, see figure 1. The ions are guided continuously by electrical fields onto a tantalum filament opposite to the entrance window. After an appropriate collection time and during the beam-off period the accumulated ions are re-evaporated as neutral atoms by a short heating pulse into the buffer gas, where they can be resonantly ionized by laser beams of suitable wavelengths. In case of resonant ionization, the created ions are subsequently transported by electrical fields onto a particle detector (Passivated Implanted Planar Silicon semiconductor detector, PIPS) with which the applied two-step photoionization is unambiguously identified by the characteristic α-decays of nuclides of interest.

In a first on-line experiment in 2007 the evaporation temperature of nobelium has been determined to be $(1200 \pm 100)\,^{\circ}$C [2]. Nevertheless, no atomic transition has been identified in a 54 h period where the frequency of the first excitation step was scanned over the frequency range predicted by the MCDF and RCC calculations. A possible reason may have been a drop in the efficiency due to buffer gas impurities, which were not monitored during that experiment. The setup has now been permanently installed at the GSI to facilitate further tests and improvements. Considerable efforts have been undertaken to optimize the electrostatic fields inside the buffer gas cell. According to ion optical simulations (SIMION), nearly 40 % of stopped ions do not reach the tip of the filament from where they can be efficiently evaporated. A recently developed filament mount promises to reduce such losses to less than 8 %. Additionally, a new entrance window with 10 % higher geometrical transmission will be used in the future. Moreover, the buffer gas purity is permanently monitored via a residual gas analyzer and can be improved further using additional gas getters and liquid nitrogen traps in the gas line. For safety reasons, the laser systems have been installed inside a dedicated container near the experimental setup and are now ready for use. On-line test experiments on the α-active ^{155}Yb, the chemical homologue of nobelium, are being prepared. The continuation of the atomic level search in ^{254}No is envisaged for the end of next year.

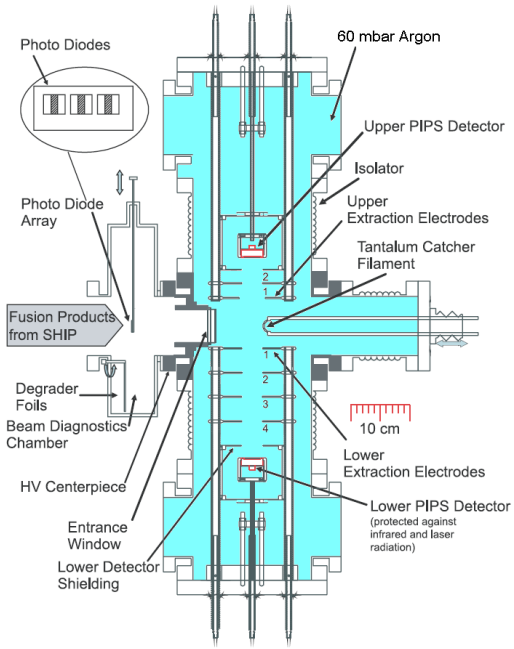

Figure 1: Buffer gas cell for laser resonance ionization spectroscopy on trans-fermium elements. The high vacuum of the velocity filter SHIP and the buffer gas volume are separated by a thin Mylar entrance window.

References

[1] H. Backe et al., Eur. Phys. J. D **45** (2007) 99.

[2] H. Backe et al., GSI Scientific Report 2007.

* Work supported by the BMBF (Grants 06 MZ 169I, 06 LM 236I) and the Helmholtz-Institut Mainz.

Digital signal processing for superheavy element studies

D. Miller[1], K. Miernik[2,3], D. Ackermann[4], R. Grzywacz[1,2], S. Heinz[4], F.P. Heßberger[4,5], S. Hofmann[4,6], J. Maurer[4], K. Rykaczewski[2], and H. Tan[7]

[1]Univ. of Tennessee, Knoxville, USA; [2]ORNL, Oak Ridge, USA; [3]Univ. of Warsaw, Warsaw, Poland; [4]GSI, Darmstadt, Germany; [5]HIM, Mainz, Germany; [6]Goethe-Universität, Frankfurt, Germany; [7]XIA LLC, Hayward, USA

Digital acquisition systems bring a host of benefits to nuclear physics experiments. Primarily, they provide a platform that is highly flexible and compact with the capability of extracting additional information from the details of the pulse shape. For recent investigations at SHIP in the first part of an experiment aimed at the detection of the superheavy element $Z = 120$ [1], digital signal processing techniques enabled detection of alpha decays as prompt as $\sim$100 ns after implantation.

During 33 days of beamtime in April-May 2011, we deployed six Pixie-16 (Rev. D) modules [2] manufactured by XIA LLC in a single 6U compact PCI crate capable of instrumenting all signals including solid-state detectors and logic signals relevant for SHIP analysis with digital sampling at 100 MHz. The digital acquisition system ran in parallel with the traditional analogue setup reproducing all essential spectra. Due to the relatively low rates of interesting decay chains, cross-correlation of the two systems was made using the internal 10 ns timestamp combined with an occasional readout containing the internal clock of the data acquisition computer to produce a human readable time within several microseconds.

Due to the FIFO buffering of the latest revisions of the Pixie-16, the system operates with effectively zero deadtime allowing the detection of all incident events. Data throughputs as high as 72 MB/s have been separately observed in high rate experiments including overhead associated with online analysis. With its simple single-crate/single-computer operation, the system also showed exceptional stability and reliability with no operative issues exhibited for the extent of the experiment.

The standard Pixie-16 firmware determines event-by-event timing and energy onboard reducing the burden of offline analysis. Several new features were also developed in the firmware. For short decay times where the signal from the radioactive decay falls on top of the tail of the implantation signal, complete trace information is needed to extract the contribution from the implantation and decay components. The newly developed firmware records traces only in the situation where such a pile-up is detected (see Figure 1). For other events, solely the timing and energy information is recorded. For maximum sensitivity to the predicted $Z = 120$ half-lives [3, 4], we recorded 9.5 μs traces for each piled-up trace. The lower limit of resolution for the pile-up inspector ($\sim$ 100 ns) depends on the convolution of the Si strip detector drift time with the preamplifier response rise time and the analogue stage Nyquist filter in the Pixie-16 modules. Recording energy and timing data for all events allows for the continuous monitoring of detector charateristics associated with the implantation

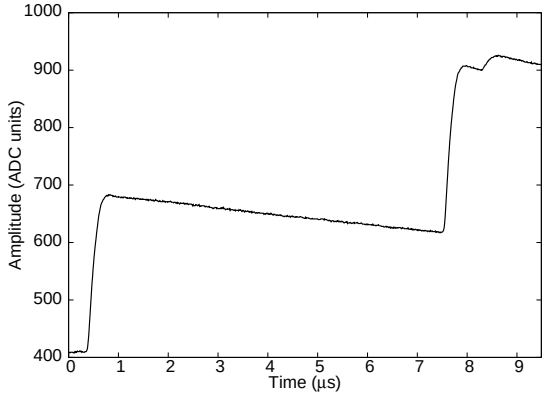

Figure 1: Trace capture selectively triggered from the pileup inspector with two successive implants followed by a low-energy alpha decay.

residues as well as remaining sensitive to longer half-lives. The reduction of data greatly simplifies the offline processing and storage. Over the month long run, a total of 397 GB of data (150 GB compressed) was recorded. If traces were recorded for every event, this would become a much more cumbersome 46 TB of raw data to analyse.

Several other features were also important for the analysis. Since traces were not captured for every event, it no longer is possible to directly determine which signals exceeded the input range of the 12-bit ADC such as those induced by fission events. These events were thus flagged onboard as "saturated" events. For saturated events, length of time out of ADC range provides an approximation of spontaneous fission pulse height. Total time out of range and several other important runtime statistics were also recorded onboard and occasionally dumped to the data stream. Initial tests were also done using the onboard QDC capabilities of the Pixie-16 to selectively integrate up to eight time intervals for each incoming signal. This allows position reconstruction from the information recorded for the position-sensitive silicon detector, though a detailed calibration and parameter optimization are still needed.

This work is supported by HI Mainz.

References

[1] S. Hofmann et al., GSI Scientific Report 2011.

[2] `http://www.xia.com/DGF_Pixie-16.html`, updated 16 Nov. 2011, accessed 16 Dec. 2011.

[3] A. Parkhomenko and A. Sobiczewski, Acta Phys. Pol. B **36**, 3095 (2005).

[4] A. Sobiczewski, Acta Phys. Pol. B **42**, 1871 (2011).

Implementation of a digital data readout system for double sided silicon strip detectors for ion and alpha particle spectroscopy*

R. R. Mändl[1,2], D. Ackermann[2], J. Adamczewski-Musch[2], L.-L. Andersson[3], M. Block[2,3], H.-G. Burkhard[2], V. Comas[4], C. Droese[5], S. Heinz[2], F. P. Heßberger[2,3], J. Hoffmann[2], S. Hofmann[2], N. Kurz[2], M. Laatiaoui[6], J. Maurer[2], E. Minaya Ramirez[3], K. Schmidt[1] and L. Zimmermann[1]

[1]Fachhochschule Frankfurt am Main, Germany, [2]GSI Helmholtzzentrum für Schwerionenforschung Darmstadt, Germany, [3]Helmholtz Institut Mainz, Germany, [4]Universität Giessen, Germany, [5]Universität Greifswald, Germany, [6]Technische Universität Darmstadt, Germany

The synthesis of superheavy elements has reached a region of short-lived nuclei with expected lifetimes shorter than 1 µs. As signal processing times for conventional analogue front-end electronics are typically larger than 10 µs, new developments are mandatory. Deadtime-free, continuously sampling ADCs are presently being implemented for various signal processing applications in particle and photon spectroscopy.

The classical VME-standard analogue front-end electronics was compared to the new flash-ADC based system developed at GSI. The in-house developed APFEL-chip (an ASIC preamplifier and shaper) and the FEBEX-module (a flash ADC circuit) [1] were characterized using α source irradiations and in heavy-ion induced fusion-evaporation reactions at GSI. Those components were used to build a fast deadtime-free data acquisition (DAQ) system. An example of recorded traces which originate from parts of a decay chain of ^{220}Th is shown in Fig. 1. The maximum time resolution of the system is 125 ns.

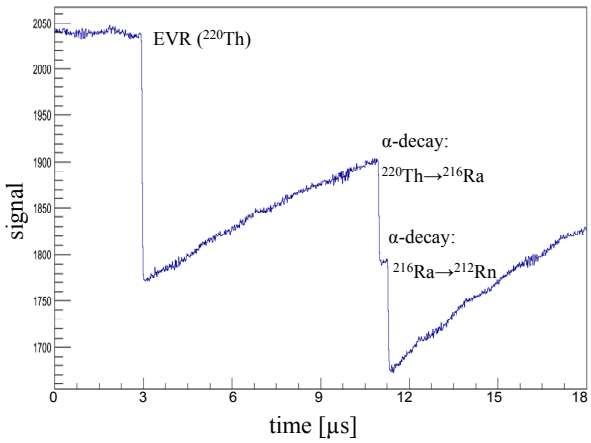

Figure 1: The curve shows an example of a trace with a length of 18.5 µs recorded on-line in the reaction ^{48}Ca + ^{176}Yb. After about 3 µs (200 samples; 1 sample = 15.4 ns) the evaporation residue (EVR) is implanted. 7.7 µs later, the first α-decay (^{220}Th ($T_{1/2}$ = 9.7 µs) appears, followed by a second one (^{216}Ra, $T_{1/2}$ = 0.18 µs) only 385 ns (25 samples) later [2].

This readout electronics is developed for a 60x60 mm^2 Double Sided Silicon Strip Detector (DSSD). The strip structure is implemented as metalized electrode areas on the surface, with 32 strips, a 1.6 mm pitch width, and perpendicular orientation front to back side. There is a gap of 75 µm between the strips to separate them electrically from each other. If an event (particle or internal decay) occurs in this region, the electric charge is divided and collected by the neighbouring strips. The value of the deposited energy can be recovered as the sum of the charge collected in these strips (lower panel in Fig. 2).

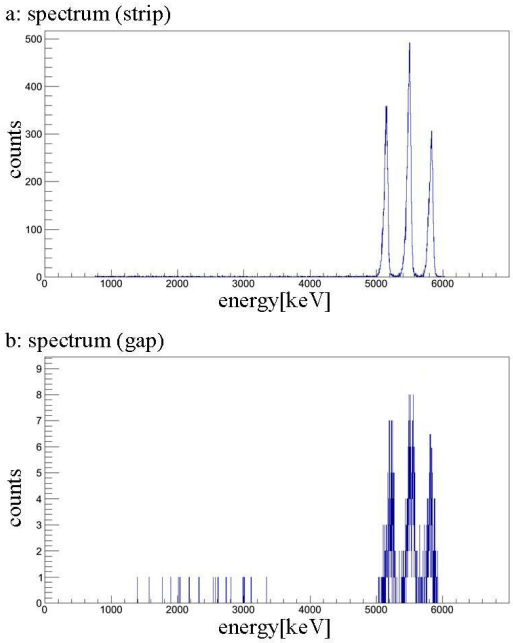

Figure 2: a) Three line α spectrum (^{239}Pu, ^{241}Am and ^{244}Cm) of a single strip. b) α spectrum recovered for a gap area from summed charges collected in the neighbouring strips [2].

In α source test irradiations we could show that summing the respective signals, yields the recovery of about 50% of the gap events at the correct energy level. The energy resolution is comparable to the single strip events. Applying this summing procedure, the sensitive area of the DSSD can be raised from 96 to 98 %.

* Supported by HI Mainz

References

[1] P. Wieczorek *et. al.*, GSI Scientific Report 2010, p. 240, PHN-IS-EE-12.
[2] R. R. Mändl, bachelor thesis FH Frankfurt, 2011.

Commissioning of a cryogenic gas cell for ion stopping at SHIPTRAP*

C. Droese[1], *K. Blaum*[2], *M. Block*[3], *S. Eliseev*[2], *F. Herfurth*[3], *M. Laatiaoui*[4,5], *F. Lautenschläger*[4], *E. Minaya Ramirez*[6], *L. Schweikhard*[1], *and P. G. Thirolf*[5]

[1]Ernst-Moritz-Arndt-Universität Greifswald, Germany; [2]Max-Planck-Institut für Kernphysik Heidelberg, Germany; [3]GSI Darmstadt, Germany; [4]Technische Universität Darmstadt, Germany; [5]Ludwig-Maximilians-Universität München, Germany; [6]Helmholtz-Institut Mainz, Germany

The Penning-trap setup SHIPTRAP is employed for high-precision mass measurements of very heavy and superheavy nuclei created in fusion-evaporation reactions. Recently, the masses of the nuclides $^{252-254}$No [1] and ^{255,256}Lr [2] were directly measured for the first time. To extend such measurements to superheavy elements, it is crucial to further increase the overall efficiency of the system. Therefore, a second-generation gas-filled stopping cell ('cryocell') was designed [3].

In a gas stopping cell the reaction products ejected from the velocity filter SHIP are slowed down in a metallic entrance window (e.g. titanium foil of about 3 μm thickness) and ultra-pure helium buffer gas at a pressure of approximately 100 mbar from several MeV to few meV.

In comparison to the first-generation gas cell [4], the new one is cooled down to cryogenic temperatures to reduce the rest-gas contamination of the stopping gas. At 40 K almost all impurities freeze out and accumulate on the walls of the chamber, which leads to a significantly improved purity of the buffer gas. As a result, ion losses due to charge exchange with contaminants are minimized. This also allows for higher electrical fields inside the cryocell to extract the radionuclides faster from the cell. In addition, ion losses due to radial diffusion will be minimized due to lower diffusion rates at cryogenic temperatures. Furthermore, baking of the system is not necessary anymore, therefore it is possible to use non-UHV compatible materials, such as printed circuit boards for voltage dividers, inside the vacuum chamber. Thus, the amount of required electrical vacuum feedthroughs was drastically reduced.

A further modification is the coaxial injection of the reaction products into the cryocell. In combination with an electrically insulated entrance window that serves as an electrode the dead volume between the stopping region and the entrance window disappears.

A sketch of the cryocell is shown in figure 1. The cryocell consists of two chambers, the outer chamber with a length of 650 mm and a diameter of 500 mm, and the inner chamber with a length of 450 mm and a diameter of 400 mm. The outer chamber is pumped down to a pressure of 10^{-6} mbar and contains a multilayer insulation foil. It serves as a thermal insulator for the inner chamber. The inner chamber is copper-plated on the outside with a thickness of 2 mm to increase the heat conductivity. It is cooled down with a single-stage cryo cooler (100 W at 77 K) to

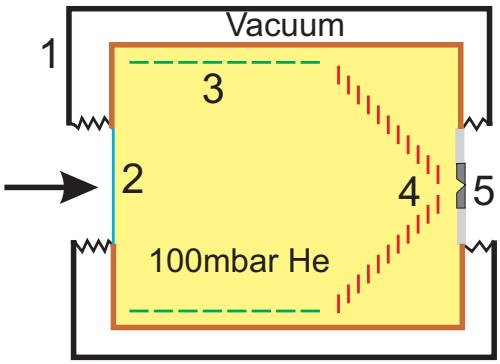

Figure 1: Sketch of the cryocell. 1. Outer Chamber 2. Entrance Window 3. DC-Cage 4. RF-Funnel 5. Extraction Nozzle

40 K. After the reaction products pass the first electrode (the entrance window), the ions are guided with an electrostatic electrode system consisting of 8 ring electrodes with a diameter of 260 mm producing a DC gradient of $>$10 V/cm to a radiofrequency funnel. The funnel consists of 76 individual ring electrodes with an initial diameter of 266 mm and a final diameter of 5 mm. Between neighbouring electrodes rf voltages with a phase shift of 180 ° in addition to a superimposed DC voltage are applied. The RF-DC mixing board is installed inside the inner chamber. The resonance frequency of the circuit is 1.017 MHz with $U_{out,pp}$=320 V at an input of $U_{in,pp}$=10 V. The ions are ejected from the cryocell through a nozzle in a supersonic gas jet. At room temperature a pressure of 10^{-8} mbar in the inner chamber was reached. In an evacuated state a temperature gradient of 20 K from the cryo cooler on the top to the CF63 pumping port on the bottom was observed. However, as soon as the chamber is filled with buffer gas the temperature distribution equilibrates due to the increased heat conductivity.

With the cryocell an increase of the efficiency of up to a factor of five is envisaged. First offline experiments with a ^{223}Ra-recoil ion source are scheduled for the beginning of 2012.

References

[1] M. Block et al., Nature 463 (2010) 785

[2] E. Minaya Ramirez et al., GSI Scientific Report 2011

[3] S. Eliseev et al., Nucl. Instr. Meth. B 266 (2008) 4475

[4] J. B. Neumayr et al., Nucl. Instr. Meth. B 244 (2006) 489

*We acknowledge the support of the German BMBF (Grants 06ML9148) and GSI (Grants LMTHIR1012 and GFMARX1012). Financial support by the Max-Planck Society is acknowledged.

IRiS - Feasibility Calculations

J. Dvorak[1] and Ch.E. Düllmann[1,2,3]

[1]Helmholtz Institut Mainz, Main, Germany; [2]Univ. Mainz, Mainz, Germany; [3]GSI Darmstadt, Germany.

The design for a new Inelastic Reactions Isotope Separator (IRiS) [1] to be installed at the GSI Darmstadt has been developed in a joint effort of an international collaboration, headed by the University Mainz, the Helmholtz Institute Mainz, and the GSI. This separator will be dedicated to the investigation of neutron-rich isotopes of heavy and superheavy elements, which can be produced exclusively in multi-nucleon transfer reactions. So far, experimental studies of transfer products with recoil separators have focused on light isotopes not far from stability for a number of reasons. These include low efficiencies for multi-nucleon transfer reactions of recoil separators that are optimized for fusion-evaporation reactions. Here, we present developments toward a dedicated facility featuring an extra-large angular acceptance separator IRiS, which will make the study of heavy neutron-rich transfer reaction products feasible.

The task of IRiS is to separate reaction products of interest from the primary beam and unwanted byproducts. The separated products will be delivered either into a detector setup or alternatively to auxiliary setups for identification and further investigation of the species of interest. For internal detection in a Si stop detector, maximum acceptable count rates are on the order of 1 kHz. For detection in auxiliary systems like a gas stopping chamber for coupling to external experimental setups, count rates up to 100 kHz appear acceptable.

In our feasibility calculations, two particular nuclear reactions were studied in detail: the reaction ^{48}Ca + ^{248}Cm at a center-of-mass beam energy E_{CM} = 209 MeV, and the reaction ^{238}U + ^{248}Cm at E_{CM} = 750 MeV. Predictions for the multi-nucleon transfer channels from theoretical models of V. Zagrebaev [2] and G. Adamian and N. Antonenko [3] were used for these studies. An ion-optical simulation was developed in framework of this study to test the performance of various potential IRiS setups for the two selected reactions. Besides the heavy n-rich products of interest, other reaction byproducts were simulated as well as they will be the major source of background.

Due to large differences in the properties (e.g., velocity, energy, angular emittance) of the studied heavy transfer products when produced in different reactions, the optimal setup differs for either of the reactions. The most versatile setup was found to be one based on a superconducting solenoid magnet as the main component, with a stored energy of E ~ 10 MJ. In the simulations, a solenoid magnet with a maximum magnetic field strength of B_{max}=4.3 T and dimensions of 2 m length and 90 cm inner diameter was used. The target is located on axis at the entrance of the solenoid. A beam dump blocking central ions is placed axially at the exit of the solenoid and the detector is located further downstream from the solenoid, see Fig. 1. Ion-optical simulations of the identified optimal setups resulted in efficiencies of roughly 20% for separation of the heaviest (Z ≥ 102) transfer products, while keeping the background rate well below 100 kHz. For the reaction ^{238}U + ^{248}Cm, the background is predicted to be below 1 kHz, when using a 500-μg/cm^2 thick target. Using thicker targets resulted in increased background. For the reaction ^{48}Ca + ^{248}Cm two setups were investigated. The setup tuned for detection of the heaviest (Z ≥ 102) transfer products resulted in background below 1 kHz and the possibility to roughly identify A and Z of the ions. When the setup was adjusted for the detection of Fm isotopes, the background increased to ~ 10 kHz.

Figure 1: Schematic drawing of a solenoid-based IRiS design in an asymmetric mode. A thin actinide target is bombarded with a heavy-ion beam. A beam dump located on axis behind the solenoid stops both, beam ions, which pass through the target without undergoing nuclear reactions (red arrow) as well as light products of transfer reaction channels (violet). Heavy transfer reaction products (blue) are focused on a disk-like detector at the exit of the solenoid. In the separator mode, the detector is removed, and the products pass through a thin window into the gas-filled stopping cell, where they are available for transport to ancillary setups.

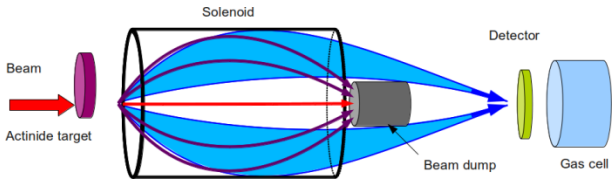

We conclude that the optimal identified setups perform better than expected for the reactions of choice. These setups will most probably not only allow for delivery of separated products into a gas stopping cell, which is the main design requirement, but also enable on-line detection in internal Si detectors. The above described setups offer enough space for inserting of multiple gas-filled detectors for precise TOF measurement and ideally also for a rough Z identification.

Acknowledgment: We thank V. Zagrebaev, G. Adamian and N. Antonenko for sharing results with us prior to publication. Work supported by the Helmholtz Institute Mainz.

References

[1] J. Dvorak et al., Nucl. Instrum. Meth. A 652 (2011) 687.
[2] priv. comm.
[3] priv. comm.

Theoretical Predictions of Properties of Element 119 and its Adsorption* on Noble Metal Surfaces

V. Pershina[1], A. Borschevsky[2] and J. Anton[3]

[1]GSI, Darmstadt, Germany; [2]A. Borschevsky, Massey University, Auckland, New Zealand; [3]Institut für Elektrochemie, Universität Ulm, Germany.

In the present work, we predict chemical properties and adsorption behaviour of element 119 that might be produced in the near future at the GSI, Darmstadt. The most promising nuclear reaction appears to be ^{50}Ti + ^{249}Bk, giving the ^{295}119 and ^{296}119 isotopes in the 4*n* and 3*n* evaporation channel, respectively. Expected lifetime, of the order of ms, is too short for study of chemical properties of this element using current gas-phase chromatography techniques. However, development of vacuum chromatography could open new prospects in this field.

An analysis of atomic properties, calculated within the Dirac-Coulomb-Breit and other relativistic approaches [1,2] has shown that the relativistic stabilization and contraction of the valence ns AO in group 1 results in the inversion of trends beyond Cs, so that element 119 will be more electronegative than K.

Chemical reactivity of element 119 in comparison with its lighter homologs K through Fr was studied for the M_2 and MAu dimers. Knowledge of properties of these compounds is indispensable for estimating important quantities measured in the chromatography studies, i.e., sublimation, ΔH_{sub}, and adsorption enthalpies, ΔH_{ads}, on gold.

Molecular calculations were performed with the use of our fully relativistic, 4-component, Density Functional Theory method in the non-collinear spin-polarized approximation [3]. Results are given in Tables 1 and 2.

Table 1. Spectroscopic properties of M_2 (M = K through element 119): bond lengths, R_e (in Å), dissociation energies, D_e (in eV) and vibrational frequencies, ω_e (in cm^{-1})[a]

Mol.	R_e	D_e	ω_e
K_2	3.942	0.515	91
	3.924	*0.520*	*92*
Rb_2	4.224	0.475	58
	4.180	*0.485*	*58*
Cs_2	4.673	0.428	41
	4.646	*0.452*	*42*
Fr_2	4.610	0.436	33
$(119)_2$	4.265	0.553	41

[a] Values in italics are experiment.

The data show that molecular properties have also a reversal of trends beyond Cs. Thus, $(119)_2$ should be most strongly bound in the row of homologs, due to the 8s(119) AO contraction, while 119Au - most weakly, due to the 8s(119) AO stabilization. ΔH_{sub} of the 119 metal and ΔH_{ads}(119) on gold were obtained via a correlation with the binding energies of the corresponding dimes in the group. Accordingly, ΔH_{sub}(119) should be larger than that of K, while -ΔH_{ads}(119) on Au (also on Pt and Ag) should be the smallest among the homologs.

Table 2. Properties of MAu (M = K through element 119): bond lengths, R_e (in Å), dissociation energies, D_e (in eV) and vibrational frequencies, ω_e (in cm^{-1})[a]

Mol.	R_e	D_e	ω_e
KAu	2.856	2.76	173
	-	*2.75*	-
RbAu	2.967	2.74	122
	-	*2.48*	-
CsAu	3.050	2.91	100
	-	*2.53*	-
FrAu	3.097	2.75	89
119Au	3.074	2.44	92

[a] Values in italics are experiment.

Predicted trends in the adsorption of group-1 elements on noble metals are shown in Fig 1. The moderate values of ΔH_{ads}(119) are indicative of the feasibility of the chromatography chemical studies.

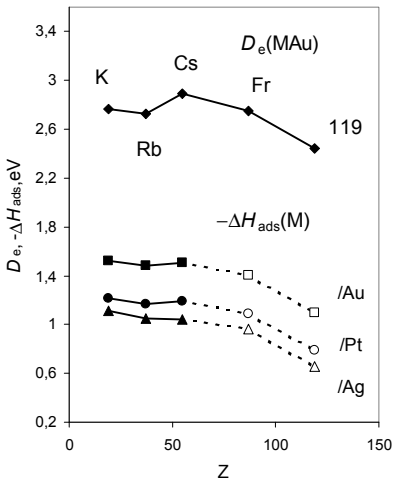

Fig. 1. Calculated D_e(MAu) and -ΔH_{ads}(M), where M = K through element 119, on Au, Pt and Ag. (The filled symbols are calculations [4], while open ones – present data).

References

[1] E. Eliav, *et al*. Chem. Phys. **311** (2005) 163.
[2] I. S. Lim, *et al*. J. Chem. Phys. **122** (2005) 194103.
[3] J. Anton, *et al*. Phys. Rev. A **69** (2004) 012505.
[4] H. Rossbach and B. Eichler, Akademie der Wissche-schaft der DDR, Report ZFK-527 (1984).

* Work supported by HI Mainz

Prediction of Atomic Properties of Ra and Element 120*

A. Borschevsky[1,2], V. Pershina[2], E. Eliav[3], and U. Kaldor[3]
[1]Massey University, Auckland, New Zealand; [2]GSI, Darmstadt, Germany; [3] Tel Aviv University, Israel

We performed relativistic benchmark calculations of polarizabilities, α, and ionization potentials, IP, of element 120 and its lighter homologues, Ba and Ra. Besides being of fundamental importance in the context of atomic studies of heavy and superheavy elements, these properties are also important for the production and identification of element 120 attempted last year at GSI, Darmstadt [1].

The first and second IPs were calculated using the Dirac-Coulomb-Breit (DCB) Hamiltonian,

$$H_{\mathrm{DCB}} = \sum_i h_D(i) + \sum_{i<j} (1/r_{ij} + B_{ij}).$$

Here, h_D is the one electron Dirac Hamiltonian,

$$h_D(i) = c\boldsymbol{\alpha}_i \cdot \mathbf{p}_i + c^2\beta_i + V_{nuc}(i),$$

where α and β are the four dimensional Dirac matrices. The nuclear potential V_{nuc} takes into account the finite size of the nucleus, modelled by a uniformly charged sphere. The two-electron term includes the nonrelativistic electron repulsion and the frequency independent Breit operator, B_{ij}, and is correct to the second order in the fine structure constant α.

Correlation was taken into account by the Fock space coupled cluster method (FSCC), augmented by the intermediate Hamiltonian approach [2] to facilitate convergence. The universal basis set [3] was used for both elements. The intermediate Hamiltonian approach allowed us to increase the model space to contain 8*s*6*p*6*d*5*f*2*g*1*h* orbitals for Ra, and 8*s*6*p*5*d*4*f*3*g*2*h* orbitals for element 120. In order to correct the IPs for higher order QED effects, we used Ref. [4] and added the self-energy, the vacuum polarization, and the frequency dependent Breit energy contributions obtained there on top of our calculated result. The composite effect of the three QED terms lowers the IP of Ra by 46.2 cm^{-1}, and that of element 120 by 101.7 cm^{-1}. The final IPs are shown in Table I in comparison with experiment for Ra and with other calculations for both atoms. The results for Ra are in excellent agreement with the experiment, achieving meV accuracy for the first IP. Similar accuracy is expected for the IPs of element 120, which are higher than those of its lighter homologue due to the relativistic stabilization of the valence *ns* orbital.

DC calculations of α were performed using the DIRAC08 package [5], employing the finite field approach. Static α of Ra has not been experimentally measured. Thus, along with α of Ra and element 120, we calculated that of their lighter homologue, Ba, for which an experimental value is known [6]. The uncontracted Faegri basis set [7] was used for both atoms and extended to convergence with respect to the calculated polarizabilities. Electron correlation was taken into account at the relativistic CC level, including single, double, and perturbative triple excitations (CCSD(T)). The αs are presented in Table I. To the best of our knowledge, this is the first calculation of α of element 120. The reliability of our prediction is confirmed by good agreement of the obtained α of Ba and Ra with previous calculations and, in case of Ba, with experiment. The decrease in α with increase in atomic number is due to the strong relativistic contraction of the *ns* orbital.

* Work supported by HI Mainz and the Marsden Fund, administered by the Royal Society of New Zealand

Table 1. First and second ionization potentials, IP (in eV), and polarizabilities, α (in a.u.), of Ba, Ra, and element 120

Property	Value	Method	Ref
		Ba	
α	272.8	DC+CCSD(T)	this
	273.5	DC+CI+MBPT	[8]
	268.2	DC+CCS	[9]
	268±22	exp.	[6]
		Ra	
IP1	5.277	DCB+FSCC	this
	5.278	exp.	[10]
IP2	10.176	DCB+FSCC	
	10.147	exp.	[10]
α	242.8	DC+CCSD(T)	this
	248.6	DK+CCSD(T)	[7]
		120	
IP1	5.834	DCB+FSCC	this
	5.863	DC+CI+MBPT	[12]
IP2	11.139	DCB+FSCC	this
	11.150	DC+CI+MBPT	[13]
α	167.4	DC+CCSD(T)	this

References

[1] D. E. Düllmann, *et al.* GSI Annual Report 2011, this issue; S. Hofmann, *et al*. ibid.
[2] E. Eliav *et al.*, J. Chem. Phys. **122**, 224113 (2005)
[3] G. L. Malli *et al.*, Phys. Rev. A **47**, 143 (1993)
[4] C. Thierfelder and P. Schwerdtfeger, Phys. Rev. A **82**, 062503 (2010)
[5] DIRAC08, written by H. J. Ja. Jensen *et al*. (2008)
[6] H. L. Schwartz *et al.*, Phys. Rev. A **10**, 1924 (1974)
[7] K. Faegri, Theor. Chim. Acta **105**, 252 (2001)
[8] S.G. Porsev and A. Derevianko, JETP **102**, 195 (2006)
[9] B. Sahoo and B. Das, Phys. Rev. A **77**, 062516 (2008)
[10] C.E. Moore, *Atomic Energy Levels* (U.S. Goverment Printing Office, Washington, DC, 1958 (1958)
[11] I.S. Lim *et al.*, Phys. Rev. A **70**, 062501 (2004)
[12] T. H. Dinh *et al*., Phys. Rev. A **78**, 022507 (2008)
[13] T. H. Dinh *et al*., Phys. Rev. A **78**, 054501 (2008)

Theoretical Studies on Formation and Adsorption of MBr_5 and $MOBr_3$ (M = Nb, Ta, and Db) on KCl/KBr Surfaces

J. Anton[1] and V. Pershina[2]
[1]Institut für Elektrochemie, Universität Ulm, Germany; [2]GSI, Darmstadt, Germany.

Volatility of halides and oxyhalides of the group-5 elements Nb, Ta and Db was studied extensively in the past both experimentally [1-3] and theoretically [4]. The case of adsorption of pure halides revealed some surprises. Thus, theoretical predictions based on the relativistic DS-DV calculations of the electronic density distribution in MBr_5 indicated higher volatility of $DbBr_5$ (as a vapour pressure over the solid) than their lighter homologs in the chemical groups [4], while experimentally, the following trend was observed: Nb ≈ Ta > Db [1-3]. New experiments are under way at the IMP, Langzhou, to shed more light on this interesting case [5].

In order to understand adsorption of bromides in these experiments, new theoretical studies were undertaken by us on the basis of the state of art fully relativistic Density Functional Theory (DFT) calculations of various halides, oxyhalides and complexes of the group-5 elements. Our 4 *component* DFT spin-polarized non-collinear method [6] allows for very accurate calculations of geometrical configurations and stabilities of the heavy-element species. With its use, formation enthalpies and their trend were predicted for the pure pentabromides and oxybromides according to the following reaction

$$M \rightarrow MOBr_3 \rightarrow MBr_5.$$

Table 1 contains calculated geometries of the group-5 species of interest together with experimental data where available. Atomization energies are given in Table 2.

Table 1. Bond lengths, R_{ax}/R_{eq} (in Å) in MBr_5, $MOBr_3$, MBr_6^-, and MBr_5Cl^- and ∠O-M-Br (in degrees) in $MOBr_3$

Molec.	Nb	Ta	Db
MBr_5	2.500/2.449	2.495/2.444	2.548/2.496
	-	2.473/2.412[a]	-
$MOBr_3$	1.704/2.442	1.716/2.440	1.788/2.484
	1.694/2.429[a]	-	-
	107.5(107.3[a])	104.5	106.0
MBr_6^-	2.554	2.547	2.598
MBr_5Cl^-	2.550/2.380	2.548/2.360	2.600/2.420

[a] Experimental values

Table 2. Atomization energies of $MOBr_3$ and MBr_5 (eV)

Molec.	Nb	Ta	Db
$MOBr_3$	20.53	21.43	20.36
MBr_5	18.32	19.41	18.86

It was shown that Db has no preference to bind oxygen, so that the trend in the $MOBr_3$ formation is Db < Nb < Ta, in difference to the earlier work [4], while the trend in the MBr_5 formation is Nb < Db < Ta. Thus, in the atmosphere of HBr/BBr_3, pure pentabromides should be formed. Their volatility as adsorption on an inert surface should have the following trend Nb < Ta < Db, in agreement with the earlier conclusions [4]. This trend is, however, not the one observed in the "one-atom-at-a-time" experiments [1-3,5], where the quartz surface is modified (e.g., with aerosol particles KCl, or KBr). Our calculations have shown that on the KBr/KCl surface, the MBr_6^- or MBr_5Cl^- complexes are formed, as is shown in Fig. 1.

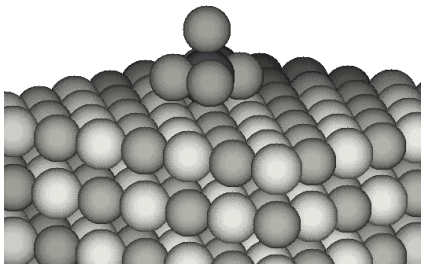

Fig. 1. Formation of MBr_6 on the KBr surface.

Their geometries are given in Table 1. Complex formation energies with respect to those of Nb, in comparison with the experimental ΔH_{ads} [2,3,5] are given in Table 3.

Table 3. Energies of the $MBr_5 \rightarrow MBr_5L^-$ (L = Br and Cl) reactions, ΔE, and of experimental ΔH_{ads} (in eV), with respect to those of Nb

$-\Delta H_{ads}$	$NbBr_5$	$TaBr_5$	$DbBr_5$
$\Delta E(MBr_5 \rightarrow MBr_6^-)$	0	-0.09	-0.21
ΔE $(MBr_5 \rightarrow MBr_5Cl^-)$	0	-0.09	-0.25
$-\Delta H_{ads}[SiO_2/KCl]$ [a]	0	-0.08	-0.29
$-\Delta H_{ads}[SiO_2/KBr]$ [b]	0	-0.08	-

[a] Refs. [2,3]; [b] Ref. [5].

The obtained ΔE (Table 3) are in excellent agreement with the experimental ΔH_{ads} [2,3,5]. Obviously, the complex formation, indeed, takes place on the KCl/KBr surface, so that the trend in the volatility should be Nb > Ta > Db.

References

[1] I. Zvara, *et al*. Sov. Radiochem. **18** (1976) 371.
[2] H. W. Gäggeler, *et al*. Radiochim. Acta **57** (1992) 93.
[3] A. Türler, *et al*. Radiochim. Acta **73** (1996) 55.
[4] V. Pershina, *et al*. J. Chem. Phys. **98** (1992) 1116.
[5] Qin Zhi, *et al.* Radiochim. Acta, submitted.
[6] J. Anton, *et al*. Phys. Rev. A **69** (2004) 012505.

Two-neutron correlations in microscopic wave functions of ^{6}He and ^{8}He *

Hans Feldmeier†[1], *Yoshiko Kanada-En'yo*[2], *and Tadahiro Suhara*[3]
[1]GSI, Darmstadt, Germany; [2]Kyoto University, Japan; [2]Yukawa Institute, Kyoto, Japan

As the neutron-neutron interaction creates at low energies a localized resonance in the $^1S_0$ channel, it is expected that spatial correlations between loosely bound neutrons are enhanced when compared to well bound nuclear many-body systems where the neutrons are in close contact to protons. Neutrons are also an example of the so called unitary limit where the scattering length is much larger than the extension of the many-body system.

Two-neutron densities obtained from microscopic wave functions of ^{6}He and ^{8}He are investigated to reveal di-neutron correlations. The correlated many-body states labeled by total spin and parity J^π are the eigenstates of a given nuclear Hamiltonian obtained by diagonalization in a many-body Hilbert space spanned by AMD-states [**?**]. The two-body correlation densities are calculated for these multi-configuration mixed eigenstates (MC).

The two-neutron density $\rho^{(2)}_{nn}$ as function of c.m. position $\mathbf{R}$ and relative distance $\mathbf{r}$ of the neutron pair with spin $S = 0, 1$ are given by

$$\rho^{(2)}_{nn,S}(\mathbf{R},\mathbf{r}) = \left\langle \Phi^{J^\pi} \right| \sum_{\substack{i\neq j \\ neutrons}}^{A} \Pi^S_{ij} \delta(\tilde{\mathbf{R}}_{ij} - \mathbf{R})\, \delta(\tilde{\mathbf{r}}_{ij} - \mathbf{r}) \left| \Phi^{J^\pi} \right\rangle ,$$

where Π^S_{ij} projects on the spin S of the pair (i,j). In the Figure we display $\rho^{(2)}_{nn,S}(\mathbf{R},\mathbf{r})$ integrated over $\mathbf{r}$. As the many-body states have $J^\pi = 0^+$ the resulting two-neutron distribution $\bar{\rho}^{(2)}_{nn,S=0}(R)$ depends only on the absolute value of the c.m. position $R = |\mathbf{R}|$ of the pair.

For a quantitative discussion of di-neutron correlations we compare with the corresponding densities of single Slater determinants which maybe regarded as uncorrelated, except for Pauli correlations. As reference states with little correlations, we prepare AMD wave functions by minimizing the energy of a single Slater determinant without any projection or constraint. After the variation this intrinsic state is projected on $J^\pi = 0^+$. This procedure is denoted by PAV (projection after variation).

In order to study the effects of the spin-orbit interaction on the two-neutron correlations we also create sample states with PAV calculations without the spin-orbit force, By switching off the spin-orbit force (PAV-ls0) spin-zero neutron pairs are favored.

In the Figure the $S = 0$ two-neutron c.m. density is displayed for ^{6}He and ^{8}He. In the case of an uncorrelated gas of neutrons one anticipates a narrow distribution for the c.m. positions of pairs because particles on opposite sides of the nucleus contribute to c.m. positions R at the center. If on the other hand due the interaction between them the neutrons like to form $S = 0$ pairs that are preferentially close in r the two-body c.m. distribution will not be as narrow as in the uncorrelated case. This effect is nicely visible in $\bar{\rho}^{(2)}_{nn,S=0}(R)$.

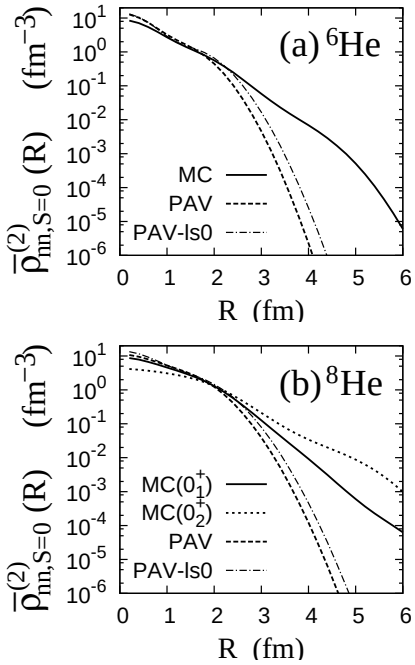

Figure 1: $S = 0$ two-neutron c.m. density $\bar{\rho}^{(2)}_{nn,S=0}(R)$ of the ^{6}He(0^+_1) and ^{8}He(0^+_1) multiconfiguration states (MC), reference states (PAV) and sample states (PAV-ls0), as well as that of the ^{8}He(0^+_2) multiconfiguration state (MC).

When compared with the reference states (PAV) and also the sample states (PAV-ls0), the two-neutron c.m. densities calculated with the MC wave functions for the ^{6}He(0^+_1) and ^{8}He(0^+_1) states are very large at the nuclear surface. In particular, ^{6}He(0^+_1) shows a significant two-neutron c.m. density in the $R > 3$ fm region. This indicates more enhanced nn correlations at the surface of ^{6}He than of ^{8}He. Even in the ^{8}He(0^+_1) ground state the two-neutron c.m. density $\bar{\rho}^{(2)}_{nn,S=0}(R)$ of the MC state at $R \sim 4$ fm is by a factor 100 larger than that of the uncorrelated reference state (PAV). The excited ^{8}He(0^+_2) state shows in the outer region remarkably large probabilities for $S = 0$ neutron pairs.

References

[1] Y. Kanada-Enyo, H. Feldmeier, T. Suhara, Phys. Rev. C 84, 054301 (2011)

* Work supported by Japan Society for the Promotion of Science (JSPS), Japanese Ministry of Education, Culture, Sports, Science and Technology (MEXT) and EMMI.

† h.feldmeier@gsi.de

Breaking of the *N*=8 shell closure in ^{12}Be

T. Neff
GSI, Darmstadt, Germany

The Beryllium isotopes are very rich in their structure. In a naive shell model picture the last neutron in ^{11}Be would occupy a $p_{1/2}$ orbit and the ground state would be $1/2^-$. However this $1/2^-$ state is the first excited state and the real ground state has a spin of $1/2^+$. The neutron separation energy $S_n = 0.504\,\text{MeV}$ is very low and the $s_{1/2}$ orbit comes down in energy. It is now an interesting question how the situation looks like in ^{12}Be. As indicated by the two-neutron separation energy ($S_{2n} = 3.67\,\text{MeV}$) the valence neutrons are much better bound than in ^{11}Be. Furthermore $(p_{1/2})^2$, $(s_{1/2})^2$ and $(d_{5/2})^2$ configurations can all mix in the 0^+ ground state. The situation is furthermore complicated by the deformation of the ^{10}Be "core" as we have to deal with the possibility of core polarization where ^{10}Be in the 2^+ state is coupled with valence neutrons in $(d_{5/2})^2$ or $(s_{1/2}d_{5/2})$ configurations.

Motivated by a recent measurement of the charge radius of ^{12}Be [1] we investigated ^{12}Be in the Fermionic Molecular Dynamics (FMD) approach [2]. FMD uses a Gaussian wave-packet basis for the single-particle states that allows to describe nuclei with clustering and halos in a consistent picture. Good quantum numbers are obtained by projecting the intrinsic many-body basis states on parity, angular and total linear momentum. The parameters of the basis states are obtained by variation after projection for the spins of the low-lying states. In the present calculation additional basis states were obtained by using the quadrupole moment of the intrinsic states as a generator coordinate. The full wave functions were obtained in a multiconfiguration mixing calculation with about 40 basis states.

We used an effective interaction derived from the Argonne V18 potential using the Unitary Correlation Operator Method with correlation functions obtained from a Hamiltonian evolved in the Similarity Renormalization Group [3]. As the effective spin-orbit splittings obtained with realistic two-body interactions are too small we introduced a phenomenological parameter η to change the strength of the spin-orbit force in the $S = 1, T = 1$ channel. A factor $\eta \approx 2$ works remarkably well for the Beryllium isotopes. This modification of the spin-orbit force leads to increased binding but it also changes the relative position of p- and sd-orbits.

Table 1: Calculated and experimental electromagnetic transition strengths in ^{12}Be.

Transition	FMD	Exp.
$B(E2; 2_1^+ \to 0_1^+)[e^2\,\text{fm}^4]$	8.75	8.0(3.0)
$B(E2; 0_2^+ \to 2_1^+)[e^2\,\text{fm}^4]$	7.45	7.0(6)
$M(E0; 0_1^+ \to 0_2^+)[e\,\text{fm}^2]$	0.90	0.87(3)

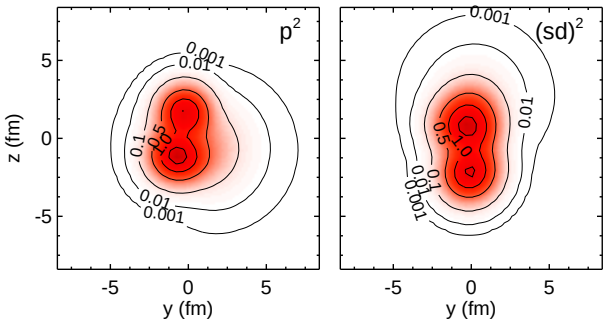

Figure 1: Cuts through the intrinsic densities of the ^{12}Be states that represent local minima in variation after projection calculation. On the left the valence neutrons are found in a p^2 configuration, on the right in a $(sd)^2$ configuration.

The intrinsic states of the Beryllium isotopes show an α-cluster structure. In the case of the 0^+ states of ^{12}Be we found two different local minima that correspond essentially to a p^2 and an $(sd)^2$ configuration as shown in Fig. 1. Whereas the charge radius of the p^2 configuration with 2.33 fm is only slightly larger than in ^{10}Be, the $(sd)^2$ configuration has a significantly larger charge radius of 2.44 fm, which is caused by both an increased distance of the α-clusters and a correlation with the neutrons which leads to an α-^{8}He like structure. The $(sd)^2$ configuration in ^{12}Be is very different from the picture in ^{11}Be where the very small neutron separation energy favors the appearance of an s-wave halo. In ^{12}Be the two neutrons are much better bound and the FMD single-particle orbits are linear combinations of d- and s-orbits. This is also reflected in the matter radius that is significantly smaller in the ^{12}Be $(sd)^2$ configuration than in ^{11}Be. Also other observables, like the monopole matrix element between the two 0^+ states and the quadrupole transition strengths of the two 0^+ states to the first 2^+ state, depend very sensitively on the mixing. We obtain a good agreement for all transitions as shown in Table 1. The $(sd)^2$ configuration contributes about 70% to the ground state. This is reflected in the charge radius which is larger than the calculated ^{11}Be charge radius by about 0.03 fm.

References

[1] A. Krieger, T. Neff, et al., *submitted to Phys. Rev. Lett.*

[2] T. Neff, H. Feldmeier, Eur. Phys. J. Special Topics **156**, 69 (2008).

[3] R. Roth, T. Neff, H. Feldmeier, Prog. Part. Nucl. Phys. **65**, 50 (2010).

Neutrino emissivities and mean free paths in hot strange quark matter*

Andreas Lohs† [1,2,3]

[1]GSI, Darmstadt, Germany; [2]Technische Universität Darmstadt, Germany; [3]Universität Heidelberg, Germany

Neutrino emission by the quark URCA processes is considered to be the dominant cooling mechanism in a possible quark phase in hot an dense matter as may be expected in the core of neutron stars. Moreover, those processes are important for neutrino transport in quark matter.

We present here a refined calculation of emissivities and mean free paths of electron neutrinos from quark URCA processes in strange quark matter assuming the following thermodynamical conditions: $T \leq 100\,\mu_e \ll \mu_{quark}$, with μ_e denoting the electron chemical potential. The reactions explicitly studied are (anti)neutrino absorption on (up) down quark and emission of (anti)neutrinos from (positron) electron capture or down quark decay. The quarks are treated as quasi free particles, with the light quarks being considered as massless. Neutrinos are assumed to leave the system so their abundances are vanishing and there is no neutrino blocking. Electrons and positrons are considered as noninteracting Fermi gases. Strong interaction is accounted for according to Landau-Fermi-Liquid theory [1]. We assume beta equilibrium between quarks and electrons.

The present calculation is an extension of earlier work of Iwamoto [3] and Burrows [2]. The former included corrections due to strong interaction but considered degenerate electrons only, while Burrows considered as well conditions for which electrons are non degenerate, yet treated the quarks as non interacting. In our calculations, we include corrections due to strong interaction and consider conditions which electrons can have any possible degeneracie. Furthermore, we have developed analytical approximations to our numerical calculations that are valid for values of T/μ_e roughly ten times bigger than the approximation presented in [3].

Additionally our calculations correctly treat momentum conservation for all conditions considered. This leads to significantly shorter mean free paths for values of T/μ_e larger than a certain threshold, which depends on the neutrino energy (see figure 1).

Figure 2 compares our ν_e and $\bar{\nu}_e$ emissivities with those computed by Iwamoto [3]. One can see that Iwamoto's approach significantly underestimates the emissivities for high T/μ_e. Previous works [2, 3] neglected positron capture as a source for antineutrinos, however our calculations show that at high temperatures positron capture is the dominant reaction for producing antineutrinos.

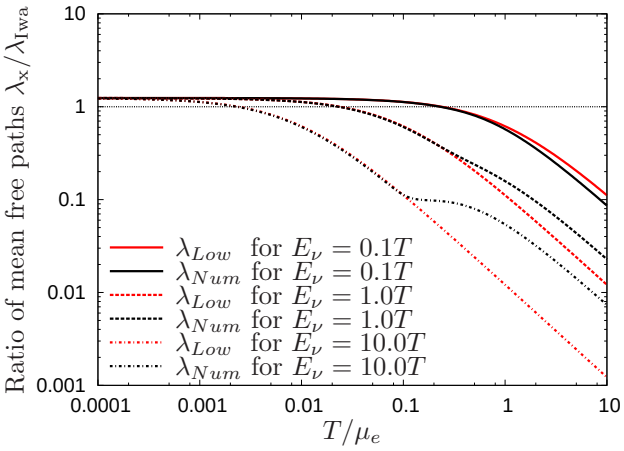

Figure 1: Ratio of mean free paths λ/λ_{Iwa} for ν_e. "Low", "Num", and "Iwa" denote the low temperature approximation, the numerical result, and the expression as given by Iwamoto in [3], respectively.

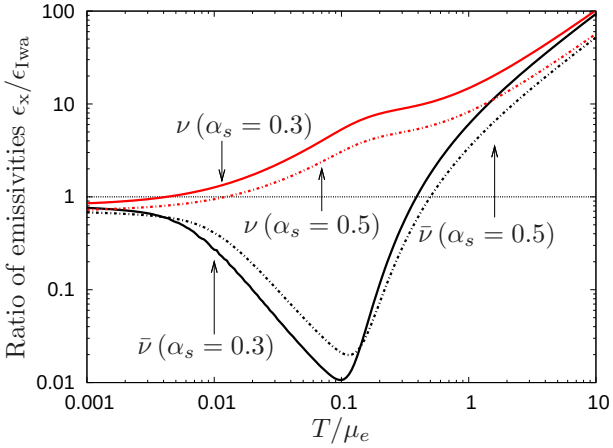

Figure 2: Ratio of ν_e (black) and $\bar{\nu}_e$ emissivities (red) ϵ/ϵ_{Iwa}. The calculations have been performed for two different values of α_s, 0.3 and 0.5

References

[1] G. Baym and S.A. Chin, Nuclear Physics A 262, 527 (1976).

[2] A. Burrows, Phys. Rev. Lett. 44, 1640 (1980).

[3] N. Iwamoto, Annals of Physics 141, 1 (1982).

* Work was supported by HGS-HIRe.

† a.lohs@gsi.de

Operator representation for realistic nucleon-nucleon potentials

D. Weber[1], *H. Feldmeier*[1], *and T. Neff* [1]
[1]GSI, Darmstadt, Germany

We present an operator representation for the Argonne potential [1], correlated with the 'Unitary Correlation Operator Method' (UCOM) [2, 3]. The correlated potential shows a more complicated operator structure than the initial Argonne interaction. However most of these additional operators only become important at high angular momentum L. In this case, due to the centrifugal barrier, the kinetic energy is dominant anyhow. Thus it is sufficient to find a reduced set of operators which can nevertheless describe the the lowest angular momentum matrix elements of the interaction with the same accuracy as the exact operator representation. We use the ansatz

$$\begin{aligned} V_{\mathrm{UCOM}}^{(\mathrm{red.})} &= \sum_{ST} \left[\mathcal{V}_{ST}^{C}(r) + \mathcal{V}_{ST}^{L2}(r) \vec{L}^{\,2} \right] \Pi_{ST} \\ &+ \sum_{T} \mathcal{V}_{1T}^{LS}(r) (\vec{L}\cdot\vec{S})\, \Pi_{1T} \\ &+ \sum_{T} \left[\mathcal{V}_{1T}^{T}(r) S_{12} + \mathcal{V}_{1T}^{Tll}(r) S_{12}(\vec{L},\vec{L}) \right] \Pi_{1T} \\ &+ \sum_{ST} \frac{1}{2} \left[\vec{q}^{\,2} \mathcal{V}_{ST}^{q2}(r) + \mathcal{V}_{ST}^{q2}(r) \vec{q}^{\,2} \right] \Pi_{ST} \\ &+ \sum_{T} \frac{1}{2} \left[q_r \mathcal{V}_{1T}^{Trq}(r) + \mathcal{V}_{1T}^{Trq}(r) q_r \right] \times \\ & \qquad S_{12}(\vec{r},\vec{q}_\Omega)\, \Pi_{1T} \quad (1) \end{aligned}$$

and fit it to the exact matrix elements of the UCOM correlated Argonne potential [4]. Thereby we obtain the radial functions $\mathcal{V}_{ST}^{\cdots}(r)$ in Eq. (1) which absorb the contributions from the neglected operators of the exact UCOM potential in the channels with low angular momentum.

Compared to the operator set of the initial Argonne interaction, the reduced set in Eq. (1) is supplemented by the momentum dependent operators $\vec{q}^{\,2}$ and $q_r S_{12}(\vec{r},\vec{q}_\Omega)$. These terms replace the strong short range repulsion and the short range tensor which are responsible for undesired scattering to high momenta. Therefore it is necessary to include these momentum dependent terms in the reduced set of operators. An ansatz excluding the momentum dependent operators in Eq. (1) cannot not even reproduce the interaction matrix elements and phase shifts in the S-wave (see Fig. 1). The full operator set in Eq. (1) however is able to reproduce these phase shifts. Only for higher L, e.g. in the F-wave, deviations appear due to the reduced set of operators. The reduced set of operators also succeeds to describe light nuclei with the same precision as the exact interaction (Tab. 1).

In that sense, the presented choice contains the minimal set of operators, which is necessary to provide an optimal description of low angular momentum phase shifts and light nuclei.

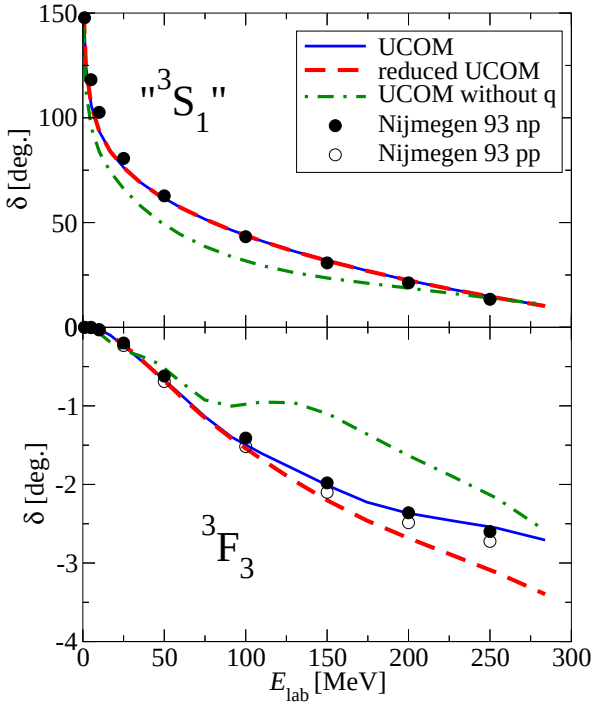

Figure 1: Nucleon-nucleon phase shifts calculated with the exact UCOM interaction (blue solid line), the reduced set of operators from Eq. (1) (red dashed line) and a operator set just neglecting the momentum dependent operators (green dot-dashed line). The dots indicate the results of the 1993 Nijmegen partial wave analysis [5].

	^{3}H	^{3}He	^{4}He
UCOM	8.38	7.67	28.53
reduced UCOM	8.37	7.67	28.51
Experiment	8.482	7.718	28.296

Table 1: Binding energies (in MeV) of some light nuclei calculated in the 'No Core Shell Model'.

References

[1] R. B. Wiringa, V. G. J. Stoks and R. Schiavilla, Phys. Rev. C, 51, 38-51, 1995

[2] H. Feldmeier, T. Neff, R. Roth and J. Schnack, Nuclear Physics A, 632, 61 - 95, 1998

[3] T. Neff and H. Feldmeier, Nuclear Physics A, 713, 311 - 371, 2003

[4] R. Roth, H. Hergert, P. Papakonstantinou, T. Neff and H. Feldmeier, Phys. Rev. C, 72, 034002, 2005

[5] V. G. J. Stoks, R. A. M. Klomp, M. C. M. Rentmeester and J. J. de Swart, Phys. Rev. C, 48, 792-815, 1993

Shell model Gamow–Teller strength distribution for ^{76}Se *

Q. Zhi [1,2], K. Langanke [1,3,4], G. Martínez-Pinedo [1,#], F. Nowacki [5,6], K. Sieja [5,6]

[1] GSI Helmholtzzentrum für Schwerionenforschung, Darmstadt, Germany; [2] School of Physics and Electronic Science, Guizhou Normal University, Guiyang, PR China; [3] Institut für Kernphysik, TU Darmstadt, Germany; [4] Frankfurt Institute for Advanced Studies, Frankfurt, Germany; [5] Université de Strasbourg, IPHC, 23 rue du Loess 67037 Strasbourg, France; [6] CNRS, UMR7178, 67037 Strasbourg, France

Recent theoretical studies predicted that, due to nuclear correlations across the N = 40 shell gap, electron captures on nuclei with proton numbers Z<40 and neutron numbers N>40 would not be strongly suppressed due to Pauli blocking of Gamow–Teller (GT) transitions [1]. This prediction has recently been confirmed by the experimental determination of the single particle occupation numbers in ^{76}Se [2]. The experiment reveals a summed strength of B(GT)=0.7±0.2 in the excitation energy interval Ex=0–5MeV mainly distributed over 6 individual states. Further GT+ strength of B(GT)=0.3±0.2 is tentatively assigned to the energy range 5–10 MeV. To explain the experiment, we present here shell model calculations for the GT+ strength distribution of ^{76}Se.

The detailed theoretical calculation can be found in [3, 4]. The NS interaction has a ^{48}Ca core and considers the full *pf* proton shell and the (*p,f5/2,g9/2*) neutron orbits. The RG and JUN45 interactions use a ^{56}Ni core and consider the (*p, f5/2, g9/2*) orbits for both protons and neutrons. Fig. 1 shows the normalized running sum of the GT distributions from experiment and shell model results. It is found that the RG and NS interactions yield quite similar energy dependencies. The JUN45 interaction predicts a relatively larger GT+ strength at low excitation energies than the other interactions. Fig. 2 compares the stellar capture rates derived from shell model and experiment. It is seen that the capture rates obtained from the experimental GT+ strength distribution are close to those obtained from theoretical calculations.

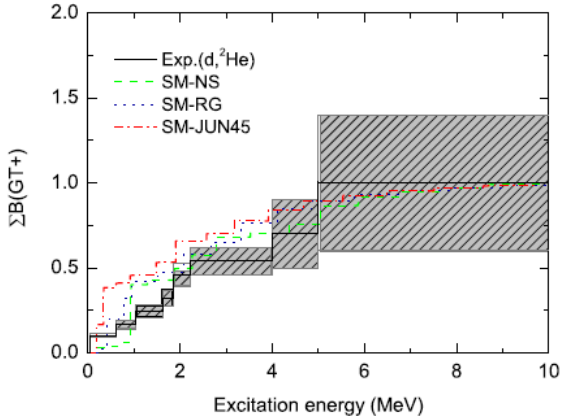

Figure 1: Comparison of Normalized running sum of GT+ strength between experiment and shell model calculations.

* Work was supported by the HA216/EMMI and the Deutsche Forschungsgemeinschaft SFB 634.

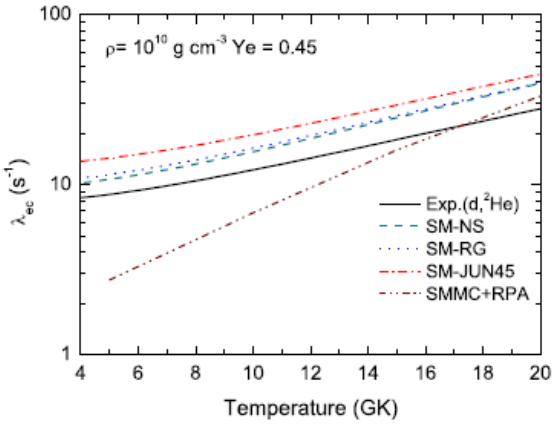

Figure 2: Comparison of stellar capture rates between theory and experiment.

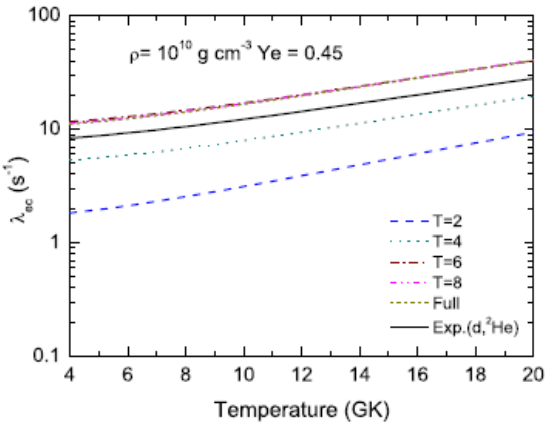

Figure 3: Stellar capture rates from shell model calculation with RG interaction as a function of truncation.

Fig. 3 shows the stellar captures rates from shell model calculation with RG interaction as a function of number of Particle-Hole excitations from *pf* shell to *g9/2* orbit. It is seen that, one needs at least 6p–6h excitations in shell model to get the experimental data.

References

[1] K. Langanke et al., Phys. Rev. Lett 90, 41102 (2003)
[2] E.W. Grewe et al., Phys. Rev. C 78, 044301 (2008)
[3] Q. Zhi et al., Nucl. Phys. A 859,172 (2011)
[4] K. Langanke, G. Martínez-Pinedo, Nucl. Phys. A 673, 481 (2000).

Fragmentation of spin-dipole strength in ^{90}Zr and ^{208}Pb

T. Marketin[1,2], E. Litvinova[3], D. Vretenar[2], and P. Ring[4]

[1]IKP, TU Darmstadt; [2]University of Zagreb, Croatia; [3]EMMI, GSI, Darmstadt; [4]TU München, Garching

Spin-isospin excitations present a very active research topic both in nuclear structure and nuclear astrophysics. In addition to the Gamow-Teller resonance, the charge-exchange spin-dipole response, made up of three components with angular momentum and parity $J^\pi = 0^-$, 1^- and 2^-, has been shown to significantly contribute to the total reaction rates and even compete with the contribution of Gamow-Teller transitions [1]. Two recent (p,n) and (n,p) measurements of the spin-dipole response of ^{90}Zr and ^{208}Pb [2] have prompted new theoretical studies, in particular investigations based on the random phase approximation. Both measurements show a high-energy tail in the spin-dipole strength distribution that cannot be described by the simple one-particle – one-hole (1p1h) random phase approximation (RPA). We introduce a charge-exchange version of the particle-vibration coupling model based on time-dependent covariant density functional theory, and apply it to an analysis of spin-dipole strength distributions in ^{90}Zr and ^{208}Pb [3].

The phonon coupling terms augment the RPA spectrum with additional p-h$\otimes$phonon components that generally lead to significant fragmentation of giant resonances [4]. In Fig. 1 we compare the spin-dipole strength distribution in ^{90}Zr calculated using the relativistic random phase approximation (RRPA), and the relativistic time-blocking approximation (RTBA).

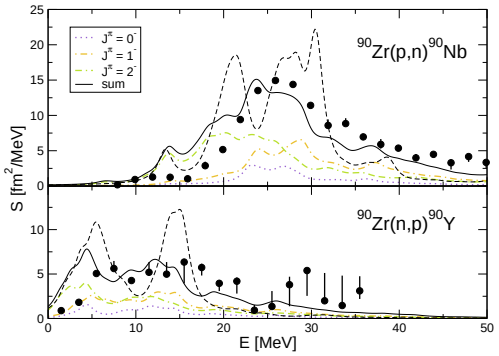

Figure 1: Spin-dipole strength distributions for the t_- (upper panel) and the t^+ (lower panel) channels in ^{90}Zr. The energy plotted on the horizontal axis is with respect to the ground state of ^{90}Zr. The solid curve represents the sum of the strength distributions of the 0^-, 1^- and 2^- components, calculated in the RTBA that includes particle-vibration coupling. The dashed curve denotes the corresponding RRPA strength function. In both cases the imaginary part of the energy is set to $\Delta = 1$ MeV. The experimental results denoted by full circles are from Ref. [2].

The prominent RRPA peaks (dashed curves) disappear when particle-vibration coupling is included in the RTBA (solid curves). In the t_- channel, for instance, only a broad resonance remains with the peak at 23.5 MeV, in very good agreement with the available data. The inclusion of particle-vibration coupling leads to a shift of the strength to higher excitation energies. A high-energy tail is formed in the region above 30 MeV where the strength decreases almost linearly with increasing energy, in close agreement with experimental results. In contrast, the RRPA strength decreases more rapidly above 30 MeV, and becomes 5 to 10 times smaller than the experimental strength above 40 MeV. In the t_+ channel the two dominant peaks predicted by the RRPA merge into a single broad structure that extends up to approximately 15 MeV excitation energy. The tail at higher energies decreases approximately linearly with increasing energy. One might notice a very good agreement with data, except in the low-energy region below 5 MeV, where both the RRPA and the RTBA predict spin-dipole strength, originating predominantly from the 2^- component, that is considerably larger than the measured distribution.

The spin-dipole strength can also provide information on basic properties of finite nuclei. In particular it is connected to the neutron skin thickness, which has been shown to constrain the neutron equation of state, and is also correlated with the nuclear symmetry energy, via the model-independent non-energy-weighted sum rule.

$$S_-^\lambda - S_+^\lambda = \frac{2\lambda+1}{4\pi}\left(N\left\langle r^2\right\rangle_n - Z\left\langle r^2\right\rangle_p\right), \qquad (1)$$

For ^{90}Zr the calculated sum rule is 9% larger than the measured value. This leads to a neutron rms radius $\sqrt{\langle r^2\rangle_n} = 4.308$ fm, and neutron skin thickness $\delta_{np} = 0.115$ fm, both at the upper limit of the experimental error bars.

References

[1] N. Paar, D. Vretenar, T. Marketin, and P. Ring, Phys. Rev. C 77, 024608 (2008).

[2] K. Yako, H. Sagawa, and H. Sakai, Phys. Rev. Lett 74, 051303(R)(2006).

[3] T. Marketin, E. Litvinova, D. Vretenar, and P. Ring, Phys. Lett. B 706, 477 (2012).

[4] E. Litvinova, P. Ring, and V. Tselyaev, Phys. Rev. C 75, 064308 (2007).

Quasiparticle-vibration coupling in relativistic framework: shell structure of Z=120 isotopes

Elena Litvinova[1]

[1]ExtreMe Matter Institute EMMI and Research Division, GSI Helmholtzzentrum für Schwerionenforschung, Planckstraße 1, D-64291 Darmstadt, Germany

For the first time, the shell structure of open-shell nuclei is described in a fully self-consistent extension of the covariant energy density functional theory. The approach implies quasiparticle-vibration coupling (QVC) in the relativistic framework being an extension of the Ref. [1] for superfluid systems [2]. Medium-mass and heavy nuclei represent Fermi-systems where single-particle and vibrational degrees of freedom are strongly coupled. Collective vibrations lead to shape oscillations of the mean nuclear potential and, therefore, modify the single-particle motion. To take this effect into account, the Dyson equation is solved with a one-body Hamiltonian that consists of a Relativistic Hartree-Bogoliubov (RHB) part $\mathcal{H}_{RHB}$ and an additional energy-dependent self-energy $\Sigma^{(e)}(\varepsilon)$ [3]:

$$\big(\varepsilon - \mathcal{H}_{RHB} - \Sigma^{(e)}(\varepsilon)\big)G(\varepsilon) = 1. \qquad (1)$$

The $\Sigma^{(e)}(\varepsilon)$ is the nucleonic self-energy of the quasiparticle-phonon coupling [3]. It contains characteristics of vibrational modes computed with the self-consistent relativistic quasiparticle random phase approximation. Solutions of the Eq. (1) provide the quasiparticle energies and the strength distributions (spectroscopic factors). The Dyson equation is formulated in the doubled quasiparticle space of Dirac spinors and solved numerically for nucleonic propagators $G(\varepsilon)$ in tin and nickel isotopes which represent the reference case: the obtained energies of the single-quasiparticle levels and their spectroscopic amplitudes are in excellent agreement with data. As an example, see Fig. 1. Selected results on the single-quasiparticle

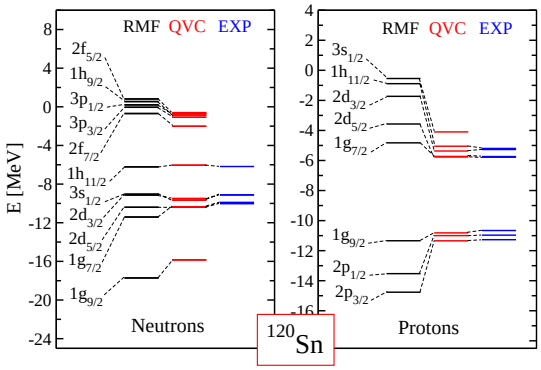

Figure 1: Single-quasiparticle spectrum of ^{120}Sn: Relativistic mean field (RMF, left column), QVC (center) and experimental data (right). In the 'QVC' and 'EXP' cases only the dominant levels are shown.

strength distributions in the neutron and the proton subsystems of the Z = 120 isotopic chain are displayed in Fig. 2. One can see the evolution of these distributions with an increase of the neutron number from N = 172 to N = 184. In the neutron subsystems both pairing and QVC mechanisms are active and show a very delicate interplay: pairing correlations tend to increase the shell gap while the QVC alone tends to decrease it and at the same time causes the fragmentation of the states in the middle of the shell. As a result, in the presence of both mechanisms the gap in the neutron subsystem remains almost steady while the newly occupied levels jump down across the gap when the neutrons are added. Thus, in contrast to the pure mean field studies [4], no sharp neutron numbers appear as the candidates for the spherical shell closures. The shell gap in the proton subsystems of the considered nuclei diminishes only slightly when the neutron number increases, so that the proton number Z = 120 remains a rather stable shell closure while the detailed structure of the proton levels shows some rearrangements induced by the neutron addition.

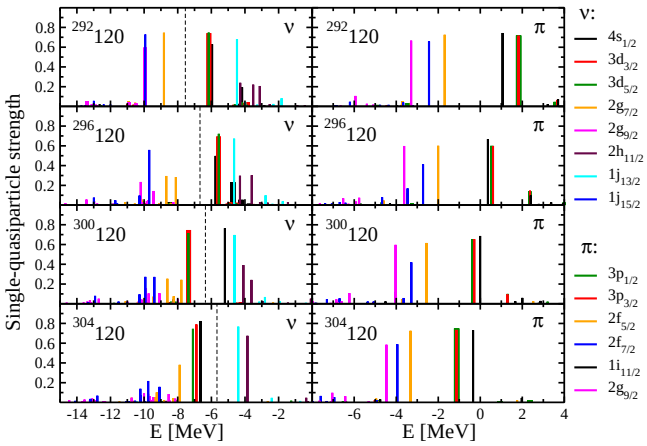

Figure 2: Single-quasiparticle strength distribution for the orbits around the Fermi surfaces in the neutron (left panels) and proton (right panels) subsystems of the Z=120 isotopes calculated in the relativistic quasiparticle-vibration coupling model. The dashed lines indicate the chemical potentials.

References

[1] E. Litvinova and P. Ring, Phys. Rev. C **73**, 044328 (2006).

[2] E. Litvinova, submitted to PRC, arXiv:1108.3508.

[3] E. Litvinova, P. Ring, and V. Tselyaev, Phys. Rev. C **78**, 014312 (2008).

[4] W. Zhang et al., Nucl. Phys. A **753**, 106 (2005).

Integrated nucleosynthesis from supernova simulations

L. Huther[*1,2], *T. Fischer*[1,2], *and G. Martinez-Pinedo*[1,2]
[1]GSI, 64291 Darmstadt, Germany; [2]TU Darmstadt, 64289 Darmstadt, Germany

The production of elements heavier than iron is mainly associated with two different processes, namely the r- and s-process (rapid and slow neutron capture processes). The astrophysical site of the s-process is known, whereas the corresponding site for the r-process is still a subject of debate.

Observations of Metal-poor stars (MPS) give insight to the solution of the problem, since these stars are expected to have fingerprints of only few nucleosynthesis events. By comparison of various MPS observations one could identify a universality of the r-process pattern in the region between the second and third r-process peak ($56 \leq Z \leq 76$), which can be also observed in the solar r-process abundance pattern. However this universality breaks down in the region of $38 \leq Z \leq 48$ and observations of different MPS show different behaviour [4]. This implies that the low-Z and high-Z r-process elements have to be created in different astrophysical sites. One possible candidate for the production of low-Z elements is the neutrino-driven wind in core-collapse supernova. Here, a newly formed proto-neutron star cools by emission of high neutrino and antineutrino fluxes ejecting matter from the surface of the proto-neutron star.

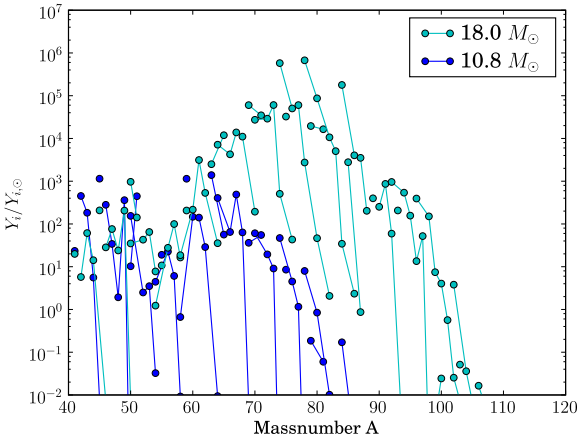

Figure 1: Isotopic abundance as a function of mass number A for setected trajectories of each simulation.

Here we present integrated nucleosynthesis results from core-colapse supernovae simulations, with different initial progenitor masses (10.8 and 18.0 $M_\odot$) and for times of several tens of seconds after the onset of explosion [2]. The ejected matter is always proton rich and is subject to νp-process nucleosynthesis [1]. Using an extended network, including all the relevant nuclear and weak rates, we have determined the integrated nucleosynthesis outcome and its sensivity to the progenitor mass.

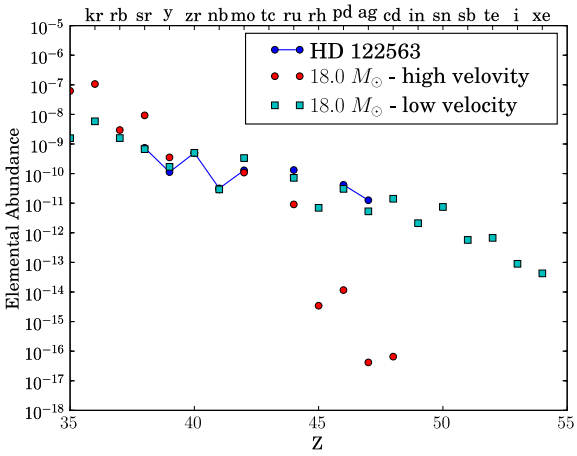

Figure 2: Integrated elemental abundances for low (cyan) and high (red) velocity in comparison to the metal poor star HD 122563

The results of our calculations lead to two conclusions. The first conclusion is, that the nucleosynthesis results of the heavier star lead to a stronger νp-process. This is due to the presence of a more massive envelope that makes the ejecta to move more slowly. This is clearly shown in figure 1, where for both progenitors the nucleosynthesis outcome of two selected trajectories is compared.

Although the simulations have been carried on for several seconds after the onset of explosion, the nucleosynthesis results depend to a large extend on the long term velocity of the ejecta. Assuming a high velocity for the ejected material at the end of the simulation, hinders the νp-process. However, if we assume a smaller velocity, the material is kept for a longer time at the relevant νp-process temperature range. In this case, we can reproduce the MPS observations of ref. [3] for the light r-process elements up to $Z = 56$.

References

[1] C.Fröhlich, **(**et al),Phys.Rev.Lett. **96**,142502 (2006)

[2] T.Fischer, **(**et al),, A&A, **517**, 80 (2010)

[3] S.Honda, **(**et al), ApJ **643**,1180 (2006)

[4] C.Sneden, **(**et al), ApJ **591**,936 (2003)

*l.huther@gsi.de

Massive star explosions: no help from collective neutrino flavor oscillations

Tobias Fischer[1,2], *Sovan Chakraborty*[3], *Alessandro Mirizzi*[3], *Ninetta Saviano*[3], *and Ricard Tomás*[3]

[1]GSI, Helmholtzzentrum für Schwerionenforschung GmbH, Darmstadt; [2]Institut für Kernphysik, Technische Universität Darmstadt; [3]Institut für Theoretische Physik, Universität Hamburg

Explosions of massive stars are related to the revival of the stalled bounce shock. It forms when the collapsing stellar core bounces back at nuclear matter densities. The bounce shock initially propagates out of the stellar core and thereby loses energy due to heavy-nuclei dissociation and neutrino losses. It stalls and turns into an accretion front. Among all shock-revival mechanisms discussed, the neutrino-driven scenario seems the favored case. In the last few years, it has been understood that the description of neutrino flavor conversions in supernovae, based on only the Mikheyev-Smirnov-Wolfenstein (MSW) effect, was incomplete. Flavor changes deep inside the stellar core can be dominated by neutrino-neutrino interactions, creating a potential which causes large and rapid conversions between different neutrino flavors. The transitions occur collectively, i.e. in a coherent fashion, over the entire energy range. An interesting observational consequence of ν–ν interactions is a swap of the ν_e and $\bar{\nu}_e$ spectra with the heavy-lepton flavors ν_x and $\bar{\nu}_x$ ($x \in (\mu, \tau)$) in certain energy ranges. Recently, it has been realized that the electron density cannot be arbitrarily large before it affects self-induced neutrino oscillations. When the electron density significantly exceeds the neutrino density, the large phase dispersion induced by the matter background suppresses collective phenomena. The outcome of such analysis depends on matter density, electron fraction and neutrino spectra, all of which are determined from the supernova simulation.

It has long been speculated whether, e.g., during the mass-accretion period of massive star explosions, such collective neutrino-flavor oscillations can have an impact, e.g., to increase the neutrino-heating efficiency. In order to investigate this question, we performed core-collapse supernova simulations of massive iron-core progenitors in the mass range of 8.8–18 $M_\odot$, in spherical symmetry based on three-flavor Boltzmann neutrino transport [1]. Note that neutrino-driven explosions can only be obtained in spherical symmetry for low-mass stars, between about 8–10 $M_\odot$. More massive stars have extended high-density silicon layers surrounding the central core which in turn leads to an extended mass accretion period which can last for several 100 ms. In order to obtain explosions for such progenitor stars, we enhance the neutrino-absorption rates artificially.

Fig. 1 shows a snapshot of the radial net electron and neutrino density profiles during the accretion phase at 200 ms after core bounce. It can be seen that the electron density largely exceeds the neutrino density[1]. Moreover, because the standing accretion shock is oscillating in radius during the accretion phase driven by neutrino heating and hence it is possible that $n_e \simeq n_{\nu_e} - n_{\nu_x}$, we compute the ν_e survival probability P_{ee}. The radial profiles are shown in Fig. 2, evaluated at selected post-bounce times (black lines) in comparison to a complete flavor swap (red line) assuming zero electron density [2]. The suppression ranges from partial to complete.

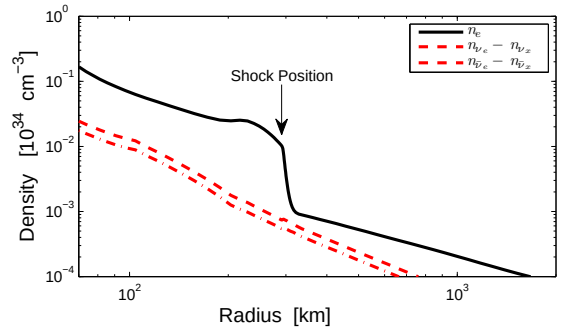

Figure 1: Radial profiles of the net electron and (anti)neutrino densities at 200 ms after core bounce.

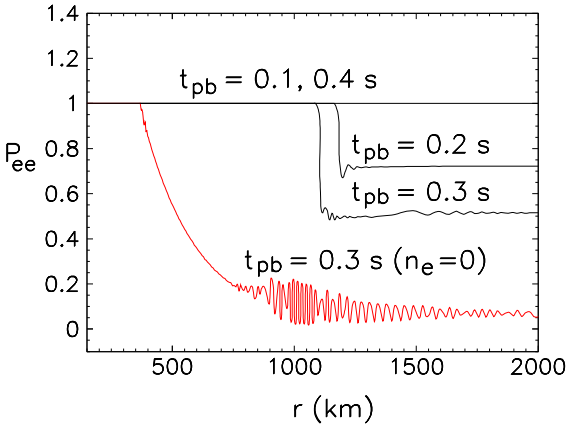

Figure 2: Radial profiles of the ν_e survival probability at selected post-bounce times during the accretion phase.

In summary, collective neutrino flavor oscillations are highly suppressed during the entire accretion phase of core-collapse supernovae and hence their impact to neutrino heating and the explosion dynamics is negligible. The results have been confirmed recently by other groups [3, 4].

References

[1] T. Fischer, et al., Astron. Astrophys., **517**, A80 (2010)

[2] S. Chakraborty, et. al. Phys. Rev. Lett. **107**, 151101 (2011)

[3] B. Dasgupta, et. al., arXiv:1106.1167

[4] S. Sarikas, et. al. arXiv:1109.3601

[1]Note the relevant quantity for the oscillation analysis is $n_{\nu_e} - n_{\nu_x}$

Calculation of neutrinoless double electron capture rates

Tomás R. Rodríguez[1,2] *and Gabriel Martínez-Pinedo*[1,2]
[1]GSI, Darmstadt, Germany; [2]TUD, Darmstadt, Germany

Neutrinoless double electron capture ($0\nu ee$) is a process that can occur beyond the standard model assuming that the neutrino is a Majorana particle. In this process two electrons from the inner shells of an atom with (N, Z) are captured by the nucleus producing an atom with $(N+2, Z-2)$ in an excited state (both nuclear and atomic levels). The capture rate of this rare process ($\lambda_{0\nu ee}$) can be written as [1]:

$$\lambda_{0\nu ee} \propto R|V_{0\nu ee}|^2 \quad (1)$$

where R is the resonance enhancement factor that depends on: the Q_{ee}-value defined as difference between the initial and final atomic masses; the energy and the width of the double electron hole in the electronic shells of the daughter atom; and the excitation energy and the width of the excited daughter nucleus. Furthermore, $V_{0\nu ee}$ is the transition amplitude between the initial and final states and it is proportional to the effective Majorana neutrino mass $m_{\beta\beta}$ and the nuclear matrix element (NME) $M^{0\nu}$. Recent advances in high precision measurements of Q_{ee}-values using Penning traps have allowed the experimental determination of the resonance enhancement factor very accurately [1, 2]. According to these results, the most promising candidates to detect this process having the initial and final nuclei in their ground states are ^{152}Gd, ^{164}Er and ^{180}W atoms. However, the NMEs cannot be determined experimentally and have to be calculated with a suitable method. In this work we have used a state-of-the-art energy density functional method (EDF) to compute $M^{0\nu}$ for these $0\nu ee$ candidates. The same framework was already developed to compute the NMEs for $0\nu\beta\beta$ decay [3] and includes particle number and angular momentum symmetry restoration and shape mixing along the axial quadrupole deformation β_2, using Gogny D1S as the underlying interaction [4]. More details of the method are provided in Ref. [3]. As an example, we show in Fig. 1(a) the ground states (0^+) of the mother ^{152}Gd and granddaughter ^{152}Sm nuclei as a function of the quadrupole deformation. We observe that both nuclei are well prolate deformed. The distribution of ^{152}Sm is wider and peaks at larger deformation ($\beta_2 \sim 0.35$) than the one of ^{152}Gd ($\beta_2 \sim 0.25$). In addition, in Fig. 1(b) we display the intensity of the Gamow-Teller part of the NME as a function of the mother and granddaughter deformation. Most of the intensity is located around the spherical shape and along the diagonal $\beta_2^{\rm ini} = \beta_2^{\rm fin}$. A similar behavior is found for the Fermi part and also for the rest of candidates studied here. However, in Fig. 1(b) we see that the actual many-body wave functions explore only regions that corresponds to quite small intensities- see the shaded area. Therefore, the NMEs are strongly suppressed whenever deformation is taken into account. The final results are summarized in the Table . The resonance enhancement factors R are extracted from Ref. [5]. We obtain quite small NMEs and, correspondingly, very long half-lives that make the experimental finding of $0\nu ee$ process rather uncertain.

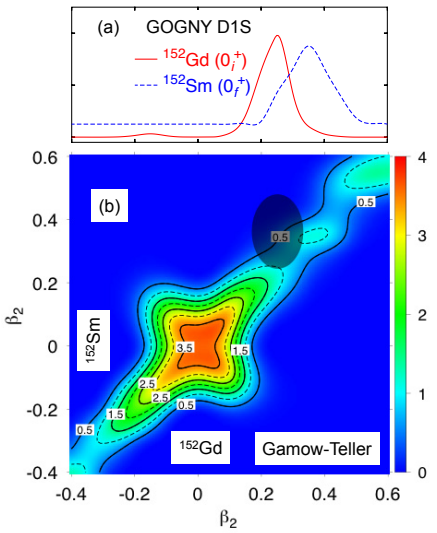

Figure 1: (a) Collective wave functions for ^{152}Sm (continuous) and ^{152}Gd (dashed) as a function of the quadrupole deformation. (b) Intensity of the NME as a function of the mother and granddaughter deformation for Gamow-Teller contributions. Shaded area corresponds to the region explored by the collective wave functions shown in (a).

Nucleus	$M^{0\nu}$	$T_{1/2}(y)$
^{152}Gd	1.07	4.2×10^{29}
^{164}Er	0.64	1.3×10^{34}
^{180}W	0.58	1.6×10^{32}

Table 1: NMEs and estimated half-lives for most probable $0\nu ee$ captures.

References

[1] S. Eliseev et *al.*, Phys. Rev. Lett. **106**, 052504 (2011).

[2] C. Droese et *al.*, arXiv:1111.6377v1. F. T. Avignone et *al.*, Rev. Mod. Phys. **80**, 481 (2008).

[3] T. R. Rodríguez and G. Martinez-Pinedo, Phys. Rev. Lett. 105, 252503 (2010).

[4] J. F. Berger et *al.*, Nucl. Phys. A **428**, 23 (1984).

[5] D. L. Fang et *al.*, arXiv:1111.6862v1.

Phases of dilute nuclear matter and electroweak interactions *

A. Sedrakian, X.-G. Huang, J. Keller, and M. Stein
Institut für Theoretische Physik, J. W. Goethe-Universität Frankfurt am Main, Germany

We study the phase structure, thermodynamics, and the transition from the weak to strong coupling regime in superfluid isospin asymmetrical nuclear matter [1, 2]. As shown recently, the formation of such isospin-asymmetric condensates is relevant to the astrophysical type-II supernovae and dilute tails of the heavy neutron-rich nuclei. Our model solves the Nozières–Schmitt-Rink equations for asymmetrical nuclear matter with a phase-shift equivalent (so-called realistic) interactions [2]. Currently, the theory includes four phases of matter: (1) the unpaired phase, (2) the homogeneous Cooper paired condensate, (3) an inhomogeneous condensate at weak coupling, (4) Bose-Einstein condensate (BEC) of deuterons at strong coupling. The phase diagram has been obtained in the density-temperature plane for fixed asymmetries between the neutrons and protons (i.e. at finite isospin chemical potential). We find that the inhomogeneous phase is favored at low-temperature and weak coupling (i. e. high densities). It goes over to the Cooper paired state at higher temperatures, and to the BEC of deuterons at lower densities.

Electroweak dynamics of baryons in dense matter has been studied within a formalism based on the re-summation of particle-hole ladders in bulk nuclear matter. The non-zero temperature and density response of neutron matter has been studied with respect to four types of perturbations which are associated with the density, spin-density, density-current and spin-density-current operators. The spectral functions of the excitations in each of these channels has been computed and their excitation spectrum has been determined [3]. At low-temperatures, the pair-breaking contribution to the response functions was evaluated in the limit of small three-momentum transfer q, within an effective theory which exploits series expansion in powers of small q/p_F, where p_F is the Fermi-momentum. The perturbative results have been compared to exact numerical results. It was shown that for typical scales of electroweak processes in neutron stars the small-q approximation is justified.

As an application, the pair-breaking neutrino bremsstrahlung – an important process contributing to the neutrino cooling of a compact star – was computed. Within the Standard Model the neutrino emission occurs via vector and axial-vector current interactions. The rate of these processes was computed initially at one-loop and, more recently, including vertex corrections. The one-loop calculations suggest that the neutrino emission via neutral vector-currents is large compared to the emission via axial-vector currents. However, the vertex corrections substantially suppress the emission via vector currents, while they leave the axial vector emission unaffected. As a result, the neutrino emission via vector currents turns out to be subdominant compared to the same emission mediated by the axial-vector current interactions.

Neutrino emission rate from baryonic matter in neutron stars via weak neutral vector interaction was computed up to order $O(v_F^6)$, where v_F is the Fermi velocity in units of speed of light. The neutrino emissivity is enhanced compared to the result at $O(v_F^4)$ order up to 10% for values $v_F \leq 0.4$ characteristic to baryons in compact stars (see Fig. 1).

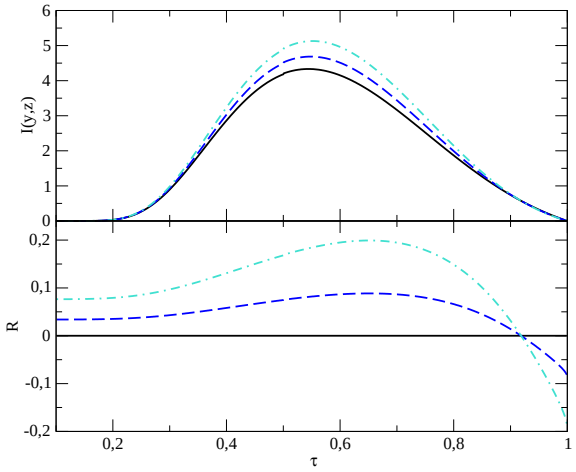

Figure 1: *Upper panel:* The temperature dependence of the (non-dimensional) neutrino emission rate, where τ is the temperature in units of critical temperature. *Lower panel:* The ratio of neutrino emissivity at order $O(v_F^6)$ over that at order $O(v_F^4)$. Dashed and dashed-dotted curves are results at order $O(v_F^6)$ for $v_F = 0.2$ and 0.4, solid lines the same at order $O(v_F^4)$.

References

[1] M. Stein, X.-G. Huang, A. Sedrakian "Phase diagram of dilute asymmetric nuclear matter including inhomogeneous phases", *in preparation*. M. Stein, Master Thesis, 2012.

[2] A. Sedrakian, "BCS-BEC crossover in spatially modulated fermionic condensates," J. Phys. Conf. Ser. **321**, 012028 (2011) [arXiv:1106.1321 [nucl-th]].

[3] J. Keller, A. Sedrakian, "Complete electroweak response functions of neutron matter", *to be submitted to Phys. Rev.*

[4] A. Sedrakian, "Vertex renormalization of weak interactions in compact stars: beyond leading order", *to be submitted to Phys. Rev.*

* Work supported by the DFG and GSI-GU R&D project.

Fermionic molecular dynamics for inhomogeneous bulk fermion systems*

K. Vantournhout[1] *and H. Feldmeier*[1]
[1]GSI, Darmstadt, Germany

The crusts and especially the mantel of a neutron star are excellent examples of inhomogeneous bulk fermion systems where spatial localisations play an important role. While the crust is understood to be a Coulomb lattice of nuclei embedded in an electron gas, the mantel represents the transition zone to the uniform core where the neutron-proton-electron system forms complex-shaped foam like structures [1].

When modelling these inhomogeneous bulk fermion systems at low temperatures—this is the case with the neutron star's crust—one has to work with antisymmetrised many-body states to get the correct fermion behaviour. Fermionic molecular dynamics (FMD) [2], which works with an antisymmetrised product of localised wave packets, should be an appropriate choice. However, due to the long-range character of the Pauli correlations, evaluating bulk fermion matter becomes a tedious task when using the standard FMD approach on a large system. Applying FMD on bulk fermion systems has therefore been a long open question. This has recently been solved within the concept of "periodic boundary conditions" in which an infinite fermion system is created by replicating a finite set of particles periodically over space and antisymmetrising this infinite system [3]. Evaluating expectation values of observables by means of standard FMD is impossible due to the infinite dimensional problem. However, as a result of the periodicity, a peculiar structure is mapped onto the equations of FMD that can be exploited. This way, expectation values of observables of the bulk system can be evaluated through finite sized equations addressing only the original set of particles while keeping track of the fermion properties of the infinite system.

When studying properties of bulk matter, it is important that the constraints of the simulation do not interfere with the result. Hence, the properties of the simulation should be equivalent with those of the macroscopic system. As the macroscopic system is non-periodic, the periodicity embedded onto the simulation should not influence the simulation's results. As long as the correlation volume of the interaction does not exceed the simulation volume, the imposed periodicity works fine. However, serious problems arise in the presence of long-range correlations. Unfortunately, the antisymmetrisation is a non-local entanglement which reaches far out of the periodically repeated unit cell. Nonetheless, the technique described in this report allows to reproduce essential features intrinsic to non-interacting bulk fermions such as the energy density and density distributions in coordinate and momentum space [see Fig. 1].

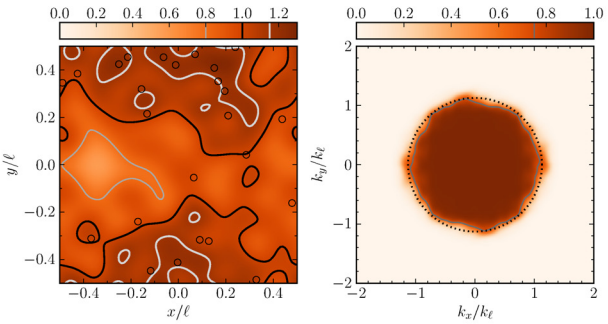

Figure 1: The density distributions (left panel: spatial $\rho_x \ell^2/N$; right panel: momentum $\rho_k k_\ell^2/N$) of $N = 25$ Gaussian wave packets. The wave packets are randomly placed in the unit cell of a square lattice with unit length ℓ and have a width parameter given by $a = (0.2\ell)^2$. The mean momentum of the individual wave packets is set to zero. The densities are normalised and coordinates are expressed in units of ℓ and $k_\ell = \sqrt{N}\pi/\ell$. For the spatial density, the black circles show the positions of the centroids of the wave packets. For the momentum density, the dotted circle represents the Fermi "sphere" of a system of free particles with the same mean density, $k_F = \sqrt{4\pi N}/\ell$.

The formalism not only reproduces intrinsic properties of non-periodic bulk fermion systems but also describes those of periodic systems such as ionic crystals [3]. Furthermore, the use of localised states makes the technique suitable to study inhomogeneous fermion matter, such as the neutron star's crust, by means of molecular dynamics or Monte Carlo methods. Hence, the next steps are to include the forces among the fermions to study the expected foam-like pasta structures and investigate the defects that the periodicity brings into the system.

References

[1] N. Chamel and P. Haensel, Living Rev. Relativity 11, 10, 2008

[2] H. Feldmeier and J. Schack, Rev. Mod. Phys. 72, 655–688, 2000

[3] K. Vantournhout, N. Jachowicz and J. Ryckebusch, Phys. Rev. C 84, 032801, 2011

* Work supported by the Helmholtz International Center for FAIR (HIC for FAIR) within the framework of the LOEWE program launched by the State of Hesse (Germany)

Constraining the nuclear matter equation of state at low densities*

M. D. Voskresenskaya[1] *and S. Typel*[1]
[1]GSI, Darmstadt, Germany

The knowledge of the equation of state (EoS) is required in a wide range of densities and temperatures for the description of astrophysical phenomena, like neutron stars and core-collapse supernovae. Here we concentrate on low densities much below nuclear saturation density, where correlations play an essential role and have an impact on the composition and thermodynamical properties of the matter. There are several ways to describe nuclear matter that are applicable in different regimes of the parameters.

One method is a model-independent approach, which describes a system of interacting particles with the help of virial corrections. Such a virial equation of state (VEoS) [1] provides the correct finite-temperature EoS in the limit of very low densities. It depends only on experimentally determined data, i.e. binding energies of nuclei and scattering phase shifts.

Another approach is based on self-consistent mean-field methods that can successfully be applied at densities near nuclear saturation. Neutrons and protons are the fundamental constituents that are considered as quasiparticles with self-energies containing the information on the interaction which is usually modeled in an effective way and not taken from a realistic nucleon-nucleon (NN) interaction. A recent publication [2] considered a quantum statistical approach to nuclear matter and devised a generalized relativistic mean-field (gRMF) model, which is an extension of the relativistic mean-field model with density dependent couplings (DD-RMF). In the gRMF model light clusters with $A \leq 4$ are included and their dissolution is modeled by a medium dependent shift of the binding energies originating mainly from the action of the Pauli principle. Even though the model contains the same relevant particles at low densities as the VEoS, it does not reproduce exactly the thermodynamical properties of the VEoS.

In this work we aim at connecting the two above approaches with the correct low and high density limits. We consider only two-body correlations and incorporate bound and scattering states effectively in the thermodynamical potential. These states are represented by quasiparticles with medium-dependent energies and degeneracy factors, see [3] for details. The low-density behavior of nuclear matter at finite temperatures is obtained in the modified gRMF approach by means of a series expansion of the grand canonical potential in powers of the nucleon fugacities. From the comparison of the fugacity expansions of the gRMF and VEoS models, consistency relations are derived that connect quasiparticle properties with the nucleon-meson couplings in vacuum and effective-range parameters of NN scattering. For a successful application of the approach, the original gRMF density dependence of the couplings is kept and effective resonance energies are calculated with NN scattering phase shifts. The effective degeneracy factors are assumed to be temperature dependent. They are derived from the consistency relations.

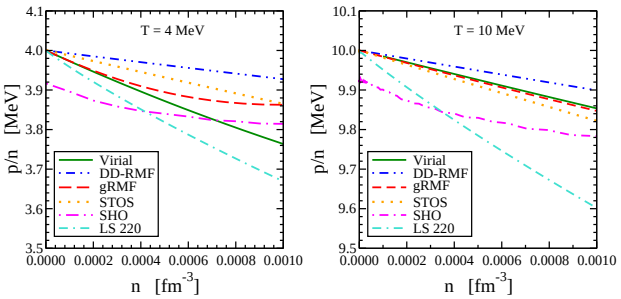

Figure 1: Ratio of pressure over total particle number density, p/n, of neutron matter as a function of the density n for temperatures of $T = 4$ MeV (left) and $T = 10$ MeV (right) in different models. See text for details.

Thermodynamical quantities, see e.g. pressure over density in Figure 1, are compared for the modified gRMF model with the VEoS, the original DD-RMF and other models used in astrophysical applications, in particular the models of G. Shen et al. [4] (SHO), H. Shen et al. (STOS) [5] and Lattimer/Swesty [6] (LS220). The gRMF model with two-body bound and scattering correlations perfectly reproduces the VEoS at very low densities. A further extension to include heavier nuclei with medium-dependent binding energies and finite-temperature excitations is possible and corresponding work is in progress.

References

[1] C.J. Horowitz, A. Schwenk, Phys. Lett. B 638 (2006) 153, Nucl. Phys. A 776 (2006) 55, E. O'Connor, D. Gazit, C.J. Horowitz, A. Schwenk, N. Barnea, Phys. Rev. C 77 (2007) 055803.

[2] S. Typel, G. Röpke, T. Klähn, D. Blaschke, H.H. Wolter, Phys. Rev. C 81 (2010) 015803.

[3] M.D. Voskresenskaya, S. Typel. arXiv:1201.1078 [nucl-th].

[4] G. Shen, C.J. Horowitz, E. O'Connor, Phys. Rev. C 83 (2011) 065808.

[5] H. Shen, H. Toki, K. Oyamatsu, K. Sumiyoshi, arXiv:1105.1666 [astro-ph.HE].

[6] J.M. Lattimer, F.D. Swesty, Nucl. Phys. A 535 (1991) 331.

* This research was supported by the DFG cluster of excellence "Origin and Structure of the Universe", CompStar, a Research Networking Programme of the European Science Foundation, the Helmholtz Nuclear Astrophysics Virtual Institute (NAVI), EMMI, HGS-HIRe and HIC for FAIR.

A Calibration Experiment for the AGATA Pulse Shape Analysis*

S. Klupp[1], *R. Gernhäuser*[1], *R. Krücken*[1,2], *M. Schlarb*[1], *D. Bazzacco*[3], *D. Bortolato*[4], *E. Farnea*[3], *and F. Recchia*[5]

[1]Technische Univerität München; [2]TRIUMF, Vancouver; [3]INFN Padova; [4]INFN LNL; [5]University of Padova

The method of γ-ray tracking will play an important role in γ-ray spectroscopy for the upcoming Prespec campaign at GSI but also for different experiments at the future FAIR facility. The most important input for reconstructing γ-ray scattering paths are the γ-ray interaction points which are determined by pulse shape analysis (PSA). The currently most successful PSA used in AGATA is based on a comparison of the experimental signal shapes to reference signals of a simulated pulse shape basis with known interaction points.

To study the performance of the PSA in terms of the position resolution online, directly at the experimental site, a calibration experiment was developed. It is based on the reconstruction of interaction points of γ-rays from positron annihilation, detected in coincidence in two opposing Ge crystals. The position resolution is extracted exploiting the fact that these γ-rays are emitted nearly back to back. For a quantitative determination of the resolution, the experimental data are compared to the results of a Geant4 based Monte Carlo simulation with adjustable position resolution. The simulation also takes into account that the current PSA algorithm reconstructs only one interaction point per segment, which corresponds to the energy weighted barycenter of all interaction positions in the segment. For mimicking a position resolution in the simulation the simulated barycenters are smeared with a Gaussian distribution. Its standard deviation σ defines the position resolution. Generally, the calibration experiment allows to study different event types. As 511 keV γ-rays undergo typically two to three interactions in Ge, the resolution of the barycenter can be determined by selecting events featuring an energy deposition of 511 keV in a single segment. Additionally, single interaction points can be studied by analyzing Compton scatterings from one segment into another segment. Independent of the event selection, a position resolution is obtained with the figure of merit d which corresponds to the distance between the source and the connection line between the barycenters in the opposing segments. As shown in fig. 1, d is strongly dependent on the position resolution. Thus, to extract the resolution the simulated spectrum of d is fitted to the experimental one.

The concept of the calibration method was verified with experimental data using the first installed crystals of the AGATA Demonstrator (c.f. fig. 2). A point-like ^{22}Na source was positioned directly at the cryostat of the A006 detector. Thus, due to the asymmetric source position, the resolution of A006 can be determined nearly independent of the other crystals A002 or A003 which detect the second γ-ray. To gain a deeper insight into different crystal regions, the measurement was conducted with various source positions. In the analysis the pulse shape bases JASS [1] and ADL [2] are compared leading to slightly different results in different regions of the crystal. This shows that there is still some room for improvement on the quality of both databases. Generally, the resolution deteriorates with increasing segment size. In summary, all obtained barycenter position resolutions are in the range $1.0\,\text{mm} < \sigma < 2.6\,\text{mm}$. Moreover, the analysis of single interactions showed that the position resolution for an energy deposit between 100 and 300 keV is approximately inversely proportional to the square root of the energy.

It was demonstrated that the coincident detection of annihilation γ-rays allows an easy and systematic investigation of the position resolution. Thus, it is an appropriate and versatile tool to optimize the simulated signal bases and prove the detector performance online.

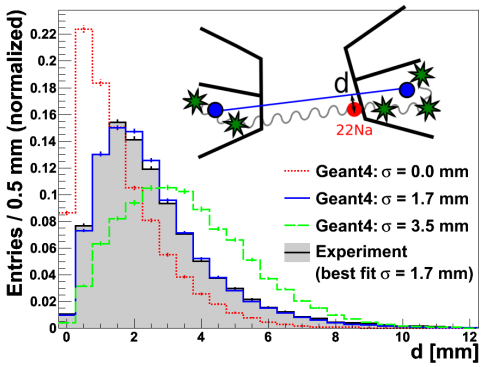

Figure 1: Influence of the position resolution on d.

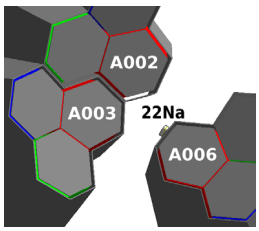

Figure 2: Experimental setup.

References

[1] M. Schlarb et al., "Pulse shape analysis for γ-ray tracking (Part I): Pulse shape simulation with JASS", Eur. Phys. J. A (2011) 47: 132

[2] B. Bruyneel et al., "AGATA Detector simulation Library (ADL) v.2.0", 2008, `http://www.ikp.uni-koeln.de/research/agata/index.php?show=download`

* Work supported by BMBF, contract No. 06MT9156.

Study of the characteristics of GEM for the FAIR experiment CBM

S. Biswas[*1], *A. Abuhoza*[1], *U. Frankenfeld*[1], *J. Hehner*[1], *C.J. Schmidt*[1], *H.R. Schmidt*[2], *M. Träger*[1], *S. Colafranceschi*[3], *A. Marinov*[3], *and A.Sharma*[3]

[1]GSI, Darmstadt, Germany; [2]University of Tübingen, Germany; [3]CERN, Switzerland

Gas Electron multipliers (GEM) will be used in CBM Muon Chamber (MUCH) located downstream of the Silicon Tracking System (STS) of the CBM experiment along with other sophisticated detectors. In GSI detector laboratory an R&D effort is launched to study the characteristics of GEM detectors for the CBM experiment. The primary goals of this R&D program are: (a) to verify the stability and integrity of the GEM detectors over a period of time, during which a charge density of the order of several Coulomb/cm^2 is accumulated in the detector; (b) to establish the functioning of a triple GEM as a precise tracking detector under the extreme condition of the CBM experiment; (c) to study usual parameters e.g., efficiency, rate capability, long term stability, spark probability by varying conditions like temperature, gas composition or radiation dose.

One triple double mask GEM detector obtained from CERN with 3 mm drift gap, 2 mm transfer gap and 2 mm induction gap has been studied systematically. The voltage to the drift plane and individual GEM plates has been applied through a voltage divider chain. Although there is a segmented readout pad the signal in this study was obtained from all the pads summed by a add up board and a single input is fed to a charge sensitive preamplifier. After that a Lab-View based data acquisition system is used. The variation of the effective gain, resolution of this detector with variation of the applied high voltage has been measured with Fe^{55} X-ray source for different gas mixtures and with different gas flow rates etc. The fraction of large signal (probable spark) relative to average signal has also been measured by setting different threshold values.

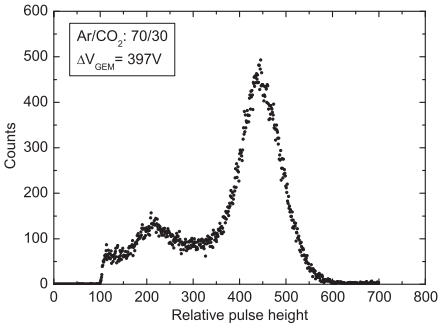

Figure 1: Pulse height distribution for 5.9 keV Fe^{55} source obtained with triple GEM detector.

The detector has been operated with Argon and CO_2 with different ratios such as 70/30, 80/20 and also with different flow rates e.g. 50 ml/min, 100 ml/min and 200 ml/min. Figure. 1 gives an example of pulse height distribution for a Fe^{55} X-ray source with Argon and CO_2 in 70/30 ratio at ΔV_{GEM} = 397V. The variation of effective gain and energy resolution (FWHM) with that of ΔV_{GEM} are shown in Figure. 2. It is clear that the gain increases exponentially and the energy resolution improves with the increase of ΔV_{GEM} [1].

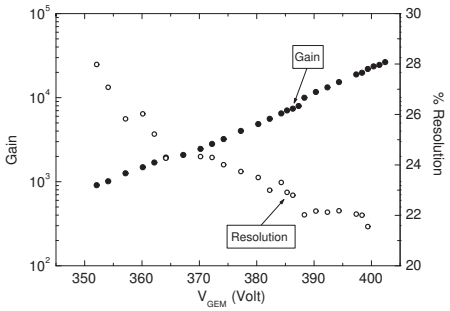

Figure 2: Effective gain curve of the triple GEM, operated in argon/CO_2 : 70/30 and energy resolution as a function of ΔV_{GEM}.

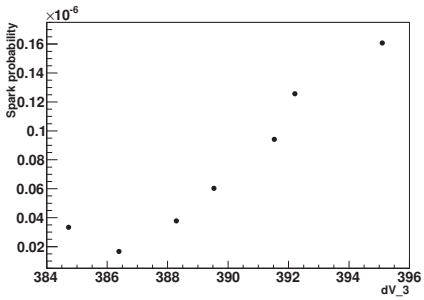

Figure 3: Spark probability as a function of ΔV_{GEM}.

Fabrication of new 10 cm $\times$ 10 cm GEM detector with newly designed box and their characterisation is also done. Testing of GEM without voltage divider chain and using a seven channel high voltage module, dedicated for triple GEM has also been performed. Both double mask and single mask triple GEM detectors have been tested at high rate at CERN SPS/H4. In this test the hadronic shower detection by GEM, the spark probability due to $\sim$ 150 GeV Pion beam has been measured. The spark probability for a double mask triple GEM with Fe block as a function of ΔV_{GEM} is shown in Figure. 3. Building and testing of large area single mask GEM is a future plan.

References

[1] S. Biswas et al., Proc. DAE Symp. on Nucl. Phys, Vol.56 (2011) 1068 .

* S.Biswas@gsi.de

Radiation Tolerant Operation of a Commercial Micro Controller for Applications in Front End Electronics*

V. Kleipa[1]

[1]GSI, Darmstadt, Germany

Abstract

The next version of front-end electronics boards to be utilized for the prototype detector development of e.g. the CBM experiment will comprise a micro controller (MCU) for the system's slow controls. The selected micro controller is a state of the art MCU without any specific radiation qualifications. It is required to determine the radiation tolerance of this device. Also a new concept of runtime software needs to be verified. The idea is to reinitialise the MCU just before any slow control command is send to the MCU and then executed. Single event upsets (SEUs) that have might occurred thus will be removed before a new command request is executed.
A RISC micro controller - Atmel ATtiny88 [1] - with Harvard architecture was selected. The program ROM is based on a flash memory. A RISC instruction set supports single cycle executions at 8 MHz clock frequency.

Hardware

A printed circuit board was designed and assembled comprising an ATtiny chip. The MCU is placed in the middle of the board, shown in Fig. 1. The PCB features a cut-out just below the MCU's position and only very few decoupling capacitors are located in its vicinity. This was done to reduce the radiation length and to minimize possible activation of material in the beam. The MCU is connected via an SPI bus and a reset line to a standard PC printer port. For the beam adjustment X-ray pictures of the MCU were taken to determine the die position.

Software

The task of the micro controller's software is to receive and to acknowledge the commands sent from the control-PC. The reception of the commands and the returned results are checked with additional CRC-bytes. A RAM area of 256 bytes is used as a sensor for SEUs and can be filled with bit-patterns. During irradiation, this buffer is read out continuously with SPI commands and compared in the PC with the default contents. Communication and RAM content are thus simultaneously checked. SEUs in the RAM or communication errors are recorded in the PC. According to the requirements the PC can initiate a reboot on the micro controller.
The SPI clock is 10 µs per bit cycle and the commands to be serviced consist of 2-6 bytes. The MCU rebooting/reset time was reduced from initially 200 µs to 15 µs. This requires the C-compiler pre-initialising the variables to be turned off.

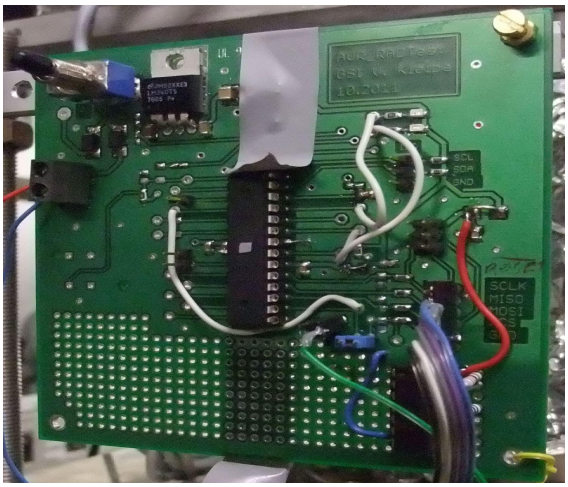

Figure 1: MCU board prepared for beam test software.

Preliminary Results

In case of the short reset time, it is straight forward to execute a complete MCU reset before a slow control command is sent. The advantage is a high probability of a SEU-cleaned micro controller.

Next Steps

The micro controller and the SW will be tested in beam in order to determine its radiation tolerance. Observables will be for instance SEUs, single-event latches (SELs). The runtime software itself, with fast reboot, will also be tested under real conditions.

References

[1] http://www.atmel.com/dyn/resources/prod_documents/doc8008.pdf

* Work supported by EU-FP7 HadronPhysics2

Radiation hardness test of the diamond Start-Veto system for the HADES.*

J.Pietraszko[1], *W.Koenig*[2], *and M.Träger* [2] *for HADES collaboration.*

[1]Institut für Kernphysik, Goethe-Universität Frankfurt, Germany; [2]GSI Helmholtz Centre for Heavy Ion Research GmbH, Darmstadt, Germany

For the heavy ion experiments with HADES it is necessary to determine the reaction time (T0) with a precision better than 50 ps (sigma). The measured T0 is a part of the Time of Flight measurement used for the particle identification. The recently upgraded HADES spectrometer, prepared for high multiplicity and high rate experiments, shows significantly improved performance [1] and is able to study reactions at Au-beam intensities of about 2-3$\times 10^6$ ions/s. Such beam intensities pose challenges on a start detector mainly in terms of the rate capability and the radiation hardness. Therefore for the heavy ion experiments a diamond based detector has been used as a start detector. The version proposed as a Start-Veto detection system based on scCVD material for upcoming Au+Au HADES run is described in [2]. As a part of this project it was important to demonstrate that the proposed system would operate satisfactorily at the required beam intensities. For this purpose a dedicated, five day long test experiment has been performed in August 2011 when in total about 1.04 $\times 10^{11}$ Au ions / mm^2 have been detected by the Start detector. Scaling with the nuclear nuclear cross section this corresponds to $\sim\times 10^{12}$ p(n) / mm^2. During the whole experiment time resolution and efficiency have been monitored. Already the very first visual surface inspection after detector dismounting indicated some deterioration of the metallization of the Start detector. In Figure 1 the damage to the surface of the metallization is shown.

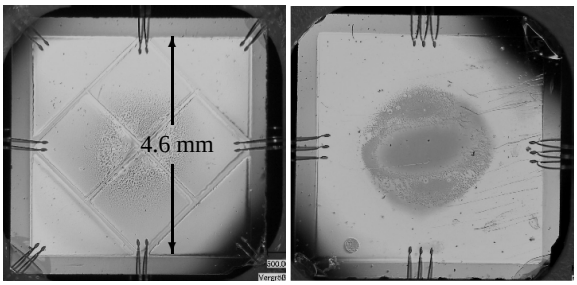

Figure 1: Photographs of the front and back sides of the Start detector after irradiation with Au beam.

As the scCVD material is well known for its excellent energy and time resolution these properties can be easily used to investigate the radiation damage to the material as shown in Figure 2. The ADC spectra measured with a mixed alpha source (^{239}Pu/^{241}Am/^{244}Cm) with the detector before irradiation - left, and after -right are shown. Note also that the right picture shows the result for the detector which has been remetallized after the test experiment. As clearly visible in the collected spectra, a strong reduction of the charge collection efficiency in the scCVD material has been observed. As the Start detector in HADES is used

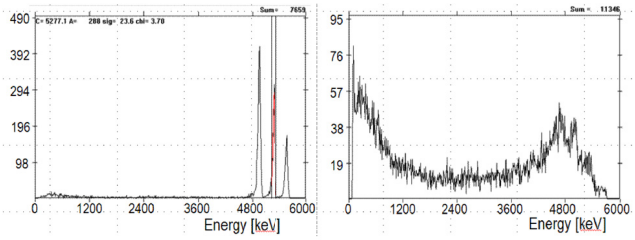

Figure 2: High resolution ADC spectra obtained with an alpha source (^{239}Pu/^{241}Am/^{244}Cm). Excellent energy resolution measured for one channel (left) compared to the result obtained after heavy irradiation (right).

to determine the T0 of the reaction also the properties in terms of time resolution have been investigated. After applying the radiation dose mentioned above the measured time resolution got worse by a factor of more than 2, going from about 40ps - before irradiation to about 100ps after irradiation.

The determined efficiency of the Start detector as a function of the radiation dose depicted in Figure 3 shows a continuous deterioration over the duration of the experiment. The visible steps in the efficiency plot corresponds to changes by a few tenths of millimeter in the beam position.

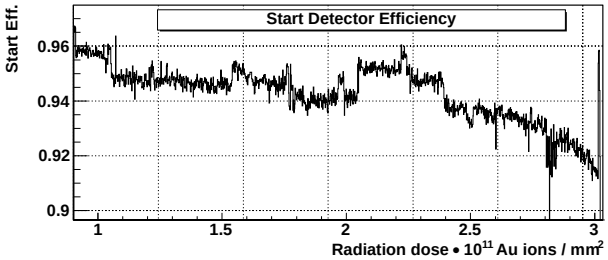

Figure 3: Dependence of efficiency of the start detector on the radiation dose for Au ions.

Acknowledgements: We highly appreciate the support of the GSI Detector Laboratory and the GSI Target Laboratory.

References

[1] J. Michel, The New Trigger and DAQ System of HADES, GSI Scientific Report (2011)

[2] J.Pietraszko et al, A diamond Start-Veto system for the HADES heavy ion experiment, GSI Scientific Report (2010)

* supported by BMBF (06 FY 9100 I), HIC for FAIR, EMMI and GSI

Development of Heteroepitaxial Single-Crystal Diamond Sensors*

E. Berdermann[1], M. Ciobanu[1,2], M. S. Rahman[1,3], M. Träger[1], M. Fischer[4], S. Gsell[4], M. Schreck[4], and C. Stehl[4]*

[1]GSI, Darmstadt, Germany; [2]ISS, Bucharest, Romania; [3]Technical University and OncoRay, Dresden, Germany; [4]University of Augsburg, Augsburg, Germany

Recent CVD diamond (CVDD) samples grown by heteroepitaxy on 4-inch Ir/YSZ/Si001 substrates [1] showed for the first time a similar behaviour to that of homoepitaxial single-crystal diamond (SC) detectors. This improvement is attributed to the use of the upper part of a thick (~ 1mm) 'quasi single-crystal' Diamond-on-Iridium (DOI) plate for the detectors. We present the hole-drift characterization results obtained from a DOI sensor (DOI954, 290µm) grown in 2011 as well as the data of the best sample grown in 2010 (DOI886-2, 320µm). We compare the DOI characteristics to that of a commercial SC sensor (SC EBS-3, 393 µm) and to a polycrystalline (PC) sample (PC-PFX350, 350 µm).

The DOI sensors have been metallized with sandwich quadrant electrodes. The individual sectors showed similar results confirming a good area-homogeneity of the films. By applying the transient-current technique (TCT) with short-range α-particles we tested the homogeneity of the crystal structure, which controls the effective internal field. Figure 1 shows the TCT signals obtained. The applied electric field is noticed in V/µm. The triangular PC signals (blue lines) illustrate impressively the incomplete charge collection in PC sensors. Moreover, the increasing signal widths at increasing bias measured in the range 0.3 - 2.9 V/µm are in contradiction to the expected decreasing trend, as a consequence of the increase of the carrier drift velocity at higher fields. This behaviour is ideally demonstrated by the SC reference sample (inset, red pulses). The trapezoidal signal shapes obtained for every value of the electric field illustrate complete carrier drift at constant velocity in the absence of charge trapping (flat-top). In spite of the high CCE > 97% measured for the DOI 886-2 sensor [2], the width of the α-TCT signals was essentially independent of the electric field. We explain this behaviour by 'capture and release' of charge carriers by shallow traps. Their trapping time is supposed to be in the microsecond range, i.e. too slow for the DBA but within the shaping time constant of the charge-sensitive amplifiers used to measure the CCE. In contrast, the development of the signals recorded with the recent DOI 954 detector (black traces) reveals convincingly both features, the increase of the drift velocity and at E > 0.3 V/µm the arrival of the charge carriers to the opposite electrode. However, the slope of the 'flat-top' indicates significant charge trapping, which occurs most likely at residual crystal dislocations. A remaining puzzle is the observed improvement of the charge-drift and collection in case of differently biased neighbouring sectors (Fig. 1, dotted signal: Q1@1.4V/µm; Q2Q3Q4@1.0V/µm). This may be due to a discharge of a previously accumulated charge reservoir in the diamond-contact interface.

A rapid increase of the drift velocity at low fields (decreasing width of the TCT signals), causes a rapid increase of the CCE to high levels - as it is demonstrated in Figure 2 by the SC sensor (red dots, 99%) and by the recent DOI sample (black diamonds, 93%). The 2010 sample achieved even 97% but at higher fields, whereas the PC sensor (blue dots, - 20%) is simply worse and cannot be used for energy measurements. Interestingly, the energy resolution is improved for samples showing a 'steep' plateau but not the highest CCE. We measured (Fig. 3) 0.1% for SC-EBS3 (red), 1.8% for DOI954 (black) and 3.5% for DOI886-2 [2] (not shown here).

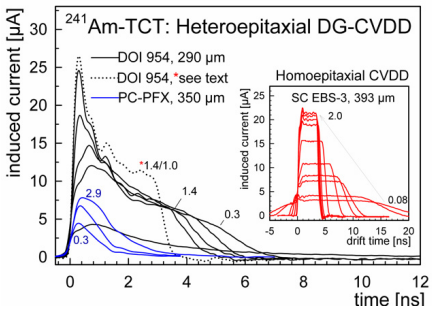

Figure 1: Averaged TCT signals at increasing field: DOI 954 (black); PC-PFX350 (blue); SC EBS-3 (red, inset).

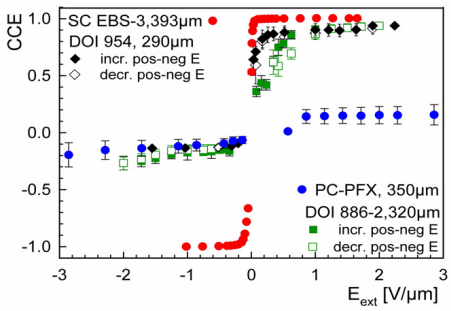

Figure 2: CCE at increasing electric field. (see text)

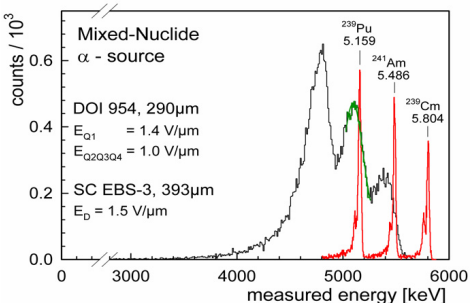

Figure 3: Mixed nuclide α-spectra of a recent DOI (black line) and of a SC diamond sensor (red line) compared.

References

[1] C. Stehl et al., GSI Annual Reports 2010, 2011.
[2] E. Berdermann et al., GSI Annual Report 2010

* Work supported by the EU, FP7 Proj. RII3-CT-227431

Growth of Heteroepitaxial CVD Diamond Films on Ir/YSZ/Si(001) for Detector Applications: Scale-Up and Crystal Quality Improvement*

C. Stehl[1], M. Fischer[1], S. Gsell[1], M. Schreck[1,#], E. Berdermann[2], M. S. Rahman[2], and M. Träger[2]

[1]Universität Augsburg, Germany; [2]GSI, Darmstadt, Germany

In the framework of the "CARAT" collaboration, which executed work package 15 of the EU FP7 "HadronPhysics2" project, the diamond group at the University of Augsburg was responsible for the development and growth of heteroepitaxial diamond films, which shall be used in particular for tracking and ToF measurements of heavy ions and minimum ionising particles.

Motivation

For future particle accelerator experiments, e.g. at FAIR, we aimed at developing novel, advanced diamond sensors grown by chemical vapour deposition (CVD), capable of replacing the commonly used silicon tracking devices and being furthermore an advantageous alternative to polycrystalline or single-crystal diamond sensors used so far in beam diagnostics and timing applications.

During the reporting periods of 2010 and 2011, very promising α-particle and heavy ion tests were conducted at GSI, showing very high values of charge collection efficiency (> 95%) and excellent time resolution (< 20 ps) of our heteroepitaxial CVD diamond films grown on Ir/YSZ/Si(001). This encouraged the scale-up of the detector crystals to lateral dimensions beyond the reach of homoepitaxial diamond single crystals. More effort was made in order to characterise the heteroepitaxial material with respect to structural crystal quality, investigating especially the role of dislocations.

Scale-up

The growth of heteroepitaxial diamond films on the Ir/YSZ/Si(001) multilayer system by microwave plasma enhanced CVD was established at the University of Augsburg in 2004 [1]. A layer of YSZ (yttria-stabilised zirconia) is deposited on a 4-inch Si wafer by pulsed laser deposition. In a second step a film of Ir is deposited on top of the YSZ layer by electron beam evaporation.

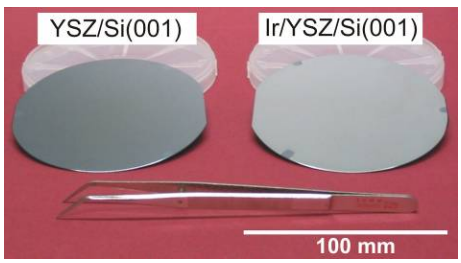

Figure 1: 4 inch silicon wafers after application of YSZ and iridium films.

* Work supported by the EU, FP7 Proj. RII3-CT-227431.

matthias.schreck@physik.uni-augsburg.de

The heteroepitaxial growth concept inherits the potential of being scaled up in order to synthesise wafer-size diamond films in the future [2]. At present, diamond nucleation and growth on large areas with high quality (i.e. esp. free of impurities and cracks) is still a huge challenge. Nevertheless, at the end of the "CARAT" project we were able to synthesise two large diamond crystals of 18 x 18 mm² lateral size (around four times the area of the largest available homoepitaxial diamond samples), one of which is shown in Fig. 2. The remaining dark spots on the sample originate from few non-epitaxial crystallites, which will be avoided in the future by further optimisation of the plasma growth parameters.

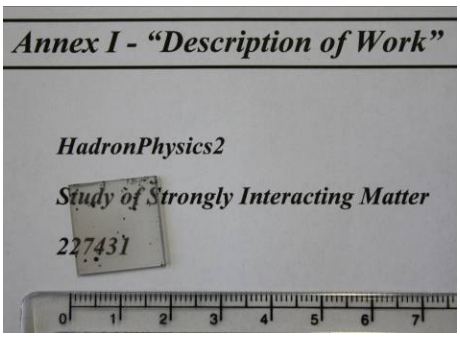

Figure 2: Large transparent heteroepitaxial diamond sample. Scale is in cm.

Crystal quality: the role of dislocations

So-called threading dislocations are the predominant crystal lattice defect in our heteroepitaxial films. Their density is assumed to decrease with larger film thickness. Indeed, the very high α-particle CCE values could only be achieved by using the upper part of a 1 mm thick diamond film for the detector. The quantitative evaluation of the dislocation density and the investigation of its evolution with increasing film thickness are in the focus of current work. First results have been obtained. This topic will be one of the main issues in the upcoming "ADAMAS" project, which is part of "HadronPhysics3" and will continue the collaboration between GSI and the University of Augsburg.

References

[1] S. Gsell, T. Bauer, J. Goldfuß, M. Schreck, and B. Stritzker, Applied Physics Letters 84 (2004) 4541.

[2] M. Fischer, S. Gsell, M. Schreck, R. Brescia, and B. Stritzker, Diamond & Related Materials 17 (2008) 1035.

GEMEX, a compact readout system*

B. Voss†, F. Baraki, B. Ernst, F. Garcia[1], J. Hoffmann, V. Kleipa, J. Kunkel, N. Kurz, S. Ndiaye[2], A. Prochazka, I. Rusanov, C.J. Schmidt, M. Shizu, P. Skott, D. Soyk, C.J. Tchatcho

GSI, Darmstadt, Germany; [1]Helsinki Institute of Physics, Helsinki, Finland;
[2]Ecole Nationale Supérieure d'Ingénieurs de Caen, Caen, France

Tracking-detector systems (see Fig. 1), like e.g. the PANDA GEM-Tracker [1] or Time-Projection Chambers (GEM-TPC) [2,3,4] currently under construction usually realize large channel numbers in the order of several 1000 to be processed. In order to avoid huge amounts of data to be transmitted over large distances, the front-end electronics employed has to be intelligent enough to perform online feature extraction in the vicinity of the detection volume. In order to cope with these demands, the GEMEX readout system has been developed in close collaboration between GSI-EE and GSI-DL departments. It comprises the functionalities of two main parts of a readout chain [5] based on the EXPLODER card and a front-end system with LVDS outputs as e.g. the NXYTER [6] ASIC (see Fig. 2). This provides access to the respective detector signals for the Multi-Branch System (MBS) [7] community in cases where an external trigger may be applied (see references for details on the system).

The GEMEX (**EX**ploder for **G**as-**E**lectron-**M**ultiplier applications, see Fig. 3) is a 256 channel front-end board with optical link extension, a pipeline ADC with a sampling rate of max. 32 Ms/s (2 ch) and a resolution of 12 bit (with an analogue range down to 600 e^- and a dynamic range of 120 ke^-). It hosts trigger- and time-stamp logics and an external clock input to a Lattice FPGA and a high precision PLL synthesizer. The size of the actual board is 104 mm x 95 mm x 1.6 mm. It is supplied with 6.3 V@2.1 A. Taking care of the heat produced by the front-end electronics is one of the pre-requisites for large detector systems in dense setups. The heat management of the GEMEX card is realized by a partial solid backing of copper and direct mounting of the ASICs on the heat spreader. Due to stringent spatial restrictions heat produced is taken away effectively via the edges where an active fluid cooling system is flanged to the surfaces.

Currently a revision of the board with reduced size, providing reduced power consumption, improved heat management (e.g. edge plating) and applying the 2nd revision of the XYTER ASIC is under construction. The so far copper-based trigger connection will be replaced by an optical link to realize a solely optical communication. The possibility of a replacement of the copper heat spreader by an aluminium one will be investigated. Tests under realistic experimental conditions with special focus on the sensibility to magnetic fields and improvements of the radiation hardness are foreseen in the near future. Moreover, the ultimate goal is the implementation of a 'triggerless' system intrinsically provided by the XYTERs architecture for future use e.g. within PANDA or SFRS.

* Work supported by EU, 7th framework program
† Corresponding author: B.Voss@GSI.de

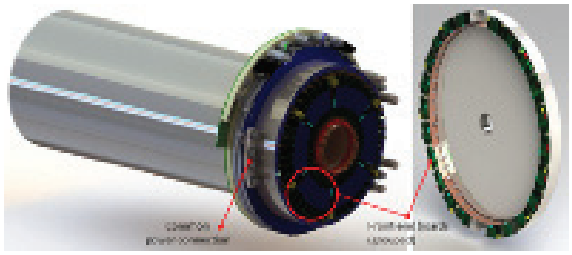

Figure 1: Sketch of GEM-TPC (left), GEM-Disc (right).

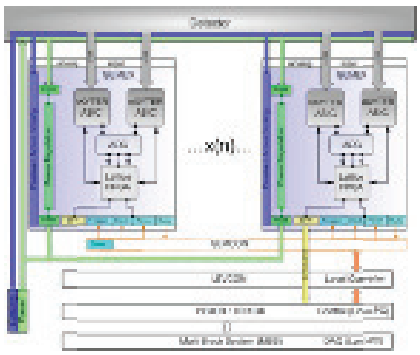

Figure 2: Sketch of the GEMEX readout chain.

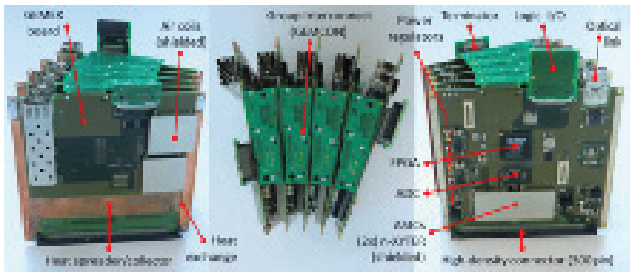

Figure 3: Photography of several GEMEX/GEMCON front-end cards forming a single readout unit.

References

[1] B. Voss et al., GSI Scientific report 2009, GSI Report 2010-1, 2010, p. 338.
[2] B. Voss et al., GSI Scientific report 2009, GSI Report 2010-1, 2010, p. 337.
[3] H. Angerer et al., GSI Scientific report 2010, GSI Report 2011-1, 2011, p. 111-115.
[4] F. Garcia et al., Proceedings of the IEEE Nuclear Science Symposium Conference 2011, 2011, Valencia, Spain, p.1788-1791
[5] http://www.gsi.de/informationen/wti/ee/elekt_entwicklung/
[6] A. Brogna et al., NIM A 568 (2006) 301-308.
[7] H.G. Essel, N. Kurz, IEEE trans. on Nucl. Science 47 (2000) 337-339; and http://daq.gsi.de

Tests for an active gas target*

M. Freudenberger[†1], *C. Eckardt*[1], *J. Enders*[1], *A. Göök*[1], *J. Hehner*[2], *P. von Neumann-Cosel*[1], *A. Oberstedt*[3,4], *S. Oberstedt*[5], *and H. Simon*[2]

[1]Institut für Kernphysik, TU Darmstadt, Germany; [2]GSI, Darmstadt, Germany; [3]Akademin för Naturvetenskap och Tekinik, Örebro Universitet, Sweden; [4]Fundamental Fysik, Chalmers Tekniska Högskola, Göteborg, Sweden; [5]EC-JRC IRMM, Geel, Belgium

Introduction

Active targets provide access to new experimental investigations with applications ranging from nuclear reactions of fast beams to decay spectroscopy. Among ohters, plans exist to utilize active targets also at the R^{3}B experiment at FAIR.

To extend the possible applicability of active targets to fission reactions, we investigate the utilization of an active gas target containing UF_6. In order to test UF_6 as an admixture to standard counting gases (e.g. argon) and to study its properties, an ionization chamber has been built at Technische Universität Darmstadt.

Experimental Setup

A chamber for testing UF_6 as a gas-admixture was designed as a Frisch-grid ionization chamber with a distance $D = 4.2\ \mathrm{cm}$ between cathode and grid, and a distance of $1\ \mathrm{cm}$ between grid and anode. The electrons, created by the energy loss of charged particles inside the active gas volume, produce a signal at the anode, which is proportional to the deposited energy. For a typical charged particle inside the active volume, the center of gravity of its charge distribution is denoted by $\overline{X}$. With the distance D between cathode and grid, one obtains the ratio $\overline{X}/D$, which defines the suppression of the signal induced at the cathode relative to the anode signal, and consequentially one can deduce the emission angle of the charged particle.

Results from the first tests

The functionality of the chamber at different temperatures between $30\ ^\circ\mathrm{C}$ and $70\ ^\circ\mathrm{C}$ was demonstrated, with special attention on the signal quality, which can be seen in Fig. 1. Only low-energy alpha particles are completely stopped inside the argon, due to the dimensions of the chamber. The produced electrons induce a signal on the cathode and drift along the field lines towards the anode. Clearly separated signals are visible in the two-dimensional plot, which indicates a high resolution due to the pure argon atmosphere. In the next step different mixtures of argon gas and small amounts of UF_6 were investigated, starting from one mass per cent of uranium up to two mass percent, in order to study the behavior of the gas mixture with respect to signal quality and electron drift velocity. Figure 2 gives an indication of the signal quality with an amount of two mass per cent uranium in the system. Adding UF_6 to the argon gas obviously distorts the signals. We note that in this case the mean free range of the alpha particles from the calibration source exceeds the dimensions of the chamber. The alpha particles are not completely stopped, and consequently the signals are washed out. Two lines with lower intensity can be seen at lower energies, as well. They originate form the alpha decays of ^{238}U and ^{234}U, respectively, which take place close to or on the surface of the electrodes.

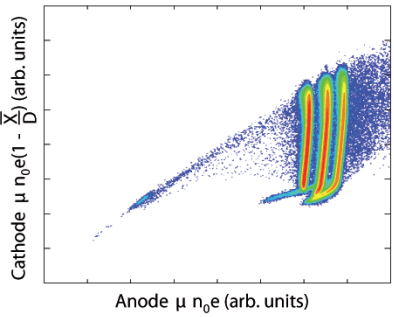

Figure 1: Two-dimensional display of the cathode signal (ordinate) vs. the anode pulse height (abscissa) in a logarithmic scale for pure Ar gas and $1055\ \mathrm{mln}$ Ar, at $70\ ^\circ\mathrm{C}$. Signals originate from a mixed α source located at the cathode.

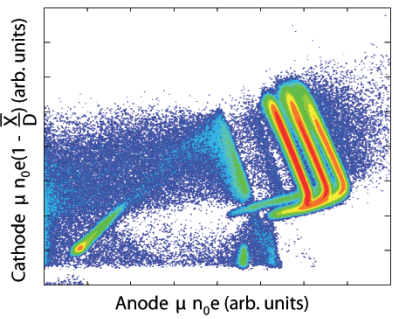

Figure 2: Two-dimensional display of the cathode signal (ordinate) vs. the anode pulse height (abscissa) in a logarithmic scale for $1055\ \mathrm{mln}$ Ar with 2 mass per cent uranium, at $70\ ^\circ\mathrm{C}$.

* Work supported through the TU Darmstadt - GSI cooperation agreement, by the state of hesse through the LOEWE center HIC for FAIR and in part through SFB634.

† mfreudenberger@ikp.tu-darmstadt.de

Memory and Polarization Effects in Heteroepitaxial 'quasi' Single-Crystal Diamond Detectors*

M. S. Rahman[1,2], E. Berdermann[1,], M. Ciobanu[1,3], M. Träger[1], M. Fischer[4], S. Gsell[4], M. Schreck[4], and C. Stehl[4]*

[1]GSI, Darmstadt, Germany; [2]Technical University of Dresden and OncoRay, Dresden, Germany; [3]ISS, Bucharest, Romania; [4]University of Augsburg, Augsburg, Germany

The trapping of drifting electrons and/or holes in the deep defect levels of defective diamond detector materials causes the build-up of an internal space charge. Subsequently created electron-hole pairs will experience an altered electric field inside the detector. A method, which is called priming or pumping, is used in order to stabilize diamonds before their usage as nuclear detectors. Priming is preferably carried out with penetrating radiation (^{90}Sr electrons) which ionizes homogenously the bulk material. The ionized charge carriers passivate the defects along their drift path. Depending on the spatial distribution and the nature of the traps, these processes lead either to polarization and/or to memory effects [1], which consequently enable detector signals at zero bias voltage. The 'memory signals' are defined as detector signals of the same polarity as of the previously biased detector (Fig. 2, left). In case of polarization, the detected signal is of opposite polarity (Fig. 2, right).

To investigate polarization and memory effects, the detector was first operated for 30 minutes in electron or hole drift configuration (Fig. 1). Due to the short range of ^{241}Am α-particles in diamond (~13µm), only one charge carrier species contributes to the detector signal. The pulses were amplified with a non-inverting diamond broadband amplifier (DBA) and monitored with a 6 GHz DSO of 20 GS/s resolution. After this time of biased operation, the high voltage was tuned as fast as possible to zero. The still appearing detector signals were continuously recorded for a long period of time (Fig. 3).

For single crystal CVD diamond (scCVDD) negligible polarization and no memory effects could be measured - in contrast to polycrystalline CVD diamond (pcCVDD) detectors, which are often influenced by both effects. Interestingly, the 'quasi single crystal' Diamond-on-Iridium (DoI) sensors showed only positive signals at zero bias, independent of the polarity of the previously applied bias (Fig. 2). That means, the memory effect in the tested DOI film exclusively appears after electron drift, whereas polarization after hole drift configuration, respectively.

Concluding, the remaining internal electric field at zero bias is comparable to the effective field generated during electron drift configuration. Therefore the polarization and memory effects in the tested DoI sample are supposed to be dominated by only one type of traps - in contrast to the pcCVDD in these measurements. Electron traps are suspected to be responsible, because the charge collection efficiency (CCE) of DoI is for electron drift significantly worse than for hole drift [2].

The count rates of detected signals were recorded in intervals of 5 min and the time constant (τ) of the rate decay of the polarization events was extracted by fitting an exponential to the experimental data (Fig. 3, right). Comparing initial count rate (f_0) and time constant, the strength of polarization in the DoI samples lies between that of pcCVDD and scCVDD, ($\tau_{PC} < \tau_{DOI} < \tau_{SC;}$ $f_{0PC} > f_{0DOI} > f_{0SC}$). Eventually, it was noticed that pcCVDD polarizes immediately after biasing, whereas scCVDD very slowly.

* Work supported by the EU, FP7 Proj. RII3-CT-227431 and MC-PAD.

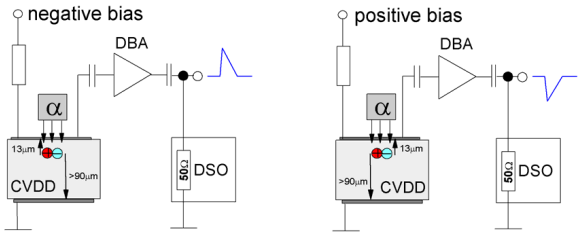

Figure 1: Measurement setup in electron drift configuration (left) and hole drift configuration (right).

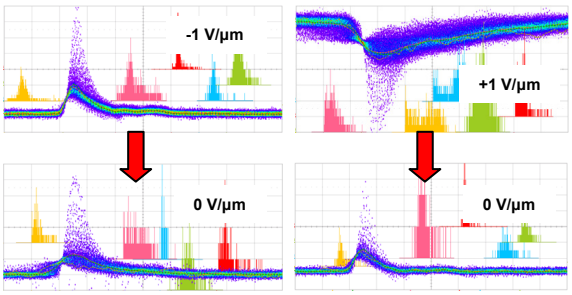

Figure 2: Illustration of memory (left) and polarization effect (right) in DoI 886-2. The DSO displays a 5 ns time window. The green traces are 'most probable' α- signals.

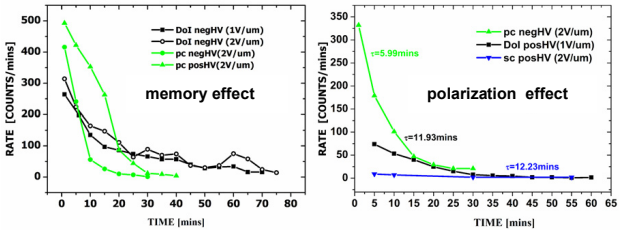

Figure 3: Count rate of memory and polarization signals versus time in different types of CVD diamond detectors.

References

[1] A. Lohstroh et al., J. Appl. Phys. 101(2007) 063711.
[2] E. Berdermann et al., this report.

The APFEL - ASIC for the Silicon Strip Detector Readout at TASCA*

P. Wieczorek[1], *H. Flemming*[1], *J.Hoffmann*[1], *N.Kurz*[1], *S.Loechner*[1], *and S.Minami*[1]
[1]GSI, Darmstadt, Germany

Introduction

The experimental program at TASCA (TransActinide Separator and Chemistry Apparatus) is focused in year 2012/13 on the search of superheavy elements - specially on element 119 and 120. For the verification of these elements the decay products will be measured with a double sided silicon strip detector. The generated charge in the detector is read out with an ASIC named APFEL (ASIC for PANDA Front-End ELectronics) developed at GSI for the PANDA experiment.

For these experiments a readout system including hard- and software was developed and produced in 2011. In this paper the analogue readout of the used silicon strip detector is described. The digitalisation, signal processing, DAQ and data analysis is presented in [1][2] and [3].

Detector Readout Electronics

The double sided silicon strip detector used at TASCA consists of 144 strips for the front readout and 48 strips on the back side. The pitch of the strips is 1 mm. With this detector and a readout system an energy resolution better than 1% is required. While looking for a new dead time less readout electronics the idea came up to use an integrated charge sensitive preamplifier which currently was developed by the GSI Experiment Electronics department for the PANDA experiment.

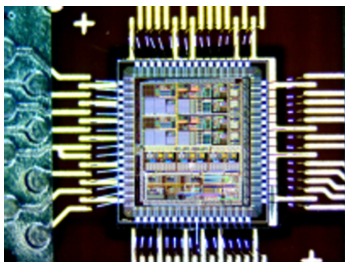

Figure 1: Photograph of the APFEL - ASIC

The APFEL - ASIC shown in figure 1 has two equivalent analogue channels each consisting of a charge sensitive amplifier, a shaper stage and differential output drivers. After the first integrator stage the signal path is splitted into two subpaths. One of these subpaths has an amplification of 32 in comparison to the other to get larger output signals in the low energy range.

The characterisation of the latest ASIC iteration at a temperature of T = $+10\,^{\circ}$C and a detector capacitance of 20 pF results in an equivalent noise charge of ENC=(3172$\pm$93) e^- (or 0.51 fC) and a maximum input charge of 6.3 pC. Therefore a dynamic range of over 10 000 follows. The peaking time of the shaped signal was measured to τ_p=(248$\pm$3) ns. The event rate independent power consumption of one channel is P=(55.2$\pm$0.5) mW. A detailed description of the ASIC can be found in [4].

* Work supported by EU and HI Mainz

First Measured Results

In August 2011 first measurements with the developed setup and a detector prototype with a reduced number of channels were successfully performed.

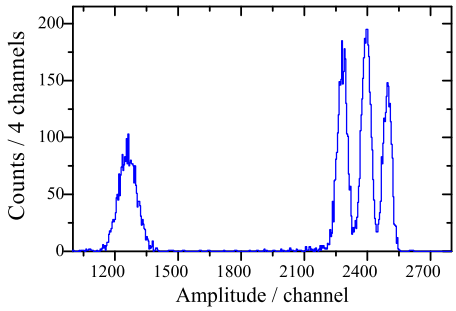

Figure 2: Measured energy resolution.

Figure 2 shows a spectrum of source with four α - lines in an energy range from 3 MeV to 6 MeV. The obtained energy resolution is 1.7 %. The measured time resolution between two α - peaks in one trace was 2 ns.

Summary

In a short period of 10 months the GSI Experiment Electronics has developed, realised and tested a new setup for the TASCA silicon strip detector. The full - scale system is now ready for the beam time in spring 2012.

References

[1] J.Khuyagbaatar et al, GSI: “Search for short-lived uranium isotopes around N=126”, GSI Scientific Report 2011

[2] J. Hoffmann et al, GSI: “New TASCA Data Acquisition Hardware Development for the Search of Element 120”, GSI Scientific Report 2011

[3] N. Kurz et al, GSI: “The MBS Data Acquisition System for the Search of Element 120 at TASCA”, GSI Scientific Report 2011

[4] P. Wieczorek and H. Flemming, “Low Noise Preamplifier ASIC for the PANDA EMC”, IEEE Nuclear Science Symposium 2010, Knoxville, USA, NSS-N47-74, Published in NSS/MIC, 2010 IEEE DOI: 10.1109/NSSMIC 2010.5873982 Page 1319 - 1322

The MBS Data Acquisition System for the Search of Element 120 at TASCA

N. Kurz, J. Hoffmann, S .Minami and W. Ott

GSI, Darmstadt

The predicted half-life of element 120 produced in the reaction Ti-50 with Cf-249 is shorter than the dead-time of the VME based MBS (Multi Branch System) running at TASCA and which has been used, e.g., for the study of element 114 in 2009 [1]. To overcome this limitation an enhanced MBS system introducing new, so called "digital" electronics has been set up for the search of element 120 in 2011 [2]. The new MBS for TASCA was composed of two sub-systems:

The first sub-system was set up in the same way as the complete system used for the 114 experiment. The 144 channels of the front side of the double sided silicon strip detector, all channels from the side walls and the ancillary detector signals were connected to peak sensing ADC boards. The dead-time for the signal conversion and readout is in the range of 30-40 µs, depending also on the number of ADC channels above threshold.

For the readout of the preamplifier signals of the 48 backside channels of the stop detector, the second subsystem equipped with digital electronics entirely developed in the EE department of GSI has been utilized. It is built up from the data concentrator board PEXOR, the MBS trigger board TRIXOR and 6 pipelining ADC boards FEBEX2.

The PEXOR acts as a data concentrator and features 4 fiber optical data input channels for the readout and control of the FEBEX2 and a 4 lane PCI Express interface as data path to the PC memory.

In this setup, 6 FEBEX2 boards where connected in 3 chains of 2 FEBEX each to 3 fiber optical inputs to the PEXOR. The FEBEX2 is an 8 input channel, 60 MHz, 12 bit pipelining ADC device. It accepts external triggers and records traces in a trigger window of up to 200 µs. The trigger window can be setup to record traces up to 34 µs before the trigger signal, thus allowing for self triggering and compensating for the trigger decision delays. A double data buffer on the FEBEX2 gives the possibility to release the dead-time already before data readout is performed. In most cases the readout takes less time than the length of the selected trigger window time (see below), which allows a quasi dead-time free operation of this subsystem.

The TRIXOR trigger module has identical functionality as its VME counterpart TRIVA5. It accepts external triggers and launches with PCI interrupts into the PC processor the readout of all FEBEX2 boards. In this setup the TRIXOR was set up as master trigger device, accepting triggers and producing total dead-time output signals for trigger suppression. The TRIXOR was connected via the trigger bus to the VME trigger module TRIVA5, which was setup in slave mode and starts the readout of the VME digitizers with interrupts after receiving a trigger request from the TRIXOR. The data from both subsystems is collected by a PC event-builder via TCP sockets. In this way the data from both sub-systems is collected fully synchronized and formatted into events composed of two sub-events. The VME - and PC readout processor as well as the PC event-builder run the real-time operating system LynxOS.

A common 60 MHz clock is provided to all FEBEX2 and 56 bit clock counters on each FEBEX2 allow signal time measurements with a granularity of 17 ns.

A trigger window length of 50 µs (3000 samples) with a pre-trigger time of 8 µs (500 samples) has been chosen for several reasons: first of all the decay of element 120 is expected in this window. Second, the readout of the FEBEX2 takes less than 50 µs, which allows with the help of the double buffer for a dead-time free operation of the FEBEX2. Third, the dead-time of the VME sub-system is well below 50 µs. If a fast alpha decay occurs within ~30-40 µs, the VME system will miss it, but it will be recorded by the FEBEX2 system.

Since full traces have been stored for all signals above a local threshold inside the trigger window, the energy of the signal has to be derived by analysis software algorithms, namely trapezoidal filters or Moving Window Deconvolution (MWD). These digital filters require summations well before the rise time of the preamplifier signals. This requirement is fulfilled with 8 µs pre-trigger time.

It is planned to implement the extraction of energy and time already in the FPGA of the FEBEX2. This will drastically reduce data sizes but require a thorough checking before going into production runs. For the search of element 119 in 2012 and further TASCA experiments, the amount of "digital" channels will rise from 48 to 640, covering all detector signals. For most of these signals the APFEL chip, developed in the EE department will be used to amplify the detector signals before feeding them in the newly developed FEBEX3 boards with 16 input channels. This system is already running as full setup in the EE laboratory.

[1] Ch.E. Düllmann et al., Phys.Rev.Lett. 104, 252701 (2010).
[2] Ch.E. Düllmann et al., this Scientific Report.

New TASCA Data Acquisition Hardware Development for the Search of Element 119 and 120

J.Hoffmann, N.Kurz, S.Loechner, S.Minami, W.Ott, I.Rusanov, S.Voltz and P.Wieczorek

GSI, Darmstadt

For the search of element 119 and 120 at TASCA in year 2012 a completely new data acquisition system was developed in Experiment Electronics (EE) department of GSI. The main hardware component of the system is a FEBEX3A module (see Figure 1).

FEBEX3A is a 16 channel ADC board containing the complete control and readout logic. The ADC resolution is 12-bit and the sampling rate is 60 MSPS respectively 16.7ns per sample. The inputs of the ADCs are differential with a range of 2V (peak-peak). In front of the ADCs high performance and high rate drivers are implemented. They allow an adjusting of the gain and input impedance.

The input connector of FEBEX3A allows connecting of different piggy-boards, equipped with 16 differential analog inputs and 16 differential LVDS I/Os. For the TASCA experiment an APFEL ASIC [1] amplifier-shaper (developed in EE department) plug-in board will be used (FEBAPF).

Up to 19 FEBEX3A boards can be connected to one backplane, mounted in a standard 3HE crate. The backplane is equipped with 20 PCI-express connectors allowing a data transfer rate of 2 Gbps. An optical interface board is plugged into the first slot of the crate which allows the connection to the PCI-express interface PEXOR3. Four crates can be controlled and readout over optical cables by one PEXOR3 card, located in a standard PC.

Trigger and control signals are distributed over the backplane of the crate to all FEBEX3A modules.

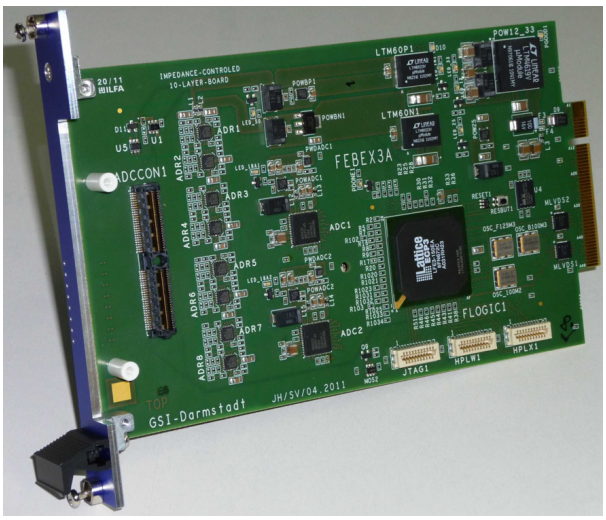

Figure 1. Photograph of FEBEX3A module.

An EXPLODER2A module serves as trigger distribution node. Up to 4 crates (1216 ADC channels) can be connected to one trigger distribution module. A multi-point LVDS standard was chosen for a trigger bus. It allows cable connection of several meters to/from up to 32 modules per chain. The interface board is equipped with a trigger-bus cable connector and allows the distribution of the trigger signals over the backplane. The complete system is in a test assembly in EE department laboratory since September 2011. One crate equipped with 6 FEBEX3A boards (96 ADC channels) was successfully tested in TASCA environment.

The logic for the FPGA chip has been programmed with Verilog HDL and VHDL. It uses GOSIP protocol with 2 modes of data transfer – address mode for read/ write access to control registers and block mode for fast

Figure 2. Photograph of FEBEX3A system.

read access to readout-buffers [2]. The 12-bit serial data from the ADCs are converted into a 12-bit parallel format and stored temporally in 16 ring-buffers with a depth of 2048. This allows the recording of ADC data up to a maximum of 34µs before a trigger occurs. When trigger signals are accepted, the data are transferred from the ring-buffers to the readout-buffers – realized as double buffers to minimize the dead time. The buffers are 32-bit in width and 4096 in depth to store ADC trace of maximum 126µs. Two different methods for signal-finding in the ADC spectra are implemented to produce self-trigger signals and to perform a data reduction on-board. One method is to find 3 consecutive samples higher than the predecessor by specified threshold. The other requires that the average of 8 samples is higher than average of 16 samples (equatable the baseline) by specified threshold with choice of 4 sampling frequency modes of 60, 30, 15 and 7.5 MHz.

[1] P. Wieczorek et al, "The APFEL-ASIC for the Silicon Strip Detector Readout at TASCA", GSI Scientific Report 2011

[2] S. Minami et al, "Design and Implementation of a Data Transfer Protocol Via Optical Fiber", IEEE Trans. Nucl. Sci., vol. 58, no. 4, p. 1816, Aug. 2011.

A CPU Controlled SEU Hardened Readout Controller for the GET4 TDC Readout

H. Flemming[1] *and J. Frühauf*[1]
[1]GSI, Darmstadt, Germany

Introduction

The current schema of the CBM-Time of Flight detector readout foresees approximately 16000 GET4 TDC ASICs[1]. Each of these ASICs has a point to point connection to the data acquisition with a modest data rate of approx. 15 MBit/s. This leads to a large number of cables, connectors and required readout controller boards.

To avoid this the idea came up to combine data of several GET4 ASICs and transmit it on a common serial link. In spring 2011 a readout controller ASIC was taped out which is able to buffer event data from the GET4, build data frames and send this to a daisy chain serial readout.

The readout controller ASIC GPRC I

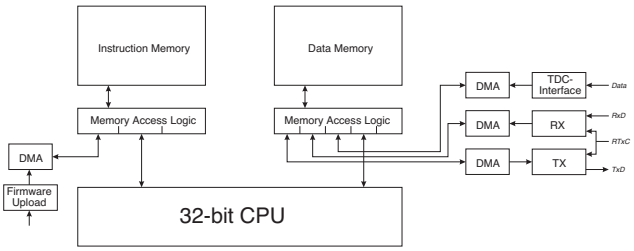

Figure 1: Block diagram of the GPRC readout controller ASIC

Figure 1 shows a block diagram of the *General Purpose Read out Controller I*. Data coming from the GET4 TDC are written by DMA into a SEU protected 4 KByte data memory. For building up a daisy chain or token ring readout structure a serial receiver and a transmitter can also access the data memory by DMA.

DMA transfers are invoked by a SEU hardened 32 bit RISC CPU which was specially designed for this readout controller. The CPU firmware is located in a one kilo words instruction memory which is initially loaded via a separate DMA upload channel.

The design is completely based on VHDL code that is synthesised to a 180 nm CMOS standard cell target library. The standard cell library and the SRAM IP cores are commercial products that are offered by *EUROPRACTICE* for educational and research use free of charge. Figure 2 shows the layout view of the GPRC I after synthesis and place and route. The SRAM IP cores for instruction and data RAM are viewable as black boxes. On the lower right side some full custom designed DACs and comparators are to see which are designed for the next GET4 iteration and implemented on the GPRC I to be tested on this ASIC.

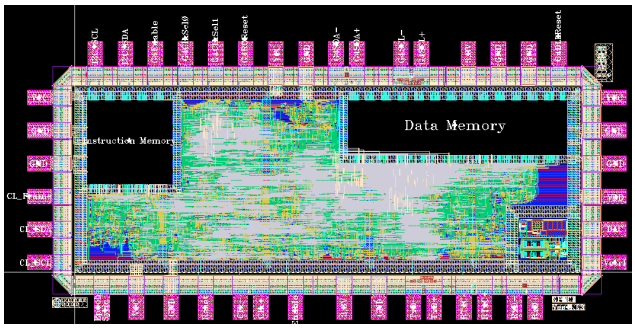

Figure 2: Layout of the GPRC I ASIC

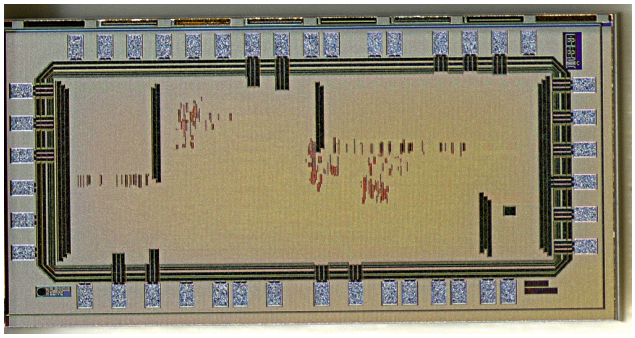

Figure 3: Die picture of the GPRC I ASIC

Tests and outlook

In summer 2011 the produced ASIC shown in figure 3 came back from the foundry. Only the bond pads and the top metal power bars are visible as the top metal layer is filled up with dummy structures which hide the structures below.

First tests on a simple test pcb have been done and were very promising. All tested sub devices are running as designed. Currently a test pcb with two GET4 TDCs and two GPRC ASIC is in preparation. First results with this test environment are expected in spring 2012.

References

[1] H. Deppe, H. Flemming, “A Wide Applicable TDC with Event-Driven Readout”, GSI Scientific report 2009

GEM TPC Data Acquisition System Development

J.Hoffmann, N.Kurz, S.Minami, W.Ott, I.Rusanov, P.Skott

GSI, Darmstadt

The GEM TPC readout module GEMEX1 has been developed and tested in the Experiment Electronics Department of GSI. Further tests are performed in the Detector Laboratory now. In this document the complete GEMEX1 based readout system is described.

GEMEX1 is a two nXYTER [1] based readout board. It contains 256 analog inputs, control, trigger and readout logic and gigabit data I/O. GEMEX1 can be easily cascaded over GEMCON connection module.

Very high density of readout pixels (c.a. 16 pro cm^2), cooling of the system, magnetic field influence and limited space were the main problems to be solved. Also the development time limit of one year was a challenge.

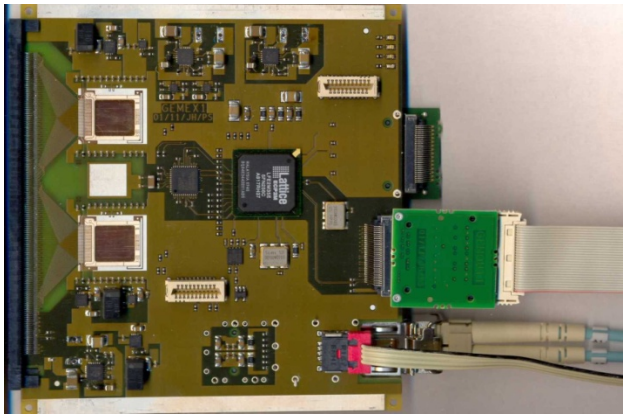

Figure 1. Photo of GEMEX1 board with cables.

Between 42 and 48 (10752 to 12288 channels) GEMEX1 boards shall be connected to the detector. Each GEMEX1 is equipped with a 300 pin connector handling 256 input channels. The input signals are conducted to two nXYTER readout ASICs.

Digital outputs of nXYTER are connected directly to field programmable gate array (FPGA) while the analog output signals go through 12 bit multi-channel pipeline ADC. The complete control and readout logic of GEMEX1 is implemented in the FPGA. It contains two main blocks: **GOSIP** (**G**igabit **O**ptical **S**erial **I**nterface **P**rotocol) slave-engine [2] and the **nXSPIP** (**nX**yter **S**erial and **P**arallel **I**nterface **P**rotocol) master-engine for control and readout of two nXYTER ASICs.

The GEMEX1 boards are designed to allow a creation of a triggered data acquisition system. Due to FPGA memory size the 96 us long trigger window is implemented. The trigger window is divided to Pre- and Post- trigger, both of them are programmable (12 bits, LSB = 31.25 ns). The length of the nXYTER data packed depends on number of registered hits. The minimum length of the packed is five 32 bit words. After processing the data are moved in block transfer mode with a rate of 2 Gbits over copper connections (up to several centimetres) or over optical links (up to several hundreds meters). To reduce the amount of output cables the GEMEX1 boards can be grouped (up to 32 boards per group). The only outputs needed for one group are two gigabit links, (transmit and receive) and an 8 fold differential multipoint trigger/control/clock bus.

The supply voltage for the boards is provided by the detector base or optionally, for test purposes or small systems, over ancillary power connector. Building the groups of GEMEX1 boards is provided through special connecting cards GEMCON. Depending on amount of GEMEX1 boards around the detector the GEMCON allows an angle of 360°/n (n=amount of GEMEX1 boards on detector). GEMCON-42SL1 is designed for 42 boards 8.57° angle.

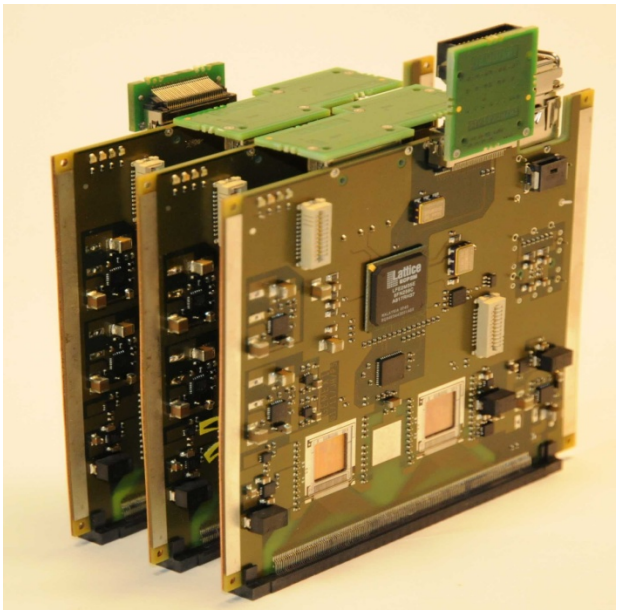

Figure 2. Photo of three GEMEX1 connected together.

The GOSIP slave-engine implemented on GEMEX1 includes also slow control functionality over the optical link. The master in the system is a PCI-express card PEXOR3 together with trigger module TRIXOR1 both plugged into standard PC running MBS [3].

References

[1] C.J. Schmidt et al. The nXyter Reference Manual. GSI Darmstadt, May 25, 2009.

[2] S. Minami et al., "Design and Implementation of a Data Transfer Protocol Via Optical Fiber", IEEE Trans. Nucl. Sci., vol. 58, no. 4, p 1816, Aug. 2011.

[3] BS N.Kurz, The general purpose data acquisition system MBS", IEEE Trans. Nucl. Sci., vol. 47, no. 2, p. 336, Apr. 2000.

The New HADES DAQ System*

J. Michel[1], *J. Adamzcewski-Musch*[2], *M. Palka*[3], *A. Tarantola*[1], *M. Traxler*[2], *and S. Yurevich*[2]
[1]Goethe-Universität, Frankfurt; [2]GSI, Darmstadt; [3]Jagiellonian University, Krakow

During the past years, the HADES read-out and trigger system was completely rebuilt. The main goal of the upgrade was to prepare the detector system for heavy ion experiments at SIS 18 and SIS 100. The old DAQ system designed more than ten years ago had strong limitations on the achievable data rates transported to the event builders as it was built to be used with a strong reduction in event rates by a LVL2 trigger. Now we run without a LVL2 trigger to collect all events without pre-selection which is benificial for our hadron physics program. Most digital front-ends were replaced by FPGA equipped platforms that are capable of sending data on optical links. Besides higher data rates, also the reduction of the electromagnetic noise caused by data transport and increasing configuration and monitoring capabilities were major aims of the upgrade. A detailed description of the HADES DAQ system can be found in [1].

This upgrade was finalized in 2011 by a four-day commissioning beam time taking place in August. During the commissioning beam time in August, the upgraded DAQ system was able to collect data from central Au+Au collisions at rates of more than 10 kHz. Additionally, a small percentage of minimum-bias events were recorded, resulting in a trigger rate of 13 kHz. The corresponding total data rate was well above 200 MByte/s. Data was sent to four servers ("Event Builders") via Gigabit Ethernet links and a central 10GbE network switch. On the servers, collected data from all sub-systems was combined and written to local disks and then forwarded to the Lustre file system for fast access by the batch farm as well to the tape robot for long-term storage. Performance tests showed that the full system with 16 independent event-building processes distributed to the servers is able to handle continuous data rates of more than 800 MByte/s.

During this four-day experiment (60 hours beam-on-target), a total of 0.84×10^9 events with a total size of 17 TB were recorded. The increase in the spectrometers rate capability is clearly visible from comparison to previous beam times: A typical four-week light ion beam time yielded in a few 10^9 recorded events and a data volume of roughly 1 TB. The typical dead time of the system was kept below 25%, leaving room for further improvements in the event rate. Figure 1 shows a typical distribution of dead-times in the HADES sub-systems and individual data-rates of some front-ends.

The new and versatile slow control and monitoring features turned out to be extremely helpful. The real-time monitoring of count rates on individual channels of the

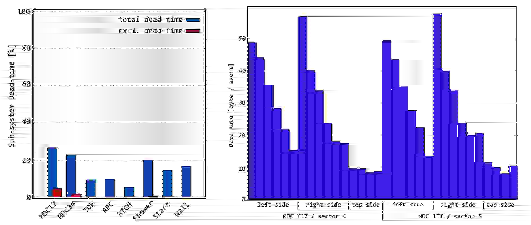

Figure 1: Left: dead-times of sub-systems. Right: data rates from indiviudal front-ends.

Start-detector provides instant information for beam monitoring and was used for fine tuning of the beam spot as well as for differential beam intensity measurements. The data is collected in the FPGA of the central trigger system and read out after each spill of the accelerator. The granularity and position in time of the acquired data is configurable at run-time. An example of the display is given in figure 2. The massive fluctuations visible in the intensity on the 100 μs scale are clearly visible (accelerator limitations), which results in a reduction of taken events by about a factor 2 compared to a smooth beam profile.

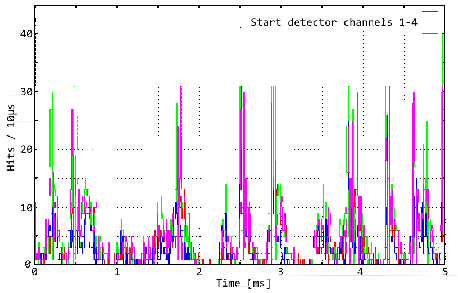

Figure 2: The structure of the beam with 10 μs granularity.

The status of each of the 500 individual front-end controllers is available to the operator. This includes reporting of buffer fill-levels, current hit rates and error reporting. Hence, even subtle and "hidden" problems are visible and can be addressed in real-time guaranteeing the highest data quality. As an example, figure 1 (right half) shows data-rates from individual front-end modules for two of the 24 drift chambers of HADES.

With the experience gained in the test experiment, we are looking forward to a full Au+Au production run in 2012.

References

[1] J. Michel et al., "The Upgraded HADES Trigger and Data Acquisition System", Journal of Instrumentation, JINST 6 C12056, December 2011.

* This work is supported by BMBF (06FY9100I), EU FP6, GSI, EMMI and HIC for FAIR.

Performance of the Global Tracking Unit for the ALICE TRD*

F. Rettig[†1], *S. Kirsch*[1,2], *D. Hutter*[1], *and V. Lindenstruth*[1]

[1]Frankfurt Institute for Advanced Studies, Goethe University Frankfurt, Germany; [3]CERN, Geneva, Switzerland

The ALICE Transition Radiation Detector (TRD) provides fast triggers based on the on-line reconstruction of charged particle tracks within a few microseconds after the collision. In total 1.2 million analog channels are processed by more than 65 500 custom multi-chip modules to find and parametrize short track segments. Via 1 080 optical detector links the track segments are transferred to the Global Tracking Unit (GTU, [1]).

The GTU consists of 109 FPGA-based dedicated processing nodes arranged in a three-stage hierarchy. In the lowest processing stage a full three-dimensional on-line reconstruction of charged particle tracks with transverse momenta above approximately 2.3 GeV is performed within 2 μs. Trigger algorithms for various physics signatures are then applied at the two higher stages.

The GTU also is a central element in the TRD read-out chain, receiving and buffering the raw data from the front-end and forming the data stream to the DAQ system.

Tracking Performance

On-line track reconstruction and several triggers were provided during the whole data taking in 2011. Comprehensive GTU tracking and trigger data were recorded in raw data for a detailed performance analysis. With the essential operation for p-p collisions shown in the 2010 campaign, a detailed understanding and performance tuning were on focus this year.

A typical correlation of track-level transverse momenta from on-line tracking and offline reconstruction is shown in Figure 1. With the initial tuning a transverse momentum resolution around 20% and tracking efficiencies above 80% were observed. Further tuning to improve resolution and fake rejection is ongoing.

Since mid-2011 a jet trigger is provided. By requiring a certain number of tracks above a given p_t threshold within one TRD stack, rejections above 10^4 maintaining good efficiencies could be demonstrated.

Additional triggers, e.g. a single high-energy electron trigger, were provided, but still in the pilot phase.

In the heavy ion data taking end of 2011 proper tracking operation could be established also for Pb-Pb collisions.

Multi-Event Buffering

Robust detector read-out for non-interlaced trigger sequences has been provided for the entire data taking since 2009. In 2011 multi-event buffering supporting interlaced trigger sequences was introduced.

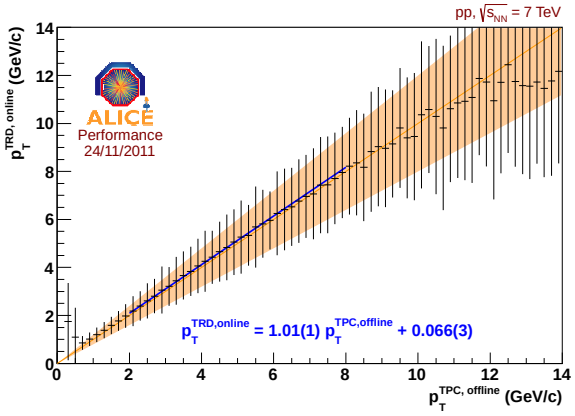

Figure 1: Correlation of transverse momenta for on-line reconstructed tracks and matching offline reference tracks. The data point is the mean and the error bars show the RMS. A deviation of 20% is marked by the area.

This facilitates decoupling of TRD front-end data taking and data shipping to the data acquisition system. Thus, a significant reduction of detector dead time can be achieved for large heavy ion events, especially. However, multi-event buffering support imposes complex requirements on the control system.

After extensive testing in stand-alone and p-p data taking ensuring reliable operation, the multi-event buffering design was successfully employed during the entire heavy ion campaign. A significant dead time reduction was observed. Under typical operating conditions the average dead time per event was reduced from 2 000 μs to 150 μs.

Also, in preparation for the 2012 campaign connectivity to three new TRD supermodules installed at the end of 2011 was established.

References

[1] S. Kirsch, et al., An FPGA-based high-speed, low-latency processing system for high-energy physics, IEEE Proc. Intl. Conf. on Field Programmable Logic and Applications (FPL), Milano, 08-2010, (2010)

[2] D. Hutter, Multi-Event Buffering und HDL-Simulationsframework für die Global Tracking Unit des ALICE-Übergangsstrahlungsdetektors, Diploma thesis, (2010)

[3] F. Rettig, et al., First High-Energy Collisions with the ALICE TRD Global Tracking Unit, GSI Scientific Report 2010, 233, (2010)

[4] J. de Cuveland, A track reconstructing low latency trigger processor for high-energy physics, Dissertation, (2009)

* Work supported by BMBF (06FY9125D).

† {rettig,kirsch}@compeng.uni-frankfurt.de

Automatic Tests to ensure the Reliability of the ALICE DCS*

R. Keidel[1], *M. Bittorf*[1], *E.S. Conner*[1], *and Th. Selig*[1]
[1]ZTT, University of Applied Sciences, Germany

The Detector Control System (DCS) for the ALICE detectors TPC and TRD are based on the software components: InterCom Layer (ICL)[1], FeeServer with State Engine, CommandCoder, DIM[1] and PVSS[2]. This system is performing reliable and stable during the last two run periods. During this time three major software updates have been shipped with far reaching changes in the code base. This was necessary to achieve performance improvements and fulfill feature requests.

Modern open-source cross-platform Enterprise Messaging systems emerged in the last years. The frameworks Qpid[3], RabbitMQ[4] and OpenAMQ[5] had been tested for the usage in DCS. The promising clarity of the interfaces was contradicted by the lack of available data throughput. So none of these tested frameworks can actually be recommended.

Prominent examples of failing software systems due to the lack of sufficient testing are the "Terminal 5 fiasco of BA"[2] or the "NASA Mars Mission's Metric Mixup"[3]. Design and testing paradigm have subsequently revolutionized the computer sciences. Behind this background and lessons learned during the years of developing the ALICE DCS several automatic test suits have been implemented and used on a daily basis to achieve nearly bug free and well performing DCS. The testing techniques are Unit Tests and Functional Tests. Unit Tests assess the interfaces of compilation units and Functional Tests assess the interfaces of the entire system or crucial parts thereof.

Examples of implemented Unit Tests are the assessment of the big and little endian conversion utility classes in the "DimUtilFramework" or the parsing of the information source names to get knowledge of the x-, y- and z-coordinates by means of regular expressions. Both utility classes are frequently used in the ICL and implementation flaws would lead to hard to track runtime errors.

The implemented Functional Tests have different goals. Integration Tests combine several modules to assess functional correctness, which is the data transport from the front-end electronics (FEDs) to the PVSS as well as the initialization of the front-end electronics by PVSS commands (see [1]). Load capacity tests have been implemented to check performance issues. The ICL can throttle the data throughput to protect the PVSS against crashes due to data overflow. A wide range of throttling adjustments is tested to expose potential concurrency issues. Contract tests have been implemented to explore and verify the interface behavior of used software frameworks. Crucial limitations in DIM could be found and appropriate counter measures have been implemented[4]. The test code coverage varies between 94% (DimUtilFramework) and 13% (jdim).

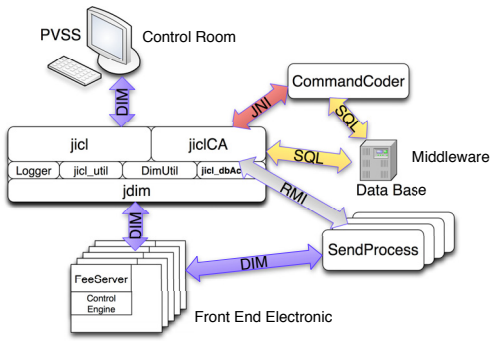

Figure 1: Block diagram of the JAVA InterCom Layer (jicl) with logger, data base access and various utility modules.

During the 2011 run-time emerged system failures of FED initiated by Single Event Upsets due to increased beam luminosity and intensity. The DCS framework will take care of this issue by frequent reboots of the FED to reduce the risk of SEUs. Major software changes are mandatory which will be supported by a thorough extension of the automatic testing framework.

References

[1] Bablok, Sebastian; Conner, Eric Sean; Hartung, G.; Keidel, Ralf; Kofler, C.; Krawutschke, T.; Lindenstruth, V.; Röhrich, D., Front-end-electronics communication software for multiple detectors in the ALICE experiment, Nuclear instruments and methods in physics research: A, Accelerators, spectrometers, detectors and associated equipment. Bd. 557. H. 2. 2006 S. 631 - 638

[2] Thomson Rebecca (2008-05-08). Lack of software testing to blame for Terminal 5 fiasco, BA executive tells MPs. ComputerWeekly.com. Online in Internet: URL: http://www.computerweekly.com/news/2240085948/Lack-of-software-testing-to-blame-for-Terminal-5-fiasco-BA-executive-tells-MPs [2011-04-01]

[3] Mars Climate Orbiter Mishap Investigation Board: Phase I Report. November 1999. Online in Internet: URL: ftp://ftp.hq.nasa.gov/pub/pao/reports/1999/MCO_report.pdf [2011-01-04]

[4] Keidel, Ralf; Bittorf, Michael; Conner, Eric Sean, Further Enhancements of the Front-End-Electronics Communication Software, GSI Scientific Report 2010. Bd. Report 2011-1. 2011 S. 234 - 234

* Work supported by GSI; Vorhaben: ALICE Softwareanwendung zur Modellierung von Prozesssteuerungsschnittstellen / EPICS; WOKEI.

[1] http://dim.web.cern.ch/dim/
[2] http://lhcb-online.web.cern.ch/lhcb-online/ecs/PVSSIntro.htm
[3] http://qpid.apache.org/
[4] http://www.rabbitmq.com/
[5] http://www.openamq.org/

The GreenIT Cube –new Data-Centers at GSI

H. Kreiser[1], *V. Lindenstruth*[1,2]

[1]GSI, Darmstadt, Germany;[2]Goethe-University Frankfurt and FIAS Frankfurt, Germany

Concept

A new data center architecture was developed which combines lowest cooling overhead with low construction cost [1]. It will host the FAIR Tier-0 data center. This center sets new standards in cooling efficiency, rendering a cooling overhead of less than 10% (PUE ≤ 1.1) and provides sufficient space for 800 19-inch racks.

Important aspects in data-center are cooling efficiency, costs, high packing density for computers resulting in a high energy density and high data transfer rate. An important issue is the length limitation of cost-effective copper cables for high performance networks. It has been demonstrated that it is possible to operate computers with up to 35kW per 19-inch rack. These racks cool the natural airflow of the computer equipment by passive heat exchangers in the rack's back door. Therefore the computer racks can be mounted in any arrangement.

The best architecture involving all aspects is a building in cube form. The data center implements a 3D steel structure, much like a high rack warehouse (figure 1). The choice of an open multi-story system allows for shorter interconnect length, which grows only with the third root of the system size as compared to the square root for 2D false floor architectures. The building costs are significantly lower than for data center of comparable size.

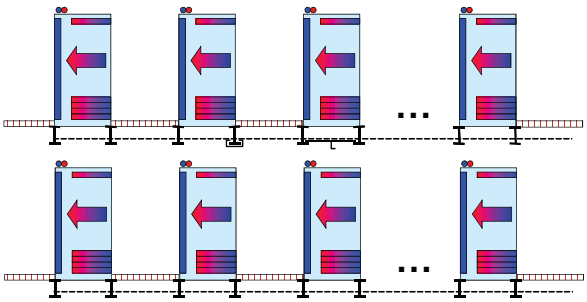

Figure 1: rack layout in 3D data center

An additional important aspect is the use of indirect free cooling the entire year using counter flow, indirect draft, wet cooling towers, allowing a cooling efficiency of less than 10% of the computers heat load. In addition the cooling water can be used for heating of neighbouring buildings.

Realization

A design study was performed for the FAIR Tier-0 data center (figure 2), which is now the basis for the construction of the building. The building cross-section measures 26x26m^2 by 23m high. The building is divided in 3 vertical (fire-)sections:

- water section with all cooling equipment, heat exchangers, high pressure pipes
- rack section with all the computing, networking and low pressure pipes
- electrical section with power distribution and transformers

These sections are surrounded by F90 concrete walls and additional F90 isolated room for tape libraries.

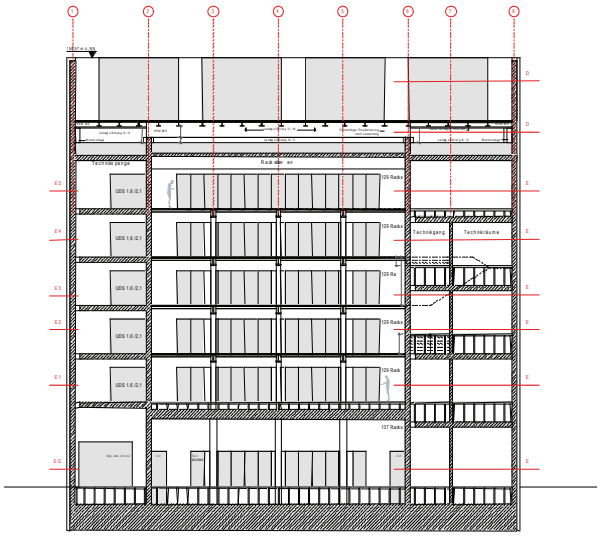

Figure 2: cross section of the new data center building.

The infrastructure inside will be designed for a maximum power input of about 16 MVA, allowing an upgrade up to 24 MVA. It should be noted that this high power consumption is not expected for the FAIR Tier-0 data center but is foreseen for future upgrades.

In the data cater core there is place for about 800 19-inch 42U computer racks (70x120cm²) with the passive heat exchanger backdoors. The racks reside on steel T-bars, which also carry the floor tiles in the isles between the racks. The steel bars also carry the cooling water distribution and also serve as support for the cable trays.

In this architecture the room temperature is at least 7 °C higher than the wet bulb temperature and therefore can reach 30°C during the summer. The computers in the GSI Test cube are operating since more than 15 months at 28 °C without problems.

An important aspect of this plan is the risk of fire, particularly given a large open volume and the very high power density. The racks implement intelligent PDUs, which monitor the power and all relevant air temperatures inside the rack. Smoke sensors in every rack result in the racks PDU to disconnect the power. Since computers do not present a significant fire load, the power termination will stop a potential fire.

Timescale

The new data center building for GSI and FAIR is fully financed by the Helmholtzgemeinschaft. The contract for the final planning is awarded, construction start will be end of 2012 and the commissioning of the new building will be beginning 2014.

The GSI MiniCube

To demonstrate this type of data center, a small version of this building is installed at GSI (figure 3). The rack space was urgently needed as the existing data center resources were already over allocated. The two storey steel structure is designed for 2x48 racks (figure 4). The electrical power supports up to 1.5 MW. The racks can be supplied with cooling water from above and below. Therefore only one cooling water supply pipe is required per rack row of both storeys. Figure 5 shows the arrangement where the racks in the ground floor have not yet been installed.

Figure 3: TeraFlop building

Figure 4: Rack installation 2nd floor

Figure 5: Cooling connection

As a first step 48 racks including 200 CPU-server with 10000 cores and 48 fileserver with 1.2 PB are installed. To interconnect these different systems InfiniBand is used.

During the first tests the CPU-servers were running with about 30kW/rack at a room temperature of 20°C. Inside the rack behind the server chassis a temperature near 47°C was measured, which was cooled down to 20°C through the heat exchanger by a water temperature of 17°C.

Figure 6: Server installation

A small cooling unit with 1.2 MW cooling power, upgradable to 1.8 MW is located nearby (figure 7). The entire cooling infrastructure is located in a 4 ft. container.

Figure 7: Cooling device

References

[1] V. Lindenstruth, H. Stöcker: Building for a computer center with devices for efficient cooling, PCT/EP2009/004704

The GSI Test Cube - a first Step to a new Data-Center

H. Kreiser[1], V. Lindenstruth[1,2] and J. de Cuveland[2]

[1]GSI, Darmstadt, Germany;[2]Goethe-University Frankfurt and FIAS Frankfurt, Germany

Introduction

A new type of a data-center [1] is tested at GSI. This center sets new standards in cooling efficiency (PUE<1.1) and supports very high energy densities of 20 kW/m². In order to evaluate several aspects of this new technology a small reference data center was built. The computers are mounted in specialized, closed 19-inch racks, which implement a heat exchanger in the back door, which absorbes the entire heat of the computer equipment inside the rack. There are no fans required or the data center cooling as the heat exchanger is entirely passive. The airflow, generated by the fans inside every server is fully sufficient to push the hot air all the way through the heat exchanger, where it is cooled back to room temperature. The heat exchangers generate a very low air backpressure, which does not generate any measurable additional power load on the fans of the servers.

To be very energy efficient, free-cooling is used during most of the year. This data center implements a chiller for the hottest temperatures. We operate this data center at temperatures of 27-30°C during the entire year.

Under pressure water cooling

To avoid water problems (water leaks in the pipes, hoses or valves) the water circuit is designed as an underpressure system. A vacuum pump connected to a big tank produces a vacuum (-200 mbar). The water flow produced by pumps is independent of the systems pressure .

Test in an old container

To test this arrangement, an old container was rebuild and equipped with 10 racks, water tank, complete water cooling system and the electrical power connection. The cooling control was designed and based on a mini computer with embedded linux. A web-based control and monitoring system controls the plant (figure 1)

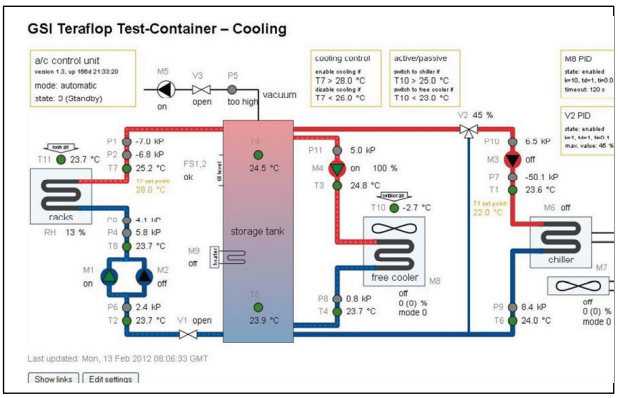

Figure 1: control and monitoring system

The primary cooling circuit, cooling the racks and te secondary cooling systems are connected by a big vaccum tank, which allows to remove any air which might come into the system due to potential leaks. Even an open half inch valve at the bottom of the system will not lead to any water leakage nor failure of the cooling system itself. Only the vacuum pump will start working.

Figure 2: back side with the heat exchanger

Figure 2 shows a picture of the data center implementing 10 racks, filled with files ervers, where about 1 PB are installed since 12 months. The power consumption is about 28 kW for the file servers, and about 1.2 kW for cooling pumps. The free cooler is regulated and requires dependent on the outside temperatures between 0 and 4.2 kW. The system also implements a chiller, in order to be able to generate low temperatures for experimental reasons. This chiller requires 24 kW when in operation.

The complete system is now running for 1.5 half years without any problems. While the temperature in the container is about 27-28°C, the hot air before the heat exchanger is about 40-45°C.We see no increased failure for servers and discs.

References

[1] V. Lindenstruth, H. Stöcker: Building for a computer center with devices for efficient cooling, PCT/EP2009/004704

Configuration Management Evolution in the GSI HPC farm

C. Huhn, E. Duve, S. Haller, B. Neuburger, V. Penso, T. Roth, W. Schön, and J. Trautmann
GSI, Darmstadt, Germany

Computing facilities are growing and their complexity is increasing over time. The management of a compute cluster must **scale** with: the number of *computers* – or rather OS instances nowadays, the number of *services* they provide and the number of *co-workers* in the team of system administrators.

For almost a decade the GSI HPC cluster has been maintained with the aid of the *Configuration Management System* (CMS) Cfengine (version 2). During that period the cluster size has grown by one order of magnitude while the manpower dedicated for its maintenance stayed constant.

Unfortunately Cfengine has its limitations and it became increasingly questionable whether it will scale with the prospective growth of the HPC installation and the HPC group's headcount.

Cfengine assets

Cfengine provides a declarative *Domain Specific Language* (DSL) to describe the nominal state of the configured system. Self-contained and autonomous agents on all nodes pull these definitions from a central server and trigger the appropriate actions to bring the system closer to the desired state (*convergence*).

Nodes are categorised in Cfengine *classes* that can be derived from other classes with algebraic set operations (unions, intersections and complements).
Cfengine is capable of phrasing minimal-invasive edit operations in configuration files instead of only handling complete files.

Cfengine drawbacks

Cfengine's pull-based approach provides very limited support for one-shot push operations that do not suit the concept of convergence. The system is monolithic and does not provide an API: interaction with Cfengine is limited to the DSL, on the other hand the extensibility of this DSL and therefore its expressiveness is limited. The deficits of the DSL steepen the learning curve – a lot of experience is neccessary to implement complex operations in a satisfactory fashion.

Cfengine is not per-se suited for multi-tenancy: Write access to the configuration on the Cfengine master is equivalent to root privileges on all managed nodes. Cfengine does not provide a global view of the Cfengine classes that are activated on the configured nodes. Configuration operations for one service cannot utilise the CMS knowledge about settings on other nodes (e.g. lists of nodes configured in a certain manner).

Chef

We started to look at the Chef CMS as a complement or even replacement for Cfengine. Chef is not only written in *Ruby* but also implements its DSL as Ruby extenions (*resources*). This implies that Chef operations (*recipes*) can be extended with normal Ruby code wherever required. These rule sets are combined to *cookbooks*.
Chef *attributes* control the behaviour of the cookbooks on the nodes to be configured. Many attributes are automatically collected by the Chef client's component *OHAI* and centrally stored on the Chef server. This information can be used to configure arbitrary services.
This separation of recipes (code) and attributes (data) in accordance with the Model View Controller paradigm enables the sharing of generic Chef cookbooks throughout the community of Chef users.
The Chef server reveals its functionality via a REST API. The command line utility `knife` provides access to this API. `knife` also supports ad-hoc push operations on the managed nodes.

Ongoing investigations

In some areas Chef does not bring improvements to Cfengine: Admin access to the Chef server implies privileged access throughout the complete cluster. Chef's capabilities of role and infrastructure modelling are not more advanced than Cfengine's. Chef cookbooks are versioned on the server, nevertheless Chef does not provide a decent *rollback* feature. And finally Chef completely lacks Cfengine's anomaly detection (*cfenvd*) features.

Considering Chef's capabilities regarding its API and Ruby foundations the implementation of these missing features seems feasible.

Conclusion

Chef promises to be more powerful and versatile than our current Cfengine setup. It is suitable for applying Software Engineering techniques to configuration management, e.g. documentation generation, coverage checks and quality assurance procedures like unit tests. These capabilities will be crucial for our CMS to scale well with our prospective growth in the next decade.
Nevertheless Chef's increased expressiveness in comparison with Cfengine may also cause an excessive increase in complexity that has to be kept in check by structuring and coding conventions.

The GSI HPC department will therefore expand and foster its Chef implementation. The complete replacement of the current Cfengine setup is a long-term effort though.

Scalable software distribution system for the new GSI computing cluster

B. Neuburger[1], *V. Penso*[1], *and F. Uhlig*[1]
[1]GSI, Darmstadt, Germany

Abstract: Many problems of the current LFS based computing cluster at GSI are due to deficiency of the Network File System NFS. NFS is used to access user software from all compute nodes of the cluster. The two main deficiency are performance issues and instabilities. The instabilities of NFS can bring a compute node in a state that manual intervention of an operator is needed to bring it back into productive mode. In this paper we describe the new scheme to distribute experiment specific software for the new computing cluster.

Requirements

The new software distribution scheme should overcome the described problems of NFS, which excludes solutions which mount external directories on each of the compute nodes. Such a solution works for a small number of compute nodes but have severe performance issues when handling many file requests at the same time. The best solution to solve the performance issues would be to install the software locally on each compute node.

To allow also the different user groups to install their individual software one needs an automatic way to install and distribute this user software to all compute nodes. Another major obstacle is the scalability of the new system. The system should scale with the number of compute nodes. It should also scale with the number of different user groups, which should not interfere with each other. To give some numbers the compute cluster in BG2 consists of 102 nodes with a total of 1632 CPU cores whereas the new cluster in the testing hall will have approximately 500 nodes with altogether 10000 CPU cores.

At the end of some evaluation we decided to use a scheme based on the CERN Virtual Machine File System (CVMFS) [1,2] to distribute the user software to the compute nodes.

CVMFS

Even if the name implies it, CVMFS has nothing to do with virtualization. CVMFS is a read-only client-server file system which was originally developed to deliver software distributions to (cernvm) virtual machines in a fast, scalable, and reliable way.

On the client side it is implemented as a filesystem in user space (FUSE) module, which makes a specially prepared directory tree stored on a web server look like a local read-only file system. The file catalog meta-data is downloaded from the repository server and cached locally in a SQLITE database. Only if a file operation really need file access the corresponding file is fetched from the repository server and cached locally. The entire communication between the client and the server is done using only HTTP. Since CVMFS internally uses hash values to identify the files this results in an deduplication of the files. Files with the same content are stored only once, because they are identified using the unique hash value.

Setup

To allow the different user groups to install their specific software we setup a dedicated build server where a software coordinator can install the needed software. This build server is used currently by all the different user groups (IT, SiSt, Alice, Hades, FairRoot), whereas each of the different user groups has their own CVMFS repository server. After the installation on the build server the software coordinator triggers an automatic synchronization of the CVMFS repository server which also creates a new version of the meta-data file catalog.

The clients will initially download the file catalog from the CVMFS repository when mounting the repository for the first time and fetch available updates after an adjustable time. Most load on the CVMFS repository servers is expected after an upload of new software since the new files are not already cached locally on the compute nodes.

Scaling and Reliability

Since CVMFS is based on HTTP, ways to scale HTTP performance are available and thoroughly tested. If a CVMFS server at one time can not handle HTTP traffic to clients any more, one solution to reduce the impact on a server is setting up a phalanx of caching proxy servers and distribute the workload horizontally. In such a scenario clients do not access the CVMFS server directly but connect to the proxies. The proxies in turn keep a copy of the repository and make sure that copy is kept updated.

To avoid unavailability of a CVMFS repository, one can also choose to clone the CVMFS server hosting that repository and use cluster high availability frameworks to make sure one of the cloned instances takes over for the primary server in case that primary server is not working correctly anymore.

Currently the load on the CVMFS repository servers is low that none of these measures are implemented yet.

References

[1] http://cernvm.cern.ch/portal/filesystem

[2] J Blomer et al.; 2011 J. Phys.: Conf. Ser. 331 042003, "Distributing LHC application software and conditions databases using the CernVM file system"

Moving towards Scalable HPC Infrastructure at GSI

V. Penso, E. Duve, S. Haller, C. Huhn, B. Neuburger, T. Roth, W. Schön, and J. Trautmann
GSI, Darmstadt, Germany

The growth in computing resources planned for the upcoming years requires fundamental changes to the system architecture [1]. To improve the scalability of the GSI HPC clusters for future needs, new management concepts are developed and tested in a prototype installation. This paper outlines the software-stack used to operate a prototype compute cluster designed with scalability as the primary goal. Furthermore it summarizes our experiences in migrating major applications to this new infrastructure.

Storage

All shared file systems for user home-directories and application software have been eliminated. Furthermore application software distribution is decoupled from data access. Software repositories, under control of the user groups, distribute applications libraries to the cluster using a cached file system called CVMFS[2]. Through scalable caching layers any compute node part of the cluster will establish its local read-only copy of the application software. Application generated output is written to Lustre, the only writable file-system in the infrastructure. Since loading application code involves reading lots of very small files, removing this duty from Lustre tremendously reduces this interference from accessing big data files.

Resource-Management

Beside suitable delivery of application software, as well as input and output data, potential limitations of the cluster configuration-, monitoring- and resource-management-systems have been considered. Large scale automation needs communication among these three systems, therefore these components have been selected according to their capability for integration. In the new cluster the resource-management-system GridEngine[3] is tightly integrated with the configuration-management-system Chef[4]. Besides Chef's responsibility for the deployment and configuration of the system software, it is used to collect static inventory information on the software and hardware of all machines. This inventory is queried by the monitoring-system and other components to automatically adjust to the infrastructure state.

Monitoring

Collecting and storing of performance metrics, like CPU load, memory utilization, or network IO, by the monitoring-system lay the foundation for the analysis of system failures and resource limitations. In connection with the inventory of the configuration-management-system it is possible to correlate system failures to the corresponding hardware and software environment. Since those systems provide programmable-interfaces, tools can be developed to query them to automatically react on problems. Thus it is feasible to remove broken nodes from the resource-management, reinstall them, and reintegrate them by a completely automatic procedure. Since the number of compute nodes is increasing dramatically such integration code will be the only way to operate the infrastructure with limited manpower.

Adoption

During a period of five months a dozen users have been working extensively with the prototype compute cluster. Many different types of applications for experiment simulation and data analysis have been executed. In total more than two million jobs have accumulated a compute time of 210 000 CPU hours. More than 19 Petabytes of input and output data have been moved between the Lustre storage and the compute nodes.

Users need to adapt their applications to the new resource-management-system and need to learn the new methods for application software distribution. Due to the missing shared home file systems users have to adjust to different, but more scalable, procedures for data handling and application development. Consequently users are much better prepared to utilize more resources with their software in the future.

Outlook

Since the new prototype cluster is in operation, the HPC department has made significant progress in automation of common maintenance tasks. In the next year it is planned to improve resilience and self-healing capabilities of the cluster. Furthermore migration of users from the legacy computing facility at GSI to the new cluster, built with all the improvements described above, will be continued.

References

[1] Schön et al., "GSI HPC Cluster and Scalability", this report

[2] F. Uhlig, et al. "Scalable software distribution system for the new GSI computing cluster", this report

[3] C. Preuss, et al., "GridEngine - A new scheduler for the GSI computing cluster", this report.

[4] C. Huhn, et al., "Configuration Management Evolution in the GSI HPC farm", this report.

GSI HPC Cluster and Scalability

W.Schön, E.Duve, S.Haller, C.Huhn, B.Neuburger, V.Penso, T.Roth, J.Trautmann[1]
[1]GSI, Darmstadt, Germany

Abstract: The GSI HPC cluster is used mainly by international collaborations to analyse experiments (GSI/LHC). The cluster will be extended to be prepare for the needs of FAIR. New concepts are developed to improve cluster scalability, being tested in prototype installations.

Introduction

The FAIR project needs more powerful computing in terms of FLOPs, I/O rates and online storage capacities. For efficient use of a cluster it is crucial to identify and eliminate bottlenecks. With increasing complexity of such a cluster, monitoring, anomaly detection and management also become crucial. In addition, IT security becomes a more and more demanding problem - especially taking into account the international usage of the cluster and the existence of broad bandwidth connections to remote sites.

Compute Power

In an environment typical for GSI, LHC or FAIR experiments, pure compute power is the problem to solve most easily. Due to the independence of the physics events, parallelization can be easy done by analyzing events simultaneously on a number of cores. No communication between the cores is necessary. The simplest solution is to increase the number of cores in the cluster to enhance the number crunching power. However, more indirect limitations will show up: I/O per node, management of a huge number of cores and nodes, power density, cooling, all can become critical.

I/O Capacity and Meta Data Perfomance

I/O is the crucial factor in analysing data of large experiments (e.g. HADES or ALICE). If the I/O capacity is not sufficient, the jobs will be I/O bound (jobs will wait for I/O instead of analysing data). In contrast, typical simulation jobs or theory calculations are much less I/O demanding. The I/O problem is solved by employing a parallel cluster file system at GSI (Lustre [1]). This cluster aggregates the capacity of single RAID groups to a file system with a global view to the whole data space. The cluster is designed, built and operated by the HPC department. With about 150 file servers and a multi-peta-byte storage capacity this cluster is of competitive size among the large clusters worldwide. GSI participates in the development and testing of the Lustre (and is a founding member of the EOFS [2]). There are limitations, however. Meta data performance is a general bottleneck of Lustre. In particular, heavy load on the meta data server can become a limiting factor of the cluster's performance. Especially massively parallel concurrent access of jobs to one and the same file can cause problems. Irrespective from the question if such an access pattern is good analysis design, it can slow down the entire cluster and thus slow down the HPC farm. The HPC department is currently developing a kind of a *meta data anomaly detection*. This is necessary because user code is often making very inefficient use of Lustre, e.g. by writing and reading huge numbers of small files instead of writing one large file. Excessive meta data usage can also be point to bad user code (e.g. nested infinite loops querying meta data). In practise, it is necessary to monitor and detect abnormal meta data operations to protect the whole system. As a future plan, the global tree of metadata will be splitted into a cluster of meta data servers serving single branches while keeping the global view.

New Concepts Managing the GSI Cluster

A prototype cluster was built to test new concepts of distributing software, taking into account all lessons learned from the management of the current cluster [3]. An important point of the new design is to avoid common shared resources for user code and system code which are potential single points of failure (stability) and to distribute the data in many instances (scalability). Access to this cluster for users is possible only via the job scheduler, no direct access is allowed. As job scheduler, an open source solution is employed, avoiding expensive commercial solutions. The new cluster is connected to the Lustre cluster for fast access to data. The new concepts are discussed in [4].

References

[1] Schön et. al. I/O Optimised Cluster for Data Analysis, GSI scientific report 2010

[2] www.eofs.org

[3] Huhn et. al. Configuration Management Evolution in the GSI HPC Farm, this report

[4] Penso et.al. Moving towards Scalable HPC Infrastructure at GSI, this report

GridEngine - A new scheduler for the GSI computing cluster

C. Preuss, V. Penso, and B. Neuburger

As our current scheduler LSF has started to become old and support will not be provided anymore on a long term basis. Therefore a discussion has been started about an update to a newer version of LSF or to look for an (free) alternative.

As the SC department has experiences with different scheduling systems due to their grid activities, they were in charge to look for the future scheduler, supported by the HPC department providing a new computing cluster with a new infrastructure and management concept.

First calculations and requests for offers on LSF 7 brought us to the idea to move to a free alternative as the costs with regard to FAIR (computing) would be enormous.

First candidate was OpenPBS/Torque (which is the free version of PBSPro) which is in use at many research centres being known as a very uncomplicated scheduler. Very fast, though, it showed problems with reliability and scaleability. The master was unstable under certain circumstances and pending jobs were not scheduled and had to be killed and resubmitted. One major problem with regards to the scaleability was that the master was not able to handle more than 10.000 running jobs.
Consequently the test phase ended soon and Torque was discarded from further evaluation.

The Second scheduler to test was Condor, which is entirely open source and has established a wide user community. As we were looking for a HighPerformanceComputing scheduler, Condor was developed as an HighThroughputComputing scheduler, getting the most computing cycles out of a computer, subsequent to this it provides neither priorities nor preemption, two features required in our environment.

(Sun)GridEngine (GE) was initially developed by Sun and is at GSI currently in a state between test and productive phase. As Sun was bought by Oracle in 2011 the future of GE has become complex. At the moment there are several different development paths and support communities, part of them commercial, some are open source.

We installed GE on a new computing cluster with a new configuration management system (Chef) and without NFS (known for being the reason for many problems on the old cluster) and started with a minimalistic GE configuration. So far mainly Alice users are doing their so called Analysis Train on it.

As the old queue based model in LSF had become more and more complicated and being reason for underutilization GE will have no experiment specific queues anymore, also (currently) no preemption. Job priorities are given by a FairShare model where users/departments will get an amount of shares which are the basis to provide priority to jobs.
How these shares are distributed is still to be decided.

The users don't have to look for queues anymore but can provide resource requests. GE will then schedule the jobs to queues which will fit best to the resource requirements. Queues are now for internal use only in order to manage the resources.

This will also help to prevent jobs from running out of control as resource requests are used as resource limits, too. Jobs, which are exceeding these limits, will be killed.

Very first experiences we got by using GE on top of LSF, to utilize unused computing resources on our old cluster.
As we have shown GE is able to raise the cluster utilization by 5-10% with a minimal administrative overhead. This was possible by moving from slot to resource based scheduling, where the scheduler provides not one job per core, but adjusts the number of jobs depending on the resource demands of each job.

After buying new hardware running under GE only, we decided to keep this model.

First experiences from ALICE and Theory are promising but also highlighted some aspects which need more investigations and in some cases software development.
Therefore a mailing list was created to share and collect knowledge from all Helmholtz centres using GridEngine.

Due to the uncertain future of GE and finding some problems (e.g. enforcing resident memory limits) the search is not over now.
In order to complete the comparison there are currently efforts in progress to install and test Slurm, which is an open source scheduler being used on many super computers.

References

http://research.cs.wisc.edu/condor/
http://gridengine.org
http://wiki.gsi.de/cgi-bin/view/Linux/GridEngineUsage
https://computing.llnl.gov/linux/slurm/

Utilization of LOEWE-CSC within the Frankfurt Cloud*

M. Zynovyev, D. Klein, A. Manafov, and V. Penso

GSI, Darmstadt, Germany

The Frankfurt Cloud project [1] has set the utilization of a subset of the LOEWE-CSC supercomputer [2] resources as one of its goals. One of the transparent ways to accomplish it is to deploy on a part of the LOEWE-CSC resources a private cloud (Figure 1). Abidance of the 'Infrastructure as Code' (IaC) principles during the deployment of SCLab, a private cloud prototype at GSI [3], and the resulting codebase have allowed to apply the SCLab architecture to a part of LOEWE-CSC.

Fifty out of 800 physical nodes, which make up the supercomputer, have been configured as hypervisors, using KVM. As a result, the private cloud at LOEWE-CSC could draw from the power of more than 1000 CPU cores. By practicing IaC, it is especially convenient to transfer the knowledge and deploy a private cloud similar to SCLab on available resources. Using VMs and isolating the infrastructure within a dedicated VLAN and subnet, it is possible to set up the OpenNebula software for VM orchestration at LOEWE-CSC just by deploying a Chef cookbook as it has been written and used for SCLab.

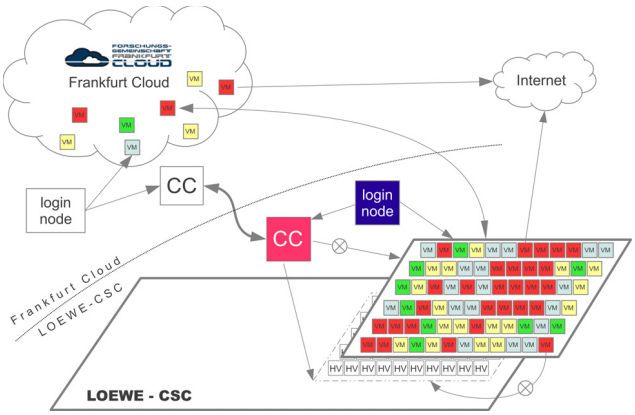

Figure 1: The envisioned architecture of the Frankfurt Cloud, incorporating a private cloud of LOEWE-CSC.

This infrastructure provides a unique opportunity to demonstrate the ability of PoD [4] and its SSH plug-in to roll out a PROOF cluster on a large number of CPU cores at a cloud and the feasibility of a PROOF analysis with several hundreds of workers and a single master. The corresponding tests have set a record for a number of workers in a PROOF cluster. PoD has been used to deploy a cluster with 975 workers, which proves to be a limit for the ROOT version 5.30, since no test has succeeded to surpass this number.

The benchmarking results demonstrate that the scaling of the analysis rate is hampered at the level of 350 worker nodes (Figure 2), and the efficiency of a cluster with more nodes and a single master goes down. The observed uneven distribution of the processed events among the workers indicates that the PROOF Packetizer may be at fault. The Packetizer is a PROOF module which schedules the workload between the worker nodes depending on the location of the data. Since some of the workers have received the load too late and have been idle until then, the single-threaded Packetizer might have failed to distribute the workload evenly in time. The PROOF and PoD developers, to whom the results have been reported, are set to eventually pinpoint the cause of this behaviour and get rid of a performance bottleneck.

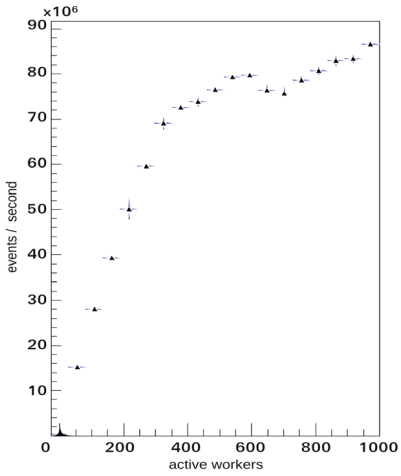

Figure 2: Event analysis rate. Efficiency threshold lies at the level of 350 workers.

To summarize, the unique results of the PROOF benchmark on a cluster of such a size have been instrumental in driving the improvement of the PROOF software for a distributed interactive ROOT analysis. This work demonstrates a synergy of the state-of-the-art computing technologies and serves as another example of the benefits of the IaC practice and the application of cloud computing technology in a scientific research environment.

References

[1] D. Klein et al, “Radiation Simulation and Nuclear Structure Calculation at Frankfurt Cloud”, GSI Scientific Report 2010.

[2] M. Bach et al, “Green IT and Efficient Computing at the LOEWE-CSC”, GSI Scientific Report 2010.

[3] V.Penso et al, “Cluster-Virtualization at GSI”, GSI Scientific Report 2010.

[4] A. Manafov et al, “PROOF on Demand”, GSI Scientific Report 2010.

* Work is part of HGS-HIRe.

High Performance Experiment Data Archiving with gStore

H.Göringer, M. Feyerabend, and S. Sedykh

GSI, Darmstadt, Germany

Overview

Experiment data archive and storage is provided with **gStore,** a client/server middleware developed at GSI. gStore is based

1. on automatic tape libraries (ATL) for long term archiving and
2. on data movers (DM) with large read and write disk caches.

Tape libraries and data movers are connected via Storage Area Network (SAN). gStore hides tape operations as far as possible from the users and provides fast and highly parallel data access 24 hours a day and 7 days a week. The data movers use high speed connections to the GSI lustre file system deployed as online storage for data analysis.

gStore is fully scalable in both, data capacity and I/O bandwidth and well prepared for the challenges of the future FAIR T0 centre. Design principles and functionality of gStore are described in more detail in several GSI reports, talks, and in a paper [1].

Hardware Status

Currently there are two tape libraries in operation. The first one is located in the computer centre (RZ) and directly accessible by gStore and user backup services. The second one is located in the remote BG2 building and contains copies of experiment (raw) and backup data. This concept prevents from loss of valuable data in case of media damage and enables disaster recovery.

In 2011 four new data movers have been installed increasing the overall disk cache capacity and I/O bandwidth. A summary of the current hardware resources can be found in table 1.

resource	used	max
storage capacities:		
3584-L23 ATL RZ:	580 TB	2.2 PB
3584-L23 ATL BG2:	170 TB	1.3 PB
overall data mover disk cache	< 90%	0.2 PB
lustre file system [2]	~80%	2.2 PB
overall gStore I/O bandwith:		
DM disk <-> tape (SAN)		1.2 GB/s
DM disk <-> clients (LAN)		5.0 GB/s
DAQ online clients ->DM disk		
all files also copied to lustre		0.5 GB/s
no copy to lustre		1.0 GB/s

Table 1: Hardware Status GSI Storage in December 2011

gStore Enhancements

1. Online data storage from running experiments. Data from running experiments can be transferred online to gStore write cache and optionally also to lustre, where data are immediately available for monitoring and online analysis. Both gStore processes have been decoupled completely in case of sequential copy mode. This assures that online storage to gStore is not affected by occasional lustre latencies and hang-ups.

The I/O bandwidth for online data storage from running experiments has been enhanced by a factor of 2 in 2011 (see table 1).

2. Recursive file operations are possible now with all relevant gstore commands using the flag '-recursive'. Additionally wildcard characters can be used in file and in (sub)directory names. In such cases the specified operations are performed for all matching files in all matching top directories and in all subdirectories.

3. Automatic process parallelization has been implemented for the gstore stage command. If a large set of files is staged, files located on different tape media are copied in parallel to read cache on different data movers. This not only considerably decreases the overall staging time, but also speeds up access to the distributed read cache files, which can be read with the overall I/O bandwidth of all the data movers involved, e.g. in parallel from many batch farm nodes.

If all files to be staged are located on a single tape, the files are divided into several groups and also staged to different data movers, one group of files after the other.

Outlook

The concept of automatic process parallelization will also be implemented for archive processes from lustre to gStore and for retrieve processes from gStore to lustre. Then with single gstore commands acting on large file sets overall transfer rates of up to 5 GB/s will be possible.

Now the next generation of tape drives is available on the market. The write density is a factor of 4 higher, and the media prices (per PByte) decrease to 40%. A tape drive upgrade in the RZ ATL would increase the storage capacity to 8.8 PByte and the I/O bandwidth to 2 GByte/s. With additional media boards, the capacity could be enhanced to 50 PByte, which approaches already the order of magnitude needed for FAIR.

References

[1] see http://www.gsi.de/informationen/wti/it/exp_daten/daten_speicherung_e.html as starting point for more info on gStore.

Status of the FairRoot simulation and analysis framework

M. Al-Turany[1], *D. Bertini*[1], *R. Karabowicz*[1], *D. Kresan*[2], *T. Stockmanns*[3], *and F. Uhlig*[1]
[1]GSI, Darmstadt, Germany; [2]TU, Darmstadt, Germany; [3]FZJ , Jeulich, Germany

The FairRoot framework is the standard simulation, reconstruction and data analysis framework for the FAIR experiments [1]. It is based on ROOT [2] and the Virtual Monte-Carlo (VMC) interface [3]. Only the general status will be presented here, more details about FairRoot developments and usage in the different experiments can be found elsewhere in this report.

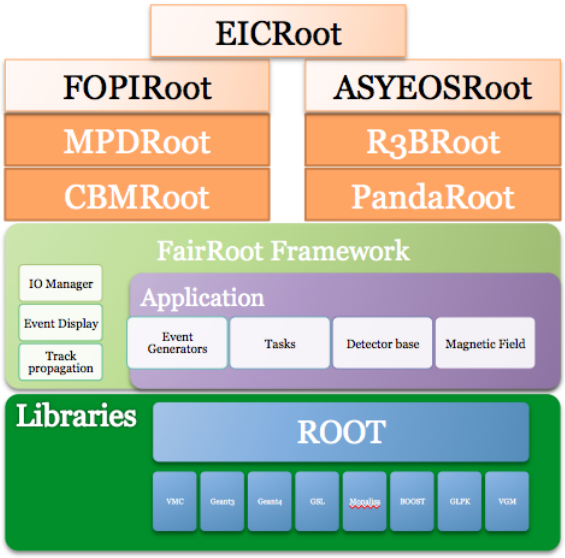

Figure 1: FairRoot at different experiments

Different implementations of experiments code based on FairRoot are shown in Figure 1. The base classes and general packages are kept in FairRoot to make them available for all experiments.The following three new implementations of FairRoot were introduced last year.

ASYEOSROOT

The international ASY-EOS collaboration, has recently been formed to study the EOS of asymmetric nuclear matter [4]. The ASYEOSRoot branch contains the detector simulation and reconstruction code of this experiment. On request of this collaboration the MBS event API [5] has been integrated into FairRoot. With the MBS API integrated one can communicate with the DAQ and/or read the list mode data files (lmd-files).

FOPIROOT

The branch FOPIRoot is mainly a TPC detector simulation, reconstruction and analysis code. The code was originally designed and implemented for the PANDA experiment. The prototype detector is tested at the FOPI experiment.

EICROOT

The Electron-Ion Collider Collaboration (EICC). EICC consists of more than 100 physicists from over 20 laboratories and universities from around the world who are working to realize a new facility in the United States. This collaboration is evaluating the FairRoot framework for their usage, some detectors are already implemented in the so called EICRoot (Figure 2.) This evaluation was mainly motivated by the modular designed of FairRoot and its large user base within the HEP community [6].

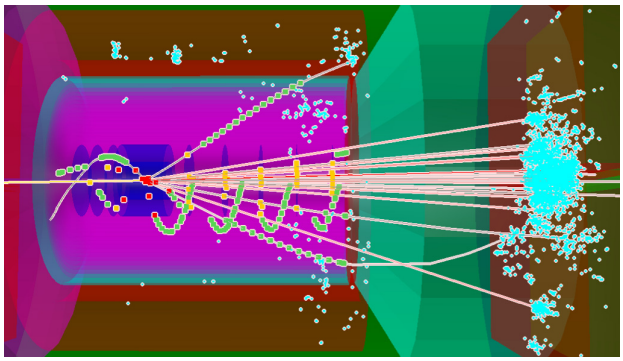

Figure 2: EIC detector implementation

Moreover the FairRoot [1] webpage has moved to a content management system (CMT) based on Drupal [7]. The new server allows more interaction with the users and offer more tools that help maintaining and documenting our project.

References

[1] FairRoot: http://fairroot.gsi.de

[2] R. Brun and F. Rademakers. Root - an object oriented data analysis framework *Nuclear Instruments and Methods in Physics Research A*, 389:81–86, Sep. 1997.

[3] R. Brun, F. Carminati, I. Hrivnacova, and A. Morsch Virtual Monte-Carlo In *Computing in High Energy and Nuclear Physics*, pages 24–28, La Jolla, California, 2003

[4] Test of the triple telescope prototype for the ASY-EOS experiment, GSI REPORT 2010

[5] http://www-win.gsi.de/daq/

[6] http://www.phenix.bnl.gov/WWW/publish/elke/EIC/TF-Meetings/eicroot_pres.pdf

[7] http://www.drupal.de/

FairRoot: Time-based simulation and reconstruction

M. Al-Turany[1] *and T. Stockmanns*[2]
[1]GSI, Darmstadt, Germany; [2]FZJ , Jeulich, Germany

The FairRoot framework [1] is the simulation, reconstruction and data analysis framework for the FAIR experiments. It includes core services for detector simulations and offline analysis. The framework, is designed to optimize the accessibility for beginners and developers, to be flexible (i.e. able to cope with future developments), and to enhance synergy between the different physics experiments within the FAIR project.

In the default mode of the software each event is treated completely independent of each other and time between events does not play a role. This is not always true in experiments, there are many cases where the time between successive events is of importance, i.e.:

- A particle hits a sensor element that is still blocked from previous hit(s)
- The read out electronic is still busy
- Hits are too close in time and cannot be distinguished

For PANDA and CBM experiments, the situation gets even more complicated as these experiments are planned without hardware trigger, i.e. continuous beam with Poisson statistics. To simulate such situations and to be able to study these cases new methods and concepts were introduced to FairRoot.

Event time

The time between two successive events can be set either during the simulation or during the reconstruction (digitization). During simulation, the time is set via the FairPrimaryGenerator, options available are:

- Set the min and max limit for event time in ns, time is set via uniform random number generator between min and max.
- Set the mean time for the event in ns (Event time is an exponential deviate)
- Set the time function for the event

The first two methods can also be used from the FairRunAna manager class during reconstruction (digitization) to set or overwrite the event time.

Time based simulation

A special buffer to store detector digits between events has been introduced (FairWriteoutBuffer). This is an abstract base class where the user (detector developer) have to inherit from and customize the behavior of his detector. This buffer holds the data that had to be stored and the absolute time of this data, if the same detector element is hit a second time this data is modified. This results in a randomized data stream stored to a TClonesArray (this simulates the input detector data as received by the DAQ in a real experiment)

It is essential for the later extraction of the data that it is sorted by its time stamp, hence a base class for the sorter (FairRingSorter) and a base class for a sorter task (FairRingSorterTask) are implemented in the software. To use them each detector has to derive his own sorter classes from them and overwrite necessary methods.

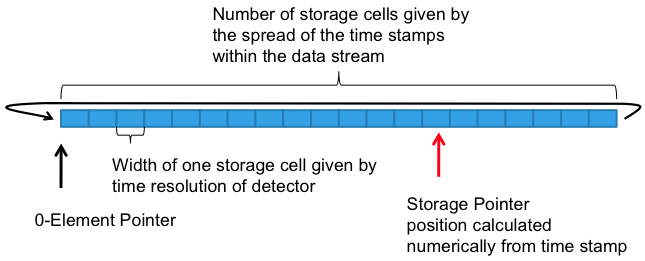

Figure 1: If a storage position is calculated which would override old data, the old data is saved to disk and the storage cell is freed

Reading back data is done via the FairRootManager, where two different methods exists:

- GetData with one functor/parameter runs always forward in time. (Data is only read once)
- GetData with two sets of functor/parameter is able to get data within a time interval. (Data can be extracted many times)

Different algorithms are available to extract data:

- All data up to a given time
- All data in a time window
- All data between time gaps of a certain size
- Other algorithms can be (easily) implemented

An example for implementing time simulation in FairRoot is available on PANDA wiki.[2]

References

[1] FairRoot: http://fairroot.gsi.de.
[2] http://panda-wiki.gsi.de/cgi-bin/view/Computing/TimeBasedSimWorkshopGSI2011

Database Interface for FairRoot

M. Al-Turany[1], *M. Babai*[2], *and D. Bertini*[3]
[1]GSI, Darmstadt, Germany; [2]KVI/RuG, Groningen, The Netherlands; [3]GSI, Darmstadt, Germany

Introduction

Since the setup of a typical nuclear experiment is varying depending on the physics case to study, the software for simulation and analysis should be able to handle a large amount of different parameters and their variation in time. For that purpose, the FairRoot framework [1] implements a database interface which provides a simple and uniform concept regardless of the data being accessed. Furthermore the database interface, using internally the ROOT TSQLServer services [2] , can access data from more than one database instance using a dedicated database connectivity implementation.

Design

The FairRoot framework already uses a parameter management system based on the original HADES runtime database [3] . The runtime database supports input from ASCII files and ROOT files. A database input will be added using TSQLServer.

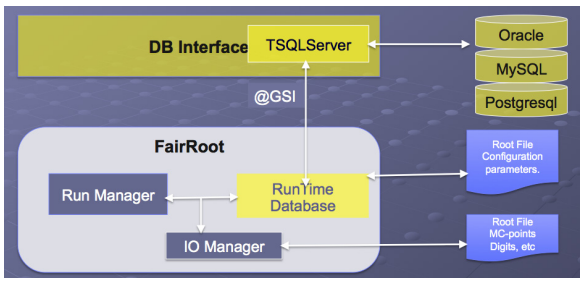

Figure 1: The Database interface in FairRoot.

Database Connectivity

The database connection is done via the ROOT TSQLServer class. For accessing the data more than one database connection can be used according to the user-defined URLs list. At initialisation time, the list order reflects the access priority. The first database in the list is used for searching the data, if it fails the next database in the list is used until the complete set of data can be retrieved. This gives the user the flexibility to create its own database from a subset of the official one and to put it ahead in the list.

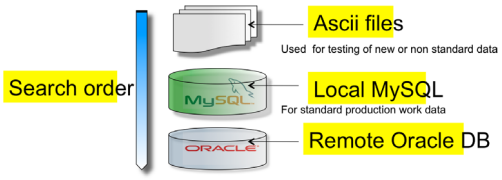

Figure 2: The ordered priority list of databases

Context sensitive version management

Ultimately, any of the data retrieved could depend on the run or the event being processed. Detector relevant parameters, such as calibration constants, will change with time and the interface has to retrieve the right ones for the current run or event.

For this reason, all requests for data through the interface must supply information about:

- The type of data: real or Monte Carlo
- The type of Detector.
- The date and time of the run or event (in UTC)

This information is called a Context. In the database all information is tagged by a Context i.e by a validation range which identifies the type of data and detector and the ranges of date times for which it is valid.

Minimizing the I/O

Another important point is to minimise I/O. Some requests, particularly for detector relevant parameters, can pull in large amounts of data but users must not load it once at the start of the job and then use it repeatedly since it may not be valid for all the data they process. Also multiple users may want access to the same data and it would be inefficient for each to have their own copy. To deal with both of the above problems, the interface uses the concept of handle or proxy and implements different levels of objects caching.

References

[1] M. Al-Turany, D. Bertini , I. Koenig, The FAIR simulation and analysis framework 2008 J. Phys.: Conf. Ser. 119 032011.

[2] http://root.cern.ch/.

[3] http://web-docs.gsi.de/ ilse/initialization.htm

Implementation and Performance of Neutron Tracking Algorithm for NEULAND *

D. Kresan[1], *M. Al-Turany*[2], *D. Bertini*[2], *R. Karabowicz*[2], *P. Malzacher*[2], *and F. Uhlig*[2]
[1]TU, Darmstadt, Germany; [2]GSI, Darmstadt, Germany

The NEULAND will be used in R3B at FAIR for the detection of fast neutrons. The focus is the recognition of multi-neutron events with precise determination of position and time of first interactions in the detector volume, which will allow momentum measurement by distance and time of flight. For the details on the proposed NEULAND layout see [1]. A fast and high performing (in terms of efficiency and resolution) neutron tracking algorithm is required.
The development of the tracking algorithm was done within R3BRoot software which is part of the FairRoot framework [2] developed at GSI for FAIR experiments. The input for the task is an array of objects of type R3BLandDigi, which contains information about time and charge deposited in one scintillator bar and read-out by two photomultipliers on the right and left end-cap. The output of the task is an array of objects of the type R3BNeutHit, which contains information about position and time of first interaction of potential incident neutron, necessary for momentum determination.

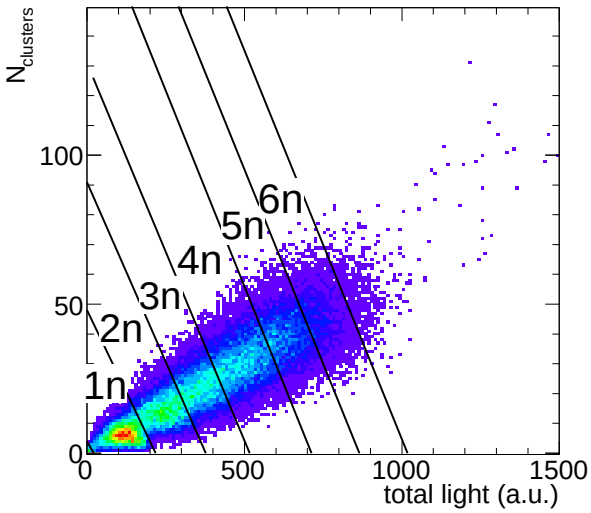

Figure 1: Distribution of the number of clusters versus total deposited energy in NEULAND. Solid lines show chosen set of cuts to separate event classes.

In the first stage of the reconstruction algorithm a number of incident neutrons is determined by cutting on values of the number of clusters and total deposited energy in the detector. Clusters are created from digis by analyzing the time and position pattern and represent tracks of charged particles. These 2-D cuts (see fig. 1) have to be calibrated on ideal case of separated event classes. In the future we will automatize the procedure of such calibration and include the values of cuts in the parameter file.
In the second stage the known number of first interactions of incident neutrons is determined. In order to exclude the secondary interactions after elastic scattering of neutrons on hydrogen we implemented a recursive function which is called for each possible pair of clusters in the loop and removes those clusters which satisfy the criteria of ellastic scattering. After such cleaning procedure, the remaining clusters are sorted with respect to absolute deviation of the velocity of potential neutron from the known beam velocity (smaller deviation has higher priority) and amount of deposited energy (higher energy has higher priority). From the list of sorted clusters the known number of first interactions is chosen starting from the top of the list.

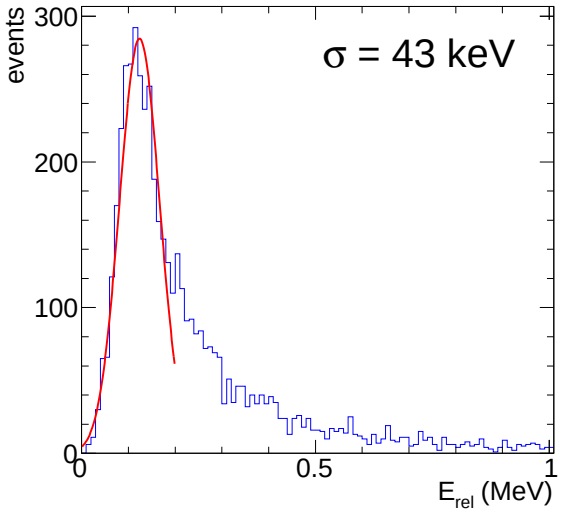

Figure 2: Simulated spectrum of tetra-neutrons (four neutrons with narrow spacial and timing distribution) with input E_{rel} = 100 keV. The tail towards higher values is due to misidentification of first interactions of incident neutrons.

Example of the algorithm performance is shown in fig. 2. The total efficiency is ≈60% with E_{rel} resolution of 43 ps.

References

[1] K.Boretzky et.al, GSI Scientific Report 2011

[2] J. Phys.: Conf. Ser. (2008) 119 032011

* Supported by Helmholtz International Center for FAIR

Implementation of unit tests for the FairRoot framework

M. Al-Turany[1], *D. Bertini*[1], *R. Karabowicz*[1], *D. Kresan*[1], *and F. Uhlig*[1]
[1]GSI, Darmstadt, Germany

Abstract: FairRoot comes with a powerful build and test system which allows the easy setup of automatic tests. To get a good test coverage of the code, we started to implement unit tests. In this paper we will summarize our evaluation of software frameworks for this task.

FairRoot test environment

Since FairRoot is now used by many experiments as a base for their own specific developments, the code has to be tested as thoroughly as possible. Up to now only **system tests** are implemented, which test a complete program at once.

To run all defined tests automatically we use the test environment CTest which comes as integrated part of our used build system CMake [1,2]. The functionality of CTest is also used by the different experiments for there own set of tests. CTest provides the functionality to run a complete test scenario, including automatic updating, configuring, building, testing, performing memory checking, performing coverage analysis, and submitting results to a CDash web server [3].

Using the results about the code coverage gathered on our CDash [4] web page, one can see that the current set of tests only cover 20-30% of the total code base, depending on the experiment. To implement more system tests to cover also the untested parts of the code base is a nearly unmanageable task. As a solution one has to use beside the system testing also **unit tests** which tests the correctness of specific code sections individually, usually at the function level.

To simplify the process of unit testing, many unit testing frameworks have been developed (see [5]).

Requirements

Since we have CTest to steer the testing procedure the unit test framework itself has only to provide the tools to setup tests in an easy to use way. It should be able to setup the test environment automatically, implement the needed assertions and generate a test report which can be sent to our web server. Beside all this it should be as easy as possible to implement the unit tests.

Most of the unit testing frameworks listed at [5] have been ruled out immediately. Either they are not developed any longer, it was impossible to get them to work or they couldn't fulfill the requirements. From the remaining 5-6 candidates we choose the two most promising frameworks (Boost Test [6] and Google Test [7]) for a thorough evaluation.

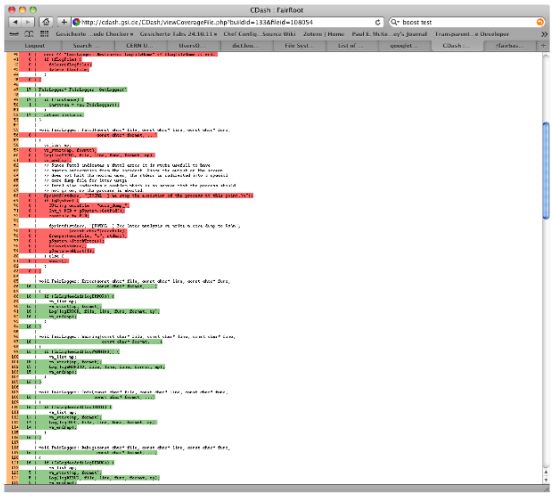

Figure 1: Coverage information for a single file.

Results

For the evaluation we tried to write a complete set of tests for the logging class of FairRoot. This set of tests should cover the complete functionality of the class and check for the correctness of the results. We choose the logging class for the evaluation, because the class is neither to complex, nor to trivial to be used as a test case.

Using our build and test environment to run the set of tests, the resulting code coverage and the results of the set of tests can be checked on our CDash web server immediately after the execution of the tests. This includes also the possibility to check which lines of the source code have been tested and which are still untested (see figure 1). This information was then used to improve the set of tests in an iterative process.

As a final result we choose to use the Google testing framework to implement unit tests for FairRoot. In contrast to the Boost unit testing framework it provides already all the needed functionality. Moreover it is much simpler to implement tests using the Google testing framework.

References

[1] K. Martin and B. Hoffmann. Mastering CMake, A Cross-Platform Build System, Kitware Inc., 2010
[2] CMake Webpage: http://www.cmake.org
[3] CDash Webpage: http://www.cdash.org
[4] FairRoot CDash: http://fairroot.gsi.de/CDash
[5] Wikipedia: http://en.wikipedia.org/wiki/List_of_unit_testing_frameworks
[6] Boost Webpage: http://www.boost.org
[7] GoogleTest Webpage: http://code.google.com/p/googletest/

PROOF on Demand

A. Manafov, P. Malzacher

GSI, Darmstadt, Germany

PROOF on Demand (PoD) [1][2] is a tool-set that automats and dramatically simplifies the process of creating private PROOF [3] clusters.

PoD dynamically sets up a PROOF cluster at a user's request on any resource management system (RMS). It provides a plug-in based system, in order to use different job submission front-ends.

In 2011 the plug-in set has been extended and supports now gLite, LSF, PBS (PBSPro/OpenPBS/Torque), Grid Engine (OGE/SGE), Condor, LoadLeveler, and SSH plug-ins. PoD makes it possible just within a few seconds to get a private PROOF cluster on those systems. If there is no RMS, then the SSH plug-in can be used, which dynamically turns a bunch of machines to PROOF workers.

User community

PoD is being very successfully used by German ALICE collaboration and has been chosen as a standard PROOF tool for FAIR computing [4].

The tool-set is official distributed to all Tier3 ATLAS sites via standard ATLAS software deployment machinery [5].

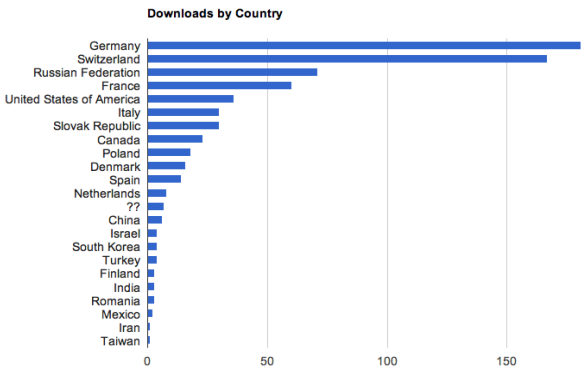

Figure 1: ~700 downloads from 22 countries (since June, 2010), with 180 downloads/year from unique IPs.

A thin client concept

Recently a new major step in PoD development has been made. It now supports not only local PoD servers, but also remote ones.

A newly developed "pod-remote" command made it possible for users to utilize a thin client concept. In order to create dynamic PROOF clusters, users are now able to select a remote computer, even behind a firewall, to control a PoD server on it and to submit PoD jobs. In this case a user interface (UI) machine is just a lightweight control center and could run on different OS types or mobile devices.

All communications are secured and provided via SSH channels. Additionally PoD automatically creates and maintains SSH tunnels for PROOF connections between the UI and a PROOF master.

Dynamic PROOF masters

Future versions of PoD are going to implement a dynamic PROOF masters feature, which is an extension of the recently developed "pod-remote". This feature is going to enable PoD to automatically assign PROOF master processes to worker nodes (WN). Users would need only to run a lightweight PoD/PROOF UI to process their analysis, as the rest will be entirely running on WNs.

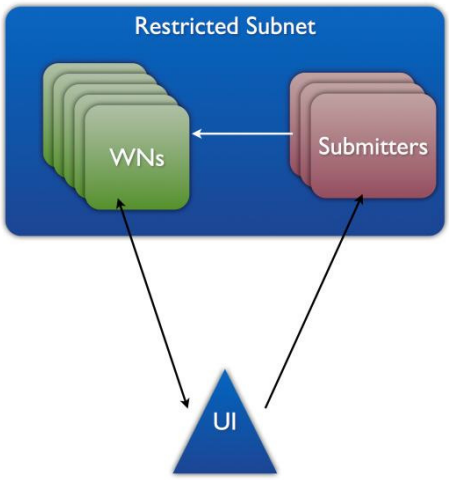

Figure 2: Dynamic PROOF masters.

Summary

As PoD matures as a product, it is used more and more as a standard for setting up dynamic PROOF clusters in many different institutions in the HEP community. With PoD there is no need to maintain a dedicated PROOF analysis facility. PoD users create themselves private dynamic PROOF clusters on general purpose batch farms, Grid or Cloud systems.

References

[1] A. Manafov et al, "PROOF on Demand", PHN-IS-IT-07, GSI Scientific Report 2010.

[2] PROOF on Demand (PoD), http://pod.gsi.de

[3] The Parallel ROOT Facility (PROOF), http://root.cern.ch/drupal/content/proof

[4] M. Al-Turany et al, "PROOF integration in FairRoot, GSI", Scientific Report 2011.

[5] ATLAS Wiki, https://twiki.atlas-canada.ca/bin/view/AtlasCanada/ManageTier3SW

PROOF integration in FairRoot

R. Karabowicz[1], *M. Al-Turany*[1], *D. Bertini*[1], *D. Kresan*[2], *A. Manafov*[1], *and F. Uhlig*[1]
[1]GSI, Darmstadt, Germany; [2]TU, Darmstadt, Germany

Abstract

Parallel ROOt Facility (PROOF[1]) is a ROOT[2] extension allowing analysis of large data sets in parallel on clusters of machines with multiple CPUs. The usage of the appliance requires the analysis to be dividable into independent subsets (in our case we imply event independency) and the code to follow a definite organization (TSelector-derived class to manage task processing).

Goals

The goal of the presented work is to allow any FairRoot[3] user to take advantage of the numerous many-core machines to effortlessly execute his analysis faster in a simple and transparent manner with few interventions into code or macros.

Implementation

The local analysis in FairRoot is managed through usage of flexible steering macros, which are developed by users. There users load libraries, set input files and parameter databases, create and set up various analysis tasks. The FairRoot management classes created in the macro initialize the analysis, loop over and analyzes available events and write the output to user-defined file.

In the case of running on the PROOF cluster separate processes are started on different CPUs (workers), also on external machines. On these workers:

- necessary libraries are uploaded using PROOF ARchive (PAR) files;
- a general FairAnaSelector class creates FairRoot analysis, connects parameter databases and triggers analysis of separate events, which are distributed by the PROOF session that controls the input data;
- creates output which is consequently merged on the master at the end of process.

One of the greatest challenges when adapting FairRoot to PROOF is the copying of the analysis tasks to the workers. As the copying of the tasks was not required in the original FairRoot concept it means that most of them have to be adapted to be compatible with PROOF.

Results and conclusions

The presented analysis has been tested on several GSI machines and the analysis time improvement of up to 5 times was observed as compared to local analysis.

In the Figure 1 the speedup factor is presented as a function of the number of events when running on a 4 CPU machine. For small number of events it is more efficient to run locally due to additional time spent initializing PROOF. For large number of events the factor saturates at about 2.5, which is considerably less than expected scaling of 4. The damping factor behind is the IO communication, which

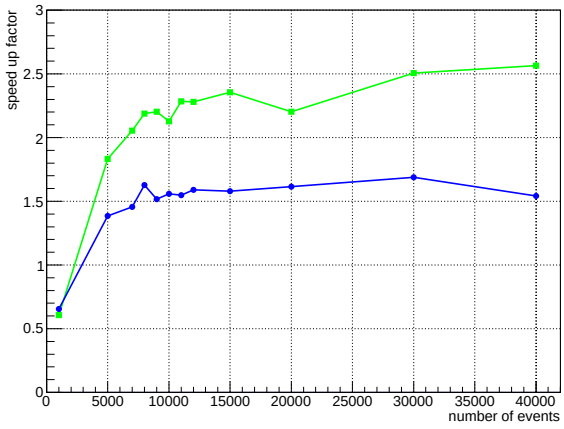

Figure 1: Speed up factor (ratio of local analysis time to PROOF analysis time) as a function of number of analyzed events on 4 (green) and 2 (blue) workers.

was tested by artificially slowing down the processing of each event - in this case this ideal scaling was achieved.

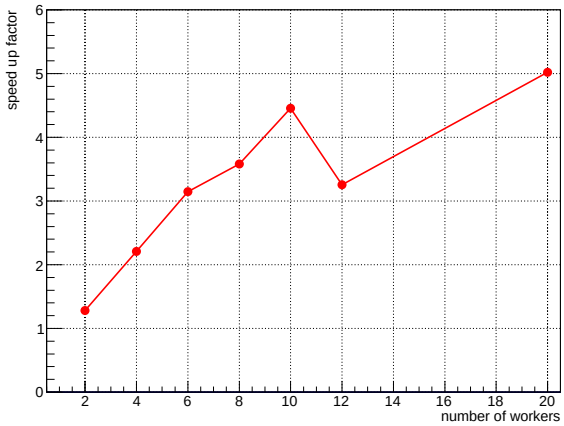

Figure 2: Speed up factor as a function of number of workers.

Figure 2 shows the speedup factor as a function of the number of workers. In this case a test PROOF cluster was set up using PoD[4] consisting of 3 machines with 4+8+8=20 CPUs altogether.

The implementation of the FairAnaSelector opens up a possibility of running FairRoot parallely on many-cores PROOF clusters. The code is available for all users of FairRoot, however further tests and developments are still needed.

References

[1] PROOF: http://root.cern.ch/drupal/content/proof
[2] ROOT: http://root.cern.ch
[3] FAIRROOT: http://fairroot.gsi.de
[4] PoD: http://pod.gsi.de

E-Science Activities at GSI

K. Schwarz for the e-science group/Scientific Computing[1]
[1]GSI, Darmstadt, Germany

This article describes the work of the GSI e-science Group with the aim to enlarge and operate an ALICE tier2 centre within the global environment of the LHC Computing Grid and to prototype a distributed computing environment for FAIR.

ALICE tier2 centre at GSI and ALICE Grid in Germany

The ALICE tier2 centre at GSI provides a computing infrastructure for ALICE Grid and for the local usage of the German ALICE groups. New data-sets are being transferred to GSI continuously and are processed on the local batch farm via daily running analysis trains. Further tasks are data calibration and quality assurance. Corresponding papers are being published. The available disk space is distributed among an xroot cluster (300 TB) and Lustre (2.3 PB). The xroot cluster is configured as a Grid Storage element and globally accessible, while Lustre is used for local data storage. Throughout the year GSI participates in centrally managed ALICE Grid productions and data analysis activities. The overall job share of GSI and Forschungszentrum Karlsruhe (ALICE tier1 centre) has been 16% of all ALICE jobs worldwide. Moreover the HHLR compute cluster at Goethe University in Frankfurt has been integrated into ALICE Grid.

Local farm management at GSI

The GSI e-science group contributes significantly to local farm management with the GSI batch farm being an integral part of the ALICE tier2 centre. One of the major projects is the transition from the commercial LSF scheduler to the open source scheduler (Sun)GridEngine [1] in close collaboration with the HPC group. The number of CPUs has been increased up to 4700 cores distributed over currently 2 clusters. The old cluster is operated via LSF while the new cluster is accessible exclusively via Grid Engine. Here the software is distributed via CVMFS and shared HOME directories are not available anymore. Monitoring is done by using MonaLisa.

Via KOSI (Kooperativer Studiengang Informatik) students from Hochschule Darmstadt the projects Cluster Virtualisation and Job Accounting are followed up. Via the first project a production version of an IaaS environment is implemented which is based on the experiences made beforehand with a prototype being able to provide 100 virtual machines via OpenNebula, libvirt, and KVM on 16 physical boxes. The new infrastructure will take into account the new network segmentation at GSI and will make use of the recently introduced service hypervisors. The idea is to be able to provide a complete Chef managed batch farm including server and virtual worker nodes with fitting applications already on board as predefined by the experiments. This can be used for software environments which are not supported anymore on the official GSI infrastructure.

PROOF on Demand

The in the context of the D-Grid project developed "PROOF on Demand (PoD) utilities" enjoy a high popularity. PoD [2] is a set of software tools developed at GSI via which each user can dynamically create individual PROOF clusters. The development is going on and and new releases are being published. Next to more supported plugins (currently PoD environments can be started via gLite, LSF, SGE, PBS, and ssh) also the user community is increasing. In the ALICE context PoD starts to be established as standard, and ATLAS started to distributee PoD as official part of their T2 software package.

Preparation for FAIR

PANDA-Grid has been extended to 18 sites, among these 3 universities from the Philippines and 1 university from Thailand. The collaboration with these sites has been strenghtened by several working visits of Asian scientists. CBMGrid is up and running. First small productions have been running successfully using the CBMGrid infrastructure. The largest CBMGrid site is Dubna, supported by the JINR-BMBF grant. Moreover in order to be able to utilise commercial computing resources for FAIR computing the capability to be able to power up an AliEn Grid site in a Cloud is being investigated. A current test case is being set up at Frankfurt Cloud [3]. The collaboration between ALICE and the FAIR experiments intensified significantly. Synergy effects have been identified within the development of the experiment frameworks AliRoot and FAIRRoot as well as in the context of Grid computing [4]. In joint workshops on regular basis (PandaGrid Workshop in conjunction with AliEn Developers Week) as well as in frequent telephone meetings the ongoing work is organised.

References

[1] C. Preuss, V. Penso, B. Neuburger, "GridEngine - A new scheduler for the GSI computing cluster", this report.

[2] A. Manafov, P. Malzacher, "PROOF on Demand", this report.

[3] M. Zynovyev, D. Klein, A. Manafov, V. Penso, "Utilization of LOEWE-CSC within the Frankfurt Cloud", this report.

[4] A. Montiel-Gonzalez, M. Dahlinger, K. Schwarz, "AliEn Database Interface Development for FAIR", this report.

ALICE tier2 at GSI

K. Schwarz[1]
[1]GSI, Darmstadt, Germany

This article describes the work of the GSI e-science Group with the aim to enlarge and operate an ALICE tier2 centre within the global environment of the LHC Computing Grid.

ALICE tier2 centre at GSI

Together with the GSI/EMMI ALICE group [1] GSI-IT is responsible for the operation of the ALICE tier2/3 computing centre at GSI. From the IT side a majore part of the work is done within the e-science group of the SC department [2]. The ALICE tier2/3 centre provides computing infrastructure for ALICE Grid and an analysis platform to all ALICE members in Germany. The activities of the GSI/EMMI ALICE group in 2011 has been focused on the analysis of the first Pb-Pb data, taken at CERN in 2010 with an energy of $\sqrt{s_{NN}} = 2.76\,TeV$ as well as on preparation and analysis of the second Pb-Pb run in 2011. Moreover the analysis of the pp data from 2010 ($\sqrt{s} = 7\,TeV$) and 2011 ($\sqrt{s} = 7\,TeV$ and $\sqrt{s} = 2.76\,TeV$) has been continued.

For this new data-sets have been transferred to GSI almost continuously. In order to achieve the necessary data rates GSI has been integrated with 10 Gb into the the HEPPI net structure of the LHC tier2 centres in Germany. The data have been processed on the local batch farm via daily running analysis trains. A train is assembled from a list of modules that are sequentially executed and is an efficient way to process a large set of data.

At the core of the ALICE tier2/3 centre is a large compute clustre (batch farm). The number of CPUs has been increased up to 4700 cores distributed over currently 2 clusters. One of the major projects is the transition from the commercial LSF scheduler to the open source scheduler (Sun)GridEngine [3]. The same compute resources are shared by local and Grid jobs. Moreover parallel data processing can be achieved by private PROOF clusters submitted to the batch farm via PROOF on Demand (PoD) [4].

The available disk space is distributed among an xroot cluster (300 TB) and a Lustre clustre (2.3 PB) which is mounted by each worker node in the batch farm. The xroot cluster is configured as a Grid Storage element and globally accessible, while Lustre is used for local data storage.

ALICE Grid in Germany

The ALICE Grid resources in Germany are provided by the tier1 centre at GridKa in Karlsruhe and the tier2 centre at GSI. Moreover the HHLR compute cluster at Goethe University in Frankfurt has been integrated in 2011. For this the interface between the ALICE Grid middleware AliEn and the local scheduling system Slurm had to be reactivated.

Throughout the year GSI and the other centres participate in centrally managed ALICE Grid productions and data analysis activities. In 2011 The overall job share of the German ALICE Grid centres have been 22% of all ALICE jobs running worldwide.

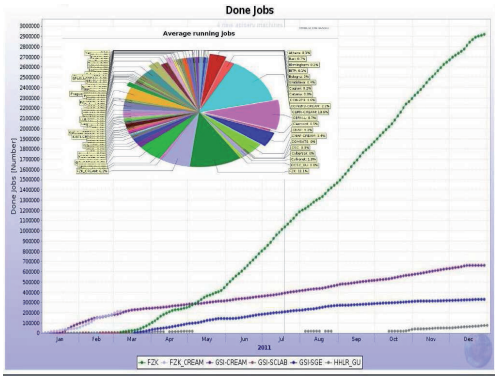

Figure 1: ALICE Grid jobs computed in Germany (GridKa, GSI, HHLR (Loewe CSC)

preparation for FAIR

ALICE and LHC computing help to prepare for FAIR computing. Synergy effects between ALICE and FAIR have been identified within the development of the experiment frameworks AliRoot and FAIRRoot as well as in the context of Grid computing. Joint workshops on regular basis (PandaGrid Workshop in conjunction with AliEn Developers Week) help to organise the ongoing work. Moreover in order to be able to utilise commercial computing resources for FAIR computing the capability to be able to power up an AliEn Grid site in a Cloud is being investigated. A current test case is being set up at Frankfurt Cloud [5].

References

[1] GSI ALICE group, “The second year of physics and data taking with the ALICE experiment at the LHC”, this report.

[2] K. Schwarz, “e-science activities at GSI”, this report.

[3] C. Preuss, V. Penso, B. Neuburger, “GridEngine - A new scheduler for the GSI computing cluster”, this report.

[4] A. Manafov, P. Malzacher, “PROOF on Demand”, this report.

[5] M. Zynovyev, D. Klein, A. Manafov, V. Penso, “Utilization of LOEWE-CSC within the Frankfurt Cloud”, this report

Software and Middleware at PandaGrid

K. Schwarz[1], *D. Protopopescu*[2], *and R. Dosdall*[3]
[1]GSI, Darmstadt, Germany; [2]University of Glasgow, UK; [3]Forschungszentrum Jülich, Germany

PANDA Grid is the computing tool of the PANDA experiment, and during the last years it has evolved beyond passive computing infrastructure, into a complete and transparent solution for physics simulation, reconstruction and analysis, an integrated toolset right at the fingertips of the physicist.

Grid Status

PANDA Grid [1] uses AliEn [**?**] middleware, developed by the ALICE experiment and used outside CERN by FAIR experiments, like PANDA and CBM. The data analysis and simulation framework, distributed via the built-in package management mechanism of AliEn, is centered on PandaRoot. Grid monitoring and data supervision are done via MonALISA [**?**]. While practically being the first up-and-running PANDA experiment component, PANDA Grid is continually evolving. It has grown to encompass 17 sites from 13 institutes in 10 countries, including EGEE/EGI sites integrated via VOBox tools. Mainz and ASTI/Philippines are joining at the time of writing.

Figure 1: Panda Grid sites distributed in Europe and Asia

Software and Middleware Tools

PandaRoot is an extension of FairRoot, a framework jointly developed by CBM and PANDA. The Grid infrastructure is used for software distribution via the package manager service (PackMan) provided by the middleware layer. PandaRoot and external software packages (boost, gsl, clhep, pythia, root, geant) are distributed separately, as interdependent source packages, compiled on sites. We possess now a completely integrated and automatic system for package installation, compilation and testing, supervised directly by PandaRoot developers. The user has only to customize a couple of scripts in order to pursue his/her own physics.

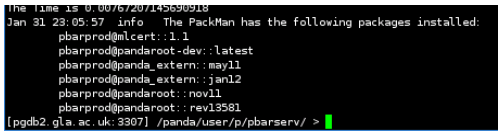

Figure 2: From the Command Line Interface of AliEn the user can see what software packages are installed on a given site

The AliEn middlewarewe itself already provides advanced data production tools: various mechanisms for job split and merging, catalogue tags and triggers, file collections, automatic data replication, etc. But besides these built-in mechanisms, the MonALISA layer provides a range of tools that make PANDA Grid both easy to administer and easy to use for large scale productions. Close communication between the groups participating in software development and Grid deployment is maintained mainly via dedicated workshops, hosted in turn by participant institutes. Four PANDA Grid workshops [**?**] were held 2010-2011, in the UK, in Switzerland, , Austria and Germany, with every second workshop being an AliEn developers workshop with the participation of the ALICE Offline team. Our Data Challenges (DC), during which large quantities of data are produced via a full chain of simulation, digitization and reconstruction, are an excellent tool for stresstesting the middleware, software, site data storage and network capabilities. The jobs run are either theoretical calculations or data simulations used for the design and prototyping of the PANDA detector. In general the PandaGrid infrastructure has been used intensively throughout the year, mainly though before conferences and collaboration meetings.

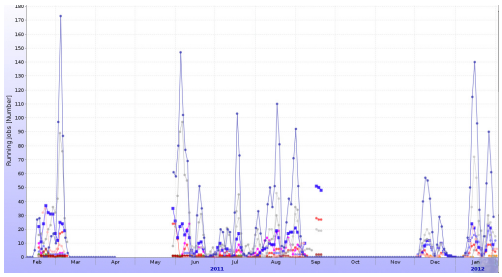

Figure 3: PandaGrid usage throughout the year.

References

[1] PANDA Grid documentation wiki at GSI:
http://pandawiki.gsi.de/cgi-bin/view/Computing/PandaGrid

Helmholtz Institutional Repositories based on CERN Invenio Software

S. Hesselbach[1], *T. Badura*[1], *K. Große*[1], *Z. Akopov*[2], *M. Köhler*[2], *T. Pazera*[2], *C. Plott*[3], *A. Wagner*[3], *L. Barake*[4], *and A.S. Diallo*[4]

[1]GSI, Darmstadt; [2]DESY, Hamburg; [3]Forschungszentrum Jülich; [4]RWTH Aachen

Since 2010 a collaboration between Deutsches Elektronensynchrotron (DESY), Forschungszentrum Jülich, GSI and Rheinisch-Westfälische Technische Hochschule (RWTH) Aachen is adapting the Digital Library System Invenio [1] to set up Institutional Repositories suitable especially for the needs of the scientists of the Helmholtz-Gemeinschaft Deutscher Forschungszentren e.V. [2]. Invenio is originally developed at CERN for the CERN Document Server CDS [3] and is now further developed internationally and used for many installations worldwide, most notably by the High-Energy Physics Literature Database INSPIRE [4].

The aims of the Institutional Repositories are to host the publication databases of the participating institutions and provide interfaces for Open Access requirements. The institutions of the Helmholtz-Gemeinschaft need to provide statistical and key data and lists of publications for their annual reports. For this a correct identification of authors, departments and projects is necessary. This is achieved in Invenio with help of authority Marc records [5, 6] which allow the mapping of the bibliographic records to the corresponding authors and departments and which can also cope with reorganizations of the institutions like renaming of departments and the existence of virtual institutes. The resulting publication lists can also be used by the departments and groups for e.g. dynamic generation of up-to-date publication lists for their own web pages.

In an ongoing effort comfortable submit masks are designed which facilitate the submission of the publication data by the scientists or departmental representatives and include automatic completion of author names with help of the authority data and enrichment from external sources like arXiv.org. This will be followed by a dedicated work flow to approve the submissions by departmental editors and librarians. Invenio includes further a powerful search engine to retrieve the content of up to several million records, which is organized in regular and virtual collection trees, social functionalities like commenting, tagging, user-defined baskets, basket sharing between users and email notifications. Figure 1 shows the start page of the GSI Institutional Repository, `http://repository.gsi.de/` with the search mask and and the navigable collection tree.

As the Helmholtz-Gemeinschaft is a signatory of the Berlin Declaration on open access [7] the Repositories of its institutions need to provide the corresponding interfaces. Furthermore it is necessary to provide a dedicated source for open access for publications resulting from EU projects (OpenAIRE [8]) based on the OAI-PMH standard [9]. With the Invenio system this can be achieved without

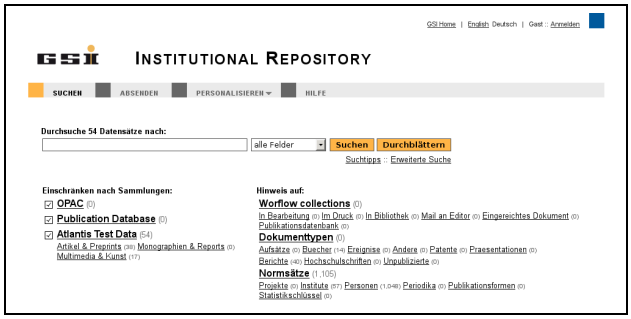

Figure 1: Example: GSI Institutional Repository.

the need of a further database as Invenio includes an OAI-PMH interface, can hold the full-texts for its bibliographic records and is able to expose a subset of the publication database for e.g. OpenAIRE. Easy export and import of data is further facilitated by the widely-used Marc 21 standard [10] for its internal records.

For the future it is planned to cover the full publication work flow from idea to final publication where the draft and preprint versions of the papers are stored in private collections of the group. Furthermore in personal baskets general lists of publications can be arranged e.g. for journal clubs or for students. Hence in this respect the Invenio system provides a true additional benefit for the scientists.

References

[1] Invenio. http://invenio-software.org/.

[2] Alexander Wagner. Veröffentlichungsdatenbank und Volltextrepositorium. *B.I.T. online*, 14(Sonderheft 1):45–48, 2011.

[3] CERN Document Server. http://cdsweb.cern.ch/.

[4] Inspire. http://www.projecthepinspire.net/.

[5] Marc 21 Format for Authority Data. http://www.loc.gov/marc/authority/.

[6] Christopher Michael Dickinson, Jean-Yves Le Meur, Abou Khaled Omar, and Pascal Felber. *Authority Control for INVENIO*. PhD thesis, Fribourg, EIA, 2011. Presented 07 Sep 2011.

[7] Berlin Declaration on Open Access to Knowledge in the Sciences and Humanities. October 2003. http://oa.mpg.de/berlin-prozess/berliner-erklarung/.

[8] OpenAIRE. http://www.openaire.eu/.

[9] The Open Archives Initiative Protocol for Metadata Harvesting. http://www.openarchives.org/OAI/openarchivesprotocol.html.

[10] Marc Standards. http://www.loc.gov/marc/.

Major Upgrade of central Oracle Database

M.Dahlinger[1]

[1]GSI, Darmstadt, Germany

In 2011 a major Hardware, Software and Security Upgrade has been performed for GSI central Oracle database services [1] offering higher performance and an enhanced scheduled 24x7 availability.

Hardware

New hardware has been taken into service:

- 2 8-core Linux Servers (SUSE SLES11) with 24 GB memory each
- Fibre Channel attached storage subsystem with 7 (max. 16) fast (15000rpm) SAS disks

Redundancy is assured exploiting redundant hardware and data paths using multipath technology.

Software

Oracle 11g R2 database enterprise edition with partitioning and RAC option and UTF-8 international character set support has been installed.

High availability and load balancing is performed using Oracle Real Application Cluster (RAC) technology. Storage is controlled via Oracle Automatic Storage Management (ASM) on a RAID6 array of fast disks with currently configured 1TB of disk space.

Online Backup is executed on a daily base using archive log features, internal hard-drives and TSM storage.

Applications can access Oracle database via transparent application failover (TAF), providing an uninterrupted database service even for most maintenance work (patches, service operations) and instance failures.

TAF exploits 11g functionalities using several virtual IP-addresses and listener daemons running on active nodes, resp.

The new database servers are located in an internal network, but are accessible from many GSI networks and external clients via the central firewall router. For further security enhancements access from outside will be directed through a proxy server in the DMZ.

Migration

Migration from former 10g databases has been completely performed by database administrators. Necessary changes in database objects (DDL) have been performed, e.g. changing default character length semantics from BYTE to Characters for all tables affected, allowing storage of the same amount of characters with Umlauts in a given VARCHAR2 cell, but using more bytes due to 2-Byte UTF-8 character coding.

Migration has been performed without interruption of read-access of running applications, achieved partly due to use of central LDAP-based naming resolution, switching database aliases used for applications to new database services running on new servers with new instance names.

References

[1] M.Dahlinger et al., “Central GSI Oracle Database Services”, GSI Scientific Report 2010.

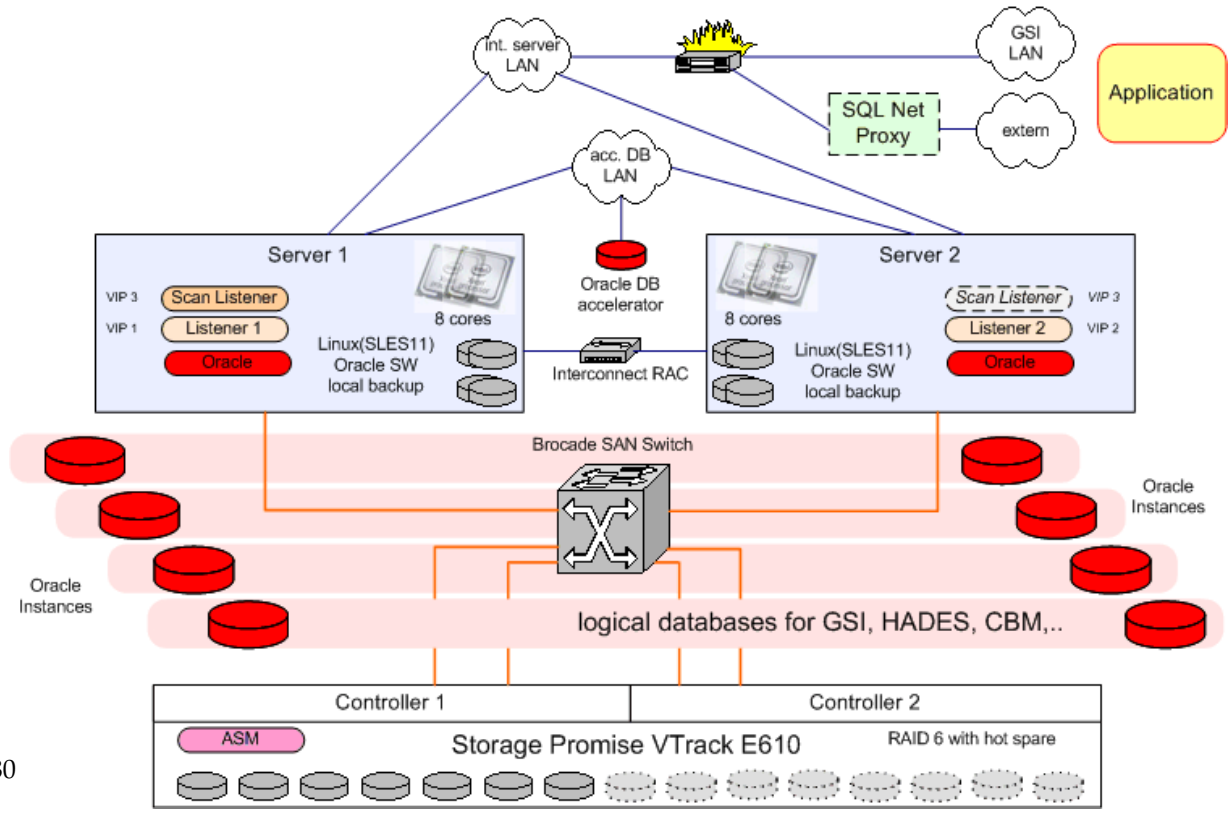

Accelerator Operation Report

W. Bayer, U. Scheeler*, P. Schuett

GSI, Darmstadt, Germany

This report describes the operation statistics of the GSI accelerator facility in the year 2011. The presented information is based on the data of the GSI electronic operation logbook OLOG [1] which allows for a detailed evaluation of operation statistics especially for the time-sharing operation mode of the accelerators.

General Overview

In 2011 GSI reduced the operation time by about 25% as compared to last year. From March till October only two beam time blocks were scheduled. In total, the SIS has been operated for 4248 hours and the UNILAC for 5032 hours. 216 hours are included for the commissioning of the accelerators after shutdown.

The first longer shutdown period lasted from January the 1st till March the 20th. This shutdown was used for a careful and detailed maintenance of the first Alvarez section, the repair of a few drift tubes in the poststripper section, the substitution of the front plate of the IH1-cavity at the High Current Injector, a vacuum upgrade of the SIS injection section and the repair of the pion target in front of the HADES cave. Technical improvements were installed at the RFQ of the High Charge State Injector, to optimize the operation behaviour. The next long shutdown started on October the 30th. It was used to maintain the second Alvarez section, to repair vacuum leaks in the single resonator section and in the ESR.

Table 1: Overall beam time of the accelerator facility

	2011	2010
Integral target time for all experiments	**8809h**	10438 h
Time for retuning	**96 h**	76 h
Time of interruption	**3518 h**	2704 h
Total beam time	**12432 h**	13218 h

In Table 1 the overall beam time of the whole facility is shown. In total, 8809 hours of beam-on-target-time were successfully delivered to the different physics experiments, about 1629 hours less than in 2010. The category 'retuning' includes the time necessary to improve the beam performance during the running experiment. The 'time of interruption' covers the categories ‘accelerator setup’ (1456 h), ‘ion source service’ (369 h) and ‘unscheduled down time’ (1693 h). These are all events which lead to a break of the running beam for the corresponding experiment. Altogether these times add up to the 'total beam time'. Due to time sharing operation this amount is higher than the sum of the operation hours. Compared to 2010 the ratio between target time and total beam time (availability of the facility) dropped by 8 percentage points to 71%. At last, the complex operation with three isotopes in parallel and a lot of short term experiments caused a lot of technical and administrative efforts.

Experimental Operation

Figure 1 gives an overview of target time for different experimental areas with the fraction of the 4 beam branches of the UNILAC on the right side, the ESR below and the different experimental caves behind the SIS on the left side. Details corresponding to the different experimental programs are given in [2].

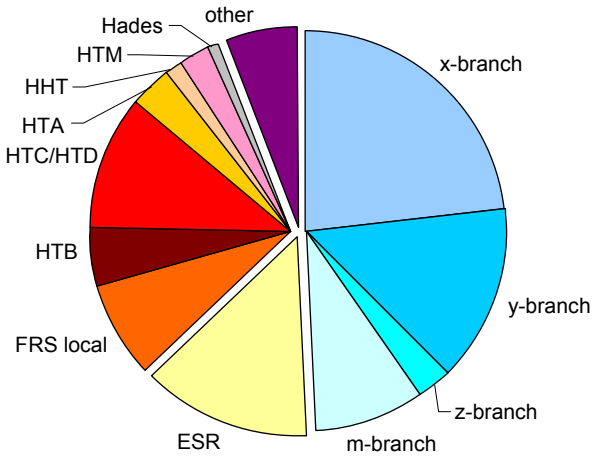

Figure 1: Distribution of target time to the different experimental areas

UNILAC Experiments

Details of the beam time for UNILAC experiments are shown in Table 2. Over the year, 11 different experiments were performed at the UNILAC. In total, 4523 hours of target time for physics experiments have been achieved. Beam was used by SHIP (1291 hours) and TASCA (1166 hours) as well as by Material Science (1410 hours). The fraction of target time decreased by 3% compared to last year. We observed an increase of times for ion source service and for accelerator setup and a decrease of unscheduled down time.

Table 2: Beam delivered to UNILAC experiments

	Time	Fraction
Target time for experiments	4523 h	76,1%
Time for retuning	33 h	0,6%
Accelerator setup	689 h	11,6%
Ion source service	279 h	4,7%
Unscheduled down time	418 h	7,0%
Total beam time	**5941 h**	**100%**

* u.scheeler@gsi.de

SIS/ESR Experiments

The heavy ion synchrotron delivered beams to 29 fixed target experiments and to 9 experiments at the ESR. In total 4286 hours of target time have been achieved. A more detailed overview is given in Table 3.

Table 3: Beam delivered to SIS/ESR experiments

	Time	Ratio
Target time for experiments	4286 h	66,1%
Time for retuning	63 h	1,0%
Accelerator setup	1005 h	15,5%
Ion source service	90 h	1,4%
Unscheduled down time	1038 h	16,0%
Total beam time	**6482 h**	**100%**

In 2011 the target time for the ESR (direct beam and beam via FRS) decreased to 1241 hours, 171 hours for HITRAP commissioning are included in this amount. About 988 hours of beam time were delivered to HTC, which was thus the main user at the SIS. For about 705 hours beam was used at local experiment of the FRS and 298 hours were delivered for producing a pion beam to HTB.

Accelerator Operation

Over the year 22 different isotopes have been accelerated. Figure 2 shows the total beam time for each isotope. The rare isotopes ^{48}Ca and ^{54}Cr were produced by the ECR ion source, which in total has been operated for 3353 h. The Penning ion source was mainly operated with ^{50}Ti and ^{197}Au (in total 4534 hours of operation). The high-current ion source was used for 3276 hours. Especially ^{36}Ar, ^{40}Ar and ^{14}N beams were delivered from the MUCIS ion source, ^{238}U was accelerated from the MEVVA ion source for 998 hours.

Table 4: Statistics of all unscheduled down time events

	Down time	No. of events
Power supplies	178 h	287
Vacuum and structures	222 h	77
Beam diagnostics	38 h	27
Operation	23 h	16
Safety-/ Interlock system	19 h	18
Ion Sources	148 h	94
RF system	469 h	479
Controls	64 h	37
Infrastructure	154 h	19
Others / ambiguous	126 h	55
Total of unscheduled down time	**1442 h**	**1109**

In Table 4 all unscheduled down time events are shown in more detail. In April a technical problem at the ECR ion source caused a break of five days in ^{48}Ca operation. In July a leak in the water supply pipeline disabled the operation for about two days. The amount of RF down time includes about 150 hours concerning problems with resonance excitation in UNILAC cavities as well as 135 hours caused by a damage of the coaxial power line of IH2. Compared to 2010 the total amount of down time remained constant, which is a relative increase in comparison to the decreased operation time.

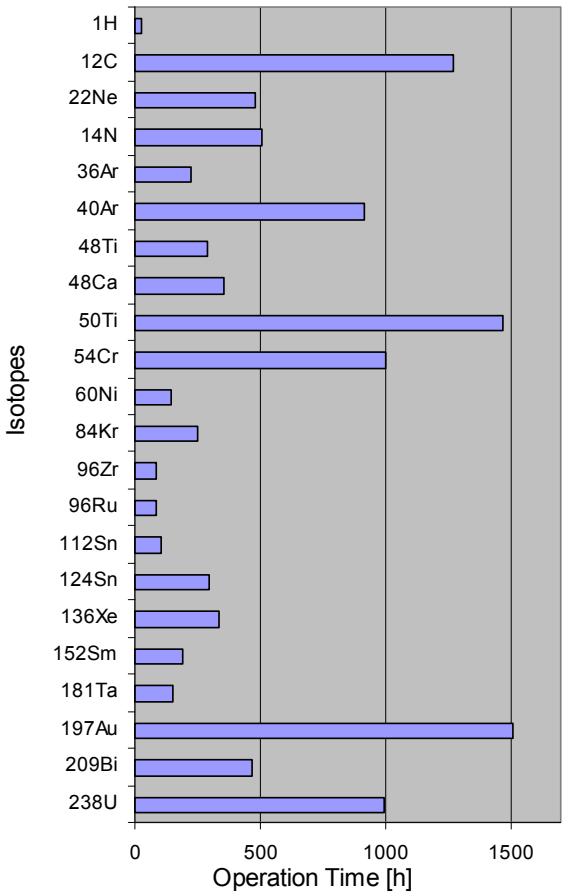

Figure 2: Total beam time for different ion species

For accelerator experiments at the UNILAC 168 hours, at SIS 253 hours, and at ESR 348 hours beam were delivered, which is for UNILAC a decrease by a factor of three compared to last year.

References

[1] P.Schuett, the GSI Operation Logbook OLog, WAO2010 (http://wao10.komac.re.kr/PDF/O-17.pdf)
[2] Report of beam time coordinator, this report

Ion source R&D Projects at the GSI Accelerator Facility

K. Tinschert[*], *R. Hollinger*[*], *A. Adonin*[*], *F. Heymach, R. Lang, J. Mäder, F. Maimone, J. Pfister, J. Roßbach, M. Stork*

GSI, Darmstadt, Germany.

ECR Ion Sources

Metal Ion Production

The investigations on the development of a ^{50}Ti beam for experiments of the Super Heavy Element (SHE) programme were extended by exploring 3 alternative approaches. Besides thermal evaporation of titanium with the resistively heated standard oven (STO) used in the GSI CAPRICE type ECR ion source (ECRIS) another type of resistively heated oven was investigated. This type of oven had been developed for the thermal evaporation of materials at very high temperatures (HTO) [1]. Furthermore the evaporation of chemical Ti-compounds at low temperatures was explored but did not lead to a useful method. The normal version of the STO is equipped with alumina (Al_2O_3) ceramics as support for the heating wire and as container for optional crucibles. However, alumina is not resistant against molten Ti and its vapor which show very high chemical reactivity with almost any material. After exploring various oven configurations using different ceramics materials and refractory metals it turned out that only yttria (Y_2O_3) based ceramics can provide improved resistance. Commercially available yttria ceramics showed insufficient mechanical form stability at the required temperature. In collaboration with the Fraunhofer institute IKTS the company in charge with the ceramics processing could optimize the ceramics sintering processes including ceramic stabilizers and could considerably improve the durability. Thus the operating conditions of the modified STO for Ti could be improved but did not show optimum reliability.

Contrary to the STO the design of the HTO avoids any ceramics in the hot volume. Instead it utilizes a free heater helix supported only at its ends. This circumvents the specific problems arising from the use of ceramics and so the application of the high temperature oven turned out to be the most promising approach. In order to optimize the HTO for routine operation its modular construction was improved in mechanical dimensional accuracy for more precise and easier mounting

Various experiments were performed with the HTO using natural Ti for most runs. For final confirmation, however, ^{50}Ti sample material had to be used. In addition the evaporation of TiO_2 was investigated, which avoids the problems related to the chemical reactivity of pure Ti at high temperatures. According to the required vapor pressure for the evaporation of TiO_2 the temperature limit of the high temperature oven could be successfully extended to 2300 °C corresponding to 560 W of electrical heating power. However, this high operating temperature reduces the lifetime of the oven. Therefore it appeared to be more favorable to use pure titanium as sample material at evaporation temperatures between 1750 °C and 1800 °C.

Several successful runs could be performed with natural titanium material and with enriched material. It could be demonstrated that the material processed in the GSI target laboratory by chemical reduction of enriched $^{50}TiO_2$ material is suitable. The charge state distribution was optimized for Ti^{8+}, which is necessary for injection into the RFQ-linac at the High Charge State Injector (HLI). The expected intensities of more than 50 µA could be easily achieved at the high level of beam stability specific for ion beams from an ECRIS. Figure 1 shows a typical spectrum for a ^{50}Ti run. The lifetime of the oven is related to the applied heating power which is also of great influence on the average ion beam intensity. At a typical lower level of heating power of 250 W (corresponding to 1750 °C) a lifetime of 6 days is obtained. This value is reduced, when the heating power is increased. The high temperature oven in its present development status is now prepared for routine operation at the accelerator.

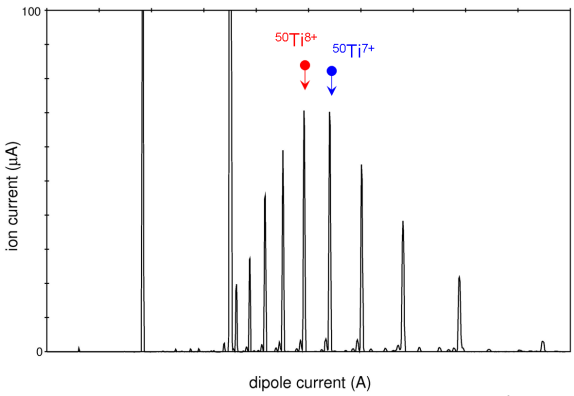

Figure 1: Typical mass/charge spectrum of ^{50}Ti.

The method of frequency tuning of the microwave injected into the ECRIS using a travelling wave tube amplifier (TWTA) can provide a considerable increase of the ion beam intensity at selected frequencies [2] and was also successfully applied during one of the Ti runs.

Multipurpose superconducting ECR ion source

An increased microwave frequency allows for enhanced plasma densities and ion currents in an ECRIS. A useful frequency of 28 GHz requires magnetic flux densities above 2.2 T implying the use of superconducting magnets. In cooperation with European institutions GSI initiated a project to build a prototype of a Multipurpose Superconducting ECR ion source (MS-ECRIS) to achieve a considerable improvement of the performances [3]. The first design of the superconducting magnet system revealed a lack of mechanical performance due to the strong interaction of the magnetic field of the 3 solenoids with the sextupole field and with its magnetic collar. Comprehensive structural analyses, calculations of the magnetic field and of the forces were performed at Bruker Ad-

[*] corresponding authors

vanced Supercon GmbH (BASC) being in charge of the fabrication of the magnet system. They confirmed these strong interactions, especially of the iron collar with the solenoidal fields. As a consequence an improved clamping of the collar by mechanical modification has been developed and is presently being implemented [4].

High Current Ion Sources

Bi and Au operation with VARIS ion source

In the frame of the project of developing the new heavy elements for SIS operation further investigations with Bi and Au have been performed. As was confirmed previously [5,6], it is not possible to provide stable high current operation of ^{197}Au and ^{209}Bi beams for SIS experiments using the cathodes made of pure Au and Bi due to the physical properties of the materials (melting point, metal vapor pressure at certain temperature, etc.). High flux of the neutrals from the cathode surface during the discharge of vacuum arc dramatically reduces the average charge state of the ions in the plasma. This effect makes it impossible to generate four fold Bi and Au beams with required for SIS pulse duration of not less than 120 µs.

Previously it was proved that this situation can be strongly improved by admixing a small amount of more refractory metal to desired elements and as the result by amending the physical properties of the cathode material. The first successful results were obtained with Bi cathodes by admixing Cu in ratio between 8 and 15% [6].

During the Bi-beamtime in August 2011 the compositions of Bi-Cu cathode material containing 10% and 15% of Cu respectively had been tested. The observable difference in operation between 10% and 15% Cu-containing cathodes was not established. However, a huge difference in beam pulse behavior and in conditioning time was noted for all examined Bi-Cu cathodes generally (independent on percentage of Cu content in the cathode material). Some of the cathodes required half an hour conditioning before they provided the stable beam the others required several hours. Some cathodes were good in operation (stable, good pulse-to-pulse reproducibility) the others were bad (too noisy pulse, poor pulse-to-pulse reproducibility). Also a notable difference in a structure of the cathode surface after operation was observed for cathodes from the same production process.

In order to understand the nature of this difference the cathodes have been investigated using an optical microscope and SEM (scanning electron microscope). Fig.2 shows the working surface and the material structure of two Bi-Cu cathodes: the top one (Fig.2a) was in operation for many hours and provided stable high current beam of Bi^{4+}; with the bottom one (Fig.2b) it was not possible to get Bi^{4+} beam at all. The photos of the working surface are shown on the right side on Fig.2. On the left side one can see the material structure of the cathodes close to the working surface. The images were captured with SEM with magnification of 420x. Light area on the images corresponds to Bi filler and randomly distributed dark spots correspond to fractions of pure Cu.

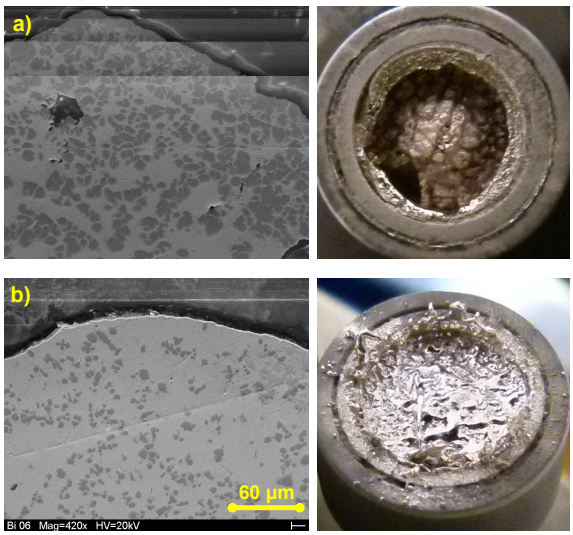

Figure 2: The surface structure of Bi-Cu cathodes (*right*) and SEM images of the longitudinal section of the cathodes (*left*); ***a)*** suitable - ***b)*** not suitable for operation.

The SEM investigations have shown that the distribution and the consistence of Cu-fractions in the examined Bi-Cu cathodes are nearly the same in the central area of the cathode (about 15% Wt. of Cu). However, close to the working surface the Cu percentage in the "good" cathodes reaches the value of up to 50% while in the case of the "bad" cathodes it was not changed. The accumulation of Cu on the cathode surface is the effect of cathode conditioning during the operation. Therefore it could be concluded that long conditioning time can be avoided by using higher Cu percentage in the cathode material (40% Wt. of Cu and more).

In November the test experiments with Au were performed on Injector North. Various cathode materials have been tested: Au-Pd (10% Wt.), Au-Cr (20% Wt.) and Au-Ti (5% and 10% Wt.). From all tested materials only Au-Cr alloy has shown stable operation with beam currents up to 6 mA of Au^{4+} (in front of the RFQ) and pulse length of 300 µs. However, from two cathodes (manufactured the same way) only one showed reliable operation. It is necessary to investigate the surface and the volume structure of both cathodes in order to understand the reason of such difference and then to find the proper composition and manufacturing process of the cathode material.

References

[1] R. Lang et al., Proceedings of the 15th International Workshop on ECR Ion Sources, University of Jyväskylä, Jyväskylä, Finland (2002) p. 180
[2] F. Maimone et al., this report.
[3] G. Ciavola et al., Rev. Sci. Instrum. 79, 02A326 (2008).
[4] K. Tinschert et al., Rev. Sci. Instrum., in print (2012).
[5] A. Adonin et al., GSI Scientific Report 2010.
[6] A. Adonin and R. Hollinger, Rev. Sci. Instrum., in print (2012).

Ion Source Operation at the GSI Accelerator Facility

R. Hollinger, K. Tinschert*, A. Adonin, M. Brühl, B. Gutermuth, F. Heymach, R. Lang, J. Mäder, F. Maimone, K. Ochs, J. Pfister, J. Rossbach, P. Schäffer, S. Schäffer, M. Stork, C. Vierheller, A. Wesp, and S. Zulauf*

GSI, Darmstadt, Germany

High Current Ion Sources

In 2011 various ion beams have been generated from the high current ion sources from Terminal North (MUCIS, CHORDIS, VARIS, MEVVA), and Terminal South (PIG ion sources). The following Table 1 gives an overview of the ion species performed from these ion sources with the most relevant beam parameters. The given analyzed ion beam current was measured in front of the RFQ and is a good mean value.

Table 1: Ion beams generated with high current ion sources in 2011. Filament driven volume type ion sources: MUCIS, MUCIS NEW and CHORDIS; Vacuum arc ion sources: VARIS and MEVVA; Penning type ion sources PIG

Ion species	Duration (days)	Ion source	Beam for experiment	Analyzed intensity (emA)
$^{14}N_2^+$	20	CHORDIS	SIS/ESR	4
$^{22}Ne^+$	20	MUCIS	SIS/ESR	6-8
$^{22}Ne^+$	2	PIG	SIS	0.1
$^{36}Ar^+$	5	MUCIS	SIS	8
$^{40}Ar^+$	21	MUCIS	SIS/UNILAC	15
$^{40}Ar^{2+}$	11	PIG	UNILAC	0.2…0.4
$^{48}Ti^{2+}$	9	PIG	UNILAC	0.05
$^{50}Ti^{2+}$	54	PIG	UNILAC	0.04…0.07
$^{60}Ni^{4+}$	6	PIG	UNILAC	0.06…0.08
$^{96}Ru^{2+}$	5	PIG	SIS	0.03
$^{96}Zr^{2+}$	4	PIG	SIS	0.02
$^{124}Sn^{5+}$	4	PIG	SIS	0.03…0.1
$^{152}Sm^{3+}$	9	PIG	SIS/ESR	0.04…0.07
$^{197}Au^{4+}$	15	PIG	UNILAC	0.4…0.6
$^{197}Au^{8+}$	39	PIG	UNILAC	0.06…0.1
$^{181}Ta^{3+}$	5	VARIS	SIS	6-8
$^{181}Ta^{4+}$	5	VARIS	SIS	6-8
$^{209}Bi^{4+}$	18	VARIS	SIS/ESR	8-12
$^{238}U^{4+}$	28	VARIS	SIS/ESR	8-12

Most of the ions, generated with the high current ion sources belong to the so called standard elements, like nitrogen, neon, argon, nickel, gold, tantalum, and uranium. These elements can be generated and operated easily. Other ions like ruthenium, zirconium, tin, and samarium belong not to the standard elements while operation is also not difficult. The operation with bismuth generated from the VARIS and titanium from the PIG ion source was challenging. Up to now it was not possible to produce fourfold charged bismuth ions from the high current ion source VARIS. Due to the low melting temperature for bismuth (271 °C) the density of neutrals in the plasma is very high. The neutrals reduce the mean charge state dramatically after a few microseconds of pulse duration [1,2]. It was decided to use a proper alloy or mixture the increase the melting temperature with a supplemental improvement of the thermal and electrical conductivity. Further on the added material should not have the same mass over charge ratio of $^{209}Bi^{4+}$ (A/ζ=52.25). Otherwise it would be not possible so separate the materials after extraction from the ion source. After some months of investigations we found the best experimental results with a mixture of bismuth and copper (80 % Bi and 20 % Cu).

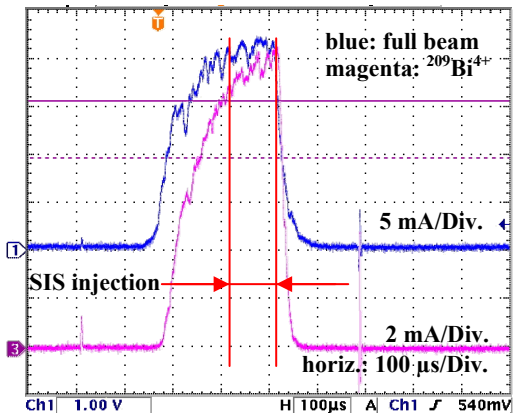

Figure 1: Typical ion beam pulse shape of full beam (blue line, 5 mA/Div.) and analyzed beam (magenta line, 2 mA/Div.), horizontal: 100 µs/Div. The injection window for the synchrotron is given by the red lines.

With this mixture 47 % of $^{209}Bi^{4+}$ compare to 0 % for pure bismuth has been reached [2]. Fig. 1 shows a typical ion beam pulse shape for full beam (blue) and analyzed beam (magenta). The ion beam current in front of the RF accelerator was about 12 emA of $^{209}Bi^{4+}$. The relatively long rise time (150 µs to the 80 % level) is not critical, because for the injection into the SIS a max. pulse length of 100 µs was required (red lines).

For the super heavy experimental program TASCA at the UNILAC, a titanium ion beam with sufficient beam intensity from the PIG ion source has been developed very quickly. This high duty factor ion beam was generated and optimized in spring 2011 very successfully. In consequence a first $^{50}Ti^{2+}$ ion beam for TASCA was offered for 54 days in the late summer for the search of the element 120. It was possible to offer an average current

* corresponding authors

at the experiment of 0.63 pμA with an uptime of 94 %. The ion beam current in front of the RF accelerator was about 40-60 eμA for $^{50}Ti^{2+}$. In the framework of optimisation of the beam conditions for the TASCA experiment, recent improvements of ion source program have been carried out. For instance the automatic reset of the sputter electrode voltage in case of a short cut and the automatic turn-on procedure of the high voltage power supplies in case of a break down increase the reliability of the ion source sufficiently.

High Charge State Injector HLI

The operation of the CAPRICE ECR ion source (ECRIS) at the High Charge State Injector (HLI) included the ion species listed in table 2.

Table 2: Ion beams delivered from the HLI in 2011.

Ion species	Auxiliary gas	Duration (days)	Analyzed intensity (eμA)
$^{12}C^{2+}$	O_2	55	100
$^{12}C^{3+}$	-	10	100
$^{40}Ar^{7+}$	He	4	90
$^{48}Ca^{10+}$	He	18	70
$^{50}Ti^{8+}$	He	6	70
$^{54}Cr^{8+}$	He	42	60
$^{112}Sn^{15+}$	He	6	22
$^{124}Sn^{17+}$	He	7	20
$^{136}Xe^{18+}$	O_2	17	44

In the beginning of the year a $^{40}Ar^{7+}$-beam was exclusively used for machine investigations of the RFQ structure at the HLI. Several beam time periods were dedicated to biophysics experiments at the SIS under therapy conditions and to biophysics experiments at the UNILAC using $^{12}C^{2+}$ in both cases.

Upon request from a user experiment the production of a $^{12}C^{3+}$-beam was investigated. Pure CH_4 was used without an auxiliary gas. Due to the experiment conditions the $^{12}C^{3+}$-beam should be used without passing through a stripper. In this case $^{12}C^{3+}$ has to be extracted from the ECRIS and has to be accelerated and transported to the injection of the synchrotron (SIS). Hence there is only a mass-to-charge separation of the ion beam in the analyzing dipole directly behind the ion source. Therefore different ion species of the same mass-to-charge ratio cannot be separated. As this is the case for $^{12}C^{3+}$ and $^{16}O^{4+}$ both components may be present in the ion beam. An estimation of the amount of beam contamination with O^{4+} from the residual gas can be achieved from the intensities of O^{3+} and O^{5+} in the mass-to-charge spectrum. At the beginning of ion source operation an O^{4+} intensity of about 30 eμA can be estimated which decreases with time to a value of less than 10 eμA. This amount remains in the spectrum and must be considered as background. Regarding an intensity of 100 eμA measured for the mass-to-charge ratio of 4, this represents a particle contamination of 8 % oxygen.

Highly enriched isotopic materials were used for the other ion beams delivered from the ECRIS. Beams of Sn isotopes were provided for different user experiments at the SIS while $^{136}Xe^{18+}$ was delivered to the local experimental area for materials research at the HLI and also to the SIS. Long runs with $^{48}Ca^{10+}$ and $^{54}Cr^{8+}$ were provided for experiments of the Super Heavy Element (SHE) programme at SHIP and at TASCA. For $^{54}Cr^{8+}$ it was tested to increase the lifetime of one filling of the oven by increasing the initial charge of ^{54}Cr sample material. Six oven fillings were necessary to cover the whole experiment run. It turned out that the lifetime increases with the charge to some extent, however, the material consumption also increases. So it became evident that an optimum charge of sample material exists giving the best compromise between oven lifetime and material consumption. The overall consumption of ^{54}Cr sample material was 4 mg/h on average with a range of fluctuation between 2 mg/h and 6 mg/h for the particular charges. Figure 2 shows a typical mass/charge spectrum of the extracted ion beam. Besides ^{54}Cr and He (auxiliary gas) it shows a very low amount of contaminations and confirms the very high degree of enrichment of the ^{54}Cr material.

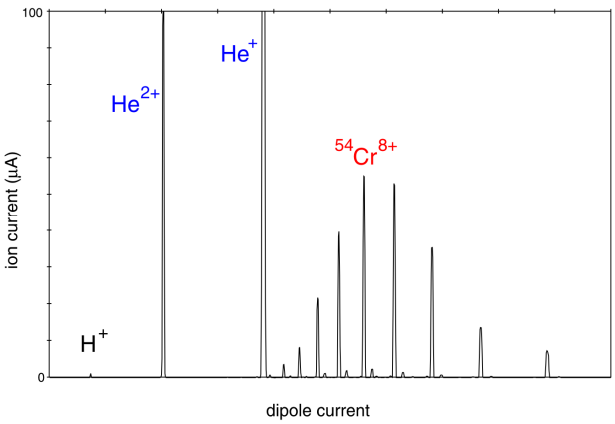

Figure 2: Typical mass/charge spectrum of ^{54}Cr.

Several days were dedicated to test the production of a $^{50}Ti^{8+}$-beam by evaporation of enriched ^{50}Ti material with the modified high temperature oven of the ECRIS at the HLI. Prior to this test extensive development work had been performed at the ECR injector test setup (EIS) at GSI [3]. In addition several test runs were performed with $^{48}Ti^{8+}$ generated from evaporation of natural titanium material. Finally these runs could confirm the positive results obtained at the EIS test bench and could prove the availability of a Ti-beam from the HLI.

References

[1] A. Adonin, R. Hollinger and P. Spädtke, GSI Scientific Report 2010, GSI Report 2011-1, p.438

[2] A. Adonin and R. Hollinger, Rev. Sci. Instrum. **83** (in print 2012).

[3] K. Tinschert et al., this report

Ion Beam Formation and Transport of a Beam, extracted from an ECRIS*

P. Spädtke[1], *R. Lang*[1], *J. Mäder*[1], *F. Maimone*[1,2], *J. Roßbach*[1], *and K. Tinschert*[1]
[1]GSI, Darmstadt, Germany; [2]Universitàa degli Studi di Catania, D.M.F.C.I, Viale A. Doria 6, 95125 Catania, Italy

Electron Cyclotron Resonance Ion Sources (ECRIS) have replaced older types of ion sources to feed particle accelerators, mainly because of the reliable long term generation of highly charged ions. Experimentally found scaling rules predict higher extractable ion currents with increasing rf frequency[1]. Simultaneously to the change in frequency the magnetic flux density within the plasma chamber has to be increased to keep the resonance condition for electrons. In addition to the mirror field a radial magnetic component is provided, for example a hexapole, which has to be increased accordingly. The influence of this increasing magnetic flux density on the ion beam extraction and on the beam properties is taken into account to determine the beam quality.

Extraction Simulation

Stronger flux density serves for a better confinement, but simultaneously it makes the extraction of ions from the plasma more difficult. The gyration radius of ions has become so small that not only the electrons but also the ions are magnetically frozen. This implies that the ions inside the plasma are guided mainly by the magnetic field. For that reason the magnetic field lines going through the extraction aperture are to be investigated. Simulations with the program TOSCA[2] have been made scanning the possible settings for all conductors of the MS-ECRIS[3]. The magnetic field is then transferred to the program KOBRA3[4] for further diagnostic, which is shown in Fig. 1. The magnetic field lines going through the extraction aperture on a radius of 5 mm are shown there. For these simulations the confinement properties are neglected, only the extraction conditions are investigated. Inside the plasma the path of an ion is strongly bound to the field line. Fig. 1 shows where ions to be extracted can come from for different magnetic settings (for the design values, for the 75% reduced design values, and for a reversed mid coil of the center solenoid). Depending on the point of origin, ions will experience different values of $\int \vec{B} ds$, which is an important quantity to investigate the beam transport.

Viewing Target Experiment

The experimental result obtained with the CAPRICE ion source by recording the beam profile on a viewing target, ramping the first magnetic solenoid in the beam line[5] has to be compared with simulation results. For that, the beam profile on the target behind this beam line solenoid (Fig. 2, left) is used to calculate the initial transverse y, z coordinates at the position of the extraction electrode. On each of these spatial coordinates the momentum space is scanned within reasonable limits, see Fig. 2, center.

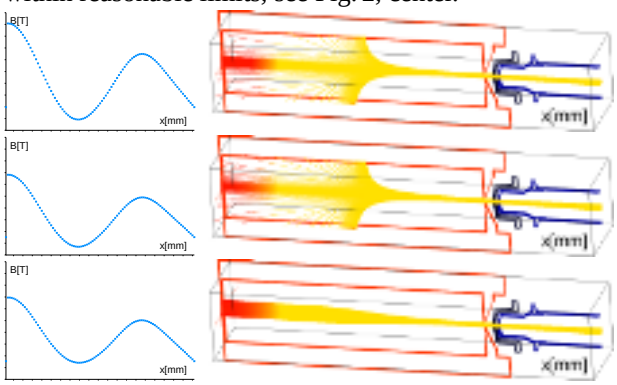

Fig. 1: Magnetic flux density on axis (left) and projection of the 3D magnetic field lines (right). 1^{st} row: Design values. 2^{nd} and 3^{rd} row: coil currents scaled down to 75%. 3^{rd} row: reversed polarity of the middle solenoid.

Only the particles having a displacement of less than the aperture radius at the position of the extraction system are selected from all backtracked particles (Fig. 2, right).

Because of the multiple sets of viewing target profiles and settings of the magnetic solenoid a wide range of simulations are to be made, but at the end it should give a better picture where the ions are coming from inside the source. The goal is to find a fixed set of magnetic setting, compatible with the experimental observed target measurements.

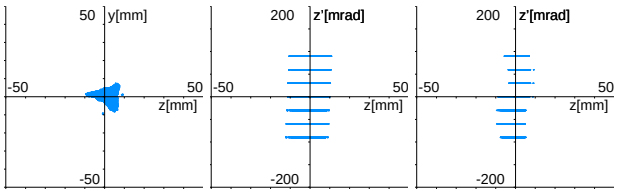

Fig. 2: Left: profile on the viewing target, center: initial phase space, right: reduced phase space.

References

[1] R. Geller, *Electron Cyclotron Resonance Ion Sources and ECR Plasmas*, IOP, London, 1996.
[2] Vectorfields, `http://www.vectorfields.co.uk`.
[3] G. Ciavola et al., Rev. Sci. Instrum. **77**, 03A303, 2006.
[4] INP Wiesbaden, Junkernstr. 99, 65205 Wiesbaden, Germany
[5] K. Tinschert et al., Rev. Sci. Instrum. **69**, 709, 1998.

* Work supported by EU, FP7, Grant agreement no 262010 ENSAR

The effect of frequency tuning on the ionization efficiency of an ECRIS*

F. Maimone[1], L. Celona[2], K. Tinschert[1], R. Lang[1], J. Mäder[1], J. Roßbach[1], P. Spädtke[1]
[1]GSI, Darmstadt, Germany; [2]INFN-LNS, Catania, Italy

The frequency tuning is a promising technique for the improvement of the performances of Electron Cyclotron Resonance Ion Sources (ECRIS) concerning the production of high charge state ion beams of higher intensity. This technique, based on the variation of the microwave frequency feeding the ECR plasma, has been experimentally investigated at GSI with the CAPRICE-type [1,2] ECRIS installed in the ECR injector test setup (EIS) [3] in 2008 [4], 2010 [5], and recently an experiment on the efficiency of frequency tuning for the production of highly charged ion beams was carried out [6]. The experimental set-up comprised a Travelling Wave Tube Amplifier (TWTA) driven by a signal generator and connected to the ion source through a WR62 rectangular waveguide. The ECRIS parameters were set in order to maximize the production of the Ar^{11+} ion current. Then frequency sweeps in the 12.5-16.5 GHz frequency range (at a microwave power of 450 W) were performed while measuring the Ar^{11+} current. The result is shown in figure 1. Some frequencies can be identified at which the Ar^{11+} current is considerably enhanced with respect to the standard operating frequency of 14.5 GHz. The charge state distributions were measured at different values of microwave power varied between 250 W and 550 W in steps of 50 W for two microwave frequencies: 14.500 GHz and 13.221 GHz, where the maximum of the Ar^{11+}-intensity appears, respectively. All other ion source parameters were kept constant. As result figure 2 shows the ratio of the ion currents corresponding to the two frequencies as function of the microwave power for the charge states Ar^{q+} (q = 8, 9, 11, 12).

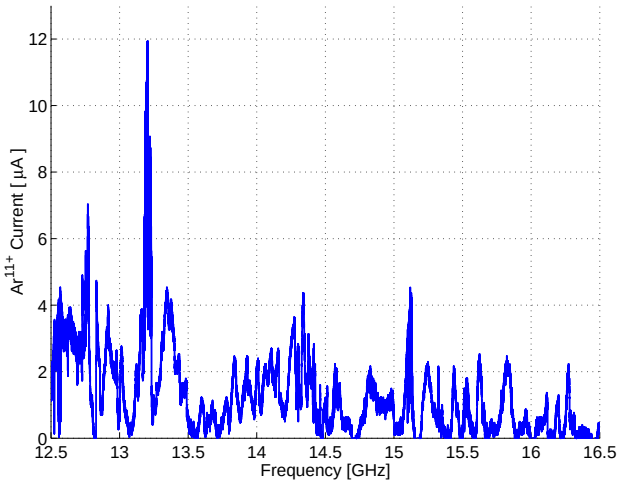

Figure 1: Ar^{11+} current measured as function of the microwave frequency

* Work supported by EU FP7 under the Grant agreement n° 262010 - ENSAR.

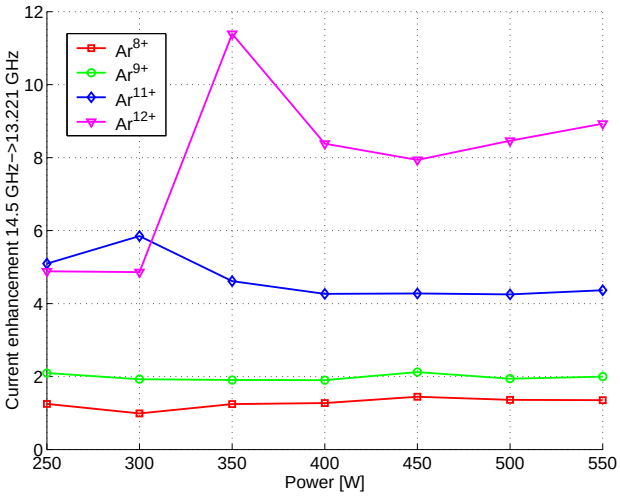

Figure 2: Current enhancement for different microwave powers when the frequency is shifted from 14.500 GHz to 13.221 GHz

Evidently a clear enhancement of the ion currents of all these charge states is achieved when the microwave frequency is set to an optimized condition. This condition could correspond to a certain electromagnetic field pattern (mode) which exists inside the ECRIS. Simulation results showing some possible modes for the CAPRICE ECRIS are reported in [5].

This effect is increasingly pronounced for the higher charge states. Over the complete power range the current enhancement factor remains constant for a given charge state of Ar^{q+} (q = 8, 9, 11). For Ar^{12+}, this enhancement factor even increases with rising power. This result may be important for the existing ECRIS and for the new generation ECRIS making use of high power microwave input (several kW) opening a promising way for optimization of high ion beam intensities.

References

[1] D. Hitz et al., Proc. 11th Int. Workshop on ECRIS, Groningen 1993, KVI-Report 996 (1993) 91.
[2] H. Schulte, K. Tinschert, J. Bossler, B. H. Wolf, J. Klabunde, L. Dahl, Th. Schwab, and J.P. Klein, Rev. Sci. Instrum. 63, 2883 (1992).
[3] K. Tinschert et al., Rev. Sci. Instrum. 69, 709 (1998).
[4] L. Celona et al., Rev. Sci. Instrum., 79 (2008).
[5] F. Maimone, L. Celona, R. Lang, J. Mäder, J. Roßbach, P. Spädtke, K. Tinschert, Rev. Sci. Instrum. 82, 123302 (2011).
[6] F. Maimone, K. Tinschert, L. Celona, R. Lang, J. Mäder, J. Roßbach, P. Spädtke, Proc. 14th Int. Conference on Ion Sources, Catania, Italy 11-16 Sept 2011, accepted for publication in Rev. Sci. Instrum.

UNILAC Status and Development

P. Gerhard[*1], *W. Barth*[1], *G. Clemente*[1], *L. Dahl*[1], *L. Groening*[1], *M. Maier*[1], *S. Mickat*[1], *M. S. Kaiser*[1], *B. Schlitt*[1], *H. Vormann*[1], *and S. Yaramyshev*[1]

[1]GSI, Darmstadt, Germany

Status of Operation

Commissioning in March with beams from HSI and HLI was followed by high current ^{40}Ar machine experiments. Regular beam operation started in April with ^{12}C from the Electron Cyclotron Resonance Ion Source (ECRIS) for experiments under therapy conditions and other biophysics experiments. This was repeated in July and October. As a major beamtime the ECRIS served in a six weeks block with ^{54}Cr for SHIP. The Cr beam was also used by biophysics experiments and for experiments in the target hall (FRS, ESR, HITRAP). ^{48}Ca was foreseen to be delivered to TASCA, SHIPTRAP and plasma physics. After a one week delay due to complications with the material, infrastructure and vacuum failures, TASCA changed to ^{50}Ti (see below). Besides the HLI delivered ^{136}Xe (material research, SIS and HITRAP), ^{112}Sn (FRS) and ^{124}Sn (HTC). Two weeks of regular beamtime were used for ^{50}Ti development [1].

Operation from the Penning Ion Gauge (PIG) source was dominated by 11 weeks of ^{50}Ti for TASCA. Plasma physics and SHIPTRAP used the same beam, predominantly as secondary users. The successful accomplishment of this beamtime paved the way for further super heavy element experiments in 2012. ^{197}Au was accelerated for eight weeks in total for material research, biophysics and SIS. Moreover ^{40}Ar, ^{60}Ni, ^{84}Kr, ^{96}Ru, ^{96}Zr, ^{124}Sn and ^{152}Sm beams were generated. The PIG was in operation for approx. 90% of the beamtime, mostly with high duty factors.

The MUlti Cusp Ion Source (MUCIS) delivered ^{40}Ar, ^{36}Ar, ^{22}Ne and ^{14}N for three weeks each, and $^{1}H_3$. The MEtal Vapor Vacuum Arc (MEVVA) ion source provided five weeks of ^{238}U, three weeks of ^{209}Bi, and ^{181}Ta. All high current beams were used by high energy experiments behind SIS as well as machine experiments.

The UNILAC was in operation for nearly 200 days, more than one third of the time with three beams [2].

High current operation was affected for six weeks by two breakdowns of the rebuncher US4BB3: A blocking of cooling channels had to be refurbished in the workshop, and after recommissioning its coupling loop had a vacuum leak. A water leak occurred in one triplet coil in the HSI LEBT. It was first converted to and later replaced by a doublet, which hindered operation for the rest of the year. Operation of the HSI was interrupted for one week by a failure of a high power rf line for an IH cavity. Large parts of the facility were affected due to several power failures (thunderstorms, short circuit of an external transformer) and the break of the main water line for GSI. Unlike the last years, there were no major failures of the Alvarez accelerator thanks to the progress of the tank revision.

* p.gerhard@gsi.de

Shutdown Activities

In spring the revision of the Alvarez tanks 1, 3 and 4 was finished, five drift tubes had to be renewed. High power tuning plates were installed into the HLI RFQ successfully. The front end cap of the IH1 tank suffered from a water leak, it was replaced by a new one. In summer the LEBT triplet was replaced by a doublet, and tests at the HLI RFQ concerning cw operation and thermal effects were accomplished. The revision of the last Alvarez tank 2 dominated the winter shutdown 2011/12. A vacuum leak in a single gap resonator necessitated opening of this section. Chemical rinsing of the cooling channels was extended to the HSI rf structures.

Upgrade Measures & Machine Experiments

An upgraded emittance device was installed between LEBT and HSI front end, and new BIF stations were commissioned, six are in operation now.

Main topic of the machine experiments was foil stripping at HSI energy [3]. Thin carbon foils were exposed to high and low intensity Ar, Sm and U beams. ^{238}U beam lifetimes in the SIS could be measured for various charge states from 28+ to 41+ and from 27+ to 35+ generated by foil and gas stripping respectively.

The overhaul of the Alvarez was reviewed by phase advance dependent emittance measurements. Investigations of the high current performance were made by emittance measurements at the HSI RFQ exit [4] with the doublet removed to achieve maximum acceptance. Twiss parameters of a $^{1}H_3^{1+}$ beam were measured in the transfer channel in preparation of emittance exchange experiments. The preparation of the cw-LINAC demonstrator and the design study for a future UNILAC were continued [5, 6].

References

[1] K. Tinschert *et al.*, "R&D and Operation of ^{50}Ti-Ion Sources", (this report)
[2] W. Bayer *et al.*, "Accelerator Operation Report", (this report)
[3] H. Vormann *et al.*, "Results of Uranium Machine Experiments at the UNILAC", (this report)
[4] W. Barth *et al.*, "UNILAC Status and Developments", GSI scientific report 2009, p. 132
[5] S. Mickat *et al.*, "Status of the cw-LINAC Demonstrator Project", (this report)
[6] B. Schlitt *et al.*, "Design Studies for the Heavy Ion High Energy LINAC", (this report)

Uranium Machine Experiments at the UNILAC

H. Vormann[1], W. Barth[1], G. Clemente[1], L. Dahl[1], P. Gerhard[1], V. Gettmann[1], L. Groening[1], S. Jacke[1], M.-S. Kaiser[1], M. Maier[1], S. Mickat[1], A. Orzhekovskaya[1], B. Schlitt[1], and S. Yaramyshev[1]

[1]GSI, Darmstadt, Germany

Uranium Experiments

The machine experiments at the UNILAC in 2011 were mainly dedicated to investigations for future accelerator operation at GSI: The uranium beam life time in the SIS was investigated for a wide range of charge states. Carbon foils were used for stripping at 1.4 MeV/u to provide medium charged uranium ions for SIS 18 injection ($U^{28+...41+}$ from carbon foils, $U^{27+...35+}$ from the gas stripper).

The preliminary life time measurements in the SIS showed that charge states $U^{38/39+}$ provide the longest life times (varying with SIS energy), extrapolated from the measured time dependent particle losses (injected typically $3*10^8$ particles per spill) [1].

The durability of 22 carbon foils (20 µg/cm^2) used for high current U^{4+} (up to 5.5 mA) beam stripping was investigated. All foils had been manufactured within a short time slot, all treated in the same way, from material of three different providers.

The durability of the foils tested in 2011 seems to be lower compared to the foils tested in 2010 (2010 up to 18 h duration without damage, 6.4 kWs/cm^2; 2011 up to 30 h operation, 13.1 kWs/cm^2, but all foils damaged). The stripping efficiency decreased within 3 hours of operation to one third of start value.

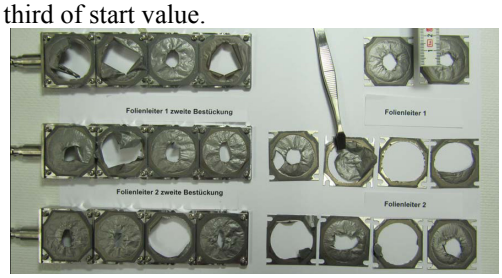

Figure 1: Carbon foils after uranium irradiation.

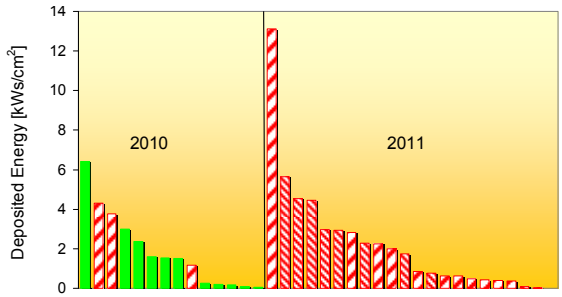

Figure 2: Deposited energy (green: foil not damaged; hatched: damaged, fine: later detected as damaged).

The beam pulses (150 µs / 1 Hz) were longer than in 2010 (50...100 µs / 1 Hz). The foils in 2010 had been tempered after production, those in 2011 not. Energy measurements in the stripper section showed no time dependent decrease of energy loss from stripping (≈ 19 keV/u). A significant variation of the emittance during the beam operation was not observed.

Furthermore, U^{41+} stripper spectra in the transfer channel at 3.07 MeV/u (a possible future post stripper input energy) showed main charge states at U^{50+} from a 55 µg/cm^2 carbon foil ($U^{46+/47+}$ for 20 µg/cm^2) [2].

Experiments with other Ion Species

In a collaboration with the Materials Research Department carbon foils have been irradiated by a low current $^{152}Sm^{22+}$ beam (3.6 MeV/u, 6 eµA/0.3 pµA, 3 Hz/1 ms,). Foil temperature, carbon particle scattering rate and beam current have been observed during 24 hours of operation, for later offline analysis. None of the foils has been damaged (W_{depos} ≈ 90 J). Tests with a gold beam had similar results.

Argon beams were used for high current optimizations in the UNILAC and the transfer channel (TK): 11 emA Ar^{10+} behind the Alvarez, 9.8 emA at TK2 were reached. Investigations on the emittance growth in the Alvarez after maintenance confirmed previous results (7.1 mA Ar^{10+}): minimum at 60°, smaller growth rates (25%) due to reduced space charge effect (larger initial emittance).

With the mobile emittance measurement device directly behind the RFQ (to avoid beam losses in the dismounted quadrupole doublet), the output emittance of the full 10 emA Ar^{1+} beam was measured ($\varepsilon_{x,y} \approx 23$ µmrad, 90% 4*rms). High gradient settings for the HSI quadrupole quartet (from DYNAMION simulations based on low current Ar^{1+} LEBT emittance measurements) provided 100% low current transmission through quartet and RFQ. Later high current U^{4+} measurements confirmed the feasibility of these settings (65% RFQ transmission, like standard).

With a $^1H_3{}^{1+}$ beam from the MUCIS preparatory emittance measurements for transversal emittance exchange experiments have been made in the transfer channel.

Radiation dose rates have been measured with a 7.1 MeV/u $^{84}Kr^{17+}$ beam at the TK entrance (faraday cup UT1DC2, av. neutron rate 12.9 mSv/h), and with a high current U^{39+} beam at the TK end (TK7DC3, 1.5 emA U^{39+}, 11.4 MeV/u, $3.6*10^{10}$ p/sec., av. rate 90 µSv/h).

The re-commissioning of the HLI RFQ (Ar^{7+} beam) after the high power upgrade showed no significant changes of the RF and beam dynamics properties, while the power handling capability was significantly increased.

References

[1] P. Spiller, "SIS 18 Operation and Upgrade Status", (this report).

[2] B. Schlitt, G. Clemente et al., "Design Studies for the Heavy Ion High Energy Linac" (this report)

Further beam dynamics investigations for the GSI cw-linac

S. Jacke[1], *W. Barth*[1,2], *V. Gettmann*[1], *S. Mickat*[1,2], *U.Ratzinger*[3], *and R.Tiede*[3]
[1]HIM, Mainz, Germany; [2]GSI, Darmstadt, Germany; [3]IAP, Goethe University, Frankfurt, Germany

Introduction

Further beam dynamics studies were made for the planned super conducting continuus wave (sc-cw) linac, based on the original design (by A. Minaev [1]). The established layout is shown in Figure 1 with the fixed lower energy part up to 3.5 MeV/u and a variable part with a final energy up to 7.3 MeV/u. As first part of the cw linac, beam dynamical simulations were carried out for the demonstrator layout [2,3] with the MIRKO and LORASR code.

Simulations and Results

First, the design output emittances from the existing High Charge Injector (HLI) were taken for the following calculations. The distances from the HLI to the demonstrator project were newly calculated according to the recent layout. The known input acceptances from the demonstrator were then taken in order to adjust the beam dynamics in MIRKO, as well as in LORASR. The studies of different final beam energies were added to those investigated earlier, where a focus was set onto the complete deactivation of complete cavities. This method provides a coarse energy variation in approximately 0.6 MeV/u steps for each deactivation of a cavity in the variable part. For small variations, phase and peak voltage of the cavities have to be altered. This was tested successfully on a few values; the desired output energies were achieved without beam losses.

Further investigations were focusing on the tolerance limits for the alignment of the sc-cw linac. These investigations used the LORASR random error distribution with 300 runs to establish a tolerance of 0.3 mm transverse offset as non-critical, as shown in the X-Z plane in figure 2. Rotational errors of 1.7 mrad are not critical either and did not result in any beam loss. For breakdown studies (randomly one of the cavities breaks down), some preliminary investigations were started and will be continued.

The existing LORASR code allowed the change of the structure with different synchronous particle energies. A new concept for the next version of LORASR has to be established, which should keep the geometry fixed, but allows the deactivation of accelerating cavities without changing the structure. It is currently being implemented. Some of the recent breakdown studies of single cavities and the coarse energy variation due to deactivation of the last cavities will be repeated with higher accuracy. It was shown preliminarily that for the last 4 out of 6 cavities in the energy variable part of the cw-linac, the missing cavity could be compensated by the neighbouring cavities, but it would need fields above 5.1MV/m.

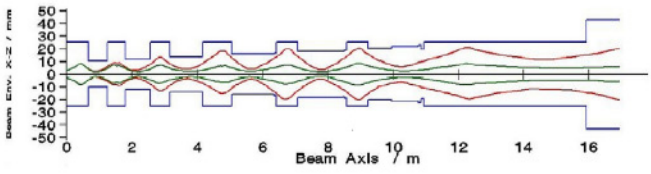

Figure 2: 300 run rotational and transverse error studies, the green beam envelope represents the ideal case, the red envelope is defined by the overlap of all 300 runs with machine errors

References

[1] A. Minaev et al., "Superconducting, energy variable heavy ion linac with constant β, multicell cavities of CH-type", Phys.Rev. ST-Acc. and Beams 12, (2009), p. 120101

[2] V. Gettmann et al., "Processing and Preparation of the sc-cw Demonstrator project", this annual report

[3] S. Mickat et al., "Status Report of the sc-cw LINAC demonstrator project", this annual report

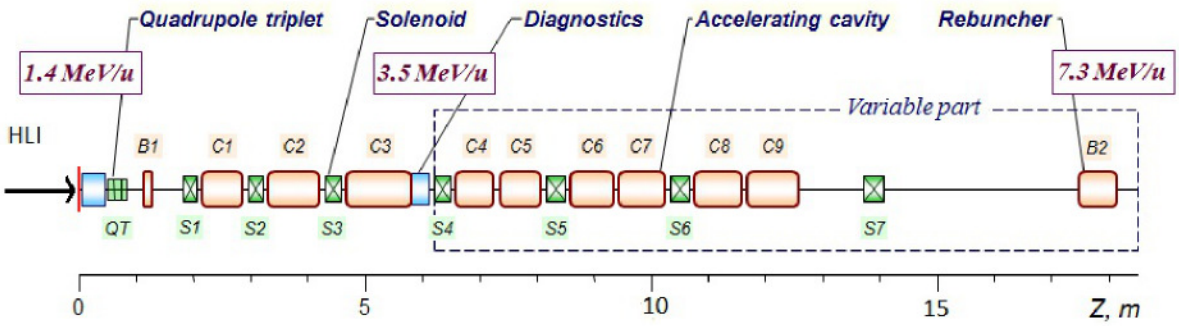

Figure 1: Conceptual layout of the sc-cw-linac with the fixed part up to 3.5 MeV/u and variable part

The Status of the sc cw-LINAC-Demonstrator

S. Mickat[1,3], M. Amberg[3], K. Aulenbacher[3,4], W. Barth[1,3], L. Dahl[1], F. Dziuba[2], V. Gettmann[3], S. Jacke[3], M. Kaiser[1], H. Podlech[2], U. Ratzinger[2], and W. Vinzenz[1]

[1]GSI Helmholtzzentrum, 64291 Darmstadt, Germany
[2]IAP Frankfurt University, 60438 Frankfurt, Germany
[3]Helmholtz-Institut Mainz (HIM), 55099 Mainz, Germany
[4]IKP Mainz University, 55128 Mainz, Germany

A new superconducting (sc) continous wave (cw) LINAC at GSI is desired by a broad community of future users [1]. A conceptual layout of an sc cw-LINAC was worked out at the Institute for Applied Physics (IAP) at Frankfurt University [2]. Here the key component, an sc Crossbar-H (CH) cavity, was developed recently [3, 4]. The first section of the proposed cw-LINAC comprising a sc CH-cavity embedded by two sc solenoids is financed by HIM as a demonstrator [5]. One important milestone of the project is a full performance test with beam of the demonstrator starting in 2013 at the GSI High Charge Injector (HLI).

cw-LINAC-Demonstrator

The demonstrator is financed by HIM mainly. It is the realisation of the first section of the proposed cw-LINAC comprising a superconducting CH-cavity embedded by two superconducting solenoids (fig. 1).

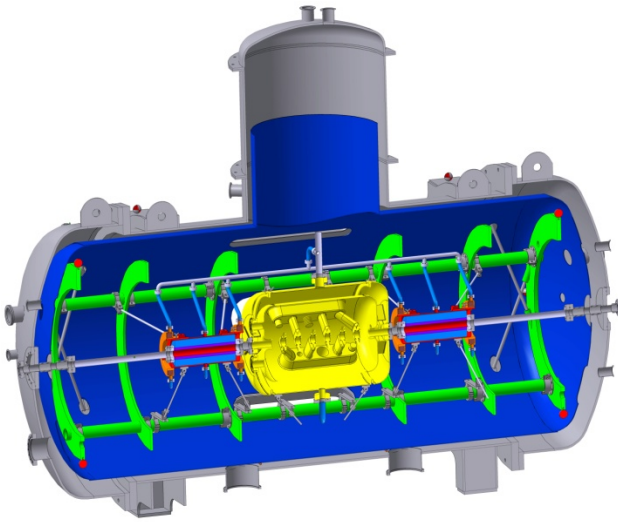

Figure 1: A scheme of the cw-LINAC Demonstrator shows the CH-cavity (yellow) in its centre embedded by two sc solenoids (red-orange). On the top space for a reservoir of liquid helium as well as of liquid nitrogen is reserved.

The sc CH-structure is the key component and offers a variety of research and development [6, 7]. The cavity designed for the cw-LINAC demonstrator is operated at 217 MHz and provides gradients of 5.1 MV/m at a total length of 0.69 m.

The solenoids provide maximum fields of 9.3 T at an effective length of 290 mm and a free beam aperture of 30 mm. The fringe fields have to be reduced from the maximum field to 50 mT at the inner NbTi-surface of the neighbouring cavity. A coil configuration with one main coil and two bucking coils was worked out by the IAP to fit the requirements at best (fig. 2).

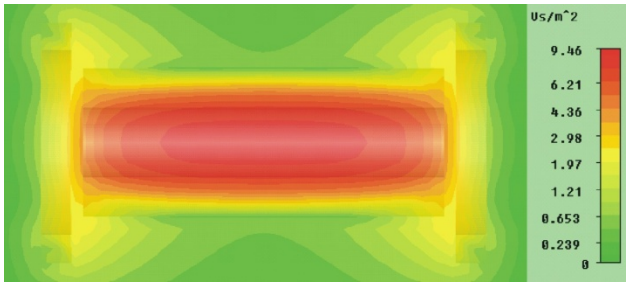

Figure 2: The solenoid field of the chosen coil configuration is calculated. Within the requirements the fringe field is shielded by the compensation coils

Setup at GSI-HLI

The location to setup the demonstrator is in straightforward direction of the HLI at GSI (fig. 3). Two existing experiments at the HLI have to move since the space is needed for the demonstrator test environment including a new radiation protection cave. The liquid helium (LHe) is provided by a 3000 ltr tank. The consumed helium is collected in a 25 m^3 recovery balloon and stored by a compressor in gas bottles. In operation a consumption of 20 ltr LHe per hour is predicted. For beam matching from the HLI to the demonstrator an existing buncher can be used. For transverse focusing an additional quadrupole doublet is needed [8]. Moreover beam diagnostics like profile grids and an emittance meter has to be integrated in the beam line in front of and behind the demonstrator as well as phase probes for time of flight (TOF) measurements.

Status

The mechanical assembly of the demonstrator at GSI-HLI is in preparation. Components like the 3000 ltr LHe-tank, the 25 m^3 recovery balloon and the compressor are in house. The order of the CH-cavity is placed to Research Instruments (RI) in Bergisch Gladbach, Germany, recently. A 5 kW rf-amplifier was delivered in May 2010. Presently the tendering of the cryostat and the solenoids is in progress.

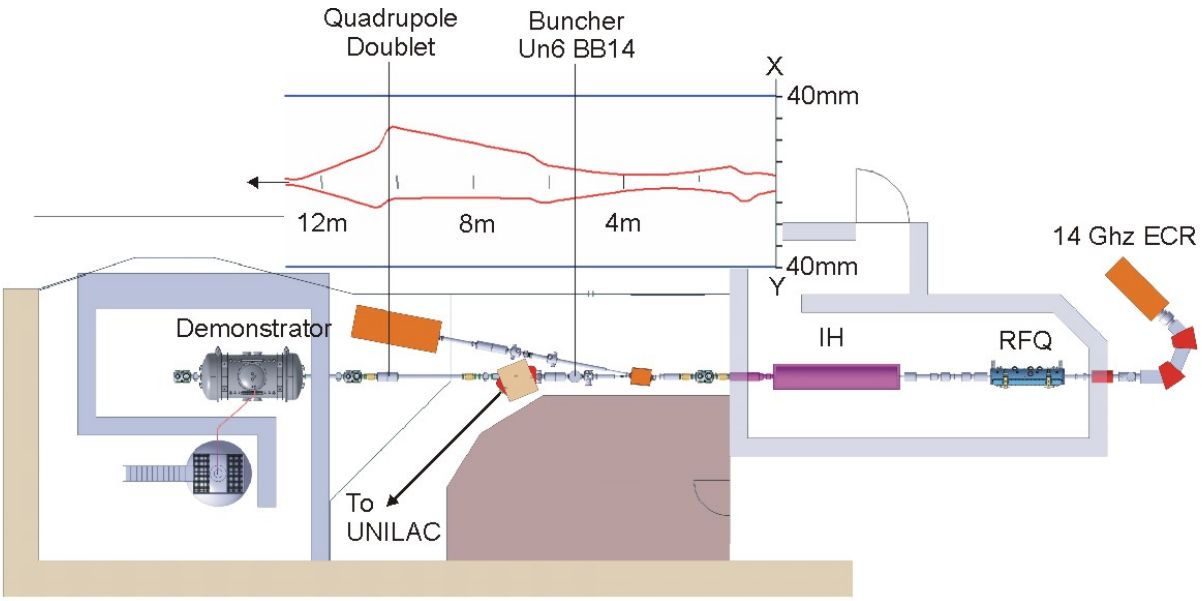

Figure 3: The existing HLI should be used as an injector for the cw-LINAC demonstrator. In longitudinal plane the existing buncher UN6BB, in transverse plane an additional quadrupole doublet should be used to match the beam to the demonstrator.

Table 4: Time Schedule

	cw-LINAC Demonstrator-Project
2010	Tendering of the demonstrator components
2011	Delivery of the LHe-supply and the rf-amplifier Ordering of the cavity, the solenoids, and the cryostat Preparation of the test environment at GSI
2012-2013	Delivery of the cavity, the solenoids and the cryostat High power rf-tests (warm + cold) at IAP
2013-14	Full performance test at GSI HLI

References

[1] S. Hofmann et al., Heavy Element Research at GSI-SHIP, EXON 2004, p. 157, Peterhof, Russia (2004)

[2] S. Minaev et al., Superconducting, energy variable heavy ion linac with constant □, multicell cavities of CH-Type, Phys. Rev. ST Accel. Beams 12, 120101 (2009)

[3] H. Podlech et al., Superconducting CH structure, Phys. Rev. ST Accel. Beams 10, 080101 (2007)

[4] F. Dziuba et al., Development of superconducting crossbar-H-mode cavities for proton and ion accelerators. Phys. Rev. ST Accel. Beams 13, 041302 (2010)

[5] S. Mickat et al.: "The status of the cw-LINACdemonstrator", ACC-RD-10, p.267, GSI SCIENTIFIC REPORT 2010

[6] M. Amberg et al., Structural Mechanical Analysis of Superconducting CH-Cavities, these proceedings, SRF2011, Chicago, USA (2011)

[7] F. Dziuba et al., Development of Superconducting CH-Cavities, these proceedings, SRF2011, Chicago, USA (2011)

[8] S. Jacke et al.: "Further beam dynamics investigations for the GSI cw-LINAC", ACC-OTHERS-03, this scientific report

RF design for the 217 MHz sc CH-Cavity*

F. Dziuba† [1], *M. Amberg*[3], *M. Busch*[1], *H. Podlech*[1], *U. Ratzinger*[1], *K. Aulenbacher*[3], *S. Mickat*[2,3], *and W. Barth*[2,3]

[1]Institut für Angewandte Physik, Goethe Universität, Frankfurt, Germany; [2]GSI, Darmstadt, Germany; [3]HIM, Johannes Gutenberg Universität Mainz, Germany

Abstract

Since in the future the existing UNILAC at GSI will be used as ion injector for FAIR, beam time availability for nuclear chemistry and especially for Super Heavy Element (SHE) production will be very limited. For this reason a new superconducting (sc) continuous wave (cw) linac (see fig. 1) at GSI is desired by a broad community of users. At present, the first cavity of the proposed cw LINAC is under development. To demonstrate the cavity capabilities under a realistic accelerator environment, a full performance test by injecting, focussing and accelerating a beam from the GSI High Charge Injector (HLI) is planned in 2013/14.

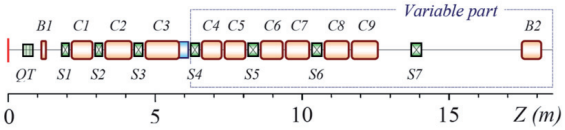

Figure 1: Schematic overview of the cw heavy ion linac. The demonstrator corresponds to C1, S1 and S2.

The 217 MHz CH-Cavity

The demonstrator cavity (see fig. 2) will provide a gradient of 5.1 $\mathrm{MV/m}$ at an inner length of 687 mm [1]. Concerning the rf design optimization of the cavity several simulations with CST MicroWave Studio and ANSYS were performed. Table 1 shows the main parameters of the 217 MHz cavity. The cavity will be supplied by all necessary auxiliaries like a 10 kW cw power coupler, frequency tuning system (including static and dynamic bellow tuners), helium vessel and flanges for cavity surface preparation. Figure 3 shows the design of a 6 cell bellow tuner. In December 2011 a construction study of the cavity was finished. Furthermore, the niobium for the cavity is ordered already. It is expected that the production of the cavity will start at the beginning of 2012 at Research Instruments (RI), Bergisch Gladbach.

References

[1] F. Dziuba et al., The Superconducting cw LINAC Demonstrator for GSI, In Proc. of IPAC 2011, San Sebastian, Spain (2011).

* Work supported by HIM, GSI, BMBF Contr. No. 06FY9089 I

† dziuba@iap.uni-frankfurt.de

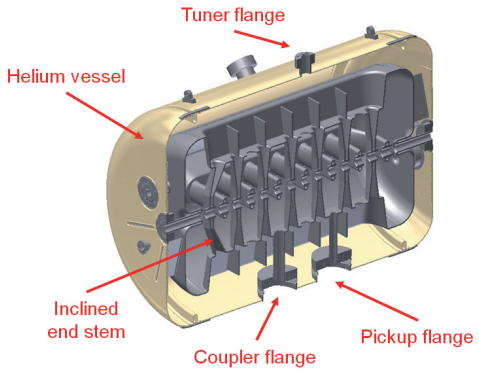

Figure 2: Sideview of the 217 MHz cavity with helium vessel, without tuners.

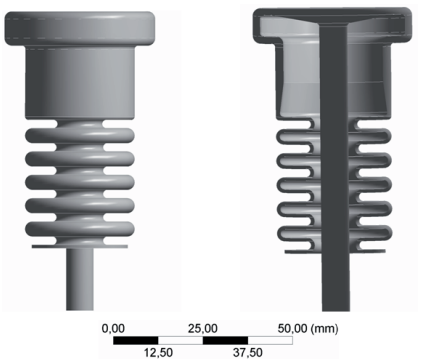

Figure 3: Bellow tuner design for the 217 MHz CH-Cavity.

Table 1: Parameters of the 217 MHz CH-Demonstrator.

Parameter	**Unit**	
Beta		0.059
Frequency	MHz	216.816
Gap number		15
Inner length	mm	687
Cavity diameter	mm	409
Aperture	mm	20
Accelerating gradient	$\mathrm{MV/m}$	5.1
E_p/E_a		6.4
B_p/E_a	$\mathrm{mT/(MV/m)}$	5.4
R/Q	Ω	3320

325 MHz sc CH-Cavity*

M. Busch†[1], *H. Podlech*[1], *U. Ratzinger*[1], *W. Barth*[2,3], *and M. Amberg*[3]

[1]Institut für Angewandte Physik, Goethe Universität, Frankfurt, Germany; [2]GSI, Darmstadt, Germany; [3]HIM, Johannes Gutenberg Universität, Mainz

Abstract

The construction of the 325 MHz CH-Cavity has reached the final phase at the end of 2011. All individual parts of the resonator have been fabricated. First cryo-tests are determinded for mid-2012. The final design of the bellow tuners has been optimised with respect to a minimization of multipacting. In order to achieve the exact frequency of 325.224 MHz for beam tests at the GSI Unilac a production concept has been elaborated. Furthermore an appropiate power coupler design developed at Fermilab will be modified to fulfill the needs of this cavity.

Status

Final simulations for the bellow tuners have been performed to lower the risk of multipacting. A 3-gap design showed promising performance in the simulations [1]. The complete RF design of the cavity is illustrated in fig. 1.

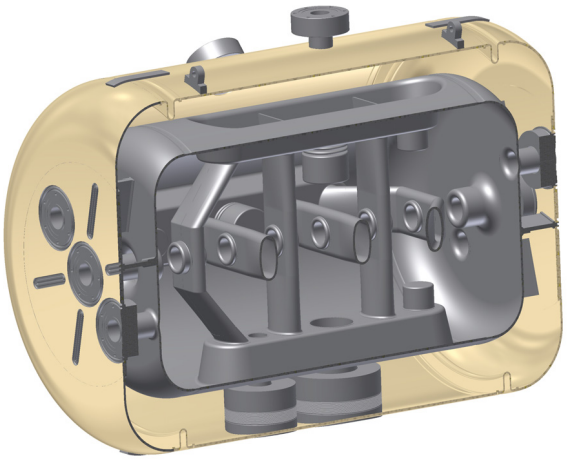

Figure 1: RF design of the 325 MHz sc CH-cavity

The fabrication of the cavity progressed in 2011. All main parts of the cavity are ready for assembly in early 2012 (see figs. 2 and 3).

Power Coupler

For beam tests at the GSI Unilac a dedicated power coupler has to be fabricated and assembled. The required 60 kW pulsed power can be fed into the cavity applying a coupler design similar to the Project-X coupler for Fermilab (see fig. 4) which has a similar specification. Thus the rf design can be adapted and the geometry has to be adjusted to the cryo system properties. As a first step ceramic windows will be ordered in january 2012.

Figure 2: Welded girders (left), end caps of the cavity (right)

Figure 3: Inclined stem (left), straight stem (right)

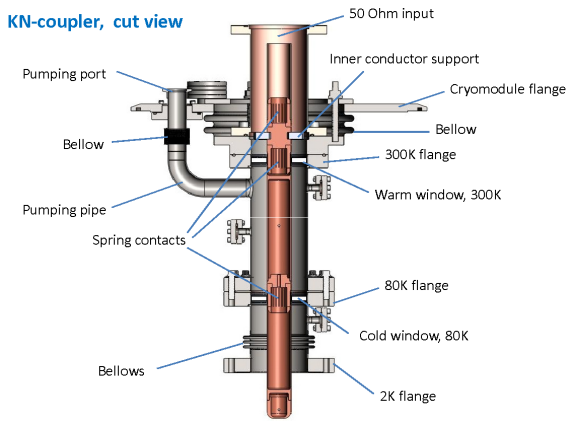

Figure 4: Power coupler design according to Project-X @Fermilab [2]

References

[1] M. Busch, F. Dziuba, H. Podlech, U. Ratzinger, W. Barth, S. Mickat, M.Amberg, K. Aulenbacher, "Status of the 325 MHz sc CH-Cavity at IAP FRANKFURT", IPAC 2011, San Sebastian, Spain.

[2] S. Kazakov, T. Nicol, T. Khabiboullinne, "325 MHz coupler designs", Project X document database, Fermilab, 2011.

* Work supported by BMBF 06FY9089 I

† busch@iap.uni-frankfurt.de

Design Studies for a New Heavy Ion High-Energy Linac at GSI

B. Schlitt, G. Clemente, W. Barth and W. Vinzenz

GSI, Darmstadt, Germany

Introduction

As the UNILAC started operation in 1975, most sections of the existing post-stripper linac will be more than 40 years old when the commissioning of FAIR will start. Due to an increased number of failures and problems at the Alvarez-type drift-tube linac (DTL), at the single-gap resonators, as well as at the corresponding rf systems during the last years, different proposals to replace the post-stripper linac are under discussion to allow for highly reliable operation of the future FAIR injector linac. Since the requirements of experiments with low-energy ion beams behind the UNILAC are contradictory to the requirements for the FAIR injector, two separate heavy-ion linacs are proposed (Fig. 1) [1]:

A new superconducting cw heavy-ion linac [2, 3, 4] behind the upgraded high charge state injector HLI should provide ion beams with high duty cycle in the MeV/u region for the GSI flagship experiments SHIP and TASCA, as well as for material research, biophysics, and plasma physics experiments.

To deliver high-intensity heavy-ion beams for FAIR, the existing post-stripper linac should be replaced by a new high-energy (HE) linac with short beam pulses, low pulse repetition rate, and fixed linac end energy [5].

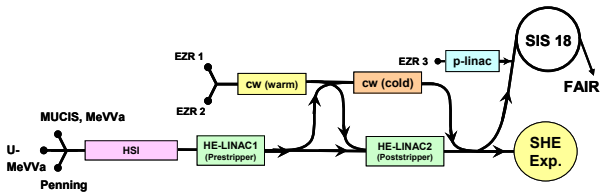

Figure 1: Proposed future GSI linac environment [1].

The proposed new high-energy linac

The high cross sections for charge exchange processes of U^{28+} in the SIS18 generate significant beam losses resulting also in an increasing vacuum pressure during synchrotron operation [6]. To reduce these effects, the use of higher uranium charge states for injection into the SIS18 was investigated [7, 8]. Higher charge states can be produced by increasing the ion beam energy at the stripper (Fig. 2). Hence, an extension of the existing high current injector HSI by four 108 MHz IH-DTL cavities is proposed (Fig. 3, Table 1), leading to a new pre-stripper end energy of 3 MeV/u and to an uranium charge state around 38+ behind the gas stripper. The existing gas-stripper and charge separation section must be dismounted and must be reassembled at the new location.

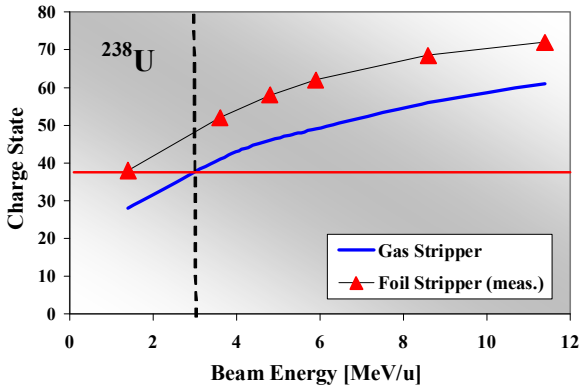

Figure 2: Main uranium charge state after stripping at different stripper materials as function of beam energy.

Table 1: Main design parameters of the proposed high-energy linac (for ^{238}U)

HE Linac	Stage 1		St. 2	
Operation freq.	108.4		325.2	MHz
Linac length	53		29	m
	pre-stripper	post-stripper		
Design charge state	4+	38+	38+	
Beam energy, in	1.4	3.0	11.4	MeV/u
Beam energy, out	3.0	11.4	22	MeV/u
Magn. rigidity, out	14.8	3.1	4.25	Tm
Max. mass / charge	59.5	6.26	6.26	
Design ion current	20	24	24	mA
Tot. accel. voltage	95	53	67	MV
No. of rf cavities (Bu = buncher)	1 Bu 4 IH	1 Bu 4 IH	1 Bu 6 CH	
No. of high-power rf amplifiers	5	5	6+1	

Since injection of an U^{38+} beam into the SIS18 at the present injection energy of 11.4 MeV/u would cause a significant increase of space charge problems, the linac end energy has to be increased to about 22 MeV/u for compensation. Overall, the realization of the new high-energy linac is proposed in two steps (Table 1):

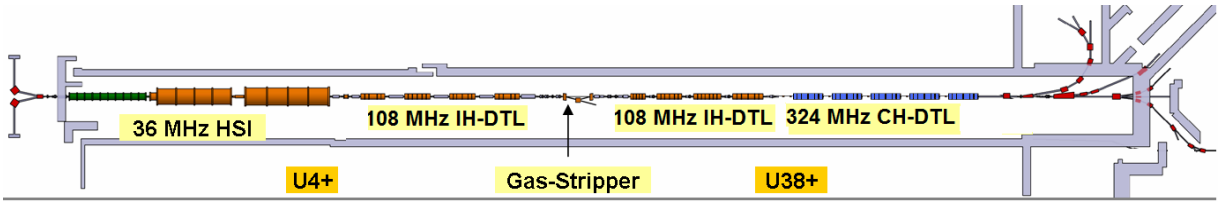

Figure 3: The proposed new high-energy (HE) linac at GSI.

1. Complete replacement of the exiting post-stripper linac by an 108 MHz IH-linac consisting of four new pre-stripper IH tanks and four new post-stripper IH tanks.
2. A 325 MHz linac using crossbar H-mode (CH) structures to boost the linac end energy up to 22 MeV/u within the exiting UNILAC tunnel.

Beam Dynamics

The beam dynamics of the entire HE linac is based on the KONUS focusing scheme, with an external magnetic quadrupole triplet lens behind each cavity. No magnets need to be installed inside the cavities – both for the 108 MHz as well as for the 325 MHz sections. Particle tracking simulations were performed for the full 108 MHz linac using the LORASR code, starting at the HSI exit with a 20 mA U^{4+} beam (Fig. 4) [5]. Immediately behind the 36 MHz HSI structures a powerful six gaps 108 MHz buncher will compensate the phase jump and will match the beams longitudinally for the acceleration along the 108 MHz IH linac. The relative rms emittance growth along the ~22 m long new pre-stripper section is limited to around 16 % in each phase plane as shown in Fig. 5.

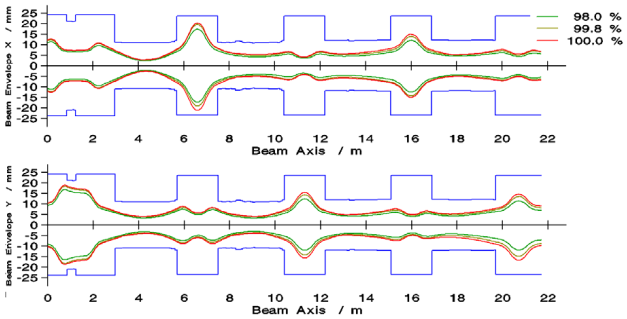

Figure 4: Transverse beam envelopes along the new 108 MHz pre-stripper section starting at the HSI exit.

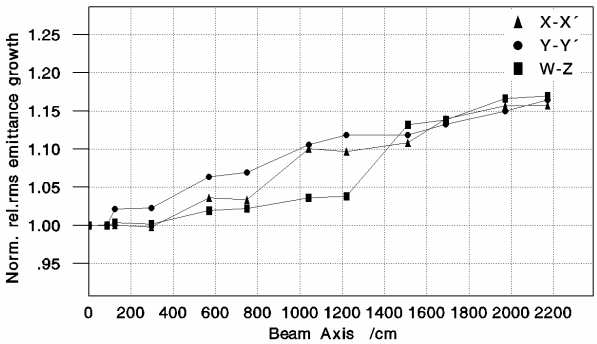

Figure 5: Relative rms emittance growth from HSI exit down to the stripper position for a 20 mA U^{4+} beam.

Cavity Design

The new linac is entirely based on highly efficient H-mode cavities. Due to the low duty cycle, room-temperature structures are planned. Each of the eight 108 MHz IH cavities will have a length between ~3 to ~3.6 meters [5]. Preliminary Microwave Studio simulations indicate that the total rf power – including beam loading – will be less than 1.3 MW for each cavity. For example, Fig.7 shows a simulation model of the first IH cavity.

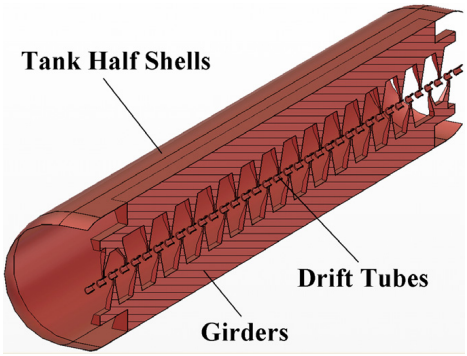

Figure 6: Simulation model of the first 108 MHz IH cavity of the new HE linac.

RF Concepts

To achieve a sufficient reliability of the existing 108 MHz rf amplifiers for the coming decades, an extensive, very costly, and man-power intensive overhauling would be necessary, including the replacement of many components. Hence, a complete substitution by new 108 MHz, 1.7 MW amplifiers for low duty cycle operation with short pulse length is proposed. Prototype studies will start in 2012 for the power amplifiers as well as for new digital low-level rf systems.

For stage 2 of the HE linac, the use of 325 MHz klystron rf amplifiers similar to those at the FAIR proton linac is proposed. Since the existing UNILAC rf gallery would be needed completely for the new 108 MHz systems, an extension of the existing building would be necessary for the 325 MHz klystron gallery.

Outlook

The high-energy linac concept presented here was proposed to the GSI supervisory board in summer 2011, but no final decision has been taken. In addition, an alternative solution has been considered, consisting of a short 108 MHz IH linac for U^{28+} as simple replacement of the existing post-stripper linac – but in contrary to the present machine only for short pulses, low duty cycle, and fixed linac end energy. Ion charge states and beam energy at injection into the SIS18 would not be increased in that case, the gas-stripper section would not have to be moved and no extension of the rf gallery would be necessary. After a decision will be made, design and construction of prototype cavities for a 108 MHz IH structure and possibly also for a 325 MHz CH structure will be planned.

References

[1] W. Barth et al., in: Proc. IPAC2011, p. 2550.
[2] S. Minaev et al., Phys. Rev. ST Accel. Beams **12**, 120101 (2009).
[3] S. Mickat et al., this report.
[4] S. Jacke et al., this report.
[5] G. Clemente, et al., in: Proc. IPAC2011, p. 2553.
[6] P. Spiller et al., in: Proc. IPAC2011, p. 2484.
[7] P. Spiller et al., in: GSI Scientific Rep. 2010, p. 270.
[8] P. Spiller et al., SIS18 Status Report, this report.

SIS18 Upgrade and Status Report

P. Spiller, O. Boine-Frankenheim, U. Blell, L. Bozyk, Y. El Hayek, G. Franchetti, A. Krämer, H.G. Koenig, H. Klingbeil, M. Kirk, K.P. Ningel, U. Laier, D. Ondreka, P. Puppel, N. Pyka, H. Ramakers, S. Ratschow, H. Reich-Sprenger, P. Schütt, J. Stadlmann

GSI, Darmstadt, Germany

FAIR Booster Operation

A major step has been achieved in increasing the static beam life time of intermediate charge state heavy ions. From previous measuremnts it was know, that the biggest amount of ionization beam loss appears in the injection straight (section 12). This was observed from static residual gas pressure measurements and by means of current measurements on the charge catcher system one section downstream (in section 1). Thus, in order to reduce the local pressure enhanced region, a set of NEG panels has been installed in the injection septum. Due to the high pumping speed, the pressure in the injection septum, which was always affected by its connection to the transfer channel, has been reduced significantly. Furthermore, pressure bumps generated by high voltage break downs in the injection septum, are now removed much faster.
As a result of the various SIS18 upgrade stages, the beam lifetime could be continuously increased. Figure 1 shows the measured lifetimes of intermediate charge state, heavy ions for different stages of the UHV system upgrade.

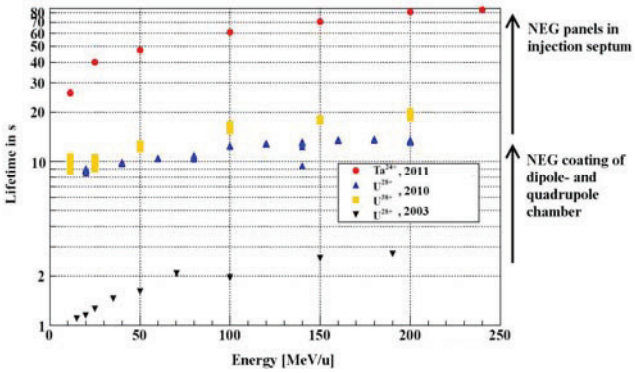

Figure 1: Measured lifetimes of intermediate charge state, heavy ions after NEG coating of the dipole- and quadrupole chambers and after inserting NEG panels in the injection septum.

After the insertion of NEG panels in the electrostatic injection septum, a perfect agreement of the single particle beam lifetime predicted by STRAHLSIM, with the measured life time as a function of energy has been achieved [1]. Before the pumping power in the injection septum has been increased, the local pressure in the injection septum has defined the overall average pressure of the machine. Thus, the beam lifetime was always restricted by this (short) enhanced pressure region. At high intensity operation, the beam halo, which is scraped of in the injection channel, has a high potential for causing high voltage break downs. High voltage break downs generate strong pressure bumps in the injection septum tank. The removal of the desorped gases by the conventional pumps attached to the septum tanke takes an unacceüptable long time. Even with the support of the new NEG panels, the recovery of the beam lifetime after a high voltage break down takes 6 minutes.

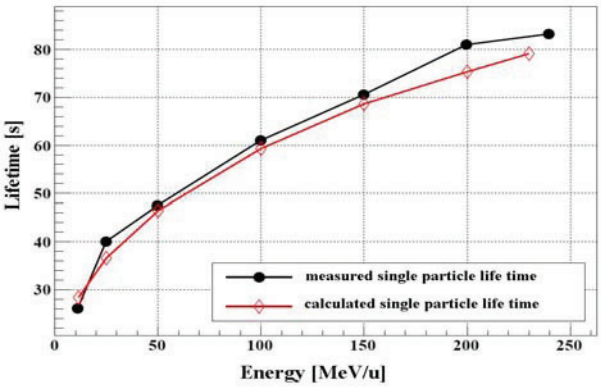

Figure 2: After the installation of NEG panels in the injection septum, a perfect agreement has been achieved between the measured and expected beam lifetime and its energy dependence.

By means of STRAHLSIM calculations, it has been shown that the intensity level reached, represents the actual machine performance defined by its technical status and the partial completion of the upgrade program.

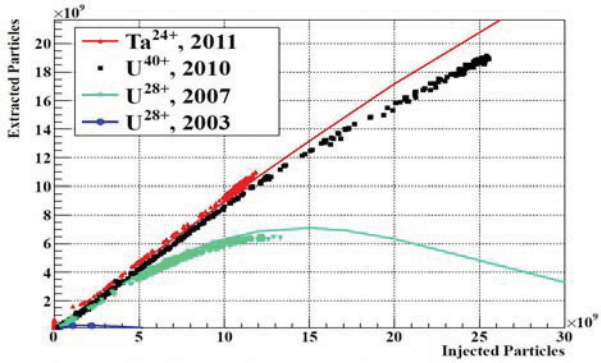

Figure 3: Dependence of the extracted versus the injected number of ions for various stages of the SIS18 upgrade program (measurements and simulations). Saturation (e.g. green curve) indicates that strong dynamic vacuum effects limit a further increase of extracted number of ions. The graph extracted intensity over injected intensity shows the limit of the machine performance determined by the technical development status of the machine.

Figure 3 shows the measured data and a STRAHLSIM extrapolation for higher number of injected ions. A linear dependence indicates that the extracted intensity is not yet

defined by dynamic vacuum effects in the synchrotron and the extracted number of ions is still depending on the injected (UNILAC) beam current. Saturation by dynamic vacuum effects limited the maximum number of extracted ions in the year 2007 to $7x10^9$ ions, while for the present situation the limit is expected at $5x10^{10}$ ions.

High Current Operation

In 2012, the highest average intensity ever reached in the SIS18 of light (N) ion beams could be accelerated. Over several weeks, a nitrogen beam with continously more than 10^{11} ions per cycle has been generated with an energy of 2 GeV/u. Due to fast ramping with 4 T/s, a short extraction time of 0.5 sec and a good extraction efficiency of more than 75 %, an average beam intensity of more than $3x10^{10}$ ions/sec has been extracted.

Multi Turn Injection

The reduction of the initial beam loss has an outstanding importance for the dynamic vacuum and FAIR the booster operation. Initial beam loss originates initial pressure bumps, which dominate the whole dynamic vacuum situation and ionization beam loss in the machine cycle. Therefore, the reduction and control of the beam loss at multi turn injection is a major issue of the machine development program. Various experiments using the scraper system in the transfer channel to minimize the losses during the injection process have been performed succesfully. In addition, the dependence of the multi turn injection efficiency on various parameters has been studies. Figure 4 show the multi turn efficiency as a function of the horizontal tune and the beam current [2].

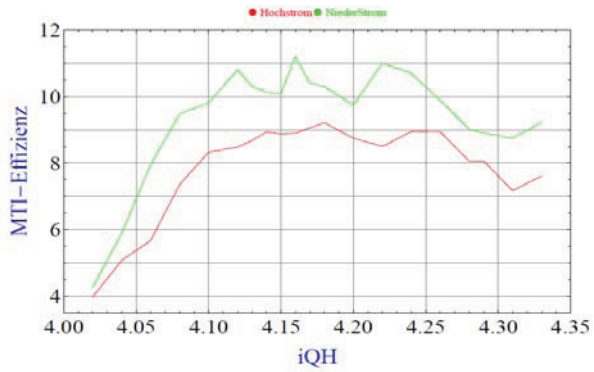

Figure 4: Dependence of the multi turn efficiency on the horizontal tune and beam current.

Bunch Merging and Fast Feed Back

The new low level Rf system developed for the FAIR project, has been installed for testing and operation of the SIS18 ferrit cavities. The new low level RF systems allows a perfect control of the Rf amplitude, phase and frequency. The new hardware was used to introduce a new scheme for the generation of single bunches after acceleration [3]. So far the single bunch has been generated by means of a debunching process at harmonic number four, followed by a coasting beam phase and a recapturing at harmonic number one. The new bunch merging scheme uses the subsequent change of the RF harmonics from 4-2-1 to generate a single bunch (see figure 5). It is expected that this scheme provides better beam control at high current operation and thereby a lower emittance conservation.

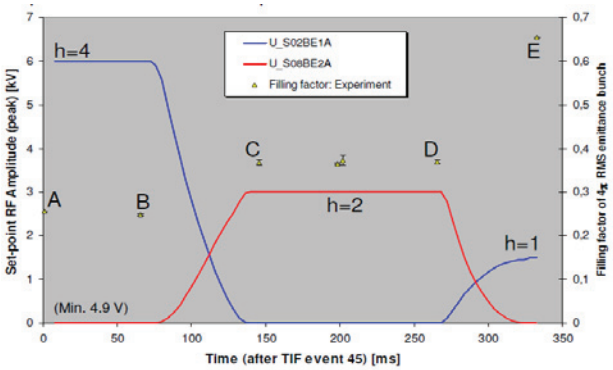

Figure 5: Rf voltage pattern of the two SIS18 acceleration cavities during the bunch merging process

By means of a tomography of the obtained measurements the phase space distribution during and after the single bunch formation could be reconstructed (figure 6) [4].

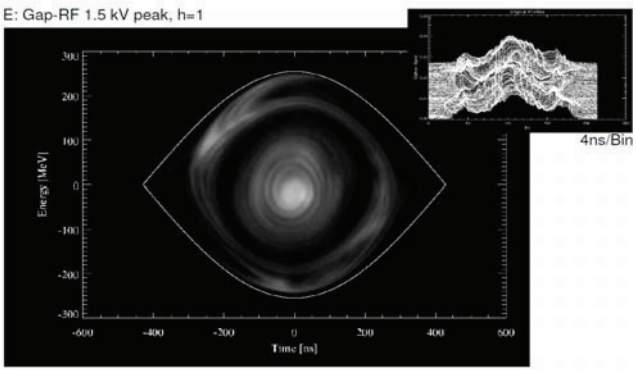

Figure 6: Phase space tomography of a single bunch generated in a subsequent bunch merging process.

Major effort devoted to the Rf systems has been taken with the focus on a reduction of the cavity impedance for high current operation. In three different machine experiments, it could been shown, that by a simple feed back of the gap voltage a reduction of the cavity impedance by a factor of 2 can be reached. The feed back system could be operated very stable over the full frequency span and it is planned to apply it at routine operation [5].

References

[1] L. Bozyk et. al, GSI internal note (2011)
[2] Y. El-Hayek,GSI internal note (2011)
[3] H. Klingbeil et.al, GSI, MemoNr.: 30062011 (2011)
[4] M. Kirk et. al, GSI internal note (2011)
[5] H.G.König, GSI internal note: "SIS18-MaschExp 020411 FB" (2011)

Simulation of the SIS18 multi-turn injection

S. Appel[1] *and O. Boine-Frankenheim*[1,2]
[1]GSI, Darmstadt; [2]TU Darmstadt

Introduction

The optimization of the Multi-Turn Injection (MTI) from the UNILAC into the SIS18 is crucial in order to reach the FAIR beam intensities required for heavy ions. In SIS18 the beam is stacked in the horizontal betatron phasespace using a closed orbit bump to bring the stacked beam close to the injection septum [1]. The orbit bump generated by four steerer magnets is decresed gradually to zero. The main beam loss is expected to occurs on the injection septum. The beam loss during the MTI in SIS18 must be minimized to avoid an intolerable increase of the dynamic vacuum pressure, which in turn leads to a reduced life-time of intermediate charge state heavy-ions [1]. The aim of the present study is the development of a detailed simulation model for the MTI including the closed orbit bump and errors, the parameters of the injected UNILAC beam, the position of the septum and other aperture limiting components, and finally the space charge force and other high-intensity effects. The model can also be used to indicate the required proton and heavy-ion beam emittances from the UNILAC and from the projected p-linac. Before the model can be applied to predict and optimize the MTI for high currents a careful validation with MTI experiments is necessary.

MTI simulation studies

The MTI efficiency depends on various machine and beam parameters. Some important parameters, like the injected beam parameters, are not precisely known from measurements. Here we compare SIS18 measurements with our simulations by using the fact that the MTI efficiency as a function of the initial radial beam position as well as of the injected beam slope exhibits maximum [2]. In the simulation the injected beam position and slope were selected such that the maximum MTI efficiency for the machine experiment settings were obtained. In Fig. 1 the depedence of the MTI beam loss on the tune is shown for low currents. In the simulation result the local beam loss maxima at fractional tunes 0, 1/2, 1/3, 1/4, are clearly visible. In order to compare the measured MTI result [3] with our simulations a constant shift of the tune has to be applied, which is consistent with the machine model. In the measurements the resonant behavior with the tune is difficult to identify. However,the overall agreement with the simulation is very good. In Fig. 2 we show simulation results for the MTI efficiency (the ratio of stored to injected number of particles of one beamlett) as a function of the bump ramp rate (see also [4]) for two beam emittances with and without space charge (sp). In the limit of very small emittances

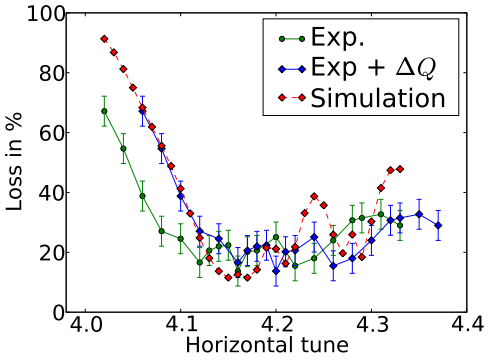

Figure 1: MTI loss as a function of the horizontal tune.

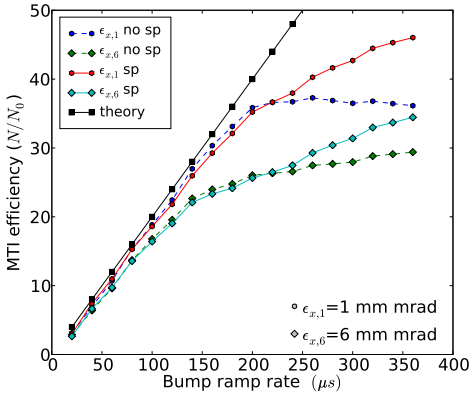

Figure 2: MTI efficiency as a function of the bump ramp.

our result follow a straight line. Our simulation show that space charge can increase the MTI efficiency. Space charge smears out the voids between the injected beamletts.

Conclusion and outlook

For low beam currents a good agreement between a simulation model and MTI measurements in SIS18 is obtained. Further well controlled measurements at low and high beam currents are required in order to fully validate the model. Our results indicatea beneficial effect of the space charge force on the injection efficiency.

References

[1] S. Paret, O. Boine-Frankenheim, HB2010, MOPD11, p. 72

[2] V. Anguelov, D. Dinev, EPAC96, MOPO62G, p. 2417

[3] Y. El-Hayek, Measurement report, GSI, 2011

[4] H. Eickhoff, Arbeitsnotiz SIS02115/IEX, GSI, 1995

Pressure Profiles of a SIS18 equivalent vacuum environment

L.Urban[1], M.C. Bellachioma[1], H. Kollmus[1], A. Krämer[1], J. Kurdal[1], H. Reich-Sprenger[1], S. Wilfert[1], M. Wengenroth[1]

[1]GSI, Darmstadt, Germany;

In particle accelerators ultra-high vacuum conditions inside of the beam pipe are necessary for an interaction free propagation of the accelerated particles. The dipole and quadrupole chambers of the heavy ion synchrotron (SIS18) were coated with thin film getters of titanium, vanadium and zirconium (NEG-layer), transforming the outgassing stainless steel of the chamber into a pumping surface [1]. Due to the lack of space inside of the magnets, it is not possible to measure a pressure profile along the magnet chambers of SIS18.

Therefore we constructed, built and put into operation a test chamber of the identical gas flow conductance, to measure the pressure profile inside the coated dipole chambers using a similar chamber but with increased wall thickness in order to mount ports for vacuum gauges. The experimental setup consists of two pumping posts on both sides of the dipole test chamber. The pumping posts are equipped with a combination of a titanium sublimation pump (TSP), an ion sputter pump and an extractor type ionization gauge. Along the dipole test chamber three more vacuum gauges were mounted. With all five gauges a pressure profile along the complete setup could be measured in a SIS18 comparable vacuum environment for different configurations. It was shown that the pressure within the test chamber coated, with activated NEG, decreases to the 10^{-12} mbar region, whereas the pressure in the pumping posts kept at 10^{-11} mbar. In addition we could show that the Vaktrak code [2] agrees with the measurements (Fig. 1). Furthermore, it was shown that the pressure increase during sublimation of the titanium pumps was not saturating the NEG layer: As one can see in figure 2, even after 12 sublimation cycles the pressure was decreasing with time. During the sublimation also argon (Ar) was released from the filaments into the vacuum (Fig. 3). The used TSP filament was an evaluation part which should not be used in the SIS18, since high Z residual gas components trigger charge exchange with a large cross section. The argon came from the filaments because the manufacturer produced them under an argon protective atmosphere.

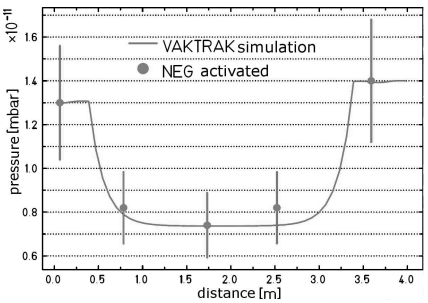

Figure 1: Pressure profile along the dipole test chamber.

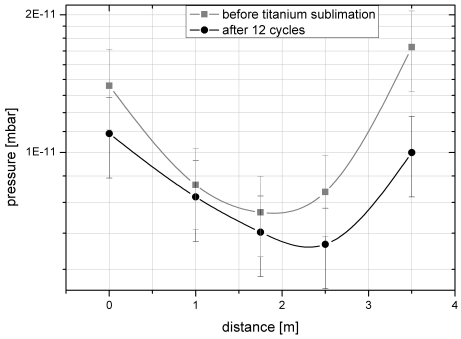

Figure 2: Pressure profile along the dipole test chamber. The grey curve shows the pressure profile before the titanium sublimation and the black curve shows the pressure profile after 12 sublimation cycles.

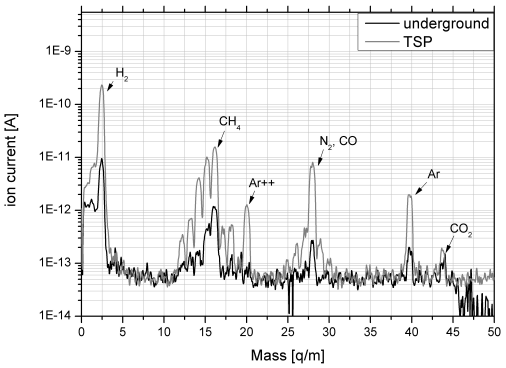

Figure 3: Comparison of the masses during the titanium sublimation

Outlook

During the measurements it was shown that the pressure in the pumping posts is limited to ~ 2 x 10^{-11} mbar. It also turned out that the two ion sputter pumps of both sides of the dipole test chamber work with different performances. This might be similar in SIS18, where these pumps are partially running since 20 years. Therefore, performance test on the SIS18 ion sputter pumps should be carried out, followed by a replacement of aged pumps. Furthermore the installation of NEG cartridges in the pumping posts should be considered in order to decrease the pressure below 10^{-11} mbar in the whole ring.

References

[1] M. C. Bellachioma et al., Vacuum 82 (2008), P. 435-439

[2] http://www.isv.uu.se/ziemann/vaktrak/

Eigenmode Computation for Ferrite-Loaded Cavity Resonators*

K. Klopfer† [1], *W. Ackermann*[1], *and T. Weiland*[1]

[1]Technische Universität Darmstadt, Institut für Theorie Elektromagnetischer Felder (TEMF), Schlossgartenstraße 8, 64289 Darmstadt, Germany

Introduction

For acceleration of charged particles at the heavy-ion synchrotron SIS18 two ferrite-loaded cavity resonators (see figure 1) are installed within the ring. During the acceleration phase the resonance frequency of the cavities has to be adjusted to the revolution frequency of the heavy-ions in order to reflect their increasing velocity. Within the flexible resonator structures dedicated biased ferrite ring cores are installed. In the elaborated setup a properly chosen bias current is used to modify the differential permeability of the installed ferrite material, which consequently enables to adjust the eigenfrequency of the whole resonator system. The goal of the current study is to numerically determine the lowest eigensolutions of accelerating ferrite-loaded cavities.

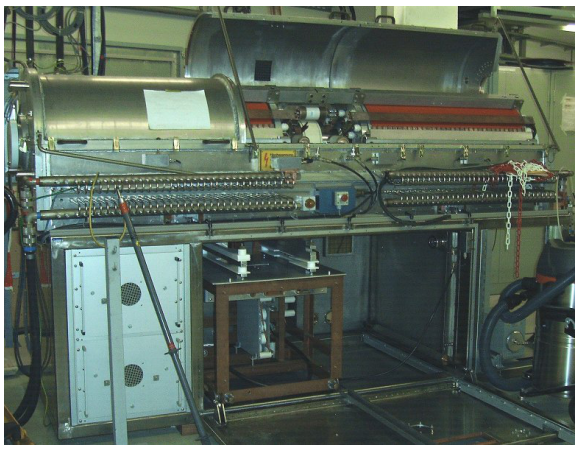

Figure 1: The SIS18 ferrite cavity at GSI.

Computational Model

The numerical modeling is based on the assumption that the amplitude of the radio frequency (RF) electromagnetic field is small compared to the bias magnetic field in the cavity. Furthermore, hysteresis effects are neglected. Applying perfect electric boundary conditions, the eigenmodes of the resonator are then determined by the fundamental relation

$$\epsilon^{-1}\nabla \times \left(\mu_d^{-1}\nabla \times \vec{E}(\vec{r},t)\right) = \omega^2 \vec{E}(\vec{r},t),\ \vec{r} \in \Omega, \quad (1)$$

$$\vec{n} \cdot \vec{E}(t) = 0,\ \vec{r} \in \partial\Omega, \quad (2)$$

wherein ϵ is the permittivity, μ_d^{-1} the differential reluctivity, ω the eigenfrequency of the corresponding RF mode and $\vec{n}$ a normal vector on the cavity boundary $\partial\Omega$. If magnetic losses are included, the eigenvalues exhibit a non-vanishing imaginary part. Since the eigenmodes depend on μ_d^{-1}, the static magnetic field generated by the bias current has to be computed in a first step. Note that μ_d^{-1} in general is a non-diagonal tensor due to both the anisotropic character of the non-linear material in the range of magnetic saturation [1] and the presence of the bias magnetic field. In order to meet these requirements a new solver has to be developed.

The current implementation is based on the Finite Integration Technique with a hexahedral staircase mesh. For modeling the resonator structure, meshing and visualization of the simulation results CST STUDIO SUITE™[2] is used. In contrast, the magnetostatic field solution and the resulting differential reluctivity are obtained with a dedicated magnetostatic solver, whereas the eigenvectors are calculated with a realization of the Jacobi-Davidson algorithm [3]. Because of the clear demand for precise calculations, particular emphasis is put on the implementation to enable high performance computations based on distributed memory machines.

Current Status and Outlook

The realization of the algorithms for the computation of the lowest eigensolutions of biased ferrite-loaded cavities has not been fully completed. Yet, the magnetostatic solver for non-linear materials and the eigensolver have successfully been verified independently through convergence studies comparing the numerical results with analytical calculations. Future work will mainly focus on the construction of the differential reluctivity matrix, which is required as an input for the aspired eigensolver, and the combination of the two algorithms.

References

[1] H. De Gersem, I. Munteanu and T. Weiland, "Construction of Differential Material Matrices for the Orthogonal Finite-Integration Technique With Nonlinear Materials", IEEE Transactions on Magnetics, 44 (6), 710-713.

[2] CST STUDIO SUITE™, CST Computer Simulation Technology, Bad Nauheimer Straße 19, 64289 Darmstadt, Germany.

[3] G. L. G. Sleijpen and H. A. van der Vorst, "A Jacobi-Davidson iteration method for linear eigenvalue problems", SIAM J. Matrix Anal. Appl., 17:401-425, 1996.

*Work supported by GSI Helmholtzzentrum für Schwerionenforschung GmbH, Darmstadt, Germany.

† klopfer@temf.tu-darmstadt.de

High Intensity Effects on Betatron Tune at SIS-18*

R. Singh[1,2], *P. Forck*[1], *P. Kowina*[1], *W. Kaufmann*[1], *K. Lang*[1], *and T. Weiland*[2]
[1]GSI, Darmstadt, Germany; [2]TEMF, TU Darmstadt, Germany

Introduction

Precise tune measurement during a full accelerating cycle is required to achieve stable high current operation at SIS-18. Recently a system has been commisioned at GSI for position, orbit and tune measurements (TOPOS). It consists of, An exciter which excites coherent betatron oscillations in the bunched beam, Fast ADCs to digitize the BPM signals at 125 MSa/s and FPGAs to calculate postion from the digitized BPM signals. Baseband tune is thus determined by Fourier transformation of the individual bunch position data [1]. Several tune measurement campaigns with high intensity beams using TOPOS were performed to emphasize the high current effects on the tune spectra.

Experiments and Results

Experiments were conducted to understand the effects of high beam intensity on tune at injection plateau of 11.4 MeV/u with Ar^{18+} ion beams upto $1.5 \cdot 10^{10}$ particles while continously excitation with noise power of upto $1\mathrm{mW/Hz}$. Coherent tune shift in dependence of beam intensity was observed as expected [2]. In addition, at high intensities ($1 \cdot 10^{10}$ Ar^{18+} particles), with $1\mathrm{mW/Hz}$ excitation, several "tune" peaks were observed in the tune spectrum as shown in Fig. 1. Further investigations in the raw data mode of TOPOS were done, where the difference between the top and bottom BPM plate was plotted over several consecutive turns for the same data. Figure 2 show two such plots with an interval of 100 turns indicating the presence of several head tail modes [3]. The distinct frequency peaks in Fig. 1 were thus understood to correspond to these head tail modes. Due to the fast dynamics involved in excitation of various modes, there is a trade-off between the frequency resolution of the evaluated spectrum and its time localization. Numerical studies on the occurence and stability of these head tail modes in view of FAIR synchrotrons has been performed in a separate study [4].

Outlook

Further experiments are planned to understand the high intensity tune spectra. Another independent base band tune measurement system (BBQ) based on the principle of direct diode detection [5] has been installed at SIS-18 and the next step is the comparision of the sensitivity of BBQ vs TOPOS.

*This work is supported by DITANET (novel DIagnostic Techniques for future particle Accelerators: A Marie Curie Initial Training NETwork),Project Number ITN-2008-215080

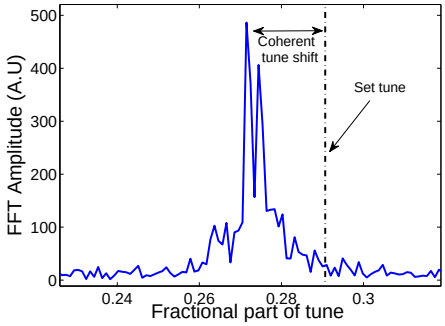

Figure 1: Vertical tune spectrum using 1024 position points of an individual bunch showing several distinct peaks. The set tune, coherent tune shift and various "tune" peaks are shown.

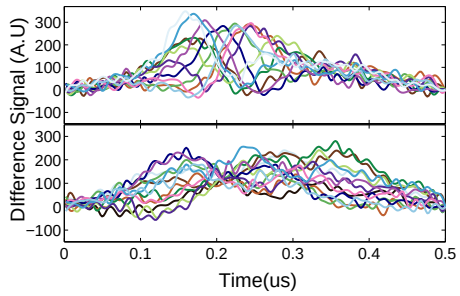

Figure 2: Difference of BPM data for the same bunch plotted over 13 consecutive turns (top) and 100 turns later (bottom). The top plot shows a predominatly second order mode while the bottom one shows bigger contribution from third order mode just after 100 turns (colours are randomly chosen to enhance clarity).

References

[1] P. Kowina et al.,"Digital baseband tune determination", Proc. BIW'10, Santa Fe, U.S.A, p .341,2010.

[2] R. Singh et al.,"Tune measurements with high intensity beams at SIS-18", Proc. of DIPAC, Hamburg, Germany, 2011.

[3] F. Sacherer, "Methods for computing bunched beam instabilities", CERN/SI-BR/72-5, Geneva, Switzerland,1972.

[4] V. Kornilov et al., "Head-Tail bunch dynamics with space charge", Proc. of HB2010, Morschach, Switzerland

[5] M. Gasior et al.,"The Principle and first results of betatron tune measurement by direct diode detection" LHC Project Report 853.

Magnetostatic contribution to the RF noise of the SIS-18 RF-KO exciter

Stefan Sorge, BPHY Department, GSI, Darmstadt, Germany

A recently developed method to measure the acceptance of a circular accelerator was applied to determine the horizontal acceptance of SIS-18. In the method transverse noise is applied to drive particle diffusion which increases the beam width. When the beam width exceeds the physical aperture the beam current decreases due to beam loss. The acceptance is obtained via modelling the process by means of particle tracking and comparing measured and simulated time behaviour of the beam current.

In the experiment a Ta^{61+} beam of $E = 100$ MeV/u was horizontally excited using the SIS-18 RF-KO exciter, see Figure 1. The modified AC voltage $U(t) = U_a \sin[2\pi f_C + \phi(t)]$ between the electrodes is characterised by the amplitude U_a, the carrier frequency f_C which should match the betatron frequency to maximise the excitation efficiency, and the phase $\phi(t)$ which is determined by a pseudorandom bit sequence where $\phi = \pi$ during a bit status 1 and $\phi = 0$ otherwise [3]. The resulting momentum kick $\Delta x^{'}(t)$ has the time behaviour of $U(t)$.

In the simulations a realistic SIS-18 lattice was used and the creation of a local closed orbit bump of -15 mm height towards the electrostatic extraction septum was taken into account. According to a common assumption, $\Delta x^{'}(t)$ was considered in the first step in evaluating the measured data as purely electrostatic. Its amplitude is

$$\Delta x^{'}_a = \Delta x^{'}_{el,a} = \frac{qU_a}{d}\frac{\Delta t}{p} = \frac{ZeU_aL}{Am_uc^2\beta^2\gamma d}, \qquad (1)$$

where p nd q are ion momentum and charge, Δt is the time for an ion to pass through the exciter, and $L = 0.75$ m and $d = 0.2$ m are the length of the electrodes and the horizontal distance between them. The obtained simulated beam current decreased much slower than the measured one, compare black and red curves in Figure 2. Adding a magnetostatic momentum kick strongly improved the

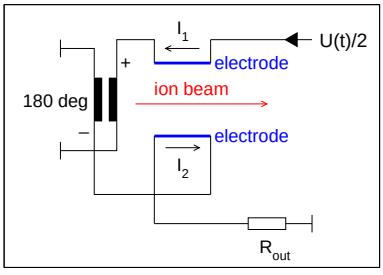

Figure 1: Scheme of the RF-KO exciter according to [2]. The voltage between the electrodes is $U(t)$. The voltage provided by the amplifier is $U(t)/2$ because of the phase rotation of the AC voltage by 180 deg.

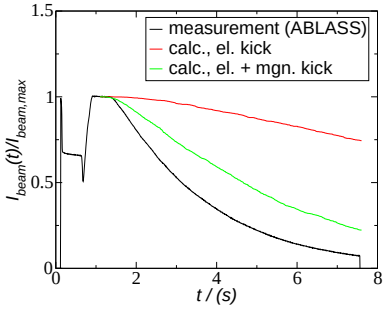

Figure 2: Beam current $I_{beam}(t)$ for $U_a = 50$ V.

agreement, see green curve in Figure 2. This kick is caused by the horizontal Lorentz force $F_{L,x} = -qvB_y$ due to the currents $I_1(t), I_2(t) = U(t)/(2R_{out})$ flowing in opposite directions through the electrodes, where $R_{out} = 50\ \Omega$ and real. Integrating $F_{L,x,a}$ along the orbit in the exciter yields

$$\begin{aligned}\Delta x^{'}_{mgn,a} = &-\frac{2Ze}{Am_uc\beta\gamma}\frac{\mu_0 I_a d}{\pi}\left\{\frac{2L}{dw_y}\right.\\
&\times\left[\arcsin\left(\frac{(w_y^2/4-x_0^2)(x_0^2+L^2)-x_0^2w_y^2/2}{(x_0^2+L^2)(w_y^2/4+x_0^2)}\right)\right.\\
&\left.-\arcsin\left(\frac{(w_y^2/4-x_0^2)x_0^2-x_0^2w_y^2/2}{x_0^2(w_y^2/4+x_0^2)}\right)\right]\\
&+\frac{2}{w_y}\left[\ln\left(\frac{w_y/2+\sqrt{w_y^2/4+x_0^2+L^2}}{\sqrt{x_0^2+L^2}}\right)\right.\\
&\left.\left.-\ln\left(\frac{w_y/2+\sqrt{w_y^2/4+x_0^2}}{x_0}\right)\right]\right\}, \qquad (2)\end{aligned}$$

i.e. $\Delta x^{'}_{mgn,a} \propto \beta\Delta x^{'}_{el,a}$, and $\Delta x^{'}_{mgn,a} = 0.86\ \Delta x^{'}_{el,a}$ at $E = 100$ MeV/u. Because of the remaining discrepancy the presented data are not proper to estimate the acceptance. However, $\Delta x^{'}_{mgn,a} \approx \Delta x^{'}_{el,a}$ implies an excitation efficiency much larger than assumed. This result suggests that efficient RF-KO extraction from SIS-100 can be performed using an amplifier of reduced power.

References

[1] S Sorge, G Franchetti, and A Parfenova, Phys Rev ST-AB **14**, 052802 (2011).

[2] P Moritz, "Zentraldokument RF-KO-Extraktion S07BO1E", GSI Darmstadt, Dec 12, 2010 and private communication.

[3] M Kirk and P Moritz, "Noise excitation parameters for the SIS-18 RF-KO excitation", GSI internal note, GSI 2006.

Electron cloud accumulation in long heavy-ion bunches

F. Petrov[1], *O. Boine-Frankenheim*[1], *and Th. Weiland*[1]
[1]TEMF, TU-Darmstadt, Darmstadt, Germany

Introduction

Electron clouds (EC) can accumulate in a circulating coasting beam and reduce the slow extraction efficiency. This is a concern for the SIS-18 and for the projected SIS-100 synchrotrons. Above a threshold beam intensity the two-stream instability and the resulting transverse coherent beam oscillations limit the electron density [1]. A gap introduced into the beam using rf barriers can significantly reduce the EC build-up. This effect is studied based on the solution of the Hill's equation for the electrons trapped in the space charge potential of the ion beam.

Results and Discussion

The basic methods to study the stability of electrons trapped in a homogeneous beam profile with a line density λ_i are given in [2]. The electron equation of motion in the linear case including the electron space charge force is

$$x'' = K(t, z_0) \cdot x = -\omega_e^2(t, z_0) \cdot x + \omega_+^2(t, z_0) \cdot x \quad (1)$$

If the transverse position at z_0 is of interest only once per revolution period P then one can use the transfer matrix $M_{tr,e}$ [2] to describe the electron oscillations. If $|Tr(M_{tr,e})| < 2$ then an electron is trapped. In our study we obtain $M_{tr,e}$ for the realistic beam line densities $\lambda_i(t, z_0)$ by numerical integration. The obtained electron Twiss parameters have dimensions of seconds because Eq. 1 is solved in time. Electrons will have different emittances $\epsilon_e = \gamma_e(t_0) \cdot x_0^2$ depending on their time of production. The maximum deviation of an electron from the beam axis is $R_{max} = \sqrt{\epsilon_e \beta_{e,max}}$. We assume that an electron is lost if its R_{max} is larger than the beam radius. To quantify the reduction of the build-up rate at point z_0 we introduce the local survival ratio δ_{z_0} defined as the number of trapped

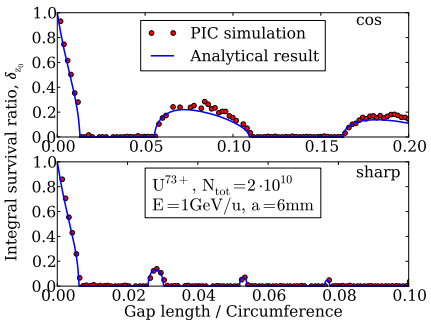

Figure 1: Comparison of δ_{z_0} obtained from PIC simulation and analytical results. Two cases: smooth cosine gap and perfectly sharp gap profiles. The agreement is very good.

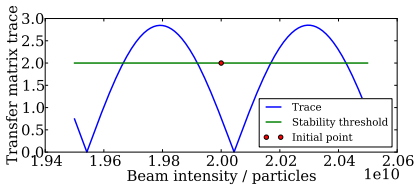

Figure 2: Stability of the beam with 10% cosine gap. Electrons are lost for values > 2. Red point shows initial electron working point. EC space charge shifts it to the left.

electrons divided by the number of produced electrons. For a homogeneous beam it is given by

$$\delta_{z_0} = \int_0^P \frac{\delta_{z_0,t_0}}{P} \frac{\lambda_i(t_0, z_0)}{\bar{\lambda}_i} dt_0 \qquad \delta_{z_0,t_0} = \frac{1}{\beta_{e,max} \cdot \gamma_{e,0}} \quad (2)$$

Here δ_{z_0,t_0} is the differential survival ratio of electrons born at time t_0. This value is averaged over one period. Beam line density $\lambda_i(t)/\bar{\lambda}_i$ is used because the production of electrons depends on it. Square root dependence disappeared because the problem is solved for round beam in 2D. Fig. 1 compares δ_{z_0} obtained from the analytic model with 2D electrostatic PIC simulations.

With increasing EC density the phase advance per one turn shifts and ω_+ in Eq. 1 increases. The upper limit for the EC density can be estimated from the phase advance shift needed to make the trace of $M_{tr,e}$ equal to 2 [3]. The threshold density is very small because $\nu_e = \omega_e P/2\pi$ under FAIR conditions is in the range of 30-100. Fig. 2 shows that for an U^{73+} beam the space charge reduction should be less than by 1%. Simulations for U^{73+} in [1] show that the instability can occur at a neutralization degree $\eta = 2\%$.

Conclusion

In [3] it is shown that by taking into account the varying beam size across the circumference reduces electron density even more. PIC simulations indicate that the EC density saturation level is smaller than our analytical estimations. Finally the η predicted in this study for SIS18 and SIS100 is lower than the instability threshold for two-stream instability [1]. We can therefore conclude, that rf barrier gaps can sufficiently suppress EC effects.

References

[1] F. Petrov et al, GSI Scientific Report 2010
[2] K.Y. Ng, Physics of Intensity Dependent Beam Instabilities, 2006
[3] F. Petrov et al, MOPS053, IPAC 2011 Proceedings

Investigation of Electron Cloud Effects in the GSI*

F. Yaman† [1], *E. Gjonaj*[1], *O. Boine-Frankenheim*[1], *and T. Weiland*[1]

[1]Technische Universität Darmstadt, Institut für Theorie Elektromagnetischer Felder (TEMF), Schloßgartenstraße 8, 64289 Darmstadt, Germany

Introduction

The space charge interaction between the ion beam and electron cloud may lead to wake fields, beam loss, trajectory change or even instability in the heavy ion synchrotron SIS18 at the GSI. In this context, the aim of our study is the numerical computation of the wake field and energy loss per unit length for an ion bunch penetrating an electron cloud residing in the beam pipe. We use two different self-consistent Particle-In-Cell (PIC) codes: a standard 2D electrostatic PIC code and a higher order 3D PIC code which is based on the full-wave approach for the Maxwell equations in the time domain.

Method

The method of investigation consists exclusively in numerical simulations. For this purpose, a self-consistent, parallel PIC code was developed. The code uses a high order and full-wave approach for the solution of 3D-Maxwell's equations in the time domain. This allows for electron cloud modeling based on first principles including, in particular, the nonlinear effects of the beam-electron cloud interaction in the transverse as well as in the longitudinal direction. For the verification of our code we compare our results with the analytical models and 2D electrostatic PIC code [3, 4].

Simulations for SIS 18

For the calculation of longitudinal wake potential, a region in the beam pipe is filled with electrons and the electron cloud density is assumed as $10^{12}\,m^{-3}$. Then the effect of electrons to the U^{73+} beam is computed for a certain SIS18 beam parameters such that the population of ion bunch is $N = 4 \times 10^{10}$, $\beta = 0.87$, bunch length $\sigma_{rms} = 0.5$ m and radius 1 cm. Afterwards, corresponding impedance is simply obtained from the Fourier transform of the wake potential, see Figure 2. Note that, the impedance presented here is normalized to the length of the electron filled region, [1, 2].

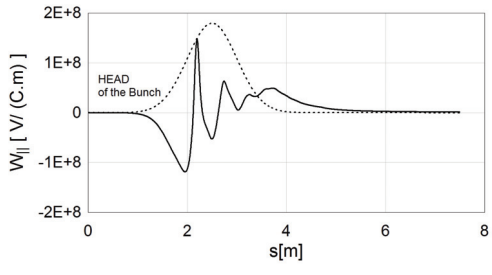

Figure 1: Longitudinal Wake Potential (dotted line shows the bunch)

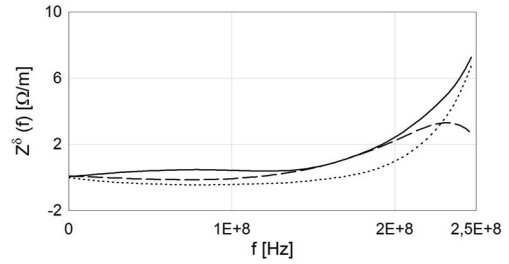

Figure 2: Longitudinal Impedance (solid line: absolute value , dashed line: real part, dotted line: imaginary part)

Outlook and Conclusions

We obtained good agreement on wake field computations for transversally uniform short relativistic bunches traveling in circular PEC beam pipes employing 3D electromagnetic and 2D electrostatic PIC codes for the parameter scope of CERN-SPS and LHC, [3, 4].

It is found that for sufficiently short bunches the energy loss can be described very well by an analytic formula and stopping power calculations due to electron cloud is already presented in [3]. For electron densities well above the typical $10^{11} - 10^{12}\,m^{-3}$ the 'shielding'-effect of space charge field of the electrons reduces the energy loss ,[3, 4].

References

[1] F. Yaman, E. Gjonaj and T. Weiland, "3D EM PIC code to study E-Cloud effects for short bunches (< 50 ns)", CERN-GSI Electron-Cloud Workshop, 7-8 March 2011, CERN.

[2] F. Yaman, E. Gjonaj and T. Weiland, "Simulation of electron cloud effects to heavy ion beams ", DPG-Frühjahrstatung 2011 (ISSN 0420-0195), Karlsruhe, Germany.

[3] O. Boine-Frankenheim , F. Yaman, E. Gjonaj, T. Weiland and G. Rumolo, "Energy Loss and Longitudinal Wakefield of Relativistic Short Ion Bunches in Electron Clouds", Proceedings of the 2nd International Particle Accelerator Conference, San Sebastian (IPAC 2011), pp. 2229-2231.

[4] O. Boine-Frankenheim, E. Gjonaj , F. Petrov, F. Yaman and T. Weiland, "Energy loss and longitudinal wake field of relativistic short proton bunches in electron clouds", submitted to Physical Review Special Topics - Accelerators and Beams, 2011.

*Work supported by GSI Helmholtzzentrum für Schwerionenforschung GmbH, Darmstadt, Germany.

† yaman@temf.tu-darmstadt.de

Experimental Studies of Beam Loss during Bunching at 4 MeV/u for HITRAP

P. Görgen[1], *O. Boine-Frankenheim*[1], *S. Appel*[2], *C. Dimopoulou*[2], *S. Litvinov*[2], *and M. Steck*[2]
[1]TEMF, TU-Darmstadt; [2]GSI Darmstadt

The Heavy Ion Trap (HITRAP)[1] experiment at GSI is supplied with electron-cooled ion beams decelerated to 4 MeV/u in the ESR. HITRAP accepts up to 1.5 μs of beam. The revolution period of 4 MeV/u ions in the ESR amounts to about 4 μs. HITRAP therefore requires rebunching in the ESR in order to capture the entire beam. Before this work RF capture at 4 MeV/u in the ESR was known to sometimes cause particle losses. Lattice errors from remanence in the magnets are more pronounced at low energy. Even a small space charge tune shift may then lead to resonance crossing and particle losses even on higher order resonances. Because of this, the space-charge tune shift leading to resonance crossing was considered the most likely loss reason. Intrabeam scattering (IBS) was considered as the dominant heating process.

For the measurements ions coming from SIS at 30 MeV/u were decelerated to 4 MeV/u in ESR. Measurements with Ar^{18+} and Cr^{23+} beams at 4 MeV/u were carried out. The emittance was determined using a residual gas ionization profile monitor. The momentum spread was obtained from the longitudinal Schottky signals. The RF capture process and the bunch dynamics were observed using a beam position monitor.

Bunching measurements Cr^{23+} and Ar^{18+} beams were bunched at 4 MeV/u with different RF voltages and the resulting bunch properties were observed. After the switch-on of the RF a sudden increase of the horizontal emittance was observed while the vertical emittance stayed constant or shrank. For the Ar^{18+} beam maximum DC currents of up to 5 μA were available. Bunching voltages of 100 V led to losses of 40% of the particles. Both particle losses and emittance growth increased with RF voltage. However even the lowest available RF voltages provided much shorter bunches than needed for HITRAP.

For Cr^{23+} beams and currents around or below 1 μA, an emittance increase but no particle losses were observed at RF voltages up to 100 V.

IBS rates It was tested whether the transverse heating rate after switching on the RF Voltage of 5 s^{-1} could be attributed to IBS. To simulate IBS, the IBS rate formalism of Bjorken and Mtingwa [2] was used. The IBS growth rates corresponding to the beam properties at bunching were calculated to be 1.3 s^{-1}. They do not explain the growth rate seen at RF capture.

Tune measurements It still remained to be shown that the small space charge tune shift at 4 MeV/u is sufficient to put the beam onto nearby resonances. For this reason the machine behaviour around the standard working point setting of $(Q_h, Q_v) = (2.27, 2.32)$ was investigated at 4 MeV/u. For variations of the focusing strength of the ESR quadrupoles, sudden particle losses were observed even during small changes in the tune of the order of 0.01. This value is of the same order of magnitude as the space charge tune shift computed from emittance and estimated peak current according to [3]. The losses are therefore attributed to resonance crossing.

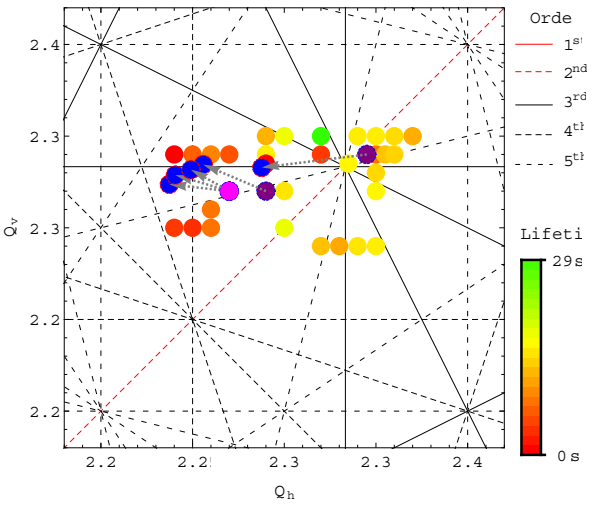

Figure 1: Resonance diagram showing color-coded lifetimes at different tune settings around the 4 MeV/u standard tune in ESR (shown in pink at (2.27, 2.32)). Set and corresponding measured tune values are shown connected by an arrow. Data was insufficient to recover the relation between actual and set tunes.

Conclusion The space-charge tune shift in the horizontal direction after bunching is close to -0.01. A tune change by this value was often followed by particle losses in our measurements. We excluded IBS as the main source of heating by comparing the calculated IBS rates to the observed heating rates. We conclude that, very likely, the space charge tune shift is the source of the particle losses. During the measurements we found tunes more stable than the standard working point. Using an optimized tune together with the lowest possible bunching voltage might allow for bunching of higher numbers of ions.

References

[1] T. Beier et al.: *HITRAP Technical Design Report* (2003).
[2] J. D. Bjorken and S. K. Mtingwa: *Intrabeam Scattering.* (1982) Part. Accel. 13 (Jul): 115-143.
[3] K. Schindl: *Space charge*, CAS 2006.

Improved Monitoring of the HITRAP Double-Drift Buncher

A. Reiter, F. Herfurth, G. Clemente, W. Vinzenz
GSI, Darmstadt, Germany

Introduction

We report on a substantial improvement of the HITRAP double-drift buncher monitoring using capacitive pick-ups. The time-of-flight measurement provided excellent energy resolution. Shifts of the order of $5 \cdot 10^{-4}$ were resolved that were induced by RF phase offsets between the bunchers. After optimisation longitudinal particle distributions were observed that agreed with model calculations of the pick-up response.

Experiment Setup

The double-drift buncher is expected to match 60–70% of the 4 MeV/u DC beam from the experimental storage ring to the IH-DTL decelerator acceptance by formation of a ∼1 ns long, peaked distribution. Beam dynamics simulations have shown that this distribution is sensitive to the phase difference between the two bunchers, which is controlled by the RF amplifier phase of Buncher 2.

During operation two capacitive pick-ups monitor the longitudinal structure, one behind Buncher 2 and one in front of the IH-DTL decelerator. The flight-time of a bunch along the path yields the mean beam energy. High-quality signal amplifiers on the pick-up outputs guarantee a good signal-to-noise ratio before the signals are transmitted to 5 GSa/s digitizers in the electronics room.

Previously, the introduction of a new data analysis [1] had suggested significant sub-structure in the longitudinal distribution (see Fig. 2 of [1]) when the bunchers were operated at what were believed to be optimum parameters. In October 2011, a dedicated measurement scanned the RF phase of the 216 MHz Buncher 2 in 10° steps over the full range. For each phase setting three to five data sets were recorded. The measurement provided a complete set of data that enabled us to investigate the previous findings.

Results

The time-of-flight data were analysed as described in [2]. The calculated mean energies are presented in Figure 1 and carry an uncertainty σ∼0.7 keV/u due to timing resolution. The observed energy shift totals 25 keV/u as expected from RF input power and cavity parameters; this implies that Buncher 2 was working properly. The energy shift equals a timing offset of only 400 ps or two digitizer sampling intervals between the two pick-up signals. Therefore, the smooth graph illustrates the excellent timing resolution of the measurement system.

Although the phase was scanned starting at the suspected optimum value, a large beam energy of 4055 keV/u was detected. From the plateau the curve drops to the minimum value of 4030 keV/u (Run 55) over a 90° range, before it steadily rises over the next 180° (Run 125) towards a second maximum region. The final quadrant records energies between 4050–4060 keV/u.

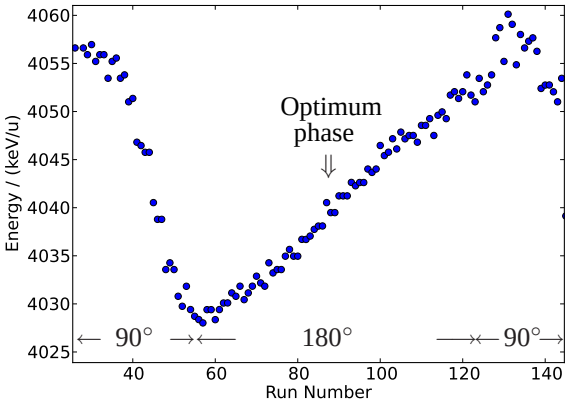

Figure 1: Measured beam energy as function of Buncher 2 phase defined by the Run Number

Clearly, the working region of Buncher 2 lies in the central 180° range. The optimum phase is found at Run 90, the centre of the working region, where Buncher 2 does not affect the primary beam energy of 4040 keV/u. With respect to the previous value, the new optimum is shifted by almost 180°. Around this position the pick-ups show signal shapes that one expects from model calculations, while amplitude and shape deteriorate outside the optimum region. There, complex distributions are formed, similar to those in [1], with significant components outside the IH-DTL acceptance at the expense of reduced performance.

Conclusions

The new monitoring approach has demonstrated its capability of optimising the HITRAP double-drift buncher. Further, it delivers an absolute phase reference for Buncher 2, the most critical setup parameter. So far, this value had to be treated as free input parameter in beam dynamics simulations; without this degree of freedom, a direct comparison with measurements should be possible.

Extending the monitoring approach to capacitive pick-ups behind the IH-DTL, we hope to gain more insight into the longitudinal structure of the decelerated beam.

References

[1] A. Reiter et al., PHN-ACC-RD-09, GSI Annual Report, 2010

[2] A. Reiter et al., MODP35, Proc. of DIPAC, Hamburg, 2011

Bead-pull Measurement on the Resonator Pick-up at IMP, Lanzhou

M. S. Sanjari[1,3], *J. X. Wu*[2], *Y. D. Zang*[2], *P. Hülsmann*[1,3], *F. Nolden*[1], *and A. Schempp*[3]
[1]GSI, Darmstadt; [2]IMP, Lanzhou; [3]IAP, Goethe Universiät-Frankfurt am Main

A new resonant pickup was built and commissioned for the CSRe storage ring at Institute of Modern Physics (IMP) in Lanzhou, China in 2011. A detailed report on the IMP resonator has appeared in [1] where a geometrical factor $R_s/Q = 71.1\ \Omega$ and a shunt impedance $R_s = 76.2\ k\Omega$ were measured for the IMP resonator. In this work we report the results of an improved measurement.

The IMP resonator is a modified pillbox with beam pipes based on a design similar to the GSI resonator [2]. Figure 1 shows the IMP resonator before installation into the CSRe storage ring. We repeated the *resonant* measurement based on RF cavity perturbation also known as the *bead pull method*. The theory relies on the work of Müller [3] and later by Slater [4][1].

Figure 1: The IMP resonant pickup before installation.

The measurement was performed in fundamental mode with a measured frequency of 242.4 MHz and an unloaded Q value of 1003. A small cylindrical copper needle of 14mm length and 4mm outer diameter was moved on the axis of the structure with a step size of 1 cm and a total of 150 points. The needle was assumed to be an equivalent ellipsoid of revolution with the same outer diameter and volume. The presence of the needle causes a shift of the resonant frequency of the structure at each position. This frequency shift can be related to the geometrical factor R_s/Q, using the definition of shunt impedance $R_s = U^2/P_L$,

[1]Detailed explanation also by Peschke in [5].

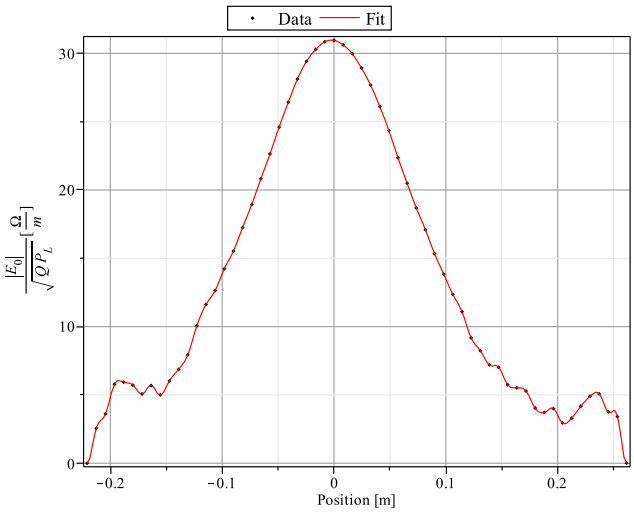

Figure 2: Measured data points and fit.

where $U = \int_0^L E_0\, ds$ is the voltage, P_L is the dissipated power, L is the effective length and E_0 is the amplitude of the electric field on axis in the fundamental mode. We have

$$\frac{R_s}{Q} = \left(\int_0^L \sqrt{\frac{M(f_0^2 - f^2)}{f^2}}\, ds \right)^2 \qquad (1)$$

where M is a constant that depends on the geometrical factors of the needle. The integrand in equation 1 shows the normalized electric field strength at each position and is plotted in figure 2. Data were corrected for drift and were cut to obtain L at points where the frequency shift was almost zero. This measurement does not account for particles' transit time factor. The resulting $R_s/Q = 42.2\ \Omega$ leads to $R_s = 42.3\ k\Omega$. MSS thanks F. Bosch, Yu. A. Litvinov, N. Winckler and D. Shubina for fruitful discussions and support of HIC-for-FAIR through HGS-HIRe.

References

[1] Y. D. Zang et al. Simulation and measurement of the resonant schottky pickup. *Chin, Phys. C*, 35(12), 2011.

[2] F. Nolden et al. A fast and sensitive resonant schottky pick-up for heavy ion storage rings. *NIM-A*, 2011.

[3] J. Müller. Untersuchungen über elektromagnetische hohlräume. *Hochfrequenztechnik*, 54:167, September 1939.

[4] L. C. Maier Jr and J. C. Slater. Field strength measurements in resonant cavities. *J. App. Phys.*, 23(1):68–77, 1952.

[5] Claudius Peschke. Messungen und berechnungen zu longitudinalen und transversalen shuntimpedanzen einer Elektronen-Positronen- Linearbeschleuniger-Struktur, 1995.

Status of the FAIR Proton Linac

L. Groening[1#], W. Barth[1], R. Brodhage[2], G. Clemente[1], N. Chauvin[3], S. Damjanovic[4], O. Delferrière[3], P. Forck[1], V. Ivanova, M.S. Kaiser[1], P. Kowina[1], B. Launé[5], C. Mühle[1], U. Ratzinger[2], G. Schreiber[1], C. Simon[3], W. Vinzenz[1], C. Will[1]

[1]GSI, Darmstadt, Germany; [2]IAP, University of Frankfurt a.M., Germany; [3]CEA/Saclay, Gif-sur-Yvette, France; [4]CERN, Geneva, Switzerland; [5]CNRS/Orsay, Orsay, France

Introduction

The FAIR proton linac [1] has to provide the primary proton beam for the production of antiprotons. It will deliver a 70 MeV beam to the SIS18 with a repetition rate of 4 Hz. The room temperature linac will be located north of the existing UNILAC complex. Its conceptual layout is shown in Fig. 1 and its main beam parameters are listed in Tab. 1.

Tab. 1: Main parameters of the proton linac for FAIR.

Final energy	70 MeV
Pulse current	70 mA
Protons per pulse	$7{\cdot}10^{12}$
Repetition rate	4 Hz
Trans. beam emittance	4.2 µm (tot. norm.)
Rf-frequency	325.224 MHz

In-Kind Contracts

A contract concerning the in-kind contributions from CEA/Saclay has been signed. It covers the delivery of the source & LEBT, external quadrupoles, the dipoles, and of the BPM mechanics. The design of the source & LEBT has started and the production of the LEBT solenoids will be completed in February. Another contract with CNRS is to be signed very soon on the delivery of the cavities, klystrons, and their converters. Finally, an agreement with GANIL on provision of magnet power converters is under preparation and should be fixed in 2012.

External Magnets

The production of the magnets is almost finished. Currently field maps of the quadrupoles and dipoles are recorded. Delivery of the magnets is expected before summer.

Civil Construction

Extensive radiation shielding simulations have been performed at GSI and CERN resulting in a re-design of the building. The compact design of the linac together with its reduced intrinsic shielding w.r.t. conventional DTLs required to include the source terminal into the linac tunnel. The plans for the building will be frozen in March. All rooms have been specified and cable lists have been provided.

Cavities

The prototype cavity (Fig. 2) [2] has been delivered to the Frankfurt University in December. Currently, it is rf-tuned. Cu-plating is planned for summer followed by high power-rf testing at the dedicated cavity test stand currently under construction on-site.

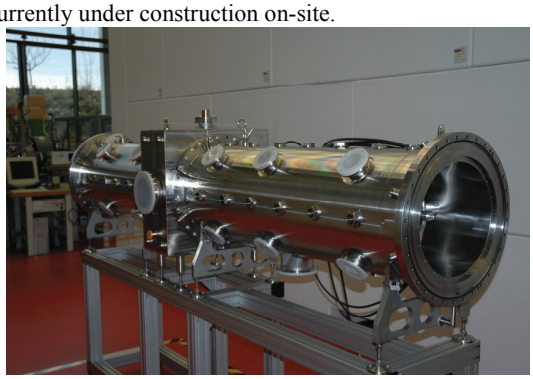

Figure 2: Prototype CCH-cavity (2.7 m) of the FAIR proton linac.

The klystron for the test stand is already on-site, the power converter will be delivered in a few months. Some equipment for test stand has been delivered through CNRS, i.e., wave guide elements, racks, analyzers, and scopes. The missing material as load, circulator, and infrastructure will be delivered this year such that the test stand should be operational in December.

BPM / Phase Probes

The suppression of signals from primary rf that sneeks to the BPMs has progressed significantly. Rf- and beam dynamics simulations indicated that beam aperture reduction close to the BPMs can provide the required suppression. However, the impact of this reduction to the loss scenario will be tested.

References

[1] *Technical Report "Proton Linac"*, https://edms.cern.ch/document/994418/1

[2] G. Clemente et al., PRST-AB **14**, 110101, (2011

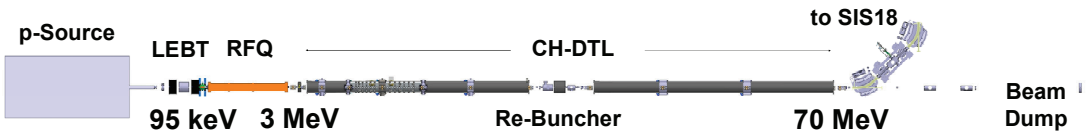

Figure 1: Conceptual layout of the FAIR proton linac.

#la.groening@gsi.de

Status of the CH-Prototype for the FAIR Proton Linac

R. Brodhage[1], T. Kanesue[1], G. Clemente[2], U. Ratzinger[1], L. Groening[2], and H. Podlech[1]
[1]IAP, University of Frankfurt, Germany; [2]GSI, Darmstadt, Germany

For the 70MeV, 35mA proton injector for FAIR a beam dynamics design based on a CH-DTL was developed successfully during the last years. This report will focus on the prototype construction of the second coupled cavity for the proton injector for FAIR. It will outline the main fabrication and assembling steps towards that novel type of proton DTL.

Introduction

The linac is mechanically grouped in two tanks, having lengths of about 9m and 10m respectively. In between there will be a 3m long diagnostics section affording two lenses and one rebuncher to get a safe beam transport.

The coupled prototype cavity

The low energy section consists of 13 gaps, followed by the coupling cell and by the 14 gap high energy section. The whole cavity has an inner length of about 2.8m.

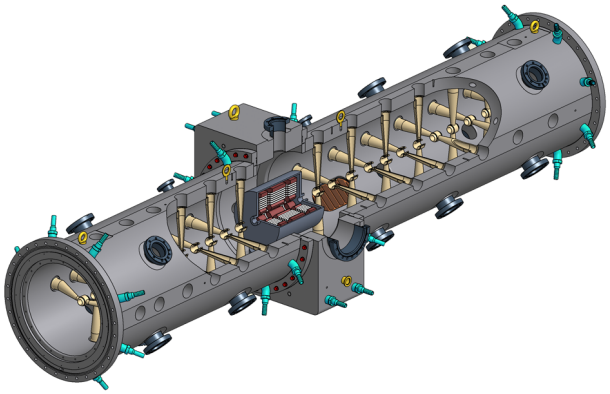

Figure 1: 3D-View of the coupled prototype cavity

Assembling Techniques

During the design period of the prototype cavity, several investigations on the welding process have been performed, to proof not only the reliability but also to mark the frontiers of conventional inert gas welding.
A special stem and tank geometry was developed, that makes it possible to insert full length stems longitudinally into the tanks and put it into an upright posture at the final position. This assembling method makes it possible to weld the stems directly to the inner tank surface in a way, that is acceptable for the following galvanic copper plating.

History of Cavity Construction

The Construction process of the prototype cavity started in the beginning of 2009. At this time only minor production steps, like drilling longitudinal cooling channels into the outer tanks, have been made.
In 2010 many optimisations and improvements have been made. Also, due to technical standardisation, that has to be complied by the manufacturing process, a short delay came up, which stalled the start of the manufacturing till the beginning of 2011.
Within 2011 all the major parts of the cavity have been manufactured and delivered to IAP.

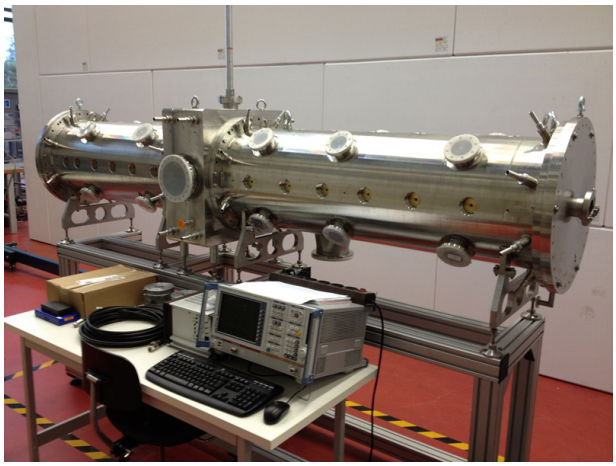

Figure 2: 3D-View of the coupled prototype cavity

Status an Outlook

At present, all major parts of the prototype have been assembled at IAP and are ready for measurements. Figure 2 shows the Cavity at the bead perturbation test stand at IAP. Some preliminary frequency measurements have been done in the end of 2011. These measurements have shown very promising results. The accelerating mode was within a 5‰ range of the simulated frequency and it was well separated from the neighbouring higher order mode.
During 2012 the RF tuning will be completed and the structure will be mechanically finished. Also the galvanic copper plating will take place in 2012, so that the high power test at GSI with the 2.5MW Klystron can be performed.

References

[1] R. Brodhage et al. ”First Coupled CH Power Cavity for the FAIR Proton Injector”, Proceedings of IPAC 2011, San Sebastian, Spain

Unintentional Coupling of the Accelerating Field to the BPM Pickups

W. Ackermann[*1], *W. F. O. Müller*[1], *and T. Weiland*[1]

[1]Technische Universität Darmstadt, Institut für Theorie Elektromagnetischer Felder (TEMF), Schlossgartenstraße 8, 64289 Darmstadt, Germany

Introduction

The acceleration of charged particles is mainly performed with the help of radio frequency (RF) electromagnetic fields. The carefully designed resonators are tightly fit together to keep the total accelerator length as short as possible. The limited space between the individual resonators is used to install additional quadrupole magnets which are essential to properly control the beam optics. The position of each quadrupole magnet has to be adjusted to the current position of the beam to enable the desired optical properties.

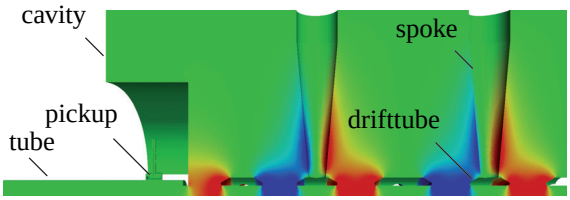

Figure 1: Longitudinal component of the accelerating RF field within the resonator near to the BPM pickup system.

Near to the magnets the transverse position of the beam is determined with the help of four pickup antennas which couple to the electromagnetic fields excited by the moving charged particles. Unfortunately, the accelerating cavities are quite near to the pickup system and the imposed large field components can unintentionally couple to the beam position monitor (BPM) if the separation is not clearly pronounced. In the current work the coupling of the RF accelerating field to the BPM pickup antennas is investigated for the proposed design parameters by means of numerical analysis.

Numerical Model

A very precise but computationally expensive numerical model is based on the solution of the full MAXWELL's equations where perfect electric boundary conditions are applied on the one hand to model the metallic surfaces of the resonator while proper port boundary conditions are used on the other hand to enable the extraction of the electromagnetic fields within the BPM structure.

The spatial discretization is based on curved tetrahedral finite elements (FEM) which finally results in a quadratic eigenvalue formulation due to the external coupling mechanism. To resolve the fine geometrical details of the pickup

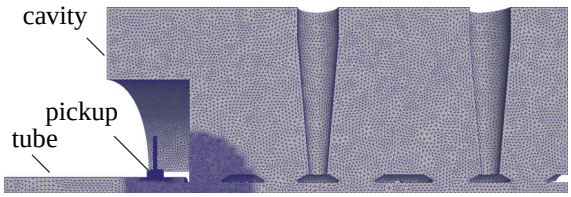

Figure 2: Discretization of the computational domain with 3.205.628 second order curvilinear tetrahedral elements using local grid refinement to resolve the fine BPM structure.

antennas and the coaxial line a proper grid resolution in the BPM region is mandatory. The meshing is performed with CST STUDIO SUITE™ [1] while the solution of the large-scale eigenvalue problem is obtained with a parallel implementation of the Jacobi-Davidson algorithm [2].

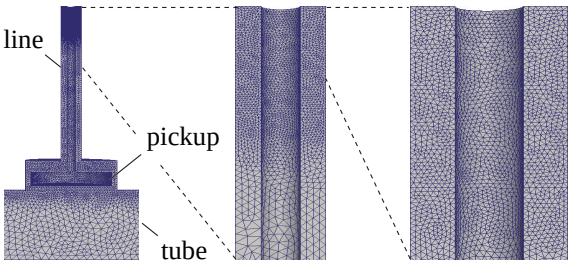

Figure 3: Special focus has to be put on a proper grid resolution to precisely model the extraction of the EM fields.

Conclusion

Following the proposed layout the unintended coupling of the high accelerating field to the BPM pickup antennas results in a peak voltage of 1.03 V which can be extracted at the coaxial line of the pickup system when the electric field strength is scaled to $E_{z,\mathrm{peak}} = 21.2$ MV/m in the first acceleration gap. Because the maximum signal intensity due to the particle beam is expected in the same voltage range a modification of the current pickup system is mandatory.

References

[1] CST Studio Suite, CST Computer Simulation Technology, Bad Nauheimer Straße 19, 64289 Darmstadt, Germany

[2] W. Ackermann, G. Benderskaya, T. Weiland, "State of the Art in the Simulation of Electromagnetic Fields based on Large Scale Finite Element Eigenanalysis", International COMPUMAG Society Newsletter, Vol. 17(2), 2010, pp. 3-12.

* ackermann@temf.tu-darmstadt.de

FAIR SIS100 and HEBT Design and Status Report

P. Spiller, F. Hagenbuck, L. Bozyk, O. Boine-Frankenheim, U. Blell, G. Franchetti, E. Fischer, E. Floch, M. Kauschke, A. Krämer, H.G. Koenig, H. Klingbeil, M. Kirk, U. Laier, A. Mierau, J. P. Meier, C. Mühle, H. Müller, D. Ondreka, P. Puppel, N. Pyka, H. Ramakers, S. Ratschow, H. Reich-Sprenger, S. Sorge, P. Schnizer, Á. Saá-Hernández, J. Stadlmann, S. Wilfert

GSI, Darmstadt, Germany

SIS100

With starting the procurement of major technical components, the SIS100 project has approached the realization phase. The main aim of the last year was to complete all systematic design studies and to fix the operation parameters for all devices. To a large extend, the device parameters are well defined and the establishment of the corresponding detailed specifications can be or are completed. In the frame of setting up an integrated project schedule, the long lead items were identified. For these items the explicit goal of initiating the tendering processes within 2012 is being followed with highest priority.

Pre-Series Dipole Magnet and Dipole Series

As an outstanding milestone for the FAIR project, and as the first major procurement process, the SIS100 dipole series has been tendered. The contract will comprise the production of a pre-series dipole magnet with the modified single layer high current coil and the production of the whole series. Additionally, a number spare moduls and spare parts have been requested. In the frame of preparing the dipole procurement, a procurement strategy and a project plan has been developed. According to the procurement strategy, GSI will subcontract the thin wall dipole chamber and the superconducting (s.c.) wire for the dipole series in separate tendering processes. Both will be supplied by GSI to the main contractor for the dipole series. Among the two technical solutions for the active cooling of the dipole chambers, a decision has been taken in favour of the cooling by means of four cooling pipes which are mounted electrically insulated on the chamber surface. The gap between the cooling pipes and the chamber surface will be closed by a ceramic filler. The positions of the cooling pipes have been again optimized with respect to their contribution to the field distortion at fast ramping. The pre-series magnet chamber will be cold tested in a test cryostat at GSI before the series production will be set free.

Sextupole Arrangement and Slow Extraction

As a result of a new beam dynamics campaign using the simulation approach developed for SIS300, a change in the position of the s.c. chromaticity sextupole magnets in the lattice cells has been suggested. The new sextupole arrangement and setting provides a larger dynamic aperture during slow extraction with Hardt condition and removes undesired phase space islands near the separatrix. As a further result, the number of warm resonance sextupole magnets could be reduced from 11 to 5 magnets. Saving the resonance sextupoles in all of the first warm sections in the straight has also provided the mssing space for the positioning of other major components. Simulations aiming for an optimized setting for slow extraction are being continued, including all nonlinear magnet imperfections.

Cryomodules

The design of the special, large cryomoduls for injection and extraction, containing four quadrupole magnets, has been further detailed. One major goal was to find a solution which enables the implementation of all BPMs at the ends of the arc cryostats. The injection beam line had to be further displaced in the injection module to resolve a collision with the BPM at the end of the cryostat. The special s.c. quadrupoles of the injection and extraction beam lines, which are part of the cryomodules had to be shortened and moved closer to each other. Thereby, a flat front face of each cryomodule could be generated which has resolves the so far existing collision with neighbouring dipole modules. Furthermore, the displacements of the injection and extraction beam lines are now sufficient to bypass the large cryostat connection bellows.

Major results have been achieved in the frame of the set-up and testing of a prototype cryo catcher system. The cryo catcher system is needed to stabilize the dynamic pressure in SIS100. By means of beam tests with various heavy ions at the SIS18 synchrotron, the necessary low effective desorption yield could be demonstrated [2].

Injection and Extraction Systems

The set-up of the prototype pulse power generator for the bipolar extraction kicker system has been continued [1]. The main aim of the set-up is to investigate the cross talk betweeen the two main thyratrons in the power stage needed to change the direction of the discharge current. The first tests have shown that an undesired switching of the second Thyratron can not be prevented at switching of the first. Thus, an alternative circuit layout which anticipates the cross between the Thyratrons talk had to be developed. All major components for a full size test of this circuit are now under procurement, aiming for a completetion of the tests and a final decision on the pulse power circuit in 2012. In parallel, simulations are performed on the effect of the impedance of the magnetic kickers on the beam dynamics.

The bipolar extraction kicker system will enable beam dumping on an internal beam dump in the synchrotron

tunnel. The performance of the very short internal machine beam dump could be improved with respect to the total absorbed beam energy. The new design uses a conical geometry and multi layer structure of verious materials and provides higher stability at high energy density.

Rf Systems

The SIS18 acceleration cavity provides all features needed for an application in SIS100. Therefore, it has been decided to use the existing, well proven cavity design, slightly modified, for the tendering process of the SIS100 series. The SIS18 cavity design has been taken over as a 3D CATIA model. Slight mechanical modifications are presently implemented to optimize the cavity in various details. It is planned to complete the design activities early in 2012 and to proceed as fast as possible with the tendering process.

Beam Instrumentation

As an important milestone, a full size prototype of the cold SIS100 BPM has been manufactured. The full size prototype covers all major technical solutions, e.g. the ceramically insulated pick-up system, which will be applied in the series. Cold tests are foreseen in for the beginning of 2012.

Furthermore, all beam instrumentation devices and dedicated diagnostics chambers have been placed at adequate positions in the warm straight sections.

Local Cryogenics System

The local cryogenics system has been presented as a Polish inkind proposal in the inkind review board. The Polish inkind proposal covers most of the technical subsystems and components which were summarized as 'local cryogenics system' in the cost book. Following the inkind proposal, the predesign of the bypass lines developed at GSI has been undisclosed to our partners for further detailing towards production of a prototype for the planned string test.

HEBT System

Ion Optical Layout

The last official transfer of the ion optical layout (IOL) to the building planners took place in March 2011. This lattice already included the p-Linac with its link to the transfer channel (TK) in GSI-NN coordinates and new layouts for section TSN1 (part of the beam line from SIS18 to NESR) as well as THS1 (from RESR to HESR), where the vertical transfer sections were repositioned such that the average height of the beam line tunnels could be reduced. Since then, several minor corrections of the beam lines had to be performed. An update of the HESR lattice, so far not represented in the IOL, was included. As the design of the Y-Cryostats proceeded, several adjustments were carried out in the positioning of the injection and extraction beam lines to and from SIS100. The focusing systems for the atomic physics and the CBM/HADES experiments had to be repositioned and updated following requests for more space around the respective targets by the experimentalists. No one of the modifications had an impact on the current building layout.

Test of FODO Optics

In order to confirm that the beam transport in a F0D0 structure, which is foreseen for the FAIR beam lines, is as predictable as a doublet structure, a machine experiment was performed. The beam line from SIS18 to HTP was operated in F0D0 mode, using only one quadrupole in every doublet or triplet. The measured beam envelopes behaved as expected and the envelopes calculated with MIRKO could be realized.

Systems Design

In order to fix the tolerable magnet errors, the influence of higher order multipole components in the beam line magnets was exemplarily investigated for the beam line from SIS100 to the APPA-Target. This beam line includes 44 quadrupoles and 29 dipoles. It turned out that an integrated field error of $\Delta BL/BL=\pm 4\cdot 10^{-3}$ for dipoles and $\Delta GL/GL=\pm 5\cdot 10^{-3}$ for quadrupoles has no major impact on the beam transverse distribution on the target.

The device parameters of almost all dipole types needed in module 0-3 are meanwhile well defined. For a major fraction (65/76), the detailed specifications will be available at the beginning of 2012. The specification contains the delivery of the corresponding supports and vacuum chambers by one main contractor.

The 3D (CATIA) modelling of the HEBT system was further improved and updated in close collaboration between the central department for engineering and an external engineering company. Drawings with all relevant geometrical information have been used in the detailed specifications of the magnets, vacuum chambers and supports.

For the first beam line sections, support structures for steerers and diagnostic chambers were added and the modelling of the beam tube vacuum system finished.

Major effort was taken for the completion of the DMU and to provide more detailed input for the building planning. E.g. a dedicated room for the current lead box had to be allocated causing a major rearrangement of the HEBT supply areas in the northern main supply building. A 3D model of the superconducting link, connecting the current lead box with the HEBT300 bypass line in the transfer building was developed and provided to FAIR S&B.

Cable lists, including cable types, numbers and start and end points have been established. Detailed requests for the supply room conditions were specified and information for component properties were handed over to the building planners.

References

[1] K. Samuelsson, this report
[2] L. Bozyk, this report

SIS100 Dynamic Vacuum Simulations*

P. Puppel[1,2], *P. Spiller*[1], *and U. Ratzinger*[2]
[1]GSI, Darmstadt, Germany; [2]Goethe-Universität, Frankfurt a.M., Germany

Introduction

Intermediate charge state heavy ions like U^{28+}, which is the reference ion of the FAIR project [1], are subject to a high probability of charge exchange reactions due to collisions with residual gas particles. The charge changed ions are deflected differently with respect to the reference ion in magnetic fields and hit the vacuum chamber after dispersive elements, where an energy-dependent strong gas desorption takes place. This gas desorption increases the pressure and therefore the rate of charge exchange reactions. This is called dynamic vacuum [2].

SIS100 has been optimized for the operation with U^{28+}. The cryogenic vacuum chambers will provide a high pumping power for residual gases, which ensures a low static pressure and the fast removal of desorbed gas particles from the beam vacuum. Furthermore, a low desorption ion catcher system will be installed in the cryogenic arcs of SIS100, which catches the lost charge changed ions in a controlled way. The prototype of the so called cryocatcher was designed and tested successfully at GSI [3].

The StrahlSim code was developed and used to simulate the charge exchange beam loss and the dynamic vacuum over a synchrotron cycle by applying space and time resolved pressure profiles [4].

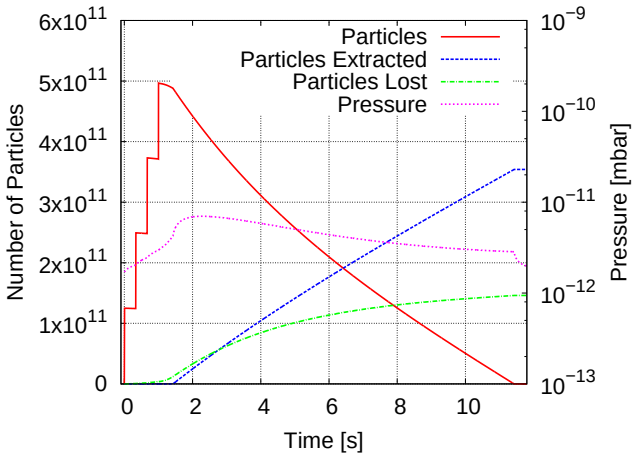

Figure 1: Number of particles and the pressure evolution over a SIS100 cycle with slow extraction.

Dynamic Vacuum in SIS100

Dynamic vacuum simulations performed with the StrahlSim code for SIS100 show, that a pumping speed for the desorbed hydrogen particles at the loss positions of the charge changed ions is necessary and sufficient to stabilize the dynamic pressure rise [5]. The cryocatcher module will be actively cooled with liquid helium and will provide the corresponding pumping power. Thereby, the catcher itself is connected to the thermal shield of the cryostat and is, therefore, thermally decoupled from the chamber to avoid the transfer of beam power into the cryogenic system [3].

SIS100 will provide fast and slow extracted beams. The extraction takes place in the second warm straight in sector 5. For slow extraction the beam ions are driven into the electrostatic septum by means of a third order sextupole resonance. Approximately 10 % of the beam ions hit the septum wires and will be fully stripped to U^{92+}. The next quadrupole doublet deflects the U^{92+} ions directly onto the chamber wall, where a pressure rise is generated [1]. The increased pressure at this position causes a higher rate of charge exchange reactions. These charge changed ions mainly hit the second ion catcher in the following cold arc in sector 5. Therefore, during slow extraction the ion currents on the catchers in sector 5 are higher than the currents in the other sectors of SIS100.

Table 1: Predicted average beam energy deposition on the ion catchers within each sector of SIS100 for a cycle with fast (FX) and slow extraction (SX). The differing numbers for sector 5 during slow extraction are given in brackets.

Ion Catcher	Load (FX) [W]	Load (SX) [W]
1	0.5	1.5 (3.1)
2	1.4	3.8 (16.7)
3	1.1	1.9 (3.7)
4	0.6	1.2 (1.4)
5 – 10	0.6	1.2

The simulated number of particles for a cycle with slow extraction over 10 s and the mean pressure are shown in figure 1. The simulated average beam power on the individual ion catchers during slow and fast extraction are listed in table 1. The total average load onto the ion catcher system is about 110 W for the operation with slow extraction and about 43 W for fast extraction.

References

[1] FAIR Technical Design Report SIS100, 2008
[2] C. Omet et al., New Jounal of Physics 8, 2006
[3] L. Bozyk et al., Proceedings of IPAC 2011
[4] P. Puppel et al., Proceedings of IPAC 2010
[5] P. Puppel et al., Proceedings of IPAC 2011

* This work is supported by HIC for FAIR.

Measurements with the SIS100 Cryocatcher Prototype *

L. Bozyk[1,2], *D.H.H. Hoffmann*[1,2], *H. Kollmus*[1], *P. Spiller*[1], *and M. Wengenroth*[1]
[1]GSI, Darmstadt, Germany; [2]TU Darmstadt, Germany

Introduction

SIS100, the main accelerator of the FAIR-facility will provide high intensity intermediate charge state heavy ion beams. In order to assure a reliable operation, a special cryogenic ion catcher system is under development. In total, 60 cryocatcher will be installed to minimize the pressure rise in the cold arcs. These ion catchers provide special low desorption yield surfaces. Thereby, the amount of ionization loss due to charge exchange in collisions with residual gas molecules is stabilized during operation.

The design of the cryocatcher [1] and its construction [2] have been presented in former scientific reports. Now the results from measurements with heavy ion beams from SIS18 will be presented.

Cryocatcher prototype test setup

The cryocatcher is a 30 cm gold coated copper block, which assure a low desorption yield. It is mounted inside a copper coated vacuum chamber. The copper coating is explosively plated before the chamber is manufactured. It ensures a homogeneous low temperature distribution around the surfaces. The chamber is connected via flexible copper bands to a liquid helium supply line, to provide cold pumping surfaces. The support structure of the cryocatcher allows to keep it at a higher temperature than the chamber. This avoids adsorption of gases on the cryocatcher's surfaces, reducing the amount of desorbed gases under ion bombardement. The vacuum chamber is located inside a cryostat vacuum chamber, containing a liquid nitrogen cooled thermal shield. The test setup was mounted at the beam line of HHT behind the SIS18. The connection of the cold test-chamber to the warm vacuum- and beam-diagnostics in front of the cryostat is realized by a cold-warm-transition. The warm section consists of several pumps, total and partial pressure gauges, a differential pumping stage, beam screens and a beam transformer.

The pressure inside the cold chamber is measured with a cold cathode gauge. A fast and beam triggered pressure measurement has been realized for a thermally shielded hot extractor gauge, located close to the cryocatcher. Several temperature sensores were mounted onto the components, to control the cooling and to verify temperature models.

Measurements at the cryocatcher prototype

The cryocatcher prototype has been tested with Gold, Tantalum and Bismuth-beams from the SIS18 in several beamtimes. The heavy ion induced pressure rise inside the chamber has been investigated as a function of beam energy and target temperature.

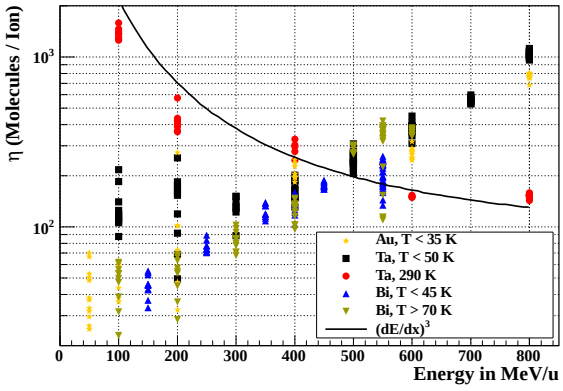

Figure 1: Energy dependent desorption yields measured at the cryocatcher. Red points represent measurements at room temperature, the black line shows the expected behaviour. All other points were measured at cryogenic temperatures.

The chamber has been cooled with liquid helium down to 12 K. Residual gas pressures in the low 10^{-12} mbar-regime were reached. The transition temperature of 18 K, underneath where a serious pumping speed for hydrogen emerges, could be verified several times.

Results

For each beam impact a maximum and a relaxation pressure were determined out of the total pressure evolution. A desorption yield was calculated using the total pressure rise, the number of hitting ions, the chamber volume, and the gas temperature. The obtained energy dependent desorption yields are shown in figure 1. For cryogenic temperatures, the desorption yield rises with the beam energy. Since this behaviour is contrary to the dependence known from room temperature, a room temperature measurement has been conducted in order to verify the measurement setup. Out of these measurements the known scaling with the electronic energy loss could be reproduced.

Simulations with StrahlSim using the measured energy scaling of the desorption yields predict a stable operation of the SIS100.

References

[1] L. Bozyk et al., GSI scientific report 2009
[2] L. Bozyk et al., GSI scientific report 2010

* Work supported by EU (FP7 project COLMAT) and FIAS

Prototype Development of SIS100 Beam Position Monitors

P. Kowina, C. Dorn, K. Gütlich, J. Macavei, and M. Schwickert
GSI, Darmstadt, Germany

Towards the SIS100 BPM Prototype

Beam Position Monitors (BPMs) of the superconducting SIS100 synchrotron are an integral part of the quadrupole doublet module. These modules consist of two quadrupoles, a BPM, a collimator, an orbit corrector (steerer) and multipole corrector magnets and all constituents will be encapsulated in a common cryostat [1]. Recent developments concerning BPM design were focused on i) optimization of the mechanical design and integration inside the quadrupole module and ii) validation of the signal path within the cryostat. As discussed in [2] the BPM design based on a metal coated ceramic cylinder was chosen since it maintains the tight requirements of mechanical stability and reproducibility even during cold/warm cycles, i.e. temperature changes between room temperature and liquid helium temperature. The BPM geometry was optimized in extensive FEM simulations as described in [2, 3]. The SIS100 BPM prototype, shown in Fig. 1, consists of a metalized Al_2O_3-ceramic pipe with an inner diameter of 135 mm (Fig. 1, right) that slides on CuBe contact ribbons on the inner surface of the BPM chassis (Fig. 1, left). The ceramic pipe is fixed only on one side to the adjacent quadrupole joke via the rigid plate shown in the middle part of Fig. 1. As vacuum signal feed-throughs N-type 50 Ω-feeds welded to CF-16 flanges are considered. For further details concerning the design and feasibility of the ceramic pipe manufacturing process refer to [4]. Cryogenic tests of the integral SIS100 BPM prototype, including the ceramic pipe, connectors, metal housing and cabling, covering also validation of the signal feed-throughs, will be performed in spring 2012.

Cryogenic Tests of Matching Transformers

A second branch of the development of the SIS 100 BPMs was focused on the signal path between BPM electrodes and low noise amplifiers installed outside the cryostat. As discussed in [5] Matching Transformers (MT) meet well the requirements of reflection-free signal transfer through the relatively long cables (2.1 m) that connect BPM electrodes with the amplifiers installed outside the cryostat. Transformers based on toroidal cores made from nanocrystalline Vitroperm-500F were tested. The structure of the windings and circuit geometry were optimized to improve linearity and allow for resonance-free transmission over the required frequency range from 0.1 to 40 MHz [6]. Due to the mechanical stress and strain during thermal cycling the transformer windings have to be mechanically stabilized using e.g. epoxy resin. The linear thermal expansion of the epoxy has to be matched to the expansion of the MT toroid material. Five different epoxy types (Fig. 2) were tested in a bath cryostat at liquid nitrogen temperature. For each epoxy type four samples were prepared and tested in 30 thermal cycles. Whereas the epoxy resins Stycast 2850 FT, Araldite CW 299-3 and Stycast 1266 A/B (Fig. 2, from right bottom to left top) were affected by many cracks in the structure, Stycast 2850 KT and Stycast 2850 GT, on the contrary, showed to be suitable for MT operation in cryogenic temperatures. In addition, the suitability of the epoxy resin for the insulation vacuum of the cryostat was proven by measurements of their outgasing rates. The results of these investigations are summarized in [6].

Figure 1: Prototype of the SIS100 BPM.

Figure 2: Matching transformers non-encapsulated (left top) and encapsulated in epoxy (others). For description see text.

References

[1] Fair Technical Design Report SIS100, p.228 (2008).
[2] P. Kowina et al., *Proc. EPAC'06*, Edinburgh, p.1022 (2006).
[3] P. Kowina et al., *Proc. DIPAC'07*, Venice, p.96 (2007).
[4] P. Kowina et al. *GSI Ann. Rep. 2009*, p.100 (2010).
[5] W. Kaufmann, et al. *Proc. DIPAC'03*, Mainz, p.208 (2003).
[6] P. Kowina et al., *Proc. DIPAC'11*, Hamburg, p.347 (2011).

A ferrite insert for passive space charge compensation

M. Mehler[1], O. Boine-Frankenheim[1,2], O. Kester[1,3]

[1]GSI, Darmstadt, Germany, [2]TU Darmstadt, Germany, [3]Goethe Universität Frankfurt, Germany

Introduction

Longitudinal space charge (sc) effects, like the reduction in the rf voltage and the loss of Landau damping [1] require countermeasures in the synchrotrons SIS-18 and SIS-100. For passively compensating the sc impedance in SIS-100, as it has been done at the PSR in Los Alamos [2] and in the proton synchrotron at KEK [3] only Finemet FT3-M [4] can be used because of its high permeability. From measured material values an insert for SIS-100 at the 10th harmonic (partially compensating the sc impedance at the 20th harmonic) has been designed as described below.

The design of the insert

The scattering parameter S_{11} has been measured at a ring core sample of Finemet FT3-M. Through this measurement the complex permeability for isotropic media [6] $\mu(\omega) = \mu'(\omega) - j\mu''(\omega)$ was determined to design the insert for SIS-100 with a sc impedance of

$$\frac{X_{SC}}{n} = -j\frac{g_0 Z_0}{2\beta\gamma^2} = -j580\Omega \qquad (1)$$

where n is the harmonic number,

$$g_0 = \frac{pq}{p^2+q^2} + 2\ln\left(\frac{p+q}{a+b}\right) \qquad (2)$$

the geometry factor [5], Z_0 the vacuum impedance, β and γ the relativistic velocity and the Lorentz factor respectively, p and q the half axis of the elliptical beam pipe and a as well as b the half axis of the elliptical beam. The sc impedance is negative and can therefore be seen as a capacitance that can be compensated by an inductive impedance. Using the series equivalent circuit of an inductivity where the capacitive impedance X_C is much lower than the inductive impedance X_L the longitudinal impedance seen by the beam

$$Z_{\parallel} = \mu''\omega L_0 + j\mu'\omega L_0 = R + jX_L \qquad (3)$$

can be used to get the dimensions of the insert for the 10th harmonic from

$$L_0 = \frac{\mu_0 l}{2\pi}\ln\left(\frac{D_A}{D_i}\right) \qquad (4)$$

The left part of the sum of $Z_{\parallel}$ in equation 3 is the real impedance R set by the imaginary part of the complex permeability μ'' and the right part the imaginary impedance X_L which has to be equal to X_{SC} is set by the real part of the complex permeability μ'. The vacuum inductivity L_0 in equation 4 contains the geometry of the insert (D_A: outer diameter, D_i: inner diameter, l: length and μ_0: vacuum permeability) and ω is the frequency. With a given l = 2 m and D_i = 130 mm of the insert determined by the horizontal inner beam pipe diameter p, D_A = 390 mm. The result for the designed sc compensating insert at n = 10 for SIS-100 is shown in Figure 1. The frequency range of interest is below 6 MHz.

Designing an insert for the 20th harmonic increases the outer diameter and doubles the impedances compared to the ones shown in Figure 1 and overcompensates the 10th harmonic.

Tests of the insert design modelled by the measured data through using equation 3 with a model from Tsutsui [7] confirms the results of Figure 1 below f = 1 MHz.

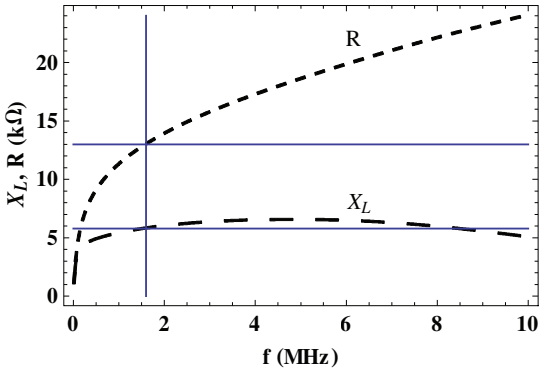

Figure 1: Imaginary and real part impedance of the designed Finemet insert. X_L = 5.8 kΩ and R = 13.0 kΩ for the 10th harmonic (f_{rf} = 1.57 MHz) indicated by the blue solid lines.

Conclusion

With the magnetic alloy Finemet FT3-M an insert can be designed for passively compensating the sc impedance of SIS-18 and SIS-100. The effects of the high resistive impedance of such an insert on the beam have to be investigated. Further it has to be shown under which conditions equation 3 is conform to the longitudinal impedance formula of the Tsutsui model.

References

[1] O. Boine-Frankenheim, et al., PRST-AB 8, 034201 (2005)
[2] M. Plum et al., PRST-AB 2, 64201, (1999)
[3] K. Koba et al., Rev. Sci. Instrum. 70, No. 7, (1999)
[4] Hitachi Metals, http://www.hilltech.com/pdf/hl-fm10-cFinemetIntro.pdf, Apr.05
[5] S. Koscielniak, Proc. PAC2001, pp.2970, (2001)
[6] C. Beltran, PhD Thesis, Indiana University (2002)
[7] H. Tsutsui, CERN-SL-2000-004 AP, (2000]

Calculation of coupling impedance and ferrite heating for the SIS-100 kicker system*

L. Hänichen[1], *O. Boine-Frankenheim*[2], *W.F.O. Müller*[1], *and T. Weiland*[1]

[1]Technische Universität Darmstadt, Institut für Theorie Elektromagnetischer Felder (TEMF), Schlossgartenstrasse 8, 64289 Darmstadt, Germany; [2]GSI, Darmstadt, Germany

Introduction

Coupling impedances are the source of coherent instabilities and corresponding beam intensity limits for the operation of high current accelerators such as the SIS-100 synchrotron for the GSI FAIR project. The coupling impedances are defined as follows:

$$Z_{||}(\omega) = \frac{1}{q^2}\int d^3x E \cdot J_{beam}, \qquad (1)$$

$$Z_{x,y}(\omega) = \frac{i}{q^2\Delta}\int d^3x \rho_{x,y}\cdot(E_{x,y} \mp vB_{y,x}), \qquad (2)$$

where E is the electric field and $E_{x,y}$ and $B_{y,x}$ are the transverse electric and magnetic fields excited by the beam. Coupling impedances can be determined through bench measurement [1], analytically [2] or numerically by solving a discretized form of Maxwell's equations [3]. This work is focused on finding suitable methods for the numerical calculation of coupling impedances for the relevant beamline components.

Impedance contribution of ferrite-based kicker magnets

The field of the beam is dominated by a monopole and a dipole pattern whereby the dipolar field depends linearly on the displacement from the symmetry axis to first order approximation. The kicker consists of a coil surrounded by a block of ferrite which represents a significant modification of the beam environment and contributes to the coupling impedance in multiple ways: the beam-driven magnetization of the ferrite material produces heat which is related to $\Re\{Z_{||}\}$.

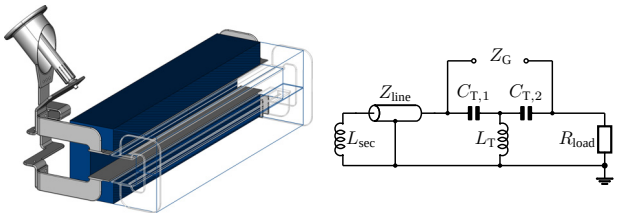

(a) Single kicker unit (b) Effective circuit in standby

Figure 1: The figure shows a single SIS-100 ferrite kicker of which up to five may be located in one tank and the effective circuit consisting of pulse transformer, matching T network and a load resistor.

* Work supported by GSI and BMBF under contract 06DA9050

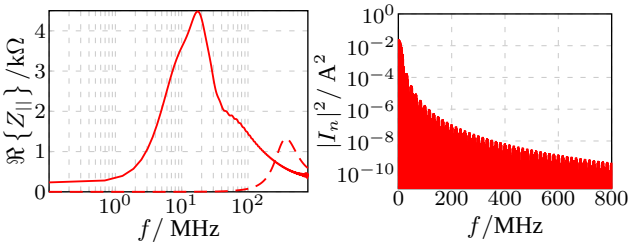

Figure 2: The left figure shows the real part of the longitudinal coupling impedance for a ferrite yoke without (solid line) and with gap (dotted line) which is used to reduce the beam-driven heat load by breaking the magnetic circuit. The right figure shows an example of the spectral beam current density for a series of 8 parabolic bunches which is used to calculate the absorbed power: $P = 2\sum_{n=1}^{\infty}|I_n|^2\Re\{Z_{||}\}$

The coil remains partly connected to a pulse forming network also during standby operation. Thus, the coil is loaded with the effective impedance Z_G which couples to the dipolar field and therefore contributes to the transverse coupling impedance.

Summary and Outlook

The coupling impedances have been calculated for different geometries using time and frequency domain simulation methods and comparing them with analytical formulations. It can be shown that the beam-induced heat is reduced from 500kW to less than 1W for the modified kicker with a gap. In the last steps the connection between the external network and the transverse impedance will be further investigated.

References

[1] F. Caspers, "Bench methods for beam-coupling impedance measurement.", Lecture Notes in Physics, 1992, Geneva.

[2] A. M. Al-Khateeb, O. Boine-Frankenheim and R.W. Hasse "Comparison of the longitudinal impedance from different source terms.", Nucl. Instruments and Meth. in Physics Res. A, 2008.

[3] B. Doliwa, H. DeGersem and T. Weiland, "Numerical calculation of coupling impedances for kicker modules.", FAIR report, 2006, Darmstadt.

[4] L. Hänichen, O. Boine-Frankenheim, W.F.O. Müller and T. Weiland "Coupling impedance contribution of ferrite devices: theory and simulation.", Proceedings of the IPAC, 2010.

Impedance calculations for the SIS100 beam pipe

U. Niedermayer [*1,2] *and O. Boine-Frankenheim*[1,2]
[1]GSI, Darmstadt, Germany; [2]TEMF, TU-Darmstadt, Germany

Introduction

Complex valued Coupling Impedances (CI) lead to coherent beam instabilities. In particular, the real (resistive) part of the dipolar transverse CI can act as the driving term for transverse beam instabilities. For the SIS18 as well as for the projected SIS100 the resistive part of the transverse CI is dominated by the beam pipe at low frequencies. The lowest coherent betatron sideband that is susceptible to impedance driven instabilities is centered at $(1-Q_f)f_0$, Q_f being the fractional part of the betatron tune and f_0 being the revolution frequency [3]. This sideband is in the range of ≈ 150 kHz for SIS18 and ≈ 90 kHz for SIS100 [3]. In this frequency range simulations in the time domain cannot be applied since an acceptable resolution would require a very long excitation bunch length and simulation duration. Therefore an approach in the frequency domain is pursued. The beam is modeled as a disc of surface charge density σ traveling with the velocity v. The beam's displacement d_x off axis (i.e. a coherent dipole oscillation) can be approximated to first order by

$$\sigma(\varrho,\varphi) \approx \frac{q}{\pi a^2}(\Theta(a-\varrho)+\delta(a-\varrho)d_x\cos\varphi). \qquad (1)$$

The transverse CI represents the force acting back on the beam from the environment and is defined as

$$\underline{Z}_{\perp,x}(\omega) = -\frac{v}{(qd_x)^2\omega}\int_{beam}\underline{\vec{E}}\cdot\underline{\vec{J}}^*_{\perp}\,\mathrm{d}V, \qquad (2)$$

where the dipolar current density is obtained from the Fourier transform of the dipolar part of $\vec{J}=\sigma\delta(z-vt)\vec{v}$, i.e. $\underline{\vec{J}}_{\perp}=\sigma_{\perp}\exp(-i\omega z/v)\vec{e}_z$. In order to determine the CI, the counteracting electric field $\underline{\vec{E}}$ in Eq. 2 has to be determined. This is usually done via the Helmholtz equation [2]

$$\left(\triangle_{\perp}-i\omega\mu\kappa-\frac{\omega^2}{\beta^2\gamma^2c^2}\right)\underline{E}_z=-\frac{i\omega\mu\sigma}{\beta^2\gamma^2}e^{-i\omega z/v}. \qquad (3)$$

Numerical model and results

For the numerical calculation of the CI of the SIS100 beam pipe shown in Fig. 1, Eq. 3 has been simplified to a 2D model

$$\left(\triangle_{\perp}-i\omega\mu\kappa+\omega^2\mu\varepsilon\right)\underline{E}_z=i\omega\mu\sigma. \qquad (4)$$

In this equation the beam is modeled as a current filament which is independent of the longitudinal coordinate, i.e. $\partial_z=0$. Such a setup can be modeled within CST EM-Studio®[4]. The resistive CI can be determined via the total power loss δP in a short ($\delta z \ll c/f$) model pipe [1]

$$\frac{\mathrm{Re}\left\{\underline{Z}_{\perp,x}(\omega)\right\}}{l}=\frac{c}{\omega d_x^2}\frac{1}{I^2}\frac{\delta P}{\delta z} \qquad (5)$$

where the the excitation has been applied by a dipolar alternating current, I, i.e. two current paths of distance d_x and 180° phase shift. The obtained horizontal CI of the proposed SIS100 pipe with cooling tubes is shown Fig.1.

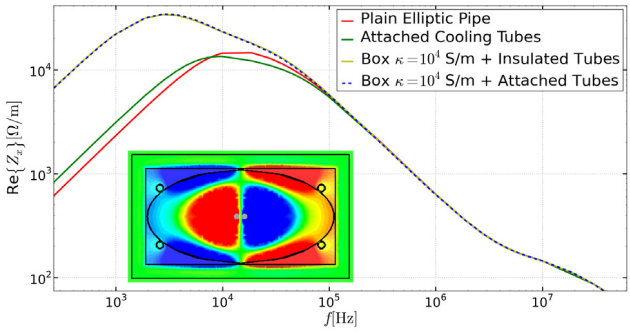

Figure 1: Horizontal CI of the SIS100 beam pipe of unit length. The poor conducting box around the pipe represents a worst case approximation for the surrounding structures.

Conclusion and outlook

The transverse CI of the SIS100 pipe has been determined numerically. The implication of the curves in Fig.1 is that the impact of outside structures is only important at extremely low frequencies, i.e. below $(1-Q_f)f_0$. The characteristic frequency for the shielding of the pipe is the maximum of the curve which represents the onset of wall current [2]. Above this frequency an impedance reduction can only be achieved by changing the pipe itself (material or thickness). In the future, the development of a numerical code that solves Eq. 3 for arbitrary structures and complex materials is foreseen.

References

[1] T. Kroyer, Simulation of the low frequency collimator impedance, CERN-AB-Note-2008-017.

[2] U. Niedermayer et al., Analytical and numerical calculations of beam pipe impedances at low frequencies with application to the thin SIS100 pipe, Proceedings of IPAC, 2011.

[3] V. Kornilov et al., Damping of Transverse Instabilities for Coasting Beams, GSI-Acc-Note-2005-10-001.

[4] CST Studio Suite 2011®, www.cst.com

[*] u.niedermayer@gsi.de

New investigations on vacuum conditions in the SIS100 dipole vacuum chamber during magnet ramping

St. Wilfert, C. Schröder, F. Walter
GSI, Darmstadt, Germany

Abstract

More than 45% of the beam line in the arches of the future SIS100 will be formed by superconducting dipole magnets operating at cryogenic temperatures. As usual in such accelerator machines, the inner surface of all cold beam line chambers, also including the dipole chambers, will be used as an effective cryopump to generate UHV pressures inside the beam pipes. However, since the dipole magnets have to be rapidly ramped at high repetition frequencies, eddy current-induced heating of the chambers is considered as a serious problem with regard to their pumping behaviour. With exceeding a critical wall temperature, previously cryopumped gas desorb from the walls and cause a pressure rise during ramping. The article presents new experimental results on further vacuum measurements carried out on the prototype dipole manufactured by BNIP (Novosibirsk) during magnet operation.

Experiments and results

The measurements were carried out at the Russian BINP (Budker Institute of Nuclear Physics) prototype magnet [1]. The used dipole chamber [2] is shown schematically in Figure 1. Note the chamber is equipped with four cooling tubes arranged at the corners of the stabilizing ribs. The cooling tubes were electrically isolated from the ribs in order to exclude power load due to eddy current through 'tubes – ribs' electrical loops. The temperatures TV01, TV02, … were measured at selected chamber positions. A quadrupole mass spectrometer installed outside the magnet was used at RT for residual gas analysis.

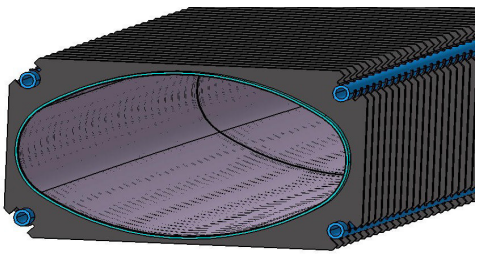

Figure 1: Cross section of the dipole chamber installed inside the BINP sc dipole magnet

The tests were carried out under real operating conditions using all relevant magnet ramping cycles for future SIS100 operation. Detailed parameters of the cycles can be found in [2]. Each cycle was driven for 20 minutes, interrupted by a short break (one minute) between each cycle. Finally, the triangular cycle (/\) was tried, but in this operation mode the magnet quenched as expected. The results of the measurements are depicted in Figure 2. They show clearly that the chamber responds immediately to magnet ramping with an increase in temperature. The highest temperature rise was observed during ramp cycle 2c. Here, the dipole chamber walls heat up from 5…7 K to maximum temperatures of max. ~ 11.5 K. As expected, at these temperatures, only He and H_2 are released from the chamber walls. All other gases remained stuck to the cold walls. Helium desorbs completely from the walls, indicating that He can not be removed by wall-pumping during machine operation. In contrast, H_2 desorbs significantly less than He. This indicates that hydrogen is pumped by the cold walls even under ramping conditions as long as the overall wall temperature is lower than 10K. Less critical were the vacuum and temperature conditions during the cycle 2a, 3a, 3c, and 4 = 5. However, in all tested cycles, helium desorbs immediately after ramping start with the same intensity.

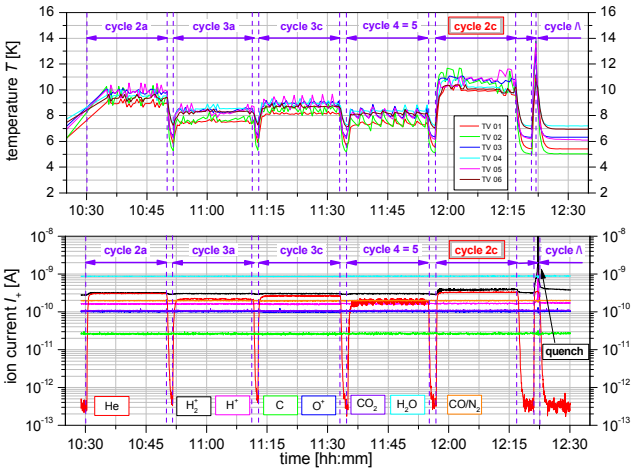

Figure 2: Chamber temperatures and partial pressure conditions during magnet ramping

Conclusions

The design concept of the tested Russian dipole chamber with supplementary LHe cooling tubes located at the rib corners has been proved to be suitable for SIS100 machine. The maximum temperature rise during 2c ramp cycle does not exceed 12 K, this is cold enough for effective cryopumping.

References

[1] E. Fischer, P. Schnizer, A. Akishin, R. Kurnyshov, A. Mierau, B. Schnizer, S. Y. Shim, and P. Sherbakov, IEEE T. Appl. Supercon., vol. 20, no. 3, 164–167, June 2010.

[2] E. Fischer, et al.: CEC/ICMC 2009, June 2009, Tuscon

Barrier Bucket Low-Level RF Development*

E. Bayer[†1], *P. Zipf*[1], *G. Schreiber*[2] *and A. Klaus*[2]
[1]Digital Technology Group, University of Kassel, Kassel, Germany; [2]GSI, Darmstadt, Germany

Abstract: This report addresses the Barrier Bucket Radio Frequency (BBRF) system for the planned synchrotron SIS100 of the new "Facility for Antiproton and Ion Research" (FAIR).

Specifications and Status of the Project

The Barrier Bucket RF system consists of two RF units, each producing single sine RF pulses of up to 15kVpeak gap voltage amplitude in a magnetic alloy loaded synchrotron cavity. The RF pulses are triggered by the circulating frequency of the particle beam and have to be shifted in time to compress the particle beam to less than one half of the SIS100 ring circumference. The barrier bucket operation requires the generation of two single sine waves in one revolution period (T_R) of the particle beam (Figure 1). Each RF cavity has to produce one of the two required pulses. The duration (period) of one single sine wave (Tb) will be fixed to 666ns (1.5 MHz). The single sine waves have to be shifted slowly in time in respect to the revolution cycle.

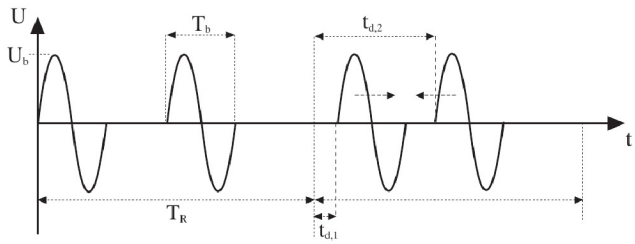

Figure 1: BB cavity signal: Two single sine waves per revolution period.

In an open loop implementation of the RF system a predisturbed driving signal is required. A rectangular offset pulse with the peak voltage U_p has to be added to the single sine wave with the ratio $U_p/U_b = 0.5$ (not shown in Figure 1).

The most challenging task is to generate a smooth phase/delay advance Δt_d of the moving barrier. A new method was found to reduce the jitter of the generated signal relative to the revolution trigger below 1 ns - the needed moving step resolution of the SIS100 BB system.

The method is developed for Field Programmable Gate Array (FPGA) platforms and is based on two main ideas. The first one is the precise measurement of the trigger arrival time using time interpolation techniques implementable in FPGA. This is necessary since the FPGA is a clocked system whose clock is uncorellated to the trigger events. The developed interpolation technique offers a precision of $\pm$ 25 ps. Once the arrival time relative to the system clock is known, internal path delays inside the FPGA are used to adjust the phase of the generated signal. The granularity of the internal phase shifter is about 150 ps. The techniques for time measurement and phase shifting make both use of the asynchronous signal runtimes. Due to the temperature dependence of the signal runtime inside the FPGA, semi-continuous calibration routines were applied to avoid performance decline at varying environment conditions.

The method was implemented and tested on existing FPGA boards available at GSI. The FAB-ADC-DAC board [1] was used to generate the shifted sine wave. The jitter of the generated signal fulfills the requirements and has the following characteristics: $\sigma = 90$ ps, peak-to-peak = 500 ps. The size of one phase shift step is variable. At the BB application it is adjusted to 600 ps. The next project steps will be the realization of the amplitude and delay control of the signal, its connection to the Central Control System (CCS) and BB machine experiments.

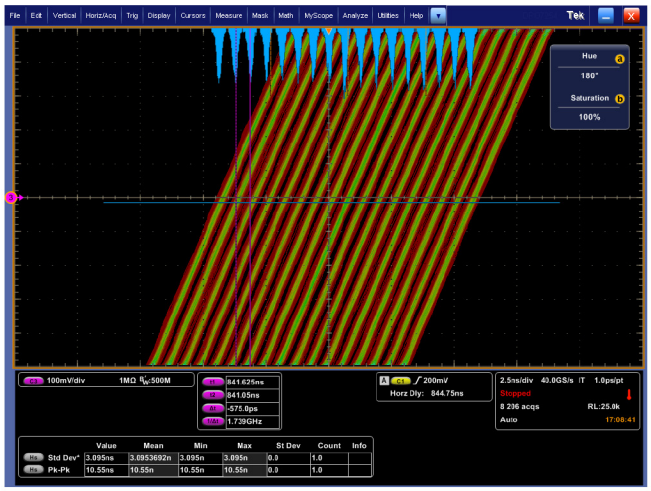

Figure 2: The rising edge of the single sine wave shifted 16 times with a step size of 600 ps.

References

[1] Bachelor Thesis Hardware and Software Implementation of a Radio Frequency High- Speed Data Conversion Unit for Digital Control Systems, S. Sanjari, 2006.

* Work supported by EU, EURONS contract No. 506065.
† e.bayer@gsi.de

Status of the superconducting magnets and cryogenic supply for FAIR

D. Acker[1], A. Bleile[1], E. Fischer[1], E. Floch[1], O. Gumenyuk[1], G. Hess[1], M. Kauschke[1], F. Klos[1], T. Knapp[1], H. Leibrock[1], J. Macavei[1], F. Marzouki[1], A. Mierau[12], J.P. Meier[1], C. Muehle[1], H Mueller[1], I. Pschorn[1], P. Schnizer[1], C. Schroeder[1], S.Y. Shim[1], A. Stafiniak[1], K. Sugita[1], F. Walter[1], M. Weipert[1], Y. Xiang[1]

[1]GSI, Darmstadt, Germany; [2]TEMF, TU-Darmstadt, Germany

Introduction

FAIR, now a project moving into its realisation phase, is gaining momentum. Its superconducting and conventional magnets together with the infrastructure for supplying the cryofluids is a major part of the total investment. The related projects, which GSI is contributing as German in-kind to FAIR, are discussed and their status is outlined.

Superconducting Magnets

Rapidly-Cycling Magnets for SIS100

The SIS100 superconducting cryomagnetic modules, consisting of the magnet, beam pipe, the helium headers, thermal shield and cryostat are one of the largest series required for SIS100.

Dipoles The SIS100 dipole design has been finalised [1,2] last year so this year was dedicated to create the appropriate specification set and start the call for tender which was finished end of the year so that the series order will be placed beginning of 2012. This marks the beginning of the FAIR project realisation. The lamination is depicted in Fig. 1 and a 3D model in Fig.2. Further theoretical investigations required for analysing the magnetic field are ongoing [3,4,5].

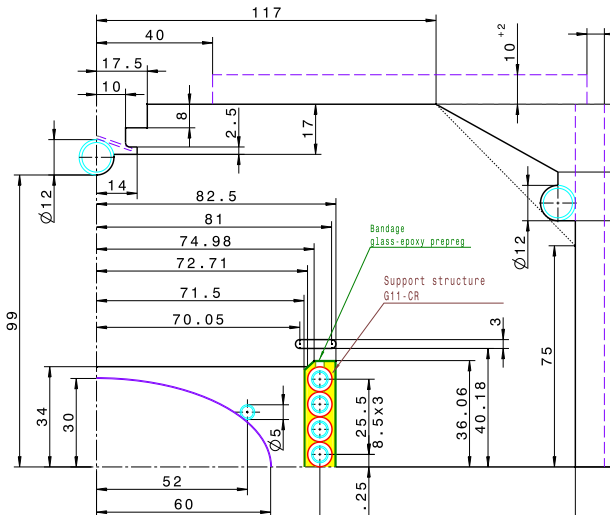

Figure 1: A quarter of the cross-section of the SIS100 dipole.

Quadrupole modules Different cable designs were foreseen for the dipole and the quadrupole resulting in not only that the bus bar of the dipole within the quadrupole module had to be made of the dipole cable but also different HTS current leads and voltage breakers were required.

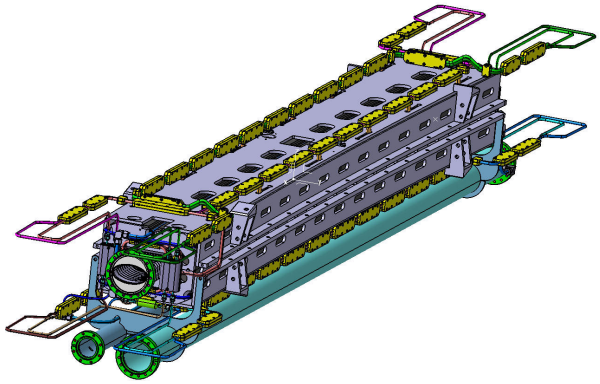

Figure 2: 3D model of the SIS100 magnet

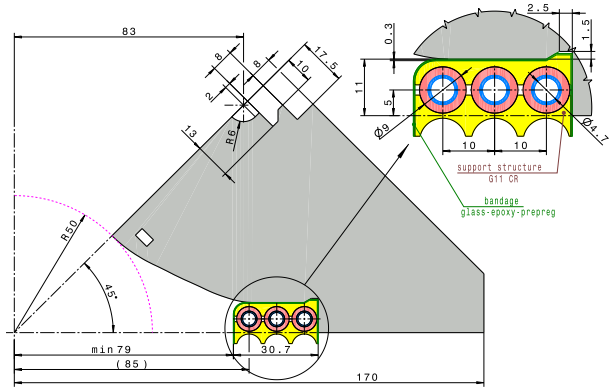

Figure 3: Lamination of the SIS100 3turn quadruple

A quadrupole was designed with 3 instead of 6 turns per poles using the high current dipole cable (see Fig 3) [2].

This simplifies not only the layout of the doublet but also:

1. uses he same cable for dipoles and quadrupoles,
2. reduces the types of HTS current leads to only one,
3. the types of superconducting joints to one,
4. requires only one type of bus bars in the dipoles, quadrupoles, bypass lines, feed in lines, superconducting links and current lead box.

This solution simplifies significantly the design of the SIS100 machine, reduces the total production costs of the main magnet and was thus supported by the machine advisory committee. The decision was taken that the quadrupole together with the correctors will be assembled into the doublet. Further the doublet will house the beam position monitor and the cryocollimator. All these elements will be mounted on a common girder (see Fig 4).

Magnets for the Super-FRS

Superferric dipole Several meetings took place with FAIR collaboration partners. It has been decided that based on the successful tests of the prototype only small modifications are necessary for the series production of the 24 superferric dipoles.

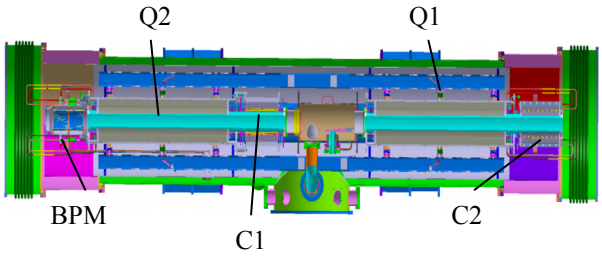

Figure 4: The SIS100 doublet. Q1… quadrupole 1, Q2…quadrupole 2, C1….corrector 1 , C2 …corrector 2, BPM .. beam position monitor

Superconducting Multiplets The superferric multiplets will be a contribution In-Kind from GSI to the FAIR-Project (see Fig. 5). A modularized concept has been developed which allows the assembling of the different types Multiplets with few standarised components. Functional specifications based on this concept are under preparations. A call for tenders for the Multiplet series production is planned for spring 2012.

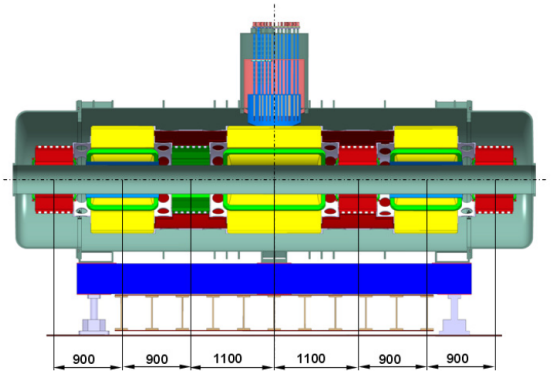

Figure 5: Concept of the most complex Multiplet with 3 quadrupoles, 3 sextupoles 2 octupoles and one steering dipole

Planning for Testing

The magnets need not only be built but also tested to prove that they will function in the machine as expected. GSI committed to the testing of all superconducting magnets by an in-kind proposal.

Prototype Test Facility Activities

The prototype test facility and the tests conducted there, actively contribute to qualify superconducting magnets and associated equipment for the FAIR project. For example A model of a curved SIS100 dipole was tested together with the vacuum chamber and the losses of the total system measured. The results show that the given vacuum chamber design can be recooled and the inner chamber temperature accepted [1].

Series Test Facility Activities

The superconducting magnets for SIS100 add up to roughly 480 magnets while all magnets for SuperFRS add up to roughly 180 magnets. Superconducting magnets of this size have only been tested at operating conditions at research centres up to now. Different options were evaluated even taking Public Private Partnerships, where a private company provides the infrastructure and is responsible for conducting and supervising craftsmen work, and GSI conducts the measurement and its associated analysis. Further different labs were contacted and different collaborations investigated.

These investigations currently concluded in that SIS100 dipoles will be tested in a yet to be built facility at GSI and the SuperFRS magnets within a collaboration.

Cryogenic Supply

The main focus was on the site and building planning for FAIR. The installation space for the components of the common cryogenic system has been fixed. The installation and operation scheme for the cryogenic system was segmented, to adapt to the planning for the buildings. The main building for the cryogenic supply of FAIR, housing the main compressor station and one of the refrigerators, was re-designed and the concept for installation and the media supply for the building revised. The list of experiments, which will be supplied by liquid helium (either continuously or by dewars), is rechecked, and the requested input for the further planning of the building provided. The interest of collaboration for the cryo control system with CERN is assured on both sides.

Again the question of radiation protection at the feed in of the helium transfer lines into experimental areas was raised and is still under investigation.

Furthermore for the synchrotrons, the SuperFRS and the HEBT the planning of the buildings went through an optimisation process. For the SuperFRS the planning of the niches is still under progress.

References

[1] E. Fischer et al IEEE T. Appl Supercon 21(3):1844 – 1848, june 2011.

[2] E. Fischer et al," Design and operation parameters of the superconducting main magnets for the SIS100 accelerator of FAIR. IPAC'11, San Sebastian, September 2011

[3] P. Schnizer at al, IEEE T. Appl. Supercon 21(3):1799 –1803, june 2011.

[4] P. Schnizer et al, "SIS100 dipole magnet optimisation and local toroidal multipoles". IEEE T. Appl. Supercon, to be published, September 2011.

[5] P. Schnizer, B. Schnizer, and E. Fischer. Magnetic field description in curved accelerator magnets using local toroidal multipoles. IPAC'11, San Sebastian, September 2011.

Large-Scale Finite-Element Simulations of the curved full-size SIS100 dipole magnet featuring a single-layer coil*

S. Koch§ [1] *and T. Weiland*[1]

[1]Technische Universität Darmstadt, Institut für Theorie Elektromagnetischer Felder (TEMF), Schloßgartenstraße 8, 64289 Darmstadt, Germany

Curved Single-Layer Dipole Magnet

The actual design of the dipole magnets for the SIS100 synchrotron features single-layer superconducting coils. This allows for a larger aperture compared to previous layouts. The total lenght of $\ell = 3.002\,\mathrm{m}$ requires a curved design, as shown in Fig. 1(a), in order to consider the deflection of the particles inside the magnet. Measurements of the field quality at an already available prototype are in progress [1]. In this report, numerical simulations are used to study the impact of the curved design on the field distribution inside the dipole magnet. On the one hand, the

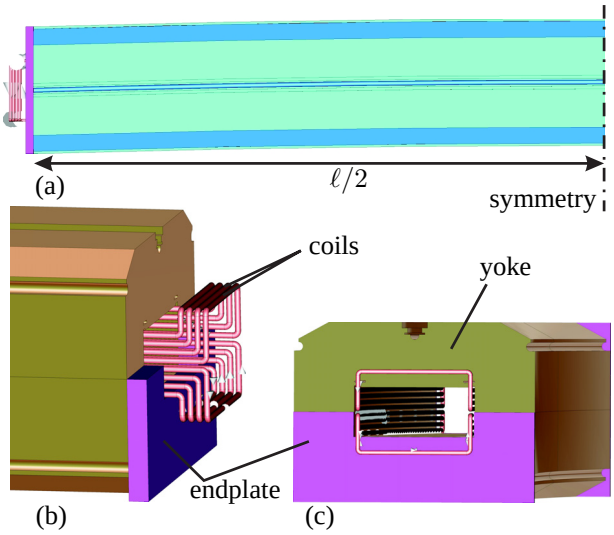

Figure 1: (a) Top view of the CAD model of the curved dipole magnet considering the longitudinal symmetry; (b) end region including the single-layer coils; (c) front view of the magnet featuring end plates.

shape of the coil heads shown in Fig. 1(b) influences the field distribution significantly as the transversal coil parts are rather close to the upper end of the aperture region. On the other hand, the end plate itself, see Fig. 1(c), is again axis-aligned as opposed to the bended shape in the inside. This breaks the transversal symmetry with respect to the curved ideal beam orbit. As a consequence, the field quality in the aperture will be affected. In order to quantify these effects, e.g., multipole coefficients suitable for this type of geometry [2] can be used.

*Work supported by GSI Helmholtzzentrum für Schwerionenforschung GmbH, Darmstadt, Germany.

§ koch@temf.tu-darmstadt.de

Table 1: Relative integral multipole coefficients for the straight as well as the curved design based on the center field integrated along w (quasi2d) and on the 3D field solution (3d) in static operation at $B_{\max} = 1.75\,\mathrm{T}$.

$r_{\mathrm{ref}} = 32\,\mathrm{mm}$		straight symmetry 1/8	straight symmetry 1/4	curved symmetry 1/8	curved symmetry 1/4
$\frac{B_2^{\mathrm{int}}}{B_1^{\mathrm{int}}}/10^{-4}$	quasi2d	–	−0.21	–	−2.77
	3d	–	0.02	–	−2.92
$\frac{B_3^{\mathrm{int}}}{B_1^{\mathrm{int}}}/10^{-4}$	quasi2d	−3.61	−3.43	–	−3.07
	3d	2.01	2.09	–	0.77
$\frac{B_4^{\mathrm{int}}}{B_1^{\mathrm{int}}}/10^{-4}$	quasi2d	–	−0.15	–	0.25
	3d	–	0.03	–	0.32
$\frac{B_5^{\mathrm{int}}}{B_1^{\mathrm{int}}}/10^{-4}$	quasi2d	−1.50	−1.49	–	−0.95
	3d	−0.63	−0.39	–	−1.07

Integral Multipole Coefficients

In order to express the 3D fields in terms of 2D circular multipole expansions, the magnetic field in the aperture is integrated along the magnet axis according to

$$\mathbf{B}^{\mathrm{int}}(x,y) = \int_{-w_{\max}}^{+w_{\max}} \mathbf{B}(u,v,w)\mathrm{d}w \,. \qquad (1)$$

For a straight layout u, v and w correspond to the cartesian coordinates while for the bended case w is the curved ideal beam orbit with u and v forming a transversal orthogonal 2D coordinate system. Thanks to the longitudinal symmetry, the longitudinal field component B_w cancels out and as a consequence $\mathbf{B}^{\mathrm{int}}$ is divergence-free. Therefore a multipole expansion can be carried out. The results for the coefficients of lower order are listed in Table 1 for the straight as well as for the curved design. While the straight layout allows for an additional symmetry which rules out the even multipole orders, the latter are present in the curved design.

References

[1] P. Schnizer, E. Fischer, H. R. Kiesewetter, A. Mierau and B. Schnizer, “Field Measurements on Curved Superconducting Magnets”, IEEE Trans. Appl. Supercond., Vol. 21(3), p. 1799–1803, Jun. 2011.

[2] P. Schnizer, E. Fischer and B. Schnizer, “Magnetic Field Description in Curved Accelerator Magnets using Local Toroial Multipoles”, Proceedings of the 2nd International Particle Accelerator Conference (IPAC2011), p. 2154–2156, Sep. 2011.

Optimization of the Ion Optical Lattice of the Collector Ring (CR)

A. Dolinskii, C. Dimopoulou, O. Gorda, K. Knie, S. Litvinov, F. Nolden, M. Steck

GSI, Darmstadt, German

During the last year optimisations and studies on critical issues of the CR lattice have been continued. The ion-optical calculations and technical studies according to the ring requirements have been refreshed.

Antiproton ion-optical mode

Tracking studies for the CR operated as an antiproton collector have been performed considering the real distribution of the magnetic field of the wide aperture quadrupole magnet. In the antiprotons mode the momentum spread of 6% and the beam emittance of 240 mm mrad must be accepted by the ring. Before stochastic cooling starts bunch rotation takes place. Quantitative studies of the amplitude-dependent tune spreads during bunch rotation have been performed. Using analytic expressions and the Monte-Carlo numerical method the amplitude-dependent tune shifts driven by sextupole magnets, the fringe field of quadrupole magnets, field errors of all magnets and kinematics effects have been calculated. As the result of these simulations two sextupole settings can be applied in order to reduce the beam loss to 4 - 7% [1]. The new betatron tunes Q_h/Q_v=4.418/4.845 for antiproton optics are defined. This allows to avoid crossing structural resonances during bunch rotation. The phase advances between SC pick-ups and kicker magnets are set exactly to 90^0.

Isochronous mode operation

In the CR the optics mode which is called "isochronous mode" gives the possibility to perform mass measurements of short-lived ($T_{1/2}$>20 μs) secondary rare isotope beams coming from the Super-FRS. In order to expand the accessible mass region to very exotic neutron-rich nuclei three ion-optical settings with different γ_{tr}=1.43, 1.67, 1.84 have been calculated. The transverse motion strongly affects the time resolution. Operating with the emittance of 100 mm mrad one can reach a mass resolving power of 10^5. However, the influence of transverse emittance can be significantly reduced applying sextupole corrections with two families. Dedicated Monte-Carlo simulations have been performed and results are given in ref. [2]. They show that a time resolution of $\Delta T/T=2\text{x}10^{-6}$ over the full acceptance of the ring can be achieved. Further improvements up to $\Delta T/T=3\text{x}10^{-7}$ can be reached using additional octupole correction.

Power converters stability

Mainly due to the fact that high mass resolving power is required in the isochronous mode of the CR there are strong demands on the stability of power converters. Considering different factors causing beam orbit instability one has to provide the stability requirements for power supplies in the frequency region from one Hz to tens of kHz. As it is shown in ref. [3] the stabilization system should suppress the relative current ripple to the order of $\Delta I/I=10^{-6}$. It is also important to avoid slow drifts of the magnet field.

Injection septum magnet

The optics of the injection scheme requires that the septum magnet deflects the incoming antiproton beam by 125 mrad onto the injection orbit. Initially, a dc septum magnet was considered but quickly abandoned for the present pulsed magnet design. This decision was taken because of both the cooling problem anticipated with a calculated 800 kW power dissipation and the high running costs. An extremely low leakage fielding on the stored beam is another key requirement for this magnet. The ion-optical simulations show that the stray field reduces the injection efficiency by 1% in the case of a dc septum magnet. The pulsed septum magnet has a average low power dissipation (up to 30 kW). But, on the other hand, the magnetic field created by the eddy currents can reduce the injection efficiency. The further design of the coil and the pulsed power supply requires more attention and care.

Closed orbit dipole correctors

14 wide aperture vertical corrector magnets, which must be placed in the arcs, are required. Last year a preliminary design of the horizontal corrector coil, which can be integrated in the main CR dipole, has been done. This coil produces the horizontal magnet field. Because of lack of space the correctors in the straight sections must be designed as combined function magnets able to produce both horizontal and vertical dipole kicks.

Beam Position Monitors (BPM)

A preliminary design of the BPM, which must be integrated in quadrupole magnets, has been done. Electronic devices should be installed directly on the BPM chamber. The detailed particle tracking in the ring in a combination with the FLUKA simulations show that the maximal radiation load for BPM electronics will be less then 5 Gy/day.

References

[1] A. Dolinskii, et.al. Proceedings of IPAC'11 Conference, San-Sebastian, 2011, WEPC054.

[2] S. Litvinov, et.al. Proceedings of STORI'11 Conference, Frascati, 2011.

[3] A.Dolinskii, et.al. Proceedings IPAC'11 Conference, San-Sebastian, 2011, WEPC055.

Simulations of Antiproton Stochastic Cooling in the CR

C. Dimopoulou, A. Dolinskii, T. Katayama, F. Nolden, C. Peschke, M. Steck[1], *D. Möhl, L. Thorndahl*[2], *and M. Dolinska*[3]

[1]GSI, Darmstadt, Germany; [2]CERN, Geneva, Switzerland; [3]University of Frankfurt

Overview

The Collector Ring (CR) of the FAIR project serves the fast cooling of the hot secondary beams, antiprotons at 3 GeV or RIBs at 740 MeV/u. After injection, bunch rotation and adiabatic debunching, the reduced momentum spread of the initialy injected bunch of secondary beams fits into the acceptance of the stochastic cooling system, so that all the particles can be cooled. For maximum antiproton production rate, stochastic cooling must reduce the transverse rms emittances from 45 down to 1.25 mm mrad and the rms momentum spread from 0.35 % down to 0.05 %, within 10 s, with the future option of 5 s (for the RIBs see [1]). The system uses the bandwidth 1-2 GHz, the foreseen installed microwave power of 4.8 kW could be upgraded.

Antiproton cooling is limited by the poor ratio of Schottky signal to thermal noise, that is why it is foreseen: (i) to keep the pickup electrodes and preamplifiers at cryogenic temperatures, (ii) to strive for large sensitivity by moving (plunging) the pickup electrodes as the beam shrinks, (iii) to choose the notch filter technique for momentum cooling, which advantageously filters out the thermal noise. The optimum choice of the ring slip factor η=-0.011 (γ_t= 3.85) guarantees sufficient momentum acceptance for the notch filter cooling, but the transverse cooling suffers from the resulting high mixing between kicker and pickup.

Simulation Results

Momentum (longitudinal) cooling can be described by the Fokker-Planck (FP) equation for the energy distribution of the particles $\Psi(E,t) \equiv \partial N/\partial E$ (formalism explained in [2], an example of the cooling force is shown in Fig. 1):

$$\frac{\partial \Psi}{\partial t} = \frac{\partial}{\partial E}\left[-F\Psi + \left(D_s\Psi + D_n\right)\frac{\partial \Psi}{\partial E}\right] .$$

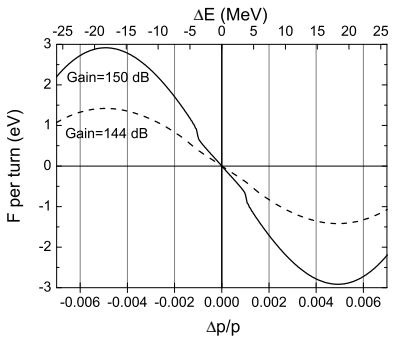

Figure 1: Coherent effect F per revolution versus Δp/p and deviation ΔE from the nominal kinetic energy of 3 GeV.

The CERN program and also the new GSI FOPLEQ code [3] numerically solve the FP equation and calculate the rms energy (momentum) spread as the 2^{nd} moment of Ψ. An example for the CR parameters is given in Fig. 2.

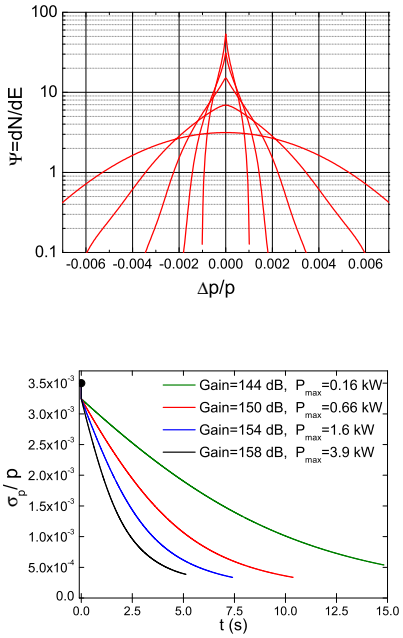

Figure 2: Evolution of Ψ during cooling of 10^8 antiprotons at 3 GeV with gain=150 dB. Plots at t=0, 2.5, 5, 7.5 and 10 s. Cooling down of the rms beam momentum spread for different gains and corresponding maximum cw power at the kickers (up to 20% Schottky, 80% thermal noise).

The required performance can be met with the notch filter momentum cooling with a gain of about 150 dB even with the conservative assumption of no plunging of the pickups. The performance of the betatron (transverse) cooling, which has to proceed simultaneously with the momentum cooling, was calculated separately with an analytical model. First results [1] indicate that, for optimum momentum cooling, the betatron cooling is slow because of the high desired mixing. This calls in the near future for detailed investigations of the interplay between momentum and betatron cooling aiming at a simultaneous optimization of both processes (including also the pickup-plunging) by distributing the available installed power accordingly.

References

[1] C. Dimopoulou et al., JaCoW Proc. COOL'11, Alushta, Ukraine, TUIOB02 (2011), www.jacow.org.

[2] D. Möhl et al., Physics Reports 58, p.73 (1980).

[3] M. Dolinska et al., JaCoW Proc. IPAC'11, San Sebastian, Spain, WEPC123 (2011), www.jacow.org.

Stochastic Cooling Developments for the FAIR Collector Ring

C. Peschke, R. Böhm, R. Hettrich, J. Krieg, W. Maier, F. Nolden, P. Petri and M. Steck[1]
[1]GSI, Darmstadt, Germany

For the stochastic cooling system at the collector ring CR of the FAIR project a number of technical developments were achieved. Here we present the linear motor drive and the optical notch filter system.

The plunging system of the CR pick-up electrodes is driven by linear motors. The most severe requirement on the motor drive is to return the electrodes within $T = 200$ ms from the final position after stochastic cooling to the position where a fresh beam can be injected. The path length S is 60 mm, and the inertial mass of the system is 6.6 kg. The atmospheric pressure acting on the vacuum bellows is counteracted by mechanical springs, which are accurately adjusted to minimize the applied load on the motor. The position of the motor is read out periodically by an optical system with a precision of 3 μm. This value is compared to the set points which are calculated from a model yielding a jerk free movement with minimum acceleration, both in the time and frequency domains. The set position is

$$s(t) = S\left[\frac{1}{2} + \frac{1}{2}\tau + \sum_{n=0}^{1} b_n \sin\left((2n+1)\pi\tau\right)\right]$$

where $\tau = 2t/T - 1$, $-1 \leq \tau \leq 1$. The parameters b_0 and b_1 are chosen by requirements on minimum accceleration [1]. The controller output is the current feeding the linear motor, given by digital sequences calculated from a PIDT1 controller model at a repetition rate of 1 kHz. The PIDT1 model parameters were optimized experimentally. A set of control parameters was found yielding a movement profile, which is sufficiently close to the requirements. The measured accelerations with the optimized profile fulfill our expectations. The measured movement profile is still reasonably stable even if the inertial mass is intentionally enlarged by 11.7 kg. The experience with the first prototype drive was used for the mechanical design of a less expensive, but more reliable drive which will be installed in the final pick-up tanks. The drive is protected against unexpected emergency cases, including a complete communication breakdown or intolerably high accelerations, which are continuously monitored by a separate device.

Longitudinal stochastic cooling at the CR makes use of the notch filter method for antiproton cooling and for the final cooling of rare isotope beams. Ideal notch filters exhibit zero transmission at all harmonics mf_0 of the equilibrium beam revolution frequency f_0. Inside the cooling bandwidth one reaches in practice only a finite, low transmission (notch depth) and there is a small deviation $f_m - mf_0$ from linearity (dispersion) of the frequencies f_m where the minima occur. These effects increase the equilibrium beam momentum width. A prototype of an optical notch filter [2] was installed for test purposes into the cooling system at GSI's ESR storage ring ($f_m = 1.96$ MHz). A block diagram is shown in Fig. 1. In order to make the filter as symmetric as possible, the signal is split into two parts only *after* laser modulation. The long optical delay line is temperature stabilized to about 0.1 K. The notches were measured to be deeper than -36 dB inside the 0.9-1.7 GHz band of the ESR cooling system. The measured frequency dispersion is smaller than 15 kHz almost everywhere inside the cooling band (see Fig. 2). It can be explained completely by the nonlinear phase behaviour of the signal subtraction in the $180°$ hybrid. Detailed cooling experiments with this system are planned for 2012.

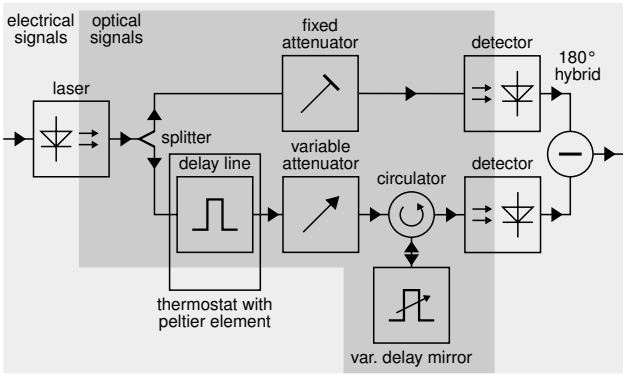

Figure 1: Block diagram of optical notch filter.

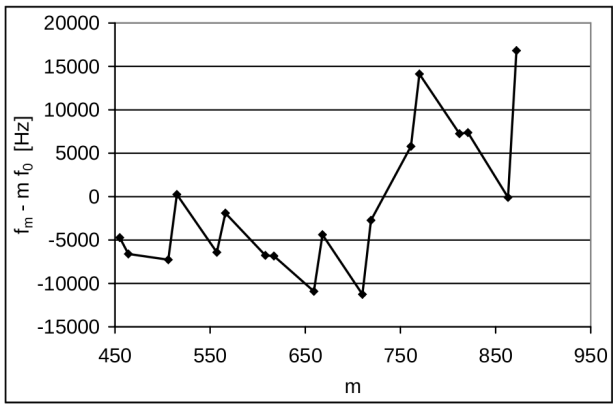

Figure 2: Dispersion of optical notch filter.

References

[1] F. Nolden et al., Prototype Pick-up Tank for CR Stochastic Cooling at FAIR, Proc. Cool 2009, 106-109

[2] F. Nolden et al., GSI annual report 2007, 58

Development of a Sensitive Schottky-System for CR *

W. Kaufmann[1], *P. Hülsmann*[1], *M. Schwickert*[1], *M. Hansli*[2], *A. Angelovski*[2], *A. Penirschke*[2], *R. Jakoby*[2], *W. Ackermann*[3], *W. Müller*[3], *and T. Weiland*[3]

[1]GSI, Darmstadt, Germany; [2]IMP, TU Darmstadt, Germany; [3]TEMF, TU Darmstadt, Germany

Introduction

This report summarizes the ongoing development of a sensitive longitudinal and transversal Schottky-Sensor for the Collector Ring CR of FAIR. A maximum sensitivity as well as operation in all modes of the CR is required. Numerical simulations with CST Microwave Studio have been carried out and the performance has been estimated with an equivalent circuit.

Basic Design of the Schottky-System

To achieve a maximum sensitivity for low beam intensities the decision was made to study a resonant cavity design. Good experiences have been made with the existing Schottky cavity for longitudinal measurements at the ESR [1]. To allow also transversal Schottky measurements, the TM_{110}, or dipole mode, will be used. This mode shows almost linear dependency between the offset of a passing particle to the center and the output signal but is excited much weaker than the monopole mode (TM_{100}). Therefore, both modes will be coupled out independently and, to suppress the monopole mode for the extraction of the transversal signal, rectangular waveguide resonators are foreseen. The basic design of the system is shown in Fig. 1.

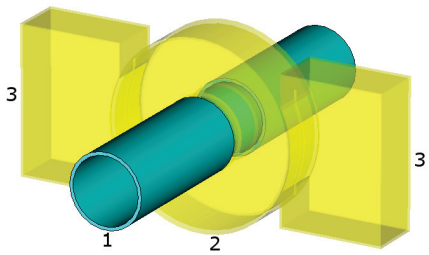

Figure 1: Basic design of the proposed sensor cavity with the beampipe (1), the pillbox-like cavity with a radius of 53 cm (2), and the rectangular waveguide filters (3).

Signal Characteristics and Optimizations

Higher measurement frequencies, and therefore higher resonance frequencies, allow shorter measurement times at a given frequency resolution as well as smaller dimensions. However, for reasonable measurements one has to stay below the Schottky band overlap of around 209 MHz. A higher quality factor of the sensor will improve the sensitivity but the demanded bandwidth limits the quality factor.

* Work supported by BMBF: 06DA90351

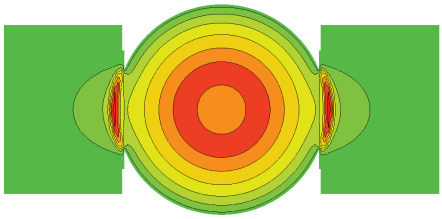

Figure 2: Absolute value of E_z of the monopole mode at 198 MHz in the cross section of the proposed sensor cavity.

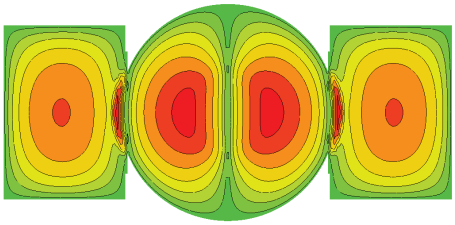

Figure 3: Absolute value of E_z of the dipole mode at 315 MHz in the cross section of the proposed sensor cavity.

To estimate the overall sensitivity of the given geometry the simulation results are used for calculating the signal-to-noise ratio by means of an equivalent circuit model [2]. Consequential, the optimization goal is to maximize the R/Q-value, and thus the sensitivity, for small beam offsets. Parameters for the optimization are the geometrical dimensions of the pillbox, the coupling slot between the pillbox and the rectangular resonators and the dimensions of the latter. A complete sequence of sophisticated FEM simulation runs is being elaborated because of the strong interdependence of the relevant parameters.

Summary and Outlook

The parameter ranges for the Schottky measurements at the CR have been determined, heading towards a resonant cavity design. First estimations on the performance using an equivalent circuit model are very promising [2]. Optimizations of the sensor geometry are ongoing.

References

[1] F. Nolden *et al.*, "A Fast and Sensitive Resonant Schottky Pick-up for Heavy Ion Storage Rings", Nuclear Instruments and Methods in Physics Research Section A, 2011.

[2] M. Hansli *et al.*, "Investigations on High Sensitive Sensor Cavity for Longitudinal and Transversal Schottky for the CR at FAIR", IPAC 2011

BPM Developments for the FAIR Collector Ring

F. Becker[1], *D. Liakin*[2], *M. Schwickert*[1]
[1]GSI, D-64291 Darmstadt, Germany; [2]ITEP, 117218 Moscow, Russia

Introduction & Focus of Development

The closed orbit measurement system for the FAIR Collector Ring (CR) will employ 18 electrostatic pickups as Beam Position Monitors (BPMs). A dense synchrotron lattice calls for an integration of the BPMs into the quadrupole magnets. Since the CR is designed for various operational scenarios, the BPM-system has to cover a wide range of different beam parameters. As a first turn diagnostic, the system will be exposed to a radioactive pion beam of 10^{10} particles. After two turns and 1,52 μs nearly all π-mesons will be decayed and 10^8 remaining anti-protons ($\bar{p}$) have to be detected. For Rare Isotope Beams (RIBs) with a design charge of q = 50+ the expected intensities range between $\leq 10^5$ and 10^9 particles. In order to cover the measurable intensity range, a low-noise amplifier chain with ∼100 dB dynamic range has to be foreseen, see also [1]. During injection, all secondary $\bar{p}$ and RI-beams will exploit the full machine aperture, with beam envelopes up to 360 x 150 mm. After cooling, the 2σ beam envelope shrinks down to about 10 mm. Therefore a linear BPM response is mandatory [2, 3].

Actual Project Status & Outlook

Starting from the given boundary conditions, an integrated mechanical design was proposed, see Fig. 2. The BPM clearance was maximized within the magnet pole shoe spacing. To reduce the antenna capacitance to 54 pF, a star-like chamber cross section was suggested. COMSOL simulations predict 300 mV_{peak} voltage on the electrodes for 10^{10} π-mesons in the first turn scenario and 3 mV_{peak} in the nominal 10^8 particles $\bar{p}$-case respectively.

An absolute position accuracy of 4 mm in the first turn application and 0.8 mm for closed orbit measurement is required. Since the amplifier layout determines the SNR and therefore the BPM resolution, this will be a major task.

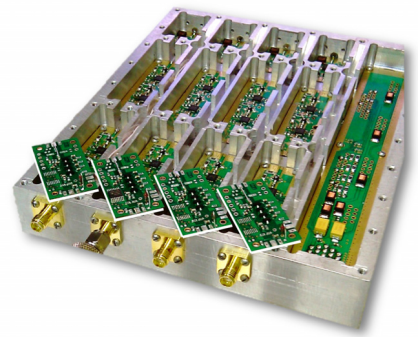

Figure 1: Photograph of the prototyped 4-channel modular amplifier unit, integrated in a full metal housing. The low-noise JFET-based preamplifier PCBs (on top) are realized in a radiation and magnetic field tolerant design.

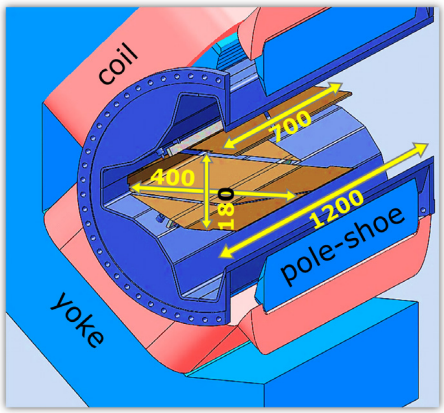

Figure 2: CAD-model of the suggested BPM assembly, integrated in the quadrupole magnet. The CF (ø = 500 mm) vacuum chamber of 1200 mm length is fitted in the spacings between the magnet pole shoes. The BPM antenna is realized as linear cut type in spiral arrangement, with 400 x 180 mm clearance and 700 mm length.

Best signal performance is achieved with the shortest high impedance path to avoid additional capacitance. Thus the impedance matching unit will either be inside the quadrupole or inside the fringe field 20 mT $\leq B \leq$ 200 mT. A preamplifier with a dedicated magnetic field tolerant design, based on parallel JFETs was proposed, see also [1]. Benefit is a SNR of about 300:1, that is ten times the SNR of a matching transformer. Technical drawback is its necessity to withstand a beam induced radiation dose of up to 250 Gy/yr. Fig. 1 shows a prototype of the analog signal chain, realized as matched high-impedance preamplifier with ≤ 3 μV_{rms} noise at 10 MHz BW and additional 20 dB amplification, followed by a modular amplifier unit with variable gain and 50 Ω line drivers. Furthermore, calibration signals can be fed to the BPM electrodes to allow online compensation of electrical drifts along the analog chain due to temperature, radiation or aging effects.

Next steps will be an extensive benchmarking of the analog components for realistic input signals. A detailed mechanical construction of the pickup and chamber will be started as well, to test the entire BPM system on a wire test bench and during dedicated beam times as soon as possible.

References

[1] M. Le Gras et al., “The COFB-system for the CERN AD”, DIPAC’99 (PT09), Chester, 1999, p. 177-179.
[2] J. Durand et al., “New electrostatic pickups for the PS’, EPAC’88, Rome, 1988, p. 1384-1386.
[3] P. Kowina et al., “Optimization of linear-cut BPMs (FEM)”, DIPAC’07 (TUPB16), Venice, 2007, p. 96-98.

LASSIE for FAIR

T. Hoffmann, H. Braeuning

GSI, Darmstadt, Germany

At all particle accelerators analogue signals are derived from detectors, rf cavities, function generators, transformers and other sources. A common way to observe these signals in order to understand, trim and operate the accelerator is the readout and signal presentation by oscilloscopes. With an increasing amount of signals at large facilities like GSI or FAIR, this solution gets expensive. Furthermore, it can not be easily integrated into a common accelerator control system, which must provide safe remote operation including data recording, storage and time-correlated presentation.

Long term experience with the cost-efficient ABLASS [1] system has already been obtained at GSI and the reduced performance in terms of resolution compared with oscilloscopes is acceptable for most of the signals. The principle of ABLASS is based on the conversion of analogue signals into frequencies, which are then counted in a modular VME system. To provide time-correlated signals acquired over the complete FAIR complex for the future digital control room, the concept of ABLASS will not only be ported to the new control system environment. In contrast to ABLASS the new DAQ system, which is called LASSIE ('Large Analogue Signal and Scaling Information Environment') is designed from the start as a distributed system. As such, LASSIE will be used at all FAIR accelerators, which are part of the modularized FAIR start version: SIS100, HESR, CR, S-FRS, HEBT and pLinac.

General Concept

The technical realisation is described in [2]. LASSIE is based on the Front-End Software Architecture (FESA) [3]. The use of the FESA framework results in a clear separation between the data acquisition part and the graphical user interface. LASSIE includes both these parts: the data acquisition using FESA and Java-based analysis and display tools. In addition, the FESA part, which is called LASA (Large Scaler Array), will strictly implement the currently emerging guidelines for FESA development at GSI. This will allow the seamless integration of the LASSIE system into the new FAIR control system by the beam diagnostics department.

JAVA Tools

The LASSIE system consists of several expert GUI tools, which are written in Java and are based heavily on CERN libraries for communication with the FESA classes and graphical display. This tool-set contains a general control and monitor tool for the LASA classes running on different distributed front-end computers, a spill structure analysis tool [Fig. 1], a counter display tool, a dose level tool and others [2]. Using the object-oriented approach of

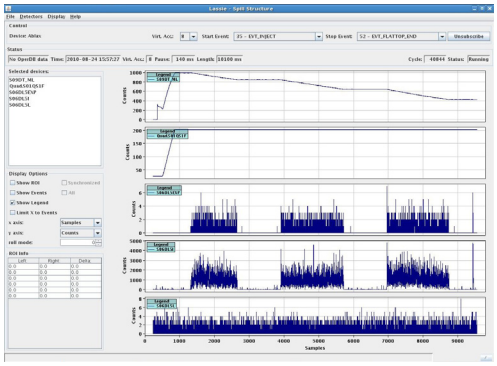

Figure 1: The Lassie spill structure tool for analysis of synchrotron signals (from top to bottom: current transformer, quadrupole ramp and beam loss monitors).

Java, the major part of the core functionality, like obtaining data from the FESA classes, storing and analyzing the obtained data and many GUI widgets, could be put into packages common to all tools. This makes the GUI part of the LASSIE system more like a framework and gives it a great flexibility with respect to developing new and dedicated tools. To synchronize the DAQ in a distributed set-up a timing system is required. Currently the virtual accelerator number and the UTC timestamp of the GSI machine timing transmitted once per cycle are used to assure the correlation of the data received and to detect timing errors. In the FAIR control system the machine timing will be handled via the White Rabbit timing system. It is based on Synchronous Ethernet, the Precision Time Protocol (PTP), new developed hardware and a field-bus like topology [4]. It provides deterministic data with sub-ns accuracy. As every event will be tagged with a time stamp, precise data correlation between the distant crates is assured. In the future this precise tagging may also allow data correlation throughout different timing domains of the accelerator complex.

The possibility to extend LASSIE with other FESA classes acquiring time-dependent data e.g. DAC driven magnet power supplies, transforms it into a powerful tool. It will provide oscilloscope-like features fully integrated into the control system, making most of the expensive cables and hardware scopes in the control room obsolete.

References

[1] T. Hoffmann et al., Proc. 11th BIW, Knoxville, Tennessee, USA, p. 294 (2004).

[2] T. Hoffmann et al., ICALEPCS 2011, Grenoble, France, MOPMN008, to be published

[3] M. Arruat et al., ICALEPCS 2007, Knoxville, Tennessee, USA, WOPA04, p. 310-312.

[4] J. Serrano et al., ICALEPS2009, Kobe, Japan, Oct 2009, TUC4, p. 93

Migration of the Operation Software from OpenVMS to Linux

R. Huhmann, G. Fröhlich, S. Jülicher[1]
[1]GSI, Darmstadt, Germany

MISSION

Presently, the accelerator's operation software at GSI runs on a cluster of DEC-Alpha machines. The computers' OS is OpenVMS. The user interface is realized by X-Window and Motif based clients. The software modules for operation of the linear accelerator (LINAC), the transfer lines, and common services are mainly written in Fortran77. The central software components for operation of the synchroton (SIS) and the storage ring (ESR) are written in Pascal. All programming languages use specific DEC extensions and a lot of OpenVMS specific system calls. We aim to get rid of OpenVMS but to reuse the main parts of the GSI operational software's source code base by porting the software to Linux. Addtionally, the migration shall enable interoperability with current or future developments, e. g. in Java on Linux.

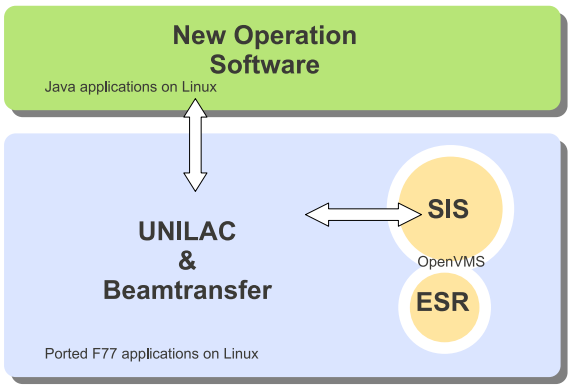

Figure 1: Groups of operation software components in step one of migration.

ISLANDS and BRIDGES

Fortunately, software components for operation of the SIS and ESR on one hand, and the LINAC and transfer lines on the other hand, are only minimally coupled. The SIS and ESR operation software will remain unchanged on OpenVMS and will be excluded from migration in step one. In a second step those components will completely be replaced by the LSA framework [2] with new Java applications.

New operation applications for the LINAC and transfer lines are developed in Java on Linux and can be bridged with the island of ported Fortran software. By the in-house developed *uv*-architecture which is described in more detail in [1] an observer pattern is realized to connect Java applications to Fortran applications for data exchange. Fortran applications serve as publisher, Java applications subcribe to *uv*-data-structures. Requests, replies, and notifications are serialized over XML-streams.

On OpenVMS, the coupling between SIS/ESR operation software and the LINAC software is realized by a service which sends binary messages from one application to another. In order to connect from VMS to the peer TCP/IP communication on Linux a proxyservice was developed on Linux [3].

STATUS and MIGRATION PATH

In 2011, the main operation applications for the LINAC and transfer lines have been ported to Linux using the in-house developed VMS system emulation libraries [1]. Some system oriented services have been reimplemented in C/C++/Java on Linux. A framework to build the complete software stack from a tagged subversion repository was developed. The above mentioned services and APIs to bridge to remaining VMS software and to new Java applications are implemented and tested. Still missing are full integration tests of all operation software components, a production run time environment on Linux, deployment to the production system, performance tests under production conditions, and control room tests without and with beam.

Currently, a test console is set up which will serve as a test site for integration tests and run time environment. In order to switch the operation software to Linux it will be neccesary to perform several temporary integration tests in the main control room, first without beam, later with beam. Now, the feasibilty studies and most of the implementation, porting, and unit testing has been completed. However, integration and launching in production environment demand further efforts and are scheduled for 2012.

References

[1] R. Huhmann, G.Fröhlich, S. Jülicher, V.RW. Schaa, "GSI OPERATING SOFTWARE MIGRATION OpenVMS TO Linux", Proceedings of PCaPAC08, Ljubljana, Slovenia, MOX02, p. 4

[2] J. Fitzek, R. Mueller, D. Ondreka, GSI, Darmstadt, Germany, "SETTINGS MANAGEMENT WITHIN THE FAIR CONTROL SYSTEM BASED ON THE CERN LSA FRAMEWORK", Proceedings of PCaPAC 2010, Saskatoon, Saskatchewan, Canada, WEPL008, p. 63

[3] R. Huhmann, G.Fröhlich, S. Jülicher, V.RW. Schaa, "GSI OPERATION SOFTWARE: MIGRATION FROM OpenVMS TO Linux", Proceedings of ICALEPCS 2011, Grenoble, France, MOPMS014, p. 351

White Rabbit Technology as Basis for the FAIR Timing System

D. Beck[1], R. Bär[1], T. Fleck[1], M. Kreider[1,2], S. Mauro[1], C. Prados[1], S. Rauch[1], W. Terpstra[1] and M. Zweig[1]

[1]GSI, Darmstadt, Germany, [2]Glyndŵr University, Wrexham, United Kingdom

The FAIR timing system has the task of triggering and synchronizing equipment actions as required by the parallel execution of different beam production chains. It must handle machine cycles from 20 ms up to several hours for storage rings. Although a precision of 1 µs is sufficient in most cases, some equipment like kickers needs timing with nanosecond precision. For synchronization of radio-frequency components, the timing system is complemented and linked to the Bunch phase Timing System BuTiS [1], but this is out of the scope of this document.

White Rabbit

The advent of the FAIR facility requires inevitable changes for the accelerator timing system due to larger distances and the need for higher precision. Furthermore, open technology shall be applied that is used by other major research facilities as well. A new timing system for FAIR will be based on a White Rabbit (WR) network [2,3]. WR is a protocol being developed further by CERN, GSI and other partners for synchronizing nodes in a packet-based network. It combines Gigabit-Ethernet, IEEE1588-2008 (PTP), precise knowledge of the link delay and Synchronous Ethernet: Time synchronization is achieved by adjusting the clock phase (125 MHz carrier) and offset (Coordinated Universal Time - UTC, or International Atomic Time - TAI) of all network nodes to that of a common grandmaster clock. It has been demonstrated, that sub-nanosecond synchronization with a jitter in the picoseconds range is achieved over distances of a few kilometers and across dedicated WR network switches.

Equipment action will no longer be directly triggered upon receiving signals from a central timing unit. Instead, timing systems using WR networks are based on the notion of absolute time. Like alarm clocks, timing receivers (TR) in a WR network are pre-programmed for autonomous execution of actions at a given date and time. Thus, distribution of information through the network and timely execution of actions are decoupled.

Complementary Building Blocks

Network. TRs are programmed to execute actions at a given time via so-called timing-events, which are broadcasted from a central master using UDP or raw Ethernet with high priority. The network must be deterministic with known upper bound latency, such that timing events are not received too late. Since packets are transmitted without handshake and may be lost, Forward Error Correction techniques such as Reed-Solomon encoding are required. Redundant links will be used at the critical parts of the timing network [4].

Etherbone (EB) is a network protocol layer meant for fast, low level communication. It connects two distant Wishbone System-on-Chip buses and provides direct memory access to network devices [5]. EB shall be deployed at WR nodes at FAIR and CERN and its use includes transmission of timing events.

Soft-CPU. WR firmware includes a small "Soft-CPU" for reusing existing open source software. This approach saves development time and FPGA area. At GSI, the LM32 from Lattice is now used in several designs for low-priority tasks, but also serves for debugging attached Wishbone devices [5].

Status and Outlook

In 2011, White Rabbit has been established as the basis for the FAIR timing system and significant progress was made on essential building blocks. This allowed detailed specification of form factors for FAIR Timing Receivers, PSP code 2.14.10.3.3. Further work included porting WR firmware from Xilinx to Altera FPGAs, the latter being used by TRs developed at GSI. The distribution of time stamps with WR has been successfully shown. The focus in the near future is on the integration of different building blocks. This is required for broadcasting timing events and demonstrating the capability of triggering synchronized actions. The authors would like to thank the "White Rabbits" at CERN for support and collaboration.

References

[1] P. Moritz, "BuTiS - Development of a Bunchphase Timing System", GSI Scientific Report 2006 (2007) 64.

[2] Tomasz Włostowski, "Precise time and frequency transfer in a White Rabbit network" Warsaw University of Technology, May 2011.

[3] E. G. Cota et al., "White Rabbit Specification: Draft for Comments" (2011) www.ohwr.org.

[4] C. Prados and M. Lipinski, "White Rabbit and Robustness: Draft for Comments" (2011) www.ohwr.org.

[5] M. Kreider et al., "Etherbone - A Network Layer for the Wishbone SoC BusS" Proc. of ICALEPCS 2011, Grenoble, France.

[6] W.W. Terpstra "The Case for Soft-CPUs in Accelerator Control Systems" Proc. of ICALEPCS 2011, Grenoble, France.

Control System Front-End Renovation: The New GµP

U. Krause[1], L. Hechler[1], K. Höppner[1,2], P. Kainberger[1], K. Kohnhäuser[1], S. Matthies[1], G. Riehl[1], and G. Schwarz[1]

[1]GSI, Darmstadt, Germany; [2]present address HIT, Heidelberg, Germany.

The GSI control system is outlined as a decentralized distributed system in which front-end VME computers to interface the equipment are cross-linked with operation layer computers. As a specific, the front-end is split into two sub layers: Equipment controllers (EC), interacting in precise real-time with the equipment via MIL field-bus, and device presentation controllers, commonly called group micro processors (GµP), serving as the access point for commands from the operation computers (see fig. 1).

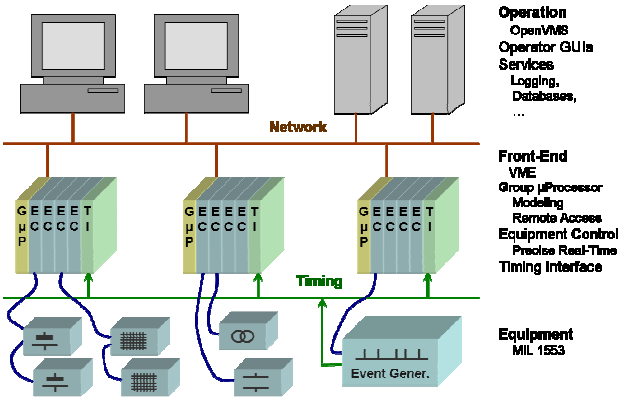

Figure 1: Control system outline.

The GµP establishes GSI's equipment modeling as devices (denoted by nomenclatures, like TK1MU1) with properties (like STATUS, CURRENTS, RESET). A library (Userface) on the operation layers nodes handles remote access to the front-end devices.

Close matching of the GµP's core software to the hardware, the highly proprietary networking protocol, and strong interdependence between all communication components impeded modifications. As result, the system was limited to OpenVMS and a specific type of 68020 VME boards running pSOS operating system.

Being in use for more than 20 years now, the GµPs urgently had to be replaced. To also overcome the limitations by the network communication, a renovation project was started: In a Gordian knot approach, network communication and core software on the GµP were rebuilt from scratch.

The project was narrowed to the communication layers: Manpower was not sufficient to adapt operation level applications, or to re-implement the bulk of the GµP's software, the user service routines (USRs) which implement the equipment specific properties.

The new communication layer software implements the control system devices as objects, to which property-objects are attached. These properties integrate the existing USR implementation as execution method (see fig. 2). Re-using the USR code easily ensures correct interconnection with the unmodified EC's software which is by common shared memory. However, the complex structures used for data exchange require the same byte order in the GµP as the big endian ECs: PowerPC is favored.

The new network communication internally uses CORBA middleware, encapsulated completely in client side interfaces which are provided for Java, C++ and Python. A wrapper additionally offers the former Userface for seamless integration into the existing operation's applications (see fig. 2).

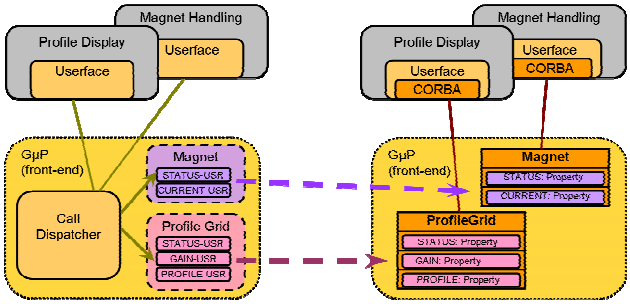

Figure 2: Replacement of communication elements.

The renovated software could be run on different operating systems and different processor architectures. Developed for Linux, it was easily ported to Windows too, both on client and server side. While first x86 based front-end controllers are already installed in the accelerator control system, e.g. for stepper motor control, focus is to replace the old GµP boards by state-of-the art PowerPC boards, running Linux.

Former functionality is fully provided, including access via Userface. Old and renovated front-end nodes can co-exist in the control system, permitting step-by-step migration of the front-ends. After a long period, in which in each shutdown period several nodes were brought to the new system, all front-end nodes in the accelerator now run the renovated front-end system.

After a long period of restriction, the renovated software now opens the control system to modern environments and offers options for the future. Front-end layer supports multiple platforms: PowerPC and x86, Linux and also Windows. Labview can be used as client. Python is as future scripting language and for interactive access replaces the former Nodal interpreter. Limitations in data size as well as restrictions in the length of nomenclatures and property names are overcome.

The front-end renovation is a prerequisite to transfer operation's applications to the Linux platform and to integrate the existing accelerator into the new FAIR control systems. Access to existing front-ends was integrated into JAPC, to be used by future Java applications, and a gateway framework on FESA front-ends provide access from existing applications to future FAIR front-ends.

Kicker goes digital – Upgrade of Kicker Electronics for ESR and SIS

M. Thieme, A. Bauer, W. Panschow

GSI Darmstadt Germany

INTRODUCTION

For the rapid deflection of an ion beam (extraction, injection) kicker magnets are used. The kicker magnets are operated in pulsed mode at high voltage. Thyratrons are used as high-voltage switches. Up to nine modules are used simultaneously for the beam deflection.

Therefore, all thyratrons must switch at the same time with minimum deviation. The effective pulse width is determined by the switching of two thyratrons (main and dump switch). Sequence control, switch synchronisation, pulse generation, switch monitoring and data logging are done by software controlled electronics.

The hardware components of the kicker control electronics from the SIS and ESR were developed about 25 years ago and have been in use even since.

Modern electronic components today open new possibilities to achieve functionality. Besides a significant higher power density and performance of today's electronic components, especially miniaturization enables the construction of compact modules. Technical advances in digital electronics and signal processing facilitate the implementation of measurement and control applications in all-digital solutions.

By using highly integrated components such as FPGAs, electronics are programmable and scalable.

PREVIOUS SOLUTION

The control electronics (timing, synchronization and pulse monitoring, see Figure 1) are built-in components in several cassettes. It consists of modules with ECL logic and mixed-signal components. Because of differing logic levels, the use of level converters is necessary.

The ignition point of each thyratron is determined by an ECL counter. The 15-bit counter is running at 50 MHz. The counter is preloaded by software and starts with a hardware start signal.

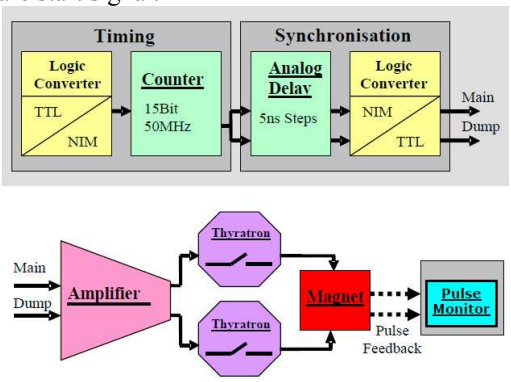

Figure 1: Previous Solution.

To ensure that all main and dump thyratrons switch synchronously, the ignition signal is passed through delay lines.

Matching of channel-dependent delay times is carried out manually by changing the hardware of the delay elements. These changes are required during the operating time of the Kicker several times and at least once before starting a new beam time.

Monitoring of the actual pulse width is done via comparators. The switching threshold must be adjusted manually.

UPGRADE ELECTRONICS

The complete control electronics (timing, synchronization and pulse monitoring, see Figure 2) is integrated in a 19" rack unit. With one rack unit, up to four Kicker channels can be controlled.

The signal processing is done fully digital in FPGAs. The ignition signal is generated by a 23-bit counter in the FPGA. The counter is clocked at 280 MHz.

Necessary delay times for synchronization are generated in the FPGA. They can be adjusted via software. The monitoring of the actual pulse width is done via software controlled comparators.

The trigger thresholds are continuously dynamically adaptable.

Continuous pulse monitoring with high resolution allows adjusting the delay time before each kicker cycle.

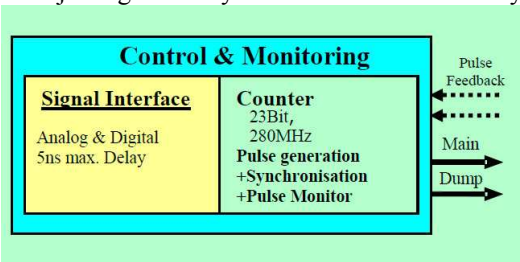

Figure 2: Upgrade.

Parameter	Previous	Upgrade
Pulse generation		
Resolution	15 Bit	23 Bit
Frequency	50 MHz	280 MHz
Minimum Pulse Width	20 ns	3.6 ns
Pulse delay generation		
Method	analog	digital
Resolution	50 ns	3.6 ns
Minimum Step	50 ns	3.6 ns
Maximum Delay	680 µs	107 ms
Pulse Monitoring		
Resolution	8 Bit	23 Bit
Minimum Pulse Width	625 ns	7 ns

Pilot Studies on Optical Transition Radiation at UNILAC

B. Walasek-Höhne[1], C. Andre[1], F. Becker[1], R. Fisher[1], P. Forck[1], H. Graf[1], A. Lumpkin[2], A. Reiter[1], M. Schwickert[1]

[1]GSI, Darmstadt, Germany; [2]Fermi National Accelerator Laboratory, U.S.A.

Introduction

The characterization of transverse ion beam profiles is an ongoing research field at GSI. Nowadays, beam profiles are often measured with secondary electron emission grids, scintillating screens, beam scrapers or beam induced fluorescence monitors [1].

As an alternative, the feasibility of optical transition radiation (OTR) has been evaluated in this pilot study with an 11.4 MeV/u (β=0.16) U^{28+} beam at the UNILAC. The present experiment was prompted by successful measurements at the CLIC Test Facility 3 with 80 keV electrons (β=0.5) and the feasibility study [2] for UNILAC and HEBT energies at GSI.

OTR is a classical electro-dynamic process: A particle of charge Q and velocity β generates optical photons when it crosses the boundary between two media of different dielectric constants. For the number of emitted photons N, theory predicts the proportionality $N \sim Q^2 \cdot \beta^2$.

Because OTR is a surface phenomenon, the use of very thin foils, e. g. aluminized Kapton (e.g. 0.1 µm Al on 6 µm Kapton), is standard for electrons and minimum-ionizing protons. The pilot study aimed to find a thermally stable OTR target for highly-ionizing heavy-ions and to detect useful transverse profiles for the first time, taking advantage of their large Q value.

Experimental Setup and First Results

The series of experiments using the non-relativistic U^{28+} beam have been performed at the X2 area. Figure 1 shows a scheme of the experimental setup consisting of an OTR target ladder and image-intensified CCD camera system (ICCD).

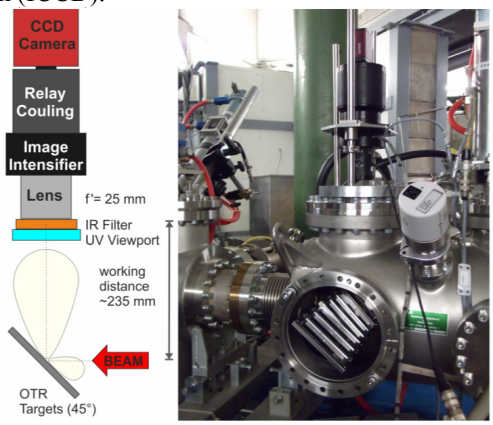

Figure 1: Scheme (left) and photo (right) of OTR experiment at the X2 beam line area.

The ICCD gating feature (down to 10 µs) was used to select preferentially the prompt OTR signal versus any background sources in the scene with a longer emission time constant like e.g. blackbody radiation from the screen. To test the Q-dependence of the light yield measured by the ICCD, a moveable 570 µg/cm^2 carbon stripping foil upstream of the target increased the mean charge to Q~73. During initial tests, a thick 500 µm stainless steel target proved superior thermal behaviour compared to the thin aluminized Kapton target which was damaged during irradiation.

For U^{73+} reasonable beam distributions were acquired above ~$2 \cdot 10^7$ ppp. Figure 2 compares raw data of beam distributions for both charge states, but same ion number of ~$7 \cdot 10^8$. The ratio of the integral ICCD intensities supports the predicted Q^2 dependence: $3.3/0.49 \sim 73^2/28^2$.

Detailed comparison with profile grid data and the analysis of spectroscopic measurements are currently evaluated.

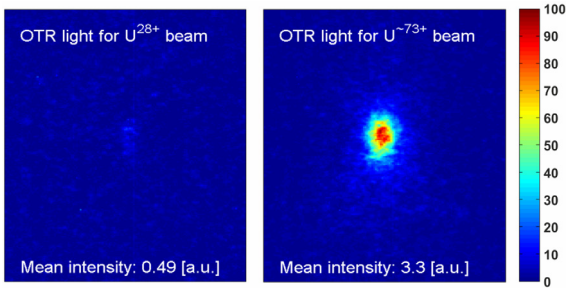

Figure 2: OTR beam spot recorded without (left) and with (right) stripping foil for constant beam parameters.

Summary

First OTR measurements with non-relativistic heavy ions at the UNILAC delivered promising data. The beam spot was clearly detectable and the Q^2 dependence was observed. The next step is to install an OTR monitor into the high energy beam transport lines to provide necessary data required for more intense high-energy ion beams as planned for the Facility for Antiproton and Ion Research FAIR.

Acknowledgments

It is a pleasure to acknowledge members of the GSI operating team, beam diagnostic group, detector and target laboratories for support and help during the experiment.

References

[1] P. Forck, "Lecture notes on Beam Instrumentation and Diagnostics", Joint Universities Accelerator School (JUAS 2010); http://www-bd.gsi.de.

[2] A. Lumpkin, "Feasibility of OTR imaging of non-relativistic ions at GSI" Workshop Proceeding, http://www-bd.gsi.de/ssabd.

Low Current Profile Measurements using a Current-to-Frequency-Converter (QFW)

M. Witthaus, J. Adamczewski-Musch, H. Flemming, J. Frühauf, S. Löchner, H. Reeg and P. Skott

GSI, Darmstadt, Germany

Overview

The development of a prototype system with 8 Current-to-Frequency Converter (QFW) ASICs [1] is a collaboration between the Beam Diagnostics and the Experiment Electronics departments at GSI since 2010 [2]. This electronic device will provide an economic alternative readout for Secondary Electron Monitor (SEM)-profile grids or similar beam diagnostic devices like Multi-Wire Proportional Chambers (MWPC) or Ionization Chambers. Transverse beam profiles with a time resolution down to the microsecond range have been recorded successfully during different test campaigns at GSI beam lines.

Hard- and Software

The developed and used hard- and software is described in [2]. The software (FPGA control unit and GO4) was improved to measure up to 100 time slices. As a result, the time resolution during the beam pulse measurement is significantly increased. Additionally, the prototype was extended to 2*32-input channels recently, whereby the control unit operates with two existing prototype motherboards.

Measurement Results

Further measurements were performed with a 2*32-wire MWPC in the HEBT beam line at GSI.

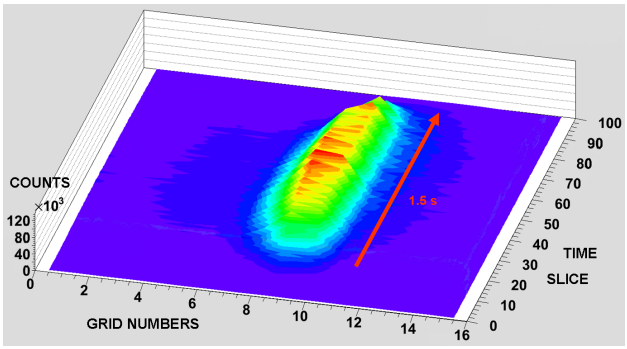

Fig. 1: Time-dependent profile of a MWPC, 300 MeV/u $^{40}Ar^{18+}$ beam

Fig. 1 shows the vertical time-dependent beam profile from the first half of the MWPC x-plane (16 out of 32 wires). The beam duration is about 1.5 s and each time slice represents 20 ms. The profile data is analysed with GSI Object-Oriented Online Offline system (GO4).

Next Development Step

After promising and successful beam campaigns with different ion species it was decided to develop a revised prototype motherboard, now with 64 input channels.

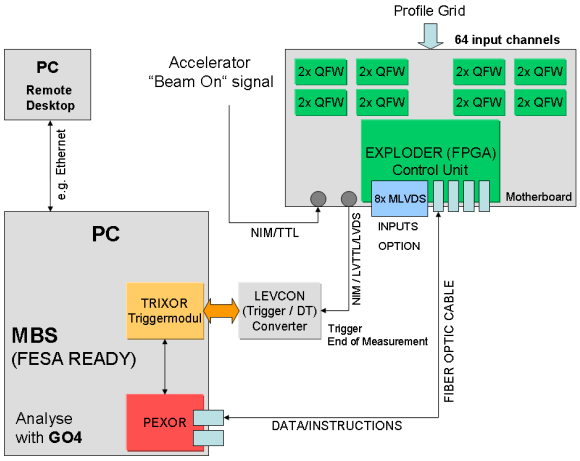

Fig. 2: Block diagram of the prospected readout system

The next development step of the readout system is shown in Fig. 2. This new board contains 16 QFW-II ASICs for 64 channel inputs in total and a FPGA Control Unit called EXPLODER [3] providing also the network communication electronics. The board sends the measured data to a PEXOR card [3] and in turn receives all the QFW parameters. The QFW parameters are set via EPICS (Experimental Physics and Industrial Control System). The measured data of the profile grids are transferred to the MBS (Multi Branch System) DAQ system by the PEXOR card. The LEVCON [3] and TRIXOR [3] modules are necessary for the MBS trigger operation. The last one is installed in a PC which is controlled by Remote Desktop Protocol. For now, the beam profiles are analyzed and displayed by GO4 software.

In this stage the VME-crate with various VME-boards is no longer necessary. The new compact design is ready for Front-end Software Architecture (FESA), and presents an economic solution for future applications at GSI and FAIR. The use of MBS will be continued for testing purposes or in case of experiments with beam, until it is replaced by FESA.

References

[1] H. Flemming and E. Badura, "A high dynamic charge to frequency converter ASIC", GSI Sci. Rep., 2004

[2] M. Witthaus et al., "SEM-Grid Prototype Electronics with Charge-Frequency-Converter", GSI Sci. Rep., 2010

[3] EXPLODER, PEXOR, TRIXOR and LEVCON are hardware boards, developed by GSI Experiment Electronics department; see: *http://www.gsi.de/informationen/wti/ee/elekt_entwicklung/module.html*

Quantitative Scintillation Screen Studies at UNILAC Energies and related Model Calculations

E. Gütlich[1], R. Haseitl[2], A. Reiter[2], B. Walasek-Höhne[2], K. Gütlich[2], P. Forck[2], and O. Kester[1,2]

[1]Goethe University Frankfurt am Main, Frankfurt, Germany; [2]GSI Helmholtzzentrum für Schwerionenforschung, Darmstadt, Germany

Scintillating screens are commonly used at accelerator facilities [1], however their imaging qualities are not well understood, especially for high current ion beam operation [2]. Due to the impact by ions, the dose rate during beam delivery is more than 10 orders of magnitude higher than for other application of scintillators in typical nuclear physics experiments. Several types of radiation-hard inorganic-materials were investigated for various ion species and energies of 4.8 and 11.4 MeV/u. To validate the imaging quality of the scintillators a scraper scan method was established. The scraper scan method gives a beam profile with higher spatial resolution than profile grids (grid spacing= 1.5 mm, scraper step size = 0.02 mm).

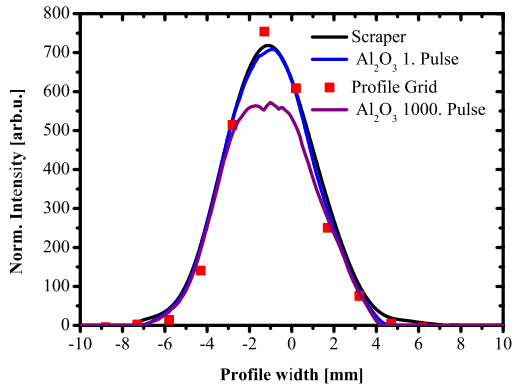

Figure 1: Comparison of reference methods with profiles obtained by Al_2O_3 screen (1^{st} and 1000^{th} macro pulse). Beam parameters:$^{48}Ca^{10+}$ @ 4.8 MeV/u, $4.3 * 10^{10}$ ppp, 13.5 μA, 5 ms, 1 Hz, P_{peak}= 317 W, P_{aver}= 1.59 W.

Ceramic Al_2O_3 showed the best agreement with reference methods (see Fig. 1) compared to other ceramics like $ZrO2 : Y$ or quartz glass $Herasil$ 102. For Al_2O_3 irradiated with a Ca beam of 4.8 and 11.4 MeV/u and a constant beam flux, these methods are compared. For 4.8 MeV/u the results are in good agreement (see Fig. 1), while for 11.4 MeV/u the screen image does not reflect the beam distribution which can not be attributed to material degradation.

Models for the response of scintillators to single particles have a long history, see e.g. [3]. A model for the response of a scintillator to an ion beam has been developed. It is based on the radial dose distribution of the ions, estimations concerning the behavior in the overlapping regions and a maximal energy dose which can be converted inside the material, as proposed by [3]. This model was applied to Al_2O_3, can describe the observed saturation effect observed at 11.4 MeV/u and is able to reconstruct saturated images. Detailed measurements are planed in the near future to validate the model for different ion energies and species.

Detailed spectroscopic investigations were performed, to determine the influence of the ion beam intensity on the luminescence spectra emitted by the materials. No significant dependence of the spectrum to the beam intensity was found for most of the scintillators [2].

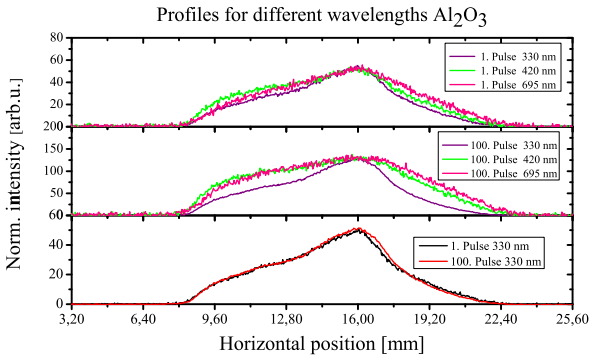

Figure 2: Wavelength-resolved beam profiles from the spectroscopic data, Beam parameters: $^{48}Ca^{10+}$ @ 4.8 MeV/u, $5.4 * 10^{10}$ ppp, 31 μA, 3.3 ms, 1 Hz, P_{peak}= 604 W, P_{aver}= 1.99 W.

In Fig. 2 the wavelength-resolved beam profiles are shown for different wavelength which can be obtained from the spectroscopic data. In the top plot the profiles of the first macro pulse are shown for F^+, F^0 and Cr^{3+}. Different profiles are recorded for each wavelength. The second plot shows the profiles of the 100^{th} macro pulse. The third row compares the profiles for 330 nm of the first and the 100^{th} macro pulse. Only small changes can be observed for the 330 nm emission. This shows that imaging property of the F^+-emission (330 nm) is more stable over time, therefore profile measurements around 330 nm can lead to better results than in the optical region of the spectrum.

References

[1] B. Walasek-Höhne et al., "Scintillating Screen Applications in Accelerator Beam Diagnostics", conference proceedings of SCINT 2011, submitted to *IEEE Transactions on Nuclear Science*.

[2] E. Gütlich et al., "Quantitative scintillation screen studies and related model calculations, " submitted to *IEEE Transactions on Nuclear Science*.

[3] K. Michaelian et al., " Scintillation response of nuclear particle detectors," in *Nucl. Instr. and Meth. in Phys. A*, 356, 1995, pp. 297.

Scintillation Screen Investigations for 300 MeV/u Ion Beams*

K. Renuka[1,2], C. Andre[1], F. Becker[1], W. Ensinger[2], P. Forck[1], R. Haseitl[1], and B. Walasek-Höhne[1]

[1]GSI, Darmstadt, Germany; [2] Technical University of Darmstadt, Germany

Scintillation screens are a prominent tool for beam alignment in accelerator facilities due to their ability of producing high- resolution two dimensional beam images at reasonable cost [1, 2]. The main aim of this work is to search for a suitable scintillating material for beam profile measurements in the high-energy beam transport section of FAIR. Different scintillation screens such as single crystals, powder screens, ceramics and glass materials were irradiated with ion beams delivered from SIS18. The experiments were performed in HTP beam line in front of the beam dump (Fig. 1). The experimental setup and measurement details are presented in detail in [3].

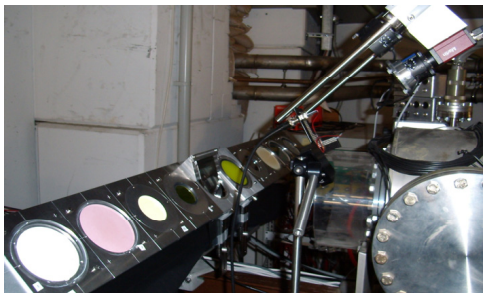

Figure 1: The target ladder with ten different scintillation screens. The scintillation light was recorded with a standard CCD camera.

Except Mg-and Y-doped ZrO_2, all of the scintillating screens showed a linear light yield for three orders of magnitude of particle intensity for carbon and uranium ion beam [3]. Apart from the ZrO_2 screens, the other scintillation screens were investigated using neon and tantalum ions with particle intensities ranging from 10^4 to 10^9 particles per pulse. Linear light yield of five orders of magnitude of particle intensity was observed from the screens (Fig. 2). The highest light yield was measured for YAG:Ce (1 mm), whereas Al_2O_3 resulted in low light yield. The light yield of Al_2O_3 was 1 order of magnitude lower than Al_2O_3:Cr. P46 powder screen gives more light yield than YAG:Ce (0.25 mm) although they are prepared from the same source materials. All the samples reproduce the beam width within the deviation of ± 4 % (Fig. 3), except YAG:Ce (1 mm) which produces a significantly broader beam width. The light yield normalised to the single particles energy loss shows a dependency on the ion species as determined for carbon, neon, argon, tantalum, and uranium. This investigation reveals that the light yield of the samples is higher for lighter ions than heavier ions showing a non-proportional behaviour on energy deposition [4]. The future work will be focused on radiation induced damage of scintillation materials.

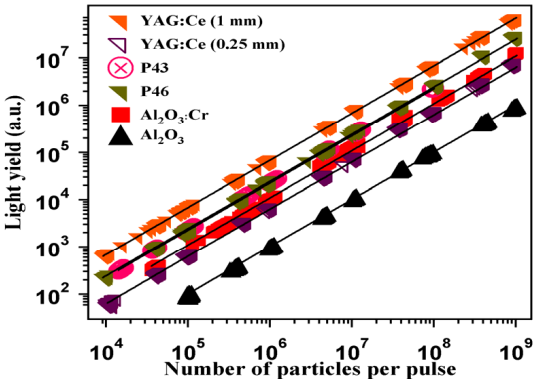

Figure 2: Light yield of scintillation screens irradiated with 275 MeV/u tantalum ions, 300 ms pulse length.

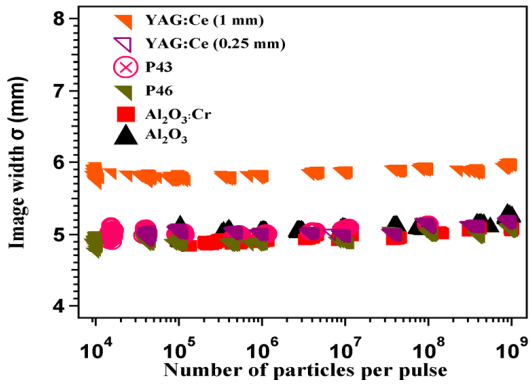

Figure 3: Imaged beam width obtained from different screens. The beam parameters are same as Fig.2.

References

[1] R. Jung *et al.*, "Single pass optical profile monitoring," in *Proceedings DIPAC*, Mainz, Germany, 2003.

[2] B. Walasek-Höhne and G. Kube, "Scintillating screen application in beam diagnostics," in *Proceedings of DIPAC 2011*, Hamburg, Germany, 2011, p. 570.

[3] P. Forck, *et al.*, "Scintillation screen investigations for high energy heavy ion beams at GSI," in *DIPAC* Hamburg, Germany, 2011.

[4] K. Renuka *et al.*, "Imaging properties of scintillation screen for high energetic ion beams" submitted in IEEE TNS, November 2011.

*This work was supported in part by the German Ministry of Science (BMBF) under contract No. 06DA9026

Frequency-variable digital filters for beam phase control *

P. Surapong[1], *C. Spies*[†1], *M. Glesner*[1], *and H. Klingbeil*[‡1,2]
[1]Technische Universität Darmstadt, Darmstadt, Germany; [2]GSI, Darmstadt, Germany

Abstract: We present a design and FPGA implementation for frequency-variable band pass filters for longitudinal beam phase control. These filters can be used to detect longitudinal bunch oscillations.

Introduction

Closed-loop beam phase control is applied for damping undesired longitudinal bunch oscillations [1]. Computation-intensive tasks, such as phase detection [2] and filtering, are handled by field-programmable logic devices (FPGAs) in order to improve the system's performance. The present paper discusses a frequency-variable digital band pass filter.

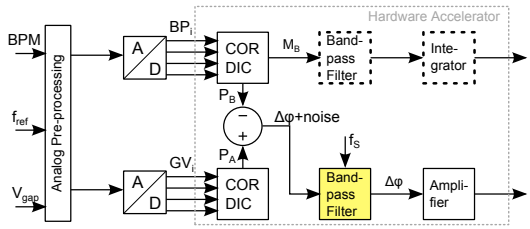

Figure 1: Signal processing block diagram for closed-loop beam phase control; future extensions are dashed.

Architecture

Our filter architecture supports a sparse coefficient vector with a maximum length of 16384 and at most 64 nonzero coefficients. A feedback factor a enables FIR ($a = 0$) or IIR ($a \neq 0$) filters. The values of up to 64 coefficients, their position in the sparse vector, the feedback factor and a scaling factor are stored in registers accessible to the DSP and can be updated at run-time. Changes become effective when the next sample arrives.

Presently, only three constant coefficients are used ($c_0 = c_2 = -\frac{1}{4}, c_1 = \frac{1}{2}$); they constitute a band-pass filter. The center frequency is modified by changing the position i of these coefficients in the coefficient vector: $i_0 = 0, i_1 = k, i_2 = 2k$, where 0 corresponds to the most recent sample. k depends on the desired pass-band center frequency f_C and the sampling interval T_S: $k = (2 \cdot f_C \cdot T_S)^{-1}$

By tuning f_C to the synchrotron frequency f_S, dipole oscillations can be detected and damped [1].

Operation

Fig. 2 shows the input and output signals of the phase detector and the bandpass filter, obtained from simulations assuming $T_S = 3.224\,\mu$s. The first two diagrams show the gap voltage and the beam position signal. In the third and fourth diagram, the phase difference between the two signals and the synchrotron frequency are shown. The last diagram shows the filtered phase difference.

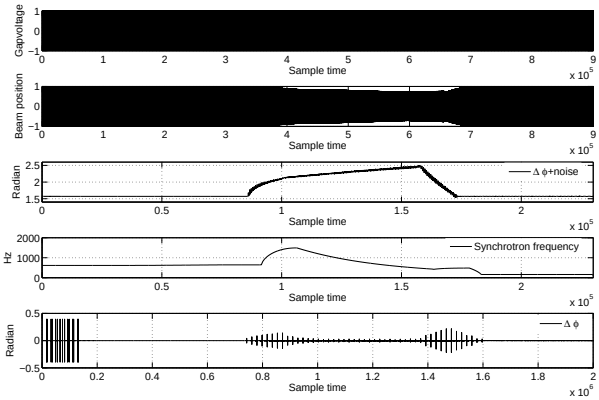

Figure 2: Hardware simulation results

Future Work

Not all features of the architecture are presently utilized. We will therefore investigate more complex filters to improve the frequency response. The filter coefficients themselves could be adapted on-line by another hardware module. Furthermore, we will optimize our filter design in order to minimize its FPGA area consumption.

Additional filters will be added (as shown in fig. 1) to process amplitude information as well. This enables detecting higher-order oscillations [3].

References

[1] H. Klingbeil, B. Zipfel, M. Kumm, P. Moritz, "A Digital Beam-Phase Control System for Heavy-Ion Synchrotrons", IEEE Trans. Nucl. Sci. 54(6), pp. 2604–2610.

[2] A. Guntoro et al., "Implementation of Realtime and High-speed Phase Detector on FPGA", Proc. Int'l. Workshop Applied Reconfigurable Computing 2006, pp. 1–11.

[3] D. Lens et al., "Damping of Longitudinal Modes in Heavy-Ion Synchrotrons by RF-Feedback", Proc. Int'l. Conf. Control Applications 2010, pp. 1737–1742.

* Work supported by GSI, contract DA/GLE1, and by BMBF, grant no. 06DA9028I

† christopher.spies@mes.tu-darmstadt.de
‡ h.klingbeil@gsi.de

Faster Parameter Sweep of the phase velocity of the wave in a Pickup-design

Joel A. Tsemo Kamga, Wolfgang F.O. Müller, Kynthia K. Stavrakakis, and Thomas Weiland
Technische Universität Darmstadt, Institut für Theorie Elektromagnetischer Felder (TEMF), Schlossgartenstrasse 8, 64289 Darmstadt, Germany

Introduction

The simulation of the Pickup design developed in [1] with CST Particle Studio [2], where the phase velocity of the wave is to be matched to the beam velocity using a ferroelectric material (see figure 1 in [1]), takes much time. In order to reduce the simulation time, a Parametric Model Order Reduction (MOR) based on the Finite Integration Technique will be studied in this work. In particular one is interested in a fast evaluation of the frequency response while taking also material variations into account.

Parametric Model Order Reduction

The particle beam velocities in the beam pipe can be modeled by respective permittivities ε_i. Different resonance curves result for each ε_i. With an appropriate $\varepsilon_{\mathrm{tune}}$ for the tunable material, the resonance frequency can be again shifted to $f = 3$ GHz. The appropriate $\varepsilon_{\mathrm{tune}}^{3\,GHz}$ can be characterized by performing a parameter sweep in CST MWS over a relatively wide range of $\varepsilon_{\mathrm{tune}}$ in order to restrict the search range. The exact $\varepsilon_{\mathrm{tune}}^{3\,GHz}$ is found by doing an optimization in MWS over this small range. The time consuming parameter sweep in MWS can be replaced by multivariate MOR techniques.

This method uses the Maxwell Grid Equations (MGE) which describe the device and which have been obtained by using the Finite Integration Technique [3]

$$\begin{array}{llll} \mathbf{C}_{\mathrm{FIT}}\widehat{\mathbf{e}} &= -\frac{\mathrm{d}}{\mathrm{dt}}\mathbf{M}_{\mu}\widehat{\mathbf{h}}, & \mathbf{S}_{\mathrm{FIT}}\mathbf{M}_{\mu}\widehat{\mathbf{h}} &= 0, \\ \widetilde{\mathbf{C}}_{\mathrm{FIT}}\widehat{\mathbf{h}} &= \frac{\mathrm{d}}{\mathrm{dt}}\mathbf{M}_{\epsilon}\widehat{\mathbf{e}} + \widehat{\widetilde{\mathbf{j}}}_{s}, & \widetilde{\mathbf{S}}_{\mathrm{FIT}}\mathbf{M}_{\epsilon}\widehat{\mathbf{e}} &= 0. \end{array} \tag{1}$$

The matrices $\mathbf{C}_{\mathrm{FIT}}, \widetilde{\mathbf{C}}_{\mathrm{FIT}}$ and $\mathbf{S}_{\mathrm{FIT}}, \widetilde{\mathbf{S}}_{\mathrm{FIT}}$ are discrete topology matrices representing the curl and divergence operators, respectively. The $\mathbf{M}_{\varepsilon}, \mathbf{M}_{\mu}$ are diagonal matrices which contain the mesh geometry and the material properties. The MGE are used to define a system with input $\mathbf{i}$, output $\mathbf{u}$, a state vector $\mathbf{x}$ and system matrices $\mathbf{A}, \mathbf{B}, \mathbf{C}$. This can be achieved by substituting $\widehat{\mathbf{h}}$ in (1), resulting in

$$\underbrace{\left(\mathbf{M}_{\varepsilon}s^2 + \widetilde{\mathbf{C}}_{\mathrm{FIT}}\mathbf{M}_{\mu}^{-1}\mathbf{C}_{\mathrm{FIT}}\right)}_{\mathbf{A}(s,\varepsilon_{\mathrm{tune}})}\widehat{\mathbf{e}} \;=\; -s\widehat{\widetilde{\mathbf{j}}}_{s} \tag{2}$$

in the frequency domain. The input at the ports are defined in terms of a matrix $\mathbf{B}$ and the generalized current $\mathbf{i}$, i.e. $-\widehat{\widetilde{\mathbf{j}}}_{s} = \mathbf{B}\mathbf{i}$. In addition, $\widehat{\mathbf{e}}$ represents the state vector, thus $\mathbf{x} = \widehat{\mathbf{e}}$. Analogously, the output is defined in terms of the vector $\mathbf{x}$ and a matrix $\mathbf{C}$. The resulting system is

$$\mathbf{A}(s, \varepsilon_{\mathrm{tune}})\mathbf{x} = s\mathbf{B}\mathbf{i}, \quad \mathbf{u} = \mathbf{C}\mathbf{x}, \tag{3}$$

with transfer function $\mathbf{Z}(s, \varepsilon_{\mathrm{tune}}) = \mathbf{C}\mathbf{A}^{-1}(s, \varepsilon_{\mathrm{tune}})\mathbf{B}$. MOR aims to reduce this typically very large n dimensional system (3) to an $m \ll n$ dimensional system.

For this, the solution vector $\mathbf{x}$ of (3) is restricted on a space spanned by orthonormal trial vectors $\mathbf{v}_1 \dots \mathbf{v}_m$. With $\mathbf{V} = [\mathbf{v}_1 \dots \mathbf{v}_m]$ we substitute $\mathbf{x} = \mathbf{V}\hat{\mathbf{x}}$.

$$\hat{\mathbf{A}}\hat{\mathbf{x}} = s\hat{\mathbf{B}}\mathbf{i}, \quad \mathbf{u} = \hat{\mathbf{C}}\hat{\mathbf{x}} \tag{4}$$

with $\hat{\mathbf{A}} = \mathbf{W}^*\mathbf{A}\mathbf{V}$, $\hat{\mathbf{B}} = \mathbf{W}^*\mathbf{B}$, $\hat{\mathbf{C}} = \mathbf{C}\mathbf{V}^*\mathbf{B}$ and transfer function $\hat{\mathbf{Z}}(s, \varepsilon_{\mathrm{tune}}) = \hat{\mathbf{C}}\hat{\mathbf{A}}^{-1}(s, \varepsilon_{\mathrm{tune}})\hat{\mathbf{B}}$. The matrices $\mathbf{V}$ and $\mathbf{W}$ are chosen such that the moments of the original and the reduced order transfer functions are matched with respect to both s and $\varepsilon_{\mathrm{tune}}$. The procedure is described briefly in [4] and in more detail in [5].

Once the projection matrices are set up, which is the most time consuming part in MOR, the s-parameter curves, resulting from the respective $\hat{\mathbf{Z}}$ for each $\varepsilon_{\mathrm{tune}}$ are calculated within seconds, and are thus faster compared to the MWS parameter sweep. For example, for a fixed $\varepsilon_i = 2.37$ the parameter sweep of $\varepsilon_{\mathrm{tune}}$ between $34 \dots 41$ using MWS 2011 takes $t_{MWS} \approx 1\mathrm{h}$. On the same machine, the multivariate MOR, which is implemented in MATLAB, takes $t_{\mathrm{MOR}} \approx 25\mathrm{min}$ to calculate $\mathbf{V}$ and to do the sweep.

Summary

A fast frequency response evaluation under consideration of material variations has been achieved in this work. Thus, the parameter sweep required for an estimation of the tunable material range, before its optimization, can be replaced by a faster parameter sweep with the help of MOR.

References

[1] J. A. Tsemo Kamga, Wolfgang F.O. Müller, K. Stavrakakis and T. Weiland, “Pickup design with Beta matching”, IPAC 2011.

[2] CST GmbH, “CST PARTICLE STUDIO”.

[3] T. Weiland, “Time Domain Electromagnetic Field Computation with Finite Difference Methods”, Int. J. Num. Modelling, 9:295-319, 1996.

[4] K. Stavrakakis, T. Wittig, W. Ackermann and T. Weiland, “Model Order Reduction Methods for Multivariate Parameterized Dynamical Systems obtained by the Finite Integration Theory”, URSI GASS, Istanbul, 2011.

[5] O. Farle “Ordnungsreduktionsverfahren für die Finite-Elemente-Simulation parameterabhängiger passiver Mikrowellenstrukturen”, PhD Thesis, Saarländische Universitäts- und Landesbibliothek, 2007.

Implementation of Resynchronisation Mechanisms in a FPGA-based Control System

K. Fricke-Neuderth, V. Wolff, M. Weß und M. Weber

University of Applied Sciences Fulda, Germany

Introduction

This project is related to the replacement of analog RF components for heavy ion synchrotrons by digital components. The advantages of digital electronics are: better stability and reproducibility and the possibility of the application of advanced control algorithms.

In this project a FPGA based (FPGA = field programmable gate array) system has been developed which controls the RF signals for the acceleration cavities in the FAIR project. The RF signals are generated by Direct Digital Synthesis (DDS) modules. Since the cavities are separated by distances of a few hundred meters, a synchronization mechanism has to be introduced in order to compensate for the delay times. In order to control the phase of the RF signal within a few degrees a precise resynchronization concept has to be investigated.

Synchronization of DDS

To accomplish the synchronization of the DDS-modules of the cavities in the remote control rooms the BuTiS reference clock [2] is used. Two synchronization clocks of 200MHz and 100 kHz are provided by this system. A data telegram containing frequency and phase information for each cavity is generated in the central control room and is subsequently transmitted to the control rooms of the acceleration cavities. The synchronization of the frequency data and trigger telegrams takes place in these control rooms using the delay-compensated BuTiS clocks. The setup of the system is shown in Figure 1.

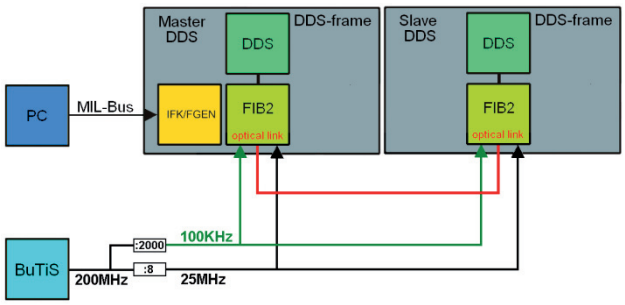

Figure 1: Implementation of the resynchronization mechanism of different DDS-units

As shown in figure 1 the Master-DDS-unit receives the frequency data from a PC by communication via a Mil-Bus. The frequency words will be sent via the optical link to the Slave-DDS-Unit. The Master-DDS-unit resynchronizes the signal relative to the BuTiS-clock. Thus the time caused by the transfer via the MIL bus is compensated. Similarly the Slave-DDS-units receive the data telegrams and synchronize the frequency words relative to the BuTiS-reference. Actually there will be 10 frequency words stored in a delay-buffer, according to a period of the 100 kHz clock cycle in all DDS-units.
Each DDS-unit takes the correct frequency word of the delay-buffer, based on the known signal propagation delay, and activates this frequency word synchronized with the rising edge of the 100 kHz clock cycle.

Realization

A Field Programmable Gate Array (FPGA) on a FIB2-Board (FPGA Interface Board) controls the DDS modules in the DDS-units. In the developed control system the FPGA of the Master-DDS-unit processes the incoming data telegram from the PC.

The FPGA printed circuit board enables the communication between the control room and the DDS modules. The main function of the FPGA on the FIB2-Board is to control the DDS-module and to configure the internal DDS registers for the required sine wave frequency output and phase. The FPGA is clocked by an external 50MHz quartz oscillator. In order to receive a quick response, the internal PLL of the FPGA increases the external 50MHz clock to the internal operation frequency of 200MHz. For the frequency generation the AD9854 DDS of Analog Device is used. The AD9854 is connected by an 8 bit bus on the FPGA and is able to generate a 100MHz sine wave output.

Discussion, Future Work

A modular FPGA-based system has been developed which is able to resynchronize the RF-system of a heavy ion beam accelerator to an absolute timescale. The system has been simulated using Modelsim.

The synchronization mechanism will be optimized and extended for other configuration-telegrams used in the RF components.

References

[1] B. Zipfel, K. Fricke-Neuderth, et al.: "Analysis of a Digital Beam Phase Control System", Workshop LLRF05, CERN, 2005

[2] P. Moritz: "BuTiS – Development of a Bunchphase Timing System", FAIR-ACCELERATORS-20, GSI Annual Report 2006.

Development of a modular Bake-Out-Controller

C. Sledz, H. Kollmus, H. Reich-Sprenger, and M. Wengenroth
GSI, Darmstadt, Germany

Abstract

For the generation of ultra-high vacuum pressures, the bake-out of the vacuum chamber is a well proven method. In general, the bake-out process of vacuum systems is rather expensive, due to the high hardware costs for the needed controller. The idea was to develop a new bake-out controller which is modularly built up, much cheaper and more flexible than the typical controllers. The developed prototype consists of three slave modules which are implementing a closed loop control for respectively 8 channels. The master module is the head of the system. It controls the whole system and provides the possibility to communicate via TCP/IP with the bake-out controller. The actual datas are rendered to a small built-in lcd screen. The whole internal communication is transacted via a RS485 bus system with a tiny ASCII protocol. The external communication with the controller is realized via a classical telnet connection or with a graphical user interface (GUI) which is also capable of logging and displaying the data of the bake-out process. The GUI is a multi-platform software providing support for Linux, Windows and MacOS X.

The Controller

Topology

The whole prototype controller consists of a master and three slave modules, connected via a RS485 bus. In case of the used bus, new slave modules can be added by simply plugging in a cable and update the master module that a new module is available. The closed-loop control of a slave module is completly independent from all other processes done on the module, like communication or calculation. It is also possible for the module to operate further if the master module is not responding anymore, so that a bake-out process can be finished regularly.

Master

The master is the core of the whole system. It controls the communication between an external user or application with the whole system. All parameters are parsed, buffered and checked for consistency on the master module, before they are sent to the corresponding slave module.

Slave

Each slave module is implementing a closed-loop control for 8 heating channels. It is also possible to use a two-point closed-loop control or a procedural integral and differential (PID) closed-loop control. The output is also fully configureable. It is feasible to change the low- or high-active behaviour for special high power output systems. The ouput pins are operated at TTL-Level. The slave module is also implementing important security functions like checking the temperature for possibility or especially checking if a thermocouple is working properly. If a failure is detected the affected channel is deactivated while the rest of the system can continue to work without being affected. A direct communication to a slave module is also possible for changing deep system settings without the need for a full reflash of the slave module, e.g. changing the module identifier or direct writing to the slave module EEPROM.

Graphical User Interface

The communication with the system can be realized via a classical telnet connection. For a more comfortable way of communication a graphical user interface (GUI) is available, which can change and visualize graphically all the parameters of the controller. The application also stores all the received data to a file for a later analyze. At the bottom of the GUI a plot of the present bake-out temperature vs. time is rendered (see Figure[1]). The application is available for Linux, MacOS X 10.6/7 and Windows.

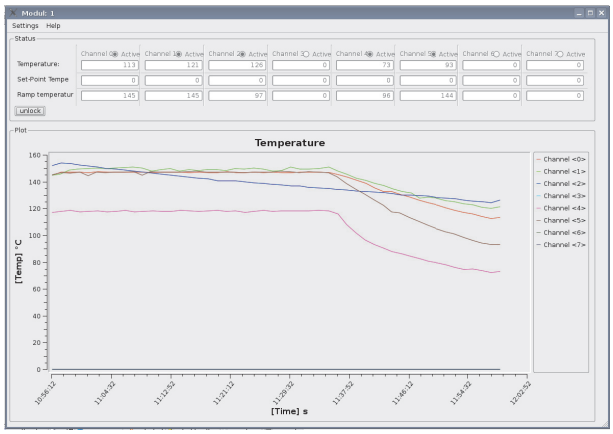

Figure 1: The realtime module view

Summary

The designed prototype has been intensively tested and the controller is working properly. It is modularly built up and flexible. The temperature control is working with an accuracy of 1-2%. The security systems capable to sense if a thermocouple is broken or not. The graphical user interface is a comfortable solution for changing and controlling all the important parameters of the bake-out controller.

Acceptance Tests and Thin Film Coatings carried out by the Vacuum Laboratory

M.C. Bellachioma, J. Cavaco, H. Kollmus, A. Kraemer, J. Kurdal, H. Reich-Sprenger, and G. Savino

GSI, Darmstadt, Germany

In the context of the technical developments for the construction of the Facility for Antiproton and Ion Research (FAIR) a large number of measurements, performed also for other groups, to define the quality of components to be mounted into the SIS 18 and in the experimental areas were carried out by the vacuum laboratory of GSI. Additionally, NEG coating of stainless steel pipes – dipole and quadrupole magnet chambers and straight pipes- were performed by means of three different magnetron sputtering systems. The experience acquired in this field during the last years allowed the vacuum laboratory to carry out also coating of NEG and Ti thin films for different universities and industries. The different works performed by the vacuum laboratory of GSI will be presented and discussed.

Acceptance Tests

Surface outgassing and presence of leaks are the main obstacles to achieving extreme vacuum. For that reason in the GSI vacuum laboratory two experimental set-ups have been built to analyse the leak rate and the released gases after heating of components, which have to be mounted in the accelerator.

Leaks may appear because of various defects of the material (presence of pores and air cracks due to mechanical or thermal stress or virtual leaks, where gas evaporates from inner excavations) and/or of the connecting areas carried our by brazing or by welding, especially between different materials (ex. ceramics-metal). The leak detection is generally performed by means of a commercial He leak detector and of a residual gas analyser optimised for the detection of the mass 4.

The outgassing study is realised performing a heating cycle up to a maximum temperature of 300°C (depending on the material) for about 48 hours and recording the pressure values and the spectra before and after heating. As an example of the measurements carried out in the last years, in Figure 1 is shown the spectra recorded for the inflector chamber of the SIS 18 before and after heating at 250°C for 48 hrs. After the heating cycle there was no evidence of gases with high masses or fluorine, poisoning for NEG, the final pressure recorded was ≈ $4x10^{-11}$ mbar, and the leak rate<$1x10^{-10}$ mbar l/s: because of these results the chamber was accepted to be mounted in the accelerator.

Thin films coating

Three different cylindrical magnetron sputtering systems

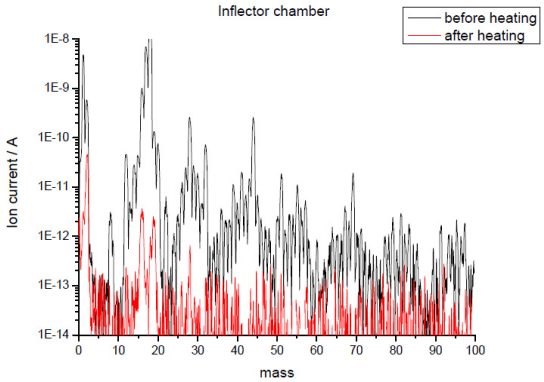

Figure 1: Spectra recorded before and after the heating cycle at 250°C for 48 hours.

were designed and commissioned at GSI starting from 2005. Essentially they consist of vacuum pumping units, equipped with a gas injection line, gauges, residual gas analysers, a manifold, and solenoids. The surface chemical composition and the good activation behaviour of the produced thin films (≈ 1 µm thick) were proved analysing small samples coated together with each vacuum pipe by means of XPS performed initially at CERN and then at the Magdeburg University. Two additional techniques for the NEG quality assurance were improved at GSI: RBS and ERDA.

During the SIS18 upgrade shutdowns from 2006 to 2009 24 dipole magnet chambers, 11 long and 5 short quadrupole chambers, and 13 straight vacuum pipes were replaced by NEG coated chambers- which corresponds to app. 65% of the SIS18 circumference. The experience acquired in this field during the last years allowed the vacuum laboratory to carry out also coating of NEG and Ti thin films for different universities and industries. In Table1 are shown the collaboration of the last two years.

INSTITUTE	N° coating
MPI Heidelberg, Germany	4
Triumf, Canada	1
FMB Feinwerk und Messtechnik, GmbH, Berlin, Germany	1
Forschungszentrum Jülich, Germany	3
Ludwig Karls Uni München, Germany	1
MIT Boston, USA	2

Table 1: Institutes and Industrial Company, which required the vacuum laboratory to deposit thin films on different vacuum pipes.

Determination of phase position for an active Rectifier circuit with sinusoidal mains current

A.Wiest, M.Dudhat, A.Döring, GSI Darmstadt, Germany

I. Introduction

In a particle accelerator magnets are used for the deflection or focusing of a particle beam. When a magnet is powered, energy is stored in its magnetic field. This energy can be fed back into the voltage intermediate link of the power converter when the current is driven to zero.

When using a power converter with classic passive feed (three phase full wave bridge rectifier, Fig. 1) the required capacity C1 of the voltage intermediate link depends on the amount of stored magnetic energy and on an acceptable voltage level. Large capacitors and high voltage levels increase cost and size of the power converter.

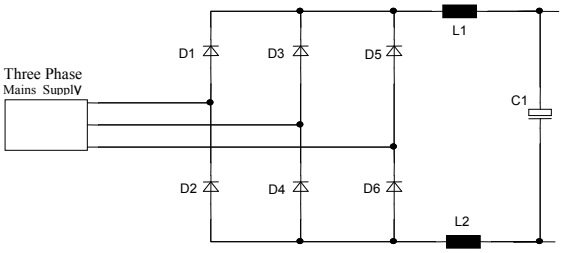

Fig. 1. Passive power supply feed

This drawback can be solved with an "Active Rectifier Circuit" (ARC), as shown in Fig.2, with a pulse width modulation strategy based on space vector analysis. With ARC the energy of the intermediate link can be fed back into the mains. Therefore the intermediate link capacity C1 can be small.

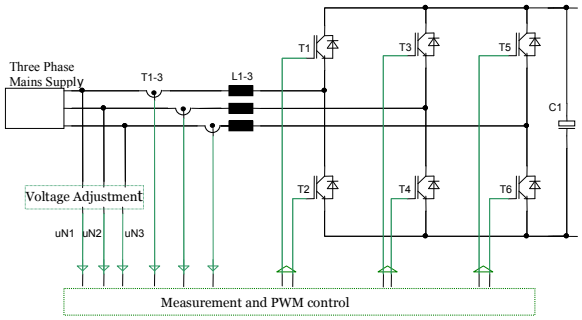

Fig. 2. Active power supply feed.

The main advantage of ARC is the sinusoidal form of the mains currents and therefore non active power is reduced.

II. Experimental implementation and results

Compared to a passive rectifier circuit, ARC requires much more hard- and software development efforts. Samples of mains currents and voltages (u_{N1},u_{N2},u_{N3}) have to be taken for the PWM (pulse width modulation) process in which the driving pattern for the transistors T1 to T6 is generated (Fig. 2).

An important part of the PWM process is the determination of the mains phase position θ, in terms of space vector notation. This is done by a complex VHDL algorithm. For this purpose a printed circuit board (PCB) with various ADCs and a FPGA- module [2] with several interfaces was developed. The VHDL implementation for calculating the mains phase angle position θ is based on a phased locked loop (PLL) as shown in Fig.3 [1].

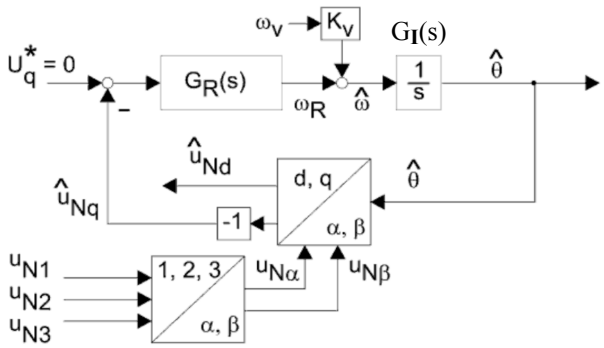

Fig. 3. PLL schematic

It includes other sub-blocks such as Clarke-transformation (αβγ), Parks-transformation (dq0), a PI controller $G_R(s)$ with anti-windup feature [3] and an integrator $G_I(s)$. The calculated phase angle θ is routed to the adaptive control unit (ACU) [4] via universal serial interface (USI) [4] on the PCB.

In operation the ADCs creates noise of about one LSB. This causes an error of the phase angle θ less than 6.7×10^{-3} degrees. This fulfils the running project requirements.

III. Conclusion

The algorithm for the active rectifier circuit is a challenge for hardware and software development. However, complex mathematical algorithms, such as the mentioned sine and cosine calculations for the PWM and other modules, can be realized using FPGA technology.

References

[1] Dirk Hasenkopf: "Regelverfahren für einen Umrichter zur Symmetrierung einphasiger Lasten in Drehstromnetzen " Book

[2] Mercury CA1 FPGA Module User Manual, Enclustra Gmbh published on 03.2011

[3] Prof. Dr.-Ing.U.Konigorski, "Digitale Regelung mechatronischer System I und II " TU-Darmstadt, Institut für Automatisierungstechnik 2007

[4] H.Ramakers, A.Döring, D.Schupp, G.Schulz, H.Welker, "Adaptive Control Unit for Digital Control of Power Converters for Magnets in GSI and FAIR Accelerators", GSI 2008

Ion Beam Tomography

H.Reichau[#1], O.Meusel[1], U.Ratzinger[1] and C.Wagner[1]

[1]Institute of Applied Physics (IAP), Goethe University, Frankfurt, Germany

Introduction

High energies and new challenging demands on the determination of relevant beam parameters require a revaluation of beam diagnostic methods. Beam tomography in combination with beam induced fluorescence measurements supports a broad spectrum of beam parameters for accelerator monitoring as well as for detailed investigations on beam dynamics in a non-invasive beam diagnostic. A new diagnostic device for beam tomography has been developed and several algorithms have been investigated for the Frankfurt Neutron Source (FRANZ) at the IAP.

Measurement Device

A rotatable vacuum chamber (Figure 1) has been developed to provide a high number of projections around the beam [1]. It has a length of 351.2 mm along the beam line and is integrated into the beam line by two CF150 flanges. Four orthogonal adapter flanges CF100 can be assembled with different measurement devices. For the measurement of beam induced fluorescence signals a CCD-Camera with a resolution of 1200 x 1600 pixel, a

Figure 1: rotatable vacuum chamber. Left: chamber with assembled CCD-camera. Right: technical construction.

shutter speed of 5µs – 60s and a wavelength sensibility of 320nm – 1000nm has been used. The chamber is able to rotate around 270° partitioned in more than 5000 angle steps. Featuring two threefold viton seals with ball bearing, the chamber is leak-proof during rotation for vacuum pressures down to 10^{-7}mbar.

Results of Tomography

Tomography has been preferentially performed with filtered back projection, since this allows a high scalability of reconstruction accuracy using a high number of profiles that can be delivered by the new rotatable vacuum chamber [1]. In preliminary inquiries the correlation between, vacuum pressure, residual gas and shutter speed has been explored [2]. First measurements have been accomplished with nitrogen at a vacuum pressure of 10^{-6} mbar and a shutter speed of 5000 ms. Projections have been taken from 180 angles around the beam (Figure 2, left), covering a length of about 70 mm of the beam in longitudinal direction. The transverse beam profile has been reconstructed with 1600 slices (Figure 2, middle) and the momentum space has been reconstructed from 180 directions around the beam (Figure 2, right).

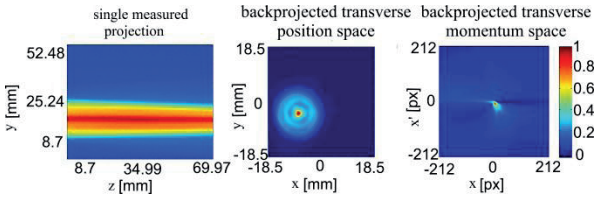

Figure 2: Left: Measured projection. Middle: back projected transversal position space. Right: back projected transversal momentum space.

Additionally, several beams have been simulated and reconstructed by the program Lintra to investigate and develop algorithms for the evaluation of the beam.

Beam Evaluation

From the reconstructed position space parameters like beam shape, beam diameter, centroid and position of the main beam axis have been identified by the investigated algorithms. The emittance of the beam has been determined from the reconstructed phase space image as RMS-emittance and from the measured projections by a gradient method as effective emittance. One major feature of the tomography approach is the beam diameter and the beam emittance determineation from several directions around the beam. Assumptions of nearly radial symmetric, Gaussian beams are not necessary when using tomography.

Outlook

In the future the determination of the longitudinal emittance will be applied for the pulsed mode of FRANZ. To use the tomography approach for beam monitoring at FRANZ the measurement and determination speed has to be improved.

References

[1] H.Reichau, Fundamentals for Routined Utilization of Tomography in Beam Diagnostics. PhD Thesis, IAP, University Frankfurt,2012

[2] C.Wagner, Entwicklung eines Teststandes für die optische Strahltomographie, Bachelor Thesis, IAP, University Frankfurt, 2011

[#]reichau@iap.uni-frankfurt.de

Analysis of the solenoid magnetic field at the PHELIX experiment

P. Schmidt[1,2], *O. Boine-Frankenheim*[1,2], *V. Kornilov*[1], *and P. Spaedtke*[1]
[1]GSI, Darmstadt, Germany; [2]TU Darmstadt, Darmstadt, Germany

Within the LIGHT-project [1], a high pulse power solenoid [2] is used for focusing of laser accelerated protons. A 3D model (see Fig. 1) of solenoid assembly was designed and simulated, using the CST Studio software [3], in order to analyse its magnetical properties. All results in this work were produced with CST [3] simulations.

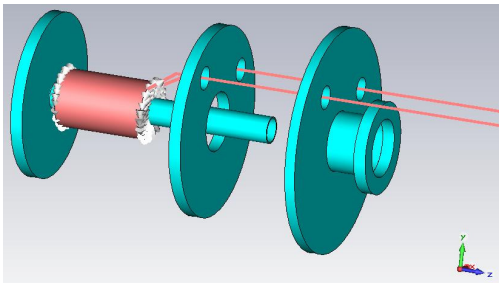

Figure 1: 3D model of the solenoid "Luftspule Darmstadt", designed with CST Studio.

First a statical simulation of the model with an operating current of $I = 9.5$ kA was done and the magnetic field from the simulation was compared to analytical calculations, where a very good agreement could be observed. Next, the simulations with a half-sine pulsed current were performed, with a maximum current $I_{max} = 9.5$ kA and with a frequency $f \approx 730.2$ Hz, in agreement with the experimental parameters. In the case of time-varying fields additional effects appear in the metal parts: The skin effect, eddy currents. Due to the induced eddy currents in the beam pipe the magnetic field strength is decreased and the field evolution is shifted in time. Figure 2 shows the time dependence of the current pulse and the magnetic field at the solenoid center from a simulation. From Fig. 2 we can see that due to the eddy currents the field reaches its maximum $\Delta t \approx 40$ μs later then the undisturbed current pulse. The losses due to the eddy currents appearing in the whole assembly are shown in Fig. 3. At its maximum, the losses are ≈ 8.6 % of the maximum operating power. Furthermore we see, that the point of minimum losses corresponds to maximum field. For the mentioned frequency the skin depth is $\delta \approx 16$ mm. The beam pipe has a wall thickness of $d = 2$mm, which means, that the skin-effect can be neglected here. On the other hand, the flanges have a thickness of about ≈ 20mm. Hence, the solenoid magnetic field is shielded due to the skin effect in the flanges (see Fig. 1) and thus vanishes almost completely behind them. For this reason, the only field appearing right behind the flanges is due to the supply wires. The supply wire field on the symmetry axes has a negative y-component with the strength of $\approx 0.34\%$ of the solenoid maximum field.

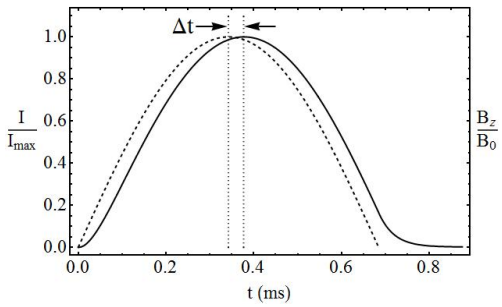

Figure 2: Time dependence of the current pulse (dashed line) and the magnetic field (full line).

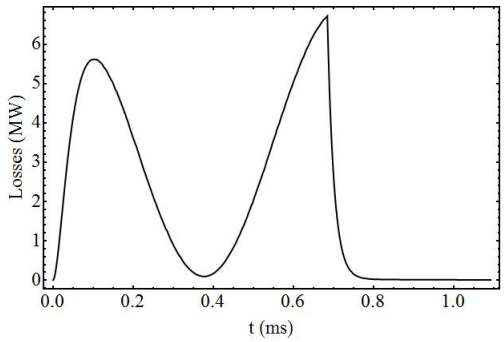

Figure 3: Simulated losses due to eddy currents in the whole assembly.

As next the emission model by [4] will be implemented into a 3D PIC simulation with CST [3] to analyse the effects of space charge.

References

[1] S. Busold et. al., Proc. of PAC 2011 Conference, p. 1960, New York, USA (2011)

[2] A. Nitzsche and B. Wustmann, "Luftspule Darmstadt", HHZ Dresden Rossendorf Abtl. FWFM, EDV-Nr. NIA15055, March 2011.

[3] CST AG, URL:"http://www.cst.com", Darmstadt, Germany, 2012

[4] P. Mora, Phys. Rev. Lett. 90, 185002 (2003).

Simulation study of TNSA from a double-layer target

Zsolt Lecz[1], *Oliver Boine-Frankenheim*[2], *and Vladimir Kornilov*[2]
[1]TU, Darmstadt, Germany; [2]GSI, Darmstadt, Germany

For intensities of the PHELIX laser [1] the Target Normal Sheath Acceleration (TNSA) is the relevant acceleration mechanism. The ion beams accelerated in this way should be collimated and transported by a solenoid to other accelerator components. Our task is to develop a model, which describes the phase-space distribution of the generated ions and electrons at μm length scale behind the target. The output of this work should be used as an input for the transport simulations. For this we use the VORPAL PIC code [2]. Here only 1D results are presented.

When a high power laser pulse ($\approx$ 100 TW) interacts with an overdense plasma a part of the electrons is heated to a relativistic temperature which leads to a very strong charge separation on the target surface with a high peak electric field (of several TV/m). The target consists of heavy ions and a very thin hydrogen-rich contamination layer on the surface. Depending on the thickness of the contamination layer the TNSA can have three regimes: quasi-static acceleration (mono-layer) [3], isothermal expansion (thick layer) [4] and an intermediate regime.

In the following we present results from two-temperature plasma expansion simulations. The hot electrons are distributed in the plasma with an exponential energy spectra, which is observed in the laser-plasma interactions: $f_e(E) \sim \exp(-E/T_h)$, where T_h is the mean kinetic energy of hot electrons, defined as the temperature. The parameters of these simulations are: $n_p = n_0$, $n_p/n_h = 10$ and $\lambda_D/\lambda_{Dc} = 80$, where n_0 is the heavy-ion density, n_p is the hydrogen layer density, n_h is the hot electron density and λ_D is the hot electron Debye length. For these numbers the cold-to-hot pressure ratio of electrons is small ($n_c T_c/n_h T_h \ll 1$). From [3] it follows that the penetration depth (δ_E) of the electric field into the target is on the order of the cold electron Debye-length (λ_{Dc}) and it is slightly increasing with decreasing the pressure ratio.

The relevant parameter for the expansion of a double-layer target is: $D = \frac{d}{\lambda_D}\frac{n_p}{n_h}$, where d is the hydrogen layer thickness. For $D \ll 1$ we find that $d \ll \delta_E$ which means the quasi-static acceleration regime, when the protons fly through the constant electric field as test particles. The heavy ions can be considered immobile on this time scale. From the spatial profile of the field [3] we can predict the maximum velocity of the quasi mono-energetic proton bunch:

$$v_{max} = 2C_s\sqrt{\ln(1 + x/(\lambda_D\sqrt{2}))} \qquad (1)$$

where $C_s = \sqrt{T_h/m_p}$ is the proton acoustic speed. The spatial extend of the electric field is about 30-40 λ_D, for which we get: $v_{max} \approx 3.5C_s$. This value is shown by the dashed horizontal lines in Fig. 1. The red points show the maximum proton velocity from the simulation at the moment of detachment, t_{det}, and the green points correspond to the end of the acceleration.

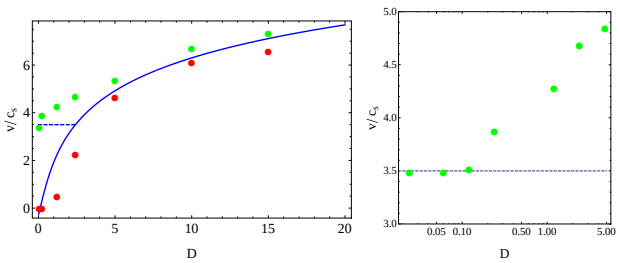

Figure 1: Theoretical prediction of maximum velocities as a function of the normalized layer thickness compared to the simulation results. The dashed lines are from Eq. (1) and the full line is given by Eq. (2)

In the other extreme case, when $d \gg \delta_E$, or $D \gg 1$, the acceleration can be described as an isothermal plasma expansion. This model holds until t_{det}, which can be calculated from the conservation of number of protons by using the results from [4]. For the proton front velocity at t_{det} we can obtain the following expression:

$$v_f = 2C_s \ln(\sqrt{2e}D) \qquad (2)$$

where $e = 2.718$. This theoretical curve is compared to the simulations in Fig. 1, left. As we can see for small and large D values the simulation result is close to the analytical solutions. The acceleration between these regimes requires more study.

Present simulations show that for large D values the electrons are co-moving with the protons after the acceleration [4], with a rapid cool-down of the electrons. In the case of the quasi-static acceleration the small proton bunch is not neutralized. The neutralization and electron cooling between these two regimes is currently under investigation.

The next step is to describe the phase-space distribution of protons and electrons beyond the 1D longitudinal acceleration, especially the energy-dependent divergence of protons is important. For this we will use the 2D simulations with the VORPAL code and the physical models discussed here.

References

[1] F. Nürnberg, Journal of Physics: Conference Series **244**, 022052 (2010)

[2] Web page: http://www.txcorp.com/products/VORPAL

[3] M. Passoni et al., Phys Rev E **69**, 026411 (2004)

[4] P. Mora, Phys. Rev. Lett., **90**, 185002 (2003)

Sensitivity Measurement of the LHC Beam Loss Monitor BLMS

A. Reiter
GSI, Darmstadt, Germany

Introduction

This short note summarises results of measurements with a LHC beam loss monitor BLMS. The tests were carried out with slowly extracted ion beams from SIS18 at the end of the HTP beam line. The BLMS detector has been developed as part of the LHC machine protection system for high-radiation environments and, therefore, is an interesting candidate for beam loss applications at FAIR, e. g. the antiproton target or selected areas of SIS100.
The response of the BLMS was compared with those of the GSI diagnostic devices in the HTP beam line. Good agreement between the measured spill structures was observed, and an estimate of the BLMS sensitivity was derived for each ion species.

Experiment Setup

Parallel to scintillating screen investigations, BLMS data were collected in two separate shifts at the beam diagnostics test area HTP using slowly extracted ion beams from the SIS18 synchrotron. The spill length was varied between 0.3 and 1.5 s. The first shift was dedicated to Uranium beams of energies between 300 and 800 MeV/u, the second to Argon and Carbon beams of 300 MeV/u. Particle numbers N_{ion} between 10^4–10^9 per spill were recorded.

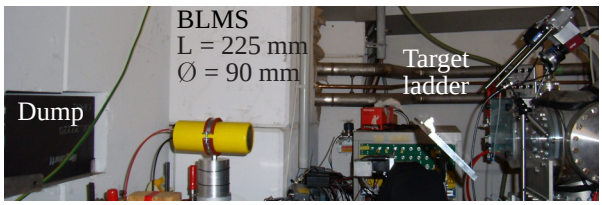

Figure 1: Setup of BLMS detector between the HTP beam dump (at left) and scintillator target ladder behind the last vacuum chamber (at right).

The BLMS detector was mounted on a pneumatic drive shown in Figure 1. The sealed stainless-steel cylinder has 5 mm thick end caps. It houses two high-voltage electrodes and a central signal electrode (60 mm diameter) from which electrons are ejected during charged particle impact. This prompt emission process remains linear up to highest count rates and provides a fast current signal.

The BLMS response was compared with those of HTP beam line devices, a secondary-electron monitor and an ionisation chamber, as well as with that of a LHC-type ionisation chamber BLMI. The latter was placed about 40 cm underneath the beam dump to monitor the particle shower. All detectors were connected to current-to-frequency converters and their output signals registered in scaler modules of the Ablass system [3]. The readout rate was set to 100 or 200 Hz.

Data Analysis and Results

For all four detectors good agreement between the measured spill structures was obtained. The BLMS sensitivity was estimated according to the Sternglass model [1] that predicts a linear correlation between electron yield N_{e^-} and stopping power dE/dX ($X = \rho \cdot x$) of the incident particle, calculated in units of MeV/(mg/cm^2):

$$N_{e^-} = Y \cdot \frac{dE}{dX} \cdot N_{ion} = S \cdot N_{ion}$$

The factor Y depends on the foil material and was derived from the measured sensitivity S. The number N_{ion} was derived from HTP devices. Energy losses along the beam trajectory up to the signal electrode were taken into account before stopping power values were calculated. The results are shown in table 1. Only the statistical uncertainty is stated, systematic effects might be as large as 50%.

Table 1: Comparison of sensitivities for Uranium, Argon, Carbon (this work), and protons (reference [2])

Ion	Energy MeV/u	S e^-/prim.	dE/dX MeV/(mg/cm^2)	Yield Y
U	800	321±3	17.9	17.9±0.2
	650	354±15	21.1	16.8±0.7
	500	575±4	36.7	15.7±0.1
Ar	300	8.8±0.4	1.08	8.1±0.4
C	300	0.9±0.1	0.097	9.0±0.9
p	63	0.25	0.014	17.9

The Uranium yield agrees with the result of [2], but a drop by a factor 2 was observed after the SIS18 energy had been reset to a previous value, probably due to beam misalignment. The smaller yields for Ar and C ions might be affected by a similar factor. Despite the inconsistency, this pilot study together with simulated responses to elementary particles [2] allows sufficiently accurate signal estimates for investigations of BLMS applications at FAIR.

The author is indebt to B. Dehning (CERN-BI) who generously made the BLMS available for the tests.

References

[1] E. J. Sternglass, Phys. Rev., Vol. 108, No. 1, 1957.
[2] D. Kramer, CERN-THESIS-2008-090, 2008.
[3] T. Hoffmann, BIW, Upton, New York, USA, 2002.

Annual neutron doses in the UNILAC experimental hall

C. Pöppe[1], P. Kewes[1]
[1]GSI, Darmstadt, Germany

Introduction

GSI has the obligation to verify that the accelerator operation is in compliance with the radiation protection ordinance and that the conditions given in the permissions of the authority (HMUELV) are fulfilled. For this purpose, dose measurements must be performed. From these dose measurements the annual dose values are derived for various radiological areas at the UNILAC and the experimental hall. The assumed definition of the different kind of radiological areas (controlled, area, survey area and free accessible areas) must be checked or – if necessary – changed.

Method of measurement

The overall dose values outside the shielding of the accelerators and experimental areas consist in most cases of neutron and photon radiation.
The GSI's Safety and Radiation Protection division provided thermoluminescence detectors (TLD, type 6776) for the dose measurements. The TLD cards consists of two ^{6}LiF (sensitive for n- and γ -radiation) and two ^{7}LiF (sensitive for γ-radiation but not for n-radiation) elements and were mounted in moderator spheres (thermal energies) made from polyethylene (PE). The TLDs are sensitive to neutrons with energies from the thermal range up to the highest energies. One advantage of this system is that the dose reading is independent on the spill structure of the beam, i.e. there are no dead time effects etc. in contrary to the active systems.

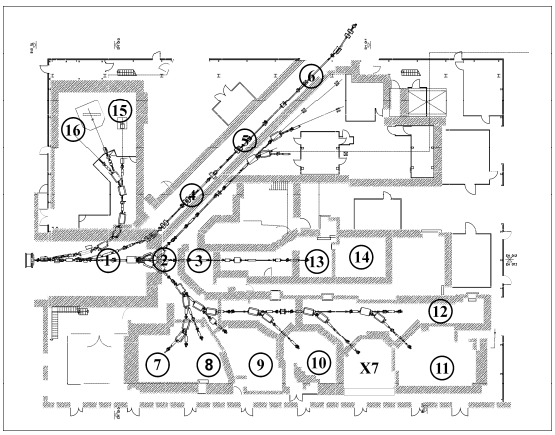

Figure 1: Measurement positions of the neutron doses in the UNILAC experimental hall outside the shielding.

Annual doses in 2010 and 2011

Figure 1 shows the downstream part of the UNILAC, a part of the TK and the experimental areas with the positions of the neutron detectors. The detectors are placed on the roof of the caves.

It can be seen (Tab. 1) that the dose values 2010 and 2011 are in the range of 0.05 mSv/a up to 8.07 mSv/a. The largest dose values in 2010 and 2011 were measured at Y7.
The dose values are generally comparable and are within the limits set by the radiation protection ordinance. The exception is Y7 where the annual dose exceeds the limit of 6 mSv/a. An experiment with a Cm-target has been the reason for the increase of the accumulated dose. Additional shielding has been placed on the roof of the cave in the beginning of 2011 which has reduced the annual dose at position 14. New measurements in 2011 (position 13) showed that it is sometimes necessary that the area around the cave must be declared as a temporarily controlled area because the dose rates are higher than 3 µSv/h (threshold dose rate value for the definition of controlled areas).
At the area X8 experiments are carried out with titanium beams in search of element 120. This 3 month beam time explains the increase of the annual dose between 2010 and 2011.
In addition to the routine measurements, an experiment was performed, to measure the dose rate in the SIS18 tunnel while a beam is stopped in TK7. Even with a uranium beam (worst case) it is possible to stay safely in the SIS tunnel.

Table 1: Measured Neutron doses in the UNILAC experimental hall outside the shielding, the positions are shown in Fig. 1

		Neutron - Dose H*(10) [mSv]	
Position	**Area**	**2010**	**2011**
1	end of UNILAC	0,09	0,08
2	end of UNILAC	0,14	0,12
3	end of UNILAC	0,12	0,11
4	TK	0,13	0,09
5	TK	0,19	0,09
6	TK	0,08	0,05
7	X 1	0,08	0,05
8	X 2,3	0,09	0,06
9	X 4	0,15	0,14
10	X 6	0,13	0,17
11	X 8	0,16	0,83
12	X 0	0,33	0,11
13	Y 7 target	-	8,07
14	Y 7 Ship	1,07	0,12
15	M 1	0,09	0,07
16	M 3	0,09	0,07

References

[1] C. Pöppe, G. Fehrenbacher, GSI annual report 2010

Annual Dose Report for SIS18 and affiliated Experimental Areas

T. Radon[1], K. Beverung[1], G. Fehrenbacher[1], P. Kewes[1], C. Pöppe[1], and J. Sauer[1]

[1]GSI, Darmstadt, Germany

High Current Beamtime

The beam times in 2011 were dominated by a high intensity experiment performed in June. A 2GeV/u N-14 beam was extracted with 6E+10 particles per second and guided to the pion production target. This is the maximum intensity which is allowed according to the SIS operation licence for this specific beam. The losses at the extraction were estimated to be in the order of 30%. In addition larger parts of the beam were lost on the following high current transfer beam line which led to very noticeable activations at several positions. This is shown in figure 1.

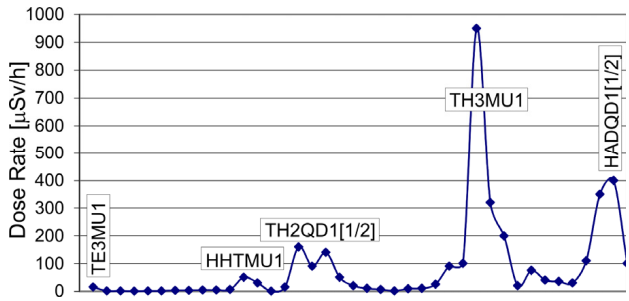

Figure 1: Residual dose rates taken 1 hour after a beam interruption at several positions along the high current transfer beam line from SIS 18 to the pion production target.

The maximum of the residual dose rates was found at the dipole TH3MU3. It was nearly 1 mSv/h. Three days after the end of this beam time block a maximum residual dose rate value of 7.5 mSv/h was measured at the magnetic extraction septum. Still up to date the activation scenario at SIS18 is influenced by this incident.

Dose Comparisons with previous years

Due to the large beam losses in the above mentioned beam time which lasted for three weeks, also the prompt dose rate outside the shielding exceeded the limits for monitored areas from the SIS extraction along the high current transfer beam line to the pion production target. This is also reflected in the annual doses for 2011, see figure 1. Annual doses in the order of 10 mSv were also measured above the SIS18 extraction area in previous years [1]. However in 2011 these values were even outreached and above the accelerator area NE5 and especially in shafts of these regions the annual doses are considerably higher compared to previous years.

References

[1] T. Radon, et al. GSI-Report 2010-1 (2010) p. 320.
[2] F. Gutermuth, T. Radon, G. Fehrenbacher, and J.G. Festag, Kerntechnik (2003), 68, 4, pp. 172-179

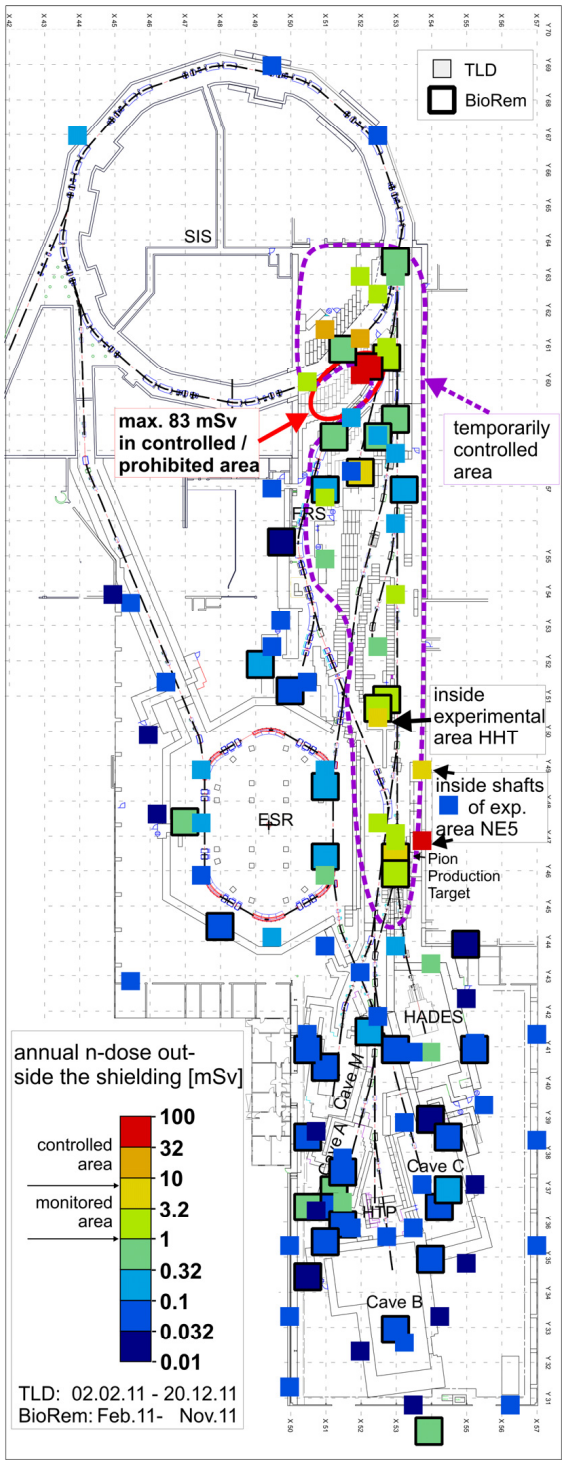

Figure 2: Map of the SIS and adjacent experimental areas. Several dose measurement positions are shown whose values were taken by active dosimeters [2] (larger squares with frame) and passive detectors [2] (smaller squares).

Dose rate calculations for the PLINAC

V. Ivanova[1], G. Clemente[1], G. Fehrenbacher[1], G. Freml[1], L. Groening[1], I. Pysmenetska[1], T. Radon[1], and W. Vinzenz[1]

[1]GSI, Darmstadt, Germany.

Introduction

The PLINAC (Proton Linear Accelerator) will accelerate protons up to the energy of 70 MeV for the injection into the synchrotron SIS 18 and the subsequent transfer to SIS100 for the production of anti-protons. The PLINAC will be situated on the 1st floor in building 20 of FAIR. The total length of the PLINAC is about of 28 m. The proton beam is generated in the source at the energy of 95 keV. Bunching and acceleration up to 3 MeV will be done in the RFQ part. Acceleration to the maximum energy of 70 MeV will be done along the two main tank groups.

Approach to the calculations

During the acceleration, beam losses along the PLINAC are expected, which will then lead to radiation fields (mainly neutron radiation) around the accelerator, the RFQ and inside the ion source region. The total beam loss in the PLINAC is about $4.3 \cdot 10^{12}$ particles/s.

34 discrete beam loss points were chosen to reproduce the calculated quasi-continuous loss scenario along the PLINAC quite exactly. The intensities and the energies of these beam losses are presented in the inserted table in Figure 1. The cave walls are considered as concrete with a density of 2.35 g/cm^3. The tank along the full beam line is made of stainless steel (type 1.4301). It has a cylindrical shape with inner and outer diameters equal to 39 cm and 48 cm, respectively. Inside the tank, the beam is surrounded by drift tubes with inner and outer diameters equal to 2 cm and 2.8 cm, respectively. Each drift tube is kept by two stems, consisting of stainless steel tubes with an axis perpendicular to the beam axis. The length of these stems is 16 cm. The stems have an inner diameter of 3 cm and an outer diameter of 3.4 cm.

For the Monte-Carlo calculations with the code FLUKA [1] an approximation of this tank structure was used. The drift tubes were presented in the form of a continuous tube with smaller inner and outer diameters for the conservation of the total volume of steel of all drift tubes. For the stems parallelepipeds were created in four perpendicular directions. The dimensions of these parallelepipeds were calculated according to the total steel volume of all stems. There are 11 quadrupole triplets included in the PLINAC with cylindrical shape having an inner diameter of 6 cm, an outer diameter of 18 cm and a length of 32 cm.

Figure 1 shows the result of the FLUKA calculations for the PLINAC. The dose rate is below 0.5 µSv/h at the entire outside of the shielding including the entrance maze which has been the goal of the calculations.

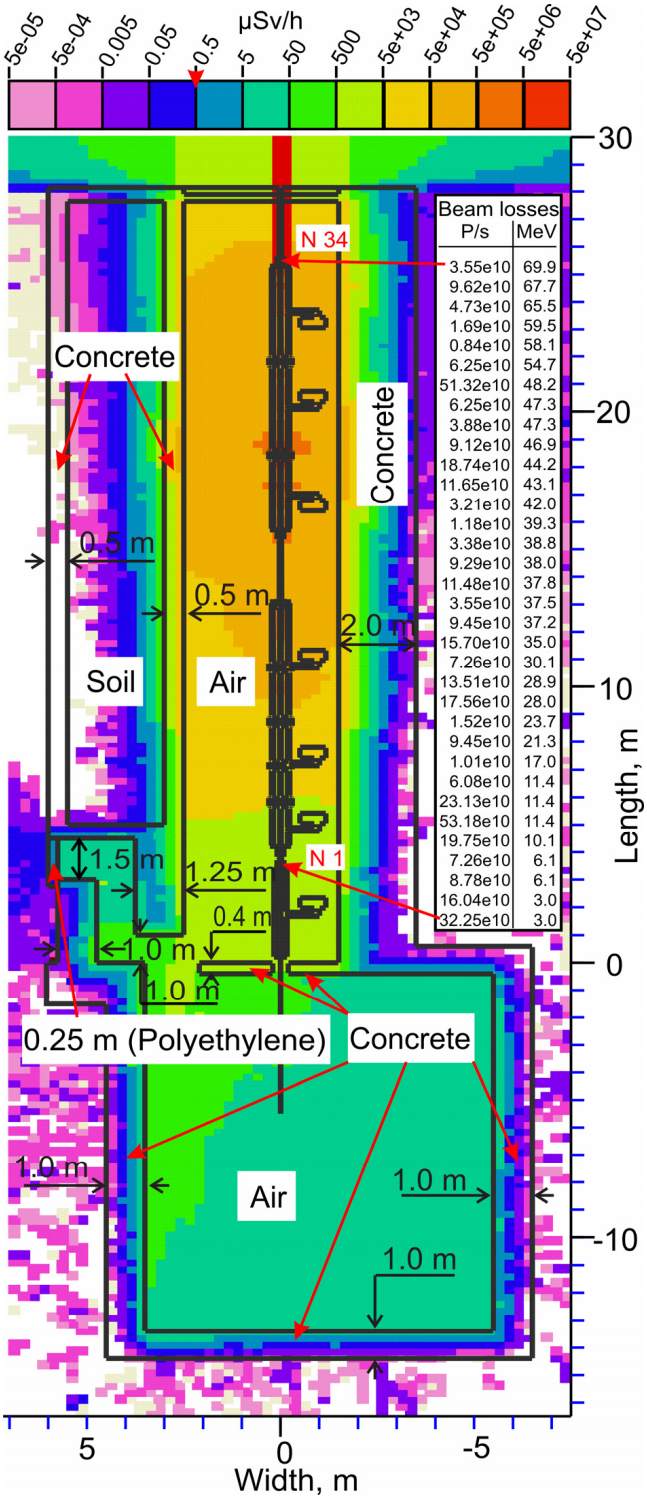

Figure 1: Total dose rate $4.3 \cdot 10^{12}$ part/s proton beam (cross section along the beam line Y = 0 m). In the table the intensities and the energies for the 34 loss points, used in calculations are represented.

References

[1] www.fluka.org.

SIS 100 extraction area

A. Sokolov[1], G. Fehrenbacher[1], N. Pyka[1], I. Pysmenetska[1], T. Radon[1], K. Vogt[1]

[1]GSI, Darmstadt, Germany

The construction of the future FAIR facility [1] requires an elaborated radiation protection scheme for the future accelerator complex to prevent considerable radiation penetration to the public and working areas. Shielding, labyrinths and ducts are approved from the radiation safety point of view using FLUKA code [2]. Besides the dose rate calculations around the beam loss points, the estimation of activation of different components of the accelerator complex during the operation is important to evaluate the way of their disposal afterwards.

A crucial part of the facility in terms of radiation is SIS100, which is used to accelerate ions like U^{28+} up to 2.7 GeV/u or protons up to 30 GeV and extract these particles into the high energy beam transport system for the use in storage rings and experiments. The beam loss of SIS100 is concentrated in the extraction straight section. In the case of slow extraction the area of beam loss is mainly situated inside the radiation resistant, water-cooled quadrupole doublet, see fig. 1. Hence, special care has been taken to elaborate adequate shielding measures to a beam loss of typically 10 % of the beam intensity. [3].

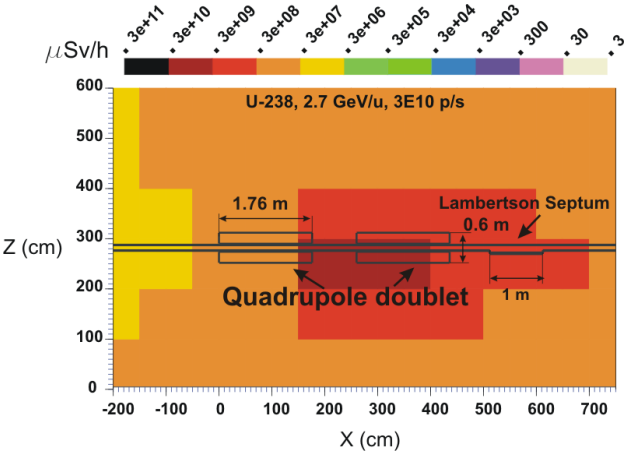

Figure 1: Section of the extraction area where the main beam loss occurs inside the quadrupole doublet in front of the Lambertson septum.

Since the design of the beam line is known, using simulations, one can estimate the activity of the optical elements, beam tube, cables, concrete, air and cooling water. Corresponding values one can find in [4]. Based on the calculations, the cooling water concept has already been planned [5].

The shielding of the maintenance tunnel adjacent to SIS100 is designed for the worst case of ^{238}U beam at maximum loss rate: 3E10 particles/s and maximum energy: 2.7 GeV/u. The equivalent dose rate in this case is below the limit of 0.5 µSv/h, see fig.2, and thus the maintenance building can be an accessible area during the synchrotron operation.

The proposed local shielding of the mentioned loss point with concrete blocks allows to remove the initially planned 1 meter of concrete along the 60 m tunnel increasing space, decreasing costs, shielding the devices placed along the tunnel's wall and localizing the highest remaining radiation during the shutdowns.

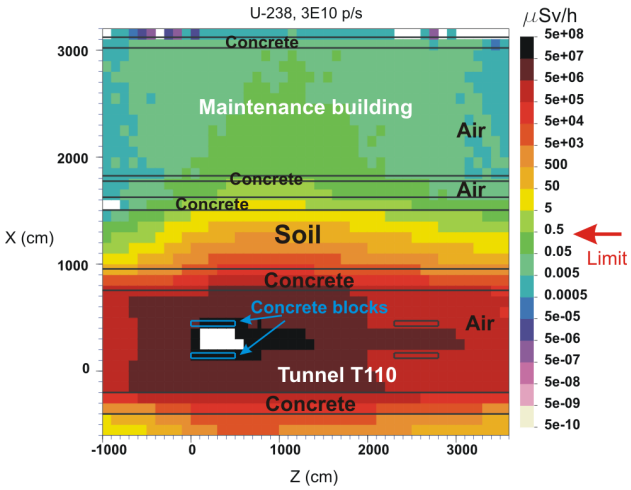

Figure 2: Equivalent dose rate in the SIS 100 tunnel and maintenance building around the loss point which is situated in between the 2 quadrupoles.

The key aspects of the extraction area are checked from the radiation safety point of view and the results are summarized in [4]. The extraction area as well as other synchrotron sections fulfils the radiation safety requirements and SIS100 plans are ready to be realized in the near future.

References

[1] FAIR Technical Design Report SIS100, P. Spiller et al., December 2008

[2] FLUKA: a multi-particle transport code, A. Fassò, A. Ferrari, J. Ranft, P. R. Sala; CERN-2005-10 (2005), INFN/TC 05/11, SLAC-R-773.

[3] Beam Loss in SIS18/100/300/HEBT, Status 24.11.2009 - Version 7.0, P.Spiller

[4] Antrag für die Errichtungsgenehmig von FAIR SIS100, K. Vogt, 2011.

[5] Konzept zur Wasserkühlung der hoch aktivierten Komponenten in der SIS100 Extraktionsgeraden N. Pyka und A. Sokolov.

FLUKA calculations with respect to radiation safety in the CBM cave.

A. Senger[1], G. Fehrenbacher[1], T. Radon [1]

[1]GSI, Darmstadt, Germany

FLUKA [1, 2] calculations were carried out for the construction permission of the building G014 (CBM Cave). One of the important components of the building G014 concerning human safety is the emergency exit.

The FLUKA dose calculations were performed out for a 35 A GeV gold beam with the intensity of 10^9 ions/s. A beam loss of 1% close to the emergency exit was assumed. The optimised geometry of the emergency exit and the FLUKA results are shown in figure 1. The dose rate level in the room behind the emergency exit is less than 0.1µSv/h.

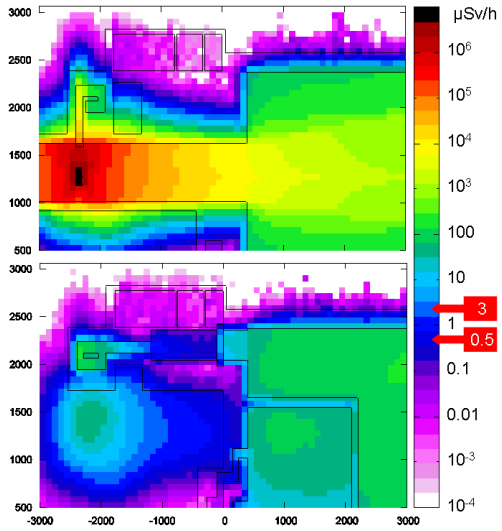

Figure 1. Dose rate (µSv/h) calculated for a gold beam of 35 A GeV with an intensity of 10^9 ions/s, and a 1% beam loss close to the exit: top – tunnel level, bottom – first floor.

The optimised geometry of the emergency exit fulfills the requirements of the radiation protection for control rooms (maximum dose rate 3 µSv/h), and can be used as a layout for the building.

A diffuser will be installed in building G004 which is connected with the CBM cave by a beam line tunnel. The diffuser is a mobile beam dump which will be used to stop the primary beam in case of an emergency.

The FLUKA dose calculations were performed for a 35 A GeV gold beam with an intensity of 5×10^{11} ions/bunch. One bunch corresponds to 1.5 s. The results of the calculations together with the geometry of the caves and the tunnel are shown in figure 2.

In order to shield the radiation from the diffuser two labyrinths were implemented in the FLUKA calculation: the first one in the tunnel and a second one at the entrance of the CBM cave. The two labyrinths are made of concrete with a total thickness of 4 m and 3 m, respectively. The vertical beam position at the diffuser in building G004 is 1.4 m below the beam line towards the CBM Cave. The maximum dose rate in the tunnel is less than 10 µSv/bunch, and below 5 µSv/bunch in the CBM cave. These values are well below the maximum permitted dose of 50 mSv/bunch for accidental radiation exposure. In conclusion, the shielding effect of the two labyrinths is sufficient to protect people in the tunnel and in the CBM cave in case of an emergency situation in G004.

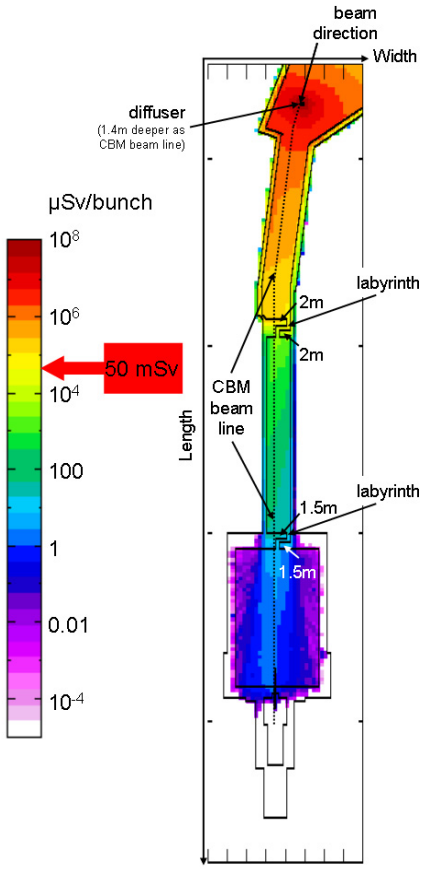

Figure 2. Dose rate (µSv/bunch) in the cave of building G004 (top of the picture), in the tunnel and in the CBM cave (bottom of the picture)

References

[1] "The FLUKA code: Description and benchmarking", G. Battistoni, S. Muraro, P.R. Sala, F. Cerutti, A. Ferrari, S. Roesler, A. Fasso`, J. Ranft, Proceedings of the Hadronic Shower Simulation Workshop 2006, Fermilab 6-8 September 2006, M. Albrow, R. Raja eds., AIP Conference Proceeding 896, 31-49, (2007)

[2] "FLUKA: a multi-particle transport code", A. Fasso`, A. Ferrari, J. Ranft, and P.R. Sala, CERN-2005-10 (2005), INFN/TC_05/11, SLAC-R-773

Shielding for the Super-FRS Tunnel 103

E. Kozlova[1], G. Freml[1], G. Fehrenbacher[1], T. Radon[1] and H. Weick[1]

[1]GSI, Darmstadt, Germany

Introduction

In the last years the shielding for the areas of the Super-FRS, where the rare isotopes are produced, was calculated. There is a pre-separator target area and a main separator [1, 2]. After production and separation, the rare-isotopes can be directed to one of the three experimental areas: the high-energy branch, the low-energy branch and the ring branch. In this report the shielding design for this branching part of the Super-FRS is presented. All three are situated in Tunnel 103. Like in all previous calculations the Monte Carlo code FLUKA [3] was used for the shielding assessment.

Prompt dose calculations

In the branches several beam losses appear: at the degrader, at the slits and dipoles. For the shielding optimization all of these possible losses were taken into account. Here only some cases are presented. Fig. 1 shows the interaction of the selected isotope ^{131}Sb with the aluminium degrader at FMF2 (Super-FRS Mid Focus 2). The calculations were done without magnetic field. In reality the selected ions will be deflected into one of the branches. The exact location of losses varies a lot with the fragment setting, instead of one scenario beam losses and targets were considered independently at many positions. For this the beam transport after the first triplet was stopped as marked in the Fig. 1.

The design goal is to limit the dose rates outside the shielding to 0.5 µSv/h. The calculations show that the shielding is sufficient to reach this goal.

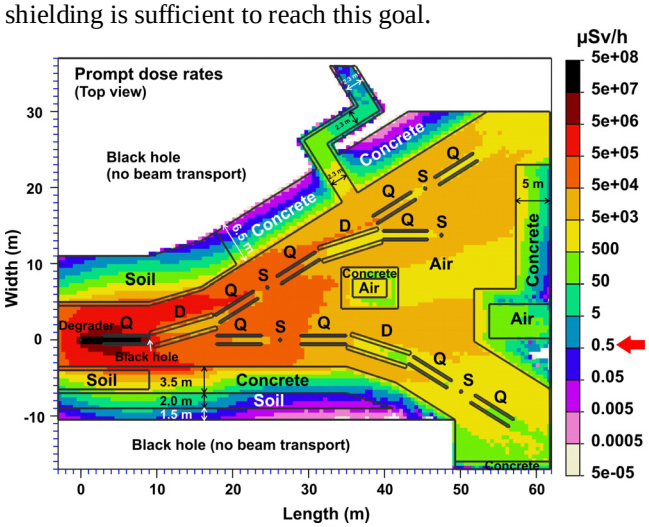

Fig.1: Horizontal view of the prompt dose rate distributions in the branch area of Tunnel 103. The antimony beam (1GeV/u, 8E9/s) interacts with the aluminium degrader (10 g/cm^2). Q – quadrupole triplet and sextupole magnets, D - dipole magnets (triplet), S – slits.

The next case is presented in Fig. 2. The interaction of the uranium beam with the slits takes place at the high-energy branch (FHF1). After the shielding, which is situated above the slits, the dose rates are below the chosen limit.

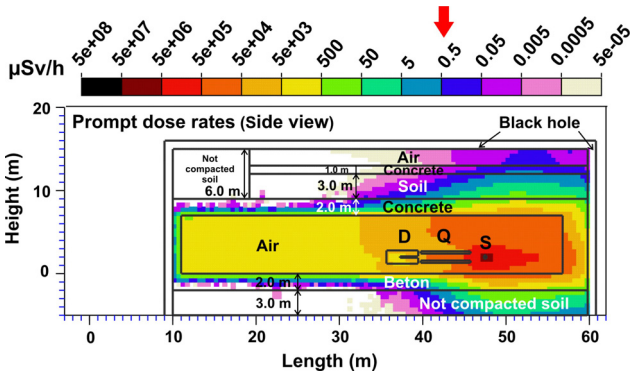

Fig. 2: Side view of the prompt dose rate distributions at the high-energy branch. 50% of the uranium beam (1GeV/u, 1E9/s) is stopped at the slits.

Fig. 3 demonstrates another important case: losses of a fragment beam represented by ^{131}Sb in the ring branch on the slits at (FRF3). In this case the dose rates in the R3B cave should be below 0.5 µSv/h. From Fig. 3 it is seen that the structure of the labyrinth and the walls thicknesses of the cave are sufficient.

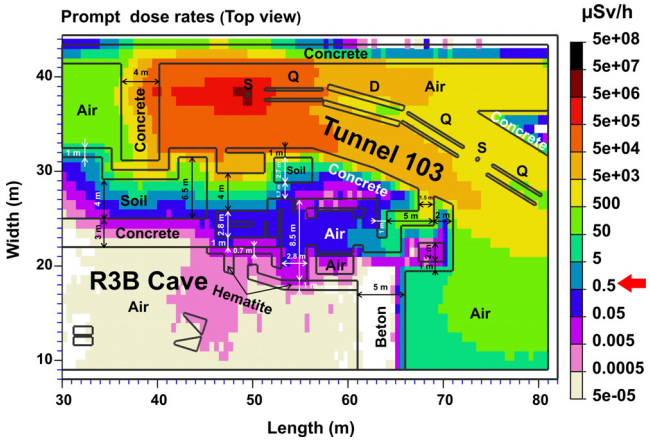

Fig. 3: Horizontal view of the prompt dose rate distributions at the ring branch. 50% of the antimony beam (740 MeV/u, 4E9/s) is stopped at the exit slit.

References

[1] E. Kozlova et al. GSI-Report 2008-1 (2008), p 247.
[2] A. Plotnikov et al. GSI-Report 2011-1 (2011), p 322.
[3] www. fluka.org

Building 50 and Tunnel 113 dosimetry calculations

A.Belousov[1,2], A.Bräuning-Demian[1], G.Fehrenbacher[1] , T.Radon[1]

[1]GSI, Darmstadt, Germany; [2]TUD, Darmstadt, Germany

Introduction

The APPA hall (building 50), as well as tunnel T113, is a part of FAIR project and will be used for experiments with high intensity heavy ion beams by the biophysics, material sciences, plasma and atomic physics groups. The beam interaction with matter results in radiation production in the cave. In order to meet the radiation safety standards, a series of calculations was performed with the Monte-Carlo code FLUKA [1].

FLUKA Calculations

The simulation geometry and the building design were fixed in a process of successive adjustment. The shielding of the experimental and beam transfer areas consists of concrete and soil layers with several meter thickness at each side. In addition, iron beam dumps with concrete cover are located in the walls at the end of each beam line. Entrance to the cave is organised as a "maze" to protect the uncontrolled area from radiation. Several "weak" points were identified and shielding solutions were found to keep all areas within the appropriate dose levels. The results of the calculations are shown as two dimensional dose rate plots with 0.5 meter spatial binning.

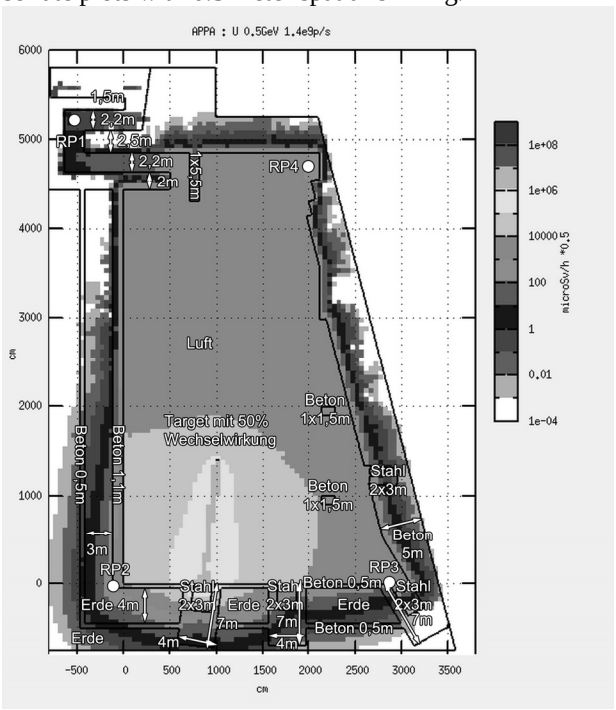

Figure 1: APPA hall dose level map example.

Bld. 50 - APPA Hall

Several scenarios with different beam types, beam directions and BD (Beam Dump) locations were simulated for the first step of the realisation of APPA:

- BD 1 – Uranium (U) 0.5GeV 1.4e9p/s with half energy losses in target.
- BD 1 - U 0.5GeV 1.4e9p/s with no losses in target
- BD 2 – Proton (p) 10GeV 5e10p/s with no losses in target
- BD 2 - U 10GeV 1e8p/s with no losses in target
- BD 3 - U 1GeV 1e8p/s with no losses in target
- BD 4 - p 4.5GeV 2.77e10p/s - no losses in target

In addition, activation calculations for soil, steel and concrete were performed for the "worst case scenario". The results indicate the remaining activity of different isotopes for each material after 30 years of beam line operation and 10 years of cool down (decommissioning scenario).

Tunnel T113

During machine operation and beam transport losses of beam particles have to be taken into account. These loss positions become significant radiation sources. The following beam loss scenarios were calculated for several locations in the tunnel 113, close to building 50, with different beam parameters:

- LP 1 - U 0.5GeV 1e10p/s with 3% losses
- LP 2 - U 0.5GeV 1e10p/s with 3% losses
- LP 3 - p 29GeV 5e12p/s with 2% losses
- LP 4 - p 29GeV 5e12p/s with 2% losses
- LP 5 - p 29GeV 5e12p/s with 2% losses

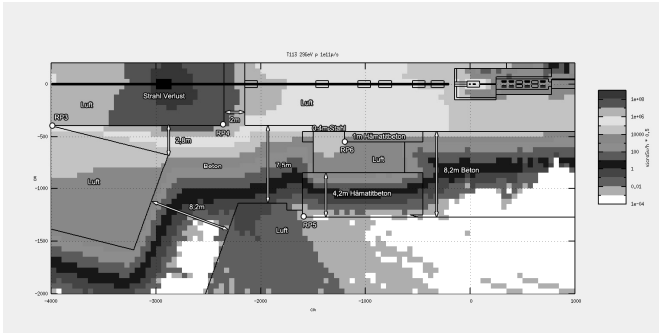

Figure 2: T113 dose level map example.

Conclusions

Due to calculations, described above, it was possible to develop architect plans for the buildings with a proper shielding design, which meets the radiation safety standards.

References

[1] www.fluka.org

First Laser Spectroscopic Observation of the Hyperfine Splitting in $^{209}Bi^{80+}$ *

M. Lochmann[1,2], Z. Andjelkovic[1,2], B. Botermann[1,2], M. Bussmann[6], A. Dax[5], N. Frömmgen[2], C. Geppert[2], M. Hammen[2], V. Hannen[4], R. Jöhren[4], Th. Kühl[1,2], Y. Litvinov[1], J. Mader[4], R. Sánchez[1,2], Th. Stöhlker[1,3], R. Thompson[8], A. Volotka[9], C. Weinheimer[4], W. Wen[7], E. Will[2], D.F.A. Winters[1,3], W. Nörtershäuser[1,2], and the E083 collaboration

[1]GSI Helmholtzzentrum, Darmstadt; [2]Universität Mainz; [3]Universität Heidelberg; [4]Universität Münster; [5]University of Tokyo; [6]Helmholtzzentrum Dresden-Rossendorf; [7]IMP Lanzhou; [8]Imperial College, London; [9]TU Dresden

Laser spectroscopic measurements of the ground state hyperfine splitting (HFS) in hydrogen-like heavy ions are of great interest because they can be used to test QED effects in extremely strong electric and magnetic fields. However, the interpretation of the experimental values is difficult since the uncertainty of the contribution of the nuclear magnetization distribution (Bohr-Weisskopf effect) conceals the size of the QED contributions. It has been suggested to overcome this limitation by measuring the HFS in both hydrogen-like and lithium-like heavy ions of the same species [1]. Thus, tests of the QED effects on the level of a few percent become feasible [2].

Bismuth is the only stable isotope where the ground state hyperfine transitions of both hydrogen-like and lithium-like ions are in a range accessible to laser spectroscopy. The HFS-transition wavelength for hydrogen-like bismuth ($^{209}Bi^{82+}$) has already been measured with a relative accuracy of 1.6×10^{-4} by Klaft *et al.*[3], but the direct search for the transition in lithium-like Bi at the ESR was so far unsuccesful.

Finally, in the beamtime in August this year, we have observed the transition for the first time. Several 10^8 ions of $^{209}Bi^{80+}$ were stored in the ESR at a fixed energy of $\approx$ 400 MeV/u ($\beta \approx 0,7$) and bunched at the second harmonic of the revolution frequency using an RF of $\approx$ 4 MHz. Due to the relativistic Doppler shift, the HFS-transition could be excited with the laser wavelength scanning at $\lambda \approx 640$ nm in collinear geometry, instead of $\lambda_0 \approx 1555$ nm in the rest frame of the ion. We used a Sirah "Cobra Stretch" dye laser, pumped by a pulsed, frequency-doubled Spectra-Physics "Quanta Ray" Nd:YAG-laser. The laser pulses were spatially and temporally overlapped in the electron cooler section with one of the two ion bunches. This bunch was used as signal bunch, whereas the other one served as a reference to correct for ion-beam-induced background. The detection took place on the oppsite side of the ESR, near the gas target section.

The moveable mirror, especially designed and built for this experiment [4, 5] turned out to be a key improvement compared to the previous beamtimes. It consists of a parabolical copper plate, centered in the beam line. The ion beam passes through a slit of ∅30 mm in the mirror. The mirror was retracted from the beam line before ion injection to the ESR, and moved in again after $\approx$ 15 s of electron cooling. The fluorescence photons emitted by the ion bunch were directed by the mirror to a photomultiplier tube. This setup proved to be significantly more efficient than the old segmented mirror section.

Data acquisition was based on a VUPROM [6] (a field programmable gate array, FPGA), designed and programmed at the experimental electronics department at GSI. A time stamp was assigned to each registered photon, synchronized to the bunching RF with a resolution of 300 MHz. In the analysis, the photon counts belonging to the reference bunch were subtracted from the signal counts. A plot of the observed resonance is shown in fig. 1. Analysis is still ongoing.

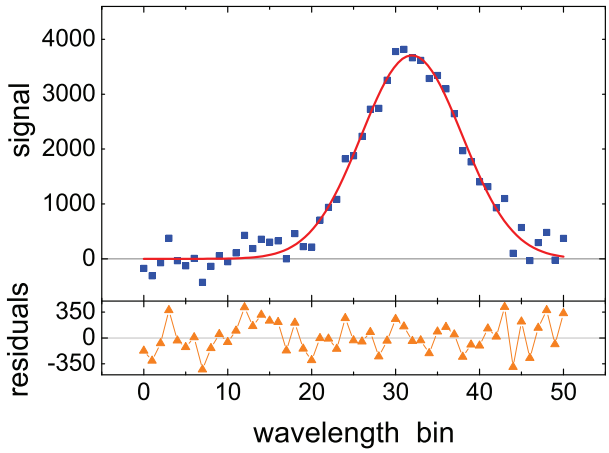

Figure 1: Background corrected signal of the HFS of $^{209}Bi^{80+}$ accumulated during $\approx$ 1 h of beamtime at the ESR. The squares are data, the line is the result of a Gaussian fit and the triangles are the fit residuals.

References

[1] V. M. Shabaev *et al.*, Phys. Rev. Lett. 86, (2001) 3959.

[2] W. Nörtershäuser, Hyperfine Interact. 199, (2011) 131.

[3] I. Klaft *et al.*, Phys. Rev. Lett. 73, (1994) 2425.

[4] D. Anielski, Diplomarbeit, Universität Münster, 2010.

[5] R. Sánchez *et al.*, GSI Scientific Report 2010, PNI-AP-10.

[6] `http://www.gsi.de/informationen/wti/ee/elekt_entwicklung/vuprom3.html`

*This work was supported by the Helmholtz Association under contract No. VH-NG-148 and by the BMBF under contract No. 06MZ9179I. The Work in Münster was supported by the BMBF under contract No. 06MS9152I.

The *g* Factor of Hydrogenlike Silicon*

A. Wagner† [1], *S. Sturm*[1,3], *F. Köhler*[2], *W. Quint*[2], *B. Schabinger*[1,3], *G. Werth*[3], *J. Zatorski*[1], *Z. Harman*[1,4], *C. H. Keitel*[1], *and K. Blaum*[1]

[1]MPI für Kernphysik, D-69117 Heidelberg; [2]GSI, D-64291 Darmstadt; [3]Institut für Physik, Johannes Gutenberg-Universität, D-55099 Mainz; [4]ExtreMe Matter Institute EMMI, D-64291 Darmstadt

The high-precision measurements of the gyromagnetic factor (g factor) of the electron bound in highly charged ions provides a very stringent test of bound-state quantum electrodynamics (BS-QED) calculations [1]. Therefore, the g factor of hydrogenlike silicon has been measured last year. Not only the nuclear charge was increased compared to the former g factor measurements of carbon [2] and oxygen [3], but also the experimental precision could be improved significantly. The determination of the g factor with a relative uncertainty of $5 \cdot 10^{-10}$ constitutes the most stringent test of BS-QED in strong fields [4].

The *g* factor measurement

To perform a g factor measurement, the Larmor frequency ν_L and the free cyclotron frequency ν_c of the ion stored in a Penning trap have to be determined. The measurement starts in the analysis trap, where the spin state of the electron can be detected with the continuous Stern-Gerlach effect. Knowing the spin state, the ion is transported to the precision trap, where the measurement of the eigenfrequencies is performed. Simultaneously to the measurement of the reduced cyclotron frequency, the Zeeman transition at the Larmor frequency is probed with microwaves. Afterwards the ion is transported back to the precision trap where again the spin state is detected. A comparison between the spin state before and after the transport to the precision trap reveals if a spin flip has been induced in the precision trap.

Repeating this cycle several hundred times and counting the number of spin flips for each frequency ratio $\Gamma = \nu_L/\nu_c$ results in a g factor resonance as shown in Fig. 1.

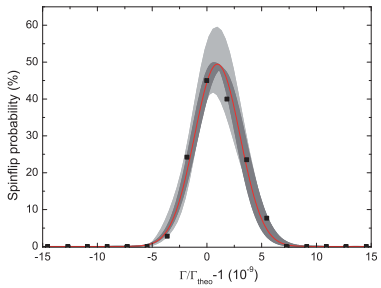

Figure 1: g-factor resonance of a single $^{28}Si^{13+}$-ion [4].

We have recorded six resonances (see Fig. 2) with different microwave powers and different axial energies to check for related systematic shifts. From the weighted average of these resonances together with the charge-to-mass ratio of electron and ion, the g factor can be determined to $g = 1.995\,348\,958\,7(5)(3)(8)$ [4]. The first number in brackets represents the statistical, the second one the systematic error and the third one the uncertainty of the electron mass.

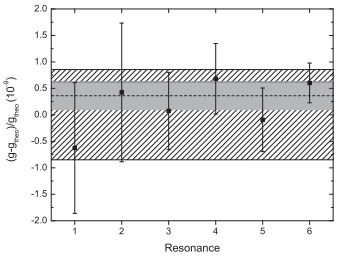

Figure 2: Experimental g factor values from six recorded resonances. The grey area indicates the experimental error, the hatched area the theoretical error. The dashed line is the weighted average of the six resonances.

A new measurement technique

Since the width of the g factor resonance is dominated by magnetic field fluctuations a new measurement technique has been developed [5], which allows for a coherent, phase-sensitive detection of the reduced cyclotron frequency. It has already been shown that the measurement noise could be reduced by one order of magnitude.

Outlook

After completing the g factor measurement of hydrogenlike silicon it is now planned to measure the g factor of lithiumlike silicon $^{28}Si^{11+}$ to rigorously test the QED theory of the electron-electron interaction.

References

[1] G. Werth *et al.*, Int. J. Mass Spectrom. **251**, 152 (2006)
[2] H. Häffner *et al.*, Phys. Rev. Lett. **85**, 5308 (2000)
[3] J. Verdu *et al.*, Phys. Rev. Lett. **92**, 093002 (2004)
[4] S. Sturm *et al.*, Phys. Rev. Lett. **107**, 023002 (2011)
[5] S. Sturm *et al.*, Phys. Rev. Lett. **107**, 143003 (2011)

* Work supported by Helmholtz Alliance HA216/EMMI and Max Planck Society.
† ankewag@uni-mainz.de

Improving the limits of the recent Local Lorentz Invariance test at the ESR*

B. Botermann[1,2], T. Kühl[1], W. Nörtershäuser[1,2], R. Sánchez[1], T. Stöhlker[1], C. Geppert[2], G. Huber[2], S. Karpuk[2], A. Krieger[2], C. Novotny[2], D. Bing[3], D. Schwalm[3], A. Wolf[3], G. Gwinner[4], T. W. Hänsch[5], S. Reinhardt[5], and G. Saathoff[5]

[1]GSI Helmholtzzentrum für Schwerionenforschung, Darmstadt, Germany; [2]Johannes Gutenberg Universität Mainz, Germany; [3]MPI für Kernphysik, Heidelberg, Germany; [4]University of Manitoba, Winnipeg, Canada; [5]MPI für Quantenoptik, Garching, Germany

Since a few years we have been performing an experimental test of Lorentz Invariance at the ESR. As reported previously [1, 2] time dilation was tested as an explicit aspect of Lorentz Invariance at the ESR using laser spectroscopy on $^7Li^+$ ions at a velocity $\beta = 0.34\ c_0$. The rest frame excitation frequency ν_0 of an electronic transition in the moving ion appears Doppler-shifted according to

$$\nu = \nu_0 \cdot \gamma \cdot (1 - \beta \cos\vartheta)\,, \qquad (1)$$

when observed under an angle ϑ relative to the laser direction in the laboratory frame. γ is the time dilation factor. For a setup with parallel and antiparallel aligned laser beams this equation simplifies to $\nu_{a,p} = \nu_0 \cdot \gamma \cdot (1 \pm \beta)$, respectively, and for the case Lorentz Invariance holds, the three frequencies ν_0, ν_a and ν_p fulfill the relation

$$\frac{\nu_a \cdot \nu_p}{\nu_0^2} = 1\,, \qquad (2)$$

which is independent of the angle ϑ and the velocity β.

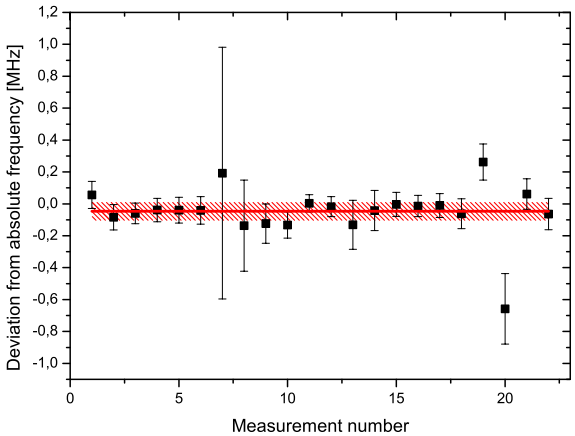

Figure 1: Results from several measurements with the Ti:Sa laser stabilized on $^{127}I_2$. The vertical axis shows the deviation from the assigned transition of the frequency stabilization. The red line is the mean value and the shaded area is the 1-σ uncertainty.

Since we are searching for deviations from equation (2), precise knowledge of the frequencies of the excitation lasers is necessary. To provide a reliable estimation for these uncertainties the stabilized frequencies of both lasers were investigated with a frequency comb referenced to a GPS disciplined Rb clock.

For this purpose, the breadboards with the laser systems that were used during our beam times at GSI were shipped to the institute for nuclear chemistry at the University of Mainz. The systems consist of a diode laser for the anti parallel light with frequency ν_a and a titanium-sapphire laser (Ti:Sa) followed by a second harmonic generation cavity which produces the light for parallel excitation with frequency ν_p. The diode laser frequency was stabilized to the $^2S_{1/2} \rightarrow {}^2P_{3/2}$ transition in atomic ^{87}Rb and the frequency of the Ti:Sa laser was stabilized to the P(42)1-14 transition in molecular $^{127}I_2$. For the diode laser as well as for the Ti:Sa an am/fm saturation spectroscopy [3] scheme was used as stabilization setup.

In both cases the heterodyne frequency between laser and the nearest comb mode was recorded. From several time series of the heterodyne frequency under varying experimental conditions, the average value of the absolute frequency and its uncertainty were extracted. For the diode laser we found

$$\nu_{DL} = (384\,228\,116.18 \pm 0.64)\,\text{MHz} \qquad (3)$$

and for the Ti:Sa

$$\nu_{Ti:Sa} = (388\,605\,083.66 \pm 0.06)\,\text{MHz} \qquad (4)$$

which are in excellent agreement with the literature values of 384 228 116.12 MHz [4] and 388 605 083.71 MHz [5], respectively. The uncertainties of these values will be used in the evaluation of the SRT test experiment.

References

[1] C. Novotny et al., Physical Review A **80**, 022107 (2009)

[2] B. Botermann et al., Canadian Journal of Physics **89**, 85-93 (2011)

[3] G. Bjorklund, Optics Letters **5**, 15-17 (1980)

[4] G. P. Barwood et al., Applied Physics B **53**, 142-147 (1991)

[5] S. Reinhardt et al., Optics Communications **274**, 354-360 (2007)

* This work was supported by the Helmholtz Association under Contract No. VH-NG-148, by the BMBF under Contract No. 06MZ9179I and by the Helmholtz Institute Mainz (HIM).

Properties of the bremsstrahlung linear polarization in polarized electron-atom collisions*

R. Märtin[1,2], R. Barday[3], J. Enders[3], Y. Fritzsche[3], U. Spillmann[2], A. Surzhykov[2,4], G. Weber[1,2], V. A. Yerokhin[2,4,5], and Th. Stöhlker[1,2,4]

[1]Helmholtz-Institut Jena, Germany; [2]GSI Helmholtzzentrum Darmstadt, Germany; [3]TU Darmstadt, Germany; [4]Universität Heidelberg, Germany; [5]Saint-Petersburg State Polytechnical University, Russia

Electron-atom bremsstrahlung is one of the most important x-ray production processes. Of particular interest is the investigation of how the photon polarization is affected if the incident electrons are themselves spin-polarized. The analysis of such a polarization transfer may reveal unique knowledge on the relativistic photon-matter interaction. While the underlying polarization correlations were already theoretical studied in the 70s [1] and have recently been revisited [2], an experimental study of the polarization transfer from incident polarized electrons to the emitted x-rays was for a long time hampered by the lack of appropriate sources for the production of polarized electrons in combination with efficient hard x-ray polarimeters. Hence the influence of longitudinal electron polarization on the orientation of the linear polarization axis of the bremsstrahlung photons has been measured only recently [3].

In a follow-up study, we applied a dedicated Si(Li) Compton polarimeter [4] in order to determine for the first time the complete linear polarization properties, i.e. the degree of the linear polarization and the orientation of the polarization axis, for different bremsstrahlung photon energies arising from transversely polarized electrons. The experiment has been performed at the test stand of the polarized electron source SPIN at the TU Darmstadt [5]. The source provides electrons with a kinetic energy of 100 keV and a high degree of electron polarization (in our case $76 \pm 5\%$). In addition to the measurement using transversely polarized electrons a reference measurement using unpolarized electrons has been performed. Figure 1 shows the azimuthal distributions of Compton-scattered photons inside the polarimeter for both settings of the electron spin orientation. Here, a thin gold foil target was used and the detector was located at an observation angle of 130°. As seen, the distribution recorded for transversely polarized electrons (squares) is shifted on the φ axis in comparison to the reference data (circles) which has been recorded for an unpolarized electron beam. This shift is equivalent to a rotation of the polarization axis which is a clear indication for the influence of a spin polarization of the incident electrons. At the same time the distribution measured using the transversely polarized electrons exhibits a stronger anisotropy which can be attributed to a higher degree of linear polarization of the emitted x-rays in comparison to the unpolarized electron case. To obtain quantitative results for the bremsstrahlung linear polarization a modified version of the Klein-Nishina formula [6] was adjusted to the Compton scattering distribution (cf. solid and dashed line in Figure 1). According to this procedure, the degree of the linear polarization P_L of the bremsstrahlung photons is increased from 28% to 31% while the axis of the polarization is rotated by an angle of $\Delta\varphi = 8°$. It should be noted that for a reliable comparison to theoretical predictions further corretions and effects, such as multiple scattering of the electrons in the target foil, has to be taken into account. Nevertheless, even the uncorrected experimental findings clearly indicate the influence of the incident electron spin polarization and deliver two separate experimental probes to study the polarization transfer in electron-atom collisions.

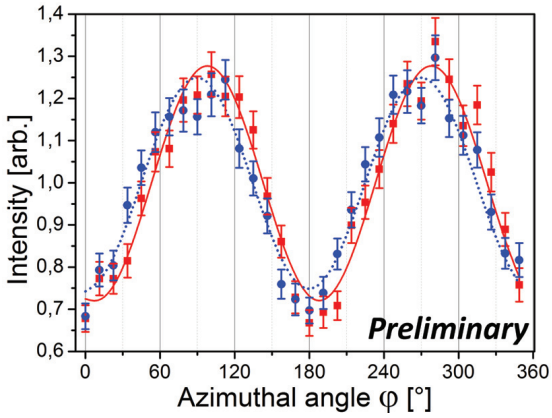

Figure 1: Projection of Compton scattering distribution on the azimuthal angle φ for the bremsstrahlung energy of 86.5±3 keV. The circles show the experimental results for an unpolarized electron beam and the dashed line indicates a fit of the Klein-Nishina equation. The squares represent the data for transversely polarized electrons. The solid line shows the respective result of the fit.

References

[1] H. K. Tseng and R. H. Pratt, Phys. Rev. A **7**, 1502 (1973).

[2] V. A. Yerokhin, and A. Surzhykov, Phys. Rev. A **82**, 062702 (2010).

[3] S. Tashenov et al., Phys. Rev. Lett. **107**, 173201 (2011).

[4] G. Weber et al., JINST 5, C07010 (2010).

[5] C. Heßler et al., Conf. Proc. EPAC08, 1482 (2008).

[6] O. Klein and Y. Nishina, Z. Physik **52**, 853 (1929).

*Work supported by DFG through SFB 634, by the state of Hesse through the LOEWE center HIC for FAIR, by the Helmholtz Gemeinschaft (Nachwuchsgruppe VH-NG-421), by GSI F+E, and by HI Jena

First Spin Flips with a Single Trapped Proton*

A. Mooser[1,2,3], *K. Blaum*[4,5], *H. Kracke*[1,2,3], *C. Leiteritz*[1], *W.Quint*[3,5], *C.C. Rodegheri*[1,4], *S. Ulmer*[6], *and J. Walz*[1,2]

[1]Institut für Physik, Johannes Gutenberg-Universität Mainz, Germany; [2]Helmholtz Institut Mainz, Mainz, Germany; [3]GSI - Helmholtzzentrum für Schwerionenforschung, Darmstadt, Germany; [4]Max-Planck-Institut für Kernphysik, Saupfercheckweg 1, Heidelberg, Germany; [5]Ruprecht Karls-Universität Heidelberg, Heidelberg, Germany; [6]present address: RIKEN Advanced Science Institute, Hirosawa, Wako, Saitama, Japan

A number of precision experiments measured the g-factor of the proton with various methods, but up to now the g-factor has never been measured directly. The most precise value for the g-factor results from measurements by Winkler *et al.* [1]. In this experiment the magnetic moment of the proton bound in atomic hydrogen has been determined with a relative precision of 10^{-8} by spectroscopy of the Zeeman effect on the hyperfine splitting. The free proton g-factor has been deduced from this measurement by subtracting theoretical bound state contributions. Our experiment, in contrast, aims for the first direct measurement of the g-factor of a single isolated proton stored in a Penning trap at a relative precision of 10^{-9} or better. The g-factor can be determined by the measurement of two frequencies of the proton in the trap. These frequencies are the Larmor frequency ω_L and the free cyclotron frequency ω_c, the g-factor is given by $g = 2\omega_L/\omega_c$.

The free cyclotron frequency is not a true eigenfrequency of the proton in trap. For the determination of ω_c all three eigenfrequencies have to be measured. A novel measurement scheme has been developed, which allows a direct measurement of the free cyclotron frequency [2]. The so called double-dressing-technique couples both radial modes to the axial mode resulting in a quintuple-dip in the axial detector. This enables the extraction of all frequency information simultaneously at the same particle position, and in thermal equilibrium with the cryogenic axial detector, see Fig. 1.

In order to measure the Larmor frequency one has to detect the orientation of spin. To this end a magnetic field inhomogeneity is superimposed, which couples the magnetic momentum to the axial mode. Hence a spin flip causes a change in the axial frequency, which is proportional to the magnetic moment and the size of the field inhomogeneity. The experimental principle has been used to compare the magnetic moments of the electron and the positron. Previous experiments thus dealt with magnetic moments on the level of a Bohr-magneton. Here the magnetic moment of the proton is on the scale of a nuclear magneton, which is about three orders of magnitude smaller. A large inhomogeneity of $3 \cdot 10^5\,\mathrm{T{\cdot}m^{-2}}$ is needed to cause a frequency jump of $190\,\mathrm{mHz}$ at an axial frequency of $600\,\mathrm{kHz}$. The angular momenta of the two radial modes couple to the axial eigenmotion, too. A large magnetic field inhomogeneity thus makes the axial mode very sensitive to energy fluctuations in the radial modes. After continuous efforts in stabilizing the radial modes of the ion, we achieved a stability of the axial frequency of a RMS value of $150\,\mathrm{mHz}$. This enabled the first observation of spin flips with a single proton in a Penning trap [3]. The spin flip resonance curve of a single proton is presented in Fig. 2.

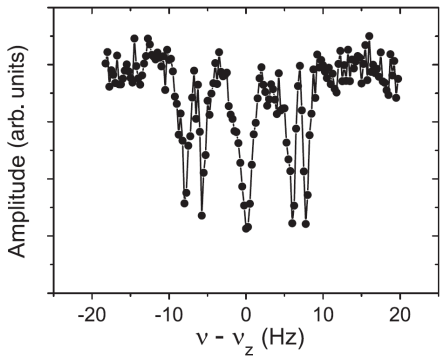

Figure 1: Quintuple-dip measurement, which carries all information on the eigenfrequencies of the trapped proton. This can be used to determine the free cyclotron frequency directly.

Taking advantage of the double Penning-trap setup, a narrow spin flip resonance is expected, which allows allows for a high precision measurement of the g-factor.

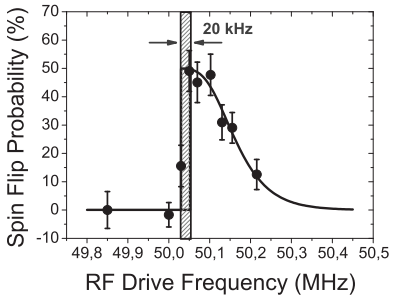

Figure 2: Proton g-factor resonance in the analysis trap, still broadened by the inhomogeneous magnetic field used for spin detection.

References

[1] P.F. Winkler. Phys. Rev., **A 5**, 83 (1972).

[2] S.Ulmer. Phys. Rev. Lett., **107**, 103002 (2011).

[3] S.Ulmer. Phys. Rev. Lett., **106**, 253001 (2011) .

* Supported by EMMI, GSI F+E

Lifetime measurement of the 2 $^3P_0$ state in He-like uranium

R.Reuschl[1,2,3], T. Gassner[1,4], U. Spillmann [1], A. Bräuning-Demian [1], A. Ananyeva [1,5], H. Beyer [1], K.-H. Blumenhagen [1,4], W. Chen [1], S. Hagmann [5],M. Hegewald [5], P. Indelicato [6], M. Schwemlein [1,2,3], S.Toleikis [7], M. Trassinelli [8], S. Trotsenko [1,9], D. Winters [1], N. Winters [1,4] and Th. Stöhlker [1,9]

[1] GSI, Darmstadt, Germany; [2] ExtreMe Matter Institute, Darmstadt, Germany; [3] Frankfurt Institute for Advanced Studies, Frankfurt, Germany; [4] Ruprecht-Karls-Universität, Heidelberg, Germany; [5] Johann Wolfgang Goethe Universität, Frankfurt, Germany; [6] Laboratoire Kastler Brossel, ENS, CNRS, UPMC, Paris, France; [7] DESY, Hamburg, Germany; [8] INSP, CNRS, UPMC Paris 6, France; [9] Helmholtzinstitut Jena, Germany

Up to now, the predictions of quantum electrodynamics (QED) have been found to be in excellent agreement with experimental data. In recent years, considerable progress in the evaluation of higher order corrections has been achieved on the theoretical side - not only for hydrogen- but also for helium-like systems - up to very heavy nuclei. He-like systems are of particular interest since they provide the simplest multi-electron configuration.

For the energy of the ground-state and the 2 $^3P_2$- state in He-like uranium experimental results have been published [1,2] . Now we are aiming at a more precise determination of the metastable 2 $^3P_0$ state. Its energy can be determined indirectly via its lifetime which has a calculated value of 57.3 ps [3,4]. The $^3P_0$ state is the longest living among all n = 2 excited states and decays via i) an E1M1 transition to the 1 $^1S_0$ state (~30%; $6*10^9$/s) and more important via ii) an E1 transition to the 2 $^3S_1$ state (~ 70%; $1.2*10^{10}$/s). This 2 $^3S_1$ state decays promptly to the ground state under emission of a 96 keV photon. By counting the number of 96 keV photons emitted by the swift projectile as a function of the distance from the target-foil, one obtains an exponential decay curve. This curve can directly be attributed to the decay of the 2 $^3P_0$ state if we assume this level to be the only feeding mechanism of the 2 $^3S_1$ state after a given time.

Previous experiments on this meta-stable state have been conducted at the BEVALAC [5] and at GSI [6]; the former providing a value of 54.4 ± 3.4 ps. With a new experimental set-up an improvement of this value to a precision of 1 ps is envisaged. The new energy-, time- and position-sensitive 2D germanium detectors permit a considerable gain in counting statistics. These detectors consist of 128 single strips with a width of 250 µm each. In order to obtain well defined data-points a Soller-slit like collimator of 1 mm thick tantalum sheets with a slit width of 1 mm is placed in front of the detector. Given a crystal width of 32 mm we should be able to measure 15 positions of the decay-curve simultaneously.

In October 2011 we have performed a test experiment with our set-up at the beamline in Cave A. A beam of U^{79+}-ions from the SIS was passed through an Al-stripper at 300 MeV/u producing U^{91+}-ions at an energy of 290 MeV/u. Afterwards the ions passed through a 1.5 mg/cm^2 nickel foil in our interaction chamber. About 5% of the initially H-like ions undergo electron capture in the Ni-foil, thus forming He-like uranium. Only a very small fraction of the electrons is directly captured into the $^3P_0$ state, but this level is fed by cascade transitions from higher n-levels. Subsequent to the 2 $^3P_0 \rightarrow$ 2 $^3S_1$ transition, the ground-state transition 2 $^3S_1 \rightarrow$ 1 $^1S_0$ occurs, whose intensity is recorded as a function of the distance from the target-foil (see figure).

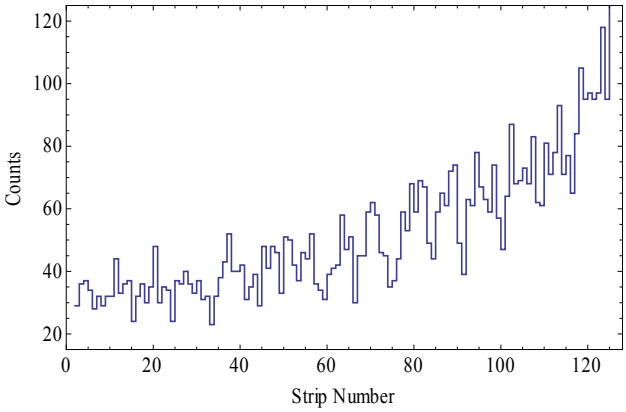

Figure 1: Decay curve measured during the beam-time with a 2D Germanium detector. Strip #125 is closest to the target (~ 5 mm), strip #1 furthest away.

The decay curve covers a span of a little more than two decay-lengths. The spectrum was obtained by applying several conditions on the data. Most important is a coincidence between the recorded x-ray and the down-charged (i.e. He-like) ion. This requires a clear separation of the charge-states behind the dipole magnet. Energy conditions were applied to select the proper transition. The limited beam time did not permit at this time to accumulate sufficient statistics for a precise value, but a preliminary analysis yields a lifetime of 57.4 ± 9.6 ps. The applicability of our method to derive lifetimes with high precision was demonstrated and the set-up is ready for a production run.

References

[1] A. Gumberidze et al., Phys. Rev. Lett. 92 (2004) 203004-1
[2] M. Trassinelli et al., EPL 87 (2009) 63001
[3] W.R. Johnson, D.R. Plante, J. Sapirstein, Adv. At. Mol. Phys. 35 (1995) 255
[4] G.W.F. Drake, Nucl. Inst. Meth. B 9 (1985) 465
[5] C.T. Munger, H. Gould, Phys. Rev. Lett. 57 (1986) 2927
[6] S. Toleikis et al., Nucl. Inst. Meth. B 235 (2005) 197

Long-lived atomic and nuclear states explored using dielectronic recombination

C. Brandau[1,2], *D. Bernhardt*[2], *C. Kozhuharov*[3], *A. Müller*[2], *S. Schippers*[2], *D. Atanasov*[3], *D. Banas*[4], *S. Böhm*[2], *A. Borovik*[2], *F. Bosch*[3], *F.J. Currell*[5], *C. Dimopoulou*[3], *A. Gumberidze*[1], *M. Heil*[3], *P. Hillenbrand*[2,3], *J. Jacobi*[2], *S. Kieslich*[2], *H. Knopp*[2], *M. Lestinsky*[3], *Yu.A. Litvinov*[3,6], *I.D. Moore*[7], *W. Nörtershäuser*[3,8], *F. Nolden*[3], *R. Reifarth*[3], *M.S. Sanjari*[3], *D. Schneider*[9], *W. Shi*[2], *D. Shubina*[6,11], *H. Simon*[3], *U. Spillmann*[3], *Z. Stachura*[10], *M. Steck*[3], *Th. Stöhlker*[3,11], *P.M. Walker*[12], *and N. Winckler*[3]

[1]EMMI/FIAS, Darmstadt; [2]Universität Gießen; [3]GSI, Darmstadt; [4]JKU, Kielce, Poland; [5]Queen's University, Belfast, U.K.; [6]MPI-K, Heidelberg; [7]University of Jyväskylä and Helsinki Institute of Physics, Finland; [8]Universität Mainz; [9]LLNL, Livermore, CA, USA; [10]IFJ, Kraków, Poland; [11]Universität Heidelberg; [12]University of Surrey, U.K.

Long-lived atomic or nuclear states are fascinating candidates for investigation and improving our understanding of transition dynamics. The hindered decay modes of metastable species are often accompanied by exotic decay pathways and/or higher order or multi-photon transitions. As a consequence of long lifetimes and extraordinary decay properties, nuclear isomers as well as atomic metastable ions play an important role in astrophysics, for precision spectroscopy, for the study of fundamental symmetries, for energy storage or —based on their small natural widths— for applications as clocks.

Storage rings provide a very clean environment with well-controlled experimental conditions for the investigation of long-lived species. Our approach for studying metastable states exploits the unique properties of the resonant process of dielectronic recombination (DR) as a spectroscopic tool. DR resonance spectra feature unique signatures associated with the long-lived excited states. Atomic metastable states show up in the DR pattern as new resonance series that originate from the initially metastable configurations. Nuclear isomeric states exhibit resonance fingerprints in the DR spectra mainly due to the distinctively different hyperfine interaction and nuclear size shifts of nuclear ground and isomeric states. In the last two years, our collaboration at the ESR storage ring has achieved substantial progress in the investigation of both, atomic and nuclear metastable states applying the DR resonance technique:

(1) Measurements with beryllium-like $^{136}Xe^{50+}$ ions were carried out that revealed resonances that could be clearly attributed to *initially metastable* $Xe^{50+}(2s2p\,^3P_0)$ ions. In Be-like ions, in the absence of nuclear spin the $^3P_0$-state can only decay via a $E1M1$ double-photon or even higher order multi-photon transitions [1]. By monitoring the intensity of resonance configurations associated with the $^3P_0$ state at time intervals 50 s apart from each other the existence of a decaying beam admixture, i.e. the metastable component was directly proven [2]. At present, the influence of unwanted effects on the decay time such as quenching of the level in the residual gas or in the magnetic fields of the ring magnets is being evaluated. As the next step, a dedicated lifetime measurement of this sought-after transition is envisaged.

(2) A pilot experiment that leveraged the DR technique for the study of nuclear isomers was successfully performed with Li-like $^{234m}Pa^{88+}$. Its isomeric state ($I^\pi = 0^-$) possesses no hyperfine splitting and decays within 1.17 min predominantly (99.84 %) due to β^--emission [3]. The $I^\pi = 4^+$ ground state features hyperfine splitting and decays substantially slower ($\tau = 6.7$ h). The fast β^--decay provides an independent way to monitor the intensity of the isomer. In our DR experiment we measured an initial resonance spectrum of $^{234(m)}Pa^{88+}$ about 30 s after beam injection, i.e., with a mixture of ground and isomeric state ions. A second data set was taken after 5 min of waiting when the isomers are expected to have completely decayed, thus resulting in a ground-state-only spectrum. Consequently, by comparison of the two data sets the DR spectrum of a nucleus in its isomeric state can be deduced.

(3) ^{235m}U is a particularly interesting nuclear isomeric state with an excitation energy as low as 76.8 eV [3]. In a preparation experiment in October 2011 we managed to produce a pure isomeric beam of Li-like $^{235m}U^{89+}$ ions by accumulation of β-decay daughters of ^{235}Pa parent ions in the storage ring. With roughly 200 ions produced every 20 mins we could perform meaningful DR experiments. The measurement highlights the sensitivity and the versatility of the combination of storage ring and the DR method. It is worth emphasizing that in contrast to Schottky techniques the DR approach is also possible for low excitation energies and thus provides access to such intriguing candidates as ^{235m}U or the famous "nuclear clock" isotope ^{229}Th [3]. These initial results on DR experiments that explore atomic and nuclear metastable states are very promising for future extensions of this method. In particular, in combination with stochastic cooling storage times of hours up to days can be achieved. This enables studies with very long-lived candidates using the DR pattern as an intensity signature.

Support is acknowledged by BMBF under contract number 06 GI 911I and by the Alliance Program of the Helmholtz Association (HA216/EMMI).

References

[1] C. Laughlin, Phys. Lett. A **75**, 199 (1979).

[2] D. Bernhardt, et al., GSI Sci. Rep. 2010, p.330; J. Phys.: Conf. Ser. in print.

[3] R.B. Firestone, et al., Table of Isotopes CD-ROM, 8th edition, 1999 update.

Mass measurements of exotic nuclei at the CSRe storage ring in Lanzhou *

X.L. Tu[1,2], H.S. Xu[1], M. Wang[1], Y.H. Zhang[1], Yu.A. Litvinov[3,4], Y. Sun[5], X.L. Yan[1,3,6], H. Schatz[7,8], X.H. Zhou[1], Y.J. Yuan[1], J.W. Xia[1], G. Audi[9], K. Blaum[6], C.M. Du[1,2], P. Geng[1,2], Z.G. Hu[1], W.X. Huang[1], S.L. Jin[1,2], L.X. Liu[1,2], Y. Liu[1], X. Ma[1], R.S. Mao[1], B. Mei[1], P. Shuai[10], B.H. Sun[11], Z.Y. Sun[1], H. Suzuki[12], S.W. Tang[1,2], J.S. Wang[1], S.T. Wang[1,2], G.Q. Xiao[1], X. Xu[1,2], T. Uesaka[13], T. Yamaguchi[14], Y. Yamaguchi[13], J.C. Yang[1], R.P. Ye[1,2], Y.D. Zang[1,2], H.W. Zhao[1], T.C. Zhao[1], X.Y. Zhang[1], and W.L. Zhan[1]

[1]IMP, Lanzhou; [2]Grad. Uni. CAS, Beijing; [3]GSI, Darmstadt; [4]NWN Uni. Lanzhou; [5]Shanghai Uni.; [6]MPIK, Heidelberg; [7]JINA; [8]MSU, East Lansing; [9]CSNSM-IN2P3-CNRS, Orsay; [10]Uni. Hefei; [11]Beihang Uni., Beijing; [12]Uni. Tsukuba; [13]RIKEN, Wako; [14]Uni. Saitama

First experiments on mass measurements of short-lived nuclei employing the isochronous mass spectrometry (IMS) at the experimental cooler-storage ring CSRe in Lanzhou, China have proven their very high potential by measuring masses of four $A = 2Z - 1$ nuclides including the astrophysically relevant ^{65}As [1]. A schematic illustration of the HIRFL-CSR facility in Lanzhou can be found in Refs. [2, 3].

Our large international collaboration continued the research program by conducting two new experiments in 2011. The data analysis of the first experiment has been already completed and the corresponding publication is in preparation. The masses of six short-lived $A = 2Z - 2$ nuclides produced in fragmentation of ^{58}Ni primary beams have been measured for the first time. These nuclides are ^{43}V ($T_{1/2} = 36.2(4)$ ms), ^{46}Mn ($T_{1/2} = 37(3)$ ms), ^{47}Mn ($T_{1/2} = 100(50)$ ms), ^{49}Fe ($T_{1/2} = 64.7(3)$ ms), ^{53}Ni ($T_{1/2} = 45(15)$ ms), and ^{55}Cu ($T_{1/2} = 40\#$ ms), where "#" denotes estimated $T_{1/2}$ values. Furthermore, masse values of ^{41}Ti ($T_{1/2} = 81(1)$ ms) and ^{45}Cr ($T_{1/2} = 50(6)$ ms), measured previously with IMS technique at GSI [4], were determined with a significantly higher accuracy. It is interesting to note that the new mass values for ^{41}Ti and ^{45}Cr are by 1.68σ and 1.04σ, respectively, more bound then the data from Ref. [4].

The second experiment has been performed in the last days of 2011, in which the neutron-rich ^{86}Kr fragments were addressed. The data analysis is presently ongoing.

The stability of the magnetic fields of the CSRe was a major factor which was limiting the mass resolving power in our first experiments (see Figure 1(a)). Therefore, a new data analysis method has been developed which allowed us to largely remove the effects due to these instabilities. The resolving power of about 170'000 has been achieved (see Figure 1(b)). The method is described in detail in Ref. [6].

In our last experiments, the magnet stability has been improved significantly. Furthermore, two vacuum chambers for two time-of-flight detectors [8] have been installed in a straight section of CSRe. The detectors will be put in operation in early 2012, thus enabling for the first time the in-ring velocity determination of each stored ion. We note, that the ILIMA project in the CR@FAIR relies on the operation of two such detectors, which can thus be tested already now.

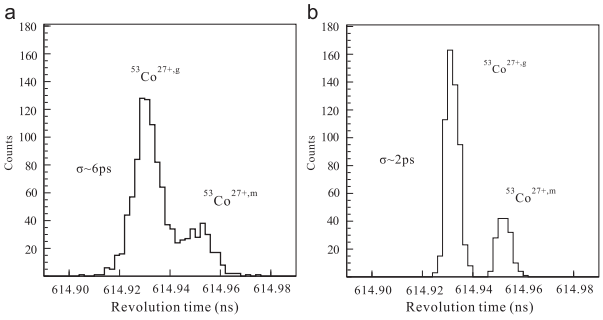

Figure 1: The revolution time spectra of ground ($T_{1/2} = 242$ ms) and isomeric ($T_{1/2} = 247$ ms, $E^* = 3174.3(1.0)$ keV [7]) states of ^{53}Co obtained with (a) the conventional method of Ref. [5] and (b) the newly developed method described in [6]. Note that the deduced excitation energy of the isomer $E^* = 3202(36)$ keV [1] is in excellent agreement with the literature value [7].

A novel resonant-cavity based Schottky detector [9] has been successfully commissioned in the CSRe [10] with which also experiments employing Schottky Mass Spectrometry are now possible.

References

[1] X.L. Tu *et al.*, Phys. Rev. Lett. **106** (2011) 112501.

[2] X.L. Tu *et al.*, GSI Annual Report 2010 (2011) 155.

[3] H.S. Xu *et al.*, Chin. Sci. Bull. **54** (2009) 4749.

[4] J. Stadlmann *et al.*, Phys. Lett. B **586** (2004) 27.

[5] B. Sun *et al.*, Nucl. Phys. A **812** (2008) 1.

[6] X.L. Tu *et al.*, Nucl. Instr. Meth. A **654** (2011) 213.

[7] A. Kankainen *et al.*, Phys. Rev. C **82** (2010) 034311.

[8] B. Mei *et al.*, Nucl. Instr. Meth. A **624** (2010) 109.

[9] F. Nolden *et al.*. Nucl. Instr. Meth. A **659** (2011) 69.

[10] Y.D. Zang *et al.*, Chin. Phys. C **35**(12) (2011) 1124.

* This work is supported by CAS and NNSFC grants 10925526, 11035007, 10675147, 10805059, 10875077, 11075103; The Major State Basic Research Development Program of China (Contract No. G2007CB815000); BMBF Grant in the framework of the Internationale Zusammenarbeit in Bildung und Forschung Projekt-Nr. CHN 11/012; H.S. is supported by NSF grants PHY06-06007 and PHY08-22648; Y.A.L is supported by CAS visiting professorship for senior international scientists (Grant No. 2009J2-23).

First Test Experiment towards Impact Parameter Sensitive Studies of Inner Shell Atomic Processes at the ESR*

A. Gumberidze[1,2], *R.D. DuBois*[1,3], *C. Kozhuharov*[4], *C. Brandau*[1,2], *M. Schwemlein*[1,5], *K.-H. Blumenhagen*[4,5], *A. Bräuning-Demian*[4], *W. Chen*[4], *R. Grisenti*†[4,6], *S. Hagmann*[4,6], *P. Indelicato*[7], *M. Lestinsky*[4], *Yu. A. Litvinov*[4], *R. Märtin*[8], *N. Petridis*[2,6], *R. Reuschl*[1,2], *U. Spillmann*[4], *S. Trotsenko*[8], *P. Verma*[9], *G. Weber*[8], *W. Wen*[10], *D.F.A. Winters*[4,5], *N. Winters*[4,5], *and Th. Stöhlker*[4,5,8]

[1]ExtreMe Matter Institute EMMI, GSI Darmstadt, Germany; [2]FIAS, Frankfurt am Main, Germany; [3]Missouri University of Science and Technology, Rolla, USA; [4]GSI Darmstadt, Germany; [5]University of Heidelberg, Germany; [6]University of Frankfurt, Germany; [7]LKB, Paris, France; [8]Helmholtz Institute Jena, Germany; [9]University of Dehli, India; [10]IMP, Lanzhou, China

At the ESR storage ring we have carried out a first test experiment aiming at impact parameter sensitive studies of inner shell atomic processes for very heavy atomic systems [1, 2]. For the measurement, the deceleration capability of the ESR was exploited. Bare bismuth (Bi^{83+}) ions were injected from the SIS into the ESR at an energy of $\sim$ 400 MeV/u and subsequently decelerated to 70 MeV/u. For the experiment, the atomic physics target chamber has been used [3]. Here, Bi^{83+} ions interacted with a supersonic jet of xenon atoms. The beam energy of 70 MeV/u was chosen as a compromise between the adiabaticity of the collision (strong perturbation) and the beam lifetime in the ring. Although the energy is not very low, one might still expect non-perturbative effects due to the heavy target. In order to obtain information concerning the impact parameter and, in particular, to pick out close collisions which are especially important for observing quasi-molecular effects, scattered Bi^{83+} ions which had undergone close collisions with xenon atoms were detected by a diamond detector mounted in a specially constructed movable pocket $\sim$3.5 m downstream from the target. The diamond detector has been constructed at GSI and consists out of four 1×1 cm strips separated by 2 mm. In the measurement position, it was covering projectile scattering angles from $\sim$0.5 - 1.0° which, for this collision, corresponds to an impact parameter range of $\sim$35 - 70 fm. In addition to the detector for the scattered projectiles, the x-rays emitted from the interaction zone were observed by an array of detectors mounted at different angles with respect to the ion beam direction. Figure 1 (top part) shows a x-ray spectrum recorded by a Ge(i) detector mounted at an observation angle of 150°. Transitions into the K-shell of H-like bismuth due to the electron transfer from the target are clearly seen, together with K and L transitions of Xe due to ionization of the corresponding shells. In addition, in the lower part, we display a coincidence time spectrum between the scattered projectile detector and a scintillator x-ray detector mounted at 35° observation angle. In spite of the few collected events, due to the relatively short measurement time, there is a strong indication of a coincidence peak resulting from x-ray emission induced by collisions well inside the K-shell radius. In future studies, we plan to use a larger particle detector along with increasing the measurement time.

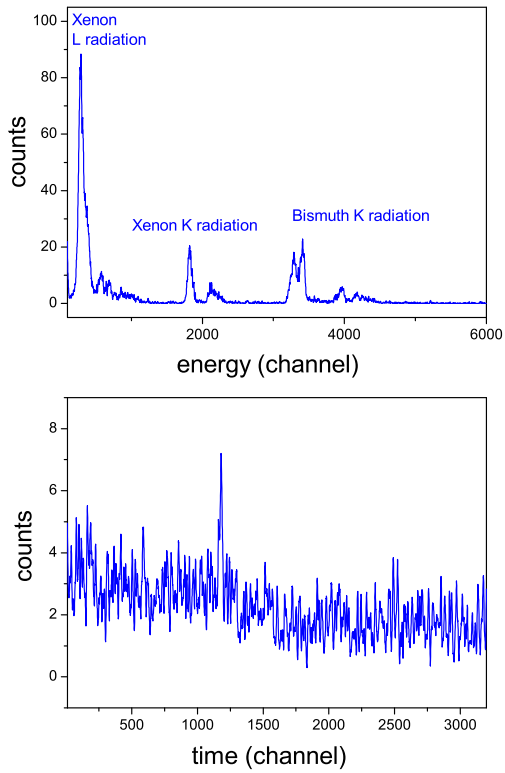

Figure 1: Top: x-ray spectrum for $Bi^{83+} \rightarrow$ Xe collisions at 70 MeV/u, recorded by a Ge(i) detector at 150° observation angle. Bottom: Coincidence time spectrum between a scintillator at 35° and the particle detector.

References

[1] Dorin-Cezar Ionescu and Thomas Stöhlker Phys. Rev. A 67 (2003) 022705.

[2] F. Bosch, in W. Greiner (ed.) Quantum electrodynamics of strong fields, Plenum Press, New York, 1983, p. 155.

[3] J. Rzadkiewicz, et al., Phys. Rev. A 74 (2006) 012511.

* Work supported by Helmholtz Alliance EMMI.
† Work supported by the Helmholtz Association (VH-NG-331).

Energy loss and cooling of HCI interacting with a H_2 droplet target beam

N. Petridis[*1,2], *A. Kalinin*[1], *U. Popp*[3], *T. Stöhlker*[3,4], *and R. E. Grisenti*[†1,3]

[1]IKF, J.W.G.-University Frankfurt; [2]FIAS, Frankfurt; [3]GSI, Darmstadt; [4]Physikalisches Institut, Ruprecht-Karls-University Heidelberg

We present measurements of the energy loss of relativistic highly charged uranium ions interacting with a target beam of near-liquid density hydrogen droplets at the experimental storage ring (ESR) at GSI [1]. The applied liquid droplet beam source has been described previously [2].

The energy loss of the ion beam was measured by employing the ESR Schottky-pickup diagnostics, which provide the revolution frequency spectrum of the circulating ions. The temporal evolution of the mean revolution frequency extracted from the Schottky spectra is used for the determination of the ion beam energy loss [3], which is plotted in Fig. 1 as a function of the (mean) target area density for the three ion energies and species investigated here. The large error bars in the target area density reflect the spatial fluctuations in the droplet target beam, which are invariably observed at the highest densities [2]. Theoretical energy losses computed with the Bethe-Bloch formula by assuming the experimental (mean) target density are shown in Fig. 1 as dashed lines, and are in fair agreement with our experimental data. Given that significantly higher energy losses would be expected due to the very high local liquid droplet density we argue that the droplets disintegrate immediately after colliding with the HCI and that our experimentally measured energy losses are primarily dominated by the interaction of the HCI with the nearly spatially uniform target consisting of the fragmentation products.

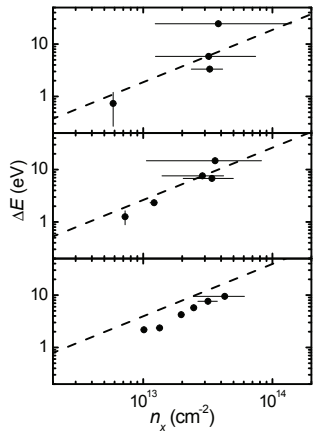

Figure 1: Experimental (filled symbols) ion energy losses of U^{91+} at 400 MeV/u (top panel), U^{91+} at 216 MeV/u (middle), and U^{89+} at 116 MeV/u (lower panel), measured as a function of the mean H_2 target area density.

The observed target density fluctuations (shown in Fig. 2(a)) can be conveniently exploited here to help in addressing the important issue concerning the ion cooling efficiency at very high target densities. The result is shown Fig. 2(b), where we plot the corresponding time evolution of the ion frequency spectrum recorded for the U^{91+} beam at 216 MeV/u and with the electron cooler turned on. The narrow frequency distribution centered at $f_0 \approx 1.6065$ MHz seen during the first 40 s recording time indicates efficient cooling of the ion beam. However, a sudden frequency shift occurring in correspondence to the $\approx 10^{15}$ cm^{-2} peak in the area density at $t \approx 50$ s can be clearly seen. This provides the most direct evidence so far for a dramatic energy loss event during interaction with a H_2 target that cannot be balanced by the electron cooler. In order to classify the observed effect, we can estimate the threshold target area density corresponding to the maximum energy loss of U^{91+} ions at 216 MeV/u that can be restored by the electron cooler by using Parkhomchuk's formula (dashed line in Fig. 2(a)). The resulting threshold density of $\approx 1.2 \times 10^{14}$ cm^{-2} is consistent with our experimental data.

Our results reveal that a liquid droplet target beam virtually behaves like a homogeneous gas jet target with respect to both energy loss and ion beam cooling. We also provide first results on ion beam cooling efficiency at high hydrogen area target densities, which are consistent with numerical estimations based on a simple model of the cooling force.

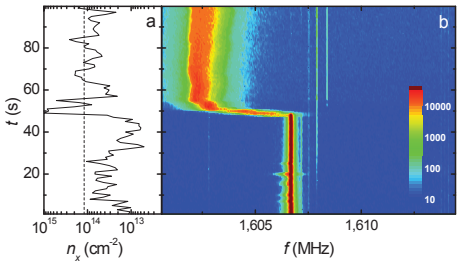

Figure 2: (a) Time evolution of the target area density measured for $T_0 \approx 27.1$ K. (b) Longitudinal Schottky frequency spectrum measured for the U^{91+} ion beam at 216 MeV/u with the electron cooler turned on.

References

[1] N. Petridis, et al., Nucl- Instr. and Meth. A 656 (2011) 1-4

[2] M. Kühnel, et al., Nucl. Instr. and Meth. A 602 (2009) 311-314.

[3] H. J. Stein, et al., Phys. Rev. ST Accel. Beams 11 (2008) 052801.

* petridis@atom.uni-frankfurt.de

† This research has been funded by the Helmholtz society under grant Nr. VH-NG-331

HITRAP – Heavy, Highly-Charged Ions at Rest – A Status Report

F. Herfurth[1], W. Barth[1], G. Clemente[1], L. A. Dahl[1], P. Gerhard[1], M. Kaiser[1], O. K. Kester[1], H.-J. Kluge[1], C. Krantz[2], N. Kotovskiy[1], C. Kozhuharov[1], M. Maier[1], D. Neidherr[1], W. Quint[1], U. Ratzinger[3], A. Reiter[1], A. Schempp[3], A. Sokolov[1], Th. Stöhlker[1], H. Vormann[1], G. Vorobjev[1], A. Wolf[2] and S. Yaramishev[1]

[1]GSI, Darmstadt, Germany; [2]MPI-K , Heidelberg, Germany; [3]IAP – Uni Frankfurt, Frankfurt, Germany

HITRAP Decelerator

The HITRAP facility is built to decelerate ions to almost rest and to provide them to the experiments [1]. First, the ions are decelerated in the experimental storage ring ESR from 400 to 4 MeV/nucleon accompanied with stochastic and electron cooling to keep the emittance small. Then, in the HITRAP linear decelerator the deceleration is performed in two additional steps. An interdigital H-type (IH) structure and a radio-frequency quadrupole (RFQ) structure are operated in inverse mode to decelerate first from 4 MeV/nucleon to 0.5 MeV/nucleon and then further to 6 keV/nucleon.

Three experimental runs were used in 2011 to commission the linear decelerator. The first run in May used a $^{54}Cr^{24+}$ beam and focused on a careful calibration of the energy analyzer after the IH. We need to know the energy of the beam after the IH with a precision of better than 1%, since the acceptance window expected for the RFQ is just 10 keV/nucleon wide at a total energy of 500 keV/nucleon. A set of thin gold foils was installed in the beam. The beam when passing through a foil is degraded in energy to produce from the 4 MeV/nucleon primary beam another beam of about 0.5 MeV/nucleon defined by the thickness and material of the foil. However, the angular straggling due to degrading together with the arrangement of two narrow slits (1 and 0.1 mm) in front of the energy analyzer reduced the beam intensity dramatically and hindered the detection of the degraded beam on the energy analyzer.

The second run was dedicated to RFQ commissioning. A huge parameter space was scanned. Since the phase acceptance of the RFQ is only about 20 degree, for every new set of IH parameters and RFQ RF-amplitude a full 360 degree phase scan had to be performed. In order to enhance the detection of decelerated particles versus the also transmitted primary beam of 4 MeV/nucleon the energy dispersive detector after the RFQ was split in two sections, one of which was covered with a mesh with a transmission of only 5%. Nevertheless, there was no beam decelerated to 6 keV/nucleon detected.

In order to investigate the detailed performance of the RFQ part in more detail and independent from the limited beam time at GSI, an off site test at the MPI for nuclear physics in Heidelberg has been set up as shown in Fig. 1. At MPI-K an electrostatic accelerator allows for a precise and broad variation of input energies as well as for a high duty cycle limited only by the thermal limit of the RFQ to about 0.2 ‰ (1 Hz ; 200µs)

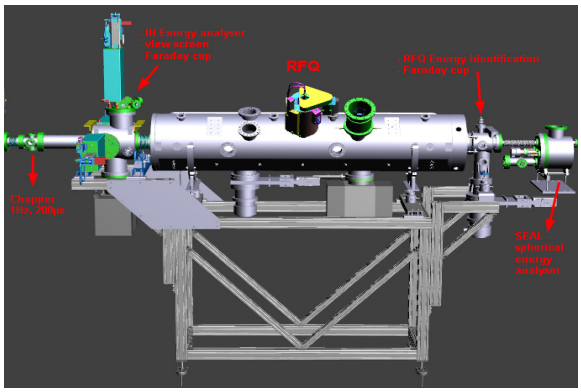

Figure 1**:** RFQ Test bench as used at MPI-K Heidelberg.

In December 2011 for the first time decelerated ions have been detected behind the RFQ. IN Fig. 2 the raw data on the energy sensitive detector are shown. A detailed characterization of required beam input energy, RF power and the resulting output energy will be done in 2012.

Additionally, the energy sensitive detector that is used at HITRAP to measure the energy spectrum after the IH structure has been calibrated. For this a beam with well known energy was sent to the detector and the resulting spectra are being compared to the ones measured during the recent experimental runs at GSI.

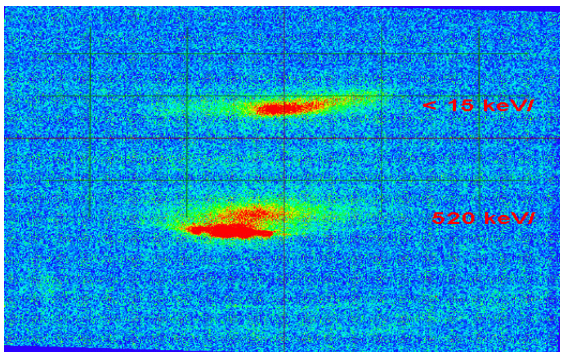

Figure 2: Raw data of the energy analyzing detector behind the RFQ. The vertical direction is energy dispersive.

The third beam time took place in September 2011 and used a $^{136}Xe^{50+}$ beam in the so called 30 MeV/nucleon SIS mode. This means that the beam is accelerated to only 30 MeV/nucleon in the SIS and will not be stripped another time after SIS extraction. This saves time in the ESR since the first declaration step from 400 to 30 MeV/nucleon can be omitted. The double drift buncher (DDB) in front of the IH was in the focus of the measurements. Together with a more detailed analysis procedure (see the 2011 annual report by A. Reiter et al.) it was

for the first time possible to relate an observed phase difference between the DDB and the IH to a phase difference in the simulation.

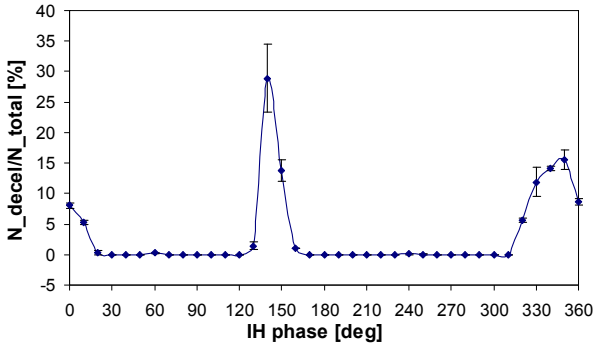

Figure 3: Fraction of decelerated particles as a function of the phase between the IH radio frequency and the one of the first cavity of the double drift buncher (DDB).

Fig. 3 shows the corresponding measurement of the IH phase relative to the phase of the first buncher cavity. Those measurements also revealed that the real gap voltage in the first buncher cavity was much smaller than required. This was later identified to be due to a to low quality factor of the resonant cavity itself which is still being investigated.

Furthermore, the energy of the primary beam from the ESR was varied in a small window of about 50 keV/nucleon to find the optimal injection energy for the IH structure. The result of both investigations was improved deceleration efficiency.

Cooler Penning Trap

This year offline tests at the HITRAP cooler Penning trap have been performed. In addition to the electron source installed in 2010 a new electron discharge ion source for delivering H_2^+ ions (m/q=2) was installed this year. Both sources are working stable and reliable and will be used in the near future to test the electron cooling of ions in the penning trap.

The electronic circuit for the axial detection of ions has been tested successfully at 4 K. At the resonance frequency of about 400 kHz the amplification is in the order of 4 to 5 with a Q-factor of 80. Nevertheless in the future the transmission of the signal out of the trap has to be improved in order to detect and identify ions with a reasonable signal to noise ratio.

In 2011 first tests in trapping mode were performed. For this electrons were injected into the Penning trap and the intensity on a faraday cup was measured (see Fig. 4). The result showed that the trapping time is only in the order of one hundred microseconds. The reason is not yet understood but this has to be improved by several orders of magnitudes if electron cooling should be used in the cooler trap.

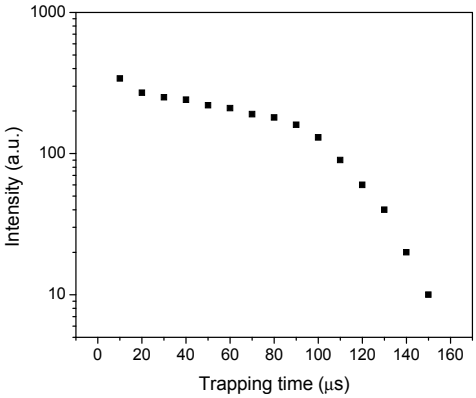

Figure 4: Intensity of trapped electrons measured at a faraday cup outside the magnetic field vs. the trapping time.

In addition, extensive theoretical studies on the collective motion of electron plasmas inside a Penning trap have been performed. By measuring the frequencies of these plasma modes it will be later possible to determine the temperature of the ions inside the trap so that one obtains information about the efficiency of the cooling process (see Fig. 5).

At HITRAP a LabVIEW based control system is in use. In 2011 also the controls of the Penning trap as well as the decelerator part in front of the trap have been included, so that a general control system is now available which simplifies the optimization of the setup.

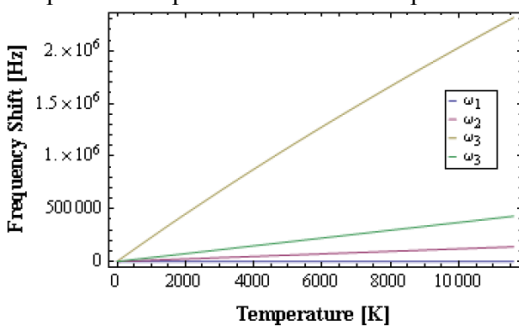

Figure 5: Temperature dependence of the frequency shifts for the first four plasma modes in HITRAP. These frequencies will be measured with an axial detection circuit.

EBIT – Vertical Beam Line

In 2011 the EBIT installed at the HITRAP platform was operating under stable conditions. For the next year it is planned to also use it for the commissioning of the vertical beam line which connects the cooler Penning trap with the different experiments. The concluding simulations of this part of the beam line are ongoing and the construction is almost finished.

The Gas Jet Target for Experiments at HITRAP*

D. Tiedemann[1], A. Malarz[6], W. Quint[2,3], K. Stiebing[1**], Th. Stöhlker[2,3,4], V. Varentsov[5†], A. Warczak[6‡] and D.F.A. Winters[2,3]*

[1]Institut für Kernphysik, Goethe University Frankfurt am Main, Germany, [2]GSI, Darmstadt, Germany, [3]University Heidelberg, Germany, [4]Helmholtz Institute Jena, Germany, [5]ITEP, Moscow, Russia, [6]Jagiellonian University, Cracow, Poland

The pulsed supersonic gas jet target for x-ray experiments with very slow highly charged ions at HITRAP [1,2] was set up at IKF in Frankfurt in 2011. The project started in 2009 and received funding from the BMBF within the framework "SPARC experiments at Fair". As HITRAP will provide the experimental beam lines with periodically injected highly charged ions, the pulsed operation mode of the gas jet target allows good vacuum conditions (~10^{-10} mbar) with a moderate pumping system (three 500 l/s turbo molecular pumps and a 2000 l/s roots pump assembly).

The design of the gas jet target was introduced in [2] and described in more detail in [3]. The arrangement of CF 100 ports assures a high flexibility for all upcoming experimental needs and especially the large CF-250 port at one side (at 90° relative to the injected beam) permits the use of different detector types and close access to the interaction region. **Figure 1** shows the setup as it was used during the first vacuum tests. Without baking the basic vacuum reached so far amounts to

is 1 10^{-9} mbar in the main chamber when the gas jet is off and 3 10^{-9} mbar when the gas jet is continuously on.

In a first step the nozzle geometry was tested by Pitot Pipe measurements and compared with theoretical calculations [4]. In these experiments the total pressure of the gas jet is recorded for different positions and distances of the Pitot Pipe relative to the nozzle. The experimental values are in good agreement with the simulations and are illustrated in **Figure 2**.

After inserting the two skimmers and careful alignment of the nozzle orientation the simulation results could be used to determine the achieved nominal[+] target thickness.

Figure 1 Setup of the gas jet target. View from the backside on the CF 250 flange and the roots pump controller.

For He and Argon target thicknesses of 4 10^{11} 1/cm² and 2 10^{11} 1/cm² could be reached respectively. Also the size of the gas jet was determined to have a diameter of approximately 0.9 mm (as predicted by geometrical considerations). The measured beam dump efficiency is in the order 97 to 99 per cent.

The gas jet target will mainly be used with Hydrogen as target gas. As depicted in [3] this requires some safety precautions. The fail safe logic units are manufactured and will be installed in the beginning of 2012.

In order to verify the above derived target parameter of the gas jet target it is planned to perform ion/atom collision experiments at the beam line of the Frankfurt RFQ-beam line For this purpose a position sensitive MCP detector will be set up behind the gas jet target to analyze the scattering of impinging ions and, in combination with a magnetic dipole, also the occurring charge transfer of the projectile.

.

References

[1] W. Quint, A. Warczak and V. Varentsov, INTAS Final Report on Research Project and Technical Information, Annex II/ GC Part D(2)
[2] K. Stiebing *et al.*, GSI Scientific Report 2009, ATOMIC-PHYSICS-26,376 (2009).
[3] D. Tiedemann *et al.*, GSI Scientific Report 2010, ATOMIC-PHYSICS-PNI-AP-21,348 (2010).
[4] Correspondence with Victor Varentsov, Liaison Officer for Russia in FAIR GmbH

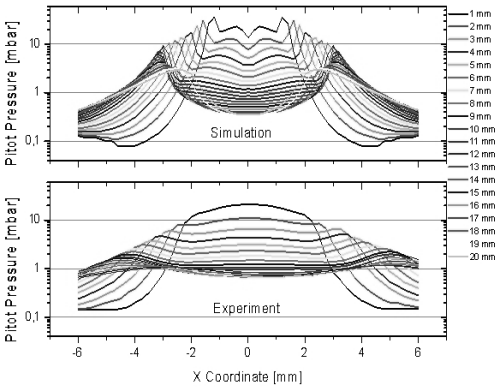

Figure 2 The total pressure was measured along the x coordinate for different distances between nozzle and Pitot Pipe.

*Work supported by EMMI
**Work supported by the BMBF (06FY9098I).
†Work supported by INTAS (Ref. Nr. 06-1000012-8956)
+nominal: the value was calculated with the specified
‡Target chamber design and construction supported by the Polish MNiSW (contract: PB 1044/B/H03/2010/38)

First trapped and cooled ions observed in SPECTRAP*

Z. Andjelkovic[1], *R. Cazan*[1], *W. Nörtershäuser*[1,2], *M. Vogel*[3], *G. Birkl*[3], *V. Hannen*[4], *R. Jöhren*[4], *C. Weinheimer*[4], *S. Bharadia*[5], *and R. Thompson*[5]

[1]Institut für Kernchemie, Johannes Gutenberg-Universität, Mainz; [2]GSI Helmholtzzentrum für Schwerionenforschung, Darmstadt; [3]Technische Univerität Darmstadt; [4]Westfälische Wilhems-Universität, Münster; [5]Imperial College London

The development of electron beam ion sources and ion storage rings about two decades ago, allowed spectroscopy experiments with highly charged ions for the first time. Their relative accuracy was limited to around 10^{-4} due to a large energy dispersion of the produced ions, and it was soon realized that a combination of ion traps with laser cooling and spectroscopy could bring an improvement of several orders of magnitude. After several years of development, the SPECTRAP experiment [1] made in 2011 the first steps towards that goal: magnesium ions were produced externally, transported into the trap and cooled to sub-Kelvin temperatures by means of laser cooling.

An overview of the experimental setup is shown in Fig.1. Situated in a laser laboratory is a frequency quadrupled fibre laser [2], producing up to 5 mW of 279 nm laser light, needed for exciting the resonance transition in singly charged magnesium used for laser cooling. After shaping and stabilizing, the beam is directed upwards, through the experimental platform, and aligned with a Penning trap on the upper level. The trap itself is located inside a Helmholtz superconducting magnet, which produces a magnetic field up to 6 T. Fluorescence is picked-up radially, directly from the trap centre. Mg ions are produced locally, as indicated in Fig.1, but the system can also accept ions through the other branch of the beamline. It is foreseen for the future connection with HITRAP, in order to gain access to highly charged ions.

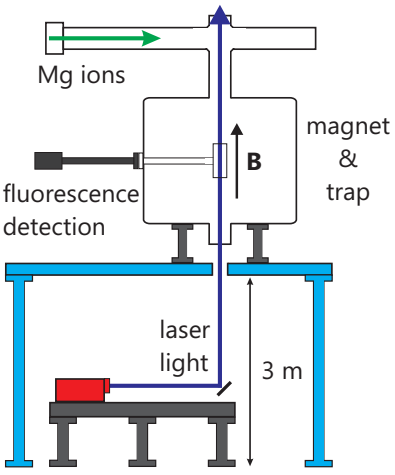

Figure 1: Overview of the SPECTRAP laser laboratory and experimental platform with the magnet and the beamline.

Mg ions were produced with a thermal source, electron impact and pulsed extraction, and then transported through the beamline into the trap. Because of the in-flight ion capture technique and the strong cooling power available with laser cooling, it was possible to store several consecutive ion source shots and accumulate up to 3000 Mg ions in the trap. After ion stacking, the trap was kept permanently closed, while the laser was scanned from approx. 1-2 GHz red detuning towards the rest frequency of the resonant transition. This was enough to cool the stored ion cloud to a sub-K temperature, as can be seen in Fig.2, by comparing the measured linewidth with the natural linewidth of the transition of 42 MHz.

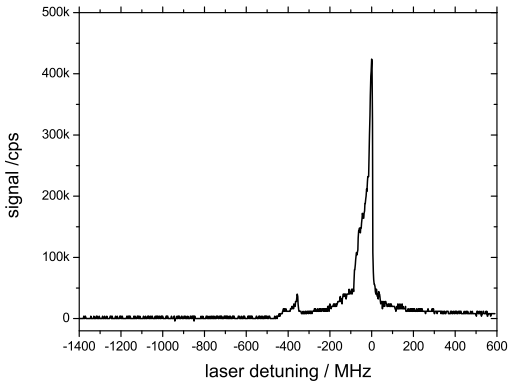

Figure 2: Fluorescence signal as a function of laser detuning. The transition width is proportional to the ion temperature.

Fluorescence was detected with a channel photo multiplier, developed in collaboration with Münster University. Its high detection efficiency and low dark count rate allowed detection of even a single trapped ion. This offered a unique opportunity to detect ions non-destructively, either by means of fluorescence detection or by electronic pick-up of the induced image charge.

The achievements are an important step towards sympathetic cooling and spectroscopy of highly charged ions, but also serve as a proof of principle for the SPECTRAP experiment.

References

[1] Z. Andjelkovic, S. Bharadia, B. Sommer, M. Vogel and W. Nörtershäuser, Hyp. Int. 196, 81 (2010)

[2] R. Cazan, C. Geppert, W. Nörtershäuser, R. Sanchez: Hyp. Int. 196, 177 (2010)

*Work supported by HGF under contract VH-NG-148 and BMBF grant 06MS9152I.

New diagnostics for laser cooling at the ESR*

M. Bussmann[1], *U. Stuhr*[1], *M. Siebold*[1], *U. Schramm*[1], *C. Geppert*[2,3], *M. Lochmann*[2,3], *W. Nörtershäuser*[† 2,3], *R. Sanchez*[2], *C. Dimopoulou*[3], *F. Nolden*[3], *M. Steck*[3], *C. Kozhuharov*[3], *Th. Kühl*[2,3,5], *Th. Stöhlker*[3,4,5], *D. Winters*[3,4], *S. Tichelmann*[6], *G. Birkl*[‡ 6], *T. Beck*[6], *Th. Walther*[† 6], *X. Ma*[7], *and W. Wen*[§ 7]

[1]Helmholtz-Zentrum Dresden-Rossendorf; [2]Johannes-Gutenberg-Universität Mainz; [3]GSI Helmholtzzentrum für Schwerionenforschung GmbH, Darmstadt; [4]Ruprecht-Karls-Universität Heidelberg; [5]Helmholtz Institut Jena; [6]Technische Universität Darmstadt; [7]Institute of Modern Physics, Lanzhou (China)

Many stored relativistic ion beams can effectively be cooled by means of laser cooling, yielding unprecedented momentum spreads of the order of $\Delta p/p \sim 10^{-7}$, as has been demonstrated at the Experimental Storage Ring (ESR) [1, 2]. These results have stimulated preparations for laser cooling at the extreme relativistic energies available at FAIR, for instance at the HESR and the SIS100/300 [3]. For this, broad-band laser cooling and efficient optical beam diagnostics have to be developed and tested [4].

We report on first results of optical bunch-length measurements of relativistic ion bunches stored in the ESR. Two new optical systems, which detect the light from the ion bunches, were installed at the internal target of the ESR. The first is a narrow-band VUV (solar blind), low dark-current photomultiplier tube with optimum efficiency around $\lambda \approx 155$ nm, which is mounted on a highly transmissive VUV CaF_2 viewport. The second system is a CsI-coated photo channeltron with an aperture of 25 mm, which is mounted inside the ESR's UHV (see Fig. 1).

Figure 1: Photograph of the VUV photo channeltron and its holder on the CF-flange. The system can be baked at 200°C and exhibited a clean residual gas spectrum at 10^{-11} mbar.

Figure 2 shows first preliminary results from a beam-time in August 2011 (E083). Here, Li-like bismuth ions, at about 70% of the speed of light, were stored in two bunches inside the ESR. The raw data, taken by both new detection systems, clearly shows the reproduceable structure of the two ion bunches. Unlike in laser cooling experiments, here the light originated from the relaxation of residual gas molecules that were collisionally excited by the ions.

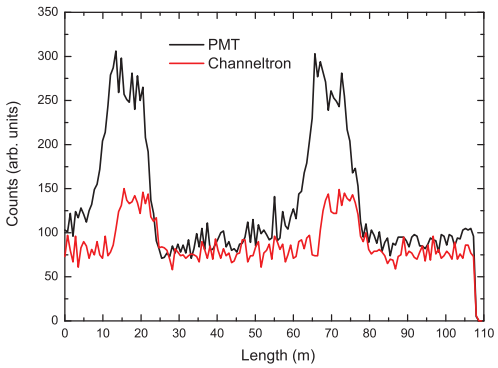

Figure 2: Preliminary data recorded in August 2011. The signals are taken by the VUV PMT and the VUV photo channeltron. The ion bunches are about 9 m in length.

For the upcoming experiment (E089) at the ESR, a diode-based CW laser system (1028 nm) with two frequency doubling stages (514 and 257 nm) and a pulsed laser system will be used for laser cooling.

With the results presented here, precise optical diagnosis of important beam parameters, such as the bunch-length, is in reach. It should be noted that, besides the integral signal from the ion bunch, also the arrival times of the individual photons are available and can potentially be used to infer correlations in the ion beam [4]. Moreover, with high photon count rates and long beam lifetimes, it should be possible to significantly increase the resolution of bunch-length measurements, surpassing the limitations of standard bunch-length measurements available at the ESR. This will also be an important step for the use of laser cooling and optical diagnostics for precision experiments at FAIR.

References

[1] U. Schramm, D. Habs, Progr. Part. Nucl. Phys. **53**, 583 (2004).

[2] M. Bussmann, U. Schramm, D. Habs *et al.*, J. Phys. Conf. Series. **88**, 012043 (2007).

[3] H. Backe, Hyp. Int. **171**, 93 (2006).

[4] M. Bussmann *et al.*, COOL09 Proceedings, IMPCAS Lanzhou, Atomic Energy Press, 22 (2009)

* Work supported by HI Jena
† Work supported by HGF, contract VH-NG148.
‡ Work supported by BMBF.
§ Work supported by DAAD.

Commissioning of the electron spectrometer at the ESR

P.-M. Hillenbrand[1,2], *S. Hagmann*[1,3], *C. Brandau*[4], *R.D. DuBois*[5], *A. Gumberidze*[4], *C. Kozhuharov*[1], *M. Lestinsky*[1], *Y.A. Litvinov*[1], *A. Müller*[2], *R. Reuschl*[4], *H. Rothard*[6], *S. Schippers*[2], *U. Spillmann*[1], *S. Trotsenko*[1,7], *D. Winters*[1], *and Th. Stöhlker*[1,7,8]

[1]GSI Darmstadt; [2]Universität Giessen; [3]Universität Frankfurt; [4]ExtreMe Matter Institute Darmstadt; [5]University of Missouri-Rolla; [6]CIRIL-Ganil, Caen, France; [7]Helmholtz Institut Jena; [8]Universität Heidelberg

While typical experiments at the ESR studying ion-atom collisions use the emitted x-rays and the up- and down-charged projectiles as observables, the variety of processes to be investigated is greatly enhanced, if the emitted fast electrons can be observed as well. Employing different combinations of coincidences, processes like *electron loss to continuum ELC* and *(radiative) electron capture to continuum (R)ECC* can be explored in parallel.

For that purpose the electron spectrometer located at the ESR downstream from the gastarget has been built to detect electrons emitted with a velocity close to the projectile velocity $v_e \approx v_p$ from the interaction point within a forward cone of $\vartheta \leq 3°$.

The spectrometer consists of two dipole magnets with an iron-free quadrupole triplet in between. The aim is to have a telescopic mode, where a given momentum interval can be selected using momentum defining slits and the corresponding emission cone is projected onto a position sensitive detector. Ideally the projection on the detector is a pure function of the emission angle and is not influenced by the selected momentum interval.

Two principle setups are possible: Either both magnets bend electrons into the same direction (+60°/+60°-configuration) or they bend into opposite directions (+60°/-60°-configuration). In order to compare both possibilities extensive simulations have been performed using the GSI beam simulation software MIRKO. It was shown that while the +60°/-60°-configuration has a high momentum resolution of theoretically up to $\Delta p/p = 2 \cdot 10^{-3}$, the +60°/+60°-configuration can lead to an achromatic system with a resolution of only $\Delta p/p = 5 \cdot 10^{-2}$. However a telescopic mode with a momentum-independent emission angle projected onto the detector can rather be realized within the +60°/+60°-configuration. Besides that it also has to be taken into account that a higher dispersion directly leads to lower countrate and thus lower statistics.

A first commissioning run using the +60°/-60°-configuration shown in Fig. 1 was done during a beamtime in August 2010, with the aim of a high electron momentum resolution. A Be-like Bi^{79+}-beam at 98 MeV/u and a N_2-target was used. By coincidence measurements the RECC and ELC reactions

$$Bi^{79+} + N \rightarrow Bi^{79+} + N^+ + e^- + \gamma \qquad (1)$$

$$Bi^{79+} + N \rightarrow Bi^{80+} + N + e^- \qquad (2)$$

could clearly be identified.

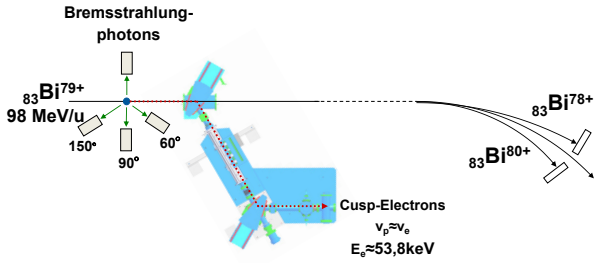

Figure 1: Experimental setup at the ESR used in 2010 (+60°/-60°-configuration: dipoles bend into opposite directions)

Fig. 2 shows the recorded x-ray-spectra under 90 °, random and in coincidence with the electron. A 2000 cm^2 Ge-detector was used. The random spectrum (blue) shows the typical structures of *radiative electron capture REC* into *L*- and *M*-shell. The background at the lower-energy side is due to bremsstrahlung. The spectrum of x-rays in coincidence with electrons having the same velocity as the projectile beam (red) corresponds to the *radiative electron capture to continuum RECC*, which is the high-energy endpoint of electron-nucleus bremsstrahlung [1].

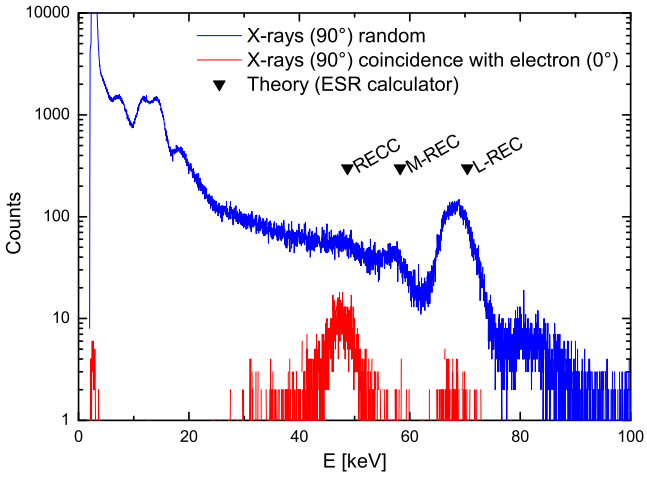

Figure 2: X-ray spectra taken with Ge-detector under 90 °

References

[1] M. Nofal *et al.*, Phys. Rev. Lett. **99** 163201 (2007)

Penning trap experiment for advanced studies with ions in extreme fields*

M. Vogel[1,2], *W. Quint*[2,3], *Th. Stöhlker*[2,3,4], *and G. Paulus*[5]

[1]TU Darmstadt; [2]GSI, Darmstadt; [3]Ruprecht Karls-Universität Heidelberg; [4]Helmholtz-Institut Jena; [5]Universität Jena

The interaction of highly intense radiation with matter and the corresponding non-linear effects have been subject of lively research, both theoretical and experimental, especially in the infrared and visible photon energy regimes. Laser systems capable of producing high intensities also at photon energies in the extreme ultra-violet (EUV) and (soft) X-ray regime open access to novel effects like non-linear Compton effects or simultaneous elastic and inelastic photon scattering, and allow multiphoton-ionisation experiments in a new domain. Recently, exceptionally strong non-linear photoionisation has been observed using high-intesity EUV laser light and been connected with the excitation of collective giant resonances. However, experiments have so far not been able to prepare and investigate well-defined particle ensembles and to non-destructively analyse the reaction products with high accuracy, nor were they able to select or prepare products for further studies in a well-defined way.

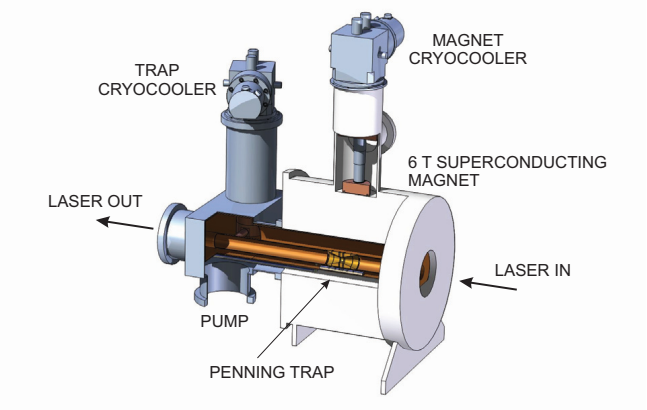

Figure 1: Schematic view of the setup. The Penning trap is located inside a horizontal superconducting magnet and traversed by the laser light. Cryogenic electronics is used for non-destructive spectrometry of confined mass and charge states.

The present development is a Penning-trap-based experiment for the advanced investigation of multiphoton-ionisation of confined particles by highly intense laser light, e.g. from free-electron lasers, see figures 1 and 2. Focus is on control over the confined particles' localization and optimized overlap with the laser light by Penning trap techniques like the use of trap electrodes as "electrostatic tweezers" and by applying a "rotating wall", respectively. Also, the non-destructive detection of reaction products is a central property.

The particles (atomic or molecular ions) are confined in a Penning trap and are subject to the laser light in a controlled manner. The reaction products are analysed in real-time by non-destructive methods. Such measurements are, for example, able to determine cross sections for multiphoton-ionisation in an energy- and intensity- regime so far not or not sufficiently examined. Additionally, the created electrons may be extracted from the trap and analysed externally. Hence, the reaction energetics may be reconstructed as completely as possible. The Penning trap setup is designed in a portable fashion, such that it can be attached to existing laser systems easily.

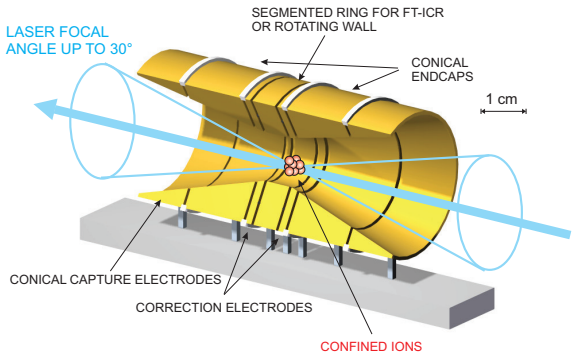

Figure 2: Schematic view of the conical open-endcap Penning trap.

As an example, the FLASH laser facility at DESY, Germany, is currently capable of producing light down to 4.5 nm (275 eV) in pulses of few fs length with peak powers of around 5 GW with repetition rates of 10 Hz [1]. This laser has previously been used for example to perform soft X-ray laser spectroscopy on highly charged ions, photo-ionization studies [2], photo-dissociation of molecular ions, and in studies of the photoelectric effect at ultra-high intensities. As a user facility, FLASH is capable of providing light under well-controlled conditions to guest experimental setups like the present one. The same is true for the PHELIX laser at GSI, Darmstadt, which can be used for studies with highly charged ions from the HITRAP facility. The potential for further studies with the same setup at even more brilliant light sources is huge, both with regard to the current upgrades to FLASH, the POLARIS laser in Jena, the future XFEL facility with photon energies up to 12.4 keV and other facilites [3].

References

[1] K. Tiedtke et al., New J. Phys. **11** 023029 (2009).

[2] M.C. Simon et al., Phys. Rev. Lett. **105**, 183001 (2010).

[3] W. Ackermann et al., Nature Photonics **1** 336 (2007).

* Work supported by HI Jena

Spectroscopic measurements of magnetic moments in highly charged ions

M. Vogel[1,2], *G. Birkl*[1], *D. von Lindenfels*[2,3], *W. Quint*[2,3], *and M. Wiesel*[2,3]
[1]TU Darmstadt; [2]GSI, Darmstadt; [3]Ruprecht Karls-Universität Heidelberg

We are currently setting up an experiment for the application of a dedicated laser-microwave double resonance technique for the precise determination of magnetic moments of highly charged ions confined in a Penning trap [1, 2]. Spectroscopic properties of highly charged ions contain valuable information both about atomic and nuclear properties of these systems and open new ways to access fundamental quantities [3, 4]. Experimental approaches to precision spectroscopy especially of forbidden transitions are manifold with novel methods under implementation which also build a bridge between optical and microwave spectroscopy [5, 6, 7]. In doing so, they allow experimental links between transition frequencies and both electronic and nuclear magnetic moments of these ions.

Figure 1 schematically shows the Penning trap design for such a measurement. The trap components have been built and assembled and will be installed soon. Components for offline-tests on the fine structure of $^{40}Ar^{13+}$ ions have been designed and partially been built. Cryo-electronics for ion manipulation and detection are currently being built. A test setup for the characterization of such cryo-components has been put into operation.

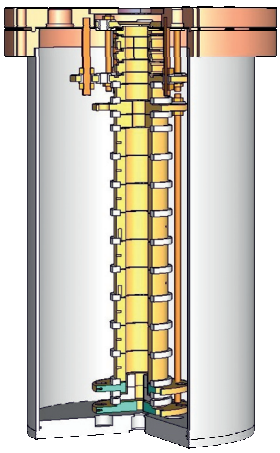

Figure 1: Electrode stack forming the Penning trap(s) inside the housing in the superconducting magnet.

Such a spectroscopic measurement of g-factors on the ppb level of accuracy allows a simultaneous and independent determination of the electronic g_J-factor and the nuclear g_I-factor on the ppb and ppm levels of accuracy, respectively. For the first time, precise values for nuclear magnetic moments can be inferred without the use of diamagnetic corrections, which currently limit the obtainable accuracy substantially. At the same time, diamagnetic shielding effects can for the first time be quantified in a spectroscopic measurement. This information may be used to benchmark corresponding theories. It furthermore allows stringent tests of theoretical values for g-factors as calculated in the framework of quantum electrodynamics of bound states in extreme electromagnetic fields.

A 7 Tesla superconducting magnet with a Penning trap designed for such spectroscopy has been set up in the framework of the HITRAP project, as can be seen in figure 2 (yelllow cube housing the superconducting magnet). Decelerated highly-charged ions will be captured and confined in the Penning trap for spectroscopic studies nearly at rest.

Figure 2: Our experimental setup at the HITRAP facility inside the ESR hall.

Following first tests in the offline mode using internally produced ions or ions from an offline-source, the experiment will be connected to the HITRAP facility within the coming year and is then to be utilized for precision spectroscopy of heavy, highly charged ions.

This work has been supported by the Deutsche Forschungsgemeinschaft.

References

[1] W. Quint, D. Moskovkhin, V.M. Shabaev and M. Vogel, Phys. Rev. A **78** (2008) 032517.

[2] M. Vogel and W. Quint, J. Phys. B **42** (2009) 154016 and Europhysics News **40** 4 (2009) 15.

[3] M. Vogel and W. Quint, Physics Reports **490** (2010) 1-47.

[4] M. Vogel, Contemporary Physics **50** (2009) 437.

[5] M. Vogel and W. Quint, New J. Phys. **11** (2009) 013024.

[6] M. Vogel and W. Quint, Hyperfine Interactions **196** (2010) 93-105.

[7] M. Vogel, W. Quint and W. Nörtershäuser, Sensors **10** (2010) 2169.

Precision Laser Spectroscopy of Forbidden Transitions in Highly-Charged Ions

S. Albrecht*[1], H. Jestädt[1], T. Murböck[1], M. Vogel[1,2], G. Birkl[1], and the SPECTRAP collaboration[2]
[1]TU Darmstadt, Darmstadt, Germany; [2]GSI, Darmstadt, Germany

Introduction

The spectroscopic investigation of hydrogen-like atomic systems has developed into an important test bed for research on atomic structure and bound-state quantum electrodynamics (QED).

Measurements of the transition energy have been realized on bunches of $^{209}Bi^{82+}$-ions in the experimental storage ring ESR. The laboratory value of the transition wavelength was determined to $243.87(4)$ nm [1, 2].

In the SPECTRAP experiment, systematic measurements on several species of highly charged ions will be possible with up to three orders of magnitude better spectroscopic resolution than in former experiments [3]. The trap will be loaded with highly-charged ions produced at the GSI accelerator facility which are decelerated and delivered by the HITRAP beam-lines and cooled to liquid helium temperatures inside the Penning trap. For efficient spectroscopy of $^{209}Bi^{82+}$ the necessary laser system should produce laser light with a power of several mW at 243.87 nm and a tuning range significantly larger then the standard deviation of 100 GHz of the previous measurement [1, 2]. In addition, the laser frequency should be stable to a precision and accuracy comparable to or below the expected Doppler-width of the transition of the ions inside the Penning trap which is expected to be approximately 30 MHz.

Laser Design and Stabilisation Scheme

We have developed, built, and characterized a laser systems which fulfils these requirements. The system consists of four major components (Fig. 1): a commercial frequency-quadrupled diode laser system (target laser) generating light at a wavelength of 243.87 nm, a pair of offset-locked diode lasers operating at 780 nm (master and transfer laser), a confocal transfer cavity locking the target laser to the transfer laser at a large wavelength offset, and a set of spectroscopic diagnostics at 780 nm (rubidium absorption cell) and 488 nm (tellurium ($^{130}Te_2$) absorption cell) for characterization of the different components of the frequency stabilisation chain. Tuning of the output frequency with high precision is achieved via a tunable rf offset lock. A sample-and-hold technique gives an extended tuning range of several THz in the UV. The modular setup with two successive frequency doubling stages gives access to three laser fields: light at 976 nm is used for frequency stabilization, light at 488 nm is used for frequency diagnostics on $^{130}Te_2$ vapour, and light at 244 nm is used for high-resolution spectroscopy of $^{209}Bi^{82+}$. The transfer cavity is stabilized to the transfer laser at 780 nm and serves for locking of the fundamental output of the target laser system by bridging the wavelength gap between 780 nm and 976 nm.

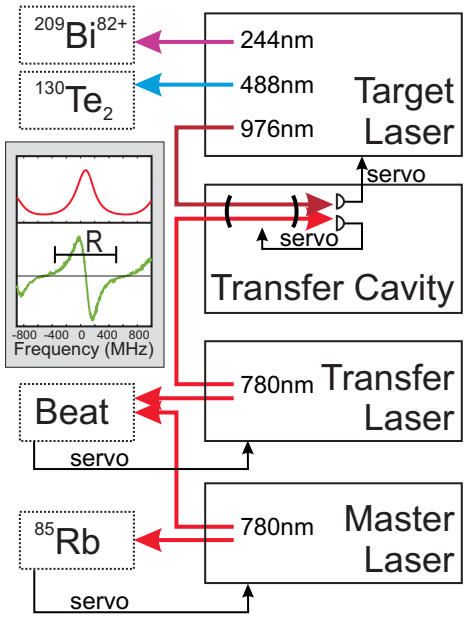

Figure 1: Schematic overview of the laser system. A stabilized transfer Cavity serves as reference. Frequency doubling and quadrupling generates light at 488 and 244 nm. In the inset (gray frame) the transmission signal (top) and the calculated dispersive signal (bottom) of the transfer cavity are shown.

Scaled to the target wavelength of 244 nm, we achieve a frequency uncertainty of $\sigma_{244nm} = 6.14$ MHz (one standard deviation) over six days of operation [4]. This scheme is universally applicable to the stabilization of laser systems at wavelengths not directly accessible to atomic or molecular resonances.

References

[1] I. Klaft et al.: Phys. Rev. Lett. **73**, 2425 (1994).

[2] S. Borneis et al.: Hyp. Int. **127**, 305 (2000).

[3] M. Vogel, D.F.A. Winters, D.M. Segal, R.C. Thompson, Rev. Sci. Ins. **76**, 103102 (2005).

[4] S. Albrecht, S. Altenburg, C. Siegel, N. Herschbach, G. Birkl, Appl. Phys. B, DOI: 10.1007/s00340-011-4732-8 (2011).

* Work supported by BMBF

Characterization of the Dresden EBIS-A as a charge breeder

A. Thorn[*1], *R. Mertzig*[1], *E. Ritter*[1], *F. Ullmann*[2], *F. Herfurth*[3], *O. Kester*[3], *and G. Zschornack*[1]

[1]Fachrichtung Physik, Technische Universität Dresden, Germany; [2]Dreebit GmbH, Dresden, Germany; [3]GSI Helmholtzzentrum für Schwerionenforschung, Darmstadt, Germany

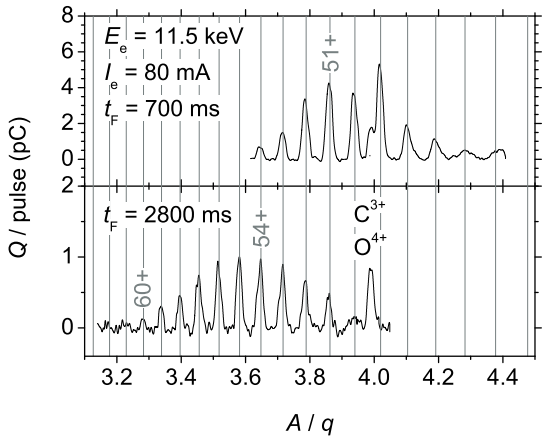

Figure 1: A/q spectrum of the Au charge state distribution after 700 ms and 2800 ms of ionization time.

Charge breeding has become an important experimental technique applied whenever highly charged ions (HCI) of a certain element or isotope are needed but only low charged ions are available from primary ion sources [1]. Over the past two years, we have reported on successful charge breeding measurements using table-top sized, room-temperature operated Dresden EBIS/T devices. This is a compilation of results continuing the studies described in [2] with the most powerful permanent magnet technology based Electron Beam Ion Source (EBIS) which currently exists, the Dresden EBIS-A [3].

The experimental setup for the charge breeding measurements with the EBIS-A was previously described in [2]. An AuGe Liquid Metal Alloy Ion Source (LMAIS) was used to provide low charged gold ions [4]. During the injection phase, the LMAIS beam was bent by 90° with the help of a quadrupole deflector and injected into the EBIS-A. During re-extraction of the charge bred gold ions the quadrupole electrodes were grounded to allow the ions to pass through towards the analysis section of the beamline consisting of a pepper - pot emittance meter (PEM) to investigate ion beam phase space distributions as well as a 90° bending magnet for A/q analysis.

Two A/q spectra measured at optimized charge breeding conditions are presented in figure 1. Charge states up to Au^{60+} were observed. The achieved breeding efficiencies of various Au charge states are summarized in table 1. These values are relatively low in comparison to those from other apparati [1] but can be raised by improving the ion beam optics in the beamline for a better match of acceptance and emittance ellipses of the incoming beam and the EBIS as well as reducing inacuracies in switching the high voltage of the quadrupole electrodes in the future.

Table 1: Breeding efficiencies ε_B reached with the current LMAIS / EBIS-A setup along with ionization times t_F, absolute ion numbers N_q, and relative abundances $N_{q,rel}$ for selected Au charge states.

q	t_F (ms)	N_q (10^5)	$N_{q,rel}$ (%)	ε_B (10^{-5})
33	100	5.1±0.5	13	6.1±1.2
43	250	4.6±0.5	14	5.7±1.2
51	700	5.3±0.5	20	6.3±1.3
55	2800	1.2±0.2	15	1.4±0.4

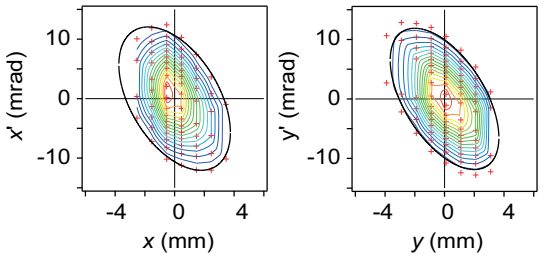

Figure 2: Trace space distributions in x and y direction of the charge bred Au beam at an ion energy of $E_i = q \cdot 8.5\,\mathrm{keV}$. The solid lines indicate the four times rms-emittance ellipses.

Finally, the PEM was used to study the HCI beam after charge breeding. The ionization time in this measurement was set to 700 ms resulting in charge state distributions around q = 51+ as shown in figure 1. The phase space distributions are presented in figure 2, the root mean square (rms) emittances at $E_i = q \cdot 8.5\,\mathrm{keV}$ resulted in $\varepsilon_{x,rms} = 10.0 \pm 4.6\,\mathrm{mmrad}$ and $\varepsilon_{y,rms} = 9.1 \pm 4.0\,\mathrm{mmrad}$.

This work has been supported by the GSI R&D cooperation project DD.ZSCH.

References

[1] F. Wenander et al.: J. Instrum. 5 (2010) C10004

[2] A. Thorn et al.: GSI Scientific Report 2010 (2011) 357

[3] V. P. Ovsyannikov et al.: J. Phys.: Conf. Ser. 58 (2007) 399

[4] L. Bischoff: Nucl. Instr. and Meth. B 266 (2008) 1846

* a.thorn@hzdr.de

The High Voltage Electron Beam Ion Trap (S-EBIT) for SPARC

Y. Ke[1], I. Orban[1,2], M. Hobein[1], S. Tashenov[1], S. Mahmood[1], O. Kamalou[1], A. Safdar[1], H. Zhang[1], and R. Schuch[1]

[1]Fysikum, Stockholm University, AlbaNova, S-10691 Stockholm, Sweden
[2]Atomic Physics Division, GSI, Darmstadt, Germany

A high voltage Electron Beam Ion Trap "Super EBIT" (S-EBIT) for a 260 keV electron beam energy has being built up at Stockholm University based on the Refrigerated Electron Beam Ion Trap (R-EBIT) [1,2] from "Physics and Technology" (Livermore, USA). This was the first of the next generation EBIT with a refrigerated (dry cryogenic) system where cold heads keeps the magnets and heat screens on 4 K and 50 K temperatures, respectively. The electron beam is compressed by a magnet field of max 4T. Singly charged ions can be injected from metal vapor source MEVVA or isotopically cleaned from a high current plasma source CHORDIS for charge breeding. The S-EBIT has a sophisticated extraction scheme with a charge cleaning magnet and a time-of-flight section for charge breeding diagnostics. So far the S-EBIT was used for ion trapping and cooling experiments, electron-ion collisions, and highly-charged ion nanocapillary studies [2-5].

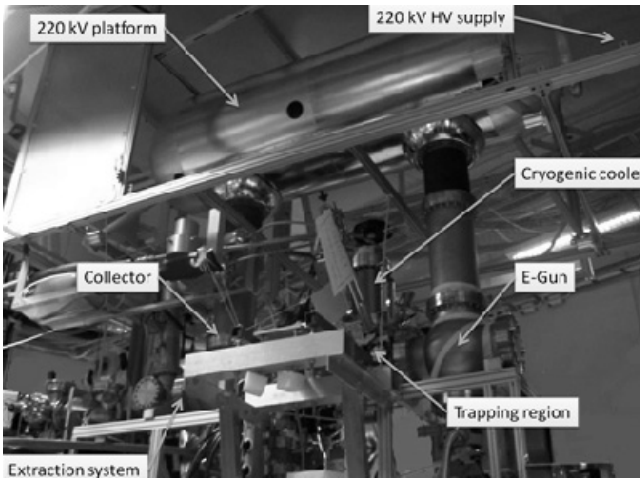

Figure 1: Foto of the assembled S-EBIT.

The upgrade of S-EBIT includes raising the electron energy from 30 keV to 260 keV, installation of a new vibration-free pulse-tube cooler, a new injection, and extraction system (Figs. 1 and 2). We also developed a new operational system for this EBIT in LabView that controls the relevant machine parameters, such as electron beam currents, vacuum, and safety interlocks. This S-EBIT with improved parameters should allow the production of fully stripped heaviest ions of all elements up to uranium. The machine is now prepared for the possible move to the HITRAP facility and finally to the Helmholtz-Institute Jena to serve as a development platform for SPARC experiments at the future FAIR facility.

Table 1: S-EBIT parameters

Magnetic field	<4 Tesla
Electron beam energy	<260 keV (trap 40kV, gun &collector -220kV
Electron beam current	<250 mA
Electron beam radius	30 μm
Central current density	<4 kA/cm^2
Trap length	2 cm

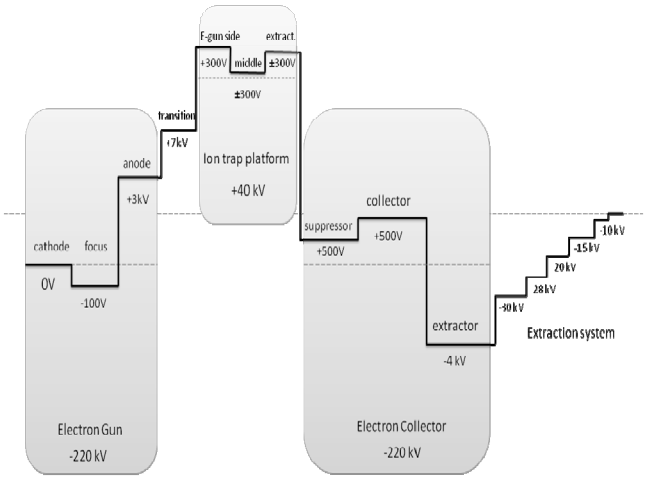

Fig. 2. S-EBIT high voltage scheme (voltage values are the upper limits of the power supplies).

We acknowledge support from the Knut & Alice Wallenberg foundation and the Swedish Research Council VR.

[1] J. McDonald and D. Schneider, NIM B 241, 870 (2005).
[2] S. Böhm et al., Journ. of Phys. Conf. Series **58**, 303 (2007).
[3] I. Orban et al., subm. to Phys. Rev.A
[4] M. Hobein, A. Solders, M. Suhonen, Y. Liu and R. Schuch, Phys. Rev. Lett. **106**, 013002 (2011).
[5] H. Zhang et al., Phys. Rev. Lett. to be published.

Development of MMC arrays for high resolution x-ray spectroscopy

S. Schäfer, C. Pies, S. Heuser, S. Kempf, A. Pabinger, J.P. Porst, T. Wolf, A. Fleischmann, L. Gastaldo, C. Enss

Kirchhoff-Institut für Physik, Universität Heidelberg, INF 227, 69120 Heidelberg, Germany

Metallic magnetic calorimeters (MMC) are calorimetric particle detectors operated at temperatures below $100\,\mathrm{mK}$, that make use of a paramagnetic temperature sensor to transform the temperature rise upon the absorption of a particle in the detector into a measurable magnetic flux change in a dc-SQUID. They combine high energy resolution, fast detector risetimes ($\tau_0 < 100\,\mathrm{ns}$) high quantum efficiency and large dynamic range [1], turning them into promising tools for numerous precision experiments in atomic and nuclear physics at GSI/FAIR. We recently started to develop two micro-fabricated linear MMC arrays, one for photon energies up to 20 keV with an energy resolution below 3 eV (FWHM), the other one for energies up to 200 keV with $\Delta E_{\mathrm{FWHM}} < 50\,\mathrm{eV}$.

Both presently developed detector arrays consist of x-ray absorbers made of electro-deposited Au, each of which connected to a paramagnetic temperature sensor made of sputtered Au:Er. A superconducting meander-shaped pickup coil made of a sputter-deposited niobium is used to generate the magnetic field in the sensor volume and to pickup the change of magnetization upon the absorption of a photon. The meander is connected to the input coil of a SQUID, forming a completely superconducting circuit. An on-chip persistent current switch is used to inject the field generating persistent current into the superconducting circuit.

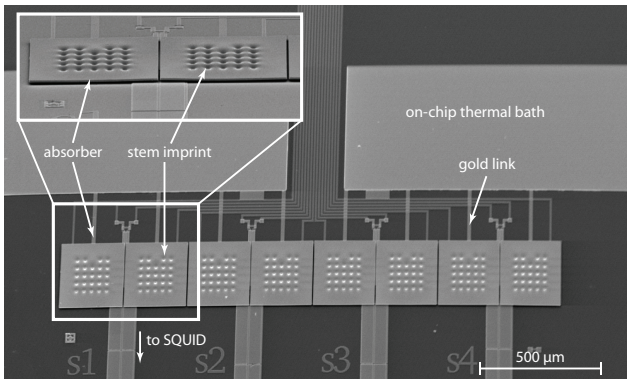

Figure 1: SEM picture of maXs-20 with 8 overhanging x-ray absorbers made of 5 μm thick gold, each $(250\,\mu\mathrm{m})^2$ in area connected to the sensor by 24 stems.

The status of development of both detector arrays, maXs-20 (shown in Fig. 1) and maXs-200, as well as their performances are discussed in detail in [2]. In summary we can note, that recent refinements in detector design, shielding and wiring made it possible to operate maXs-20 even in the harsh environment (vibrations and emi) of a closed cycle pulse-tube cooled ADR cryostat with an instrumental linewidth of $\Delta E_{\mathrm{FWHM}} = 3.4\,\mathrm{eV}$, close to the design value and not degraded by crosstalk between the pixels. Similarly positive is the status of maXs-200.

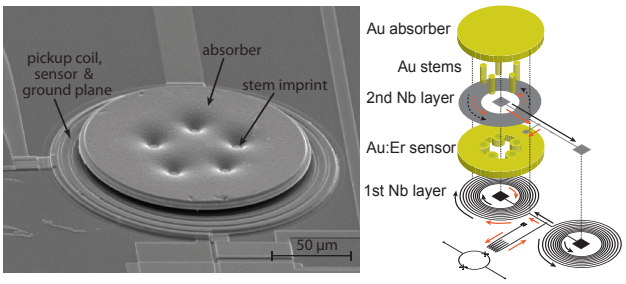

Figure 2: SEM picture and sketch of an MMC with sandwiched paramagnetic sensor.

To further improve the energy resolution of MMCs, we recently developed and studied a first single-channel detector where the sensor is sandwiched between a planar superconducting spiral coil and a superconducting top plane (Fig. 2), which improves the magnetic flux-coupling between paramagnetic sensor and SQUID close to its maximum value [1]. Already the first characterization measurements delivered very promising results. Fig. 3 shows the fine structure splitting of the K_α x-ray fluorescence line of ^{55}Mn as measured with this MMC. Deconvolving the measured lineshape by the natural one we deduce an instrumental linewidth of $\Delta E_{\mathrm{FWHM}} = 2.0\,\mathrm{eV}$. The results also suggest that $\Delta E_{\mathrm{FWHM}} < 1.6\,\mathrm{eV}$ should be achievable by further fine-tuning, which would correspond to the highest resolving power achieved with micro-calorimeters so far.

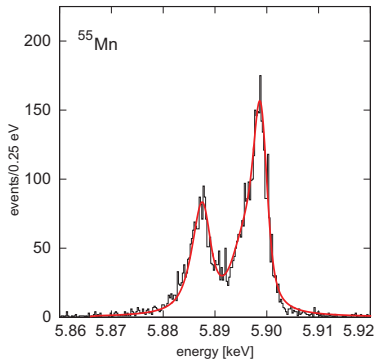

Figure 3: K_α line of ^{55}Mn.

This work was supported by the GSI R&D grant HDENSS and by the BMBF grant 06HD9118I.

References

[1] A. Fleischmann et al., *Metallic magnetic calorimeters*, AIP Conf. Proc. **1185**, 571 (2009)

[2] C. Pies et al., *maXs: Microcalorimeter Arrays for High-Resolution X-ray Spectroscopy at GSI/FAIR*, accepted for publication in Journal of Low Temperature Physics, LTD-14 Conference Proceedings (2012)

Sensor Optimization Studies on the CCC for FAIR *

F. Kurian[1,2], R. Geithner[3,4], M. Schwickert[1], P. Kowina[1], P. Hülsmann[1,2], H. Reeg[1] and R. Neubert[3]

[1]GSI, Darmstadt; [2]Goethe Universität, Frankfurt am Main; [3]Friedrich-Schiller-Universität Jena;
[4]Helmholtz-Institut Jena, Germany

High intensity and high energy of ion beams and anti-protons in the FAIR facility demand for the installation of Cryogenic Current Comparators (CCC), providing online measurement of beam currents precisely down to nA-range. CCCs are foreseen in various HEBT sections of the FAIR facility. An improved version of a CCC prototype is under development in collaboration between FSU/HI Jena, MPI-K Heidelberg.

Magnetic Shielding for CCC

In a Cryogenic Current Comparator, the azimuthal component of the magnetic field of the ion beam is detected by a superconducting pick up coil and the signal is measured using a DC SQUID, a high sensitivity magnetic flux detector. The magnetic field produced by the beam in the required current limits will be several orders of magnitude lower than the field components of electromagnetic noise. Hence the pick-up coil must be shielded with meander-shaped superconducting magnetic shield geometry. The goal is to strongly attenuate all field components except for the azimuthal component of the field produced by the beam which carries the information about the beam current. To realize optimum shielding efficiency, a mathematical model of the attenuation by the meander-shaped shield geometry is under development with the help of an FEM simulation package.

Field Attenuation by the Shield Geometry

The field attenuation is studied for different diameter and length of the superconducting shield. For meander-shaped shield, the attenuation is studied with respect to the length of the coaxial cylinder and the results are confirmed with the theoretical estimation [1]. The attenuation is also studied for different radii of the cylindrical gap and gap width (see Fig.1). To evaluate the relation between attenuation and geometrical shield parameters the attenuation values were fitted with exponential functions. As a next step the estimation will be compared to measurements of the field attenuation through a meander-shaped shield of a CCC developed for dark current measurements of the TESLA cavities at DESY [4].

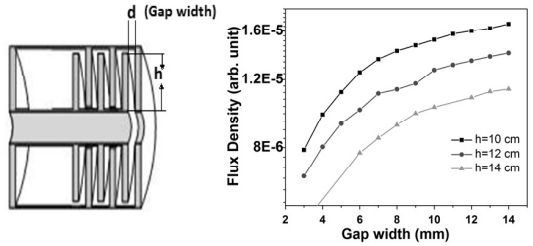

Figure 1: The variation of field attenuation with increase in gap width for different h values.

* Work supported by EU, DITANET, Project No. ITN-2008-215080, GSI F+E, HI Jena

Sensor Characterization

Searching for ferromagnetic core materials with a high relative permeability μ_r and therewith a high inductance factor for given coil dimensions three Nanoperm M764 cores from the manufacturer Magnetec with the final dimensions were ordered and characterized at GSI. Measurements of the temperature and frequency dependent inductance $L_S(\nu)$ and serial resistance $R_S(\nu)$ with an LCR-Meter at 4.2 K had shown that these cores fulfil the requirements for FAIR [2]. The noise contribution of the cores is evaluated by using the Fluctuation-Dissipation-Theorem (FDT) [3] and applying the measured $L_S(\nu)$ and $R_S(\nu)$ of the toroidal coils with a single-turn superconducting winding and the inductance of the input coil of the SQUID sensor L_{SQUID}.

$$PSD\_I = 4k_B T \frac{R_S(\upsilon)}{\left(2\pi\upsilon\left(L_{SQUID} + L_S(\upsilon)\right)\right)^2 + \left(R_S(\upsilon)\right)^2} \quad (1)$$

From FDT we calculate a three to six time lower current noise for Nanoperm M-764 (see Fig. 2, curve c) compared to the pickup coil of the CCC in a former project with DESY (DESY-CCC) with a Vitrovac 6025F core [4].

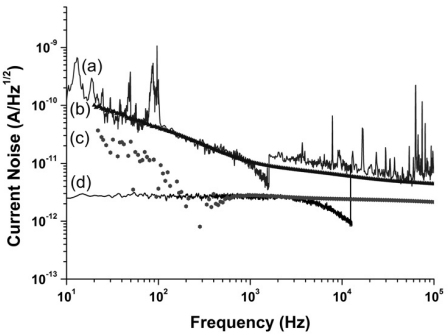

Figure 2: Measured current noise of the DESY-CCC pickup coil (a) and the SQUID (d) as well as the calculated current noise from FDT of the DESY-CCC pickup coil (b) and Nanoperm M-764 core 2 (c).

The white current noise of such a coil is 2.5 pA/Hz$^{1/2}$ and seems to be limited by the SQUID noise (see Fig. 2, curve (d)).

References

[1] F.Kurian et al., DITANET International Conference, Nov 2011, Sevilla, Spain
[2] R. Geithner et al., Proc. of DIPAC 2011, TUPD66, pp. 458 – 460, Hamburg, Germany
[3] H. P. Quach, T. C. P. Chui, Cryogenics 44 (2004) 6, 445.
[4] R. Geithner et al., Rev. Sci. Instrum. 82 (2011), 013302.

Digital readout of segmented solid state detectors based on Febex2

K.-H. Blumenhagen[1], *E. Badura*[2], *H. Bräuning*[2], *J. Hoffmann*[2], *K. Koch*[2], *N. Kurz*[2], *R. Märtin*[1,3], *S. Minami*[2], *W. Ott*[2], *Th. Stöhlker*[1,2,3], *U. Spillmann*[2], *G. Weber*[3], *and M. Weber*[4]

[1]PI, Universität Heidelberg, Germany; [2]GSI, Darmstadt, Germany; [3]HI Jena, Germany; [4]IPE, KIT, Karlsruhe, Germany

In atomic physics at GSI, solid state detectors are used to measure the energy of X-rays with a high resolution. Both segmented and non-segmented detectors were successfully employed in several works [1, 2] and will be an essential part of future spectroscopy experiments within the SPARC-collaboration [3] at FAIR. Up to now, the readout of these detectors has been performed with NIM and VME modules. Limitations of this system include insufficient rate acceptance and pile-up rejection as well as a hight cost per channel. To overcome these, a fully digital readout system is under development within the High Data Rate Initiative (HDRI) [4] of the Helmholtz Association. With this approach, not only cost and space of the readout system is reduced, one can also gain additional information by performing a digital pulse shape analysis. In this work, already available digitizer systems were used to read out different detectors. The preamplifier pulses – generated by an ^{241}Am source mounted in front of the detector – were digitized with a fixed sampling frequency and then stored entirely. These pulses were analyzed with software employing digital filters. A comparison of different filters was performed. The first setup was a HPGe-detector which was read out by a digitizer card (CompuScope card) that is built in a Windows-XP computer. First, the timing properties of several filter configurations have been investigated. The best time resolution obtained was $7.8\,\mathrm{ns} \pm 1\%$. Then the pulseheight spectrum was generated for different filters. A reference spectrum of ^{241}Am was used to perform the energy calibration. The quantity calculated for each filter in order to compare them was the FWHM at 59.54 keV (fit of a gaussian with linear background in the energy spectrum). The best value obtained was $0.38\,\mathrm{keV} \pm 1.6\%$ which corresponds to the result of a measurement with the same setup, but analog readout. The energy spectrum that gave this value with digital readout is shown in figure 1. The second setup was a segmented Si(Li)-detector [5] which was read out by the Febex2 card [6] and additional electronics which was all developed at GSI. The detector has 32 strips on the front side and orthogonal to them 32 strips on the backside of its crystal. In this work eight strips on the front side were read out and one of them was investigated (only energy resolution, no timing). The best value obtained was $1.98\,\mathrm{keV} \pm 1.6\%$. The corresponding spectrum is shown in figure 2. Similar results were obtained with analog electronics. One future activity is the development of a hardware-based pulse analysis. For this, the Febex2 card's built-in FPGA applies simple digital filters online to obtain time and energy information.

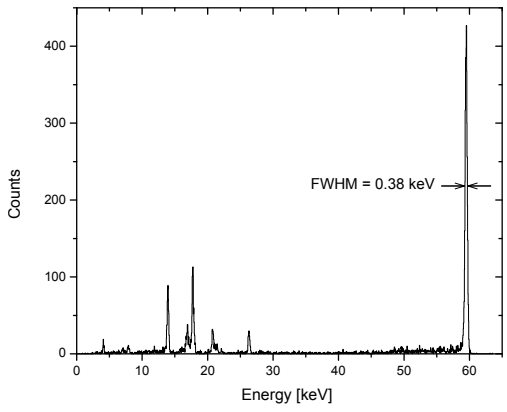

Figure 1: ^{241}Am spectrum of HPGe-detector.

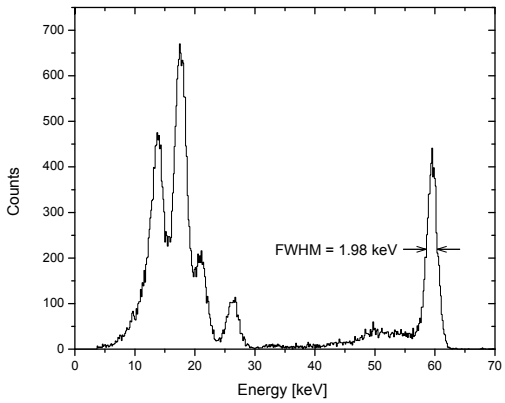

Figure 2: ^{241}Am spectrum of Si(Li)-detector.

References

[1] A. Gumberidze et al., Electron-Electron Interaction in Strong Electromagnetic Fields: The Two-Electron Contribution to the Ground-State Energy in He-like Uranium, Phys. Rev. Lett., 92, 20, May 2004.

[2] G. Weber et al., Performance of a position sensitive Si(Li) x-ray detector dedicated to Compton polarimetry of stored and trapped highly-charged ions, JINST 5,C07010, 2010.

[3] Th. Stöhlker et al., SPARC: The Stored Particle Atomic Research Collaboration At FAIR, AIP Conference Proceedings, 1336, 1, p. 132-137, 2011.

[4] HDRI - High Data Rate Processing and Analysis Initiative, http://www.pni-hdri.de/e102421/e121571/index_ger.html.

[5] D. Protic, E. L. Hull, T. Krings, K. Vetter, Large-volume Si(Li) orthogonal-strip detectors for Compton-effect-based instruments, IEEE Transactions on Nuclear Science, 2005.

[6] J. Hoffmann, "FEBEX2, preliminary specification", 2011, https://www.gsi.de/onTEAM/grafik/1130845854/febex2.pdf.

Detector systems for the SPECTRAP and LIBELLE experiment*

J. Mader†[1], *Z. Andjelkovic*[2,3], *D. Bonaventura*[1], *W. Buglak*[1], *C. Geppert*[2,3], *V. Hannen*[1], *M. Lochmann*[2,3], *R. Jöhren*[1], *W. Nörtershäuser*[2,3], *H.-W. Ortjohann*[1], *R. Sánchez*[2,3], *and C. Weinheimer*[1] *for the SPECTRAP collaboration*

[1]WWU Münster, Institut für Kernphysik, Wilhelm-Klemm-Str. 9, 48161 Münster; [2]Johannes Gutenberg-Universität Mainz, Institut für Kernchemie, Fritz-Straßmann-Weg 2, 55128 Mainz; [3]GSI Helmholtzzentrum für Schwerionenforschung GmbH, Planckstr. 1, 64291 Darmstadt

The development and characterization of detector systems capable of single-photon counting and dedicated and optimized for the SPECTRAP experiment and the related ESR measurements is the contribution of the Institut für Kernphysik in Münster to these experiments. The wavelengths of interest range from the UV (244 nm) to the near infrared (1550 nm).

Movable mirror system for ESR

During the LIBELLE experiment a new photodetection system based on a movable parabolic Cu mirror [1] has been used to measure the HFS transition in Li-like Bi [2]. Simulations have shown [1] that the mirror system strongly increases the collection efficiency of forward emitted and therefore Doppler shifted photons compared to the segmented mirror section installed in the ESR. During the meassurement the inserted mirror lead to a loss in beam current of about 5 % but did not disturbe the lifetime of the ions (Fig. 1). At certain beam settings it was even possible to leave the mirror in the beam position during injection of the ions. With 2.2 mA beam current we obtained a signal rate at the resonance of 41 cps on top of a background of about 564 cps.

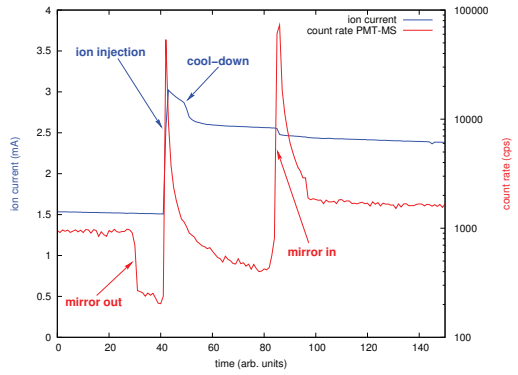

Figure 1: Ion current (blue) and PMT count rate (red) vs. time in arbitrary units.

Detector setups for SPECTRAP experiment

Avalanche Photo Diodes (APDs) of type S0223 manufactured by Radiation Monitoring Devices Inc. (RMD) [3] will be used as detector at the SPECTRAP experiment to cover the wavelength region from 400 nm to 1100 nm [4]. By cooling the APDs to approximately $-170\,^{\circ}\mathrm{C}$ and using extremely low noise preamplifiers one can obtain gains exceeding $2 \cdot 10^4$ near the breakdown voltage. The photodetection efficiency with a discriminator threshold of 6 mV for 628 nm photons has been found to be $(67 \pm 7)\%$ at a dark count rate of 200 cps, for 1020 nm photons it is $(13 \pm 3)\%$ [5]. The experimental set-up for this region consisting of a vacuum chamber where the APD is kept near liquid nitrogen themperature and a shutter system, was presented in [4] and is completed by now (Fig. 2). For longer wavelengths

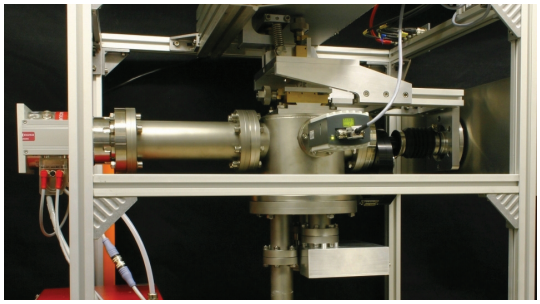

Figure 2: APD detection system for the SPECTRAP experiment

up to 1650 nm a selected photomultiplier module of type H10330A-75 [6] with a notably high quantum efficiency of almost 10 % manufactured by Hamamatsu was aquired. The module is equipped with a thermoelectric cooler and HV unit. A dark count rate of 150 kcps has been obtained at 30 mV threshold. The count rate is highly temperature dependent, so a temperature stabilized environment is needed. As an alternative to NIR PMTs the usability of large area InGaAs APDs for photon counting at 1550 nm will be investigated in the coming year.

References

[1] D. Anielski, Diplomarbeit, Universität Münster, 2010.

[2] M. Lochmann *et al.*, GSI Scientific Reports 2010, 2011.

[3] RMD product information: Silicon Avalanche Photodiodes (APDs), `http://www.rmdinc.com/products/p006.html`.

[4] R. Jöhren *et al.*, GSI Scientific Reports 2008, 2009, 2010.

[5] R. Jöhren *et al.*, APDs as Single-Photon Detectors for Visible and Near-Infrared Wavelenghts down to Hz Rates arXiv:1111.6948

[6] Hamamatsu Photonics, *Thermoelectrically cooled NIR-PMT Module H10330A-75*, datasheet 2011

* Supported by BMBF under contract number 06MS9152I

† jonas.mader@uni-muenster.de

A novel ultra cold atom target for collision experiments with heavy ion beams*

S. Götz[1], B. Höltkemeier[1], C. Hofmann[1], B. DePaola[2], M. Weidemüller[1]

[1]Physikalisches Institut, Universität Heidelberg, Germany; [2]Kansas State University, Manhattan, KS, U.S.A.

In the past few decades, kinematically complete high-resolution studies of ionization processes have been studied extensively using COLTRIMS [1,2,3]. The targets are provided by supersonic expansions of gas jets, which limits the resolution to the thermal spread of the target atoms and the available atomic target to species without active electrons. These limits can be overcome by combining the novel technique of RIMS with state-of-the-art laser cooling, where the target atoms can be trapped and cooled to very cold temperatures well below 1mK in magneto-optical traps (MOTRIMS) [4]. As compared to COLTRIMS targets, systems with one or more active electrons can be explored. This is in particular interesting for multiple charge exchange experiments, since the energy difference between the transferred electrons is non negligible [5]. Furthermore, the ability to state-prepare and polarize the target atoms leads to the possibility of exploring new physics, as for example the initial state dependence in multielectron threshold ionization of the target atoms [6].

Our setup combines a high-resolution recoil ion momentum spectrometer with a high density magneto-optical trap (Fig. 1). Using a two-dimensional magneto optical trap (2D MOT) [7] as a source of Rb atoms, we can achieve extremely short loading times of 300ms which allow measurements of processes with very low probability such as multi electron charge transfer, which are otherwise disguised by the far more dominant single charge transfer channel. Compared to loading from background gas, the 2D MOT also allows a much better pressure in the main chamber, which means longer trapping times of the atoms and a much lower signal from background ions.

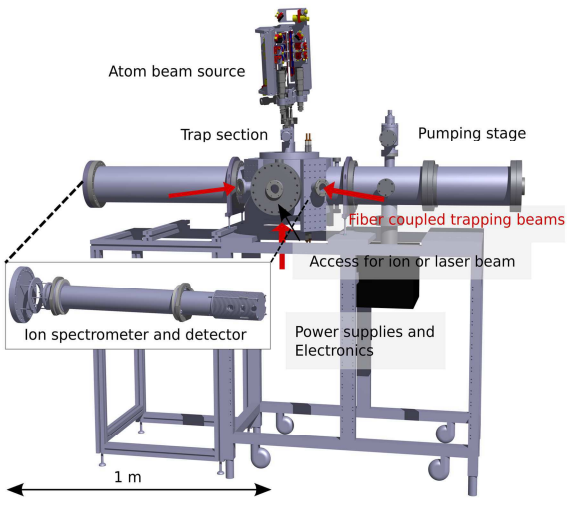

Figure 1: MOTRIMS setup.

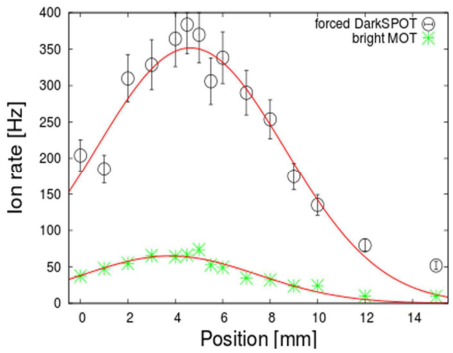

Figure 2: Density profile of MOT/DarkSPOT.

By implementing a so called DarkSPOT we could also increase the atom density by one order of magnitude to a maximum of $2 \cdot 10^{11}$ atoms/cm^{-3}. Figure 2 shows the density profile of both the conventional MOT and the DarkSPOT, which was measured by moving the focus of a pulsed laser beam through the atom cloud and measuring the rate of atoms being ionized in a two-photon process. With the pulsed laser beam we could also test the momentum resolution of our RIMS spectrometer to be 0.10 a.u. which is sufficient to study multiple charge transfers of the neutral atoms with highly charged ions.

In conclusion, we have developed a new target with very high atom densities and a very high loading flux. We also achieved a momentum resolution of the recoil ions, that is in the range of similar experiments and is sufficient to study fundamental processes in collisions with highly charged ions such as multiple charge transfers. To perform these kind of measurements, the setup is going to be transported to GSI in Darmstadt where it will be implemented in the HITRAP beamline. This will allow us to study collisions of our trapped rubidium atoms with highly charged ions up to bare uranium.

References

[1] J. Ullrich, et al., Comments At. Mol. Phys. 30, 415 (1994)
[2] J Ullrich et al, Rep. Prog. Phys. 66 (2003)
[3] R. Dörner, et al., Phys. Report 330, 95 (2000)
[4] B. DePaola, R. Morgenstern, N. Anderen, Advances In Atomic, Molecular, and Optical Physics 55, 139 (2008)
[5] S. Knoop et al., Eur. Phys. J. D 74, 992 (2006)
[6] G. Zhu et al., Phys. Rev. Lett. 103, 103008 (2009)
[7] K. Dieckmann et al., Phys. Rev. A 58, 3891 (1998)

*supported by EMMI

A transverse electron target for the FAIR storage rings *

S. Geyer[1,2], O. Meusel[2] and O. Kester[1,2]

[1]GSI, Darmstadt, Germany; [2]Goethe-Universität Frankfurt, Germany

A transverse electron target is a well suited concept for storage ring experiments. Using the crossed beam technique, the investigation of electron-ion interaction processes with high energy resolution will become possible.

Experimental Perspective

A transverse target of free electrons promises a better energy resolution than an internal gas target by one order of magnitude. It additionally allows the detection of emitted photons and electrons under large solid angles. Therefore a transverse electron target opens the perspective to new types of experiments. One application of the target will be the measurement of absolute cross sections in the low energy regime for astrophysical data as well as for plasma and ion beam physics (eg. for beam lifetimes in storage rings and beam transport, like from an ECRIS to the subsequent LINAC at the FAIR facility). Due to its design, the influence of electrostatic fields on the different interaction processes can be examined.

Interaction Rates and energy resolution

To approximate the rates to be expected for the electron target, calculations for the direct electron impact ionization (DI) and the radiative recombination (RR) have been performed using semi-empirical expressions for the cross sections [1,2]. For a 50keV argon beam of the charge states depicted in fig.1, with a current of 1μA interacting in a 10cm long region with the 0.5A/cm^2 dense electron beam, the rates amount to ~10^{3}kHz for the DI and ~10^{2}Hz for the RR due to [3].

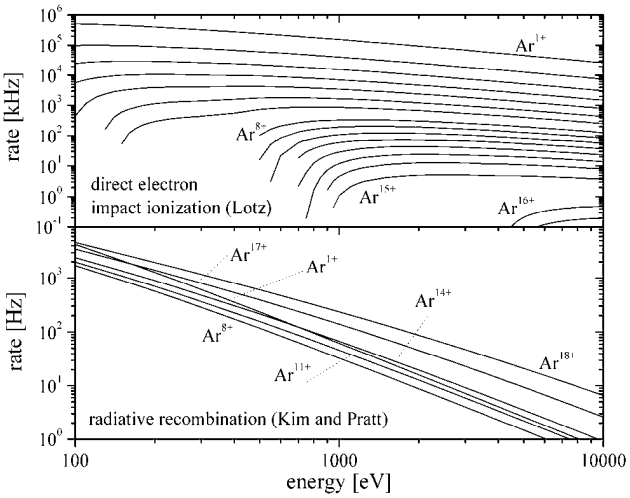

Figure 1: Energy dependence of the rates for the DI and the RR for different charge states of Ar.

The energy resolution mainly depends on the three factors: thermal energy spread of the electrons, divergence of the ion beam and the potential depression of the electron beam in the interaction region [4]. The last factor dominates with several ten eV the energy resolution. A higher resolution is achievable by compensation of the depression by residual gas ions.

Target Design

The electron target relies on a simple concept using electrostatic fields to focus the sheet beam (fig. 2). Using a rectangular instead of a cylindrical geometry not only allows for a higher perveance limit but also leads to a smaller potential depression, important for a high energy resolution. The adjustable electron energy ranges between several 10eV and a few keV. To optimize the beam optics and to get the electron trajectories as parallel as possible in the interaction region, simulations with the EGUN code [5] have been performed. To determine the overlap factor for absolute cross section measurements the animated beam technique will be used to scan the ion beam.

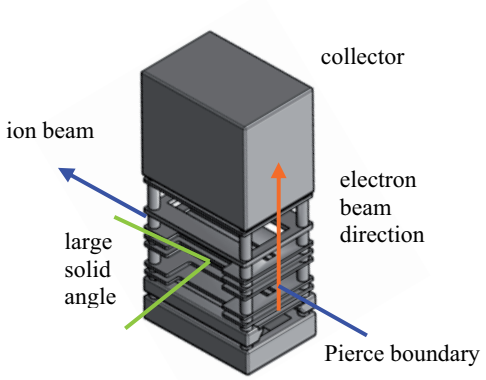

Figure 2: Preliminary design of the electron target

Summary

The target is dedicated to the FAIR storage rings in the future, but will be tested at the Frankfurt Low Energy Storage Ring (FLSR) at Frankfurt University [6]. After finalizing the simulations and completion of the construction of the target it will be characterized on a test bench.

References

[1] W. Lotz, *Zeitschrift für Physik* 206 (1967) 205
[2] Y. S. Kim *and* R. H. Pratt, *Phys. Rev. A* 27 (1983)
[3] A. Müller *et al,*. J. Phys. B 13 (1980)
[4] R. Becker *et al,. NIM B* 9 (1985)
[5] W. B. Hermannsfeldt, *Electron Trajectory Program, SLAC* 226 (1979)
[6] K. E. Stiebing *et al., NIM A* 614 (2010)

* Work supported by GSI F+E, HIC4FAIR

Test of many-electron QED effects in the hyperfine splitting of heavy ions*

A. V. Volotka[1,2], *D. A. Glazov*[2], *O. V. Andreev*[2], *V. M. Shabaev*[2], *I. I. Tupitsyn*[2], *and G. Plunien*[1]

[1]Technische Universität Dresden, Germany; [2]St. Petersburg State University, Russia

Investigations of a specific difference of the hyperfine splitting values of H- and Li-like ions with the same nucleus give an access to the stringent test of many-electron QED effects in strong electromagnetic fields [1]. This difference $\Delta' E = \Delta E^{(2s)} - \xi \Delta E^{(1s)}$, where $\Delta E^{(1s)}$ and $\Delta E^{(2s)}$ are the hyperfine splittings of H- and Li-like ions, respectively, can be calculated to a rather high accuracy independently of the employed nuclear magnetization distribution model. Accurate measurements of the ground-state hyperfine structure were performed for several H-like ions: ^{209}Bi, ^{165}Ho, ^{185}Re, ^{187}Re, ^{207}Pb, ^{203}Tl, and ^{205}Tl. Recently, the hyperfine splitting of the ground state Li-like Bi ion has been directly observed at GSI for the fist time [2].

Achievements of the required theoretical accuracy for the specific hyperfine splitting difference for H- and Li-like heavy ions demand for the rigorous evaluation of various QED and interelectronic-interaction effects. Since the influence of one-electron QED corrections is considerably reduced in the specific difference, the total value of $\Delta' E$ is essentially determined by the screened radiative and interelectronic-interaction corrections. The screened self-energy and a dominant part of the screened vacuum-polarization contributions have been calculated rigorously within a systematic QED approach [3, 4]. Recently, we completed the evaluation of the second-order interelectronic-interaction corrections within a rigorous QED approach [5]. As the most interesting application of these results we present here improved theoretical predictions for the specific difference between the ground-state hyperfine splitting values of H- and Li-like Bi ions.

For the case of Li-like Bi we utilize the following values for the nuclear properties: $\langle r^2 \rangle^{1/2} = 5.5211$ fm, $I^\pi = 9/2-$, and $\mu = 4.1106(2)\mu_N$. The cancellation of the Bohr-Weisskopf effect appears with $\xi = 0.16886$. In Table 1 we present the current status of individual contributions to the specific difference. The rigorous evaluation of the two-photon exchange corrections improves the accuracy of the interelectronic-interaction term by an order of magnitude in comparison with previous calculations [3, 4]. The accuracy of the screened QED contribution has been also increased due to recent rigorous evaluations of the Wichmann-Kroll parts of the electric and magnetic loops [6], which was accounted for in Refs. [3, 4] within some approximations. Thus, the remaining theoretical uncertainty for the specific difference comes from the uncalculated Wichmann-Kroll parts of the screened vacuum-polarization correction and from the $1/Z^3$ and higher orders interelectronic-interaction term. The second uncertainty in the total value of $\Delta' E$ arises from the uncertainty of the nuclear magnetic moment, the nuclear polarization corrections, and other nuclear effects, which do not completely cancel in the specific difference. Employing the experimental value of the $1s$ hyperfine splitting $\Delta E^{(1s)}_{\rm exp} = 5.0840(8)$ eV [7] and the theoretical result for the specific difference, one can easily find the hyperfine splitting for Li-like Bi $\Delta E^{(2s)} = 797.16(14)$ meV, where the accuracy is fully determined by the uncertainty of the experimental value. As one can see from Table 1, the one-electron QED corrections are strongly canceled in the specific difference and the dominant QED contributions comes from the many-electron effects. Therefore, the theoretical accuracy achieved now for the specific difference allows to test the many-electron QED effects on the few percent level, provided the hyperfine splittings in H- and Li-like bismuth are measured with a relative accuracy of about 10^{-6}. When the QED corrections will be tested and found to be valid, the comparison between the theoretical and experimental values will enable the determination of the nuclear magnetic moments and their volume distribution.

Table 1: Individual contributions to the specific difference $\Delta' E$ for ^{209}Bi in meV.

	$\Delta E^{(2s)}$	$\xi \Delta E^{(1s)}$	$\Delta' E$
Dirac value	844.829	876.638	−31.809
Interel. interaction			
$\sim 1/Z$	−29.995		−29.995
$\sim 1/Z^2$	0.258		0.258
$\sim 1/Z^3$ and h. o.	−0.003(3)		−0.003(3)
QED	−5.052	−5.088	0.036
Screened QED	0.193(2)		0.193(2)
Total			−61.320(4)(5)

Finally, we have significantly increased the accuracy of the specific difference, thus providing the theoretical prerequisite for a test of many-electron QED effects in the strongest electromagnetic fields available at present for experimental studies.

References

[1] V. M. Shabaev *et al.*, Phys. Rev. Lett. **86**, 3959 (2001).

[2] http://www.uni-mainz.de/FB/Chemie/AK-Noertershaeuser/

[3] A. V. Volotka *et al.*, Phys. Rev. Lett. **103**, 033005 (2009).

[4] D. A. Glazov *et al.*, Phys. Rev. A **81**, 062112 (2010).

[5] A. V. Volotka *et al.*, arXiv:physics/1111:5663.

[6] O. V. Andreev *et al.*, arXiv:physics/1112.3882.

[7] I. Klaft *et al.*, Phys. Rev. Lett. **73**, 2425 (1994).

* Work supported by DFG and GSI

Parity nonconservation effect in the resonant recombination of polarized electrons with heavy hydrogenlike ions *

A. V. Maiorova[1], *V. M. Shabaev*[1], *A. V. Volotka*[1,2], *V. A. Zaytsev*[1], *G. Plunien*[2], *and T. Stöhlker*[3,4,5]

[1]St. Petersburg State University, Russia; [2]TU Dresden, Germany; [3]GSI Darmstadt, Germany; [4]Universität Heidelberg, Germany; [5]Helmholtz-Institut Jena, Germany

Investigations of parity nonconservation (PNC) effects in heavy few-electron ions can give new possibilities for tests of the Standard Model. This is due to the fact that in highly charged ions the electron-correlation effects, being suppressed by a factor 1/Z (Z is the nuclear charge number), can be calculated to a very high accuracy by perturbation theory. PNC experiments with highly charged ions were first discussed in [1], where it was proposed to use the close opposite-parity levels in He-like ions at $Z \sim 6$ and $Z \sim 29$. Later, most of the theoretical studies of the PNC effects with heavy ions exploited the near-degeneracy of the 2^1S_0 and 2^3P_0 levels in He-like ions at $Z \sim 64$ and $Z \sim 90$, where the PNC effect is strongly enhanced [2, 3, 4, 5, 6, 7, 8].

In [9], we study the PNC effect in the resonant recombination of a polarized electron with unpolarized H-like thorium ($Z = 90$) and gadolinium ($Z = 64$) ions into a doubly excited state of the He-like ion. The incident electron energy is chosen to get in resonance with a doubly excited state of the He-like ion assuming that the photons with energy corresponding to the decay of this state to either the 2^1S_0- or the 2^3P_0-state are detected at a given angle. We have considered the resonant recombination processes which correspond to the following dielectronic recombination (DR) channels (without the admixture due to the weak interaction):

1) $\bar{e} + 1s \to (2s_{1/2}2p_{1/2})_1 \to (1s_{1/2}2p_{1/2})_0 + \gamma$
2) $\bar{e} + 1s \to (2s_{1/2}2p_{3/2})_1 \to (1s_{1/2}2p_{1/2})_0 + \gamma$
3) $\bar{e} + 1s \to (2p_{1/2}2p_{3/2})_1 \to (1s_{1/2}2s_{1/2})_0 + \gamma$
4) $\bar{e} + 1s \to (2s_{1/2}3p_{1/2})_1 \to (1s_{1/2}2p_{1/2})_0 + \gamma$
5) $\bar{e} + 1s \to (2s_{1/2}3p_{3/2})_1 \to (1s_{1/2}2p_{1/2})_0 + \gamma$

For these processes the PNC effect should be most pronounced, due to the fact that the main decay channel considered is the magnetic dipole (M1) transition to the $2^1S_0 = (1s_{1/2}2s_{1/2})_0$ or the $2^3P_0 = (1s_{1/2}2p_{1/2})_0$ state, while the PNC-mixing opens the channel for the electric dipole (E1) transition.

The requirement that should be imposed on the luminosity L, provided the PNC effect is measured to a relative accuracy η, can be written as [5, 10]:

$$L > L_0 = \frac{\sigma_+ + \sigma_- + 2\sigma_{\rm b}}{(\sigma_+ - \sigma_-)^2 \eta^2 T}\,. \qquad (1)$$

where $\sigma_{\rm b}$ is the background magnitude and T is the acquisition time (we set it equal 2 weeks).

Table I presents numerical results for the differential cross section in case of thorium at the angles θ corresponding to the minimum values of the luminosity (with $\sigma_{\rm b} = 0$).

Table 1: Cross sections for a resonant recombination of a polarized electron with H-like Th at the photon emission angle θ corresponding to the minimum value of L_0. The number N refers to the process defined in the text.

N	ε_i [keV]	θ [deg]	L_0 [cm^{-2}s^{-1}]	σ_0 [barn]	$\sigma_{\rm PNC}$ [barn]
1	60.91	0	1.2×10^{30}	1.076	6.1×10^{-5}
2	65.04	56	1.9×10^{30}	1.247	-5.2×10^{-5}
4	79.21	0	1.9×10^{30}	0.429	3.0×10^{-5}
5	80.41	53	3.2×10^{30}	0.779	-3.2×10^{-5}
3	64.96	43	2.0×10^{31}	0.287	7.7×10^{-6}

σ_0 is the cross section without the PNC effect and $\sigma_{\rm PNC}$ is the PNC contribution, N is the process number in the list above. It is found that, although in some cases (when the main channel is the two-electron magnetic dipole transition, which is additionally suppressed by a factor $1/Z$, whereas the PNC-mixing channel is the one-electron electric dipole transition) the contribution of the PNC effect to the dielectronic recombination itself is rather big (up to 12%), the corresponding contribution to the total recombination cross section does not exceed 0.1%. This is due to a large screening of the main dielectronic recombination channel by the radiative recombination and the dielectronic recombination via close states. This work may stimulate further efforts for studying the PNC effects in resonant scattering processes with heavy ions.

* Work supported by DFG and RFBR, by GSI and DAAD.

References

[1] V. G. Gorshkov and L. N. Labzowsky, JETP Lett. **19**, 394 (1974); Sov. Phys. JETP **42**, 581 (1975).

[2] A. Schäfer *et al*, Phys. Rev. A **40**, 7362 (1989).

[3] L. N. Labzowsky *et al*, Phys. Rev. A **63**, 054105 (2001).

[4] L. N. Labzowsky and A. Prozorov, J. Phys.: Conf. Ser. **72**, 012010 (2007).

[5] A. V. Maiorova *et al*, J. Phys. B **42**, 205002 (2009).

[6] V. M. Shabaev *et al*, Phys. Rev. A **81**, 052102 (2010).

[7] F. Ferro *et al*, Phys. Rev. A **81**, 062503 (2010).

[8] F. Ferro, A. Surzhykov, and T. Stöhlker, Phys. Rev. A **83**, 052518 (2011).

[9] A. V. Maiorova *et al*, J. Phys. B **44**, 225003 (2011).

[10] G. F. Gribakin *et al*, Phys. Rev. A **72** 032109 (2005); **80** 049901(E) (2009).

Parity–violation effects on the radiative recombination of hydrogen–like ions *

J. Gunst[1], *A. Surzhykov*[1,2], *S. Tashenov*[1], *A. N. Artemyev*[1,2], *and Th. Stöhlker*[1,2,3]

[1]Physics Institute, University of Heidelberg, Germany; [2]GSI Helmholtzzentrum für Schwerionenforschung, Darmstadt, Germany; [3]Helmholtz Institute Jena, Germany

Measurements of the parity–violation (PV) effects in atomic systems attract considerable attention as a valuable tool for testing the Standard Model in the low–energy regime [1]. In the past, the PV studies have mainly dealt with the valence–shell transitions in neutral atoms. Even though the results of these studies have revealed unique information on the Weinberg angle and the nuclear anapole moment, their interpretation was often hindered by the precision of atomic–structure calculations. This difficulty can, to a large extent, be overcome by the use of highly–charged, heavy ions. During the recent years a number of proposals have been made to perform PV–experiments with these heavy few–electron species (see eg. Ref. [2]). Many of these proposals, however, require application of spin–polarized ion beams and/or performing *circular* polarization x–ray measurements; the experimental tasks which can not be easily accomplished today.

An alternative approach to explore PV phenomena in heavy, highly–charged ions was recently pursued by Maiorova and co–workers [3] who considered the radiative recombination of a free electron into excited states of (finally) helium–like ions. It was shown that the angle–differential cross section of this process might be sensitive to the parity violation effects if only photons of a particular *linear* polarization are recorded by x–ray detectors. In this contribution, we lay out an extension of the method of Ref. [3] which is based on the analysis of the *rotation* of the linear polarization of RR photons. Owing to the recent advances in energy– and position–sensitive solid state detectors, such a rotation is likely to be detected in the near future with a sub–degree accuracy opening, thus, a new route to the PV studies with heavy ions.

Similarly to the scenario from Ref. [3], we consider the recombination of unpolarized electrons into the $1s2p_{1/2}\,^3P_0$ state of (finally) helium–like ions. Due to a significant PV–mixing between the 2^3P_0 state and the opposite–parity $1s2s_{1/2}\,^1S_0$ level, the direction of the RR linear polarization is slightly tilted with respect to the parity–conserved (i.e. purely electromagnetic) case. That is, based on the density matrix approach we found that the angle of the linear polarization is given:

$$\chi_0 = \chi_0^{\rm em}\,(1 + \xi\,\mathcal{R}(Z, T_p)) + \mathcal{O}(\xi^2)\,, \qquad (1)$$

where ξ represents the weak mixing coefficient, $\chi_0^{\rm em}$ defines the angle of the RR linear polarization if a parity is preserved ($\chi_0^{\rm em}$ = 0° or 90° if both incident ions and electrons are unpolarized), and $\mathcal{R}$ is the function which depends only on the collision parameters. To understand this effect qualitatively we recall that the weak interaction processes prefer emission (or absorption) of electrons with the particular helicity. For the case of the radiative recombination such an asymmetry results in a dependence of the capture cross section on the projection of the electron spin and, hence, in the rotation of the RR linear polarization.

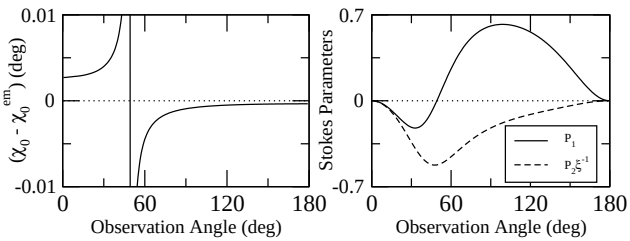

Figure 1: The rotation angle (left) and the Stokes parameters (right) of the linear polarization of the photons emitted due to the radiative recombination of electrons into $1s2p_{1/2}\,^3P_0$ state of finally helium–like gadolinium ions with a projectile energy of 300 MeV/u. Results are presented as function of the RR photon emission angle.

In order to estimate the size of the PV effect on the rotation angle χ_0 calculations have been performed for the electron capture by (initially unpolarized) gadolinium ions with projectile energy T_p = 300 MeV/u. For this energy we displayed in the left panel of Fig. 1 the difference between the polarization rotation angles as obtained with and without account for the parity mixing between the $2\,^3P_0$ and $2\,^1S_0$ states. In the right panel, the Stokes parameters that characterize (apart from the angle) the degree of RR polarization are displayed. As seen from the figure, the PV–induced tilt may reach the value of 0.01° in the angular region where the degree of the polarization is large enough to be detected by the Compton polariemeters.

Together with the high–precision measurements of the RR tilt angle, the practical realization of the proposed scenario requires distinction between the electron capture into $2\,^3P_0$ and almost degenerate $2\,^1S_0$ state. This can be achieved by the analysis of the subsequent characteristic emission and by employing the significant difference between the lifetimes of both excited states. Theoretical study along this line is currently underway.

References

[1] I. B. Khriplovich, "Parity Nonconservation in Atomic Phenomena", Gordon and Breach, New York, 1991.

[2] A. Bondarevskaya et al., Phys. Rep. **507** 1 (2011).

[3] A. V. Maiorova et al., J. Phys. B **42** 205002 (2009).

* Work supported the Helmholtz Gemeinschaft and GSI (Nachwuchsgruppe VH-NG-421).

Relativistic calculations of the K-K charge transfer and K-vacancy production probabilities in low-energy ion-atom collisions*

I. I. Tupitsyn[1], *Y. S. Kozhedub*[1], *V. M. Shabaev*[1], *A. I. Bondarev*[1], *G. B. Deyneka*[2], *I. A. Maltsev*[1], *S. Hagmann*[3], *G. Plunien*[4], *and Th. Stöhlker*[3,5,6]

[1]St. Petersburg State University, Russia; [2]St. Petersburg State University of Information Technologies, Mechanics and Optics, Russia; [3]GSI, Darmstadt, Germany; [4]TU Dresden, Germany; [5]Universität Heidelberg, Germany; [6]Helmholtz-Institut Jena, Jena, Germany

Here we report that the method [1] has now been extended for the evaluation of electron-excitation and charge-transfer processes in low-energy collisions of H-like ions with neutral atoms [2]. This extention is based on the active electron approximation, in which only the active electron participates in the charge transfer and excitation processes while the passive electrons provide the screening potential. The time-dependent Dirac wave function of the active electron is represented as a linear combination of atomic-like Dirac-Fock-Sturm orbitals, localized at the ions (atoms). The screening density functional theory (DFT) potential is calculated using the overlapping densities of each ions (atoms), derived from the atomic orbitals of the passive electrons. The atomic orbitals are generated by solving numerically the one-center Dirac-Fock and Dirac-Fock-Sturm equations by means of a finite-difference approach with the potential taken as the sum of the exact reference ion (atom) Dirac-Fock potential and of the Coulomb potential from the other ion within the monopole approximation.

To examine the approach we calculate the K-K charge transfer and K-vacancy production probabilities for low-energy collision of H-like F (F^{8+}) and neutral Ne, the process which has been investigated both experimentally [3] and theoretically [4, 5, 6]. In the case of the projectile energy of 230 keV/u our results are in perfect agreement with experimental ones. For the projectile energy of 130 keV/u the probabilities $P(b)$ of the Ne K-shell-vacancy production (solid line) and of the K-K-shell charge transfer (dotted line) as functions of the impact parameter b are presented in Fig. 1. As one can see, in this case our theoretical results for the K-vacancy production probability are in a good agreement with the experimental ones at small impact parameters. However, the agreement is not so good for medium and large impact parameters, although the theoretical predictions for the maximum and minimum positions agree rather well with the experimental ones. Let us mention that in [2] we also evaluated the probabilities of the K-K charge transfer and K-vacancy production in Xe – Xe$^{53+}(1s)$ collisions.

To investigate the role of the relativistic effects the same calculations in the nonrelativistic limit are performed. It is demonstrated that the relativistic and nonrelativistic probabilities as functions of the impact parameter exhibit the same oscillatory behavior at low energies but the relativistic curves are shifted toward lower impact parameters compared to the nonrelativistic ones.

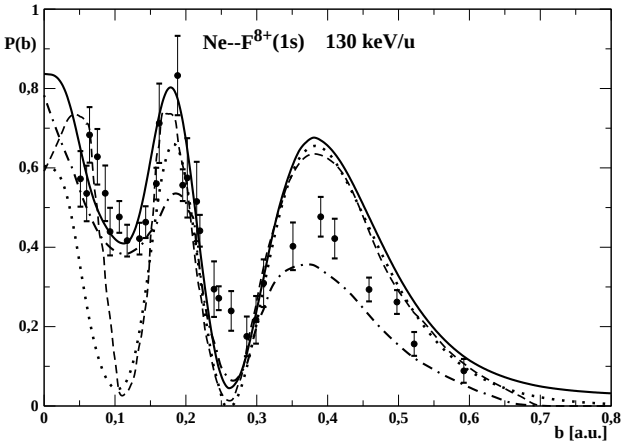

Figure 1: The probabilities $P(b)$ of the Ne K-shell-vacancy production (solid line) and of the K-K-shell charge transfer (dotted line) as functions of the impact parameter b for the Ne-F$^{8+}(1s)$ collision at the projectile energy of 130 keV/u. The circles indicate experimental results by Hagmann *et al.* [3]. The dashed and dash-dotted lines present theoretical results by Lin *et al.* (taken from Ref. [3]) and by Thies *et al.* [6], respectively.

In our further investigation we plan to continue calculations of low-energy heavy-ion collisions that are of interest for current and nearest future experiments at GSI and FAIR facilities in Darmstadt [7]. Special attention will be paid to the critical regime, when the quasimolecular ground-state level of the united system dives into the negative-energy Dirac continuum.

References

[1] I.I. Tupitsyn *et al.*, Phys. Rev. A **82**, 042701 (2010).

[2] I.I. Tupitsyn *et al.*, submitted to Phys. Rev. A, E-prints/physics/arXiv:1112.3223.

[3] S. Hagmann *et al.*, Phys. Rev. A **36**, 2603 (1987).

[4] W. Fritsch and C. D. Lin, Phys.Rev.A **31**, 1164 (1985);

[5] A. Toepfer *et al.*, Phys. Lett. A **126**, 11 (1987);

[6] B. Thies *et al.*, Phys. Lett. A **139**, 161 (1989).

[7] S. Hagmann *et al.*, AIP Conf. Proc. 1336, 115-118 (2011).

* Work supported by DFG and GSI

Electron dynamics accompanying slow heavy–ion collisions *

S. R. McConnell[1], *A. N. Artemyev*[1,2], *A. Surzhykov*[1,2], *and Th. Stöhlker*[1,2,3]
[1]GSI, Darmstadt, Germany; [2]Physikalisches Institut Heidelberg, Germany; [3]Helmholtz Institute Jena, Germany

The past few years have witnessed a revival of interest in the study of heavy quasi–molecular systems formed in slow ionic and/or atomic collisions. New experiments along this line are planned to be performed at the future Facility for Antiproton and Ion Research (FAIR) and will provide unique tests of the quantum electrodynamics (QED) in extremely strong electromagnetic fields. In order to better understand the strong–filed QED phenomena, the experimental findings have to be supplemented by a detailed theoretical analysis of the structure and dynamic behaviour of heavy quasi–molecules. In the simplest case of the "one–electron—two–nuclei" system, such an analysis can be traced back to eigenfunctions of the time–dependent Dirac Hamiltonian:

$$\hat{\mathbf{H}} = -i\boldsymbol{\alpha}\boldsymbol{\nabla} - \frac{\alpha Z_1}{r_1(t)} - \frac{\alpha Z_2}{r_2(t)} + \beta, \qquad (1)$$

where $r_{1,2} = |\mathbf{r} \pm \mathbf{R}(t) \cdot Z_{1,2}/(Z_1 + Z_2)|$ is the distance between an electron and nucleus with the charge $Z_{1,2}$ and $\mathbf{R}(t)$ is the inter–nuclear distance.

Integration of the time–dependent Dirac problem (1) is in general rather complicated task which requires application of approximate methods. Apart from the well–established LCAO (linear combination of atomic orbitals) techniques which allow accurate treatment of the two–center system at rather large distances $\mathbf{R}$ (see eg. Ref. [1]), the so–called monopole approximation was also frequently used in the past [2]. Such an approximation employs solely the spherically–symmetrical part of the (two–center) interaction potential in Eq. (1), thus reducing the problem to the spherically symmetric one, with a total nuclear charge distributed homogeneously on a spherical shell with diameter equal to the internuclear distance. Although the monopole approximation indeed provides very good results for small internuclear distances, it encounters difficulties if ions are placed relatively far from each other.

In this contribution, therefore, we have worked out an extension of the monopole approximation towards the account of the higher terms in the interaction–potential expansion. Such an extended, "multipole–decomposition" approach still allows solution of the two–center problem (1) in the spherical coordinates in which the wavefunction of the electron is written as:

$$\Psi(\mathbf{r}, t) = \sum_n a_n(t)\, \psi_n(\mathbf{r}, R(t))\, \mathrm{e}^{-iE_n t}\,, \qquad (2)$$

* Work supported the Helmholtz Gemeinschaft (Nachwuchsgruppe VH-NG-421) and the International Max Planck Research School for Quantum Dynamics (IMPRS–QD).

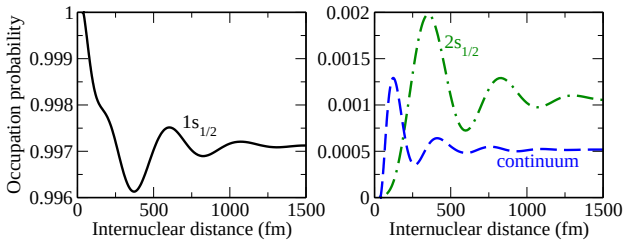

Figure 1: The occupation probabilities of the ground and the first excited states of the hydrogen–like led ion Pb^{81+}, as well as the electron ionization probability following the α–decay of polonium Po^{83+}. Calculations have been performed for the energy of α–particle of 6.713 MeV.

where eigenfunctions ψ_n of the Dirac Hamiltonian are calculated by using the B–spline method in a dual kinetically balanced basis [3], and expansion coefficients a_n found from the solution of the corresponding system of coupled channel equations.

While our approach can be applied for the description of the (single–) electron dynamics in the collision of arbitrary two nuclei, test calculations have been performed for the α–decay of hydrogen–like polonium Po^{83+} ion. By considering this process, we were able to restrict the theoretical analysis to the zero–impact–parameter case. The populations of the ground and the first excited state of (finally) led ion Pb^{81+} are displayed for such a case in Fig. 1 as functions of the inter–nuclear distance R. Moreover, the ionization probability (dashed line) has been evaluated and found to be about $P_{\rm ion} = 5\times10^{-4}$ for large R. This prediction is in a good agreement with the value $P_{\rm ion} = 4\times10^{-4}$ obtained based on the perturbative treatment [4] of the α–decay induced ionization, thus confirming the accuracy of our method.

Based on the developed approach, we aim to investigate in the future the laser–assisted ion–ion scattering. Here we will address the question of how the intense laser may catalyze the process of electron–positron pair production caused by the extremely strong electromagnetic fields produced by high–Z heavy projectiles.

References

[1] I. I. Tupitsyn et al., Phys. Rev. A 82, 042701 (2011).
[2] U. Müller–Nehler and G. Soff, Phys. Rep. 246, 101 (1994).
[3] V. M. Shabaev et al., Phys. Rev. Lett. 93, 130405 (2004).
[4] S. R. McConnell at al., J. Phys. B 44, 145204 (2011).

Angular correlations in radiative cascades following resonant electron capture by highly charged ions*

O. Matula[†1,2], *S. Fritzsche*[1,3], *and A. Surzhykov*[1,2]

[1]Physikalisches Institut, Universität Heidelberg, Germany; [2]GSI, Darmstadt, Germany; [3]Department of Physical Sciences, University of Oulu, Finland

Dielectronic recombination (DR) is a resonant process, in which a free electron is captured into an ion under the simultaneous excitation of one (or several) bound electrons, and the resulting multiple-excited state stabilizes by a cascade of characteristic x-ray photons. The first and second subsequent photon are conventionally denoted as the hypersatellite (HS) and satellite (S) one respectively. Whereas in the last decades a number of studies have been performed to determine the total DR rates [1], much of today's interest is focused on the angular properties of the characteristic x-ray photons. These angle-resolved studies provide a unique tool to probe relativistic, many-body and QED effects in the high-Z regime. For example, a strong E1-M2 multipole-mixing for the emission of the HS photon has been observed recently for K-LL DR into (initially) hydrogenlike U^{91+} ions at the electron storage ring (ESR) at GSI [2]. Apart from the *individual* HS and S transitions, the nondipole effects may also significantly affect the angular correlations *between* the subsequent photons.

In this contribution we perform a theoretical analysis of the $\gamma - \gamma$ correlations within the radiative cascades following resonant electron capture into highly-charged ions. Our analysis that extends previous work by Zakowicz and co-authors [3] is based on a density matrix approach and relativistic Dirac theory. Here we pay special attention to higher-order, nondipole effects in the expansion of the electron-photon interaction.

To quantify the angular correlations, a proper observable is given by the angular distribution of the S photons measured in coincidence with the HS photons emitted under a specific angle $\Omega_1 = \{\theta_1, \varphi_1\}$. This distribution (also denoted as correlation function) can be written as

$$W_{abc}(\Omega_1, \Omega_2) = \frac{1}{4\pi} \left(1 + W_{ab}(\Omega_1)^{-1} \sum_{k_1 k_2 k} \beta^{abc}_{k_1 k_2 k} \times \{ Y_{k_1}(\Omega_1) \otimes Y_{k_2}(\Omega_2) \}_{k0} \right), \quad (1)$$

where $W_{ab}(\Omega_1)$ is the angular distribution of the HS photon, and $\{ Y_{k_1}(\Omega_1) \otimes Y_{k_2}(\Omega_2) \}_{k0}$ is a standard notation for a tensor product of spherical harmonics. Furthermore, Eq. (1) depends on the so-called generalized anisotropy parameters $\beta^{abc}_{k_1 k_2 k}$, which account for the free-bound and bound-bound transition matrix elements. The free-bound transition amplitudes have been evaluated within a multiconfiguration Dirac-Fock (MCDF) approach taking into account the full Dirac-Coulomb-Breit interaction, whereas the bound-bound amplitudes have been computed within an independent particle model (IPM), which is known to give accurate results in the high-Z regime [4].

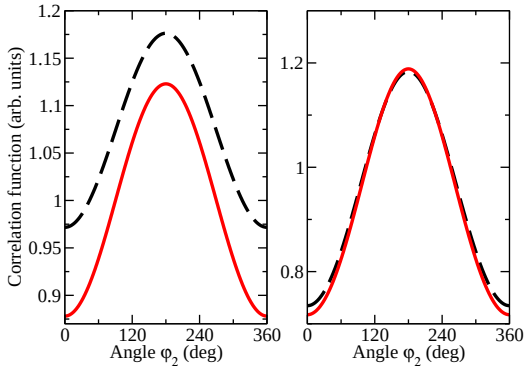

Figure 1: Correlation function for the decay of the $L_{1/2}L_{3/2}$ resonance group proceeding via the $1s_{1/2}2l_{1/2}(J = 1)$ intermediate states. Results obtained within the electric–dipole approximation (- -) are compared to those of the exact theory (–) for the two particular geometries mentioned in the text.

Our general formalism has been applied to compute the correlation function for the radiative decay of the $L_{1/2}L_{3/2}$ resonance of finally heliumlike uranium. This resonance is populated at an electron energy of about 68.5 keV and stabilizes afterwards by emission of two subsequent photons via the intermediate $1s_{1/2}2l_{1/2}(J = 1)$ states. In Fig. (1) the correlation function is shown with (–) and without (- -) multipole mixing effects taken into account for two different geometries: $\varphi_1 = 0, \theta_1 = 20°, \theta_2 = 18°$ (left) and $\varphi_1 = 0, \theta_1 = \theta_2 = 45°$ (right). In the left panel the multipole mixing can be seen to significantly influence the angular distribution over the whole φ_2-range with effects up to 10%. In the right panel, however, the nondipole contributions are seen to be neglectable. As a conclusion, multipole mixing may significantly affect the correlations in the decay of the $L_{1/2}L_{3/2}$ resonance for specific geometries.

References

[1] C. Brandau *et al.*, Phys. Rev. Lett. **91**, 07320297 (2003).

[2] X. Ma *et al.*, Phys. Rev. A **68**, 042712 (2003).

[3] S. Zakowicz, W. Scheid, and N. Grün, J. Phys. B: At. Mol. Opt. Phys. **37**, 131 (2004).

[4] O. Matula *et al.*, Phys. Rev. A **84**, 052723 (2011).

* Work supported by Helmholtz Gemeinschaft, Nachwuchsgruppe VH-NG-421

† omatula@physi.uni-heidelberg.de

Two-photon absorption of few-electron heavy ions *

S. Fritzsche[1,2], *P. Indelicato*[3], *J. P. Santos*[4], *P. Amaro*[4], *and A. Surzhykov*[1,5]

[1]GSI, Darmstadt, Germany; [2]Department of Physics, University of Oulu, Finland; [3]Laboratoire Kastler Brossel, Paris, France; [4]Departamento de Física, Universidade Nova de Lisboa, Portugal; [5]Physikalisches Institut Heidelberg, Germany

The recent progress in developing coherent light sources have opened new avenues for studying two- and multi-photon transitions in ions, atoms and molecules. For example, the $ns \to n's$ and $ns \to n'd$ two-photon excitation of atomic hydrogen and deuterium has been explored in great during recent years and and helped determine the *fundamental* constants with unprecendented accuracy [1, 2]. Less attention, however, has been paid until now to *induced* two-photon absorption processes in multiple and high-Z atoms and ions, though they are exptected to provide new insights into relativistic, many-body and QED phenomena in strong electromagnetic fields and, hence, may serve as a valuable alternative to x-ray absorption (XAS) spectroscopy and related techniques [3]. Moreover, induced two-photon excitations have been proposed as a promising tool for studying parity-violating interactions in high-Z ions [4].

To explore and better understand the two-photon absorption in strong fields, we have recently worked out a (unified) relativistic formalism that enables one to describe the (spatial and polarization) properties of light in a consistent manner [5]. Using second-order perturbation theory and Dirac's relativistic equation, expressions were derived for the two-photon excitation cross sections and rates, including the important many-electron effects as well as all (higher) multipoles in the expansion of the electron-photon interaction. For the absorption of a photon, arriving from the direction $\hat{\boldsymbol{k}} = (\theta, \phi)$ with regard to the quantization (z) axis, such an expansion of the electron-photon operator $\hat{\mathcal{R}} = \sum_m \boldsymbol{A}_m(\boldsymbol{k}, \boldsymbol{\epsilon})$ into spherical tensors reads as [6]

$$\boldsymbol{A}_m(\boldsymbol{k}, \boldsymbol{\epsilon}) = 4\pi \sum_{pLM} i^{L-|p|} \left(\boldsymbol{\epsilon} \cdot \boldsymbol{Y}^{(p)*}_{LM}(\hat{\boldsymbol{k}}) \right) \boldsymbol{a}^p_{LM,m}(k) \,,$$

where $\boldsymbol{Y}^{(p)}_{LM}(\hat{\boldsymbol{k}})$ is a vector spherical harmonics and the index p describes either the electric (p = 1), magnetic (p = 0), or longitudinal (p = –1) component of the electromagnetic field. In this formalism, in addition, the properties of the incident light are described conveniently by means of the (so-called) *angular-polarization* tensor, and which is known to contain the complete information about the direction and polarization states of the incident photons in the two-photon absorption process.

While our derived expressions are general and independent of the particular shell structure of the ion, detailed computations have been carried out for the two-photon absorption of hydrogen-, helium-, and beryllium-like ions, and they are compared with the available theoretical and experimental data [5]. Figure 1, for example, displays the (reduced) cross section $\alpha_0 = \sigma_{2\gamma}/g(\omega)G^{(2)}$ for the $1s \to 2s$ and $1s \to 2p_{1/2}$ absorption of hydrogen-like ions. Here, $G^{(2)}$ is the two-photon statistical factor and $g(\omega)$ is the line-shape function. As seen from the figure, the relativistic contraction of the wave functions toward the nucleus as well as the nondipole effects in the electron-photon interaction lead to a faster decrease of the cross sections than predicted by the non-relativistic $\alpha_0(1s \to 2s) \sim Z^6$ and $\alpha_0(1s \to 2p) \sim Z^4$ scalings. Further computations have been performed for the (excitation) probabilities of the two-photon induced $1s2p\ ^3P_0 \to 1s2s\ ^1S_0$ and $1s^22s^2\ ^1S_0 \to 1s^22s2p\ ^3P_0$ transitions of helium-like and beryllium-like ions.

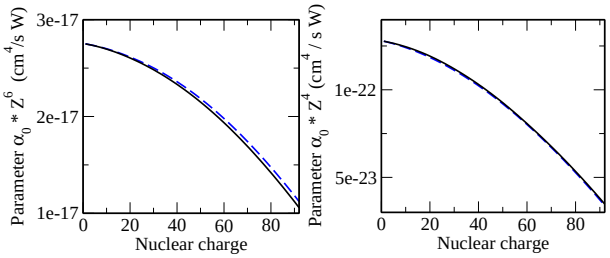

Figure 1: The parameter α_0 for the two–photon $1s \to 2s$ (left panel) and $1s \to 2p_{1/2}$ (right panel) absorption of hydrogen–like ions. Predictions have been obtained within the electric dipole (dashed line) approximation as well as by taking the higher terms into account (solid line).

In conclusion, our studies demonstrate the importance of relativistic and higher-multipole effects upon the two-photon absorption rates. Reliable theoretical rates are however required to plan and prepare future experiments on the parity violation in high-Z ions as they will be performed at the future Facility for Antiproton and Ion Research (FAIR) in Darmstadt. A new generation of such two-photon absorption experiments with helium-like ions is currently being planned at the GSI facility in Darmstadt and the Helmholtz Institute in Jena.

References

[1] B. de Beauvoir et al., Eur. Phys. J. D 12, 61 (2000).

[2] O. Arnoult et al., Eur. Phys. J. D 60, 243 (2010).

[3] C. Szymanowski et al., Europhys. Lett. 37, 391 (1997).

[4] M. Maul et al., J. Phys. B 31, 2725 (1998).

[5] A. Surzhykov et al., Phys. Rev. A84, 022511 (2011).

[6] S.P. Goldman and G.W.F. Drake, PRA 24, 183 (1981).

* Work supported the Helmholtz Gemeinschaft and GSI (Nachwuchsgruppe VH-NG-421).

Triple ionization of lithium-like ions by photon impact*

A.I. Mikhailov[1], *A.V. Nefiodov*[1], *A. Pernice*[2], *and G. Plunien*[2]

[1]PNPI, 188300 Gatchina, St. Petersburg, Russia; [2]TU Dresden, Mommsenstr. 13, D-01062 Dresden, Germany

Due to the single-particle character of the electron-photon interaction, the multielectron ionization of atoms by a single photon is entirely caused by the electron correlations. Lithium-like ions allow one to study both the inner- and inter-shell electron correlations. In addition, these are the simplest systems, in which three electrons can be ionized simultaneously by a single photon.

In paper [1], we have considered the triple ionization of Li-like ions by photon impact within the framework of the sudden approximation. According to this model, the process is viewed as the double ionization of inner K-shell electrons followed by ejection of the outer-shell electron. It is also assumed that $Z \gg 1$ and $\alpha Z \ll 1$, where α is the fine-structure constant.

In the high-energy non-relativistic limit, the triple-to-single photoionization ratio can be cast into the following scaling form ($\hbar = 1$, $c = 1$) [1]:

$$R^{3+}(\mathrm{Li}) = \frac{\sigma^{3+}(\mathrm{Li})}{\sigma^{+}(\mathrm{Li})} = \frac{16}{17}\, R^{2+}(\mathrm{He})\, W_{2s} = \frac{0.085}{Z^2}\, W_{2s}\,. \quad (1)$$

The notations He and Li imply the members of isoelectronic sequences of He and Li, respectively, which have the same nuclear charge Z. The quantity W_{2s}, which is the total probability for ejection of the $2s$ electron into the continuum due to sudden change of the atomic field, has rather complicated dependence on the the nuclear charge Z. For the particular case of the neutral Li atom, we obtain $W_{2s} = 0.406 \times 10^{-2}$ and $R^{3+} = 0.38 \times 10^{-4}$.

Equation (1) is applicable for ionization of the non-relativistic targets by high-energy photons. If the energy-dependent ratio $R^{2+}(\mathrm{He})$ is employed, then one can check the range of applicability of the model under consideration. The universal function $Z^2 R^{2+}(\mathrm{He})$ with respect to the photon energy has been calculated in work [2]. By using this result, we have drawn the curve R^{3+} as a function of the excess energy for the case of Li atom (see Fig. 1). The agreement of the model predictions with the experimental measurements is remarkably good, that seems to be due to different time scales for ionization of the $1s$ and $2s$ electrons.

As a by-product of the scaling (1), one can also estimate the triple-to-double photoionization cross section ratio. In the asymptotic high-energy region, it yields [1]

$$\frac{\sigma^{3+}(\mathrm{Li})}{\sigma^{2+}(\mathrm{Li})} = 0.294\, W_{2s}\,. \quad (2)$$

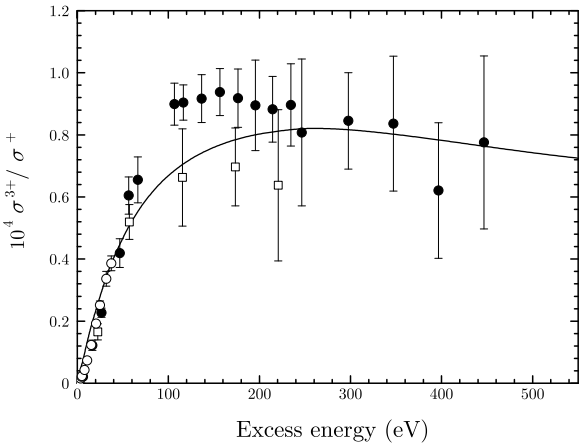

Figure 1: Triple-to-single photoionization ratio in the Li atom. Experimental data: open squares, [3]; open circles, [4]; black circles, [5].

This formula is valid for arbitrary Li-like targets with moderate values of the nuclear charge Z. If $Z = 3$, we get $\sigma^{3+}/\sigma^{2+} = 0.12 \times 10^{-2}$, which is in agreement with the experimental measurement [5] and prediction of the half-collision model [6].

By using the sudden approximation, we have also considered the triple ionization of Li-like targets by Compton scattering of high-energy photons. The triple-to-single Compton ionization ratio can be written as follows [1]

$$R^{3+}_{\mathrm{C}}(\mathrm{Li}) = \frac{\sigma^{3+}_{\mathrm{C}}(\mathrm{Li})}{\sigma^{+}_{\mathrm{C}}(\mathrm{Li})} = \frac{0.033}{Z^2}\, W_{2s}\,. \quad (3)$$

In the particular case of neutral Li atom, we get $R^{3+}_{\mathrm{C}} = 0.15 \times 10^{-4}$.

Finally, the triple-to-double ionization ratio in high-energy Compton scattering is estimated as [1]

$$\frac{\sigma^{3+}_{\mathrm{C}}(\mathrm{Li})}{\sigma^{2+}_{\mathrm{C}}(\mathrm{Li})} = 0.227\, W_{2s}\,. \quad (4)$$

References

[1] A.I. Mikhailov, A.V. Nefiodov, and G. Plunien, Phys. Lett. A 375 (2011) 823.

[2] A.I. Mikhailov et al., JETP Lett. 78 (2003) 110.

[3] R. Wehlitz et al., Phys. Rev. Lett. 81 (1998) 1813.

[4] R. Wehlitz et al., Phys. Rev. A 61 (2000) 030704(R).

[5] P.N. Juranić and R. Wehlitz, Phys. Rev. A 78 (2008) 033401.

[6] T. Pattard and J. Burgdörfer, Phys. Rev. A 63 (2001) 020701(R).

* Work supported by GSI

PEBSI - A Monte Carlo simulator for polarized-electron bremsstrahlung*

G. Weber[1,2], *R. Märtin*[2,3], *A. Surzhykov*[2,3], *M. Yasuda*[4], *V. A. Yerokhin*[5,2,3], *and Th. Stöhlker*[1,2,3]

[1]Helmholtz-Institut Jena, Germany; [2]GSI, Darmstadt, Germany; [3]Universität Heidelberg, Germany; [4]Osaka Prefecture University, Japan; [5]St. Petersburg State Polytechnical University, Russia

Electron-atom bremsstrahlung, also referred to as ordinary bremsstrahlung, is one of the basic photon-matter processes and has attracted continuous interest both theoretically and experimentally during the last decades [1, 2, 3]. Of particular importance is the study of the bremsstrahlung polarization properties resulting from polarized electrons as it reveals subtle details of the so-called polarization transfer, i.e. a modified degree of linear polarization and a rotation of the polarization axis, from charged particles to the emitted x-rays [4]. Recently, a series of polarization-resolved bremsstrahlung measurements has been carried out at the test stand of the polarized electron source SPIN [5] at the TU Darmstadt. In these experiments the polarization transfer was studied in collisions of polarized electrons with gold foils of about 100 μg/cm^2 thickness and at an impact energy of 100 keV [6, 7].

A crucial point when drawing conclusions from the experimental data is the question to what extend the bremsstrahlung characteristics, in particular concerning the polarization, are altered by effects due to multiple collisions inside the target. One can expect that the linear polarization shows a high sensitivity to the target thickness as the straggling of incident electrons followed by bremsstrahlung emission leads to a superposition of different degrees of polarization and polarization orientations, resulting in a decrease of the degree of linear polarization and a modified orientation of the polarization axis. To quantify these effects, the Monte Carlo code PEBSI (Polarized Electron Bremsstrahlung SImulator) was developed for modeling the bremsstrahlung arising from polarized electrons during their passage through matter [8].

Indeed, preliminary calculations show that for the target thicknesses of interest the straggling of the electrons within the target foils leads to a significant reduction of both the degree of linear polarization P_L and the rotation of the polarization vector $\Delta\chi$. As an example, we present in Fig. 1 the degree linear polarization and the rotation of the polarization axis of bremsstrahlung stemming from polarized electrons with an kinetic energy of 100 keV impinging on a thin gold foil. We assumed the electron polarization to be oriented perpendicular to the incident electron direction (transversal polarization) and to lie within the reaction plane, being defined by the incident electron momentum and the direction of the emitted photon. It is interesting to note that while the value of P_L significantly decreases with decreasing photon energy, the rotation angle $\Delta\chi$ exhibits only a very weak dependence on the bremsstrahlung energy. Moreover, for the highest photon energy considered, the degree of linear polarization remains constants for target thicknesses above 500 μg/cm^2.

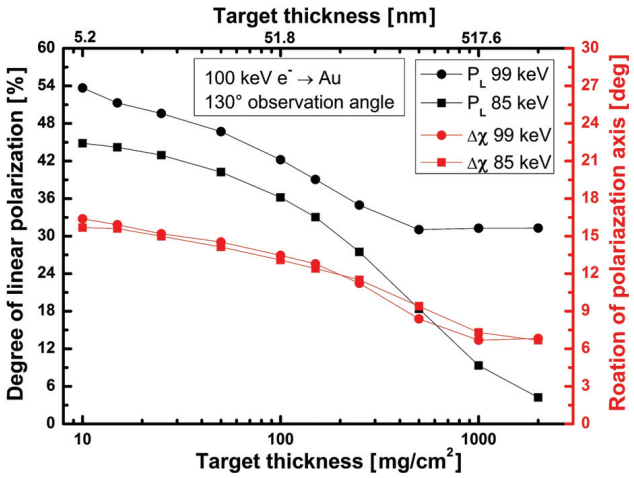

Figure 1: Preliminary PEBSI results for the degree of linear polarization and the orientation of the polarization axis for bremsstrahlung arising from polarized electrons impinging on a gold foil of various thicknesses. The bremsstrahlung is emitted at an angle of 130° with respect the incident electron direction and two photon energies at the high-energy end of the bremsstrahlung distribution are considered.

Summarizing, according to the presented PEBSI results, a rigorous analysis of polarization-resolved bremsstrahlung measurements using high-Z solid-state target foils has to take into account the effects of electron straggling on the bremsstrahlung properties.

References

[1] W. Nakel, Phys. Rep. **243**, 317 (1994).

[2] C. A. Quarles, Rad. Phys. Chem. **59**, 159 (2000).

[3] C. A. Quarles and S. Portillo, Rad. Phys. Chem. **75**, 1187 (2006).

[4] V. A. Yerokhin and A. Surzhykov, Phys. Rev. A **82**, 062702 (2010).

[5] C. Heßler et al., Proceedings of EPAC08 (2008).

[6] R. Märtin et al., AIP Conf. Proc. **1336**, 94 (2011).

[7] S. Tashenov et al., Phys. Rev. Lett. **107**, 173201 (2011).

[8] G. Weber et al., Nucl. Inst. Meth.B. in print.

* Work supported by the Helmholtz Gemeinschaft (Nachwuchsgruppe VH-NG-421) and by HI Jena

MD simulations of the dynamics of heavy ions in HITRAP*

J. Steinmann, P.-G. Reinhard, G. Zwicknagel
Institut für Theoretische Physik, Universität Erlangen, Germany

In previous simulation studies [1, 2] we investigated the dynamics of the electron cooling process and the related phase space distribution of highly charged ions in HITRAP based on a molecular dynamics (MD) simulation scheme. There the motion of each ion is numerically calculated taking into account the electric and magnetic fields in the trap and the stopping force due to collisions with magnetized electrons which is taken from microscopic calculations [3]. Only the Coulomb interaction between the ions was neglected so far, which is expected to be important only in the very last phase of cooling when the ions already move rather slowly. In more recent implementations of such simulations we thus also included the ion-ion Coulomb interaction. But this considerably enhances the numerical effort and should be restricted preferably to the final part of the cooling process. To study the relevance of the ion-ion interaction we therefore compare simulations with and without taking it into account.

Some first results have been obtained by performing corresponding MD simulations with $N = 9216$ bare uranium ions U^{92+}, which is already close to the designed 10^5 ions in the real trap, are shown in Figs. 1 and 2. The magnetic field along the trap axis is $B = 6$ T. The electric fields in the trap are, however, replaced for these tests by a simple potential well along the trap axis with infinitely high walls and with an additional small harmonic trapping potential of a few tens of eV in the center of the trap. Also the detailed cooling forces are replaced by a simple friction force $\vec{F}_f = -\eta\vec{v}$. To reduce here the relevant time scale some artificially enlarged friction was used. Considering the whole simulation period of about 12 μs on the scales given in Figs. 1 no differences between both cases are visible, both curves lie on top of each other. But a more detailed view on the spatial ion distribution at later times $t \gtrsim 7\mu$s reveals deviations as can be seen in Fig. 2 (top). In the presence of the ion-ion Coulomb interaction, the repulsion of the ions prevent the ion cloud to be axially squeezed in the center of the harmonic trapping potential. The transverse spatial distribution is ruled by the confinement due the strong axial magnetic field and does not significantly differ in both cases as shown in Figs. 2 (center and bottom) for $t \approx 11.5\mu$s. As expected, the influence of the ion-ion interaction is significant only at low ion energies.

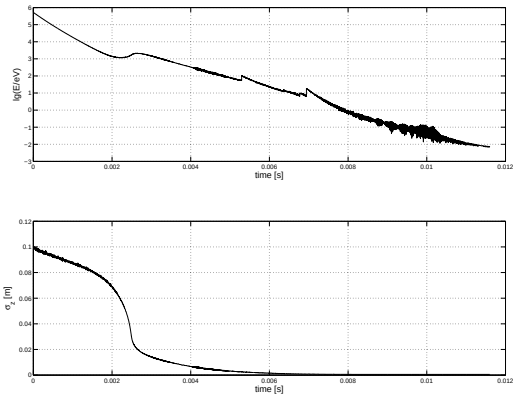

Figure 1: Top: temporal evolution of the mean energy E of the ions. Bottom: standard deviation σ_z of the spatial ion distribution along the trap axis.

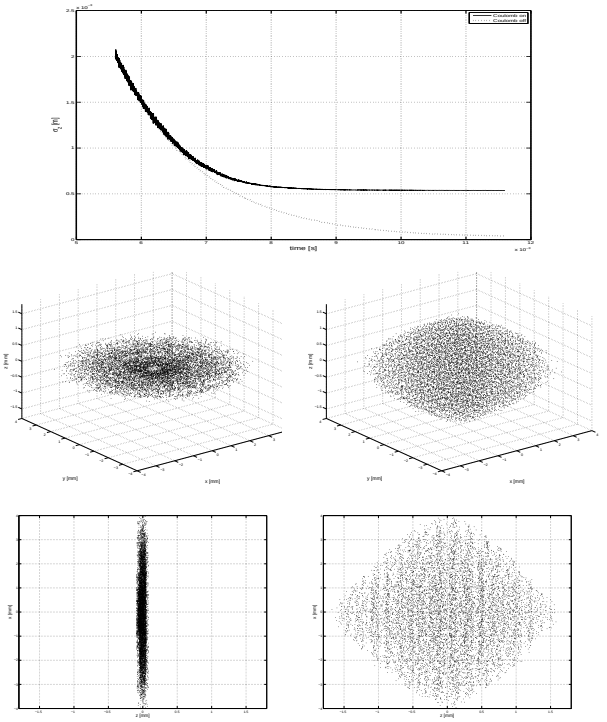

Figure 2: Top: standard deviation σ_z as in Fig. 1 for $t \gtrsim 5.5\mu$s. Center and bottom: spatial ion distribution at $t \approx 11.5\mu$s, left panels without, right panels with ion-ion interaction.

References

[1] G. Zwicknagel, GSI Report 2009-1, p. 307; GSI Report 2011-1, p. 367

[2] B. Möllers, PhD-thesis, University Erlangen 2007, `www.opus.ub.uni-erlangen.de/opus/volltexte/2007/547/`.

[3] H. Nersisyan, C. Toepffer, G. Zwicknagel, *Interactions Between Charged Particles in a Magnetic Field* (Springer, Berlin Heidelberg New York 2007)

*Work supported by the BMBF (06ER9064)

Simulation of Ion Clouds in Penning traps using graphic boards*

J. Steinmann[1,2], *S. Fedotova*[1], *J. Groß*[2], *F. Herfurth*[1], *and G. Zwicknagel*[3]

[1]GSI Helmholtzzentrum, Darmstadt, Germany; [2]University of Applied Sciences, Darmstadt, Germany; [3]University, Erlangen-Nuernberg, Germany

The HITRAP (Highly charged Ions Trap) facility at the GSI was developed for the investigation of slow highly charged ions up to U^{92+}. The ion trap was designed to store up to 10^5 ions by superimposing appropriate magnetic and electric fields. The ions are injected into the Penning trap with an energy of 6 keV/u and are cooled down to 10 eV/u due to electron cooling. Following the electron cooling and collecting of the ions in the center of the trap, resistive cooling is performed to cool the ion cloud down to 0.3 meV/u. During this process the ion density increases and the characteristics of the ion cloud are increasingly determined by the Coulomb interaction. The motion of the j-th ion is governed by the equation

$$\ddot{\vec{x}}_j = -\frac{q_j}{m_j}\cdot\left(\vec{\nabla}V - \dot{\vec{x}}_j \times \vec{B}\right) + \frac{q_j}{m_j}\cdot\sum_{k=1,j\neq k}^{N}\frac{q_k\cdot(\vec{x}_j-\vec{x}_k)}{|\vec{x}_j-\vec{x}_k|^3} + \frac{\vec{F}_{cooling}}{m_j}$$

x_j , x_k are the position vectors of ion no. j resp. no. k, q_j, m_j are the charge resp. the mass of ion no. j, V is the electric potential and B the magnetic field, both at the ion position. $F_{cooling}$ is a frictional force.

For N ions, this leads to an ODE-system of $3N$ equations, which in general can only be solved by using a numerical integration scheme. The computational effort to solve the ODE-system is proportional to N^2 and quickly leads, with increasing number of ions, to simulation times of several years. The simulation time for such a huge ODE-system can be reduced immensely by using graphic boards. The special architecture of the graphic boards allows to use them as parallel computers, so that in the ideal case the computational effort scales with N, only.

The graphic board mainly consists of a number of arithmetic logical units (ALU), which are arranged into work groups of similar size. Each work group got a local memory, for fast communication between ALU of the same work group. The work groups themselves communicate via the global memory of the graphic board. The access time of the local memory is more than one hundred times faster than the access time of the global memory, and it should therefore be used as often as possible. Figure 1 illustrates the simplified work flow of a graphic board. The example board consists of 3 work groups, where each of them holds 3 ALU. In total 27 threads must be processed. The threads are sorted into 9 blocks of equal size. Due to the 3 work groups 3 blocks (9 threads or in our case the trajectories of 9 ions) can be calculated at the same time. Compared to a system using a single ALU (like older CPUs) the graphic board enables a calculation, which performs nine times faster.

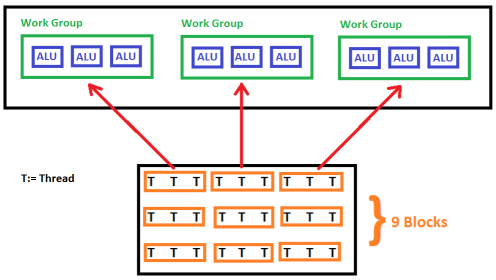

Figure 1: Operation scheme of a grafic board

In figure 2 a comparison of the simulation time for two types of graphic boards and a CPU is shown. The device specifications are listed in table 1. The comparison is made for simulations over a period of 50 timesteps, using single precison and a fourth order Runge-Kutta algorithm. The

Device	GFLOPS	Memory global [MB]	Memory local [kB]
ATI FirePro V8800	2640	2048	32
NVIDIA Quadro FX 880M	174.2	1024	16

Table 1: Device Specifications

strong magnetic field (6 T) in the HITRAP Penning trap is a limiting factor for the maximal step size, allowed. Due to the large cyclotron frequency $\omega_c \propto 10^8 s^{-1}$, the maximal step size should be at most $\approx 10^{-9} s$. The simulation of a cooling cycle for a cloud of 10^4 ions over a duration of 10^{-2} s and a stepsize of 10^{-9} s lasts approximately seven days on the ATI device. The same simulation on the CPU needs approximately 2 years.

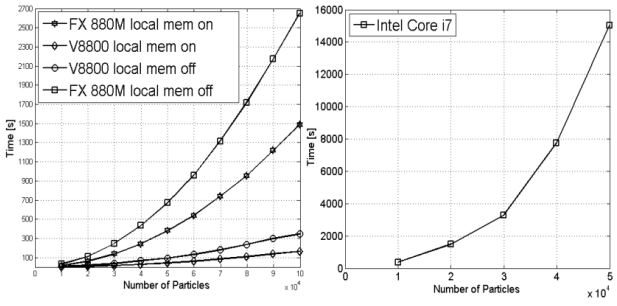

Figure 2: Comparison of simulation time

With the code developed it is already possible to simulate the cooling process of a system of 10^4 ions, where the cooling is performed through a frictional force. The next step is to adapt the code to simulate electron and resistive cooling.

* Work supported by FE, Project-Number DAGROS1012.

Two–Dimensional Thermal Simulations of an Aluminum Beam Stripper for Experiments at SPIRAL2*

N.A. Tahir[1], V. Kim[2], E. Lamour[3], I.V. Lomonosov[2], A.R. Piriz[4], J.P. Rozet[3], Th. Stöhlker[1], V. Sultanov[2], and D. Vernhet[3]

[1]GSI, Darmstadt, Germany; [2]IPCP, Chernogolovka, Russia; [3]Institut des NanoSciences de Paris,UMR CNRS–Université Pierre et Marie Curie, Paris, France; [4]UCLM, Ciudad Real, Spain

Based on 2D numerical simulations, we propose design of a wheel shaped Al stripper for use in the FISIC (Fast Ion-Slow Ion Collision) experiments at the SPIRAL2 facility. The inner radius, R_1 of the target is 32 cm, the outer radius, R_2 is 35 cm while the beam is perpendicular to the target surface at a radius, R_0 = 33 cm (see Fig. 1). The target is rotated at a rate of 2000 rpm.

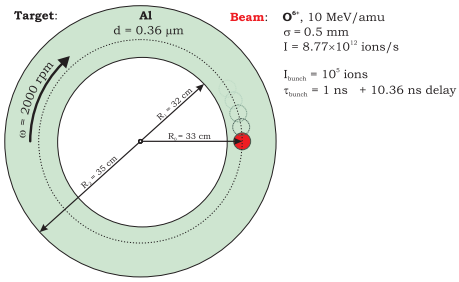

Figure 1: Stripper geometry.

First test calculations are presented using a typical beam of ${}_{18}O^{6+}$ at 10 MeV/u with a current = 1.4 pμA that leads to 8.77x10^{12} particles per second. The beam comprises of particle bunches with bunch length = 1 ns and bunch frequency = 88 MHz while the transverse intensity distribution is Gaussian with σ = 0.5 mm. This means that each bunch comprises of 10^5 ions. The Al stripper thickness is 100 μg/cm^2 that corresponds to 0.36 μm. 2D thermodynamic response of the target is calculated using a numerical model, PIC3D [1] and the results are presented in Fig. 2 where we plot the target temperature at the focal spot center, T_{R0}, at the inner target radius, T_{R1} and at the outer target radius, T_{R2} vs time . In one set of calculations we include thermal conduction only, while in the other case we consider thermal conduction as well as radiation losses from the target surface. It is seen in Fig. 2 that excluding the radiation losses, the temperature at all the above three target locations continues to increase during the considered time of 6 s. On the other hand, when the radiation losses are included, the temperature saturates at around 3 s with T_{R0} = 307 K, T_{R1} = 300 K and T_{R2} = 296 K.

Fig. 3 shows the evolution of T_{R0} over 200 s including and excluding the radiation losses. It is seen that the temperature saturates at 307 K in the former case while the temperature continues to increase in the latter case and melting occurs at t = 180 s. Therefore heat conduction alone is not sufficient to cool the target and the radiation losses are very important in this respect. Further details can be found in [2].

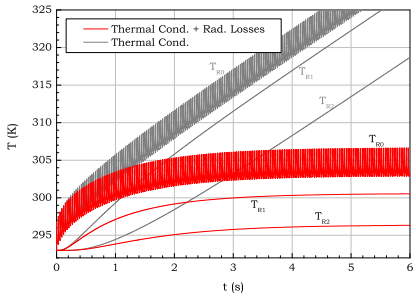

Figure 2: Temperature, T_{R0} at the center of the focal spot, T_{R1}, at the inner target radius and T_{R2}, at the outer target radius; red curve including heat conduction and radiation losses, black curve including only heat conduction vs time.

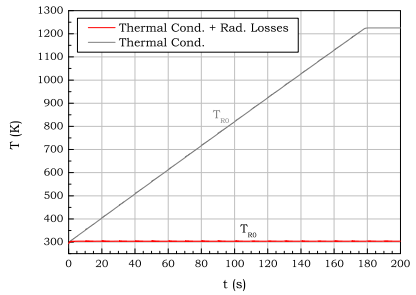

Figure 3: Same as in Fig. 2, but up to 200 s after irradiation.

These simulations have shown that the stripper is stable corresponding to the above beam parameters, however, much higher beam intensities will also be used. Typical beam parameters are as below.

(a) ${}_{18}O^{6+}$ with current between 15 – 70 pμA.
(b) ${}_{20}Ne^{7+}$ with current between 15 – 60 pμA.
(c) ${}_{40}Ar^{13+}$ with current between 8 – 30 pμA.

It is, therefore, important to check the stripper behavior for the above parameters. This work is in progress.

References

[1] V.E. Fortov et al., Intnl. J. Impact Eng. 33 (2006) 244.

[2] N.A. Tahir et al., Nucl. Inst. Meth B (2012) Submitted.

* Work supported by the BMBF

Swift Heavy Ion-Induced Amorphization of $CaZrO_3$ Perovskite*

M. Lang[1#], F.X. Zhang[1], W.X. Li[1], D. Severin[2], M. Bender[2], S. Klaumünzer[3], C. Trautmann[2], and R.C. Ewing[1]

[1] University of Michigan, Ann Arbor, MI, U.S.A.; [2] GSI, Darmstadt, Germany; [3] HZB, Berlin, Germany

Perovskite structures (ABO_3) are an important class of ceramics with a large variety of derivative structure-types (e.g., cubic, hexagonal, and orthorhombic). Owing to this structural flexibility, perovskites have very different physical and chemical properties leading to numerous technological applications. Radiation damage in perovskites is of interest due to their potential as actinide waste forms.

Powder $CaZrO_3$ perovskite was irradiated with 940-MeV Au ions at the UNILAC M2-beamline [1]. The irradiations were performed in steps of 1×10^{12} ions/cm^2 up to a fluence of 8×10^{12} ions/cm^2 with two additional exposures at 1×10^{13} ions/cm^2 and 1.5×10^{13} ions/cm^2. During beam interruptions, the structure of the powder material was analysed by *in situ* X-ray diffraction (XRD) measurements. The instrument is a standard 4-circle X-ray diffractometer (Cu-K_α) operating in vacuum and equipped with a position-sensitive detector. Within the maximum X-ray range of about 10 μm, the electronic energy loss (dE/dx) of the Au ions was with ~36 keV/nm nearly constant, and the nuclear dE/dx was well below 0.5% of the total energy loss (SRIM 2008). Samples from irradiations at two different fluences were additionally investigated by transmission electron microscopy (TEM).

Ion-induced amorphization is evidenced in the XRD patterns by a decrease in diffraction intensity and an increase in diffuse scattering (Fig. 1a,b). The crystalline and amorphous contributions were quantified by peak-fitting the diffraction profiles at each irradiation step yielding position, FWHM, intensity, and area of the diffraction maxima. With increasing fluence, the normalized area of the 101 and 020 peaks (~22°) decreases quickly (Fig. 1c: filled circles). Concurrently, the normalized area of the broad amorphous peak (~30°) grows linearly in the initial stage and finally reaches saturation at higher fluences (Fig. 1c: filled squares). This behaviour can be understood in terms of the direct-impact model, where amorphization is described by the accumulation of individual amorphous tracks. At larger fluences, tracks begin to overlap, and the increase/decrease in amorphous/crystalline fraction becomes sub-linear. The amorphization cross-section per incident ion, σ, was determined by fits to the XRD data (Fig. 1c), and a track diameter d was extracted by assuming cylindrical track geometry ($\sigma = \pi\cdot(d/2)^2$). Based on the average of several diffraction maxima (including the broad amorphous peak), individual tracks have a calculated diameter of 6.0 ± 0.6 nm. This is in good agreement with independent TEM measurements yielding a track diameter of 6.7 ± 0.4 nm.

With accumulating radiation, the 2θ positions of all diffraction maxima showed a complex behaviour, indicating contributions from several processes. The experimentally determined FWHM of the main diffraction maxima increased significantly with ion fluence. Based on a Williamson-Hall plot, strain-induced broadening is the dominant process with microstrains approaching the elastic limit [1].

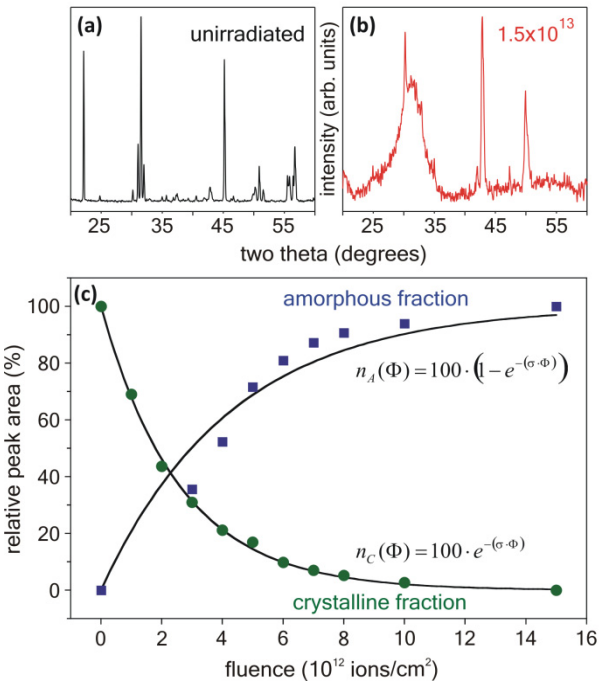

Figure 1: XRD patterns of $CaZrO_3$ perovskite (a) before and (b) after irradiation with 940-MeV Au ions, indicating full amorphization at 1.5×10^{13} ions/cm^2 (remaining peaks are due to copper sample holder and Si substrate). (c) Relative peak area, of amorphous, n_A, (diffuse peak at ~30°) and crystalline, n_C, (peak at ~22°) fraction as a function of increasing fluence. The curves are fits to the data by the given Eqs. and provide the amorphization cross-sections, σ, and track diameter d.

References

[1] M. Lang, F.X. Zhang, W.X. Li, D. Severin, M. Bender, S. Klaumünzer, C. Trautmann, R.C. Ewing, Nucl. Instr. Meth. B (2012) in press, doi:10.10/16/j.nimb.2011.12.028.

* This work was supported as part of the Materials Science of Actinides, an Energy Frontier Research Center funded by the U.S. Department of Energy, Office of Science, Office of Basic Energy Sciences under Award Number DE-SC0001089.

#mklang@umich.edu

Radiation response of pressurized Y_2O_3

B. Schuster[1,2,#], B. Merk[1,2], A. Romanenko[1.,2], and C. Trautmann[2]

[1]GSI, Darmstadt, Germany; [2]Technische Universität Darmstadt, Germany

The combination of high pressure and swift heavy ion irradiation has proven to be an effective tool to manipulate the phase behavior of solids. Under these extreme conditions, it is possible to induce structural phase transitions in simple oxide structures far beyond their actual stability field or even stabilize usually unstable structures [1].

Here we describe the response of yttrium sesquioxide (Y_2O_3), with several interesting properties such as high crystallographic stability and diversity, high mechanical strength, and a good protective behavior as coating material in highly reactive environments.

At ambient conditions, Y_2O_3 exists in a cubic modification, while upon pressure increase it performs structural phase transitions. At about 13 GPa it changes into a monoclinic structure, and at about 25 GPa into a hexagonal structure. When the pressure is released, the high pressure hexagonal structure transforms to the monoclinic one which then remains stable to ambient pressure. The original cubic structure is not recovered [2].

Under heavy-ion irradiation at high fluences, the original cubic structure is partially converted into the monoclinic phase [3]. The effect is minor, because even after the exposure to a high fluence of 1×10^{13} Au-ions/cm^2 (11.1 MeV/u), the cubic structure is still dominating.

If the irradiation is performed under high pressure (several GPa), the response behavior of the material is quite different. As expected, Y_2O_3 pressurized to 9 GPa, is cubic, while the irradiation with 2×10^{12} Au-ions/cm^2 leads to a X-ray diffraction pattern (see Fig. 1), that does not belong to any of the known crystal structures of Y_2O_3 discussed in literature.

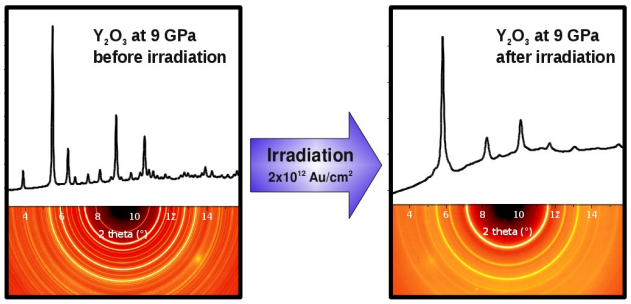

Figure 1: X-ray diffraction image and spectra of pressurized (9 GPa) Y_2O_3 before and after irradiation with 2×10^{12} Au-ions/cm^2.

*Financial support from the DFG (Project No. FU 308/12) and GSI F+E is gratefully acknowledged.

beatrice.schuster@physik.tu-darmstadt.de

Similar irradiations at higher pressure (30 GPa), also show an unexpected behavior. The diffractogram is dominated by a peak around 5.8° that can not be attributed to any known Y_2O_3 structure. The broad and weak signal of the sample indicates amorphization of the material (Fig. 2).

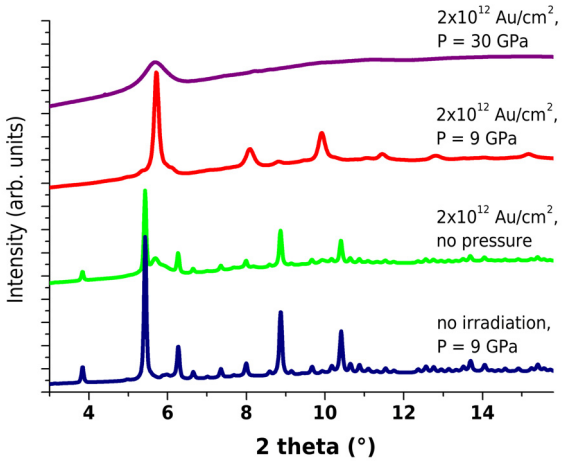

Figure 2: X-ray analysis of Y_2O_3 at ambient pressure showing data of samples irradiated at 9 - 30 GPa and ambient pressure, as well as a pressure-treated sample as reference.

After pressure release, the new material structure remains stable at ambient conditions. Reference samples that have either only been irradiated or pressurized do not show this effect.

The nature of this new structure of Y_2O_3 is not yet clarified, but it is evident, that the combination of pressure and heavy ion irradiation can induce unusual structural behavior, and grant access to new routes in the p-T phase diagram, stabilizing structures that are normally not accessible under ambient conditions..

References

[1] B. Schuster, F. Fujara, B. Merk, R. Neumann, C. Trautmann; NIMB doi: 10.1016/j.nimb.2011.12.060, (2012)111

[2] I. Halevy, R. Carmon, M.L. Winterrose, O. Yeheskel, E. Tiferet, and S. Ghose; J. Phys. Conf. Series **215** (2010) 012003

[3] S. Hémon, C. Dufour, A. Bethelot, F. Gourbilleau, E. Paumier, S. Bégin-Collin; NIMB **166-167** (2000) 339-344

Ion Hammering of NiO

S. Klaumünzer[1, #], D. Severin[2], and M. Bender[2]

[1]Helmholtz-Zentrum Berlin; [2]GSI, Darmstadt, Germany;

During bombardment with heavy ions, amorphous samples (thickness >> projected ion range R_p) deform as if each ion would act as a little hammer, i.e. the sample dimensions perpendicular to the ion beam grow while the dimension in beam direction shrinks maintaining a constant mass density. This effect arises from shear stress relaxation of the transiently fluid matter in the ion tracks [1]. The constitutive equation for ion hammering reads

$$\dot{\varepsilon} = \boldsymbol{C}\,\frac{D\,\boldsymbol{\sigma}}{Dt} + \boldsymbol{A}\,\Phi + \boldsymbol{F}\,\Phi\,\boldsymbol{\sigma} \qquad (1)$$

where $\dot{\varepsilon}$ denotes the strain rate tensor, D/Dt an invariant time derivative, and Φ the ion flux. The first term on the right hand side is essentially Hooke's law with the elastic compliance tensor $\boldsymbol{C}$ and stress tensor $\boldsymbol{\sigma}$. In the second term, $\boldsymbol{A}=\boldsymbol{A}(S_e,T_i)$ is the deformation yield tensor [1], that depends on the electronic energy loss S_e of the ions and the irradiation temperature T_i. The last term is Newtonian flow with a fluidity tensor $\boldsymbol{F}\,\Phi$. The components of $\boldsymbol{F}$ are specified in ref. [2] and depend on the Poisson number ν.

For a thick plane target, eq. (1) has the steady-state solution

$$v_x(z) = 6A\Phi\sin\alpha\cos\alpha \int_{-R_p\cos\alpha}^{z} A(S_e(\zeta))d\zeta \qquad (2)$$

where we have ignored the tensorial character of $\boldsymbol{F}$. The velocity v_x is directed along the projection of the ion beam onto the sample surface and z runs in direction of the surface normal. An isolated, elastically rigid crystalline grain rotates in this velocity field with a rate

$$\dot{\Omega} = \frac{1}{2}\frac{\partial v_x}{\partial z} = 3A\Phi\sin\alpha\cos\alpha \qquad (3)$$

If the irradiated layer contains numerous grains, sliding between the grains occurs and the rotation rate is expected to approach zero when the grains fill the total irradiated layer.

Surprisingly, ion hammering occurs also in nanocrystalline materials and grain rotation turns out to be very large [3-5]. We have tested the applicability of eq. (1) to the grain rotation of nanocrystalline NiO by irradiating various (111)-oriented NiO single crystals with 4.8 MeV/u Au ions at T_i between 20 and 50°C. The measurements were done in-situ with the 4-circle diffractometer at the M2-beamline at the UNILAC. The single crystals transform rapidly ($\Phi t < 10^{12}$ Au/cm^2) into well-aligned nanocrystals (∅~30 nm), which undergo a tilt Ω as a function of Φt. A typical example is shown in fig. 1. The rotation rate $\partial\Omega/\partial\Phi t$ is plotted in fig. 2 and compared with eq. (3) and the equivalent solution of eq. (1) taking into account the tensorial character of $\boldsymbol{F}$. The fit is only slightly improved when the more complicated solution of eq. (1) is considered. Fig. 2 demonstrates that eq. (1) also provides a phenomenological basis for the grain rotation in nanocrystalline NiO, i.e. the structure of $\boldsymbol{A}$ is essentially determined by the cylindrical symmetry of the ion tracks. Further investigations have to show if this conclusion holds also for other nanocrystalline materials.

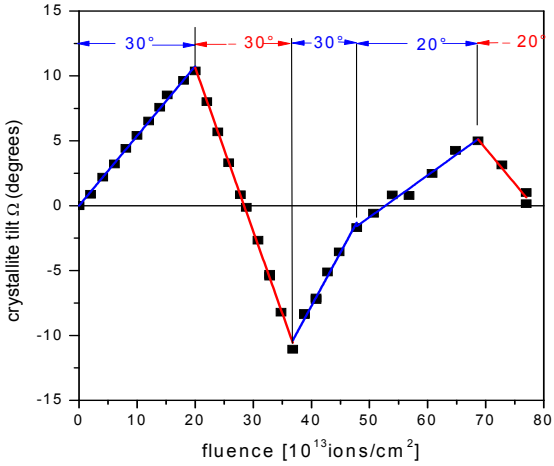

Figure 1: Tilt Ω vs. ion fluence for α = ±30° and ±20°, with α being the angle of ion beam incidence with respect to the sample normal.

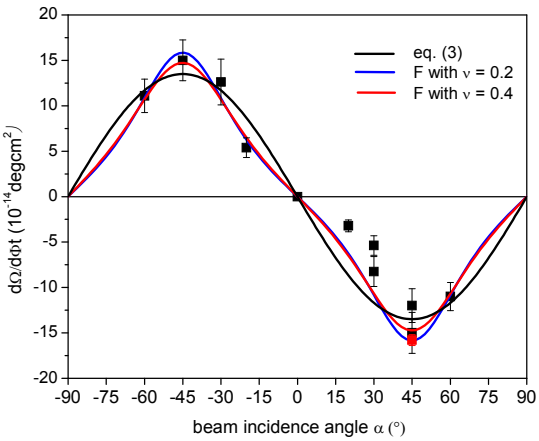

Figure 2: Rotation rate vs. beam incidence angle α.

[1] H. Trinkaus and A. I. Ryazanov, Phys. Rev. Lett. 74 (1995) 5072 .
[2] H. Trinkaus, Nucl. Instr. Meth. B107 (1995)155.
[3] W. Bolse, B. Schattat, and A. Feyh, Appl. Phys. A77 (2003) 11; W. Bolse, Nucl. Instr. Meth B 244 (2006) 470.
[4] I. Zizak et al., Phys. Rev. Lett. 101 (2008) 065503.
[5] M. Seita, D. Muff, and R. Spolenak, Acta Mat. 59 (2011) 5351.

#klaumuenzer@helmholtz-berlin.de

Ion Tracks in Amorphous $Fe_{80}B_{20}$: The Effect of Pre-Irradiation Annealing

M. D. Rodríguez[1,#], C. Trautmann[2], B. Afra[1], N. Kirby[3], and P. Kluth[1]

[1]Australian National University, Canberra, Australia, [2]GSI, Darmstadt, Germany, [3]Australian Synchrotron, Melbourne, Australia.

Amorphous metals, also called metallic glasses, are metallic alloys with a disordered non-crystalline atomic structure. The amorphous structure is quenched from the liquid state by rapid cooling with rates of 10^5 to 10^6 K/s. Metallic glasses are of particular interest due to their special physical properties including high mechanical strength, great wear and corrosion resistance, and high elasticity [1]. The means of tailoring the structurally governed amorphous metal properties have the potential to benefit advanced technological applications.

Ions at energies of some MeV/u lose their energy predominantly to the electronic system when passing through matter. Energy transfer from the electronic system to the atoms due to electron-phonon coupling may finally lead to the formation of long columnar defects along the ion trajectories, so called ion tracks.

Studying single, non-overlapping ion tracks in amorphous metals is challenging and has been reported for a few cases using chemical etching [2], scanning probe [3] and transmission electron microscopy [4]. Recently, we have shown that small angle x-ray scattering (SAXS) is well suited for measuring ion tracks in these materials [5]. Here, we have investigated the effect of pre-irradiation annealing of the metallic glasses on ion track formation using simultaneous SAXS and wide angle x-ray scattering (WAXS). The measurements were performed at the Australian Synchrotron. Previous track-etching experiments showed that pre-irradiation annealing leads to the absence of typical etch pits resulting from track formation [2].

Ribbons of $Fe_{80}B_{20}$ (29±1µm thick) were annealed for 30, 60 and 120 minutes applying temperatures of 100, 200, 300 and 400 ºC. The process was performed in argon to avoid oxidation of the material. All annealing temperatures were below the recrystallization temperature of 448°C. The annealed samples and an unannealed reference sample were irradiated at the UNILAC using 11.2 MeV/u Au ions and a fluence of 1×10^{11} ions/cm^2. A 48±1µm thick aluminium degrader foil covered half of the sample, to shift the energy to 5.5 MeV/u thus increasing the stopping power.

The SAXS measurements provide clear evidence for the existence of ion tracks in all samples. The SAXS data were analysed by fitting a simple cylindrical track model with constant density in the track, different from that of the surrounding matrix (for details see reference [5]). The WAXS measurements confirmed that all samples retained their amorphous structure.

SAXS track radii extracted for $Fe_{80}B_{20}$ samples pre-annealed at different temperatures (120 min) are plotted in Fig. 1. The track radii do not vary significantly up to 300°C. At 400°C, close to the recrystallization temperature of the material, the radii drop to approximately 60% of the value of the unannealed reference sample. Track radii produced in samples annealed at 400°C are shown in Fig. 2 as a function of annealing time and reveal a gradual decrease.

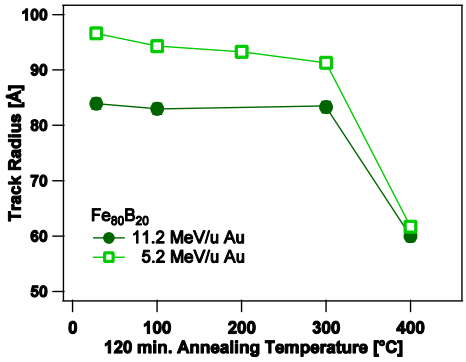

Figure 1: Track radii deduced from SAXS data versus annealing temperature (120 min annealing). The uncertainties of the fit are smaller than the symbols.

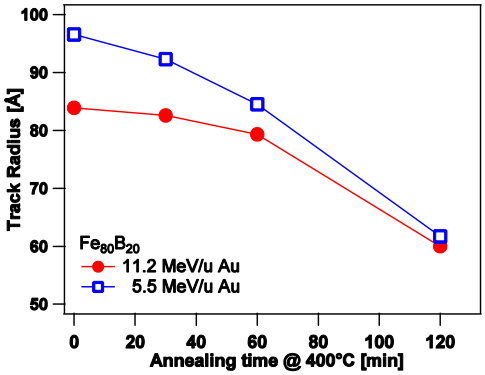

Figure 2: Track radii deduced from SAXS data versus annealing time (400°C annealing temperature).

The observed reduction in track radii upon pre-irradiation annealing is likely a consequence of a relaxation of the material and a possible means of increasing the radiation resistance of such materials.

[1] M. Telford, Materials Today 7 (2004) 36
[2] C. Trautmann *et al.*, Nucl. Instr. Meth. B 107 (1996) 397
[3] A. Audouard *et al.*, Europhys. Lett. 40 (1997) 527
[4] G. Rizza *et al.*, J. Phys: Cond. Matter 16 (2004) 1547
[5] M.D. Rodríguez *et al.*, J. Non-Cryst. Solids 358 (2012) 571

#Matias.rodriguez@anu.edu.au

Feasibility of *in situ* determination of elastic stiffness coefficients by resonant ultrasound spectroscopy during irradiation with swift heavy ions *

B. Winkler [1,#], E. Haussühl[1], B. Schuster[2], C. Trautmann[2] and S.C. Vogel[3]

[1]Goethe University, Frankfurt, Germany; [2]GSI, Darmstadt, Germany; [3]LANSCE, Los Alamos, USA

The characterisation of irradiation-induced changes of structural and physical properties of crystalline and amorphous materials is of interest in numerous applications, such as in understanding the process of metamictisation of minerals, the structural stability of materials used in the nuclear industry or for encapsulation of nuclear waste. In order to detect transient phenomena *in situ* measurements have to be performed. This project explores the feasibility to determine changes in the elastic properties of materials during irradiation with swift heavy ions. The first tests were performed on Cr-rich steel and SiO_2 glass.

The irradiation experiments were performed in cave A at the SIS synchrotron using 620 MeV/u ^{209}Bi ions. The energy was chosen so that the ions completely penetrated the samples, which are rectangular parallel epipeds with dimensions of ~6×7×9 mm^3. The samples were very gently clamped between two corundum rods (Fig. 1) which transmit ultrasound waves from and to the two transducers. This set-up allows the on-line collection of high-quality resonant ultrasound spectra [1].

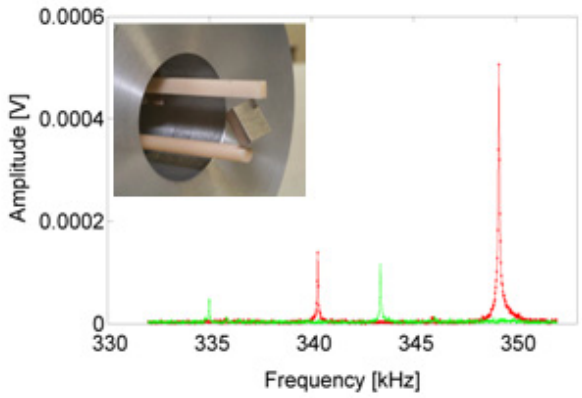

Figure 1: Typical resonant ultrasound spectra of steel sample during irradiation with 620-MeV/u Bi ions. The green spectrum shows the maximum frequency shift we observed during the measurements. The red spectra was recorded after the beam had been switched off for a few minutes, it is virtually indistinguishable from the starting spectrum. During irradiation, the sample is gently clamped between corundum rods, which serve to transmit ultrasound waves (inset).

Typical spectra recorded during and after beam exposure are shown in Fig. 1. During irradiation, the resonance frequencies shift significantly. This clearly demonstrates that resonant ultrasound spectra can be measured with this setup. In the present study, the total accumulated fluence was 2.6 × 10^{11} ions/cm^2. As the spectra before and after irradiation are virtually indistinguishable, we conclude that the observed shifts are due to beam-induced temperature increases of the sample. Independent experiments with a furnace showed that the resonance frequencies shift linearly with temperature. We therefore could convert resonance frequencies measured during irradiation into sample temperatures. We have then established a simple model for the energy balance, taking into account heating by the ion beam and cooling by radiative losses. This two-parameter model describes the flux dependence of the sample temperature exceedingly well (Fig. 2).

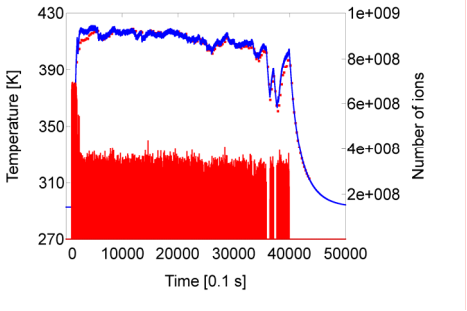

Figure 2: Sample temperature of steel sample during irradiation (red dots, left hand scale) as obtained from the measured resonance frequency, sample temperature from model calculation (blue line, left hand scale), and beam intensity (red histogram, right hand scale).

For the SiO_2-glass sample the model works equally well. The temperature increase in the steel sample (120 K) is significantly larger than in the SiO_2-glass sample (30 K). The computed energy transfer per ion as derived from our data analysis is approximately 10^{-9} J/ion. This is the same order of magnitude as the value obtained from calculations using LISE++ [2].

Future experiments with this newly developed in-situ monitoring technique will be extended to other materials in which significant radiation damages is known to occur.

References

[1] D. Arbeck, E. Haussühl, L. Bayarjargal, B. WInkler, N. Paulsen, S. Haussühl, and V. Milman „Piezoelastic properties of retgersite determined by ultrasonic measurements" European Physical Journal B, **73**, (2010) 167-175

[2] O.B. Tarasov and D.Bazin– "LISE++: Radioactive beam production with in-flight separators." Nuclear Instruments and Methods in Physics Research Section B 266 (2008) 4657-4664.

* Financial support for B.S. from the DFG (Project No. FU 308/12) and GSI F+E and for B.W. and S.C.V. from Los Alamos National Laboratory is gratefully acknowledged.

b.winkler@kristall.uni-frankfurt.de

Dilation of Al_2O_3 single crystal due to swift heavy ion irradiation

N. Ishikawa[1 #], N. Okubo[1], R. Neumann[2] and C. Trautmann[2]

[1]JAEA, Tokai, Ibaraki, Japan; [2]GSI, Darmstadt, Germany

Introduction

Aluminum oxide, Al_2O_3, is one of the promising materials in the field of nuclear energy because it is highly radiation-resistant compared with other materials. For example, Al_2O_3 is suitable as window for plasma diagnosis in a fusion reactor and is also expected to be used as an inert matrix for geological disposal of high level radioactive waste. However, when aluminum oxide is exposed to swift heavy ions, prominent damage is introduced provided the electronic energy deposition is sufficiently high [1]. Especially at high fluences when ion tracks heavily overlap, amorphization takes place [2]. The amorphization at high fluence has been ascribed to the high-density electronic energy deposition [3]. This paper investigates the radiation resistance of Al_2O_3 at high fluences and highest electronic energy deposition.

Experimental

Single crystals of Al_2O_3 with typical dimensions of about 5×5×0.35 mm^3 were irradiated with 2.7-GeV U ions at room temperature. The irradiated surface was analysed by optical color laser microscope VK-8510 (Keyence) in order to characterize the surface profile of the irradiated specimens.

Results and Discussion

The specimen irradiated at the highest fluence of 1.0×10^{13} ions/cm^2 broke into pieces as shown in Fig. 1, probably due to accumulated strain. The sample exposed to 1.6×10^{12} ions/cm^2 remained intact but exhibits a pronounced surface curvature (Fig. 2 and 3). The profile is convex, indicating that the lattice is dilated due to highly accumulated strain.

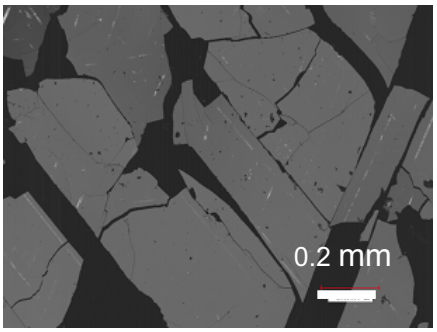

Figure 1: Optical image of surface of fractured Al_2O_3.

#ishikawa.norito@jaea.go.jp

According to the SRIM-2003 code [4], the projected range of 2.7-GeV U in Al_2O_3 is about 65 µm. Since the thickness of the specimen is ~350 µm. only the upper irradiated part of the specimen undergoes a volume increase, resulting in the convex shape. More systematic and quantitative curvature measurements are needed for characterizing the resistance against highly accumulated strain introduced by the irradiation.

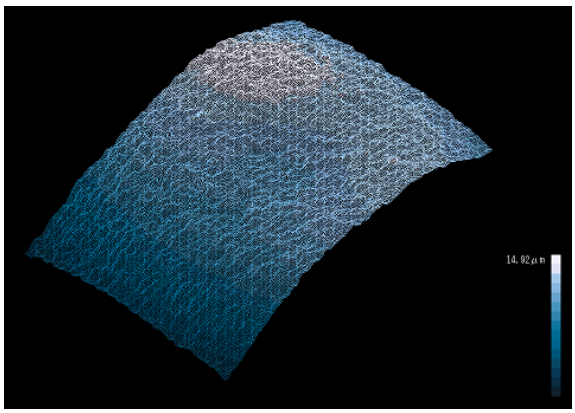

Figure 2: Surface profile measured for 1.0×1.4 mm^2 area for Al_2O_3 irradiated with 2.7-GeV U at 1.6×10^{12} ions/cm^2.

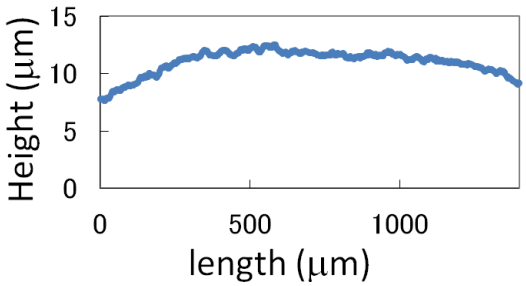

Figure 3: Surface profile near the highest point of Al_2O_3 irradiated with 2.7-GeV U at 1.6×10^{12} ions/cm^2.

References

[1] B. Canut et al., Phys. Rev. B 51 (1995) 12194.
[2] T. Aruga et al., Nucl. Instr. Meth. B 166-167 (2000) 913-919.
[3] G. Szenes, J. Nucl. Mater. 336 (2005) 81-89.
[4] J.F. Ziegler, Nucl. Instr. Meth. B 219-220 (2004) 1027.

EXAFS spectroscopy study on swift heavy ion irradiated Gd_2O_3-doped CeO_2

Y. Tahara[1], A. Iwase [1,#], R. Neumann[2] and C. Trautmann[2]

[1]Osaka Prefecture University, Sakai, Osaka, Japan; [2]GSI, Darmstadt, Germany

Introduction

To investigate the effects of high energy fission products on fission fuels doped with burnable poison (Gd_2O_3-doped UO_2), we investigated Gd_2O_3-doped CeO_2 as a surrogate for fission fuel material [1, 2]. To better understand atomic rearrangements induced by GeV ions, we applied Extended X-ray Absorption Fine Structure (EXAFS) spectroscopy. EXAFS is an effective method to study short range atomic arrangements around selected atoms. In this paper, we report specific irradiation effect on the local structure around Ce or Gd atoms revealed by EXAFS.

Experimental

Specimens used in this study were 5mol% Gd_2O_3-doped CeO_2 pellets. They were irradiated at room temperature with 8.6 MeV/u (1.7 GeV) Au ions at the UNILAC accelerator. Ion fluences were 5×10^{11}, 1×10^{12}, 2×10^{12}, and 5×10^{12} ions/cm^2. After the irradiation, we recorded EXAFS spectra around the X-ray energies of Ce-L3and Gd-L3 absorption edges.

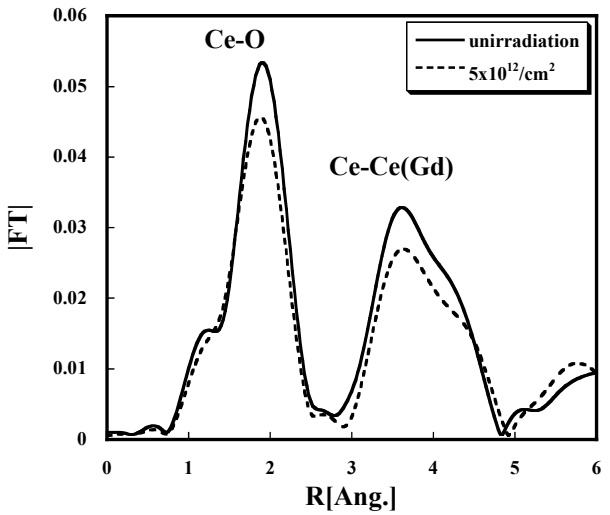

Figure 1: EXAFS-FT spectra near the Ce-L3 edge for irradiated (5×10^{12} /cm^2) and unirradiated specimens.

Results and discussion

Figure 1 shows the Fourier Transform (FT) of EXAFS spectra near the Ce-L3 edge for an irradiated and unirradiated specimen. The first peak corresponds to the first coordination of Ce atoms, that are O atoms. The second peak corresponds to the second coordination of Ce atoms, that are Ce(Gd) atoms. Figure 2 shows the EXAFS-FT spectra near the Gd-L3 edge for the irradiated and unirradiated specimens. The first peak corresponds to the first coordination of Gd atoms, that are O atoms. The second peak corresponds to the second coordination of Gd atoms, that are Ce(Gd) atoms. As can be seen in Fig. 1, the intensity of the two peak decreases by the ion irradiation, whereas in Fig.2 only the second peak intensity decreases by the ion irradiation. The result suggests that the effect of ion irradiation on short range atomic arrangement around Ce atoms is different from that around Gd atoms. The intensity decrease is an indication that the ion irradiation decreases the coordination number and/or increases the Debye-Waller factor. Information on such beam-induced local disordering of the atomic arrangement around Ce or Gd atoms can only be identified by EXAFS spectroscopy. Quantitative analysis to determine the values of coordination numbers and Debye-Waller factors is in progress.

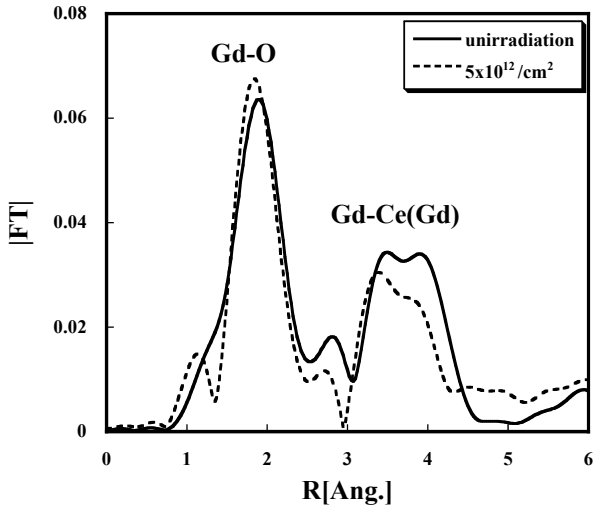

Figure 2: EXAFS-FT spectra near Gd-L3 edge for irradiated (5×10^{12} /cm^2) and unirradiated specimens.

References

[1] Y. Tahara, B.Zhu, S. Kosugi, N. Ishikawa, Y. Okamoto, F. Hori, T. Matsui, A. Iwase, Nucl. Instr. Meth. B (2011) 886-889.

[2] Y. Tahara, K. Shimizu, N. Ishikawa, Y. Okamoto, F. Hori, T. Matsui, A. Iwase, Nucl. Instr. Meth. B in press.

[#]iwase@mtr.osakafu-u.ac.jp

Damage accumulation model for overlapping of swift ion tracks*

M. Sorokin[1,#], K. Schwartz[2], and C. Trautmann[2]

[1]NRC Kurchatov Institute, Moscow, Russia; [2]GSI, Darmstadt, Germany.

In many different materials, swift heavy ions produce radiation damage along their trajectories. In some cases, the size of the damaged track zone can directly be measured e.g. by small angle x-ray scattering, transmission electron or scanning probe microscopy. Many other techniques, such as optical absorption, X-ray and Raman spectroscopy or electron-spin and nuclear-magnetic resonance spectrometry yield integral values of the damaged material. The corresponding track radius r_0 is deduced by analysing the sublinear evolution of the damage as a function of ion fluence due to track overlapping [1].

The model of overlapping damage zones was initially suggested for elastic cascades [2] and later applied for swift ion tracks [1,3]. In a direct impact process, the track damage A produced by the ions depends on the fluence Φ and follows the Poisson law $A \sim \left(1-\exp\left(-\pi r_0^2 \Phi\right)\right)$ [2,3]. This model can also take into account if two or more ion hits are required for damage production [1,4,5]. A drawback of this model is that it considers an unrealistic homogeneous damage within the track cross section πr_0 instead of considering the radial dependence of the dose distribution deposited around the ion trajectory, which is in particular crucial during gradual damage accumulation by manifold track overlapping.

We can select an arbitrary point on the material surface. The distance r between this point and the ion impact is a uniformly distributed random value. The radial energy distribution around the ion trajectory gives the absorbed energy fraction $g(r)$ in the selected point with

$$\int g(r)dr = 1.$$

Assuming the reciprocity law, the number N of independent ions ($N = \Phi S$, where S denotes the surface area) provides in the selected point the fraction of NE (E is the energy deposited by the ion), corresponding to the convolution

$$G(r) = (g_1 * g_2 * \ldots * g_N)(r)$$

Generally it means that $G(r)$ should be found numerically, but for some model distributions the analytical form of the convolution is known. The exponential radial energy distribution $(1/r_0)\exp(-r/r_0)$, e.g., gives an absorbed energy fraction $G(r)$ in the selected point that follows a gamma distribution (fig. 1):

$$g(r) = \left(r/r_0^2\right)\exp(-r/r_0) \quad \text{and} \quad G(r) = \frac{r^{2N-1}\exp(-r/r_0)}{r_0^{2N}\Gamma(2N)}$$

where $\Gamma(n) = (n-1)!$ is the gamma function.

The average material damage is given by:

$$\langle \eta(E\Phi G) \rangle = \int F(G)\eta(E\Phi G)dG = \int \eta(E\Phi G(r))dr$$

where $\eta(G)$ is the dose-dependent damage production efficiency, and $F(G) = 1/\left|G'(r(G))\right|$ is the probability distribution for the absorbed energy at the selected point.

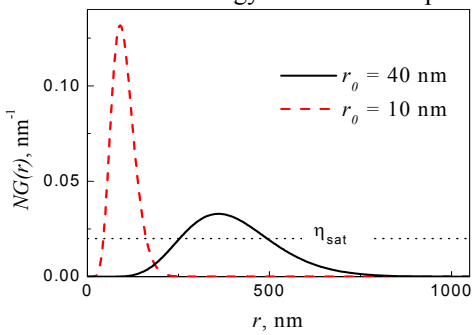

Figure 1: Local distribution of absorbed energy for N =10 ion impacts for different track radii r_0.

The damage saturating with increasing fluence can be simulated by the efficiency function:

$$\eta(E\Phi G) = \min(E\Phi G, \eta_{sat}),$$

where η_{sat} is the saturation value at high fluence. Depending on radius r_0, the local energy deposition surpasses the saturation level (Fig. 1).

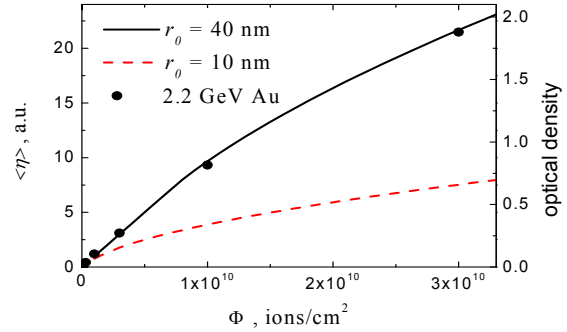

Figure 2: Effective damage accumulation versus fluence using r_0 = 40 nm gives good agreement with experimental data for colour centres in ion-irradiated LiF.

The calculated damage accumulation can be compared with the fluence dependence of experimentally measured color centers. The $\langle \eta \rangle$ damage accumulation versus fluence curve using a track radius of r_0 = 40 nm is in excellent agreement with optical absorption data of F-centres produced by irradiating LiF crystals with 11.1 MeVu Au ions (Fig. 2).

[1] P. Thevenard *et al.*, Radiat. Eff. 32 (1977) 83.
[2] J.F. Gibbons, Proc. IEEE 60 (1972) 1062.
[3] K. Schwartz *et al.*, Phys. Rev. B 70 (2004) 184104.
[4] A. Benyagoub, Nucl. Instr. Meth. B 218 (2004) 451.
[5] W.J. Weber, Nucl. Instr. Meth. B 166-167 (2000) 98.

* Work supported by DFG, Project TR 973/1-1.

m40@lab2.ru

Evidence for SHI induced Spinodal-like Dewetting of a Fe_2O_3-Film on Si*

W. Bolse[1#], S. Amirthapandian[2], and F. Schuchart[1]

[1]Institut für Halbleiteroptik und Funktionelle Grenzflächen, Universität Stuttgart, Stuttgart, Germany,
[2]Material Physics Division, Indira Gandhi Centre for Atomic Research, Kalpakkam, India.

When investigating the dewetting of molten polymer films it was found, that in some cases the breakup of the film occurs due to periodic (or more precise: correlated) undulations of the film thickness similar to the compositional fluctuations during spinodal decomposition of fluid mixtures [1]. Because of this similarity the process is called "spinodal dewetting". It is due to a capillary instability, where preferential self-amplification of capillary waves of a certain wave length occurs and the film rupture sets in as soon as the valleys reach the substrate [2].

Recently we found that dewetting also occurs during swift heavy ion (SHI) irradiation of thin oxide films on Si, even the irradiation was performed far below the coatings melting point [3]. In some cases the final dewetting patterns were quite similar to those attributed to spinodal dewetting of liquid polymer films. After the installation of our in-situ scanning electron microscope (SEM) [4] at the M-branch of the UNILAC, we are now able to monitor one and the same surface area throughout an entire irradiation process and to study the development of the surface morphology as a function of ion fluence.

The sample consisted of a 50 nm thin Fe_2O_3-film on Si, which had been pre-irradiated with ^{197}Au-ions of 1 MeV/u to a fluence of 1×10^{14}/cm^2. Because of this, the film already exhibited dewetting holes of 1 µm in diameter. The sample was then irradiated in our in-situ SEM setup with 3.6 MeV/u ^{197}Au-ions to a total fluence of 11.5×10^{14}/cm^2 in steps of 0.5×10^{14}/cm^2. After each step SEM images of one and the same surface area were taken.

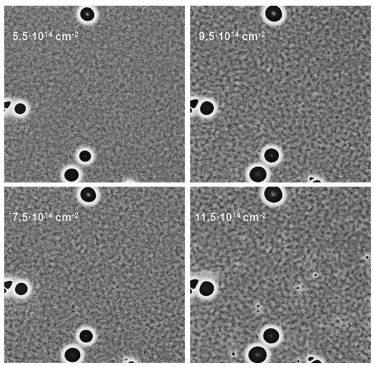

Figure 1: SEM images of sample surface after irradiation at different fluences, taken at one and the same spot.

The development of the film during irradiation is illustrated in Fig. 1. First the existing holes grow, but almost no new holes nucleate. However, the surface becomes more and more undulated and finally, at the highest fluences, the number of holes increases exponentially, with the new holes nucleating in the troughs of the wavy surface. This clearly points at a "spinodal-like" dewetting mechanism.

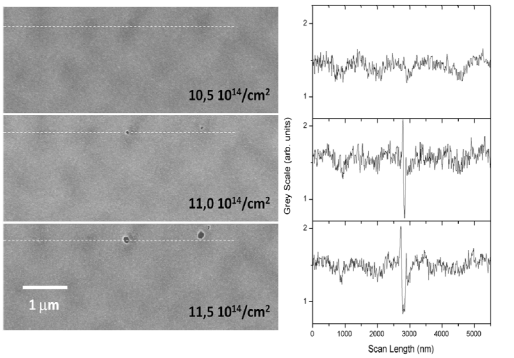

Figure 2: SEM images of irradiated surface in an initially hole-free area (left) and gray-scale scans along the lines indicated in the SEM images (right).

In the higher-magnification images taken at the highest fluences (see fig. 2), the undulations are clearly visible. From the gray-scale scans along the lines indicated in the SEM images, a typical wave-length of ~ 1µm can be deduced (verified by 2D-Fourier transformation). The images also clearly prove, that the new holes nucleate in the wave-troughs. Hence, we conclude that like for spinodal dewetting of liquid polymer films the holes nucleate as soon as the valleys of the self-amplifying undulations reach the substrate. However, because the film did not melt globally, capillary waves cannot be the reason for the wavy surface. On the other hand, Asaro and Tiller [5] and later also Grinfeld [6] predicted, that the surface of a thin film under compression becomes instable against undulations of a certain wave-length. Trinkaus [7] has shown, that the transient melting of a SHI track leads to compressive stresses perpendicular to the ion trajectory. We therefore conclude that in the present case, the SHI irradiation generated compressive in the aforementioned surface instability and the "spinodal-like" dewetting process.

References

[1] S. Herminghaus, et al., Science 282, 916 (1998).
[2] F. Brochard, et al., Can. J. Phys. **68**, 1084 (1990).
[3] T. Bolse, et al., Nucl.Instr. Meth. B244, 115, (2006).
[4] S. Amirthapandian, et al., Rev. Sci. Instr. 81, 033702 (2010).
[5] R. J. Asaro, et al., Metall. Trans. **3**, 1789 (1972).
[6] M.A. Grinfeld, Doklady Akademii Nauk SSSR **265**, 836 (1982); Europhys. Lett. **22**, 723 (1993).
[7] H. Trinkaus, et al., Phys. Rev. Lett. 74, 5072 (1995).

* Work supported by BMBF under contract 05KK7VS1.
#w.bolse@ihfg.uni-stuttgart.de

Temperature dependent conductivity measurements of single ion tracks in ta-C*

H.-G. Gehrke[1#], J. Krauser[2], C. Trautmann[3], A. Weidinger[4], U. Vetter[1] and H. Hofsäss[1]

[1] II. Physikalisches Institut, Universität Göttingen, Germany; [2]Hochschule Harz, Wernigerode, Germany; [3]GSI Helmholtzzentrum, Darmstadt, Germany; [4] Helmholtz-Zentrum Berlin für Materialien und Energie, Berlin, Germany.

The swift heavy ion irradiation of tetrahedral amorphous carbon (ta-C), a diamond-like carbon with low hydrogen content and a high sp^3 bond fraction, leads to conductive tracks along the ion trajectory. The sp^3-rich phase is transformed to a sp^2-rich phase by the high energy deposition within the track volume resulting in 8 nm wide nano-filaments embedded in the insulating ta-C film [1,2].

The ta-C samples were synthesized by mass selected ion beam deposition of 100 V C^+ ions onto conductive n-type silicon (0.015 Ωcm). The 70 nm thick films were irradiated with 1 GeV U-ions at the UNILAC. In order to lower the initial 11.1 MeV/u to this energy and to adjust the projectile to equilibrium state, an Al-degrader was mounted in front of the sample. Fluences applied were 2, 4, and 11×10^9 ions/cm^2 corresponding to a track coverage of the surface between 0.1 and 0.6%. Effects due to overlapping tracks can be disregarded because even at highest fluence only 1% of tracks overlap.

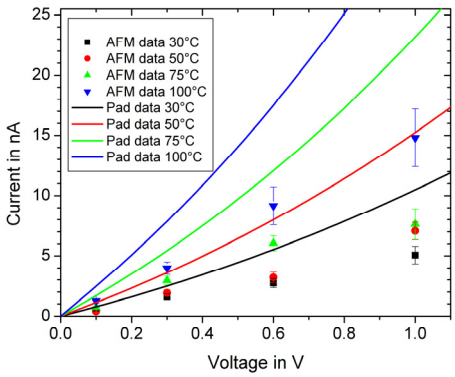

Figure 1: I-U-characteristics of averaged single ion tracks from AFM (data points) and contact-pad measurements (lines) with a fluence of 2×10^9 ions/cm^2.

The electrical conductivity of the samples was analysed by two approaches. Track ensembles were contacted macroscopically in parallel by evaporating Cr/Au-pads onto the films, covering millions of tracks each. I-U-characteristics of these ensembles were recorded at different temperatures (30 - 100°C). In the second experiment, individual tracks were analysed microscopically by atomic force microscopy (AFM) using a conductive tip. Earlier experiments showed considerable conductivity variations of individual tracks [3], even if the tracks were only 100 nm apart. For a representative result, the conductivity data of all tracks in a randomly chosen area of 1 μm^2 were averaged. For each 1 μm^2 area the current was mapped at different bias voltages and temperatures (30 - to 100°C). In order to compare the results of both experiments (Fig. 1), the average current of single tracks was calculated. The results of the two measurements show the same trend but in absolute numbers differ for a given temperature by nearly factor of two. The reduced conductivity of the tracks in AFM analyses could possibly originate from a higher contact resistivity of the small tip compared to an evaporated metal film. The temperature dependence (slope in Arrhenius plot) of both measurements agrees well within experimental uncertainties. The macroscopic pad analyses of samples exposed to different fluences show a linear dependence of the conductivity and fluence in the selected fluence range.

Figure 2 shows the conductivity of the data given in Figure 1 as a function of temperature. The solid lines are fits to the data in order to calculate the activation energy.

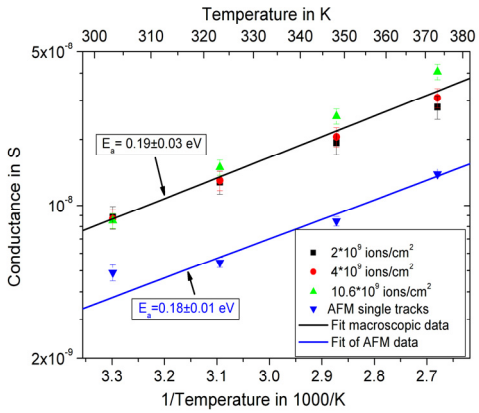

Figure 2: Arrhenius-plot showing the conductance of ion tracks measured by AFM and contact pads at different temperatures. The fitted slope (solid line) provides the activation energy E_a

We have successfully measured the temperature dependence of the conductivity of individual ion tracks in ta-C. These microscopic AFM measurements differ only by a factor of two from macroscopic contact pad measurements (averaging millions of tracks in parallel) probably due to different contact resistance. The deduced activation energy is 0.18 ± 0.01 eV and agrees well within the uncertainty of both experimental settings.

References

[1] M. Waiblinger, et al. J. Appl. Phys. 69 (1999) 239
[2] J. Krauser, et al. J. Appl. Phys. 94 (2003) 1959
[3] J. Krauser et al. NJOP, 13(2011)083023

* Work supported by DFG (Ho1125/17-1).
#hgehrke1@gwdg.de

Tuning the conductivity of VO_2 thin films by swift heavy ion irradiation

P. Ehrhardt[1], M. Brötzmann[1], H.-G. Gehrke[1], H. Hofsäss[1], K. Zhang[1], U. Vetter[1], J. Krauser[2], C. Trautmann[3], C. Ko[4], and S. Ramanathan[4]

[1] II. Physikalisches Institut, Universität Göttingen, Germany; [2] Hochschule Harz, Wernigerode, Germany; [3] GSI, Darmstadt, Germany; [4] Harvard School of Engineering and Applied Sciences, Harvard University, Cambridge, USA

The first order semiconductor-to-metal phase transition in vanadium dioxide has been of great interest for half a century. The transition can be triggered by thermal [1], optical [2] and electrical excitation [3], and even by pressure or strain [4]. This work was inspired by previous experiments irradiating tetrahedral amorphous carbon (ta-C) with swift heavy ions and creating electrically conductive tracks along the ion path [5]. Due to extremely rapid annealing and quenching during the passage of the heavy projectile, specific processes are expected such as freezing in a conductive high-temperature phase of VO_2, defects formation, or a slight change of the stoichiometry. Also, track formation is often correlated with mechanical stress. Here, we explored if ion-induced changes to the VO_2 lattice can increase the conductivity along ion tracks.

Thin vanadium dioxide films (thickness: 100-200 nm) were grown by the Harvard group using magnetron sputter deposition. The substrate was n-type silicon, sapphire or strontium titanate. The samples were irradiated at the UNILAC with 1 GeV Au or U ions of electronic energy loss 37 and 47 keV/nm, respectively.

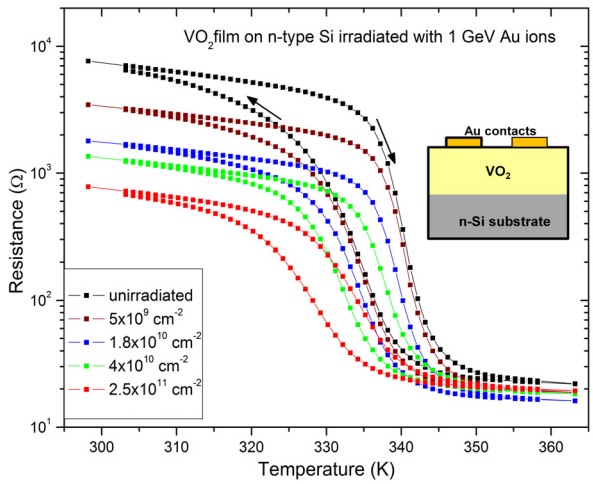

Figure 1: Resistance versus temperature curves for unirradiated and irradiated VO_2 films measured with two gold top-contacts. Arrows specify curves recorded while heating or cooling the sample. The irradiations were performed with 1-GeV Au ions (fluence regime identical to irradiated ta-C reference samples).

The electrical conductivity of the films was characterized by two methods. For the macroscopic study we used 0.9 mm diameter Au contact-pads as electrodes. The I-V curves show a decrease in film resistivity with increasing fluence in the semiconducting regime, while above the transition temperature the resistivity remains nearly unchanged (Fig. 1). The irradiation induces a slight shift of the transition temperature towards lower temperatures, but the hysteresis width is almost constant. Further analysis was performed by atomic force microscopy (AFM) with a conducting tip (Fig. 2). Topography AFM images show no indication for the creation of surface hillocks, but current maps give evidence of well conducting regions around ion tracks possibly due to stress (see lower right region in Fig. 2). More details on this persistent increase in electrical conductivity in thin VO_2 film are described in [6].

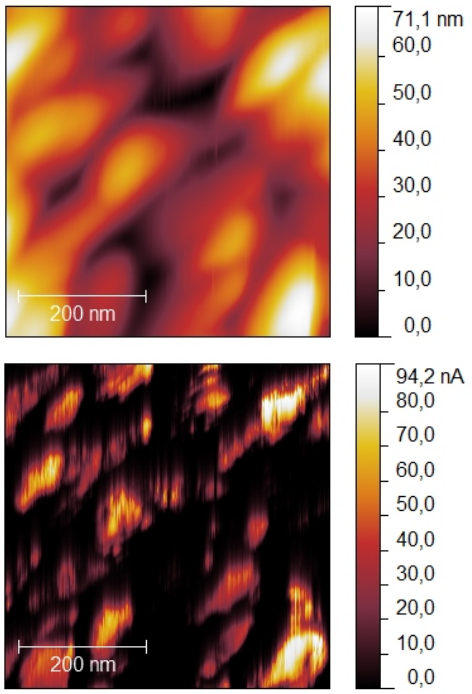

Figure 2: AFM images of VO_2 film on n-type silicon irradiated with 1 GeV Au ions of fluence 10^{10} cm^{-2}: topography (top) and current map (bottom)

*Work supported by DFG, Project Ho 1125/17-1.

paul.ehrhardt@uni-goettingen.de

References

[1] F.J. Morin, Phys. Rev. Lett. 3 (1959) 34.
[2] G. Stefanovich, A. Pergament and D. Stefanovich, J. Phys.: Condens. Matter 12 (2000) 8837.
[3] A. Cavalleri et al., Phys. Rev. Lett. 87 (2001) 237401.
[4] T. Kikuzuki and M. Lippmaa, Appl. Phys. Lett. 96 (2010) 132107.
[5] A. Nix et al., Rev. Adv. Mat. Sci. 15 (2007) 192.
[6] H. Hofsaess et al., AIP Advances 1 (2011) 032168

Defects in 6H SiC created by swift heavy ion irradiation

R. Stübner[1,#], M. Bender[2], D. Severin[2], and J. Weber[1]

[1]Technische Universität Dresden, Germany; [2]GSI, Darmstadt, Germany

SiC is an ideal material to study intrinsic defect formation by particle irradiation. The simple Si vacancy V_{Si} is stable at room temperature and transforms by annealing up to 700°C into a complex consisting of a carbon vacancy next to a C_{Si} antisite defect. At even higher temperatures the very stable $Si_C(C_{Si})_2$ complex forms denoted as D_1 defect [1].

In this project, we irradiated 6H SiC crystals with 4.8-MeV/amu Au ions up to a fluence of 4×10^{10} ions/cm^2. The signature of intrinsic defects was studied by means of in-situ luminescence which is associated with ion-beam induced excitation of the electrons. The samples were mounted on a closed-cycle He-cryostat and kept at a temperature of T = 26 K. The ion beam had a frequency of 1 Hz and a pulse length of 5 ms corresponding to 6×10^7 ions per pulse. The luminescence light was analysed with a fixed grating outside the vacuum chamber and registered with a CCD detector. During each beam pulse a full spectrum was recorded. The investigated samples were SiC single crystalline slices cut from a wafer. N-type samples were doped with 6.4×10^{17} cm^{-3} nitrogen atoms (Si face up). They also contained a trace amount of aluminium, as evidenced in the photoluminescence spectra. P-type samples were doped with 1.1×10^{18} cm^{-3} aluminium atoms and showed C face up.

For the n-type 6H SiC:N sample, the evolution of the luminescence with increasing fluence is shown in Fig. 1, top. The spectrum recorded after the first beam pulse (Fig. 1, bottom) is typical for photoluminescence spectra known from low temperature investigations. It consists of a large peak at about 475 nm that is correlated with the recombination of nitrogen-aluminium donor-acceptor pairs. A second broad band at about 620 nm is assigned to boron impurities [2]. With increasing ion fluence, the intensity of these two peaks decreases rapidly following a double-exponential behaviour (Fig. 2). Simultaneously a new broad peak appears around 527 nm reaching maximum intensity at a fluence of 2.8×10^9 cm^{-2}, while further irradiation also causes an intensity drop. In contrast to the 475 nm and 620 nm peaks, this decrease follows a single-exponential. Subsequent photoluminescence investigations identified this new peak at 527 nm as D_1 luminescence that is usually only found in irradiated samples after an additional annealing process at 700°C.

The luminescence of the p-type 6H SiC:Al sample seems to be more stable. At the highest fluence of 4×10^{10} cm^{-2}, the original signal intensity is reduced only by about 10%. After this irradiation, we could identify a new peak close to the Al-related band at 2.65 eV.

[#] ronald.stuebner@physik.tu-dresden.de

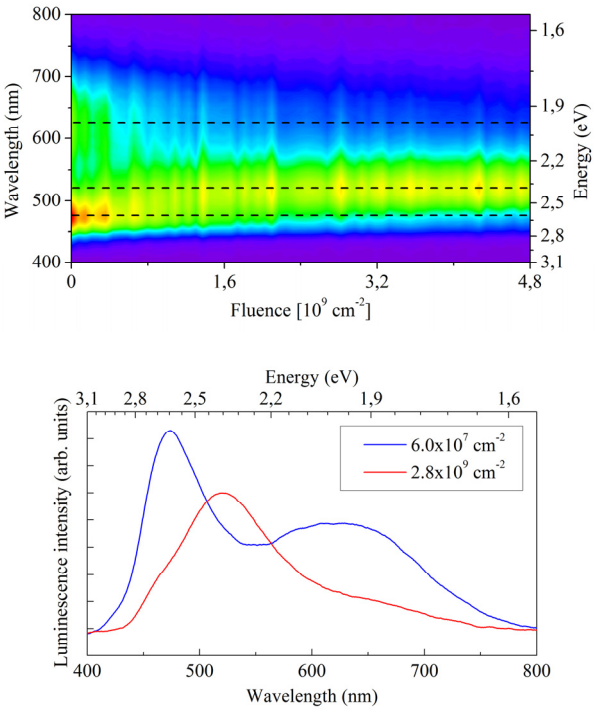

Figure 1: (top) Evolution of luminescence spectra of n-type 6H SiC with increasing ion fluence (ample irradiated at T=26 K); (bottom) spectra recorded after two different ion fluences.

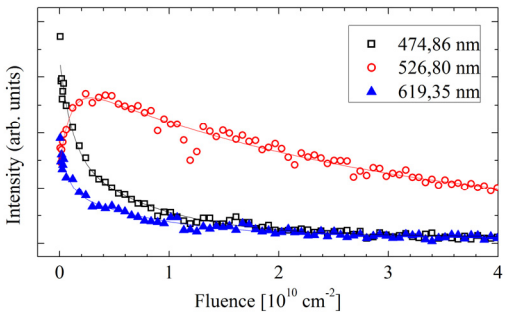

Figure 2: Intensity of three different luminescence bands as a function of ion fluence.

References

[1] E. Rauls *et al.*, „A New Model for the D_I-luminescence in 6H-SiC“, Materials Science Forum Vols. 483-485 (2005) 465.

[2] W. Suttrop *et al.*, „Boron-Related Deep Centers in 6H-SiC“, Appl. Phys. A 51 (1990) 231.

In-situ SEM Investigations of Ion-Induced Damage in Novel Diamond-Copper Composite Materials for LHC Collimator Jaws *

M. Tomut[1,2,#], R. Assmann[3], A. Bertarelli[3], W. Bolse[4], A. Dallocchio[3], R. Ferhati[4], M. Kitzmantel[5], N. Mariani[3], E. Neubauer[5], J. Stadlmann[1], C. Trautmann[1]

[1]GSI, Darmstadt, Germany; [2]NIMP, Bucharest, Romania; [3]CERN, Genève, Switzerland; [4]Universität Stuttgart, Germany; [5]RHP-Technology, Seibersdorf, Austria

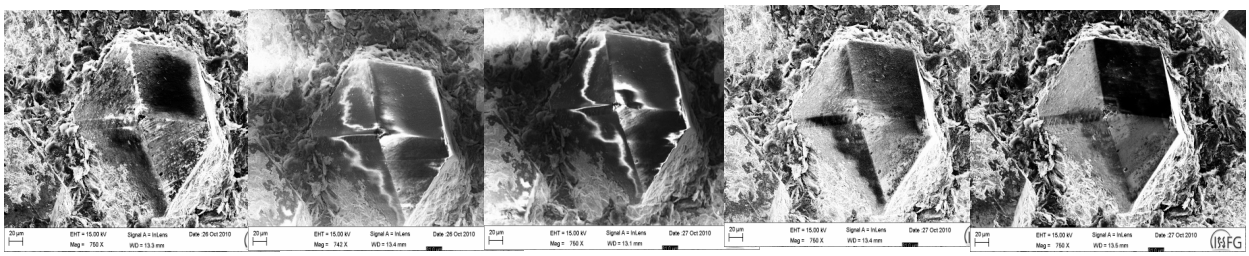

pristine 5×10^{12} i/cm^2 1×10^{13} i/cm^2 5×10^{13} i/cm^2 1.7×10^{14} i/cm^2

Figure 1. Sequence of in-situ SEM micrographs of a diamond-copper composite sample showing the evolution of a surface-near diamond with increasing fluence using a beam of 4.8 MeV/u ^{238}U ions.

The LHC collimation system has to intercept beam losses at intensities never experienced before [1]. Phase I collimator jaws were designed to stand abnormal beam losses and were made of carbon-carbon composites due to their good thermo-mechanical properties. These materials have though low cleaning efficiency and high RF impedance, which could lead to instabilities of the LHC. Phase II collimators are expected to overcome these limitations and in addition stand extreme working conditions. With metal-diamond composites, a new family of materials with promising thermal, electrical, and mechanical properties has been identified within the EU FP7 ColMat project. These materials combine exceptional thermal conductivity with good electrical and mechanical properties in the unirradiated state. Nevertheless, nothing is known about their radiation hardness and irradiation- induced degradation of functional properties.

First radiation hardness tests with heavy ions beams have been performed at the Materials Department at GSI, within the ColMat project [2]. Copper-diamond composite, developed by the RHP-Technology [3], has been the first advanced material considered. The composites are obtained by Rapid Hot Pressing (RHP) of metallic Cu, with addition of small quantities of boron powder, mixed with small synthetic diamonds [3].

To study radiation-induced microstructural changes, diamond-copper composites samples were exposed to 4.8 MeV/u ^{238}U ions, up to a fluence of 1.7×10^{14} ions/cm^2, at the M1 beamline at the UNILAC and monitored in-situ using a high resolution scanning electron microscope (SEM). Different sites at matrix-diamond interfaces and individual diamond particles were analysed. The samples were irradiated on the microscope sample stage and SEM inspected between different fluence steps. The rotation of the stage allowed us to recover with high precision the same sample positions.. Micrographs were recorded using a secondary electron and in-lens detector. Magnifications of 750, 7000 and 70000 have been used. No crack formation or diamond detachment at the diamond-matrix interfaces are observed. The evolution of the diamonds charging behaviour with increasing fluence shows that beam-induced charge trapping defects are formed. The charging effect is present up to 5×10^{12} ions/cm^2 and quenches above 1×10^{13} ions/cm^2 (Fig. 1). Off-line Raman investigations of irradiated individual diamonds within the composite material show a decrease of the Raman peak intensity and an increase of the luminescence background of the spectra, attributed to optical active defects induced with increasing fluence (Fig. 2). The change of the background of the Raman spectra and the quenching of the charging effects in SEM take place at fluences corresponding to overlapping regime of ion-induced defects in diamond.

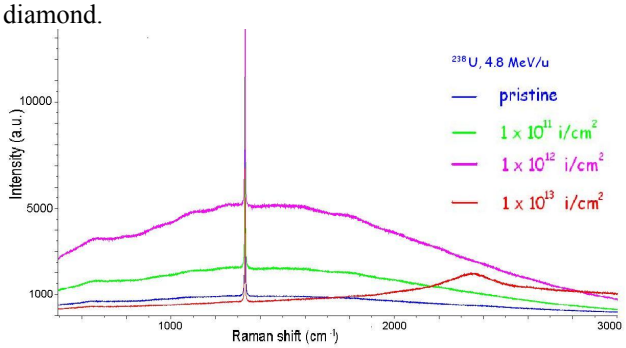

Figure 2. Sequence of Raman spectra of a diamond on the surface of a diamond-copper composite sample exposed to 4.8 MeV/u ^{238}U ions at different fluences.

[1] R. Assmann et al., PAC'09, Vancouver, May 2009.
[2] J. Stadlmann et al., IPAC2011, San Sebastián, Spain.
[3] E. Neubauer et al., Adv. Mat. Res. 59 (2009) 214.

* Work supported by EU, EuCARD contract No 53102
#m.tomut@gsi.de

Microstructural Investigation of Failure Mode of Carbon Stripper Foils Exposed to Intense Heavy Ion Beams

M. Tomut[1,2,#], O. Ersen[3], S. Moldovan[3], W. Barth[1], P. Gehard[1], M. S. Kaiser[1], B. Lommel[1], M. Maier[1], J. Steiner[1], H. Vormann[1], C. Trautmann[1]

[1]GSI, Darmstadt, Germany; [2]NIMP, Bucharest, Romania; [3]IPCMS, Strasbourg, France

High beam intensities at FAIR request to overcome the space charge limit problem at SIS, scaling with A/Q^2. One option for the starting phase and for high-current low-duty operation could be the combination of the gas stripper at 1.4 MeV/u and of the foil stripper at the transfer line (11.4 MeV/u) with a thin stripper foil at 1.4 MeV/u, which directly produces the intermediate charge state. First tests at UNILAC in 2010 have shown that ^{238}U ions of charge state ~39+ can be delivered to the SIS18 by using a 20 µg/cm^2 amorphous carbon stripper foil produced by the GSI Target Laboratory [1]. The lifetime of the stripper foils was up to 20 h. Further systematic irradiation experiments are needed for reliable lifetime prediction. This work presents an experimental approach to understanding the failure mechanism of carbon stripper foils with high intensity beams.

Several factors limit the lifetime of carbon foils under these conditions including beam-induced temperature rise, mechanical stress, fatigue, sublimation, radiation damage, mismatch between coefficients of thermal expansion for foils and frames. Most probably a combination of several of these factors determines the failure. Foil manufacturing technique and microstructure play also a major role in lifetime. Beam tests in accelerator combined with material characterization is the reliable way to identify failure modes of stripper foils.

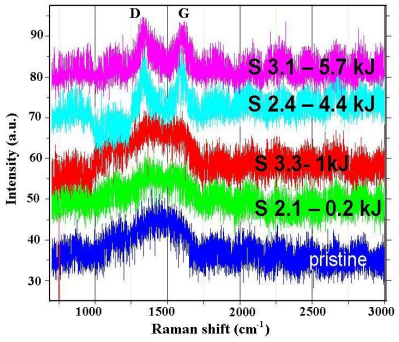

Figure 1. Raman spectra of carbon stripper foils exposed to ^{238}U at 1.4 MeV/u for different deposited energies.

Irradiation experiments with controlled beam parameters were performed at the gas stripper location of the UNILAC. 20 µg/cm^2 amorphous carbon foils were exposed to 50 - 100 µs long beam pulses of 1.4-MeV/u ^{238}U ions (1 Hz repetition rate and 5emA intensity) after being conditioned with a low intensity ^{40}Ar beam. Structural changes of stripper foil material that accumulated different total beam deposited energies were investigated by Raman spectroscopy, transmission electron microscopy (TEM), and electron energy-loss near-edge fine structure spectroscopy (ELNES). The Raman spectra give evidence that graphitization of amorphous carbon starts at a beam energy deposition as low as 4.4 kJ, as indicated by the increase of the graphitic peak (G) in Figure 1.

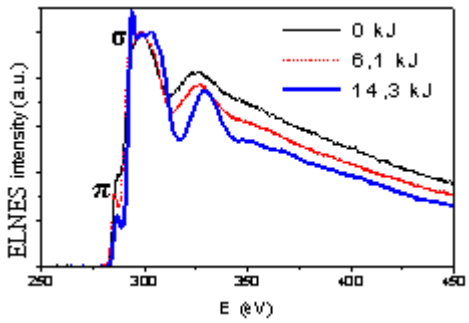

Figure 2. ELNES spectra for: pristine carbon foil (black, thin line); foil irradiated with ^{238}U at 1.4 MeV/u, deposited energy 6.1 kJ (red dotted line); foil irradiated in similar conditions, 14.3 kJ deposited energy (blue thick line).

The increase of sp^2-bonding fraction in the irradiated stripper foils is also indicated by the ELNES spectra, which exhibit the features of typical sp^2 coordinated carbon atoms, such as the sharp π peak around 286 eV and the exciton peak of σ at 293 eV (Figure 2). Beam- induced partial crystallization of the amorphous stripper foil leads to in-plane tensile stresses due to the higher density of the crystalline phase. For the high-current, low-duty cycle irradiation regime tested in this experiment, TEM micrographs (Figure 3) show that the failure is mainly due to stress-induced opening of pre-existing cracks in the foil, leading to pinholes that act further as stress concentrators. Future efforts on extending the lifetime of the stripper foil will concentrate on reducing the energy deposition by mounting them on a rotating wheel and find a starting material microstructure which does not experience densification under ion irradiation.

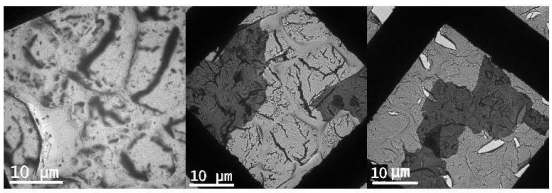

Figure 3. Low magnification TEM micrographs: pristine amorphous foil (left), irradiated foil with 6.1 kJ (centre) and 14.3 kJ (right) deposited energy.

[1] W. Barth et. al., LINAC2010, Tsukuba, Japan (2010).

m.tomut@gsi.de

In-situ resistivity monitoring of defect accumulation and recovery by thermal annealing during swift heavy ion-irradiation of graphite*

S. Fernandes[1,#], M. Avilov[1], M. Bender[2], W. Mittig[3], M. Krause[2,4], F. Pellemoine[1], M. Schein[1], D. Severin[2], M. Tomut[2,5], C. Trautmann[2,4]

[1]FRIB, MSU, East Lansing, MI, USA; [2]GSI, Darmstadt, Germany;
[3]NSCL, MSU, East Lansing, MI, USA; [4]TU Darmstadt, Germany; [5]NIMP, Bucharest, Romania.

We report here the characterization of radiation damage effects caused by 8.6MeV/u ^{197}Au beam in polycrystalline graphite for studying its suitability as high-power target material for the production of secondary nuclear beams for the Facility for Rare Isotope Beams FRIB (USA) and the Facility for Antiproton and Ion Research FAIR (Germany). This work was performed at GSI and is part of a scientific collaboration work which started in 2010 [1].

Continuous irradiation by charged heavy projectiles may give rise to degradation of the material properties of the graphite target. The target performance can decrease over time and ultimately generate failure during operation. The structural behaviour of the production targets will depend not only on the irradiation history, but also on the source material, manufacturing process, chemical environment, and temperature. Overheating and increased stress load variations during irradiation are main concerns when operating these targets. Under these circumstances drastic changes in the graphite target material structure, electrical resistivity and thermal conductivity are likely to occur and the ultimate stress for rupture may be exceeded.

The irradiated samples were made of two grades of purified polycrystalline isotropic graphite foils supplied by Mersen USA [2] grades 2320 and 2360 and a mean grain size of 13 and 5μm respectively, both with a nominal thickness of 74 μm. Table 1 provides the graphite irradiation conditions and initial resistivity ρ at the estimated maximum irradiation temperature T_{irrad}. The samples were irradiated with external electric ohmic heating using currents up to ~ 40 A. The dimensions of the irradiated region were accessed by geometry and visual control.

Table 1 Graphite irradiation conditions and ρ at T_{irrad}.

Grade	T_{irrad} (°C)	Mean flux (x10^{10}cm^{-2}s^{-1})	Fluence (cm^{-2})	ρ (Ωcm) [2]
2320	350	1.6 (±2%)	10^{14}	8.45 ×10^{-4}
	1600	5.6 (±24%)	10^{15}	9.30 ×10^{-4}
2360	500	4.4 (±14%)	10^{14}	8.80 ×10^{-4}
	650	3.1 (±9%)	10^{14}	8.55 ×10^{-4}
	1200	4.1 (±4%)	10^{14}	8.80 ×10^{-4}
	1500	4.0 (±10%)	10^{15}	9.20 ×10^{-4}

The graphite radiation damage was monitored by "in-situ" electrical resistance measurements during and after irradiation until its stabilization and cooling at room temperature. The change of electrical resistance provided an assessment of electrical resistivity change and of the accumulation and recovery of irradiation-produced defects as a function of ion fluence and annealing temperature. It was assumed that during irradiation the variation of the total electrical resistance was associated to the variation of electrical resistivity in the irradiated region.

The dependence of the relative change of electrical resistivity with fluence for irradiated samples is shown in Figure 1. The saturation of defects occurs faster at low irradiation annealing temperatures for both graphite grades 2320 and 2360. Moreover, higher irradiation temperatures lead to less pronounced swelling and dimensional changes of the irradiated region as observed in [1] due to a more efficient recombination of the irradiation produced defects. The higher ion flux for the high temperature 2320 graphite sample might lead to faster defect annihilation, resulting in less defect build-up than in the other tested graphite samples.

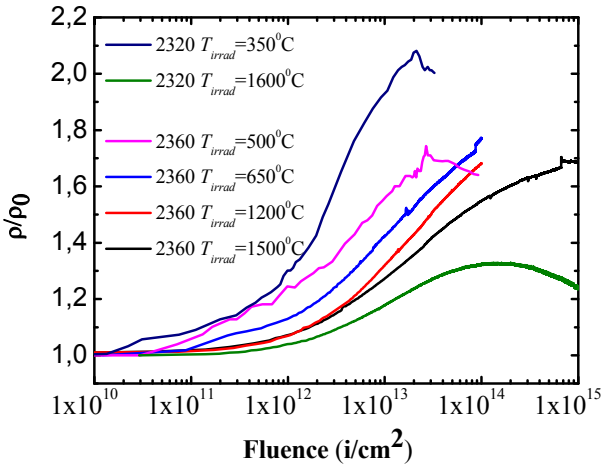

Figure 1: Ion fluence dependence of the ratio of in-situ measured resistivity to initial resistivity of the pristine sample at different high irradiation temperatures for two graphite grades 2320 and 2360.

This work supports the use of graphite at high temperature and fluence for high-power production targets and for beam dump and wedge applications for beam accelerators.

[1] M. Avilov et al., GSI Scientific Report 2010, 383.
[2] Mersen group. www.mersen.com.

* Work supported by U.S. Department Of Energy, Office of Science under Cooperative Agreement DE-SC0000661
# Fernandes@frib.msu.edu

A Photothermal Radiometry Study of Thermal Diffusivity Degradation of High-Temperature Heavy Ion-Irradiated Graphite*

N. Horny[1], M. Chirtoc[1], M. Tomut[2,3,#], M. Avilov[4], M. Bender[2], W. Mittig[5], F. Pellemoine[4], M. Schein[4], D. Severin[2], C. Trautmann[2]

[1]GRESPI-CATHERM, Univ. Reims, France; [2]GSI, Darmstadt, Germany; [3]NIMP, Bucharest, Romania; [4]FRIB, MSU, East Lansing, MI, USA; [5]NSCL, MSU, East Lansing, MI, USA; [6]TU Darmstadt, Germany

Thermal conductivity degradation plays an important role in the failure of targets, beam catchers, beam windows and collimators for the new generation of high power accelerators (LHC, FAIR, FRIB). Information on ion-induced thermal conductivity degradation in target materials is extremely scarce. We present first experimental data on thermal diffusivity measurements on graphite ribbons (thickness l ~75 µm) irradiated with 8.6 MeV/u ^{197}Au ions at temperatures of 445, 1000, and 1600 °C [1].

Photothermal radiometry (PTR) set-up (see Figure 1) allows the determination of thermal diffusivity $a=k/C$, with k- thermal conductivity and C- volume specific heat capacity. In order to estimate the thermal conductivity, it is necessary to know the volume specific heat capacity.

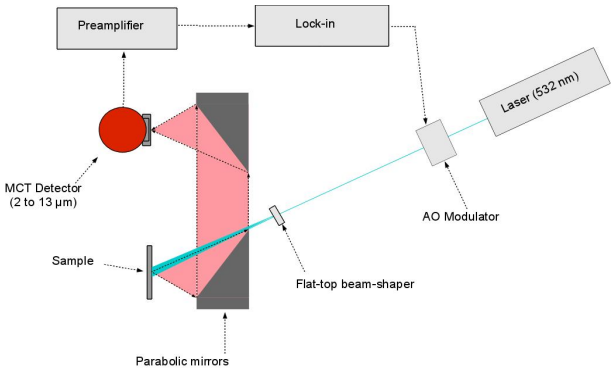

Figure 1: Photothermal radiometry set-up.

The experiment consists of heating the sample with a laser beam and detecting the thermal response of the sample. The laser beam is sinusoidal modulated with an acousto-optic modulator. The Gaussian beam is transformed by a flat-top beam-shaper in order to provide a one dimensional excitation. The variation of the sample temperature generates a variation of IR radiation which is collected by the off-axis parabolic mirrors and sent to the IR detector. The modulation frequencies are varied from 0.1 Hz to 1 MHz. With PTR, a results from the simultaneous fit of amplitude A and phase ϕ signals in the thermally thin/thick transition region (1 - 100 Hz) which corresponds to a frequency around $f_c = a/(\pi l^2)$.

Figure 2 shows the amplitude (A)*sqrt(frequency) and the phase as a function of the modulation frequency for a graphite ribbon irradiated with 1×10^{14}Au ions/cm^2 at a temperature of 1600°C, simulating the operation conditions of a high power target. The solid lines are generated by the model describing the transition between thermally thin (low frequency, A proportional to 1/f, ϕ = -90°) and thermally thick (high frequency, A proportional to 1/sqrt(f), ϕ = -45°) behaviour [2]. This transition gives the thermal diffusivity.

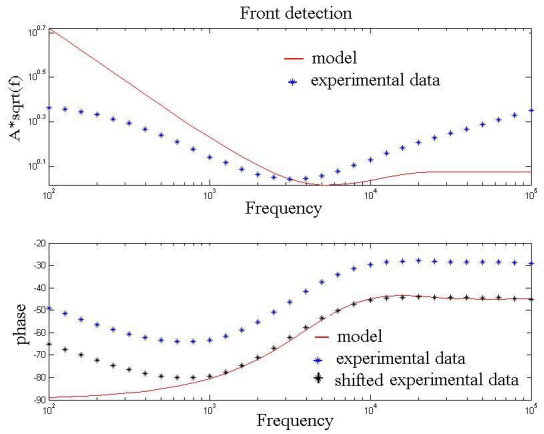

Figure 2: Experimental results for CL2320 graphite sample irradiated with 1×10^{14}Au ions/cm^2 at 1600°C.

Despite the fact that there is a bias of the experimental data probably due to the roughness of the sample, the thermal diffusivity of graphite ribbons irradiated with 8.6 MeV/u Au ions could be calculated (Table 1). We note that swift heavy ion irradiation could decrease the thermal diffusivity up to a factor of 24 at low temperature irradiation, where the defect recovery mechanism is less effective (low vacancy mobility). Whereas at high irradiation temperatures, the degradation of thermal diffusivity is less pronounced due to enhanced vacancy mobility.

Samples- Mersen CL2320 graphite	Thermal diffusivity (mm^{2}s^{-1})
Pristine	90 ± 10
Irradiated at 445°C	3.3 ± 0.2
Irradiated at 1000°C	7.3 ± 0.3
Irradiated at 1600°C	25.5 ± 1.0

Table 1. Thermal diffusivity of graphite samples exposed at different temperatures to 10^{14}Au ions/cm^2 (8.6 MeV/u).

[1] M. Avilov et al., GSI Scientific Report 2010, 383.
[2] M. Chirtoc, Chap. 2 , Ed. E. Marín Moares, Transworld Research Network, Trivandrum, Kerala, 2009, pp. 29-63.

* Work supported by EU, EuCARD contract No. 53102
# m.tomut@gsi.de

Positron Annihilation Lifetime Spectroscopy Investigation of Vacancy Clustering in High-Temperature Ion-Irradiated Graphite

M. Krause[*1,2], *W. Egger*[3], *W. Ensinger*[1], *C. Hugenschmidt*[4], *B. Löwe*[3], *L. Ravelli*[3], *M. Tomut*[2,5], *and C. Trautmann*[2]

[1]Technische Universität Darmstadt, Germany; [2]GSI, Darmstadt, Germany; [3]Universität der Bundeswehr München, Neubiberg, Germany; [4]TU München, Germany; [5]NIMP, Bucharest, Romania

The rare isotope production target that is forseen at the future Super-FRS facility of FAIR [1] consists of isotropic graphite (R6650 grade, SGL Carbon). Beam induced temperatures of up to 750 °C within the ^{238}U-beam spot are predicted by ANSYS calculations. Former experiments on Highly Oriented Pyrolytic Graphite (HOPG) exposed at room temperature (RT) to various GeV ions and analyzed by positron annihilation lifetime spectroscopy (PALS) with the unique Pulsed Low-Energy Positron System (PLEPS) [2] at the FRM II in Munich, revealed the creation of vacancy clusters V_n (chain) with $n = 2 - 4$ [3].

For monitoring the clustering behavior of vacancies at high irradiation temperatures, the new *in-situ* heater setup at the UNILAC M3-Beamline was used. HOPG samples were irradiated at temperatures up to 750 °C and analyzed by PALS using PLEPS. Measured spectra were fitted with POSWIN software [4]. Best spectral deconvolution was archieved using three different lifetimes τ_1, τ_2 and τ_3.

Fig. 1 shows the fitted positron lifetimes for HOPG samples irradiated at a fluence of 1×10^{13} ions cm^{-2} using 1.1 GeV Ru and 1.4 GeV U ions. The data are shown as a function of positron implantation energy and thus as depth within the sample. For reason of completeness also the mean lifetime $\tau_m = \sum I_i \times \tau_i$ is displayed. τ_1 denotes the (reduced) bulk lifetime, while lifetime components τ_2 and τ_3 are specific for vacancy related defects. In all irradiated samples we find a large positron lifetime τ_3, but the intensity is typically below $0.5 \pm 0.1\%$ which is too small to confirm voids possibly formed within the core of the ion tracks.

Lifetime τ_2 is strongly influenced by the irradiation conditions. For the RT irradiation with Ru ions τ_2 has a value of 278 ± 2 ps at highest implantation energy of 16 keV (bulk, Fig. 1a). In agreement with earlier results for the irradiation with 2.2 GeV Au ions [3], τ_2 is attributed to V_n (chain) clusters with $n = 2 - 4$. At elevated temperatures τ_2 has an average value of 359 ± 5 ps at positron implantation energies ≥ 8 keV (Fig. 1b,c). This lifetime is in good agreement with the lifetime reported for experimental results on neutron irradiated graphite for the particular stable V_6 (disc) vacancy cluster and with the *ab-initio* calculated lifetime of 352 ps by Tang *et al.* [5]. At low implantation depths τ_2 shows a tendency towards a value of 361 ± 13 ps, similar as discussed for surface states in combination with the defect specific lifetime. For the benchmark case of the Super-FRS graphite target operating conditions (Fig. 1c), mainly the formation of V_6 (disc) vacancy clusters which are stable up to a temperature of 1500 °C [5] are expected.

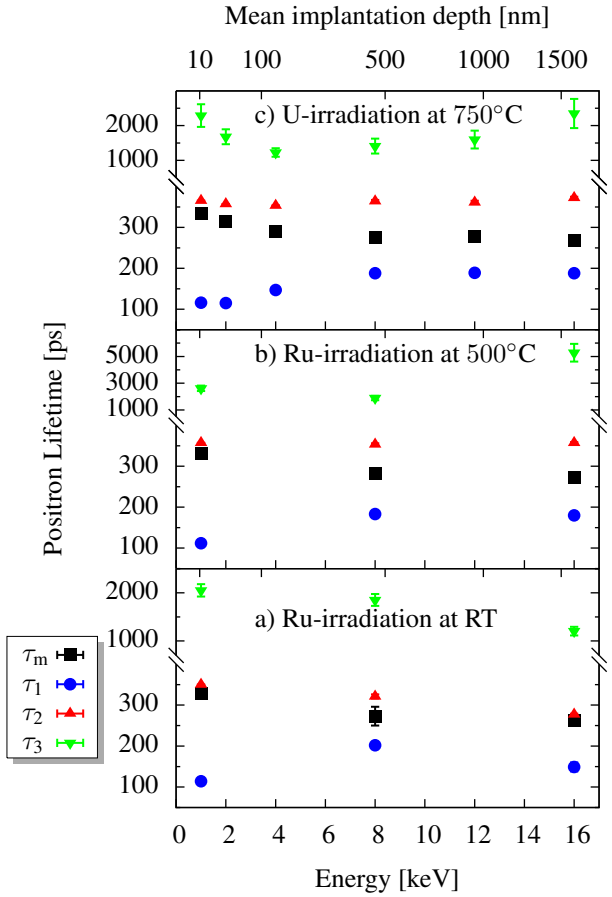

Figure 1: Positron lifetime components as a function of positron energy and thus mean depth for HOPG samples irradiated with 1×10^{13} ions cm^{-2} 1.1 GeV Ru ions (a) at RT , (b) at 500 °C and (c) 1.4 GeV U ions at 750 °C.

[1] M. Winkler *et al.*, Nuc. Inst. Meth. B. 266 (2008) 4183.
[2] W. Egger *et al.*, Phys Stat. Sol. C 4 (2007) 3969.
[3] M. Krause *et al.*, GSI Report (2011-1) 384.
[4] D. Bochert, Diploma thesis, Universität der Bundeswehr München, 2004.
[5] Z. Tang *et al.*, Phys. Rev. Lett. 82 (1999) 2532.

* m.krause@gsi.de

Thermal gravimetric analysis of ion-irradiated polyimide*

T. Seidl[1, 2,#], D. Severin[1], C. Trautmann[1], and W. Ensinger[2]

[1]GSI, Darmstadt, Germany; [2]Technische Universität Darmstadt

Based on their excellent properties, aromatic polyimides are frequently used in particular for electronic and aerospace applications. Polyimides are also prime candidates for the insulation of the superconducting magnets of the FAIR project due to their high radiation resistance that is linked to the chemical structure consisting of a fully conjugated aromatic polymer backbone. Radiation induced degradation is typically characterized by bond scission, formation of unsaturated compounds, carbonization, and gas evolution of small volatile degradation products [1]. When polyimdes are exposed to heavy ions in the MeV-GeV energy regime, significant radiolysis has been observed. The process is known to scale with the energy loss of the ions used.

This study focuses on thermal degradation processes after the irradiation with protons and with Ta ions. The experiments were performed on irradiated Kapton foils analyzed by means of thermal gravimetric analysis in combination with mass spectrometry (TG-MS). TG analysis measures the loss of weight of a given sample while heating and is a standard characterization method for polymers. Coupling TG analysis to mass spectrometry allows characterization of the evolved gas species during each step of the pyrolysis. Both techniques provide useful information on (i) the chemical structure of the analyzed sample and (ii) the involved degradation mechanisms.

Polyimide samples (Kapton HN) were irradiated at the UNILAC with Ta ions (E = 11 MeV/u) and with protons (E = 21 MeV) at ITEP (Russia). According to the TRIM-2010 code, the electronic energy loss of the Ta ions and protons is 15 and 0.003 keV/nm, respectively. TGA measurements were performed with a Netsch TG209 F1 instrument with a heating rate of 20°C/min in nitrogen atmosphere.

Figure 1 shows the TG curves of proton and Ta-ion irradiated samples in the temperature range up to 800 ºC. The ion irradiation clearly modifies the course of the radiolysis process resulting in reduced degradation temperatures and significant residual weight values due to char residues. Beam-induced effects are less pronounced for protons than for Ta ions. Compared to virgin samples, Ta-ion irradiated foils decompose at lower temperatures. For the highest ion fluence applied, the residual weight increases from below 60% to ~70%. The tendency to form char is strongly determined by the chemical structure of a given polymer. Char easily forms in case of dehydrogenated, substituted, or condensed aromatic rings, while a negative char-forming tendency is observed for aliphatic groups connected to aromatic groups. Under proton or low-fluence Ta-ion irradiation, the pristine structure of Kapton is obviously changed in a way that char does not form easily, probably by scission of aromatic rings leading to aliphatic structures. In contrast, high-fluence ion irradiation is known to create carbon clusters which do not degrade thermally within the temperature regime tested. Therefore samples irradiated at high fluences already contain char prior to the TG analysis. Moreover, carbon particles suspended in polymers are known to catalyse thermal degradation and support the char-forming process [2]. It is not possible to distinguish between beam-induced structural changes and carbon cluster formation.

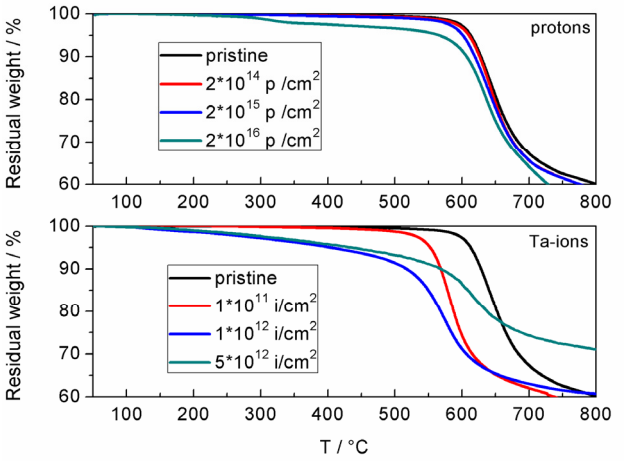

Figure 1: TG-analysis for proton (upper) and Ta-ion (bottom) irradiated polyimide samples.

The analysis of the gas evolution of the sample irradiated with 5×10^{12} Ta ions reveals that at 400°C mainly the formation of CO_2 is increased. Surprisingly, at 550°C the typically observed CO formation is totally absent. This is probably due to the proposed heavy-ion induced production of carboxylic acids [1,3] or the rearrangement of an imide into an isoimide. Both cases would be quite in analogy to thermal degradation of polyimide where the degradation route via CO formation leads to carboxylic acids. Assuming degradation by heavy ion irradiation favours this degradation path explains the increased formation of CO_2 at lower temperatures as well as the total absence of CO production at higher temperatures. For proton irradiated foils, we did not detect any significant changes in gas evolution, presumably because the low energy loss of protons does not lead to major changes of the chemical structure.

References

[1] T. Steckenreiter et al. Nucl. Instr. and Meth. B 161-168 (1999) 151
[2] H. Hatori et al., Carbon, Vol. 34 Issue 2 (1996) 201
[3] O. Baake et al., Rev. of Sci. Instr. 82 (2011) 045103

* work was partially financed by BMBF 06DA9025I

#t.seidl@gsi.de

Mechanical Strength Tests on Ion Irradiated Glass Fibre Reinforced Epoxies

V. Lima[1,2,#], T. Seidl[1,2], E. Bruder[2], E. Mustafin[1], E. Floch[1], and W. Ensinger[2]

[1]GSI, Darmstadt, Germany; [2]Technische Universität Darmstadt, Germany

Introduction

Superconducting magnets used in high-power accelerator facilities have to withstand harsh conditions since they are exposed to high levels of radiation. Radiation induced material degradation limits the lifetime of various components thus posing a threat to their reliable function. Most of the superconducting magnets of the FAIR project will use a G11-type glass fibre reinforced epoxy polymer as structural support material for the magnet coil. In this application the material has to withstand dynamic mechanical loads which derive from Lorentzian forces during pulsed magnet operation. A simple mechanical failure in the coil may cause drastic and costly breakdowns.

In order to estimate the lifetime of superconducting magnets in radiation environments, several studies with gamma and neutron irradiations were performed showing radiation induced degradation of mechanical and electrical properties [1,2]. At FAIR, the secondary radiation consists of a complex spectrum including gammas, neutrons, protons, and heavy ions. Because of their large energy deposition, heavy ions are known to induce extensive damage at rather low fluences. The degree of damage depends on the type of material (insulators e.g. being more sensitive than metals) and scales with the stopping power of the ion. This study focuses specifically on the mechanical strength of ion irradiated G11 composite material.

Experimental

G11 specimens were irradiated in air with uranium ions (E=500 MeV/u) at the SIS18 synchrotron. Four different sample stacks were irradiated with fluence 10^{10} ions/cm^2 (0.04 MGy), 10^{11} ions/cm^2 (0.4 MGy), 3.3×10^{11} ions/cm^2 (1.3 MGy) and 10^{12} ions/cm^2 (4 MGy). Each stack consisted of six G11 samples (thickness 2 mm). After the beam-induced activation of the samples was close to background, Ultimate Tensile Strength (UTS) measurements were performed in warp direction (i.e. along glass fibres).

Figure 1: Photograph of G11 tensile test specimen irradiated with 500 MeV/u uranium ions (10^{12} cm^{-2}).

Results and Discussion

The ion beam induces a change of the original green colour to brown at low fluence, and finally black at high fluence. Figure 1 shows a tensile test specimen colored in the central region due to the exposure to 10^{12} U-ions cm^{-2}. The coloration is ascribed to the formation of carbon clusters and polymer degradation products with conjugated bonds [3].

The UTS measurements show no significant changes within the experimental error up to a fluence of 3.3×10^{11} ions/cm^2 (dose 1.3 MGy). At higher fluence (10^{12} ions/cm^2 / 4 MGy), the tensile strength decreased by 26 % from originally 315 to 238 MPa. The UTS in warp direction is mainly governed by the strength of the fibres and by the fibre-polymer interface. In order to monitor the changes occurring at the interface between the polymeric matrix and the glass fibres, fractured specimens were inspected by means of scanning electron microscopy. Already at a fluence of 3.3×10^{11} ions/cm^2 the composites show signs of degradation and the matrix starts to separate from the fibre. For gamma irradiation such delamination and debonding effects occur only at much higher doses (6-25 MGy) [4]. The increased deterioration induced by heavy ions definitely should be considered for lifetime estimations for the FAIR magnets. In the radiation spectrum, the number of energetic heavy projectiles may be orders of magnitude smaller than the number of neutrons, protons, or light fragments. However, given by their high energy deposition, their damage efficiency is much larger. For the final design of the FAIR magnets, it is recommended to shield polymeric materials, in particular against the direct exposure to heavy ion fragments.

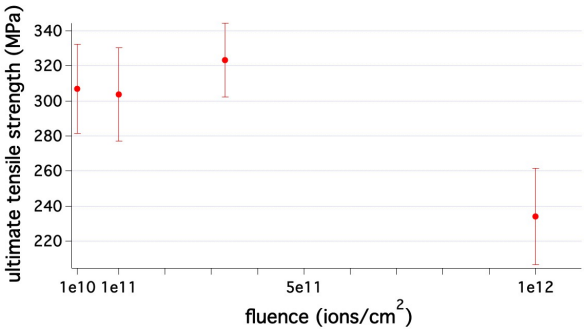

Figure 2: Ultimate tensile strength of G11 composite as function of fluence (U ions of 500 MeV/u). Error bars correspond to the standard deviation of 6 samples.

References

[1] R.R. Coltman Jr. and C.E. Klabunde, J. of Nucl. Mat. 113 (1983) 268

[2] K. Bittner-Rohrhofer *et al.*, Cryogenics 42 (2003) 697

[3] J.M. Costantini *et al.*, Nucl. Instr. and Meth. B 234 (2005) 458

[4] C.E. Klabunde and R.R. Coltman Jr., J. of Nucl. Mat. 117 (1983) 345

v.lima@gsi.de

In-situ FTIR spectroscopy of polyvinyl formal irradiated with gold ions

U. H. Hossain[1,2#], T. Seidl[1, 2], O. Baake[1], A. O. Delgado[3], V. Lima[1,2], D. Severin[2], M. Bender[2] and W. Ensinger[1]

[1]Technische Universität Darmstadt, Germany; [2]GSI, Darmstadt, Germany; [3]University of São Paulo, Brazil.

When polymers are exposed to ionizing radiation, they undergo plenty of changes both in structure and composition. Degradation induced by swift heavy ions has been studied for many years, see e.g. [1]; however, various aspects of the complex process are still not understood. This study concentrates on polyvinyl formal, with Formvar® being a registered trade name of the commercial product. Its complex structure bears three subunits: acetale, alcohol, and acetate. Given by its outstanding chemical and physical properties, this high performance polymer is of interest for application in the future FAIR magnets. For lifetime estimations of the magnet insulation, it is important to better understand damage processes which energetic ions induce in polyvinyl formal.

Formvar® foils having a thickness of 12 µm were synthesized and irradiated at room temperature with Au ions up to energies of 4.4 MeV/u and fluences of $6x10^{11}$ ions/cm^2. The experiment was performed at the M3 beamline of the UNILAC which is described elsewhere [2].

Fourier transform infrared (FTIR) measurements were performed using a Nicolet 6700 spectrometer. For each scan the range from 400 to 4000 cm^{-1} was recorded with 2 cm^{-1} resolution

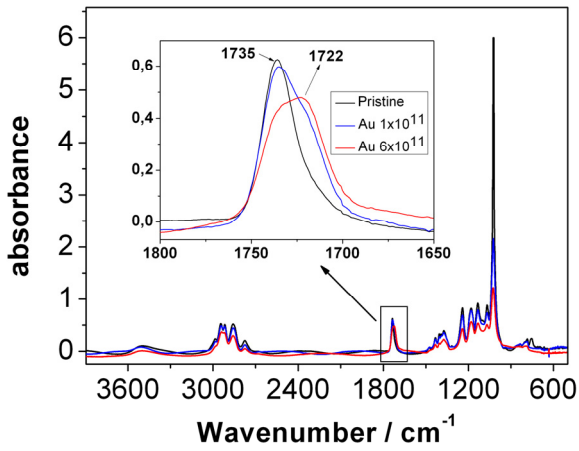

Figure 1: FTIR spectra of 12-µm thick Formvar® foils before and after irradiation with Au ions. The inset shows the newly formed absorption band at 1722 cm^{-1}.

Figure 1 shows the infrared absorption spectrum of Formvar® before and after ion exposure. The region between 1500 and 500 cm^{-1} (fingerprint region) usually contains a complex series of absorption bands. The irradiation leads to an overall decrease of these band intensities.

The very broad absorption centred at about 3490 cm^{-1} originates from the stretching vibration of the OH-groups. The broadness of the absorption band indicates a combination of alcohol, carboxylic acid, and the ester carbonyl vibration. The five intense absorption bands in the 3040-2700 cm^{-1} region are from the symmetric and asymmetric modes of the backbone i.e. –CH and -CH_2. Ion irradiation within the explored fluence regime leads to a decrease in intensity of these bands mirroring the molecular degradation of the polymer. The strong sharp band at 1735 cm^{-1} (A) is attributed to the stretching vibrations of the carbonyl group from the acetate side chain. With increasing fluence, this band decreases and a new band appears at around 1722 cm^{-1} (B). The band increase of B is assigned to the formation of a ketone type C=O bond. The appearance of this ketone can be explained by enol formation which tautomerizes, in analogy to gamma-induced degradation of polyvinyl alcohol [3].

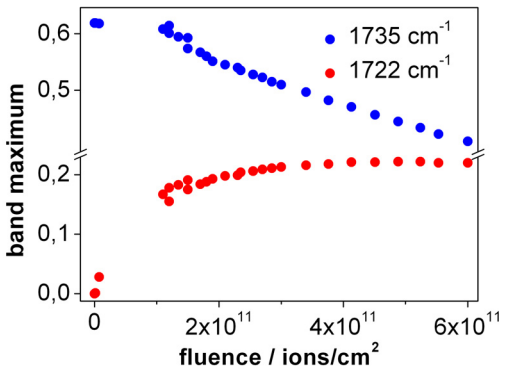

Figure 2: Maximum intensity of absorption bands at 1735 and 1722 cm^{-1} as a function of fluence for 12-µm Formvar® foils irradiated with 4.4 MeV/u Au ions.

Fig. 2 shows the evaluation of the maximum intensities of band A and B after background subtraction as a function of fluence. While the band intensity of A is decreasing, the production of B is increasing and finally saturates at about 3×10^{11} cm^{-2}. The shape of the saturating curve follows an exponential function as characteristic for single ion-hit processes. We note that the beam-induced creation of this ketone takes place at a much lower fluence compared to the production of specific degradation products (e.g. alkynes) found in aromatic polymers. This obviously mirrors the sensitivity of Formvar® to ion irradiation compared to other aromatic polymers such as polyethylene terephthalate or polyimide [1].

[1] T. Steckenreiter, E. Balanzat, H. Fuess, and C. Trautmann, Nucl. Inst. Meth. B 131 (1997) 159.

[2] O. Baake, T. Seidl, U. H. Hossain, A. O. Delgado, M. Bender, D. Severin, and W. Ensinger, Rev. Sci. Instr. 82 (2011) 045103.

[3] M. Ilčin, O. Holá, B. Bakajová and J. Kučerík, J. Radioanal. Nucl. Chem. 283 (2010) 9

#u.h.hossain@gsi.de

Dielectricity and Resistivity Changes in Polymers under Ion Irradiation

B. Körber[1], *M. Bender*[1], *D. Severin*[1], *and C. Trautmann*[1]
[1]GSI, Darmstadt, Germany

We investigated dielectricity and conductivity changes of polyimide foils during exposure to swift heavy ions. Changes of these properties can reveal the aging process of insulators under harsh high-dose environments [1, 2] such as at nuclear power plants or high power particle accelerators. The future FAIR facility requires radiation resistant insulating materials for various devices including magnets. The experimental setup is similar to an impedance spectrometer. As sample we used a 7.5-μm thick Kapton foil that was Al-coated on both sides and as such can be considered as a parallel-plate capacitor which is integrated into an oscillating circuit inside a voltage divider (fig. 1). A sinus signal is applied to the circuit and the frequency is swept around the oscillators resonance frequency. The ratio between ingoing and outgoing amplitude is plotted versus frequency (fig. 2, top). From the resonance curve, two important values can be extracted: the resonance frequency f_R and the FWHM of the resonance curve. A shift of f_R is due to changes of the foil capacity as

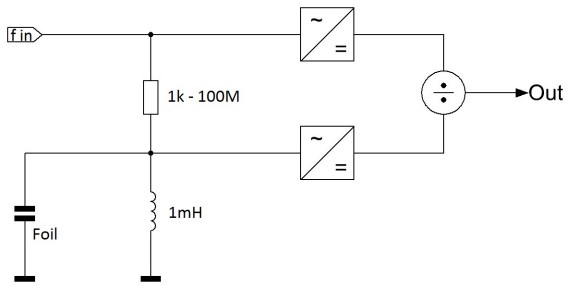

Figure 1: Signal flow of the impedance spectrometer.

$$f_R = \frac{1}{2\pi\sqrt{LC}} \quad (1)$$

where L is the constant inductivity of the coil and C the capacity of the foil which varies as a function of irradiation dose. It has to be mentioned, that the total capacity is composed of the sum of the irradiated foil and the electric cables of the set-up. The change of the foil capacity is proportional to the relative dielectricity of the polymer.

Irradiation experiments were performed at the UU-beamline at the high-charge injector using 1.4 MeV/u Xe ions and at the M3-Branch of the UNILAC using 4.8 MeV/u Au ions. The beam flux was kept below about 1.5×10^8 $ions/s\ cm^2$ to prevent thermal damage. After fluence steps of 5×10^9 or 1×10^{10} $ions/cm^2$ a frequency sweep was performed up to a total fluence of about 5×10^{12} $ions/cm^2$.

Fig. 2 displays a series of resonance curves for a Kapton foil irradiated with different fluences of 4.8 MeV/u Au ions together with the evolution of the resonance maximum as function of fluence.

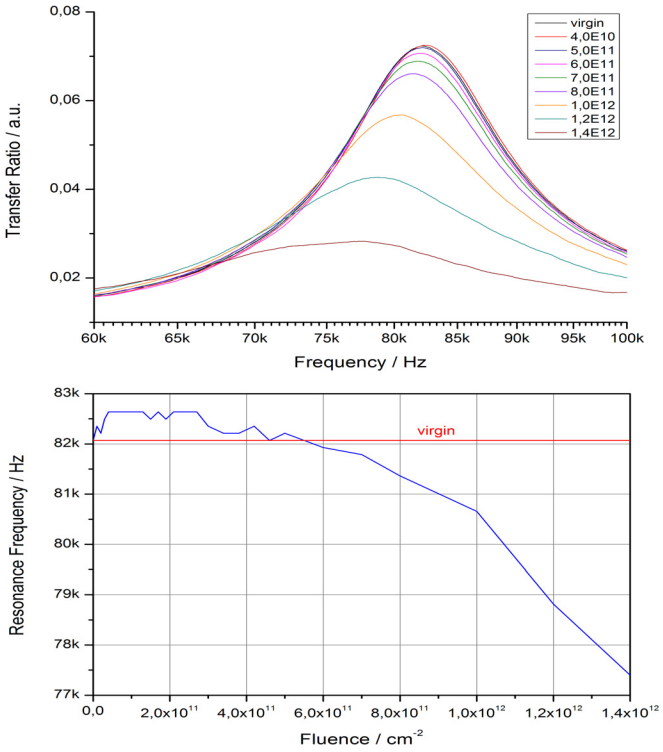

Figure 2: Frequency sweep for different fluences (top) and shift of resonance maximum (bottom) versus fluence.

With increasing fluence, the resonance maximum shifts towards lower frequencies revealing higher capacity values. Moreover, the total area of the resonance curve decreases and the FWHM increases, giving evidence that the conductivity of the foil becomes larger.

In conclusion, by combining irradiation experiments with this new *in-situ* analysis technique it is possible to step by step monitor the degradation of polymer foils exposed to ion beams. This technique is not only suitable for polymer foils but for any other metallized thin insulator acting as capacitor. For a more complex investigation of the degradation process, it can easily be combined with other monitoring methods (e.g. rest gas analysis or infra red spectroscopy) available at the M3-beamline.

References

[1] J.-M. Costantini et al., Nucl. Instr. Meth. **B** 234 (2005) 458-466

[2] J.-P. Salvetat et al., Nucl. Instr. Meth. **B** 116 (1996) 284-288

In-situ analysis of ion-beam-induced degradation and post-irradiation oxidation in poly(vinylidene fluoride)

T. Yamaki[1,#], M. Asano[1], H. Koshikawa[1], Y. Maekawa[1], D. Severin[2], T. Seidl[2], C. Trautmann[2]

[1]Japan Atomic Energy Agency (JAEA), Takasaki, Gunma, Japan; [2]GSI, Darmstadt, Germany

For several years, we have been working on ion-track membranes of poly(vinylidene fluoride) (PVDF) because they have attracted a renewed interest for their applications to fuel-cell materials [1]. The main conclusion from past experiments was that not only heavy ions of high LET, but also post-irradiation heating in air promotes chemical etching, both in the core and in the halo of the track. This leads to an increased etching sensitivity and to larger pore diameters [2]. The effect of the post-irradiation heating as an etching pre-treatment process originates from an oxidation of the radiolysis products within the latent tracks, which lowers the hydrophobicity of the polymer and thus increases the wettability in aqueous etching solutions. Therefore, there has been a strong motivation to investigate the detailed chemistry of heavy-ion-induced degradation and the post-irradiation oxidation. We report here the results of our first experiments in this regard performed at the newly installed M-branch.

Commercially available 25-µm thick PVDF films were irradiated at room temperature with 4.8-MeV/u ^{238}U at fluences up to 6×10^{11} ions/cm^2. The irradiation was performed in the multi-purpose chamber of the M3 beamline at the UNILAC equipped with a Fourier-transform infrared (FTIR) transmission spectrometer as well as a residual gas analyzer [3]. The FTIR spectra were recorded in-situ as a function of fluence in the course of irradiation. The irradiated film was also FTIR-analyzed just after ventilation of the irradiation chamber with air.

Original sharp IR bands assigned to CH_2 stretching were originally observed at approximately 2990 and 3030 cm^{-1}; they decreased during the irradiation. For irradiation fluences above 1×10^{10} ions/cm^2, the film showed new absorption bands around 1710, 1750, and 3300 cm^{-1}, identified as double-bond stretching vibrations of in-chain unsaturations –CH=CF– and fluorinated vinyl groups –CF_2–CH=CF_2, and CH_2 stretching vibration of R–CH_2–C≡CH, respectively. Their intensity became more prominent with increasing fluence (Fig. 1). This observation is in agreement with results from earlier ex-situ experiments [e.g., 4].

A special advantage of in-situ analysis is the possibility to record FTIR spectra at the very initial stage of oxidation reactions of the degradation products. This allowed us to monitor a change in the spectral profile for the film irradiated at the highest fluence as a function of time after chamber ventilation (Fig. 2). After three minutes, a small absorption band appeared at 1800-1850 cm^{-1} that could be ascribed to the stretching vibration of the C=O group in acid fluoride –CH_2COF and fluorinated carboxylic acid –CF_2COOH, indicative of the formation of new functionalities due to the rapid oxidation of the radiolysis products. Conventional offline analysis has very limited access to accurate information on short-term dynamic processes. Further investigations at the M-branch are now in progress in order to get a basic insight into the reactivity of latent tracks.

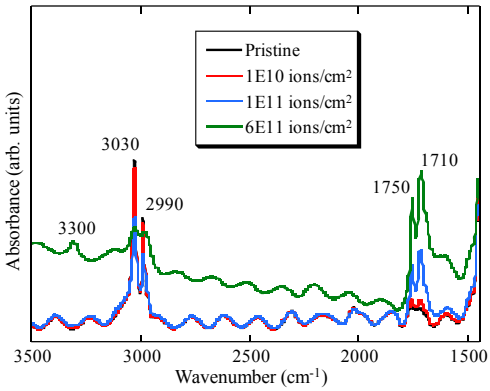

Figure 1: FTIR spectra of PVDF irradiated with 4.8-MeV/u U ions of different fluences.

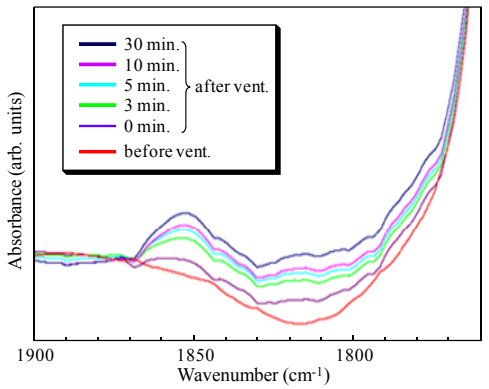

Figure 2: FTIR spectra of PVDF irradiated with 6×10^{11} U/cm^2 at different times after ventilation.

References

[1] T. Yamaki, Y. Kozone, A. Hiroki, M. Asano, H. Kubota, M. Yoshida, ECS Transactions 3 (2006) 103.

[2] R. Rohani, T. Yamaki, H. Koshikawa, S. Takahashi, S. Hasegawa, M. Asano, Y. Maekawa, K.-O. Voss, C. Trautmann, R. Neumann, Nucl. Instr. Meth. B 267 (2009) 554.

[3] D. Severin, C. Trautmann, R. Neumann, GSI Scientific Report 2008 (2009) 362.

[4] A Le Bouëdec, N. Betz, S. Esnouf, A. Le Moël, Nucl. Instr. Meth. B, 151 (1999) 89.

[#] yamaki.tetsuya@jaea.go.jp

Annealing of dislocations and heavy-ion induced tracks in calcite *

Sebastian Dedera[1], Michael Burchard[1], Ulrich A. Glasmacher[1], Christina Trautmann[2]

[1]Institute of Earth Sciences, University of Heidelberg, Heidelberg, Germany; [2]GSI, Darmstadt, Germany

Natural calcite crystals typically bear dislocations in variable quantities. Dislocations can be visualized by the etching technique and often exhibit a similar morphology as etch pit originating from ion tracks. To distinguish between ion tracks and dislocations, minerals can be heated for a certain time which often leads to the annealing of the ion tracks at lower temperatures than the dislocations.

In this project, natural calcite crystals were irradiated with ^{197}Au or ^{238}U ions (11.1 MeV/u) at a fluence of 10^6 U/cm^2, and 10^6 and 10^8 Au/cm^2 at the UNILAC. During irradiation the surface of the calcite crystals was covered with a hexagonal mask to create neighboring irradiated and non-irradiated sites on the crystal surface. As chemical etchant we used a 1:1 solution of ethylenediaminetetraacetic acid (Na-EDTA) + 5% acetic acid for 20 s at 21 °C [1]. The etch pits from ion tracks have an elongated hexagonal shape and are denoted as Type I.

Applying the same etching conditions to non-irradiated crystals revealed two different types of etch pits: Type A has a very similar shape as those of ion tracks (Type I). Type B etch pits differ significantly from Type I, they are more shallow and look like a flat depression on the crystal surface (Fig. 1.)

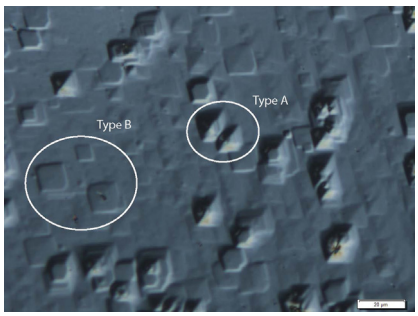

Fig. 1: Type A and B etch pits from dislocations (optical microscope with Nomanski-Interference Contrast).

Type A etch pits do not have a distinct dark central spot as seen for etched ion tracks of Type I. The density of Type A and B etch pits increases close to cracks, scratches or any other deformation of the crystal, while Type I etch pits are evenly distributed on the entire crystal surface. If they represent etched dislocations, heat treatment of non-etched calcite crystals is expected to clearly differentiate them from etched ion tracks. To test this hypothesis, ion-irradiated calcite samples were heated for 100 h at temperatures between 200 – 500 °C. After heat treatment the calcites were etched with the same solution and at identical conditions as described above. For comparison, we exposed non-irradiated calcite crystals to the same annealing process (100 h, 200–500 °C).

* Work supported by BMBF Verbundprojekt 05K10VH1

ulrich.a.glasmacher@geow.uni-heidelberg.de

The areal density of the etch pits of irradiated calcite reduces dramatically between 200 and 300 °C, while at 200 °C the density was within errors the same as the one at room temperature (RT) corresponding to the ion fluence of 10^6 Au ions/cm^2. After annealing at 300 °C, the etch pit density was reduced to 0.04×10^6 cm^{-2}. The etch pits were inhomogeneously distributed on the surface of the calcite crystal. In contrast, the non-irradiated crystal revealed the same areal density (0.04×10^6 etch pits/cm^2) before and after the heat treatment (Fig. 2 & 3)

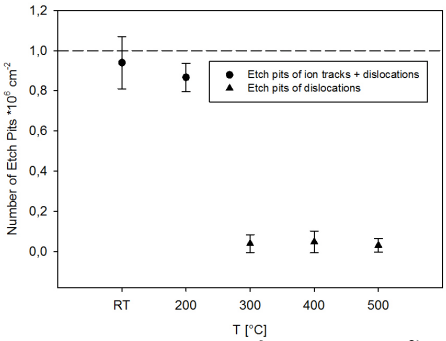

Fig. 2: Irradiated calcites (10^6 Au ions/cm$^{2)}$ treated at temperatures of 200-500 °C for 100 h. Etch pit areal density reduces dramatically between 200 and 300 °C; (dashed line indicates the nominal fluence of the ion irradiation).

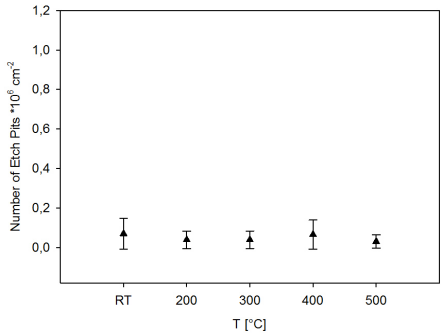

Fig. 3: Non-irradiated calcites treated at temperatures of 200-500 °C for 100 h. The areal density of dislocations etch pits remains stable at approx. 10^4 cm^{-2}

These results point towards the possibility to distinguish between etch pits of ion tracks and etch pits of dislocations by heating calcite prior to etching above 300 °C. Further investigations will follow to quantify the thermal stability of ion tracks and dislocations, and to provide more precise information on the annealing behavior of ion tracks in calcite.

[1]: S. Dedera et al., “Etch pit morphology of heavy ion tracks in calcite”, GSI-Report 2011, this volume

Etching of heavy ion tracks in calcite*

Sebastian Dedera[1], Michael Burchard[1], Ulrich A. Glasmacher[1#], Christina Trautmann[2]

[1]Institute of Earth Sciences, University of Heidelberg, Heidelberg, Germany; [2]GSI, Darmstadt, Germany

Carbonate minerals such as calcite ($CaCO_3$) are abundant in carbonate rocks in nature. Their dissolution behavior under natural conditions plays a major role in the understanding of the CO_2-balance on planet Earth and therefore, on the degree of climate change. In the past, dissolution experiments have been performed on natural carbonate minerals by using a combination of flow cells, SEM and AFM-techniques [1]. The revealed total dissolution rate comprises the etching rate of the undisturbed crystal along dislocations, and spontaneous fission tracks originating from the radioactive decay of ^{238}U. As the amount of fission tracks is a function of the ^{238}U-content and rock age, the etching rate of fission tracks is of major importance for the understanding of the dissolution of calcite, in general. Furthermore, neither dislocations nor fission tracks are homogenous distributed in natural calcite. This inhomogeneity might lead to selected dissolution of calcite and therefore, carbonate rocks in nature. Our investigation aims at separating and quantifying the etching rate of undisturbed calcite crystals, dislocations, and ion tracks.

Here, we present the first data of selective etching of heavy ion tracks induced in calcite. Calcite was irradiated with 11.1 MeV/u ^{238}U or ^{197}Au ions at the UNILAC, applying fluences between 10^6 and 10^8 ions/cm^2. Even though U and Au ions are much heavier than fission fragments, we chose these beams to make sure to create etchable tracks far above the etching threshold. During irradiation, the surface of some calcite crystals was covered with a hexagonal mask to create irradiated and non-irradiated sites next to each other. In a first step, various etching solutions and conditions have been tested with respect to their effectiveness to selectively attack the tracks and produce etch pits.

Solution agents tested are formic acid (CH_2O_2), sodium hydroxide (NaOH), hydrochloric acid (HCl), and a 1:1 mixture of disodium-ethylenediaminetetraacetic acid (Na-EDTA) and 5% acetic acid. So far the EDTA mixture revealed the best etch pit morphology. The evolution of the etch pit morphology was tested by using the EDTA mixture at 21°C with etching time 5, 10, 15, and 20 s (Figs. 1, 2).

The etch pits have an elongated hexagonal shape designated as Type I. Part of the etched ion channel is visible in optical microscopy. Related to the fluence of 10^6 ions/cm^2, the best visibility (well developed, no overlap) of the etch tracks is provided after 20 s etching.

* Work supported by BMBF Verbundprojekt 05K10VH1

ulrich.a.glasmacher@geow.uni-heidelberg.de

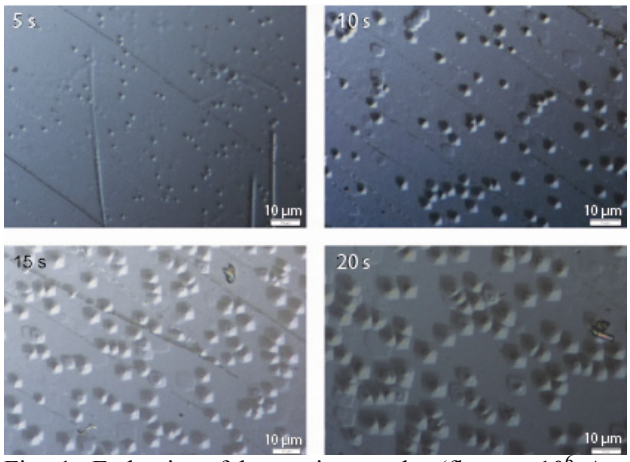

Fig. 1: Etch pits of heavy ion tracks (fluence 10^6 Au-ions/cm^2) on surface of calcite after various etching times in a Na - EDTA based solution. (optical microscope with attached Nomarski Interference Contrast)

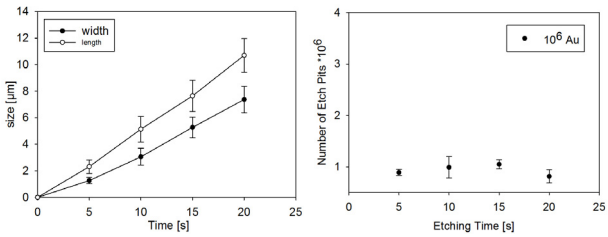

Fig. 2: Etch pit size (crossectional length and width) (left) and areal density (right) as a function of etching time. (same samples as in Fig. 1)

We also performed experiments to understand the influence of a thin surface cover (such as a red edding paint and grease) on etching behavior. As it can be seen on figure 3 in the area of the thin cover the etch pits are less developed. Therefore, it is strongly recommended to clean the surface as much as possible with solutions before etching.

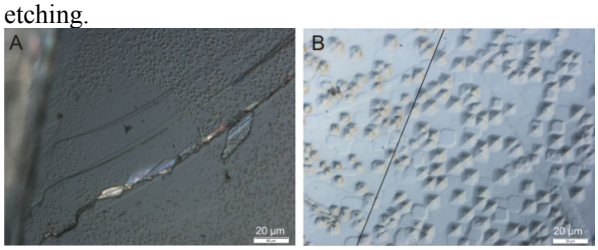

Fig. 3: Influence of thin surface cover on the etching behavior of ion tracks. A: cover with red edding paint; B: left side was covered with grease.

[1] A.Lüttge et al., "Interferometric study of the dolomite dissolution: A new conceptual model for mineral dissolution", Geochimica et Cosmochimica Acta 67 (2003) 1099.

The thermal signal of the Ries meteorite impact

F. Krieger[1,2,3], A. Kleber[1],J.-M. Lange[2], B. Wauschkuhn[3], R. Jonckheere[3] and L. Ratschbacher[3]

[1]Institut für Geography, TU Dresden, Germany; [2]Sektion Petrographie, SNSD, Germany;
[3] Geologisches Institut, TU BA Freiberg, Germany

Introduction

The Ries crater in south Germany was formed ca. 14.6 Ma ago by a meteorite impact [1]. The impact is associated with extreme heating, melting and vaporization of the projectile and target rocks. Earlier post-impact cooling histories were based on numerical models. Low-temperature geothermochronometers, such as the fission-track method, provide a modern empirical tool for constraining palaeotemperature estimates and unravelling the thermal signal of impact events.

Measurement

The fission-track method was applied to apatites from 19 cores from the *Forschungsbohrung Nördlingen*. Their ages were determined with the ζ-method. The track length measurements were carried out on mounts irradiated with 2×10^6 cm^{-2} 8.3 MeV/amu ^{197}Au ions at the Unilac accelerator. These ion tracks act as etchant conduits permitting full-length fission tracks inside the apatite grains to be etched and measured [2].

Three sample groups can be distinguished based on the ages and track length distributions: (a) reset (event) samples, with ages of ~14.6 Ma and long mean track-lengths, (b) overprinted samples with ages between 28.0±2.7 and 86.7±7.9 Ma and broad track-length distributions, and (c) unaffected basement samples, with ages >85 Ma and short mean track lengths. The oldest age is from a basement fragment within the fall-back suevite just above the crater floor (Fig. 1)

Discussion

These results are not compatible with the existence of a long lasting, elevated post-equilibration temperature after the meteorite impact, because of (a) the occurrence of (almost) unreset basement ages near the crater floor, and (b) the large age variations over short vertical distances. The results thus suggest that the formation of the Ries crater was a cooler process than hitherto assumed and that less heat remained in the basement after the impact. This does not exclude transient extreme heating of the basement during the compression stage.

The fall-back suevite experienced temperatures above those for complete annealing of the fission tracks. This took place during ejection or a short time after deposition. The thermal signal of the basement rocks reflects the inhomogeneous pre-equilibrium temperature distribution due to differential heating by the shock wave and conductive heating close to the contact with the fall-back suevite. Some annealing due to shock pressure cannot be excluded, however. No major annealing occurred after temperature equilibration. The undisturbed basement samples reveal a fossil Permian partial annealing zone and Late Cretaceous exhumation. These are thought to be related to the post-Variscan formation of the Central European Basin System and its subsequent inversion due to the Europe-Africa collision.

#Raymond.Jonckheere@geo.tu-freiberg.de

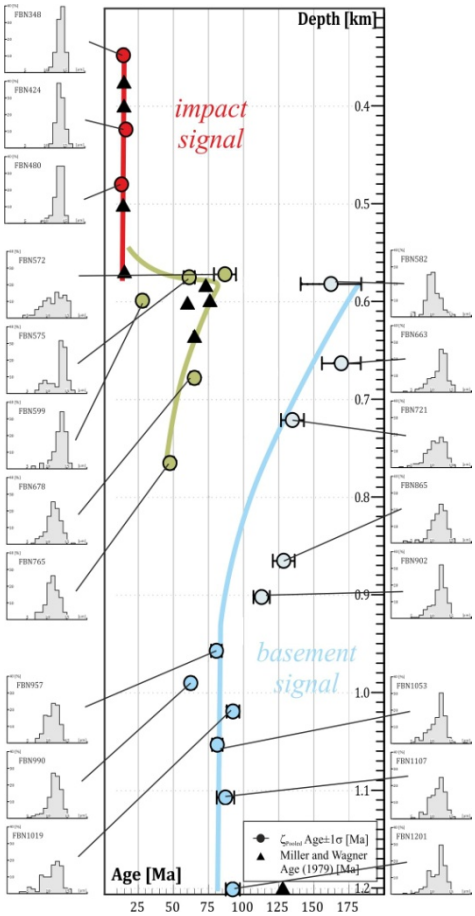

Figure 1: Apatite fission-track ages [3; this work] and mean track-length distribution [this work].

References

[1] E. Buchner, W.H. Schwarz, M. Schmieder and M. Trieloff, Meteorit. Planet. Sci. 45 (2010) 662-674.

[2] R. Jonckheere, E. Enkelmann, M. Min, C. Trautmann and L. Ratschbacher, Chem. Geol. 242 (2007),:202-217.

[3] D.S. Miller, G.A. Wagner, Earth Planet. Sci. 43 (1979):351-358.

Single Event Effect Measurements in 90nm CMOS Circuits at the Microbeam Facility for the Project FATAL*

M. Hofbauer[1,#], K. Schweiger[1], H. Dietrich[1], H. Zimmermann[1], U. Schmid[2], B. Merk[3], K.O. Voss[3]

[1]TU Wien, EMCE, Austria; [2]TU Wien, ECS, Austria; [3]GSI, Darmstadt, Germany

Introduction

Final goal of the project FATAL is a simulation model which considers radiation induced effects, like single event transients (SETs) and single event upsets (SEUs), in asynchronous logic. Using this model, it will be possible to develop a design and simulation framework for designing radiation tolerant asynchronous logic. For synchronous logic such frameworks are already available. Synchronous logic is sensitive to single event effects (SEEs) at the clock edge only. Therefore it is sufficient to know the arising pulse widths of the SETs in order to design radiation tolerant synchronous logic [1]. In asynchronous logic there is no clock available. Thus it is sensitive to SEEs all the time. Furthermore, handshaking and data signals work with voltage transitions. Since SETs are nothing else than voltage transitions they can easily be misinterpreted as data or handshaking signals. To consider single event effects in a simulation model for asynchronous logic, it is necessary to know the exact shape of the arising SETs and the propagation of these pulses through the circuitry.

Simulation

For investigation of SEEs, extensive 3D semiconductor simulations have been performed. The final simulation model will be significantly less complex in order to reduce the computational effort. This simplified model has to be verified by measurements and 3D semiconductor simulations that are very sensitive to process parameters like doping profiles. Therefore the 3D semiconductor simulations have to be calibrated with help of measurements. First measurements have been performed in 2011 at the micro-beam facility using 945-MeV gold ions.

Measurement

Simulation results showed a strong position dependency of SEEs. Therefore it is necessary to be able to accurately deposit the ions at the desired position. Furthermore, the effects of several ions should not overlap. According to this, the circuit should be hit by only one single ion at a time. These two requirements are perfectly met by the micro-beam facility at the UNILAC. It is able to deposit single ions in a region with a diameter of approximately 500nm. For measurement of the arising SETs and SEUs, test chips with integrated sense amplifiers have been designed and fabricated. These sense amplifiers allow measurement of the voltage transients with negligible influence on the test circuit and pulse shapes. Fig. 1 shows the measurement setup. The micro-beam scans the surface of the chip. Every time an ion hits the chip, the channeltron generates a signal which triggers the oscilloscope and forces the system control to log the position of the beam in order to correlate the hit position with the measured pulses. Basic logic circuits like inverter chains and Muller-C pipelines have been investigated. Muller-C Gates are basic memory elements for asynchronous logic. SETs and SEUs could be observed.

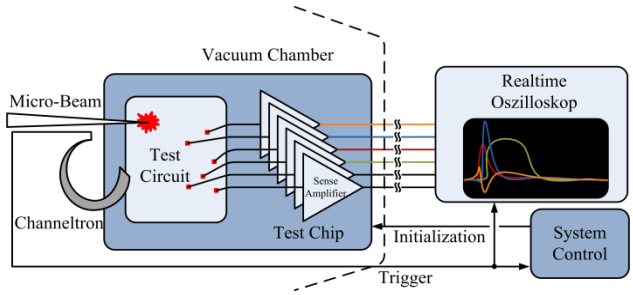

Figure 1: measurement setup

Results

Fig. 2 shows a voltage transient recorded in a single inverter. Using on chip sense amplifiers, it was possible for the first time to directly measure the voltage pulse shapes of SETs and SEUs. More detailed information is published in [2].

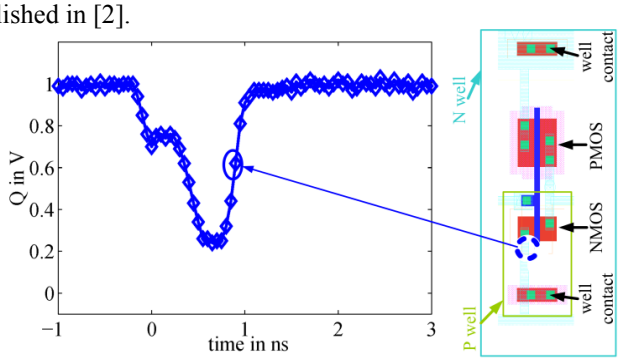

Figure 2: measurement result

References

[1] M. J. Gadlage et al., "Scaling Trends in SET Pulse Widths in Sub-100 nm Bulk CMOS Processes," IEEE Transactions on Nuclear Science, 57 (2010) 3336.

[2] K. Schweiger, M. Hofbauer et al, “Position Dependent Measurement of Single Event Transient Voltage Pulse Shapes under Heavy Ion Irradiation”, accepted in Electronics Letters.

* This research is supported by the Austrian Science Fund (FWF): P21694

Michael.Hofbauer@tuwien.ac.at

Immersion Optics for the Horizontal Online Microscope at the GSI Microbeam

K.-O. Voss[1], *B. E. Fischer*[1], *B. Jakob*[1], *and B. Merk*[1,2]
[1]Helmholtzzentrum für Schwerionenforschung GSI; [2]Technische Universität Darmstadt

Introduction

For many years, the term ”sub-cellular targeting” in the field of microbeam irradiators is being used synonymously with directing particles into either the cell nucleus or, in rare cases, into regions in the cytoplasm of eukariotic cells. These two typical targets have sizes of the order of tens of micrometers. For this reason, the microscopes used to locate the target objects at an ion microbeam usually do not strive for utmost optical resolution. Instead, a large field of view with many target objects imaged at the same time and very large working distance between objective and cell dish with lower chance of collision are advantageous for these types of experiments. However, with truly sub-cellular target objects on the scale of about a micron or so [1] and with time resolved online microscopy in mind [2], one can no longer afford the luxuries of low numerical aperture, low magnification, and long working distance objectives. Here, we report on the implementation of high numerical aperture water immersion optics into the horizontal GSI microbeam.

Setup and Performance

Immersion optics employ a film of optically transparent high refractive index material between sample and objective lens to collect light from solid angles that would otherwise be refracted out of the objective entrance. This results in a higher numerical aperture and ultimately in brighter images with better spacial resolution. Typical immersion media are oil and water. In our case, microscopy is performed through a refractively water-like culture medium. As a consequence, we minimize the refractive mismatch along with its optical aberrations using water as immersion film. For GSI’s horizontal ion beam to reach the cell culture, the cell dish needs to be mounted vertically. Any liquid immersion medium between objective and the cover glass of the cell dish will thus tend to flow downwards. The movement of the microscope stage will increase this loss of liquid from the immersion film. For this reason, water is pumped through a PVC tube fixed on the objective ending just above the objective front lens. Droplets of water from the tube are pulled into the gap between lens and cell dish cover glass by surface tension and thus replenish the immersion film. Excess water separates from the immersion film by gravity flowing vertically downward on the cover glass. This excess water collects at the rim of the cell dish where a silicone o-ring holds the cover glass in place. Here, suction removes water through a bent glass tube that is hooked over the curvature of the o-ring. The suction tube is fixed on the microscope stage and thus moving along synchronously with the additional force acting upon the cell dish being small and constant. Figure 1 shows this setup.

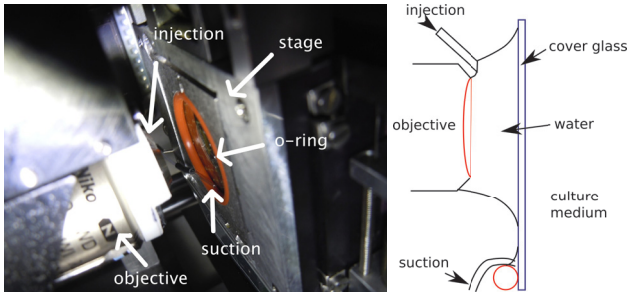

Figure 1: Immersion objective retracted from the cell dish. Water is injected through a PVC tube fixed just above the front lens (left). Excess water is sucked through a glass capillary from the lower rim of the o-ring closing the cell dish (right). The newly designed larger cell dish allows for collision-free movement of the microscope stage.

Figure 2 depicts a micrograph of 200 nm diameter green fluorescent beads imaged as resolution standard. Clearly, beads with central distance 400 nm can easily be resolved. The immersion setup has been employed for a number of *in-situ* microscopy and laser bleaching experiments [3] in 2011.

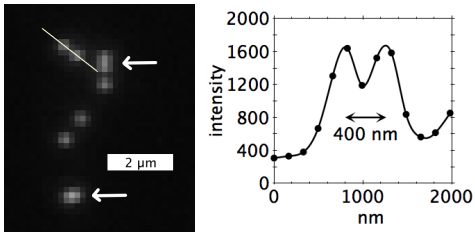

Figure 2: 200 nm diameter green fluorescent beads imaged for resolution estimation (left). 400 nm distant beads clearly separate (profile right, spline-connected). Critical distance beads top right (arrow); Sub-resolution distance bottom (arrow).

References

[1] Burkhard Jakob, Jörn Splinter, Sandro Conrad, Kay-Obbe Voss, Daniele Zink, Marco Durante, Markus Löbrich and Gisela Taucher-Scholz, Nucleic Acids Research **39** (2011) 6489

[2] B. Merk, K.-O. Voss, B. E. Fischer, B. Jakob, G. Taucher-Scholz, and M. Durante, GSI Scientific Report 2010, 394

[3] B. Merk, K.-O. Voss, I. Müller, B. E. Fischer, B. Jakob, G. Taucher-Scholz, C. Trautmann, and M. Durante, GSI Scientific Report 2011, Biophysics section of this issue

Power generation from concentration gradient in ion-selective nanochannel*

L. Cao[1], W. Guo[1], M.E. Toimil-Molares[2], C. Trautmann[2], M. Ali[2], and Y. Wang[1,#]

[1]Peking University, Beijing, China; [2]GSI, Darmstadt, Germany

In recent years, smart synthetic nanopores have been proposed to serve as artificial ion channels that mimic the ion selectivity of the biological counterparts [1]. In nature, some organisms have the inherent skill to convert Gibbs free energy in the form of a salinity gradient into bioelectricity with highly selective ion channels and pumps on its cell membrane. One remarkable example is the electric eel, which is capable of generating considerable electric shocks [2]. Inspired by these biological systems, an abiotic nanofluidic system is demonstrated converting a salinity gradient into electricity [3]. This facile and efficient energy conversion system has the potential to power biomedical tiny devices or construct future clean-energy.

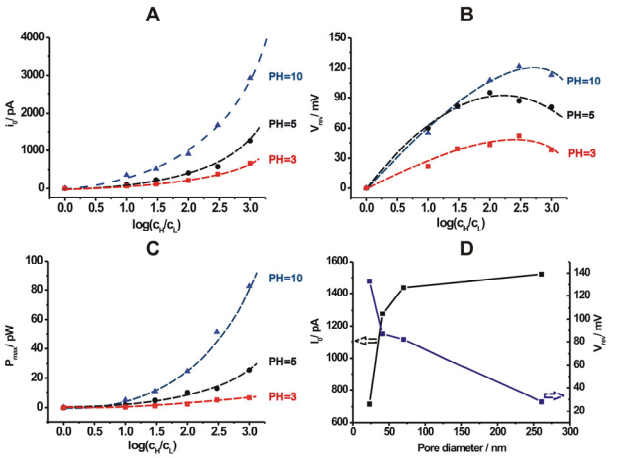

Figure 1. Power generation of single conical nanopores. (A–C) i_0, V_{rev}, and P_{max} as a function of the logarithm of the KCl concentration gradient at different pH value for a 41-nm pore-tip diameter. (D) i_0 (black) and V_{rev} (blue) evolution versus pore-tip diameters.

The nanopores were fabricated by the ion-track etching technique. Polyimide films (12 μm thick) were irradiated with one single heavy ion at the UNILAC accelerator. Subsequent chemical etching with NaClO from one side led to the formation of a single conical nanopore. We measured the I-V curves of the nanopores mounted in an electrolytical cell applying several KCl gradients. The current i_0 and voltage V_{rev} are the short-circuit current and the open-circuit voltage of the nanofluidic power source, respectively (Fig. 1A and B). The corresponding maximum energy production capability of the nanopore is calculated by $P_{max}=1/4(i_0 \times V_{rev})$ (Fig. 1C). In addition, experiments were conducted on nanopores with different tip diameters, showing that i_0 increases while V_{rev} decreases with pore size (Fig. 1D).

* Work supported by National Nature Science Foundation of China No. 10675009, 90923004.

ygwang@pku.edu.cn

We further investigated the performance of the energy converting system in relation to the electrolyte type and the charge selectivity of the nanopore using both experimental and theoretical approaches [4]. Experimental results show that i_0, V_{rev}, and the resulting electric power are very sensitive to the ionic composition of the electrolyte solution.

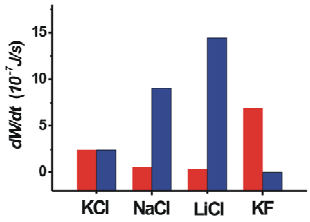

Figure 2. Electric power generation in unit time (dW/dt) in a single cation- (red) or anion-selective (blue) nanopore using KCl, NaCl, LiCl, and KF as electrolyte.

Assuming the same surface charge density, the calculated electric power generation in cation- or anion selective nanopore is nearly identical when using KCl as electrolyte (Fig. 2, we note a quantitative comparison with experimental data of Fig. 1 is not possible due to different pore parameters). However, the difference in power generation between the two kinds of nanopores becomes evident when the cations and anions in the electrolyte solution have asymmetric mobility. In the case of NaCl and LiCl electrolyte, the power generation in anion selective nanopores is significantly higher than that in cation selective nanopores. Note that this trend can be opposite when using KF as electrolyte, with cation selective nanopores showing a better performance because in the KF solution, the cations diffuse faster than the anions.

The concentration-gradient driven nanofluidic energy conversion system does not rely on any mechanical moving parts, such as turbines or motors, and uses simple inorganic electrolyte as fuel, which is innocuous to life processes. The power generation can be further improved by increasing the pore number, engineering the pore geometry, and tailoring the surface chemistry of the pore wall. Therefore, this technology may have a bright future for power supply components of, e.g., implantable biomedical devices that harvest electricity in vivo.

References

[1] Z. Siwy, Adv. Func. Mater. 16 (2006) 735.
[2] J. Xu, D. A. Lavan, Nat. Nanotechnol. 3 (2008) 666.
[3] W. Guo, L. Cao, J. Xia, F.-Q. Nie, W. Ma, J. Xue, Y. Song, D. Zhu,Y. Wang and L. Jiang, Adv. Funct. Mater. 20 (2010) 1339.
[4] L. Cao, W.Guo, W. Ma, L. Wang, F. Xia, S. Wang, Y. Wang, L. Jiang, and D. Zhu, Energy Environ. Sci. 4 (2011) 2259.

Tailoring of keV-ion beams by image charge when transmitting through rhombic shaped nanocapillaries *

HQ. Zhang[1], N. Akram[1], P. Skog[1], I. L. Soroka[1], C. Trautmann[2], and R. Schuch[1,#]

[1]Physics Department, Stockholm University, Stockholm, Sweden; [2] GSI Helmholtzzentrum Darmstadt, Germany.

In recent years, the transmission of slow Highly Charged Ions (HCI) through nanocapillaries in various insulating materials (e.g., polyethylene terephthalate, SiO_2, Al_2O_3, or glass) has been studied by several groups [1-4]. It is shown that the ions are guided through the channels by self-organized charge patches on the inner walls due to initial ion impact [1-3]. Subsequent particles are then guided through the capillaries by Coulomb forces derived from a self-arranged potential. Maximum transmission is achieved once the charge patches inside the capillaries have reached a state of equilibrium between the incident ions and the draining through various discharge channels. The majority of the transmitted ions typically retain their initial charge state without any substantial loss of kinetic energy. The phenomenon provides the possibility of ion transport through insulating channels at angles much larger than the angle allowed by their aspect ratio. This is of great interest for new ion-beam optics.

In contrast to previous guiding experiments utilizing capillaries of circular cross-sections with complete rotational symmetry, we present first results on rhombic cross-sections. The capillaries were fabricated by irradiating 20-µm thick muscovite mica sheets at the UNILAC with 11.1 MeV/u Pb-ions at a fluence of 5×10^7 cm^{-2}. The projectiles pass through the entire thickness of the samples and produce tracks. By chemical track etching highly-parallel nanocapillaries with oriented rhombic cross sections are produced. 10 min etching in 20% aq. solution of hydrofluoric acid (RT) yielded channels with a long axis of 248 nm and a short axis of 142 nm (Fig. 1).

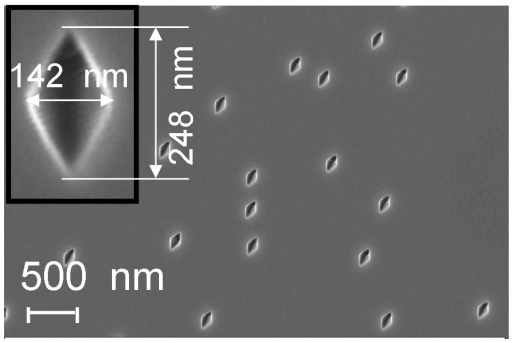

Figure 1: Scanning electron micrograph of muscovite mica irradiated with 11.1 MeV/u Pb-ions. Subsequent track etching results in capillaries of rhombic cross section oriented along the same axis. The inset shows a single channel (acute angle 60°, obtuse angles of 120°).

* Support by Swedish Research Council (VR) and European network ITSLEIF is gratefully acknowledged.

#schuch@fysik.su.se

Ion-beam transmission measurements were performed at the Stockholm ECR and S-EBIT source using Ne^{7+}-ions of kinetic energy between 1-10 keV/q. The intensity of the beam (2×2 mm^2) was between 8 and 80 pA/mm^2 at the membrane position. The beam divergence was collimated to less than 0.2°. By mounting the capillary membrane on a goniometer, the capillaries could be adjusted independently in three spatial directions and around two rotational axes. The transmitted ions were imaged using micro-channel plates with a resistive anode. Downstream of the membrane, an electrostatic deflector allowed the analysis of the charge states of the transmitted ion.

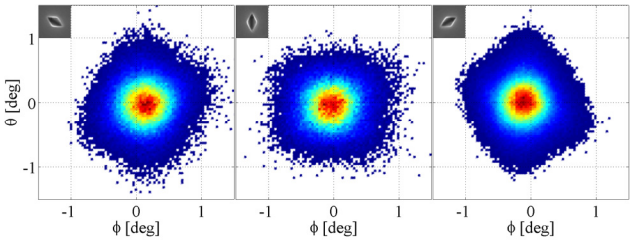

Figure 2: Transmission profiles for 7-keV Ne^{7+}-ions incident on a muscovite mica membrane with the capillary axes aligned along beam direction. The insets (upper left corner of profile) indicate the orientation of the rhombi in a plane perpendicular to the beam.

Surprisingly, we find that the ion beam profiles are tailored in an intriguing way by the geometrical shape of the nanocapillaries: rhombic cross sections produce rectangular shaped ion transmission profiles with the long side aligned along the short axes of the rhombi (Fig. 2). Obviously, the transmission profile is directly influenced by the shape of the capillary cross section. The effect on the angular distribution does not originate from the shape of the primary beam, because when varying the rhombus orientation, the profile rotates accordingly (Fig. 2). More details on this novel beam shaping mechanism including data on rectangular-shaped capillaries are described in forthcoming publications [5-7].

References

[1] N. Stolterfoht et al., Phys. Rev. Lett. 88 (2002) 133201.
[2] P. Skog, HQ. Zhang, R. Schuch, Phys. Rev. Lett. 101 (2008) 223202.
[3] P. Skog et al. Nucl. Instr. Meth. B 258 (2007) 145.
[4] Y. Yamazaki, Nucl. Instr. Meth. B 258 (2007) 139
[5] HQ. Zhang et al., Phys. Rev. A., to be submitted.
[6] N. Akram et al., J. Phys. B., to be submitted.
[7] HQ. Zhang et al., Phys. Rev. Lett., to be publ.

Lithography with photo and polymer pens using track-etched glass templates *

Pradeep Ramiah Rajasekaran[1], Chuanhong Zhou[1], Christina Trautmann[2], Kay-Obbe Voss[2], Punit Kohli[1,#]

[1]Department of Chemistry and Biochemistry, Southern Illinois Univ., Carbondale, U.S.A; [2]GSI, Darmstadt, Germany

Nanolithography is a high impact research area with a plethora of application from biotechnology to electronics. In this project we perform lithography using conical pores fabricated in ion-tracked glass samples. Chemical etching of ion tracks is performed under ordinary laboratory conditions and does not require clean room facilities. The instrumentation involved is inexpensive, and all elements of the fabrication process can be performed in wet laboratory conditions. Using conical pores, we investigate and demonstrate an inexpensive, fast, and easy to implement lithographic technique.

The starting material is a 70 µm thick glass chip that is exposed to heavy ions (e.g. Au or U) of ~11 MeV/u specific energy available at the UNILAC accelerator. The applied fluence is between 10^2 and 10^5 ions/cm^2 to obtain well separated pores. Preferential etching of the track material leads to conical pores. Figure 1 shows the schematic of the etching apparatus which consists of two half-U tubes sandwiching the tracked glass chips. The conical pores were formed due to anisotropic etching of the chip of which one side was exposed to HF (24.5%) solution in 0.5 M NaCl (etching solution), while the other side of the glass chip was in contact with saturated $Ca(NO_3)_2$ (blocking solution) [1].

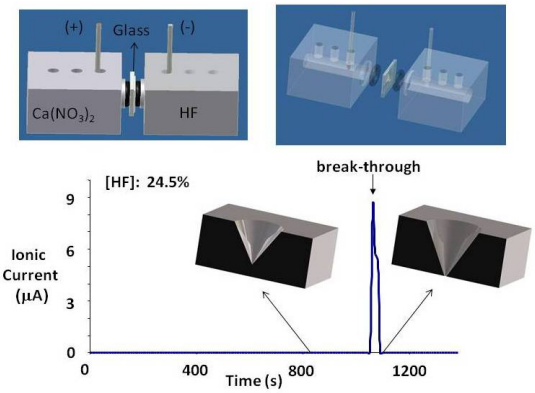

Fig. 1: Top: apparatus for track etching procedure. Bottom: monitoring the electric current during etching allows us to stop the process right after pore break-through.

In the following, we demonstrate the applications of track-etched glass chips as photo pens [2] and as templates to fabricate polymer pens. In the first case, the chip containing the conical pores is used as mask, mounted on a home-assembled xyz piezoelectric stage to accurately control the exposure at the pattern positions. Figure 2 shows a bright fluorescent pattern of photo responsive polydiacetylene films fabricated on a glass substrate. These experiments clearly indicated that the pattern size depends on the exposure time, and that it can be easily modulated without changing the pore size (Fig. 2). This will be extremely useful in photolithography and can significantly reduce the cost and down time for photo-patterning.

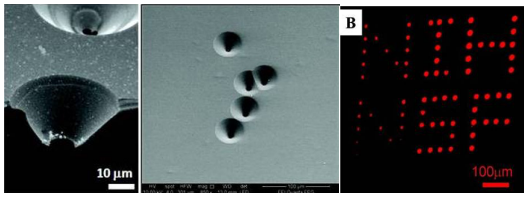

Fig. 2: Cross sectional (left) and top view (centre) SEM image of track-etched pores in glass. Photolithographic patterns (right) produced using different exposure times.

In the second case, the conical pores in the glass were used as templates [3] for making polymeric structures by replication [4]. The resulting polymer pens were mounted on the xyz piezoelectric stage and dipped in fluorescent ink. Just by altering the force applied, the same polymer pens can be used to make patterns from micron to submicron range (Fig. 3, right).

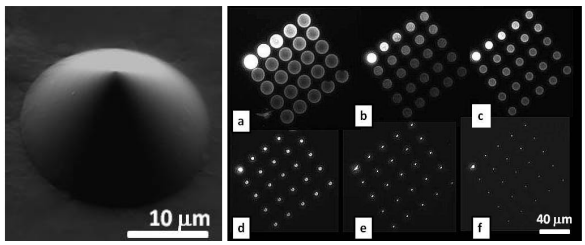

Fig. 3: Left: polymer pen formed by replication of pore in track-etched glass templates. Right: patterns produced by dipping the pens in fluorescent ink and printing with different pressures (a-f).

References

[1] Pradeep Ramiah Rajasekaran; Justin Wolff; Chuanhong Zhou; Mary Kinsel; Christina Trautmann; Samir Aouadi; Punit Kohli. "Two dimensional anisotropic etching in tracked glass", *J. Mater. Chem*. 19 (2009) 8142–8149.

[2] Chuanhong Zhou; Pradeep Ramiah Rajasekaran; Justin Wolff; Xuelian Li; Punit Kohli. "Photo-Pens: A Simple and Versatile Tool for Maskless Photolithography", Langmuir 26 (2010) 17726–17732.

[3] C.R. Martin, "Nanomaterials: A Membrane-Based Synthetic Approach", Science266 (1994) 1961–1966.

[4] Pradeep Ramiah Rajasekaran; Chuanhong Zhou; Christina Trautmann; Kay-Obbe Voss; Punit Kohli; "Lithography with nano-pen and nano-eraser duo". in preparation.

* Work supported by National Science Foundation, National Institute of Health, ORDA at SIUC, and Materials Technology Center at SIUC.

pkohli@chem.siu.edu

Rough $Bi_{1-x}Sb_x$ Nanowires for Thermoelectrics*

S. Müller† [1], *O. Picht*[1], *W. Sigle*[2], *P. Kopold*[2], *M. Rauber*[1,3], *I. Alber*[1], *R. Neumann*[1], *and M. E. Toimil-Molares*[1]

[1]GSI, Darmstadt, Germany; [2]MPI for Intelligent Systems, Stuttgart, Germany; [3]TU Darmstadt, Darmstadt, Germany

Thermoelectric effects have been known since the 19th century, but for technological application the efficiency still requires significant improvement. Hicks and Dresselhaus suggested to improve the thermoelectric efficiency by the confinement of charge carriers into one-dimensional structures leading to beneficial quantum-size effects [1]. For $Bi_{1-x}Sb_x$, Rabin et al. predicted such quantum-effects for nanowires (NWs) with several tens of nm diameter [2]. Recently, new calculations for InSb indicate a minimum in the thermoelectric power factor for NWs with diameters $10-20$ nm, and a significant increase for thinner NWs [3]. To gain thermoelectric efficiency, it is in general of interest to decrease the thermal conductivity κ of a given material. An interesting approach was demonstrated by Hochbaum et al. who reported a 100-fold decrease in κ for rough Si NWs, presumably due to enhanced phonon scattering at the surface [4].

In this project, we fabricated rough $Bi_{1-x}Sb_x$ NWs by electrodeposition in poly(ethylene terephthalate) (PET) etched ion-track membranes [5]. PET foils were irradiated at the UNILAC accelerator at 11.1 MeV/n and subsequently etched with 6 mol/l sodium hydroxide solution at 50 °C. The fabricated channels were electrochemically filled at a potential of -225 mV versus a saturated calomel electrode in a three-electrode configuration. The electrolyte contained hydrochloric acid and Bi(III)- and Sb(III)-chloride in a combined concentration of 0.1 mol/l.

* We thank the Deutsche Forschungsgemeinschaft (DFG) for supporting this work within the priority program SPP 1386

† sven.mueller@gsi.de

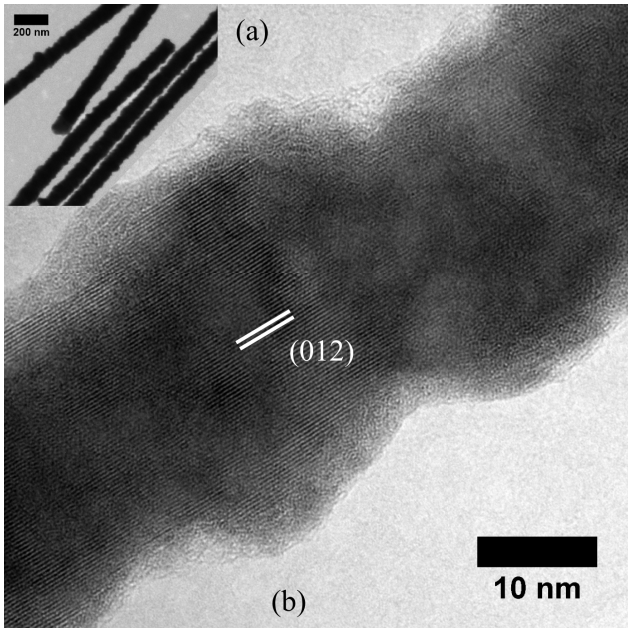

Figure 1: $Bi_{1-x}Sb_x$ NWs grown in a PET template: (a) SEM image, $d \approx 90$ nm (b) HRTEM image, $d \approx 20$ nm.

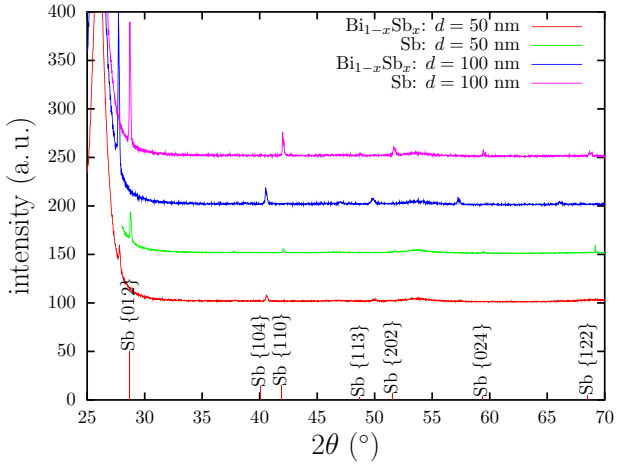

Figure 2: X-ray diffractograms of $Bi_{0.6}Sb_{0.4}$ and Sb NWs grown in PET templates. The vertical lines given correspond to a Sb powder standard (JCPDS file no. 35-732).

Figure 1 shows scanning and transmission electron microscopy images of $Bi_{0.85}Sb_{0.15}$ NWs of 90 and 20 nm diameter, respectively. The surface of the NWs is a replica of the rough inner surface of the nanochannels in semicrystalline PET. The high resolution image (Fig. 1(b)) clearly shows the (012) lattice planes, and the length of the crystallites is in general much longer than the diameter of the NW. Furthermore, the variation in diameter of the rough NW can make up to 30%.

X-ray diffractograms of $Bi_{0.6}Sb_{0.4}$ and pure Sb NWs reveal a $\{012\}$ texture in all cases (Fig. 2). However, for the samples with smaller NW diameters of $d = 50$ nm and also for the alloy NWs, the $\{012\}$ texture is less pronounced. It is noteworthy, that in none of our NWs the $\{104\}$ reflections appear although it is as strong as the $\{110\}$ reflections in random oriented polycrystalline powder.

References

[1] L. D. Hicks, M. S. Dresselhaus, Physical Review B 47 (1993) 16631–16634.

[2] O. Rabin et al., Applied Physics Letters 79 (2001) 81–83.

[3] J. E. Cornett, O. Rabin, Applied Physics Letters 98 (2011) 182104–1–3.

[4] A. I. Hochbaum et al., Nature 451 (2008) 163–167.

[5] S. Müller et al., Journal of Crystal Growth (2011), doi:10.1021/cg200685c.

Localized Surface Plasmon Resonances in Single Nanowires and Dimers

I. Alber [#,1], W. Sigle[2], S. Müller[1], R. Neumann[1], O.Picht[1], M. Rauber[1,3], P.A. van Aken[2], and M.E. Toimil-Molares[1]

[1]GSI, Darmstadt, Germany; [2]MPI for Intelligent Systems, Stuttgart, Germany, [3]TU Darmstadt, Darmstadt, Germany

In recent years, the excitation of localized surface plasmon resonances (LSPR) on metallic nanowires (NWs) has attracted strong interest due to the high field enhancement generated close to the wire surface [1]. It has been shown that even higher field enhancements can be generated in a small gap separating two nanowires, a so-called nanowire dimer (ND) [2].

At GSI, single NWs and NDs were prepared using electrodeposition of metals into the nanopores of ion-track etched polymer templates. The NDs were synthesized by deposition of segmented Au/Ag/Au NWs and subsequent solving the Ag segments. This results in nanogaps with dimensions down to 5 nm. For more details on the preparation route see Ref. [3]. The LSPR on NWs and NDs with different aspect ratios and gap sizes were measured using scanning transmission electron microscopy combined with electron energy-loss (EEL) spectroscopy.

Fig. 1a displays a LSP intensity map of a single NW consisting of 50 EEL spectra. Each horizontal line of the map corresponds to one spectrum measured at a specific point along the red arrow in the TEM image of the NW. The colour in the map represents the number of counts at a specific position and energy-loss, which varies from left to right from 0.2 to 3.0 eV. In Fig. 1b one exemplary EEL spectrum is shown. It was measured at the position of the red dot in the TEM image (right inset).

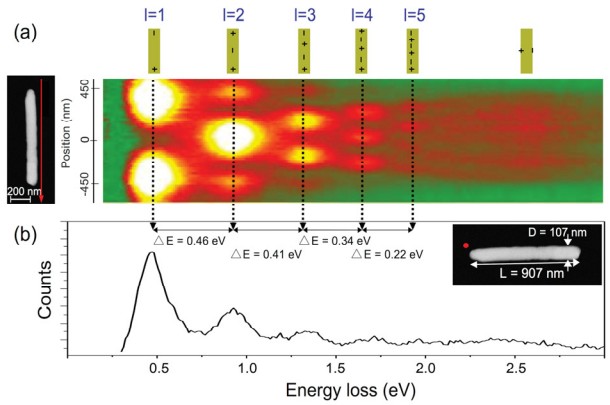

Fig. 1: (a) Plasmonic map along a NW obtained from 50 EEL spectra, (b) spectrum extracted from the map at the position of the red dot in the TEM image. [1]

In the map five different longitudinal LSPR can be distinguished (l = 1 to l = 5). With increasing l the number of intensity maxima along the NW increases, whereas their intensity decreases. Furthermore, our results reveal that for single NWs the distance between two consecutive modes decreases continuously.

Fig. 2a shows a plasmonic intensity map consisting of 60 EEL spectra of a ND with wires of length L_1 = 784 ± 5 nm, and L_2 = 808 ± 5 nm, diameter D =112 ± 5 nm, and a gap size of only 8 nm. Fig. 2b displays three single spectra measured at the two ends of the wire (blue and green spectra), as well as at the position of the gap (red spectrum). From the map we can resolve six longitudinal LSPR. The spacing between two consecutive longitudinal modes of the ND does not follow the same rule as for the single NW. In the case of the ND each mode of an individual NW splits into a mode pair [4] (see schematics on top of Fig. 2a). The so-called bonding modes have a charge distribution with charges of opposite sign located at opposite gap sides, whereas for the antibonding modes charges of the same sign are present at opposite gap sides. In Fig. 2, a bonding and an antibonding mode corresponding to the same multipole order are closer in energy than two consecutive modes corresponding to two neighbouring pairs. The energy difference of a mode pair depends on gap size and aspect ratio. In addition, it is displayed in Fig. 2 that with increasing l the energy difference between bonding and antibonding mode decreases. Our measurements can resolve splitting into bonding and antibonding modes on NDs for the first time up to the third order.

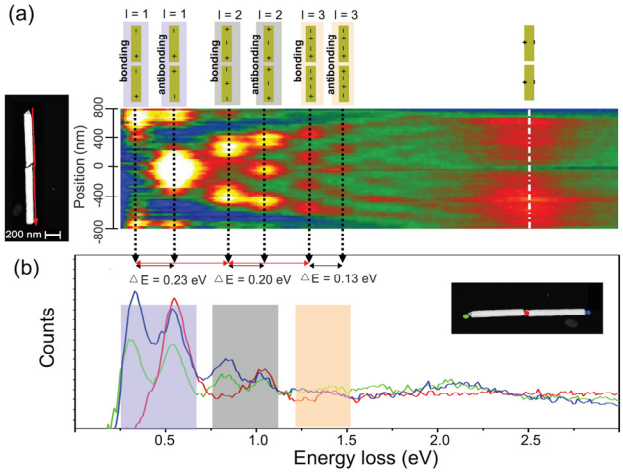

Fig. 2: (a) Plasmonic map along a ND (diameter 112 nm, gap size ~ 8 nm), (b) three spectra measured at the positions of the coloured dots in the TEM image. [1]

References

[1] B. N. Khlebtsov et al., J. Phys. Chem. C 111 (2007) 11516.
[2] J. Aizpurua et al., Phys. Rev. B 71 (2005) 235420.
[3] I. Alber et al., ACS Nano 5 (2011) 9845.
[4] B. Willingham et al., Appl. Phys. B 93 (2008) 209.

i.alber@gsi.de

[1] Reprinted with permission from Ref. [3]. Copyright 2011 American Chemical Society.

Pipetting Nanowires: In-Situ Visualisation of Solid-State Nanowire-to-Nanoparticle Transformation Driven by Surface Diffusion-Mediated Capillarity

Maria Eugenia Toimil-Molares[1,#], Lars Röntzsch[2,3], Wilfried Sigle[4], Karl-Heinz Heinig[2], Christina Trautmann[1], Reinhard Neumann[1]

[1]GSI Materials Research, Darmstadt, Germany; [2] Helmholtz-Centre Dresden-Rossendorf, Dresden, Germany; [3] Fraunhofer Institute IFAM, Dresden, Germany; [4] MPI for Intelligent Systems, Stuttgart, Germany

Recently, numerous applications for nanotubes have been explored and discussed, including storage and encapsulation of atoms or small molecules and catalysts for chemical reactions [1]. In the case of encapsulated solid materials, capillary processes can be triggered by enhancing diffusion processes at elevated temperatures. The improved understanding of both filling and draining processes driven by capillary action at the nanoscale is highly important for applications in nanoelectronics, biology and medicine [2]. We report the geometrical transformation of metallic Cu nanowires (NWs), confined in graphitic coating, into crystalline nanoparticles of up to tenfold increased diameter. In-situ transmission electron microscopy (TEM) images at 500 °C recorded as movies provide an exceptional real-time visualization of Cu draining out of the carbon coating [3].

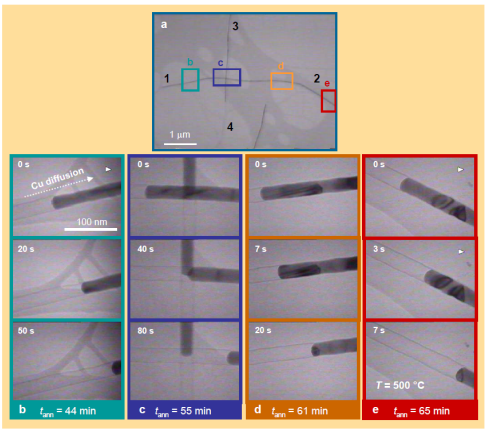

Fig. 1: Snapshots recorded on four areas (a) at different annealing times: (b) 44, (c) 55, (d) 61, and (e) 65 min [3].

Cu NWs are fabricated by electrochemical deposition in porous 30-µm thick ion track-etched polymer membranes. The polycarbonate membranes are prepared by irradiation with GeV heavy ions at the UNILAC accelerator and subsequent chemical etching of the ion tracks in 6M NaOH at 50 °C. For TEM investigations, the polymer matrix is dissolved in dichloromethane, and some drops of the solution containing individual wire sections are dispersed on a carbon coated TEM grid. We used a JEOL JEM2000FX microscope with a high-temperature specimen holder operated in vacuum (10^{-6} mbar) at 500 °C (heating rate 100 K·min^{-1}).

At such temperatures, the presence of carbon (presumably from polymer residues on the wire surface) results in the formation of graphene layers entirely coating the nanowires. The low-magnification TEM image in Fig. 1a displays two encapsulated Cu NWs intersecting each other on a TEM grid. Fig. 1(b–e) display series of snapshots taken after different annealing times and at four fixed positions between wire ends 1 and 2 (respective color-boxes b–e in Fig. 1a). The images indicate strongly that the carbon tubes provide drainage at their open ends and that Cu mass transport takes place by diffusion. From the image series effective longitudinal drainage velocities of 2.1, 1.8, 4.8, and 14.8 nm·min^{-1} are deduced, thus evidencing an increase of the velocity of the Cu edge with time and location while the temperature was kept constant. The morphology of the Cu front remains faceted and diffraction contrasts along the Cu wire originating from planar defects such as twin or grain boundaries are visible, excluding melting and verifying that the NW is in the solid state. Fig. 2a–d presents the sequence of TEM images taken after 9, 50, 65, and 75 min annealing, showing the formation of a protrusion (about 300 nm before wire end 2) that increases progressively in size as Cu diffuses. After ~70 min, every Cu NW on the TEM grid had morphologically transformed into a facetted nanoparticle (Fig. 2e–h).

3D lattice kinetic Monte-Carlo (KMC) simulations yield qualitatively a very similar behaviour indicating that surface diffusion is responsible for the draining of the metal-filled tube (Fig. 2i–n).

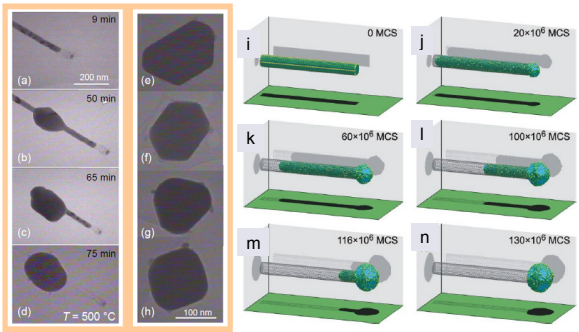

Fig. 2: (a–d) TEM images of Cu NW close to end 2 showing growth of nanoparticle during annealing process, (e–h) facetted Cu particles at different wire ends, (i–n) KMC simulations showing the draining process [3].

[1] A. Bianco et al., Current Opinion Chem. Biology 9 (2005) 674.
[2] M. Moseler et al., ACS Nano 4 (2010) 7587
[3] M.E. Toimil-Molares et al., Adv. Funct. Mater. 2012 DOI: 10.1002/adfm.201102260.

m.e.toimilmolares@gsi.de

Field emission properties of novel copper nanocone cathodes

P. Serbun[1*], F. Jordan[1], A. Navitski[1], G. Müller[1], I. Alber[2], M. E. Toimil-Molares[2], C. Trautmann[2]

[1]Physics Department, University of Wuppertal, Germany; [2]GSI Helmholtz Centre, Darmstadt, Germany

Structured cold cathodes with randomly distributed freestanding gold nanowires (NWs) fabricated by electrochemical deposition into cylindrical pores of etched ion-track polycarbonate templates showed high efficiency at suitable onset field and good alignment of field emission (FE) patches [1]. The FE current limits of NW patches, however, varied strongly due to random destruction of individual wires caused by their insufficient substrate contact [2]. In order to improve the contact and achieve higher emission currents, we modified the emitter shape from cylindrical to conical geometry by means of asymmetric etching of the ion-tracks from one side only [3].

Table 1: Parameters of fabricated Cu-NC cathodes.

Parameters \ Cathodes	Unstructured		Structured	
	A	B	C	D
Etching time, min	15	15	13	15
Depos. voltage, mV	40	90	40	40
Number density cm^{-2}	10^7		$< 10^6$	
Length, µm	~28		< 28	
Tip radius, nm	~190	~120	~ 95	~220
Aspect ratio	147	233	295	127

Four types of such cathodes with copper nanocones (Cu-NCs) were fabricated using various parameters as listed in table 1. The resulting Cu-NCs on unstructured and patch-structured cathodes are mechanically very stable as shown in Fig. 1. Some Cu-NCs in the patches, however, grow incomplete yet.

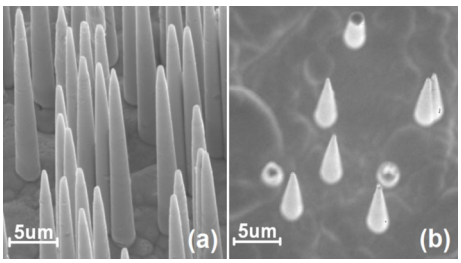

Figure 1: SEM images of Cu-NCs of similar length but different number density and tip diameter: (a) 10^7 cm^{-2}, ~380 nm; (b) < 10^6 cm^{-2}, ~190 nm, respectively.

The FE properties of these Cu-NC cathodes were measured with the field emission scanning microscope (FESM) at 10^{-7} Pa using a tungsten anode of diameter $Ø_a$ = 30 µm as described elsewhere [4]. Fairly distributed FE (at onset fields E_{on}(1nA) around 50 (20) V/µm) was obtained for the unstructured (structured) cathodes (Fig. 2). Obviously, there are multiple emitters per patch, and the resulting FE is well-aligned to the triangular array.

*contact: serbun@physik.uni-wuppertal.de

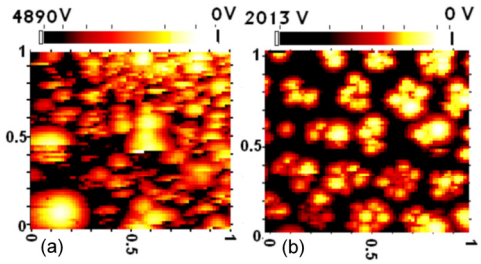

Figure 2: Voltage maps (1 nA fixed FE current, $Ø_a$ = 30 µm) of cathode A (Δz = 40 µm, left) and structured cathode C (Δz = 25 µm, $Ø_{patch}$ = 150 µm, pitch 320 µm, right).

The effective field enhancement factor β and maximum achievable stable current I_{max} of these Cu-NC cathodes was measured with the same anode for selected emitters of the voltage maps. As expected for the different number density, the mean E_{on}(1nA) values were higher for the unstructured (52 V/µm) than for the structured (22 V/µm) cathodes, in accordance with the mean β values of 267 (84) [4]. The I_{max} values achieved for all samples are given in Fig. 3. Moderate I_{max} result for the fast-grown unstructured sample (B, 20-700 nA) and for the rather incomplete-grown structured sample (C, 0.1-20 µA). In contrast, slow and complete Cu-NC growth lead to much improved performance, i.e. I_{max} < 280 µA at ~100 V/µm for unstructured sample A, and I_{max} < 100 µA at 60 V/µm for the better but still incomplete-grown structured sample D. In conclusion, these first results of Cu-NC are very promising for the further optimization of conical nanostructures.

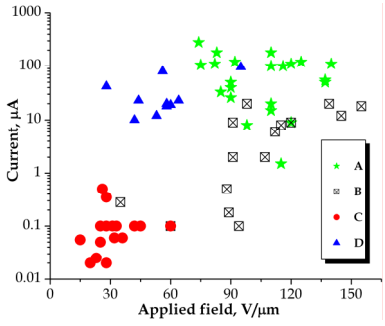

Figure 3: I_{max} vs. E for all measured spots on the four Cu-NC cathodes (A - D).

References

[1] A. Navitski et al., Eur. Phys. J. Appl. Phys. **48**, 30502 (2009).

[2] A. Navitski et al., Techn. Digest IVNC 2010, Palo Alto, IEEE Cat. No. CFP10VAC-PRT, p. 163 (2010).

[3] I. Alber et al., Techn. Digest IVNC 2011, Wuppertal, IEEE Cat. No. CFP11VAC-ART, p. 106 (2011).

[4] P. Serbun et al., Techn. Digest IVNC 2011, Wuppertal, IEEE Cat. No. CFP11VAC-ART, p. 230 (2011).

Operation and Improvements of PHELIX*+

V. Bagnoud[1], C. Brabetz[2], U. Eisenbarth[1], J. Fils[1], S. Götte[1], T. Kühl[1,3], S. Kunzer[1], M. Kreutz[1], C. Lempa[1], T. Merz-Mantwill[1], D. Reemts[1], T. Stöhlker[1,4] , A. Tauschwitz[1], L. Tymura[1], B. Zielbauer[4]

[1]GSI, Darmstadt, Germany; [2]Johann Wolfgang Goethe University Frankfurt, Germany; [3]Johannes Gutenberg University Mainz, Germany; [4]Helmholtz Institute Jena, Germany

General overview

PHELIX[1], the high-energy short-pulse laser facility of GSI, has completed in 2011 its third year of operation. PHELIX is a Helmholtz user facility opened to the international scientific community and a unique opportunity for combined ion-laser experiments to support the science programs of the Plasma Physics and Atomic Physics departments of GSI. In 2011, PHELIX was a very reliable machine requiring very little maintenance. This allowed freeing up time for internal development activities without impacting the beam time offer for user groups. In particular, the theme of temporal contrast improvement has received a lot of attention with different ideas being pursued in parallel. For the main goal, which is the generation of temporally clean short laser pulses, most of the hardware has been implemented, so that tests and commissioning experiments are scheduled for 2012.

From an operation point, 2011 was a successful year in which 18 beamtimes serving 14 experimental proposals were conducted. The amount of days per beamtime has been reduced compared to last year, as wished by users who are now trained to use the allocated days very efficiently. This resulted however in an increase in the demand on setup time; a time which is work intensive and when the creativity of the laser team is challenged.

Internal developments and beamtime

As recommended by the PHELIX and Plasma Physics Program Advisory Committee (PPAC) that met in November 2010, the effort to improve the temporal contrast of the PHELIX short pulse has been strengthened. This effort has been boiled down to three projects that address different aspects of the temporal contrast issue. First, an electro-optical element has been inserted into the laser to improve the isolation between the pre- and main-amplifiers. By creating a 10-ns temporal gate, this Pockels cell replaces the Faraday isolator used so far. This allows reducing dramatically the long term pulse pedestal that was damageable to ultra-thin targets. Second, the project to increase the picosecond and nanosecond temporal contrast by use of an ultrafast parametric amplifier (uOPA project) was continuing in collaboration with the Helmholtz Institute Jena. For this project, the main milestone has been the delivery of a laser amplifier developed in Jena at GSI. The amplifier is made of a fiber pre-amplifier and a laser-diode-pumped regenerative amplifier. The fiber amplifier setup has been re-engineered to meet the PHELIX standards and it is now a turn-key well documented device synchronized to PHELIX. The regenerative amplifier delivers the expected energy and aside from spectral modulation performs satisfactorily. This amplifier is now used to pump the uOPA and gains of 10^4 have been measured. Further steps will be done to quantify the impact of the amplifier on the contrast. Last, a beam time has been dedicated to the implementation of a plasma mirror setup at the back end of the laser, in the target chamber. This setup has been developed and tested at PHELIX in collaboration with the group of David Neely from the CLF in the UK[2].

The second improvement to the PHELIX laser system has been the upgrade of the PHELIX timing system to offer more experimental capabilities. The most notable effects are the use of the UNILAC 108 MHz clock as the reference timing signal for PHELIX to reduce the jitter between both machines to less than 1 ns as required by the LIGHT project, and the possibility to operate both ns- and fs-frontends synchronously. For this step, a significant change to the short pulse laser oscillator had to be made, and slow electronics like NIM crates were exchanged for faster electronic devices. With this upgrade, the injection of laser accelerated particles into conventional accelerator structures from the UNILAC is possible. Additionally, a 1 MHz synchronization signal necessary for the uOPA project has been added and was successfully tested.

The third area of development at PHELIX is the preparation of the PHELIX target area in the laser hall for full petawatt operation. In order to do this, the target area in the PHELIX laser hall has been shielded using 20 tons of steel that will significantly ease the operation at the target chamber by moving the shielding outside the chamber. In parallel, the beamline going from the compressor to the target chamber has been upgraded to larger mirrors and their corresponding holder. The next step is the procurement of a target chamber that can accept the 25 cm PHELIX beam and focus it to a tight focus.

The fourth area of development has been the upgrade of the PHELIX data storage scheme to a more flexible database system (the PHELIX database project PSDB), used to store all the information gathered by the PHELIX control system and users[3]. The effort has been put on interfacing the PHELIX control system to the database and the development of graphical user interface that presents the data in a way relevant to experiments conducted at PHELIX. The database becomes active in 2012 and will shortly replace the old system after some commissioning time.

* The acronym stands for **P**etawatt **H**igh **E**nergy **L**aser for heavy **I**on e**X**periments.

+ This work is supported by EMMI, the Helmholtz Institude Jena and GSI

The last area of development relates to the control of the laser beam quality. For experiments aiming at shaping proton beams accelerated by lasers for instance, the precise control of the laser focal spot shape is necessary. There, significant results of interest to the general user community have been obtained on laser focal spot shaping[4]. In parallel to this project, it became clear that more control over the phase distortion happening in the system is necessary for many advanced setups. In particular, the adaptive optics system available at PHELIX was used to demonstrate a new method for direct reference-free focal spot optimization[5].

Operation of the laser facility

As can been seen in Figure 1, the time dedicated to beamtime at PHELIX was close to 80% in 2011. While the time dedicated to operation for external users (defined as days with high-energy target shots) remains stable at 40% compared to the last two years, more time was necessary for setting up experiments because of the increasing complexity of the experimental setups at PHELIX. Although this had been foreseen and mitigated thanks to a more aggressive planning where experiments sharing the same setup have been combined, the increase of setup time has been unavoidable.

A notable evolution compared to last year has been the amount of time dedicated to internal beamtime development. Based on the recommendation of the PPAC, 32 days of beamtime have been spent on temporal contrast related issues like the uOPA project, the LAPC project and the development of a plasma mirror setup at the back end of the laser.

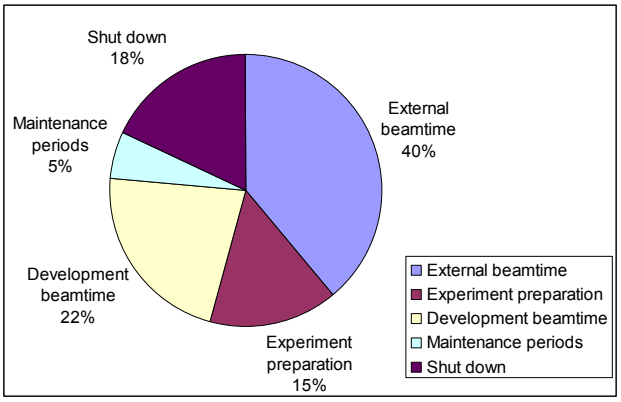

Figure 1: PHELIX usage in 2011

The second evolution has been an increase of the shutdown time at PHELIX. Except for single-event reasons like the upgrade of the shielding in the PHELIX laser hall in the framework of the UPTA project, some cyclic downtime due to the periodic upgrade of the control system software to the latest supported LabVIEW™ version has taken place. The impact of the building up phase of FAIR on PHELIX downtime has been so far low in 2011 but it must be anticipated that this will change starting in 2012.

In the end, the time dedicated to the maintenance of the machine was drastically reduced to a level that is not sustainable in the long run. This means that more maintenance time will have to be provided in the future.

Contribution to the scientific program and outreach

This year, seven peer reviewed articles were published on data collected at PHELIX[6, 7, 8, 9, 10, 11, 12]. Typically, these publications report on results obtained during beamtime that occurred in the last 18 months.

In May, the PHELIX group held the second Laserlab-NAHEL (Network Activity on High Energy Lasers) meeting at the Lichtenberg House in Darmstadt. This meeting aims at exchanging information and sharing the experience gathered on operation of mi-size laser facilities. The meeting included participants from the four laboratories participating in NAHEL In addition, PHELIX has given one beam time to experiments supported by Laserlab in the fields of X-ray laser generation

Outlook for 2012

The PPAC met in November to review and recommend new experiments for the GSI director. In total, 13 new or continuing experiments were granted, amounting for 250 shifts in total. The new experiments will be scheduled starting in the spring of 2012.

References

[1] V. Bagnoud et al., Appl. Phys. B 100 (1) 137-150 (2010)
[2] B. Zielbauer et al. this report
[3] U. Eisenbarth et al, this report
[4] C. Brabetz et al., this report
[5] U. Eisenbarth et al., this report
[6] M. N. Quinn et al., Plasma Phys. Control. Fusion, 53 (2011) 025007
[7] O Tresca et al., Plasma Phys. Control. Fusion 53 (2011) 105008
[8] T. Burris-Mog et al., Phys. Rev. ST Accel. Beams 14, 121301 (2011)
[9] N. Orlov et al., Laser and Part. Beams (2011), 29, 69–80
[10] O. N. Rosmej et al, NIMA 53260, 653 (2011) 52–57
[11] T. Heßling et al., Phys. Rev. E 84, 016412 (2011)
[12] B. Aurand et al., Nucl. Instr. Meth. Phys. Res. A 653 (2011) 130–133

The PHELIX shot database

U. Eisenbarth, S. Götte, T. Stöhlker and V. Bagnoud

GSI, Darmstadt, Germany.

In the past years of operation, PHELIX has delivered more than 2000 experiment shots serving over 30 experiments performed by national and international research groups. Hence, a proper and reliable documentation of the shot operation becomes more and more important. So far most of the relevant machine data have been manually recorded using electronic lists. This method turned out to be unnecessarily elaborate and error-prone since all measurement data are already electronically available through the PHELIX control system (*PCS*). Earlier attempts of a data storage solution turned out to be not reliable enough and inflexible in terms of data retrieval.

Requirements

In the turn of the year a new documentation system has been developed in order to overcome these shortcomings. For the new system a bunch of requirements were defined. At first, reliability of the data storage is of central importance. In addition the new system must be able to handle arbitrary types of data. The PHELIX facility permanently undergoes changes and upgrades with new devices being implemented or older ones removed. All these changes must be handled by the system with as little maintenance effort as possible. Furthermore, with more and more shots delivered, efficient data retrieval methods become important which allow for grouping shots belonging to a particular experiment or comparing measurement data of one specific device such as a series of camera images. In addition, experimental groups are usually only interested in a limited set of shot data. Hence, it must be possible to generate experiment-specific presentations of relevant laser data (views). Finally the documentation system must allow for easy data access from everywhere.

Implementation

Above requirements lead to the development of a database application with two interfaces. The first interface was programmed mainly for writing data to the database by the control system. The initial development was based on LabVIEW 8.2.1 / *CS* 3.1 but recently upgraded to LabVIEW 2009 / *CS* 3.2. For the second interface, a web application based on the Ruby on Rails 3.1 framework has been developed to allow for comfortable data retrieval. Both interfaces do not depend on a specific database management system but use itself abstract interfaces for reading and writing. For PHELIX the Oracle database system served by GSI's IT-infrastructure is used.

The database design has been carefully chosen with a maximum flexibility in mind. The system can record several data types such as numbers or string as well as more complex data like images, spectra etc. New types can easily be added without changes of the database layout. New instances or class types introduced by the control system are seamlessly integrated without structural changes. Only the web application needs information on how to present the data. Default presentations exist though and measurement data from old hardware remains accessible all time. Furthermore, all datasets connected to a device contain version information, which allow for tracking changes in the programming interface. Further flexibility is added due to the possibility to attach arbitrary data files to either an experiment entry (e.g. experiment drawings or proposals) or a shot (e.g. data from a device which is not controlled by the *PCS*).

Manual operation has been reduced to a minimum: New Experiments need to be set up once through the web interface. During the shot procedure only the experiment name (selectable from a list), the shot type, and optionally a shot comment needs to be given. All these data can be modified afterwards through the web interface.

As the *PCS* follows the concept of distributed computing, each device/instance directly writes its data to the database. This writing procedure is coordinated by the data controller which writes the general shot information, such as a unique shot id as well as the shot comment and shot type. Then it sends write requests to all instances. This approach has the advantage of a better performance since it allows parallel write operations to the database. In addition it is robust against failures of single instances (e.g. hardware errors). In this case the troubled instance does not lead to a complete hang of the system. A former system was based on a data collector model which suffered from these issues.

Operation

Over the year the PHELIX shot database has been tested and improved during several beam times while writing to a test database. This time also gave us the opportunity to test the database performance and scalability. In this time period nearly 1000 shots were recorded with more than 180 instances/devices delivering measurement data. This lead to over 1.1 million measurement data sets with an average memory consumption of 2.8 MByte per shot with no performance issues observed so far.

Outlook

The flexible design and the independency from a specific database management system might also be interesting for other facilities working with the *CS* with shot/-based data. All parts of the software are released under the GNU public license. In the near future this system is also going to be integrated for the POLARIS laser facility located at the Helmholtz-Institute Jena in close collaboration with PHELIX.

Optifocus: A reference-free focal spot optimization for PHELIX*

U. Eisenbarth, C. Brabetz, C. Lempa, T. Stöhlker, and V. Bagnoud

GSI, Darmstadt, Germany

Nowadays, many high intensity laser systems include adaptive optics modules for controlling the beam wavefront [1]. Besides the effect of thermal aberrations, complex high power laser systems usually consist of a large amount of optical components whose manufacturing imperfections sum up to a considerable static wavefront distortion. Most control systems directly measure the wavefront using sensors following the Shack-Hartmann principle or interferometric methods [2]. Above sensors measure the wavefront relative to a given reference. For an absolute measurement a flat wavefront is needed first which is not always easy to achieve. The wavefront is normally measured at a location within the beam path of the laser system. For most high intensity laser experiments however the performance is strongly determined by the focal spot quality at the end of the laser chain. Compensation of wavefront aberrations at the sensor's position therefore does not necessarily lead to the best focal spot quality for the experiment.

In this paper, we propose and demonstrate a simple method to directly optimize the focal spot of a high intensity laser by sequentially optimizing the Zernike coefficients associated with a deformable mirror (DM) located upstream the laser chain. This method makes use of the orthogonality of the Zernike polynomials which are used to describe the wavefront and their influence on the focal spot size. Due to the orthogonality this can be done individually for each coefficient. Hence, after iterating over all coefficients up to a certain order the best overall focal spot size can be achieved. The main advantage of the method lies in the strong reduction of the number of optimization variable hence in its speed and its reference-free nature.

At PHELIX, a 65-mm diameter DM with 30 actuators is located at the output of the PreAmplifier. A local Shack-Hartmann sensor is used to control and calibrate the DM. The calibration is necessary at first to compute the response matrix of each actuator on the phase deformation. The response matrix is recorded by stepwise applying a constant control voltage to each one mirror actuator respectively and a measurement of the resulting wavefront using a local Shack-Hartmann sensor. For this step no absolute wavefront reference is necessary, because the response matrix only contains the relative change of the wavefront while applying a voltage to one actuator. Using the pseudo-inverse of this response matrix then afterwards allows for calculating the voltage pattern necessary to vary a single Zernike coefficient during the focus optimization.

For the calculation of the focal spot size the radius of the encircled energy turned out to be the most robust criterion. For this the radius of a circle around the beam centroid is increased until a given fraction of the total energy is covered. The focus optimization procedure starts with finding the best value for the third Zernike coefficient representing defocus. Lower Zernike coefficients (piston and tilt) do not contribute to the focal spot size and are therefore omitted. The defocus coefficient resulting in the smallest energy radius is set after the variation. This procedure is repeated stepwise for all higher order coefficients. The entire algorithm can be repeated starting again with the third coefficient in order to further optimize the spot size due to remaining coupling effects of the Zernike modes.

We used this algorithm to optimize the focal spot measured after the PHELIX main amplifier configured for a 28cm diameter beam. Without correction (Figure 1.a), the beam suffers some astigmatism arising from alignment as well as optics imperfections. Figure 1.b shows focal spot images after the optimization procedure with a significant improvement of the focal spot quality. The Strehl ratio increases from 0.23 to 0.66 (+/- 0.1).

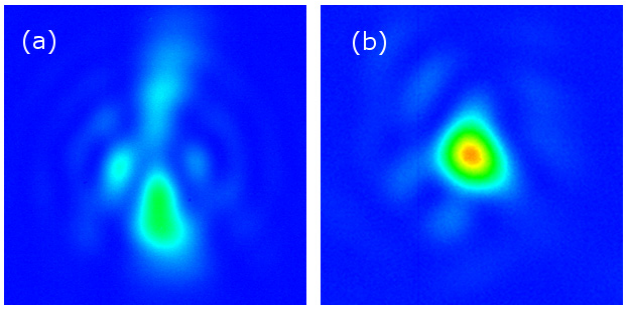

Figure 1: Focal spots profiles at the MainAmp sensor before (a) and after (b) the optimization.

Typically, 9 Zernike coefficients and 2 iterations were used so that the optimization is finished on a minutes scale. Once the focus optimization is finished the new wavefront can be used as reference for well-established closed loop wavefront control methods, which regulate towards the newly derived reference in short time.

The presented method allows for correcting static aberrations in high intensity laser systems without the need for a flat reference wavefront. A significant increase of the peak intensity in the focal plane can be achieved, which many today's experiments can benefit from.

References

[1] J-P. Zou et al., Appl. Opt. 47, 704-710 (2008)

[2] J. Sheldakova, A. Kudryashov, V. Zavalova, P. Romanov, *Proc. SPIE* **7194**, pp.71940B, 2009

* Work supported by HIC for FAIR

Hollow Beam creation with continuous diffractive phase mask at PHELIX*

C. Brabetz[2], V. Bagnoud[1], T. E. Cowan[3], U. Eisenbarth[1], J. Fils[1], S. Götte[1], O. Kester[1,2], T. Kühl[1], S. Kunzer[1], D. Reemts[1], T. Stöhlker[1], B. Zielbauer[1]

[1]GSI Darmstadt, Germany; [2]JWGU, Johann Wolfgang Goethe University, Frankfurt, Germany; [3]HZDR, Helmholtz center Dresden Rossendorf, Germany

Overview

In the framework of the Laser Ion Generation Handling and Transport (LIGHT) research project at GSI, the reduction of the divergence of the laser accelerated ions is a central issue. One solution, illustrated by theoretical studies and some preliminary experimental data [1], is based on engineering the electron sheath using in TNSA for reducing the initial divergence of the ion beam. For such a scheme, a precise control over the laser beam parameters is essential in order to reliably shape the ion beam. Laser focus shaping has been used for example in optical trapping in relatively small laser systems [2]. But such a manipulation of the laser beam appears quite complicated at large laser apertures. During the year we demonstrated the focal spot shaping of the high-energy high-intensity laser PHELIX using diffractive phase plates confirmed by simulations. The main part of the work was in the definition of diffractive elements which turn the Gaussian beam of the laser front end into a top-hat beam that focuses into a hollow beam.

Hollow Beams

Because it is very hard to directly shape the focus of a high-intensity laser, we decided to act on the beam at the front end of the laser and use beam shapes that are propagation invariant. Laguerre-Gaussian (LG) beams fulfill this conditions and the LG01 mode is of particular interest because of its annular intensity distribution. The beam shaping is done by applying a transmission phase mask with a helical shape so that a discontinuity is introduced at the centre of the beam. This implies that the singularity in the beam, that is, its hollow character, is constant along the propagation axis of the beam, and in particular is realized also in the far-field at its focus. The LG mode also guarantees that no peak intensity is present in the intermediate field and the risk of damage to the laser chain is low. However, a pure LG01 mode exhibits a large hole in the middle of the beam that is not compatible with the need for energy extraction in a large laser amplifier. In other words, the amount of energy that the LG01 beam would carry is small compared to the standard PHELIX "top hat" beam of the same dimension. For this reason, we use an amplitude mask together with the phase mask to shape the Gaussian beam of the front end into the desired hollow beam. Thanks to image plane transport in the laser system, the process does not depend on the image plane chosen to do the beam shaping. For obvious cost and convenience reasons, we decided to implement it at the input of the pre-amplifier, where the beam dimension is only several millimeters wide as shown in Figure 1.

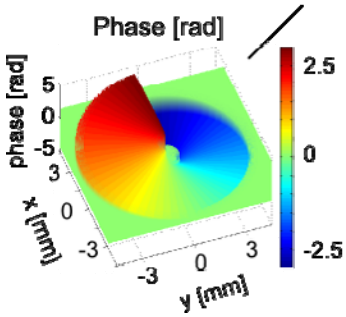

Figure 1: Phase that is applied to the PHELIX laser beam.

Report on the 2011 Beamtime

We spent a week of beamtime to study the propagation of the beam on the PHELIX system and validate our scheme. We have performed measurements of the beam profile along the beam path in the PHELIX system (after the main amplifier shown in Figure 2). As we had seen during the offline tests, beam distortion either in the main beam or occurring in the diagnostic channels made it not possible to transport the special hollow beam mode through the PHELIX system. Therefore we decided to investigate the phase distortions in the PHELIX main amplifier, since the wavefront distortion in the pre-amplifier is negligible. After optimizing the injection into the main-amplifier, and optimization of the large main-mirror 1 in the chain, we were able to achieve a satisfactory wavefront and therefore a less astigmatic focus. The corrections of the astigmatism applied to the main-amplifier were sufficient so now it is possible to transport the hollow beam through the PHELIX chain past the short pulse compressor with the desired hollow character (see Figure 2).

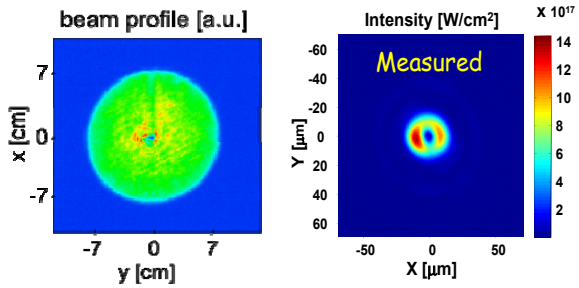

Figure 2: beam profile (left) and resulting focus (right).

References

[1] J. Fuchs et al, Phys. Rev. Lett. 91 (2003) 255002
[2] T. Kuga et al, Phys. Rev. Lett. 78 (1997) 4713

* Work supported by HIC for FAIR.

First experiments with the new PHELIX 100 TW beamline: Towards new applications for laser ion sources*

S. Busold[1], *O. Deppert*[1], *C. Brabetz*[2], *T. Burris-Mog*[3], *M. Joost*[3], *A. Blazevic*[4], *B. Zielbauer*[4,5], *V. Bagnoud*[4], *O. Kester*[2,4], *T. Cowan*[3], *and M. Roth*[1]

[1]TU Darmstadt, Institut für Kernphysik, Germany; [2]JWG Universität Frankfurt, Institut für angewandte Physik, Germany; [3]Helmholtzzentrum Dresden-Rossendorf, Germany; [4]GSI, Darmstadt, Germany; [5]Helmholtz Institut Jena, Germany

The technique of ion acceleration by ultra-short, high-intensity lasers ($> 10^{19}$ W/cm^2) provides ion beams with unique beam parameters. However, due to the large divergence and full energy spread of laser accelerated ions, further treatment of these ions is necessary for many possible applications. Therefore, in the frame of the LIGHT project (Laser Ion Generation, Handling and Transport, [1]), the new 100 TW beamline of PHELIX was build, which now provides the necessary short pulse laser at the experimental area Z6 at GSI. Here we meet the full conventional accelerator infrastructure and have the perfect test bed for combining both technologies. The aim of the LIGHT project is to demonstrate injection and bunching in conventional accelerator structures of laser accelerated ions, starting with protons.

In the following, experimental setup and results of the first laser ion acceleration experiments at the Z6 area are described.

Experimental setup

At the moment, PHELIX provides for the high-power option at Z6 up to 10 J of laser energy in 500 fs on target. The beam enters the target chamber with a diameter of 120 mm and is focussed down by a parabolic off-axis mirror to 10–15 μm (FWHM) into the target chamber center. There it impacts on a thin (5–10 μm) gold foil and a bunch of protons is accelerated via the TNSA mechanism [2].

A few centimeters behind the the target, the key element for collimation and energy-selection of the proton beam is placed: a pulsed high-field solenoid, which was developed together with the necessary pulsed power supply by our collaborators at HZDR. It has an aperture of 40 mm and can reach a maximum magnetic field of > 10 T. Due to the chromatic aberrations of this ion-optical lens, protons of different energies are focussed at different distances behind the solenoid. Placing a pinhole at the right position therefore easily provides good energy selection.

As proton beam diagnostic, RCF stack detectors were used at different positions: before the solenoid to detect the initial spectrum, directly behind the solenoid and at a position in the Z6 beamline behind the target chamber. A full beam analysis is possible with these detectors via RIS (Radiochromic-film Imaging Spectroscopy, [3]). A sketch of the experimental setup is shown in figure 1.

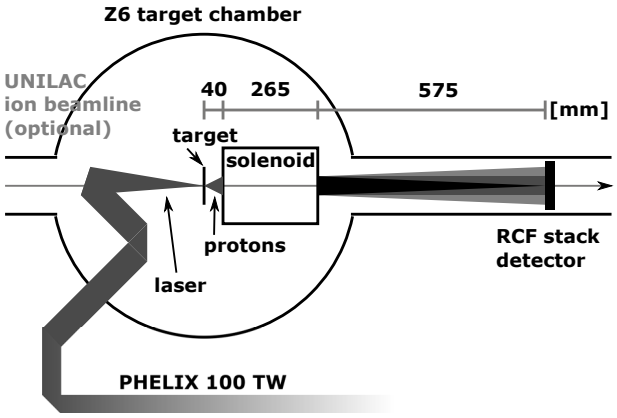

Figure 1: Experimental setup at the Z6 area. The laser beam, coming from PHELIX, hits the target from the left side and a proton beam expands to the right side. The protons are captured and focussed energy-dependendly by a pulsed solenoid and transported into the Z6 ion beamline.

Results and Outlook

Two experimental runs (each one week) were done in 2011, where the first one was used for beamline commissioning only (no solenoid). Proton energies above 10 MeV already could be reached in this commissioning phase. In the second campaign, the pulsed power system including the solenoid was successfully installed and applied at Z6. Focussing to a spot size of a few millimeters and transport to up to 880 mm behind the target of laser accelerated protons in the Z6 beamline could be demonstrated.

The next steps planned for 2012 are: to optimize the ion transport and to add a RF cavity to the beamline for phase-space-rotation of the proton beam in strong cooperation with the GSI accelerator department.

References

[1] S. Busold *et al.*, proceedings of PAC'11, New York, USA

[2] S. C. Wilks *et al.*, Phys. Plas., 8, 542-549 (2001)

[3] F. Nürnberg *et al.*, Rev. Sci. Instr., 80, 033301 (2009)

* This work is supported by the Helmholtz Institute Jena and HIC for FAIR.

Development of a Plasma Mirror Setup for Pulse Contrast Enhancement at PHELIX

B. Zielbauer[1,2], J. Green[3], D. Neely[3,4], M. Roth[5], G. Scott[3,4], T. Stöhlker[1,2], F. Wagner[5], V. Bagnoud[1,2]

[1]GSI, Darmstadt, Germany; [2]Helmholtz Institute Jena, Jena, Germany; [3]Rutherford Appleton Laboratory, [4]Strathclyde University, Glasgow, UK; Didcot, UK; [5]Institut für Kernphysik, TU Darmstadt, Germany

One of the most critical issues in high-power laser-matter interaction is the so-called laser pulse contrast, i.e., the ratio between the amount of laser light arriving at the target prior to the main pulse and the peak intensity. In recent years, several techniques have been developed to increase this important figure of merit to up to 10^{12} for high-energy lasers [1, 2]. These include the use of plasma mirrors (PM) which is based on the fast reflectivity change on an antireflection-coated surface into a reflective plasma during the interaction with an intense laser pulse. For proper operation the intensity on the PM has to be chosen carefully in order to achieve high reflectivity and to conserve the beam profile and focus quality.

In a dedicated machine beamtime at PHELIX, the implementation of a PM has been tested and investigated with specially developed diagnostics.

Setup

The plasma mirror is placed at a distance of several cm to the target chamber center (TCC) where the laser beam would have been focused without the PM (figure 1). The beam is thereby reflected towards the diagnostics which are set up in an additional smaller target chamber. We use a scattering screen in combination with a camera to record the laser near field distribution. A rectangular hole is cut into the screen to let a part of the beam propagate to a calorimeter. A special calibration of the setup which has been carried out during the experiment allows for an exact determination of the reflectivity.

We vary the intensity on the PM by changing its distance to TCC as well as the energy of the beam.

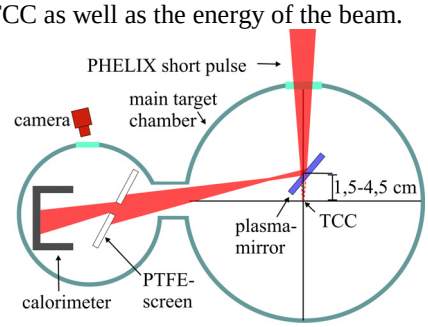

Figure 1: Setup

Experimental results

Figure 2 shows the change of reflectivity with varying maximum intensities on the PM. According to [1] the reflectivity first increases for rising intensities. This occurs due to plasma formation at an earlier time at the rising edge of the pulse which leads to reflection of a bigger part of the pulse. If the plasma formation starts too early, the main pulse hits an expanding underdense plasma. This leads to reduced reflectivity due to absorption in the plasma as well as breakup of the reflected beam. In our setup the optimum is found to be around 10^{15} W/cm^2.

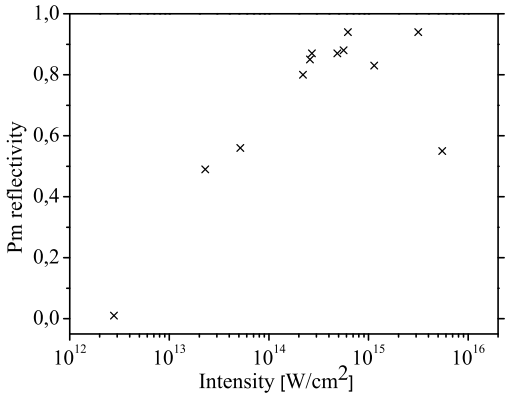

Figure 2: PM reflectivity for different intensities

In figure 3 the near field image of the reflected beam is shown for two different intensities. At a lower intensity (left) the nearfield distribution is not affected by the PM while at the higher intensity (right) the breakup can clearly be seen.

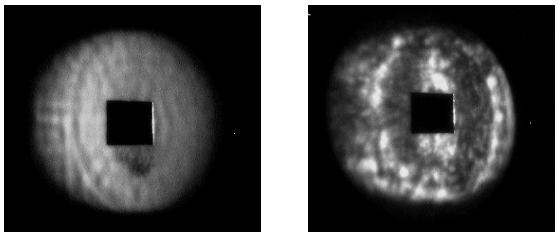

Figure 3: Image of the beam after the plasma mirror at 2,7*10^{14} W/cm^2 (left) and 5,5*10^{15} W/cm^2 (right)

Conclusion and Outlook

During this beamtime we successfully characterized and optimised our PM setup. With the PM, a contrast improvement of more than two orders of magnitude is possible. For 2012 we plan to develop a setup with two consecutive plasma mirrors. Together with an uOPA system which will be implemented at the PHELIX frontend, we predict that the pulse contrast will reach a level of at least 10^{10} .

References

[1] B. Dromey et al, Rev. Sci. Instrum. 75 (2004) pp. 645
[2] A. Jullien et al, Opt. Lett. 30 (2005) pp. 920-922

Improvement of the PHELIX-laser short-pulse contrast using shielding foils

M. Povarnitsyn[1], *N. Andreev*[1,2], *P. Levashov*[1,2], *K. Khishchenko*[1,2], *and O. Rosmej*[3]
[1]JIHT RAS, Moscow, Russia; [2]MIPT, Dolgoprudny, Moscow region, Russia; [3]GSI, Darmstadt, Germany

Laser contrast is a key parameter in experiments with high-intensity high-energy pulses. For relativistic intensities of the main pulse $\geq 10^{19}$ W/cm^2, even high-contrast beams can produce plasma on the target surface due to a long nanosecond prepulse action which results in an undesirable early smearing of the target. To avoid the influence of the long laser prepulse a thin foil can be placed in front of the target. The analysis of the multi-stage foil dynamics is performed using a wide-range two-temperature hydrodynamic model [1], which correctly describes the foil expansion starting from the normal solid density at room temperature. Modeling of shielded and unshielded target dynamics demonstrates the effectiveness of this technique. However, the prepulse energy re-emission by the shielding foil plasma can be sizable producing an undesirable early heating of the target placed behind the foil.

Series of simulations are performed for the laser pulses with wavelength $\lambda_L = 1.053$ μm and typical intensity contrast ratio of nanosecond prepulse $C_{\rm ns} = 10^{-8}$. The main pulse is assumed to be Gaussian with different peak intensities $10^{19} \leq I_{\max} < 10^{20}$ W/cm^2 achieved at $t = 0$ ps, and full width at half maximum (FWHM) pulse duration is $\tau_0 = 0.5$ ps. The picosecond-scale prepulse appearing just before the main pulse is also Gaussian with FWHM duration $\tau_1 = 20$ ps and contrast ratio $C_{\rm ps} = 10^{-4}$. These parameters correspond particularly to the petawatt high-energy laser for heavy ion experiments (PHELIX), which is planning to be used for X-ray generation at GSI.

In presented numerical result the shielding foil is initially located at $0 \leq z \leq 0.1$ μm and the bulk target of aluminum is placed behind the foil so that it occupies $500 \leq z \leq 600$ μm. Initial moment is $t = -2000$ ps. The gap of ~ 500 μm between the foil and target helps to avoid the hydrodynamic interaction between them during the simulation. It is seen that the soft X-ray re-emission radiation flux results in the target material expansion ~ 50 μm by moment -995 ps. The position of the critical electron density is situated at 10, 13 and 17 μm away from the initial target surface position for instants -995, -512 and -30 ps, respectively, see Fig. 1(a). The characteristic temperature of electrons and ions in the near-surface plasma is about 20 eV during the prepulse action. This target preheating is the result of thermal radiation action only since the laser beam does not reach the target till the moment $t = -5$ ps. As one can see in Fig. 1 there is no visible difference in target plasma parameters for moments -30 and -10 ps while the foil plasma demonstrates a sizable growth of $\langle Z \rangle$ and T_e. Thus, for the described parameters some target preheating takes place despite the laser light screening.

Simulation without the shielding foil demonstrates much more intensive target heating and expansion. The leading plasma edge at the moment -30 ps reaches the position ~ -400 μm and the entire plasma extent is about 900 μm that is much larger than ~ 150 μm for the shielded target.

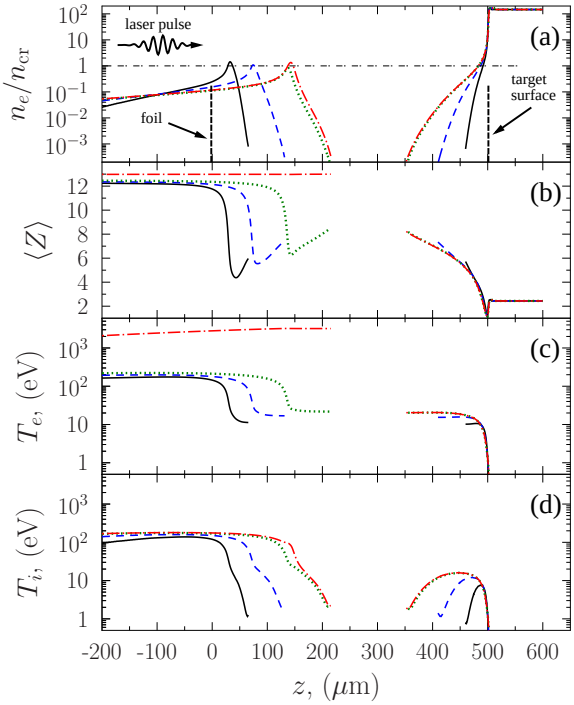

Figure 1: Evolution of the main parameters in the foil for laser pulse with $I_{\max} = 5 \times 10^{19}$ W/cm^2. Electron density normalized to the critical one—(a); mean charge of ions—(b); electron temperature—(c); ion temperature—(d). Instants: solid (black) curve— -995 ps; dashed (blue) curve— -512 ps; dotted (green) curve— -30 ps; dash-and-dot (red) curve— -10 ps. Initial foil and target positions are marked by arrows in panel (a).

To remedy the problem of the prepulse energy re-emission by the shielding foil and consequent undesirable heating and rarefaction of the main target, one can use the foil material with less nuclear charge (light elements or compounds like CH or CH_2 to reduce the integral radiation flux in the direction of the target) and also increase the gap between the foil and the target. These simulations are in sight.

References

[1] M. Povarnitsyn *et al.*, "Dynamics of thin metal foils irradiated by moderate-contrast high-intensity laser beams", Physics of Plasmas (2012). Accepted manuscript.

Experimental results and calculation of the energy loss of argon ions penetrating laser-generated carbon plasma

A. Frank[1], *A. Blazevic*[2], *M. Basko*[3], *M. Börner*[1], *W. Cayzac*[1], *P.L. Grande*[5], *T. Hessling*[2], *A. Pelka*[1], *G. Schiwietz*[6], *D. Schumacher*[1], *T. Stöhlker*[2], *An. Tauschwitz*[4], *and M. Roth*[1]

[1]TU Darmstadt, Germany; [2]GSI, Darmstadt, Germany; [3]ITEP, Moscow, Russia; [4]Uni Frankfurt, Germany; [5]Univ. Rio Grande, Porto Allegre, Brazil; [6]Helmholtz-Zentrum Berlin, Germany

The interaction of swift heavy ions with plasmas is a field of research which has been under intense investigation at GSI for a long time. Over the last years, a huge increase in the understanding of the different underlying processes of the interaction, namely the different ways of charge-transfer and the energy loss to bound and free electrons, has been achieved [1]. Furthermore the development of an improved wollaston interferometer as plasma [2] and a charge state spectrometer as heavy ion beam diagnostics [3] as well as the possibility to use the frequency-doubled option of the Phelix and the nhelix laser have made it possible to modify the experimental setup substantially. The plasma is now created by two laser beams from opposite sides as shown in Fig. 1, which leads to a significant suppression of inhomogeneities in the plasma target. These

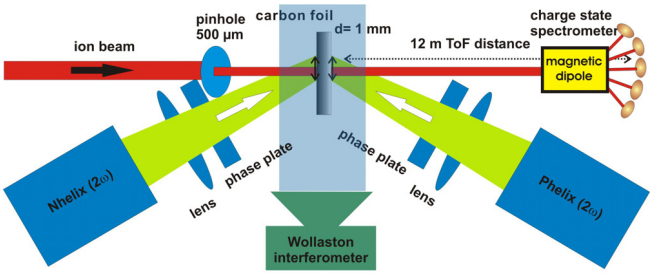

Figure 1: Experimental setup of the energy loss experiment.

inhomogeneities have led to a decrease of up to 40 % of the ion beam's energy loss below the value for the cold target during the laser-plasma interaction in earlier experiments [4]. As a consequence the experiments were governed for a rather long time to larger degree by the target's hydrodynamic response than by the atomic physics processes of the energy transfer. With the new setup it is now possible to conduct a detailed investigation of the different underlying processes. Fig. 2 shows the projectile charge state distribution of Ar at an energy of 4 MeV/u after having penetrated the cold foil (for t<0 ns) and the hot fully ionized carbon plasma (t>0 ns) with a temperature of 140-200 eV. After the interaction with the plasma target a stronger population of the higher charge states (16+ and 17+) is observed while the population of the lower charge states (14+ and 15+) decreases. However these changes in the charge state distribution remain moderate so that they only account for an increase of about 5 % to the total increase of a factor of 2

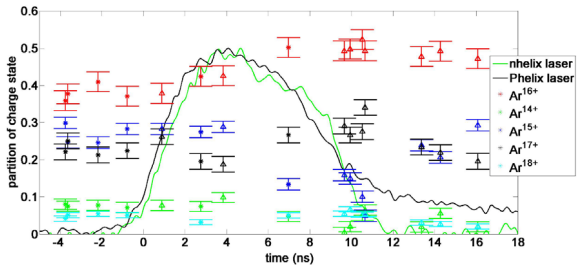

Figure 2: Experimental results of the projectile charge state distribution.

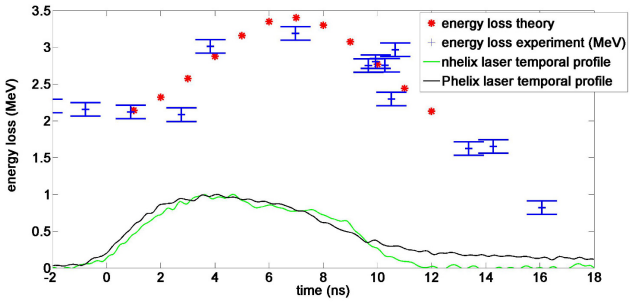

Figure 3: Comparison between experimental results and theoretical calculations for the energy loss.

in the stopping power in the plasma compared to the solid state. The main differences for the energy loss observed in the experiments shown in Fig. 3 arise from the more efficient energy transfer to the free electrons in the fully ionized carbon plasma in the experiment. This increase in the energy loss can be very well calculated with the aid of a specially developed Monte-Carlo code which allows the calculation of both the charge-transfer of the heavy ion beam while penetrating the plasma target and the energy loss with the aid of an extended version of the CasP code. No decrease below the value of the cold target is observed in the experiment and as shown by the theoretical curve in Fig. 3 experimental results and theoretical predictions are in a very good agreement.

References

[1] A. Frank et al, Phys. Rev. E 81, 026401 (2010)

[2] M. Boerner et al, GSI annual report 2010, 407

[3] W. Cayzac et al, GSI annual report 2009, 398

[4] A.Frank et al, GSI annual report 2009, 390

Indirectly plasma heating and energy loss experiments with PHELIX

D. Schumacher[1], *S. Bedacht*[1], *A. Blaževi*ć[2], *S. Busold*[1], *A. Frank*[1], *A. Ortner*[1], *G. Schaumann*[1], *and M. Roth*[1]

[1]TU Darmstadt, Germany; [2]GSI, Darmstadt, Germany

Introduction

The energy loss of heavy ions in plasma is one of the fields of research of our group. So far, only directly laser heated plasmas have been investigated [1]. To probe more homogeneus, slower expanding and denser plasmas an indirect heating scheme has been developed, where the plasma is heated by soft x-ray radiation. In this scheme the x-ray radiation is generated by a laser driven hohlraum. This hohlraum radiation is used to heat a secondary hohlraum, containing a carbon foil. The carbon foil is then heated to plasma temperature and can be investigated by ions. This year was the first time that energy loss experiments in indirectly heated plasma have been performed.

Target design

For this purpose beside the old target design, introduced in the last scientific report, a new target has been developed (fig. 1) and assambled at the target laboratory at the TU Darmstadt. The target is cuboid shaped and divided by a gap in two parts. The upper part is used as converter hohlraum, where the laser radiation is coupled in. The lower part is the target part, where the carbon foils are heated by the x-ray radiation.

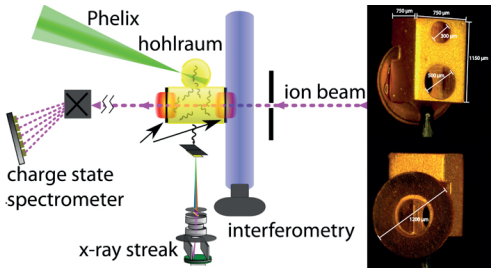

Figure 1: Setup with target and diagnostics.

Experiment setup

For both experiment campaigns in 2011 at Z6, using the 527 nm frequency doubled laser option of the PHELIX facility, the temperature of hohlraums was determined (fig. 1). The second harmonic of the laser wavelength was used for the better x-ray conversion of shorter laser wavelength and to avoid strong back reflection of the first harmonic due to stimulated brillouin scattering. As diagnostics for the temperature measurements a x-ray streak camera was used. For the energy loss experiments during the second campaign a ion charge state spectrometer was attached.

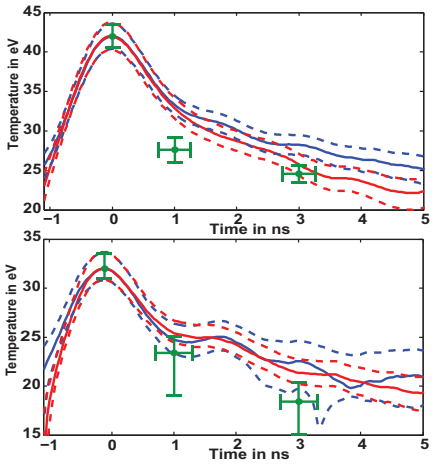

Figure 2: Temperature evolution for new (upper) and old (lower) hohlraum design. Depicted are the fits to the spectrum (green) and temperature derived from intensity at two different wavelength (red and blue).

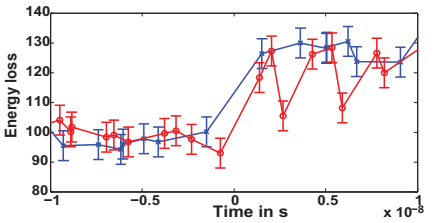

Figure 3: Energy loss of old (red) and new (blue) design.

Results

The temperature profile of the secondary part of both designs was determined through fitting of a planckian curve to the spectrum at different times and through measure the intensity of the spectrum at fixed wavelength. The results of this is shown in figure 2. Figure 3 depicts the energy loss for both hohlraum designs whereat the energy loss of the cold foil is scaled to 100 %.

References

[1] A. Frank, “Energy loss of argon in a laser-generated carbon plasma”, Phys. Rev. E 81, February 2010

A foam-filled cylindrical hohlraum for ion stopping measurements*

M. M. Basko[1,2,3], *J. A. Maruhn*[1,2], *An. Tauschwitz*[1,2], *V. G. Novikov*[4], *and A. S. Grushin*[4]
[1]EMMI, Darmstadt, Germany; [2]University of Frankfurt, Germany; [3]ITEP, Moscow, Russia; [4]KIAM, Moscow, Russia

We describe a novel cylindrical hohlraum target which allows to heat a sample material uniformly by the hohlraum radiation to a high temperature. The proposed configuration is optimized for ion stopping measurements in laser-produced plasmas. The main goal was to achieve a quasi-homogeneous plasma state with a temperature $T \simeq 100$ eV (sufficient to fully ionize carbon atoms) with typical PHELIX laser beam parameters. The hohlraum consists of two chambers: the primary one for laser absorption, and the secondary containing the sample material. Figure 1 shows the initial computational region for the Au hohlraum, filled with a carbon foam, together with the entering laser beam.

The hohlraum wall of solid gold is 15 μm thick. The carbon foam has a density of 3×10^{-3} g/cm^3, and is separated from the primary chamber by 15 μm of gold foam at the same density. The primary hohlraum and the outer buffer zone are filled with an Au vapor. Because of its shape, this hohlraum was dubbed an "Ω-hohlraum" [1]. In simulations the cylindrical Ω-hohlraum was assumed to have infinite length. In experiments an elliptical laser spot might be used. The ion beam should propagate along the cylinder axis. It was simulated with the radiation-hydrodynamics code RALEF-2D [2]. The equations of state, thermal conduction coefficients and LTE spectral opacities have been provided by the THERMOS code [3]. A special calculation for an empty Ω-hohlraum has shown that adding a second chamber leads to a $\simeq 10\%$ temperature reduction compared to the empty spherical configuration.

In simulations, the laser energy of 100 J/mm was delivered in a 1.2 ns long pulse with linear 0.3 ns rise and fall ramps. Figure 2 shows a spatial distribution of temperature at $t = 0.9$ ns, where the maximum carbon temperature of $T_{cp} \approx 90$ eV is reached near the hohlraum center. At such temperatures carbon becomes transparent for thermal x-rays over the entire spectrum. This leads to a homogeneous temperature distribution across the secondary hohlraum chamber. The temporal evolution of the average matter and radiation temperatures near the center ($r < 0.1$ mm) is shown in Figure 3. Note that the inward shock in C, driven by the wall ablation, limits the time window for the uniform plasma state to $\Delta t \simeq 0.5$ ns. By $t = 3.5$ ns the radius of C-plasma shrinks to $r \approx 0.1$ mm.

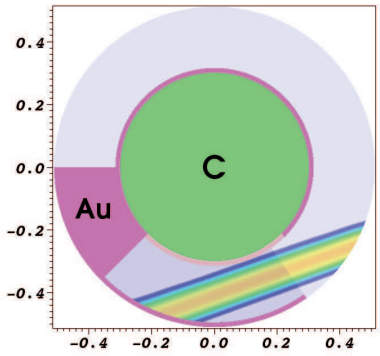

Figure 1: Numerical region for the C-filled Ω-Hohlraum. The colours are the density contours and the laser heating.

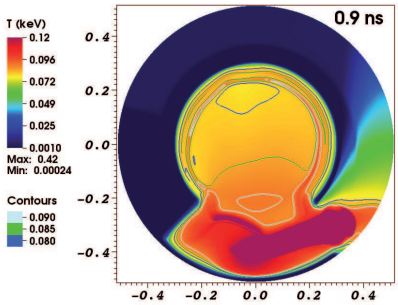

Figure 2: Contour plot of the matter temperature T [keV] at $t = 0.9$ ns.

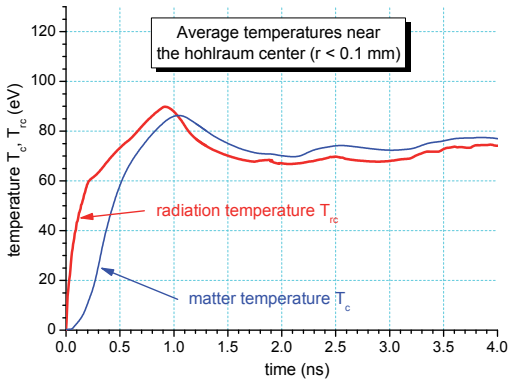

Figure 3: Temporal evolution of the average matter and radiation temperatures near the center of the hohlraum.

References

[1] M. M. Basko, J. A. Maruhn, An. Tauschwitz, V. G. Novikov, A. S. Grushin, GSI Report 2011-03.

[2] M. M. Basko, J. A. Maruhn, and An. Tauschwitz, GSI Report 2010-1 (GSI Scientific Report 2009), p. 410.

[3] A. F. Nikiforov, V. G. Novikov, V. B. Uvarov, *Quantum-statistical models of hot dense matter: methods for computation of opacity and equation of state*, Birkhäuser, 2005.

* supported by Helmholtz Alliance EMMI

First steps into the nonlinear regime of ion stopping in plasma*

W. Cayzac[1,2], *A. Blaževi*[3], *A. Frank*[1], *L. Hallo*[4], *G. Malka*[2], *A. Ortner*[1], *M. Roth*[1], *G. Schaumann*[1], *and T. Schlegel*[3]

[1]TU Darmstadt, Germany; [2]CELIA, Talence, France; [3]GSI, Darmstadt, Germany; [4]CEA/CESTA, Le Barp, France

While the precise knowledge of ion stopping in plasma is crucial for inertial confinement fusion and high energy density physics, this topic is still incompletely understood. In recent experiments, thin carbon foils were irradiated from both sides with frequency-doubled pulses from the PHELIX and *nhelix* laser systems [1]. The generated hot (200eV) and dense (10^{20-21}cm^{-3}) plasma was then probed by swift ion beams from the UNILAC accelerator at an energy of 4MeV/u, and a good characterization and understanding of the interaction has been achieved. There the ion velocity was significantly higher than the electron thermal velocity ($v_{ion}/v_{th} > 4$) and the plasma was ideal (coupling coefficient $\Gamma \approx 0{,}01$). This corresponds to weak beam-plasma correlation and thus to the linear regime of the beam-plasma interaction. The purpose of the present work, led in collaboration with the CEA and CELIA in France, is to investigate experimentally the ion energy loss when stepping out of that linear regime. This means decreasing v_{ion}/v_{th} while increasing $Z_p\Gamma^{3/2}$, with Z_p the ion charge. In that largely unknown parameter region, strong discrepancies appear between the various theoretical approaches [2], which points out the need for experimental data to benchmark the existing models.

As a first experimental step, the energy loss of slow ions (energy $\leq$ 500keV/u) will be investigated, where Z_p is first deliberately chosen low (e.g. carbon projectile) to simplify the theoretical analysis. This corresponds, for the plasma in [1], to v_{ion}/v_{th} =1-2, which is the region of the stopping power maximum (around the Bragg peak). Even in such an ideal plasma ($Z_p\Gamma^{3/2} \approx 0{,}015$), this velocity region is almost unknown and is expected to exhibit important deviations of the stopping power from the standard approaches. Following [1], the same well-characterized plasma can thus be used while the ion beams are slowed down by means of a carbon foil of about 40μm thickness (Fig.1).

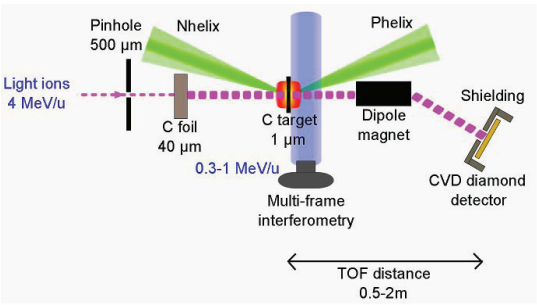

Figure 1: Setup of the experiment with slowed down ions.

The beam straggling in energy and in angle caused by the slowing down process was calculated with TRIM, which resulted, for an energy of 500keV/u, in $10\,\%$ and $1{,}5\,°$, while the energy resolution of the employed diamond detector is estimated to be better than 60keV. Because of this angular divergence, it is necessary to position the slowing down target only a few millimeters from the plasma target. Moreover, to prevent ion pulse overlapping due to energy straggling, a much shorter time-of-flight distance for the measurements, namely 0,5-1m, has to be used. Experimental work to test these aspects is underway.

Furthermore, for determining the optimal experimental parameters to reach a higher $Z_p\Gamma^{3/2}$, hydrodynamic simulations of carbon plasmas were performed with the ESTHER 1D code developed at CEA [3]. As was found, for dense plasmas heated with X-rays at a radiative temperature T_{rad} = 40-50eV out of a 1μm thick carbon foil target and probed by carbon projectile ions below 500keV/u, the relevant parameters reach the values $Z_p\Gamma^{3/2}$ =1-3 and v_{ion}/v_{th} =4-10 during the whole interaction time (duration of an ion pulse, 2-3ns) and in most of the target (Fig.2). Then a strong reduction of the stopping power of the carbon ions of 30-50 $\%$ is expected in comparison with the linear result [2]. The progress in work with cavity X-ray heating of carbon targets opens the way to such experiments [4]. In the near future, the development of cryogenic deuterium foils [5] will enable to extend this concept to a deuterium plasma.

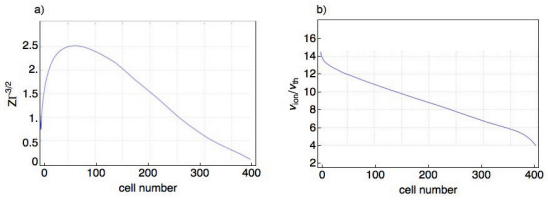

Figure 2: a) $Z_p\Gamma^{3/2}$ and b) v_{ion}/v_{th} for E_{ion}=400keV/u, after 2ns of the interaction of hohlraum X-rays at T_{rad}=45eV with a 1μm thick carbon foil target, as a function of the grid cell number, as simulated with ESTHER. The 400 cells originally correspond to the 1μm thickness and then evolve with the plasma expansion.

References

[1] A. Frank, this annual report

[2] D.O. Gericke and M. Schlanges, Phys. Rev. E, Vol.60, 1999

[3] J.P. Colombier, P. Combis, Phys. Rev. B 71, 165406, 2005

[4] D. Schumacher, this annual report

[5] S. Bedacht, this annual report

* This project is supported by CEA/CESTA and the Région Aquitaine

MPQeos-JWGU: A new equation-of-state package for warm/hot dense matter*

S. Faik[1], *An. Tauschwitz*[1,2], *J. A. Maruhn*[1,2], *and I. L. Iosilevskiy*[2,3,4]

[1]ITP, Goethe-Universität, Frankfurt am Main; [2]EMMI, GSI, Darmstadt; [3]JIHT-RAS, Moscow; [4]MIPT, Moscow

MPQeos-JWGU is a computer code that can generate EOS tables for arbitrary materials, also mixtures. It is an improved version of the code MPQeos, which is described in [1]. The underlying physical model is the "quotidian equation-of-state model (QEOS)" [2].

The MPQeos model. The original MPQeos code can only generate EOS of chemical elements. Thermodynamic quantities, like pressure, specific internal energy, specific entropy, are derived from the specific Helmholtz free energy $F = E - TS$, which is composed of three contributions: the electronic part, the ionic part, and the phenomenological bonding correction. For any element, the MPQeos model requires two empirical parameters: the density ρ_0 and the bulk modulus $K_0 = \rho\,(\partial p/\partial\rho)$ at a reference value of temperature T_0 and zero pressure $p_0 = 0$.

The electronic contribution is calculated by using the Thomas-Fermi (TF) model. An advantage of the TF model is that the TF equation and all thermodynamic quantities scale with the atomic number Z, and therefore must be calculated only once, e. g. for hydrogen. The most important drawback of the TF model is the absence of attractive (bonding) forces between neutral atoms. Hence, pressures near the normal conditions are overestimated.

MPQeos uses a bonding correction from Ref. [3]. It adjusts the EOS at p_0 and T_0 to have the correct values of ρ_0 and K_0. The bonding correction has the strongest effect on the EOS near the solid density. At higher densities the TF electronic contribution dominates.

The ionic contribution to thermodynamic quantities is independent of that from electrons. It is calculated with the Cowan model as described in Ref. [2], which employs analytical formulae to smoothly interpolate between the Debye solid, the normal solid and the liquid states. The ionic internal energy and pressure are of purely thermal nature.

Improvements for MPQeos-JWGU. Three important changes were introduced into the original MPQeos code.

1. The QEOS model overestimates the critical pressure p_c and the critical temperature T_c. This problem was solved by replacing the TF cold curve and the bonding correction for densities $\rho < \rho_0$ with a soft-sphere function proposed in [4]: $\epsilon_{cold}(\rho, T = 0) = A\rho^n - B\rho^m + \epsilon_{coh}$. Here ϵ_{coh} is the cohesive energy. The constants A and B are adjusted so as to make the total pressure and the internal energy be equal to zero at ρ_0 and T_0: $p(\rho_0, T_0) = \epsilon(\rho_0, T_0) = 0$. The free parameters m and n are used to fit the experimentally (or theoretically) known critical point. At ρ_0 the sound velocity is allowed to be discontinuous.

2. A well known rule for the TF mixing of elements [2] was added to MPQeos-JWGU. The ionic contribution and the bonding correction are handled as a single species with a mean atomic number $\bar{Z}$ and weight $\bar{A}$. For the electronic contribution of a mixture the partial volumes of all species k are iteratively adjusted in order to equilibrate the TF pressures $p_{e,k}$ and to fulfill an additive volume rule.

3. In the original MPQeos the liquid-vapor phase coexistence was calculated for each isotherm below T_c by using Maxwells computationally very intensive geometrical rule. In MPQeos-JWGU a new routine, which calculates the saturated vapor pressure for each isotherm below T_c by equating the values of the Gibbs free energy and pressure on the liquid and vapor branches of the binodal, is applied.

Fig. 1 shows the EOS of SiO_2 calculated with MPQeos-JWGU. The parameters, $\rho_0 = 2.2$ g/cm^3, $T_0 = 300$ K, and $K_0 = 37$ GPa, were used. The parameters of the soft-sphere model, $\epsilon_{coh} = 9.74$ kJ/g, $m = 0.8$, and $n = 2.8$, were adjusted such as to make the critical point approach data by Iosilevskiy and Gryaznov: $T_c = 6300$ K, $p_c = 3500$ bar, and $\rho_c = 0.65$ g/cm^3.

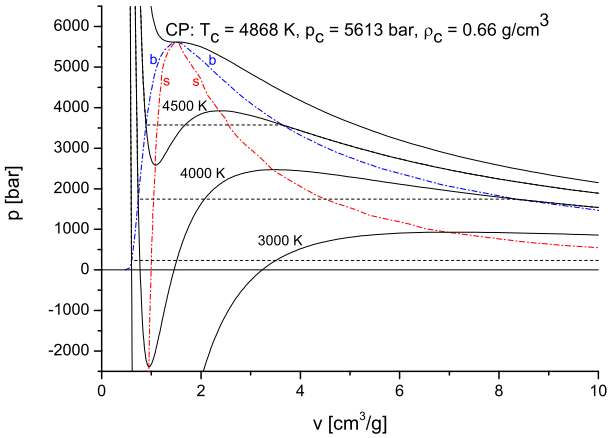

Figure 1: Equation of state of SiO_2 on the volume-pressure phase plane. Shown are the isotherms with and without the Maxwell construction; the binodal and the spinodal touch each other at the critical point CP.

References

[1] A. Kemp, J. Meyer-ter Vehn, Technical Report 229, Max-Planck-Institut für Quantenoptik (1998).

[2] R. M. More et. al., Physics of Fluids 31 (1988) 3059.

[3] J. F. Barnes, Physical Review 153 (1967) 269275.

[4] D. A. Young, E. M. Corey, J. of Appl. Phys. 78 (1995) 3748.

* supported by BMBF (Projects 06FY9085) and by Helmholtz Alliance EMMI

Dynamics of volumetrically heated matter passing through metastable states *

S. Faik[1], *M. M. Basko*[2,3], *An. Tauschwitz*[1,2], *I. L. Iosilevskiy*[2,4,5], *and J. A. Maruhn*[1,2]

[1]ITP, Universität Frankfurt; [2]EMMI, GSI, Darmstadt; [3]ITEP, Moscow; [4]JIHT-RAS, Moscow; [5]MIPT, Moscow

A self-consistent model for simulating the dynamic behavior of matter passing through the metastable states in the two-phase liquid-vapor region of the phase diagram is formulated [1]. It is based on the local criterion of explosive boiling, derived by applying the theory of homogeneous nucleation in superheated liquids and can be used in situations where the distribution of thermodynamic parameters is non-uniform. Figure 1 gives a schematic trajectory of a volumetrically heated sample passing through the metastable states. Initially, the sample of a thickness l is heated uniformly in a quasi-static manner, which means slowly by comparison with the sonic time, $t_s = l/c_s$ (c_s is the speed of sound). The first-order quasi-static solution for the fluid velocity is $u(t,x) = ax$, where $a = \Gamma q/c_s^2$. Here Γ is the Grüneisen coefficient and q is the heating rate. The condition for the quasi-static solution is hereby $at_s \ll 1$. At the Fig. 1 the trajectory of the heated foil starts from the point O at $T = 0$, crosses the binodal at B_0 and undergoes an explosive boiling $B_1 \to B_2$ at B_1.

The criterion for the instantaneous and irreversible transition to the equilibrium EOS at point B_1 is given by

$$NV_c \left(\frac{3\sigma}{\pi m}\right)^{1/2} \left[\frac{d}{dt}\left(-\frac{W_c}{T}\right)\right]^{-1} \exp\left(-\frac{W_c}{T}\right) = \frac{\rho_l(T_2) - \rho}{\rho_l(T_2) - \rho_v(T_2)}\,.$$

Here, N is the concentration of molecules, V_c is the volume of a critical bubble, W_c is the minimum work needed to create a critical bubble and m is the mass of one molecule. ρ_l and ρ_v are the densities along the liquid and the vapor branches of the binodal. The equilibrium temperature T_2 is implicitly defined by the transition constraints of constant density and specific internal energy. One can prove that $T_2 > T_1$ and $p_2 > p_1$.

To illustrate the method, simulations for a thin foil made of SiO_2 heated volumetrically with $q = 10^{11}$ J g^{-1} s^{-1} are performed. Equations of state for SiO_2 are provided by the MPQeos-JWGU model [2]. The foil of a thickness $l_0 = 10\,\mu$m is divided into 100 mesh intervals. At $t = 0$ the linear velocity profile $u(0,x) = ax$ is assumed to suppress quasi-static oscillations ($u_{l_0} = u(0,l_0) = 3528$ cm/s). Figure 2 shows the trajectories of three selected Lagrangian cells. For illustrative reasons the initial pressure is set equal to $p_0 = 0.5$ kbar. The foil obeys the metastable EOS until the criterion for explosive boiling is fulfilled at $t_b = 52.95$ ns and $T_1 = 3923$ K. During the transition the temperature raises to $T_2 = 3964$ Kelvin and the pressure jumps up to $p_2 = 1.65$ kbar. At the moment of explosive boiling a jump in the surface velocity u_l by a factor of 10 is observed. This could be used to measure t_b in the ion beam experiments at the HHT area. It is seen from the Fig. 2, that after the transition the trajectories of the inner foil elements virtually stick to the binodal. Such behavior is caused by a large drop in c_s across the binodal.

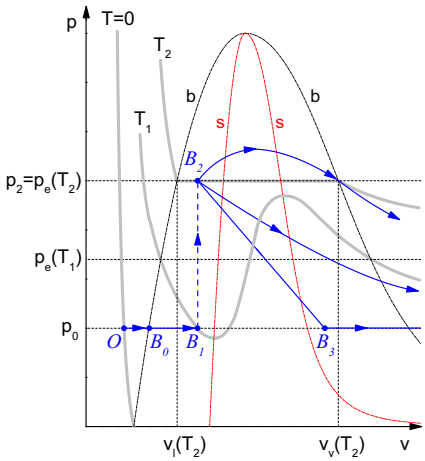

Figure 1: Schematic view of the evolution of the thermodynamic state of heated matter. p_0 is an external pressure.

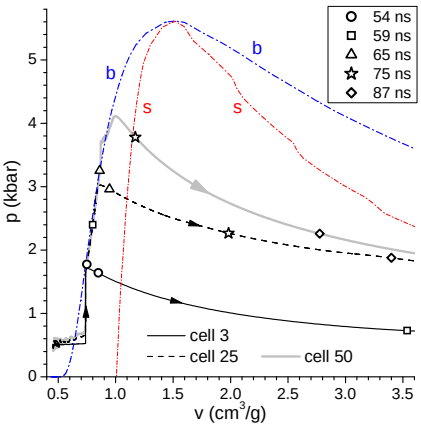

Figure 2: Trajectories of three selected Lagrangian cells of the simulated SiO_2 foil on the (v,p) phase plane.

References

[1] S. Faik, M. M. Basko, An. Tauschwitz, I. L. Iosilevskiy, and J. A. Maruhn, submitted for publication.

[2] S. Faik, et. al.; "MPQeos-JWGU: A new equation-of-state package for warm/hot dense matter", this report.

* supported by BMBF (Projects 06FY9085) and by Helmholtz Alliance EMMI

Analysis of self-consistent field models for warm dense matter*

A. S. Grushin[1], *V. G. Novikov*[1], *An. Tauschwitz*[2,3], *J. Otto*[3], *A. Tauschwitz*[4], *and P. Neumayer*[2,4]

[1]KIAM, Moscow, Russia; [2]EMMI, Darmstadt, Germany; [3]Frankfurt University, Germany; [4]GSI, Darmstadt, Germany

The quasizone model [1, 2] and the INFERNO model [3, 4] implemented in the TH_BAND code and in the RESEOS code developed at the Keldysh Institute of Applied Mathematics are analyzed in view of warm dense matter opacity calculations. Both models use an average atom approximation with local exchange in the electroneutral spherical cell, where the self-consistent interatomic potential is calculated, but the boundary conditions for electron wave functions are extremely different.

In the INFERNO model the spherical atomic cell is merged in an uniformly distributed ion background of positive charge with density $\overline{\rho}$. The electron density outside the cell is assumed to be constant and equal to its asymptotic value $\overline{\rho}$. The Dirac equation is used to obtain the one-electron wave functions in the self-consistent potential $V(r)$, and the resonant wave function is a special solution for the Dirac equation with certain boundary conditions. The potential is obtained from the free energy minimum condition. In the quasizone model the most general boundary conditions for the wave function resulting from translational symmetry are used. At the boundary of the spherical cell ($r = r_0$) we have for the wave function $\Psi_\gamma(\vec{r})$ $|\Psi_\gamma(\vec{r})|^2 = |\Psi_\gamma(-\vec{r})|^2$ or $\Psi_\gamma(\vec{r}) = e^{i\vec{k}\vec{r}}\,\Phi_{\gamma\vec{k}}(\vec{r})$, where γ is the set of quantum numbers for one-electron states, $\vec{k}$ is an arbitrary real constant vector (quasi-momentum) and $\Phi_{\gamma\vec{k}}(\vec{r})$ is a periodic function.

When increasing the matter density the upper energy levels in the INFERNO model are merged into continuum. In this case the sharp maxima for the continuum density of states are located in a very narrow intervals of energy (the resonances), which are similar to that of the bound levels. With further density increase the maxima dissolve in the continuum spectrum providing smooth transitions from bound states to continuous states. An example for such behavior is shown in Fig. 1. In the quasizone model we get energy bands instead of bound levels when the density of matter is increased. Again, as a result one obtains a smooth dependence of thermodynamic and optical properties over temperature and density. Figure 2 shows results for energy bands $\varepsilon_{n\ell m}(k)$ in gold at a temperature of $T = 1$ eV and a density of $\rho = 125$ g/cm^3. For energies greater than 12 eV the bands are overlapped and form a continuum.

The correct description of the spectrum structure in view of resonant states and quasizones allows to obtain reasonable and smooth thermodynamic and optical characteristics of dense plasmas in a wide range of temperature and density. A comparison of transmission in the XUV region calculated with the RESEOS code for heated bismuth foils [5] is presented in Fig. 3.

* supported by Helmholtz Alliance EMMI

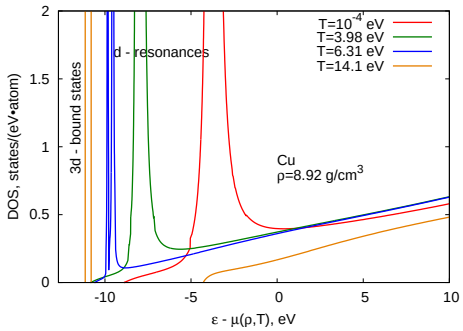

Figure 1: Density of states for Cu at 1 eV temperature and 8.92 g/cm^3 matter density.

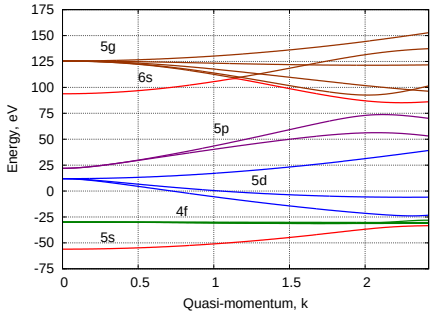

Figure 2: Energy spectrum for Au at 1 eV temperature and 125 g/cm^3 density.

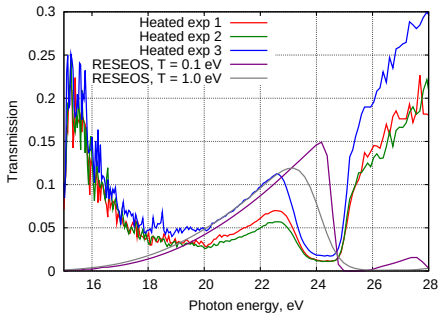

Figure 3: Transmission of heated Bi: theory vs experiment.

References

[1] A. F. Nikiforov, V. G. Novikov, V. B. Uvarov, Quantum-Statistical Models of Hot Dense Matter, Birkhäuser, 2005.

[2] V. G. Novikov, A. S. Grushin, Quasizone model of matter, XXIV Int. Conf. on Interaction of Intense Energy Fluxes with Matter, Elbrus, Kabardino-Balkaria, Russia, 2007.

[3] D. A. Liberman, Phys. Rev. B **20** (1979) 4981.

[4] A. Bar-Shalom, J. Oreg, M. Klapish, JQSRT **99** (2006) 35.

[5] A. Tauschwitz et al., GSI Report 2011-1, 417.

Spatial and temporal distribution of Hohlraum radiation in experiments with ns-PHELIX-laser pulses

T. Rienecker[2]; O.N. Rosmej[1]; Maeder, R.[2]; Suslov, N. [3] ; Blazevic, A.[1] ; Otto, J.[2]; Derkach, V.[3] ; Zhao, Y. [4] ; Zhao, H.[4]; Borisenko, N. [5] ; Vergunova, G.[5], M. Basko[6]

[1]GSI, Darmstadt, Germany; [2]Goethe-University Frankfurt, Germany; [3]VNIIEF-Sarov, Russia; [4]Institute of Modern Physics, China Academy of Science, Lanzhou, China; [5] Lebedev Physical Institute, Moscow [6]Institute of Theoretical and Experimental Physics, Moscow; Russia

For indirect homogeneous heating of low-Z triacetate-cellulose (TAC) foam targets, used in experiments on ion energy loss in plasma, a large (Ø > 1 mm) soft X-ray source with a Planckian equivalent radiative temperature of 30 to 50 eV is required. In this temperature region soft X-rays are effectively absorbed by low Z low density polymer layers. More energetic radiation above 1 keV passes through the 200 µg/cm^2 TAC-layer without attenuation giving no input into the process of foam heating.

As a X-ray source an Au-hohlraum constructed as a 1,8 mm long cylinder of 1,3 to 1,5 mm in diameter, driven by the PHELIX-laser (Nd:glass at 2 ω) with a pulse length of 1,4 ns, a spot diameter of 200 µm and a laser energy of up to 180 J. The thickness of the Au-wall is 12,5 µm, the Au-cylinder is surrounded by an Al-holder. The hohlraum top served as an entrance laser hole, the bottom was covered with a foam layer of 0.5 – 1 mm thickness.

The experimental setup includes spectral, spatial and temporal measurements by grating and mica spectrometers, pinhole cameras and X-ray diodes [1].

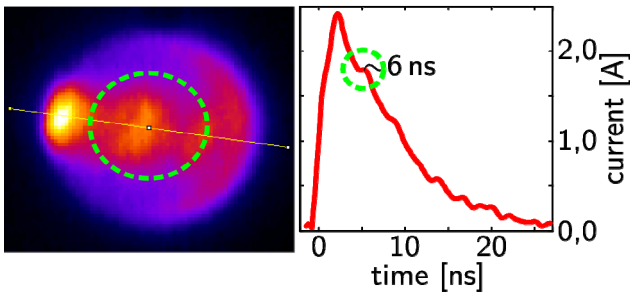

Figure 1: Pin-hole image of the hohlraum plasma in the photon energy region >200 eV and temporal evolution of the soft x-ray signal measured by means of an X-ray diode (XRD)

The pinhole images of the both sides Au-hohlraum have been made. One can observe more heterogeneous structure of the hohlraum plasma radiation compared to the experiments with 1ω PHELIX-option [1]. The XRD signal shows long lasting (> 10 ns) X-ray emission with a small second peak at 6 ns (fig.1).

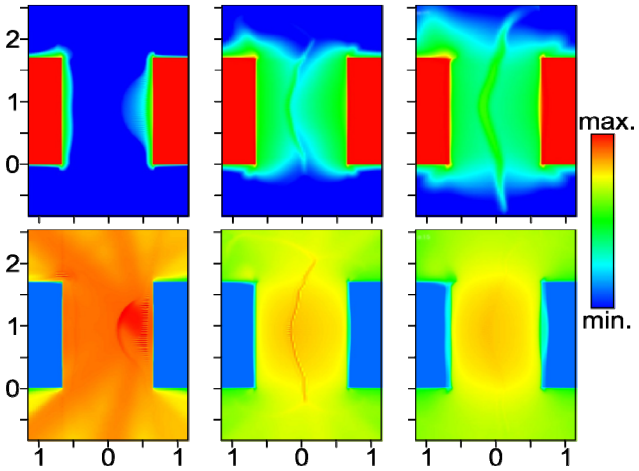

Figure 2: Simulations of the hohlraum plasma, density (upper line) and temperature (lower line) distribution at 1 ns, 6 ns and 15 ns, axes are in millimetre, (code RALEFII), $E_{Laser} = 100$ J, $I = 10^{14}$ W/cm^2

According to hydrodynamic simulations carried out using the code RALEF II [3] this heterogeneity is caused by the radiation of the hot plasma in the laser - hohlraum wall interaction region and by the near centre collision of the plasma plums, propagating from the opposite sides of the hohlraum wall, at around 5-6 ns (see fig.2). After 10 ns hohlraum plasma reaches thermodynamic equilibrium with the themperature of 30 eV providing long lasting soft X-ray source for effective heating of the foam layer.

* Work supported by DFG contract No. 586477; WTZ-Project, GSI and EMMI

References

[1] O.N. Rosmej et al. NIMA 653(2011)52-57
[2] O.N, Rosmej et al. GSI-report 2010
[3] M. Basko, An. Tauschwitzt et al, GSI-Preprint N 2011

Transmission properties of X-ray heated low density foam layers

[1]O.N. Rosmej, [2]V. Derkach, [2]N. Syslov, [2]N. Zhidkov [3]T. Rienecke,[3]J. Otto, [3]J. Jacoby, [4]G. Vergunova, [4]N. Borisenko, [5]Y. Zhao, [5]H. Zhao,

[1]GSI, Darmstadt, Germany; [2]VNIIEF-Sarov, Russia, [3] Goethe University Frankfurt, Germany, [4]Lebedev Physical Institute , Moscow, Russia, [5]Institute of Modern Physics , Lanzhou, China

For combined experiments on interaction of heavy ion beams with ionized matter a high density plasma target with homogeneous plasma parameters is required. For these purposes we develop the combined target which consists of the Au-hohlraum (converter) and low density foam target heated by the hohlraum radiation before probed with an ion beam. Foam targets are rather promising due to the effective conversion of the deposited radiation energy into the internal plasma energy and slow hydrodynamic response on the heating [1]. Such CHO - plasma with expected electron temperature of T=20-30 eV and electron density of ne=10^{21} is in the thermodynamic equilibrium (TE).

In experiments carried out in March and August 2011 in the frame of the experimental projects P014 and U266, transmission properties of the 2 mg/cc 0.5 – 1mm thick polymer layers heated by hohlraum radiation have been investigated. Hydrodynamic calculations including radiation transport [1] showed a strong dependence of the CHO-plasma transmission properties for soft X–rays (50-1000eV) on the hohlraum temperature and the temperature of the heated to plasma foam. According to numerical simulations, transmission of 1mm thick 2 mg/cc CHO foam layers used in experiments is changing in this photon region from 7% up to 70% if the hohlraum temperature rises from 20 to 50 eV.

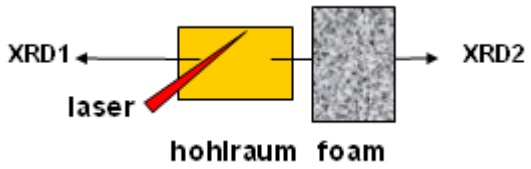

Figure 1a: experimental scheme

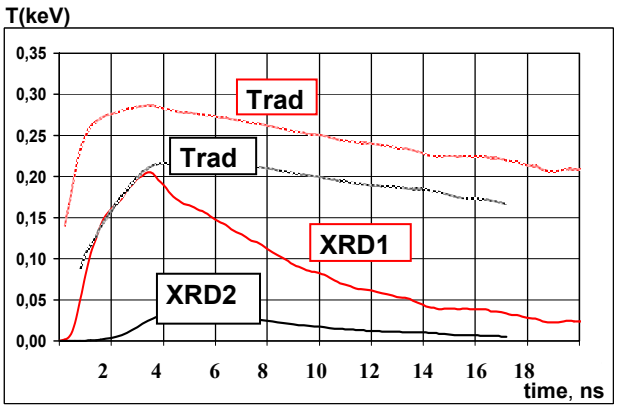

Figure 1b: X-ray diode signals: XRD1- hohlraum radiation, XRD2 – hohlraum radiation transmitted by 1mm thick CHO plasma layer. Trad1- an equivalent hohlraum radiation temperature; Trad2 – the hohlraum "temperature" viewed through the CHO-plasma.

For the measurements of the CHO-plasma transmission properties in dependence on the hohlraum temperature two cross-calibrated X-ray vacuum diodes with Carbon cathodes covered with 0.9 mm Mylar filters were used. XRD1 was placed in front of the opened part of the hohlraum measuring the temporal evolution of the hohlraum radiation (fig. 1a). The similar X-ray diode, XRD2, was placed from the target back-side measuring the hohlraum radiation after transmission through 1mm thick foam layer heated by this radiation to a plasma state. Fig. 1b shows the time evolution of both signals. Since the XRDs are absolutely calibrated, one can conclude about the evolution of the hohlraum temperature Trad1, Trad2.

The ratio of these two signals gives the time evolution of the TAC-plasma transmission (see fig.2) for soft X-ray generated in the Au-hohlraum.

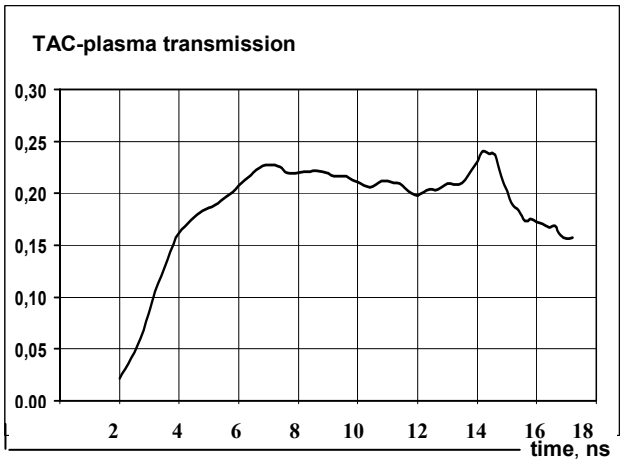

Figure 2: time evolution of the CHO-plasma transmission

The measured plasma transmission varies between 18 and 22 %, according to the numerical simulations is of 18%.The best agreement between the numerical simulations and experimental data occurs at the foam temperature of 25-27 eV.

References

[1] G. Vergunova et al, Journal of Russian Laser Research, **31**, N5(2010)504-5013
[2] O.N. Rosmej et al, NIMA **653**(2011)52-57

Work supported by DFG grant No.586477; WTZ-Project, GSI and EMMI

Measurements of the Heavy Ion Stopping in X-ray heated low-density nanostructured targets*

Maeder, R.[2]; Rosmej, O.[1]; Rienecker, T.[1,2]; Suslov, N[3]; Zhao, Y.[4]; Blazevic, A.[1]; Otto, J.[2]; Martsovenko, D.[3]; Borisenko, L.[5]; Borisenko, N.[7] Zhao, H.[4]; Cheng, R.[4]; Cao. L.[6]; Gao, Y.[6]

[1]GSI, Darmstadt, Germany; [2]University Frankfurt am Main, Germany; [3] VNIIEF, Sarov, Russia;
[4]Institute of Modern Physics, China Academy of Science, Lanzhou, China; [5] Moscow State University, Russia;
[6] Laser Fusion Research Center, China ; [7]Lebedev Physical Institute, Moscow.

Goal of the experimental project U266 using the combination of the petawatt PHELIX-laser (2ω; 180J; 1,4ns) and UNILAC ion beam, were measurements of the difference between the ion energy loss in cold and ionized matter.

In order to achieve reliable data, a plasma target with homogeneous in time- (~5ns) and space- (~1mm) plasma parameters, such as density, temperature and ionization degree has to be used.

To create such a plasma, low density (2mg/cc), up to 1mm thick CHO-foam layers were volumetrically heated by soft X-rays. This indirect heating was realised through a nanosecond PHELIX laser pulse fired at the Au-hohlraum, which transformed the laser's energy into soft-X-ray radiation.

A cellulose-triacetate-(TAC)-foam ($C_{12}H_{16}O_8$) was used, for effective conversion of the absorbed radiation energy into internal plasma energy, thus creating, within a sub-nanosecond time-scale, a homogeneous, hydrodynamic stable plasma, with an electron density of $n_e \sim 10^{21}$ cm^{-3} and temperatures of 20-30 eV.

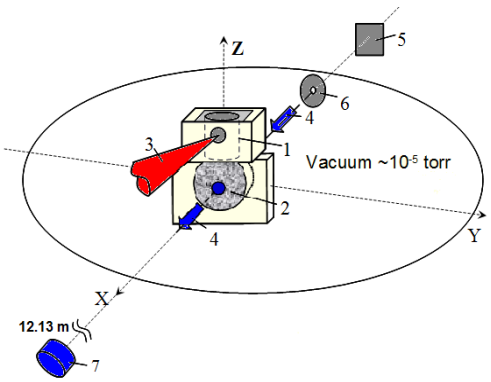

Figure 1: Construction within the Z6-Targetchamber

In experiments (Fig. 1), the Au-hohlraum (1) was irradiated by a nanosecond PHELIX-laser pulse (3) with a 200um spot size on the wall. Soft-X-ray radiation with close to the Planckian spectral distribution was propagating into the foam layer (2) and heating it volumetrically to the plasma state.

* Work supported by DFG contract No. 586477; WTZ-Projects, GSI and EMMI

The 4.77 MeV/u Ti^{12+}-beam with 36MHz RFQ-frequency, enters the target chamber opposite to the laser beam direction (fig.1). The Ti^{12+}beam was striped in the target chamber up to the equilibrium charge state distribution by means of the 90 μm/cm^2 carbon foil (5) and collimated on to the foam target using a carbon collimator (6) having a hole of 0.5mm in diameter.

The ion energy loss was analysed by means of Time of flight (TOF) method using a diamond detector (7) placed 12.13m apart the interaction region.

The Ti-ions energy loss in cold (ΔE_{cold}) and ionized (ΔE_{Pl}) matter was measured by comparing the ion TOF after interaction with the target with TOF in vacuum (Fig.2). Measurements were carried out for different delays (Δt) between laser- (green-line) and ion- (red-line) pulses .

We obtained up to 1,8 enhancement in Ti-ion energy loss in plasma compared to cold target (Tab.1).

Shot	Δt [ns]	$\frac{\Delta E_{Pl}}{\Delta E_{Cold}}$
No. 18	4,667	1,852
No. 26	17,170	1,595
No. 27	14,050	1,283
No. 28	13,053	1,625
No. 31	8,853	1,624
No. 32	9,200	1,615

Table 1: Measurements

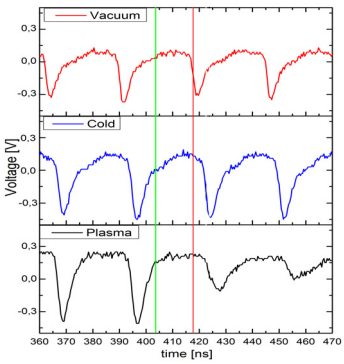

Figure 2: Shot 27-TAC 4.4

During our next beam-time, we plan to analyse the gold-plasma dynamics inside the hohlraum, as well as the lifetime of homogeneous plasma.

We would like to thank A. Blazevic, W. Cayzak and M. Roth for their support with the ion energy-loss measurements .

References

[1] A.M. Khalenko et al., Laser Part. Beams **24**(2006)283-290
[2] G. Vergunova et al, Journal of Russian Laser Research, **31**, N5(2010)504-5013
[3] 2. O.N. Rosmej et al, NIMA **653**(2011)52-57

First X-ray scattering experiments with shock-compressed matter at GSI

D. Kraus[*1], *A. Otten*[1], *A. Frank*[1], *V. Bagnoud*[2], *A. Blazevic*[2], *D. O. Gericke*[3], *G. Gregori*[4], *A. Ortner*[1], *G. Schaumann*[1], *D. Schumacher*[1], *J. Vorberger*[3], *F. Wagner*[1], *K. Wünsch*[3], *and M. Roth*[1]

[1]TU Darmstadt, Germany; [2]GSI, Darmstadt, Germany; [3]University of Warwick, UK; [4]University of Oxford, UK

Introduction

X-ray Thomson scattering is a very powerful technique to study warm dense matter which means materials around solid density and temperatures of 0.5 to 10 eV [1]. It gives the possibility for the direct measurement of plasma parameters like temperature, density of free electrons, degree of ionization and the microscopic structure of a warm dense matter sample. Therefore, X-ray Thomson scattering is a central diagnostics for all three upcoming plasma physics experiments at FAIR (HIHEX, LAPLAS, WDM) which aim for a precise characterization of warm dense matter [2]. Hence, the accumulation of experience with X-ray Thomson scattering experiments at GSI and using the laser system PHELIX as pulsed X-ray source of high brilliance is of major importance for the success of these future experiments at FAIR.

Experiment

At GSI, a first X-ray Thomson scattering experiment for the characterization of warm dense matter created by laser-driven shocks was realized in April 2011 [3]. The laser system nhelix with pulse energies of 65 J and pulse durations of 10 ns was used for the compression of graphite samples (fig. 1). The ns-option of the PHELIX system at Z6 (150 J, 1 ns) was focused on a Ti foil and created enough X-rays of Ti-He-α line radiation (4.75 keV) for a successful X-ray scattering experiment. In fact, a conversion efficiency of up to 5×10^{-3} could be achieved. The scattering angle was chosen to be $(126\pm10)^\circ$ which ensures scattering in the non-collective regime (scattering on single electrons). As a pre-experiment the thermodynamic state in the shock wave was characterized by a classical measurement of shock velocity and particle velocity. The shock speed was measured by looking at the self emission of the shock breakout with a visible streak camera. Additionally, the particle velocity was measured via the expansion of the shock release with a multi-frame shadowgraphy instrument.

Results

The resulting pressure of the shocked carbon was around 1 Mbar. In this region, the stable state of the shocked graphite is either hexagonal diamond or liquid carbon. X-ray Thomson scattering is able to resolve this change in microscopic structure. Within the applied angle range the elastic contribution to the scattering increases strongly for hexagonal diamond and liquid carbon compared to cold graphite whereas the inelastic part remains nearly unchanged for all three phases and the chosen geometry. These characteristics were directly seen in the experiment. The total transit time of the shock through the 190 µm thick carbon sample was 16 ns. As the duration of the X-ray source is only 1 ns, it is possible to follow the motion through the sample by using different time delays. As the photons enter the sample from the opposite side of the shock drive the signal rises stronger at later times in this backscattering geometry. Due to the exponential attenuation the probed regions closer to the X-ray source contribute most to the recorded signal. The contribution of the hot plasma of the shock drive to the scattering can be estimated to be only $\sim$1 % and, thus, can be neglected. With the results of this experiment it is not yet possible to distinguish between hexagonal diamond or liquid carbon as the final state after the shock. However, this will be possible in a future experiment where additional scattering angles will be covered (scheduled for February/March 2012).

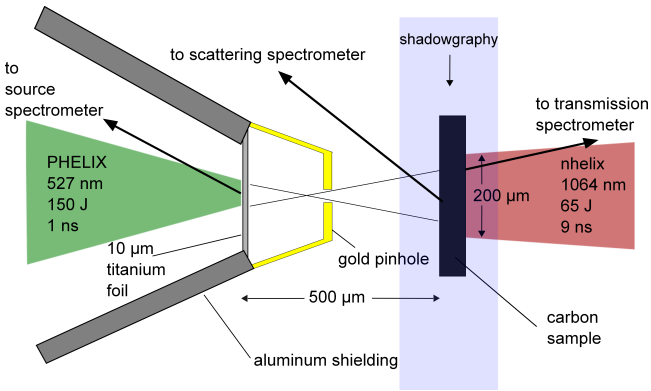

Figure 1: Sketch of the experimental setup at Z6: For the target design, it is crucial to ensure the shielding of the scattering spectrometer from a direct line-of-sight to the X-ray source. Additionally, the scattering angle has to be well defined. This was realized with special micro-machining and galvanic techniques in the target laboratory of TU Darmstadt.

References

[1] S. H. Glenzer, R. Redmer, Rev. Mod. Phys. 81, 1625 (2009)

[2] FAIR Baseline Technical Report (2006)

[3] D. Kraus et al., High Energy Density Physics 8, 46-49 (2012)

* d.kraus@gsi.de

Generation of picosecond narrow bandwidth X-ray pulses from a Laser-Thomson-Backscattering source at HZDR

J. A. Irman[1], A. Jochmann[1], S. Trotsenko[2,3], U. Lehnert[1], J.P. Couperus[1], M. Kuntzsch[1], A. Wagner[1], A. Debus[1], H.P. Schlenvoigt[1], K.D. Ledingham[4], T.E. Cowan[1], R. Sauerbrey[1], Th. Stöhlker[2,3] and U.Schramm[1]

[1]Helmholtz Zentrum Dresden-Rossendorf, Dresden, Germany; [2]GSI, Darmstadt, Germany; [3]Helmholtz-Institut Jena, Jena, Germany; University of Stratclyde, Glasgow, Scotland

Intense ultrashort hard X-ray can serve as a novel tool for structural analysis of complex systems with unprecedented temporal and spatial resolution [1]. However, hard X-ray generation based on insertion devices like undulators in conventional accelerators requires GeV range electron energies and thus large installations. The most prominent examples of such sources are the X-ray free electron laser projects that are currently under construction [2].

Here, we propose the replacement of the magnetic undulator by an optical light wave and the implementation of this scheme, also well-known as the Thomson backscattering [3], at the radiation source ELBE. In this scheme, electrons oscillating in the light field emit Doppler-upshifted radiation (proportional to the square of the relativistic energy γ) into a relativistically contracted solid angle cone (proportional to 1/γ) in the laboratory. Although the brilliance as well as the total number of photons expected from this process cannot compete with the XFEL approach, it should be sufficient for a number of applications where the short pulse duration and the simultaneous availability of 100 TW class laser radiation can be exploited. Pump-probe experiments analysing laser induced melting and re-crystallization or temporal X-ray probing of warm dense matter only represent a small range of applications that will be the topic of further proposals.

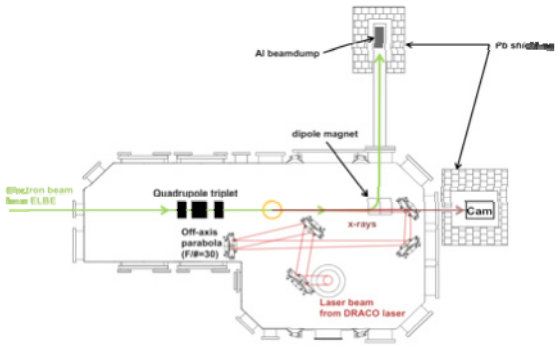

Fig. 1: Thomson backscattering experimental setup.

Experimental setup

A schematic drawing of the setup is presented in figure 2. Electron beams with energy of 24, 27 and 30 MeV and charge of 70 pC from the radiation source ELBE were transported into the interaction chamber located in room 111b of the ELBE building. Inside the chamber these electron beams were focused by a set of permanent quadrupole magnets onto the interaction point, where they collided with synchronized counter-propagating laser beams from the DRACO Tisa laser system. The scattered X-ray photons pass a kapton window at the end of the vacuum chamber and enter the diagnostic area shielded with lead bricks. A dipole magnet was installed downstream of the interaction point to deflect the electron beams towards the electron beam dump made from a thick aluminium block.

Preliminary Results

The generated x-rays are highly collimated and can be reliably adjusted from 5.5 to 23.5 keV by tuning the electron energy (24 MeV to 30 Mev) and the laser intensity. Ensuring the spatio-temporal overlap at the interaction point and suppressing the Bremsstrahlung background we have achieved a signal to noise ratio of greater than 300. Together with the use of an x-ray camera (resolution of 250 eV FWHM) to record the x-ray beam profile (in Fig.2) and the energy spectrum (in Fig.3), we were able to resolve the angular-energy correlation and to study the influence of the beam emittance on the observed bandwidth. This experiment serves as an important step towards a compact tuneable source of ultrashort hard x-ray pulses at the ELBE.

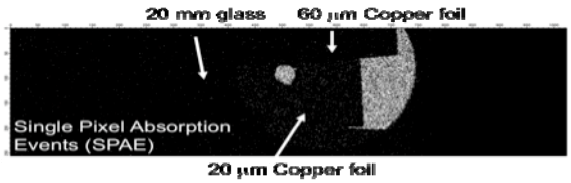

Fig. 2: The measured x-ray beam profile on the CCD.

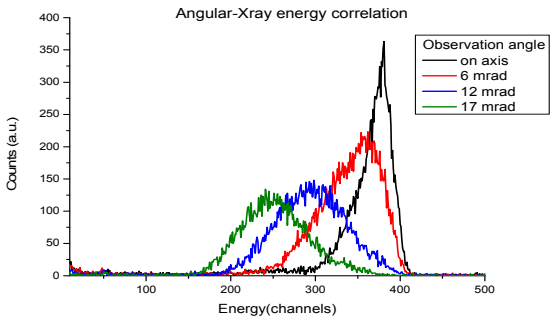

Fig. 3: Angular-energy correlation of the x-ray beams.

References

[1] T. Guo, Laser and photonics Rev. 3, 591 (2009)
[2] XFEL project DESY, Hamburg, Germany
[3] E. Esarey, et al., Phys. Rev. E. 48, 3003 (1993)

Laser Driven X-ray Radiography on Warm Dense Matter*

D. C. Hochhaus[1,2,3,#], B. Aurand[1,4], M. Basko[1,8], B. Ecker[4,6], T. Kühl[2,4], T. Ma[7], F. Rosmej[5], B. Zielbauer[2,6], D. Zimmer[2] and P. Neumayer[1,3]

[1]EMMI, Darmstadt; [2]GSI, Darmstadt; [3]FIAS, Frankfurt; [4]University of Mainz, Mainz; [5]UPMC, Paris, France; [6]HIJ, Jena; [7]LLNL, Livermore, USA; [8]ITEP, Moscow, Russia

Matter at high energy density (HED), at pressures exceeding 1 Mbar, is prevalent in many compact astrophysical objects. In the laboratory HED matter can be generated by use of high-intensity drivers, such as powerful lasers or heavy ion facilities. This offers the opportunity to test modelling of dense matter properties, such as the equation-of-state or opacities.

Using GSI's high-energy short-pulse laser facility PHELIX we have recently employed hot electrons to isochorically heat solid density matter. Upon laser irradiation of matter at relativistic intensities (>10^{18}W/cm^2) about 10% of the laser energy is converted to a fraction of energetic ("hot") electrons with ranges of several 100µm in matter at solid density. In our experiment we have irradiated Titanium wires (diameters 50 and 80µm) with laser pulses of up to 50J of energy. The K-alpha fluorescence excited within the target by the fast electrons is recorded with an absolutely calibrated spectrometer providing a spatial resolution of 25µm along the wire axis.

We have modelled the fast electron transport and K-alpha generation within the wire both with a 1D collisional model, where we include ohmic heating using the "rigid beam model" [1], and with the 3D hybrid PIC code ZUMA. Both models accurately reproduce the K_α emission emitted along the wire. This allows us to assess the energy deposited by the hot electrons in the bulk target. We find a temperature distribution reaching from >150 eV (wire-tip) down to ~2 eV (1000 µm from the tip).

The relaxation time of the hot electron population is of the order ps, short compared to the hydrodynamic evolution of the target. Thus the rapid heating is well separated in time from the subsequent expansion of the target.

We have employed the second laser beam of the new double-beam option of PHELIX to drive an intense hard x-ray back-lighter to take radiographic images of the exploding wire [2]. Variation of the delay between the heater and the back-lighter laser pulse allowed us to follow the wire expansion in time. Careful characterization of the x-ray back-lighter spectrum was required to determine the absolute mass density of the expanding matter for comparison of the radiographic images to radiation hydrodynamic calculations (fig. 1). The energy deposition as determined from the K_α emission was used as initial condition. Comparing simulations in 1D- and 2D-cylindrical geometry with and without radiation revealed that 2D effects as well as effects from radiation transport are negligible, and the expansion is well described as a 1D isentropic expansion.

* Work supported by EMMI and the Helmholtz Institue Jena.

#d.hochhaus@gsi.de

With this clean experimental realization of HED matter, these measurements hold the potential of an alternative method for testing EOS models in the WDM regime [4].

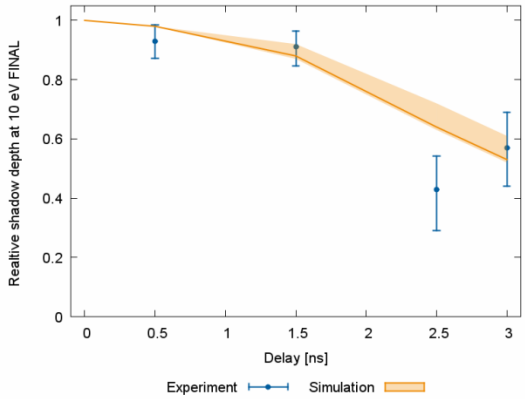

Figure 1: Comparison of radiographic shodow depth vs. 1D hydro-simulation of Titanium expanding at initially 10 eV and solid density

While the temporal and spatial resolution of the measurement are sufficient, improvements in the image signal-to-noise and back-lighter spectrum characterization are required to reduce the uncertainty of the absolute density measurement. We expect this to be feasible by shielding the intense x-ray emission from the tip of the laser irradiated wire and adding a static calibration target at the imaging plane.

To assess the potential of laser driven hard x-ray sources as back-lighters for dense plasmas created at FAIR, we have performed Monte-Carlo simulations of the back-lighter spectrum for various laser irradiation conditions. The calculations were benchmarked with results of the recent experiment on the back-lighter spectral composition. Our modelling shows that a 100J-class ps-laser driven x-ray source will provide a sufficient flux of x-ray radiation energetic enough to penetrate the high ρ-r targets as produced in HIHEX scheme

We believe this adds to the strong case for a high energy short pulse laser as diagnostic tool for plasma physics experiments at FAIR.

References

[1] J. R. Davies, Phys. Rev. E **68**, 056404 (2003)
[2] D.C. Hochhaus, GSI Sci. Rep. (2010)
[3] N.A. Tahir et al., Phys. Rev. Lett. **95**, 035001 (2005)
[4] M. E. Foord et al., Rev. Sci. Instr. **75**, 2586 (2004)

Intense-laser heating of micro-droplet targets at the PHELIX laser*)

P. Neumayer[1,2], B. Aurand[1,5,6], A. Gumberidze[1,2], D. Hochhaus[1,4], T. Kühl[1,3,5,6], R. Reuschl[3], D. Winters[3], N. Winters[3], Z. Yin[3], R. A. Costa Fraga[4], R. Grisenti[4], A. Kalinin[4], B. Ecker[5,6], M. C. Kaluza[7], J. Polz[7]

[1]EMMI/GSI, Darmstadt, Germany; [2]Frankfurt Institute of Advanced Studies, Germany; [3]GSI, Darmstadt, Germany; [4]Univ. Frankfurt, Germany; [5]Univ. Mainz, Germany; [6]Helmholtz-Institut Jena, Germany; [7]Univ. Jena, Germany;

Laser irradiation of matter at relativistic intensities results in a significant fraction of laser energy converted to hot (~MeV) electrons. When using "reduced-mass targets" with dimensions smaller than the range of these energetic electrons (~mm) electrostatic sheath fields confine the majority of the electrons to the target volume. This allows concentrating a large fraction of the laser energy to a small amount of matter, thus efficiently producing matter at extreme energy densities with moderate size laser systems (see e.g. [1,2]). Here we have used for the first time Rayleigh droplet beams (RDBs) as reduced mass targets, which offer an attractive alternative compared to individually mounted micron-sized targets that have been employed so far. A RDB is produced by forcing a liquid in a laminar flow through a small orifice into vacuum. Initially, the liquid emerges as a continuous, cylindrical jet, before it eventually spontaneously breaks up as a result of surface tension instabilities into a stream of spherical droplets. Liquid jets deliver a uniquely functional, boundary-free and self-replenishing target beam, and have found widespread applications in diverse interdisciplinary fields.

The experiments were carried out at the PHELIX facility at the GSI Helmholtz-Center for Heavy Ion Research at Darmstadt/Germany. For our experiment we have extracted laser pulses after the pre-amplifier stage, at an energy level of up to 5J. After temporal compression down to 370 fs, pulse energies of up to 2.5 J were available for irradiation of the droplet beams. The pulses were focused with a 90° off-axis parabola to a focal spot size of <6µm, producing peak intensities of 10^{19} W/cm^2. Synchronization of the droplets with the laser system is achieved by triggering the entire laser amplifier chain off a signal derived from the HF-oscillator that excites the piezo driving the Raleigh break-up of the droplet beam. The x-ray emission of the Argon droplets is spectrally dispersed by a cylindrically curved graphite crystal and the spectra are recorded using a back-illuminated scientific grade CCD-camera (Andor DX420-BN). The spectral range of the spectrometer was designed to cover the entire K-shell emission spectrum of Argon, reaching from the cold K-alpha line at 2.96keV to the Hydrogen-like Argon 1s-2p transition (Ly-alpha) at 3.32 keV. Fig. 1 shows a typical spectrum obtained from a 20µm diameter Ar-droplet, irradiated with 2.4 J of laser energy. The strong He-like line emission at 3.14 keV as well as the Ly-alpha line is attributed to the high-temperature (kT~keV) blow-off plasma, where the laser pulse is absorbed at the critical density. The K-alpha line originates from fluorescence decay following collisional ionization of K-shell electrons by the relativistic electron population produced in the intense laser plasma interaction. The total yield of K-alpha radiation indicates a coupling of 1.5% of the laser energy to relativistic electrons.

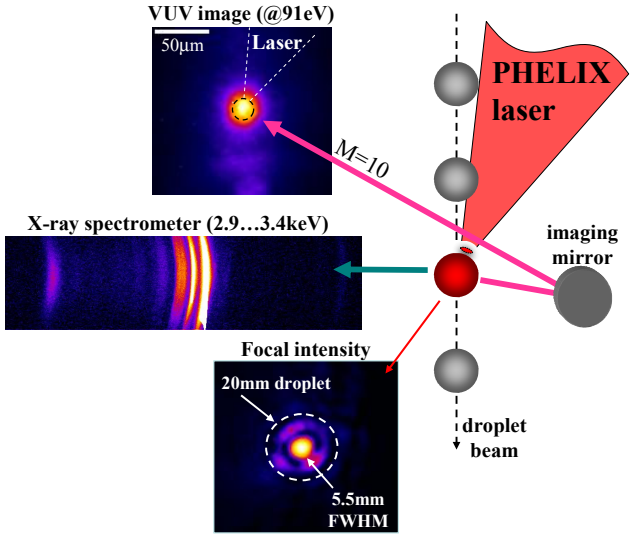

Figure 1: Schematic of the experimental setup

The strong K-alpha line observed from our spectra is emitted from Ar-ions with charge states Ar1+ to Ar8+. Higher charge states appear as satellites at higher photon energies. Detailed fitting of these spectra shows an increased charge state indicating heating of the solid-density droplet by thermalization of the relativistic electron population to temperatures well above 100 eV. Time-integrated high-resolution 2D-images of the droplet thermal XUV emission in a narrow spectral range around 13.7 nm indicate that the droplet remains close to its initial size for an extended time, thus supporting the conclusion that the droplets are in fact isochorically heated to matter in the regime high-energy density.

This demonstrates the potential of droplet beams as a self-replenishing source of mass-limited targets enabling generation of samples of matter at high-energy density at high repetition rates for precision experiments. Using the recent data, our modelling suggests that matter at Gbar pressures can be reached when using the full laser energy available from PHELIX. Future experiments are planned to explore this potential.

References

[1] P.M. Nilson *et al.*, Phys. Rev. E 79 (2009) 016406.
[2] P. Neumayer *et al.*, High Energy Density Phys. 5 (2009) 244.

*) this work is supported by the Helmholtz Institute Jena and EMMI

Towards seeded X-ray lasers at PHELIX*

B. Ecker[1,2,#], E. Oliva[6], B. Aurand[2,3,4], D. C. Hochhaus[3], T. Kuehl[2,4], P. Neumayer[3], H. Zhao[4], B. Zielbauer[4], K. Cassou[5], S. Daboussi[5], O. Guilbaud[5], S. Kazamias[5], D. Ros[5], T. Le[6] and P. Zeitoun[6]

[1]Helmholtz Institute Jena, Germany; [2]Johannes Gutenberg University Mainz, Germany; [3]ExtreMe Matter Institute EMMI, Germany; [4]GSI Helmholtzzentrum fuer Schwerionenforschung, Germany; [5]LASERIX-CLUPS / Laboratoire de Physique des Gaz et des Plasmas, France; [6]Laboratoire d'Optique Apliquée, ENSTA, École Polytechnique, France

Plasma-based X-ray lasers (XRL) possess several disadvantageous properties that are related to their generation process. Being based on the amplification of spontaneous emission (ASE), XRL can not provide a significant degree of spatial coherence and the beam profiles are dominated by characteristic speckle-patterns. The circumvention of these undesired properties consists in injection-seeding the XRL medium with a spectrally matched XUV pulse of a second source, which is typically either based on high-order harmonic generation (HHG) [1, 2] or a second XRL [3, 4]. HHG sources provide high-quality XUV beams but suffer from small conversion efficiencies. The spectral overlap between one of the harmonic lines and the XRL transition needs to be ensured, which can be problematic especially when working with a Nd:Glass laser like PHELIX [5]. The spectral width of HH radiation is significantly larger compared to the line width of the XRL transition. This alleviates the spectral matching but reduces the efficiency of the seeding process. Utilizing a second XRL for seeding is more demanding on the laser system in terms of the required pump energy and can not provide the beam quality offered by HHG. However, successful seeding experiments have been reported utilizing these techniques, demonstrating fully coherent and diffraction limited XRL beams.

On the road of improving the beam quality of the XRL at GSI we developed a setup that allows us to operate two independent XRL targets simultaneously. The setup is based on the in-house developed DGRIP pumping technique [6], allowing for an efficient pumping including the travelling wave excitation (TW) for both of the targets. The setup also relies on the PHELIX double-beam option originally developed for pump-probe experiments that is available since November 2010. This way, each of the two XRL targets can be pumped by its individual pump beam (Fig. 1). Due to the symmetry of the setup the XRL output of the two targets is propagating in opposite directions. The XRL pulses can be diagnosed separately or be combined in a seed/ amplifier configuration. For the latter option one can use a spherical XUV mirror to image the output of the first XRL target into the gain zone of the second.

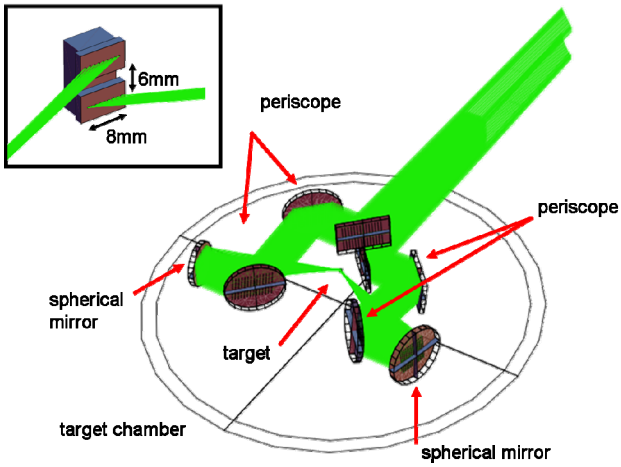

Figure 1: The Butterfly Configuration. The inset gives a more detailed view of the target arrangement [7].

A first successful experiment using this experimental scheme that we refer to as Butterfly configuration has been carried out in 2011. The results hold the promise of the determination of the life time of the gain in a transient, Ni-like silver XRL [8]. Simulations of the temporal development of the seeded XRL signal utilizing the Maxwell-Bloch code DeepOne [9] are in progress. A succeeding beam-time in 2012 is planned using molybdenum as target material, allowing us to carry out the experiment at higher laser repetition-rate and thus provide more valuable input for the development of the DeepOne code.

References

[1] Ph. Zeitoun et al., Nature 431, (2004).
[2] Y. Wang et al., Nature Photonics 2, 94-98 (2008).
[3] M.Tanaka et al., Optics Letters 28, 1680-2 (2003).
[4] M. Nishikino et al., Physical Review A 68 (2003)
[5] D. C. Hochhaus et al., Applied Physics B (2010).
[6] D. Zimmer et al., Optics Express 13, 2403 (2008).
[7] B. Ecker et al., Proc. of SPIE, San Diego (2011).
[8] B. Ecker et al., to be published.
[9] E. Oliva et al., Phys. Rev. A 84, 013811 (2011).

* Work supported by EMMI and the Helmholtz Institute Jena.

#b.ecker@gsi.de

Characteristic X-rays generation under the action of femtosecond laser pulses on nano-structured targets

O.F. Kostenko[1], *M.B. Agranat*[1], *N.E. Andreev*[1], *O.V. Chefonov*[1], *V.E. Fortov*[1], *A.V. Ovchinnikov*[1], *O.N. Rosmej*[2], *J.L. Duan*[3], *and J. Liu*[3]

[1]Joint Institute for High Temperatures RAS, Moscow, Russia; [2]GSI Helmholtzzentrum für Schwerionenforschung, Darmstadt, Germany; [3]Institute of Modern Physics, Chinese Academy of Sciences, People's Republic of China

Enhancement of K_α yield from a metal foil covered with metal rods of submicron sizes, with low aspect ratio, irradiated by a p-polarized femtosecond laser pulses of about 10^{17} W cm^{-2} intensity is demonstrated [1]. Obtained relative increase in K_α X-ray line emission is explained with a model of vacuum heating of fast electrons [2, 3].

An absolute yield of X-ray characteristic K_α-radiation for p-polarized laser pulses was investigated experimentally depending on a target type. There were three target types used: Cu foils of 8 and 31 μm thicknesses and a target with Cu rods. The Cu nano-rods target consists of about 10^8 rods cm^{-2}, each of 500 nm in diameter and about 1 μm of height (about 20% of the solid density). The nano-rods were supported by the 8 μm thick Cu layer, obtained by means of electrochemical deposition. This layer serves as a bulk material for production of K_α-radiation by hot electrons generated in the interaction of ultrashort laser pulses with the nano-structured surface.

A laser energy value in the experiments was 9.2 ± 0.5 mJ. With pulse duration of 40 fs and laser spot diameter of 14 μm, it results in the maximum laser intensity on a target surface of 1.4×10^{17} W cm^{-2}. Amplified spontaneous emission intensity in the nanosecond time domain does not exceed 10^{-8}. The angle between a target surface normal and a p-polarized laser beam was set to be $45 \pm 2^\circ$. X-ray characteristic spectra were investigated using absolutely calibrated focusing crystal von Hamos spectrometer. The angle of inclination of the spectrometer axis to the target surface normal was 30°.

In spite of the high contrast laser pulses used in the discussed experiments, pilot modeling of the surface modifications under the action of the nano-second prepulse showed some smearing of the initial inhomogeneity of the target surface covered with micron sized rods. At the same time, a surface roughness with the typical scale on the order of micron remains, keeping sharp density gradients. To estimate the influence of a clustered surface on K_α generation, we considered the model of characteristic X-ray emission from a foil covered with half-spherical clusters (as an approximate model of the surface with rods of low aspect ratio modified by prepulses) taking into account given laser pulse and target parameters.

Calculations carried out for polished copper foils of 8 and 31 μm thicknesses according to the model with Maxwellian distribution of hot electrons [2] give K_α yields from the foil front side of 4.4×10^8 and 6×10^8 photons, respectively. Taking into account isotropic emission of X-rays in the context of considered model, these numbers (recalculated per steradian) are in reasonable agreement with measured K_α yields $(0.95 \pm 0.2) \times 10^8$ and $(1.3 \pm 0.2) \times 10^8$ photons (steradian$\times$pulse)$^{-1}$, respectively, and reproduce well the relative increase of K_α emission with increase of the foil thickness.

For a foil, as in case of a solid substrate [3], dependence of K_α yield on the cluster size shows a sharp maximum at $\rho = \pi D/\lambda \approx 1$, with D being the cluster diameter (Fig. 1). Measured relative increase in X-ray yield from the foil of 8 μm thickness with clustered surface equal to 1.7 is best fitted by the clusters of 0.5 μm diameter at $\rho = 2$. This increase is caused by enhancement of accelerating electric field at the cluster surface [3].

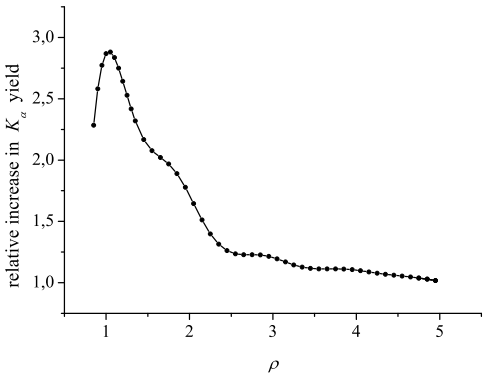

Figure 1: Relative increase in K_α yield from a copper foil of 8 μm thickness versus ρ.

Obtained results indicate an applicability of the used model, based on the vacuum heating of electrons, under conditions of carried out experiments and show an availability of nano-structured targets for increasing of K_α radiation under the action of high contrast femtosecond laser pulses.

References

[1] A. V. Ovchinnikov, O. F. Kostenko, O. V. Chefonov, O. N. Rosmej, N. E. Andreev, M. B. Agranat, J. L. Duan, J. Liu, and V. E. Fortov, Laser Part. Beams **29**, 249 (2011).

[2] O. F. Kostenko and N. E. Andreev, Contrib. Plasma Phys. **51**, 463 (2011).

[3] O. F. Kostenko and N. E. Andreev, Phys. Scr. **81**, 055505 (2010).

Classical radiation effects on relativistic electrons in ultraintense laser fields *

T. Schlegel[1] *and V.T. Tikhonchuk*[2]

[1]Helmholtz-Institute, Jena and GSI, Darmstadt, Germany; [2]University Bordeaux 1 - CNRS - CEA, CELIA, UMR 5107, F-33400 Talence, France

The propagation of relativistic electrons with the initial energies $> 100\,\mathrm{MeV}$ in a number of simple laser field configurations with circular polarization was studied by solving the relativistic equation of motion in the Landau-Lifschitz approach [1], to account for the radiation friction force. The radiation back-reaction on the electron dynamics becomes visible at dimensionless field amplitudes $a > 10$ at these high particle energies. Analytical expressions could be derived for the energy and the longitudinal momentum of the electron, the frequency shift factors of the light scattered by the electron and the particle trajectories. These findings were compared with the numerical solutions of the basic equations. A strong radiation damping effect results in reduced light scattering forming at the same time a broad quasi-continuous spectrum [2].

In this Contribution, the electron dynamics in the strong field of a quasistationary laser piston is reported (see Fig. 1), which may serve as an efficient ponderomotive ion acceleration scheme [3]. The radiation friction force may stop an escaping relativistic electron after the propagation over several laser wavelengths at high laser field strengths, which supports the formation of a stable piston regime.

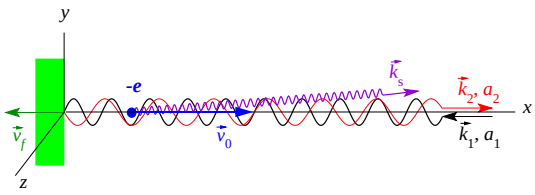

Figure 1: Interaction scheme: A relativistic classical electron escapes the quasistationary laser piston, which is pushed by an ultraintense plane laser wave (amplitude a_1, wave vector $\vec{k}_1$, carrier frequency $\omega_1 = k_1\, c$) with the velocity $\vec{v}_f$. The electron has the initial velocity $\vec{v}_0$ and interacts with the fields of the incident $\vec{k}_1$ and reflected $\vec{k}_2$ laser waves. Thereby, high-energy photons are transmitted due to nonlinear Thomson scattering as well as due to emission by the electron itself.

It is instructive to study the electron trajectories and the related radiation spectra. The spectral intensities of the first ten harmonics emitted in the drift direction of the electron along the x-axis (towards the incident wave) at disregarded radiation damping are displayed in Fig.2 (a). Panel (b) shows the corresponding spectra for the case of a standing wave, when a laser wave with the same field amplitude is totally reflected by a static mirror. The spectra of both demonstrated cases are normalized with help of the corresponding upshift factors M_p and M_s. The analytical estimate for the piston case is $M_p = (1+\overline{\beta_x})/(1-\overline{\beta_x})$, with the averaged drift velocity $\overline{\beta_x} = \beta_0\sqrt{1-2a_1^2/[\gamma_0^2(1+\beta_f)]}$, where β_f is the piston velocity v_f normalized to the speed of light. It amounts to ≈ 21 for the initial parameters used in this figure. In the standing wave case, we get $M_s = 16$ for $\overline{\beta_x} = \beta_0\sqrt{1-2a_1^2/\gamma_0^2}$.

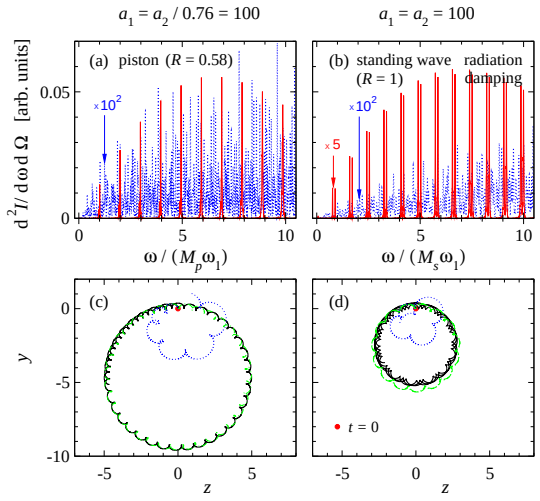

Figure 2: Electron motion in the ultrastrong field behind a stationary laser piston (a, c), and in a standing wave with the same incident laser field. Spectral intensities of the radiation emitted in the direction of the electron drift motion without the radiation damping effect (solid lines) and with the account for this effect (dotted curves in the background) are plotted in the upper panels (a) and (b), the transverse projections of the electron trajectories with radiation damping (dotted curves) and without it (solid lines) are depicted in the lower panels (c, d). The initial electron energy is $\gamma_0 = 300$, the laser field strenghts are given in the panel titels. The dot-dashed curves display analytical estimates derived in the proper frame of the electron.

References

[1] L.D. Landau, E.M. Lifshitz, *The Classical Theory of Fields* (New York: Pergamon) 1994.

[2] T. Schlegel and V.T. Tikhonchuk, subm. *New J. Phys.* (2012).

[3] T. Schlegel et al., *Phys. Plasmas* **16** (2009) 083103.

* Work supported by the Region Aquitaine under project No. 34293, by the European support program Marie Curie IRSES project # 230777, and by EURATOM in the framework of keep-in-touch activities

Cryogenic Targets for Laser and Particle Beams*

S. Bedacht[1], *G. Schaumann*[1], *A. Blazevic*[2], *M. Roth*[1], *and D.H.H. Hoffmann*[1]

[1]Technische Universität Darmstadt, Darmstadt, Germany; [2]GSI Helmholtzzentrum für Schwerionenforschung GmbH, Darmstadt, Germany

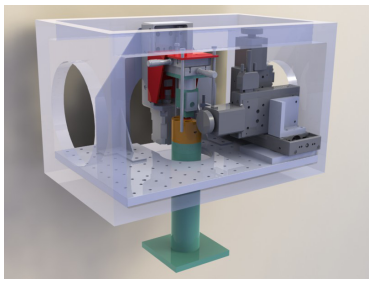

Figure 1: Drawing of the cryogenic test rig

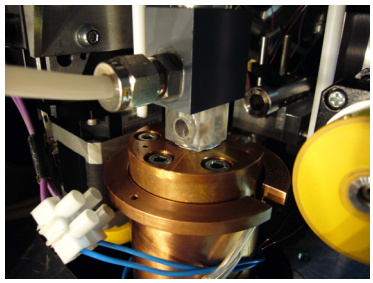

Figure 2: Photograph of the growing chamber

Abstract

Laser driven particle acceleration and measurements of ion energy loss in plasma largely rely on suitable targets to achieve good particle beam and plasma quality. Recent research results [2] indicate that cryogenic targets allow for very high ion energies. Advantages of our cryogenic targets include high purity at solid density in a self-supported structure as well as fitness for medium repetition rates.

Within the HIGH POWER LASER ENERGY RESEARCH (HiPER) collaboration our group works on thin cryogenic targets from deuterium and hydrogen to be used in experiments on laser driven ion acceleration and energy loss in plasma.

Experimental Setup

Our setup for making cryogenic targets consists of a vacuum chamber with a cooling head attached, a custom-built growing chamber, and various diagnostics. With this setup we are able to make cryogenic targets from a large variety of gases, including argon, deuterium, hydrogen, and neon (see [1]).

In 2011 we improved the experimental setup for growing the targets significantly and we were able to make solid cryogenic targets with an initial thickness of some micrometers from deuterium. We installed an actively cooled shield for shielding the target from thermal radiation and a heating device so that the temperature inside the growing chamber can be adjusted accurate to 0.1 Kelvin.

To measure the thickness of the target in real-time we installed an interferometer with an accuracy better than 0.1 micrometer. A motorized three axis system of linear stages to scan the target surface and generate a surface profile is currently under construction. A drawing of our experimental test rig and a photograph of the growing chamber are shown in Figure 1 and Figure 2, respectively.

Outlook

For 2012 we have been granted several weeks of beamtime at both the PHELIX and the UNILAC facilities for experiments with cryogenic targets. The beamtime granted will be divided in at least two experimental campaigns.

One of these campaigns will aim at accelerating protons to energies above 100 MeV by exploiting the BREAKOUT AFTERBURNER (BOA) regime [2]. Therefore, targets with thicknesses in the range of tens of nanometers to few micrometers are necessary.

In another experimental campaign we will use cryogenic targets to generate homogenous plasma at high densities. Therefore, we will heat the target directly with the PHELIX beam and measure the energy loss of heavy ions accelerated by the UNILAC transversing plasma created. [3]

References

[1] J. Menzel, Aufbau und Inbetriebnahme einer Kryoanlage zur Targeterzeugung für Experimente mit Hochenergielasern und Schwerionenstrahlen, PhD Thesis, 2010

[2] L. Yin et al., Monoenergetic and GeV ion acceleration from the laser breakout afterburner using ultrathin targets, Phys. Plasmas 14, 056706 (2007)

[3] W. Cayzac et al., Towards the nonlinear regime of ion stopping in plasma, this Scientific Report

*Work supported by HIGH POWER LASER ENERGY RESEARCH (HiPER) and BUNDESMINISTERIUM FÜR BILDUNG UND FORSCHUNG (BMBF).

Spherical theta pinch for plasma stripper applications

C. Teske[1], Ge Xu[1], J. Jacoby[1], Ying Liu[1], and J. Wiechula[1]
[1]Inst. für Angewandte Physik, J. W. Goethe-Universität, D-60438 Frankfurt am Main, Germany

A spherical theta pinch (spherical θ-pinch) plasma source has recently been investigated by the authors for a large variety of applications such as pulsed ion sources and plasma strippers. The progression of the corresponding experimental setup with discharge energies starting from 100 J and leading up to the recent device with more than 2 kJ has been documented in a variety of publications [1, 2]. A major feature of the discharge device is a large spherical vessel surrounded by a multi-turn induction coil which is connected to a capacitor bank via low inductance transmission line. The resulting resonant circuit usually has an eigenfrequency of 10 kHz up to 30 kHz, depending on the overall capacitance. Experimental data thus far shows that the spherical θ-pinch has an excellent energy transfer efficiency of up to 85% if the resonant circuit is matched to the discharge. Further, it has been demonstrated that this pulsed inductive discharge device can be driven by power semiconductors, thus, enabling a higher pulse repetition rate [1, 2].

Based on the latest insights regarding the spherical θ-pinch a plasma stripper is now being set up with pulse energies of more than 4 kJ and induction fields of 1 T which is supposed to be assembled at the GSI facility.

The measurements performed with the current experimental setup of the spherical θ-pinch revealed further support for the suggested high energy transfer efficiency of the experimental device and its potential to be used as a high efficient plasma source [1]. The issue of transformer coupling between the primary circuit and the discharge plasma and its importance concerning the transfer efficiency has also been investigated [1]. Finally, a firm evidence of the plasma contraction in form of a photographic sequence has been presented [1, 2], which is of considerable interest for the application as a stripper device to enhance the charge states of high energy ions.

Since higher pulse repetition rates are desirable for the application as a plasma stripper, a suitable solid state switch for the pulsed inductive discharge has been developed and tested [2]. The authors have already made some experiments with a smaller stack for inductive discharge generation, though the current rise times were limited to less than 1 kA/µs and the pulse energy was well below 100 J. However, for the setup of a pulsed inductive plasma stripper device a more sophisticated switch had to be designed in order to achieve the required pulsed power specifications. First experiments with the spherical θ-pinch have shown that a transfer efficiency of up to 85% can be achieved with the current experimental setup. The authors conclude that the energy transfer efficiency achieved is mostly due to the improved transformer coupling between primary circuit and discharge plasma. Also, the transfer efficiency as a function of the gas pressure and the load voltage of the capacitors has been measured. The experimental evidence presented in [1, 2] shows a shift of the transfer efficiency maximum to higher gas pressures with higher load voltages. Mean power values reached more than 2 MW inside the plasma.

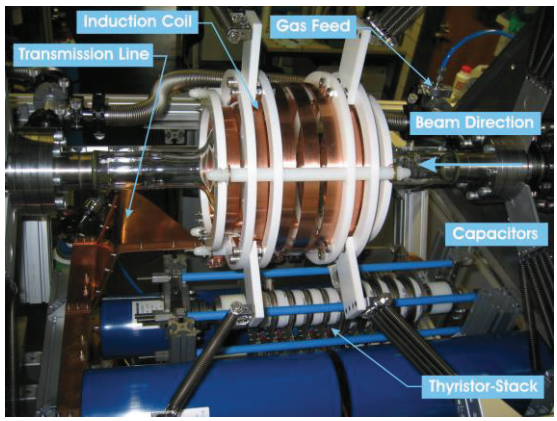

Fig. 1: Experimental setup of the plasma stripper device.

Further investigations will include beam plasma interactions at the Z 6 experimental location in order to determine the achievable charge states of the beam ions while traversing through the pinch plasma.

Acknowledgments

The authors wish to acknowledge the support of the BMBF (German Ministry for Education and Science) under the contract 06FY9082I.

References

[1] C. Teske, J. Jacoby, F. Senzel and W. Schweizer: *Energy transfer efficiency of a spherical theta pinch*. Phys. Plasmas **17**, 043501 (2010).

[2] C. Teske, Y. Liu, S. Blaes and J. Jacoby: *Electron density and plasma dynamics of a spherical theta pinch*. Phys. Plasmas **19**, 029203 (2012).

Investigating a colliding plasma

J. Wiechula[1,3], Ch. Hock[1], M. Iberler[1], J. Jacoby[1], B.-J. Lee[2], J. Otto[1, 3], T. Rienecker [1], A. Schönlein[1,3] and C. Teske[1]

[1] Inst. Für Angewandte Physik, Goethe-Universität, Frankfurt am Main, Germany; [2]Pohang Accelerator Laboraty, Pohang, Korea; [3]ExtreMe Matter Institute, Darmstadt, Germany.

The collision of two plasma sheets, induced by two identical coaxial plasma accelerators (PAs) is under investigation to provide an intense UV/VUV radiation source. The acceleration of the plasma sheets is based on the Lorentz force and can be described by the snowplough model (SPM) [1].

According to the SPM a plasma sheet accelerated by the Lorentz force drags the neutral gas out of the PA. The magnetic field behind the plasma sheet functions as a magnetic piston. Due to the acceleration of the plasma a strong shockwave is formed, that is able to pre-ionize the neutral gas. This preceding shockwave is used as an additional heating in the collision area.

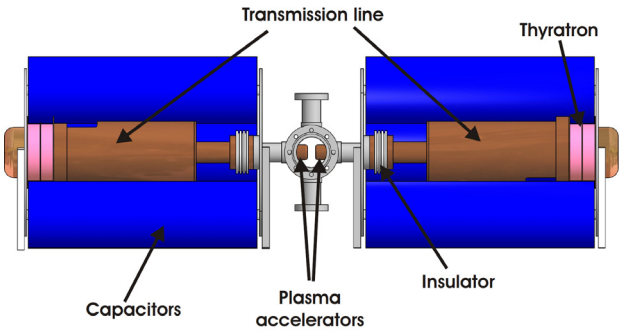

Fig.1: Experimental setup

The used PAs shown in Fig 1 consist of massive outer and massive inner electrodes made of copper. PEEK is used as an insulator between both electrodes. First experiments were performed using three parallel connected capacitors (4000 V, 3 µF) on one side and on both sides. Due to low inductance a maximum current of 34kA was reached with this configuration.

A single accelerator was used to optimize the PAs. Therefore plasma parameters, like electron density, the transfer efficiency and the velocity as well as the discharge behaviour of the plasma have been studied. To determine the transfer efficiency the damping of RLC circuits from a short circuit was compared to that in plasma operation. A maximum efficiency of 45% was reached. It was shown that with increasing gas pressure the efficiency is decreasing. The electron density was measured using the Stark broadening of the Hβ Line. The electron density is increasing with increasing gas pressure and had a maximum of $3*10^{15}$ cm^{-3}. The velocity was measured using a photodiode array. A typical sequence is shown in fig. 2. The results given by the photodiode array have been compared with a sequence of pictures taken from a fast shutter CCD camera. Both results were found to be in good agreement with each other. The maximum measured velocity with a stored energy of 72 Joule was around 23 km/sec.

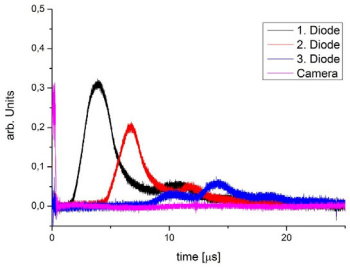

Fig.2: Photodiode signals

Recently first pictures taken from a fast shutter CCD camera provided first information about the collision of the two plasma sheets (fig 3.). Each picture from the collision area has a delay of 1µsec. The propagation as well as the collision of the plasma sheets can be seen. Starting with picture 3 a flash in the middle of the two plasma fronts appears that ends on picture 5.

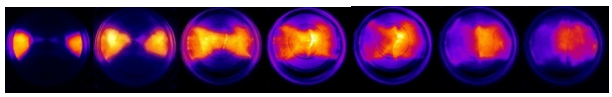

Fig.2: CCD Pictures from a plasma collision

It is intended to conduct further experiments with stored energies up to 1.35 kJ, an applied voltage up to 10 kV on each side and to compare the results from a single accelerator to those of the collision case. By increasing the stored energy stepwise it is possible to reveal the behaviour of the emitted UV/VUV radiation depending on the stored energy.

References

[1] J. Jacoby, C. Bickes, D.H.H. Hoffmann, C. Hofmann, J. Philipps, "Experimental study to accumulate, accelerate and focus a massive plasma beam onto a target", Fusion Engineering and Design, 44: 331-334, 1999.

Non-invasive, electron beam based profile measurement of strongly focused, intense heavy ion beams*

S. El Moussati[1], S. Udrea[1], D.H.H. Hoffmann[1], A. Hug[2], D. Varentsov[2]

[1]TU Darmstadt, Germany; [2]GSI, Darmstadt, Germany

At the HHT area of GSI strongly focused intense beams of heavy ions are used to generate high energy density (HED) and warm dense matter (WDM) through their impact on solid targets. Typically experiments are carried out with $^{238}U^{73+}$ beams with a specific energy of 200 – 500 AMeV, an intensity of 10^8 – $5{\cdot}10^9$ particles and pulse durations between 100 and 1000 ns FWHM.

In order to reach the physical states of interest these beams have to be strongly focused at the target into a spot with diameter of less than 1 mm. Since energy deposition in the target depends on the transverse beam intensity distribution, this distribution has to be precisely determined. Typical measurement techniques, which employ wire grids or solid state scintillators, are not applicable because such detectors have a strongly non-linear response at very high intensities and also get destroyed after few shots.

Gas as scintillator has been also investigated in the last few years [1]. While promising results have been already obtained, the optimization of this measurement method is still problematic.

An alternative, non-invasive method to determine the transverse intensity distribution of an intense ion beam is to use an electron beam and measure its deflection, as caused mainly by the electrical field of the ion beam. This method has been already applied to diagnose charged particles at different accelerator facilities [2, 3]. Nevertheless, for keeping the setup as simple as possible, a single shot system is under consideration. Thus the electron beam is supposed to have a larger diameter than the ion beam and the alteration of its transversal intensity distribution is to be measured by means of a thin, plane scintillator. To estimate the feasibility of the method we have performed numerical simulations, which are presented in this article. For this we used a custom developed code which tracks the electrons in a given electrical field.

Simulations

To show that one can distinguish between different ion beam distributions and widths the calculations were performed assuming Gaussian and Lorentz transversal charge distribution respectively. For the ion beam an energy of 350 AMeV, an intensity of $3{\cdot}10^9$ particles and a duration of 100 ns were considered. The electron beam had an energy of 10 keV, a Gaussian transversal intensity distribution and a divergence of 10^{-2} rad. The results are shown in figures 1 and 2.

* Supported by BMBF and the Helmholtz Russia Joint Research Group.

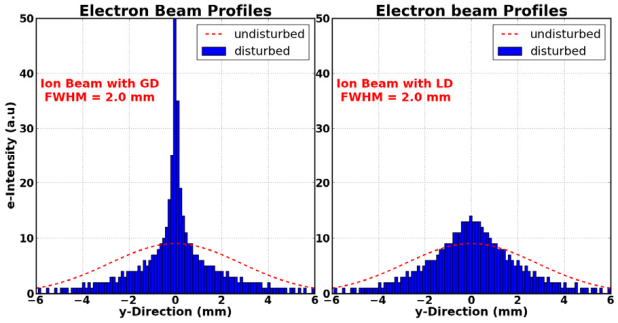

FIG. 1: The alteration of the electron beam profiles at the detector after passing through an ion beam with Gaussian (left) and Lorentz (right) transversal intensity distributions, both with 2.0 mm FWHM.

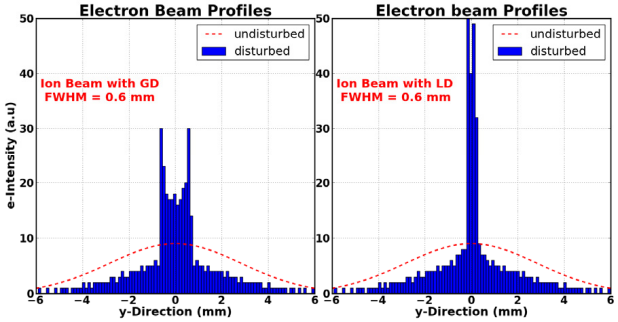

FIG. 2: The alteration of the electron beam profiles by ion beams with transversal intensity distributions like those in FIG. 1, and with 0.6 mm FWHM.

Conclusion

An electron beam diagnostic device for the measurement of the transverse intensity distribution of strongly focused, high intensity heavy ion beams is presently under development at the HHT experimental area. First numerical simulations show that such a system is suitable to distinguish between different cylindrical symmetric transversal distributions of the ion beam and allow for the measurement of the width of the given distribution.

References

[1] D. Varentsov *et al*, Contributions to Plasma Physics, **48**, pp. 586-594 (2008).

[2] Prabir K. Roy *et al*, Review of Scientific Instruments, **76**, 023301 (2005).

[3] W. Blokland *et al*, Proceedings of HB2010, Morschach, Switzerland, pp. 438-442 (2010).

Simulations of Beam–Matter Interaction Experiments at the HiRadMat Facility at CERN*

N.A. Tahir[1], J. Blanco Sancho[2], A. Shutov[3], R. Schmidt[2], and A.R. Piriz[4]

[1]GSI, Darmstadt, Germany; [2]CERN, Geneva, Switzerland; [3]IPCP, Chernogolovka, Russia; [4]UCLM, Ciudad Real, Spain

The Super Proton Synchrotron (SPS) at CERN accelerates 288 bunches of 440 MeV protons with each bunch having about 1.15×10^{11} particles (nominal parameters). The bunch length is 0.5 ns and two neighboring bunches are separated by 25 ns so that the duration of the entire beam is 7.2 μs. The focal size can go down to 0.1 mm σ_{rms}, thus providing a very dense beam (energy/size). The spot size can be tuned ranging from 0.1 mm to 2 mm. We have carried out numerical simulations of heating of solid copper cylindrical targets that are impacted by the SPS beam. We consider three different focal spot sizes characterized by σ = 0.1 mm, 0.2 mm and 0.5 mm, respectively, which are the typical parameters that will be used in the experiments to be carried out at the HiRadMat facility [1]. The target length is 1.5 m and its radius is 5 cm. These simulations have been carried out using the energy deposition code, FLUKA and the 2D hydro code, BIG2, iteratively.

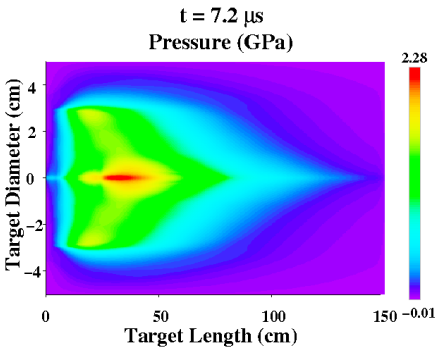

Figure 1: Pressure distribution at t = 7.2 μs.

In the present contribution we summarize results for one case only, namely, σ = 0.5 mm while further details can be found in [2]. These simulations show that at t = 7.2 μs (end of the beam), a maximum specific energy of about 7 kJ/g is deposited along the axis which leads to a temperature of around 11000 K. The corresponding thermal pressure distribution is presented in Fig. 1 which shows a maxima of 2.28 GPa. The minimum density is of the order of 1.2 g/cm^3 (about 13 % of the solid density). This shows that the inner part of the target is severely damaged. Study of the long term evolution of pressure is also very important for the target stability during the experiments. In Fig. 2 we plot the pressure distribution at t = 12 μs. where the pressure wave has just arrived at the cylinder surface and the pressure has a value = 0.8 GPa. Fig. 3 shows that

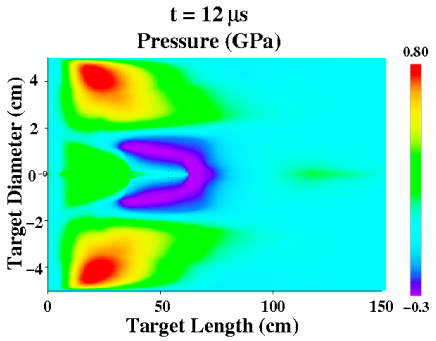

Figure 2: Pressure distribution at t = 12 μs.

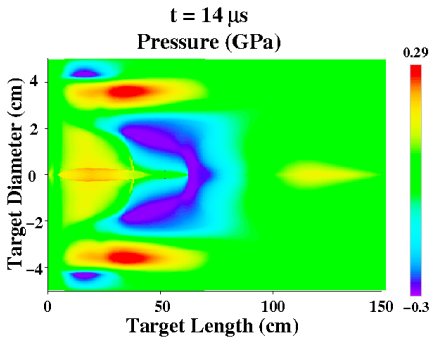

Figure 3: Pressure distribution at t = 14 μs.

at t = 14 μs, the pressure wave is reflected at the boundary along the radial direction. Negative pressure near the surface shows the action of the tensile force to restore the target to its original shape. Moreover, the maximum pressure has been reduced to 0.29 GPa while the negative pressure is -0.3 GPa. It is also interesting to note that there is a V–shaped region of negative pressure in the inner part of the target. Simulations have been done up to t = 20 μs which show that the von Mises parameter in the solid part of the target always remains less than 1 which implies that the material is in an elastic state.

References

[1] J. Blanco Sancho et al., Proc. IPAC11, San Sebastian, September 5 – 9, 2011.

[2] N.A. Tahir et al., Phys. Rev. Special Topics Accel. Beams (2012) Submitted.

* Work supported by the BMBF and EuCARD

Simulations of Interaction of 7 TeV/c LHC Protons With a Carbon Beam Stopper*

N.A. Tahir[1], J. Blanco Sancho[2], A. Shutov[3], R. Schmidt[2], and A.R. Piriz[4]

[1]GSI, Darmstadt, Germany; [2]CERN, Geneva, Switzerland; [3]IPCP, Chernogolovka, Russia; [4]UCLM, Ciudad Real, Spain

The Large Hadron Collider (LHC) is designed to collide two counter rotating ultra relativistic proton beams with unprecedented particle energy of 7 TeV. These beams have a fine time structure with each beam comprising of 2808 bunches, each bunch is made of 1.15×10^{11} protons (nominal intensity). The bunch length is 0.5 ns and separation between two neighboring bunches is 25 ns. This leads to a total beam duration of around 89 μs. The typical transverse intensity distribution is Gaussian with σ = 0.2 mm. The total number of protons per beam is 3×10^{14} that corresponds to an amount of energy of 362 MJ, sufficient to melt 500 kg copper. Safety of operation is an extremely important issue when working with such extremely powerful beams. An accidental release of even a very small fraction of the beam energy can result in severe damage to the equipment. One of the critical failure scenarios is when the entire beam is lost at a single point. To assess the damage caused in such an accident, we have carried out numerical simulations of the thermodynamic and the hydrodynamic response of a solid carbon cylindrical target that is facially irradiated by one LHC beam. These simulations have been performed using an energy deposition code, FLUKA, and a 2D hydrodynamic code, BIG2, iteratively. The iteration interval is determined by the time during which the target density is reduced by 10–15 %. The target length is 6 m, the radius is 5 cm (only inner 2 cm radius is shown in these figures) and the material density is 2.28 g/cm^3. In Fig. 1

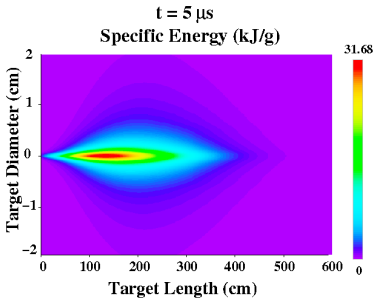

Figure 1: Specific energy deposition distribution at t = 5 μs.

we present the specific energy distribution in the target at t = 5 μs (200 bunches delivered). It is seen that the maximum specific energy deposition is arournd 30 kJ/g and the beam has penetrated up to 4 m. Fig. 2 shows the same variables as Fig. 1, but at t = 15 μs (600 bunches delivered). It is seen that the maximum specific energy deposition has increased to about 45 kJ/g while the beam has penetrated the entire 6 m length of the target due to the hydrodynamic tunneling phenomenon. This effect is occurs because the energy deposition by a few 10's of bunches leads to very high thermal pressure that launches an outgoing compression wave which leads to density depletion at the target axis. This allows the protons that are delivered in the subsequent bunches to penetrate deeper into the target, thereby causing a considerable range lengthening. The density depletion can be clearly seen in Fig. 3, where we present density distribution at t = 15 μs. These simulations have shown that the density depletion front moves in longitudinal direction with a speed of 25 cm/μs that implies that the beam will penetrate up to 25 m in solid carbon in 89 μs. The inner part of the target is severely damaged. Further details can be seen in [1].

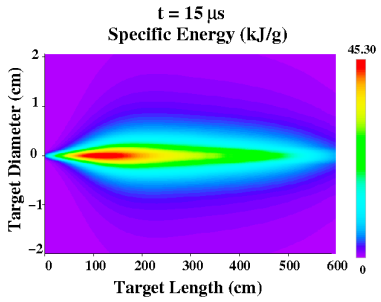

Figure 2: Same as in Fig. 1, but at t = 15 μs.

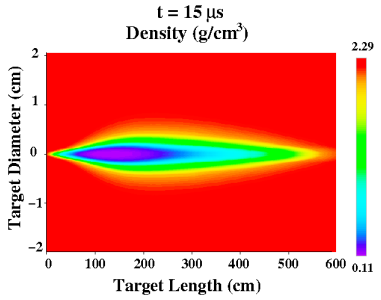

Figure 3: Density distribution in the target at t = 15 μs.

References

[1] N.A. Tahir et al., Phys. Rev. Special Topics Accel. Beams (2012) Submitted.

* Work supported by the BMBF and EuCARD

Data acquisition system for HHT experiments *

A. Hug[1], B. Ionita[2], A. Kantsyrev[3], L. Shestov[3], S. Udrea[2], and D. Varentsov[1]
[1]GSI, Darmstadt, Germany; [2]TU Darmstadt, Darmstadt, Germany; [3]ITEP, Moscow, Russia

At the HHT area of GSI intense focused beams of energetic heavy ions are used to generate high-energy-density (HED) states in matter, or so-called warm dense matter (WDM), by their impact on solid targets. This ongoing research is currently being done in the framework of a Helmholtz-Russia Joint Research Group *"Experimental Study on WDM by Intense Heavy Ion Beams"* with a goal to develop essential diagnostic instruments and methods for future HEDgeHOB experiments at FAIR.

The HED physics experiments at HHT run in repetitive single-shot mode where the data has to be acquired from numerous diagnostics instruments such as multi-channel digitizers and oscilloscopes, iCCD and streak cameras, target manipulators and delay generators. A highly heterogeneous detector and experimental instruments landscape makes the development of a corresponding hardware control (HC) and data acquisition (DAQ) systems a challenging task.

The developed DAQ system [1] is realized entirely in Python [2] — a powerful and easy-to-learn scripting language — exploring a scalable client-server architecture. The conceptual elements of the DAQ are the *Device Drivers*, *Device Servers*, and *Clients* (see Fig. 1). The main idea is to provide an access to any (remote) device independently of its nature, properties, function and hardware connection though a unified interface realized as a Python class (Device API). All the particularities of a device and its low-level access code are hidden from device users (clients) in a Device Driver object which is made visible to the outside by a Python script called Device Server. PYRO (Python Remote Objects) RPC library was chosen for client-server communications. It is important to note that the system is designed to be platform-independent and runs under any operating system.

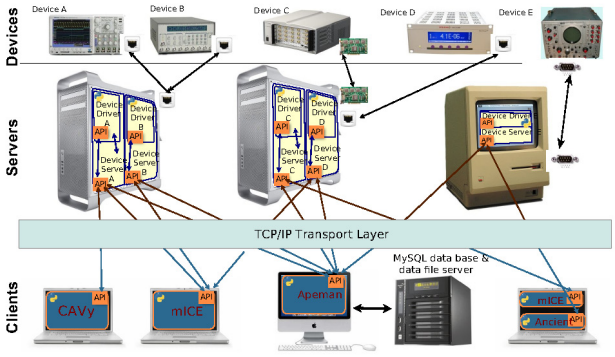

Figure 1: HHT DAQ architecture.

The experiment is controlled by a special client — Apeman which is checking the status of all devices to be used for the following shot, arms the devices, sends beam request to the accelerator, acquires the data from the devices and stores the acquired data in a MySQL database and on a file server (see Fig. 2).

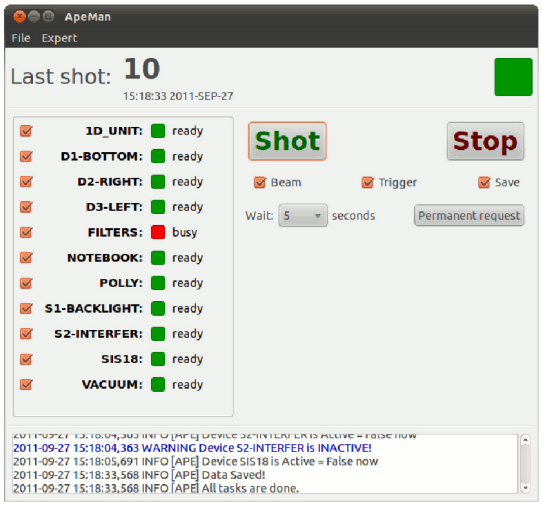

Figure 2: Apeman — client for controlling the experiment.

Besides device specific clients, there're also a few general purpose DAQ applications developed such as mICE (*devIce Control for Experiments*) for setting parameters of arbitrary device, CAVy (*Camera Adjustment View*) for controlling and adjusting CCD or other cameras, and OWL (*prOperty Watchdog Owl*) for on-line monitoring of device parameters and status (see Fig. 3).

Figure 3: Owl clients on the status screen.

The DAQ system has been successfully commissioned during a HED physics experiment at HHT in September 2011. It is planned to employ the developed system for the future proton microscopy (the PRIOR project) experiments at GSI as well as for similar experiments at ITEP and later — at FAIR.

References

[1] `http://www-linux.gsi.de/~hug/daq/`.
[2] `http://www.python.org`.

* Supported by Helmholtz-Russia Joint Research Group 112 and FRRC

Development of a high current gas discharge switch for the FAIR magnetic horn

Ch. Hock, M. Iberler, J. Jacoby, G. Loisch, A. Schönlein, J. Wiechula
J. W. Goethe University Frankfurt, Institut für Angewandte Physik, 60438 Frankfurt

The planed Facility for Antiproton and Ion Research (FAIR) is a new international accelerator laboratory at the GSI in Darmstadt, Germany. The main research topic at this facility is aimed to heavy ion research and protons and anti protons colliding experiments. To produce this antiprotons (3GeV), protons (29GeV) will be shot on a target (e.g. Iridium). In order to focus these antiprotons for experiments, a strong magnetic field will be applied by a so called magnetic horn. To generate for this application the necessary high magnetic field the designed stripline of the pulse forming network (PFN) has to handle a peak current of 400kA with a pulse length of 20µs. Currently the only possibility to handle this high current is the use of mercury filled Ignitrons. Another application for the need of high power switches is to control the FAIR SIS injection and extraction magnets. The requirements for this switch are a hold off voltage of about 80kV and maximum currents of about 8kA with a pulse length in the range of µs.

The working group plasma physics at the University of Frankfurt develops a mercury free switch, which is able to replace the Ignitrons in the PFN of the magnetic horn. The challenge for the development of a switch for such high currents is to reduce the local electrode erosion. For that we propose a gas switch that generates an accelerated plasma to minimize the attrition.

The experimental setup of the switch consists of coaxial electrodes, similar to the geometry used for plasma focus devices [1]; the inner electrode is surrounded by an outer electrode. To reach a high hold off voltage, the setup is designed for the left hand side of the paschen branch. One important feature of a high voltage and high current switch is the reliability for triggering. The main discharge between the coaxial electrode system will be initiated by a trigger predischarge. With an external triggering a gas breakdown is initiated at the outer electrodes and forms a conductive plasma sheath which penetrates through holes to the inner electrodes.

The ignition of the discharge during the trigger phase occurs over the long distances of the cathode back space [2]. As a trigger we already used for single LDS a semiconductor surface trigger [3].

After the ignition of the main discharge between the coaxial electrode system and due to the interaction of the induced radial magnetic field with the plasma, the gas discharge will be accelerated to the open end of the coaxial electrode system. This acceleration of the plasma sheet is due to the Lorentz force. The Lorentz force which interacts with the discharge is given by:

$$\vec{F} = \int dV\, J \times B \qquad (1)$$

The switch will be therefore called as Lorentz Drift Switch (LDS). For already designed LDS the maximum current was approximately 33 kA with a current rise time of 15 kA/µs. As a working gas Nitrogen and Argon was used.

For a further reduction of erosion and to provide enough charged particles for the current transport, several of these coaxial devices will be stacked together in a parallel, multiple electrode system. The outer electrodes will be connected with each other to synchronize the single plasma sheets of every device.

The following fig. 1 shows a schematic drawing of the experimental set up of the multi gap LDS.

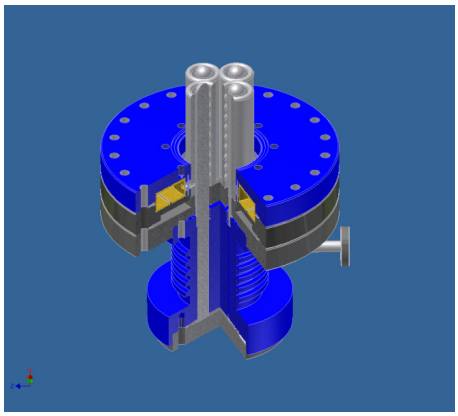

Figure 1: Schematic drawing of a two gap Lorentz Drift Switch.

The designed multi gap Lorentz Drift Switch is a low inductive, fast current, low pressure gas discharge switch. Due to the simple setup and the reduction of erosion we will introduce a low cost, and rugged high current switch for applications in further high energy experiments. With the introduced setup we hope to provide a real alternative for such high current applications of common Ignitrons at FAIR. This work is funded by a HGS-HIRe scholarship.

References

[1] J. Jacoby, C. Bickes, D.H.H. Hoffmann, C. Hofmann, J. Philipps, Experimental Study to Accumulate, Accelerate and Focus a Massive Plasma Beam onto a Target Fusion Engineering and Design 44 (1999) 331.

[2] A. Görtler, "Untersuchungen von gepulsten Oberflächenentladungen an Dielektrika und deren Anwendung zur Triggerung eines Pseudofunkenschalters", Diplomarbeit, Universität Erlangen-Nürnberg (1986)

[3] M. Iberler, R. Bischoff, K. Frank, I. Petzenhauser, A. Rainer, J. Urban, Fundamental investigation in two flashover-based trigger methods for low-pressure gas discharge switches, IEEE on Plasma Science, Vol 32 (1), 208-214, 2004.

Laser acceleration in the radiation-pressure-regime from ultra-thin foils

B. Aurand[1,2,4,5], J. Bierbach[2,3], S. Herzer[2,3], O. Jäckel[2,3], S. Kuschel[2,3], J. Polz[2,3], C. Rödel[2,3], H. Zhao[1,6], P.Gibbon[5,7], A. Karmakar[5,7], B. Elkin[8], G.G. Paulus[2,3], M.C. Kaluza[2,3] and T. Kühl[1,2,4,5]

[1] GSI , Darmstadt, Germany; [2] Helmholtz Institute Jena, Jena, Germany; [3] Institute for Optic and Quantum Electronics, Jena, Germany; [4] Johannes Gutenberg University, Mainz, Germany; [5] EMMI Extreme Matter Institute, Darmstadt, Germany; [6] Institute of Modern Physics, Lanzhou, China; [7] Research Center Jülich, Jülich, Germany; [8] Fraunhofer Institute for Interfacial Engineering and Biotechnology, Stuttgart, Germany

Introduction

Acceleration of matter using the momentum of light was first time proposed by Marx [1] in the 1960's. It became a realistic prospect for laser-particle acceleration by use of chirped pulse amplification (CPA) [2]. Today, typical laser-systems deliver peak intensities in the range of 10^{20-21} W/cm². To work in the radiation pressure acceleration (RPA) regime, beside the high laser intensities, ultra thin target materials with a thickness in the range of a few nanometers are necessary. This was so far only realized using ultra-thin diamond-like-carbon (DLC) foils. Just very few results on this mechanism were presented [3].

Experiment

Our experiment took place at the JETI laser-system , delivering pulses of 1J in 27 fs, with a pulse contrast in the range of better than 10^6. Using a plasma mirror set-up integrated into the laser beam line [4], a laser-contrast of $>10^9$ was achieved (Fig. 1).

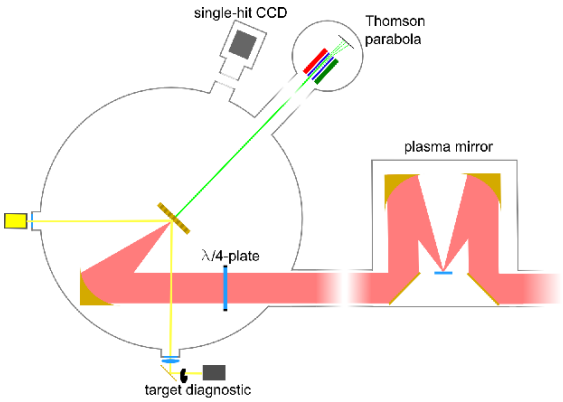

Fig.1 : Experimental set-up : The beam from the JETI laser system is delivered via a plasma mirror into the target chamber. Polarization can be controlled by the use of a λ/4 plate. The beam is focussed by an off-axis parabola to an intensity of 5 10^{19} /cm^2. Accelerated particles from the ultra-thin targets are analyzed by a Thomson parabola

Results

Under these conditions we observed mono-energetic ion-features on top of the thermal spectrum (Fig.2). The surprising finding is that the peaks for the different charge states of carbon appear at nearly the same energy while the energy of the protons is considerably higher. This behavior hints at a two step acceleration process, starting with an RPA phase where protons and the other ions are accelerated together, and a second step where a separation of the protons from the other ions is leading to an additional energy gain for the protons. This could be consistent with a transition from a leaky-light-sail [5] to a directed-coulomb-explosion [6] interpretation. 2d- simulations reproduce the energy of the proton peaks within a factor of 2. Detailed results will be publicated soon.

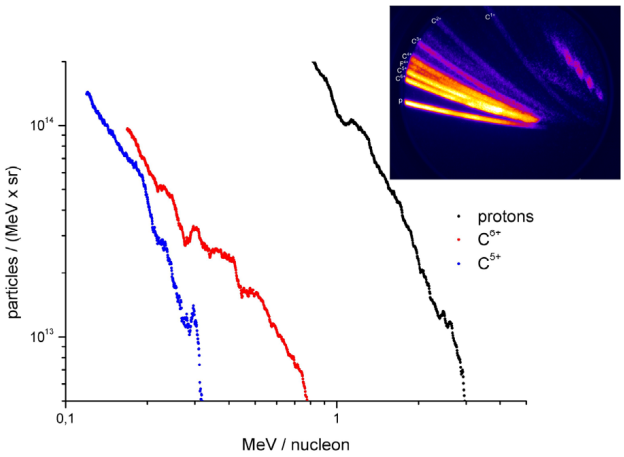

Fig. 2: energy spectra with peaks in protons and carbon ions. For different charge states of carbon the peak appears at e same position which indicates a collective acceleration.

References

[1] G. Marx, "Interstellar Vehicle propelled by terrestrial laser beam", Nature 21, 22 (1966)

[2] D. Strickland and G. Mourou, "Compression of amplified chirped optical pulses", Opt. Commun. 56, 219 (1985)

[3] A. Henig *et al.*, "Radiation-Pressure Acceleration of Ion Beams Driven by Circularly Polarized Laser Pulses", PRL 103, 245003 (2009)

[4] C. Rödel *et al. ,"* High repetition rate plasma mirror for temporal contrast enhancement of terawatt femtosecond laser pulses by three orders of magnitude" Apl. Phys. B. 103 4329 (2010)

[5] B. Qiao *et al.*, "Radiation-Pressure Acceleration of Ion Beams from Nanofoil Targets: The Leaky Light-Sail Regime" PRL 105, 155002 (2010)

[6] S. S. Bulanov, *et al.,* " Accelerating monoenergetic protons from ultrathin foils by flat-top laser pulses in the directed-Coulomb-explosion regime"Phys. Rev. E 78, 026412 (2008)

Creating circularly polarized light with a fully reflective wave-plate assembly

B. Aurand[1,2,3,4], C. Rödel[2,5], H. Zhao[1,6], S. Kuschel[2,5], M. Wünsche[2,5], O. Jäckel[2,5], M. C. Kaluza[2,5], M. Heyer[7], F. Wunderlich[7], G. G. Paulus[2,5] and T. Kühl[1,2,3,4]*

[1]GSI, Darmstadt, Germany; [2]Helmholtz-Institut Jena, Jena, Germany; [3]University, Mainz, Germany; [4]EMMI ExtreMe Matter Institute, Darmstadt, Germany; [5]Institut for Optic and Quantum Electronic, Jena, Germany; [6]Institut of Modern Physics, Lanzhou, China; [7]Layertec GmbH, Mellingen, Germany

Introduction

Circularly polarized light is typically created using a quarter-wave plate made of mica, quartz glass or other crystalline material. However, this method is not generally applicable to ultra-high intensity short-pulse lasers due to nonlinear effects, the damage threshold of the material, and the fact that ultra-thin wave-plates have a chromaticity that prevents their usage for broadband laser sources. An alternative way is the use of reflective elements using the polarization dependent phase shift on the surface. We developed and tested a system which can easily be implemented in the laser system enabling to switch the polarization between linear- and circular- polarized within seconds [1, 2].

Setup

Dielectric coatings are a well-known technique to produce e.g. mirrors with a high reflectivity. Advanced designing of the layer stack allows an influence of the reflected phase behavior. Within an optimization process we designed a mirror inducing a phase shift of 90° between the s- and the p- polarized component for a broad wavelength range of (800 ± 40) nm having a reflectivity of 98%. Benchmarking this mirror we realized an ellipticity of (98.3±0.6) % for a 10 cm diameter beam. This method will be well applicable even for ultra-short pulses in the range of a few femtoseconds, since the calculated group-delay-dispersion (GDD) amounts to only 40fs². By implementing three mirrors specially designed without a phase shift, we developed in a second step a reflective wave-plate assembly (Fig. 1), which can be implemented in a laser-system creating circular polarized light without major changes.

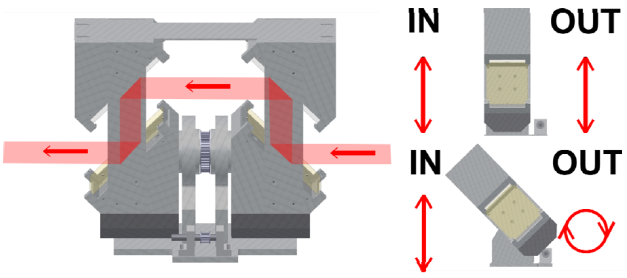

Figure 1: Setup of the reflective wave-plate using four mirrors. Depending on the polarization of the assembly, linear polarized light stays linear polarized, or becomes circular polarized.

Experiment

All tests of the single PSM and the reflective wave-plate assembly were done on a Ti-Sapphire laser-system delivering pulses of 27fs and a multi-kilohertz repetition rate. The bandwidth of the system [(800±50) nm] is within the design range of the device. Using polarizing beam splitters we measured the angular dependent intensity variation and calculated the field distribution in front and behind the mirror. The maximum ellipticity for the full setup was found to be (90.0±0.1) % (Fig. 2). The pulse broadening of a 27 fs pulse in the PSM and the full reflective wave-plate assembly was smaller than the measurement accuracy of 1 fs of the autocorrelator used in the experiment, which is in agreement with the calculated value GDD of 40fs². Comparison of the spectrum in front and behind the assembly showed no changes due to interferences in the complex layer design. Another big advantage of the reflective design is the high damage threshold, measured to be $5x10^{12}$ W/cm², which is a factor of 400 higher compared to typical transmissive quartz retardation-plates[3].

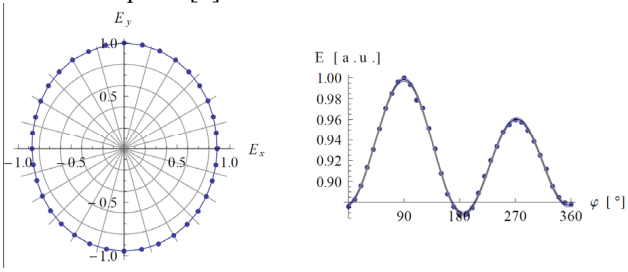

Fig. 2: Field distribution for the maximum achievable ellipticity of the full system is (90.0±0.1)%.

Outlook

Phase modulation systems based on this idea are proposed to be implemented into the new POLARIS system at Jena University, and will be used for a proposed experiment at the PHELIX laser facility at GSI in the next year.

References

[1] B. Aurand, *et al.*; Creating circularly polarized light with a phase-shifting mirror; Optics Express, Vol. 19, Issue 18, 17151, (2011).

[2] B. Aurand, et al.; A large aperture reflective wave-plate for high-intensity short-pulse laser experiments; (submitted to Ref. of. Sci. Inst.)

[3] A.A. Said, et al.; Measurement of the optical damage threshold in fused quartz.; Appl. Opt., Vol. 34, Issue. 18, 3374-3376, (1995)

Progress Report on the SIS 18 h=2 System

P. Hülsmann, R. Balss, H. Klingbeil, U. Laier, D. Mondry, K.P. Ningel, S. Schäfer, M. Sam and T. Winnefeld

GSI, Darmstadt, Germany

Abstract

The new RF accelerating cavity is based on novel magnetic alloy materials (MA-materials) for operation at harmonic number two (f=0.43-to 2.8 MHz) to provide the necessary accelerating voltage for SIS18 injector operation with high intensity heavy ion beams in a fast operation mode with three cycles per second.

The acceleration system consists of three units which are able to operate independently from each other. That is important since each ion for FAIR has to pass the h=2 RF system and in the case of a damage a reduced operation can be ensured.

The cavity is filled with Finemet FT-3M ring cores from Hitachi Metals Ltd. which is an iron based MA-material and thus, due to the high saturation field strength of Finemet (1.2 T), the overall length of all three cavity units can be very short. This is an important feature since due to many insertions, which were additionally installed in the synchrotron ring SIS12/18 in the meantime, the available length for the cavity units is limited to 3.8 m. [1]. On the other hand these ring cores are very lossy and therefore the cavities show a broadband behaviour and due to that no cavity tuning during the acceleration ramp will be necessary.

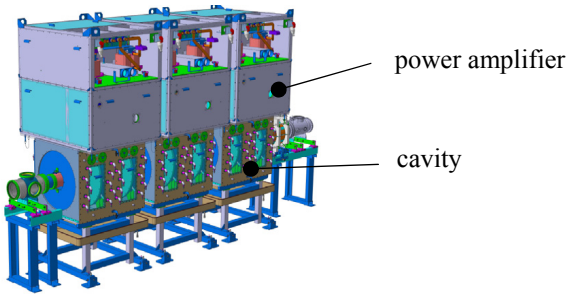

Fig. 1: h=2 RF System (3 units)

One unit of the RF System consists of a tetrode based push pull RF power amplifier on top of the cavity, a broadband magnetic alloy cavity itself and a power supply unit. Last but not least a low level RF system (LLRF) is also part of the whole unit.

RF power amplifier

The RF power amplifier feeds the cavity in push pull mode using two Thales TH 537 tubes with an anode dissipation power of 300 kW. A 2 kW solid state amplifier will drive the power amplifier. The power is transmitted via a ferrite loaded toroidal transformer (with grounded center tap) in order to drive the steering grid of both tubes in push pull mode. Due to space limitation in the SIS 18 synchrotron the power amplifier will be mounted on top of the cavity. (see Fig. 1).

MA cavity

All three units of the RF system will provide 50 kV gap voltage in total over the full frequency range from 0.4 up to 2.8 MHz (harmonic number h=2). One cavity unit is filled with a total number of 16 MA ring cores and it consists of two ceramic gaps which are connected in parallel. This measure is necessary to keep the bandwith of the cavity as large as possible since it avoids unwanted parasitic capacitances. Cavity cooling will be done by direct oil cooling with mineral oil in order to avoid corrosion of the ring cores and large parasitic capacitances between adjacent ring cores.

Supply unit

The supply unit contains the different power supplies like anode, screen grid, control grid, and filament supply. Power up and -down as well as the interlock procedure will be done by a programmable logic control (PLC).

The anode supply for instance will provide a voltage of U_{ADC}=15 kV and a current of I_{ADC}=40 A

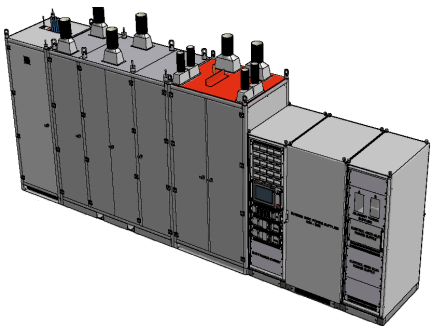

Fig. 2: Supply unit for the h=2 RF system

Outlook

Next steps will be the assembly of the RF power amplifier and the MA cavity for the first unit. The delivery of the supply unit will take place at the end of July 2012 and the commissioning of the supply unit will be carried out. Afterwards commissioning and testing of the whole RF system will be done.

After successful lab tests and optimizations the first system will be installed in the SIS18 tunnel.

The second and the third RF system will be realized immediately afterwards.

References

[1] P. Hülsmann: “Development of a new broadband accelerating system for the SIS 18 Upgrade at GSI”, 2010

ESR Operation and Development

C. Dimopoulou, A. Dolinskii, O. Gorda, P. Görgen, R. Hettrich, S. Litvinov, W. Maier, F. Nolden, C. Peschke, P. Petri, U. Popp, I. Schurig, M. Steck
GSI, Darmstadt, Germany

The ESR storage ring was predominantly operated for physics experiments. Machine development focussed on the properties of cooled ion beams after deceleration, which is documented in a separate report [1], and investigations on the limits of beam accumulation for future physics experiments at the ESR. Some of the experiments at higher energies suffered from an unexplained beam loss when the beam was stored close to the central orbit. The remedy was to store of the beam on orbits with some momentum offset with respect to the loss region. This was possible without significant constraints to the scheduled experiments. In dedicated machine experiments systematic tune measurements were performed with a Cr^{23+} beam in the energy range 30 to 400 MeV/u. No significant deviations of the tune from the expected values were found.

During the summer a leak in the coil of an extraction septum caused an interruption of the ESR operation. This was the second time a leak in the brazing of the thin septum conductor occurred and is attributed to aging.

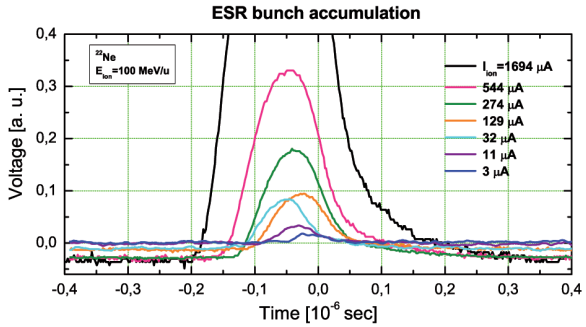

Figure 1: Bunch signal for different intensities during accumulation of a 100 MeV/u Ne^{10+} beam.

The feasibility to accumulate high intensities for a rare isotope beam of $^{21}Ne^{10+}$ was investigated with a $^{22}Ne^{10+}$ beam. Single bunches with a length of 150 ns of about 4×10^7 ions at 100 MeV/u were injected into the ESR. Longitudinal stacking was performed by synchronizing the SIS and ESR rf system such that the bunch arrived in the ESR at the unstable fixed point of the ESR rf system operated at harmonic number $h = 1$. Continuous electron cooling was applied to the ions stored in the ESR. Maximum currents of about 2 mA, corresponding to 1×10^9 particles could be accumulated reliably. For large rf amplitudes the intensity was limited by instabilities of the short bunch of cooled ions. For weak bunching with small rf amplitude and a correspondingly longer bunch the tails of the circulating ESR bunch were kicked out by the injection kicker which covered nearly 80 % of the ring circumference. The loss is due to the increase of the bunch length with increasing beam intensity (Fig. 1).

As part of the activities on the new stochastic cooling systems for the Collector Ring CR of FAIR [2] an optical notch filter was developed and installed for tests with beam at the ESR. Only a few hours at the end of the ESR operation time were available, but were sufficient to demonstrate for the first time notch filter cooling at the ESR. Additional experiments are planned to optimize the optical notch filter system for the use both at the ESR and at the CR.

A large fraction of the ESR beamtime was devoted to commissioning of the HITRAP facility. In order to reduce the cycle time to less than 30 s the beams were injected at 30 MeV/u and decelerated to 4 MeV/u. As this cycle can be favorably performed with lighter ions which are injected close to the equilibrium charge state, these ions have longer lifetimes in the residual gas. With Cr^{23+} and N^{7+} ions stored at 4 MeV/u with lifetimes of 11 s and 45 s, respectively, it was for the first time possible to measure the tune systematically and consecutively to optimize the working point for the decelerated beam. Bunching the low energy beam at 4 MeV/u with the second rf cavity operated at 253 kHz (harmonic number $h = 1$) is now available within the deceleration cycle, but so far was not used for HITRAP commissioning. As the HITRAP decelerator relies on a precise energy of the beam after deceleration the accelerating voltage of the electron cooler which defines the energy of the extracted beam was carefully checked and the expected energy of 4 MeV/u could be confirmed with an uncertainty of less than 0.1 %.

Various experiments at different energies used stable uranium and bismuth beams in high charge states and the internal target operated with hydrogen and nitrogen gas and electron cooling to compensate the target heating. As in the previous year a primary ^{238}U beam was used in combination with a 10 mm thick Be target in front of the ESR to produce $^{235}U^{89+}$ secondary ions for precision dielectronic recombination spectroscopy employing the electron cooler also as electron target. The program of beta decay studies and the detection of single ions was continued with a primary Sm beam and secondary $^{142}Pm^{60+}$ ions injected at 400 MeV/u from the FRS. A complication occurred in these experiments due to the reduced stability of the accelerating voltage of the electron cooler which was attributed to poor quality of the insulating gas in the high voltage power supply. This resulted in variations of the revolution frequency of the stored ions on the 10^{-6} level.

References

[1] P. Görgen et al., this annual report.
[2] C. Peschke et al., this annual report.

Progress of standards and tools for the accelerator part of the FAIR project

G.Aberin-Wolters, P.Busch, G.Hickler, U.Weinrich

GSI, Darmstadt, Germany

Introduction

In 2011 the duties of the project within the accelerator division steadily increased. At the end of the year the project office was responsibly for the following processes of the accelerator part of the FAIR project:

1. establishment of FAIR Technical Guidelines
2. preparation of In-Kind-Contributions
3. coordination of accelerator schedule
4. Establishment of a document management system.

The named processes reflect that the project has evolved from the pure planning and development phase to the start of the real procurement of components. The main achievements are described in this report.

Establishment of FAIR Technical Guidelines

The FAIR Technical Guidelines are a set of actually 170 documents which define technical quality assurance standards. They include for example material definitions, design principles and special test procedures. Only parts of them are referenced for each components class. They can be grouped in the following manner:

Technical Group	Number of documents
Control System	5
Cryogenics	41
Electrical design	1
Media supply	3
Transport	3
Vacuum	49
Survey and alignment	12
Stands and support	36
Data exchange	1
Radiation hard Materials	1
Magnet design and tests	18

Table 1 Groups of Technical Guidelines

A lot of effort had to be spent to establish these documents. 20 authors from different technical departments were needed to produce a total amount of 563 pages.

In addition a lot of meetings were organised to elaborate standards accepted by the different accelerator departments.

The establishment of the full set of documents valid for many or all classes of components was finished in Beginning of June 2011. It now serves as reference for the authors of the other documents and is subject to change management procedures [1].

Preparation of In-Kind-Contributions

In 2011 the FAIR Council attributed a significant number of In-Kind-Contributions to the FAIR member countries and their institutions. The project office created the corresponding GSI proposals and gave significant support to the Slovenian in-kind-contribution.

Since March 2011 the project office took over the responsibility to coordinate the preparation of in-kind contributions from GSI. The amount of money involved and the contractual framework require quite some different processes as for standard GSI procurements. Procedures are now fixed which are agreed on by the concerned departments of technical directorate, the administrative directorate and the accelerator division. The procedures describe the workflows for technical aspects, financial aspects and contractual aspects.

The following six GSI in-kind-contribution are actually under the coordination of the project office: CR Debuncher system, SIS100 dipole modules, Superferric multiplets, magnet testing of superconducting magnets, parts of the proton linac and accelerator control system. In total they represent an investment value of more than 100 million Euros.

Coordination of accelerator schedule

From June 2011 on the project office took over the responsibility to further develop the FAIR accelerator schedule by improved integration of the expertise of the work package leaders and machine project leaders. At the same time the planning depth was increased. In order to get consistency of scheduling in all 47 work packages a series of meetings with the work package leaders, the corresponding machine project leaders and the responsible for the scheduling were organised. In this first round of meetings the detailed structure and defined milestones were agreed with the main aim to have the components ready for assembly when the building progress allows the start of assembly. The total amount of lines has meanwhile reached the range of ten thousand activities and milestones.

At the end of the year the work one focus was laid on getting together with the colleagues from the FAIR GmbH the technical issues of the MS Project Server handled in order to be able to extract relevant data for reporting and steering. In addition a lot of work was dedicated to provide sound assembly schedules.

Establishment of a document management system

After having reached the released set of FAIR Technical Guidelines in June 2011 it was necessary to start the change management on these documents. For practical reasons it turned out that a document management system under the administration of the project office was necessary for this process. A quick and cheap solution was found by creating a GSI EDMS knot for this purpose in November. All FAIR Technical Guidelines were migrated on the knot. At the end of year the release process for many other specification documents for the actual in-kind-contributions was launched.

It was also decided to archive important FAIR documents like minutes on the GSI EDMS knot. The preparation of this has started.

Summary

A complete set of released FAIR Technical Guidelines was achieved. Further specification documents are under release now.

Procurement procedures have been worked out and agreed on for the first six GSI In-Kind-contributions. They will serve as reference now.

The accelerator schedule has been substantially improved in quality and detailing until the end of component the production phases. The scheduling process itself and the assembly scheduling are under development.

A document management system under the administration of the project office within the accelerator division has been started.

Outlook

Many project processes are not yet running at the required speed or are even not yet started. The increase of the duties of the project office will therefore persist. Coordination or at least significant support from the project office will be needed in for the set up of the component database, the reporting, the financial controlling and the risk management. All these processes have to be strongly improved during the year to come.

References

[1] U.Weinrich, “The Specification Process for the Large Scale Accelerator Project FAIR”, IPAC`11, San Sebastian, September 2011, TUPS076; http://www.JACoW.org

Project Status of the New Setting Generation System for GSI and FAIR

D. Ondreka, O. Chorniy, J. Fitzek, R. Hellmich, M. Kirk,H. Liebermann, R. Müller, S. Reimann, B. R. Schlei, J. Struckmeier

GSI, Darmstadt, Germany

Since 2008, a project group at GSI is developing a new unified setting generation system for the accelerators of GSI and FAIR. The system is realized using the CERN LSA (LHC Software Architecture) framework [1]. This report summarizes the development progress during the year 2011.

Concerning the LSA framework, major progress has been made through the implementation of arbitrary length changes to cycles or super cycles. This work has eliminated the most serious limitation of the LSA framework which so far prevented a realistic modelling of the flexible operation of the GSI/FAIR accelerator complex. While a workaround had already been implemented in 2010, this was nothing but a way of testing the validity of the algorithms for calculating the actual length changes. It would have been of little practical use because the internal structures of the LSA framework and, correspondingly, all applications built on it, would never have been aware of the changes.

The extension of the LSA system to allow length changes was realized by the LSA collaboration with CERN. Two collaboration meetings were held to complete the task: During the first meeting in May the general strategy for implementing the changes was worked out. In the following months, a preliminary implementation was realized in the GSI clone of the LSA framework. When this implementation became functional, the final implementation was elaborated and finished during the second meeting in December.

This limitation removed, the LSA framework now provides basically everything that is needed to model the synchrotrons of the GSI/FAIR facility. Therefore, the focus will now shift to the modelling of storage rings. While the LSA framework has in fact been designed to operate a storage ring, namely the LHC, the differences in operation when compared to the storage rings in the GSI/FAIR accelerator complex are quite significant. The logical next step is thus to implement a minimal model of the ESR and check for possible limitations. This task was originally planned for 2011 but had to be postponed in favor of the work concerning the flexible cycle lengths.

Another topic relating to the LSA framework itself concerns the modelling of the planned parallel operation within the GSI/FAIR facility. This issue has already been informally addressed during the December LSA collaboration meeting and shall be pursued this year.

In contrast to the previous year, there were no major improvements to the physics model. Rather, the existing model was investigated more closely to ensure its completeness and correctness: On one hand, the data basis was extended to include realistic FAIR HEBT beamline sections from the SIS100 to the SFRS and the pbar target. Thus, it is now possible to compute realistic set values for those beam lines. Further investigations were done relating to the timing constraints on the corresponding power supplies from the planned parallel operation scenarios. On the other hand, the RF model was cross checked by performing multi-particle simulations including space charge with the ramps generated by the LSA system. Even though the simulation work is not yet finished, the first results indicate that the physics model implemented in LSA is indeed valid for heavy ion operation

Apart from the work on the LSA framework and the physics model, a number of additional activities were pursued. First of all, the development of an LSA application for parameter control was started. This application can be considered an LSA version of SISMODI and serves two purposes: On the fundamental level, it is a prototype for all LSA applications to be developed within the GSI/FAIR control system; on the practical level, it shall improve the usability of the LSA system to control the SIS18 during machine experiments.

Next, the Java based offline version jMIRKO of the ion optical simulation program MIRKO has reached a stable state. It is now available as a single user application for use under Linux and Windows. As mentioned in the last scientific report, the next step is the development of an online version of jMIRKO as a replacement for the MIRKO Expert program running in the control room. Contrary to original plans, this online version will not be implemented using the Device Access interface to the hardware, but will use the LSA client interface instead. While this change in strategy has a lot of advantages from the technical point of view and fits very nicely into the development of the new setting generation system, it implies that the online version of jMIRKO cannot become productive before the LSA system does.

And finally, the work on the quadratic interpolation function generator for ramped devices was continued. In contrast to previous expectations, it could not yet be finished due to resource limitations.

In 2012, the project group will focus on the following issues: Concerning the LSA framework, the major topics are the modelling of storage rings and the beam patterns arising from parallel operation. Concerning the physics model, the emphasis will be on the proton cycle in SIS100 with all its RF manipulations as well as on a generic model for slow extraction.

References

[1] Grzegorz Kruk et al, “LHC Software Architecture (LSA) - Evolution Toward LHC Beam Commissioning”, ICALEPCS’07, WOPA03.

Status Report on RF Knock-Out Extraction

M. Kirk, P. Moritz, D. Ondreka, and P. Spiller

GSI, Darmstadt, Germany

This article details the design efforts towards an RF Knock-Out (KO) system for the resonant beam extraction out of the SIS-100 FAIR synchrotron.

The foremost concern is the extraction of the lowest q/m ions at the highest possible rigidity of 100 Tm. The present requirement is a transmission >90% in 500 ms which was shown in a tracking simulation. Transmissions up to 99% were demonstrated in figure 1 fixing the center frequency of the exciter half way between the horizontal tune of the lattice and the third integer resonant tune, and maintaining a constant 5 kV peak voltage as described in [1]. This way ions remain highly resonant until extracted.

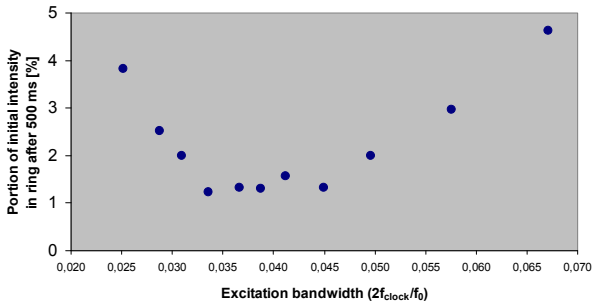

Figure 1: Optimising the bandwidth.

In practice the spill envelope should be almost flat. This can be done by modulation of the exciter's voltage amplitude either through feed-forward or feed-back. The latter can maintain flat spill envelopes for a changing initial beam distribution. A feedback process based on PI control has been shown to work well [2] and could be used in SIS-100. Thus 90% transmission may be exceeded as shown in figure 2 at the cost of longer spill duration; the exciter's power amplifier being a limitation. Additional transverse B-field deflection of beam can be achieved with oppositely flowing electrode currents.

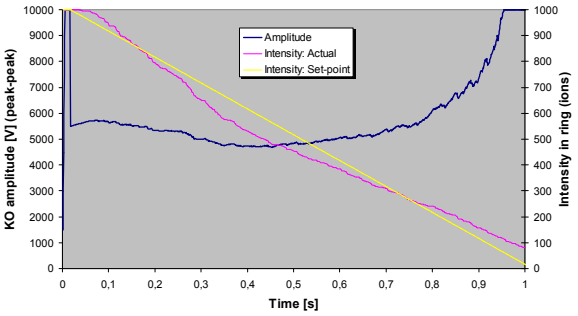

Figure 2: Machine intensity profile due to PI-control.

RF-KO was chosen because it provides a stable beam spot at the target since the currents in the power supplies to the first and second extraction septa do not have to be ramped, thus allowing operation at optimum stability. However, preliminary results from SIS-18 RF-KO simulations have shown levels of variation in spill current at resolutions of ~10 µs which appear to be greater than that obtained when the machine tune is moved towards the resonance without transverse RF excitation. Machine tune ripple was absent in both cases. The rough spill during RF-KO is believed to be caused by the excitation signal's influence on the beam. Attempts to optimise these spill current fluctuations without causing excessive beam loss have so far brought only small improvements.

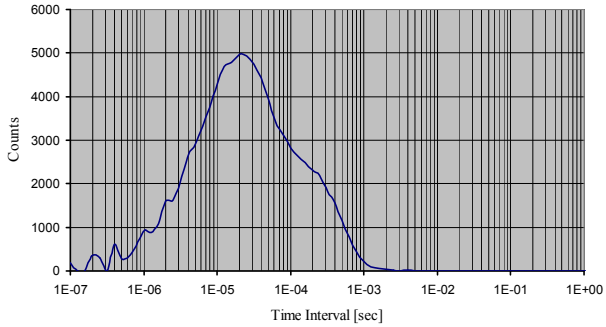

Figure 3: Time interval distribution of FRS fragments.

SIS-18 spill is measured by pulse counting. The multi beam-diagnostic DAQ and online analysis systems ABLASS and ABLAX at GSI can offer resolutions in spill count rates as low as 10 µs with a plastic scintillator for an average count rate $<10^6$ s^{-1} to avoid pile-up at ~50 ns between pulses. Better resolution however is possible with a relatively new system [3] at the GSI FRS in which firmware does the pulse counting as well as the online spill analysis at the mid- and end-focal plane targets. A histogram of the time interval between consecutive q/m selected primary beam fragments, such as in figure 3, are measureable down to the event pile-up at 50-100 ns. Spill fluctuations would show up as departures from a Poisson distribution. In principle NIM pulses from constant fraction discriminator could sent to ABLASS/X for analysis in the accelerator complex's main control room.

References

[1] M. Kirk et al, "SIS100 RF-KO Requirements Analysis: SIS-100 RF Knock-Out System", CERN EDMS Note, April 2011.

[2] A. Peters et al, "Operational Status and Future Enhancements of the HIT Accelerator Facility", IPAC'10, Kyoto, May 2010.

[3] H. T. Johansson, "LAND TRLO II trigger logic in VULOM and TRIDI", Chalmers, Göteborg 2010, http://fy.chalmers.se/~f96hajo/shows/htj_feb2011_trlo_ii.pdf

Pulse Power and HV Device Developments for FAIR

U.Blell[1], J.Florenkowsi[1], K.Knie[1], M.Petryk[1], I.Petzenhauser[1], P.Spiller[1] A.Staubach[2], C.Tenholt[3]

[1]GSI, Darmstadt, Germany; [2]Fachhochschule Gelsenkirchen, University of Applied Sciences; [3]IAP, University of Frankfurt

Pulsed power and high voltage components are required for different applications at FAIR. This paper presents some systems currently under development at the synchrotrons group of GSI.

High voltage resistors for electrostatic septa

Electrostatic septa consist basically of two electrodes, one typically on ground potential and one at high voltage. The electric field is used to deflect the ion beam in the synchrotron, e.g. for injection or slow extraction. To prevent damage in case of voltage breakdown between the electrodes, a resistor is used to limit the discharge current. In the SIS 100 extraction septum, a 300 Ω resistor made of tungsten-rhenium wire is used until now. To limit the peak discharge current to an even lower value, three film resistors with a resistance of 300 kΩ each are connected in parallel to form a resistance of 100 kΩ. To prove the applicability of this setup, different tests were performed. In one experiment the resistors were tested in vacuum with dc power. The power input was increased up to 125 W. At that power, the resistors reach temperatures of ~270°C, well within their specifications. In another test, the electrodes of a septum were connected. The cable that connects the power supply and the septum was charged up to voltages up to 80 kV and then the energy was discharged via a spark gap switch to the resistor. The results are very promising so far, but the tests have to be continued to finally prove the advantages of the new resistors.

Iron-free high current pulsed quadrupoles

For the final focussing in the HHT beamline a pulsed quadrupole doublet is intended. With a beam spot width of 0.5 mm at the target, the aperture dimensions and beam requirements lead to currents in the coil up to 200 kA and an inductivity of 5 µH. The current produces a magnetic field strength of about 4 T at the edges of the lens. Warm quadrupole magnets have a maximum magnetic field of 1.8 T due to saturation of their iron cores. As a consequence the magnet has to have an iron free design. A pulsed power supply operable up to 25 kV is necessary. The advantage of a pulsed power supply is high savings of energy by just operating while beam bunches pass through the quadrupole. The whole design with its power supply forms a resonant circuit with a SCR-stack power switch. Choosing the right SCRs and bringing them together in an adequate constellation with the capacitors, which also have to fit to the inductivity of the lens will be a challenge. The pulse duration of a half wave would be approximately 100 µs the Lorentz-Forces on the conductors of ca. 50 kN outwards create a big challenge. Furthermore, flexible wires, which are insulated and twisted with each other to avoid a strong skin effect, are ideally applicable to the design of the coil (an adequate cos(2θ) field distribution). The design of the quadrupoles with its technical challenges will be the next activity.

Pulse power for the magnetic horn of the pbar target

To accumulate a large number of antiprotons produced at the antiproton target, a focusing element is required. At FAIR a magnetic horn will fulfil this task. Basically, a magnetic horn is a specially shaped coaxial conductor. When a current runs through it, charged particles travelling between the inner and the outer conductor are deflected and thereby focused. While the basic layout of such a system is quite simple, the engineering task is difficult. On the one hand the structure has to withstand high mechanical forces due to the produced magnetic field. On the other hand, the electrical circuit is also challenging, because to focus a decent number of antiprotons, a current flow in the order of 400 kA is needed. Cables and a strip line will be used to connect the energy storage (i.e. a capacitor bank) to the horn. The strip line is required due to the high radiation levels near the horn that would destroy the insulation of cables. The charging voltage should be <12 kV to reduce cost and improve lifetime of the pulsed power system. First simulations have shown the feasibility of the preliminary design. Additional calculations and simulations will help to finalize the design and to provide the required performance, lifetime and cost-efficiency.

Pseudospark switches for kicker magnets

To operate the kicker magnets at FAIR, high-voltage switches are required. They have to handle operating voltages of up to 70 kV and current pulses of more than 6 kA. The pulse duration can be as high as ~7 µs. The current rise rate should exceed $4*10^{10}$ A/s and the lifetime should exceed 10^8 shots. Low-pressure gas discharge switches combine these properties. Thyratrons are intended to be used as switches in this application. But due to a shrinking market for these switches their availability for more than 30 years is questionable. Therefore an alternative switch, the so-called pseudospark switch was adapted to the FAIR specification. The development is not yet finalized, but the first prototype built in the workshop at GSI has proven its ability to work beyond 50 kV and has a good switching behaviour for currents above ~1.5 kA. With lower currents there is still a quenching behaviour (i.e. current interruptions), but this problem was significantly reduced by adding a low percentage of argon to the hydrogen working gas.

Cross-Talk between two Thyratrons in a Bipolar Test Set-up

K. Samuelsson[1,2], U. Blell[1], J. Florenkowski[1], I. Petzenhauser[1], P. Spiller[1], and V. Hinrichsen[2]

[1]GSI, Darmstadt, Germany; [2]TU Darmstadt, High Voltage Laboratories, Darmstadt, Germany

Introduction

For the FAIR synchrotron SIS100 a bipolar kicker system is to be developed as described in [1]. One concern is the possibility of cross-talk between the two thyratrons, which implies that both thyratrons are conductive although only one has been triggered. In [1] first investigations were made with charging voltages of up to 35 kV, higher voltages were not possible at that time because of the limitations of the high voltage source. Up to this voltage level no problems occurred. The high voltage source has been changed to one which can deliver voltages up to the required charging voltage of 80 kV. In the following the findings with the new source will be presented.

Measurements

Two different thyratrons are used and thus the specified currents which can be handled by the switch differ. The CX2004X can handle currents up to 10 kA, but the CX1171 can only handle currents up to 3 kA. Therefore the circuit of the test set-up described in [1] had to be modified, not to exceed the allowed current of CX1171. The resistance was doubled to reach at least 50 kV charging voltage without excessive current. A higher resistance value was not used to avoid even higher impedance mismatching. The modified circuit can be seen in figure 1.

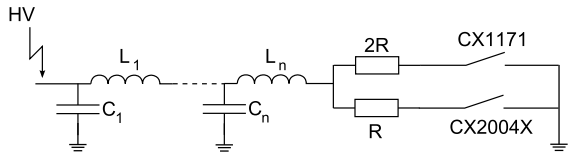

Figure 1: Equivalent circuit of the test set-up, with L_x = 2.5 µH, C_x = 77 nF, R = 5.7 Ω and n = 8.

With the new voltage source cross-talk was observed already at 20 kV charging voltage. As a countermeasure an electromagnetic shield, in form of a metal plate, was installed between the two thyratrons, see figure 2.

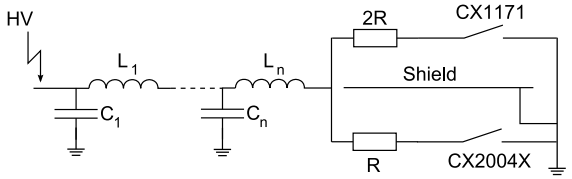

Figure 2: Equivalent circuit for the test set-up with the electromagnetic shield.

With this countermeasure a charging voltage of 50 kV was achieved. At higher charging voltages the problem of cross-talk re-occurred. The discharge current through the termination resistor for CX2004X can be seen in figure 3 and respectively for CX1171 in figure 4. Because of the changed resistance a higher reflection will occur for CX1171. These can be seen in the graphs as the bumps after the main pulse.

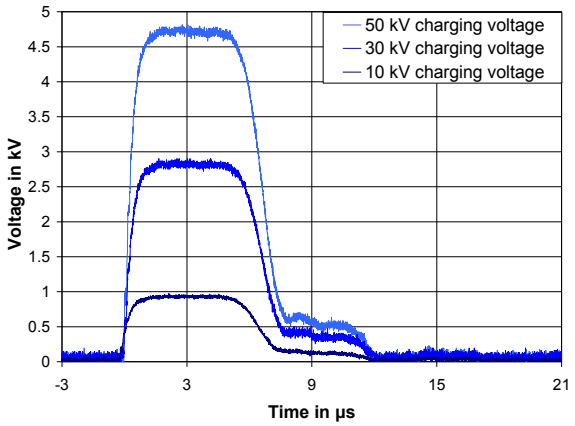

Figure 3: Discharge current with triggering of CX2004X.

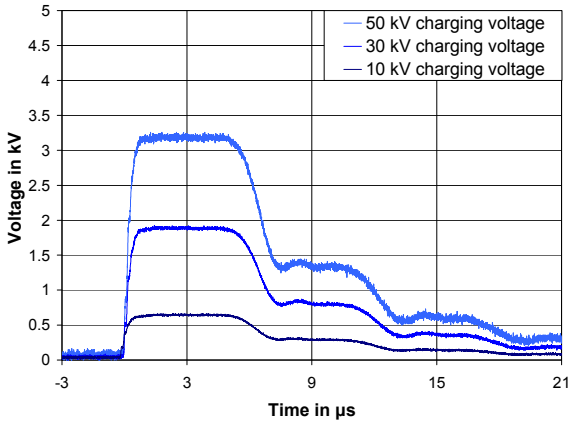

Figure 4: Discharge current with triggering of CX1171.

Further investigations

For a better understanding of the cross-talk further investigations are necessary. Firstly measurements will be made to gain knowledge on which of the gaps of the non-triggered thyratron is conducting first in the case of cross-talk. New shielding boxes have been built and are ready to be tested.

References

[1] K. Samuelsson, Development of a Bipolar Kicker System for SIS100, GSI Scientific Report 2010.

SPARC Experiments at the HESR: A Feasibility Study

Th. Stöhlker[1,2,3], R. Schuch[4], S. Hagmann[1,5], Yu. A. Litvinov[1,2], for the SPARC Collaboration[*] ,
C. Dimopoulou[1], A. Dolinskii[1], T. Katayama[6], M. Steck[1], and H. Stockhorst[7]

[1]GSI Helmholtzzentrum für Schwerionenforschung; [2]Ruprecht-Karls-Universität Heidelberg; [3]Helmholtz Institute Jena; [4]Stockholm University; [5]Goethe-Universität Frankfurt; [6]RIKEN, Saitama, Japan; [7]Forschungszentrum Jülich

Only a very small part of the originally envisioned atomic physics program contained in the Conceptual Design Report (CDR) [1] is foreseen within the Modularized Start Version (MSV) of the FAIR project [2]. However, the major part of the original experimental program is focused on experiments with stored and cooled ions to be either conducted at the NESR or on using the NESR as an intermediate beam transport and deceleration facility for FLAIR [3]. The NESR is not a part of MSV and it cannot be expected that the NESR will be operational for experiments within the next 10 years. Since this creates a difficult perspective for the atomic physics community, the impact of the MSV for SPARC was to some extent compensated by the decision, to keep the ESR accessible for experiments until the NESR will be available [2].

The MSV has triggered efforts to investigate alternatives which may allow to perform already within the MSV unique experiments in the realm of atomic physics using stored and cooled ion-beams at FAIR. The High-Energy Storage Ring (HESR) [4], whose primary aim is to allow for experiments with stored and cooled antiprotons, turned out to be a well-suited facility which can accommodate a range of SPARC experiments with high-energy stored heavy-ion beams. A feasibility study has been conducted and the corresponding report can be found in [5].

The HESR can store cooled beams at energies of up to a few GeV/u and thus can enable unique atomic physics experiments which would even not be feasible at the NESR or at any other place in the world. This is in particular true for the use of cooled ion beams at highly relativistic energies ($\gamma \approx 2$ to 6). We note, that possible experimental activities for atomic physics at the HESR were already mentioned and discussed at a very early stage of the international FAIR project, i.e. within the CDR [1]. Moreover, with respect to the experimental installations needed for SPARC at HESR, we like to emphasize that most of the equipment already specified within the SPARC technical report [3] for experiments at the NESR can be transferred to the HESR and is covered by the FAIR cost book. This is in particular true for the prototype detectors and target stations already developed for SPARC@NESR [3].

A possible location of the SPARC setup in the HESR could be the missing dipole straights in arc sections of the ring (see Figure 1). The already foreseen electron-cooling and stochastic cooling will allow to cover from the very beginning the whole energy regime accessible for heavy ions at the HESR. Although these installations have been optimized for the storage of antiprotons it turns out that they are also well suited for heavy-ion beams. Also the ion optic simulations have shown that the foreseen target position appears to meet very well the requirements of the planned experiments.

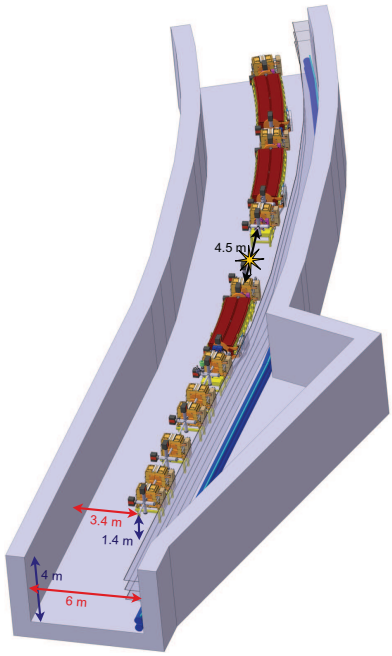

Figure 1: Possible location of the experimental installations in the HESR (shown with a yellow star). The dimensions of the tunnel are indicated on the drawings.

Thus, the HESR appears to be almost ideally suited for the envisioned experimental program of the SPARC collaboration for the high and relativistic energy domain. Beam cooling will allow for an up to now unprecedented beam quality when compared to single-pass experiments at conventional relativistic ion accelerators in combination with a gain of luminosity by orders magnitude.

References

[1] FAIR CDR, http://www.gsi.de/GSI-Future/cdr/

[2] FAIR Green Paper, http://www.gsi.de/documents/

[3] SPARC Tech. Proposal, http://www.gsi.de/forschung/fair_experiments/sparc/documents.html

[4] HESR TDR, http://www-win.gsi.de/fair-eoi/PDF/TDR_PDF/TDR_HESR-TRV3.1.2.pdf

[5] http://lxcms1.gsi.de/typo3/fileadmin/SPARC/documents/SPARC%40HESR_FS_V26.pdf

[*] *http://lxcms1.gsi.de/typo3/start/fair/fair_experimente_und_kollaborationen/sparc/*

Progress Report on the Bunch Phase Timing System (BuTiS)

P. Moritz, B. Zipfel

GSI, Darmstadt, Germany

Abstract

The Bunch Phase Timing System (BuTiS) performs as the precision time reference for the FAIR complex. Its construction has reached a preliminary state of operation. Since the first report [1] a number of improvements have been realized. These are reported here.

Loose Fiber Tube Optical Distribution Cables

The decision to use loose fiber tube optical cables for reference signal distribution was emphasized by the investigation of their exceptional delay stability [2]. The loose fiber tube structure is shown in figure 1.

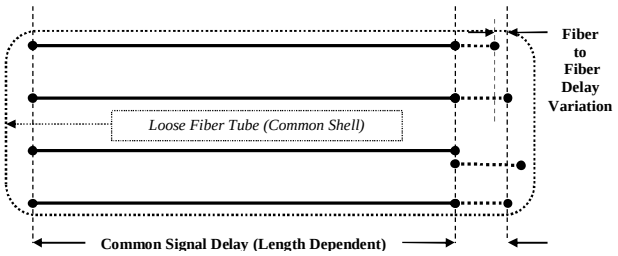

Figure 1: Internal structure of the fiber tube

The delay tracking over temperature between the fibers comprising the cable is shown in figure 2.

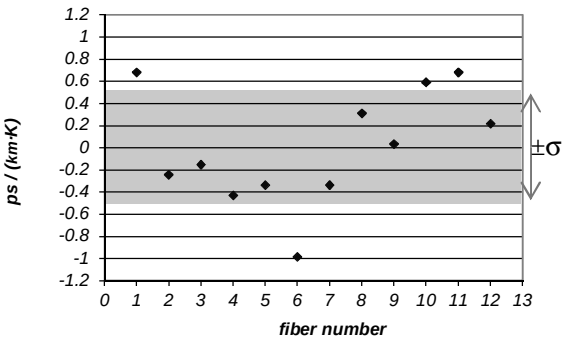

Figure 2: Typical relative thermal delay variation between fibers within a BuTiS fiber optical line of 1km length.

The expected fiber to fiber delay deviation of a 1km run of distribution cable in a tunnel with typical temperature deviation of 10°C stays within 10ps.

BuTiS Feedback Channel

As shown in figure 1, if the delay of one fiber is measured, the delay of each other fiber is known. This enables an additional feedback path with known delay properties using one of the extra fibers.

Clock Distribution Modules

The main task of the BuTiS is to provide a reliable reference clock for the low-level rf modules for the FAIR synchrotrons [3]. Several modules require synchronous electrical clock signals. They are derived from the local reference synthesizer by the clock distribution module. Inside these modules individual clock division ratios as well as individual fine delay adjustments in the picosecond range can be performed.

Interfacing to White Rabbit

The White Rabbit Control and Timing Network [4] will be used for FAIR accelerator control. The White Rabbit timing master is synchronized to BuTiS so that commands and control system events are also synchronous. Control commands and events will be sent as data burst in advance to the next BuTiS time reference pulse T_0 (period of 10µs) and become valid at T_0. UTC correlation of timing is achieved through GPS synchronization of both systems.

System Status

The BuTiS center prototype is operational. The optical distribution rack including the delay measurement switch is available for 16 BuTiS distribution lines. Local Reference Synthesizers as well as optical receivers are industrially available. The clock distribution modules are under construction. The field testing for 6 complete local nodes is ongoing.

BuTiS center control software is working. The software includes the delay measurement system as well as the network control of the local reference nodes. Control system software to access BuTiS system status and a data base containing the line delay measurement values is under development.

References

[1] P. Moritz, "BuTiS - Development of a Bunchphase Timing System", GSI Scientific Report 2006, (2007)

[2] B. Zipfel and P. Moritz, „Recent Progress on the Technical Realization of the Bunch Phase Timing System BuTiS", Proc. IPAC 2011, Spain, p. 418-420

[3] "New digital low-level rf system for heavy-ion synchrotrons", Harald Klingbeil, et.al. Phys. Rev. ST Accel. Beams 14, 102802 (2011)

[4] "FAIR Timing System and White Rabbit Project", http://www-bd.gsi.de/dokuwiki/lib/exe/fetch.php?media=fair_timing_fair_technikforum.pdf

Control Theory for RF Feedback and Longitudinal Beam Stability*

D. Lens† [1], *J. Adamy*[1], *J. Grieser*[1], *K. Groß*[1], *and H. Klingbeil*[1,2]

[1]Technische Universität Darmstadt, Darmstadt, Germany; [2]GSI, Darmstadt, Germany

Introduction

Progress in digital hardware solutions such as field programmable gate arrays (FPGA) has raised the question of how to design the algorithms of RF feedback. This especially applies to the feedback of the RF cavities and the longitudinal beam feedback for SIS100. For example, FPGAs currently allow FIR (finite impulse response) filter lengths of several tens of taps. This number of degrees of freedom requires the appropriate modeling of the RF feedback loops and a subsequent analysis and design. The status of current control theory projects for RF feedback loops is described.

Progress in RF Feedback Analysis

Several aspects of the modeling of longitudinal single-bunch oscillations and their RF feedback have been studied [1]. In particular, the dynamics of the quadrupole mode damping loop were modeled and a stability analysis of the feedback parameter space was performed. Measured and simulated amplitude signals for three different experiments agree well as shown in Figure 1. In addition, it has been shown that the feedback of the sextupole mode behaves distinctively different in linear vs. nonlinear simulations. This result implies that the consideration of nonlinearities is necessary for a proper analysis of the bunch feedback. Therefore, the approach of [1] has been extended to include arbitrary nonlinear RF potentials [2]. The extended models rely on a moment approach and can be applied for small and long bunches in the stationary and acceleration case and for single and dual-harmonic operation. In the latter case, a linearization of the RF voltage is not feasible even for small bunch oscillations. To obtain models suitable for controller design, a simplification is made that neglects Landau damping. This makes the stability analysis of the feedback more conservative. However, this may be improved by including additional damping terms that approximate the Landau damping rate. Comparison with simulations shows a good agreement between the models and the full nonlinear beam dynamics. Collective effects are not covered explicitly, but may be incorporated in principle within a robust feedback design.

In a design study, a so-called Fuzzy Controller was developed and simulated to examine a different feedback approach [3]. This feedback uses linguistic rules to calculate the necessary phase shift for damping dipole oscillations. Simulations show good results in keeping the rms emittance at a very low level compared to Landau damping. In a further work, RF models have been derived which include Fourier coefficients [4]. This enables the analysis of beam loading.

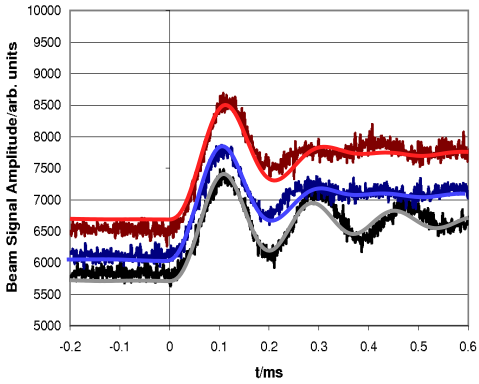

Figure 1: Experiment without feedback (black), with amplitude feedback (blue), and additional phase feedback (red). Simulated curves lie on top of the measured curves.

Practical Implications

The analysis of RF loops has the following practical implications: Due to dynamical coupling between modes, a strong feedback that may damp a specific mode may therefore excite another. Thus, higher order modes should be taken into account during the feedback design process. The models reflect also the well-known fact that the RF phase modulation acts on odd modes, wheres the RF amplitude modulation acts on even modes. This is however only true for the stationary case. During acceleration, the phase modulation has a significant additional impact on the odd modes. However, a simple transformation may decouple this effect.

References

[1] H. Klingbeil, D. Lens, M. Mehler, and B. Zipfel, “Modeling longitudinal oscillations of bunched beams in synchrotrons”, arXiv:1011.3957v1 [physics.acc-ph], Nov. 2010

[2] D. Lens, J. Grieser, and H. Klingbeil: “Longitudinal Closed-Loop Beam Control in Heavy Ion Synchrotrons: Simulation Methods and Results”, Simtech, June 2011, Stuttgart

[3] J. Grieser, H. Klingbeil, and J. Adamy, “Fuzzy Controller for Beam Stabilization in a Heavy-Ion Synchrotron”, ICA 2011, Nov. 2011, Bandung, Indonesia

[4] K. Groß, D. Lens, and H. Klingbeil: “Modeling Longitudinal Beam Dynamics by Combining Fourier Coefficients and Moments”, LLRF 2011, Oct. 2011, DESY Hamburg

* Work partly supported by GSI-TU Darmstadt cooperation contract and by BMBF through contract 06DA9016.

† dlens@rtr.tu-darmstadt.de, H.Klingbeil@gsi.de

Code development: Implementation of compensation electrons for space charge dominated beams

M. Droba[1], A. Almomani[1], O. Meusel[1], D. Noll[1], U. Ratzinger[1], J. Wagner[1], C. Wiesner[1]

[1]Institut für Angewandte Physik, Goethe Universität, Frankfurt am Main, Germany.

Space charge dominated beams in LEBT and MEBT sections of linacs like in FRANZ project or in laser driven proton beam sources of the LIGHT collaboration (***L**aser **I**on **G**eneration, **H**andling and **T**ransport*) poses some unique features in presence of compensation electrons. Especially trapping of the electrons in high magnetic and electric fields can change the beam properties dramatically. An example of the simulated proton beam dynamic for the FRANZ chopper system is shown by Figure 1.

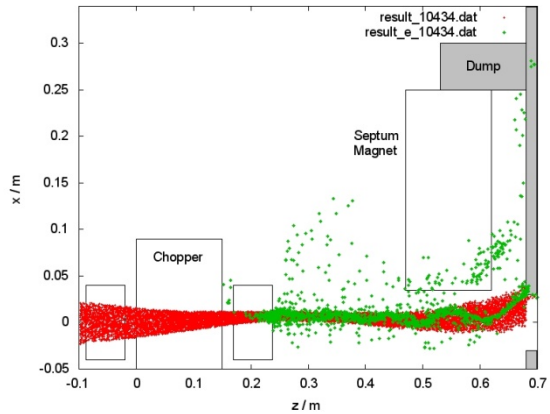

Figure 1: An example of the beam dynamic through the LEBT ExB chopper system for the FRANZ project. The proton beam is depicted in red. Secondary electrons produced on the aperture are in green.

The 3D simulation code LASIN is developed for multi-species (electrons, protons and ions) beam tracking through a solenoidal magnetic field with high space charge forces and at rapidly varying geometric bunch dimensions (from 10 µm to 5 cm transversely along a longitudinal drift of about 50 cm). The magnetic field is calculated by the Biot-Savart solver using a numerical integration scheme from a given distribution of current elements. At every exact particle position at a given time step, the B-field is calculated accordingly.

In case of space charge forces, the charge density is integrated on a cylindrical mesh from a particle distribution by PIC (Particle-In-Cell) techniques [1]. Afterwards, the Poisson equation is solved numerically by the iteration method BiCGSTAB (Bi-Conjugate Gradient Method-Stabilized) [2] on the mesh resulting in the potential distribution. For the tracking algorithm the electric field is interpolated at the particle position.

A symplectic middle step scheme [3] in Cartesian coordinates is used to follow the particle motion in given fields. The code is implemented at the Frankfurt Center for Scientific Computing CSC cluster by fully exploiting the parallel processing capabilities. Typically, 50 processors and up to 10^7 macroparticles are used in proton tracking simulations from the laser target (TNSA) to the CH accelerating structure. For optimization purposes and memory requirement reduction the sparse format of stored vectors and matrices is used.

The space charge force action on the beam dynamics of the single proton pulse along the magnetic solenoid was investigated in detail.

Detailed investigation showed how the trapped electron column influences the beam focusing and spectral distribution of the proton pulse in the first 40ps after generation (Fig. 2). The momentum exchange between the species is present and results in a distribution splitting in phase space. This is a major factor for injection into a proposed CH-structure for further post-acceleration. As a consequence an optimized CH-linac was designed. Overall 72% transmission was reached in simulation from the target position to the end at energies of 40MeV.

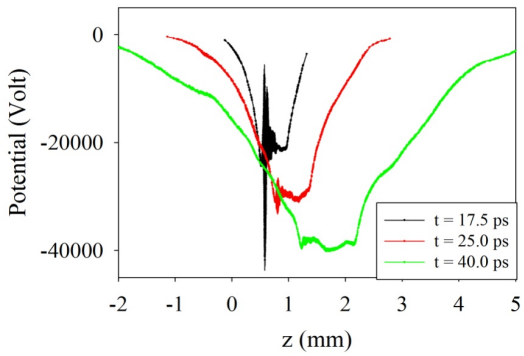

Figure 2: An example of the on axis potential distribution of a laser generated single proton pulse with co-moving electrons in a focusing solenoid. The electrons are trapped by a magnetic field on axis, while protons expand.

A new simulation code is under development. It will cover the problematic of multi species in a more general and allow for arbitrary geometries by using various space charge methods (FEM, Multigrid, Gradient Methods).

References

[1] J. M. Dawson, Rev. Mod. Phys. 55, 403-447 (1983).

[2] M. M. T. Wang and T.W.H. Sheu, Journal of Computational and Applied Mathematics 79, 147-165 (1997).

[3] T. J. Stuchi, Braz. J. Phys. Vol.32 no.4 (2002) doi:10.1590/S0103-97332002000500022.

Transport and rebunching of a laser generated proton beam

S. Yaramyshev[1], W. Barth[1], I. Hoffman[1], A. Orzhekhovskaya[1], B. Zielbauer[1]

[1]GSI, Darmstadt, Germany.

An impressive advantage of Laser Ion Sources is an extremely high beam brilliance. The LIGHT (**L**aser **I**on **G**eneration, **H**andling and **T**ransport) collaboration [1] is dedicated to build up at GSI a test stand for an investigation of the proton beam, accelerated with GSI laser PHELIX [2]. The installation is already integrated into a beam line (Fig. 1) of the GSI heavy ion high current linac UNILAC [3]. It provides for an unique possibility to tune the beam line and to calibrate diagnostics devices with an ion beams.

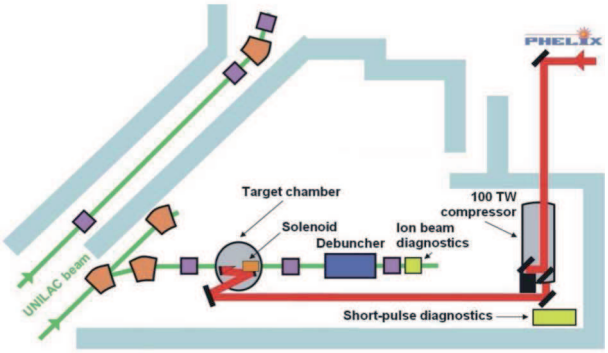

Figure 1. Integration of the LIGHT test stand into existing UNILAC beam line.

Generally the LIGHT collaboration combines together three different tasks:

- Development of the powerful laser and delivery of the laser beam to the target;
- Simulations of the very early expansion of the laser generated electron-ion cloud and an optimization of the target;
- Capture, collimation and rotation of the ion beam including its matching to the conventional accelerator.

The versatile multiparticle code DYNAMION [4] was implemented to perform beam dynamics simulations for the transport line, which comprises a solenoid for transverse beam focusing and an rf cavity decreasing the energy spread of the protons (bunch rotation) [5]. General feature of the code is a solving of the full 3D-equation of particle motion in 3D electromagnetic field. Therefore non-linear effects, as well as high order chromatic aberrations, are included into the simulations automatically.

The initial beam parameters (Tab. 1) for the simulations are based on the experimental data and dedicated calculations of plasma expansion.

The bunch rotation is foreseen by means of an existing GSI 3-gap 108 MHz buncher [6]. It is planned to be installed into the beam line this year. A 3D electrical field inside the buncher was calculated with the DYNAMION package for the measured topology of the gaps and tubes. A comparison of the calculated and measured electrical field [7] shows good coincidence.

Table 1: Estimated input parameters of the proton beam

Energy	10 MeV
Energy spread	± 50%
Phase spread	± 0.75° (at 108 MHz)
Transverse emittance	< 5 mm*mrad
Transverse divergence	± 172 mrad
Transverse radius	± 0.03 mm

A good energy resolution behind the buncher can be observed on Fig. 2. This result is especially promising for the planned experimental parameter study of the laser generated beam at the LIGHT test stand.

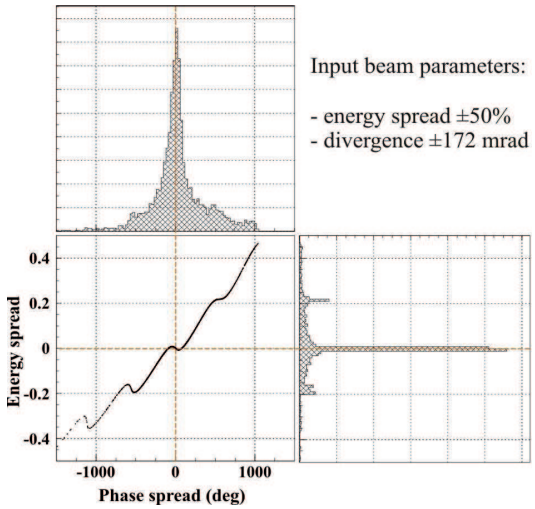

Figure 2. A longitudinal beam phase portrait at the end of the transport line.

An unique installation for the transport, collimation and rotation of the proton beam, generated by powerful laser PHELIX, is integrated into GSI UNILAC beam line.

An ion beam with variable energy from UNILAC can be used for tuning the beam line settings and for calibration of the beam diagnostics devices.

Beam dynamics simulations by means of DYNAMION code are used for the design and optimization of the beam line.

Experiments at GSI with laser generated proton beam, focused by the solenoid and rotated with the buncher, are already planned for 2012.

References

[1] S. Busold et al., PAC-2011, WEP256.
[2] V. Bagnoud et al., APP. Phys. B, 2009.
[3] W. Barth et al., NIM A, 577(1), p. 211, 2007.
[4] S. Yaramyshev et al., NIM A, 558(1), p. 90, 2005.
[5] I. Hofmann et al., Phys. Rev. 031304, 2011.
[6] S. Yaramyshev et al., IPAC-2011, MOODB03.
[7] W. Vinzenz, GSI Scientific Report, 1991.

ColMat activities at GSI*

J. Stadlmann†[1], *L. Boyzk*[1,2], *H. Kollmus*[1], *E. Mustafin*[1], *N. Pyka*[1], *P. Spiller*[1], *I. Strasik*[1], *N.A. Tahir*[1], *M. Tomut*[1,3], *and C. Trautmann*[1,2]

[1]GSI, Darmstadt, Germany; [2]TU Darmstadt, Germany; [3]NIMP, Bucharest, Romania

Introduction

ColMat is the name of WP8 of the joined R&D initiative EuCARD funded by the EU in FP7 [1]. The topics of WP8 are collimators and suitable collimator materials for modern high power, high brightness accelerators. Contributors are more than ten European institutes and universities.

Contribution by GSI groups to ColMat

GSI covers prototyping and testing of a cryogenic ion catcher for SIS100, simulations and studies on activation of accelerator components e.g. halo collimators as well as irradiation experiments on materials foreseen to be used in FAIR accelerators and the LHC upgrade program.

Cryo-catcher for SIS100

One of the main deliverables within ColMat is a prototype of the cryogenic ion catchers which will be placed in the arcs SIS100 to control beam losses due to charge exchange. Controlling such losses prevent dynamic vacuum effects and is mandatory to obtain the high beam intensities foreseen for FAIR facility. The prototype was delivered to GSI and tested with SIS18 beam in 2011 [2, 3].

Ion induced damage in materials for collimators

To study radiation-induced dimensional changes and degradation of thermo-mechanical properties, graphite and AC 150 carbon-carbon composite samples were irradiated with heavy and light ions. The irradiation experiments were performed at energies of 11.1 MeV/u, with GSI the UNILAC accelerator at GSI. Similar studies have been started on new candidate materials such as diamond-metal composites. Depending on the specific modifications and functional properties, the most suitable material will be selected for the construction of collimators to be used for FAIR and the LHC upgrade [4].

Beam-halo collimation studies for SIS100

SIS100 will be operated with high intensity proton and ion beams. The ions will have intermediate charge states (design Ion U^{28+}). To collimate the beam particles two different multi stage solutions are foreseen. Heavy ions will interact with a charge striper foil and loose all electrons. Due to the lower magnetic rigidity of those stripped ions they will be deflected and dumped by the two warm quadrupoles in the extraction section of SIS100 similar to beam losses during slow extraction. The protons will be scattered by a different primary collimator and dumped in secondary beam stoppers. Studies on this collimator systems are performed within ColMat and are presented in this report [5].

Simulation of beam interaction with collimators

The high intensities of modern accelerators require already very robust collimator designs to withstand the beam loss during standard operation. In case of accidental beam losses the risk of damage is very high. Numerical simulations on the possible damage by LHC and SPS beams to different targets have been performed within ColMat [6]. The studies concentrate on full impact of all or parts of the LHC and SPS beams. The results obtained at GSI are benchmarked with other contributor's codes and future experiments at the HighRadMat facility at CERN's SPS. [7].

Summary and outlook

Several new collaborations with other institutes and industry participating in the EuCARD framework could be established. Most GSI milestones and deliverables defined in ColMat have already been achieved, some ahead of schedule. The overall success led to a follow-up proposal within the next EU accelerator R&D framework EuCARD[2] which is supposed to start in 2013.

References

[1] ColMat web page `http://eucard.web.cern.ch/eucard/activities/research/WP8/`

[2] L. Bozyk et. al., "SIS100 Prototype Cryocatcher" *IPAC 2011 Conf. Proc. (TUPS007)*, San Sebastian, (2011).

[3] L. Bozyk et al., "Measurements with the SIS100 Cryoctacher Prototype" within this GSI Sci. Rep. 2011.

[4] M. Tomut et al., "In-situ SEM investigations of ion- induced damage in novel diamond-copper composite materials for LHC collimators jaws" within this GSI Sci. Rep. 2011.

[5] I. Strasik and E. Mustafin "Halo Collimation of Protons and Heavy Ions in SIS100" within this GSI Sci. Rep. 2011.

[6] N.A. Tahir et. al., "Simulations of Interaction of 7 TeV/c LHC Protons with a Carbon Beam Stopper" within this GSI Sci. Rep. 2011.

[7] N.A. Tahir et. al., "Simulations of BeamMatter Interaction Experiments at the HiRadMat Facility at CERN" within this GSI Sci. Rep. 2011.

* Work supported by EU, Grant Agreement No: 227579 EuCARD

† j.stadlmann@gsi.de

Status of the Antiproton Production Area for FAIR

V. Gostishchev, K. Knie and M. Steck
GSI, Darmstadt, Germany.

The first simulations of the expected radiation levels for the antiproton target area were already reported [1,2]. In order to ensure that a sufficient radiation protection of the neighboring areas can be achieved, a series of extensive simulations were performed for the latest layout of the antiproton production area for FAIR.

The Monte-Carlo particle transport code FLUKA [3,4] was used for the simulations. A very detailed geometry file was needed as input to obtain reliable results. The latest architect drawings of the pbar target area were used as a basis for the geometry in the FLUKA input file. The magnetic fields in the magnetic horn right after the target, all quadrupole magnets and all dipole magnets were taken into account in the simulations.

The region used for a simulation was slightly increased in comparison with the previous simulations. Due to the high energies and the long ranges of the primary and secondary particles a large region of 50 × 30 × 200 m³ ($x \times y \times z$) was used in the FLUKA calculations (see Fig. 1). In the simulations the antiproton production area of FAIR was extended in the direction of the CR/RESR building by about 50 m. Thus the geometry used for the FLUKA calculations became more realistic than before.

Concrete is used as shielding material between and above the tunnels. Between antiproton target building (6c) levels and neighboring buildings 6c and 7, encapsulated soil is used for shielding. Inside the tunnels wet air is used to account for the moderation of neutrons. The target and magnetic horn are located in an iron shielding with 1.6 m thickness on the downstream side and 1.0 m thickness on all other sides.

It was important to know the expected radiation level in the CR/RESR building caused by operation of the pbar separator. The CR/RESR hall is separated into two parts, inner part and the ring tunnel, by the central wall. It protects the inner part of the hall, equipment and personnel, during operation, either from radiation in the tunnel or from activation induced by the pbar separator. It is planned to have a free access to the inner part of the hall during CR operation. According to the German Radiation Protection Ordinance areas with dose rates below 0.5 µSv/h (purple and white) are accessible without any restriction. It was found out that activation caused by antiproton production gave an increase of the radiation level in the inner part of the building to values which could not be accepted. In order to reduce the radiation level there a part of the central wall was enforced by means of additional 1.5 m of concrete. The entrance walls of the CR/RESR hall were modified as well in order to reduce activation coming from the pbar separator.

The shielding wall between pbar target tunnel and the building 50 was modified according to the latest drawings and used in the simulations. Its thickness is about 8 m and it is enough for the protection of the neighboring building 50 during antiproton production (see Fig. 1). Encapsulated soil layer was successfully introduced between the antiproton target and the CR/RESR buildings instead of large concrete volume. It is obviously a cheaper solution than before and it can be used as demonstrated in Fig. 1.

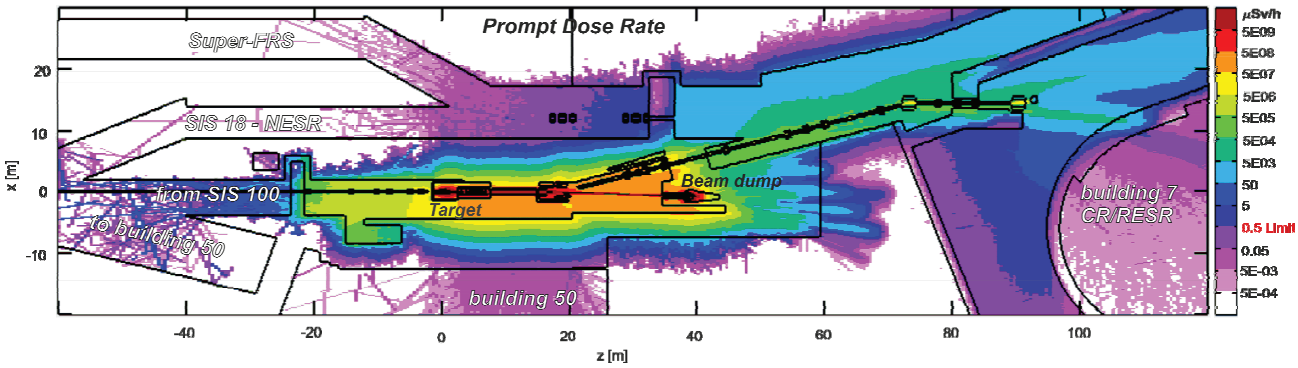

Figure 1: Prompt dose rates during operation with 2×10^{13} protons per pulse and a repetition rate of 0.1 Hz. The data are averaged over a height interval of ± 1.0 m relative to the beam line. The target is located at (0,0). The primary beam is dumped at $z \approx 40$ m, the antiprotons are transported to the CR/RESR hall.

References

[1] GSI Scientific Report (2007) 59.
[2] GSI Scientific Report (2008) 84.
[3] A. Fassò, A. Ferrari, J. Ranft, and P.R. Sala, CERN-2005-10 (2005), INFN/TC_05/11, SLAC-R-773.
[4] G. Battistoni, S. Muraro, P.R. Sala, F. Cerutti, A. Ferrari, S. Roesler, A. Fassò, J. Ranft, Proceedings of the Hadronic Shower Simulation Workshop 2006, Fermilab 6-8 September 2006, M. Albrow, R. Raja eds., AIP Conference Proceeding 896, 31-49, (2007)

DNA Damage after High-LET Exposure

M. Ensminger[1], S. Conrad[1], O. Barton[1], G. Taucher-Scholz[2] and M. Löbrich[1]
[1]Darmstadt University of Technology, Germany; [2]GSI, Darmstadt, Germany

It has been known for several years that DNA double-strand breaks (DSBs) evoked by particle radiation are generally more slowly repaired than breaks induced by photon irradiation. Moreover, the fraction of residual breaks after prolonged repair incubation correlates with the cell killing capacity of high-LET radiation. However, the understanding of the molecular processes is still incomplete.

In this study we focus on the complexity of DSBs induced by heavy ions, especially carbon-ions. Owing to the high ionisation density of high-LET particles, heavy ion irradiation induces DSBs that are generally more complex with additional lesions in very close proximity to the DSB. Recently we have reported that complex breaks require processing before repair, performed by the nuclease Artemis that is operating in a common repair pathway with the kinase ATM. Cells deficient in one of these factors are specifically defective in the repair of DSBs with slow repair kinetics and the level of unrepaired breaks seems to depend upon the complexity of the DSB ends. After α-particle irradiation a higher proportion of DSBs is repaired in an ATM and Artemis dependent manner than after X-irradiation. By contrast ATM and Artemis are dispensable for the repair of "clean" DSBs induced by the topoisomerase II inhibitor etoposide [1].

To determine the amount of complex DSBs after heavy ions, we irradiated HeLa cells with 2 Gy ^{12}C (LET: 170keV/µm) ions using the UNILAC at the GSI. We depleted the nucleases Artemis and CtiP in these cells by siRNA prior to irradiation, to measure the importance of these factors on the repair of complex DSBs. The repair of the DSBs was monitored by a cell cycle specific γH2AX immunofluorescence assay. Artemis- and CtIP-depleted cells were seeded on cover slips and irradiated with ^{12}C ions under a small angle to the beam. γH2AX foci along the ion tracks were analysed in G1 and G2 cells. In Artemis deficient cells a high repair defect was detected with this approach in G1(Fig.1 B) and G2-phase (Fig. 1A) of the cell cycle, therefore supporting our notion that Artemis is indispensible for the repair of complex DSBs. Interestingly, CtIP-depleted cells also showed a pronounced repair defect after irradiation in both cell cycle phases.

Downregulation of CtIP and Artemis together revealed that these factors work in the same repair pathway, because no pronounced epistatic effect was present in these cells. The defect of the double knockout was comparable to the repair defect observed in Artemis deficient cells. Together, these results demonstrate that the nucleases Artemis and CtIP are indispensible for the repair of complex DSBs induced by high-LET particle irradiation.

A) G2-cells

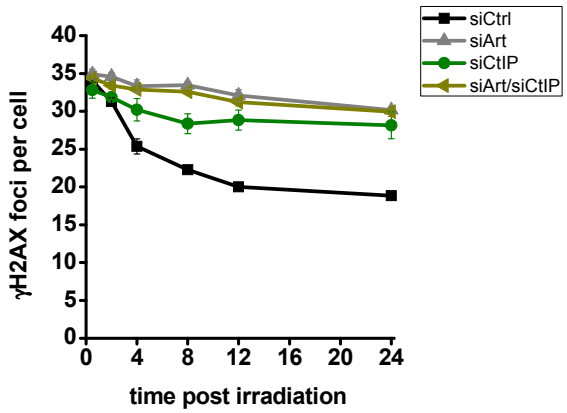

B) G1-cells

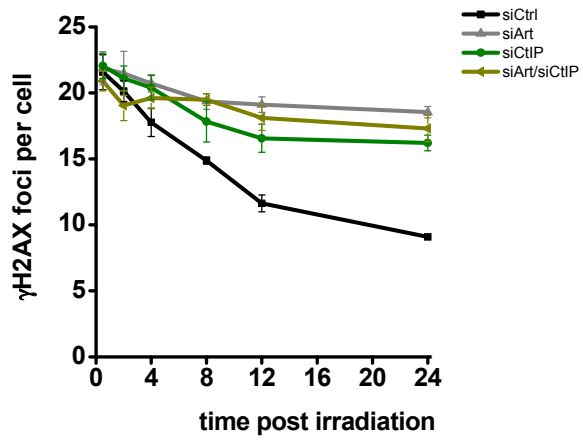

Fig.1: DSB repair kinetic of HeLa cells treated with different siRNA prior to irradiation with 2 Gy carbon ions. Artemis- and CtIP- downregulated cells exhibit a pronounced repair defect in G2 (A) and G1 (B).

References

[1] E. Riballo, M. Kühne, N. Rief, A. Doherty, et al., Molecular Cell 16 (2004) 715-724

Accumulation of H4K16 acetylation at heavy ion induced damage sites*

M. Herrlitz[1], I. Müller[2], A.L. Leifke[2], G. Becker[2], M. Durante[2,3] and G. Taucher-Scholz[2]

[1]FIAS, Frankfurt Institute for Advanced Studies, Germany; [2]GSI, Darmstadt, Germany; [3]TUD, Darmstadt, Germany

Introduction

Chromatin is a well organized complex of DNA and proteins. If damage occurs the DNA is repaired in a clearly defined process involving repair proteins and chromatin modifications. Here chromatin modifications are regulating binding affinities of different proteins at sites of DNA double-strand breaks as well as the compaction of DNA. Histone modifications, especially Histone acetylation at defined Lysine residues, play a major role in changing the density of chromatin.

Since it is shown that a local decompaction of heterochromatic regions takes place at sites of DNA damage [1], we investigated the acetylation of different histone residues that might be involved in this process. We investigated the histone residues H4K16 as well as H3K56. It is known that these residues play a role in the DNA damage response after irradiation with X-Rays and UV-Laser [2,3].

Methods

Mouse embryonic fibroblast and human osteosarcoma cells were irradiated under low angle, causing a streak pattern which is produced as an accelerated heavy ion passes the nucleus. After fixing the cells at different timepoints, immunostaining and confocal microscopy were used to visualize proteins of interest. To examine their accumulation at damage sites a colocalization with γH2AX was assessed.

Results and Conclusions

Acetylated H4K16 is increased at damage sites after irradiation with heavy ions

H4K16ac showed (in a fraction of cells) an increased signal at damage sites causing a streak pattern (white arrow in figure 1) that is clearly distinguishable from the H4K16ac signal in the whole nucleus. An accumulation of H3K56ac was not observed (data not shown).

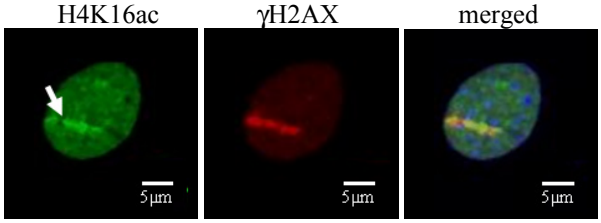

Figure 1: Accumulation of H4K16ac in mouse embryonic fibroblasts. Cells were irradiated with Au ions (LET: 13000 keV/µm; Fluence: $3x10^6$ p/cm^2) under low angle and fixed after 1 hour. H4K16ac (green) is increased at damage sites. DNA damage is shown by γH2AX staining (red). DNA is counterstained with ToPro3 (blue).

No visible recruitment of MOF in human osteosarcoma cells

To get insight into the role of H4K16ac in the damage response, we focused on MOF, which is known as the major acetylase modifying H4K16 [3]. First we analyzed if MOF is recruited to damage sites after irradiation with heavy ions. A colocalization of MOF with γH2AX indicating recruitment to damage sites was not visible (figure 2).

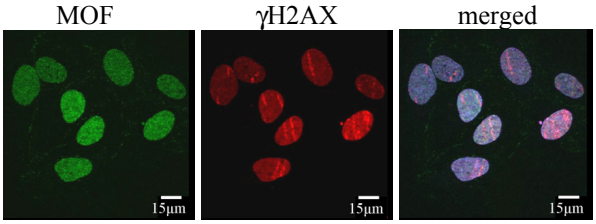

Figure 2: MOF is not recruited to damage sites after irradiation with heavy ions. After irradiation of human osteosarcoma cells with Au ions (LET: 13000 keV/µm; Fluence: $3x10^6$ p/cm^2), cells were fixed after 2 hours and stained for MOF (green). DNA damage is shown by γH2AX staining (red). DNA is counterstained with ToPro3 (blue).

H4K16ac accumulates at damage sites after irradiation with Au-ions whereas an accumulation of H3K56ac at damage sites could not be observed. These findings suggest that H4K16ac might play also a role in the damage response after irradiation with heavy ions. Since it is known that acetylation of H4K16 changes chromatin to a more open conformation it has to be elucidated if H4K16 acetylation is involved in decompaction of DNA at damage sites.

Recently, it has been proposed that MOF is the major enzyme acetylating H4K16 [3]. Since we do not see an increase of MOF at damage sites, we suppose that even low amounts of MOF assembled at damage sites are sufficient to acetylate H4K16.

Further experiments are needed to elucidate the role of H4K16 acetylation in the ion – induced damage response more closely.

References

[1] Jakob, B. et al. (2011) Nucleic Acids Research, vol. 39, p.6489 – 6499

[2] Miller, K. M. et al. (2010) Nature Struct. & Mol. Biol., vol. 17, p.1144 – 1152

[3] Li, X. et al. (2010) Mol. & Cell. Biol., vol. 30, p. 5335 – 5347

*Supported by the Beilstein – Institut, Frankfurt/Main, Germany, within the research collaboration Nano BiC and BMBF grant 02S8355. Work is part of HGS-HIRe.

ACF1 and CHD4 are not recruited to sites of DNA damage after heavy ion irradiation*

I. Müller[1], F. Haster[1], A. L. Leifke[1], R. Khan[1], M. Durante[1,2] and G. Taucher-Scholz[1]

[1]GSI, Darmstadt, Germany; [2] TUD, Darmstadt, Germany.

Introduction

Emerging evidence suggest that the DNA damage response has a major impact on the surrounding chromatin within the cell nucleus. Changes in histone modifications and recruitment or release of different chromatin interacting proteins have been reported. One main role hereby plays the local decondensation of chromatin, which is thought to enhance access of repair proteins to sites of DNA damage. In a recent paper [1] we showed that we can visualise this chromatin decondensation after heavy ion induced DNA double strand breaks (DSB) directly by fluorescent DNA staining (DAPI), but only within the heterochromatic areas of mouse embryonic fibroblast cells. Heterochromatin represents the transcriptional inactive and therefore more compacted part of the chromatin within the cell nucleus. Other than in human cells in mouse cells these heterochromatic areas are concentrated in DAPI bright spots, the so called chromocentres. Being even more compacted, these areas probably need a more efficient or an additional pathway, compared to euchromatic regions, for opening up the DNA before repair.

Chromatin decondensation is carried out by so called chromatin remodelling complexes, which uses ATP hydrolysis to remove or translocate nucleosomes along the DNA or by changing the nucleosome histone composition. Two good candidates for triggering an early decondensation event after heavy ion irradiation within heterochromatin are displayed by the NuRD and the ACF1 chromatin remodelling complexes. Both reported to participate in the DNA damage response pathway and additionally exhibiting specialised function in heterochromatin. While the ACF1 complex is responsible for decondensation within hetrochromatin to allow DNA to become replicated and is responsible for the recruitment of Ku70/80 at the DSB [2], the NuRD complex assembles at pericentric heterochromatin and is reported to be phsophorylated by ATM, one of the main kinases in DNA repair [3].

Results

Many proteins which are involved in the repair machinery accumulate within so called repair foci around DSB. So looking for the recruitment of a protein to the side of damage is one of the easiest ways for testing the involvement and the time dependency of the chosen protein in repair.

After laser induced DNA damage a fast (within seconds) accumulation of GFP-fusion proteins of ACF1 and CHD4 (the ATPase of the NuRD complex) was reported [3;4] and could be verified for both proteins with our newly established 405nm Laser system (Khan same GSI report). After heavy ion induced DNA damage however no obvious accumulation of either ACF1-GFP (Figure 1) or CHD4-GFP (data not shown) can be observed.

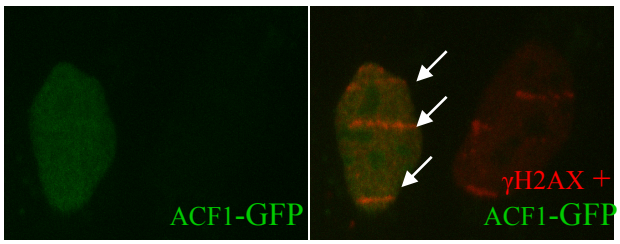

Figure 1: No obvious accumulation of ACF1-GFP at sites of DSB. Mouse fibroblast cells were transiently transfected with ACF1-GFP (green) and irradiated with gold ions at the UNILAC (13.000 keV/µm). Counterstaining with γH2AX (red) indicates sites of DSB (arrows).

Conclusion

While after irradiation with laser direct recruitment of ACF1- or CHD4-GFP to the DSB can be observed, no such accumulation is visible after irradiation with heavy ions, which might be due to very high local doses delivered by laser [4]. Further and more direct experiments will help to study the influences of ACF1 and CHD4 on chromatin decondensation in heterochromatic areas at early timepoints after irradiation with heavy ions.

References

[1] Jakob et al, Nucleic acids research 39, 6489-99.
[2] Lan et al, Molecular cell 40, 976-87.
[3] Larsen et al, The Journal of cell biology 190, 731-40.
[4] Splinter et al, Mutagenesis 25, 289-97.

Acknowledgements

Thanks to Karsten Rippe for the ACF1-GFP construct and Jiri Lukas for the CHD4- GFP construct.

* Work supported by BMBF (02NUK001A, 02NUK001C and 02S8355)

An attempt to see chromatin structure change after heavy ion irradiation at the GSI microbeam

B. Merk[1,2,#], K.-O. Voss[1], I. Müller[1], B.E. Fischer[1], B. Jakob[1], G. Taucher-Scholz[1], C. Trautmann[1], and M. Durante[1,2]

[1]GSI, Darmstadt, Germany; [2]Technische Universität Darmstadt, Germany

Introduction

In collaboration of GSI Biophysics and Material Research, the microbeam is routinely employed for targeted irradiation of living cells in culture [1]. A custom-made epi-fluorescence microscope is used for beam targeting and cell observation via fluorescent dyes which specifically highlight biological proteins of interest.

Over the past two years, we added a dedicated laser system to the microbeam to locally bleach these fluorescent markers [2]. Following up the intensity distributions after bleaching it is possible to gain information about dynamic processes after DNA damage induction induced by ion irradiation.

Experiments with laser induced DNA damage have shown a change in chromatin structure after exposure with UV light [3].

Therefore, we used the new laser system at the GSI microbeam with the aim to see if there is a chromatin structure change after heavy ion irradiation analog to the one reported after UV irradiation [3].

Experiment

The basic idea is to use the laser system to bleach a specific pattern into the fluorescence tagged chromatin of a cell nucleus. The bleached structure is expected to shift or distort after DNA damage induction produced by irradiation with ions.

To measure chromatin structure changes we used a stable HeLa-H2B-GFP cell line[1] where the structural histone H2B is tagged with green fluorescent protein. To visualize the DNA damage after ion irradiation these cells had an additional red fluorescent marker (RFP) tagged on repair protein XRCC1[2].

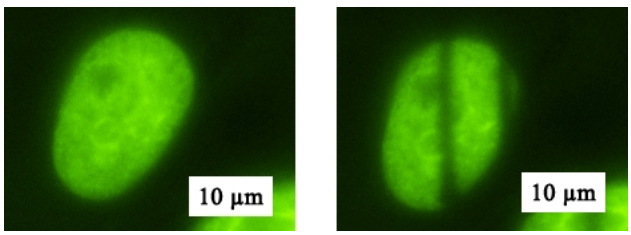

Figure 1: Hela-H2B-GFP cell nucleus before (left) and after bleaching (right).

On the left side of figure 1 one cell nucleus is visible before bleaching. On the right side the same nucleus is shown after the focused 488 nm laser [2] has bleached two vertical lines into the GFP tagged H2B.

The borders of the bleached lines have been irradiated with 4.5 µm long lines of 9 Au ions as shown in Fig. 2 left (white lines). DNA damage locations were verified by XRCC1-RFP (Fig. 2 right).

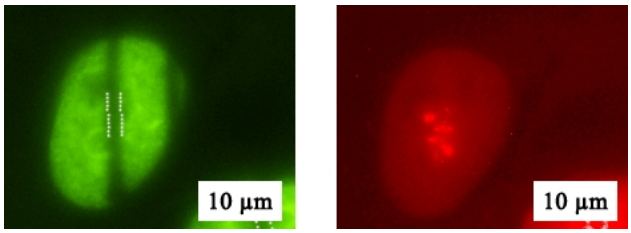

Figure 2 left side: Bleached HeLa-H2B-GFP cell nucleus before irradiation with gold ions. Every white point was irradiated with one ion.
Right side: In red the same cell nucleus, but after irradiation with gold ions DNA damage sides are visible by XRCC1-RFP accumulation.

As a measure for damage mediated chromatin movement we evaluated the width of the GFP bleach lines where the surrounding DNA has been damaged by ion irradiation relative to the width where the local DNA was spared from damage.

Results

In these first measurements not major change in chromatin structure was observable. As only 7 cell nuclei have been involved in the experiment additional measurements are required. Nevertheless this first experiment demonstrates the capability of the dedicated laser system.

References

[1] M. Heiß, B. E. Fischer, B. Jakob, C. Fournier, G. Becker, and G. Taucher-Scholz , Radiation Research 165 (2006) 231

[2] B. Merk, K.-O. Voss, B. E. Fischer, B. Jakob, G. Taucher-Scholz, and M. Durante, GSI Scientific report 2010, p. 394

[3] M. J. Kruhlak, A. Celeste , G. Dellaire, O. Fernandez-Capetillo, W. G. Müller, J. G. McNally, D. P. Bazett-Jones, and A. Nussenzweig, The Journal of the Cell Biology 172 (2006) 823-834

B.Merk@gsi.de

[1] stably transfected HeLa-H2B-GFP cell line kindly provided by D. Zink, LMU München, Germany

[2] XRCC1-RFP kindly provided by N. Averbeck, GSI, Darmstadt, Germany

DNA double strand break resection after heavy ion irradiation

N. B. Averbeck[1], O. Ringel[1], M. Herrlitz[1], B. Jakob[1], F. Tobias[1], A. L. Leifke[1], M. Durante[1, 2], and G. Taucher-Scholz[1]

[1]GSI Helmholtzzentrum für Schwerionenforschung GmbH, Darmstadt, Germany;
[2]TUD, Institut für Festkörperphysik, Darmstadt, Germany

It is well known that DNA double strand break (DSB) resection occurs as a pre-requisite of the repair pathway of homologous recombination that takes place in the late S and G2 cell cycle phase. We study DSB repair with heavy ion irradiation; it represents an excellent tool for investigating DSB repair as one can generate strictly localized DSBs within the nucleus and analyze the recruitment of repair factors to these lesions by immunofluorescence. Applying this technique we were able to show that several heavy ion irradiation induced DSBs in the cell cycle phase G1 require also resection as RPA located at DSBs in G1 (Figure 1); RPA is a protein that binds and protects single stranded DNA, which is generated during DSB resection. Since heavy ions represent high LET radiation that causes DSBs with high complexity, most likely lesion complexity plays a critical role in the decision of DSB resection in G1.

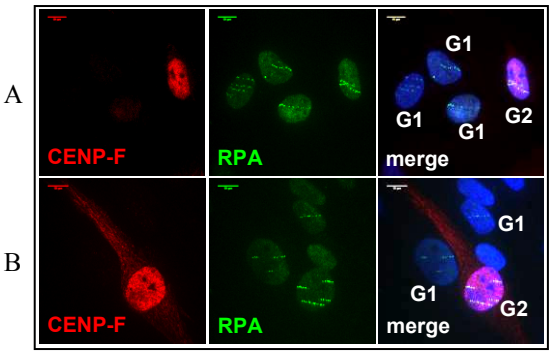

Figure 1: RPA is recruited to DSBs in G1 after heavy ion irradiation. Human tumor cells U2-OS (A) as well as human fibroblasts (B) were irradiated with ^{197}Au ions (LET: 13000 keV/µm; fluence: 3 x 10^6 p/cm^2) and fixed 1 h after irradiation. Cells were immuno-stained for CENP-F and RPA. DNA was visualized by DAPI staining. No CENP-F signal: G1 cell; strong CENP-F signal: G2 cell. Scale: 10 µm

The question arises, which nuclease is responsible for the DSB resection in G1. In G2 the endonuclease CTIP is crucial for DSB resection [1]. Thus, in a first step we tested whether or not CTIP is recruited to heavy ion induced DSBs in G1. By immunofluorescence analysis we were able to show that CTIP is indeed recruited to DSBs in G1 (Figure 2). We further demonstrated that CTIP is important for the observed resection in G1 as down regulation of CTIP expression by RNA interference (*knock down*, k. d.) diminishes resection in G1 (Figure 3). A decrease of CTIP expression reduces resection to the same degree in G1 as well as S/G2 cells, suggesting that CTIP plays an equal important role in G1 as well as S and G2 after heavy ion irradiation (Figure 3).

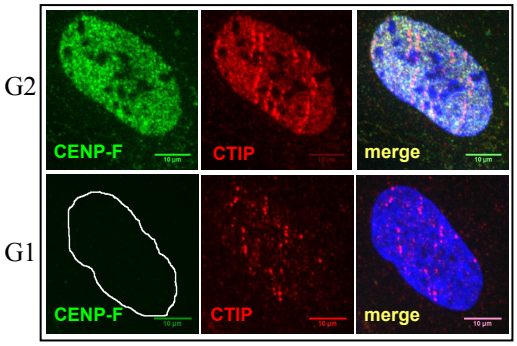

Figure 2: CTIP is recruited to DSBs in G1. Cells were irradiated with ^{238}U ions (LET: 15000 keV/µm; fluence: 3 x 10^6 p/cm^2) and fixed 1 h after irradiation. Cells were immuno-stained for CENP-F and CTIP. DNA was visualized by DAPI staining. Scale: 10 µm

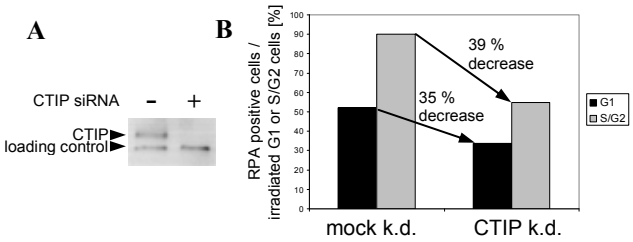

Figure 3: Down regulation of CTIP expression (CTIP k. d.) diminishes resection in G1 as well as S/G2 cells to the same degree. **A** Successful CTIP knock down; **B** Relative number of RPA positive irradiated G1 and S/G2 cells, respectively. Cells were irradiated with ^{119}Sn ions (LET: 7900 keV/µm; fluence: 3 x 10^6 p/cm^2) and fixed 1 h after irradiation.

Taken together, resection seems to represent an important step in DSB processing upon heavy ion irradiation – not only in S and G2 cells but even in G1 cells. In future experiments we want to further characterize this G1 resection and find out whether this is coupled to a specific repair pathway.

References

[1] A. Sartori *et al.* (2007) Human CtIP promotes DNA end resection, Nature, vol. 450, p. 509 - 515

Acknowledgements

This work is part of HGS-HIRe and partially funded by BMBF grants 02NUK001A and 02S8355.

FRET imaging based analysis of protein interactions in living human cells*

F. Tobias[1], R. Khan[1], A.L. Leifke[1], M. Durante[1,2], B. Jakob[1] , and G. Taucher-Scholz[1]

[1]GSI, Darmstadt, Germany; [2]Technische Universität Darmstadt, Institut für Festkörperphysik, Darmstadt, Germany

Introduction

The correct repair of damaged DNA is most crucial for cells to survive exposure to ionizing radiation. Cells possess various mechanisms to cure damaged DNA. In these processes many distinct proteins are involved, interacting with each other in a complex network. However it is highly challenging to measure protein interactions in living cells. A process called Förster Resonance Energy Transfer (FRET) enables interaction-measurements of fluorescently tagged proteins. FRET describes energy transfer within a range of typically a few nm from an excited donor- to an acceptor fluorescent protein. Our experimental setup, measuring FRET by fluorescence polarization anisotropy was described and validated for green/red fluorescent proteins in a previous report [1]. Here we present the capability of our setup for measuring interactions between blue/yellow tagged proteins and first experimental results in the cellular response to charged particle irradiation.

Results

Blue/yellow fluorescence protein interaction

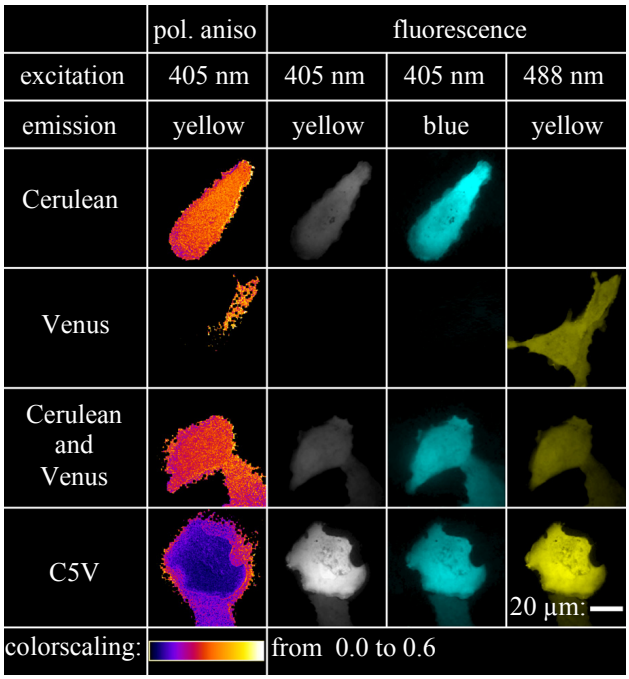

Figure 1: Blue (Cerulean) and yellow (Venus) fluorescent proteins in living human U2OS cells. C5V describes Cerulean linked with Venus by 5 amino acids.

To test the system for the capability of measuring interactions between the blue and yellow fluorescent proteins Cerulean and Venus, respectively, human U2OS cells were transfected with only Cerulean, only Venus, Cerulean and Venus or with a construct referred to as C5V in which each Cerulan is linked with a Venus by 5 amino acids† [2]. In the C5V construct each Cerulean protein is in close contact to a Venus protein resulting in a high FRET efficiency. The energy transfer from the donor (Cerulan) to the acceptor (Venus) provokes a reduction of the acceptor fluorescence polarization anisotropy [3]. The clearly reduced yellow polarization anisotropy of C5V with Cerulean excitation is in agreement with previous studies [4] and proofs our setup for detecting protein interactions between blue and yellow tagged proteins.

53BP1 after Au ion irradiation

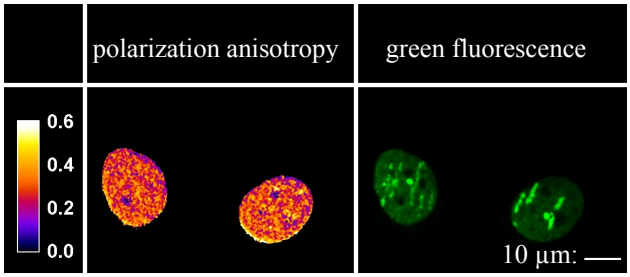

Figure 2: Human U2OS cells transfected with 53BP1-GFP, after low angle Au-ion irradiation.

Fluorescence polarization anisotropy based FRET measurements provide the unique possibility to detect FRET between identical tagged proteins. Reduced polarization anisotropy would indicate protein oligomerization. Here the DNA repair protein 53BP1-GFP was analyzed after Au-ion irradiation. However no reduction of polarization anisotropy along the streak patterned 53BP1-aggregates at the DNA damage could be detected. Hence it is unlikely that GFP proteins of different 53BP1 molecules come in close proximity of a few nm even after irradiation with high LET particles.

Conclusion

Our fluorescence polarization anisotropy based FRET setup was validated for measuring protein interactions between blue/yellow tagged proteins in living cells. Furthermore the repair protein 53BP1 did not show indications for local oligomerization at sites of damaged DNA.

References

[1] Tobias et al. , GSI report 2010 (2011).
[2] Koushik et al. , Biophysical Journal (2006).
[3] Piston et al. , Methods in Cell Biology (2008).
[4] Rizzo et al. , Biophysical Journal (2005).

* This work is partially funded by BMBF grants 02NUK001A and 02S8355. Work is part of HGS-HIRe

† Plasmids were kindly provided by S. V. Koushik, Laboratory of Molecular Physiology, Bethesda, USA

Repair of DNA double-strand breaks (DSBs) by particular mechanisms is detectable in human hematopoietic stem and progenitor cells

D. Kraft[1], A. Czernok[3], L. Bauer[1], H. Bönig[2], M. Durante[1], C. Fournier[1] and L. Wiesmüller[3]

[1]GSI, Darmstadt, Germany; [2]Institute for Transfusion Medicine and Immunohaematology, Frankfurt, Germany; [3]Department of Obstetrics and Gynecology, University of Ulm, Germany

Introduction

Galactic cosmic rays are a complex mixture of high- and low-LET radiation types, but high-LET exposure induces formation of more complex DNA and chromosomal damage [1, 2]. Even though stem and progenitor cells of the hematopoietic system (HSPC) are the origin of radiation-induced leukemogenesis [3], very little is known about the repair of radiation-induced DNA damage in HSPC, particularly in human HSPC or in response to high-LET radiation treatment. Consequently, we established a DSB repair assay for the assessment of the removal of radiation-induced DNA damage for this cell type. Importantly, the assay discriminates between error-prone and error-free DSB repair mechanisms, which is particularly relevant regarding the repair of complex DNA damage following charged particle radiation [1, 2]. Moreover, error-prone DSB repair activities are thought to be responsible for generating chromosomal rearrangements that can lead to hematopoietic malignancies [4].

Materials and Methods

Human HSPC were isolated and cultivated for 72h as described [2]. Subsequently, cells were nucleofected according to an Amaxa® protocol (Lonza) with DNA substrates designed for the analysis of specific DSB repair pathways (figure 1A) [5]: Non-homologous end joining (NHEJ), homologous recombination (HR), and homology-directed DSB repair, i.e. both HR and single-strand annealing (SSA). For DSB formation within the substrate, the nucleofection mixture also contained expression plasmid for endonuclease I-*Sce*I. Alternatively, HSPC were exposed to X rays (16 mA, 250 kV) 2h after nucleofection. The assay monitors reconstitution of wild-type *EGFP*, so that EGFP-positive cells were quantified by the diagonal gating method in the FL1/FL2 dot plot (FACS Calibur®, BD). Each measurement was accompanied by the analysis of split samples after nucleofection with the same DNA mixture plus wild-type *EGFP* expression plasmid for normalization of repair frequencies.

Results

Our previous work has led to the development of a powerful fluorescence-based assay for DSB repair with unique applications in the detection of cancer risk through discrimination of error-prone and error-free repair pathways [5]. Here, we optimized the conditions for fluorescence-based testing of DSB repair in HSPC and then applied the specific substrates for comparison of the major mechanisms. Upon targeted DSB repair formation within the substrate, we measured NHEJ and HR activities, both in the order of 10^{-4} and overall homology-directed DSB repair in the order of 10^{-3} (figure 1B). Lack of major data scattering indicated robust detection of these repair activities. Importantly for our research goals in this project, treatment of these cells with 2 Gy of X rays caused a 5-fold increase of homology-directed DSB repair. The challenge will now be to characterize DSB repair in HSPC and mature cells of the hematopoietic system, i.e. lymphocytes, in terms of DSB repair pathway-usage in response to X rays and particle irradiation as well as in response to low- versus high-LET irradiation.

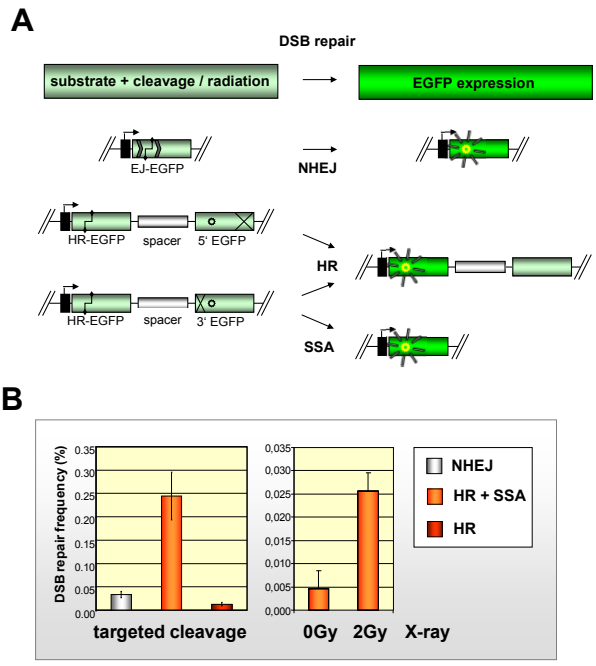

Figure 1: Analysis of DSB repair in human HSPC. (A) Design of DNA substrates for the detection of NHEJ, HR, and both HR and SSA. (B) DSB repair triggered by DNA lesions after expression of endonuclease I-*Sce*I for targeted cleavage (✂) or exposure to X-ray (B). Mean values and SEMs from N = 3-12

Work is in part funded by BMBF 02S8355

References

[1] Durante et al (2001), Radiat Res, 156(5 Pt 2):662–667
[2] Becker et al (2009), Int J Radiat Biol, 85(11):1051-1059
[3] Rithidech et al (2007), Radiat Environ Biophys, 46(2):137-145
[4] Mohrin et al (2010), Cell Stem Cell, 7(2):174-185
[5] Keimling et al (2011), FASEB J, 25(11):3849-3860

Transient Ion Irradiation Induced Pan-nuclear H2AX Phosphorylation*

B. Meyer[1], KO. Voss[1], B. Jakob[1], A. L. Leifke[1], G. Becker[1], M. Durante[1,2] and G. Taucher-Scholz[1]

[1]GSI, Darmstadt, Germany; [2]TUD, Darmstadt, Germany.

Introduction

The histone H2AX is phosphorylated on serine 139 to form γH2AX locally at DNA double strand breaks after ionizing radiation. However, heavy ion irradiation induces the nuclear-wide phosphorylation of H2AX despite the localized dose deposition of low energy ions. We reported earlier that the pan-nuclear γH2AX is bound to chromatin, directly dependent on the dose applied to the cell nucleus and not connected to apoptosis [1]. We further characterized this response with respect to time dependency compared to the kinetics of γH2AX foci.

Results

To investigate the kinetics of the nuclear-wide H2AX phosphorylation we measured the immunofluorescence signal of γH2AX as formerly described [2]. First, we measured pan-nuclear γH2AX at different times after defined microbeam irradiation of confluent human fibroblasts with single carbon ions aimed at one spot within the cell nucleus. The signal increases within the first hour followed by a rapid decrease until 6 to 8 hours with a low remaining signal up to 24 hours after irradiation (Fig. 1 A).

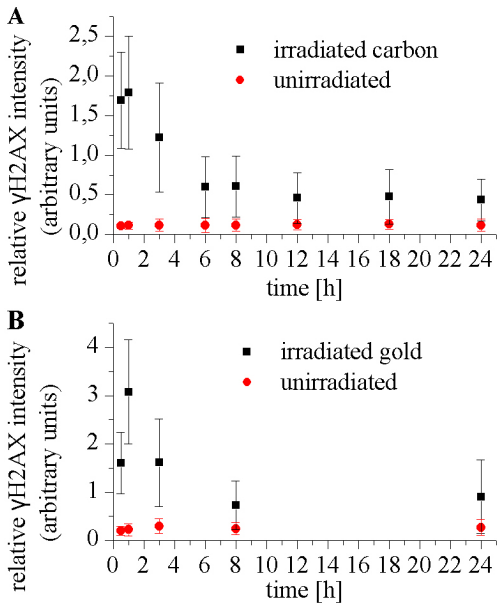

Figure 1: Confluent human fibroblasts (AG1522) were irradiated with (A) 40 carbon ions (290 keV/µm) or (B) 2 gold ions (12800 keV/µm) per nucleus and the pan-nuclear γH2AX signal was measured at different time points. Error bars show the standard deviation.

Next, we tested if this kinetics is changed by irradiation with a higher dose and LET. However, after irradiation of human fibroblasts with 2 gold ions per nucleus a similar increase and decrease of pan-nuclear γH2AX could be detected (Fig. 1 B). To check whether the regulation of the pan-nuclear γH2AX is connected to the kinetics of γH2AX foci at DNA damage we analysed the γH2AX foci after low angle irradiation. After carbon irradiation a strong decrease of γH2AX foci was visible after 24 hours (Fig. 2 A), whereas the ion tracks are largely preserved 24 hours after irradiation with gold ions (Fig. 2 B).

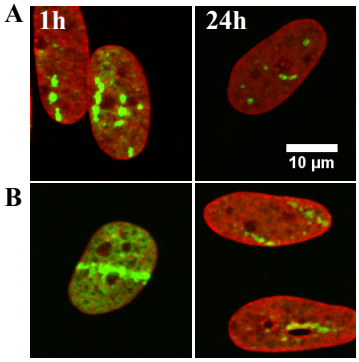

Figure 2: The immunofluorescence signal of γH2AX foci (green) at the ion trajectories were investigated 1 and 24 hours after low angle irradiation of confluent human fibroblasts with $3 \cdot 10^6$ p/cm^2 (A) carbon (170 keV/µm) or (B) gold ions (12800 keV/µm). The DNA was stained with ToPro-3 (red).

Conclusions

We report that the heavy ion irradiation induced pan-nuclear response is fully activated only within few hours after irradiation with a strong decline to nearly control level after several hours. In contrast to DSB repair as observed by γH2AX foci detection the kinetics of the pan-nuclear H2AX phosphorylation was not influenced by dose and LET though a clear dose dependency was shown for the magnitude of the pan-nuclear response [1]. This indicates a different mechanism for the regulation of the nuclear-wide γH2AX response and of γH2AX at DNA double strand breaks.

References

[1] B. Meyer et al., "Characterization of the Nuclear-wide γH2AX Response after Ion Irradiation", GSI Scientific Report 2010, 2011, p.440.

[2] B. Meyer et al., "Evaluation of a Nuclear-wide γH2AX Response after Ion Irradiation", GSI Scientific Report 2009, 2010, p. 465.

* Work supported by BMBF Grant 02NUK001A.
Work is part of HGS-HIRe.

X-rays or heavy ions-induced γH2AX distribution is correlated to the GC content in the human genome*

F. Natale[1,2,#], A. Rapp[3], M. Durante[1,2,3], G. Taucher-Scholz[2] and M. C. Cardoso[3]

[1]FIAS, Frankfurt; [2]GSI, Darmstadt; [3]Technische Universität Darmstadt

Introduction

Despite the DNA double strand break marker γH2AX being extensively studied, its distribution in the context of chromatin density (eu-/heterochromatin) remains not fully understood. As previously reported[1], ChIP-Seq technology allows the mapping of DNA-protein interactions sequencewise and genomewide. In our work, we used ChIP-Seq to provide a genome scale sequence-based map of γH2AX signature induced by different types of ionizing radiation (IR: X-rays, heavy ions). Compaction state of chromatin domains was characterized by multi-parametric analysis (e.g. GC content) and the distribution of IR-induced γH2AX along such chromatin domains was investigated.

Methods

Unsynchronized HepG2 cells showing a rather high γH2AX background (~10 γH2AX foci per cell in immunofluorescence experiments) were irradiated with 10 Gy X-rays (250 kV, 16 mA) or nickel ions (1 GeV/u, 174 keV/µm) and incubated for convenient times to allow γH2AX propagation. Following a multi-step biochemical procedure[1],§, the DNA associated to γH2AX-enriched chromatin fractions is collected and sequenced. The sequences are then compared to the reference human genome and further bioinformatic analysis is performed.

γH2AX positively correlates to GC content

First, we measured the abundance of γH2AX along each chromosome. Figure 1 shows a typical ChIP-Seq profile (only γH2AX profile of chromosome 1 is shown). As expected, unirradiated cells (grey) show low abundance of γH2AX with the exception of the *p*-telomere. This observation was reported previously[2] and we were able to reproduce it in our experimental conditions. Even in absence of IR, the γH2AX distribution appears to be uneven. After IR exposure (incubation time: 0.5 hours) the overall amount of γH2AX is increased (orange) but the distribution remains non homogenous. Specifically, chromatin domains encompassed in giemsa dark bands (GDB) showed a lower γH2AX signal when compared to non-GDB. GDB show a very low GC content (black line) and several other features of heterochromatic domains, suggesting that γH2AX is either less efficiently propagating or rapidly removed from low GC / heterochromatic domains.

Conversely, non-GDB domains, including the *p*-telomere, show high GC content and high γH2AX signal.

Figure 1

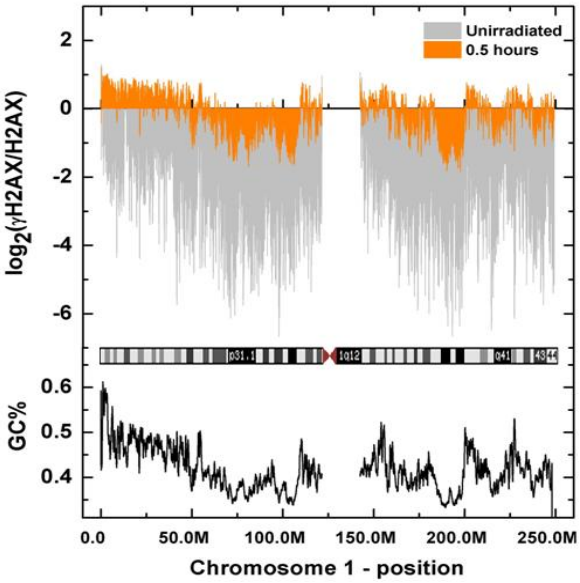

Conclusions and Perspectives

Overall, our findings show that γH2AX is positively correlated to GC content. Such feature can be associated to the compaction state of the chromatin suggesting that a less compact state (high GC content) could be a more favourable environment for γH2AX spreading.

To confirm our hypothesis, other parameters (e.g. transcriptional activity, other histone modifications) are being investigated and will integrate the present data.

References

[1] F. Natale *et al.*, "ChIP-Seq genome wide analysis of γH2AX induced by X-rays or heavy ions", GSI Report 2010

[2] J. S. Jacovoni *et al.*, "High-resolution profiling of gamma-H2AX around DNA double strand breaks in the mammalian genome", EMBO J. 2010

* Work supported by Beilstein Stiftung (NanoL project)

§ http://grcf.jhmi.edu/hts/protocols/11257047_ChIP_Sample_Prep.pdf

f.natale@gsi.de

Aknowledgements. The authors thank A. Gogol-Doering and W. Chen (MDC Berlin) for technical and scientific support.

Design and validation of a photo activation setup with 405 nm laser*

R. Khan[1,2], M. Herrlitz[1], B. Jakob[1], M. Durante[1,2], and G. Taucher-Scholz[1]
[1]GSI, Darmstadt, Germany; [2]TU Darmstadt, Germany

Introduction

Here we describe and characterize a new setup to photo bleach or activate fluorescent proteins in living cells with a 405 nm laser. The setup was validated using live cell measurements of protein recruitment [1] and photobleaching of GFP-tagged proteins.

Description of the setup

The experimental setup is based on a Leica IRE2 inverted microscope equipped with LED light sources and a climate chamber controlling temperature, humidity and COa concentration for long term live cell observations. Image acquisition is done by a Hamamatsu C7190 EB-CCD camera. A 405 nm diode laser was coupled to galvo-scanning mirrors (Fig. 1) .

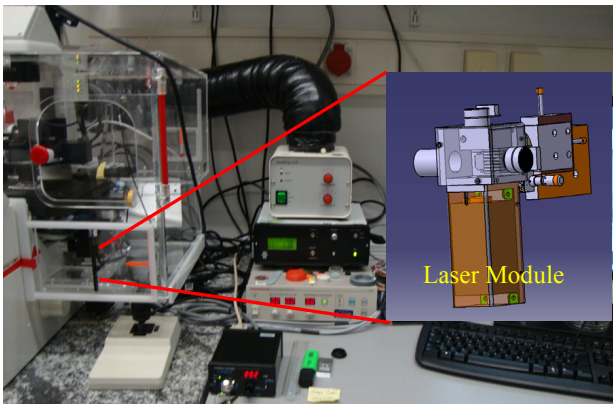

Figure 1: Experimental setup and a detailed view of the designed galvanometer module. The collimated laser can be moved precisely with the help of galvano-mirrors in both x and y directions

The laser beam is than directed to a dichroic mirror mounted in a special holder in the filter revolver (Fig. 2) which reflects it to the specimen. In the developed Labview based software, one can select different patterns like circles, line scans or point illumination at defined coordinates by mouse click.

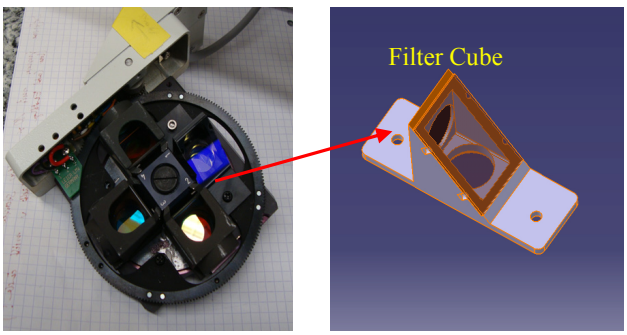

Figure 2: Filter revolver with dichroic in a holder turned by 90° to the normal fluorescence light path.

The whole control of laser, galvanometers has been integrated in our in house developed long term live cell imaging software.

Results

The collimated laser results in a 2.5 µm spot diameter (FWHM) at the specimen using a 63x NA 1.3 oil immersion lens. During first tests, it could be demonstrated that the system works satisfactorily. However due temperature dependent shifts, calibration should be performed on a daily basis.
Examples for laser induced recruitment of chromatin remodeler ACF1 and CHD$ using our new setup are described in [1, 2]. Photobleaching of GFP-tagged H2B in living Hela-Cells by the 405 laser is demonstrated in Fig. 4. By turning and paning of the laser circle, the logo of the Beilstein Stiftung was visualised by pseudocolouring of the bleached regions.

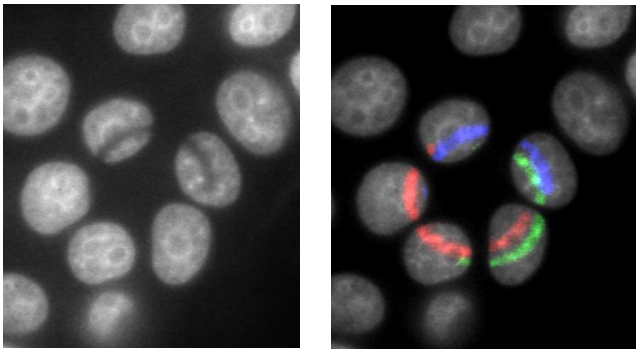

Figure 4: Living HeLa cells expressing histone H2B tagged to GFP were photobleached. Bleaching within a region of three sectors of a circle depletes fluorescence from the bleached region. Colors of the three regions were adjusted with ImageJ and the different channels were merged.

Conclusion

A microscopic setup was established that enables targeted local laser irradiation with 405 nm in combination with live cell imaging. The setup can now be used for photoactivation, FRAP or protein recruitment studies related to the DNA damage response in living cells.

References

[1] Florian Hastert Bachelor Thesis 2011 TU Darmstadt FB Biologie
[2] Müller I. et al. GSI Scientific report (2011)

* Work supported by BMBF grants 02NUK001A, 02NUK001C,and the Beilstein Institute NanoBIC. This work is part of HGS-HIRe

Influence of PARP on irradiation induced foci dynamics

A. Becker, B. Jakob, A.L. Leifke, G. Becker, M. Durante and G. Taucher-Scholz

GSI, Darmstadt, Germany

When cells are exposed to ion irradiation they exhibit changes in their chromatin structure along the ion traversal. These ion traversals can be visualized by occurring foci of DNA repair related proteins which are recruited to the sites of double strand breaks (DSB) (Fig.1). The appearing track structure in the cell nucleus after irradiation with heavy particles can be detected over many hours and stays relatively stable in its position besides a fast small scale Brownian-like motion of repair foci [1]. Here, the influence of PARP, a signal protein in DNA repair, on dynamics of irradiation induced foci was determined by live cell experiments in different cell systems.

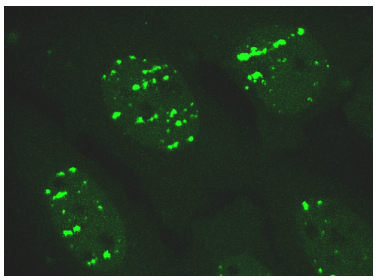

Figure 1: U2OS cell expressing 53BP1-GFP 1 hour after irradiation with Au ions (LET 13000 keV/µm). Foci of 53BP1 along tracks show traversals of ions through the cell nucleus.

As the earliest modification which occurs after DNA damage Poly-ADP-Ribose-Polymerase (PARP) is known to cross-link chromatin structure due to the very fast formation of PAR moieties which bind covalently to histones and proteins surrounding the DSB. This generates a fast signalling cascade to recruit other DNA repair proteins like XCRR1 as well as chromatin remodelers. Through PARylation and the recruitment of chromatin remodelers like the NuRD complex PARP influences changes in chromatin structure after DNA damage. Both the crosslinking as well as the modification of chromatin structure might lead to a different mobility of irradiation induced foci, which should be determined in this study.

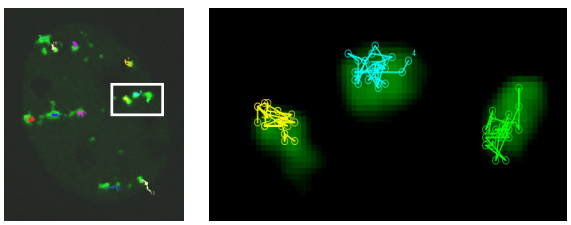

Figure 2: Movement of 53BP1 foci was tracked as shown for a single U20S nucleus (left) for 2 h after Au irradiation. Trajectories of motion of single IRIF (right).

The dependence of PARP on irradiation induced foci stability was analyzed in living cells after charged particle irradiation in different mammalian cell lines. We used PARP deficient mouse cells as well as human cells treated with siRNA knockdown or inhibition of PARP. DNA damage at various densities was generated by traversing Sn, Au or C ions. A transient expression of the fluorescent marker protein 53BP1-GFP was used to detect ionizing radiation induced foci (IRIF). Movement of these 53BP1 foci was tracked starting 30 min post irradiation for a period of 2 hours after irradiation as shown in Fig. 2.

For wild type cells the movement of foci showed diffusion like characteristics with a mean square displacement (msd) around 0.6 µm^2/h independent on ion species for the two cell lines examined. This confirms earlier results of Brownian-like motion of repair foci on this time scale [1]. Deficiency or inhibition of PARP did not result in significant changes in foci movement (Fig.3). This result indicates that there is no direct influence of PARP on the dynamic behaviour of ion induced IRIF in the cell nucleus in the observed time window.

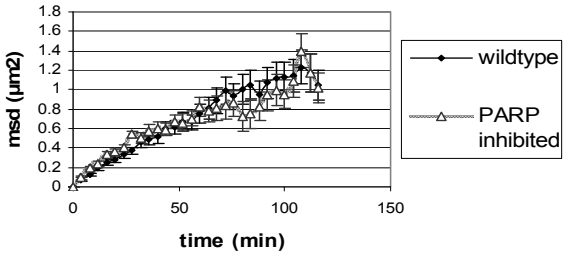

Figure 3: Mean square displacement (msd + SEM) of 53BP1 foci tracked over 2 hours in U2OS cells after C irradiation (LET 168 keV/µm).

Even though IRIF stay in a quite stable position in the nucleus, examples of changes in chromatin structure and altered mobility of DSBs related to the recruitment of DNA repair factors to the breaks have been shown [2]. As shown here, PARP does not influence foci mobility in the expected manner. Further research needs to determine factors which contribute to positional stability or instability of IRIF and might be directly related to the formation of chromosomal translocations.

References

[1] B. Jakob et al., PNAS (2009)
[2] Polo and Stephen, Genes and Development (2011)

This work is part of HGS-HIRe and supported by DFG-funded Graduiertenkolleg (GRK 1657) and BMBF Grant 02NUK001A.

Relocation of heterochromatic DNA lesions to euchromatin is ATM-dependent *

M. Beuke[1], I. Müller[1], B. Jakob[1], K.-O. Voss[1], B. Merk[1], G. Becker[1], M. Durante[1,2], G. Taucher-Scholz[1]
[1]GSI, Darmstadt, Germany; [2]TUD, Darmstadt, Germany

DNA is highly compacted by wrapping around histones and folding into higher order structures building chromatin. This chromatin can be subdivided in two classes: the highly transcriptional active, sparse euchromatin and the densely packed heterochromatin. The heterochromatin is transcriptionally inert but essential for the regulation of the gene expression and the entire architecture of the nucleus [1]. Here, we studied the ATM dependency of DNA damage response within the heterochromatin. For an aimed irradiation of distinct heterochromatic mouse chromocenters with single ions we made use of the unique submicrometer resolution of the GSI microprobe.

Results and Discussion

Recent work in our group [2] indicated that there is damage induced H2AX phosphorylation in heterochromatin after ion irradiation, accompanied by a local decondensation at the sites of ion hits. Moreover we observed a damage relocation of initially central hit chromocenters toward their periphery within the first 20 minutes after damage induction. In order to uncover the mechanistic background behind this relocation process we checked for the role of one of the most prominent key players in DNA damage response – ATM.

For analysis we divided the γH2AX-tracks in three classes: (i) centrally located tracks, where the damage marker signal peak is totally enclosed by bright DNA staining, (ii) intermediately located tracks which are only in part enclosed depending on the direction of the intensity profile and (iii) peripherally located tracks which generally flank the chromocenter. We monitored these γH2AX-tracks in wildtype cells and observe a decrease in the central and intermediate fraction in favour of the peripheral fraction within the first half hour after damage induction (Fig. 1 A).

By monitoring the relocation kinetic in an ATM deficient cell line we prove a distinct influence of ATM on damage relocation. As mentioned above in WT cells the predominant majority of DNA lesions is relocated within the first half hour after damage induction. In contrast, the relocation process in ATM deficient cells is clearly delayed. After more then one hour a large fraction of DNA lesions is still central or intermediate (Fig. 1 B). However, preliminary results indicate that after two hours all DNA lesions are relocated.

ATM is known to play a crucial role in the recruitment of DNA repair factors and chromatin remodeling. ATM deficiency can be partly compensated by other kinases (like ATR and DNA-PK) which might also substitute in the observed residual relocation ability.

It will be important to determine whether a delay in relocation is directly related to a diminished damage repair.

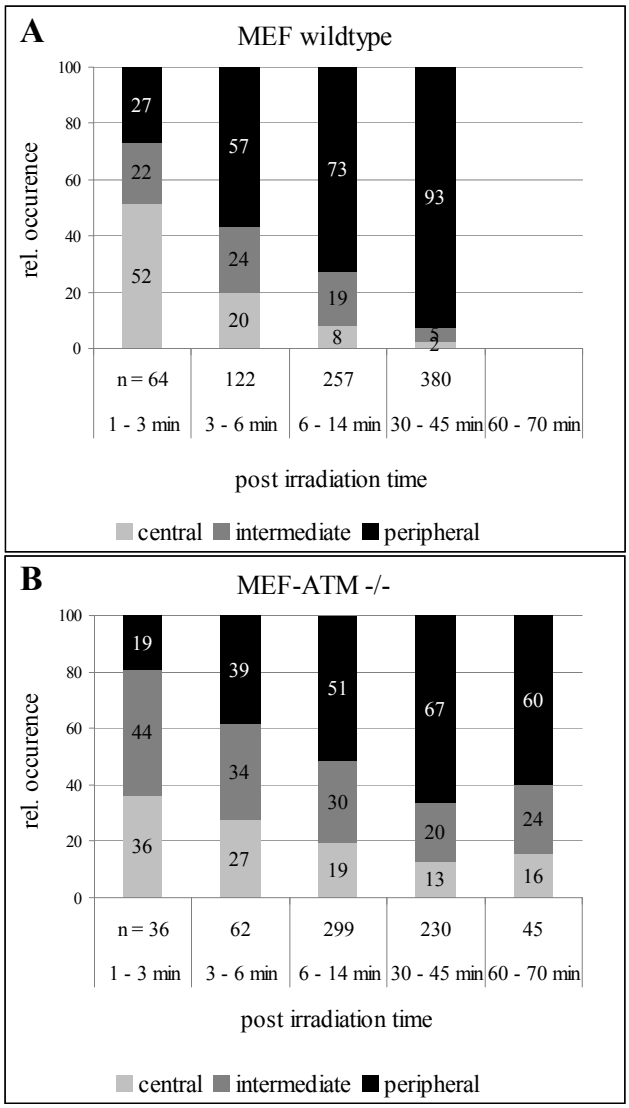

Figure 1: (A) MEF wt cells and ATM deficient cells (B) irradiated with Au ions (4.8 MeV/u, 12815 keV/µm) or Ni ions (4.8 MeV/u, 3800 keV/µm), targeted at chromocenters at the GSI microprobe, fixed between 1 and 70 min post irradiation.

References

[1] A.A. Goodarzi et al., DNA Rep. 9 (2010) 1273-1282
[2] B. Jakob et al, Nucleic Acids Research (2011), Vol. 39, No. 15, 6489-6499

*This work was partly supported by BMBF contract [02NUK001A].
Work is part of HGS/HIRe.

Effects of X-rays and Carbon Ions on the Cardiac Differentiation of Mouse Embryonic Stem Cells*

A. Helm[1,2], D. Pignalosa[1], M. Durante[1,2], P. Layer[2], D. Szypkowski[1] and S. Ritter[1,#]
[1]GSI, Darmstadt, Germany; [2]Technische Universität Darmstadt, Germany

The impact of ionizing radiation on early embryonic development is poorly understood [1]. An ideal model system to study these effects *in vitro* are pluripotent mouse embryonic stem cells (mESCs) that are isolated from the inner cell mass of blastocysts. *In vitro* these cells give rise to all three germ layers and subsequently to a broad spectrum of differentiated cells, among them cardiomyocytes. Embryonic stem cell derived cardiomyocytes display features typically found *in vivo,* i.e. express cardiac specific genes, form sarcomeric structures and contract spontaneously [2]. Hence, the development of cardiomyocytes in an embryo can be recapitulated *in vitro* and this process can be easily monitored by observing beating cells. Due to these advantages this system (referred to as *Embryonic Stem Cell Test*, EST) has been used since several years to screen the embryotoxic potential of drugs [3, 4].

In the present study we examined the effects of high and low LET radiation on the development of cardiomyocytes from mESCs. For the experiments the mESC line D3 was used. Cells were irradiated with either X-rays (250 kV, 16 mA) or Carbon ions (25-mm extended Bragg peak, energy range: 106-147 MeV/u with a mean LET of 75 keV/µm at sample position). One day later cells were passaged, while initiation of the differentiation was induced 3 days post-irradiation by creating *embryoid bodies* (EBs) as described elsewhere [5]. Per sample 48 EBs were generated and 10 days after initiation of differentiation the fraction of spontaneously beating EBs was determined (Fig. 1). The error was calculated according to Bernoulli's distribution. Fisher's exact test was used for significance evaluation. Additionally, to prove the formation of cardiomyocytes, beating EBs were enzymatically dissociated and cells were reseeded. Subsequently, the cardiomyocyte-specific structural protein Troponin I was visualized with a fluorescence labelled antibody and samples were analysed under a fluorescence microscope (Fig. 2).

As displayed in Fig. 1, after irradiation with 1 Gy Carbon ions the fraction of beating EBs was significantly lower than in the control (i.e. 73 vs. 38%, $p < 0.001$). In contrast, the exposure to 1 Gy X-rays did not affect the fraction of beating EBs formed: about 88% of EBs derived from irradiated or unirradiated samples were beating. Furthermore, as shown in Fig. 1, both control values differ slightly, but are within the range normally observed for controls (i.e. 70% up to 100%). Further experiments are currently performed over a broader range of doses.

The low number of beating EBs formed after Carbon ion exposure might result from an impaired cell survival that was observable up to 3 days post-irradiation (data not shown). Heavy ion induced changes in the expression pattern of genes that are involved in cardiac development might be another reason. In further studies we will focus on the latter point. *Quantitative Reverse Transcriptase Polymerase Chain Reaction* (qRT-PCR) will be used to quantify the expression of cardiac specific genes such as *NKX2-5* or *NPPA*.

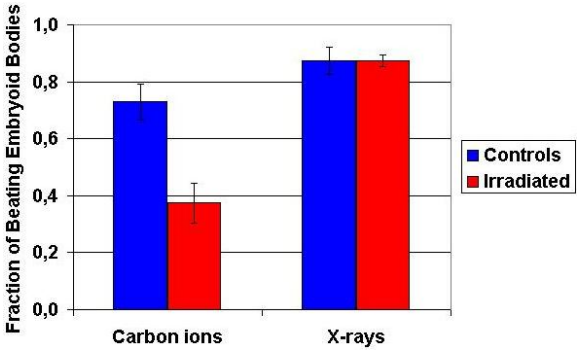

Fig. 1: Fraction of beating EBs. Undifferentiated D3 cells were exposed to 1 Gy of X-rays or Carbon ions, differentiated and after 10 days the number of beating EBs was determined (Error bars: Bernoulli's distribution).

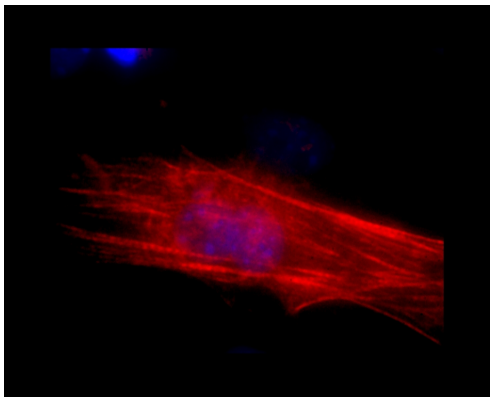

Fig. 2: Differentiated cardiomyocyte derived from mESCs (100x). Cell nuclei are stained blue, whereas the cardiac-specific structural protein Troponin I is stained red.

References

[1] ICRP (2003) Biological Effects after Prenatal Irradiation (Embryo and Fetus), ICRP Publication 90
[2] Wobus et al., Physiol Rev, 2005, 85, 635-678
[3] Scholz et al., Cells Tissue Organs, 1999, 165, 203-211
[4] ECVAM (2002) Embryonic Stem Cell Test (EST): INVITTOX no. 113. Embryotoxicity/Teratogenicity
[5] Helm et al., GSI Scientific Report 2010, 455

#s.ritter@gsi.de
*Funded by the Euratom 7th Framework Programme under grant agreement n° 295823, Work is part of HGS-HIRe

Application of the Embryonic Stem Cell Test in Radiobiological Studies: Validation with Retinoic Acid*

M. Materna[1,2], A. Helm[1,3], M. Durante[1,3], W. Mäntele[2] and S. Ritter[1,#]
[1]GSI, Darmstadt, Germany; [2]Goethe-Universität, Frankfurt, Germany; [3]Technische Universität Darmstadt, Germany

Pluripotent mouse embryonic stem cells (mESCs) differentiate *in vitro* spontaneously to cardiomyocytes thereby providing a tool to study the effects of ionizing radiation on cardiac development and on cardiomyocytes themselves [1]. So far, the system has been used in the pharmacological industry to screen the embryotoxic potential of drugs or chemical compounds and has been validated by the *European Centre for the Validation of Alternative Methods* (ECVAM) [2]. To evaluate the quality of the assay, the ECVAM-protocol recommends the use of a positive control in each experiment.

Likewise, we examined whether retinoic acid can be used as a positive control in radiobiological experiments. All-*trans*-retinoic acid (RA) is known to be strongly embryotoxic and to affect the *in vitro* cardiac differentiation of mESCs [3]. During embryonic development (i.e. under physiological conditions) RA functions as an important signalling factor in a variety of processes, among them the organogenesis of the heart [4].

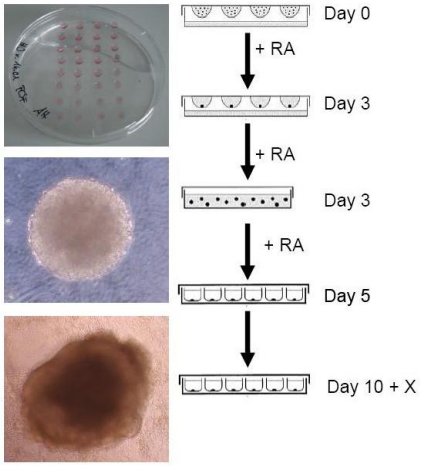

Fig. 1: Experimental schedule: RA was added at day 0 when hanging drops were formed, at day 3 after the transfer of embryoid bodies into suspension, at day 5 when cells were plated into 24-well-plates and when medium was changed.

In vitro differentiation of the pluripotent mESC line D3 into cardiomyocytes through *embryoid bodies* (EBs) was performed as described elsewhere [1]. Retinoic acid (Sigma Aldrich) was dissolved in ethanol to reach a concentration of 3 mg/ml. Thereafter, RA was serially diluted in cell culture medium and the effect of 1 nM and 5 nM RA on the formation of EBs was examined. As displayed in figure 1, mESC were exposed to RA in the beginning of the differentiation process, when hanging drops were formed (day 0), when EBs were transferred to suspension culture (day 3) and finally, when EBs were seeded into 24-well tissue culture plates. In parallel, two controls were performed, i.e. a blank control and a solvent control (ethanol dilution $1{:}2\text{x}10^6$).

In two independent experiments we examined the effect of 5 nM on the formation of beating EBs (see Fig. 2). The solvent control did not differ from the blank control. As observed by others (e.g. Scholz et al. [3]) the addition of 5 nM RA to the cell culture medium resulted in a strong inhibition of differentiation of D3 cells into beating cardiomyocytes compared to control samples. At day 10 the difference was most pronounced, but became smaller with increasing age of the EBs.

In a further experiment, where 1 nM RA was applied, the fraction of beating EBs was similar to those measured for 5 nM. Likewise, the time-course of beating EBs was comparable (data not shown). Interestingly, measurements of the size of the EBs showed that the RA-treated ones were remarkably smaller than the untreated EBs (data not shown). In this experiment the control levels of beating EBs were similar to other cardiac differentiation assays performed before (e.g. ≥ 70% on day 10).

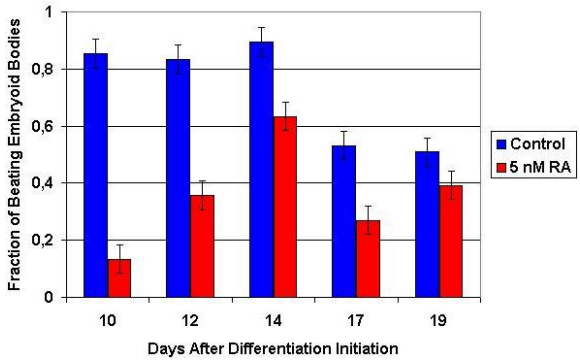

Fig. 2: Fraction of beating EBs after RA treatment. The combined data of 2 independently performed experiments are shown.

Our experiments confirm that the effect of RA on the differentiation of mESCs to cardiomyocytes is significant and reproducible. Therefore, RA will be used in further radiobiological studies as a positive control.

References

[1] Helm et al., GSI Scientific Report 2010, 455
[2] ECVAM (2002) Embryonic Stem Cell Test (EST): INVITTOX no. 113. Embryotoxicity/Teratogenicity
[3] Scholz et al., Cells Tissue Organs, 1999, 165, 203-211
[4] Campo-Paysaa et al., Genesis, 2008, 46, 640-656

#s.ritter@gsi.de
*Funded by the Euratom 7th Framework Programme under grant agreement n° 295823

Mouse embryonic stem cells surviving γ ray exposure carry stable chromosomal aberrations with low complexity

D. Pignalosa[1], P. Rebuzzini[2], S. Garagna[2], M. Durante[1,3] S. Ritter[1]
[1]GSI, Darmstadt; [2]Pavia University, Pavia, Italy; [3]TUD, Darmstadt, Germany .

Embryonic stem cells (ESCs) are undifferentiated cells derived from the inner cell mass (ICM) of the blastocyst and are characterized by an unlimited self-renewal capability *in vitro*. They are considered pluripotent since they contribute to the formation of all tissues of an individual and they are able to differentiate in vitro into cells of the 3 embryonic germ layers. Because of their biological role, it has been proposed that ESCs have a strict control of their genome integrity. Indeed, recent studies have reported that DNA repair mechanisms are more active in ESCs than in their differentiated counterparts [1]. It has also been reported that ESCs with a high mutational burden are preferentially lost from the population [2], but further studies are needed to clarify the mechanism and the extent of this elimination process. In particular, nothing is known about the perpetuation of the DNA damage at chromosomal level.

Due to the increasing interest in using ESCs for stem cell therapy, the investigation of their cytogenetic stability is essential. The aim of our work was to analyse the residual cytogenetic damage in the progeny of R1 mouse ESC (mESC) surviving the exposure to high doses of γ-rays. We performed karyotype analysis with multicolour fluorescent probes (mFISH), a widespread method that allows the simultaneous detection of structural and numerical (aneuploidies) abnormalities involving any chromosome of the genome. R1 cells were cultured on glass slides and chromosome spreads were prepared 96 hours (equivalent to roughly 8 cell divisions) after irradiation with 2 or 5 Gy γ-rays. Cell culture, irradiation and preparation of chromosome samples were performed at the University of Pavia. Slides were shipped to GSI, where chromosome fluorescent labelling was carried out following the protocol recommended by the manufacturer (MetaSystems). Metaphase images were captured using an automatic Zeiss Imager Z1 microscope and the analysis was performed with the ISIS software (MetaSystems). For each sample, around 100 metaphases were scored. Analysis criteria have been extensively described elsewhere (3).

In the control sample the yield of metaphases with a normal diploid karyotype (i.e. 40, XY) was low (20%). In the progeny of irradiated cells a similar yield was found. The most commonly aneuploidies observed (Fig.1a) were the gain of a chromosome number 8 (72±5% of aneuploid cells) or 11 (43±4%) or the loss of chromosome Y (30±3%). These observations confirm previous studies on other mESC lines, where trisomy of chromosome 8 was observed in 70% of the cells (4) and loss of the Y chromosome in 25% (5).

In the control sample also a high rate of structural aberrations was found (20%, Fig. 1b). Radiation exposure significantly increased the yield of aberrant cells in a dose-dependent manner, from 25±5% to 41±6% for 2 and 5 Gy γ-rays, respectively. In control cells only simple exchanges (translocations and dicentrics) and fragments were observed. These aberration types were also detected in the progeny of irradiated cells, but also a few stable complex exchanges were found (Fig. 1a). The complexity of these rearrangements represented by the mean number (± SD) of chromosomes participating in the exchange was similar (1.9±0.9 and 2.0±0.7 after 2 or 5Gy, respectively). More than 80% of the exchanges observed were stable, i.e. transmissible to the progeny. Further experimental results are described elsewhere [3].

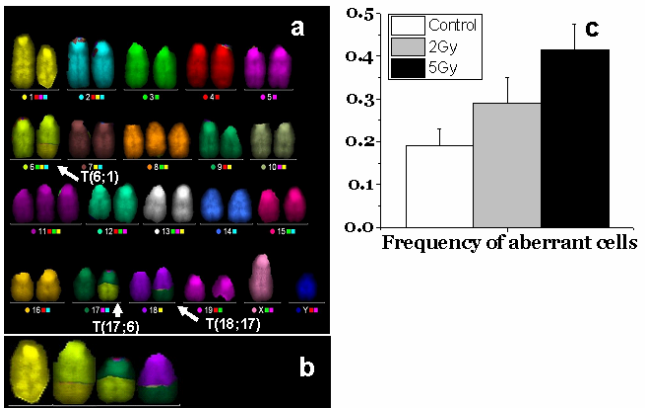

Figure 1: (a) Aberrant karyotype from R1 cell line exposed to 5 Gy γ-rays and visualized with mFISH. Additional copies of chromosome 8 and 11 are present and a stable complex exchange. (b) Chromosomes 1, 6, 17 and 18, involved in the complex exchange presented in (a). (c) Frequency of chromosomal aberrations observed in mESCs 96 h after the exposure to 2 and 5Gy γ-rays.

In conclusion, the high level of abnormalities (numerical and structural) observed in the control sample suggests that careful cytogenetic analysis should be carried out when working with ESCs, especially for therapeutic purposes. In the progeny of the cells surviving the radiation exposure we found more damaged cells than in the control population and aberrations were mostly of the simple and stable type. Obviously, cells carrying unstable aberrations had already been successfully eliminated at 96 h post-irradiation. Interestingly, aneuploidies appear to be tolerated by mESCs.

References

[1] Saretzki et al. *Stem Cells.* 26, 455-64 (2008).
[2] Roos et al. *Nature.* 14, 1422-1432 (2007).
[3] Rebuzzini et al. *J Cell Physiol* 227:1242– 49 (2011)
[4] Sugawara et al. *Comp Med* 56:31– 34 (2006).
[5].Guo et al. *In Vitro Cell Dev Biol Anim* 41:278– 83 (2005).
This work was partly funded by the BMBF, grant 02S8497.

Radiation response of pluripotent stem cells derived from early mouse embryos*

S. Luft[1], A. Helm[1], D. Pignalosa[1], P. Hessel[1], M. Durante[1,2], P. Layer[2], S. Ritter[1]

[1]GSI, Darmstadt, Germany; [2]Technische Universität Darmstadt, Germany.

Embryonic stem cells (ESC) are intrinsically different from differentiated, somatic cells. One characteristic feature of ESC is the ability of self-renewal, a mechanism which ensures that the stem cell population is maintained. Another characteristic feature is the cell pluripotency. A pluripotent cell is able to give rise to all cell types of the three germ layers [1].

Since there is not much known about the risks of an irradiation during early pregnancy (preimplantation period), we used the murine embryonic stem line D3 as a model system. D3 cells were isolated by Doetschman et al. (1985) from the inner cell mass of a 4 days old blastocyst of the mouse strain 129S2/SvPas. First, we tested the ability of unirradiated D3 cells for self-renewal. For this reason, the cells were passaged every 2-3 days up to 78 days. Based on the number of cells seeded and harvested, the cumulative population doublings (CPD) were calculated and the cell generation time was determined. As shown in figure 1, the CPD of D3 cells increased steadily, while the growth curves of ageing, primary cells typically exhibit a shoulder (after about 50 cell divisions, see dotted line).

Furthermore, in first experiments we investigated the effect of X-ray (0.5, 2, 3 and 4 Gy) and carbon-ion exposure (0.5, 1, 2 and 3 Gy, extended Bragg peak, 107-147 MeV/u, LET=75 keV/µm) on D3 cells. The pluripotency markers Oct3/4 and Sox2 [2] were visualised by immunohistochemical staining (see fig. 2) and quantified by flow cytometry at different time-points after exposure. Additionally, cells were stained with the DNA-dye Hoechst 33 342 and the number of apoptotic cells was determined based on morphological criteria [3] and cell survival was measured by the colony forming assay.

The fluorescence intensity of the cells, resembling the amount of pluripotency markers in irradiated and unirradiated cells was measured up to 29 days after exposure and did not show any significant difference (data not shown). Analysis of the apoptotic index revealed that the frequency of apoptotic cells increased with culture time and was higher in irradiated samples (3 Gy carbon ions) than in control cultures. At 24 h and 72 h after carbon ion exposure the apoptotic index amounted to 20 % and 80 %, while in the control 10 % and 56 % were measured.

Determination of the cell survival showed that carbon ions were more effective than X-rays (see fig. 3).

In further experiments, we will extend these studies to human ESC, since there are essential differences between rodent and human ESC (like DNA repair mechanisms [4]), and data obtained for murine ESC cells cannot be directly applied to human cells.

* Work supported by BMBF, Bonn (contract 02S8497) and by the ESA-IBER project.

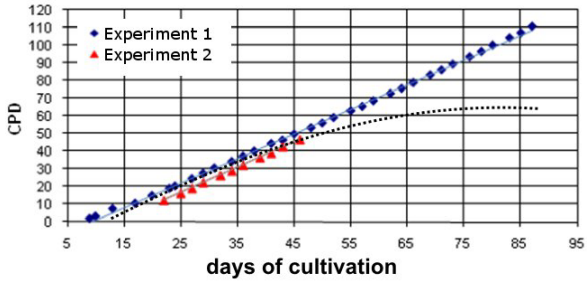

Figure 1: CPD of D3 cells measured in 2 independent experiments. No shoulder is seen, as it is typical for ageing, primary cells (dotted line). Based on the data the generation time of ESC was determined to be 17,0 ±0,2 h.

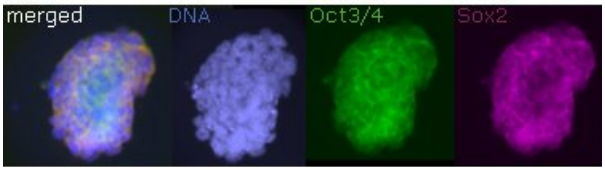

Figure 2: Immunohistochemical staining of the pluripotency factors Oct3/4 (green) and Sox2 (red) in unirradiated D3-colonies after 15 days of cultivation.

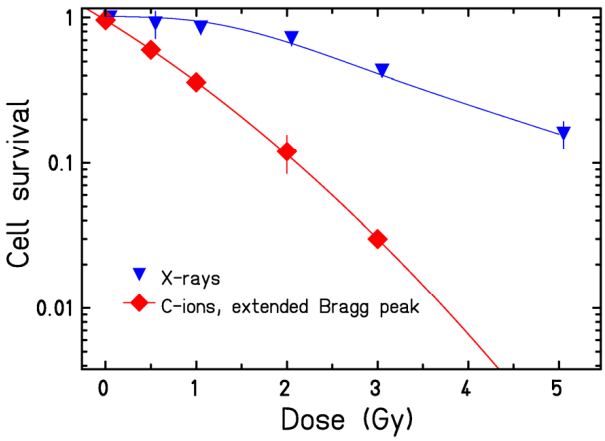

Figure 3: Cell survival of D3 cells after x-ray and carbon ion irradiation (n=1). Datapoints are the mean (± SD) from 3 independent samples.

References

[1] Koestenbauer et al., Am. J. Reprod. Immunol. 55, 169-180 (2006)
[2] Niwa et al., Cell Struct. Funct. 26, 137-148 (2001)
[3] Luft, Diploma thesis, TU Darmstadt, 2011
[4] Banuelos et al., DNA Repair (Amst). 7, 1471-1483 (2008).

Cellular survival of human lung adenocarcinoma cell line (A549) after carbon ion irradiation under different oxygenation conditions

F. Kamlah[1], S. Rudolph[1], V. Bill[1], B. Bischoff[1], F. Rose[1], R. Engenhart-Cabillic[1], A. Arenz[1], W. Kraft-Weyrather[2], M. Scholz[2], C. Fournier[2], G. Taucher-Scholz[2], and J. Hänze[3]

[1]Dept. of Radiotherapy and Radiooncology, University of Marburg, Germany; [2]GSI, Darmstadt, Germany; [3]Department of Urology and Pediatric Urology, University of Marburg, Germany

Hypoxia inducible factors (HIF) regulate adaptive cellular processes in response to hypoxia. Also, HIF can be activated by non-hypoxic stimuli such as oncogenes and in particular by reactive oxygen species which are affected by irradiation [1]. Clinical trials demonstrated a direct relationship between tumor hypoxia and poor clinical outcome after photon radiation (X-ray) [2]. Here, we compared the effect of different irradiation qualities (heavy ions (^{12}C) and X-ray irradiations) under hypoxic and normoxic conditions on the clonogenic survival of human non small lung adenocarcinoma cell line (A549).

For hypoxia treatment, we seeded the cells in non-vented cell culture flasks and placed them for 24 h in a hypoxic chamber at 37 °C in humidified atmosphere containing 5% CO_2 and 1% O_2. After immediate closing of the culture flasks, cells were submitted to irradiation with ^{12}C (LET 70 keV/µm, energy 120.45-135.16 MeV/u on target, spread out bragg peak [SOBP]) and photons (6 MV-X). Under these conditions, we found increased HIF-1α abundance as analysed by Western Blot (data not shown) when compared to normoxia. The survival curves of A549 cells are shown in Figure 1. The relative biological effectiveness (RBE) of 10% survival was nearly 3.0. The oxygen enhancement ratio (OER) for X-Rays was 1.29 ± 0.06 and the OER for ^{12}C irradiation was 1.05 ± 0.07 in accordance with the literature [3].

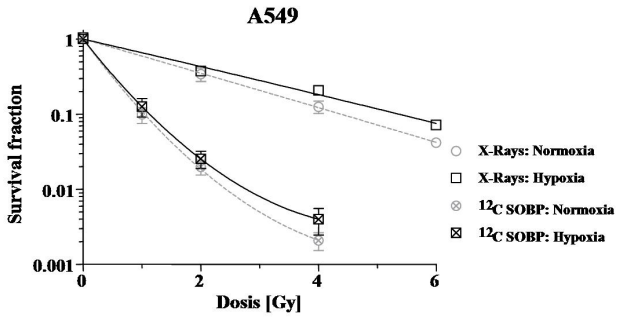

Figure 1. Survival curves of A549 cells after irradiation with carbon ions (^{12}C SOBP), and 6 MV-X-rays. The curves were fitted by least squares to a linear-quadratic equation.

In the next step we plan to analyse the role of HIF-1α for cellular survival in hypoxia after silencing of HIF-1α using siRNA. Initially, we tested the influence of transfection itself employing a random siRNA (siRNA-control) in complex with Lipofectamine 2000™.

We compared the plating efficiency (PE) of untransfected (untreated) and siRNA control transfected cells. We found a slight increase of PE in the group of transfected cells (Figure 2) that was not significant different, reflecting that the transfection procedure does not principally interfere with the assay. In further experiments we will study the cellular survival of hypoxic A549 cells that are treated with si-RNA-HIF-1α.

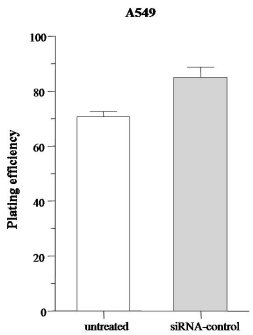

Figure 2. Plating efficiency of A549 cells, which were untransfected (untreated) and transfected with scrambled siRNA (siRNA-control). Data reflect the mean ± s.e.m. (n=13 [untreated] n=9 [siRNA-control]).

References

[1] Semenza, G. L. (2003) Targeting HIF-1 for cancer therapy. *Nat Rev Cancer* **3**, 721-732

[2] Brizel, D. M., Dodge, R. K., Clough, R. W., and Dewhirst, M. W. (1999) Oxygenation of head and neck cancer: changes during radiotherapy and impact on treatment outcome. *Radiother Oncol* **53**, 113-117.

[3] Hall EJ, Giaccia AJ: *Radiobiology for the radiologist.* 6th edition. Philadelphia: Lippincott Williams and Wilkins; 2006.

Construction of a new chamber for hypoxia experiments

A. Maier[1,2], *M. Scholz*[1], *M. Durante*[1,3], *and W. K.Weyrather*[1]
[1]GSI, Darmstadt, Germany; [2]TU Ilmenau, Ilmenau, Germany; [3]TU Darmstadt, Darmstadt, Germany

Introduction

Cancer is one of the most common causes of death in Germany. It is known that hypoxia is a characteristic feature in solid tumors resulting from an inefficient growth of blood vessels in the tissue. These hypoxic cells show an aggressive phenotype resulting in enhanced migration and risk for metastasis. [1]

Material and Methods

In the past a in-house developed videomicroscopy system was used to investigate the effect of different states of oxygenation on the behavior of the cells. For these experiments CHO-K1 (Chinese hamster ovary) cells were used. The observation time was 48 hours.
But with this systems it was only possible to perform experiments in the state of reoxygenation. To get chronic hypoxic (0,5% O_2) or anoxic (0% O_2) conditions the cells were gased for 2 hours in previously designed hypoxic chambers [2],[3] and then kept in the incubator for 24 hours. To look at the cells under the microscope the chamber had to be opened and so the cells where in the phase of reoxygenation when starting the measurement.
To observe cells directly in hypoxia or anoxia a new chamber had to be developed.
For this new hypoxic chamber there was a set of specifications. The camber has to be adapted to the available space under the microscope to get pictures with a high quality and reproducible positions of the cells. This is important to identify cells during the experiment. But the chamber also must be gas proof to enable experiments directly under hypoxic or anoxic conditions.

Results

The body of the chamber is made of PEEK (Polyetheretherketon). It is a radio- and alcoholresistant material that has no adverse effect on the behavior of the cells.
The system consists of an upper and a lower part which are connected by an o-ring seal. The gassing is realised by automatically closing couplings. And the view through the chamber is allowed over two windows made of acrylic glas. Inside the chamber the cell cultivation vessels are fixed in their position by a sample holder made of aluminum so that reproducible results are possible.
A picture of the new hypoxic chamber can be seen in figure 1. In first tests after construction the picture quality, gas proof and the fit to the microscope stage where checked.

Figure 1: Hypoxic chamber

As these tests where successfull first experiments with CHO cells where done. The results can be seen in table 1. In this experiments, cells where cultivated under oxic and hypoxic conditions for 48 hours. For the measurement with the microscope, positions in the cultivations vessels were manually selected. Then the microscope automatically took pictures every 30 minutes from this positions. So it was possible to calculate the local doubling time at this positions. The doubling time between the oxic and the hypoxic cells is nearly the same. The difference in the number of cells corresponds to this minor differences in the local doubling time.

Table 1: Influence of oxygen on cell growing

O_2-State	local doubling time [h]	number of cells
oxic	11,5 $\pm$ 1,0	64547 $\pm$ 5680
hypoxic	12,6 $\pm$ 3,4	43518 $\pm$ 7260

These results fit together with the experiments presented in [4] that CHO-K1 cells have nearly the same doubling time in hypoxic and oxic state but are more radioresistant during hypoxia.

References

[1] K. Ameri et al., Circulating tumour cells demonstrate an altered response to hypoxia and an aggressive phenotype, British Journal of Cancer Band 102, p. 561-569 (2010)

[2] C. Schicker, C. von Neubeck, U. Kopf, W. Kraft-Weyrather, Patent: Ep 09 002 402.7, Zellkultur-Bestrahlungskammer, 2009.

[3] C. Schicker, C. von Neubeck, U. Kopf, W. Kraft-Weyrather, Patent: De 10 2008 010 918.5, Zellkultur-Bestrahlungskammer, 2008.

[4] Ma N, et al. GSI scientific report 2010: p. 460 (2011)

E-cadherin gene response to carbon ions under different state of oxygenation *

W. Tinganelli[1], M.Durante[1], and W. K.Weyrather[1]

[1]GSI, Darmstadt, Germany

Cadherins, named for Calcium- Dependent Adhesion, are a class of trans-membrane proteins important for the cell adhesion. Dependent on calcium ion (Ca^{2+}) cadherin permits that the tissues are bound together [1]. The amount of E-cadherin decreases under hypoxic conditions and this could be one of the causes for the metastatic increase in tumors with high grade of hypoxia. High incidence of metastases in fact is associated with low oxygen tension in the primary tumor [2]. In this report the E-cadherin gene profile expression is shown through PCR Real Time, for 2 different states of oxygenation and after carbon and X-ray irradiation.

Material and Methods

- PC3 cell line (human prostate cancer cells).
- For the hypoxic condition, cells were kept for 72 hours in hypoxia: 0.5% oxygen, 94.5% nitrogen, 5% carbon dioxide, 37˚C. Oxic cells were kept for 72 hours in norm-oxia, 5% CO_2, 37˚C. After this time all cells were irradiated under oxic condition with different doses and then reseeded in tissue culture flasks. Seventy two hours later then, analyzed with PCR Real Time (endogenous gene: GAPDH).
- Carbon irradiation was performed using a 1cm extended Bragg peak at a dose averaged LET of 100keV/μm.

Results

The cells were irradiated with 0, 0.4, and 1.6 Gy with carbon ions and with 0, 0.4, 1.6 and 6 Gy with X-rays. E-cadherin gene expression was down-regulated after 72 hours of hypoxia, confirming a well known result in literature [3] and was even more down-regulated after X-ray irradiation, at least at low doses (Fig 1). The E-cadherin gene expression for carbon ion (Fig 2), instead, was surprisingly high at 0.4 Gy doses, almost 6 times more the reference condition, 0 Gy oxic, for the oxygen condition and 4 times more expressed for the hypoxic condition

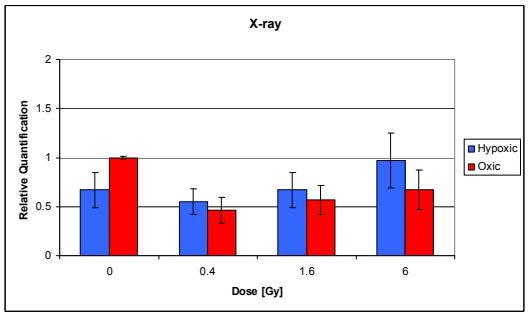

Figure 1: Real time PCR for E-cadherin after X-ray irradiation, in 2 different states of oxygenation

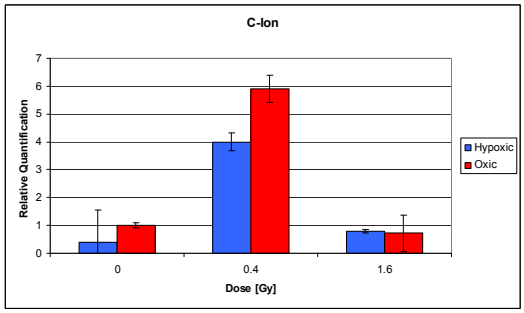

Figure 2: Real time PCR for E-cadherin after carbon ion irradiation, in 2 different states of oxygenation.

Further analysis has been done to measure the protein expression in anoxia (24 hours 0% oxygen) and norm-oxic with Western blot analysis (Fig 3).

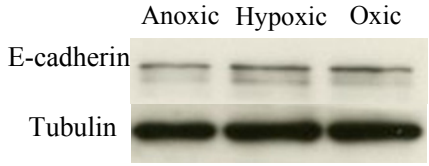

Fig 3. Western blot analysis of E-cadherin in anoxic and oxic conditions.

Conclusions

E-cadherin is one of many proteins responsible for the correct adhesion and migration of cells in all the tissue of the human body. It is now clear that anomaly in cadherin expression is a cause for a poor prognosis of a tumour. Hypoxia is one of the most common causes of metastatic increase. The understanding mechanisms between hypoxia and cadherin expression under irradiation could be important to predict the metastatic grade after tumour irradiation for different oxygen conditions.

References

[1] Eur J Cancer. 2000 Aug; 36 (13 Spec No):1607-20. The E-cadherin-catenin complex in tumour metastasis: structure, function and regulation.

[2] K Sundf0r1 et al. British Journal of Cancer (1998) 78(6), 822-827 Rofstad2 Tumour hypoxia and vascular density as predictors of metastasis in squamous cell carcinoma of the uterine cervix.

[3] Tsutomu Imai et al. Am J Pathol. 2003 October; 163(4): 1437–1447. Hypoxia Attenuates the Expression of E-Cadherin via Up-Regulation of SNAIL in Ovarian Carcinoma Cells

* Work supported by EU, PARTNER PROJECT No. 215840.

Effect of C-ions with Differing LET on the Cell Cycle Progression of Human Lymphocytes from G0/G1- to S-Phase*

R. Lee[1], E. Nasonova[1,2], P. Hessel[1], M. Durante[1,3] and S. Ritter[1,#]

[1]GSI, Darmstadt, Germany; [2]JINR, Dubna, Russia; [3]TU Darmstadt, Darmstadt, Germany

Human peripheral blood lymphocytes are a commonly used model system in radio-biological research, in particular to estimate the individual dose after accidental, occupational, or medical exposure to ionizing radiation and to assess possible health consequences. The main biological endpoint employed is the formation of structural chromosome aberrations [1, and references therein]. However, one major problem in quantifying high LET induced aberrations in cycling cells is the cell-cycle delay, which depends on LET, dose and cell type studied. So far, studies investigating the relationship between radiation-induced cell cycle delay and the expression of aberrations in lymphocytes concentrated on the G2-arrest [1, 2].

To gain information whether the transition of lymphocytes from the G0/G1-phase to S-phase is affected by C-ion or X-ray exposure, BrdU-incorporation into DNA was measured up to 72 h post-irradiation. For the analysis, aliquots of chromosome samples were used [1], i.e. lymphocytes were differentiated in ultrapure water after Giemsa-staining [3]. BrdU-labeled nuclei appear blue, while non-labeled nuclei are rose as shown in Fig. 1. At each dose- and time-point about 2000 cells were scored.

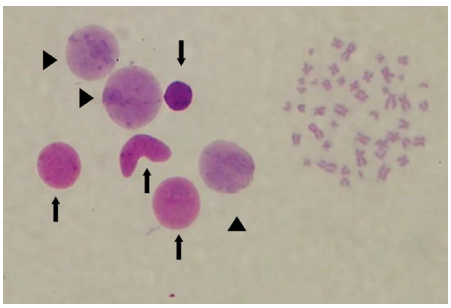

Fig. 1: BrdU-positive (blue) and negative lymphocytes (rose) marked with triangles and arrows, respectively.

Analysis of the labeling indices revealed a dose-dependent delay in the progression of the cells into S-phase as exemplarily shown in Fig. 2 for 9.5 MeV/u C-ions with LET=175 keV/µm. When iso-doses are compared (2 Gy), 175 keV/µm LET C-ions were found to be more effective than X-rays (Fig. 2). To examine the effect of C-ions with differing LET, labeling indices measured at 72 h post-irradiation were compared. As shown in Fig. 3, the effectiveness of X-rays and C-ions with LET values of 14 and 29 keV/µm were found to be similar (RBE=1). In contrast, C-ions with higher LET values (60-85 keV/µm and 175 keV/µm) induced a more severe progression delay into S-phase, in other words a higher fraction of cells suffered a prolonged arrest in the G0/G1-phase, yielding an RBE of about 4.

Altogether these data demonstrate for the first time that heavy ion exposure affects not only the G2/M-transition of human lymphocytes but also their progression from G0/G1- to S-phase. The relevance of both effects on the fate of damaged cells remains to be elucidated.

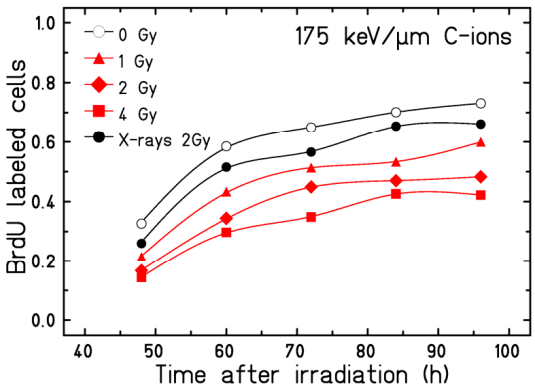

Fig. 2: Fraction of BrdU-labeled lymphocytes as a function of time after irradiation with 9.5 MeV/u C-ions (LET=175 keV/µm) or X-rays (for details see [1,3]).

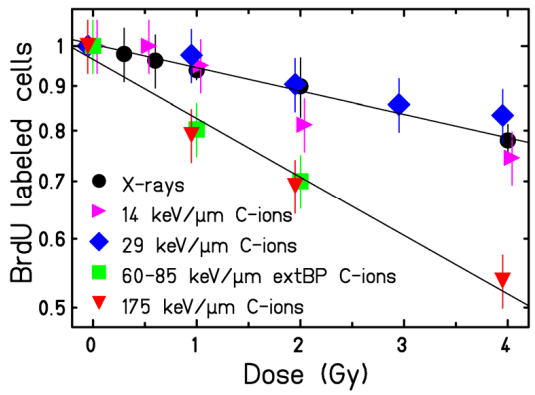

Fig. 3: Fraction of BrdU labeled cells 72 h after exposure to X-rays and C-ions with various LET values. Error bars represent sample variations within an experiment and were in the range of 5-8%.

References

[1] Lee et al., Radiat. Environ. Biophys. 50 (2011) 371.
[2] Gotoh and Durante, J Cell Physiol. 209 (2006) 297.
[3] Nasonova et al., Int J Radiat Biol 80 (2004) 621.

* Work supported by BMBF, Bonn, under contract 02S8497.

s.ritter@gsi.de

Establishment of fluorescence staining protocols for formaldehyde-fixed, paraffin-embedded tissue of carbon ion exposed rat lung

T. Dettmering, P. Simoniello, H. Faber, P. van Luijk, M. Durante, R. P. Coppes, C. Fournier

[1]GSI, Darmstadt, Germany; [2]UMCG, Groningen, The Netherlands

Introduction

To investigate radiation damage to the lung, the analysis of histological samples provides a better understanding of radiation effects than cell cultures. An initial step must be the identification of cell types such as fibroblasts, macrophages and epithelial cells, which can be performed by a staining of characteristical surface antigens of the cell types.

There are two main options for preparing and staining tissue sections: First, cryosections, which are easier to stain because the antigens are not stressed by fixation. Cryosections need constant freezing from the moment of sectioning and are therefore hard to transport. Second, formalin-fixed, paraffin-embedded (FFPE) tissue sections are more difficult to stain because antigens are obscured during fixation and embedding, but are easier to store. The former method is more suitable for weak signals and immunofluorescence, while it is more common to use a peroxidase-based, chromogenic method for FFPE tissue sections due to its superior signal amplification.

The imaging infrastructure at GSI Biophysics is fluorescence-based, with different epifluorescence and confocal microscopes being available. For logistical reasons, only FFPE tissue sections can be used. Fluorescence imaging of FFPE sections is challenging, because fixation enhances the already strong autofluorescence of lung tissue. Together with the low antigen signal of FFPE sections, the signal-to-noise ratio is low, which hinders a fluorescence staining. We established strategies to perform immunofluorescence on FFPE tissue sections and improve the signal-to-noise ratio, of which one is presented here.

Materials and Methods

Rats were irradiated with carbon ions at the SIS facility (GSI) and FFPE rat lung tissue was prepared at UMC (Groningen) after sacrificing the animals at different times after exposure. Deparaffinization was performed in Xylene, Antigen-retrieval was performed by boiling the slides for 10 min in 0.1 M citrate buffer, pH 6.0. Permeabilization was performed in 0.1% Triton X-100 in PBS for 20 min. 10% goat serum in PBS for 30 min was used for blocking. To quench the autofluorescence, slides were incubated 0.1% Sudan Black B (Sigma) in 70% EtOH for 10 min after the secondary Ab incubation.

All primary antibodies were chosen for IHC(P) compatibility and for specificity against rat antigens. Goat-anti-rabbit-Alexa568 and goat-anti-mouse-Alexa488 (both Invitrogen) were used as secondary antibodies.

Results and Discussion

The autofluorescence of the paraffin-embedded tissue was very strong in DAPI and FITC channels, so measures to reduce it had to be taken. Red and far-red channels are not as prone to autofluorescence as channels with shorter wavelengths. It was reported previously [1] that Sudan Black B is able to reduce autofluorescence with good results in brain tissue.

Incubation with Sudan Black B was able to completely abolish autofluorescence in the DAPI channel and reduce it in the FITC channel without noticeably reducing the actual signal from the secondary antibody.

Erythrocytes showed a strong autofluorescence in the FITC channel, which proved problematic if blood leaked into the tissue during preparation. The erythrocyte autofluorescence could not be reduced using Sudan Black B. Due to their different fluorescence spectrum, it was possible to remove the erythrocytes from the image using a linear unmixing algorithm in a first test.

After autofluorescence reduction, all antibody signals were well distinguishable from the background (Fig. 1). If an antibody has been tested for IHC(P) by the manufacturer, it can be safely assumed that it works also for fluorescence based detection in FFPE tissue.

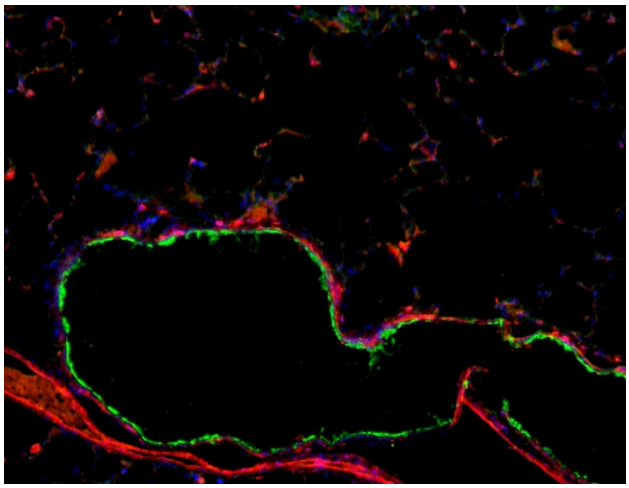

Fig. 1: Detection of fibroblasts (FSP1, red) and ciliated epithelium (alpha-Tubulin, green) in a 4 µm section of FFPE rat lung tissue.

Work is part of HGS-HIRe and FOI Bad Gastein.

References

[1] Baschong, W., R. Suetterlin, et al. (2001). J Histochem Cytochem 49(12): 1565-1572.

Cellular response of CHO-K1 cells to X-ray and carbon-ion irradiation under different states of oxygenation

N. Ma[1,2,3], M. Durante[1,4], S. Lai[1,2,3], A.Maier[1], W. Tinganelli[1,4] and W. K. Weyrather[1]
[1]GSI, Darmstadt, Germany; [2]Department of Radiation Oncology, Fudan University Shanghai Cancer Center, Shanghai, China; [3]Department of Oncology, Shanghai Medical School, Fudan University, Shanghai,China; [4]TU Darmstadt, Germany

Hypoxia is known to contribute to radiation therapy resistance directly by depriving cells of oxygen and indirectly by influencing cell physiological factors [1]. To investigate the influence of chronic oxygen depletion on cell survival, the Chinese hamster ovary cell line CHO-K1 was irradiated with x-ray and carbon ions under different states of oxygenation. The cell survival and cell cycle distribution were measured.

Material and Methods

CHO-K1 cells, cultivated under standard conditions, were investigated under normoxia (air), hypoxia (0.5% O_2, 94.5% N_2; 5% CO_2) or anoxia (95% N_2; 5% CO_2). The method of gassing and irradiation using the hypoxia exposure chamber has been described in [2]. For experiments under chronic conditions, cells were kept for 24 hours in hypoxia or anoxia. Irradiation was done using 250 kVp x-ray and carbon-ions with a 1 cm extended Bragg peak, corresponding to a dose-averaged LET value of 100 keV/µm. Cell survival was measured with a colony forming assay. Cell cycle analysis was performed with the flow cytometer PAS III (Partec).

Results and Discussion

From survival curves under different oxygenation states, we can see that CHO cells have a similar survival under both acute and chronic hypoxia (data not shown). In contrast, survival after irradiation under chronic anoxia is slightly reduced compared to acute anoxia. A similar reduction of survival can be seen for cells irradiated within 1 hour after reoxigenation from chronic anoxia compared to oxic cells. This is true for x-ray as well as for carbon irradiation (fig. 1). To understand this effect, the cell cycle distribution after reoxygenation from chronic anoxia and hypoxia has been measured and compared to normoxic cells. This results for chronic anoxia are shown in fig. 2. They show a block in G1 and a nearly complete depletion of S-phase cells directly after release from chronic anoxia. The distribution changed rapidly in the first 12 hours and is comparable to normoxic cells after 15 hours. Cell survival measured 15 hours after reoxygenation showed no enhanced sensitivity compared to normoxic cells (data not shown). For chronic hypoxia, a fairly uniform distribution of cell cycle under reoxygenation resulted in similar survival for 1 hour and 24 hours of reoxygenation.

Furthermore, the cell cycle distribution after irradiation with x-rays was performed with 2 Gy and 6 Gy under oxic conditions and 2 Gy, 6 Gy and 11.6 Gy under chronic anoxia. This reduced the cell survival to 64%, 18% and 80%, 50% and 18%, respectively.

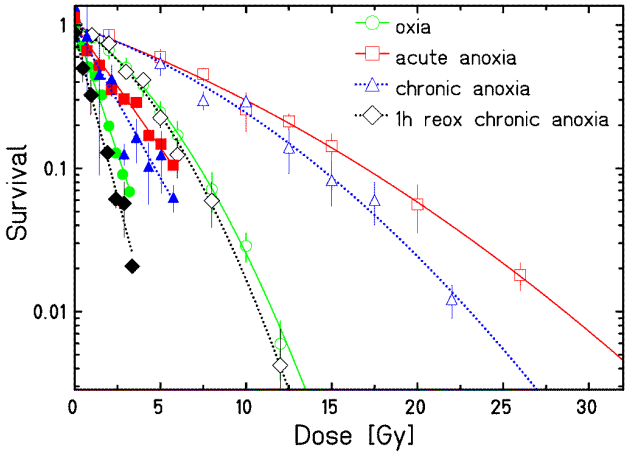

Figure 1 Survival of CHO-K1 cells under different states of oxygenation (open symbols: x-ray irradiation, closed symbols: carbon irradiation)

A dose-dependent reduction of cells in G1 and S phase and a dose-dependent accumulation of cells in G2/M phase were shown after x-ray irradiation under oxic conditions. The distribution of irradiated cells treated with 2 Gy and 6 Gy after chronic anoxia changed rapidly in the first 12 hours and was comparable to normoxic cells after 15-20 hours. There was no G2-block shown after irradiation at both doses. There was a small G2-block shown after 12-20 hours after irradiation with 11.6 Gy.

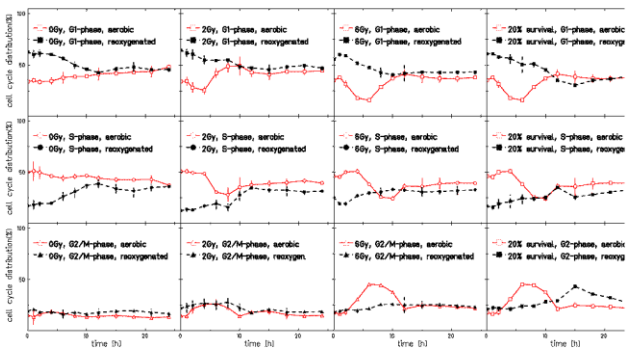

Figure 2 Cell cycle distribution under normoxia and during reoxygenation after chronic anoxia.

The study illustrates that for measurement in cell cultures, changes in survival and OER (Oxygengen Enhancement Ratio) after chronic oxygen depletion are due to changes in cell cycle distribution.

References

[1] Wouters A, et al. Oncologist. 12:690-712(2007).
[2] Ma N, et al. GSI scientific report 2010: 460 (2011).

Inflammatory effects of ionizing radiation in keratinocytes in comparison to UVB

J. Zink[1], G. Alphonse[2], M. Esposito[1,3], P. Simoniello[1], M. Durante[1,3], C. Rodriguez-Lafrasse[2], C. Fournier[1]

[1]GSI, Darmstadt, Germany; [2] EMR3738 Faculté de Médecine Lyon-Sud, Oullins, France; [3]TU Darmstadt, Germany

Introduction

Apoptosis and necrosis, two major types of cell death, are important processes which are involved in the inhibition or stimulation of inflammatory effects [1]. We have used the immortalized keratinocyte cell line HaCaT to perform experiments on the impact of exposure to ionizing radiation on cell growth, cell cycle regulation and the occurrence and mechanisms of cell death. We have used UVB as a naturally occurring radiation for comparison. Previously obtained results indicate that HaCaT cells undergo apoptosis after irradiation with UVB and high doses of γ-irradiation (10-20 Gy) [2].

Methods

HaCaT cells (DKFZ, Heidelberg) were irradiated with X-rays (2 and 10 Gy), carbon ions (0,5 and 2 Gy, 170 keVμm^{-2}) and UVB (15 and 60 mJcm^{-2}) and experiments were conducted between 6 hours and 10 days after irradiation. Clonogenic survival was assessed after X-ray irradiation up to 5 Gy by counting the colonies after 7 days. Morphological changes like occurrence of anaphase bridges, apoptotic bodies, cells micronuclei as well as multinucleated, giant and aberrant mitotic cells were determined after nuclear staining (DAPI, fluorescent microscopy). To discriminate between the occurrences of apoptosis or necrosis, cells were stained with Annexin-V and propidium iodide. Attached cells and detached cells in the cell culture supernatant were counted. The expression of apoptosis related proteins like activated Caspase 3 and 2 were analysed by western blot, lysis was performed by combining or separating attached and detached cells.

Results and Discussion

The response of keratinocytes to UVB light represents the major challenge of the upper layer of the skin due to environmental radiation exposure. Already shortly after irradiation with UVB apoptosis could be detected for the lower energy of 15 mJcm^{-2} with a maximum at 48 hours. In contrast, following exposure to 60 mJcm^{-2} HaCaT cells rather died by necrosis with maximum frequencies at 72 hours after irradiation. This result reveals that HaCaT cells undergo apoptosis after treatment with low doses of non-ionizing radiation whereas at higher doses they die by necrosis (data not shown).

Clonogenic survival after X-ray irradiation with up to 5 Gy showed that HaCaT cells are rather resistant to ionizing irradiation (SF2 = 0,64). Also the morphology of the cell nuclei demonstrated that the cells continue to proliferate after irradiation. However, starting from 48h an increasing number of morphological changes could be detected (figure 1) indicating mitotic catastrophe after a high but also after a lower dose (not shown).

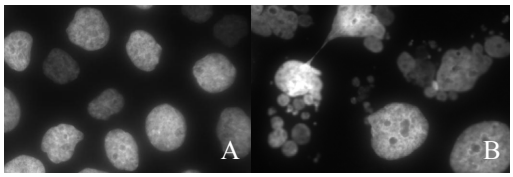

Figure 1: DAPI stained cell nuclei of HaCaT cells five days after X-ray irradiation (A: control; B: 10 Gy).

No molecular changes typical for early apoptosis were observed, but at later times (maximum values at 5 days after exposure) activated Caspase-3 (cleaved form, figure 2) and Caspase-2 (not shown) could be detected, indicating that the observed mitotic catastrophe is followed by apoptosis. This confirms published data [3]. In addition an increasing number of necrotic cells could be detected. In the samples with detached cells separated from attached cells we observed that the majority of cells with activated Caspase-3 had been detached from the cell culture dish indicating cell death.

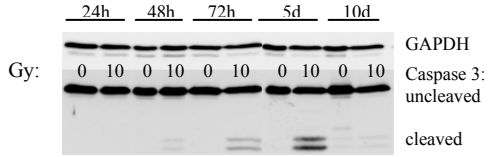

Figure 2: Western blot analysis of uncleaved and cleaved Caspase 3 in HaCaT cells (attached and detached cells combined) after irradiation with X-rays.

The observation that HaCaT cells do not undergo primary apoptosis after irradiation with X-rays could be caused by the mutation of p53 in HaCaT [4]. Mitotic catastrophe is caused by defective cell cycle check points [3]. In contrast, after irradiation with UVB a p53 independent pathway is probably responsible for cell death via apoptosis [5]. Based on our data we conclude that ionizing and non-ionizing irradiation induce different types of cell death in this cell type. We hypothesize that the effect of ionizing irradiation on HaCaT cells is related to mitotic catastrophe and late apoptosis or necrosis and thereby influence inflammatory processes.

Supported by DFG-funded Graduiertenkolleg (GRK 1657), HGS-HIRe and FOI

References

[1] Voll et al. (1997), *Nature*. 390: 350-351.
[2] Petit-Frère et al. (2000), *Carcinog.* 21: 1087-1095.
[3] Castedo et al. (2004), *Oncogene* 23: 4362-4370.
[4] Boukamp et al. (1988), *J. Cell Biol.* 106: 761-771.
[5] Aragane et al. (1998), *J. Cell Biol.* 140: 171-182.

Interaction of human lymphocytes to endothelial cells in a co-culture model under laminar flow conditions

Anna-Sophia Bothe[3], Jonas Klinger[1], Marco Durante[1,2], Gerhard Kraft[1] , Claudia Fournier[1]
[1]GSI, Darmstadt, Germany; [2]TU Darmstadt, Germany; [3]Hochschule Darmstadt, Germany

Introduction

Chronic inflammatory diseases are efficiently treated by irradiation with low doses of photons or α-particles, but the cellular and molecular background remains widely unknown [1,2]. The reduction of adhesion by low doses of X-ray as a result of a changed interaction of peripheral blood mononuclear cells (PBMC) and endothelial cells (EC) is discussed as an effect possibly attributed to low dose radiotherapy [3]. Adhesion of PBMC on the EC wall of the blood vessels is one of the initial steps in the inflammation cascade to recruit immune cells to inflamed tissue. EC are exposed to a constant shear stress because of blood circulation. In the previously reported experiments EC were all cultured under static conditions. The goal of the present study was to establish a system providing laminar flow conditions which mimics the wall shear stress imposed on EC in blood vessels, to investigate possible changes in the adhesion of peripheral blood lymphocytes (PBL) after irradiation .

Materials and Methods

A flow-chamber system was built, based on a publication by Freyberg et al. [4]. The system was modified to cultivate up to 8 samples in parallel. The flow chamber was composed of a petridish (Ø 3,5 cm), two silicone membranes and a polycarbonate inlet (perfusion chamber). The flow was generated from a peristaltic pump through the perfusion chamber. Human umbilical cord vein endothelial cells (HUVEC) were used for the experiments. They were cultivated for 72h prior to exposure to X-rays (250kV, 16mA). After irradiation EC were stimulated with TNF-α (1ng/ml) and incubated for 24h under laminar flow conditions. Afterwards the complete medium was exchanged by medium w/o TNF-α supplementation. In parallel PBL were stained with the membrane dye PKH67 (Sigma) and subsequently suspended in the circulating cell medium. Afterwards they were conducted over the EC monolayer in a constant flow for 30min. The unbound PBL were removed by washing the samples with PBS and afterwards EC were fixed with paraformaldehyde. Analysis was performed using a fluorescent microscope. As a comparison all experiments were performed as well under static conditions.

Results and Conclusion

In order to achieve laminar flow conditions, the flow rates of the peristaltic pump were determined at different pump speed settings (data not shown). To verify the laminar flow conditions the Reynold's number was calculated for each flow rate. Laminar flow conditions are defined at Reynold's numbers ≤2300 which was the case for all determined flow rates. In a next step the cell growth was determined at different flow rates (data not shown). The optimal cell growth was achieved at a flow rate of 0.037 m/s. Furthermore the cultivation of EC under static and dynamic flow conditions was compared. Therefore morphological differences between both cultivation methods were analysed. As shown in [Fig. 1] ECs were more aligned in the direction of flow after a dynamic- [A] compared to static cultivation [B]. Furthermore the changes in adhesion of PBL to EC were investigated after irradiation. First results indicate a different impact of irradiation on dynamic cultivated HUVEC compared to the static cultivated cells (data not shown). Whereas HUVEC showed under static cultivation no changes in adhesion after irradiation, the same cells showed under dynamic cultivation a reduced adhesion of PBL after irradiation with 0.5Gy.

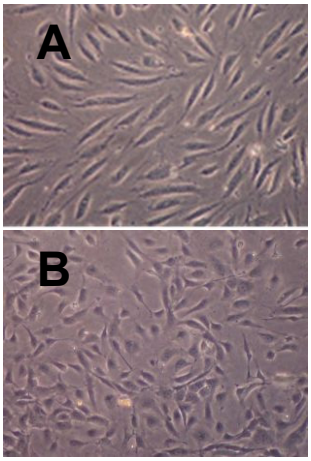

Figure 1: *Comparison of dynamic-* (**A**) *and static* (**B**) *cultivation conditions of endothelial cells (HUVEC). EC were cultured for 72h, images were acquired with a Leica phasecontrast microscope at an optical magnification of 200.*

Taken together, we have successfully cultured EC under laminar flow conditions using the flow-chamber system. The comparison of the static and dynamic cultivation revealed clear morphological differences between the cultivated EC. These results are in good agreement with the results published by Freyberg et al. Furthermore the cultivation conditions had an influence on the response of EC upon irradiation with respect to the adhesion of PBL. We assume that the dynamic cultivation is more comparable and less artificial to the situation *in vivo* as the static cultivation. The differences in the radiation response observed in our first experiments point to the importance of dynamic culture conditions to investigate radiation induced changes in the interaction of the cell types relevant for adhesion.

References

[1] Seegenschmiedt et al., *Strahlenther. Onkol.* 180: 718-730 (2004).
[2] Falkenbach et al., *Rheumatol Int*. 25(3): 205-10 (2005)
[3] Rödel et. al., *Strahlenter Onkol*., 180:194-200 (2004)
[4] Freyberg et al, *Cytotechnology* 26: 49–58. (1998)

*Work is part of HGS-HIRe and FOI Gastein (Austria)

New Collaborative Project on Cardiovascular Risk from Exposure to Low-dose and Low-dose Rate Ionizing Radiation (ProCardio) launched*

S.Ritter[1#], C. Fournier[1], M. Durante[1, 2], S. Tapio[3] and M. Atkinson[3]

[1]GSI, Darmstadt, Germany; [2]TU Darmstadt, Darmstadt, Germany; [3]HMGU, München, Germany

Cardiovascular disease, i.e. any disease involving the heart and blood vessels such as coronary heart disease, hypertension or arteriosclerosis, is estimated to be the leading cause of death in developing countries. One of the well-recognized risk factors for cardiovascular disease is the exposure to a high dose of ionizing radiation. For example, several studies have shown an increased risk of heart disease and stroke in patients after radiotherapy for cancer (reviewed in [1, 2]). More recently, also a link between moderate doses of ionizing radiation (> 500 mGy) and an increased risk of adverse cardiovascular effects was established, but considerable uncertainties remain about the health effects at low doses (e.g. <100 mGy) [3].

To fill the gap in knowledge on cardiovascular effects of low-doses and low-dose rates of ionizing radiation the ProCardio consortium was formed comprising a multidisciplinary international team of epidemiologists, radiation biologists and physicists, molecular biologists and mathematical modellers. The project started on 1 October 2011 and is funded for a period of 3 years with an amount of 3 million Euros by the Euratom 7th Framework Programme. It is coordinated by Prof. Michael Atkinson, Helmholtz Centre for Environmental Health Munich (HMGU).

Within the workpackage "Radiation Quality" treated by the biophysics group at GSI we will examine the influence of high and low LET radiation on both, beating cardiac myocytes and human cardiac microvascular endothelial cells (HCMEC). High LET exposure will be performed at the SIS accelerator at GSI using C-ions or Fe-ions at energies of 200-1000 MeV/u, LET in water will range from 20 to 400 keV/microns with a dose-rate of about 1 Gy/min. Low LET irradiation will be applied using Cs137 gamma- or X-rays.

One of the endpoint studied is the impact of high and low LET radiation on cardiomyocyte electrophysiology. The electrical properties of cardiac myocytes will be non-invasively analyzed up to 2 weeks after exposure using a microelectrode array system (MEA). This novel tool allows a functional analysis of cell-cell interactions in electrogenic tissue [4]. Endpoints such as beating frequency, arrhythmia and conduction velocity can be measured with a high spatial and temporal resolution.

Concomitant, cellular parameters such as the intracellular coupling between cells, cell death, and premature senescence will be examined. First, doses of 0.5 and 2 Gy will be applied. If there is an effect, doses from 100 mGy downwards will be studied. Since a large number of functional (beating) cardiomyocytes is required for these experiments, cardiac myocytes will be derived from mouse embryonic stem cells. The differentiation protocol for the mouse embryonic stem cell line D3 has been recently established and is currently improved [5, 6].

Furthermore, the influence of radiation quality on HCMEC (commercially available) will be investigated. Cells will be exposed to 0.01, 0.5 and 2 Gy heavy ions or photons and the cytokine release related to an inflammatory response will be analysed at 4 h, 24 h and 1 week after irradiation, which includes the time frames for both acute and chronic phenotypic changes after low-dose irradiation (Tapio et al., unpublished data). In preliminary experiments the assay has already been successfully used to characterise the response of various endothelial cell lines following X-ray exposure (Fournier et al., unpublished data).

Finally, HCMEC and cardiomyocytes exposed at GSI to high and low LET radiation will be shipped to partner institutes for a detailed analysis of phenotypic changes affecting the transcriptome, epigenome and proteome. For example, proteomic alterations will be studied at HMGU to identify potential biomarkers, and at the same time provide insight into mechanisms affecting the heart at low doses. For this analysis protein extracts from sham and irradiated samples will be labelled, mixed, and separated. Differentially expressed proteins will be identified by mass spectrometry. Proteomic alteration patterns typical for low LET, high LET or both will then be analysed using bioinformatics tools.

In summary, the ProCardio project aims to establish a scientific data base for accurate risk estimation of low-doses and low-dose rates of ionizing radiation. In cellular experiments, as performed at GSI or HMGU, mechanisms that may influence the disease processes at low doses will be examined. These *in vitro* studies will complement *in vivo* studies using mouse models and epidemiological studies of childhood cancer survivors performed at partner institutes. Finally, in one workpackage mathematical models of circulatory disease will be developed and tested against new biological information and available epidemiological data.

References

[1] Adams et al. Crit Rev Oncol Hematol, 2003, 45, 55-75
[2] Shankar et al., Pediatrics, 2008, 121, 387-396.
[3] Little et al., Radiat Environ Biophys, 2010, 49, 139-153.
[4] Steger et al., GSI Report 2011-1, p450.
[5] Materna et al., GSI Scientific Report, this issue.
[6] Helm et al., GSI Scientific Report, this issue.

#s.ritter@gsi.de

*Funded by the Euratom 7th Framework Programme under grant agreement no 295823

Phagocytosis of radiation-induced apoptotic lymphocytes*

J. Klinger[1], M. Durante[1,2], B. Frey[3], U. Gaipl[3], A. Groo[1], G. Kraft[1], C. Fournier[1],
[1]GSI, Darmstadt, Germany; [2]TU Darmstadt, Germany; [3]Universitätsklinkum Erlangen, Germany

Introduction

Chronic inflammatory diseases such as arthritic disorders are efficiently treated by irradiation with low doses of photons or α-particles [1,2]. However, the molecular and cellular background of induction of anti-inflammation by low dose irradiation remains widely unknown. It was shown that the phagocytosis of irradiation induced apoptotic cells is increased in comparison to viable ones and that immunosuppressive effects are observed only in activated macrophages after phagocytosis [3,4,5]. The induction of apoptosis in these studies was achieved by UV irradiation. In the present work the question was raised if the induction of apoptosis through ionizing radiation would have the same effect on the macrophages phagocytotic activity as described for UV irradiation. Furthermore possible differences between photon- and charged-particle irradiation were investigated. To achieve this goal, in a first step a simple phagocytosis assay was established for a quantitative measurement of phagocytotic activity.

Materials and Methods

Three different macrophage subsets were generated by *in vitro* differentiation for 7d with distinct stimulation factors (M-CSF/GM-CSF) or by spontaneous differentiation. For the phagocytosis assay human peripheral blood lymphocytes (PBL) were stained prior to irradiation with the membrane dye PKH67 (Sigma). Irradiation of PBL was performed using X-rays (250kV, 16mA) or carbon ions (LET 63-85keV/µm) and effective doses were chosen with respect to the induction of apoptosis. After irradiation PBL were cultured for 24h. Afterwards they were co-cultured with human macrophages for 1.5h +/-LPS (100ng/ml) or +/-TNF-α (1ng/ml). After co-incubation remaining PBL were removed by washing with PBS. Subsequently the macrophages were detached and analysed by flowcytometry. The mean fluorescent intensity (MFI)of the dye PKH67 was measured, as an indication for phagocytotic activity to compare the phagocytosis of unirradiated vs. irradiated PBL.

Results and Conclusion

In a first approach we compared the phagocytotic activity of the different macrophage subsets. All subsets showed a diverse behaviour concerning the phagocytosis of apoptotic PBL. The macrophages generated by spontaneous differentiation showed the highest phagocytotic activity, but interestingly they showed no significant difference between the phagocytosis of unirradiated and apoptotic PBL following exposure to 6Gy X-rays (data not shown). Compared to the unstimulated macrophages, the M-CSF- and GM-CSF subsets showed a lower phagocytotic activity, but in contrast the, co-incubation with irradiated PBL increased the phagocytotic activity of both subsets significantly (shown in *Fig. 1*). The most pronounced difference between the uptake of unirradiated and apoptotic PBL was observed for the M-CSF stimulated macrophages. In further experiments a possible influence of a pro-inflammatory stimulation of the macrophages (LPS or TNF-α) was examined. In all performed experiments no difference in phagocytotic activity in the presence or absence of pro-inflammatory compounds was observed (data not shown). In first experiments the effect of photons was compared to carbon ion exposure. Freshly isolated PBL were irradiated either with X-ray (6Gy) or carbon ions (0.5 or 2Gy) prior to the phagocytosis assay. Interestingly, X-ray irradiation caused a more pronounced increase of phagocytotic activity compared to carbon ions, although carbon ions were as effective as photons in inducing apoptosis (data not shown).

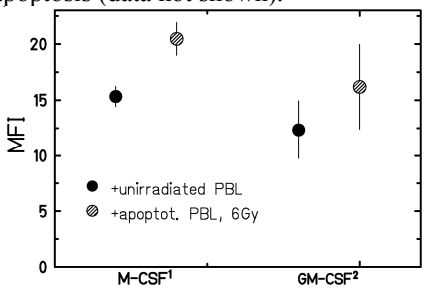

Figure 1: *MFI as an indication for phagocytotic activity of human macrophages, co-cultivated with unirradiated- or apoptotic PBL, irradiated with X-ray (6Gy). Co-incubation was performed for 1.5h. Error bars are shown as SEM.* (N=3-4, n=11-15)

Our results show that the phagocytotic activity depends considerably on the macrophage subsets. The macrophage subset that had undergone differentiation in the presence of M-CSF showed significantly higher phagocytotic activity for viable and irradiated PBL compared to the GM-CSF subset. While GM-CSF generated macrophages are described as pro-inflammatory, M-CSF generated macrophages are discussed to have an anti-inflammatory role [6]. Therefore, for *in vivo* differentiation it is likely that M-CSF participates, if macrophages are involved in the uptake of apoptotic cells, which in turn might contribute to an anti-inflammatory reaction. Future experiments have to be carried out analysing the cytokine profile of activated M-CSF macrophages after Phagocytosis to sustain this hypothesis. Our results further indicate that a pro-inflammatory stimulation has no effect on the amount of phagocytosed apoptotic cells. At the moment we have no explanation why carbon ions were less efficient in increasing the uptake of the irradiated PBL by macrophages, although they were as efficiently as X-rays in inducing apoptosis (data not shown).

*Work is part of HGS-HIRe and FOI Gastein (Austria)

References

[1] Seegenschmiedt et al., *Strahlenther. Onkol.* 180: 718-730 (2004).
[2] Falkenbach et al., *Rheumatol Int*. 25(3): 205-10 (2005)
[3] Fadok et al., *J. Clin. Invest.* 101(4): 890–898 (1998)
[4] Voll et al., *Nature* 390(6658): 350–351 (1997)
[5] Munoz et al., *J. Leukoc. Biol.* 81(1): 6–14 (2007)
[6] Verreck et al., *Proc. Natl. Acad. Sci.* 101(13): 4560–4565 (2004)

Predicting chromosome aberration yield at different time points after exposure to energetic heavy charged particle radiation*

J. Deperas-Standylo† [1,2], *R. Lee*[3], *S. Ritter*[3], *M. Durante*[3], *and E. Gudowska-Nowak*[1]

[1]Jagiellonian University, Krakow, Poland; [2]JINR, Dubna, Russia; [3]GSI, Darmstadt, Germany

Cytogenetic data accumulated from the experiments with peripheral blood lymphocytes exposed to densely ionizing radiation [1] clearly demonstrate that for particles with LET>100 keV/μm the derived RBE will strongly depend on time after exposure. A reasonable prediction of radiation-induced chromosome damage and its distribution among cells can be achieved by exploiting Monte Carlo methodology along with the information about the radius of the penetrating ion-track and the LET of the ion beam. In

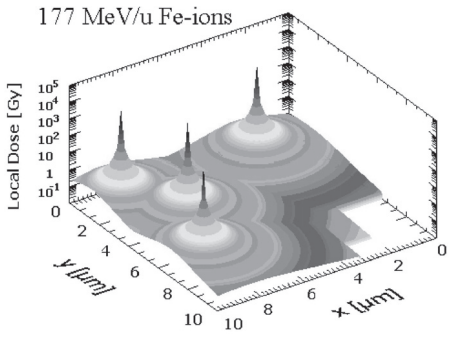

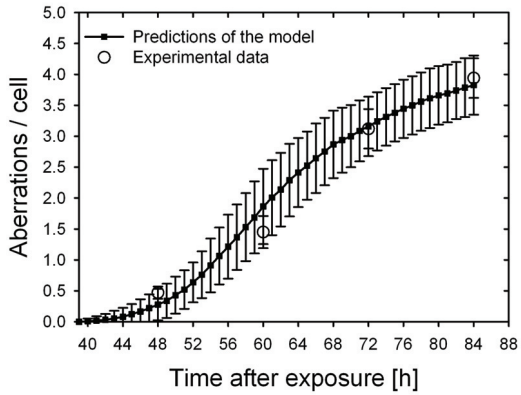

order to examine the relationship between the track structure and the distribution of aberrations induced in human lymphocytes and to clarify the correlation between delays in the cell cycle progression and the aberration burden visible at mitosis, we have analyzed chromosome aberrations in lymphocytes exposed to Fe-ions with LET values of 335 keV/μm and formulated a Monte Carlo model which reflects time-delay in mitosis of aberrant cells. Within the model the frequency distributions of aberrations among cells follow the pattern of local energy distribution and are well approximated by a time-dependent compound Poisson statistics. On the other hand, the passage or flux of undamaged and aberrant cells and chromosome aberrations through mitosis are modelled as a renewal process represented by a random sum of (independent and identically distributed) random elements $S_N = \sum_{i=0}^{N} X_i$. Here N stands for the number of particle traversals of cell nucleus, each leading to a statistically independent formation of X_i aberrations. The parameter N is itself a random variable and reflects the cell cycle delay of heavily damaged cells [3]. The probability distribution of S_N follows a general law for which the moment generating function satisfies the relation $\Phi_{S_N} = \Phi_N(\Phi_{X_i})$.

Within the current project we focus on derivation of the Monte Carlo model which allows to predict expected fluxes of aberrant and non-aberrant cells based on several input information: (i) experimentally measured mitotic index in the population of irradiated cells (ii) scored fraction of cells in first cell cycle (iii) estimated average number of particle traversals per cell nucleus. By reconstructing the local dose distribution in the biological target, the relevant amount of lesions induced by ions is estimated from the biological effect induced by photons at the same dose level. Moreover, the total amount of aberrations induced within the entire population is determined. For each subgroup of intact (non-hit) and aberrant cells the flux of cells passing through mitosis has been analyzed reproducing correctly an expected correlation between mitotic delay and the number of aberrations carried by a cell [3]. As discussed previously [2, 4], this observation is of particular importance for the proper estimation of the biological efficiency of ions and for the estimation of health risks associated with radiation exposure.

References

[1] S. Ritter and M. Durante, Mutation Research 701 (2010) 38.

[2] M. Scholz et al., Adv. Space Res. 18 (1996) 5.

[3] E. Gudowska-Nowak et al., Int. J. Radiat. Biol. 81 (2005) 23.

[4] J. Deperas-Standylo et al., Eur. Phys. J. D 60 (2010) 93.

* This work is supported by the International PhD Projects Programme of the Foundation for Polish Science within the European Regional Development Fund of the European Union, agreement no. MPD/2009/6. E.N. and R.L. were funded by the German Federal Ministery of Education and Research (BMBF), Bonn, under contract No. 02S8497

† joannadeperas@wp.pl

Survival of RAT-1 cells irradiated with x-rays or carbon ions under hypoxic and co-culture conditions

S. Lai[1,2,3], N. Ma[1,2,3], C. Hartel[1], W. K. Weyrather[1], W. Tinganelli[1,4] and M. Durante[1,4]

[1]GSI, Darmstadt, Germany; [2]Department of Radiation Oncology, Fudan University Shanghai Cancer Center, Shanghai, China; [3]Department of Oncology, Shanghai Medical School, Fudan University, Shanghai, China; [4]TU Darmstadt, Germany

The purpose of this study was to investigate the effects of x-ray or carbon ion irradiation under different oxygen supply conditions on two rat cell lines grown together under co-culture conditions. Previous results of co-culture experiments had shown, that after x-ray irradiation the normal cells, IEC-6, had a proliferation gain, whereas it could not be found in the cancer cell line, RAT-1 [1]. However, to verify these results and to investigate whether there is an additional effect from formerly hypoxic tumor cells on the growth of the normal cells, a set of experiments was carried out.

Materials and Methods

Cell lines and culture

RAT-1 cells (R3327 AT-1 from rats) and IEC-6 cells (the intestinal epithelium cells of rats) were cultured in RPMI-1640 medium supplemented with 10% fetal calf serum (FCS) and 1% Penicillin/Streptomycin, and kept in a humidified atmosphere of 5% CO_2 at 37°C.

Chronic hypoxia and clonogenic survival assay

Acute hypoxia (2 h) and two kinds of chronic hypoxia (24 h) were performed in this study, using a standard hypoxia incubator or specially designed hypoxia chambers. The concentration of the oxygen was 0.5%. Cells were irradiated under hypoxic conditions, or were irradiated after reoxygenation. Then the clonogenic survival assay was carried out and the survival curves fitted with linear-quadratic formula.

Co-culture

RAT-1 and IEC-6 were reseeded together in tissue culture flasks after certain treatments, hypoxia or/and irradiation (x-ray or Carbon ion beam) for the survival analysis.

Results and Discussion

Survival under hypoxia

Fig. 1A shows the high effectiveness of C-ions in killing the RAT-1 cells, compared to x-rays. No difference was observed in the survival of cells after chronic hypoxia + reoxygenation, compared to normal oxic conditions. RAT-1 cells irradiated in acute hypoxia showed a pronounced radioresistance to x-rays (Fig 1B). Cells irradiated under chronic hypoxia have only a slight survival advantage, compared to cells kept under normal oxic conditions. In contrast to X-rays, the effect of the oxygen status on the cell survival is small after carbon irradiation, confirming that carbon ions are advantageous for the clinical application in treating tumors with hypoxic areas.

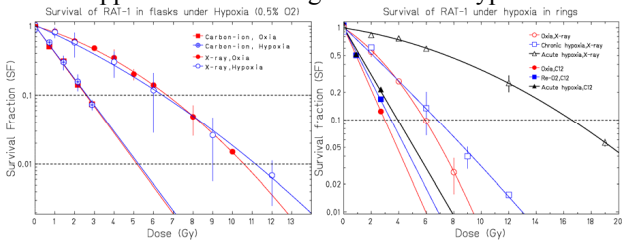

Fig.1 Survivals of RAT-1 irradiated with X-ray and Carbon ions. A) Cells irradiated in reoxygenated conditions after chronic hypoxia and normal oxic conditions. B) Cells irradiated in acute hypoxia, chronic hypoxia and normal oxic conditions.

Co-culture of RAT-1 and IEC-6

The plating efficiency of IEC-6 cells was higher in co-culture conditions than in mono-culture, confirming previous results (data not shown). Regarding the cell survival, co-culture conditions have only slight influences (Fig 2). The survival ratios (survivals in co-culture divided by survivals in mono-culture) of IEC-6 cells irradiated with X-ray were slightly higher than 100% under oxic condition and under hypoxia. In contrast, RAT-1 cells irradiated with C-ions under hypoxia show a decreased survival level in co-culture (Fig 2D), however, due to the limiting beam-time this experiment was performed only once, thus, for a reliable conclusion more works would be necessary.

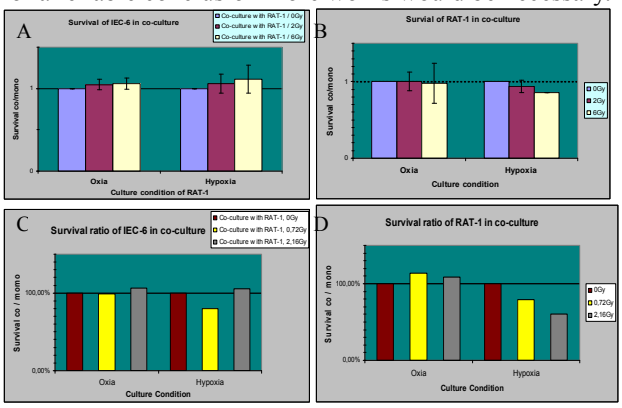

Fig. 2 Co-culture of RAT-1 & IEC-6. A) IEC-6 irradiated with X-ray; B) RAT-1 treated with X-ray; C) IEC-6 irradiated with C^{12}; D) RAT-1 treated with C^{12}

References

[1] S. Lai, et al. GSI Scientific Report: 459(2010).

[2] Ma N, et al. GSI Scientific Report: 460 (2010).

Targeting cancer stem cells in head and neck squamous cell carcinoma to overcome resistance to X-ray or carbon ion irradiation.

Alphonse G[1,2,3], Bertand G[1,2], Maalouf, M[1,2], Battiston-Montagne P[1,2], Taucher-Scholz[4], Fournier C[4], and Rodriguez-Lafrasse C[1,2,3]

[1]Université Lyon I, Faculté de Médecine-Lyon-Sud, F-69921 Oullins, France. [2]Laboratoire de Radiobiologie Cellulaire et Moléculaire, EA3738, F-69921 Oullins, France. [3]Hospices-Civils-Lyon, CHLS, Pierre-Bénite, F-69495, France. [4]GSI Helmholtz Center for Heavy Ion Research, Biophysics Department, 64291 Darmstadt, Germany..

Introduction

It is now well-established that heavy ion radiotherapy can offer some potential merits over conventional radiotherapy. Elucidating the molecular mechanisms involved after carbon ions exposure is therefore a crucial step for improving hadrontherapy, particularly for the treatment of radioresistant tumors.

Since recent clinical trials had shown that the local treatment of HNSCC by hadrontherapy is much less efficient than that of other radioresistant cancers [1], we thus initiated fundamental studies on the mechanisms of cell death in two p53-mutated head and neck squamous cell carcinoma (HNSCC) with opposite radiosensitivity following carbon ions and X-rays exposure, We first showed that carbon ion irradiation does not modify the type of death involved, but amplifies it. In the radiosensitive SCC61 cell line, an early ceramide-dependent apoptotic cell death occurred after irradiation. In contrast, the radioresistant SQ20B cells underwent G2/M arrest associated with Chk1 activation and Cdc2 phosphorylation. Furthermore, 5 days after carbon ion irradiation, SQ20B cells bypassed the G2/M arrest and underwent mitotic catastrophe cell death. Although a majority of SQ20B cell finish mitotic catastrophe by a ceramide-dependent apoptosis mechanism, a subpopulation of cells was able to escape mitotic catastrophe and continue to proliferate [2,3].

Recently, the involvement of Cancer Stem Cells (CSC) in solid tumors recurrences following conventional irradiation has been demonstrated. We have then investigated whether CSC might be the subpopulation of SQ20B cells resistant to carbon ion irradiation.

Results

We first demonstrated that a subset of SQ20B cells presents different markers of CSC such as CD44 expression, Hoechst efflux, ALDH over activation and spheroids formation. We then separated a SQ20B/SP/ALDH+/CD44+ subpopulation as putative HNSCC cancer stem cells. The radiation response of this subpopulation of cancer cells that are likely to be critical for success or failure of cancer therapy was then studied.

The CD44+ SQ20B cells seems to be more resistant to photon irradiation than the CD44- cells as the surviving factors at 2 Gy (SF2) were respectively 0,81 and 0,54 in CSC and non-CSC. In response to carbon ions the same pattern of response is observed since the SF2 was 0.21 for the CSC compared to 0.09 for the non-CSC population.

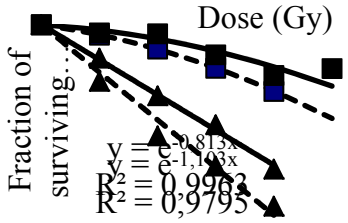

Fig.1: Cell survival curves after photon or carbon irradiation for both SQ20B/CD44+ and SQ20B/CD44- cells.

After the analysis of cell cycle we demonstrated that the lack of apoptosis induction due to an extend G2/M phase arrest induced by carbon ion irradiation are responsible for this radioresistance.

In light of these results, we investigated whether the inhibition of G2/M arrest, by UCN-01 could radiosensitize the SQ20B/CD44+ cells and induce apoptotic cell death. As shown in Figure 2 a significant inhibition of the G2/M arrest was observed after carbon irradiation. Accordingly, the combination of UCN-01 and irradiation amplify the apoptotic cell death since the percentage of SQ20B/CD44+ cells in sub-G1 phase without UCN-01 treatment was less than 30%, at 240 hours and raised more than 70% following the addition of UCN-01.

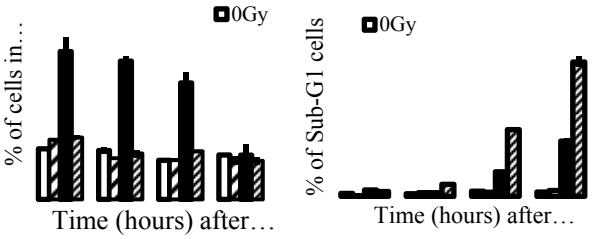

Fig.2: Percentage of SQ20B/CD44+ cell in sub-G1 or G2/M phase after carbon irradiation +/- UCN-01.

Our results demonstrated that targeting specifically apoptosis in CSC led to a significant sensitization to carbon irradiation. Thus, targeting of the HNSCC-CSCs would provide a critical step to disrupt the resistance mechanism and to improve overall tumor control with radiation treatment.

Reference

[1] JE. Mizoe *et al*. IJROBP. **2004** Oct 1;60(2):358-64.
[2] G. Alphonse *et al., Submited*
[3] M. Maalouf *et al.,* IJROBP. 2009;74(1):200-209

Multimodal Treatment Planning with TRiP98 *

M. Krämer[1], *E.Scifoni* [1], *and M. Durante*[1]
[1]GSI, Darmstadt, Germany

In ion beam radiotherapy dose optimization via inverse planning, fully including radiobiological properties, is the de-facto standard, pioneered by GSI's TRiP98 treatment planning system (TPS) [1]. In the context of the European ULICE project, several new methods of "adaptive treatment planning" have been implemented in addition.

Combined Photon-Ion Boost Plans

In GSI's radiotherapy pilot project about one third of patients received photon treatment with an additional carbon ion boost on a tumour subvolume. Both treatments were planned separately, however. In order to improve dose conformation one may use the "prior knowledge" from preirradiation for ion plan optimization. As a proof of concept, Figure 1 shows dose distributions for ion boost plans on top of preirradiation base plans. The optimization algorithm is able not only to fill the non-irradiated parts of the target volume, but also compensates for the shallow dose gradient of the base plan by allowing some extra dose at x=85mm. The benign particle fluence maps of Fig. 2 show that the solution of the inverse problem is reasonably stable.

Multi-Ion Plans

So far all clinical sites use a single ion species per patient plan. However, in certain cases it might be advantageous to combine different ions in one irradiation. Hypoxic subvolumes, for example, might require extra high LET radiation such as stopping carbon or even oxygen beams [2], whereas the bulk of the volume could be irradiated with less critical radiation, such as protons. Thus it appears attractive to provide the means to generate multi-ion treatment plans. As a proof of concept, Figure 3 shows simultaneously optimized dose distributions for combined irradiation with protons and ^{12}C. If only the target volume would be considered, both partial fields would contribute equally. An additional dose constraint ($< 20\%$ target dose) for the organ at risk, however, leads to an automatic preference for ^{12}C (and corresponding deemphasis for protons) at the inner target edges. The benign particle fluence maps of Fig. 4 show that the solution of the inverse problem is reasonably stable also for this scenario.

References

[1] Krämer M., Durante M, Eur. Phys. J. D, 60 (2010) 195.

[2] Scifoni E. et al., this report

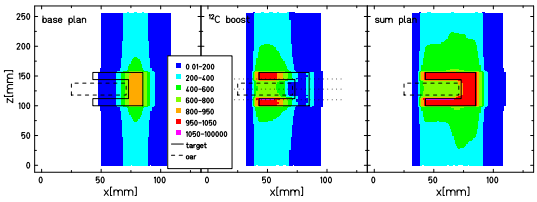

Figure 1: Dose distributions for combined plans. Left: base plan, middle: ^{12}C compensation, right: combined plan

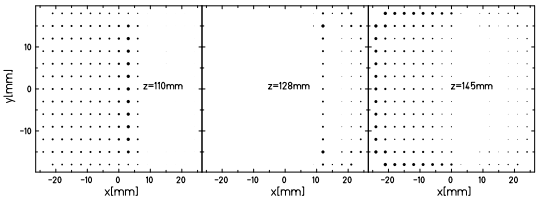

Figure 2: Fluence maps for positions indicated in Fig. 1

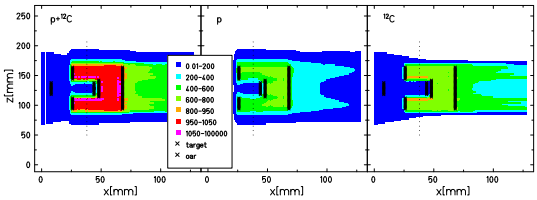

Figure 3: RBE-weighted dose distributions for multi-ion plans. Left: combined, middle: protons, right: ^{12}C

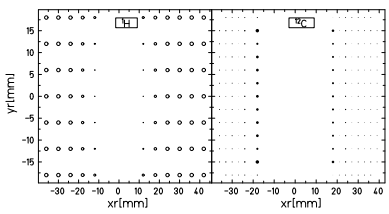

Figure 4: Fluence maps for position indicated in Fig. 3

* Work co-funded by the European Commission under FP7 Grant Agreement Number 228436

TRiP98: Results of the parallelization of dose calculation

J. Trautmann[1,2], W. Heenes[2], M. Krämer[1], C. Bert[1], and M. Durante[1]

[1]GSI, Darmstadt, Germany; [2]TU Darmstadt, Germany

Introduction

TRiP98 is a treatment planning program, which was used in the pilot project of heavy ion radiotherapy with scanned ion beam at GSI [1]. Over 400 patients have been treated from 1997 to 2008 [2].

At the moment, TRiP98 is only used for research purposes. One current research topic concerns 4D treatment planning for moving tumors (e.g. lung tumors), that requires handling large time-resolved 4D data sets [3]. Despite this increased amount of data, fast calculations are requested by the user. To increase computation speed, the dose calculation algorithm was parallelized [4] using the application programming interface OpenMP.

Measurements

Measurements to determine the speedup of the OpenMP implementation have been done for four patient data sets taken from the GSI pilot project. They were recalculated using the standard version of TRiP98 and the new parallel approach. In both versions the recalculation was done for the absorbed [1] and the biologically effective [5] dose taking alternative algorithms into account. For the OpenMP version different amounts of threads have been used up to the maximum of 32 threads available on the IBM BladeServer PS701 (IBM Power7, 8 cores, 4-way-SMT) with 32 GB main memory. The speedup factor differs between the data sets depending on the amount of dose voxels.

For both kinds of dose calculations Patient 290 was chosen as an average example. For up to 8 threads a linear growth of the speedup factor was determined (see fig. 1).

Absorbed dose

For the absorbed dose there are three algorithms which differ in the level of detail and therefore have differences in the execution time. The most complex one is the multiple scatter (ms) algorithm. Here the best performance has been reached with a speedup factor of 20.8 (fig. 1).

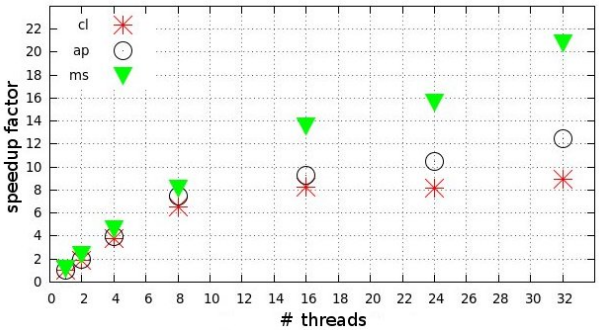

Figure 1: speedup for patient 290
(absorbed doses)

Biologically effective dose

In case of the biologically effective dose, there are two alternative algorithms. The more complex classic (cl) algorithm uses a two-level random number distribution in which a data dependency was discovered and solved. To make the calculation times comparable, this was changed in the parallel and original version of TRiP98.

For the cl algorithm the speedup factor reaches a saturation value of 11.8 already at 24 threads (fig. 2). We attribute this to cache limitations due the larger amount of data which the cl algorithm takes into account.

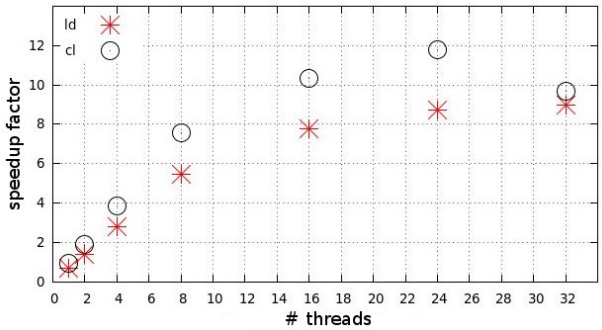

Figure 2: speedup for patient 290
(biologically effective doses)

Outlook

It was possible to demonstrate the potential of parallelization with acceptable amount of work for TRiP98. To reduce the calculation time for the new developments of TRiP98, further parts should be parallelized. A good starting point should be the dose optimization, which uses a lot of functions that were already parallelized for the presented dose calculation algorithms.

Alternative parallelization techniques like GPU-based ones will require more severe changes in the current code.

References

[1] M. Krämer et al., “Treatment planning for heavy-ion radiotherapy: physical beam model and dose optimization”, Phys.Med.Biol., 45 (2000) 3299-3317

[2] O. Jäkel et al., “Treatment planning for heavy ion radiotherapy: clinical implementation and application”, Phys.Med.Biol., 46 (2001) 1101-1116

[3] D. Richter et al., “Status of 4D Treatment Planning Implementations for TRiP98”, GSI Scientific Report 2010, 476

[4] J. Trautmann et al., “TRiP98: Parallelization of Dose Calculation”, GSI Scientific Report 2010, 478

[5] A. Gemmel et al., “Biological dose optimization with multiple ion fields”, Phys.Med.Biol. 53 (2008) 6991-7012

Using Parallel Hardware for Biophysical Modelling: A Parallelized Implementation of the Local Effect Model*§

O. Steinsträter[1], U. Scholz[1], M. Durante[1], and M. Scholz[1]

[1]GSI, Darmstadt

Introduction

In the past, the rapid increase in processor clock speed and transistor density led automatically to an accompanying increase in the performance of existing software. But due to problems with power consumption and heat-dissipation, virtually all vendors have switched to multi-core CPUs to increase the processing power. Unfortunately, this means that existing sequential code will no longer run automatically faster on faster hardware. On the other hand, parallel programming is challenging, error-prone and needs a high degree of experience. This is in particular true for the programming of GPUs (graphics processing units) on graphic cards [1].

In contrast, software developing in the scope of a biophysical research project is characterised by a high degree of heterogeneity: some software components will last for a long time, while other parts will only be used for a limited live time as the underlying model may turn out to be less effective than expected. In addition the programming skills of the involved scientist are as heterogeneous as the used hardware: from the laptop of a student to a high performance cluster system.

A good example is the implementation of the Local Effect Model [2], LEM, developed at the GSI. Due to improvements in the underlying biophysical model, the software is under constant development but is used at the same time by other researchers for the generation of reliable and reproducible simulation results. Although an increase of the performance of the simulation software is very desirable its reliability and availability must also be ensured.

Using the implementation of the Local Effect Model as an example, we tried to investigate to what extend software developed in an academic environment can profit from the trend to highly parallel hardware.

Method

We expected that typically only low resources for the development of parallel software is available and in general reliability is more important than speed. Therefore, and as experiences in parallel programming can not generally be expected from biophysicists which will contribute to the LEM code in the future, the software should mainly stay in its sequential state. We therefore used OpenMP [3], an API (application programming interface) which allows the parallelization of existing code mainly by adding hints to the compiler (compiler directives). If a compiler does not understand these directives or if the compiler is instructed to ignore them, the code falls back to its pure sequential, i.e. original version.

In addition we try to participate from the high theoretical processing power of a potentially available graphic card by substituting the generation of random numbers (monte carlo simulation) by a library function which uses a graphic card as a coprocessor: CURAND library (part of the NVIDIA's CUDA toolkit [4]) .

Results

On an Intel Xeon processor L5506 (4 cores) we found that the parallel version of the LEM software typically ran around 5.5 times faster than the serial version. By using the graphic card an increase of the performance on a system with an Intel Core i7-2600K CPU and an NVIDIA GeForce GTX 570 graphic card around 35% was observed. As the graphic card has to calculate random number in large blocks (here 310,000,000 random numbers), its use is connected with a significant overhead. When random numbers are calculated by CPU and GPU in the same way (the same overhead), for the GPU solution we observed an increase in speed of more than 100%.

Discussion and Conclusion

Without significantly changing the original LEM code we could increase the processing speed on a four core processor by a factor of 5.5. The code is still basically sequential and runs on hardware independent on the number of processing units. If needed the parallelization could be turned off by a simple compiler switch. The reliability of the code is therefore not negatively influenced by the parallelization. The performance increase due to the graphic card was significant lower, but a performance gain of 35% could be reached simply by substituting a library function.

We conclude that at least in simple cases parallelization of existing software can be easy and does not require a significant change of the structure of the program. If a basic knowledge about the principles of parallel software is available, sequential code could be structured and commented to ease a later parallelization.

References

[1] D. B. Kirk and W. W. Hwu, "Programming Massively Parallel Processors", Elsevier, 2010.

[2] T. Elsässer et al., Int. J. Radiation Oncology Biol. Phys. 78 (2010) 1177.

[3] S. Hoffmann and R, Lienhart, "OpenMP", Springer, 2008.

[4] http://developer.nvidia.com/cuda-toolkit-40.

* Work supported by Siemens Healthcare.

§ Work is part of HGS-HIRe.

The shape of dose response curves generated by the full simulation extension of LEM IV*

U. Scholz[†1,2], *O. Steinsträter*[1], *T. Friedrich*[1], *M. Durante*[1,2], *and M. Scholz*[1]

[1]GSI, Darmstadt, Germany; [2]Institut für Festkörperphysik, Technische Universität Darmstadt, Darmstadt, Germany

The purpose of the Local Effect Model (LEM) is to calculate the relative biological effectiveness of charged particle radiation with respect to conventional photon radiation [1]. In the current LEM IV realization the biological effectiveness of a single charged particle traversing a cell nucleus is deduced by its double strand break (DSB) distribution pattern [2]. While the initial slope α_{I} of the linear-quadratic-linear (LQL) ion dose response curve is obtained by means of Poisson statistics, the curvature β_{I} is deduced by the assumption that the maximal slope of the curve is the same as for photon radiation. Additionally, the threshold dose D_t (the dose where the response curve gets linear) for ion radiation is assumed to be identical to the one of photon radiation.

In contrast to the low dose algorithm described above, in the full simulation extension of LEM IV the DSB distribution pattern and the resulting biological effect is analyzed for arbitrary patterns of multiple traversals for the radiation type of interest [3]. Since an LQL description is used for the reference radiation, the predicted ion dose response curves are expected to exhibit also an LQL-like behavior. Fitting of LQ parameters then will depend on the dose range as depicted in Fig. 1, where $\Delta\chi^2$ is plotted, i.e. the change of the χ^2 fit value obtained by altering the fit range. The fit gets worse by increasing the fit range above

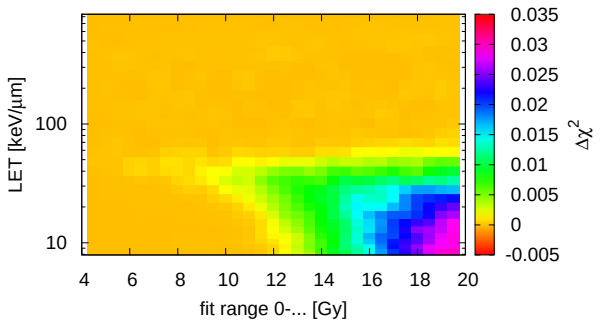

Figure 1: $\Delta\chi^2$ of LQ carbon ion dose response curve fits. Photon input values: $\alpha_\gamma = 0.25\,\mathrm{Gy}^{-1}$, $\beta_\gamma = 0.05\,\mathrm{Gy}^{-2}$, $D_t = 11\,\mathrm{Gy}$.

11 Gy for the lowest LET, which is the photon input value for D_t in this case. With increasing LET the dose at which the fit gets worse decreases, i.e. the LQ model describes the data decreasingly well in the same dose range. At LET values higher than $80\,\mathrm{keV}/\mu\mathrm{m}$ no increase of $\Delta\chi^2$ is observable as the dose response curves are almost linear in the whole fit range. To be close to experimental conditions when fitting the measured dose response curves we now fit the dose response within the cell survival level between 100 % and 1 % by an LQ formula. The obtained values α_{I} and β_{I} are then fixed in order to fit D_t on the same survival curve by an LQL formula up to a maximal dose of 20 Gy.

In Fig. 2 the parameters α_{I}, β_{I} and D_t, obtained by the procedure mentioned above, and the LQL parameters of the low dose algorithm are plotted. In the case of $\beta = 0$ values for D_t are mathematically undefined, depicted by the dotted line for the low dose values. By construction the D_t behavior is different to the one of the full simulation algorithm: here D_t decreases with increasing LET. The D_t bump in mid-LET region is an understood artefact, originating from fitting the dose response values by an LQ model where they actually are not purely linear-quadratic.

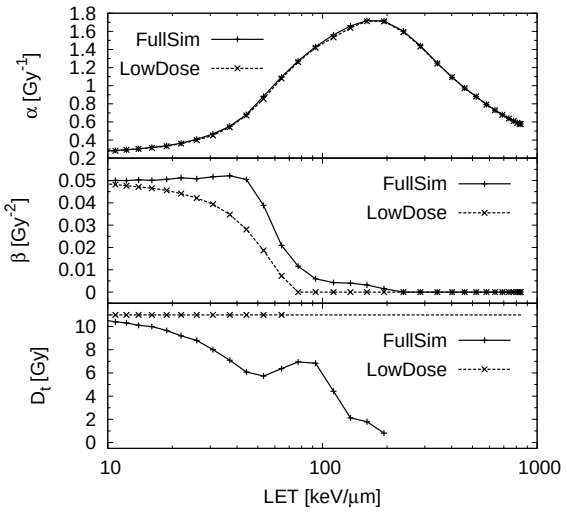

Figure 2: Obtained LQL parameters for cell response after carbon ion irradiation. Input parameters as in Fig. 1.

The presented two-step fit procedure allows us to describe fully simulated LEM IV dose response curves by LQL parameters. Future tasks will be to investigate their dependence on photon input parameters and to implement the tabulated values for different ion species in treatment planning software.

References

[1] M. Scholz et al., Radiat. Environ. Biophys., 36 (1997) 59.

[2] T. Elsässer et al., Int. J. Radiat. Oncol. Biol. Phys., 78 (2010) 1177.

[3] U. Scholz et al., GSI Scientific Report, 2010.

* Work is part of HGS-HIRe.

† u.scholz@gsi.de

Possible approaches toward experimental validation of LEM mechanistic bases*

F. Tommasino[1], T. Friedrich[1], U. Scholz[1], M. Durante[1, 2] and M. Scholz[1]

[1]GSI, Darmstadt, Germany; [2]Institut für Festkörperphysik, Technische Universität, Darmstadt, Germany

The main aim of the Local Effect Model is to predict the Relative Biological Effectiveness (RBE) after ion irradiation starting from the corresponding experimental photon data and an amorphous track structure model [1]. According to the model, the increased effectiveness of ions can be partially traced back to the increased yield of DNA Double Strand Breaks (DSB), resulting from the induction of Single Strand Breaks (SSB) closer than a threshold distance [2], then the local density of DSB resulting from the spatial distribution of the damage inside the nucleus also determines the biological effect[3]. This mechanism of DSB production becomes relevant when the local dose deposited in the cell nucleus exceeds few hundreds grays, and plays consequently a primary role in the yield of DSB during particle irradiation, when the local deposition of dose in sub-volumes of cell nucleus can reach and overcome that values. Although at the moment a fixed value of 25bp is assigned to this threshold genomic distance, not full agreement has been found up to now in the literature, where values in the range between 3 and 60bp are actually under discussion.

Due to the importance of the parameter in DSB yield calculations, a direct comparison between the predictions of the LEM in terms of increased induction of DSB and experimental data is actually under development. The γH2AX flow cytometric assay [4] will be employed to experimentally quantify the yield of DSB. The method is based on the measurement of an integral fluorescent signal coming from the cell nucleus which is expected to be proportional to the number of induced DSB. A broad range of ion species and beam energies will be investigated, aiming at the analysis of a broad range of ionization densities. This will allow the study of radiation qualities which are expected to determine significant variations in the amount of induced DSB. By comparing different ions at the same LET, useful informations concerning the impact of the track structure will be obtained. The effect of changes in the value of the SSB cluster threshold distance will be examined, and this will allow to appreciate the relevance of this parameter in a direct comparison with the flow cytometric data.

Moreover, the recent version of the LEM is based on a detailed consideration of the spatial distribution of the initial damage (DSB) [3]. The structure of the chromatin organization in the cell nucleus is taken into account, assuming that 'giant loops' of DNA [5], comprising about 2Mbp of DNA, represent the critical higher order structure of the DNA. This allows the definition of two different classes of damage, namely 'isolated' (iDSB) and 'clustered' (cDSB) double strand breaks, when only one and two or more than two DSB are induced in the loop structure respectively. The cell response to these two types of induced damage is expected to be different, since the repair is hypothesized to be easier to perform for the iDSBs compared to the cDSBs. Consequently, a higher probability of cell killing can be associated to the clustered component of damage. Affecting the total number of induced DSB, the SSB threshold distance is naturally expected to play a role in the resulting proportion of induced iDSB and cDSB. In Fig. 1, results for the induction of iDSB and cDSB after carbon ion irradiation (LET =150keV/ μm) are reported. Obviously, compared to the standard 25bp, a larger value of the threshold distance corresponds to a higher number of induced DSB, and consequently to an induction of less iDSB and more cDSB in a given nuclear volume, and the opposite behaviour is observed for a smaller value of the threshold. Considering the crucial role played by the clustered component of damage in the final cell survival calculations, it becomes clear that a more accurate description of the SSB threshold distance will help to improve the predictive power of the model.

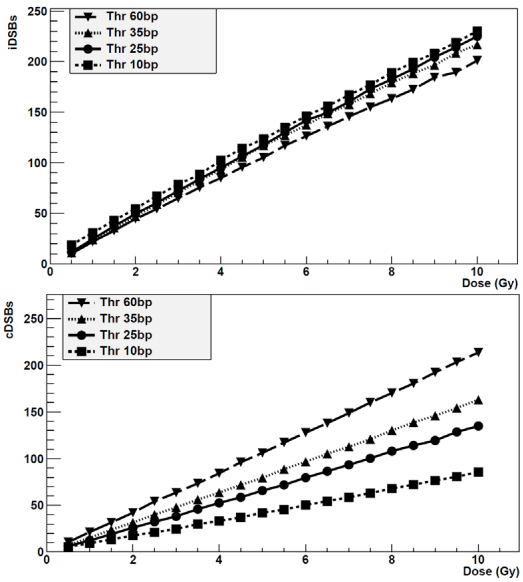

Figure 1: simulated induction of iDSB and cDSB after carbon ion irradiation (LET=150kev/μm) for different values of the SSB cluster threshold

References

[1] M. Scholz et al., Radiat. Envir. Biophys. 36 (1997) 59.

[2] Elsässer et al., Int. J. Radiat. Oncol. Biol. Phys., 167 (2008) 319.

[3] Friedrich et al., Int. J. Radiat. Biol., 88 (2012) 103.

[4] MacPhail et al., Int. J. Radiat. Biol., 79 (2003) 351.

[5] Yokota et al., J. Cell Biol., 130 (1995) 1239.

* This work is supported by DFG-funded Graduiertenkolleg (GRK 1657) and is part of HGS-HIRe enthalten

Nonlinear Dose Optimization Using the Inverse BFGS-Method

M. Horcicka[1], *C. Meyer*[2], *M. Durante*[1], *and M. Krämer*[1]

[1]GSI Helmholtzzentrum für Schwerionenforschung GmbH, Biophysics; [2]TU Dortmund, Dep. for Mathematics

Introduction

In the GSI therapy pilot project from 1997 until 2008 about 450 cancer patients were successfully treated with carbon ions. Due to the promising healing rates the clinical radiotherapy facility HIT was opened in 2009.

For the treatment planning (TP) the software TRiP [1] is used. A crucial part of the TP is the dose optimization with the goal to achieve a homogeneous target dose distribution as close as possible to the prescribed dose distribution by an appropriate sparing of critical structures, e.g. the brainstem. These requirements can be mathematically expressed by the minimization of a functional, where the free optimiziation parameters are the particle numbers in the individual raster spots.

Mathematics of the Optimization

The objective function is defined as follows [2]:

$$X^2(\vec{N}) = \sum_{i \in Target} \frac{(D^i_{pre} - D^i_{bio}(\vec{N}))^2}{\Delta D^2_{pre}}$$

$$+ \sum_{i \in OAR} \frac{(D^i_{max} - D^i_{bio}(\vec{N}))^2}{\Delta D^2_{max}} \cdot \Theta(D^i_{bio}(\vec{N}) - D^i_{max})$$

$\vec{N}$: vector that contains the particle numbers

D_{pre} : prescribed dose within the target

D_{max} : maximum dose within OAR (Organ-At-Risk)

D^i_{bio} : RBE-weighted dose at voxel i

Θ : Heaviside function

The nonlinearity of the RBE-weighted dose D^i_{bio} leads to the nonlinearity of X^2 and the minimization task can only be solved with numerical methods. We tested the inverse BFGS-method. As a startmatrix we use the identity matrix and the stepsize is controlled with the Armijo-rule [3]. A so called angle test is implemented to force a stronger decrease of X^2. The full algorithm is described in [2].

The number of rasterspots and voxels are several ten thousands, which leads to long computation times [4].

Results and Discussion

The results of the inv. BFGS are illustrated in Fig. 1,2 and compared to the Fletcher-Reeves variant of the method of conjugated gradients (KGV). The KGV shows the best results in comparison to other algorithms, which we published in [5]. The data were taken from the plan #135.

The convergence results show, that the BFGS-method works as efficient as the KGV concerning the iteration steps (Fig. 1). However, due to the matrix update in the BFGS iteration procedure this method requires by a factor of approx. 1.5 more computation time than the KGV (Fig. 2).

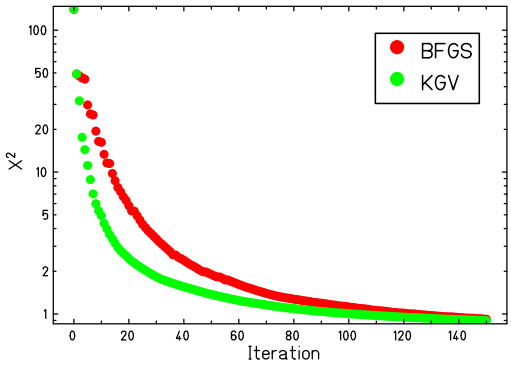

Figure 1: Minimization of the X^2-function in terms of iterations.

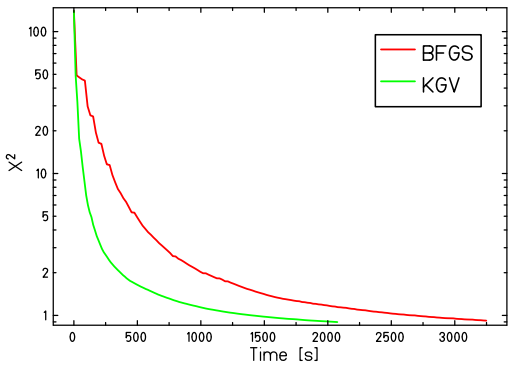

Figure 2: Minimization of the X^2-function in terms of computation time.

Summary

The results show, that currently the KGV is the best algorithm for the optimization step in our TP-procedure. With this method complete patient plans can be optimized in an acceptable computation time. Furthermore, this method is robust and requires only modest amounts of RAM.

References

[1] M. Krämer et al, Eur. Phys. J. D., 60 (2010) 195-202.

[2] M. Horcicka, Master-Thesis, GSI, TUD (2011).

[3] W. Alt, *Nichtlineare Optimierung*, Vieweg, 2002.

[4] A. Gemmel et al, Phys. Med. Biol., 53/23 (2008) 6991.

[5] M. Horcicka et al, GSI Scientific Report 2009, 488.

Impact of enhancements of the Local Effect Model (LEM) on the prediction of RBE-weighted doses for chordoma treatments*

R. Grün[1,2,3], T. Friedrich[1], O. Steinsträter[1], M. Krämer[1], M. Durante[1,4], and M. Scholz[1]

[1]GSI, Darmstadt, Germany; [2]Institut für Medizinische Physik und Strahlenschutz,TH-Mittelhessen, Gießen, Germany; [3]Philipps-Universität Marburg, Germany; [4]Institut für Festkörperphysik, Technische Universität Darmstadt, Germany

Introduction

Dose-response curves for the tumor control of skull base chordoma have been published by Schulz-Ertner et al. [1] based on clinical data with photons, protons and carbon ions. For the analysis, RBE-weighted doses for carbon ion irradiation have been estimated using the Local Effect Model (LEM I) [2]. Therefore the median isoeffective dose related to the clinical results is based on RBE predictions of the LEM I and the question arises in how far the dose-response relationship is changing when the RBE predictions of the improved version LEM IV [3] and more recent α and β estimates are considered.

Methods

For the analysis two different so called RBE tables based on LEM IV were used in exchange with the RBE-table (LEM I) used in the pilot project. For the simulation of the irradiation process the software package TRiP98 was used [4]. The same physical dose profiles leading to isoeffective doses of 75 Gy(IsoE) and 96.25 Gy(IsoE) based on RBE predictions of the LEM I were used to predict the isoeffective dose when using instead the RBE-table based on RBE predictions of the LEM IV. The considered target volumes are related to the PTV2 as described in Schultz-Ertner et al. represented by a sphere with the corresponding diameter.
The first RBE-table AB2 IV is based on experimental data with the rat spinal cord and therefore represents the endpoint of normal tissue complication [5]. The photon input data for the second RBE-table AB2.45 IV is derived from clinical local control data for chordoma and therefore represents the endpoint tumor control [6]. The dose-response relationship was determined with the logistic dose-response model [5]. The two free parameters were adjusted using the maximum likelihood procedure for a binomial distribution.

Results

Recalculating the TCP-curve with different mathematical software and procedures was done to evaluate the method for further use with other experimental data from clinical trials. In Fig. 1 the TCP curve is adjusted with respect to the generated response data points due to the RBE predicted by the RBE-table AB2.45 IV. The original data points related to RBE predictions with the LEM I were replaced by the new ones. The change in the TCP curve illustrates the influence of the LEM IV on the dose-response relationship for skull base chordoma considering the smallest (13.6 ml), median (78.3 ml) or largest (578.9 ml) planning target volume (PTV2) according to Schulz-Ertner et al. [1]. Median dose values are only slightly shifted between LEM I and LEM IV predictions, as indicated by the arrows. For comparison also the corresponding response data points representing the smallest and largest PTV2 and the resulting TCP curves are given.

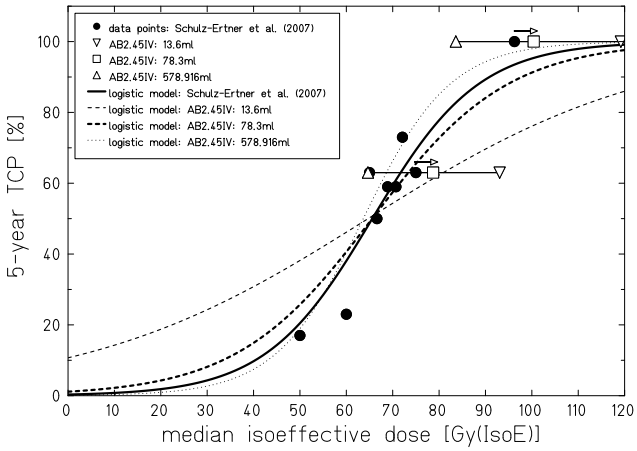

Figure 1: Adjustment of the dose-response curve for the tumor control of skull base chordoma according to Schulz-Ertner et al. [1] considering the response data points resulting from calculations with the RBE-table AB2.45 IV in comparison to the original ones.

Conclusion

On balance the RBE predictions of the LEM IV are in good agreement with the dose-response relationship assumed so far. Hence it can be concluded that the LEM IV does represent the clinical results in the same way the LEM I does.

References

[1] D. Schulz-Ertner et al.,Int J Radiat Onc Biol Phys (2007) 68.

[2] M. Scholz et al., Radiat Environ Biophys 36 (1997) 59.

[3] T. Elsässer et al., Int J Radiat Onc Biol Phys (2010) 78.

[4] M. Krämer and M. Scholz, Phys Med Biol, 11(2000) 45.

[5] C.P. Karger et al., Int J Radiat Onc Biol Phys (2006) 66.

[6] F.C. Henderson et al., Neurosurgery (2009) 64.

* Work is part of HGS-HIRe

Hypoxia driven treatment planning with TRiP98*

E. Scifoni[†1], *M. Krämer*[1], *G. Fattori*[2], *and M. Durante*[1]
[1]GSI, Darmstadt, Germany; [2]Politecnico di Milano, Milan, Italy

After the success in leading the GSI pilot project for ion beam therapy, the TRiP98 code [1], first complete treatment planning system for ion beams, is further developing as a research prototype for all the growing centres now dealing with particle therapy. One of the main direction where ion beam therapy is promising new outcomes is the battle against hypoxic tumors [2], and then naturally this has become also a major direction of TRiP98 development.

The possibility to introduce a selective treatment of differently oxygenated areas of a tumor, painting the dose accordingly, has been exploited: after developing a parametric description of the oxygen enhancement ratio (OER) as a function of LET and pO_2 [3], this has been introduced into the code allowing not only to perform forward planning but also to inverse plan, getting to an effective OER driven optimization. In figure 1 the scheme of the code implementation is given, including the ongoing PET data conversion module *ptx-tool* (collaboration with PoliMi), which is intended to handle the input from hypoxia imaging into the TPS. In figure 2 an exemplary tumor tissue with differently oxygenated regions is considered and the performance of the code in compensating the dose is shown.

The targeted irradiation of hypoxic regions is going to be tuned in different ways in order to maximize the high LET beam components, also taking advantage on the possibility to use different ions, e.g. in the HIT facility, a feature that has been already implemented in the new multi-ion version of TRiP98 [4]. The relative advantage of using oxygen, e.g. as compared to carbon, with the constraint to keep the same survival in the entrance channel, is shown in fig.3.

The code has been also experimentally verified with dedicated extended volume irradiation experiments during the 3 carbon beamtimes held in 2011. Details on these results, as well as on the implementation of the code are given in a forthcoming publication [5].

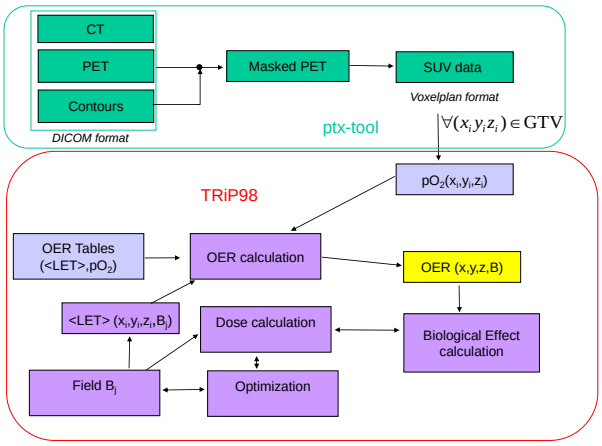

Figure 1: Scheme of the implementation of hypoxia driven treatment planning in TRiP98.

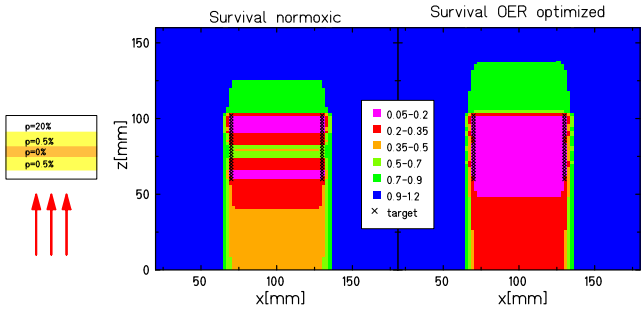

Figure 2: TRiP98 computed survival profiles, without (left) and with (right) taking into account the non uniform oxygen concentration of the target tissue into the optimization.

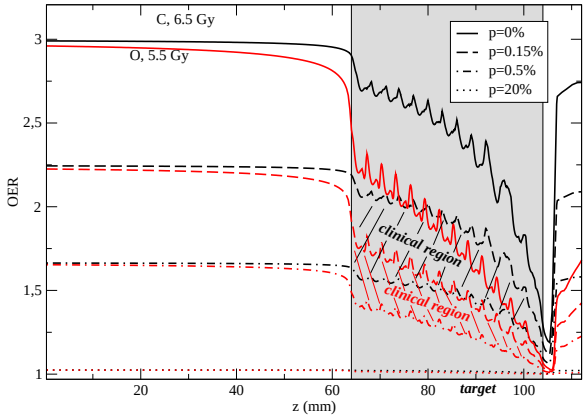

Figure 3: Comparison of the computed OER along a target tissue, for carbon (black curves) and oxygen (red curves) at different pO_2 levels. Hatched areas represent the clinical interesting regions for hypoxia ($0.15 < pO_2 < 0.5\%$).

References

[1] M. Kramer and M. Durante, Eur. Phys. J. D. 60 (2010) 195.

[2] S. M. Bentzen and V. Gregoire, Semin Radiat Oncol 21, 101 (2011).

[3] E. Scifoni, M. Krämer and M.Durante, GSI Rep.2010, p.489

[4] M. Krämer, E. Scifoni and M.Durante, "Multi modal Treatment Planning with TRiP98" this Report.

[5] E. Scifoni, M. Krämer, W. Tinganelli, W.Kraft-Weyrather, and M. Durante, in prep.for Phys. Med. Biol.

* Work supported by EU, ULICE contract No.228436.
† e.scifoni@gsi.de

Sensitivity analysis of input parameters in the Local Effect Model*

T. Friedrich[1], *R. Grün*[1], *U. Scholz*[1,2], *T. Elsässer*[1], *M. Durante*[1,2], *and M. Scholz*[1]
[1]GSI, Darmstadt, Germany; [2]Institut für Festkörperphysik, TU Darmstadt, Darmstadt, Germany

Introduction

One rationale for using carbon ions in radiation therapy is the enhanced effectiveness of carbon ions in comparison to photon radiation, parameterized by the relative biological effectiveness (RBE). This quantity depends on both physical (particle species, energy, dose) and biological parameters (radiosensitivity of the cells or tissue type). The Local Effect Model (LEM) which has been developed at GSI is able to predict the RBE. In its recent version LEM IV the RBE is determined by a comparison of the spatial distribution of induced double strand breaks after photon and ion irradiation [1, 2]. With the LEM a biological oriented treatment planning is possible, which optimally respects the RBE for each voxel of a treatment plan. For the clinical usage modelled RBE values must reveal sufficient accuracy, which in turn means that the model parameters of the LEM have to be determined correctly. The sensitivity analysis is concerned with all relevant parameters and their influence on the modelled RBE values.

Methods

The LEM has two different classes of model parameters: Some parameters are fixed while others represent input data related to the cell or tissue type under investigation. The latter specify the radioresistance or the geometric extensions of the cell nuclei. In the current implementation we use the linear quadratic - linear (LQL) model, where the radiobiological effect is given by a linear quadratic dose response with coefficients α and β for low doses and enters into a constant slope beyond a threshold dose D_t. The general strategy for a sensitivity analysis is to monitor the change in RBE when changing one of the input parameters. We chose a $\pm$ 25% change of each of the input parameters and recorded the changes in the RBE in the limit of low doses (RBE_α) and for 10 % survival level (RBE_{10}). We carried out this analysis for different particle species for a typical situation of in-vitro cell lines irradiated under track segment conditions, where two cases of the dose response curves have been considered, distinguished by the photon parameter ratio $\alpha/\beta = 2$ Gy and $\alpha/\beta = 10$ Gy.

Results

Figure 1 shows exemplarily the changes of the RBE_α vs LET relationships for carbon ions under parametric variation of the photon parameters α and β for both $\alpha/\beta = 2$ Gy and 10 Gy. An increase of α (β) implies a decrease (increase) of the corresponding RBE. The following trends were found: (i) The relative change of the RBE never exceeds the relative change of the input parameter. (ii) For higher doses and higher effects, RBE values become more robust against parameter changes. (iii) Similarly, changes in RBE are largest for small α/β. (iv) The relative change in RBE is comparable for different ion species.

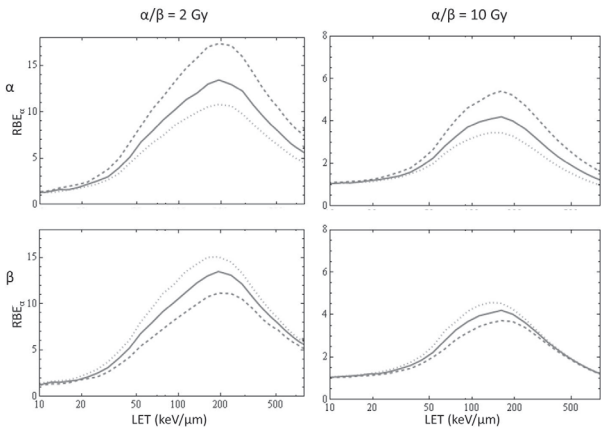

Figure 1: RBE_α vs LET for cells irradiated with carbon ions with $\alpha = 0.1\,\mathrm{Gy}^{-1}$ ($0.5\,\mathrm{Gy}^{-1}$), $\beta = 0.05\,\mathrm{Gy}^{-2}$, and $D_t = 8$ Gy (14 Gy) for $\alpha/\beta = 2\,\mathrm{Gy}$ (10 Gy) as solid lines along with the corresponding curves after lowering or rising α (upper row) or β (lower row) about 25% of its initial value (dashed and dotted lines, respectively).

Conclusions and further work

The sensitivity analysis can be used to assess uncertainties of calculated RBE values. The results are helpful for the interpretation of, e.g., in-vitro cell survival experiments. All findings can be understood by the radiobiological meaning of the parameters within the LEM. An extension of the work to a more treatment like situation of tissue within a spread out Bragg peak was also carried out following the same strategy, which allows to assess calculated RBE values as modelled by the LEM with respect to RBE values obtained from clinical studies.

References

[1] T. Elsässer, Int. J. Radiat. Onc. Biol. Phys. 78 (2010) 1177.

[2] T. Friedrich et al., Int. J. Radiat. Biol. 88, (2012) 103.

* Work supported by Siemens Healthcare. Work is part of HGS-HIRe.

Chromosomal aberrations observed up to three years after *in vivo* irradiation with photons and carbon ions*

C. Hartel[1], M. Durante[1,2] P. Hessel[1], S. Ritter[1], and A. Nikoghosyan[3].

[1]GSI, Darmstadt, Germany; [2]Condensed Matter Physics, TU Darmstadt, Darmstadt, Germany; [3]Radiology Clinics, University of Heidelberg, Heidelberg, Germany

One of the major concerns in modern radiotherapy is the risk of possible late effects like secondary cancers. This point is becoming more relevant the more successful a therapy is and the longer the patients live thereafter. To assess the relative risk for late effects after carbon ion radiotherapy, compared to conventional treatment, a study investigating chromosomal aberrations in radiotherapy patients was performed. Chromosomal aberrations in peripheral blood lymphocytes are a useful biomarker for radiation exposure, and can predict the relative risk for late effects. Lymphocytes in the peripheral blood are constantly replaced by new ones produced in the bone marrow, thus originally irradiated peripheral lymphocytes will die out over time. However, if bone marrow cells were irradiated, they could pass their radiation damage to their daughter cells which differentiate into lymphocytes. Thus, not only the aberration yield at the end of therapy is of interest, but also its development over time.

For the present study, blood samples were obtained from prostate cancer patients treated with carbon ion irradiation combined with conventional IMRT (called C+IMRT, n=13) or IMRT alone (called IMRT, n=5). For more details, see [1,2]. The analysis was performed using the mFISH technique, which allows assigning different artificial colours to the 22 human chromosome pairs plus the sex chromosomes (see fig. 1A), and thus can be used to detect exchanges of DNA between different chromosomes (see figure 1B). From all patients several blood samples were obtained, including one at the end and one 1 year after therapy. From selected patients (all from C+IMRT group) an additional sample 2-3 years after treatment was taken (n=5). For each time point at least 1200 cells were analyzed.

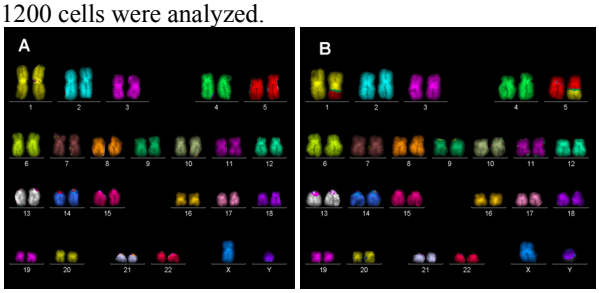

Figure 1: Examples of karyotypes found in a patient 2.5 years after radiotherapy. A: normal human male karyotype. B: Human karyotype with an aberration in chromosomes Nr.1 and Nr 5.

The results at the end of therapy showed no higher yield of chromosome aberrations after C+IMRT, compared to IMRT, indicating that there is no higher risk for late effects after carbon ion therapy [3].

* Work supported by Federal Ministry of Education and Research (BMBF, Bonn, Germany) under contract number 02S8497.

In the year after therapy, a significant decline in aberration frequency of about 25% was observed. No further significant decrease in the aberration frequency after 2-3 years compared to 1 year after treatment was found.

mFISH allows to identify many different types of chromosomal aberrations. For the present study, it is useful to distinguish transmissible and non-transmissible aberrations, i.e. aberrations which can or cannot be passed to the daughter-cells. Regarding simple chromosomal interchanges, these aberrations are translocations (transmissible, example is shown in Fig 1B) and dicentric chromosomes (non-transmissible, not shown). These aberration types are expected to be induced with similar frequencies [4]. This was confirmed in the present study, the ratio of dicentrics to translocations was about 1 directly after therapy. However, in the year after therapy, a significant change in the ratio to about 0.5 was observed, indicating that some non-transmissible aberrations had "died-out", while the number of translocations stayed constant. No further significant difference was found between the samples taken 1 and 2-3 years after therapy. These results show that bone marrow was exposed during the radiotherapy (which is in line with the treatment plans) and that the bone marrow cells were damaged by the treatment and passed this damage to their progenies.

In summary, the results at the end of therapy showed, that no higher risk for late effects after carbon therapy compared to conventional therapy must be feared. The results of the three-year follow-up period showed that the aberration yield decreases significantly with time, and that the bone marrow exposure during radiotherapy leads to a change in the aberration pattern, underlining the biological relevance of treating bone marrow as an "organ at risk" during treatment planning.

References

[1] C. Hartel et al. (2008) *GSI scientific report 2007*, p.361

[2] C. Hartel (2010) "Qualitative and quantitative investigation of the cytogenetic effects of densely ionizing radiation in vitro and in vivo". Dissertation, TU Darmstadt; *http://tuprints.ulb.tu-darmstadt.de/2179/*

[3] C. Hartel et al. (2010) "Chromosomal aberrations in peripheral blood lymphocytes of prostate cancer patients treated with IMRT and carbon ions" *Radiother Oncol* 95, p.73-78

[4] J.N. Lucas et al. (1996). "Theoretical predictions on the equality of radiation-produced dicentrics and translocations detected by chromosome painting." *Int J Radiat Biol*, 69(2),p.145-153.

Calculation of the Effect of Mixed Radiation Based on Linear-Quadratic-Linear Dose Response Curves*§

O. Steinsträter[1], U. Scholz[1], M. Durante[1], and M. Scholz[1]

[1]GSI, Darmstadt, Germany

Introduction

The treatment planning system TRiP98 [1] developed at GSI for heavy ion radiotherapy predicts the biological effect of an ion beam based on an externally calculated set of dose response curves for all contributing ion types (the primary ion, e.g. carbon, as well as its fragments) at all relevant energies. The response curves are calculated according to the Local Effect Model (LEM) [2], also developed at GSI. They are provided in the framework of the Linear-Quadratic (LQ) model (characterized by the parameters α and β) extended by a threshold parameter D_t marking the high-dose transition from linear-quadratic to purely linear dose response (LQL model). In addition to a Monte Carlo based technique, a much faster method based on the Theory of Dual Radiation action (TDRA) [3] is used in TRiP98 to derive mixed beam α and β parameters as dose-mean values of the monoenergetic response parameters. The D_t parameter is difficult to include in this theory, but as the previous versions of LEM do not provide an individual D_t for each ion type, the constant D_t could be added after the calculation of the mixed beam α and β values as the dose where the slope of the dose response curve of the mixed beam becomes constant. The most recent version of the LEM now provides individually calculated α, β, and D_t values for each ion (characterised by type and energy) and an extension of the internal structure of the TDRA based model for mixed beams is therefore needed.

Methods

The TDRA relates the linear part (α) of the LQ curve to the effects (mean numbers of lethal events) $\varepsilon_\alpha^{(i)}$ of individual ions i and the quadratic part (β) to the interaction of events originated from different ions i, j: $\varepsilon_\beta^{(i,j)}$. This leads to $\varepsilon(D)=\sum_i \varepsilon_\alpha^{(i)}(D)+\sum_{i,j}\varepsilon_\beta^{(i,j)}(D)$ for the total effect ($D=\sum D_i$ total dose, D_i individual dose contributions of ions i). As D_t describes the transition from quadratic to linear response, in the theory proposed here, the linear part of the TDRA model is kept unchanged $(\mu_i = D_i / D)$: $\varepsilon_\alpha^{(i)}(D)=\alpha_i\mu_i D$. The D_t transition is added to the quadratic part:

$$\varepsilon_\beta^{(i,j)}(D)=\beta_i^{1/2}\beta_j^{1/2}\mu_i\mu_j D^2$$

for $D \le D_t^{(i,j)}$, and otherwise

$$\varepsilon_\beta^{(i,j)}(D)=2\beta_i^{1/2}\beta_j^{1/2}\mu_i\mu_j D_t^{(i,j)}\left(D-D_t^{(i,j)}\right)+\beta_i^{1/2}\beta_j^{1/2}\mu_i\mu_j\left(D_t^{(i,j)}\right)^2.$$

Here, the threshold dose for the interaction of two ions i and j is modelled as $D_t^{(i,j)} = (D_t^{(i)})^{1/2}(D_t^{(j)})^{1/2}$.

Results

If no explicit D_t is used ($D_t = \infty$) the proposed model is identical to the original TDRA model. In the case of a constant D_t the proposed model is identical to the D_t extension currently used in TRiP98.

In Figure 1 a mixture of two beams according to three different models is shown. In addition to the models already discussed, the mixed beam model proposed by Lam [4] is shown which is similar to the beam mixing realised in the Monte Carlo branch of TRiP98.

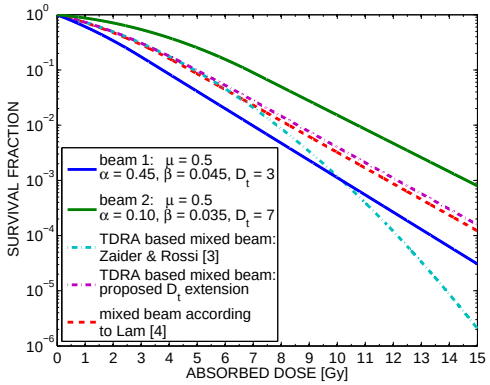

Figure 1: Mixture of two beams (solid lines) according to different models (dashed lines).

Discussion and Conclusion

As shown in the Fig., for $D \le D_t^{(1)} < D_t^{(2)}$, the TDRA based model and our extension are identical. For $D > D_t^{(1)}$ results based on our model are typically only slightly different from results based on the model proposed by Lam [4]. We conclude that the proposed model is therefore a reliable extension of the TDRA mixed beam model.

References

[1] M. Krämer et al., Phys. Med. Biol., 45 (2000) 3299.
[2] T. Elsässer et al., Int. J. Radiation Oncology Biol. Phys. 78 (2010) 1177.
[3] M. Zaider & H. H. Rossi, Radiat. Res., 83 (1980) 732.
[4] G. K. Y. Lam, Radiat. Res., 110 (1987) 232.

* Work supported by Siemens Healthcare.
§ Work is part of HGS-HIRe.

Risk of second cancers in paediatric patients after radiotherapy

M.Durante[1,2] and W. Newhauser[3]

[1]GSI, Darmstadt, Germany; [2]Darmstadt University of Technology, Germany; [3]LSU, Baton Rouge, LO, USA.

Recent advances in radiotherapy have enabled the use of different types of radiotherapy, such as proton and heavy ion therapy, as well as refinements to the treatment of tumours with standard radiotherapy sources (X-rays). However, the risk of second malignant neoplasms (SMN) arising in long-term survivors continues to be a problem. The long-term risk from treatments such as particle therapy, have not yet been determined and are unlikely to become apparent for many years hence. Therefore, there is a need to try and develop risk assessments based on our current knowledge of radiation-induced carcinogenesis.

Modeling SMN

Contemporary SMN risk models typically take into account a variety of host related factors that influence predicted risk, including age at exposure, attained age, and sex. Typically, risks are larger for females, decrease with age at exposure, and continue to increase with attained age decades after exposure. To accurately predict radiogenic risk using the models described above, one must calculate the radiation doses in the tumor as well as in healthy tissues and organs throughout the entire body. Fortunately, this is now entirely possible, thanks to strident progress in radiation transport models, nuclear interaction data and models, and high-performance computing. This means that, in principle, we can now calculate the dose to the patient and transform it in a cancer-risk map in the body (Fig. 1). In fact, our understanding of the physics of particle therapy is advanced, and for the purposes of SMN risk assessment, nearly complete. Most of the uncertainty remains in the biology. The risk estimates in Fig. 1 are therefore only qualitative, but the calculation with the color-scale clearly shows how the dose is a poor predictor of risk, and large organ-specific differences can be found between incidence and mortality risks [1].

Particles vs. X-ray therapy

Studies comparing SMN risks associated with contemporary proton and photon therapies have consistently found that proton therapy confers smaller overall predicted risk of SMN for children with medulloblastoma and adults with prostate cancer and liver cancer. The models found a negligible difference between lifetime risk of SMN incidence from passive versus scanned proton craniospinal irradiation: the risk was mostly attributable to therapeutic radiation, not leakage neutrons. These studies revealed that the largest reductions in predicted risk were obtained by replacing IMRT with proton therapy, even after taking into account the stray and leakage neutrons associated with proton therapy.

Future plans

The SMN model described in Figure 1 will be extended to heavy ions, and will include different biological models: non-targeted effects, genetic predisposition, fractionation effect, age-dependence for different organs as a function of the dose to the organ. The final goal will be to produce a reliable tool for the radiotherapist providing comparison of treatment plans for different modalities not only in terms of dose to the target volume and organs at risk, but also as risk of SMN.

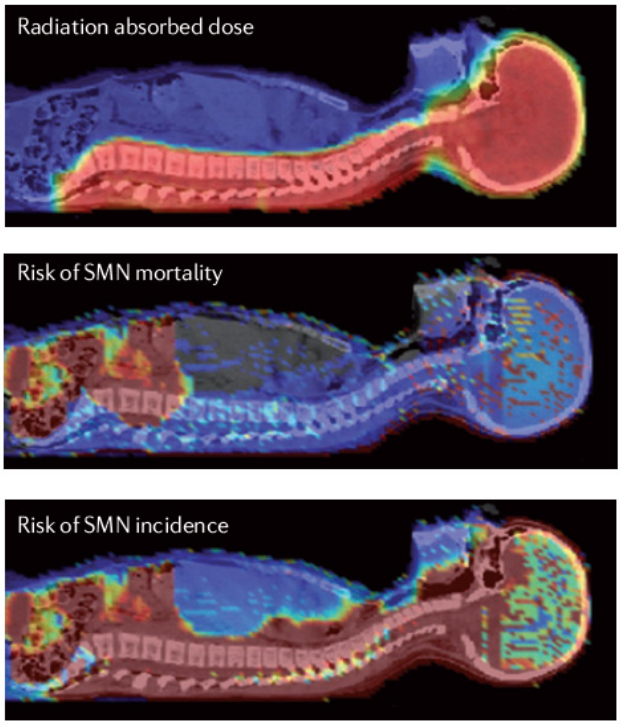

Figure 1 This 9-year old girl received craniospinal irradiation for medulloblastoma using passively scattered proton beams at M.D. Anderson Cancer Center. The color scale illustrates the difference for absorbed dose, incidence and mortality cancer risk in different organs. Risk of SMN incidence and mortality varies strongly with radiation dose, but it also varies strongly between organs, with the patient's age at exposure and attained age, sex, genetic profile, and other factors [1].

References

[1] W. Newhauser and M. Durante, "Assessing the risk of second malignancies after modern radiotherapy" *Nature Rev. Cancer* **11** (2011) 438-448.

GSI-NIRS International Open Laboratory: measurements of oxygen effect*

M.Durante[1,2],E. Scifoni[1], W. Tinganelli[1,3] and Y. Furusawa[3]

[1]GSI, Darmstadt, Germany; [2]Darmstadt University of Technology, Germany; [3]NIRS, Chiba, Japan.

The GSI-NIRS International Open Laboratory (IOL) "Radiation Quality Research Unit" had a delayed kick-off caused by the earthquake in Japan. The kick-off meeting was held in Darmstadt on 5.9.2011. An inter-IOL meeting was held in Chiba on 21.1.11, where the links among the 4 different IOL were discussed (see http://www.gsi.de/forschung/bio/nirs_iol.html). During these meeting we outlined the detailed program of the Radiation Quality Research Unit and applied for beam time at HIMAC.

IOL Goal

This Research Unit will concentrate on clinical radiobiology, and specifically on the oxygen effect (Figure 1). The final goal will be to allow the fulfillment of an adaptive treatment planning system where tumor oxygen concentration is taken into account, through filling a long-standing experimental data gap, and a molecular understanding of the interplay between hypoxia and radiation therapy in tumor metastatization.

Detailed plans

Year 1: measurements of the OER-LET relationship at different oxygen concentration (Figure 2), between anoxic and oxic conditions; in vivo tests on tumor metastatic potential after irradiation.

Year 2: further measurements of the OER-LET relationship at different oxygen concentration, with different ions, between anoxic and oxic conditions; role of hypoxia in tumor metastatic potential after irradiation.

Year 3: incorporation of the new OER-LET data at different O_2 concentration into the treatment planning system and further validation experimental tests; molecular analysis of the mechanism of metastasis formation after X-rays or C-ions.

Budget

Budget will be used to pay the salary of a postdoc from GSI working full time at NIRS and to support 1-2 visits from other GSI scientists per year.

Collaborations

The unit can have several links with all the other 3 units: molecular analysis (particularly the adhesion molecule E-catherins) can be performed in collaboration with Particle Therapy Molecular Target Unit; in vivo carcinogenesis/metastasis with the Space Radiation Research Unit; modeling the oxygen effect in collaboration with the Radiation Response Model Unit.

* Supported by the NIRS IOL grant to GSI

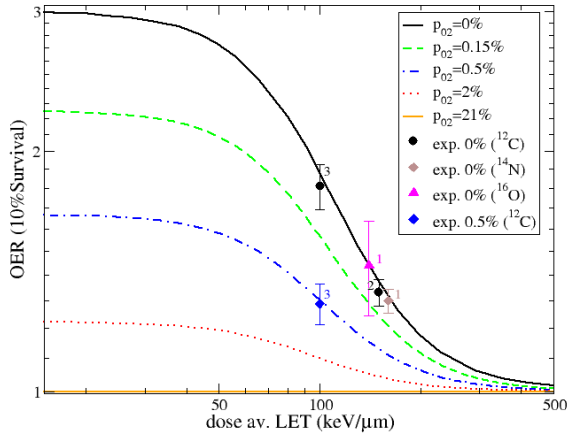

Figure 1: Model of the dependence of OER from LET for different oxygen partial pressures under implementation in TRiP98 [2] (lines) and independent experiments performed at GSI (points). The IOL will be used to measure experimental points, clearly at the moment lacking, to test the model and eventually modify it.

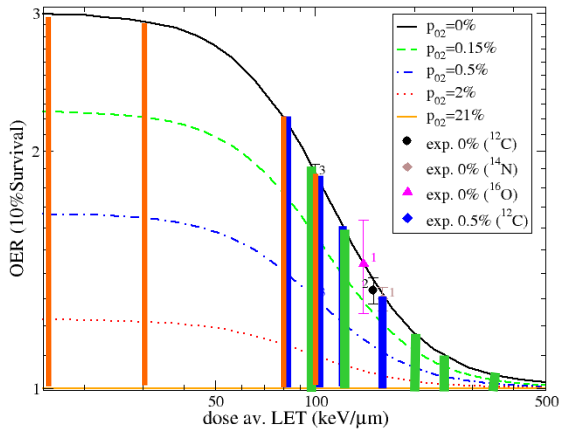

Figure 2: The bars overlapped to the plot in Figure 1 represent the LET values that will be measured at HIMAC within this IOL project. Different ions will be used: orange, ^{12}C; blue, ^{20}Ne; green, ^{28}Si.

References

[1] M. Durante and Y. Furusawa, "Program of the new International Open Laboratory at NIRS" GSI Report 2010, p.492.

[2] E. Scifoni, M. Krämer and M. Durante, "Hypoxia driven treatment planning with TRiP98", this report

Attenuation of a therapeutical carbon beam in bone-like materials

A. Eichhorn[1,2], *C. La Tessa*[1], *M. Rovituso*[3], *and M. Durante*[1,2]

[1]TUD, Darmstadt, Germany; [2]GSI, Darmstadt, Germany; [3]University of Catania, Catania, Italy

The extension of heavy ion therapy to further types of cancer might require a detailed characterization of the interaction of the primary particles with specific biological materials. The majority of data available in literature is measured in water targets, since the latter is considered tissue equivalent representing up to 70% of the human body composition. However, when treating tumors seated, for example, in the skull or in the prostate, the amount of bones that the primary ions have to transverse can range from a few mm up to 5 cm.

In this study, the attenuation of a ^{12}C beam was investigated using different targets with varying thickness of Gammex RMI 450 as an equivalent of compact bones and Gammex RMI 456 as an equivalent of spongious bones. For the measurement two different beam energies (200 and 400 MeV u^{-1}) were used.

Target	Density $\left(\frac{g}{cm^3}\right)$	Atomic number $\left(\frac{g}{mol}\right)$
Spongious	1.133	10.895
Compact	1.819	14.017

Table 1: Material properties of the different types of bone used as target [1].

Experimental setup

A scheme of the experimental setup is shown in Fig. 1. It consists of three different detectors: two plastic scintillators (Start and Veto) and a barium fluoride detector (BaF); the targets were placed between the Start and the Veto detectors.

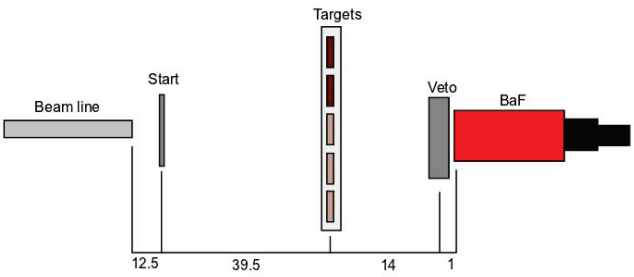

Figure 1: Scheme of the experimental setup.

Results

The survival fraction is the ratio between incident N_{in} and outgoing N_{out} primary ions from the target and is related to the total charge-changing cross section σ_{cc} according to the following formula:

$$\frac{N_{out}}{N_{in}} = \exp\left(-\frac{\sigma_{cc}\rho N_a d}{A}\right) \quad (1)$$

where N_a is the Avogadro number and ρ and d the density and thickness of the target, respectively. An estimate of σ_{cc} can be obtained by fitting the attenuation values with an exponential function of the form of Eq. 1. The results for 400 MeV u^{-1} carbon beam in all targets are shown in Fig. 2. The attenuation increases with increasing density of the target, therefore the value for spongious bones is a bit higher than for water. From the survival fraction curves, the total charge-changing cross sections in compact and spongious bones were calculated to be 730 $\pm$ 51 mb and 780 $\pm$ 50 mb, respectively. Both the survival fraction and the total charge-changing cross section were found to be energy independent in the range of selected energies. The energy loss measured in the targets was compared with values predicted by LISE and a very good agreement was found. In the future, the measured data will be implemented in the treatment planning system and a rescaling factor has to be found to mix the amount of compact and spongious bones as present in the human body.

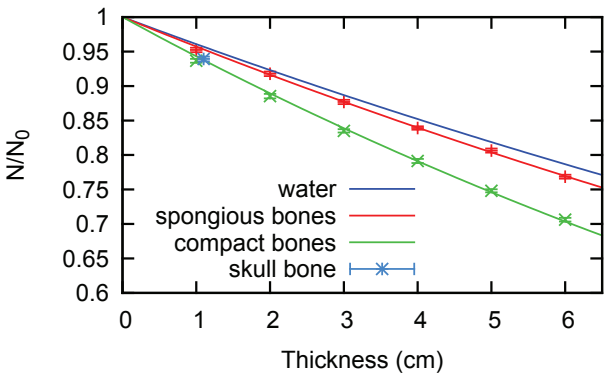

Figure 2: Survival fraction of a 400 MeV u^{-1} carbon beam in spongious and compact bones as function of the target thickness; a single value was also measured for a real skull bone 1.1 cm thick. The survival fraction in water [2] is added for comparison.

References

[1] O. J äkel, C. Jacob, D. Schardt, et. al, Med. Phys. **28** (2001), p. 701.

[2] T. Toshito, K. Kodama, L. Sihver et al., Phys. Rev. C **75** (2007), p. 054606.

Characterization of a 160 MeV/u ^{4}He beam interacting with water*

C. La Tessa[1], *C. Schuy*[1], *A. Rusek*[3], *M. Sivertz*[3], *and M. Durante*[1,2]
[1]GSI, Darmstadt, Germany; [2]TU Darmstadt, Germany; [3]NSRL (BNL), USA

Radiotherapy with charged particles has shown several advantages compared to conventional treatments [1] and its application is being extended to a wider range of clinical cases. Furthermore, several particles have been considered as alternative candidates to protons and carbon ions; among them, helium and oxygen projectiles appears to be the most promising. The former suffers less lateral scattering and has a higher relative biological effectiveness (RBE) than protons, while it undergoes less fragmentation and deposits less energy in the entrance channel than carbon ions. Oxygen shows great benefits for the treatment of tumors characterized by a higher radioresistance caused, for example, by the presence of an extensive hypoxic region, which require a higher LET to be "killed". In this frame, the interaction of 160 MeV/u ^{4}He and 360 MeV/u ^{16}O beams with water targets were investigated at NSRL (NASA Space Radiation Laboratory), Brookhaven National Laboratory (BNL), Upton, USA. The results of the experiment with helium ions are reported here while the characterization of the oxygen beam is described in [2].

Data analysis

The production of primary ions, secondary charged particles and neutrons was investigated for several thicknesses of water in correspondence with the plateau (5 cm), slope (15 cm) peak (17 cm) and tail (19 cm) of the Bragg curve. Particle identification was achieved with a ΔE-E telescope composed of a 9 mm plastic scintillator and a 14 cm long BaF_2 placed at 3 m from the targets. A detailed description of the experiment setup can be found in [2]. The measurements were repeated placing the detector telescope at difference angles (0, 5, 15 and 30 deg from the beam direction) to study the angular distribution of all particle types. ΔE-E spectra were acquired as well Time-Of-Flight (TOF) spectra between the start detector placed just downstream of the exit window and the ΔE-E telescope. Furthermore, the collection of the BaF_2 signals with a short (70 ns) and a long (2 μs) gate allowed particle discrimination though the pulse shaping technique. An example of a TOF versus ΔE plot collected at 5 deg after 15 cm of water is given in Fig. 1. The quality of the radiation field was characterized through the measurements of microdosimetrical spectra collected with a TEPC (Tissue Equivalent Proportional Counter) at different water depths both in-beam and out-of-field at distances of 2, 5 and 10 cm from the beam direction. The yd(y) spectra recorded at several positions are shown in Figure 2.

The analysis of the data is currently in progress. The results will provide the energy spectra of charged and uncharged particles at different target thicknesses and positions compared to the primary beam direction from which the angular distribution can be estimated. As a satisfactory statistics could not be achieved for all target-angle combinations, the measurements are planned to be completed next summer; moreover, the attenuation of the primary beam in water will be investigated.

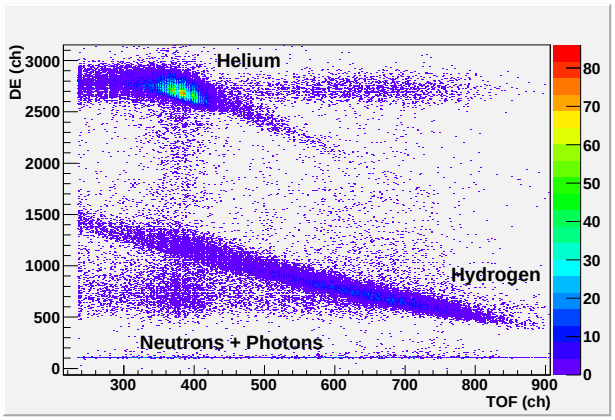

Figure 1: TOF versus ΔE plot recorded at 5 deg from the beam direction after 15 cm of water.

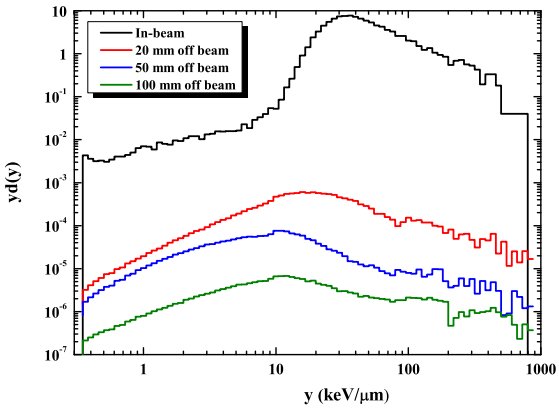

Figure 2: yd(y) spectra measured in-beam at the Bragg peak position (175 mm depth in water) and at 20, 50 and 100 mm off-beam (150 mm depth in water).

References

[1] W. Newhauser and M. Durante, Nat. Rev. Cancer **11**, 1-11 (2011)

[2] C. Schuy, C. La Tessa, A. Rusek et al., GSI Scientific Report (2011).

* Nasa space radiation health program (NSRHP)

Characterization of 360 MeV/u ^{16}O beam interacting with water targets*†

C. Schuy[1,2], *C. La Tessa*[1], *A. Rusek*[3], *M. Sivertz*[3], *and M. Durante*[1,2]
[1]GSI, Darmstadt, Germany; [2]TU Darmstadt, Germany; [3]NSRL (BNL), USA

Clinical trials have shown benificial effects using particle therapy with protons and carbon ions compared to conventional radio therapy. As a likely alternative for particle therapy, the characteristics of the radiation field generated by ^{16}O ion beams in water targets was investigated in NSRL (NASA Space Radiation Laboratory) at BNL (Brookhaven National Laboratory), Upton, USA.

Experimental setup

Schemes of the experimental setups are shown in Figs. 1, 2 and 3.

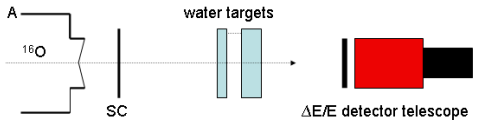

Figure 1: Setup used for measuring the attenuation of the primary beam.

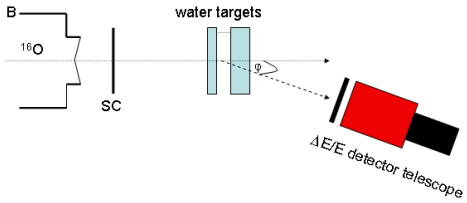

Figure 2: Setup used for measuring the angular distribution of the primary ions surviving the target as well as charged and uncharged fragments.

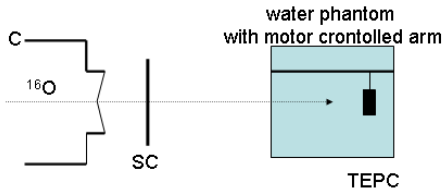

Figure 3: Setup used for measuring microdosimetrical spectra and dose distributions in-beam and out-of-field.

- Setup A was used to investigate the attenuation of the primary beam traversing water targets of thicknesses between 2.5 and 19 cm. Charged fragments and primary ions were identified with a ΔE-E telescope.
- The angular distribution of changed and uncharged fragments was studied with setup B. The primary ions traversed water thicknesses of 5, 15.5, 17 and 19 cm and the ΔE-E spectra of all outgoing particles were measured under different angles (0, 5, 15, 30 degrees) as well as their Time-Of-Flight (TOF).
- Lineal-energy distributions were measured inside a water phantom both in-beam and out-of-field (2, 5 and 10 cm from the beam position) at different water depths.

In all setups, a 2 mm plastic scintillator (Sc) was placed just downstream of the exit window to monitor the primary ions; when the intensity of the oxygen beam exceeded a rate of 10^5 particle/s, the scintillator was replaced by a 12 mm thick ion chamber. Particle identification was achieved with a telescope composed of a 9mm plastic scintillator to measure the energy loss (ΔE) and a 14 cm BaF_2 scintillator to measure the residual energy (E). The microdosimetrical spectra were acquired with a TEPC (Tissue Equivalent Proportional Counter).

Status of analysis

The analysis of the data is currently in progress. As soon as all the results are available they will be compared to Monte Carlo simulations and implemented into the treatment planning TRiP.

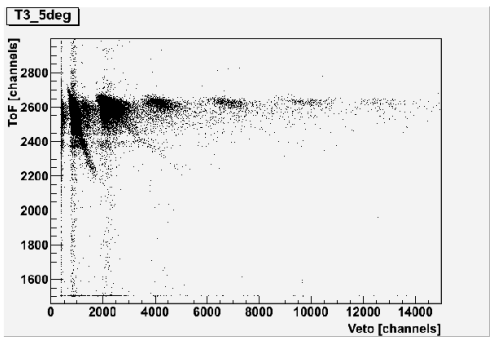

Figure 4: TOF versus ΔE (Veto) distribution recorded at 5 deg from the beam direction for ^{16}O ions after transversing 5 cm of water.

References

[1] H. Iwase and D. Schardt, GSI Scientific Report 2008, p.387.
[2] C. La Tessa et al., GSI Scientific Report 2011(submitted)

* Nasa space radiation health program (NSRHP)
† Work is part of HGS-HIRe.

Photoneutron spectra in radiotherapy

R. Kaderka[1,4,5], *D. Schardt*[1], *M. Durante*[1,4], *T. Berger*[3], *U. Ramm*[2], *J. Licher*[2], *and C. La Tessa*[1]
[1]GSI, Germany; [2]KGU, Germany; [3]DLR, Germany; [4]TU Darmstadt, Germany; [5]HGS HIRe, Germany

The ALLEGRO project (grant agreement no. 231965) investigated the late health effects following radiotherapy. Among the goals of the study was a comparison of the out-of-field dose in conventional and particle therapy [1, 2]. In fact, side effects induced by radiation treatment are well known to be related to the exposure of normal tissue surrounding the tumor. Furthermore, the characterization of secondary neutrons produced in photon therapy was addressed specifically because of their potentially high biological effectiveness.

Methods and materials

Experiments were performed using a water phantom and an anthropomorphic phantom. In the former, an 18 MV photon beam was used to irradiate an area of 5×5 cm^2 and photoneutron spectra were recorded on the water surface and in a water depth of 10 cm at several positions.

The anthropomorphic phantom was equipped with 5 detector holders along its main axis and was irradiated with a 25 MV IMRT beam delivered through 7 fields for treating a target volume of $5 \times 2 \times 5$ cm^3 at the center of the head.

For both experimental geometries, the neutron spectra were measured with a bubble detector spectrometer (BDS) from BTI, Canada, composed of a set of 6 different types of detectors, each with a specific sensitivity threshold covering an energy range between 10 keV and 25 MeV. The raw data were unfolded with the BUNTO code [3].

Results and discussion

Fig. 1a shows the results from the irradiation of the water phantom. The shape of the spectra are similar for all positions except for the one in-field which peaks at a higher energy. Out-of-field, the dependency of the spectra on the distance to the target is very weak whereas the water depth has a large influence on the amount of neutrons detected.

The measurements performed with the anthropomorphic phantom are shown in Fig. 1b. As for the simpler geometries, the spectra are very similar out-of-field regardless of the distance to the target. A large difference can only be seen in-field where the spectrum peaks at a higher energy.

The emission of secondary neutrons during photon irradiation is a direct consequence of the photo absorption by the target nuclei. The cross section related to this process was observed to have a broad giant resonance (Giant Dipole Resonance) in the energy range typical of high-energy photon radiotherapy. In detail, the GDR leads to the production of two types of neutrons: a fast and forwardly directed component directly emitted after the absorption and and an isotropic and lower-energy component due to the de-excitation of the target nuclei through evaporation. The energy of the photoneutrons is in the area of their maximum biological effectiveness (around 1 MeV), as also observed in the figure. Therefore, it is strongly advised to employ countermeasures in photon therapy to minimize the dose deposited by secondary neutrons outside the tumor volume and thus decrease the risk of inducing a secondary malignancy. The measurements have confirmed the strong neutron attenuation capability of water, recommending it as an optimal shielding material in photon therapy.

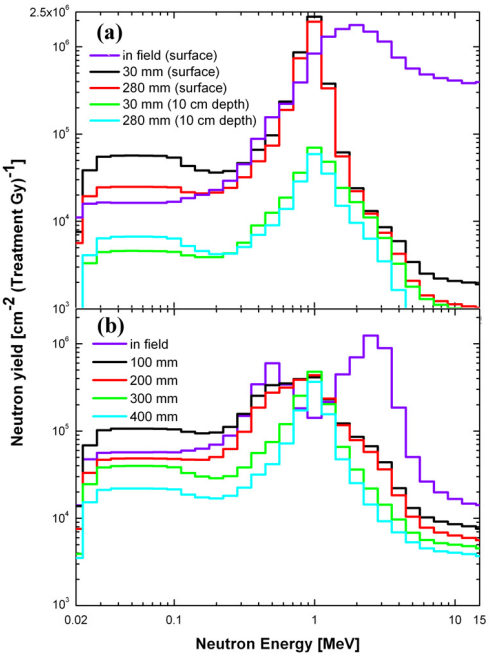

Figure 1: Photoneutron spectrum measured at several distances to the field in (a) a water phantom during its irradiation with 18 MV photons, (b) an anthropomorphic phantom during its irradiation with 25 MV IMRT photons.

References

[1] Kaderka et al. “Out-of-field dose measurements in a water phantom using different radiotherapy modalities”, submitted to Radioth. Oncol. (2012)

[2] La Tessa et al. “Out-of-field dose studies with an anthropomorphic phantom: comparison of X-rays and particle therapy treatments”, submitted to Radioth. Oncol. (2012)

[3] Ongaro et al. “Unfolding technique with passive detectors in neutron dosimetry”, Proc. Neutron Spectrometry and Dosimetry: Exp. Techniques and MC Calculations (2001)

Detection of secondary particles from ^{12}C fragmentation in an anthropomorphic phantom for SOBP position monitoring

M. Vanstalle[1], *C. La Tessa*[1], *C. Schuy*[1], *A. Sarti*[2], *L. Piersanti*[2], *V. Patera*[2], *A. Sciubba*[2], *and M. Durante*[1,3]

[1]GSI, Darmstadt, Germany; [2]Università di Roma La Sapienza, Roma, Italy; [3]TUD, Darmstadt, Germany

The real time monitoring of the Spread-Out-Bragg-Peak (SOBP) position represents one of the major concerns in modern ion therapy as it would allow a direct check of the patient alignment in combination with the treatment planning delivered. A possible method to achieve this goal is to exploit the fragmentation of the primary ions in the patient, correlating the production of secondary particles with the tumor position. Results have already been obtained with prompt gammas [1] but no data are available so far for secondary charged particles. A first experiment was performed at GSI in cave M with carbon ions. The goal of this measurement was to study the relation between the SOBP location and the yield of secondary particles (ions, neutrons and gammas) as a function of their angular distribution.

Material and methods

The experimental setup is similar to the one described in [2]. The carbon ions beam was impinging on an anthropomorphic RANDO phantom according to different configurations of irradiation:

- a spot irradiation with a monoenergetic pencil beam of 200 MeV/u stopped at the center of the phantom head;
- a 3D irradiation for treating a 2x5x7.6 cm^3 volume placed at the center of the phantom head;
- a 3D irradiation for treating a C-shaped volume placed at the center of the phantom head and having a length of 7.8 cm along the beam direction and a height of 2 cm.

All irradiations were performed under full treatment conditions. A scheme of the experimental apparatus is shown in Figs. 1 and 2. The primary ions outgoing from the exit window were monitored with a 2 mm plastic scintillator (start counter). On the upper and left arm, two drift chambers were placed to reconstruct the trajectories of secondary charged particles. Two $\Delta E - E$ telescopes composed of a plastic scintillator (VETO) for measuring the energy loss (ΔE) and a barium fluoride (BaF_2) to determine the residual energy (E) were placed on the upper arm, behind the chamber, and on the right arm, behind a lead collimator (1 mm aperture pointing at the center of the SOBP). On the left arm, a plastic scintillator was placed upstream of the drift chamber while a LYSO scintillator was positioned downstream. Both lateral arms could be rotated around he head to allow the study of the production of secondary particles as a function of the angle. The data acquisition system was triggered when a coincidence between the start counter and either one of the BaF_2 or the LYSO occurred. Particle identification will be possible thanks to Time-Of-Flight (TOF) measurement between the start counter and the BaF_2 or LYSO detectors as well as from 2-dimensional $\Delta E - E$ plots. Furthermore, the signals of the BaF_2s were integrated over a short (70 ns) and a long (2 μs) gate to apply the technique of pulse shaping.

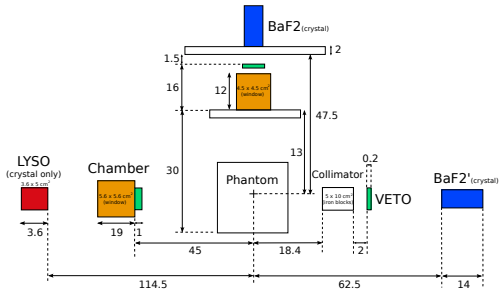

Figure 1: Scheme of experimental setup, lateral view.

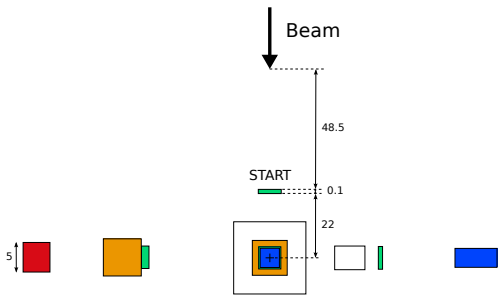

Figure 2: Scheme of experimental setup, top view.

Prospects

The data analysis is still in progress. The first step is to identify the peak of the prompt γ in the TOF spectrum for the time calibration. Monte Carlo simulations of the full setup will be carry out to estimate the geometry acceptance and compare the number of tracks measured with the expected values.

References

[1] M. Testa, M. Bajard, M. Chevallier et al., Radiat. Environ. Biophys. 49(3):337-43 (2010).

[2] K. Gunzert-Marx, H. Iwase, D. Schardt et al., New J. Phys. 10:1-21 (2008).

TRAX Code Extensions

C. Wälzlein[*1,2], *M. Krämer*[1], *E. Scifoni*[1], *and M. Durante*[1]
[1]GSI, Darmstadt, Germany; [2]FIAS, Frankfurt, Germany

The GSI track structure Monte Carlo (MC) code TRAX [1], whose purpose is to properly describe creation and transport of low energy electrons, has been extended. Electrons with initial energies below 1 keV are the most relevant for radiation damage. TRAX is intended to be suitable for a variety of different target materials and projectiles. One of our goals is to reproduce the data from the GSI Toroid experiment [2].

Auger electrons

The creation of Auger electrons was implemented in the TRAX code. Auger electron data tables are now part of the base data set automatically loaded on startup. The data was taken from the Livermore Evaluated Atomic Data Library [3]. The data contains the probabilities for the different Auger transitions as well as the flourescence yields.
So far, Auger data are only implemented for some atomic materials like carbon and oxygen. Auger yields for other materials can easily be added.
The implementation of the Auger effect was neccesary to reproduce data from the GSI Toroid experiment [2] where Auger electrons could be clearly seen in the electron spectra (Figure 1). One of the ideas of the Toroid experiment was to use the Auger electrons as a probe for interaction processes inside the target. This purpose failed as most of the Auger electrons are coming from the surface and not from inside the target.

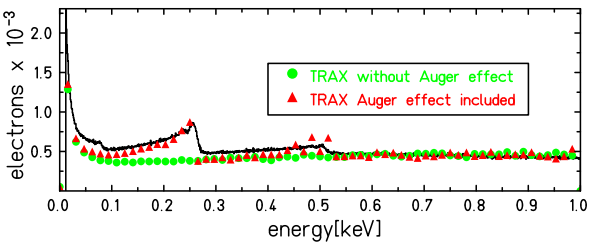

Figure 1: Electron spectrum behind a 15.9 nm thick carbon foil irradiated with 8.77 MeV protons from the Toroid experiment [2]. TRAX simulations without implementation of Auger effect could reproduce the continous part of the spectrum. With implemented Auger effect, reasonable agreement with experimental data was achieved. Auger electrons from carbon and oxygen were detected. Deviations probably are due to unknown molecular surface contaminations. To account for surface contaminations in the simulation, 3 nm of atomic carbon and oxygen were placed behind the carbon target.

* Work supported by Beilstein Institute (NanoBiC project). Work is part of HGS-HIRe.

Elastic Ion Scattering

The elastic scattering of ions has been neglected so far in the TRAX code, only excitation and ionization were considered. The elastic scattering of electrons was already implemented. Screened Rutherford cross sections according to Berger [4] are used to describe ion elastic scattering.
The correct implementation of the scattering was tested by reproducing experimental results. The data were taken from experiments by Gottschalk [5]. As an example, the angular distribution of 158.6 MeV protons incident on several different target materials and thicknesses was simulated with TRAX and showed good agreement to Gottschalk's results (Figure 2). The target materials ranged from light materials such as beryllium and carbon to heavy materials like iron, lead and uranium.
Additionally, the results were compared to Highlands's formula [6] which is a parametrized approximation of the Molière theory.

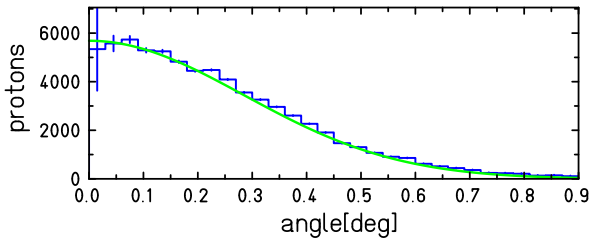

Figure 2: Simulated angular distribution of 158.6 MeV protons incident on 0.3018 cm carbon with TRAX. The binning of the histogramm in the TRAX simulation is 0.03°. Fitting a Gaussian distribution to the simulated data resulted in a gaussian width of $\sigma = 0.28(1)°$. Gottschalk determined this width to be 0.26(1)°. Highlands formula led to a width of 0.24°.

References

[1] M. Krämer, M. Durante, Eur. Phys. J. D, 60 (2010) 195.

[2] N. Lineva et al.. NIM B 267 (2000) 891.

[3] S.T. Perkins, D.E. Cullen, et al., "Tables and Graphs of Atomic Subshell and Relaxation Data Derived from the LLNL Evaluated Atomic Data Library (EADL), Z = 1 - 100", UCRL-50400, Vol. 30, Lawrence Livermore National Laboratory (1991).

[4] M. J. Berger, Methods in Computational Physics, Vol. 1, (1963) 135.

[5] B. Gottschalk, NIM B 74 (1993) 467-490.

[6] V.L. Highland, NIM 129 (1975) 497-499.

Estimation of carbon ion induced activity distributions with the yield approach

M. Priegnitz[1], *W. Enghardt*[1,2], *K. Laube*[2], *and F. Fiedler*[1]

[1]Helmholtz-Zentrum Dresden-Rossendorf, Germany; [2]OncoRay, TU Dresden, Germany

Phantom irradiation with pencil-like beams of carbon ions have been performed at GSI Darmstadt. The induced β^+-activity has been monitored by means of the dedicated in-beam PET scanner mounted at the irradiation site. On the basis of the yield approach ion beam induced positron emitter distributions have been predicted for these irradiation and activity distributions have been estimated. The comparison of predicted and measured activity profiles provides promising results.

Introduction

Tumor therapy with ion beams allow for a precise irradiation with high tumor conformality and protection of the surrounding healthy tissue. However, in order to take advantage of this high precision a monitoring of the dose delivery is required. Currently, the only method in clinical application is positron emission tomography (PET). The first in-beam PET installation has been operated at GSI Darmstadt. Carbon ion treatment of more than 400 patients has been monitored there and thus, the clinical benefit of this method was proven [1].

In-beam PET data evaluation aiming at the validation of the correct dose application requires a comparison of the measurement with a simulated expected activity distribution. Currently, this prediction is performed by means of Monte Carlo simulations, which depend on partial cross sections for all nuclear reactions occuring in the tissue and leading to positron emitting nuclei. These cross sections are available only for a few reaction channels in the required energy range. For several other reaction channels, especially for the use of other therapeutically interesting ions than carbon, these cross sections have not been measured in the required energy range yet and semi-empiric modeling often provide insufficient accuracy. Thus, an approach for activity prediction has been developed, which is based on experimental positron emitter yields rather than on cross sections. The feasibility of this yield approach has been shown by comparing measured activity profiles of phantom irradiation with the predicted ones.

Materials and Methods

Monoenergetic pencil beams of ^{12}C-ions with therapeutically relevant energies have been applied to homogeneous targets consisting of water, graphite and polyethylene. The ion beam induced β^+-activity has been measured by means of the in-beam PET scanner implemented at the former therapy site at GSI Darmstadt [1]. From these irradiation depth dependent thick target yields of induced positron emitters have been deduced. With the yields of these reference materials a database has been compiled from which the prediction of positron emitter distribution in any target consisting predominantly of carbon, hydrogen and oxygen is possible. By taking into account the actual time course of irradiation, i.e. the duration of beam extraction pulses and of the pauses within, the expected activity distribution in those materials can be predicted [2].

Results

Figure 1 shows the prediction of depth dependent positron emitter yields in a homogeneous polymethyl methacrylate (PMMA) target, which was irradiated with a carbon beam of two energies. The prediction was made from the database of the positron emitter yields in the reference materials mentioned above. The lower part of the figure shows the derived predicted activity distribution compared with the measurement. The positions of the activity peaks differ less than 1 mm. It is shown that the yield approach is a suitable alternative to rather extensive partial cross section measurements.

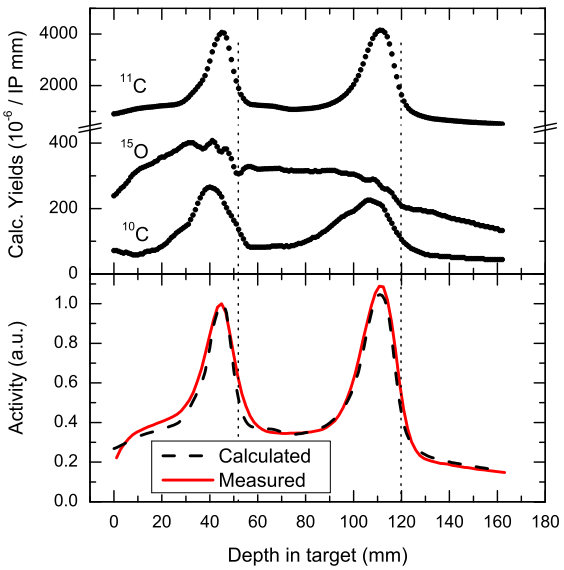

Figure 1: Top: Calculated yields of ^{11}C, ^{15}O and ^{10}C in a PMMA target irradiated with $163A$MeV and $260A$MeV carbon ions. Bottom: Comparison between measured and predicted activity. The vertical dotted lines indicate the primary particle ranges.

References

[1] W. Enghardt, P. Crespo, F. Fiedler *et al.*, Nucl. Instr. Meth. A 525, pp 284-288, 2004.

[2] M. Priegnitz, F. Fiedler, D. Kunath *et al.*, IEEE Trans. Nucl. Sci., DOI 10.1109/TNS.2011.2172629, in print, 2011.

Verification of ion range in moving targets with in-beam PET*

K. Laube[1], *C. Bert*[3], *F. Fiedler*[2], *S. Helmbrecht*[1], *M. Priegnitz*[2], *N. Saito*[3], *and W. Enghardt*[1,2]

[1]OncoRay, Dresden, Germany; [2]HZDR, Dresden, Germany; [3]GSI, Darmstadt, Germany

Introduction

Continuous density changes due to intra-fractional motion can strongly affect the particle range in ion beam therapy. Although using complex beam delivery techniques like gating, tracking or rescanning and choosing optimal beam directions where density changes are low and no organs at risk are likely to move into the beam path there remains a remarkable risk for an inaccurate dose deposition. (In-beam) positron emission tomography (PET) can visualize the autoactivation of the tissue occuring under treatment along the beam path. The distal fall-off of the β^+-activity distribution is correlated to the Bragg peak position and is used as an indication of the particle range. Under target motion blurring effects have to be compensated during reconstruction to determine the correct distal edge position.

Materials and Methods

Plexiglas targets ($13.5\times20\times9\,\mathrm{cm}^3$) were irradiated with monoenergetic ^{12}C ions at the former medical treatment site at GSI. The applied treatment plan consisted of 60 rescans at a 14 cm long horizontal line at isocenter height. The pencil beam of about 295 AMeV passed an 8 cm thick absorber imitating the wedge system for range compensation [1] and had a residual range of about 6 cm in the target. The one-dimensional (1D) sinusoidal target motion (2 cm peak-to-peak amplitude, 6 s period) parallel to the scanning direction of the incident beam was compensated by lateral beam tracking. Cuboid structures of 1 cm width and different thicknesses (1.75 cm, 0.75 cm and 1.25 cm) at the proximal target surface caused systematic underranges in the target. The induced β^+-activity distribution in the target was measured in listmode operation with the double head in-beam PET scanner BASTEI [2] during the irradiation and 5 minutes afterwards with ongoing target motion. A static follow-up measurement of the residual activity with the target positioned at the isocenter was done for about 6.5 minutes to be used as a reference for the moving target measurement. PET images were generated from both data sets regardless of motion by the well-established 3D maximum likelihood expectation maximization (MLEM) algorithm with median filtering of the image after each iteration step. Corrections for attenuation, limited solid angle coverage of the scanner and its detection efficiency were included. Another reconstruction using the motion information was done by a 4D MLEM algorithm [3, 4]. For that, listmode data were divided into 9 phases based on the target motion amplitude. The 3D and 4D MLEM results of the moving target measurement were compared to the static reference by an automated range verification system [5].

* Work supported by EU, ENVISION contract No. 241851.

Results

The reconstructed β^+-activity distributions are visualized in the top row of figure 1. The static activity distribution of the reference measurement is well reproduced under target motion by the 4D MLEM algorithm. With the uncorrected 3D MLEM reconstruction the range influence of the 1 cm wide structures is not correctly reproduced in the resulting activity. The gaps in the activity distribution at maximal particle depth are almost vanished due to blurring effects. Consequently, overranges similar to the thicknesses of the cuboids are found at these positions by the range verification system as it is shown in the bottom row of figure 1. A nearly ideal identity in range is found between the reference and the 4D MLEM along the whole width of the activity distribution. These experiments confirmed that the 4D MLEM algorithm compensates correctly the motion influence onto the distal edge position in PET images to allow for a precise ion range verification.

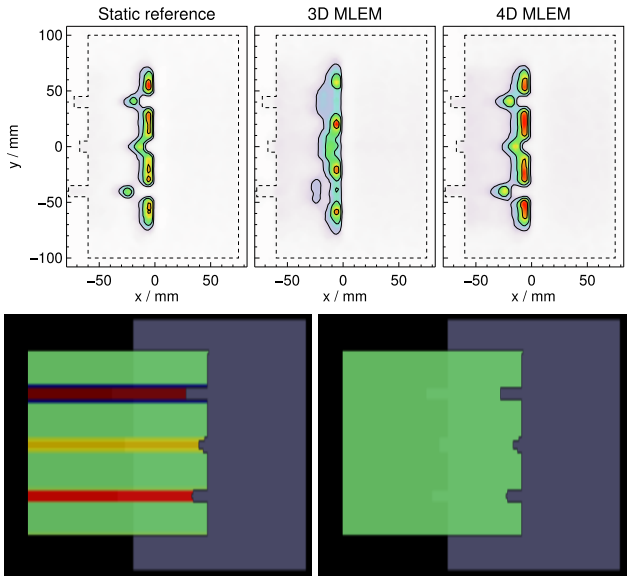

Figure 1: Top: Color coded β^+-activity distribution (maximum in red and minimum in white) in the target (dashed line) shown in bird's eye view (incident beam impinges the target from the left) for the static reference (left) and the moving target measurement reconstructed by 3D (middle) and 4D MLEM (right). Bottom: Detected range deviations (superposed to the CT) between the static reference and the 3D MLEM (left) and the 4D MLEM (right), respectively. Unmodified ranges are shown in green, underranges in blue and overranges in yellow, red and brown.

References

[1] N. Saito *et al.*, Phys. Med. Biol. 54, 2009, pp. 4849–62

[2] W. Enghardt *et al.*, Nucl. Instr. Meth. A 525, 2004, pp. 284–8

[3] T. Li *et al.*, Med. Phys. 33, 2006, pp. 1288–98

[4] F. Qiao *et al.*, Phys. Med. Biol. 51, 2006, pp. 3769–83

[5] S. Helmbrecht *et al.*, Phys. Med. Biol., accepted

Proton therapy and radiography project (PaNTERA)

M. Durante[1,2] *and D. Varentsov*[1]

[1]GSI, Darmstadt, Germany; [2] TU Darmstadt, Germany

Proton therapy is now a well established method in treatment of cancer and noncancer diseases [1]. The rationale of using protons with energies between 60 and 250 MeV is based on the favourable depth-dose distribution, so that the targets can be located on a spread-out Bragg peak while the normal tissue is exposed on the plateau region. However, the proton beam is broadened by multiple scattering in the beamline materials and in the patient's body. This broadening produces a "dose halo" in the treatment plan and worsens the dose contours. For a charged particle with atomic number z and mass number A, the lateral scattering is roughly proportional to $z/A\beta^2$, and therefore the lateral scattering can be reduced either using heavy ions such as carbon, or by increasing the particle velocity. In the latter case, using protons in the GeV region the targets cannot be exposed on the Bragg peak (for instance, the range of 1 GeV protons is ~3.2 m in water), and then requires various beams cross-fired to the target from different angles, similarly to X-ray therapy.

The advantage of the "plateau" (non-Bragg-peak) radiotherapy will be a stable beam profile providing very sharp dose contours for sparing of critical organs. For this reason, relativistic protons were proposed for plateau stereotactic radiosurgery already in Berkeley. The only clinical experience comes from St. Petersburg in Russia: more than 1,000 patients have been treated with 1 GeV protons at the Petersburg Nuclear Physics Institute (PNPI) since 1975 [2].

A major advantage of relativistic protons is that the beam crossing the patient can be exploited for proton radiography. Proton radiography was investigated since the early 1970s because of its low radiation dose and high density resolution, but until recently the image blurring due to multiple Coulomb scattering was limiting its practical applications. However, about a decade ago researchers of Los Alamos National Laboratory (LANL) have introduced a magnetic lens after the object for imaging and chromatic aberration corrections. This allowed to reach unprecedented spatial resolution with high-energy protons, as proved by many dynamic experiments with 800 MeV beam at LANL. (Fig. 1). A project for proton microscopy at FAIR (PRIOR project) plans to exploit a 4.5 GeV proton beam for radiography, reaching a spatial resolutions below 10 µm and a time resolution below 10 ns. The high-precision in beam delivery combined with online high-resolution imaging and dose verification leads to reduced target margins and improved image-guided stereotactic proton radiosurgery (IGSpRS) for cancer (e.g. small brain metastasis, pituitary adenoma, vestibular Schwannoma) and noncancer (e.g. arteriovenous malformations, trigeminal neuralgia, epilepsy, intracranial aneurysm, macular degeneration) lesions (Fig. 2).

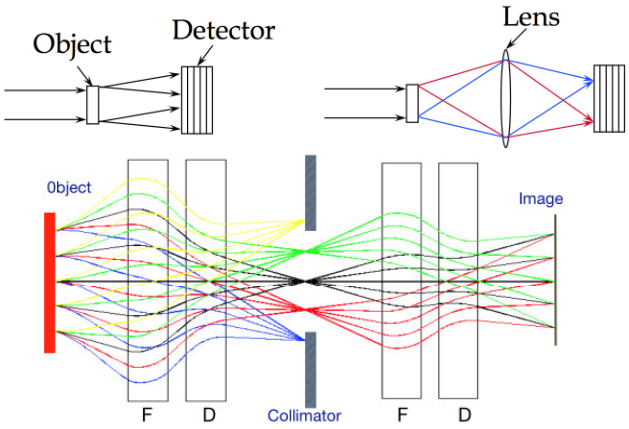

Figure 1. Correction of image blurring in proton radiography using magnetic lenses. The idea was originally proposed by Morris and Zumbro (LANL Technical Report LA-UR-974172, 1997).

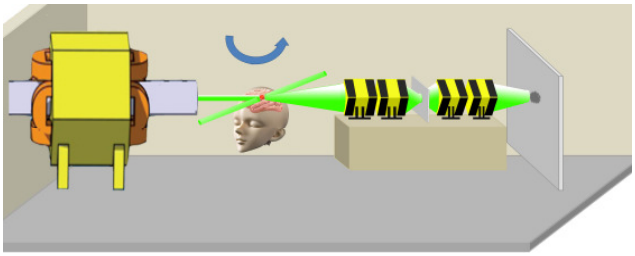

Figure 2: Proposed setup for IGSpRS using relativistic protons. Patient has to be rotated to allow cross-firing of the proton beam from different angles. A magnetic lens system is used for high-resolution radiography. This imaging system makes possible online guidance.

A first test has been performed at ITEP in Moscow (Russia), where a proton radiography setup is installed on the 800 MeV beamline [3]. Moreover, we have completed a full biophysical characterization of a 1 GeV proton beam (Brookhaven National Laboratory, Upton, NY, USA), measuring the dose profile in 3D and cell survival (relative biological effectiveness) in 3 different mammalian cell lines [4]. These preliminary results support the rationale of the PaNTERA project.

References

[1] Durante M and Loeffler JS 2010 *Nature Rev. Clin. Oncol.* **7** 37

[2] Abrosimov NK, et al. 2006 *J. Phys.* **41** 424

[3] Varentsov D et al. "High-energy proton microscopy of radiobiology-relevant targets" 2012 this report

[4] La Tessa C et al. "Dosimetry and biological effectiveness of a 1 GeV proton beam for image-guided stereotactic radiosurgery" 2012 this report

High energy proton microscopy of radiobiology-relevant targets *

D. Varentsov[1], *A. Bogdanov*[2], *V.S. Demidov*[2], *M. Durante*[1,3], *A.A. Golubev*[2], *A. Kantsyrev*[2], *P.M. Lang*[3], *D.N. Nikolaev*[4], *N. Markov*[2], *F. Natale*[1], *L. Shestov*[2], *P. Simoniello*[1], *and G.N. Smirnov*[2]

[1]GSI, Darmstadt, Germany; [2]ITEP, Moscow, Russia; [3]TUD, Darmstadt, Germany; [4]IPCP, Chernogolovka, Russia

High energy proton microscopy (HEPM) provides unique capabilities in penetrating radiography including the combination of high spatial resolution and field-of-view, dynamic range of density for measurements, in addition to the key attribute of reconstructing the density variations to less than 1% inside volumes and *in situ* environments [1]. The PRIOR (*Proton Microscope for FAIR*) facility which is currently being constructed at the HHT area of GSI will use a 4.5 GeV proton beam from SIS-18 synchrotron and allow for a significant step forward in spatial resolution ($< 10\,\mu m$) to advance high-energy-density physics and heterogeneous materials research. Recently, it was proposed to employ PRIOR to radiobiological and medical therapy studies (the PaNTERA project [2]).

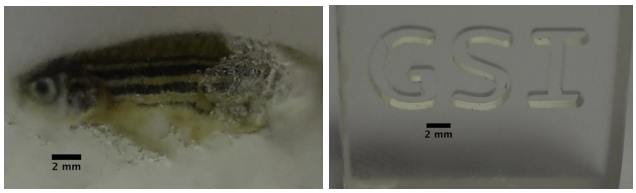

Figure 1: Zebrafish (*Danio rerio*) embedded in 1 cm-thick paraffin (left) and a 8 mm-thick PMMA slab with 1 mm-thick, 1 mm-deep letters milled on its surface (right).

A first test of using HEPM for biological objects has been performed at ITEP in Moscow (Russia) in December 2011, using a 800 MeV proton beam from the TWAC synchrotron facility and the PUMA x4 proton microscope. A set of biological targets has been prepared at GSI. The targets included small fishes and fish organs fixed in paraffin slabs and in tubes with agarose gel to be installed inside a vacuum target chamber. In addition, a few PMMA phantom targets have been prepared at IPCP (see Fig. 1).

Since the microscope has been prepared for high explosives dynamic experiments and was not optimized for high-precision measurements, the obtained spatial resolution was about $150\,\mu m$ (RMS) only. The proton beam intensity was up to $2.5 \cdot 10^{10}$ per image. In order to enhance the contrast, several images have been collected for each irradiated target. The white field images had to be recorded separately and the beam position at the object was considerably fluctuating for every shot due to unstable beam extraction conditions. This did not allow for the perfect white field correction. The obtained HEPM images of a zebrafish fixed in paraffin and a PMMA phantom target are shown in Fig. 2 and Fig. 3, respectively.

It is planned to continue the PaNTERA experiments at GSI in 2012–2013. It is expected that by the optimized PRIOR microscope and high-energy protons from SIS-18, the spatial resolution, contrast and imaging quality will be significantly improved.

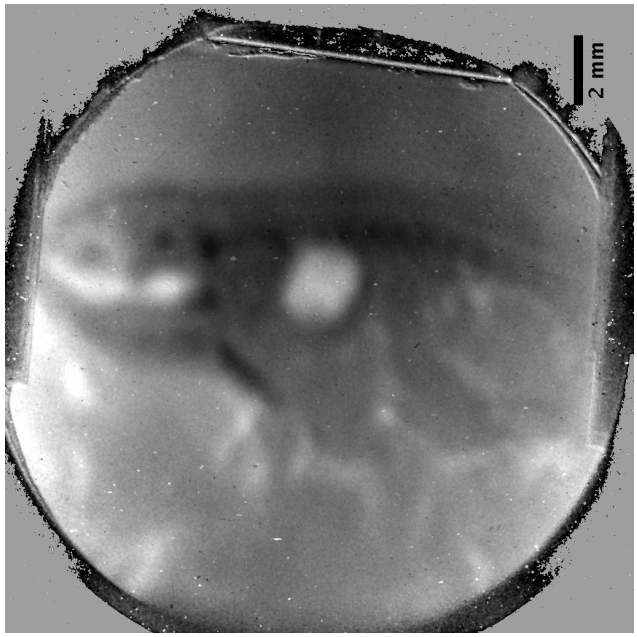

Figure 2: HEPM image of zebrafish (Fig. 1, left).

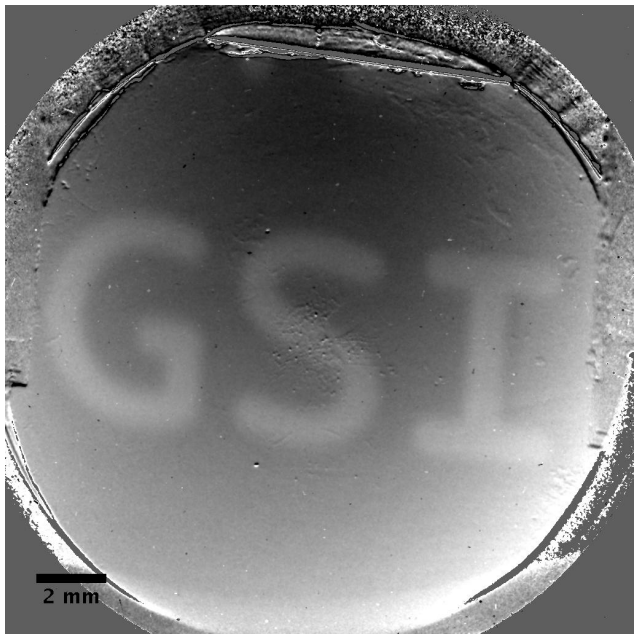

Figure 3: HEPM image of PMMA slab (Fig. 1, right).

[1] http://1.usa.gov/y9hQha.
[2] Durante M et al. 2012 this report.

* Supported by HRJRG-112 and FRRC.

Dosimetry and biological effectiveness of a 1 GeV proton beam for image-guided stereotactic radiosurgery*

C. La Tessa[1], A. Rusek[2], M. Vanstalle[1],Z. Yu[1,3] and M.Durante[1,4]

[1]GSI, Darmstadt, Germany; [2]NSRL Brookhaven National Laboratory, Upton, NY, USA; [3]Fudan Cancer Center, Shanghai, China; [4]TU Darmstadt, Germany

In the framework of the PaNTERA project [1], we measured the physical and radiobiological characteristic of 1 GeV protons for possible applications in stereotactic radiosurgery (image-guided plateau-proton radiosurgery).

Materials and Methods

A proton beam was accelerated at 1 GeV at the Brookhaven National Laboratory (Upton, NY). A target in polymethyl methacrylate (PMMA) with a maximum thickness of 20 cm was used to simulate the target. A broad-beam (10x10 cm) was used for beam tuning and tests of proton radiography (Fig. 1) while a 1.79 cm FWHM small beam was used for measurements of radiosensitivity in 3 mammalian cell lines.

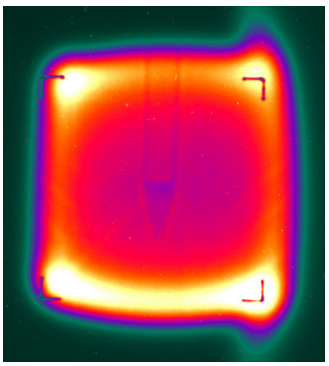

Figure 1: proton radiography with a pixel chamber of a centrifuge tube containing cells in tissue culture medium.

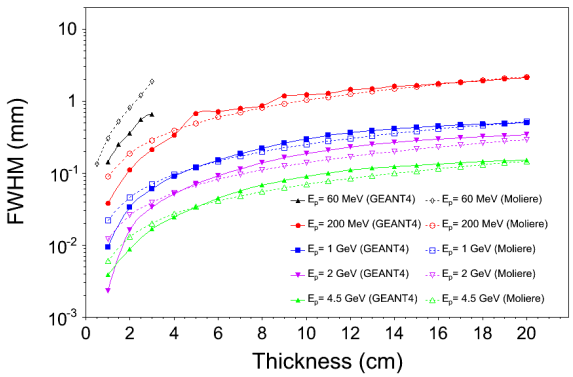

Figure 2: FWHM of proton beams at different energies in PMMA. Simulations either by the Monte Carlo code GEANT4 or by the Molière approximation.

Results

Measurements and simulations demonstrate that the lateral scattering of the beam is very small (Fig. 2).

* Experiment supported by NASA SRHP grant

The lateral dose profile was measured with or without the 20 cm plastic target, showing no significant differences up to 2 cm from the axis (Fig.3). The relative biological effectiveness at 10% survival level ranged between 1.0 and 1.2 (Fig.4).

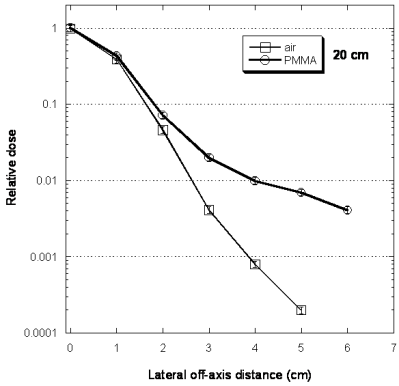

Figure 3: Lateral dose profile of the small beam after 20 cm air or PMMA

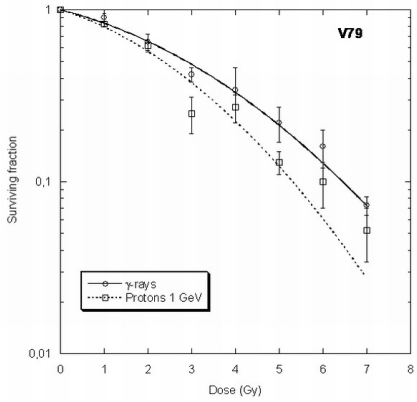

Figure 4: Survival of V79 hamster cells exposed to graded doses of 1GeV protons or ^{137}Cs γ-rays.

Conclusions

The very low lateral scattering of relativistic protons and the possibility to use online proton radiography during the treatment make them attractive for image-guided plateau (non-Bragg-peak) stereotactic radiosurgery. The data presented here should be incorporated in treatment plans for comparison to other stereotactic X-ray techniques.

References

[1] M. Durante and D. Varentsov, "Proton therapy and radiography project (PaNTERA)", 2012 this report.

First biology test- experiments at PHELIX*

D.Pignalosa [1], Günter Lenz [1], Petra Hessel [1], Oliver Deppert [2], Andreas Maier [1], Sylvia Ritter [1], Markus Roth [2], Knut Harres [2], Marco Durante [1,2], Gerhard Kraft [1,2], Wilma Kraft-Weyrather [1]

[1]GSI, Darmstadt, [2]TUD, Darmstadt Germany;.

Laser driven ion acceleration, LDIA, has been frequently discussed to be used in particle therapy because its compactness compared to conventional acceleration, [1]. But the medical quality requirements are very strict and will prevent a medical use of LDIA in near future. However, the extreme short pulse lengths of a few picoseconds of the LDIA created secondary particle beams can be used to study the kinetics of the cellular response to exposure of ionizing radiation in a time scale that was not accessible up to now.

Such experiments carried out with mammalian cells need some special set up where the beam is extracted from vacuum into normal air under atmospheric conditions. Therefore, a re-entry tube with special sample holders have been installed as shown in fig.1&2

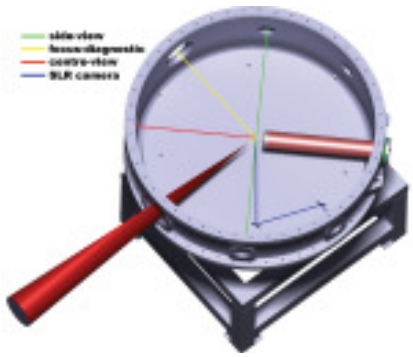

Figure 1: Experimental set up: the laser beam enters the reaction chamber from the lower left side and hit the target foil under 45° at the center. The re-entry tube enters from the left under and angle of 90° to the target foil

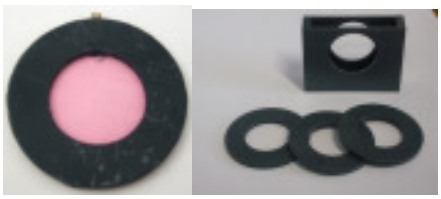

Figure 2: The sample holders (left) are filled with medium and cells from the top and put together with two distance rings in a sample box (right) for exposure

Experimental setup

The re-entry tube with a total length of 625 mm had a 12-16 µm Ti entrance window of 30 mm in diameter and of 50 mm in distance from the Laser target point. The cell sample box could be placed in various distances behind the window. The free space inside the entry tube was filled with solid material and closed with a blind flange in order to reduce the air volume that could inflate the reaction chamber in case of a vacuum leak.

The holder for the biological target was a plastic ring covered at both sides with biocompatible foils having cells attached at one foil (fig.2). The spacing between the rings was 2 mm filled with medium. With additional absorber foils in front of the samples energy and intensity could be varied (fig 3).

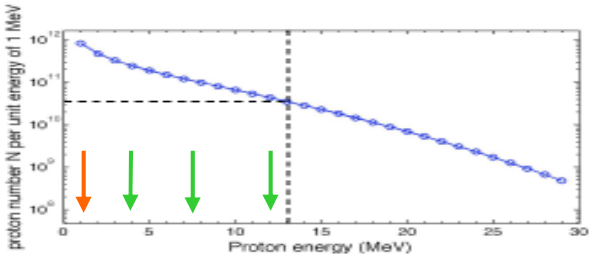

Figure 3: Typical proton energy spectrum. Arrows indicate the cut off in energy but also in intensity by the exit window (red) and additional absorber foils of 100, 200 and 300 mg/cm²

Experiment

For the experiment 9 laser pulses within one week could be used, two of them for dosimetry. First problem was the stability of the entrance window which was stable for the 16µm foils but imploded for the thinner ones.

The optimal exposure conditions seem to be 10 cm from the laser target where the beam was homogenous over most of the target area with a fluence in order of exp 11 part/cm². With these high particle intensities layers of human AG fibroblast cells were exposed and processed according to standard γH2AX procedures in order to visualize the induced double strand breaks DSB (fig 4).

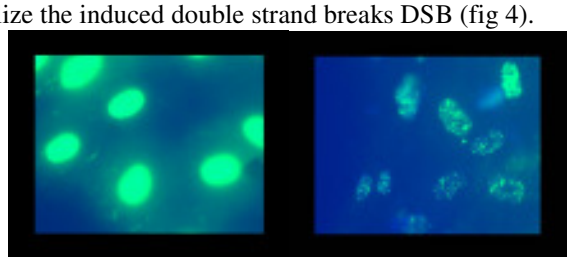

Figure 4: Distribution of DSBs in the exposed cell nuclei, in the center (left) and at the very border of the samples (right).

[1] G.Kraft ,S.D.Kraft **Research needed for improving heavy-ion therapy** New J. Phys. *Focus on Heavy Ions in Biophysics and Medical Physics*, **11** :025001-(16pp) (2009)

* Work is part of HGS-Hire

A patient study for comparison of two motion detection systems*

P. Steidl[1,2], *R. Brevet*[1], *J. Bürkelbach*[3], *H. Hof*[3], *T. Haberer*[4,5], *M. Durante*[1,2], *and C. Bert*[1]

[1]GSI, Darmstadt, Germany; [2]Technical University Darmstadt, Darmstadt, Germany; [3]University Clinic Heidelberg, Heidelberg, Germany; [4]Heidelber Ion Beam Therapy Center, Heidelberg, Germany; [5]Goethe University Frankfurt, Frankfurt, Germany

Introduction

Treatment of tumours situated in organs which are affected by breathing motion is a big challenge in radiation therapy. Tumour motion tracking is often done by measuring the breathing motion by means of a surrogate signal, e.g. the thorax skin motion or the abdominal expansion during breathing. In this case good correlation between the external surrogate signal and the internal actual tumour motion is essential [3]. A patient study is presented which was performed to investigate and compare the correlation of two external motion detection systems in respect of the actual tumour motion.

Material and Methods

At the University Clinic Heidelberg two motion monitoring systems are available: the Anzai system (Anzai Medical Co.,Ltd, Tokyo, Japan) and the VisionRT system (VisionRT Ltd., London, UK). The Anzai system includes a belt which measures the abdominal or thoracic expansion. The VisionRT system is a stereoscopic camera system which measures the thorax motion in 3D. A certain pre-defined region of interest can be tracked.

During the conventional photon treatment of five lung cancer patients (one to five fractions, six or seven fields) these two systems were used to generate an external motion signal temporal correlated to MV fluoroscopy. For four patients the Anzai belt was put around the abdomen while in one case it measured the extension of the thorax due to an abdominal compression. The VisionRT system always tracked the motion of the sternum. Due to technical issues in some cases temporal correlation was not possible which reduced the number of correlated data sets.

After data acquisition the tumour motion was extracted from the MV fluoroscopy sequences [1, 2]. Since base line drifts, signal jumps and phase shifts were observed minima and maxima were estimated and all signals were normalized to the local amplitude to correct for base line drifts and signal jumps. Correction for phase shifts was performed by adapting the temporal correlation. After that for the uncorrected and corrected signals the correlation coefficient was calculated.

Results and Discussion

In all of the three signals base line drifts or jumps occurred. Phase shifts of up to one second could be observed. In the four cases the Anzai belt was placed around the abdomen phase shifts between the Anzai system and fluoroscopy were below 140 ms while in the one case where the thorax motion was measured the phase shifts were larger (up to 400 ms). Phase shifts between sternum motion (VisionRT) and fluoroscopy ranged between 500 ms and 1 s. This leads to the impression that there can occur a phase shift between thoracic and abdominal motion. The lung tumour motion seems to be most affected by the abdominal motion.

The mean correlation coefficients of Anzai system versus VisionRT system turned out to be 0.43, 0.64 and 0.81 for uncorrected, phase shift corrected and base line drift corrected signals, respectively. The mean values for Anzai system versus fluoroscopy were 0.73, 0.73 and 0.89, and for VisionRT versus fluoroscopy 0.29, 0.57 and 0.78, respectively. Thus, phase shifts showed a large impact on the correlation which is reasonable. The results for the corrected signals showed that the difference between Anzai system and VisionRT system seem to be a result of phase shifts and base line drifts. Since these occurred in signals of all systems and the number of data sets was very low a general difference between the VisionRT system and the Anzai system cannot be concluded from this data. Further investigation is necessary which leads to a continuation of this project.

Conclusion

To compare the two external motion monitoring systems of VisionRT and Anzai we acquired their signals parallel to MV fluoroscopy during conventional photon therapy of five lung cancer patients. Based on correlation to the internal motion no difference between the two systems could be observed based on the data. Since data basis was small further investigations are needed. Anyhow it should be kept in mind that phase shifts between internal and external motion of up to 1 s can occur when using an external motion monitoring system e.g. for gating.

References

[1] R. Brevet, “Internal/External Motion Correlation”, Diploma thesis, Université de Strasbourg, 2011

[2] R. Brevet et al., “Analysis of internal/external motion correlation”, GSI Scientific Report 2011, 2012

[3] C. Bert and M. Durante, “Motion in radiotherapy: particle therapy”, Physics in Medicine & Biology, 56(16):R113–R144, 2011

* Work supported by DFG (KFO 214 TP 5)

Analysis of internal/external motion correlation*

R. Brevet[1], P. Steidl[1,2], M. Durante[1,2] and C. Bert[1]

[1]GSI, Darmstadt, Germany; [2]Technical University Darmstadt, Darmstadt, Germany

Introduction

For tumors located in the abdomen or in the thorax motion can be induced during radiotherapy treatment because of breathing or heart pulsation.[1] Especially for scanned beam ion beam therapy this intra-fractional motion can result in underdosage. Several motion mitigation strategies require motion detection. Possible techniques are fluoroscopy (internal motion detection) or external signals such as the motion of the chest. External surrogates are potentially not as precise as imaging internal motion but have the advantage to avoid additional imaging dose to the patient.

To study the correlation between internal and external motion we developed algorithms that allow tracking the motion of lung tumors out of fluoroscopic sequences from MV photon beam treatments. These were then used to analyze the correlation of external and internal signals.

Tumor tracking with MV fluoroscopy

Among the proposed methods for this purpose is template matching[2], which consists in computing a template based on several frames and comparing it with each incoming frame of the current sequence to find the position where the correlation score (eq. 1) is the highest.

$$s = \frac{\sum_m \sum_n (R_{mn} - \bar{R})(T_{mn} - \bar{T})}{\sqrt{(\sum_m \sum_n (R_{mn} - \bar{R})^2)(\sum_m \sum_n (T_{mn} - \bar{T})^2)}} \quad (1)$$

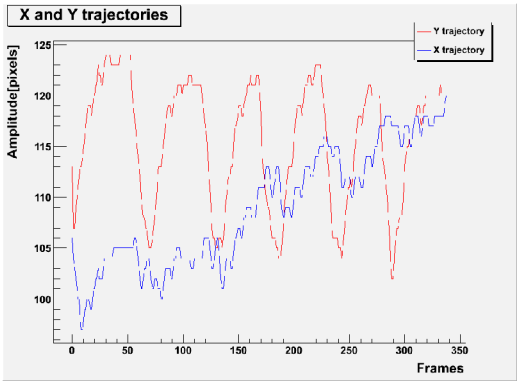

Figure 1: Example of the motions on vertical and horizontal directions extracted from the MV-fluoroscopic sequences.

In eq. 1, R_{mn} and T_{mn} are respectively the values of the pixel $[m,n]$ of the current frame and of the previous one and $\bar{R}$ and $\bar{T}$ are respectively the mean grayscale values of the current frame and of the previous one.

This correlation score s was also used for the here presented work. After a preprocessing step to enhance contrast[3], to reduce noise[4] and to remove stripes artefacts, the correlation score was directly calculated with successive frames of the fluoroscopic sequence. The position of the tumor on the second frame was determined by the highest value of s. The analysis is performed in two regions of interest (ROI). The ROI of the first frame contains the tumor area. The position of the ROI in the second frame is dynamically moved based on the detected tumor position in the previous frame.

Fig. 1 displays an example of detected tumor position. These data allow studying the correlation with external motion signals.

Correlation analysis

Correlation has been studied with two external sensors, namely the GateRT (VisionRT Ltd, London) and the ANZAI AZ-733 (ANZAI Medical Co. Ltd.). ANZAI data are acquired using a belt placed around the chest of the patient measuring pressure. VisionRT is based on a stereoscopic camera which detects the motion of a tracking point (for instance on the chest).

Fluoroscopic and ANZAI data showed a good correlation ($0.6 < s < 0.9$). Because of phase shifts and less stable trajectories, it was more difficult to study VisionRT data. However the global behaviors were the same or were inverted once the phase shifts are removed.

Conclusion

Even for the very low-contrast MV fluoroscopy sequences, motion of lung tumors was successfully tracked. Correlation studies between internal motion and external signals from the ANZAI and VisionRT systems showed comparable behavior. To obtain better and more precise results, a further correlation analysis has been done with enhanced ANZAI and VisionRT data.[5]

References

[1] C. Bert and M. Durante, 2011 Phys. Med. Biol. 56, R113-R144.

[2] H. Animura et al, 2009 Phys.Med.Biol.54,665-677.

[3] B. Jähne, 2005 “Digital Image Processing”.

[4] R. C. Jain, 1995 “Machine Vision”.

[5] P. Steidl et al, “A patient study for comparison of two motion detection systems”, 2012 GSI Scientific Report

* RB is funded as an ESR within the EU-FP-7 ENTERVISION framework, Grant Agreement no. 264552. Further funds received by DFG KFO 214.

Experimental validation of motion phase interpolation when tracking a moving tumor with a scanned ion beam* †

A. Constantinescu[1,2], *R. Lüchtenborg*[1,2], *M. Durante*[1,2], *and C. Bert*[1]
[1]GSI, Darmstadt, Germany; [2]Technische Universität Darmstadt, Germany

Introduction

Time-resolved Computed Tomography scans (4DCTs) are the basis of treatment planning and delivery for intra-fractionally moving tumors. The respiratory motion of the patient is subdivided into N quasi-stationary sections (motion phases). In every motion phase a regular 3DCT is reconstructed. One method for treating a moving tumor with a scanned ion beam is tracking, i.e. adapting the beam position to the current tumor position at any time of the treatment session. Using this technique, motion look up tables (MLUT) provide the needed compensation vectors (lateral and longitudinal direction) for each rasterpoint/motion phase combination [2]. During the irradiation the motion of the tumor is continously assigned to one of the N motion phases and the corresponding compensation vector is applied. Information on the tumor motion within a motion phase is not utilized. Interpolation in between the known motion phases during irradiation could improve this [1] and was implemented into the GSI therapy control system. The results of the experimental tests will be presented here.

Material and Methods

All measurements were carried out on KODAK X-OMAT V films, which were mounted on a motion slide and moved periodically in a left-right direction (from beam's eye view) with a peak-to-peak amplitude of $x_m = 4\,\mathrm{cm}$. The target trajectory was measured using a displacement sensor [2]. The allocation of the voltage signal to the corresponding motion phase was based on the amplitude. Different experiments were carried out. Measurements of tracking without interpolation included variations in the number of used motion phases in the corresponding MLUTs (2, 11, 21, 41 motion phases). In the measurements in which tracking was combined with motion phase interpolation, a MLUT with only 2 motion phases was used. For reference also a non-moving film was irradiated. The obtained results were classified by analyzing the dose deposition on the film. The standard deviation σ and the mean value μ of the optical density within a region of interest (3x3 cm^2) in the target area (5x5 cm^2) was determined, resulting in homogeneity H according to

$$H = 1 - \frac{\sigma}{\mu}. \qquad (1)$$

Results and Conclusion

In table 1 the result for the homogeneity of the optical density is listed for the different irradiations. For beam tracking experiments the homogeneity increases with the number of used motion phases in the MLUT (see also fig.1). With a high number of motion states results comparable to the static case are obtained. When using beam tracking with interpolation, only two motion phases are needed in order to obtain the same result.

Exp.	static	w/o interpol				interpol
No.MP	-	2	11	21	41	2
$H[\%]$	95	23	86	92	91	94

Table 1: Homogeneity of the optical density within the region of interest. MP: motion phase

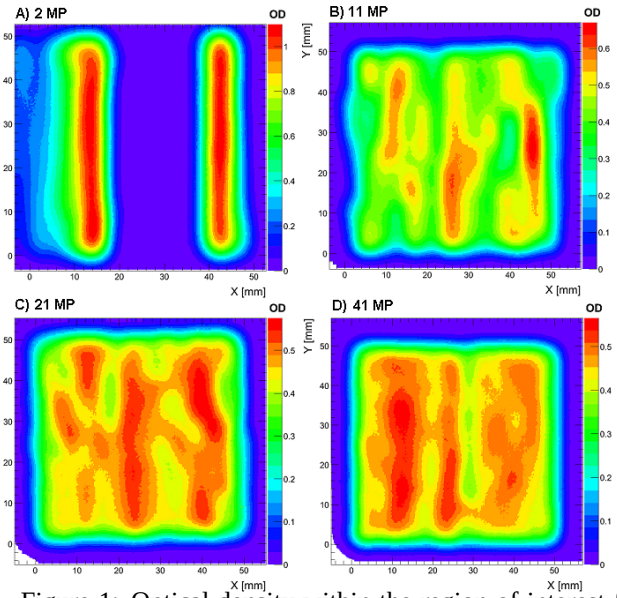

Figure 1: Optical density within the region of interest for tracking experiments (w/o interpolation). The number of used motion phases in the MLUT are: A) 2 MP, B) 11 MP, C) 21 MP and D) 41 MP.

Studying the interpolation between motion phases of the MLUT it can be concluded that the implemented modality can drastically improve tracking of a moving target for this simplified geometry. Studies with patient data are planned.

References

[1] Y.Suh et al., PMB 54, 3821, 2009

[2] N.Saito et al., PMB 54, 4849, 2009

* Work is in part supported by Siemens AG, Particle Therappy
† Work is part of HGS-HIRe

Experimental verification of real-time dose compensation*

R. Lüchtenborg[1,2], *N. Saito*[1], *M. Durante*[1,2], *and C. Bert*[1]
[1]GSI, Biophysics, Darmstadt, Germany; [2]TU Darmstadt, Germany

Introduction

Scanned particle beams are used successfully for treatment of tumors showing no considerable motion during irradiation [1]. Interference between tumor motion and dynamic beam delivery yields distinct patterns of under- and overdose if no countermeasures are taken [2, 3]. Different beam delivery techniques aiming at preserving dose homogeneity in the presence of tumor motion are currently investigated [4]. One of these techniques, namely *beam tracking* (BT), adapts the beam position to the changing tumor position [5]. Taking into account more complex motions than pure translations dose inhomogeneities will occur despite the use of *beam tracking* (BT) [6]. These dose deviations are typically not predictable and thus can only be counteracted in real-time during beam delivery.

A method for *real-time dose compensation combined with beam tracking* (RDBT) has been implemented to the GSI therapy control system (TCS) [7]. While initial results on a rotated but stationary phantom were already presented in [8] results on a phantom moving during dose delivery are presented here.

Material & Methods

A method to evaluate dose changes based on real-time motion measurements and a pre-calculated base data has been implemented to the GSI TCS. Motion induced dose changes for each raster position of the treatment plan are accumulated during beam delivery and the deposited particle number of the respective beam position is adjusted accordingly. Details concerning the TCS implementation can be found in [7].

Treatment plans for a BOX and a SPHERE geometry have been optimized. Nominal dose was 1 Gy. A water phantom equipped with an array of pinpoint ionization chambers has been used for dose measurements [9]. The phantom was placed on a dedicated rotational table. Three different delivery modes have been measured:

- REF: Phantom was in reference position, i.e., not rotated.
- BT: Phantom was rotating between $-14°$ and $10°$. BT was applied.
- RDBT: Phantom was rotating between $-14°$ and $10°$. RDBT was applied.

Dose differences between REF and BT as well as between REF and RDBT have been evaluated. Under- and overdoses were analyzed seperately. RDBT is not expected to shift the mean in the dose difference distribution but rather to yield a more narrow distribution around zero. Thus the Bartlett test at 5% significance level has been used to assess the significance of variance changes in the dose difference distributions of BT and RDBT, respectively.

Results

As can be seen in Table 1 the measured under- as well as overdoses could be reduced when RDBT was used compared to when BT was used. The Bartlett test showed significant variance changes for both geometries.

Table 1: Average ($\pm$ 1 standard deviation) measured under- as well as overdoses in BT and RDBT compared to REF. Dose values are in mGy. Nominal dose was $1000\,$mGy. Only ionization chambers (IC) inside the target volume are considered. The number of ICs for each geometry is listed. Table from [7].

geometry	# ICs	underdose	
		BT	RDBT
BOX	20	$52\,(\pm 36)$	$12\,(\pm 14)$
SPHERE	12	$30\,(\pm 30)$	$24\,(\pm 13)$
geometry	**# ICs**	**overdose**	
		BT	RDBT
BOX	20	$53\,(\pm 30)$	$37\,(\pm 32)$
SPHERE	12	$27\,(\pm 33)$	$13\,(\pm 26)$

Conclusion

The RDBT implementation to the GSI TCS has successfully been verified. Measured under- as well as overdoses were significantly reduced when RDBT was used instead of BT.

References

[1] M. Durante and J. S. Loeffler *Nat. Rev. Clin. Oncol.* **7** (2010).
[2] M. H. Phillips et al. *Phys. Med. Biol.* **37** (1992).
[3] C. Bert et al., *Phys. Med. Biol.* **53** (2008).
[4] C. Bert et al., *Phys. Med. Biol.* **56** (2011).
[5] C. Bert et al., *Med. Phys.* **34** (2007).
[6] C. Bert and E. Rietzel, *Rad. Onc.* **2** (2007).
[7] R. Lüchtenborg et al., *Med. Phys.* **38** (2011).
[8] R. Lüchtenborg et al., *GSI Scientific Report* (2010).
[9] C. Karger et al., *Med. Phys.* **26** 1999.

* Work supported by Siemens Healthcare, Imaging & Therapy, Particle Therapy, Erlangen. Robert Lüchtenborg is member of HGS-HIRe.

Fractionated treatment of moving tumours with scanned carbon ions

J. Wölfelschneider[1,2], T. Friedrich[1], C. Graeff[1], M. Scholz[1], K. Zink[2], M. Durante[1] and C. Bert[1]

[1]GSI, Biophysics, Darmstadt, Germany; [2]TH Mittelhessen, Gießen, Germany

Introduction

Tumour treatment of moving targets with scanned particles induces interplay effects, which cause inhomogeneous dose distributions [1]. These effects have to be compensated. Fractionation is one possible method for motion mitigation and can also actually be implemented in clinical practice. Studies at the National Institute of Radiological Sciences (*NIRS*) in Japan showed promising results with hypo-fractionation of non-small cell lung cancer (*NSCLC*) [2]. Nevertheless, hypo-fractionation seems to be contra-productive for motion mitigation.

In this study, the influence of different fractionation schemes on the homogeneity of the target dose distribution was investigated for lung cancer treatment.

Material & Methods

4D-CT data, including 10 motion states, of a male patient with a NSCLC in the right lower lobe of the lung were used. Using a 4D extension of the treatment planning system TRiP98 together with transformation fields, an internal target volume was created by a propagation of the clinical target volume (*CTV*) from the reference state (end-exhale) to the other motion states. The 3D motion amplitude at isocentre was 21 mm and the tumour volume 160 cm³. To compare the results with the data from NIRS, comparable beam geometries and treatment plan parameters were used. This resulted in four different beam angles per fraction for which the beam intensities were determined in a simultaneous multifield optimization to the RBE-weighted dose.

Dose-per-fraction values for the different fractionation schemes studied were derived from clinical tumour control probability (*TCP*) data of carbon beam treatment in 18 fractions [3]. The dose per fraction was derived via eq. 1 that describes the TCP for different fractionation schemes:

$$TCP = \sum_i \frac{1}{\sqrt{2\pi\sigma}} \cdot e^{-\frac{(\alpha_i-\alpha)^2}{2\sigma^2}} \cdot e^{-Ne^{-n\alpha_i d\left(1+\frac{d}{\alpha_i/\beta}\right)+\frac{0.693T}{T_d}}} \quad (1)$$

To simulate realistic breathing parameters, a surface motion according to Lujan et al. [4] was chosen and 72 possible dose outcomes per fraction were calculated. Thereby, different breathing periods of 2, 4 and 6 s and starting phases of 0, 90, 180 and 270° were varied.

To get the total RBE-weighted dose after each fractionation scheme, randomly chosen dose distributions were taken out of the possible outcomes. By application of the Linear-Quadratic-Linear Model (*LQL*) a total effect per voxel E_v was determined, using equations 2 and 3 [5]:

$$E_v = \alpha D + \beta D^2 \qquad D < D_t \quad (2)$$

$$E_v = \alpha D_t + \beta D_t^2 + (\alpha + 2\beta D_t)(D - D_t) \qquad D \geq D_t \quad (3)$$

A summation of the effect per voxel after each fraction results in the total effect per voxel, which could be recalculated into an effective dose using the LQL-model inversely.

Results

The analysis was mainly focused on the Dose-Volume-Histograms (*DVH*). The figure shows the average DVHs after one, five and ten fractions in a Box-Plot. The error bars indicate the minimum and maximum values; the box quantifies lower and upper quartiles as well as the median.

With increasing number of fractions, the DVHs getting steeper and the error bars shrink. While the interquartile range is greatly reduced after ten fractions, the maximum error range remains at up to 12 %.

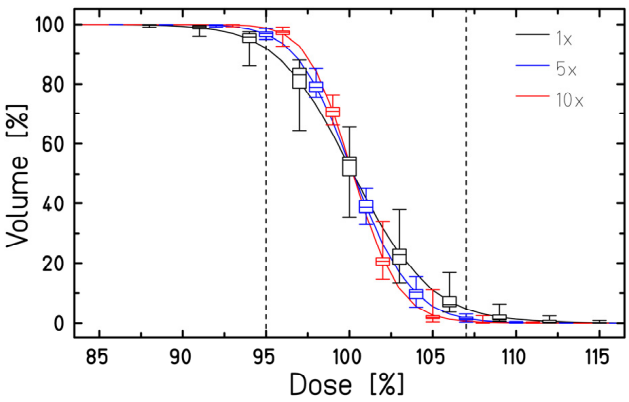

Whisker-Box-Plot of DVHs after 1, 5 and 10 fractions.

Discussion

The homogeneity of the dose distributions improves with a higher number of fractions. But even after ten fractions considerable uncertainty remains and the quality of the stationary irradiation is not reached.

Nevertheless, fractionation with scanned particles is a clinically available possibility to treat moving tumours.

References

[1] Phillips et al., Phys. Med. Biol. 37(1), 1992
[2] Miyamoto et al., Int. J. Radiat Oncol Biol. Phys. 67(3), 2007
[3] Kanai et al., Int. J. Radiat. Oncol. 64(2), 2006
[4] Lujan et al., Med. Phys. 26(5), 1999
[5] Krämer and Scholz, Phys. Med. Biol. 45(11), 2000

Image registration for moving tumour treatment with ion beam*

N. Saito[1], M. Durante[1,2] and C. Bert[1]

[1]GSI, Darmstadt, Germany; [2]TU-Darmstadt, Darmstadt, Germany

Introduction

Image registration technique is widely used to analyse multi-dimensional images. For radiotherapy of moving organs, time-resolved (4D) computed tomography (CT) can be used to extract anatomical changes. A 4DCT data set consists of several 3-dimensional (3D) CT volumes (typically 10), and each volume corresponds to the anatomical 3D image at a motion phase of the breathing cycle. By comparing two image volumes in a 4DCT set, internal motion including organ deformation can be extracted. Image registration has many degrees of freedom to meet a good matching of the images. In this report, the choice of the registration parameters and quality assessment of the performed deformable registration is presented.

Materials and Methods

At GSI biophysics two image registration tools are installed and used for 4D treatment planning studies. This year, the deformable registration software plastimatch [1] has been used for most of the available 4DCT data sets at GSI. Registration parameters have been investigated under a trial with the 4DCT data set that was provided by DIRLab [2,3] with anatomical landmark information in lung. As a measure of registration quality landmark displacement between the reference landmark and the transformed landmark was used and correlation to the corresponding plastimatch score (based on pixel-wise CT value difference) was investigated. Plastimatch B-spline mode was selected to perform deformable registration. Registration has been tested with various combinations of parameters (grid spaces, number of iterations, CT resolutions). The optimized parameters have been used for 10 DIRLab 4DCT data sets.

Results

Correlation of landmark displacement and the plastimatch score showed a linear relation. Therefore the plastimatch score can be used as a measure of registration quality for the tested lung cases. The optimized parameters resulted in two stage B-spline registrations with grid space of 35 and 11 for the first stage and the second stage respectively. An averaged displacement of 300 landmark pairs is shown for each DIRLab 4DCT data set (case 1 to 10) together with the results of DIRLab group [2] in Figure 1. In comparison to the displacements without registration (Fig.1 label noR) the plastimatch registration achieves a good accuracy for all cases except for the cases 7 and 8 with a total average displacement of 1.8mm. The case 8 has CT artefacts that makes the registration difficult. The cases 7 and 8 need further optimization of parameters or improved implementation of the registration algorithm.

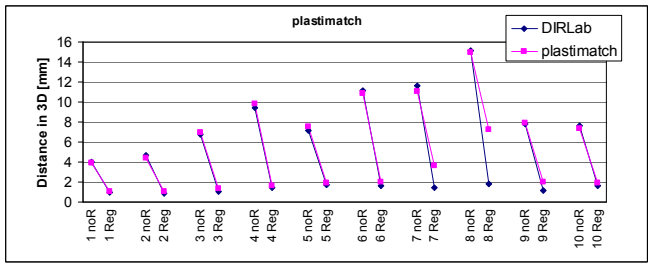

Figure 1: Image registration results as an averaged landmark displacement without registration (noR) and with registration (Reg) by plastimatch (square) and DIRLab (circle) for 10 cases of 4DCTs.

Discussion

In this study the landmark displacement and the plastimatch score showed a linear relation. However in general, pixel-wise matching can be arbitrarily achieved if the structural constrain (e.g. regularization) has not been applied. Therefore inspection of transformation vectors is, in general, worthwhile to be done to judge registration quality when landmark information is not available. The parameters chosen were optimized for case 5 that has a midium motion amplitude among the data in this study. The optimization of parameters could be done in case of insufficient accuracy that can be judged by the output score. As a general tendency, finer spacing of the B-spline grid makes finer adjustment in CT matching, therefore small grid space is preferable at least for the last stage of the registration process. However, it is time consuming and may catch local artefacts. Inspection and regularization of transformation vectors can avoid unrealistic local warps and leads to more practical image registration for treatment planning.

Conclusion

Image registration of 4DCT data sets has been performed with an optimized parameter sets for thorax 4DCT. The accuracy of plastimatch registration was tested with DIRLab data and resulted in 1.8 mm as average displacement for all 10 cases.

References

[1] J.A. Shackleford, et al., Phys. Med. Biol., Vol 55, No 21, pp 6329-6351, Nov 7, 2010

[2] http://www.dir-lab.com

[3] E. Castillo et al, Phys. Med. Biol. 55 305 (2010)

* Work supported by Siemens AG, particle therapy

Range-Dependent Internal Target Volumes for IMPT in Ion Therapy*

C. Graeff[1], *M. Durante*[1], *and C. Bert*[1]

[1]GSI, Darmstadt, Germany

Introduction

Particle therapy offers benefits over conventional photon therapy but also introduces sensitivity to the water-equivalent path length (WEPL) and its potential changes in case of a moving target such as a lung tumor. A common approach to address target motion is the internal target volume (ITV), defined as the CTV but including any target movement, i.e. the union of all CTVs in all motion states (GEO-ITV). Together with e.g. rescanning to counter interplay effects, this allows for sufficient target coverage in the absence of WEPL-changes.

Methods

An ITV that also covers range changes can be defined as the union of all CTVs converted to a WEPL-equivalent axis along beam's eye view [1]. The resulting ITV is field-specific and not suited for Intensity Modulated Particle Therapy (IMPT) [2]. An IMPT-compatible solution can be achieved by using the geometric union of all CTVs as a common target for all fields. A field-specific transformation function converts the WEPL of the geometric union to the actual WEPL-ITV for each field. Such implicitly defined margins are not visible to other fields.

The inhomogeneous fields used in IMPT cause additional problems. Though the fields gradients will match in the reference phase, this is in general no longer the case for other motion phases with differing water ranges. A 4D optimization approach carried out in multiple phases can alleviate this problem. To this end, the optimization is given additional constraints in the form of target voxels from other motion phases, which are combined with the original raster of beam positions to form a new, larger dose correlation matrix. The optimization algorithm itself is not changed.

A complete 4D-optimization includes the CTV in all motion phases but leads to a prohibitively large optimization problem. This approach appears feasible for gating with a reduced number of motion phases. As an alternative, the WEPL-ITV in the reference phase is combined with the CTV from a selected subset of other phases (4D-WEPL-ITV). The selected phases must be representative for the breathing cycle, e.g. end-exhale and end-inhale, to minimize the residual error from neglected motion phases.

Patient Study

The developed methods were applied to a lung tumor patient using a 4 field-treatment plan geometry typically applied at National Institute of Radiological Sciences, Chiba, Japan [3]. For this simulation the CTV and the heart as an OAR with a tolerance dose of 50% of the target dose were considered in the optimization. Heart and CTV partially overlap, so that perfect dose coverage is not possible. The dose was computed using TRiP4D, with a simulated 5 s breathing period and 15 rescans.

Figure 1 shows the DVH for the 4D-dose distribution. While the GEO-ITV leads to a considerable underdose (V95: 90.6%), the WEPL-ITV can correct this at the cost of overdose (V107: 5.6%). The 4D-WEPL-ITV leads to a conformal plan (V95: 98.0%, V107: 1.7%), comparable to a static plan on the CTV in the reference phase. In addition, the more precise range estimate over the whole breathing cycle leads to a reduced OAR dose; in 3D optimization the beam is partially stopped in the OAR.

The 4D-optimization leads to a more homogeneous dose distribution to the individual motion phases, making the method more robust against irregular breathing.

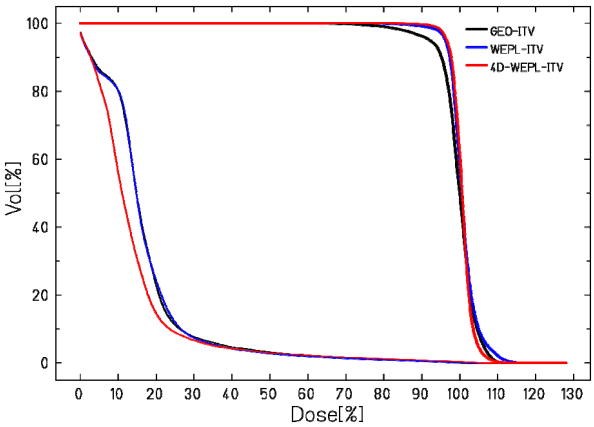

Figure 1: DVH of the 4D-dose to the CTV (bold lines) and the OAR for the 3 ITV plans.

Conclusions

We developed a method to define an ITV that includes changes in range, which together with rescanning can readily be applied to clinical use.
IMPT and the 4D-WEPL-ITV allows for enhanced OAR sparing and good dose coverage of a moving target.

References

[1] E. Rietzel and C. Bert, Med. Phys. 37(2), 2010
[2] A. Gemmel, B. Hasch, M. Ellerbrock et al., Phys. Med. Biol. 53, 2008
[3] T. Miyamoto, N. Yamamoto, H. Nishimura et al. Radiotherapy and Oncology, 66(2), 2003

* Work supported by Siemens AG, Healthcare Sector, Imaging & Therapy Division, Particle Therapy

Raster-file transformation as a first step in adaptive prostate cancer treatment*

S. Hild[1,2], K. Zink[1,2], M. Durante[1,3], and C. Bert[1,#]

[1]GSI, Darmstadt, Germany; [2]TH Mittelhessen, Germany; [3]TU Darmstadt, Germany

Introduction

We are currently developing different treatment approaches for slow moving tumors e.g. tumors of prostate. As the prostate is located between the bladder and the rectum its location and shape is not stable over the entire treatment or even a single treatment course [1]. Sparing the radiation sensitive rectum and ensuring a significantly high prostate dose can therefore be improved with adaptive treatment approaches.

By means of daily computer tomography (CT) scans we plan to adapt or re-optimize the treatment plan with the aim to correct for changes of internal geometry. The time spent for optimization and treatment is limited by the fact that the likelihood of prostate displacement increases with elapsed time [2].

Materials and Methods

To avoid the time consuming biological optimization we adapted the treatment plan calculated on a planning CT to the daily-CT. The raster file is thereby modified in raster point position and energy using the transformation matrix gained from a rigid registration of the daily scan to the planning-CT. Due to a decrease of energy loss in the Bragg peak region with increasing initial energy (Figure 1) the particle numbers also have to be adapted in order to avoid over/under dosage in the target volume:

$$N' = N \frac{(dE/dz)_{peak}}{(dE/dz)'_{peak}} \qquad (1)$$

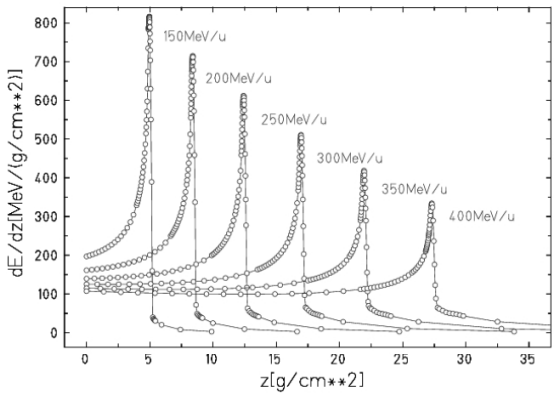

Figure 1: depth dose distribution of C^{12} in H_2O (Basedata extracted from TRiP98 [3])

Results / Current status

We showed the basic proof of concept with simulations on spherical geometries. The over dosage of the adapted plans could be compensated by changing the particle numbers (Figure 2). Changing the particle numbers also effects the pre-irradiation which is responsible for most of the dose to proximal seated raster position. This fact causes the simple approach of adapting the particle number to over / under compensate depending on direction and magnitude of displacement. Simple shifts of up to 2.5cm which would correspond to an extreme prostate displacement could never the less be compensated for.

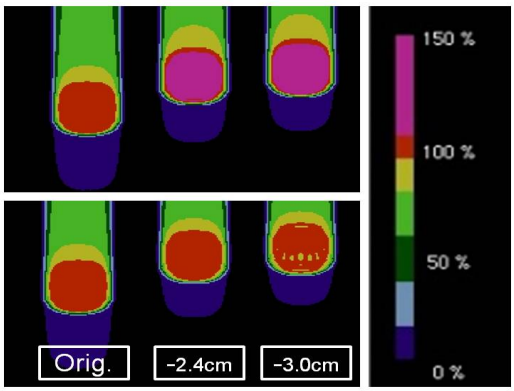

Figure 2: Plan adaptation results on shifted prostate – like geometry. TOP: no particle correction, BOTTOM: with particle correction

Outlook

This adaptation method serves as a first step into fast plan adaptation. It is a rather straight forward method with clear limits concerning its performance. Future work will focus on more elaborate methods to adapt the particle numbers to improve the results and maintain the calculation speed of this process.

[1] C. Peng et al. “Characterizing interfraction variations and their dosimetric effects in prostate radiotherapy”, Int. J. Radiation Oncology Biol. Phys., 2011 Vol 79, No 3, 909-914

[2] K.Langen et al. “Observations on real-time prostate gland motion using electromagnetic tracking”, Int. J. Radiation Oncology Biol. Phys., 2008 Vol 71, No 4, 1084-1090

[3] Krämer et al. “Treatment planning for heavy-ion radiotherapy: calculation and optimization of biologically effective dose” Phys. Med. Biol., 2000 Vol 45, 3319–3330

* In part funded by Siemens AG, Particle Therapy.

#c.bert@gsi.de

Rescanning - phase dependence experiments with a moving phantom*

D. Müssig[1,2,3], M. Durante[1,2], and C. Bert[1]

[1]GSI, Darmstadt, Germany, [2]TU Darmstadt, Germany, [3]HGS-HIRe

Introduction

Treatment of moving targets can result in local over and under dosage due to interference effects of the beam application and the motion of the target. First experimental studies [1] as well as theoretical works [2, 3] showed that multiple irradiations with an accordingly reduced dose per irradiation reduce these inhomogeneities due to averaging effects. If the multiple irradiations are performed within one fraction this method is called rescanning.

Since rescanning is based on statistical smoothing of the dose, there is - at least for low rescan numbers - a certain likelihood that the generated cold and hot dose spots are beyond the ICRU-50 limits of 95/107% of the prescribed dose.

In the scope of this work we performed irradiations of radiographic films with simple geometries with slice by slice rescanning. Different starting phases were investigated.

Material & Methods

Experiments were performed at the Heidelberger Ion Beam Therapy Center (HIT). The experiment plan was designed close to extreme moving conditions expected in patients since it can be assumed that more realistic conditions will yield even better results. We chose an amplitude of 5 cm peak-to-peak perpendicular to the beam direction with a sinusoidal motion and a period of 5 seconds.

The irradiation plan was designed with the following parameters. We used an energy of 200.28 MeV/u, a raster grid of 2x2 mm^2 with a particle number of 1.6×10^6 per rasterpoint, a beam intensity of 8×10^7 s^{-1} and slice-by-slice rescanning with a scanpath perpendicular to the motion direction [4]. To account for motion we expanded the target area of 5x5 cm^2 to an internal target area of 10x5 cm^2.

To achieve comparable motion conditions for each single measurement we build a phantom which can move up to six Kodak X-Omat V films simultaneously with a phase difference of 60°. Films are stacked in beam direction. To minimize the influence of slightly different depth and of different conditions in the developing process, a homogeneous area was irradiated on each film without motion. All data are normalized to this area.

We report absolute homogeneity $H = \sigma/\mu$ values, with σ as the standard deviation and μ as the mean value of the optical density of the X-ray films in the target area.

Results

Figure 1 shows the dependence of the homogeneity in the target area on the number of rescans. As expected, the homogeneity approaches the reference value with increasing rescan numbers and is in some cases even superior. Notably, the rescan numbers R = 5 and 7 show the statistical character since there is always some likelihood that the homogeneity decreases despite an increased number of rescans. In addition, the strong phase dependence of rescanning is very obvious in this region

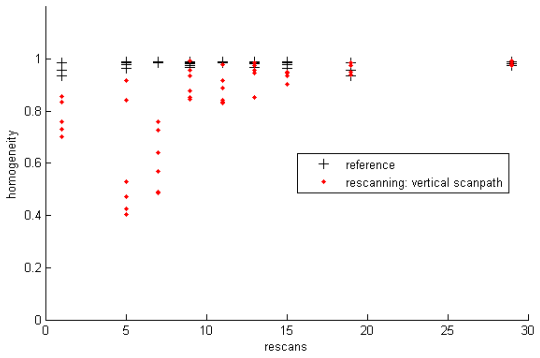

Figure 1: phase dependence of the homogeneity as a function of the rescan number

Discussion

A recently published article [5] shows simulation results for proton beam therapy that state that even in the region $1 \leq R \leq 6$ there is almost no difference in the homogeneity due to phase variations if all the other parameters are kept constant. These results are conflictive with our experimental findings. This might be due to the fact that patient plans were used in these simulations. Due to multiple fields and numerous iso-energy slices patient plans benefit of an intrinsic rescanning effect (each field can be considered as a volumetric rescan, proximal energy slices are rescanned due to dose contributions from distal slices). Patient plans therefore tend to give better outcome than artificially designed plans.

For comparison, we plan rescanning simulations for patient geometries with a carbon beam as a next step.

References

[1] Bert et al., GSI Scientific Report 2008, 397
[2] Philips et al., Phys. Med. Biol. 37 (1992), 223-243
[3] Bortfeld et al., Phys. Med. Biol. 47 (2002), 2203-2220
[4] Seco et al., Phys. Med. Biol. 54 (2009), 283-294
[5] Knopf et al., Phys. Med. Biol. 56 (2011), 7257-7271

* This work is in part supported by Siemens AG, Particle Therapy and the EU-FP7 project ULICE (Union of Light Centres in Europe)

Simulation of uncompensated and gated treatments of a liver cancer patient with scanned carbon ions*

D. Richter[1,2], *N. Saito*[1], *P. Steidl*[1,2], *M. Härtig*[3], *O. Jäkel*[4], *M. Durante*[1,2], *and C. Bert*[1]

[1]GSI, Darmstadt, Germany; [2]Technische Universität Darmstadt, Physics Dep., Germany; [3]Universitätsklinikum Heidelberg, Germany; [4]Deutsches Krebsforschungszentrum, Heidelberg, Germany

Introduction

In scanned ion beam radiotherapy interference of the dynamic beam delivery and moving organs can lead to clinically unacceptable under- and over-dosage in the target volume and critical irradiation of healthy tissue [1]. Gating is a proposed technique to mitigate these effects by irradiation of the target in a pre-defined window only [2] and clinically available at HIT. The choice of the gating window (GW) size is an issue in treatment planning for gated beam delivery. We compared uncompensated and gated beam delivery with different GW sizes for a patient with hepatocellular carcinoma in treatment planning simulations.

Materials and Methods

A 4DCT of a liver patient was used as the basis for the treatment planning simulations. Deformable registration of the 4DCT was performed with the open source software *Plastimatch* [3]. The target volume and critical structures were delineated by a physician on a 3DCT of the patient and propagated to the end exhale 4DCT phase. Contour propagation, treatment plan optimization and dose calculations were performed with the in-house 4D treatment planning system TRiP4D [4]. The target dose of the reference phase CTV was optimized to 8.1 Gy(RBE) using a carbon ion beam. The standard beam parameters for liver treatments at HIT were used (2 mm raster, 3 mm iso-energy slice spacing, 10 mm beam FWHM).

Inputs to the 4D treatment simulations were the treatment plan, a breathing trajectory of the patient and a simulated beam delivery sequence (BDS) describing the chronology of the irradiation. For uncompensated treatment sixteen different starting phases were chosen by shifting the patient trajectory in 200 ms steps. GWs of 20, 30 and 50 % of the amplitude range around the end exhale phase were used for gating. Simulation of the BDS was performed using a dedicated software which takes into account the technical framework of the HIT accelerator and the respective motion trajectory (for gating). Analysis was performed by visual inspection of the dose distributions and calculation of dose volume histograms (DVHs).

Results

Figure 1 displays DVHs for uncompensated (gray) and gated treatments (blue) for the CTV, the Liver and the remaining tissue. Under- and over-dose is improved for gating in general and increasing for smaller GWs. For gating with a 20% GW more than 99 % of the volume receive at least 95 % of the planned dose. Dose to the healthy tissue dose remains largely unaffected for both the uncompensated and gated treatments.

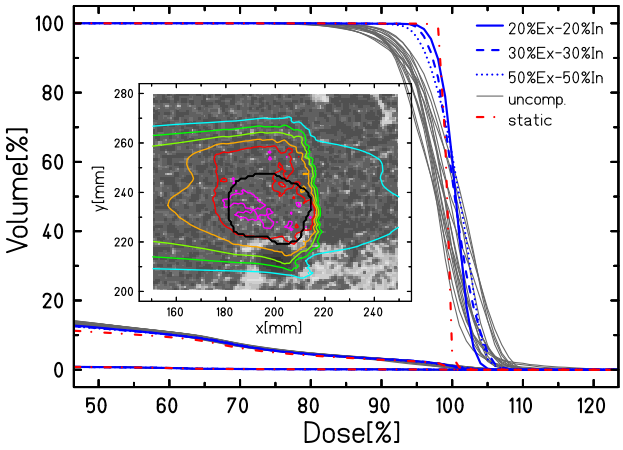

Figure 1: DVHs for uncompensated (gray) and gated treatments (blue). The small figure shows a representative dose distribution out of the 16 calculated distributions.

Discussion

Results indicate that dose coverage can be significantly improved using gated beam delivery compared to uncompensated treatment. Additional use of an internal target volume (ITV) is expected to further improve dose coverage. However, also healthy tissue dose is expected to increase. In this particular case we could not observe a strong impact of interplay on the healthy tissue dose which can be attributed to the motion pattern and the plan geometry.

Acknowledgments

We thank N. Chaudhri, D. Habermehl and K. Parodi from the university clinic of Heidelberg and HIT for providing us with the patient and base beam data for this study.

References

[1] J. Lambert et al., *Phys. Med. Biol.* (2005) **50**:4853–62.

[2] S. Minohara et al., *Int. J. Radiat. Oncol.* (2000), **47**:1097–1103.

[3] G. Sharp et al., *Phys. Med. Biol.* (2007) **52**:5771-83.

[4] D. Richter et al., *GSI Scientific Report* (2010) 476.

* Work is part of HGS-HIRe for FAIR

4D Optimization for Ion Rasterscanning of Moving Tumors*

J. Eley[1], *C. Gräff*[2], *M. Durante*[2], *W. Newhauser*[3], *and C. Bert*[2]

[1]The University of Texas Graduate School of Biomedical Sciences, Houston, TX, USA;
[2]GSI Helmholtz Centre for Heavy Ion Research GmbH, Darmstadt, Germany;
[3]Louisiana State University, Baton Rouge, LA, USA

Introduction

Efforts to mitigate dosimetry problems caused by organ motion during ion scanning have been underway for several years [1] and show potential that scanned ion beams may eventually be used to treat moving tumors, e.g., lung cancers. However, the optimal motion mitigation approach has not been fully established and likely depends on the specific site of organ motion. The purpose of the current work was to develop a spatiotemporal (4D) optimization approach for scanned ion therapy of moving tumors using beam tracking [2]. The focus was to reduce dose to nearby healthy tissues, compared to a 3D optimized beam tracking approach. The rationale was that 4D optimization of ion fluence provides more degrees of freedom to attain plan objectives than 3D optimization approaches for moving tumors.

Methods and Materials

4D optimization algorithms were developed using the C programming language and implemented in a research version (TRiP4D) of the TRiP98 treatment planning system [3, 4]. Existing conjugate gradient (3D) optimization codes in TRiP4D were extended to perform 4D optimization. For example, the calculation of a dose correlation matrix (i.e., dose per number of incident particles for each pencil beam) was extended to include correlations for (1) all pencil beams to (2) all target and organ-at-risk voxels for (3) all motion states.

Carbon ion dose distributions were simulated using TRiP4D for 3D optimized tracking and 4D optimized tracking. For 3D optimized tracking, pencil beam fluence, planned for a reference motion state, was equally distributed to each motion state with appropriate beam tracking offsets. For 4D optimized tracking, pencil beam fluence was varied for individual pencil beams for each motion state to reach plan objectives, i.e., 100% of prescription dose to the target and less than 10% of prescription dose to the avoidance volume.

To evaluate the 4D optimization code, a hypothetical, spherical target with 3 cm diameter was simulated in a moving water slab phantom with an avoidance volume positioned in a proximal, static 2 cm depth water slab. Sphere target motion was described by $x(t) = A_x sin^4(\omega t/2)$ with an amplitude $A_x = 2$ cm and angular frequency $\omega = 2\pi/4$ (radians / s).

* Work supported in part by Rosalie B. Hite Fellowship, The University of Texas M. D. Anderson Cancer Center, Houston, USA.

Results and Discussion

Results of 4D optimized ion tracking therapy are compared with 3D optimized tracking in Figure 1. Both methods achieved similar target dose coverage, indicated by the red colorwash region (95-105% of prescription dose), and similar dose fall-off lateral and distal to the target. However, dose in the static avoidance volume was greatly reduced using 4D optimized tracking instead of 3D optimized tracking. In order to maintain target dose coverage, fluence for pencil beams that did not intersect the avoidance volume was increased, resulting in higher dose regions in the proximal slab lateral to the avoidance volume for 4D optimized tracking, compared with 3D optimized tracking.

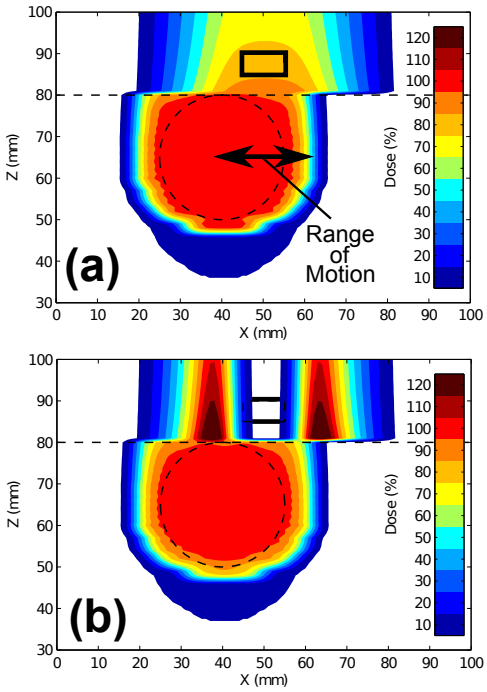

Figure 1: Dose color planes for (a) 3D and (b) 4D optimized tracking. Moving sphere target (dashed circle) with static avoidance volume (black rectangle). Carbon beams incident in $-z$ direction.

References

[1] C. Bert and M. Durante, Phys Med Biol, **56** (2011) R113-44.
[2] S. Grözinger et al, Radiother Oncol, **73** (2004) S77-9.
[3] M. Krämer et al, Phys Med Biol, **45** (2000) 3299-317.
[4] D. Richter et al, GSI Annual Report, 2010.

The Status of the FIRST Project

R. Pleskac on behalf of the FIRST collaboration

GSI Helmholtzzentrum für Schwerionenforschug GmbH, Darmstadt, Germany

The FIRST experiment (Fragmentation of Ions Relevant for Space and Therapy) [1,2] started extensive measurements on projectile fragmentation with the ^{12}C at 400 MeV/u beam on a thin 8 mm graphite and 0,5 mm Au target behind the SIS18 accelerator in cave C in August 2011.

The original ALADiN detector setup was modified several times in order to perform high-accuracy measurement [3]. The major changes were done mainly in the target region in front of the magnet. The target vacuum chamber was completely omitted and all small area detectors as a start scintillator, a beam monitor, a target holder with several targets, a silicon vertex and a Kentros detector were mounted in the air. The pre-target reaction probability is less than one percent in this case [4] and technical realization of the detector setup is much simpler. The start detector [5] is a 250 μm thin scintillator disc delivering the trigger signal for the DAQ system and start signal for time-of-flight measurements. The beam monitor [5] is a drift chamber consisting of 6 planes of vertical and horizontal wires, filled with the Ar/CO_2 (80/20) gas mixture and determining trajectory of primary beam particles in front of the target. The silicon pixel detector [6] is based on MIMOSA26 sensors organized in 4 planes and performing the tracking of charged particles in front of the magnet in a very accurate way. The Kentros [7] is measuring the energy deposition and time-of-flight of charge particles at angles from 5º to 90º relative to the beam. Behind the magnet large area detectors from the former ALADiN experiment as TP -MUSIC-IV and TOF wall were applied in order to measure the position, energy loss and time-of-flight of charge particles at small angles relative to the beam. At the end the LAND was included to measure high-energy neutrons.

Preparative works for the experiment started already in September 2009. The MUSIC detector, its gas purification system and the TOF wall were tested both in cave B and C at GSI experimental facility. A large area vacuum window for the rear side of the ALADiN magnet was produced and tested in the technology laboratory at GSI. The target region consisted fully from brand-new detectors. The start detector, beam monitor and vertex detector were developed, built and tested in different beams by INFN in Italy and by IPHC in France. The Kentros detector was planned and built within one year by INFN. During the main experiment all detectors showed a very good and stable performance apart the large MUSIC which had to be completely excluded from the measurement because of a problem with the HV on the cathode (~ 20 kV). The exact cause will be investigated in the detector laboratory at GSI during first months in 2012. The time resolution of the start scintillator was 150 ps with an outstanding stability of 5 ps during the whole experiment. The position resolution of the beam monitor was 140 μm and time resolution of the Kentros about 250 ps.

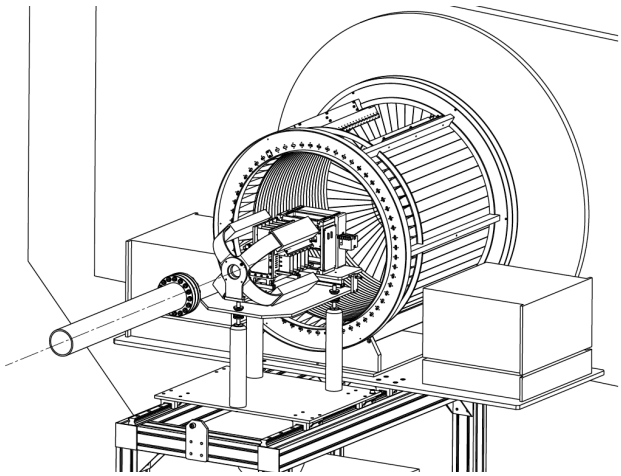

Figure 1: interaction region of the FIRST experimental setup (area in front of the ALADiN magnet)

The data was collected by MBS based DAQ system with the rate of ~ 350 Hz and about of 37 million of events were recorded for both reaction systems. Although the MUSIC was completely excluded from the DAQ system, tracks of charged particles can be reconstructed by means of the silicon vertex detector and complete data analysis can be performed. Preliminary results show a good quality of the data. At present the collaboration considers a possibility to replace the MUSIC by another tracking detector in order to increase the accuracy of the measurement in our future experiments.

References

[1] FIST Collaboration, "Extensive Study of Nuclear Reactions of Interest for Medical and Space Applications", Project Proposal, January 2009

[2] R. Pleskac, "The Status of the FIRST experiment", GSI Scientific Report, Darmstadt, 2009

[3] R.Pleskac et al., "The FIRST experiment at GSI", submitted to NIM A, January 2012

[4] T.T. Böhlen, "The FIRST experiment: Status of vertex analysis", this issue

[5] E. Iarocci et al., "Beam Monitor and Start Counter detectors for the FIRST experiment", this issue

[6] Ch. Schuy., "The FIRST experiment: Status of vertex analysis", this issue

[7] Ch. Golosio., "The Kentros detector for the FIRST experiment", this issue

[8] C. Schuy, "The FIRST experiment: Status of the MUSIC", GSI Scientific Report, Darmstadt, 2010

The FIRST experiment: Status of vertex analysis

C. Schuy on behalf of FIRST collaboration[*1,2]
[1]GSI, Darmstadt, Germany; [2]TU Darmstadt, Germany

Overview

The FIRST (Fragmentation of Ions Relevant for Space and Therapy) experiment was performed in August 2011 at GSI's cave C with the aim to measure double-differential cross sections using ^{12}C ions at 400 MeV/u on carbon and gold targets. The experimental setup as well as the reconstruction software is based on the ALADIN setup [1] with a newly designed interaction region [Figure 1]. It consists of thin EJ-228 scintillator attached to 4 PMTs as a start counter, a drift chamber with 36 sensing wires arranged in 6 planes as beam monitor, 8 MIMOSA-26 silicon pixel sensors [3] arranged in 4 planes with an active area of 21.2*10.6 mm^2 each as Vertex Detector and KENTROS (Kinetic Energy and Time Resolution optimized on Scintillator) to measure time of flight and energy release of fragments. The data acquisition was developed using the GSI Multi Branch System (MBS [4]) utilizing all the needed readout modules as well as handling the trigger logic. Because of an anomaly in the detector the TP-MUSIC IV could not be used durring the experiment which lead to an increase of the event rate to 350 Hz. A total of 37 million events were collected as well as runs with special conditions used for e.g. calibration purposes. A detailed description of the experimental setup is reported in [2]. A full report on detector performance will be submitted in the near Future.

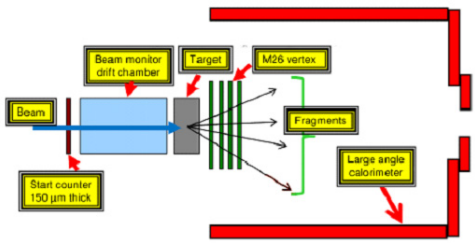

Figure 1: Schematic of interaction region.

Status of vertex analysis

Alongside improvements in the data reconstruction framework, implementation of the alignment the low level analysis is currently in progress and will yield first results in early 2012. Currently the analysis of the vertex is focused on:

- Multiplicity analysis of number of tracks in vertex vs. number of hits in TOF wall and Kentros
- Angular distribution of tracks in vertex
- Matching of beam monitor and vertex

Preliminary analysis of number of events with reconstructed tracks vs. number of physical trigger shows a tracking efficiency of about 98%. Most of these tracks consist of four or more clusters. The distribution of the total number of clusters per plane is quite uniformly.
The code for the multiplicity analysis is currently under development and a first version, with vertex and TOF wall implemented, shows reasonable results. The final code should be avaliable early 2012.
The angular distributions of reconstructed tracks is currently calculated for all available runs. First plots show reasonable behavior.

The low level analysis results will be compared to a monte carlo simulation as soon as all results are avaliable.

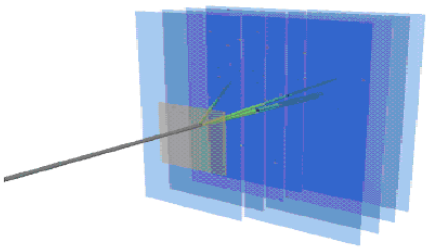

Figure 2: Vertex event display: the target and incoming beam and the 8 sensor planes are shown. The reconstructed clusters and tracks of a fragmented event are also depicted [5].

References

[1] C. Schuy and R. Pleskac on behalf of FIRST collaboration, "FIRST project: Status of TP-MUSIC IV", GSI scientific report, 2010.

[2] R. Pleskac et al., "The FIRST experiment at GSI", Nuclear Instruments and Methods in Physics Research, 2012 (in press)

[3] http://www.iphc.cnrs.fr/-CMOS-ILC-.html

[4] N. Kurz, http://www-win.gsi.de/daq/Docs/mbs_Apr-2006.pdf

[5] C. Fink, personal communication 2011

* Work is part of HGS-HIRe.

Beam Monitor and Start Counter detectors for FIRST experiment

E. Iarocci[c,h], *A. Paoloni*[c], *V. Patera*[c,h], *L. Piersanti*[c,h], *A. Sarti*[c,h], *and A. Sciubba*[c,h]

[c]Istituto Nazionale di Fisica Nucleare - Laboratori Nazionali di Frascati, Italy; [h]Dipartimento di Scienze di Base e Applicate per l'Ingegneria, "La Sapienza" Università di Roma, Italy

for the FIRST collaboration.

The Beam Monitor and Start Counter detectors for the FIRST experiment

The FIRST (Fragmentation of Ions Relevant for Space and Therapy) experiment[1] is performed at GSI heavy ion synchrotron (SIS) in Darmstadt. Its aim is to measure carbon fragmentation at different energies between 100 and 1000 MeV/u. The requested precision on fragment mass separation directly translates into performance requirements (time and momentum resolution) for all the detectors that are used in the FIRST experiment. Here we review two Interaction Region target upstream detectors: the thin scintillation counter (Start Counter) and the drift chamber (Beam Monitor) .

The Start Counter has been designed for triggering and timing purposes. It has been optimized through a careful balancing of detector time resolution (time of flight measurements will be used to disentangle the different fragments) and thickness minimization. The design goal was to have a pre–target beam interaction probability nearly 1% with respect to the on–target one, reducing to a negligible amount the Start Counter contribution to the cross section measurement systematics.

In FIRST a 5–8 mm thick graphite target was foreseen, so the final final Start Counter layout, taking into account the different material density and interaction cross sections, was designed as a 250 μm thick disc, 52 mm diameter, of plastic scintillator (EJ-228). Light is collected by means of 160, 1 mm diameter, step-index plastic optical fibers (reference standard: IEC 60793-2-40) radially glued and grouped in four bundles, and finally connected to four fast Hamamatsu UBA H10721-201 photo-multipliers (40% quantum efficiency). The fibers have a low attenuation (¡ 200 dB/km) for the scintillator output wavelength (400 nm) and their layout has been chosen in order to maximize the light collection from the scintillator. A picture of the Start Counter is shown in Fig. 1.

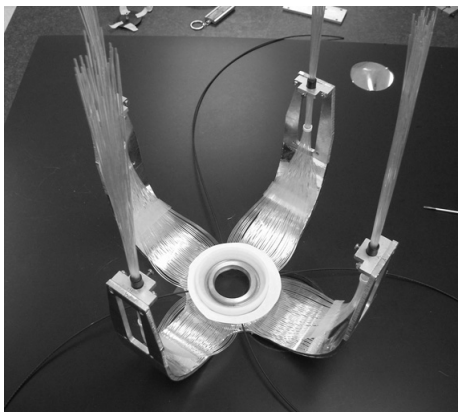

Figure 1: Start Counter picture.

The Beam Monitor is a drift chamber designed for charged particles trajectory reconstruction. This detector provides the ion position on the target, together with valuable information on possible projectile pre–target fragmentation. The design performances for fragmentation measurements in FIRST are a single cell spatial resolution $<$ 200 μm with an high particle detection efficiency. The detector is made of alternated horizontal and vertical wire layers (or planes). Each layer is composed of three rectangular cells, 16 mm x 10 mm along the beam direction, for a total of 36 sense wires. The geometrical layout has been optimized in order to minimize beam interactions with the wires. The twelve planes (six on each "view") provide tracking redundancy and ensure a high tracking efficiency and an excellent spatial resolution. In order to minimize tracking ambiguities, the consecutive layers of each view are staggered by half drift cell.

Detector performance in the FIRST experiment at GSI

The FIRST experiment took data on August 2011, performing 400 MeV/u ^{12}C on 8 mm graphite and Au collisions. In order to assess the Start Counter efficiency we required at least one photomultiplier fired when a carbon ion is traversing the detector. The efficiency, for an applied threshold of 30 mV was stable around 99.5% during the whole data taking. Also time resolution has been measured fitting with a gaussian the distribution of the time difference between two selected photomultipliers. The time resolution showed an outstanding stability during all the experiment, with a fluctuation of ≈ 5 ps around an average value of $\sigma_t \approx 150$ ps. The Beam Monitor was operated, at GSI, at 1.8 kV with and Ar/CO_2 (80%/20%) gas mixture. Drift chamber spatial resolution was found to be really stable during the data taking with an average value of $\sigma_x = 140$ μm.

References

[1] V. Patera, "Nuclear physics experiment for hadrontherapy application", Nuovo Cimento C 34, n.6

Monte Carlo Simulation of the FIRST Experiment*

T.T. Böhlen on behalf of the FIRST Collaboration[1,2]

[1]European Organization for Nuclear Research CERN, CH-1211, Geneva 23, Switzerland; [2]Medical Radiation Physics, Karolinska Institutet and Stockholm University, Box 260 S-171 76 Stockholm, Sweden

Introduction

Nuclear fragmentation processes of ions are of importance in several fields of basic and applied physics. Detailed fragmentation measurements are required in particular for the development and verification of models describing radiation fields for ion beam radiotherapy and space radiation protection. The scientific program of the FIRST (Fragmentation of Ions Relevant for Space and Therapy) experiment at GSI (Gesellschaft für Schwerionenforschung, Germany) aimes to provide accurate measurements of ion fragmentation cross sections at beam energies between 100 and 1000 MeV/u, details see [1, 2]. The general Monte Carlo (MC) simulation of the FIRST experiment provides simulated detector response data of a full FIRST event. It aims at supporting design decisions, the optimization of the experimental set-up and providing training data for the reconstruction software in the preparatory stage of the experiment. In the data analysis phase, it facilitates the evaluation of acceptances, reconstruction efficiencies and other systematics. The simulation of the particle transport and interactions is based on the multipurpose MC code FLUKA [3, 4]. In addition to an accurate description electromagnetic processes, FLUKA was shown to provide a modelling of nuclear interactions which is judged to be satisfactory in the energy regime of FIRST [5, 6].

Structure of the simulation

The implementation of the general FIRST simulation breaks up into several sub-sectors: (1) description of set-up configuration (beam phase space, set-up geometry and materials, parameters describing detector properties and the magnetic field), (2) particle transport with the MC code FLUKA and retrieval (scoring) of basic physical quantities of the tracks (i.e., primary particles and created secondary particles which are propagated through the detector geometry) and hits (i.e., energy depositions of tracks in sensitive detector elements), (3) modelling of the subdetector responses and digitization, and (4) storing of simulated track, hit and detector signal data for further processing and analysis. The data flow of the simulation is illustrated in figure 1. In order to facilitate a flexible and object-oriented coding of the geometry and processing of the MC simulation data, the FORTRAN77-based FLUKA code was interfaced with C++. Amongst others this allows the smoothless conversion and storage of virtually arbitrarily large simulated event samples in the ROOT tree format [7]. The reconstruction and analysis software of the FIRST experiment reads and processes the MC events from the ROOT files.

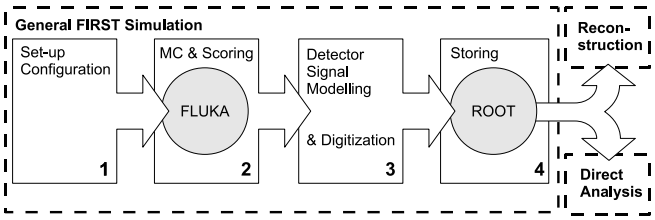

Figure 1: Data flow of the simulation.

The experimental set-up was implemented including all eight sub-detectors and the ALADiN spectrometer. The geometry of the detectors is modelled with a considerable detail, e.g. including wires of the beam monitor and the 192 scintillator slats of the two walls of the TOFWALL, and implementing materials such as vacuum windows and gases which the primary beam and the created fragments traverse before their detection.

The focus of the signal modelling in the general simulation is to be able to predict the sub-detector responses in terms of their principal features, the characteristics of the measured signals and eventual effects on the reconstructed physical quantities, such as charge collected, position resolution, etc.

Conclusion

The FIRST MC simulation supports the FIRST experiment in the design phase and during data analysis. The deployment and evaluation of the software is currently in progress.

References

[1] V. Patera et al., Nucl. Instrum. Meth. A (2012), submitted.

[2] Z. Abou-Haidar et al., J. of Instrum. (2012), accepted.

[3] G. Battistoni et al., "The FLUKA code: Description and benchmarking", Proceed. of the Hadronic Shower Simulation Workshop 2006, AIP Conference Proceed. 896 (2007) 31–49.

[4] A. Ferrari et al., "FLUKA: a multi-particle transport code", CERN-2005-10, INFN/TC_05/11, SLAC-R-773 (2005).

[5] T.T. Böhlen et al. Phys. Med. Biol. 55 (2010) 5833–5847.

[6] F. Sommerer et al., Phys. Med. Biol. 51 (2006) 4385-4398.

[7] R. Brun, F. Rademakers, Nucl. Instrum. Meth. A 389 (1996) 81-86.

* This research project has been supported by a Marie Curie Early Initial Training Network Fellowship of the European Community's Seventh Framework Programme under contract number (PITN-GA-2008-215840-PARTNER).

The KENTROS detector for the FIRST experiment*

B. Golosio[1,2] for the FIRST collaboration

[1]Università di Sassari, Italy; [2]Istituto Nazionale di Fisica Nucleare, Sezione di Cagliari, Italy.

KENTROS (Kinetic ENergy and Time Resolution Optimized on Scintillator) is a relatively compact detector for charged particles energy deposition and time of flight (TOF) measurement. The angular region covered by KENTROS goes from about 5 degrees up to about 90 degrees polar angle between the detected particles and the beam direction. The active part of the KENTROS detector is made of organic scintillator modules and scintillating fibers. The modules are made using the EJ-200 fast scintillator by Eljen technology, which has a decay time of 2.1 ns, 10000 photons/MeV light yield, 425 nm wavelength of maximum emission, 1.58 refractive index, 4 meters attenuation length. The scintillating fibers are 1 mm diameter BCF-10 fibers by Bicron, which have a decay time of 2.7 ns, 8000 photons/MeV light yield, 432 nm wavelength of maximum emission, 1.60 core refractive index, 2.2 meters attenuation length. The signal is read using silicon photomultipliers (SiPM) by AdvanSiD, 4x4 mm^2 active area, which are relatively cheap and have excellent timing resolution. The scintillation light is driven from the scintillator modules to the SiPM using plexiglass light guides.

The detector, shown in Fig. 1, has a cylindrical shape, and is structured in three main parts: a barrel, which will detect particles with polar angle between about 36 and about 90 degrees, a big endcap, for particles with polar angle between about 15 and about 36 degrees, and a small endcap, for particles with polar angle between about 5 and about 15 degrees. In Fig. 2, the TDC time as a function of the QADC counts, measured by a single module of the KENTROS small endcap, is shown. The shape of the distribution is influenced by the time-walk effects which must be corrected. The two regions in the scatter plot on the top-left and on the bottom-right correspond to the ion fragments with Z=1 and Z=2, respectively. The time resolution of the detector in our experimental conditions was measured to be about 250 ps. The time of flight and the energy release, combined with the information on the tracks reconstructed by the vertex detector, will be used to evaluate the fragment kinetic energy.

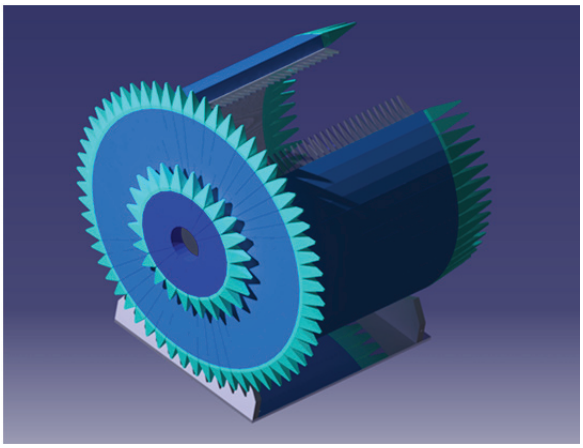

Figure 1: three-dimensional view of the KENTROS detector.

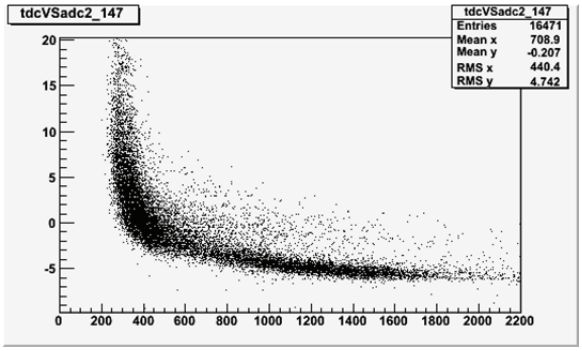

Figure 2: TDC vs QADC counts measured by a single module of the small endcap. The two regions in the scatter plot on the top-left and on the bottom-right correspond to the ion fragments with Z=1 and Z=2, respectively.

The ESA Space Radiation Laboratory at GSI*

M. Durante[1,2] and O.Angerer[3]

[1]GSI, Darmstadt, Germany; [2]TU Darmstadt, Germany; [3]ESA-ESTEC, The Nordwijk, The Netherlands.

The IBER-08 project has been successfully carried out at GSI and has produced interesting preliminary results for risk estimates [1-3]. The new announcement of opportunity IBER-10 has been issued by ESA in 2010. A workshop with scientists potentially interested, who had submitted a LoI, was held at GSI on 24.11.2010. During the workshop, the investigators of the previous IBER project presented their results and status reports.

The GSI Bio-PAC met at ESTEC on February 21-22, 2011. A total of 15 out of 28 proposals were selected with scores from "very good" to "excellent". The topic distribution of the proposals is given in Table 1.

Main Topic	Subtopic	Proposals
Noncancer effects	Cardiovascular diseases	2
	Eye	2
	Membranes	1
	Bones	1
	CNS	1
Carcinogenesis	DNA repair	4
	Biodosimetry	2
Countermeasures	Biological	1
	Physical	1

Table 1: topics of the selected proposals

As to the geographical distribution, 10 proposals are fom Germany, 3 from Italy, and one each from Belgium and Greece. The reports of the selected experiments follows this report and represent the ESA-section in the 2011 Annual Report.

Figure 1: inauguration of the ESA Space Radiation Laboratory (SRL), former Annex building, at GSI on 16.11.2011

* Project supported by the ESA-TIBER grant

To host the new research program, the ESA Space Radiation Laboratory (ESA SRL - former Annex building for therapy) has been inaugurated officially on 16.11.2011 (Figure 1).

Figure 2. The air conditioning supply for the ESA SRL installed at GSI. The system allows air exchange and temperature control.

The air conditioning-filter-air exchange system is shown in Figure 2. The new chemistry and tissue culture laboratories include state-of-the-art S1 flowboxes and incubators. ESA SRL includes two office spaces and a warehousing (Lager). It will be used by external users in the 1st IBER-10 beamtime in 2012 (March-April).

References

[1] O.Angerer and M.Durante, "Status of the ESA project at GSI", GSI Annual Report 2010, p. 493, http://www.gsi.de/informationen/wti/library/scientificreport2010/index.html#HEALTH.

[2] M.Durante, D. Schardt, S. Metzger and O.Angerer "Status of the ESA projects at GSI", GSI Annual Report 2009, p. 509, http://www.gsi.de/informationen/wti/library/scientificreport2009/#RADIATION-BIOPHYSICS

[3] M. Durante, G. Reitz and O. Angerer, Space radiation research in Europe: flight experiments and ground-based studies. *Radiat. Environ. Biophys.* **49** (2010) 295-302.

Analysis of electrophysiological characteristics of cardiomyocytes following radiation exposure*

F. Steger[1,2], S. Ritter[2]
A. Daus[1], J. Frieß[1] and C. Thielemann[1]

[1]biomems lab, University of Applied Sciences Aschaffenburg, [2]biophysics division, GSI, Darmstadt

Motivation

There is increasing evidence that the exposure to ionising radiation can have adverse effects on the cardiovascular system [1, 2]. These effects usually occur many years after the exposure. Yet, little is known on the effects of high LET radiation. With the increasing use of heavy ions in cancer therapy, an assessment of their possible cardiovascular late effects is important, in particular when young patients are treated. Likewise, for manned space missions the risk of developing adverse cardiovascular effects by exposure to space radiation must be seriously considered [3]. To address the question, if and to what extent an exposure to heavy ions affects cardiac function, avian cardiomyocytes were irradiated with C-ions and the electrophysiological functionality of the cardiac cells was measured with microelectrode array chips (MEAs). For comparison cells were exposed to X-rays.

Material and Methods

Cardiomyocytes were isolated from embryonic chickens at stage E8 and cultivated [4]. To detect electrophysiological changes, cells were seeded onto MEAs (Fig. 1). These chips contain an array of 60 microelectrodes with a diameter of 30 µm able to extracellularly record cardiac action potentials.

To study the effects of low and high LET radiation, cardiomyocytes were exposed at GSI to X-rays (250 kV, 16 mA, 1 mm Al and 1 mm Cu filtering) or C-ions (25-mm extended Bragg peak, energy range: 106-147 MeV/u with a mean LET of 75 keV/µm at sample position). While cell samples can be exposed to X-rays in a horizontal position, irradiation with C-ions at the SIS18 requires that samples are in a vertical position. Therefore, for C-ion exposure, MEA containers were covered tightly with Parafilm and adjusted upright into the ion beam (Fig.1). The dose rate was in the range of 1-6 Gy/min for heavy ions, resulting in an irradiation time in the order of 1-5 min. X-ray exposures were done with a dose rate of about 2-3 Gy/min.

Figure 1: Covered MEA container with cell medium. The MEA is attached to a water filled cell culture flask to enable irradiation in an upright position. The markers allowed an easy tracking by the Ion-Beam.

The electrophysiological properties of the cells were measured before and after exposure. Signals could be recorded for about one week and were analysed in terms of signal amplitude, shape, beat rate, and spreading velocity.

Results

The experiments revealed a high robustness of the cells to radiation damage. In no case the functionality of the cells was severely affected. All networks remained active and uniformly contractive (Fig. 2). Also no influence on signal amplitude and shape was observed. However, slight changes of beating rate and signal propagation could be detected at higher doses (data not shown). Further experiments are required to statistically verify radiation induced effects.

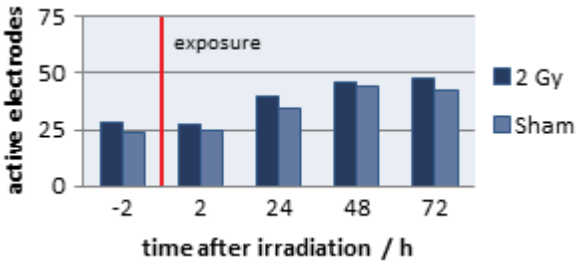

Figure 2: Beating rate of cells after exposure to high LET C-ions.

Conclusions

The study of cardiac electrophysiology allows for a rapid assessment of the cardiac functionality as a function of dose rate of exposition to low and high LET radiation. Complementary immunohistochemical studies on radiation-induced cell death and the intracellular coupling of cells (i.e. the expression of connexins) will be performed in the future.

References

[1] R. Roychoudhuri et al., BMC Cancer. 2007 Jan 15;7:9.
[2] M. Hooning et al., J Natl Cancer Inst. 2007 Mar 7;99(5):365-75.
[3] M. Durante and F. Cucinotta, Nat Rev Cancer. 2008 Jun 8(6):465-72.
[4] A.W. Daus, et al., Bioelectromagnetics. 2011 Jul ;32(5):351-9.

* This work is partly supported by the Association for the Promotion of Tumor Therapy with Heavy Ions

Slice cultures as a tool to study effects of irradiation on human brain tumors*

F. Merz[1], G. Taucher-Scholz[2], M. Durante [2,3], F. Gaunitz [5], A. Giese [6], H. Stoecker [2,4] and I. Bechmann [1,4#]

[1]Institute of Anatomy, University of Leipzig, [2] GSI Helmholtzzentrum für Schwerionenforschung mbH, Darmstadt, Germany, [3] Technical University Darmstadt, [4] Frankfurt Institute for Advanced Studies, [5]Klinik und Poliklinik für Neurochirurgie, Universitätsklinikum Leipzig, [6] Neurochirurgische Klinik und Poliklinik, Universitätsklinikum Mainz

Introduction

Heavy ions (HI) currently raise dual interest in biomedical research: they can be used for tumor treatment, but may also provide harm to healthy brain tissue, e.g. in astronauts during long-term space missions. We have set up tools to explore the effects of radiation on human brain tumor and intact brain tissue. As for the former, we prepared slice cultures from human glioblastoma multiforme (GBM) tissue and developed a method to expose them to photons or HI as well as combined treatment with chemotherapeutics or novel compounds (Merz et al., 2010; Müller et al., 2010; Merz and Bechmann, 2011). Organotypic cultures provide a model system close to the in vivo situation because of the maintenance of all cells in the tissue and the connective tissue to keep up the 3D matrix which is crucial for cell behavior and differentiation. Still, several therapy options can be tested on the same tumor which could be helpful for patient treatment in the future.

Experimental Setup

Tissue slice preparation and irradiation

Brain tumor biopsies were obtained from surgery and 350 µm thick slice cultures were prepared. Slices were then transferred to membrane culture inserts and cultivated on a liquid-air- interface. One day before irradiation, treatment with Temozolomide, a cytostatic compound widely used in GBM therapy (TMZ), was started in half of the cultures. Irradiation with Carbon ions (^{12}C) was performed at GSI with 2 Gy and with Xrays at Leipzig university hospital with 4 Gy. The Carbon dose was chosen because the RBE is 2 compared to Xrays in GBM cells (Combs et al., 2009). 24 h after irradiation, medium was changed and new TMZ added. After 72 h, slices were fixed.

Immunohistochemistry and quantification of cell death

For morphological analysis, paraffin sections of 6µm were stained with Hematoxilin/Eosin. Cell nuclei were counterstained with Hoechst 33342, and cell death was visualized with Caspase-3-antibody staining, an apoptosis marker. Pictures were taken using a confocal microscope, and then analyzed with the help of ImageJ software (NIH) by measuring the area of apoptotic cells and total nuclei.

Results

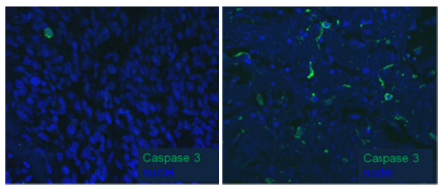

Figure 1: Cell death in human GBM slice cultures visualized by Caspase 3 staining. Left: control, right: ^{12}C ions and 200µM Temozolomide. Cas3 positive cells (green) are present more often in treated than in untreated samples, and there is significant cell loss in treated slices visible by a smaller cell density (blue nuclei)

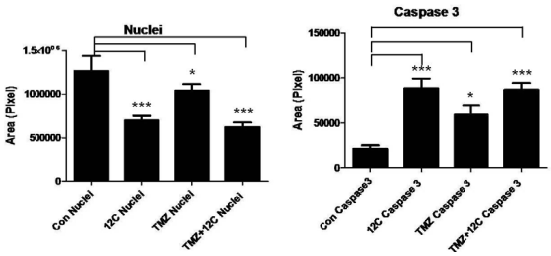

Figure 2: Cell death in human GBM slice cultures 48 hours after irradiation or combined treatment with Carbon ions (2 Gy) and Temozolomide (200µM). Activity of caspase-3 is upregulated in all treated samples, but most in irradiated and double treated slices (right). The area of nuclei is less in treated samples which implies a cell loss due to earlier cell death (left). Again, the cell loss is largest in samples which were irradiated or double treated. (Bars= SEM, One-way ANOVA, $p<0,05$).

Conclusion

Our newly developed slice culture model is suitable for the use in irradiation experiments on human tumor tissue. With its unique feature to perform several experiments on one tumor, it could provide an important tool for the optimization of therapy in the future.

References

[1] Merz F et al, Radiat Environ Biophys (2010) 49(3):457-62
[2] Mueller M et al, EPJD (2010) 60(1):171-176
[3] Merz F, Bechmann I. Future Oncol. (2011) 7(4):489-91.
[4] Combs SE et al, Int J Radiat Biol. (2009)

Studies on the Role of Backup Pathways of NHEJ in Heavy Ion Carcinogenesis: 50WB0929

Alena A. Bencsik-Theilen[1], Emil Mladenov[1], Satyendra Kumar Singh[1], Swetlana Konkow[1], Burkhard Jakob[2], Gisela Taucher-Scholz[2] and George Iliakis[1]

[1]Institut für Medizinische Strahlenbiologie, Universität Duisburg-Essen, Universitätsklinikum Essen, Hufelandstr. 55, 45122 Essen; [2]GSI Helmholzzentrum für Schwerionenforschung GmbH, Abteilung Biophysik, Planckstraße 1, 64291 Darmstadt

To repair double-strand breaks (DSBs) induced by heavy ions, cells utilize, in addition to homologous recombination repair (HRR) and the DNA-PKcs-dependent non-homologous end joining (D-NHEJ), also an alternative backup pathway (B-NHEJ) operating with slower kinetics and implicated in chromosomal translocations and telomere fusions, which are the general hallmark of carcinogenesis. In this project we investigate the contribution of B-NHEJ to the repair of DSBs generated by high- and low-LET radiation (heavy ions, neutrons and X-rays). Briefly, the goals of the project are:

Specific Aim 1: Determine the contribution of B-NHEJ to the repair of DSBs as a function of LET.

Specific Aim 2: Determine the contribution of HRR as a function of LET using Rad51 foci formation as endpoint.

Specific Aim 3: Examine variations in checkpoint signaling in G1 and G2 phase cells after exposure to radiations of different LET at the cellular and the molecular level.

Survival studies using colony formation as endpoint indicate that in the absence of operational D-NHEJ the increased killing efficiency of high-LET radiation is compromised in both exponentially growing and plateau phase cells in comparison to wild-type cells. Notably, the difference in radiosensitivity between M059K and M059J cells is blurred after exposure to heavy ions.

Pulsed-field gel electrophoresis results (Fig. 1) indicate a slight reduction in DSB repair efficiency when wild-type cells are exposed to heavy ions as compared to X-rays. Notably, this difference is exacerbated in *LIG4*$^{-/-}$ cells, suggesting that when the bulk of DSBs is analyzed B-NHEJ is compromised by the increased lesion complexity of high LET radiation to a greater extend that D-NHEJ and more DSBs are repaired slowly.

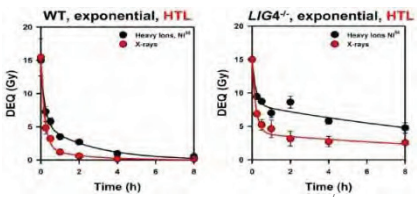

Fig.1: Exponentially growing wt or LIG4$^{-/-}$ MEFs were irradiated with 15 Gy, 1 GeV, Ni^{58} and X-rays. After irradiation samples were processed by HTL and analyzed by PFGE. Kinetics are shown as dose equivalent (DEQ) versus time. Results represent the average and the standard deviation from 4 determinations in one experiment.

The severe biological consequences of high-LET radiation derive from the increased complexity and spatial proximity of DNA lesions induced along the particle track. To be effective in the repair of DSBs both HRR and B-NHEJ require processing of DNA ends resulting in the formation of ssDNA regions as intermediates of the repair process.

To investigate how the increase in LET affects the ability of cells to process DNA ends, we have monitored appearance and decay of RPA70 foci as a surrogate for the formation of ssDNA regions (Fig. 2). These results clearly show that in DNA-PKcs deficient cells, irradiated with X-rays, RPA foci are evident 1h after irradiation and increase linearly to reach maximum at 24h. When cells are irradiated with ^{56}Fe ions, the number of RPA foci does not significantly increase over time at low doses (0.5Gy) suggesting that all of the generated breaks are subjected to end-processing less than 3h after irradiation. At higher doses, the number of RPA foci nearly doubles at 24h, indicating that some of the generated DSBs undergo end-processing more than 3h after irradiation. These results suggest that end-processing of DSBs is not compromised after exposure to high-LET radiation and may even be accelerated at low radiation doses. These results are in agreement with experiments showing the formation of Rad51 foci, a marker of ongoing HRR.

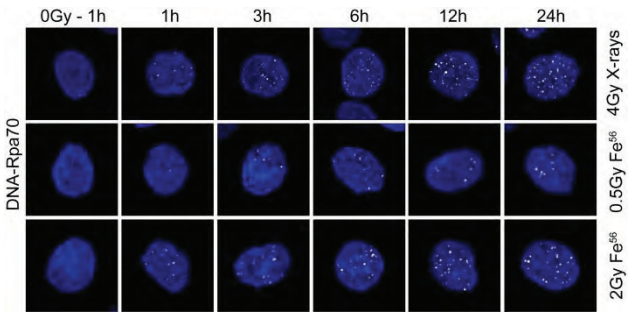

Fig.2: Exponentially growing M059J cells were irradiated with 1 GeV, Fe^{56} or X-rays. After irradiation samples were fixed and stained with an antibody against RPA70. Nuclei were counterstained with DAPI.

In summary, the results suggest that after exposure to heavy ions, B-NHEJ is compromised. This compromised function may increase the probability of misjoining and thus the formation of chromosome aberrations, a hallmark of this type of radiation. The role of HRR in this process and the possibility that abrogated HRR feeds DSBs to B-NHEJ requires further investigation.

Cell cycle and radiation associated activation of ion channels in the plasma membrane of primary lymphocytes

Roth B[1], Kraft D[2], Knoop J[1,2], Klinger J[2], Fournier C[2] and Thiel G[1]

[1]Membrane Biophysics, Technische Universität Darmstadt; [2]GSI, Darmstadt, Germany

Introduction

Peripheral blood lymphocytes (PBLs) generally have in the resting state a low proliferation activity. For experimental purposes mitotic division can be induced by the mitogen phytohaemagglutinin (PHA) [1]. This induction process is associated with a complex signal transduction cascade including the activation of particular K^+ channels [1, 2]. In the present study we examine, whether ionizing radiation has any effect on the ensemble of active ion channels in lymphocytes and if this is linked to a modulation of cell propagation.

Material and Methods

PBLs were isolated from the peripheral blood of healthy donors. As PBLs rest in the G_0-phase after isolation (figure 1a) cells were cultured for 48-72h in expansion media supplemented with PHA to allow cell cycle entry (figure 1c). Patch Clamp experiments were performed on a port-a-patch device according to standard conditions [3].

Results

After the Patch-Clamp technique had been optimized for primary PBLs we were able to record the K^+ channels in these cells with high confidence. The results show that the ensemble of K^+ channels, which is active in these cells, is modulated by PHA treatment. The data show that the activity of Kv1.3 channels is absent in non-stimulated cells in G_0-phase (figure 2 a-b) and appears after stimulation of cell proliferation (figure 2c-d). In pilot experiments we have also established a protocol to measure the activity of the membrane channels in non-stimulated lymphocytes after irradiation with sparsely ionizing X-rays or densely ionizing heavy ions. First experiments imply that also radiation alters the ensemble of active channels in lymphocytes and elicits activity of Kv1.3 (not shown).

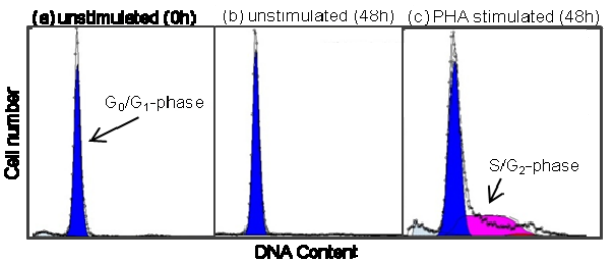

Figure 1: Cell cycle distribution of cultured PBLs: unstimulated cells directly after isolation from peripheral blood (a). After 48h cultivation without PHA cells remain in the G_0/G_1 phase (b). If cells are treated with PHA they progress under the same conditions to S/G_2 -phase (c).

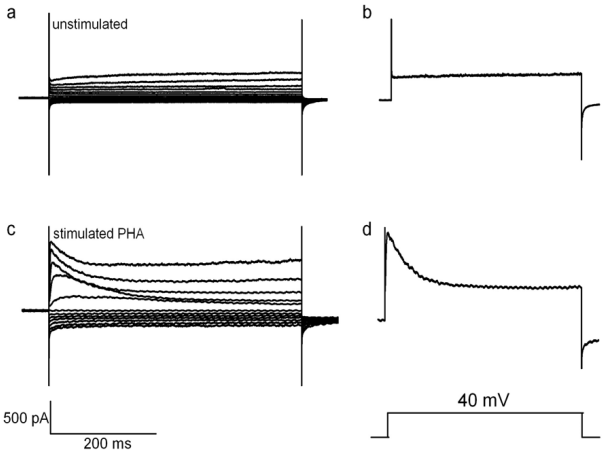

Figure 2: Exemplary current-responses of PBLs before (a) and after (c) stimulation with PHA. Currents were recorded in whole cell mode using the port-a-patch device. Exemplary Kv1.3 currents with c-type inactivation were elicited by a voltage step from the holding potential to +40 mV for 800 ms before (b) and after stimulation with PHA (d).

Discussion

Our work has so far established the methods for measuring channel activity in PBLs as a function of the cell cycle distribution. Experiments indicate that PHA stimulation but also ionizing radiation alters the ensemble of active channels in these cells. Following experiments are designed to uncover the signal transduction cascade between radiation damage and channel regulation. The experiments will further examine whether and how the activation of these channels is related the further differentiation of PBLs. In the next step the same experiments will be conducted in CD3 and CD19 enriched lymphocyte populations to discriminate the reaction between these different cell types.

Funded by BMBF 02S8355 and HGS-HIRe

References

[1] Verheugen JAH, Vijverberg HPM (1995). Cell calcium 17:287-300

[2] Wulff H, Knaus H-G. Pennington M., Chandy KG (2004). The Journal of Immunology 173:776-786

[3] Fertig N, Blick RH, Behrends JC (2002). Biophysical Journal 82: 3056-3062.

Cellular effects of space radiation with relevance to cardiovascular diseases*

C. Thielemann[1], S. Ritter[2], and P. Layer[3]
J. Frieß[1], A. Daus[1], F. Steger[1] and A. Heselich[3]
[1]University of Applied Sciences Aschaffenburg, Germany, [2]GSI Darmstadt, Germany, [3]Technical University of Darmstadt, Germany

Motivation

There is emerging epidemiological evidence of an increased risk of adverse cardiovascular effects at low or moderate doses of ionizing radiation occurring many years after the exposure. However, essentially no information is available on the potential cardiovascular risks associated with the exposure to heavy ions. To address this issue the induction of cellular late effects of particle exposure in beating cardiac myocytes grown in a two- or three-dimensional cell culture environment is studied.

Experiments

For the experiments beating cardiac myocytes derived from chicken and mammalian embryonic cells will be used. Cells will be grown as monolayer or three dimensional cell culture systems, so called spheroids. The latter model resembles more closely the in vivo situation in particular with regard to the number of cell-cell contacts. Myocytes will be irradiated with high energy heavy ions as described below. For comparison X-ray experiments will be done to enable a comparison of high and low LET radiation. Furthermore the effect of high and low LET radiation on prestressed cardiac myocytes, i.e. after pharmaceutical induction of arrhythmia will be examined.

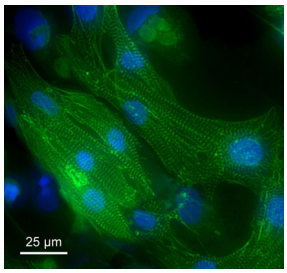

Figure 1: Cardiac myocytes from embryonic rat, green: FITC labelled α-actinin, blue: DAPI labeling of nuclei.

Electrophysiology

The electrical properties of cardiac myocytes will be measured by use of a microelectrode array system. This novel tool allows a functional analysis of cell-cell interactions in electrogenic tissue. Endpoints such as beating frequency, arrhythmia and conduction velocity can be measured with a high spatial and temporal resolution. The system has been already successfully used to study the anti- and pro-arrhythmic effects of pharmacological substances on cardiac cells [1,2] and is expected to provide new insights into the impact of heavy ion exposure on the electrical and mechanical activity of cardiac myocytes.

Biochemical endpoints

Recent evidence suggests that the development of apoptosis, or "programmed cell death" in response to pathological, physiologic, and/or genetic signals, may be a key developmental factor in causing cardiac arrhythmias [3, 4]. For example, apoptosis associated with atrophy and fibrofatty replacement of right ventricular tissue has been identified as the likely mechanism for arrhythmia development in arrhythmogenic right ventricular dysplasia, a condition that may lead to sudden death in otherwise healthy young individuals [5]. Based on this indication we intend to investigate apoptosis of cardiac myocyte cells induced by low and high LET radiation. Additionally, the intracellular formation of ROS will be measured, which plays a vital role in the aging of cardiomyoctes and as well as the development of radiation induced cardiovascular diseases. Persistently elevated levels of ROS have been associated with the appearance of nuclear and mitochondrial DNA damage, mitochondrial dysfunction and altered morphology, genomic instability, membrane damage and premature cellular senescence [6-10].

Summary

For the first time the MEA technique, a non-invasive method to investigate the electrical activity of cardiac myocytes, will be applied for the analysis of the impact of heavy ion irradiation on the mechanical and cardiac activity of cardiac cells. As further endpoints with relevance to cardiovascular disease cellular parameters such as the intercellular coupling between cells, cell death, and premature senescence will be studied. The comparative evaluation of these parameters will help to clarify the role of high LET radiation in the etiology of radiation induced cardiovascular disease.

References

[1] Pottek et al. (2006), MST News (January)
[2] Reppel et al. (2007). Cell Physiol Biochem 19:213-
[3] Colucci. N Engl J Med 1996 Oct 17; 335(16):1224-6.
[4] James. Annu Rev Physiol (1998) 60:309-25.
[5] Mallat et al. N. Engl. J. Med. (1996) 335(16): 1190-6.
[6] Haendeler et al. (2004) Circ Res 94: 768-775.
[7] Kim et al. (2006) Mutagenesis 21: 361-367.
[8] Nugent et al. (2007) Radiat Res 168: 134-142.
[9] D. Bernhard et al. Gerontology 2008; 54:24-31.
[10] Lakatta et al. Comp. Biochem & Physiol Pt. A 132, 699-721, 2002.

*This work is supported by the ESA IBER-10 program.

Gene expression and cytokine monitoring for biodosimetry and radiation sensitivity screening (GYMBRASS)*

R. Quintens[1], S. Baatout[1], M. Moreels[1]

[1]Radiobiology Unit, Belgian Nuclea Research Centre, SCK•CEN, Belgium.

Introduction

In deep space, the ionizing radiation quantity and quality is very different from that on Earth or in low Earth orbit because of the shielding characteristics of the Earth's atmosphere and electromagnetic field. Whereas typical terrestrial radiation mostly consists of low linear energy transfer (LET) radiation such as X- and gamma rays, space radiation is comprised of high-energy protons and high-charge and energy (HZE) nuclei. The increased cancer risk due to exposure to ionizing radiation from galactic cosmic rays and solar particle events is considered as the most important hindrance to interplanetary space travel [1,2]. Besides cancer, also other adverse health effects (e.g. impaired immune system, cardiovascular diseases, cataract) may arise in astronauts after exposure to cosmic radiation. In order to better understand and define these risks it is important to identify biomarkers of exposure and of prediction of individual sensitivity towards radiation-induced biological damage. High throughput bioassays for gene expression (microarrays) or cytokine monitoring (Luminex assays) can be powerful tools to achieve these goals. In this project, human peripheral blood samples from healthy donors will be irradiated *ex vivo* with heavy ions using different doses and energies. To investigate possible differences related to radiation quality, results will be compared to X-irradiated samples.

Objectives

The main aim of this project is to identify biomarkers (genes, exons, microRNAs, secreted proteins) that can be used for tracing exposure to radiation (biodosimetry) as well as to predict individual radiosensitivity to heavy ions. We will therefore irradiate peripheral blood mononuclear cells (PBMCs) from healthy volunteers with different doses (ranging from 0.05 Gy to 1 Gy) of HZE particles with high LET values which are relevant for human space flight.

Microarray analysis will be performed at different time points after irradiation in order to identify genes, exons and/or microRNAs that can be used to classify samples depending on the received doses. Based on these data, we will select proteins (cytokines) to be used for multiplex protein quantification (Luminex system) as a screen to test their usefulness as radiation biomarkers. For each condition, results will be compared with samples which will be exposed to similar doses of X-rays. This will allow us to verify whether differences exist in the biological response to high- versus low-LET radiation.

Concomitantly, we will quantify DNA damage (γ-H2AX phosphorylation) in response to high doses of X-rays in order to score the different donors for their individual radiosensitivity. These results will be integrated with data (microarrays, Luminex) from HZE and X-ray irradiations as a means to identify biomarkers for individual radiosensitivity.

* Work supported by Belspo, PRODEX-9 project "MOSAIC-2 (42-000-90-380)".

Preliminary results from X-irradiations [3]

Until now, studies which aimed at identifying gene expression signatures as biomarkers for radiation exposure have focussed on doses within the range of 0.5 to 10 Gy, which are less relevant for astronauts in the ISS or during an interplanetary mission. In our laboratory, we have performed preliminary experiments on isolated PBMCs from healthy donors which were irradiated with doses of 0.1 and 1 Gy of X-rays. Gene expression was analyzed in these cells using Affymetrix Human Gene 1.0 ST Arrays, which allow simultaneous detection of gene expression, exon expression (transcript variation) and expression of pre-microRNAs. The data indicated that both at low and high doses, mainly genes involved in DNA damage response were induced, albeit in a dose-dependent manner. Therefore, based on the expression levels of specific genes, we could accurately separate samples which had been irradiated with different doses. Our data further indicate that gene expression signatures may be used to accurately predict radiation exposure to doses below 0.1 Gy, which is below the sensitivity range of most classically used radiation biomarkers such as chromosomal aberrations and micronuclei. These experiments also showed that this sensitivity might be further enhanced by using the expression levels of single exons instead of genes. We further observed that individual differences exist in the regulation of transcript variants in response to radiation, indicating that these differences may explain, at least in part, individual differences in radiation sensitivity.

Our project will further elaborate on these very promising results, by using heavy ion (and X-ray) irradiations of PBMCs at doses of as low as 0.05 Gy.

References

[1] F.A. Cucinotta and M. Durante (2006). "Cancer risk from exposure to galactic cosmic rays: implications for space exploration by human beings." Lancet Oncol **7**(5): 431-5.

[2] M. Durante and F. A. Cucinotta (2008). "Heavy ion carcinogenesis and human space exploration." Nat Rev Cancer **8**(6): 465-72.

[3] R. Quintens (2010). "Identification of radiation-dependent gene / splice variation signatures". ESA Topical Team meeting. Brussels, Belgium, 6-7 July 2010.

IBER-10 SPARTACUS annual report

C. Lobascio[1#] and E. Tracino[1]

[1]Thales Alenia Space Italia, Torino, Italy

Project Status

The SPARTACUS "SPAce Radiation Testing in Accelerator of CoUntermeasureS (SPARTACUS)" project, selected for the definition phase as per ESA letter HSO-AS/2011 – 23 could not be started so far. As for the other Italian selected projects in the frame of IBER 2010, national funding for this activity is not secured, and no planning can be performed on funding availability. In fact, several requests for clarification in this respect have been made to the Italian Space Agency (ASI), in the persons of Dr. F. Svelto and Dr M. Cosmo. The latest (informal) answer was provided in mid July by Dr Svelto, reporting that since the ASI PTA (3-y Activity Plan) was not approved yet, there could be no basis to issue a Call dedicated to the ESA approved IBER proposals. In fact, as of today there is no further public information on the issue of the PTA and of the expected dedicated national Call to support the IBER-10 projects.

A letter addressed to the president of the Italian Space Agency was written by all the selected Italian science team leader to request information about the issue of a dedicated tender and the foreseen funding to sustain the proposal; for the time being the letter remains without any answer.

This stall situation, resulting in an inability on our side to proceed, performing adequate resource allocation, procurement and planning, is cause of deep concern for our team**.**

Project objectives

The objective of the project is to assess through tests in accelerator the efficacy of novel Habitat Protection Structures (HPS) to shield the crews in view of the envisaged extended presence of humans in space foreseen by the new exploration scenarios.

A HPS "integrated shielding structures" is the ensemble of primary structure, the micro-meteoroids and debris protection system and the thermal protection system.

Building on the strong knowledge acquired in the past decade on physical passive radiation shielding systems, we propose to develop and test new HPS configurations comparing them with the more classical ones.

In particular, a new approach will be followed to select new materials and design innovative structures through the use of Monte Carlo simulations - based on Geant4/GRAS tool - and experimental data.

The selection of the materials and configurations will be driven by radiation protection considerations as opposed to the usual approach where the shielding effectiveness is a secondary characteristic. New space materials have been identified and will be subjected to experimental tests as necessary to prove their radiation shielding capabilities. Secondary structures and internal outfitting will be tested and simulated, as well as the presence of additional materials dedicated to the radiation shielding.

The following quantities will be used to characterize the different targets:

a) Bragg Curve
c) Microdosimetry of the radiation field behind the target

To determine these quantities the measurement of the dose and the lineal energy spectra will be performed.

Project plans

Thales Alenia Space Italia will continue requesting the necessary information to ASI about the funding of the project and will kept ESA and GSI informed about the evolution of the situation.

An excessive kick-off delay in the mid term could result in fact in schedule conflicts and difficult (or even impossible) exploitation of available GSI beam-time windows.

Visual System Activation by Ionizing Radiation: experiments and models (VISAIR)

L. Narici for the VISAIR collaboration

Department of Physics, University of Rome Tor Vergata & INFN Tor Vergata, Rome Italy.

The Italian Space Agency still does not have set up the procedures for providing financial support for the project. For this reason the experimentation did not start yet.

In the following a brief summary of background and strategy of the project.

Risks due to cosmic radiation are a major issue when planning deep space manned missions. However, the concept of radiation dose (also dose equivalent, effective dose) appears inadequate to univocally assess the associated risks and may be even more so in the study of the functional effects on exposed tissues (e.g. the CNS).

Experiments in space showed that the phosphenes (anomalous Light Flashes; *LF*) observed by astronauts are triggered by single particles, suggesting that single ions can trigger the CNS multiplicative cascade processes and generate functional anomalies [1]. The reported effects of radiation on sensory channels other than visual suggest a direct action on neurons or neural networks. Recent findings suggest that also low LET ions can elicit *LF* [2]

Our previous work on the mechanisms of LF generation [3] shows that radicals produced by radiation in, or near the retina can activate rhodopsin and start the photo-transduction cascade mediating in vision. In this previous work, we demonstrated the effect, but did not approach the issue of the efficiency of the interaction at different LET and Z, and, being based on spectrophotometric measurements, could not produce information on single particle effects.

In this project, A LET/charge modulation of rhodopsin activation is hypothesized.

We will i) study experimentally the behavior with LET and Z and ii) provide detailed simulations of the radiation driven radical generation, to help the extrapolation of the results to single ion/track effect. Two kind of simulations will be provided, one entirely based on a biophysical Monte Carlo code, PARTRAC, and a second one based on experimental results in literature about radical formation and analytical functions. The comparison between these two approaches will be of help not only for this particular project but also for the other many investigations aimed at defining the radical role in the risk assessment.

In more detail we will

- Define the modulation with Z and LET of the chemiluminescence effect. The hypothesis is that this modulation will be linked to the efficiency of different Z/LET in producing free radicals. The approach will be experimental (as previously, measuring with spectrophotometric techniques the rhodopsin activation after irradiation) and modelistic, using stochastic and deterministic codes to provide insights on the single track behavior to be linked to the results of the measurements). The results will be also used to identify possible processes where LET and dose plays a weak role, and also to provide inputs on the radiation selective mechanisms of action on the retinal functional organization that we observed in the mice experiments and finally help estimate the biological/functional hazard in greater detail.
- Test the efficiency of different kind of scavengers as countermeasures to prevent rhodopsin bleaching. The approach will be experimental, concurrent with the previous irradiation / spectrophotometric measurements
- Provide preliminary results on possible direct effect of radiation on calcium signaling in the photo-transduction cascade. These information will help to identify mechanisms of neuronal interaction possibly common to all sensory modalities.
- Finally based on previous results, countermeasures will be proposed.

References

[1] L. Narici “Heavy ions light flashes and brain functions: recent observations at accelerators and in space-flight” New J. Phys. 10 (2008) 075010

[2] E. Khan, F. Maréchal, R. Dendale, C. Mabit, Calugaru, L. Desjardin, L. Narici, "Anomaluos Phosphenes in Ocular Protontherapy" Adv. Space Res. 45:846-849 (2010)

[3] L. Narici, A. De Martino, V. Brunetti , A. Rinaldi , W.G. Sannita, M. Paci “Radicals excess in the retina: A model for light flashes in space” Rad Meas. 44:203-205 (2009)

Osteoblast Like Cell Culture Model Systems In Response to Space relevant Qualities of Ionizing Radiation (OSIRIS 2.0)

P. Lau[1], C. Baumstark-Khan[1], C.E. Hellweg[1], Y. Hu[1], E. Tobiasch[2], and G. Reitz[1]

[1]DLR, Köln, Germany; [2]University of Applied Sciences, Bonn Rhein-Sieg, Rheinbach, Germany.

Space radiation produces distinct biological damage compared to radiation on Earth, leading to large uncertainties in the projection of cancer and further health risks. On these terms, almost all human physiological systems are affected. However, the detailed impact on the skeletal system has not been defined. Our hypothesis is that exposure to ionizing radiation of different qualities effects the commitment and differentiation of multipotent human mesenchymal stem cells to the osteoblastic lineage. This may result in a severe reduction of osteoblast function leading to an elevated fracture risk.

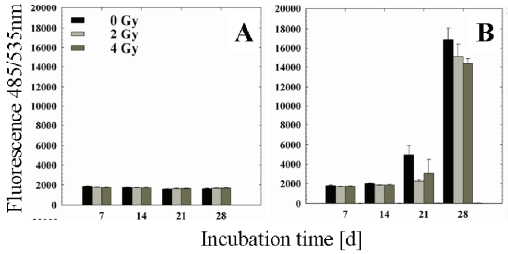

Figure 1: Calcium deposition of osteogenic-differentiated human adipose tissue derived stem cells. Single doses of 2 Gy and 4 Gy were applied. Calcium deposition was measured at day 7, 14, 21 and 28. Non-induced ATSCs (A) and induced cells (B).

To understand how differentiation is affected after exposure to ionizing radiation, we intend to use multipotent stem cells with the potential to differentiate into several different cell types, like osteoblasts, myoblasts, adipocytes or chondrocytes, given the appropriate conditions. Adipose tissue derived stem cells (ATSCs) were isolated out of lipoaspirate of human donors (Zuk et al., 2001). Preliminary data from our lab showed that ATSCs expressed the characteristic stem cell markers CD70, CD90 and CD105. Furthermore, we were able to demonstrate the osteogenic lineage-specific differentiation by histochemical staining of the extracellular calcium depositions. Osteoblastic function was further quantified by fluorescent staining of the calcium deposition (Fig.1). The quantification is based on specific binding of the fluorescent OsteoImage™ staining reagent to the hydroxyapatite portion of the bone-like nodules deposited by osteoblasts.
In addition, the human osteosarcoma cell line SaOs-2 was included in the experiments, known to be easily inducible to the osteoblastic lineage. It has further been suggested that accumulated DNA damage could be a principal mechanism underlying age-dependent stem cell decline.

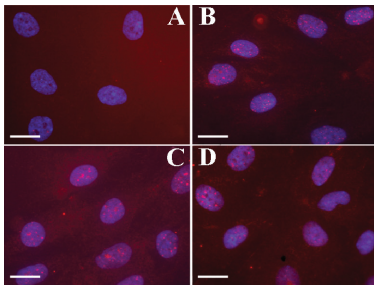

Figure 2: DSB induction and repair in ATSCs as measured by γ-H2AX foci formation. γ-H2AX foci, (A) 30 min 0 Gy , (B) 2 h after 1 Gy, (C) 4 h after 1 Gy, (D) 6 h after 1 Gy. The Scale bars correspond to 20 µm.

Therefore, assessment of H2AX phosphorylation as a reporter of DNA damage will be performed after exposure to low and high LET radiation (Fig.2).

Culture conditions

ATSCs were cultivated under established culture conditions (37°C with 5% $C0_2$). Media was changed twice a week. DMEM was supplemented with 50 µM Ascorbic Acid, 10mM ß-Glycerophosphate, 100nM Dexamethasone for osteogenic differentiation.

Outlook

Giving the fundamental requirements, ATSCs provide a promising tool in further research related to radiation effects on bone tissue. In future work, we will evaluate ALP activity and the number of mineralized bone nodules by alizarin red S staining. Real time RT-PCR will allow us to identify any modulation of the bone matrix proteins osteopontin, BSPII (bone sialoprotein II), osteocalcin and collagen I. Additionally we aim to evaluate the expression of genes involved in osteoblast differentiation. The proposed experiment OSIRIS 2.0 will thus provide valuable information necessary for estimating the health risk of astronauts, especially regarding long term space scenarios for exploration of Moon and Mars.

References

[1] P.A. Zuk, Zhu. M., H. Mizuno, J. Huang, J.W. Futrell, A.J. Katz, P. Benhaim, H.P. Lorenz, and M.H. Hedrick, Multilineage cells from human adipose tissue: implications for cell-based therapies. (2001) Tissue Eng., 7, 211-228

Protective measures for vertebrate photoreceptors against heavy ionizing radiation, as analysed in 3-dimensional cell culture models

Florian Frohns[1], Johanna Kramer[1], Marco Durante[1,2], Claudia Fournier[2], Paul G. Layer[1]
[1] Technische Universität Darmstadt, Germany; [2] GSI, Darmstadt, Germany

Introduction

Long-term space flights go along with a long-term exposure of astronauts to unpredictable doses of space radiation. Due to its ionizing character, this radiation might have deleterious effects on the genomic integrity of the exposed persons, thereby probably evoking the degeneration of various tissues or cancer development. Since there are only few studies about the impact of ionizing radiation on the retina, as our light-sensitive tissue, we started to analyze the development of this tissue after its exposure to X-rays by using three-dimensional cell culture models as well as in vivo experiments.

Materials and Methods

The impact of ionizing radiation (IR) on retinal tissue from the chick as a model system for distinct colour vision was analyzed by using different experimental setups. Three-dimensional retinal cell spheres, so called retinospheroids, arising from dissociated retinae of six days old chick embyos, mimicking the retinal structure in vitro, as well as whole chick embryos were used for irradiation experiments. After irradiation, spheroids and retinae were analyzed for their histotypical structure by immunostainings of cryosections against retinal marker proteins.

Results and Conclusion

Irradiation of chick spheroids

To analyze the impact of IR on the structure of the retinal tissue alone, without any interference from its surrounding tissues, we irradiated chick retinospheroids after five days in vitro with various doses of X-rays.

Figure 1: *Analysis of the influence of IR on the Müller glia scaffold and the connectivity of amacrin cells in retinal spheroids. Staining of nuclei (blue), Müller glia specific glutamine synthetase (red) and Calretinin in amacrine cells (green) show no differences within their organization in controls and spheres treated with 6 Gy X-Ray (90kV, 33,7 mA) 24 hours past irradiation.*

When analyzed 72 hours after the irradiation, we observed no changes within the alignment of Müller glia and interneuronal amacrine cells, even after high doses up to 6Gy (see Fig.1).

Irradiation of chick embryos

To analyze the impact of whole body irradiation on retinal integrity, 13 day-old chick embryos were exposed to 1Gy of X-rays. Rod photoreceptor (PR) morphology and their expression of typical proteins were analyzed 5 days after the treatment by immunostainings of retinal cryosections against rhodopsin (see Fig. 2). DAPI-stainings revealed no alterations within the appearance of PR-nuclei after irradiation, when compared to untreated controls. Furthermore, irradiation showed no effect on the development of the outer segments of PRs: In both cases, photoreceptors developed these typically elongated structures which contained high amounts of the light-sensing protein rhodopsin.

Figure 2: *Rod photoreceptor development is not affected after whole body irradiation with 1Gy of X-rays. Retinae of 18 day old control embryos and embryos that received 1Gy of X-rays (90kV, 33,7 mA) 5 days before were stained against nuclei with DAPI (a, c) and rhodopsin (b, d).*

Conclusion and Outlook

In this project we have, and will further analyze the impact of IR on the structuring and the protein expression patterns of the retina, thereby trying to evaluate the risks of long-term space irradiation exposure of astronauts for their visual capacities. Up to now, our experiments show a surprising resistance of this tissue against IR-induced degeneration.

Aknowledgements

We thank ESA-IBER for the funding of this project and Prof. M. Löbrich for providing X-ray facilities.

Repair of heavy-ion induced DNA double-strand breaks in mice models

S.Conrad[1], J.Mirsch[1], and M.Löbrich[1]

[1]Darmstadt University of Technology, Germany.

DNA double-strand breaks (DSBs) represent an important lesion induced by ionizing radiation since unrepaired or incorrectly repaired DSBs can lead to chromosomal instability and cancer development. It is therefore not surprising that cells respond to the presence of DSBs and are usually capable to repair the lesions within hours after irradiation.

However, recent work from our group has shown that cells in culture fail to repair DSBs efficiently which are induced by low to very low radiation doses of X-rays (in the order of a few milli-Gray). Moreover, persisting DSBs are also observed in various tissues of living mice which were irradiated with milli-Gray doses of X-rays [1,2].

Intriguingly, cells in culture are able to repair DSBs after low doses efficiently if they are treated prior to irradiation with H2O2 which, at the concentration used, does not induce DSBs itself but induces a significant amount of radicals which lead to single-strand breaks and base damages.

Thus, repair of DSBs requires an inducible response. After high doses, this response is provided by the radiation itself but after low doses, cells need to be exposed to a certain radical level to repair their DSBs efficiently. In this study, we aim to investigate the repair of DSBs induced by single high-energy high-LET particles in various tissues of living mice.

The distribution of damage following high energy high-LET particle irradiation is distinct to that after X-irradiation involving cells which are directly hit by the particle track receiving fairly high doses and cells in the surrounding of the hit cells which receive much lower doses (Fig. 1).

One aim of this study is to investigate if the cells receiving low doses fail to repair their DSBs efficiently, similar to the situation after X-irradiation, or if they are able to repair their DSBs because the inducible response needed for efficient repair is provided by the neighboring cells receiving high doses. We plan to irradiate mice at the SIS facility and will detect DSBs in various tissues by using several immunofluorescence markers.

As a long-term goal, we plan to modify the cellular capacity to repair DSBs after low doses by pre-treating cells and mice with agents that reduce or increase the intra-cellular radical level. These studies are of outmost importance to evaluate and modify the carcinogenic risk of high-energy high-LET particle irradiation.

A) Ions

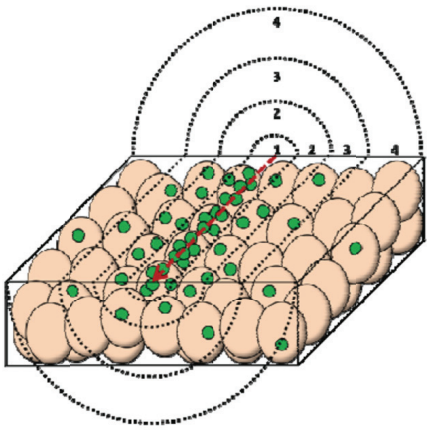

B) X-rays

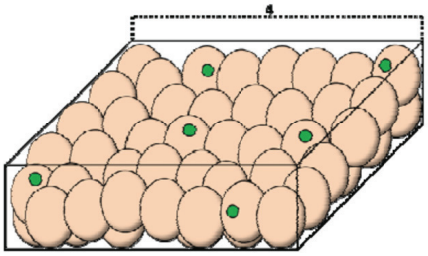

Figure 1: Schematic draw of the dose distribution of a tissue section irradiated by a heavy ion (A) or by X-rays (B). The ellipses represents cells in a tissue, the red line indicates an ion traversing the tissue. Green dots represent DSBs marked by yH2AX. The numbered circles indicate different dose-regions applied by delta-electrons in the penumbra of the ion track.

References

[1] K. Rothkamm and M. Lobrich, “Evidence for a lack of DNA double-strand break repair in human cells exposed to very low x-ray doses”, PNAS 2003 April 29;100(9):5706-15

[2] Grudzenski et al., Inducible response required for repair of low-dose radiation damage in human fibroblasts. ,PNAS 2010 Aug 10 107(32):14205-10.

AO-10-IBER-16: Ground based radiation field simulation of the MATROSHKA experiment: Physical and Biological Experiments for Radiation Risk Assessment – PART II

T. Berger[1], G. Reitz[1], C. Baumstark-Khan[1], C. Hellweg[1], M. Hajek[2], P. Bilski[3], J. K. Pálfalvi[4], L. Hager[5], S. Burmeister[6], L. Sihver[7], C. La Tessa[8]

[1]DLR, Germany; [2]TU Vienna, ATI, Austria; [3]IFJ, Poland; [4]AERI, Hungary; [5]HPA, UK; [6]CAU, Germany, [7]CTH, Sweden; [8]GSI, Germany.

Introduction

The work to be performed within the AO-10-IBER-16 proposal is a follow up to the ESA-IBER experiment **AO-08-IBER-12**: "Ground based radiation field simulation of the MATROSHKA experiment: Physical and Biological Experiments for Radiation Risk Assessment". Within the previous experiment three beam times at GSI have been performed using 1 x Fe and 2 x Ni with 1 GeV/n in the years 2009 and 2010 with LET values of 150 and 174 keV/µm.

The rationales and motivation for the AO-10-IBER-16 experiment proposal "Ground based radiation field simulation of the MATROSHKA experiment: Physical and Biological Experiments for Radiation Risk Assessment PART II" are the following:

- To include ions with lower LET range (as for example 1 GeV/n C) up to 100 keV/µm
- To include ions with higher LET range starting from around 200 keV/µm
- To irradiate the applied phantom head not only in CAVE A but also in CAVE M applying the GSI developed 3D spot scanning technique
- To increase the data gathered by passive and active radiation detectors applied for depth dose measurements for further benchmarking and simulation with radiation transport codes as GEANT4 and PHITS

Phantom Head Exposures

Irradiation of the detectors within the head of the phantom upper torso will include :

Irradiation of passive detectors within the head of the phantom upper torso under simulated space radiation environmental conditions.

Including TLDs and CR-39 track etch detectors together in the simulated organ dose boxes for the estimation of the dose equivalent – based on a simulated space radiation "heavy ion field"

Comparison of the data from the passive organ dose boxes with the active Silicon Szintillation Detectors provided by the Christian Albrechts University zu Kiel.

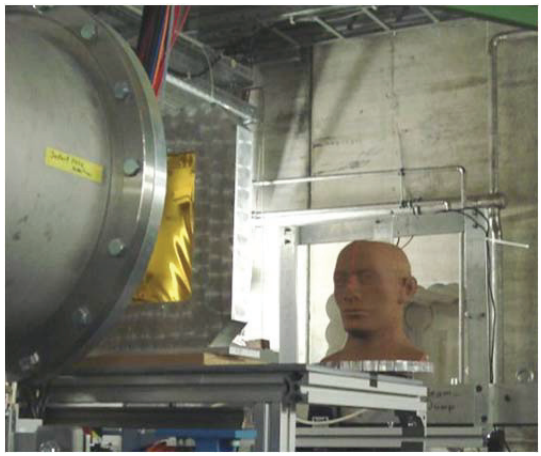

Figure 1: Head of the phantom at Cave A

There is a lack of experimental data for the radiation transport through the phantom material for high-energy ion beams. It is therefore planned to compare the measured results with the model output for the irradiation conditions and also thereby benchmark the radiation transport codes. PHITS and GEANT4 will be used as Monte Carlo codes within the experiment.

Detector Characteristics

Irradiation of the TLD materials applied during the MATROSHKA experiment onboard the ISS under identical irradiation conditions (heavy ions available from GSI, Co-60 and Cs-137 photon fields), using equivalent detector holders to precisely determine TL efficiency and harmonize the generated dosimetric data.

* The work performed within the proposal up to September 2011 was supported by the FP7 Project HAMLET http://www.fp7-hamelt.eu (Project # 28817).

Cardiovascular tissue degeneration, altered platelet production and adhesion, and thrombus formation in space crews: effects of high-LET ion exposure on platelet production and platelet endothelium interaction (AO-10-IBER-9)

L. De Marco[1], A. Balduini[2], G. Grossi[3],

[1]C.R.O.-IRCCS Aviano, Italy; [2]Università di Pavia, Italy; [3]Università di Napoli „Federico II, Italy.

The Italian Space Agency still did not set the procedures for providing financial support for the project. For this reason the experimentation did not start yet. In the following a brief summary of background and strategy of the project.

Ionising radiation exposure can result in an increased risk of late-occurring cardiovascular disease. However, it is still unclear to what extent Galactic Cosmic Radiation (GCR) may impact cardiac tissue, whose progressive loss of function is related to vascular damage. Being the maestro of thromboregulation, endothelial cells (ECs) represent the target for the pathogenesis of cardiovascular radiation injury. Space mission crews are not likely to experience acute microvascular injuries, typical of high doses. On the other hand, chronic high-LET radiation may cause accelerated cellular senescence, which is inducible *in vitro* by a variety of stressors, hence termed stress-induced premature senescence or SIPS, and can be associated with telomere length shortening and genomic instability. Moreover, space radiation may alter platelet homeostasis and induce abnormal platelet interaction with ECs through release of high-molecular weight von Willebrand factor (vWF), which is required for platelet adhesion. Increased platelet adherence results in a higher probability of pathologic occlusion of vessels and thrombus formation. Radiation is already known to exert a prothrombotic effects since an increased release of von Willebrand factor (vWF) stored in ECs and to have a major impact in megakaryocytes maturation.

With these premises, we will expose cardiac fibroblasts, the dominant cell type in the myocardium, or ECs of umbilical and aortic origin and CD34+ stem cells to high-LET particles. The onset of SIPS will be studied using β-galactosidase activity and will be related to telomere length. The latter will be measured by IQ-FISH. To assess the influence of ion irradiation on the antithrombotic activity of the endothelial lining of the arteries, platelet-endothelium interaction will be studied under different flow conditions with a new video-imaging apparatus (SMART CLOT). The influence of ion irradiation will be also studied on the different stages of megakaryocyte maturation, platelet production and platelet function using either using a static system or our newly developed 3D bioreactor.

The adipocyte-derived hormone leptin as novel tool for immunodepression consequent to cosmic ray exposure

G. Matarese[1], C. Procaccini[1], V. De Rosa[1], M. Galgani[1], F. Natale[2], S. Pappata3, and A. La Cava[4]

[1]Laboratorio di Immunologia, IEOS-CNR, Napoli, IT; [2]GSI Darmstadt, [3]Nuclear Medicine, IBB-CNR, Napoli, IT; [4]Dept. of Medicine, UCLA, Los Angeles, CA, USA

Leptin is an adipocyte-derived cytokine-like hormone that links nutritional status to neuroendocrine and immune functions. The presence of leptin is important for immune homeostasis and survival of immune cells. An increased radiosensitivity has been reported in either leptin (*ob/ob*) or leptin receptor deficient (*db/db*) obese mice. Since astronauts are exposed to space radiation (chronic but also possibly acute, in case of solar particle events) under conditions of severe immunosuppression induced by the space environment (including microgravity), we propose the use of leptin as a countermeasure and possible immune-reconstituting agent for acute and late effects of exposure to cosmic radiation. Recent reports have shown that leptin administration has the capacity to stimulate the immune system in cases of immunosuppression and infections, and actually clinically used in leptin deficient individuals, which are susceptible to infections in young age. We will investigate in human lymphocytes and in different groups of mice either normal or leptin/LepR deficient how recombinant leptin replacement can be effective in preventing or treating immune depression and immune depletion observed upon exposure to X-rays and heavy ions at doses of 0.5 and 5 Gy. Parallel haematological and physiological parameters (including body weight and fat mass) will be also investigated. The results should indicate whether leptin supplementation can be used as a countermeasure for space radiation exposure and immune suppression/depletion during spaceflight.

Preliminary data

Our group of research has generated substantial evidence that supports the notion that leptin is able to maintain survival of human and mouse T lymphocytes. In humans leptin has been shown to be a safe and effective treatment to increase the number of T cells in leptin-deficient subjects. Our group has been contributing to such study in humans. Also, it has been shown that leptin and LepR deficient mice have an increased susceptibility and reduced survival to radiation exposure.

Mouse: We have shown in leptin deficient mice that leptin increases the number of T cells and increases the size of lymphoid organs such as spleen and thymus upon 0.5 Gy X-ray irradiation.

Human: In malnourished humans the condition of immune depletion resembles that observed in individuals exposed to low doses of radiations. In this context, we have currently a clinical trial, in which women with hypothalamic amenorrhea and malnutrition (HA subjects) show a reduced number of T cells in the periphery similar to radiation exposed humans. Leptin *vs* placebo treatment (36 weeks) showed in these women a significant increase in lymphocytes of the $CD4^+$ T cell subset in the periphery, suggesting the capacity of leptin to revert the immune depletion and immune suppression observed in HA and malnutrition. The other cell types were not affected such as B and NK cells. Also in the $CD4^+$ subset both memory and naive T cells were significantly restored at levels comparable to normal individuals. These data suggest that leptin replacement is affective and safe in reversing immune suppression in individuals with reduced nutritional intake. Taken together mouse and human data suggest that leptin in vivo could be considered and tested as possible countermeasure to treat radiation exposed-individuals, due to it marked and effective capacity to increase survival of immune cells in conditions of leptin deficiency and reduced caloric intake.

References

[1] De Rosa V, Procaccini C, Calì G, Pirozzi G, Fontana S, Zappacosta S, La Cava A, Matarese G.A key role of leptin in the control of regulatory T cell proliferation. Immunity. 2007 Feb;26(2):241-55.

[2] Galgani M, Procaccini C, De Rosa V, Carbone F, Chieffi P, La Cava A, Matarese G. Leptin modulates the survival of autoreactive CD4+ T cells through the nutrient/energy-sensing mammalian target of rapamycin signaling pathway. J Immunol. 2010 Dec 15;185(12):7474-9.

[3] La Cava A, Matarese G.The weight of leptin in immunity.Nat Rev Immunol. 2004 May;4(5):371-9.

Novel and *in situ* shielding materials for protection of planetary bases from cosmic rays*

M.Durante[1,2] and F.A. Cucinotta[3]

[1]GSI, Darmstadt, Germany; [2]TU Darmstadt, Germany; [3]NASA Johnson Space Center, Houston, TX, USA.

Shielding is very difficult in space: the very high energy of the cosmic rays and the severe mass constraints in spaceflight represent a serious hindrance to effective shielding. Active shielding would have to overcome challenging technical hurdles to protect against GCR. Passive shielding can be effective for solar particle events; however, it is limited for galactic cosmic rays (GCR). Development of novel materials and exploitation of in situ resources for shielding may greatly reduce the radiation risk on planetary bases [1].

Novel materials

Polyethylene has been identified as a useful structural polymer for spacecraft shielding with various fabrication strategies developed for damage tolerant stiff structure and inflatable vehicles. An important challenge is how to form high-density polyethylene fiber with polyethylene matrix and bond the resulting composite face sheets to form polyethylene foams. Approaches considered are plastic thermo-sets, aliphatic systems and e-beam curing. Aliphatic systems lose strength at both low and high temperatures to be expected under space conditions. Wilson has discussed the usage of aliphatic/aromatic hybrid polymers as improvement to a purely aliphatic systems. Carbon nano-tubes with high hydrogen content offer a distinct approach and are under investigation for improved structural layouts.

In situ materials

Because of the high costs of launch mass in-situ shielding on the lunar or Mars surface are of interest and may require distinct approaches since a higher relative fraction of astronaut exposures on the Mars surface are due to neutrons compared to the lunar surface due to the Mars atmosphere both depleting heavy ions and adding neutrons. The exposure to astronauts will depend on which region of Mars a habitat occupies, because large variations in secondary neutrons can occur due to the soil composition as well as seasonal variations due to the presence of protective ice (water or perma-frost) as shown in Fig. 1. Landing sites will likely be chosen by science requirements, however may require distinct shielding approaches dependent on the fractional contribution from neutrons to the total risk. Digging regolith to shield planetary habitats with bring along equipment is one approach considered. Certainly, exposures could be reduced substantially if several meters of regolith are used to cover a habitat albeit the view and creation of astronaut moles is not preferred.

* Work supported by ESA-ISRU grant

The moon is known to contain lava tubes as well as craters that partially shield space radiation, and Mars has similar geographical features to increase habitat shielding. In situ hydrogen or perhaps launched boron could be used to create regolith shielding bricks, however will require new manufacturing approaches on planetary surfaces.

Accelerator tests

A campaign of measurements of novel and in situ materials for heavy ion shielding is under way at GSI and supported by ESA [2]. Materials will be produced in blocks and tested for (a) dose attenuation (Bragg curves); (b) neutron production; and (c) microdosimetry spectra. Results will be used to develop new shielding strategies on planets.

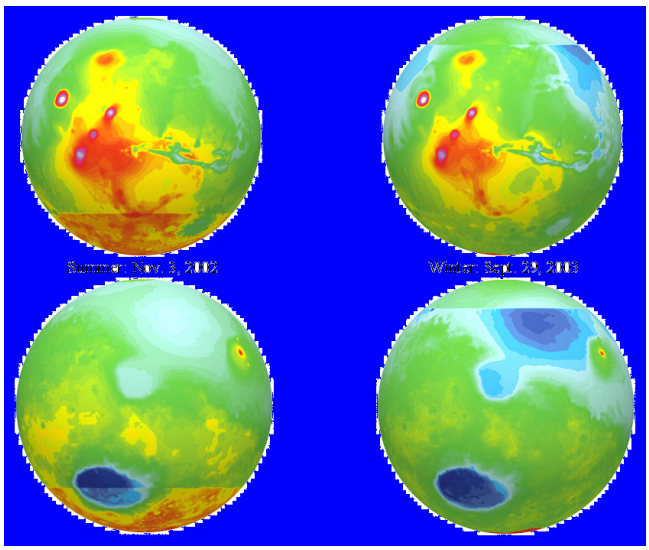

Figure 1 Seasonal variation of the integral neutron fluence above 10 MeV on Mars due to ice buildup reducing regolith backscattered neutrons [1].

References

[1] M. Durante and F.A. Cucinotta, "Physical basis of radiation protection in space travel" *Rev. Mod. Phys.* **83** (2011) 1245-1281.

[2] ESA, Appendix 1 to ESTEC/ITT AO/1-6765/11/NL/AT – Statement Of Work "Radiation Shielding by ISRU and/or innovative materials for EVA, vehicles and habitats" TECEES/2010.623/PN Issue 0.1 Rev. 1, 01 March 2011

WoS publications to the programme 'Physics of hadrons and nuclei' published in 2011

K. Götzen[1], *P. Karampougiouki*[1], *Y. Leifels*[1], *M.V. Ricciardi*[1], *C. Sturm*[1], *and L. Wunderlich*[1]
[1]GSI, Darmstadt, Germany

001 Aamodt, K.; Abel, N.; Abeysekara, U.; Quintana, A. A.; Abramyan, A.; Adamova, D.; Aggarwal, M. M.; Rinella, G. A.; Agocs, A. G.; Salazar, S. A.; Ahammed, Z.; Ahmad, A.; Ahmad, N.; Ahn, S. U.; Akimoto, R.; Akindinov, A.; Aleksandrov, D.; Alessandro, B.; Molina, R. A.; Alici, A.; Avina, E. A.; Alme, J.; Alt, T.; Altini, V.; Altinpinar, S.; Andrei, C.; Andronic, A.*; Anelli, G.; Angelov, V.; Anson, C.; Anticic, T.; Antinori, F.; Antinori, S.; Antipin, K.; Antonczyk, D.; Antonioli, P.; Anzo, A.; Aphecetche, L.; Appelshauser, H.; Arcelli, S.; Arceo, R.; Arend, A.; Armesto, N.; Arnaldi, R.; Aronsson, T.; Arsene, C.*; Asryan, A.; Augustinus, A.; Averbeck, R.*; Awes, T. C.; Aysto, J.; Azmi, M. D.; Bablok, S.; Bach, M.; Badala, A.; Baek, Y. W.; Bagnasco, S.; Bailhache, R.*; Bala, R.; Baldisseri, A.; Baldit, A.; Ban, J.; Barbera, R.; Barnafoldi, G. G.; Barnby, L. S.; Barret, V.; Bartke, J.; Barile, F.; Basile, M.; Basmanov, V.; Bastid, N.; Bathen, B.; Batigne, G.; Batyunya, B.; Baumann, C.; Bearden, I. G.; Becker, B.; Belikov, I.; Bellwied, R.; Belmont-Moreno, E.; Belogianni, A.; Benhabib, L.; Beole, S.; Berceanu, I.; Bercuci, A.; Berdermann, E.*; Berdnikov, Y.; Betev, L.; Bhasin, A.; Bhati, A. K.; Bianchi, L.; Bianchi, N.; Bianchin, C.; Bielcik, J.; Bielcikova, J.; Bilandzic, A.; Bimbot, L.; Biolcati, E.; Blanc, A.; Blanco, F.; Blanco, F.; Blau, D.; Blume, C.; Boccioli, M.; Bock, N.; Bogdanov, A.; Boggild, H.; Bogolyubsky, M.; Bohm, J.; Boldizsar, L.; Bombara, M.; Bombonati, C.; Bondila, M.; Borel, H.; Borisov, A.; Bortolin, C.; Bose, S.; Bosisio, L.; Bossu, F.; Botje, M.; Bottger, S.; Bourdaud, G.; Boyer, B.; Braun, M.; Braun-Munzinger, P.*; Bravina, L.; Bregant, M.; Breitner, T.; Bruckner, G.; Brun, R.; Bruna, E.; Bruno, G. E.; Budnikov, D.; Buesching, H.; Buncic, P.; Busch, O.; Buthelezi, Z.; Caffarri, D.; Cai, X.; Caines, H.; Calvo, E.; Camacho, E.; Camerini, P.; Campbell, M.; Roman, V. C.; Capitani, G. P.; Romeo, G. C.; Carena, F.; Carena, W.; Carminati, F.; Diaz, A. C.; Caselle, M.; Castellanos, J. C.; Hernandez, J. F. C.; Catanescu, V.; Cattaruzza, E.; Cavicchioli, C.; Cerello, P.; Chambert, V.; Chang, B.; Chapeland, S.; Charpy, A.; Charvet, J. L.; Chattopadhyay, S.; Chattopadhyay, S.; Cherney, M.; Cheshkov, C.; Cheynis, B.; Chiavassa, E.; Barroso, V. C.; Chinellato, D. D.; Chochula, P.; Choi, K.; Chojnacki, M.; Christakoglou, P.; Christensen, C. H.; Christiansen, P.; Chujo, T.; Chuman, F.; Cicalo, C.; Cifarelli, L.; Cindolo, F.; Cleymans, J.; Cobanoglu, O.; Coffin, J. P.; Coli, S.; Colla, A.; Balbastre, G. C.; del Valle, Z. C.; Conner, E. S.; Constantin, P.; Contin, G.; Contreras, J. G.; Morales, Y. C.; Cormier, T. M.; Cortese, P.; Maldonado, I. C.; Cosentino, M. R.; Costa, F.; Cotallo, M. E.; Crescio, E.; Crochet, P.; Cuautle, E.; Cunqueiro, L.; Cussonneau, J.; Dainese, A.; Dalsgaard, H. H.; Danu, A.; Das, I.; Dash, A.; Dash, S.; de Barros, G. O. V.; De Caro, A.; de Cataldo, G.; de Cuveland, J.; De Falco, A.; De Gaspari, M.; de Groot, J.; De Gruttola, D.; De Marco, N.; De Pasquale, S.; De Remigis, R.; de Rooij, R.; de Vaux, G.; Delagrange, H.; Delgado, Y.; Dellacasa, G.; Deloff, A.; Demanov, V.; Denes, E.; Deppman, A.; D'Erasmo, G.; Derkach, D.; Devaux, A.; Di Bari, D.; Di Giglio, C.; Di Liberto, S.; Di Mauro, A.; Di Nezza, P.; Dialinas, M.; Diaz, L.; Diaz, R.; Dietel, T.; Divia, R.; Djuvsland, O.; Dobretsov, V.; Dobrin, A.; Dobrowolski, T.; Donigus, B.*; Dominguez, I.; Don, D. M. M.; Dordic, O.; Dubey, A. K.; Dubuisson, J.; Ducroux, L.; Dupieux, P.; Majumdar, A. K. D.; Majumdar, M. R. D.; Elia, D.; Emschermann, D.; Engel, H.; Enokizono, A.; Espagnon, B.; Estienne, M.; Esumi, S.; Evans, D.; Evrard, S.; Eyyubova, G.; Fabjan, C. W.; Fabris, D.; Faivre, J.; Falchieri, D.; Fantoni, A.; Fasel, M.*; Fateev, O.; Fearick, R.; Fedunov, A.; Fehlker, D.; Fekete, V.; Felea, D.; Fenton-Olsen, B.; Feofilov, G.; Tellez, A. F.; Ferreiro, E. G.; Ferretti, A.; Ferretti, R.; Figueredo, M. A. S.; Filchagin, S.; Fini, R.; Fionda, F. M.; Fiore, E. M.; Floris, M.; Fodor, Z.; Foertsch, S.; Foka, P.*; Fokin, S.; Formenti, F.; Fragiacomo, E.; Fragkiadakis, M.; Frankenfeld, U.*; Frolov, A.; Fuchs, U.; Furano, F.; Furget, C.; Girard, M. F.; Gaardhoje, J. J.; Gadrat, S.; Gagliardi, M.; Gago, A.; Gallio, M.; Ganoti, P.; Ganti, M. S.; Garabatos, C.; Trapaga, C. G.; Gebelein, J.; Gemme, R.; Germain, M.; Gheata, A.; Gheata, M.; Ghidini, B.; Ghosh, P.; Giraudo, G.; Giubellino, P.; Gladysz-Dziadus, E.; Glasow, R.; Glassel, P.; Glenn, A.; Jimenez, R. G.; Santos, H. G.; Gonzalez-Trueba, L. H.; Gonzalez-Zamora, P.; Gorbunov, S.; Gorbunov, Y.; Gotovac, S.; Gottschlag, H.; Grabski, V.; Grajcarek, R.; Grelli, A.; Grigoras, A.; Grigoras, C.; Grigoriev, V.; Grigoryan, A.; Grigoryan, S.; Grinyov, B.; Grion, N.; Gros, P.; Grosse-Oetringhaus, J. F.; Grossiord, J. Y.; Grosso, R.; Guber, F.; Guernane, R.; Guerra, C.; Guerzoni, B.; Gulbrandsen, K.; Gulkanyan, H.; Gunji, T.; Gupta, A.; Gupta, R.; Gustafsson, H. A.; Gutbrod, H.; Haaland, O.; Hadjidakis, C.; Haiduc, M.; Hamagaki, H.; Hamar, G.; Hamblen, J.; Han, B. H.; Harris, J. W.; Hartig, M.; Harutyunyan, A.; Hasch, D.; Hasegan, D.; Hatzifotiadou, D.; Hayrapetyan, A.; Heide, M.; Heinz, M.; Helstrup, H.; Herghelegiu, A.; Hernandez, C.; Corral, G. H.; Herrmann,

N.*; Hetland, K. F.; Hicks, B.; Hiei, A.; Hille, P. T.; Hippolyte, B.; Horaguchi, T.; Hori, Y.; Hristov, P.; Hrivnacova, I.; Hu, S.; Huang, M.; Huber, S.; Humanic, T. J.; Hutter, D.; Hwang, D. S.; Ichou, R.; Ilkaev, R.; Ilkiv, I.; Inaba, M.; Innocenti, P. G.; Ippolitov, M.; Irfan, M.; Ivan, C.*; Ivanov, A.; Ivanov, M.*; Ivanov, V.; Iwasaki, T.; Jacholkowski, A.; Jacobs, P.; Jancurova, L.; Jangal, S.; Janik, R.; Jena, C.; Jena, S.; Jirden, L.; Jones, G. T.; Jones, P. G.; Jovanovic, P.; Jung, H.; Jung, W.; Jusko, A.; Kaidalov, A. B.; Kalcher, S.; Kalinak, P.; Kalisky, M.; Kalliokoski, T.; Kalweit, A.*; Kamal, A.; Kamermans, R.; Kanaki, K.; Kang, E.; Kang, J. H.; Kapitan, J.; Kaplin, V.; Kapusta, S.; Karavichev, O.; Karavicheva, T.; Karpechev, E.; Kazantsev, A.; Kebschull, U.; Keidel, R.; Khan, M. M.; Khan, S. A.; Khanzadeev, A.; Kharlov, Y.; Kikola, D.; Kileng, B.; Kim, D. J.; Kim, D. S.; Kim, D. W.; Kim, H. N.; Kim, J.; Kim, J. H.; Kim, J. S.; Kim, M.; Kim, M.; Kim, S. H.; Kim, S.; Kim, Y.; Kirsch, S.; Kisel, I.*; Kiselev, S.; Kisiel, A.; Klay, J. L.; Klein, J.; Klein-Bosing, C.; Kliemant, M.; Klovning, A.; Kluge, A.; Knichel, M. L.*; Kniege, S.; Koch, K.*; Kolevatov, R.; Kolojvari, A.; Kondratiev, V.; Kondratyeva, N.; Konevskih, A.; Kornas, E.; Kour, R.; Kowalski, M.; Kox, S.; Kozlov, K.; Kral, J.; Kralik, I.; Kramer, F.; Kraus, I.; Kravcakova, A.; Krawutschke, T.; Krivda, M.; Krumbhorn, D.; Krus, M.; Kryshen, E.; Krzewicki, M.*; Kucheriaev, Y.; Kuhn, C.; Kuijer, P. G.; Kumar, L.; Kumar, N.; Kupczak, R.; Kurashvili, P.; Kurepin, A.; Kurepin, A. N.; Kuryakin, A.; Kushpil, S.; Kushpil, V.; Kutouski, M.; Kvaerno, H.; Kweon, M. J.; Kwon, Y.; La Rocca, P.; Lackner, F.; de Guevara, P. L.; Lafage, V.; Lal, C.; Lara, C.; Larsen, D. T.; Laurenti, G.; Lazzeroni, C.; Le Bornec, Y.; Le Bris, N.; Lee, H.; Lee, K. S.; Lee, S. C.; Lefevre, F.; Lenhardt, M.; Leistam, L.; Lehnert, J.; Lenti, V.; Leon, H.; Monzon, I. L.; Vargas, H. L.; Levai, P.; Li, X.; Li, Y.; Lietava, R.; Lindal, S.; Lindenstruth, V.; Lippmann, C.; Lisa, M. A.; Liu, L.; Loginov, V.; Lohn, S.; Lopez, X.; Noriega, M. L.; Lopez-Ramirez, R.; Torres, E. L.; Lovhoiden, G.; Soares, A. L. F.; Lu, S.; Lunardon, M.; Luparello, G.; Luquin, L.; Lutz, J. R.; Ma, K.; Ma, R.; Madagodahettige-Don, D. M.; Maevskaya, A.; Mager, M.; Mahapatra, D. P.; Maire, A.; Makhlyueva, I.; Mal'Kevich, D.; Malaev, M.; Malagalage, K. J.; Cervantes, I. M.; Malek, M.; Malkiewicz, T.; Malzacher, P.*; Mamonov, A.; Manceau, L.; Mangotra, L.; Manko, V.; Manso, F.; Manzari, V.; Mao, Y.; Mares, J.; Margagliotti, G. V.; Margotti, A.; Marin, A.*; Martashvili, I.; Martinengo, P.; Hernandez, M. I. M.; Davalos, A. M.; Garcia, G. M.; Maruyama, Y.; Chiesa, A. M.; Masciocchi, S.*; Masera, M.; Masetti, M.; Masoni, A.; Massacrier, L.; Mastromarco, M.; Mastroserio, A.; Matthews, Z. L.; Matyja, A.; Mayani, D.; Mazza, G.; Mazzoni, M. A.; Meddi, F.; Menchaca-Rocha, A.; Lorenzo, P. M.; Meoni, M.; Perez, J. M.; Mereu, P.; Miake, Y.; Michalon, A.; Miftakhov, N.; Milano, L.; Milosevic, J.; Minafra, F.; Mischke, A.; Miskowiec, D.*; Mitu, C.; Mizoguchi, K.; Mlynarz, J.; Mohanty, B.; Molnar, L.; Mondal, M. M.; Zetina, L. M.; Monteno, M.; Montes, E.; Morando, M.; Moretto, S.; Morsch, A.; Moukhanova, T.; Muccifora, V.; Mudnic, E.; Muhuri, S.; Muller, H.; Munhoz, M. G.; Munoz, J.; Musa, L.; Musso, A.; Nandi, B. K.; Nania, R.; Nappi, E.; Navach, F.; Navin, S.; Nayak, T. K.; Nazarenko, S.; Nazarov, G.; Nedosekin, A.; Nendaz, F.; Newby, J.; Nianine, A.; Nicassio, M.; Nielsen, B. S.; Nikolaev, S.; Nikolic, V.; Nikulin, S.; Nikulin, V.; Nilsen, B. S.; Nilsson, M. S.; Noferini, F.; Nomokonov, P.; Nooren, G.; Novitzky, N.; Nyatha, A.; Nygaard, C.; Nyiri, A.; Nystrand, J.; Ochirov, A.; Odyniec, G.; Oeschler, H.; Oinonen, M.; Okada, K.; Okada, Y.; Oldenburg, M.; Oleniacz, J.; Oppedisano, C.; Orsini, F.; Velasquez, A. O.; Ortona, G.; Oskarsson, A.; Osmic, F.; Osterman, L.; Ostrowski, P.; Otterlund, I.; Otwinowski, J.*; Ovrebekk, G.; Oyama, K.; Ozawa, K.; Pachmayer, Y.; Pachr, M.; Padilla, F.; Pagano, P.; Paic, G.; Painke, F.; Pajares, C.; Pal, S.; Pal, S. K.; Palaha, A.; Palmeri, A.; Panse, R.; Papikyan, V.; Pappalardo, G. S.; Park, W. J.*; Pastircak, B.; Pastore, C.; Paticchio, V.; Pavlinov, A.; Pawlak, T.; Peitzmann, T.; Pepato, A.; Pereira, H.; Peressounko, D.; Perez, C.; Perini, D.; Perrino, D.; Peryt, W.; Peschek, J.; Pesci, A.; Peskov, V.; Pestov, Y.; Peters, A. J.; Petracek, V.; Petridis, A.; Petris, M.; Petrov, P.; Petrovici, M.; Petta, C.; Peyre, J.; Piano, S.; Piccotti, A.; Pikna, M.; Pillot, P.; Pinazza, O.; Pinsky, L.; Pitz, N.; Piuz, F.; Platt, R.; Ploskon, M.; Pluta, J.; Pocheptsov, T.; Pochybova, S.; Lerma, P. L. M. P.; Poggio, F.; Poghosyan, M. G.; Polak, K.; Polichtchouk, B.; Polozov, P.; Polyakov, V.; Pommeresch, B.; Pop, A.; Posa, F.; Pospisil, V.; Potukuchi, B.; Pouthas, J.; Prasad, S. K.; Preghenella, R.; Prino, F.; Pruneau, C. A.; Pshenichnov, I.; Puddu, G.; Pujahari, P.; Pulvirenti, A.; Punin, A.; Punin, V.; Putis, M.; Putschke, J.; Quercigh, E.; Rachevski, A.; Rademakers, A.; Radomski, S.; Raiha, T. S.; Rak, J.; Rakotozafindrabe, A.; Ramello, L.; Reyes, A. R.; Rammler, M.; Raniwala, R.; Raniwala, S.; Rasanen, S. S.; Rashevskaya, I.; Rath, S.; Read, K. F.; Real, J. S.; Redlich, K.*; Renfordt, R.; Reolon, A. R.; Reshetin, A.; Rettig, F.; Revol, J. P.; Reygers, K.; Ricaud, H.; Riccati, L.; Ricci, R. A.; Richter, M.; Riedler, P.; Riegler, W.; Riggi, F.; Rivetti, A.; Cahuantzi, M. R.; Roed, K.; Roohrich, D.; Lopez, S. R.; Romita, R.*; Ronchetti, F.; Rosinsky, P.; Rosnet, P.; Rossegger, S.; Rossi, A.; Roukoutakis, F.; Rousseau, S.; Roy, C.; Roy, P.; Rubio-Montero, A. J.; Rui, R.; Rusanov, I.*; Russo, G.; Ryabinkin, E.; Rybicki, A.; Sadovsky, S.; Safarik, K.; Sahoo, R.; Saini, J.; Saiz, P.; Sakata, D.; Salgado, C. A.; da Silva, R. S. D.; Salur, S.; Samanta, T.; Sambyal, S.; Samsonov, V.; Sandor, L.; Sandoval, A.; Sano, M.; Sano, S.; Santo, R.; Santoro, R.; Sarkamo, J.; Saturnini, P.; Scapparone, E.; Scarlassara, F.; Scharenberg, R. P.; Schiaua, C.; Schicker, R.; Schindler, H.*; Schmidt, C.*; Schmidt, H. R.*; Schossmaier, K.; Schreiner, S.; Schuchmann, S.; Schukraft, J.; Schutz, Y.; Schwarz, K.*; Schweda, K.; Scioli, G.; Scomparin, E.; Scott, P. A.; Segato, G.; Semenov, D.; Senyukov, S.; Seo, J.; Serci, S.; Serkin, L.; Serradilla, E.; Sevcenco, A.; Sgura, I.; Shabratova, G.; Shahoyan, R.; Sharkov, G.; Sharma, N.; Sharma, S.; Shigaki, K.; Shimomura, M.; Shtejer, K.; Sibiriak, Y.; Siciliano, M.; Sicking, E.; Siddi, E.; Siemiarczuk, T.; Silenzi, A.; Silvermyr, D.; Simili, E.;

Simonetti, G.; Singaraju, R.; Singh, R.; Singhal, V.; Sinha, B. C.; Sinha, T.; Sitar, B.; Sitta, M.; Skaali, T. B.; Skjerdal, K.; Smakal, R.; Smirnov, N.; Snellings, R.; Snow, H.; Sogaard, C.; Soloviev, A.; Soltveit, H. K.; Soltz, R.; Sommer, W.; Son, C. W.; Son, H.; Song, M.; Soos, C.; Soramel, F.; Soyk, D.*; Spyropoulou-Stassinaki, M.; Srivastava, B. K.; Stachel, J.; Staley, F.; Stan, E.; Stefanek, G.; Stefanini, G.; Steinbeck, T.; Stenlund, E.; Steyn, G.; Stocco, D.; Stock, R.; Stolpovsky, P.; Strmen, P.; Suaide, A. A. P.; Vasquez, M. A. S.; Sugitate, T.; Suire, C.; Sumbera, M.; Susa, T.; Swoboda, D.; Symons, J.; de Toledo, A. S.; Szarka, I.; Szostak, A.; Szuba, M.; Tadel, M.; Tagridis, C.; Takahara, A.; Takahashi, J.; Tanabe, R.; Takaki, J. D. T.; Taureg, H.; Tauro, A.; Tavlet, M.; Munoz, G. T.; Telesca, A.; Terrevoli, C.; Thader, J.; Tieulent, R.; Tlusty, D.; Toia, A.; Tolyhy, T.; de Matos, C. T.; Torii, H.; Torralba, G.; Toscano, L.; Tosello, F.; Tournaire, A.; Traczyk, T.; Tribedy, P.; Troger, G.; Truesdale, D.; Trzaska, W. H.; Tsiledakis, G.; Tsilis, E.; Tsuji, T.; Tumkin, A.; Turrisi, R.; Turvey, A.; Tveter, T. S.; Tydesjo, H.; Tywoniuk, K.; Ulery, J.; Ullaland, K.; Uras, A.; Urban, J.; Urciuoli, G. M.; Usai, G. L.; Vacchi, A.; Vala, M.; Palomo, L. V.; Vallero, S.; van der Kolk, N.; Vyvre, P. V.; van Leeuwen, M.; Vannucci, L.; Vargas, A.; Varma, R.; Vasiliev, A.; Vassiliev, I.*; Vasileiou, M.; Vechernin, V.; Venaruzzo, M.; Vercellin, E.; Vergara, S.; Vernet, R.; Verweij, M.; Vetlitskiy, I.; Vickovic, L.; Viesti, G.; Vikhlyantsev, O.; Vilakazi, Z.; Baillie, O. V.; Vinogradov, A.; Vinogradov, L.; Vinogradov, Y.; Virgili, T.; Viyogi, Y. P.; Vodopianov, A.; Voloshin, K.; Voloshin, S.; Volpe, G.; von Haller, B.; Vranic, D.; Vrlakova, J.; Vulpescu, B.; Wagner, B.; Wagner, V.; Wallet, L.; Wan, R.; Wang, D.; Wang, Y.; Wang, Y.; Watanabe, K.; Wen, Q.; Wessels, J.; Westerhoff, U.; Wiechula, J.*; Wikne, J.; Wilk, A.; Wilk, G.; Williams, M. C. S.; Willis, N.; Windelband, B.; Xu, C.; Yang, C.; Yang, H.; Yasnopolskiy, S.; Yermia, F.; Yi, J.; Yin, Z.*; Yokoyama, H.; Yoo, I. K.; Yuan, X.; Yurevich, V.; Yushmanov, I.; Zabrodin, E.; Zagreev, B.; Zalite, A.; Zampolli, C.; Zanevsky, Y.; Zaporozhets, S.; Zarochentsev, A.; Zavada, P.; Zbroszczyk, H.; Zelnicek, P.; Zenin, A.; Zepeda, A.; Zgura, I.; Zhalov, M.; Zhang, X.; Zhou, D.; Zhou, S.; Zhu, J.; Zichichi, A.; Zinchenko, A.; Zinovjev, G.; Zoccarato, Y.; Zychacek, V.; Zynovyev, M.*: **Production of pions, kaons and protons in pp collisions at root s=900 GeV with ALICE at the LHC.** *Eur. Phys. J. C* **71**(6): 1655, 2011. DOI: 10.1140/epjc/s10052-011-1655-9

002 Aamodt, K.; Abelev, B.; Quintana, A. A.; Adamova, D.; Adare, A. M.; Aggarwal, M. M.; Rinella, G. A.; Agocs, A. G.; Agostinelli, A.; Salazar, S. A.; Ahammed, Z.; Ahmad, N.; Masoodi, A. A.; Ahn, S. U.; Akindinov, A.; Aleksandrov, D.; Alessandro, B.; Molina, R. A.; Alici, A.; Alkin, A.; Avina, E. A.; Alt, T.; Altini, V.; Altsybeev, I.; Andrei, C.; Andronic, A.*; Anguelov, V.; Anson, C.; Anticic, T.; Antinori, F.; Antonioli, P.; Aphecetche, L.; Appelshauser, H.; Arbor, N.; Arcelli, S.; Arend, A.; Armesto, N.; Arnaldi, R.; Aronsson, T.; Arsene, I. C.*; Arslandok, M.; Asryan, A.; Augustinus, A.; Averbeck, R.*; Awes, T. C.; Aysto, J.; Azmi, M. D.; Bach, M.; Badala, A.; Baek, Y. W.; Bailhache, R.*; Bala, R.; Ferroli, R. B.; Baldisseri, A.; Baldit, A.; Ban, J.; Baral, R. C.; Barbera, R.; Barile, F.; Barnafoldi, G. G.; Barnby, L. S.; Barret, V.; Bartke, J.; Basile, M.; Bastid, N.; Bathen, B.; Batigne, G.; Batyunya, B.; Baumann, C.; Bearden, I. G.; Beck, H.; Belikov, I.; Bellini, F.; Bellwied, R.; Belmont-Moreno, E.; Beole, S.; Berceanu, I.; Bercuci, A.; Berdermann, E.*; Berdnikov, Y.; Bergmann, C.; Betev, L.; Bhasin, A.; Bhati, A. K.; Bianchi, L.; Bianchi, N.; Bianchin, C.; Bielcik, J.; Bielcikova, J.; Bilandzic, A.; Biolcati, E.; Blanco, F.; Blanco, F.; Blau, D.; Blume, C.; Boccioli, M.; Bock, N.; Bogdanov, A.; Boggild, H.; Bogolyubsky, M.; Boldizsar, L.; Bombara, M.; Bombonati, C.; Book, J.; Borel, H.; Borissov, A.; Bortolin, C.; Bose, S.; Bossu, F.; Botje, M.; Bottger, S.; Boyer, B.; Braun-Munzinger, P.*; Bravina, L.; Bregant, M.; Breitner, T.; Broz, M.; Brun, R.; Bruna, E.; Bruno, G. E.; Budnikov, D.; Buesching, H.; Bufalino, S.; Bugaiev, K.; Busch, O.; Buthelezi, Z.; Caffarri, D.; Cai, X.; Caines, H.; Villar, E. C.; Camerini, P.; Roman, V. C.; Romeo, G. C.; Carena, F.; Carena, W.; Carlin, N.; Carminati, F.; Diaz, A. C.; Caselle, M.; Castellanos, J. C.; Hernandez, J. F. C.; Catanescu, V.; Cavicchioli, C.; Cepila, J.; Cerello, P.; Chang, B.; Chapeland, S.; Charvet, J. L.; Chattopadhyay, S.; Chattopadhyay, S.; Cherney, M.; Cheshkov, C.; Cheynis, B.; Barroso, V. C.; Chinellato, D. D.; Chochula, P.; Chojnacki, M.; Christakoglou, P.; Christensen, C. H.; Christiansen, P.; Chujo, T.; Cicalo, C.; Cifarelli, L.; Cindolo, F.; Cleymans, J.; Coccetti, F.; Coffin, J. P.; Balbastre, G. C.; del Valle, Z. C.; Constantin, P.; Contin, G.; Contreras, J. G.; Cormier, T. M.; Morales, Y. C.; Cortese, P.; Maldonado, I. C.; Cosentino, M. R.; Costa, F.; Cotallo, M. E.; Crescio, E.; Crochet, P.; Cuautle, E.; Cunqueiro, L.; Dainese, A.; Dalsgaard, H. H.; Danu, A.; Das, I.; Das, D.; Dash, S.; Dash, A.; De, S.; Moregula, A. D.; de Barros, G. O. V.; De Caro, A.; de Cataldo, G.; de Cuveland, J.; De Falco, A.; De Gruttola, D.; Delagrange, H.; Sanchez, E. D.; Mercado, Y. D.; Dellacasa, G.; Deloff, A.; Demanov, V.; De Marco, N.; Denes, E.; De Pasquale, S.; Deppman, A.; Erasmo, G. D.; de Rooij, R.; Di Bari, D.; Dietel, T.; Di Giglio, C.; Di Liberto, S.; Di Mauro, A.; Di Nezza, P.; Divia, R.; Djuvsland, O.; Dobrin, A.; Dobrowolski, T.; Dominguez, I.; Donigus, B.*; Dordic, O.; Driga, O.; Dubey, A. K.; Ducroux, L.; Dupieux, P.; Majumdar, M. R. D.; Majumdar, A. K. D.; Elia, D.; Emschermann, D.; Engel, H.; Erdal, H. A.; Espagnon, B.; Estienne, M.; Esumi, S.; Evans, D.; Evrard, S.; Eyyubova, G.; Fabjan, C. W.; Fabris, D.; Faivre, J.; Falchieri, D.; Fantoni, A.; Fasel, M.*; Fearick, R.; Fedunov, A.; Fehlker, D.; Fekete, V.; Felea, D.; Feofilov, G.; Tellez, A. F.; Ferretti, R.; Ferretti, A.; Figueredo, M. A. S.; Filchagin, S.; Fini, R.; Finogeev, D.; Fionda, F. M.; Fiore, E. M.; Floris, M.; Foertsch, S.; Foka, P.*; Fokin, S.; Fragiacomo, E.; Fragkiadakis, M.; Frankenfeld, U.*; Fuchs, U.; Furano, F.; Furget, C.; Girard, M. F.; Gaardhoje, J. J.; Gadrat, S.; Gagliardi, M.; Gago, A.; Gallio, M.; Gangadharan, D. R.; Ganoti, P.; Garabatos, C.; Garcia-Solis, E.; Gemme, R.; Gerhard, J.; Germain, M.; Geuna, C.; Gheata,

M.; Gheata, A.; Ghidini, B.; Ghosh, P.; Gianotti, P.; Girard, M. R.; Giubellino, P.; Gladysz-Dziadus, E.; Glassel, P.; Gomez, R.; Ferreiro, E. G.; Gonzalez-Trueba, L. H.; Gonzalez-Zamora, P.; Gorbunov, S.; Gotovac, S.; Grabski, V.; Graczykowski, L. K.; Grajcarek, R.; Grelli, A.; Grigoras, C.; Grigoras, A.; Grigoriev, V.; Grigoryan, S.; Grigoryan, A.; Grinyov, B.; Grion, N.; Gros, P.; Grosse-Oetringhaus, J. F.; Grossiord, J. Y.; Guber, F.; Guernane, R.; Gutierrez, C. G.; Guerzoni, B.; Guilbaud, M.; Gulbrandsen, K.; Gulkanyan, H.; Gunji, T.; Gupta, R.; Gupta, A.; Gutbrod, H.; Haaland, O.; Hadjidakis, C.; Haiduc, M.; Hamagaki, H.; Hamar, G.; Han, B. H.; Hanratty, L. D.; Harmanova, Z.; Harris, J. W.; Hartig, M.; Hasegan, D.; Hatzifotiadou, D.; Hayrapetyan, A.; Heide, M.; Heinz, M.; Helstrup, H.; Herghelegiu, A.; Corral, G. H.; Herrmann, N.*; Hetland, K. F.; Hicks, B.; Hille, P. T.; Hippolyte, B.; Horaguchi, T.; Hori, Y.; Hristov, P.; Hrivnacova, I.; Huang, M.; Huber, S.*; Humanic, T. J.; Hwang, D. S.; Ilkaev, R.; Ilkiv, I.; Inaba, M.; Incani, E.; Innocenti, G. M.; Ippolitov, M.; Irfan, M.; Ivan, C.*; Ivanov, V.; Ivanov, A.; Ivanov, M.*; Jacholkowski, A.; Jacobs, P. M.; Jancurova, L.; Jangal, S.; Janik, M. A.; Janik, R.; Jayarathna, P. H. S. Y.; Jena, S.; Jirden, L.; Jones, G. T.; Jones, P. G.; Jovanovic, P.; Jung, W.; Jung, H.; Jusko, A.; Kaidalov, A. B.; Kalcher, S.; Kalinak, P.; Kalisky, M.; Kalliokoski, T.; Kalweit, A.*; Kamermans, R.; Kanaki, K.; Kang, J. H.; Kang, E.; Kaplin, V.; Uysal, A. K.; Karavichev, O.; Karavicheva, T.; Karpechev, E.; Kazantsev, A.; Kebschull, U.; Keidel, R.; Khan, M. M.; Khan, P.; Khanzadeev, A.; Kharlov, Y.; Kileng, B.; Kim, S.; Kim, B.; Kim, D. J.; Kim, S. H.; Kim, D. S.; Kim, D. W.; Kim, J. H.; Kim, J. S.; Kim, M.; Kirsch, S.; Kisel, I.*; Kiselev, S.; Kisiel, A.; Klay, J. L.; Klein, J.; Klein-Bosing, C.; Kliemant, M.; Kluge, A.; Knichel, M. L.*; Koch, K.*; Kohler, M. K.; Kolojvari, A.; Kondratiev, V.; Kondratyeva, N.; Konevskih, A.; Kornas, E.; Don, C. K. K.; Kour, R.; Kowalski, M.; Kox, S.; Meethaleveedu, G. K.; Kozlov, K.; Kral, J.; Kralik, I.; Kramer, F.; Kraus, I.; Krawutschke, T.; Kretz, M.; Krivda, M.; Krizek, F.; Krus, M.; Kryshen, E.; Krzewicki, M.*; Kucheriaev, Y.; Kuhn, C.; Kuijer, P. G.; Kurashvili, P.; Kurepin, A.; Kurepin, A. B.; Kuryakin, A.; Kushpil, S.; Kushpil, V.; Kvaerno, H.; Kweon, M. J.; Kwon, Y.; de Guevara, P. L.; Lafage, V.; Lakomov, I.; Lara, C.; Lardeux, A.; La Rocca, P.; Larsen, D. T.; Lazzeroni, C.; Lea, R.; Le Bornec, Y.; Lee, K. S.; Lee, S. C.; Lefevre, F.; Lehnert, J.; Leistam, L.; Lenhardt, M.; Lenti, V.; Leon, H.; Monzon, I. L.; Vargas, H. L.; Levai, P.; Li, X.; Lien, J.; Lietava, R.; Lindal, S.; Lindenstruth, V.*; Lippmann, C.; Lisa, M. A.; Liu, L.; Loenne, P. I.; Loggins, V. R.; Loginov, V.; Lohn, S.; Lohner, D.; Loizides, C.; Loo, K. K.; Lopez, X.; Noriega, M. L.; Torres, E. L.; Lovhoiden, G.; Lu, X. G.; Luettig, P.; Lunardon, M.; Luparello, G.; Luquin, L.; Luzzi, C.; Ma, K.; Ma, R.; Madagodahettige-Don, D. M.; Maevskaya, A.; Mager, M.; Mahapatra, D. P.; Maire, A.; Malaev, M.; Cervantes, I. M.; Mal'Kevich, D.; Malzacher, P.*; Mamonov, A.; Mangotra, L.; Manko, V.; Manso, F.; Manzari, V.; Mao, Y.; Marchisone, M.; Mares, J.; Margagliotti, G. V.; Margotti, A.; Marin, A.*; Markert, C.; Martashvili, I.; Martinengo, P.; Martinez, M. I.; Davalos, A. M.; Garcia, G. M.; Martynov, Y.; Mas, A.; Masciocchi, S.*; Masera, M.; Masoni, A.; Massacrier, L.; Mastromarco, M.; Mastroserio, A.; Matthews, Z. L.; Matyja, A.; Mayani, D.; Mazzoni, M. A.; Meddi, F.; Menchaca-Rocha, A.; Lorenzo, P. M.; Perez, J. M.; Meres, M.; Miake, Y.; Midori, J.; Milano, L.; Milosevic, J.; Mischke, A.; Miskowiec, D.*; Mitu, C.; Mlynarz, J.; Mohanty, B.; Mohanty, A. K.; Molnar, L.; Zetina, L. M.; Monteno, M.; Montes, E.; Morando, M.; De Godoy, D. A. M.; Moretto, S.; Morsch, A.; Muccifora, V.; Mudnic, E.; Muhuri, S.; Ller, H. M.; Munhoz, M. G.; Musa, L.; Musso, A.; Nagle, J. L.; Nandi, B. K.; Nania, R.; Nappi, E.; Nattrass, C.; Navach, F.; Navin, S.; Nayak, T. K.; Nazarenko, S.; Nazarov, G.; Nedosekin, A.; Nicassio, M.; Nielsen, B. S.; Niida, T.; Nikolaev, S.; Nikolic, V.; Nikulin, S.; Nikulin, V.; Nilsen, B. S.; Nilsson, M. S.; Noferini, F.; Nooren, G.; Novitzky, N.; Nyanin, A.; Nyatha, A.; Nygaard, C.; Nystrand, J.; Obayashi, H.; Ochirov, A.; Oeschler, H.; Oh, S. K.; Oleniacz, J.; Oppedisano, C.; Velasquez, A. O.; Ortona, G.; Oskarsson, A.; Ostrowski, P.; Otwinowski, J.*; Oyama, K.; Ozawa, K.; Pachmayer, Y.; Pachr, M.; Padilla, F.; Pagano, P.; Paic, G.; Painke, F.; Pajares, C.; Pal, S. K.; Pal, S.; Palaha, A.; Palmeri, A.; Pappalardo, G. S.; Park, W. J.*; Pastircak, B.; Patalakha, D. I.; Paticchio, V.; Pavlinov, A.; Pawlak, T.; Peitzmann, T.; Peresunko, D.; Lara, C. E. P.; Perini, D.; Peryt, W.; Pesci, A.; Peskov, V.; Pestov, Y.; Peters, A. J.; Petracek, V.; Petran, M.; Petris, M.; Petrov, P.; Petrovici, M.; Petta, C.; Piano, S.; Piccotti, A.; Pikna, M.; Pillot, P.; Pinazza, O.; Pinsky, L.; Pitz, N.; Piyarathna, D. B.; Platt, R.; Ploskon, M.; Pluta, J.; Pocheptsov, T.; Pochybova, S.; Podesta-Lerma, P. L. M.; Poghosyan, M. G.; Polak, K.; Polichtchouk, B.; Pop, A.; Pospisil, V.; Potukuchi, B.; Prasad, S. K.; Preghenella, R.; Prino, F.; Pruneau, C. A.; Pshenichnov, I.; Puddu, G.; Pulvirenti, A.; Punin, V.; Putis, M.; Putschke, J.; Qvigstad, H.; Rachevski, A.; Rademakers, A.; Radomski, S.; Raiha, T. S.; Rak, J.; Rakotozafindrabe, A.; Ramello, L.; Reyes, A. R.; Rammler, M.; Raniwala, R.; Raniwala, S.; Rasanen, S. S.; Rathee, D.; Read, K. F.; Real, J. S.; Redlich, K.*; Reichelt, P.; Reicher, M.; Renfordt, R.; Reolon, A. R.; Reshetin, A.; Rettig, F.; Revol, J. P.; Reygers, K.; Ricaud, H.; Riccati, L.; Ricci, R. A.; Richter, M.; Riedler, P.; Riegler, W.; Riggi, F.; Cahuantzi, M. R.; Rohr, D.; Rohrich, D.; Romita, R.*; Ronchetti, F.; Rosinsky, P.; Rosnet, P.; Rossegger, S.; Rossi, A.; Roukoutakis, F.; Rousseau, S.; Roy, P.; Roy, C.; Montero, A. J. R.; Rui, R.; Ryabinkin, E.; Rybicki, A.; Sadovsky, S.; Safarik, K.; Sahoo, R.; Sahu, P. K.; Saiz, P.; Sakaguchi, H.; Sakai, S.; Sakata, D.; Salgado, C. A.; Sambyal, S.; Samsonov, V.; Castro, X. S.; Sandor, L.; Sandoval, A.; Sano, S.; Sano, M.; Santo, R.; Santoro, R.; Sarkamo, J.; Saturnini, P.; Scapparone, E.; Scarlassara, F.; Scharenberg, R. P.; Schiaua, C.; Schicker, R.; Schmidt, C.*; Schmidt, H. R.*; Schreiner, S.; Schuchmann, S.; Schukraft, J.; Schutz, Y.; Schwarz, K.*; Schweda, K.; Scioli, G.; Scomparin, E.; Scott, R.; Scott, P. A.; Segato, G.; Selyuzhenkov, I.*; Senyukov, S.; Serci, S.; Serradilla, E.; Sevcenco, A.; Sgura,

I.; Shabratova, G.; Shahoyan, R.; Sharma, S.; Sharma, N.; Shigaki, K.; Shimomura, M.; Shtejer, K.; Sibiriak, Y.; Siciliano, M.; Sicking, E.; Siemiarczuk, T.; Silvermyr, D.; Simonetti, G.; Singaraju, R.; Singh, R.; Singha, S.; Sinha, T.; Sinha, B. C.; Sitar, B.; Sitta, M.; Skaali, T. B.; Skjerdal, K.; Smakal, R.; Smirnov, N.; Snellings, R.; Sogaard, C.; Soltz, R.; Son, H.; Song, M.; Song, J.; Soos, C.; Soramel, F.; Spyropoulou-Stassinaki, M.; Srivastava, B. K.; Stachel, J.; Stan, I.; Stefanek, G.; Steinbeck, T.; Steinpreis, M.; Stenlund, E.; Steyn, G.; Stocco, D.; Stokkevag, C. H.; Stolpovskiy, M.; Strmen, P.; Suaide, A. A. P.; Vasquez, M. A. S.; Sugitate, T.; Suire, C.; Sukhorukov, M.; Sumbera, M.; Susa, T.; Symons, T. J. M.; de Toledo, A. S.; Szarka, I.; Szostak, A.; Tagridis, C.; Takahashi, J.; Takaki, J. D. T.; Tauro, A.; Munoz, G. T.; Telesca, A.; Terrevoli, C.; Thader, J.; Thomas, D.; Thomas, J. H.; Tieulent, R.; Timmins, A. R.; Tlusty, D.; Toia, A.; Torii, H.; Toscano, L.; Traczyk, T.; Truesdale, D.; Trzaska, W. H.; Tsuji, T.; Tumkin, A.; Turrisi, R.; Turvey, A. J.; Tveter, T. S.; Ulery, J.; Ullaland, K.; Uras, A.; Urban, J.; Urciuoli, G. M.; Usai, G. L.; Vajzer, M.; Vala, M.; Palomo, L. V.; Vallero, S.; van der Kolk, N.; Vande Vyvre, P.; van Leeuwen, M.; Vannucci, L.; Vargas, A.; Varma, R.; Vasileiou, M.; Vasiliev, A.; Vechernin, V.; Veldhoen, M.; Venaruzzo, M.; Vercellin, E.; Vergara, S.; Vernekohl, D. C.; Vernet, R.; Verweij, M.; Vickovic, L.; Viesti, G.; Vikhlyantsev, O.; Vilakazi, Z.; Baillie, O. V.; Vinogradov, Y.; Vinogradov, A.; Vinogradov, L.; Virgili, T.; Viyogi, Y. P.; Vodopyanov, A.; Voloshin, K.; Voloshin, S.; Volpe, G.; von Haller, B.; Vranic, D.; Ovrebekk, G.; Vrlakova, J.; Vulpescu, B.; Vyushin, A.; Wagner, B.; Wagner, V.; Wan, R.; Wang, Y.; Wang, Y.; Wang, M.; Wang, D.; Watanabe, K.; Wessels, J. P.; Westerhoff, U.; Wiechula, J.*; Wikne, J.; Wilde, M.; Wilk, A.; Wilk, G.; Williams, M. C. S.; Windelband, B.; Karampatsos, L. X.; Yang, H.; Yasnopolskiy, S.; Yi, J.; Yin, Z.*; Yokoyama, H.; Yoo, I. K.; Yoon, J.; Yuan, X.; Yushmanov, I.; Zabrodin, E.; Zach, C.; Zampolli, C.; Zaporozhets, S.; Zarochentsev, A.; Zavada, P.; Zaviyalov, N.; Zbroszczyk, H.; Zelnicek, P.; Zenin, A.; Zgura, I.; Zhalov, M.; Zhang, X.; Zhou, D.; Zhou, F.; Zhou, Y.; Zhu, X.; Zichichi, A.; Zinovjev, G.; Zoccarato, Y.; Zynovyev, M.*: **Higher Harmonic Anisotropic Flow Measurements of Charged Particles in Pb-Pb Collisions at root s(NN)=2.76 TeV.** *Phys. Rev. Lett.* **107**(3): 032301, 2011. DOI: 10.1103/PhysRevLett.107.032301

003 Aamodt, K.; Quintana, A. A.; Adamova, D.; Adare, A. M.; Aggarwal, M. M.; Rinella, G. A.; Agocs, A. G.; Agostinelli, A.; Salazar, S. A.; Ahammed, Z.; Ahmad, N.; Masoodi, A. A.; Ahn, S. U.; Akindinov, A.; Aleksandrov, D.; Alessandro, B.; Molina, R. A.; Alici, A.; Alkin, A.; Avina, E. A.; Alme, J.; Alt, T.; Altini, V.; Altsybeev, I.; Andrei, C.; Andronic, A. *; Anguelov, V.; Anson, C.; Anticic, T.; Antinori, F.; Antonioli, P.; Aphecetche, L.; Appelshäuser, H.; Arbor, N.; Arcelli, S.; Arend, A.; Armesto, N.; Arnaldi, R.; Aronsson, T.; Arsene, I. C.; Asryan, A.; Augustinus, A.; Averbeck, R.*; Awes, T. C.; Aysto, J.; Azmi, M. D.; Bach, M.; Badala, A.; Baek, Y. W.; Bailhache, R.*; Bala, R.; Ferroli, R. B.; Baldisseri, A.; Baldit, A.; Ban, J.; Barbera, R.; Barile, F.; Barnafoldi, G. G.; Barnby, L. S.; Barret, V.; Bartke, J.; Basile, M.; Bastid, N.; Bathen, B.; Batigne, G.; Batyunya, B.; Baumann, C.; Bearden, I. G.; Beck, H.; Belikov, I.; Bellini, F.; Bellwied, R.; Belmont-Moreno, E.; Beole, S.; Berceanu, I.; Bercuci, A.; Berdermann, E.*; Berdnikov, Y.; Bergmann, C.; Betev, L.; Bhasin, A.; Bhati, A. K.; Bianchi, L.; Bianchi, N.; Bianchin, C.; Bielcik, J.; Bielcikova, J.; Bilandzic, A.; Biolcati, E.; Blanc, A.; Blanco, F.; Blanco, F.; Blau, D.; Blume, C.; Bock, N.; Bogdanov, A.; Boggild, H.; Bogolyubsky, M.; Boldizsar, L.; Bombara, M.; Bombonati, C.; Book, J.; Borel, H.; Borissov, A.; Bortolin, C.; Bose, S.; Bossu, F.; Botje, M.; Bottger, S.; Boyer, B.; Braun-Munzinger, P.*; Bravina, L.; Bregant, M.; Breitner, T.; Broz, M.; Brun, R.; Bruna, E.; Bruno, G. E.; Budnikov, D.; Büsching, H.; Bufalino, S.; Busch, O.; Buthelezi, Z.; Caffarri, D.; Cai, X.; Caines, H.; Villar, E. C.; Camerini, P.; Roman, V. C.; Romeo, G. C.; Carena, F.; Carena, W.; Carminati, F.; Diaz, A. C.; Caselle, M.; Castellanos, J. C.; Catanescu, V.; Cavicchioli, C.; Cepila, J.; Cerello, P.; Chang, B.; Chapeland, S.; Charvet, J. L.; Chattopadhyay, S.; Chattopadhyay, S.; Cherney, M.; Cheshkov, C.; Cheynis, B.; Chiavassa, E.; Barroso, V. C.; Chinellato, D. D.; Chochula, P.; Chojnacki, M.; Christakoglou, P.; Christensen, C. H.; Christiansen, P.; Chujo, T.; Cicalo, C.; Cifarelli, L.; Cindolo, F.; Cleymans, J.; Coccetti, F.; Coffin, J. P.; Balbastre, G. C.; del Valle, Z. C.; Constantin, R.; Contin, G.; Contreras, J. G.; Cormier, T. M.; Morales, Y. C.; Maldonado, I. C.; Cortese, P.; Cosentino, M. R.; Costa, F.; Cotallo, M. E.; Crescio, E.; Crochet, P.; Cuautle, E.; Cunqueiro, L.; Erasmo, G. D.; Dainese, A.; Dalsgaard, H. H.; Danu, A.; Das, D.; Das, I.; Dash, A.; Dash, S.; De, S.; Moregula, A. D.; de Barros, G. O. V.; De Caro, A.; de Cataldo, G.; de Cuveland, J.; De Falco, A.; De Gruttola, D.; De Marco, N.; De Pasquale, S.; De Rooij, R.; Sanchez, E. D.; Delagrange, H.; Mercado, Y. D.; Dellacasa, G.; Deloff, A.; Demanov, V.; Denes, E.; Deppman, A.; Di Bari, D.; Di Giglio, C.; Di Liberto, S.; Di Mauro, A.; Di Nezza, P.; Dietel, T.; Divia, R.; Djuvsland, O.; Dobrin, A.; Dobrowolski, T.; Dominguez, I.; Donigus, B.; Dordic, O.; Driga, O.; Dubey, A. K.; Ducroux, L.; Dupieux, P.; Majumdar, A. K. D.; Majumdar, M. R. D.; Elia, D.; Emschermann, D.; Engel, H.; Erdal, H. A.; Espagnon, B.; Estienne, M.; Esumi, S.; Evans, D.; Evrard, S.; Eyyubova, G.; Fabris, D.; Faivre, J.; Falchieri, D.; Fantoni, A.; Fasel, M.; Fearick, R.; Fedunov, A.; Fehlker, D.; Fekete, V.; Felea, D.; Feofilov, G.; Tellez, A. F.; Ferreiro, E. G.; Ferretti, A.; Ferretti, R.; Figueredo, M. A. S.; Filchagin, S.; Fini, R.; Finogeev, D.; Fionda, F. M.; Fiore, E. M.; Floris, M.; Foertsch, S.; Foka, P.*; Fokin, S.; Fragiacomo, E.; Fragkiadakis, M.; Frankenfeld, U.*; Fuchs, U.; Furano, F.; Furget, C.; Girard, M. F.; Gaardhoje, J. J.; Gadrat, S.; Gagliardi, M.; Gago, A.; Gallio, M.; Ganoti, R.; Garabatos, C.*; Garcia-Solis, E.; Gemme, R.; Gerhard, J.; Germain, M.; Geuna, C.; Gheata, A.; Gheata, M.; Ghidini, B.; Ghosh, P.; Gianotti, R.; Gi-

rard, M. R.; Giubellino, P.; Gladysz-Dziadus, E.; Glässel, P.; Gomez, R.; Gonzalez-Trueba, L. H.; Gonzalez-Zamora, P.; Gorbunov, S.; Gotovac, S.; Grabski, V.; Graczykowski, L. K.; Grajcarek, R.; Grelli, A.; Grigoras, A.; Grigoras, C.; Grigoriev, V.; Grigoryan, A.; Grigoryan, S.; Grinyov, B.; Grion, N.; Gros, P.; Grosse-Oetringhaus, J. F.; Grossiord, J. Y.; Guber, F.; Guernane, R.; Gutierrez, C. G.; Guerzoni, B.; Gulbrandsen, K.; Gulkanyan, H.; Gunji, T.; Gupta, A.; Gupta, R.; Gutbrod, H.; Haaland, O.; Hadjidakis, C.; Haiduc, M.; Hamagaki, H.; Hamar, G.; Hanratty, L. D.; Harmanova, Z.; Harris, J. W.; Hartig, M.; Hasegan, D.; Hatzifotiadou, D.; Hayrapetyan, A.; Heide, M.; Heinz, M.; Helstrup, H.; Hergheleiu, A.; Corral, G. H.; Herrmann, N.; Hetland, K. F.; Hicks, B.; Hille, P. T.; Hippolyte, B.; Horaguchi, T.; Hori, Y.; Hristov, R.; Hrivnacova, I.; Huang, M.; Huber, S.; Humanic, T. J.; Hwang, D. S.; Ilkaev, R.; Ilkiv, I.; Inaba, M.; Incani, E.; Innocenti, G. M.; Ippolitov, M.; Irfan, M.; Ivan, C.*; Ivanov, A.; Ivanov, M.*; Ivanov, V.; Jachalkowski, A.; Jacobs, P. M.; Jancurova, L.; Jangal, S.; Janik, M. A.; Janik, R.; Jayarathna, P. H. S. Y.; Jena, S.; Jirden, L.; Jones, G. T.; Jones, P. G.; Jovanovic, P.; Jung, H.; Jung, W.; Jusko, A.; Kalcher, S.; Kalinak, P.; Kalisky, M.; Kalliokoski, T.; Kalweit, A.*; Kamermans, R.; Kanaki, K.; Kang, E.; Kang, J. H.; Kaplin, V.; Uysal, A. K.; Karavichev, O.; Karavicheva, T.; Karpechev, E.; Kazantsev, A.; Kebschull, U.; Keidel, R.; Khan, M. M.; Khan, P.; Khanzadeev, A.; Kharlov, Y.; Kileng, B.; Kim, D. J.; Kim, D. S.; Kim, D. W.; Kim, J. H.; Kim, J. S.; Kim, M.; Kim, S.; Kim, S. H.; Kirsch, S.; Kisel, I.*; Kiselev, S.; Kisiel, A.; Klay, J. L.; Klein, J.; Klein-Bosing, C.; Kliemant, M.; Kluge, A.; Knichel, M. L.; Koch, K.; Köhler, M. K. *; Kolojvari, A.; Kondratiev, V.; Kondratyeva, N.; Konevskih, A.; Kornas, E.; Don, C. K. K.; Kour, R.; Kowalski, M.; Kox, S.; Meethaleveedu, G. K.; Kozlov, K.; Kral, J.; Kralik, I.; Kramer, F.; Kraus, I.; Krawutschke, T.; Kretz, M.; Krivda, M.; Krizek, F.; Krus, M.; Kryshen, E.; Krzewicki, M.; Kucheriaev, Y.; Kuhn, C.; Kuijer, P. G.; Kurashvili, P.; Kurepin, A.; Kurepin, A. B.; Kuryakin, A.; Kushpil, S.; Kushpil, V.; Kweon, M. J.; Kwon, Y.; La Rocca, P.; de Guevara, P. L.; Lafage, V.; Lakomov, I.; Lara, C.; Larsen, D. T.; Lazzeroni, C.; Le Bornec, Y.; Lea, R.; Lechman, M.; Lee, K. S.; Lee, S. C.; Lefevre, F.; Lehnert, J.; Leistam, L.; Lenhardt, M.; Lenti, V.; Monzon, I. L.; Vargas, H. L.; Levai, P.; Li, X.; Lietava, R.; Lindal, S.; Lindenstruth, V.; Lippmann, C.; Lisa, M. A.; Liu, L.; Loggins, V. R.; Loginov, V.; Lohn, S.; Lohner, D.; Loizides, C.; Loo, K. K.; Lopez, X.; Noriega, M. L.; Torres, E. L.; Lovhoiden, G.; Lu, X. G.; Luettig, P.; Lunardon, M.; Luparello, G.; Luquin, L.; Luzzi, C.; Ma, K.; Ma, R.; Madagodahettige-Don, D. M.; Maevskaya, A.; Mager, M.; Mahapatra, D. P.; Maire, A.; Malaev, M.; Cervantes, I. M.; Mal'Kevich, D.; Malzacher, P.; Mamonov, A.; Manceau, L.; Manko, V.; Manso, F.; Manzari, V.; Mao, Y.; Marchisone, M.; Mares, J.; Margagliotti, G. V.; Margotti, A.; Marin, A.*; Markert, C.; Martashvili, I.; Martinengo, P.; Martinez, M. I.; Davalos, A. M.; Garcia, G. M.; Martynov, Y.; Mas, A.; Masciocchi, S.*; Masera, M.; Masoni, A.; Massacrier, L.; Mastromarco, M.; Mastroserio, A.; Matthews, Z. L.; Matyja, A.; Mayani, D.; Mazzoni, M. A.; Meddi, F.; Menchaca-Rocha, A.; Lorenzo, P. M.; Perez, J. M.; Meres, M.; Miake, Y.; Midori, J.; Milano, L.; Milosevic, J.; Mischke, A.; Miskowiec, D.*; Mitu, C.; Mlynarz, J.; Mohanty, B.; Molnar, L.; Zetina, L. M.; Monteno, M.; Montes, E.; Morando, M.; De Godoy, D. A. M.; Moretto, S.; Morsch, A.; Muccifora, V.; Mudnic, E.; Muller, H.; Muhuri, S.; Munhoz, M. G.; Musa, L.; Musso, A.; Nandi, B. K.; Nania, R.; Nappi, E.; Nattrass, C.; Navach, F.; Navin, S.; Nayak, T. K.; Nazarenko, S.; Nazarov, G.; Nedosekin, A.; Nendaz, F.; Nicassio, M.; Nielsen, B. S.; Nikolaev, S.; Nikolic, V.; Nikulin, S.; Nikulin, V.; Nilsen, B. S.; Nilsson, M. S.; Noferini, F.; Nooren, G.; Novitzky, N.; Nyanin, A.; Nyatha, A.; Nygaard, C.; Nystrand, J.; Obayashi, H.; Ochirov, A.; Oeschler, H.*; Oh, S. K.; Oleniacz, J.; Oppedisano, C.; Velasquez, A. O.; Ortona, G.; Oskarsson, A.; Ostrowski, P.; Otterlund, I.; Otwinowski, J.*; Ovrebekk, G.; Oyama, K.; Ozawa, K.; Pachmayer, Y.; Pachr, M.; Padilla, F.; Pagano, P.; Paic, G.; Painke, F.; Pajares, C.; Pal, S.; Pal, S. K.; Palaha, A.; Palmeri, A.; Pappalardo, G. S.; Park, W. J. *; Paticchio, V.; Pavlinov, A.; Pawlak, T.; Peitzmann, T.; Peresunko, D.; Lara, C. E. P.; Perini, D.; Perrino, D.; Peryt, W.; Pesci, A.; Peskov, V.; Pestov, Y.; Peters, A. J.; Petracek, V.; Petran, M.; Petris, M.; Petrov, P.; Petrovici, M.; Petta, C.; Piano, S.; Piccotti, A.; Pikna, M.; Pillot, P.; Pinazza, O.; Pinsky, L.; Pitz, N.; Piuz, F.; Piyarathna, D. B.; Platt, R.; Ploskon, M.; Pluta, J.; Pocheptsov, T.; Pochybova, S.; Podesta-Lerma, P. L. M.; Poghosyan, M. G.; Polichtchouk, B.; Pop, A.; Pospisil, V.; Potukuchi, B.; Prasad, S. K.; Preghenella, R.; Prino, F.; Pruneau, C. A.; Pshenichnov, I.; Puddu, G.; Pulvirenti, A.; Punin, V.; Putis, M.; Putschke, J.; Quercigh, E.; Qvigstad, H.; Rachevski, A.; Rademakers, A.; Radomski, S.; Raiha, T. S.; Rak, J.; Rakotozafindrabe, A.; Ramello, L.; Reyes, A. R.; Rammler, M.; Raniwala, R.; Raniwala, S.; Rasanen, S. S.; Rathee, D.; Read, K. F.; Real, J. S.; Redlich, K.; Renfordt, R.; Reolon, A. R.; Reshetin, A.; Rettig, F.; Revol, J. P.; Reygers, K.; Ricaud, H.; Riccati, L.; Ricci, R. A.; Richter, M.; Riedler, P.; Riegler, W.; Riggi, F.; Cahuantzi, M. R.; Rohr, D.; Rohrich, D.; Romita, R.*; Ronchetti, F.; Rosinsky, P.; Rosnet, P.; Rossegger, S.; Rossi, A.; Roukoutakis, F.; Rousseau, S.; Roy, C.; Roy, R.; Montero, A. J. R.; Rui, R.; Ryabinkin, E.; Rybicki, A.; Sadovsky, S.; Safarik, K.; Sahoo, R.; Sahu, P. K.; Saiz, P.; Sakai, S.; Sakata, D.; Salgado, C. A.; Sambyal, S.; Samsonov, V.; Sandor, L.; Sandoval, A.; Sano, M.; Sano, S.; Santo, R.; Santoro, R.; Sarkamo, J.; Saturnini, R.; Scapparone, E.; Scarlassara, F.; Scharenberg, R. P.; Schiaua, C.; Schicker, R.; Schmidt, C.; Schmidt, H. R.*; Schreiner, S.; Schuchmann, S.; Schukraft, J.; Schutz, Y.; Schwarz, K.; Schweda, K.; Scioli, G.; Scomparin, E.; Scott, P. A.; Scott, R.; Segato, G.; Senyukov, S.; Seo, J.; Serci, S.; Serradilla, E.; Sevcenco, A.; Sgura, I.; Shabratova, G.; Shahoyan, R.; Sharma, N.; Sharma, S.; Shigaki, K.; Shimomura, M.; Shtejer, K.; Sibiriak, Y.; Siciliano, M.; Sicking, E.; Siemiarczuk, T.; Silvermyr, D.; Simonetti, G.; Singaraju, R.; Singh, R.; Singha, S.; Sinha, B. C.;

Sinha, T.; Sitar, B.; Sitta, M.; Skaali, T. B.; Skjerdal, K.; Smakal, R.; Smirnov, N.; Snellings, R.; Sogaard, C.; Soltz, R.; Son, H.; Song, J.; Song, M.; Soos, C.; Soramel, F.; Spyropoulou-Stassinaki, M.; Srivastava, B. K.; Stachel, J.; Stan, I.; Stefanek, G.; Stefanini, G.; Steinbeck, T.; Steinpreis, M.; Stenlund, E.; Steyn, G.; Stocco, D.; Stock, R.; Stokkevag, C. H.; Stolpovskiy, M.; Strmen, P.; Suaide, A. A. P.; Vasquez, M. A. S.; Sugitate, T.; Suire, C.; Sukhorukov, M.; Sumbera, M.; Susa, T.; Swoboda, D.; Symons, T. J. M.; de Toledo, A. S.; Szarka, I.; Szostak, A.; Tagridis, C.; Takahashi, J.; Takaki, J. D. T.; Tauro, A.; Munoz, G. T.; Telesca, A.; Terrevoli, C.; Thader, J.; Thomas, D.; Thomas, J. H.; Tieulent, R.; Timmins, A. R.; Tlusty, D.; Toia, A.; Torii, H.; Tosello, F.; Traczyk, T.; Truesdale, D.; Trzaska, W. H.; Tumkin, A.; Turrisi, R.; Turvey, A. J.; Tveter, T. S.; Ulery, J.; Ullaland, K.; Uras, A.; Urban, J.; Urciuoli, G. M.; Usai, G. L.; Vajzer, M.; Vala, M.; Palomo, L. V.; Vallero, S.; van der Kolk, N.; van Leeuwen, M.; Vyvre, R. V.; Vannucci, L.; Vargas, A.; Varma, R.; Vasileiou, M.; Vasiliev, A.; Vechernin, V.; Veldhoen, M.; Venaruzzo, M.; Vercellin, E.; Vergara, S.; Vernekohl, D. C.; Vernet, R.; Verweij, M.; Vickovic, L.; Viesti, G.; Vikhlyantsev, O.; Vilakazi, Z.; Baillie, O. V.; Vinogradov, A.; Vinogradov, L.; Vinogradov, Y.; Virgili, T.; Viyogi, Y. P.; Vodopyanov, A.; Voloshin, K.; Voloshin, S.; Volpe, G.; von Haller, B.; Vranic, D.; Vrlakova, J.; Vulpescu, B.; Vyushin, A.; Wagner, B.; Wagner, V.; Wan, R.; Wang, D.; Wang, M.; Wang, Y.; Wang, Y.; Watanabe, K.; Wessels, J. P.; Westerhoff, U.; Wiechula, J.; Wikne, J.; Wilde, M.; Wilk, A.; Wilk, G.; Williams, M. C. S.; Windelband, B.; Yang, H.; Yasnopolskiy, S.; Yi, J.; Yin, Z.; Yokoyama, H.; Yoo, I. K.; Yuan, X.; Yushmanov, I.; Zabrodin, E.; Zach, C.; Zampolli, C.; Zaporozhets, S.; Zarochentsev, A.; Zavada, P.; Zaviyalov, N.; Zbroszczyk, H.; Zelnicek, P.; Zenin, A.; Zgura, I.; Zhalov, M.; Zhang, X.; Zhou, D.; Zhou, F.; Zhou, Y.; Zhu, X.; Zichichi, A.; Zinovjev, G.; Zoccarato, Y.; Zynovyev, M.: **Rapidity and transverse momentum dependence of inclusive J/psi production in pp collisions at root s=7 TeV.** *Phys. Lett. B* **704**(5): 442–455, 2011. DOI: 10.1016/j.physletb.2011.09.054

004 Aamodt, K.; Quintana, A. A.; Adamova, D.; Adare, A. M.; Aggarwal, M. M.; Rinella, G. A.; Agocs, A. G.; Salazar, S. A.; Ahammed, Z.; Ahmad, N.; Masoodi, A. A.; Ahn, S. U.; Akindinov, A.; Aleksandrov, D.; Alessandro, B.; Molina, R. A.; Alici, A.; Alkin, A.; Avina, E. A.; Alt, T.; Altini, V.; Altinpinar, S.; Altsybeev, I.; Andrei, C.; Andronic, A.*; Anguelov, V.; Anson, C.; Anticic, T.; Antinori, F.; Antonioli, P.; Aphecetche, L.; Appelshauser, H.; Arbor, N.; Arcelli, S.; Arend, A.; Armesto, N.; Arnaldi, R.; Aronsson, T.; Arsene, I. C.*; Asryan, A.; Augustinus, A.; Averbeck, R.*; Awes, T. C.; Aysto, J.; Azmi, M. D.; Bach, M.; Badala, A.; Baek, Y. W.; Bagnasco, S.; Bailhache, R.*; Bala, R.; Ferroli, R. B.; Baldisseri, A.; Baldit, A.; Ban, J.; Barbera, R.; Barile, F.; Barnafoldi, G. G.; Barnby, L. S.; Barret, V.; Bartke, J.; Basile, M.; Bastid, N.; Bathen, B.; Batigne, G.; Batyunya, B.; Baumann, C.; Bearden, I. G.; Beck, H.; Belikov, I.; Bellini, F.; Bellwied, R.; Belmont-Moreno, E.; Beole, S.; Berceanu, I.; Bercuci, A.; Berdermann, E.*; Berdnikov, Y.; Betev, L.; Bhasin, A.; Bhati, A. K.; Bianchi, L.; Bianchi, N.; Bianchin, C.; Bielcik, J.; Bielcikova, J.; Bilandzic, A.; Biolcati, E.; Blanc, A.; Blanco, F.; Blanco, F.; Blau, D.; Blume, C.; Boccioli, M.; Bock, N.; Bogdanov, A.; Boggild, H.; Bogolyubsky, M.; Boldizsar, L.; Bombara, M.; Bombonati, C.; Book, J.; Borel, H.; Bortolin, C.; Bose, S.; Bossu, F.; Botje, M.; Bottger, S.; Boyer, B.; Braun-Munzinger, P.*; Bravina, L.; Bregant, M.; Breitner, T.; Broz, M.; Brun, R.; Bruna, E.; Bruno, G. E.; Budnikov, D.; Buesching, H.; Busch, O.; Buthelezi, Z.; Caffarri, D.; Cai, X.; Caines, H.; Villar, E. C.; Camerini, P.; Roman, V. C.; Romeo, G. C.; Carena, F.; Carena, W.; Carminati, F.; Diaz, A. C.; Caselle, M.; Castellanos, J. C.; Catanescu, V.; Cavicchioli, C.; Cerello, P.; Chang, B.; Chapeland, S.; Charvet, J. L.; Chattopadhyay, S.; Chattopadhyay, S.; Cherney, M.; Cheshkov, C.; Cheynis, B.; Chiavassa, E.; Barroso, V. C.; Chinellato, D. D.; Chochula, P.; Chojnacki, M.; Christakoglou, P.; Christensen, C. H.; Christiansen, P.; Chujo, T.; Cicalo, C.; Cifarelli, L.; Cindolo, F.; Cleymans, J.; Coccetti, F.; Coffin, J. P.; Coli, S.; Balbastre, G. C.; del Valle, Z. C.; Constantin, P.; Contin, G.; Contreras, J. G.; Cormier, T. M.; Morales, Y. C.; Maldonado, I. C.; Cortese, P.; Cosentino, M. R.; Costa, F.; Cotallo, M. E.; Crescio, E.; Crochet, P.; Cuautle, E.; Cunqueiro, L.; D'Erasmo, G.; Dainese, A.; Dalsgaard, H. H.; Danu, A.; Das, D.; Das, I.; Dash, A.; Dash, S.; De, S.; Moregula, A. D.; de Barros, G. O. V.; De Caro, A.; de Cataldo, G.; de Cuveland, J.; De Falco, A.; De Gruttola, D.; De Marco, N.; De Pasquale, S.; De Remigis, R.; de Rooij, R.; Delagrange, H.; Mercado, Y. D.; Dellacasa, G.; Deloff, A.; Demanov, V.; Denes, E.; Deppman, A.; Di Bari, D.; Di Giglio, C.; Di Liberto, S.; Di Mauro, A.; Di Nezza, P.; Dietel, T.; Divia, R.; Djuvsland, O.; Dobrin, A.; Dobrowolski, T.; Dominguez, I.; Doniguss, B.*; Dordic, O.; Driga, O.; Dubey, A. K.; Ducroux, L.; Dupieux, P.; Majumdar, A. K. D.; Majumdar, M. R. D.; Elia, D.; Emschermann, D.; Engel, H.; Erdal, H. A.; Espagnon, B.; Estienne, M.; Esumi, S.; Evans, D.; Evrard, S.; Eyyubova, G.; Fabjan, C. W.; Fabris, D.; Faivre, J.; Falchieri, D.; Fantoni, A.; Fasel, M.; Fearick, R.; Fedunov, A.; Fehlker, D.; Fekete, V.; Felea, D.; Feofilov, G.; Tellez, A. F.; Ferretti, A.; Ferretti, R.; Figueredo, M. A. S.; Filchagin, S.; Fini, R.; Finogeev, D.; Fionda, F. M.; Fiore, E. M.; Floris, M.; Foertsch, S.; Foka, P.*; Fokin, S.; Fragiacomo, E.; Fragkiadakis, M.; Frankenfeld, U.*; Fuchs, U.; Furano, F.; Furget, C.; Girard, M. F.; Gaardhoje, J. J.; Gadrat, S.; Gagliardi, M.; Gago, A.; Gallio, M.; Ganoti, P.; Garabatos, C.; Gemme, R.; Gerhard, J.; Germain, M.; Geuna, C.; Gheata, A.; Gheata, M.; Ghidini, B.; Ghosh, P.; Girard, M. R.; Giraudo, G.; Giubellino, P.; Gladysz-Dziadus, E.; Glassel, P.; Gomez, R.; Gonzalez-Trueba, L. H.; Gonzalez-Zamora, P.; Santos, H. G.; Gorbunov, S.; Gotovac, S.; Grabski, V.; Grajcarek, R.; Gramling, J. L.; Grelli, A.; Grigoras, A.; Grigoras, C.; Grigoriev, V.; Grigoryan, A.; Grigoryan, S.; Grinyov, B.; Grion, N.; Gros, P.; Grosse-Oetringhaus, J. F.; Grossiord,

J. Y.; Grosso, R.; Guber, F.; Guernane, R.; Gutierrez, C. G.; Guerzoni, B.; Gulbrandsen, K.; Gulkanyan, H.; Gunji, T.; Gupta, A.; Gupta, R.; Gutbrod, H.; Haaland, O.; Hadjidakis, C.; Haiduc, M.; Hamagaki, H.; Hamar, G.; Harris, J. W.; Hartig, M.; Hasch, D.; Hasegan, D.; Hatzifotiadou, D.; Hayrapetyan, A.; Heide, M.; Heinz, M.; Helstrup, H.; Herghelegiu, A.; Hernandez, C.; Corral, G. H.; Herrmann, N.*; Hetland, K. F.; Hicks, B.; Hille, P. T.; Hippolyte, B.; Horaguchi, T.; Hori, Y.; Hristov, P.; Hrivnacova, I.; Huang, M.; Huber, S.*; Humanic, T. J.; Hwang, D. S.; Ichou, R.; Ilkaev, R.; Ilkiv, I.; Inaba, M.; Incani, E.; Innocenti, G. M.; Innocenti, P. G.; Ippolitov, M.; Irfan, M.; Ivan, C.*; Ivanov, A.; Ivanov, M.*; Ivanov, V.; Jacholkowski, A.; Jacobs, P. M.; Jancurova, L.; Jangal, S.; Janik, R.; Jayarathna, S. P.; Jena, S.; Jirden, L.; Jones, G. T.; Jones, P. G.; Jovanovic, P.; Jung, H.; Jung, W.; Jusko, A.; Kalcher, S.; Kalinak, P.; Kalisky, M.; Kalliokoski, T.; Kalweit, A.*; Kamermans, R.; Kanaki, K.; Kang, E.; Kang, J. H.; Kaplin, V.; Karavichev, O.; Karavicheva, T.; Karpechev, E.; Kazantsev, A.; Kebschull, U.; Keidel, R.; Khan, M. M.; Khanzadeev, A.; Kharlov, Y.; Kileng, B.; Kim, D. J.; Kim, D. S.; Kim, D. W.; Kim, H. N.; Kim, J. H.; Kim, J. S.; Kim, M.; Kim, M.; Kim, S.; Kim, S. H.; Kirsch, S.; Kisel, I.*; Kiselev, S.; Kisiel, A.; Klay, J. L.; Klein, J.; Klein-Bosing, C.; Kliemant, M.; Klovning, A.; Kluge, A.; Knichel, M. L.*; Koch, K.*; Kohler, M. K.; Kolevatov, R.; Kolojvari, A.; Kondratiev, V.; Kondratyeva, N.; Konevskih, A.; Kornas, E.; Don, C. K. K.; Kour, R.; Kowalski, M.; Kox, S.; Meethaleveedu, G. K.; Kozlov, K.; Kral, J.; Kralik, I.; Kramer, F.; Kraus, I.; Krawutschke, T.; Kretz, M.; Krivda, M.; Krumbhorn, D.; Krus, M.; Kryshen, E.; Krzewicki, M.; Kucheriaev, Y.; Kuhn, C.; Kuijer, P. G.; Kurashvili, P.; Kurepin, A.; Kurepin, A. B.; Kuryakin, A.; Kushpil, S.; Kushpil, V.; Kweon, M. J.; Kwon, Y.; La Rocca, P.; de Guevara, P. L.; Lafage, V.; Lara, C.; Larsen, D. T.; Lazzeroni, C.; Le Bornec, Y.; Lea, R.; Lee, K. S.; Lee, S. C.; Lefevre, F.; Lehnert, J.; Leistam, L.; Lenhardt, M.; Lenti, V.; Monzon, I. L.; Vargas, H. L.; Levai, P.; Li, X.; Lietava, R.; Lindal, S.; Lindenstruth, V.*; Lippmann, C.; Lisa, M. A.; Liu, L.; Loggins, V. R.; Loginov, V.; Lohn, S.; Lohner, D.; Loizides, C.; Lopez, X.; Noriega, M. L.; Torres, E. L.; Lovhoiden, G.; Lu, X. G.; Luettig, P.; Lunardon, M.; Luparello, G.; Luquin, L.; Luzzi, C.; Ma, K.; Ma, R.; Madagodahettige-Don, D. M.; Maevskaya, A.; Mager, M.; Mahapatra, D. P.; Maire, A.; Malaev, M.; Cervantes, I. M.; Malinina, L.; Mal'Kevich, D.; Malzacher, P.*; Mamonov, A.; Manceau, L.; Mangotra, L.; Manko, V.; Manso, F.; Manzari, V.; Mao, Y.; Mares, J.; Margagliotti, G. V.; Margotti, A.; Marin, A.*; Martashvili, I.; Martinengo, P.; Martinez, M. I.; Davalos, A. M.; Garcia, G. M.; Martynov, Y.; Mas, A.; Masciocchi, S.*; Masera, M.; Masoni, A.; Massacrier, L.; Mastromarco, M.; Mastroserio, A.; Matthews, Z. L.; Matyja, A.; Mayani, D.; Mazza, G.; Mazzoni, M. A.; Meddi, F.; Menchaca-Rocha, A.; Lorenzo, P. M.; Perez, J. M.; Mereu, P.; Miake, Y.; Midori, J.; Milano, L.; Milosevic, J.; Mischke, A.; Miskowiec, D.*; Mitu, C.; Mlynarz, J.; Mohanty, B.; Molnar, L.; Zetina, L. M.; Monteno, M.; Montes, E.; Morando, M.; De Godoy, D. A. M.; Moretto, S.; Morsch, A.; Muccifora, V.; Mudnic, E.; Muller, H.*; Muhuri, S.; Munhoz, M. G.; Munoz, J.; Musa, L.; Musso, A.; Nandi, B. K.; Nania, R.; Nappi, E.; Nattrass, C.; Navach, F.; Navin, S.; Nayak, T. K.; Nazarenko, S.; Nazarov, G.; Nedosekin, A.; Nendaz, F.; Newby, J.; Nicassio, M.; Nielsen, B. S.; Nikolaev, S.; Nikolic, V.; Nikulin, S.; Nikulin, V.; Nilsen, B. S.; Nilsson, M. S.; Noferini, F.; Nooren, G.; Novitzky, N.; Nyanin, A.; Nyatha, A.; Nygaard, C.; Nystrand, J.; Obayashi, H.; Ochirov, A.; Oeschler, H.; Oh, S. K.; Oleniacz, J.; Oppedisano, C.; Velasquez, A. O.; Ortona, G.; Oskarsson, A.; Ostrowski, P.; Otterlund, I.; Otwinowski, J.*; Ovrebekk, G.; Oyama, K.; Ozawa, K.; Pachmayer, Y.; Pachr, M.; Padilla, F.; Pagano, P.; Paic, G.; Painke, F.; Pajares, C.; Pal, S.; Pal, S. K.; Palaha, A.; Palmeri, A.; Pappalardo, G. S.; Park, W. J.*; Paticchio, V.; Pavlinov, A.; Pawlak, T.; Peitzmann, T.; Peresunko, D.; Lara, C. E. P.; Perini, D.; Perrino, D.; Peryt, W.; Pesci, A.; Peskov, V.; Pestov, Y.; Peters, A. J.; Petracek, V.; Petris, M.; Petrov, P.; Petrovici, M.; Petta, C.; Piano, S.; Piccotti, A.; Pikna, M.; Pillot, P.; Pinazza, O.; Pinsky, L.; Pitz, N.; Piuz, F.; Piyarathna, D. B.; Platt, R.; Ploskon, M.; Pluta, J.; Pocheptsov, T.; Pochybova, S.; Podesta-Lerma, P. L. M.; Poghosyan, M. G.; Polak, K.; Polichtchouk, B.; Pop, A.; Pospisil, V.; Potukuchi, B.; Prasad, S. K.; Preghenella, R.; Prino, F.; Pruneau, C. A.; Pshenichnov, I.; Puddu, G.; Pulvirenti, A.; Punin, V.; Putis, M.; Putschke, J.; Quercigh, E.; Qvigstad, H.; Rachevski, A.; Rademakers, A.; Rademakers, O.; Radomski, S.; Raiha, T. S.; Rak, J.; Rakotozafindrabe, A.; Ramello, L.; Reyes, A. R.; Rammler, M.; Raniwala, R.; Raniwala, S.; Rasanen, S. S.; Read, K. F.; Real, J. S.; Redlich, K.*; Renfordt, R.; Reolon, A. R.; Reshetin, A.; Rettig, F.; Revol, J. P.; Reygers, K.; Ricaud, H.; Riccati, L.; Ricci, R. A.; Richter, M.; Riedler, P.; Riegler, W.; Riggi, F.; Rivetti, A.; Cahuantzi, M. R.; Rohr, D.; Rohrich, D.; Romita, R.*; Ronchetti, F.; Rosinsky, P.; Rosnet, P.; Rossegger, S.; Rossi, A.; Roukoutakis, F.; Rousseau, S.; Roy, C.; Roy, P.; Montero, A. J. R.; Rui, R.; Rusanov, I.*; Ryabinkin, E.; Rybicki, A.; Sadovsky, S.; Safarik, K.; Sahoo, R.; Sahu, P. K.; Saiz, P.; Sakai, S.; Sakata, D.; Salgado, C. A.; Samanta, T.; Sambyal, S.; Samsonov, V.; Sandor, L.; Sandoval, A.; Sano, M.; Sano, S.; Santo, R.; Santoro, R.; Sarkamo, J.; Saturnini, P.; Scapparone, E.; Scarlassara, F.; Scharenberg, R. P.; Schiaua, C.; Schicker, R.; Schmidt, C.*; Schmidt, H. R.*; Schreiner, S.; Schuchmann, S.; Schukraft, J.; Schutz, Y.; Schwarz, K.*; Schweda, K.; Scioli, G.; Scomparin, E.; Scott, P. A.; Scott, R.; Gegato, S.; Senyukov, S.; Seo, J.; Serci, S.; Serradilla, E.; Sevcenco, A.; Shabratova, G.; Shahoyan, R.; Sharma, N.; Sharma, S.; Shigaki, K.; Shimomura, M.; Shtejer, K.; Sibiriak, Y.; Siciliano, M.; Sicking, E.; Siemiarczuk, T.; Silenzi, A.; Silvermyr, D.; Simonetti, G.; Singaraju, R.; Singh, R.; Sinha, B. C.; Sinha, T.; Sitar, B.; Sitta, M.; Skaali, T. B.; Skjerdal, K.; Smakal, R.; Smirnov, N.; Snellings, R.; Sogaard, C.; Soloviev, A.; Soltz, R.; Son, H.; Song, M.; Soos, C.; Soramel, F.; Spyropoulou-Stassinaki, M.; Srivastava, B. K.; Stachel, J.; Stan, I.; Ste-

fanek, G.; Stefanini, G.; Steinbeck, T.; Stenlund, E.; Steyn, G.; Stocco, D.; Stock, R.; Stolpovskiy, M.; Strmen, P.; Suaide, A. A. P.; Vasquez, M. A. S.; Sugitate, T.; Suire, C.; Sumbera, M.; Susa, T.; Swoboda, D.; Symons, T. J. M.; de Toledo, A. S.; Szarka, I.; Szostak, A.; Tagridis, C.; Takahashi, J.; Takaki, J. D. T.; Tauro, A.; Tavlet, M.; Munoz, G. T.; Telesca, A.; Terrevoli, C.; Thader, J.; Thomas, D.; Thomas, J. H.; Tieulent, R.; Timmins, A. R.; Tlusty, D.; Toia, A.; Torii, H.; Toscano, L.; Tosello, F.; Traczyk, T.; Truesdale, D.; Trzaska, W. H.; Tumkin, A.; Turrisi, R.; Turvey, A. J.; Tveter, T. S.; Ulery, J.; Ullaland, K.; Uras, A.; Urban, J.; Urciuoli, G. M.; Usai, G. L.; Vacchi, A.; Vala, M.; Palomo, L. V.; Vallero, S.; van der Kolk, N.; van Leeuwen, M.; Vande Vyvre, P.; Vannucci, L.; Vargas, A.; Varma, R.; Vasileiou, M.; Vasiliev, A.; Vechernin, V.; Venaruzzo, M.; Vercellin, E.; Vergara, S.; Vernet, R.; Verweij, M.; Vickovic, L.; Viesti, G.; Vikhlyantsev, O.; Vilakazi, Z.; Baillie, O. V.; Vinogradov, A.; Vinogradov, L.; Vinogradov, Y.; Virgili, T.; Viyogi, Y. P.; Vodopyanov, A.; Voloshin, K.; Voloshin, S.; Volpe, G.; von Haller, B.; Vranic, D.; Vrlakova, J.; Vulpescu, B.; Wagner, B.; Wagner, V.; Wan, R.; Wang, D.; Wang, Y.; Wang, Y.; Watanabe, K.; Wessels, J. P.; Westerhoff, U.; Wiechula, J.*; Wikne, J.; Wilde, M.; Wilk, A.; Wilk, G.; Williams, M. C. S.; Windelband, B.; Yang, H.; Yasnopolskiy, S.; Yi, J.; Yin, Z.; Yokoyama, H.; Yoo, I. K.; Yuan, X.; Yushmanov, I.; Zabrodin, E.; Zampolli, C.; Zaporozhets, S.; Zarochentsev, A.; Zavada, P.; Zbroszczyk, H.; Zelnicek, P.; Zenin, A.; Zgura, I.; Zhalov, M.; Zhang, X.; Zhou, D.; Zhu, X.; Zichichi, A.; Zinovjev, G.; Zoccarato, Y.; Zynovyev, M.*: **Two-pion Bose-Einstein correlations in central Pb-Pb collisions at root(S)NN=2.76 TeV.** *Phys. Lett. B* **696**(4): 328–337, 2011. DOI: 10.1016/j.physletb.2010.12.053

005 Aamodt, K.; Quintana, A. A.; Adamova, D.; Adare, A. M.; Aggarwal, M. M.; Rinella, G. A.; Agocs, A. G.; Salazar, S. A.; Ahammed, Z.; Ahmad, N.; Masoodi, A. A.; Ahn, S. U.; Akindinov, A.; Aleksandrov, D.; Alessandro, B.; Molina, R. A.; Alici, A.; Alkin, A.; Avina, E. A.; Alt, T.; Altini, V.; Altinpinar, S.; Altsybeev, I.; Andrei, C.; Andronic, A.*; Anguelov, V.; Anson, C.; Anticic, T.; Antinori, F.; Antonioli, P.; Aphecetche, L.; Appelshauser, H.; Arbor, N.; Arcelli, S.; Arend, A.; Armesto, N.; Arnaldi, R.; Aronsson, T.; Arsene, I. C.*; Asryan, A.; Augustinus, A.; Averbeck, R.*; Awes, T. C.; Aysto, J.; Azmi, M. D.; Bach, M.; Badala, A.; Baek, Y. W.; Bagnasco, S.; Bailhache, R.*; Bala, R.; Ferroli, R. B.; Baldisseri, A.; Baldit, A.; Ban, J.; Barbera, R.; Barile, F.; Barnafoldi, G. G.; Barnby, L. S.; Barret, V.; Bartke, J.; Basile, M.; Bastid, N.; Bathen, B.; Batigne, G.; Batyunya, B.; Baumann, C.; Bearden, I. G.; Beck, H.; Belikov, I.; Bellini, F.; Bellwied, R.; Belmont-Moreno, E.; Beole, S.; Berceanu, I.; Bercuci, A.; Berdermann, E.*; Berdnikov, Y.; Betev, L.; Bhasin, A.; Bhati, A. K.; Bianchi, L.; Bianchi, N.; Bianchin, C.; Bielcik, J.; Bielcikova, J.; Bilandzic, A.; Biolcati, E.; Blanc, A.; Blanco, F.; Blanco, F.; Blau, D.; Blume, C.; Boccioli, M.; Bock, N.; Bogdanov, A.; Boggild, H.; Bogolyubsky, M.; Boldizsar, L.; Bombara, M.; Bombonati, C.; Book, J.; Borel, H.; Bortolin, C.; Bose, S.; Bossu, F.; Botje, M.; Bottger, S.; Boyer, B.; Braun-Munzinger, P.*; Bravina, L.; Bregant, M.; Breitner, T.; Broz, M.; Brun, R.; Bruna, E.; Bruno, G. E.; Budnikov, D.; Buesching, H.; Busch, O.; Buthelezi, Z.; Caffarri, D.; Cai, X.; Caines, H.; Villar, E. C.; Camerini, P.; Roman, V. C.; Romeo, G. C.; Carena, F.; Carena, W.; Carminati, F.; Diaz, A. C.; Caselle, M.; Castellanos, J. C.; Catanescu, V.; Cavicchioli, C.; Cerello, P.; Chang, B.; Chapeland, S.; Charvet, J. L.; Chattopadhyay, S.; Chattopadhyay, S.; Cherney, M.; Cheshkov, C.; Cheynis, B.; Chiavassa, E.; Barroso, V. C.; Chinellato, D. D.; Chochula, P.; Chojnacki, M.; Christakoglou, P.; Christensen, C. H.; Christiansen, P.; Chujo, T.; Cicalo, C.; Cifarelli, L.; Cindolo, F.; Cleymans, J.; Coccetti, F.; Coffin, J. P.; Coli, S.; Balbastre, G. C.; del Valle, Z. C.; Constantin, P.; Contin, G.; Contreras, J. G.; Cormier, T. M.; Morales, Y. C.; Maldonado, I. C.; Cortese, P.; Cosentino, M. R.; Costa, F.; Cotallo, M. E.; Crescio, E.; Crochet, P.; Cuautle, E.; Cunqueiro, L.; Erasmo, G. D.; Dainese, A.; Dalsgaard, H. H.; Danu, A.; Das, D.; Das, I.; Dash, A.; Dash, S.; De, S.; Moregula, A. D.; de Barros, G. O. V.; De Caro, A.; de Cataldo, G.; de Cuveland, J.; De Falco, A.; De Gruttola, D.; De Marco, N.; De Pasquale, S.; De Remigis, R.; de Rooij, R.; Delagrange, H.; Mercado, Y. D.; Dellacasa, G.; Deloff, A.; Demanov, V.; Denes, E.; Deppman, A.; Di Bari, D.; Di Giglio, C.; Di Liberto, S.; Di Mauro, A.; Di Nezza, P.; Dietel, T.; Divia, R.; Djuvsland, O.; Dobrin, A.; Dobrowolski, T.; Dominguez, I.; Donigus, B.*; Dordic, O.; Driga, O.; Dubey, A. K.; Dubuisson, J.; Ducroux, L.; Dupieux, P.; Majumdar, A. K. D.; Majumdar, M. R. D.; Elia, D.; Emschermann, D.; Engel, H.; Erdal, H. A.; Espagnon, B.; Estienne, M.; Esumi, S.; Evans, D.; Evrard, S.; Eyyubova, G.; Fabjan, C. W.; Fabris, D.; Faivre, J.; Falchieri, D.; Fantoni, A.; Fasel, M.*; Fearick, R.; Fedunov, A.; Fehlker, D.; Fekete, V.; Felea, D.; Feofilov, G.; Tellez, A. F.; Ferretti, A.; Ferretti, R.; Figueredo, M. A. S.; Filchagin, S.; Fini, R.; Finogeev, D.; Fionda, F. M.; Fiore, E. M.; Floris, M.; Foertsch, S.; Foka, P.*; Fokin, S.; Fragiacomo, E.; Fragkiadakis, M.; Frankenfeld, U.*; Fuchs, U.; Furano, F.; Furget, C.; Girard, M. F.; Gaardhoje, J. J.; Gadrat, S.; Gagliardi, M.; Gago, A.; Gallio, M.; Ganoti, P.; Garabatos, C.; Gemme, R.; Gerhard, J.; Germain, M.; Geuna, C.; Gheata, A.; Gheata, M.; Ghidini, B.; Ghosh, P.; Girard, M. R.; Giraudo, G.; Giubellino, P.; Gladysz-Dziadus, E.; Glassel, P.; Gomez, R.; Gonzalez-Trueba, L. H.; Gonzalez-Zamora, P.; Santos, H. G.; Gorbunov, S.; Gotovac, S.; Grabski, V.; Grajcarek, R.; Grelli, A.; Grigoras, A.; Grigoras, C.; Grigoriev, V.; Grigoryan, A.; Grigoryan, S.; Grinyov, B.; Grion, N.; Gros, P.; Grosse-Oetringhaus, J. F.; Grossiord, J. Y.; Grosso, R.; Guber, F.; Guernane, R.; Gutierrez, C. G.; Guerzoni, B.; Gulbrandsen, K.; Gunji, T.; Gupta, A.; Gupta, R.; Gutbrod, H.; Haaland, O.; Hadjidakis, C.; Haiduc, M.; Hamagaki, H.; Hamar, G.; Harris, J. W.; Hartig, M.; Hasch, D.; Hasegan, D.; Hatzifotiadou, D.; Hayrapetyan, A.; Heide, M.; Heinz, M.; Helstrup, H.; Herghelegiu, A.; Hernandez, C.; Corral, G. H.; Herrmann,

N.*; Hetland, K. F.; Hicks, B.; Hille, P. T.; Hippolyte, B.; Horaguchi, T.; Hori, Y.; Hristov, P.; Hrivnacova, I.; Huang, M.; Huber, S.*; Humanic, T. J.; Hwang, D. S.; Ichou, R.; Ilkaev, R.; Ilkiv, I.; Inaba, M.; Incani, E.; Innocenti, G. M.; Innocenti, P. G.; Ippolitov, M.; Irfan, M.; Ivan, C.*; Ivanov, A.; Ivanov, M.*; Ivanov, V.; Jacholkowski, A.; Jacobs, P. M.; Jancurova, L.; Jangal, S.; Janik, R.; Jayarathna, S. P.; Jena, S.; Jirden, L.; Jones, G. T.; Jones, P. G.; Jovanovic, P.; Jung, H.; Jung, W.; Jusko, A.; Kalcher, S.; Kalinak, P.; Kalisky, M.; Kalliokoski, T.; Kalweit, A.*; Kamermans, R.; Kanaki, K.; Kang, E.; Kang, J. H.; Kaplin, V.; Karavichev, O.; Karavicheva, T.; Karpechev, E.; Kazantsev, A.; Kebschull, U.; Keidel, R.; Khan, M. M.; Khanzadeev, A.; Kharlov, Y.; Kileng, B.; Kim, D. J.; Kim, D. S.; Kim, D. W.; Kim, H. N.; Kim, J. H.; Kim, J. S.; Kim, M.; Kim, M.; Kim, S.; Kim, S. H.; Kirsch, S.; Kisel, I.*; Kiselev, S.; Kisiel, A.; Klay, J. L.; Klein, J.; Klein-Bosing, C.; Kliemant, M.; Klovning, A.; Kluge, A.; Knichel, M. L.*; Koch, K.*; Kohler, M. K.; Kolevatov, R.; Kolojvari, A.; Kondratiev, V.; Kondratyeva, N.; Konevskih, A.; Kornas, E.; Don, C. K. K.; Kour, R.; Kowalski, M.; Kox, S.; Kozlov, K.; Kral, J.; Kralik, I.; Kramer, F.; Kraus, I.; Krawutschke, T.; Kretz, M.; Krivda, M.; Krumbhorn, D.; Krus, M.; Kryshen, E.; Krzewicki, M.*; Kucheriaev, Y.; Kuhn, C.; Kuijer, P. G.; Kurashvili, P.; Kurepin, A.; Kurepin, A. B.; Kuryakin, A.; Kushpil, S.; Kushpil, V.; Kweon, M. J.; Kwon, Y.; La Rocca, P.; de Guevara, P. L.; Lafage, V.; Lara, C.; Larsen, D. T.; Lazzeroni, C.; Le Bornec, Y.; Lea, R.; Lee, K. S.; Lee, S. C.; Lefevre, F.; Lehnert, J.; Leistam, L.; Lenhardt, M.; Lenti, V.; Monzon, I. L.; Vargas, H. L.; Levai, P.; Li, X.; Lietava, R.; Lindal, S.; Lindenstruth, V.*; Lippmann, C.; Lisa, M. A.; Liu, L.; Loggins, V. R.; Loginov, V.; Lohn, S.; Lohner, D.; Lopez, X.; Noriega, M. L.; Torres, E. L.; Lovhoiden, G.; Lu, X. G.; Luettig, P.; Lunardon, M.; Luparello, G.; Luquin, L.; Luzzi, C.; Ma, K.; Ma, R.; Madagodahettige-Don, D. M.; Maevskaya, A.; Mager, M.; Mahapatra, D. P.; Maire, A.; Malaev, M.; Cervantes, I. M.; Mal'Kevich, D.; Malzacher, P.*; Mamonov, A.; Manceau, L.; Mangotra, L.; Manko, V.; Manso, F.; Manzari, V.; Mao, Y.; Mares, J.; Margagliotti, G. V.; Margotti, A.; Marin, A.*; Martashvili, I.; Martinengo, P.; Martinez, M. I.; Davalos, A. M.; Garcia, G. M.; Martynov, Y.; Mas, A.; Masciocchi, S.*; Masera, M.; Masoni, A.; Massacrier, L.; Mastromarco, M.; Mastroserio, A.; Matthews, Z. L.; Matyja, A.; Mayani, D.; Mazza, G.; Mazzoni, M. A.; Meddi, F.; Menchaca-Rocha, A.; Lorenzo, P. M.; Perez, J. M.; Mereu, P.; Miake, Y.; Midori, J.; Milano, L.; Milosevic, J.; Mischke, A.; Miskowiec, D.*; Mitu, C.; Mlynarz, J.; Mohanty, B.; Molnar, L.; Zetina, L. M.; Monteno, M.; Montes, E.; Morando, M.; De Godoy, D. A. M.; Moretto, S.; Morsch, A.; Muccifora, V.; Mudnic, E.; Muller, H.*; Muhuri, S.; Munhoz, M. G.; Munoz, J.; Musa, L.; Musso, A.; Nandi, B. K.; Nania, R.; Nappi, E.; Nattrass, C.; Navach, F.; Navin, S.; Nayak, T. K.; Nazarenko, S.; Nazarov, G.; Nedosekin, A.; Nendaz, F.; Newby, J.; Nicassio, M.; Nielsen, B. S.; Nikolaev, S.; Nikolic, V.; Nikulin, S.; Nikulin, V.; Nilsen, B. S.; Nilsson, M. S.; Noferini, F.; Nooren, G.; Novitzky, N.; Nyanin, A.; Nyatha, A.; Nygaard, C.; Nystrand, J.; Obayashi, H.; Ochirov, A.; Oeschler, H.; Oh, S. K.; Oleniacz, J.; Oppedisano, C.; Velasquez, A. O.; Ortona, G.; Oskarsson, A.; Ostrowski, P.; Otterlund, I.; Otwinowski, J.*; Ovrebekk, G.; Oyama, K.; Ozawa, K.; Pachmayer, Y.; Pachr, M.; Padilla, F.; Pagano, P.; Paic, G.; Painke, F.; Pajares, C.; Pal, S.; Pal, S. K.; Palaha, A.; Palmeri, A.; Pappalardo, G. S.; Park, W. J.*; Paticchio, V.; Pavlinov, A.; Pawlak, T.; Peitzmann, T.; Peresunko, D.; Lara, C. E. P.; Perini, D.; Perrino, D.; Peryt, W.; Pesci, A.; Peskov, V.; Pestov, Y.; Peters, A. J.; Petracek, V.; Petris, M.; Petrov, P.; Petrovici, M.; Petta, C.; Piano, S.; Piccotti, A.; Pikna, M.; Pillot, P.; Pinazza, O.; Pinsky, L.; Pitz, N.; Piuz, F.; Piyarathna, D. B.; Platt, R.; Ploskon, M.; Pluta, J.; Pocheptsov, T.; Pochybova, S.; Podesta-Lerma, P. L. M.; Poghosyan, M. G.; Polak, K.; Polichtchouk, B.; Pop, A.; Pospisil, V.; Potukuchi, B.; Prasad, S. K.; Preghenella, R.; Prino, F.; Pruneau, C. A.; Pshenichnov, I.; Puddu, G.; Pulvirenti, A.; Punin, V.; Putis, M.; Putschke, J.; Quercigh, E.; Qvigstad, H.; Rachevski, A.; Rademakers, A.; Rademakers, O.; Radomski, S.; Raiha, T. S.; Rak, J.; Rakotozafindrabe, A.; Ramello, L.; Reyes, A. R.; Rammler, M.; Raniwala, R.; Raniwala, S.; Rasanen, S. S.; Read, K. F.; Real, J. S.; Redlich, K.*; Renfordt, R.; Reolon, A. R.; Reshetin, A.; Rettig, F.; Revol, J. P.; Reygers, K.; Ricaud, H.; Riccati, L.; Ricci, R. A.; Richter, M.; Riedler, P.; Riegler, W.; Riggi, F.; Rivetti, A.; Cahuantzi, M. R.; Rohr, D.; Rohrich, D.; Romita, R.*; Ronchetti, F.; Rosinsky, P.; Rosnet, P.; Rossegger, S.; Rossi, A.; Roukoutakis, F.; Rousseau, S.; Roy, C.; Roy, P.; Montero, A. J. R.; Rui, R.; Rusanov, I.*; Ryabinkin, E.; Rybicki, A.; Sadovsky, S.; Safarik, K.; Sahoo, R.; Sahu, P. K.; Saiz, P.; Sakai, S.; Sakata, D.; Salgado, C. A.; Samanta, T.; Sambyal, S.; Samsonov, V.; Sandor, L.; Sandoval, A.; Sano, M.; Sano, S.; Santo, R.; Santoro, R.; Sarkamo, J.; Saturnini, P.; Scapparone, E.; Scarlassara, F.; Scharenberg, R. P.; Schiaua, C.; Schicker, R.; Schmidt, C.*; Schmidt, H. R.*; Schreiner, S.; Schuchmann, S.; Schukraft, J.; Schutz, Y.; Schwarz, K.*; Schweda, K.; Scioli, G.; Scomparin, E.; Scott, P. A.; Scott, R.; Segato, G.; Senyukov, S.; Seo, J.; Serci, S.; Serradilla, E.; Sevcenco, A.; Shabratova, G.; Shahoyan, R.; Sharma, N.; Sharma, S.; Shigaki, K.; Shimomura, M.; Shtejer, K.; Sibiriak, Y.; Siciliano, M.; Sicking, E.; Siemiarczuk, T.; Silenzi, A.; Silvermyr, D.; Simonetti, G.; Singaraju, R.; Singh, R.; Sinha, B. C.; Sinha, T.; Sitar, B.; Sitta, M.; Skaali, T. B.; Skjerdal, K.; Smakal, R.; Smirnov, N.; Snellings, R.; Sogaard, C.; Soloviev, A.; Soltz, R.; Son, H.; Song, M.; Soos, C.; Soramel, F.; Spyropoulou-Stassinaki, M.; Srivastava, B. K.; Stachel, J.; Stan, I.; Stefanek, G.; Stefanini, G.; Steinbeck, T.; Stenlund, E.; Steyn, G.; Stocco, D.; Stock, R.; Stolpovskiy, M.; Strmen, P.; Suaide, A. A. P.; Vasquez, M. A. S.; Sugitate, T.; Suire, C.; Sumbera, M.; Susa, T.; Swoboda, D.; Symons, T. J. M.; de Toledo, A. S.; Szarka, I.; Szostak, A.; Tagridis, C.; Takahashi, J.; Takaki, J. D. T.; Tauro, A.; Tavlet, M.; Munoz, G. T.; Telesca, A.; Terrevoli, C.; Thader, J.; Thomas, D.; Thomas, J. H.; Tieulent, R.; Timmins, A. R.; Tlusty, D.;

Toia, A.; Torii, H.; Toscano, L.; Tosello, F.; Traczyk, T.; Truesdale, D.; Trzaska, W. H.; Tumkin, A.; Turrisi, R.; Turvey, A. J.; Tveter, T. S.; Ulery, J.; Ullaland, K.; Uras, A.; Urban, J.; Urciuoli, G. M.; Usai, G. L.; Vacchi, A.; Vala, M.; Palomo, L. V.; Vallero, S.; van der Kolk, N.; van Leeuwen, M.; Vande Vyvre, P.; Vannucci, L.; Vargas, A.; Varma, R.; Vasileiou, M.; Vasiliev, A.; Vechernin, V.; Venaruzzo, M.; Vercellin, E.; Vergara, S.; Vernet, R.; Verweij, M.; Vickovic, L.; Viesti, G.; Vikhlyantsev, O.; Vilakazi, Z.; Baillie, O. V.; Vinogradov, A.; Vinogradov, L.; Vinogradov, Y.; Virgili, T.; Viyogi, Y. P.; Vodopyanov, A.; Voloshin, K.; Voloshin, S.; Volpe, G.; von Haller, B.; Vranic, D.; Vrlakova, J.; Vulpescu, B.; Wagner, B.; Wagner, V.; Wan, R.; Wang, D.; Wang, Y.; Wang, Y.; Watanabe, K.; Wessels, J. P.; Westerhoff, U.; Wiechula, J.*; Wikne, J.; Wilde, M.; Wilk, A.; Wilk, G.; Williams, M. C. S.; Windelband, B.; Yang, H.; Yasnopolskiy, S.; Yi, J.; Yin, Z.*; Yokoyama, H.; Yoo, I. K.; Yuan, X.; Yushmanov, I.; Zabrodin, E.; Zampolli, C.; Zaporozhets, S.; Zarochentsev, A.; Zavada, P.; Zbroszczyk, H.; Zelnicek, P.; Zenin, A.; Zgura, I.; Zhalov, M.; Zhang, X.; Zhou, D.; Zichichi, A.; Zinovjev, G.; Zoccarato, Y.; Zynovyev, M.*: **Strange particle production in proton-proton collisions at root s=0.9 TeV with ALICE at the LHC.** *Eur. Phys. J. C* **71**(3): 1594, 2011. DOI: 10.1140/epjc/s10052-011-1594-5

006 Aamodt, K.; Quintana, A. A.; Adamova, D.; Adare, A. M.; Aggarwal, M. M.; Rinella, G. A.; Agocs, A. G.; Salazar, S. A.; Ahammed, Z.; Ahmad, N.; Masoodi, A. A.; Ahn, S. U.; Akindinov, A.; Aleksandrov, D.; Alessandro, B.; Molina, R. A.; Alici, A.; Alkin, A.; Avina, E. A.; Alt, T.; Altini, V.; Altinpinar, S.; Altsybeev, I.; Andrei, C.; Andronic, A.*; Anguelov, V.; Anson, C.; Anticic, T.; Antinori, F.; Antonioli, P.; Aphecetche, L.; Appelshauser, H.; Arbor, N.; Arcelli, S.; Arend, A.; Armesto, N.; Arnaldi, R.; Aronsson, T.; Arsene, I. C.*; Asryan, A.; Augustinus, A.; Averbeck, R.*; Awes, T. C.; Aysto, J.; Azmi, M. D.; Bach, M.; Badala, A.; Baek, Y. W.; Bagnasco, S.; Bailhache, R.*; Bala, R.; Ferroli, R. B.; Baldisseri, A.; Baldit, A.; Ban, J.; Barbera, R.; Barile, F.; Barnafoldi, G. G.; Barnby, L. S.; Barret, V.; Bartke, J.; Basile, M.; Bastid, N.; Bathen, B.; Batigne, G.; Batyunya, B.; Baumann, C.; Bearden, I. G.; Beck, H.; Belikov, I.; Bellini, F.; Bellwied, R.; Belmont-Moreno, E.; Beole, S.; Berceanu, I.; Bercuci, A.; Berdermann, E.*; Berdnikov, Y.; Betev, L.; Bhasin, A.; Bhati, A. K.; Bianchi, L.; Bianchi, N.; Bianchin, C.; Bielcik, J.; Bielcikova, J.; Bilandzic, A.; Biolcati, E.; Blanc, A.; Blanco, F.; Blanco, F.; Blau, D.; Blume, C.; Boccioli, M.; Bock, N.; Bogdanov, A.; Boggild, H.; Bogolyubsky, M.; Boldizsar, L.; Bombara, M.; Bombonati, C.; Book, J.; Borel, H.; Bortolin, C.; Bose, S.; Bossu, F.; Botje, M.; Bottger, S.; Boyer, B.; Braun-Munzinger, P.*; Bravina, L.; Bregant, M.; Breitner, T.; Broz, M.; Brun, R.; Bruna, E.; Bruno, G. E.; Budnikov, D.; Buesching, H.; Busch, O.; Buthelezi, Z.; Caffarri, D.; Cai, X.; Caines, H.; Villar, E. C.; Camerini, P.; Roman, V. C.; Romeo, G. C.; Carena, F.; Carena, W.; Carminati, F.; Diaz, A. C.; Caselle, M.; Castellanos, J. C.; Catanescu, V.; Cavicchioli, C.; Cerello, P.; Chang, B.; Chapeland, S.; Charvet, J. L.; Chattopadhyay, S.; Chattopadhyay, S.; Cherney, M.; Cheshkov, C.; Cheynis, B.; Chiavassa, E.; Barroso, V. C.; Chinellato, D. D.; Chochula, P.; Chojnacki, M.; Christakoglou, P.; Christensen, C. H.; Christiansen, P.; Chujo, T.; Cicalo, C.; Cifarelli, L.; Cindolo, F.; Cleymans, J.; Coccetti, F.; Coffin, J. P.; Coli, S.; Balbastre, G. C.; del Valle, Z. C.; Constantin, P.; Contin, G.; Contreras, J. G.; Cormier, T. M.; Morales, Y. C.; Maldonado, I. C.; Cortese, P.; Cosentino, M. R.; Costa, F.; Cotallo, M. E.; Crescio, E.; Crochet, P.; Cuautle, E.; Cunqueiro, L.; Erasmo, G. D.; Dainese, A.; Dalsgaard, H. H.; Danu, A.; Das, D.; Das, I.; Dash, A.; Dash, S.; De, S.; Moregula, A. D.; de Barros, G. O. V.; De Caro, A.; de Cataldo, G.; de Cuveland, J.; De Falco, A.; De Gruttola, D.; De Marco, N.; De Pasquale, S.; De Remigis, R.; de Rooij, R.; Delagrange, H.; Mercado, Y. D.; Dellacasa, G.; Deloff, A.; Demanov, V.; Denes, E.; Deppman, A.; Di Bari, D.; Di Giglio, C.; Di Liberto, S.; Di Mauro, A.; Di Nezza, P.; Dietel, T.; Divia, R.; Djuvsland, O.; Dobrin, A.; Dobrowolski, T.; Dominguez, I.; Donigus, B.*; Dordic, O.; Driga, O.; Dubey, A. K.; Ducroux, L.; Dupieux, P.; Majumdar, A. K. D.; Majumdar, M. R. D.; Elia, D.; Emschermann, D.; Engel, H.; Erdal, H. A.; Espagnon, B.; Estienne, M.; Esumi, S.; Evans, D.; Evrard, S.; Eyyubova, G.; Fabjan, C. W.; Fabris, D.; Faivre, J.; Falchieri, D.; Fantoni, A.; Fasel, M.*; Fearick, R.; Fedunov, A.; Fehlker, D.; Fekete, V.; Felea, D.; Feofilov, G.; Tellez, A. F.; Ferretti, A.; Ferretti, R.; Figueredo, M. A. S.; Filchagin, S.; Fini, R.; Finogeev, D.; Fionda, F. M.; Fiore, E. M.; Floris, M.; Foertsch, S.; Foka, P.*; Fokin, S.; Fragiacomo, E.; Fragkiadakis, M.; Frankenfeld, U.*; Fuchs, U.; Furano, F.; Furget, C.; Girard, M. F.; Gaardhoje, J. J.; Gadrat, S.; Gagliardi, M.; Gago, A.; Gallio, M.; Ganoti, P.; Garabatos, C.; Gemme, R.; Gerhard, J.; Germain, M.; Geuna, C.; Gheata, A.; Gheata, M.; Ghidini, B.; Ghosh, P.; Girard, M. R.; Giraudo, G.; Giubellino, P.; Gladysz-Dziadus, E.; Glassel, P.; Gomez, R.; Gonzalez-Trueba, L. H.; Gonzalez-Zamora, P.; Santos, H. G.; Gorbunov, S.; Gotovac, S.; Grabski, V.; Grajcarek, R.; Grelli, A.; Grigoras, A.; Grigoras, C.; Grigoriev, V.; Grigoryan, A.; Grigoryan, S.; Grinyov, B.; Grion, N.; Gros, P.; Grosse-Oetringhaus, J. F.; Grossiord, J. Y.; Grosso, R.; Guber, F.; Guernane, R.; Gutierrez, C. G.; Guerzoni, B.; Gulbrandsen, K.; Gulkanyan, H.; Gunji, T.; Gupta, A.; Gupta, R.; Gutbrod, H.; Haaland, O.; Hadjidakis, C.; Haiduc, M.; Hamagaki, H.; Hamar, G.; Harris, J. W.; Hartig, M.; Hasch, D.; Hasegan, D.; Hatzifotiadou, D.; Hayrapetyan, A.; Heide, M.; Heinz, M.; Helstrup, H.; Herghelegiu, A.; Hernandez, C.; Corral, G. H.; Herrmann, N.*; Hetland, K. F.; Hicks, B.; Hille, P. T.; Hippolyte, B.; Horaguchi, T.; Hori, Y.; Hristov, P.; Hrivnacova, I.; Huang, M.; Huber, S.*; Humanic, T. J.; Hwang, D. S.; Ichou, R.; Ilkaev, R.; Ilkiv, I.; Inaba, M.; Incani, E.; Innocenti, G. M.; Innocenti, P. G.; Ippolitov, M.; Irfan, M.; Ivan, C.*; Ivanov, A.; Ivanov, M.*; Ivanov, V.; Jacholkowski, A.; Jacobs, P. M.; Jancurova, L.; Jangal, S.; Janik, R.; Jayarathna, S. P.; Jena, S.; Jirden, L.; Jones, G. T.; Jones, P. G.; Jovanovic,

P.; Jung, H.; Jung, W.; Jusko, A.; Kalcher, S.; Kalinak, P.; Kalisky, M.; Kalliokoski, T.; Kalweit, A.*; Kamermans, R.; Kanaki, K.; Kang, E.; Kang, J. H.; Kaplin, V.; Karavichev, O.; Karavicheva, T.; Karpechev, E.; Kazantsev, A.; Kebschull, U.; Keidel, R.; Khan, M. M.; Khanzadeev, A.; Kharlov, Y.; Kileng, B.; Kim, D. J.; Kim, D. S.; Kim, D. W.; Kim, H. N.; Kim, J. H.; Kim, J. S.; Kim, M.; Kim, M.; Kim, S.; Kim, S. H.; Kirsch, S.; Kisel, I.*; Kiselev, S.; Kisiel, A.; Klay, J. L.; Klein, J.; Klein-Bosing, C.; Kliemant, M.; Klovning, A.; Kluge, A.; Knichel, M. L.*; Koch, K.*; Kohler, M. K.; Kolevatov, R.; Kolojvari, A.; Kondratiev, V.; Kondratyeva, N.; Konevskih, A.; Kornas, E.; Don, C. K. K.; Kour, R.; Kowalski, M.; Kox, S.; Meethaleveedu, G. K.; Kozlov, K.; Kral, J.; Kralik, I.; Kramer, F.; Kraus, I.; Krawutschke, T.; Kretz, M.; Krivda, M.; Krumbhorn, D.; Krus, M.; Kryshen, E.; Krzewicki, M.*; Kucheriaev, Y.; Kuhn, C.; Kuijer, P. G.; Kurashvili, P.; Kurepin, A.; Kurepin, A. B.; Kuryakin, A.; Kushpil, S.; Kushpil, V.; Kweon, M. J.; Kwon, Y.; La Rocca, P.; de Guevara, P. L.; Lafage, V.; Lara, C.; Larsen, D. T.; Lazzeroni, C.; Le Bornec, Y.; Lea, R.; Lee, K. S.; Lee, S. C.; Lefevre, F.; Lehnert, J.; Leistam, L.; Lenhardt, M.; Lenti, V.; Monzon, I. L.; Vargas, H. L.; Levai, P.; Li, X.; Lietava, R.; Lindal, S.; Lindenstruth, V.*; Lippmann, C.; Lisa, M. A.; Liu, L.; Loggins, V. R.; Loginov, V.; Lohn, S.; Lohner, D.; Loizides, C.; Lopez, X.; Noriega, M. L.; Torres, E. L.; Lovhoiden, G.; Lu, X. G.; Luettig, P.; Lunardon, M.; Luparello, G.; Luquin, L.; Luzzi, C.; Ma, K.; Ma, R.; Madagodahettige-Don, D. M.; Maevskaya, A.; Mager, M.; Mahapatra, D. P.; Maire, A.; Malaev, M.; Cervantes, I. M.; Mal'Kevich, D.; Malzacher, P.*; Mamonov, A.; Manceau, L.; Mangotra, L.; Manko, V.; Manso, F.; Manzari, V.; Mao, Y.; Mares, J.; Margagliotti, G. V.; Margotti, A.; Marin, A.*; Martashvili, I.; Martinengo, P.; Martinez, M. I.; Davalos, A. M.; Garcia, G. M.; Martynov, Y.; Mas, A.; Masciocchi, S.*; Masera, M.; Masoni, A.; Massacrier, L.; Mastromarco, M.; Mastroserio, A.; Matthews, Z. L.; Matyja, A.; Mayani, D.; Mazza, G.; Mazzoni, M. A.; Meddi, F.; Menchaca-Rocha, A.; Lorenzo, P. M.; Perez, J. M.; Mereu, P.; Miake, Y.; Midori, J.; Milano, L.; Milosevic, J.; Mischke, A.; Miskowiec, D.*; Mitu, C.; Mlynarz, J.; Mohanty, B.; Molnar, L.; Zetina, L. M.; Monteno, M.; Montes, E.; Morando, M.; De Godoy, D. A. M.; Moretto, S.; Morsch, A.; Muccifora, V.; Mudnic, E.; Muller, H.*; Muhuri, S.; Munhoz, M. G.; Munoz, J.; Musa, L.; Musso, A.; Nandi, B. K.; Nania, R.; Nappi, E.; Nattrass, C.; Navach, F.; Navin, S.; Nayak, T. K.; Nazarenko, S.; Nazarov, G.; Nedosekin, A.; Nendaz, F.; Newby, J.; Nicassio, M.; Nielsen, B. S.; Nikolaev, S.; Nikolic, V.; Nikulin, S.; Nikulin, V.; Nilsen, B. S.; Nilsson, M. S.; Noferini, F.; Nooren, G.; Novitzky, N.; Nyanin, A.; Nyatha, A.; Nygaard, C.; Nystrand, J.; Obayashi, H.; Ochirov, A.; Oeschler, H.; Oh, S. K.; Oleniacz, J.; Oppedisano, C.; Velasquez, A. O.; Ortona, G.; Oskarsson, A.; Ostrowski, P.; Otterlund, I.; Otwinowski, J.*; Ovrebekk, G.; Oyama, K.; Ozawa, K.; Pachmayer, Y.; Pachr, M.; Padilla, F.; Pagano, P.; Paic, G.; Painke, F.; Pajares, C.; Pal, S.; Pal, S. K.; Palaha, A.; Palmeri, A.; Pappalardo, G. S.; Park, W. J.*; Paticchio, V.; Pavlinov, A.; Pawlak, T.; Peitzmann, T.; Peresunko, D.; Lara, C. E. P.; Perini, D.; Perrino, D.; Peryt, W.; Pesci, A.; Peskov, V.; Pestov, Y.; Peters, A. J.; Petracek, V.; Petris, M.; Petrov, P.; Petrovici, M.; Petta, C.; Piano, S.; Piccotti, A.; Pikna, M.; Pillot, P.; Pinazza, O.; Pinsky, L.; Pitz, N.; Piuz, F.; Piyarathna, D. B.; Platt, R.; Ploskon, M.; Pluta, J.; Pocheptsov, T.; Pochybova, S.; Podesta-Lerma, P. L. M.; Poghosyan, M. G.; Polak, K.; Polichtchouk, B.; Pop, A.; Pospisil, V.; Potukuchi, B.; Prasad, S. K.; Preghenella, R.; Prino, F.; Pruneau, C. A.; Pshenichnov, I.; Puddu, G.; Pulvirenti, A.; Punin, V.; Putis, M.; Putschke, J.; Quercigh, E.; Qvigstad, H.; Rachevski, A.; Rademakers, A.; Rademakers, O.; Radomski, S.; Raiha, T. S.; Rak, J.; Rakotozafindrabe, A.; Ramello, L.; Reyes, A. R.; Rammler, M.; Raniwala, R.; Raniwala, S.; Rasanen, S. S.; Read, K. F.; Real, J. S.; Redlich, K.*; Renfordt, R.; Reolon, A. R.; Reshetin, A.; Rettig, F.; Revol, J. P.; Reygers, K.; Ricaud, H.; Riccati, L.; Ricci, R. A.; Richter, M.; Riedler, P.; Riegler, W.; Riggi, F.; Rivetti, A.; Cahuantzi, M. R.; Rohr, D.; Rohrich, D.; Romita, R.*; Ronchetti, F.; Rosinsky, P.; Rosnet, P.; Rossegger, S.; Rossi, A.; Roukoutakis, F.; Rousseau, S.; Roy, C.; Roy, P.; Montero, A. J. R.; Rui, R.; Rusanov, I.*; Ryabinkin, E.; Rybicki, A.; Sadovsky, S.; Safarik, K.; Sahoo, R.; Sahu, P. K.; Saiz, P.; Sakai, S.; Sakata, D.; Salgado, C. A.; Samanta, T.; Sambyal, S.; Samsonov, V.; Sandor, L.; Sandoval, A.; Sano, M.; Sano, S.; Santo, R.; Santoro, R.; Sarkamo, J.; Saturnini, P.; Scapparone, E.; Scarlassara, F.; Scharenberg, R. P.; Schiaua, C.; Schicker, R.; Schmidt, C.*; Schmidt, H. R.*; Schreiner, S.; Schuchmann, S.; Schukraft, J.; Schutz, Y.; Schwarz, K.*; Schweda, K.; Scioli, G.; Scomparin, E.; Scott, P. A.; Scott, R.; Segato, G.; Senyukov, S.; Seo, J.; Serci, S.; Serradilla, E.; Sevcenco, A.; Shabratova, G.; Shahoyan, R.; Sharma, N.; Sharma, S.; Shigaki, K.; Shimomura, M.; Shtejer, K.; Sibiriak, Y.; Siciliano, M.; Sicking, E.; Siemiarczuk, T.; Silenzi, A.; Silvermyr, D.; Simonetti, G.; Singaraju, R.; Singh, R.; Sinha, B. C.; Sinha, T.; Sitar, B.; Sitta, M.; Skaali, T. B.; Skjerdal, K.; Smakal, R.; Smirnov, N.; Snellings, R.; Sogaard, C.; Soloviev, A.; Soltz, R.; Son, H.; Song, M.; Soos, C.; Soramel, F.; Spyropoulou-Stassinaki, M.; Srivastava, B. K.; Stachel, J.; Stan, I.; Stefanek, G.; Stefanini, G.; Steinbeck, T.; Stenlund, E.; Steyn, G.; Stocco, D.; Stock, R.; Stolpovskiy, M.; Strmen, P.; Suaide, A. A. P.; Vasquez, M. A. S.; Sugitate, T.; Suire, C.; Sumbera, M.; Susa, T.; Swoboda, D.; Symons, T. J. M.; de Toledo, A. S.; Szarka, I.; Szostak, A.; Tagridis, C.; Takahashi, J.; Takaki, J. D. T.; Tauro, A.; Tavlet, M.; Munoz, G. T.; Telesca, A.; Terrevoli, C.; Thader, J.; Thomas, D.; Thomas, J. H.; Tieulent, R.; Timmins, A. R.; Tlusty, D.; Toia, A.; Torii, H.; Toscano, L.; Tosello, F.; Traczyk, T.; Truesdale, D.; Trzaska, W. H.; Tumkin, A.; Turrisi, R.; Turvey, A. J.; Tveter, T. S.; Ulery, J.; Ullaland, K.; Uras, A.; Urban, J.; Urciuoli, G. M.; Usai, G. L.; Vacchi, A.; Vala, M.; Palomo, L. V.; Vallero, S.; van der Kolk, N.; van Leeuwen, M.; Vyvre, P. V.; Vannucci, L.; Vargas, A.; Varma, R.; Vasileiou, M.; Vasiliev, A.; Vechernin, V.; Venaruzzo, M.; Vercellin, E.; Vergara, S.; Vernet, R.; Ver-

weij, M.; Vickovic, L.; Viesti, G.; Vikhlyantsev, O.; Vilakazi, Z.; Baillie, O. V.; Vinogradov, A.; Vinogradov, L.; Vinogradov, Y.; Virgili, T.; Viyogi, Y. P.; Vodopyanov, A.; Voloshin, K.; Voloshin, S.; Volpe, G.; von Haller, B.; Vranic, D.; Vrlakova, J.; Vulpescu, B.; Wagner, B.; Wagner, V.; Wan, R.; Wang, D.; Wang, Y.; Wang, Y.; Watanabe, K.; Wessels, J. P.; Westerhoff, U.; Wiechula, J.*; Wikne, J.; Wilde, M.; Wilk, A.; Wilk, G.; Williams, M. C. S.; Windelband, B.; Yang, H.; Yasnopolskiy, S.; Yi, J.; Yin, Z.3390; Yokoyama, H.; Yoo, I. K.; Yuan, X.; Yushmanov, I.; Zabrodin, E.; Zampolli, C.; Zaporozhets, S.; Zarochentsev, A.; Zavada, P.; Zbroszczyk, H.; Zelnicek, P.; Zenin, A.; Zgura, I.; Zhalov, M.; Zhang, X.; Zhou, D.; Zhu, X.; Zichichi, A.; Zinovjev, G.; Zoccarato, Y.; Zynovyev, M.*: **Centrality Dependence of the Charged-Particle Multiplicity Density at Midrapidity in Pb-Pb Collisions at root s(NN)=2.76 TeV.** *Phys. Rev. Lett.* **106**(3): 032301, 2011. DOI: 10.1103/PhysRevLett.106.032301

007 Aamodt, K.; Quintana, A. A.; Adamova, D.; Adare, A. M.; Aggarwal, M. M.; Rinella, G. A.; Agocs, A. G.; Salazar, S. A.; Ahammed, Z.; Ahmad, N.; Masoodi, A. A.; Ahn, S. U.; Akindinov, A.; Aleksandrov, D.; Alessandro, B.; Molina, R. A.; Alici, A.; Alkin, A.; Avina, E. A.; Alt, T.; Altini, V.; Altinpinar, S.; Altsybeev, I.; Andrei, C.; Andronic, A.*; Anguelov, V.; Anson, C.; Anticic, T.; Antinori, F.; Antonioli, P.; Aphecetche, L.; Appelshauser, H.; Arbor, N.; Arcelli, S.; Arend, A.; Armesto, N.; Arnaldi, R.; Aronsson, T.; Arsene, I. C.; Asryan, A.; Augustinus, A.; Averbeck, R.; Awes, T. C.; Aysto, J.; Azmi, M. D.; Bach, M.; Badala, A.; Baek, Y. W.; Bagnasco, S.; Bailhache, R.*; Bala, R.; Ferroli, R. B.; Baldisseri, A.; Baldit, A.; Ban, J.; Barbera, R.; Barile, F.; Barnafoldi, G. G.; Barnby, L. S.; Barret, V.; Bartke, J.; Basile, M.; Bastid, N.; Bathen, B.; Batigne, G.; Batyunya, B.; Baumann, C.; Bearden, I. G.; Beck, H.; Belikov, I.; Bellini, F.; Bellwied, R.; Belmont-Moreno, E.; Beole, S.; Berceanu, I.; Bercuci, A.; Berdermann, E.*; Berdnikov, Y.; Betev, L.; Bhasin, A.; Bhati, A. K.; Bianchi, L.; Bianchi, N.; Bianchin, C.; Bielcik, J.; Bielcikova, J.; Bilandzic, A.; Biolcati, E.; Blanc, A.; Blanco, F.; Blanco, F.; Blau, D.; Blume, C.; Boccioli, M.; Bock, N.; Bogdanov, A.; Boggild, H.; Bogolyubsky, M.; Boldizsar, L.; Bombara, M.; Bombonati, C.; Book, J.; Borel, H.; Bortolin, C.; Bose, S.; Bossu, F.; Botje, M.; Bottger, S.; Boyer, B.; Braun-Munzinger, P.*; Bravina, L.; Bregant, M.; Breitner, T.; Broz, M.; Brun, R.; Bruna, E.; Bruno, G. E.; Budnikov, D.; Buesching, H.; Busch, O.; Buthelezi, Z.; Caffarri, D.; Cai, X.; Caines, H.; Villar, E. C.; Camerini, P.; Roman, V. C.; Romeo, G. C.; Carena, F.; Carena, W.; Carminati, F.; Diaz, A. C.; Caselle, M.; Castellanos, J. C.; Catanescu, V.; Cavicchioli, C.; Cerello, P.; Chang, B.; Chapeland, S.; Charvet, J. L.; Chattopadhyay, S.; Chattopadhyay, S.; Cherney, M.; Cheshkov, C.; Cheynis, B.; Chiavassa, E.; Barroso, V. C.; Chinellato, D. D.; Chochula, P.; Chojnacki, M.; Christakoglou, P.; Christensen, C. H.; Christiansen, P.; Chujo, T.; Cicalo, C.; Cifarelli, L.; Cindolo, F.; Cleymans, J.; Coccetti, F.; Coffin, J. P.; Coli, S.; Balbastre, G. C.; del Valle, Z. C.; Constantin, P.; Contin, G.; Contreras, J. G.; Cormier, T. M.; Morales, Y. C.; Maldonado, I. C.; Cortese, P.; Cosentino, M. R.; Costa, F.; Cotallo, M. E.; Crescio, E.; Crochet, P.; Cuautle, E.; Cunqueiro, L.; Erasmo, G. D.; Dainese, A.; Dalsgaard, H. H.; Danu, A.; Das, D.; Das, I.; Dash, A.; Dash, S.; De, S.; Moregula, A. D.; de Barros, G. O. V.; De Caro, A.; de Cataldo, G.; de Cuveland, J.; De Falco, A.; De Gruttola, D.; De Marco, N.; De Pasquale, S.; De Remigis, R.; de Rooij, R.; Delagrange, H.; Mercado, Y. D.; Dellacasa, G.; Deloff, A.; Demanov, V.; Denes, E.; Deppman, A.; Di Bari, D.; Di Giglio, C.; Di Liberto, S.; Di Mauro, A.; Di Nezza, P.; Dietel, T.; Divia, R.; Djuvsland, O.; Dobrin, A.; Dobrowolski, T.; Dominguez, I.; Donigus, B.*; Dordic, O.; Driga, O.; Dubey, A. K.; Dubuisson, J.; Ducroux, L.; Dupieux, P.; Majumdar, A. K. D.; Majumdar, M. R. D.; Elia, D.; Emschermann, D.; Engel, H.; Erdal, H. A.; Espagnon, B.; Estienne, M.; Esumi, S.; Evans, D.; Evrard, S.; Eyyubova, G.; Fabjan, C. W.; Fabris, D.; Faivre, J.; Falchieri, D.; Fantoni, A.; Fasel, M.*; Fearick, R.; Fedunov, A.; Fehlker, D.; Fekete, V.; Felea, D.; Feofilov, C.; Tellez, A. F.; Ferretti, A.; Ferretti, R.; Figueredo, M. A. S.; Filchagin, S.; Fini, R.; Finogeev, D.; Fionda, F. M.; Fiore, E. M.; Floris, M.; Foertsch, S.; Foka, P.*; Fokin, S.; Fragiacomo, E.; Fragkiadakis, M.; Frankenfeld, U.*; Fuchs, U.; Furano, F.; Furget, C.; Girard, M. F.; Gaardhoje, J. J.; Gadrat, S.; Gagliardi, M.; Gago, A.; Gallio, M.; Ganoti, P.; Garabatos, C.; Gemme, R.; Gerhard, J.; Germain, M.; Geuna, C.; Gheata, A.; Gheata, M.; Ghidini, B.; Ghosh, P.; Girard, M. R.; Giraudo, G.; Giubellino, P.; Gladysz-Dziadus, E.; Glassel, P.; Gomez, R.; Gonzalez-Trueba, L. H.; Gonzalez-Zamora, P.; Santos, H. G.; Gorbunov, S.; Gotovac, S.; Grabski, V.; Grajcarek, R.; Grelli, A.; Grigoras, A.; Grigoras, C.; Grigoriev, V.; Grigoryan, A.; Grigoryan, S.; Grinyov, B.; Grion, N.; Gros, P.; Grosse-Oetringhaus, J. F.; Grossiord, J. Y.; Grosso, R.; Guber, F.; Guernane, R.; Gutierrez, C. G.; Guerzoni, B.; Gulbrandsen, K.; Gunji, T.; Gupta, A.; Gupta, R.; Gutbrod, H.; Haaland, O.; Hadjidakis, C.; Haiduc, M.; Hamagaki, H.; Hamar, G.; Harris, J. W.; Hartig, M.; Hasch, D.; Hasegan, D.; Hatzifotiadou, D.; Hayrapetyan, A.; Heide, M.; Heinz, M.; Helstrup, H.; Herghelegiu, A.; Hernandez, C.; Corral, G. H.; Herrmann, N.*; Hetland, K. F.; Hicks, B.; Hille, P. T.; Hippolyte, B.; Horaguchi, T.; Hori, Y.; Hristov, P.; Hrivnacova, I.; Huang, M.; Huber, S.*; Humanic, T. J.; Hwang, D. S.; Ichou, R.; Ilkaev, R.; Ilkiv, I.; Inaba, M.; Incani, E.; Innocenti, G. M.; Innocenti, P. C.; Ippolitov, M.; Irfan, M.; Ivan, C.*; Ivanov, A.; Ivanov, M.*; Ivanov, V.; Jacholkowski, A.; Jacobs, P. M.; Jancurova, L.; Jangal, S.; Janik, R.; Jayarathna, S. P.; Jena, S.; Jirden, L.; Jones, G. T.; Jones, P. G.; Jovanovic, P.; Jung, H.; Jung, W.; Jusko, A.; Kalcher, S.; Kalinak, P.; Kalisky, M.; Kalliokoski, T.; Kalweit, A.*; Kamermans, R.; Kanaki, K.; Kang, E.; Kang, J. H.; Kaplin, V.; Karavichev, O.; Karavicheva, T.; Karpechev, E.; Kazantsev, A.; Kebschull, U.; Keidel, R.; Khan, M. M.; Khanzadeev, A.; Kharlov, Y.; Kileng, B.; Kim, D. J.; Kim, D. S.; Kim, D. W.; Kim, H. N.; Kim, J. H.; Kim, J. S.; Kim,

M.; Kim, M.; Kim, S.; Kim, S. H.; Kirsch, S.; Kisel, I.*; Kiselev, S.; Kisiel, A.; Klay, J. L.; Klein, J.; Klein-Bosing, C.; Kliemant, M.; Klovning, A.; Kluge, A.; Knichel, M. L.*; Koch, K.; Kohler, M. K.; Kolevatov, R.; Kolojvari, A.; Kondratiev, V.; Kondratyeva, N.; Konevskih, A.; Kornas, E.; Don, C. K. K.; Kour, R.; Kowalski, M.; Kox, S.; Kozlov, K.; Kral, J.; Kralik, I.; Kramer, F.; Kraus, I.; Krawutschke, T.; Kretz, M.; Krivda, M.; Krumbhorn, D.; Krus, M.; Kryshen, E.; Krzewicki, M.*; Kucheriaev, Y.; Kuhn, C.; Kuijer, P. G.; Kurashvili, P.; Kurepin, A.; Kurepin, A. B.; Kuryakin, A.; Kushpil, S.; Kushpil, V.; Kweon, M. J.; Kwon, Y.; La Rocca, P.; de Guevara, P. L.; Lafage, V.; Lara, C.; Larsen, D. T.; Lazzeroni, C.; Le Bornec, Y.; Lea, R.; Lee, K. S.; Lee, S. C.; Lefevre, F.; Lehnert, J.; Leistam, L.; Lenhardt, M.; Lenti, V.; Monzon, I. L.; Vargas, H. L.; Levai, P.; Li, X.; Lietava, R.; Lindal, S.; Lindenstruth, V.*; Lippmann, C.; Lisa, M. A.; Liu, L.; Loggins, V. R.; Loginov, V.; Lohn, S.; Lohner, D.; Loizides, C.; Lopez, X.; Noriega, M. L.; Torres, E. L.; Lovhoiden, G.; Lu, X. G.; Luettig, P.; Lunardon, M.; Luparello, G.; Luquin, L.; Luzzi, C.; Ma, K.; Ma, R.; Madagodahettige-Don, D. M.; Maevskaya, A.; Mager, M.; Mahapatra, D. P.; Maire, A.; Malaev, M.; Cervantes, I. M.; Mal'Kevich, D.; Malzacher, P.*; Mamonov, A.; Manceau, L.; Mangotra, L.; Manko, V.; Manso, F.; Manzari, V.; Mao, Y.; Mares, J.; Margagliotti, G. V.; Margotti, A.; Marin, A.; Martashvili, I.; Martinengo, P.; Martinez, M. I.; Davalos, A. M.; Garcia, G. M.; Martynov, Y.; Mas, A.; Masciocchi, S.*; Masera, M.; Masoni, A.; Massacrier, L.; Mastromarco, M.; Mastroserio, A.; Matthews, Z. L.; Matyja, A.; Mayani, D.; Mazza, G.; Mazzoni, M. A.; Meddi, F.; Menchaca-Rocha, A.; Lorenzo, P. M.; Perez, J. M.; Mereu, P.; Miake, Y.; Midori, J.; Milano, L.; Milosevic, J.; Mischke, A.; Miskowiec, D.*; Mitu, C.; Mlynarz, J.; Mohanty, B.; Molnar, L.; Zetina, L. M.; Monteno, M.; Montes, E.; Morando, M.; De Godoy, D. A. M.; Moretto, S.; Morsch, A.; Muccifora, V.; Mudnic, E.; Muller, H.*; Muhuri, S.; Munhoz, M. G.; Munoz, J.; Musa, L.; Musso, A.; Nandi, B. K.; Nania, R.; Nappi, E.; Nattrass, C.; Navach, F.; Navin, S.; Nayak, T. K.; Nazarenko, S.; Nazarov, G.; Nedosekin, A.; Nendaz, F.; Newby, J.; Nicassio, M.; Nielsen, B. S.; Nikolaev, S.; Nikolic, V.; Nikulin, S.; Nikulin, V.; Nilsen, B. S.; Nilsson, M. S.; Noferini, F.; Nooren, G.; Novitzky, N.; Nyanin, A.; Nyatha, A.; Nygaard, C.; Nystrand, J.; Obayashi, H.; Ochirov, A.; Oeschler, H.; Oh, S. K.; Oleniacz, J.; Oppedisano, C.; Velasquez, A. O.; Ortona, G.; Oskarsson, A.; Ostrowski, P.; Otterlund, I.; Otwinowski, J.*; Ovrebekk, G.; Oyama, K.; Ozawa, K.; Pachmayer, Y.; Pachr, M.; Padilla, F.; Pagano, P.; Paic, G.; Painke, F.; Pajares, C.; Pal, S.; Pal, S. K.; Palaha, A.; Palmeri, A.; Pappalardo, G. S.; Park, W. J.*; Paticchio, V.; Pavlinov, A.; Pawlak, T.; Peitzmann, T.; Peresunko, D.; Lara, C. E. P.; Perini, D.; Perrino, D.; Peryt, W.; Pesci, A.; Peskov, V.; Pestov, Y.; Peters, A. J.; Petracek, V.; Petris, M.; Petrov, P.; Petrovici, M.; Petta, C.; Piano, S.; Piccotti, A.; Pikna, M.; Pillot, P.; Pinazza, O.; Pinsky, L.; Pitz, N.; Piuz, F.; Piyarathna, D. B.; Platt, R.; Ploskon, M.; Pluta, J.; Pocheptsov, T.; Pochybova, S.; Podesta-Lerma, P. L. M.; Poghosyan, M. G.; Polak, K.; Polichtchouk, B.; Pop, A.; Pospisil, V.; Potukuchi, B.; Prasad, S. K.; Preghenella, R.; Prino, F.; Pruneau, C. A.; Pshenichnov, I.; Puddu, G.; Pulvirenti, A.; Punin, V.; Putis, M.; Putschke, J.; Quercigh, E.; Qvigstad, H.; Rachevski, A.; Rademakers, A.; Rademakers, O.; Radomski, S.; Raiha, T. S.; Rak, J.; Rakotozafindrabe, A.; Ramello, L.; Reyes, A. R.; Rammler, M.; Raniwala, R.; Raniwala, S.; Rasanen, S. S.; Read, K. F.; Real, J. S.; Redlich, K.*; Renfordt, R.; Reolon, A. R.; Reshetin, A.; Rettig, F.; Revol, J. P.; Reygers, K.; Ricaud, H.; Riccati, L.; Ricci, R. A.; Richter, M.; Riedler, P.; Riegler, W.; Riggi, F.; Rivetti, A.; Cahuantzi, M. R.; Rohr, D.; Rohrich, D.; Romita, R.*; Ronchetti, F.; Rosinsky, P.; Rosnet, P.; Rossegger, S.; Rossi, A.; Roukoutakis, F.; Rousseau, S.; Roy, C.; Roy, P.; Montero, A. J. R.; Rui, R.; Rusanov, I.*; Ryabinkin, E.; Rybicki, A.; Sadovsky, S.; Safarik, K.; Sahoo, R.; Sahu, P. K.; Saiz, P.; Sakai, S.; Sakata, D.; Salgado, C. A.; Samanta, T.; Sambyal, S.; Samsonov, V.; Sandor, L.; Sandoval, A.; Sano, M.; Sano, S.; Santo, R.; Santoro, R.; Sarkamo, J.; Saturnini, P.; Scapparone, E.; Scarlassara, F.; Scharenberg, R. P.; Schiaua, C.; Schicker, R.; Schmidt, C.*; Schmidt, H. R.*; Schreiner, S.; Schuchmann, S.; Schukraft, J.; Schutz, Y.; Schwarz, K.*; Schweda, K.; Scioli, G.; Scomparin, E.; Scott, P. A.; Scott, R.; Segato, G.; Senyukov, S.; Seo, J.; Serci, S.; Serradilla, E.; Sevcenco, A.; Shabratova, G.; Shahoyan, R.; Sharma, N.; Sharma, S.; Shigaki, K.; Shimomura, M.; Shtejer, K.; Sibiriak, Y.; Siciliano, M.; Sicking, E.; Siemiarczuk, T.; Silenzi, A.; Silvermyr, D.; Simonetti, G.; Singaraju, R.; Singh, R.; Sinha, B. C.; Sinha, T.; Sitar, B.; Sitta, M.; Skaali, T. B.; Skjerdal, K.; Smakal, R.; Smirnov, N.; Snellings, R.; Sogaard, C.; Soloviev, A.; Soltz, R.; Son, H.; Song, M.; Soos, C.; Soramel, F.; Spyropoulou-Stassinaki, M.; Srivastava, B. K.; Stachel, J.; Stan, I.; Stefanek, G.; Stefanini, G.; Steinbeck, T.; Stenlund, E.; Steyn, G.; Stocco, D.; Stock, R.; Stolpovskiy, M.; Strmen, P.; Suaide, A. A. P.; Vasquez, M. A. S.; Sugitate, T.; Suire, C.; Sumbera, M.; Susa, T.; Swoboda, D.; Symons, T. J. M.; de Toledo, A. S.; Szarka, I.; Szostak, A.; Tagridis, C.; Takahashi, J.; Takaki, J. D. T.; Tauro, A.; Tavlet, M.; Munoz, G. T.; Telesca, A.; Terrevoli, C.; Thader, J.; Thomas, D.; Thomas, J. H.; Tieulent, R.; Timmins, A. R.; Tlusty, D.; Toia, A.; Torii, H.; Toscano, L.; Tosello, F.; Traczyk, T.; Truesdale, D.; Trzaska, W. H.; Tumkin, A.; Turrisi, R.; Turvey, A. J.; Tveter, T. S.; Ulery, J.; Ullaland, K.; Uras, A.; Urban, J.; Urciuoli, G. M.; Usai, G. L.; Vacchi, A.; Vala, M.; Palomo, L. V.; Vallero, S.; van der Kolk, N.; van Leeuwen, M.; Vyvre, P. V.; Vannucci, L.; Vargas, A.; Varma, R.; Vasileiou, M.; Vasiliev, A.; Vechernin, V.; Venaruzzo, M.; Vercellin, E.; Vergara, S.; Vernet, R.; Verweij, M.; Vickovic, L.; Viesti, G.; Vikhlyantsev, O.; Vilakazi, Z.; Baillie, O. V.; Vinogradov, A.; Vinogradov, L.; Vinogradov, Y.; Virgili, T.; Viyogi, Y. P.; Vodopyanov, A.; Voloshin, K.; Voloshin, S.; Volpe, G.; von Haller, B.; Vranic, D.; Vrlakova, J.; Vulpescu, B.; Wagner, B.; Wagner, V.; Wan, R.; Wang, D.; Wang, Y.; Wang, Y.; Watanabe, K.; Wessels, J. P.; Westerhoff, U.; Wiechula, J.*; Wikne,

J.; Wilde, M.; Wilk, A.; Wilk, G.; Williams, M. C. S.; Windelband, B.; Yang, H.; Yasnopolskiy, S.; Yi, J.; Yin, Z.*; Yokoyama, H.; Yoo, I. K.; Yuan, X.; Yushmanov, I.; Zabrodin, E.; Zampolli, C.; Zaporozhets, S.; Zarochentsev, A.; Zavada, P.; Zbroszczyk, H.; Zelnicek, P.; Zenin, A.; Zgura, I.; Zhalov, M.; Zhang, X.; Zhou, D.; Zichichi, A.; Zinovjev, G.; Zoccarato, Y.; Zynovyev, M.*: **Suppression of charged particle production at large transverse momentum in central Pb-Pb collisions at root s(NN)=2.76 TeV.** *Phys. Lett. B* **696**(1-2): 30–39, 2011. DOI: 10.1016/j.physletb.2010.12.020

008 Aamodt, K.; Quintana, A. A.; Adamova, D.; Adare, A. M.; Aggarwal, M. M.; Rinella, G. A.; Agocs, A. G.; Salazar, S. A.; Ahammed, Z.; Ahmad, N.; Masoodi, A. A.; Ahn, S. U.; Akindinov, A.; Aleksandrov, D.; Alessandro, B.; Molina, R. A.; Alici, A.; Alkin, A.; Avina, E. A.; Alt, T.; Altini, V.; Altinpinar, S.; Altsybeev, I.; Andrei, C.; Andronic, A.; Anguelov, V.; Anson, C.; Anticic, T.; Antinori, F.; Antonioli, P.; Aphecetche, L.; Appelshauser, H.; Arbor, N.; Arcelli, S.; Arend, A.; Armesto, N.; Arnaldi, R.; Aronsson, T.; Arsene, I. C.; Asryan, A.; Augustinus, A.; Averbeck, R.; Awes, T. C.; Aysto, J.; Azmi, M. D.; Bach, M.; Badala, A.; Baek, Y. W.; Bagnasco, S.; Bailhache, R.; Bala, R.; Ferroli, R. B.; Baldisseri, A.; Baldit, A.; Ban, J.; Barbera, R.; Barile, F.; Barnafoldi, G. G.; Barnby, L. S.; Barret, V.; Bartke, J.; Basile, M.; Bastid, N.; Bathen, B.; Batigne, G.; Batyunya, B.; Baumann, C.; Bearden, I. G.; Beck, H.; Belikov, I.; Bellini, F.; Bellwied, R.; Belmont-Moreno, E.; Beole, S.; Berceanu, I.; Bercuci, A.; Berdermann, E.; Berdnikov, Y.; Betev, L.; Bhasin, A.; Bhati, A. K.; Bianchi, L.; Bianchi, N.; Bianchin, C.; Bielcik, J.; Bielcikova, J.; Bilandzic, A.; Biolcati, E.; Blanc, A.; Blanco, F.; Blanco, F.; Blau, D.; Blume, C.; Boccioli, M.; Bock, N.; Bogdanov, A.; Boggild, H.; Bogolyubsky, M.; Boldizsar, L.; Bombara, M.; Bombonati, C.; Book, J.; Borel, H.; Bortolin, C.; Bose, S.; Bossu, F.; Botje, M.; Bottger, S.; Boyer, B.; Braun-Munzinger, P.; Bravina, L.; Bregant, M.; Breitner, T.; Broz, M.; Brun, R.; Bruna, E.; Bruno, G. E.; Budnikov, D.; Buesching, H.; Busch, O.; Buthelezi, Z.; Caffarri, D.; Cai, X.; Caines, H.; Villar, E. C.; Camerini, P.; Roman, V. C.; Romeo, G. C.; Carena, F.; Carena, W.; Carminati, F.; Diaz, A. C.; Caselle, M.; Castellanos, J. C.; Catanescu, V.; Cavicchioli, C.; Cerello, P.; Chang, B.; Chapeland, S.; Charvet, J. L.; Chattopadhyay, S.; Chattopadhyay, S.; Cherney, M.; Cheshkov, C.; Cheynis, B.; Chiavassa, E.; Barroso, V. C.; Chinellato, D. D.; Chochula, P.; Chojnacki, M.; Christakoglou, P.; Christensen, C. H.; Christiansen, P.; Chujo, T.; Cicalo, C.; Cifarelli, L.; Cindolo, F.; Cleymans, J.; Coccetti, F.; Coffin, J. P.; Coli, S.; Balbastre, G. C.; del Valle, Z. C.; Constantin, P.; Contin, G.; Contreras, J. G.; Cormier, T. M.; Morales, Y. C.; Maldonado, I. C.; Cortese, P.; Cosentino, M. R.; Costa, F.; Cotallo, M. E.; Crescio, E.; Crochet, P.; Cuautle, E.; Cunqueiro, L.; D'Erasmo, G.; Dainese, A.; Dalsgaard, H. H.; Danu, A.; Das, D.; Das, I.; Dash, A.; Dash, S.; De, S.; Moregula, A. D.; de Barros, G. O. V.; De Caro, A.; de Cataldo, G.; de Cuveland, J.; De Falco, A.; De Gruttola, D.; De Marco, N.; De Pasquale, S.; De Remigis, R.; de Rooij, R.; Delagrange, H.; Mercado, Y. D.; Dellacasa, G.; Deloff, A.; Demanov, V.; Denes, E.; Deppman, A.; Di Bari, D.; Di Giglio, C.; Di Liberto, S.; Di Mauro, A.; Di Nezza, P.; Dietel, T.; Divia, R.; Djuvsland, O.; Dobrin, A.; Dobrowolski, T.; Dominguez, I.; Donigus, B.; Dordic, O.; Driga, O.; Dubey, A. K.; Ducroux, L.; Dupieux, P.; Majumdar, A. K. D.; Majumdar, M. R. D.; Elia, D.; Emschermann, D.; Engel, H.; Erdal, H. A.; Espagnon, B.; Estienne, M.; Esumi, S.; Evans, D.; Evrard, S.; Eyyubova, G.; Fabris, D.; Faivre, J.; Falchieri, D.; Fantoni, A.; Fasel, M.; Fearick, R.; Fedunov, A.; Fehlker, D.; Fekete, V.; Felea, D.; Feofilov, G.; Tellez, A. F.; Ferretti, A.; Ferretti, R.; Figueredo, M. A. S.; Filchagin, S.; Fini, R.; Finogeev, D.; Fionda, F. M.; Fiore, E. M.; Floris, M.; Foertsch, S.; Foka, P.; Fokin, S.; Fragiacomo, E.; Fragkiadakis, M.; Frankenfeld, U.; Fuchs, U.; Furano, F.; Furget, C.; Girard, M. F.; Gaardhoje, J. J.; Gadrat, S.; Gagliardi, M.; Gago, A.; Gallio, M.; Ganoti, P.; Garabatos, C.; Gemme, R.; Gerhard, J.; Germain, M.; Geuna, C.; Gheata, A.; Gheata, M.; Ghidini, B.; Ghosh, P.; Girard, M. R.; Giraudo, G.; Giubellino, P.; Gladysz-Dziadus, E.; Glassel, P.; Gomez, R.; Gonzalez-Trueba, L. H.; Gonzalez-Zamora, P.; Santos, H. G.; Gorbunov, S.; Gotovac, S.; Grabski, V.; Graczykowski, L. K.; Grajcarek, R.; Grelli, A.; Grigoras, A.; Grigoras, C.; Grigoriev, V.; Grigoryan, A.; Grigoryan, S.; Grinyov, B.; Grion, N.; Gros, P.; Grosse-Oetringhaus, J. F.; Grossiord, J. Y.; Grosso, R.; Guber, F.; Guernane, R.; Gutierrez, C. G.; Guerzoni, B.; Gulbrandsen, K.; Gulkanyan, H.; Gunji, T.; Gupta, A.; Gupta, R.; Gutbrod, H.; Haaland, O.; Hadjidakis, C.; Haiduc, M.; Hamagaki, H.; Hamar, G.; Harris, J. W.; Hartig, M.; Hasch, D.; Hasegan, D.; Hatzifotiadou, D.; Hayrapetyan, A.; Heide, M.; Heinz, M.; Helstrup, H.; Herghelegiu, A.; Hernandez, C.; Corral, G. H.; Herrmann, N.; Hetland, K. F.; Hicks, B.; Hille, P. T.; Hippolyte, B.; Horaguchi, T.; Hori, Y.; Hristov, P.; Hrivnacova, I.; Huang, M.; Huber, S.; Humanic, T. J.; Hwang, D. S.; Ichou, R.; Ilkaev, R.; Ilkiv, I.; Inaba, M.; Incani, E.; Innocenti, G. M.; Innocenti, P. G.; Ippolitov, M.; Irfan, M.; Ivan, C.; Ivanov, A.; Ivanov, M.; Ivanov, V.; Jacholkowski, A.; Jacobs, P. M.; Jancurova, L.; Jangal, S.; Janik, M. A.; Janik, R.; Jayarathna, S. P.; Jena, S.; Jirden, L.; Jones, G. T.; Jones, P. G.; Jovanovic, P.; Jung, H.; Jung, W.; Jusko, A.; Kalcher, S.; Kalinak, P.; Kalisky, M.; Kalliokoski, T.; Kalweit, A.; Kamermans, R.; Kanaki, K.; Kang, E.; Kang, J. H.; Kaplin, V.; Karavichev, O.; Karavicheva, T.; Karpechev, E.; Kazantsev, A.; Kebschull, U.; Keidel, R.; Khan, M. M.; Khanzadeev, A.; Kharlov, Y.; Kileng, B.; Kim, D. J.; Kim, D. S.; Kim, D. W.; Kim, H. N.; Kim, J. H.; Kim, J. S.; Kim, M.; Kim, M.; Kim, S.; Kim, S. H.; Kirsch, S.; Kisel, I.; Kiselev, S.; Kisiel, A.; Klay, J. L.; Klein, J.; Klein-Bosing, C.; Kliemant, M.; Klovning, A.; Kluge, A.; Knichel, M. L.; Koch, K.; Kohler, M. K.; Kolevatov, R.; Kolojvari, A.; Kondratiev, V.; Kondratyeva, N.; Konevskih, A.; Kornas, E.; Don, C. K. K.; Kour, R.; Kowalski, M.; Kox, S.; Meethaleveedu, G. K.; Kozlov, K.; Kral, J.; Kralik, I.; Kramer, F.; Kraus,

I.; Krawutschke, T.; Kretz, M.; Krivda, M.; Krumbhorn, D.; Krus, M.; Kryshen, E.; Krzewicki, M.; Kucheriaev, Y.; Kuhn, C.; Kuijer, P. G.; Kurashvili, P.; Kurepin, A.; Kurepin, A. B.; Kuryakin, A.; Kushpil, S.; Kushpil, V.; Kweon, M. J.; Kwon, Y.; La Rocca, P.; de Guevara, P. L.; Lafage, V.; Lara, C.; Larsen, D. T.; Lazzeroni, C.; Le Bornec, Y.; Lea, R.; Lee, K. S.; Lee, S. C.; Lefevre, F.; Lehnert, J.; Leistam, L.; Lenhardt, M.; Lenti, V.; Monzon, I. L.; Vargas, H. L.; Levai, P.; Li, X.; Lietava, R.; Lindal, S.; Lindenstruth, V.; Lippmann, C.; Lisa, M. A.; Liu, L.; Loggins, V. R.; Loginov, V.; Lohn, S.; Lohner, D.; Loizides, C.; Lopez, X.; Noriega, M. L.; Torres, E. L.; Lovhoiden, G.; Lu, X. G.; Luettig, P.; Lunardon, M.; Luparello, G.; Luquin, L.; Luzzi, C.; Ma, K.; Ma, R.; Madagodahettige-Don, D. M.; Maevskaya, A.; Mager, M.; Mahapatra, D. P.; Maire, A.; Malaev, M.; Cervantes, I. M.; Malinina, L.; Mal'Kevich, D.; Malzacher, P.; Mamonov, A.; Manceau, L.; Mangotra, L.; Manko, V.; Manso, F.; Manzari, V.; Mao, Y.; Mares, J.; Margagliotti, G. V.; Margotti, A.; Marin, A.; Martashvili, I.; Martinengo, P.; Martinez, M. I.; Davalos, A. M.; Garcia, G. M.; Martynov, Y.; Mas, A.; Masciocchi, S.; Masera, M.; Masoni, A.; Massacrier, L.; Mastromarco, M.; Mastroserio, A.; Matthews, Z. L.; Matyja, A.; Mayani, D.; Mazza, G.; Mazzoni, M. A.; Meddi, F.; Menchaca-Rocha, A.; Lorenzo, P. M.; Perez, J. M.; Mereu, P.; Miake, Y.; Midori, J.; Milano, L.; Milosevic, J.; Mischke, A.; Miskowiec, D.; Mitu, C.; Mlynarz, J.; Mohanty, B.; Molnar, L.; Zetina, L. M.; Monteno, M.; Montes, E.; Morando, M.; De Godoy, D. A. M.; Moretto, S.; Morsch, A.; Muccifora, V.; Mudnic, E.; Muller, H.; Muhuri, S.; Munhoz, M. G.; Munoz, J.; Musa, L.; Musso, A.; Nandi, B. K.; Nania, R.; Nappi, E.; Nattrass, C.; Navach, F.; Navin, S.; Nayak, T. K.; Nazarenko, S.; Nazarov, G.; Nedosekin, A.; Nendaz, F.; Newby, J.; Nicassio, M.; Nielsen, B. S.; Nikolaev, S.; Nikolic, V.; Nikulin, S.; Nikulin, V.; Nilsen, B. S.; Nilsson, M. S.; Noferini, F.; Nooren, G.; Novitzky, N.; Nyanin, A.; Nyatha, A.; Nygaard, C.; Nystrand, J.; Obayashi, H.; Ochirov, A.; Oeschler, H.; Oh, S. K.; Oleniacz, J.; Oppedisano, C.; Velasquez, A. O.; Ortona, G.; Oskarsson, A.; Ostrowski, P.; Otterlund, I.; Otwinowski, J.; Ovrebekk, G.; Oyama, K.; Ozawa, K.; Pachmayer, Y.; Pachr, M.; Padilla, F.; Pagano, P.; Paic, G.; Painke, F.; Pajares, C.; Pal, S.; Pal, S. K.; Palaha, A.; Palmeri, A.; Pappalardo, G. S.; Park, W. J.; Paticchio, V.; Pavlinov, A.; Pawlak, T.; Peitzmann, T.; Peresunko, D.; Lara, C. E. P.; Perini, D.; Perrino, D.; Peryt, W.; Pesci, A.; Peskov, V.; Pestov, Y.; Peters, A. J.; Petracek, V.; Petris, M.; Petrov, P.; Petrovici, M.; Petta, C.; Piano, S.; Piccotti, A.; Pikna, M.; Pillot, P.; Pinazza, O.; Pinsky, L.; Pitz, N.; Piuz, F.; Piyarathna, D. B.; Platt, R.; Ploskon, M.; Pluta, J.; Pocheptsov, T.; Pochybova, S.; Podesta-Lerma, P. L. M.; Poghosyan, M. G.; Polak, K.; Polichtchouk, B.; Pop, A.; Pospisil, V.; Potukuchi, B.; Prasad, S. K.; Preghenella, R.; Prino, F.; Pruneau, C. A.; Pshenichnov, I.; Puddu, G.; Pulvirenti, A.; Punin, V.; Putis, M.; Putschke, J.; Quercigh, E.; Qvigstad, H.; Rachevski, A.; Rademakers, A.; Rademakers, O.; Radomski, S.; Raiha, T. S.; Rak, J.; Rakotozafindrabe, A.; Ramello, L.; Reyes, A. R.; Rammler, M.; Raniwala, R.; Raniwala, S.; Rasanen, S. S.; Read, K. F.; Real, J. S.; Redlich, K.; Renfordt, R.; Reolon, A. R.; Reshetin, A.; Rettig, F.; Revol, J. P.; Reygers, K.; Ricaud, H.; Riccati, L.; Ricci, R. A.; Richter, M.; Riedler, P.; Riegler, W.; Riggi, F.; Rivetti, A.; Cahuantzi, M. R.; Rohr, D.; Rohrich, D.; Romita, R.; Ronchetti, F.; Rosinsky, P.; Rosnet, P.; Rossegger, S.; Rossi, A.; Roukoutakis, F.; Rousseau, S.; Roy, C.; Roy, P.; Montero, A. J. R.; Rui, R.; Rusanov, I.; Ryabinkin, E.; Rybicki, A.; Sadovsky, S.; Safarik, K.; Sahoo, R.; Sahu, P. K.; Saiz, P.; Sakai, S.; Sakata, D.; Salgado, C. A.; Samanta, T.; Sambyal, S.; Samsonov, V.; Sandor, L.; Sandoval, A.; Sano, M.; Sano, S.; Santo, R.; Santoro, R.; Sarkamo, J.; Saturnini, P.; Scapparone, E.; Scarlassara, F.; Scharenberg, R. P.; Schiaua, C.; Schicker, R.; Schmidt, C.; Schmidt, H. R.; Schreiner, S.; Schuchmann, S.; Schukraft, J.; Schutz, Y.; Schwarz, K.; Schweda, K.; Scioli, G.; Scomparin, E.; Scott, P. A.; Scott, R.; Segato, G.; Senyukov, S.; Seo, J.; Serci, S.; Serradilla, E.; Sevcenco, A.; Shabratova, G.; Shahoyan, R.; Sharma, N.; Sharma, S.; Shigaki, K.; Shimomura, M.; Shtejer, K.; Sibiriak, Y.; Siciliano, M.; Sicking, E.; Siemiarczuk, T.; Silenzi, A.; Silvermyr, D.; Simonetti, G.; Singaraju, R.; Singh, R.; Sinha, B. C.; Sinha, T.; Sitar, B.; Sitta, M.; Skaali, T. B.; Skjerdal, K.; Smakal, R.; Smirnov, N.; Snellings, R.; Sogaard, C.; Soloviev, A.; Soltz, R.; Son, H.; Song, M.; Soos, C.; Soramel, F.; Spyropoulou-Stassinaki, M.; Srivastava, B. K.; Stachel, J.; Stan, I.; Stefanek, G.; Stefanini, G.; Steinbeck, T.; Stenlund, E.; Steyn, G.; Stocco, D.; Stock, R.; Stolpovskiy, M.; Strmen, P.; Suaide, A. A. P.; Vasquez, M. A. S.; Sugitate, T.; Suire, C.; Umbera, M. S.; Susa, T.; Swoboda, D.; Symons, T. J. M.; de Toledo, A. S.; Szarka, I.; Szostak, A.; Tagridis, C.; Takahashi, J.; Takaki, J. D. T.; Tauro, A.; Tavlet, M.; Munoz, G. T.; Telesca, A.; Terrevoli, C.; Thader, J.; Thomas, D.; Thomas, J. H.; Tieulent, R.; Timmins, A. R.; Tlusty, D.; Toia, A.; Torii, H.; Toscano, L.; Tosello, F.; Traczyk, T.; Truesdale, D.; Trzaska, W. H.; Tumkin, A.; Turrisi, R.; Turvey, A. J.; Tveter, T. S.; Ulery, J.; Ullaland, K.; Uras, A.; Urban, J.; Urciuoli, G. M.; Usai, G. L.; Vacchi, A.; Vala, M.; Palomo, L. V.; Vallero, S.; van der Kolk, N.; van Leeuwen, M.; Vyvre, P. V.; Vannucci, L.; Vargas, A.; Varma, R.; Vasileiou, M.; Vasiliev, A.; Vechernin, V.; Venaruzzo, M.; Vercellin, E.; Vergara, S.; Vernet, R.; Verweij, M.; Vickovic, L.; Viesti, G.; Vikhlyantsev, O.; Vilakazi, Z.; Baillie, O. V.; Vinogradov, A.; Vinogradov, L.; Vinogradov, Y.; Virgili, T.; Viyogi, Y. P.; Vodopyanov, A.; Voloshin, K.; Voloshin, S.; Volpe, G.; von Haller, B.; Vranic, D.; Vrlakova, J.; Vulpescu, B.; Wagner, B.; Wagner, V.; Wan, R.; Wang, D.; Wang, Y.; Wang, Y.; Watanabe, K.; Wessels, J. P.; Westerhoff, U.; Wiechula, J.; Wikne, J.; Wilde, M.; Wilk, A.; Wilk, G.; Williams, M. C. S.; Windelband, B.; Yang, H.; Yasnopolskiy, S.; Yi, J.; Yin, Z.; Yokoyama, H.; Yoo, I. K.; Yuan, X.; Yushmanov, I.; Zabrodin, E.; Zampolli, C.; Zaporozhets, S.; Zarochentsev, A.; Zavada, P.; Zbroszczyk, H.; Zelnicek, P.; Zenin, A.; Zgura, I.; Zhalov, M.; Zhang, X.; Zhou, D.; Zhu, X.; Zichichi, A.; Zinovjev, G.; Zoc-

carato, Y.; Zynovyev, M.: **Femtoscopy of pp collisions at root s=0.9 and 7 TeV at the LHC with two-pion Bose-Einstein correlations.** *Phys. Rev. D* **84**(11): 112004, 2011. DOI: 10.1103/PhysRevD.84.112004

009 Ablikim, M.; Achasov, M. N.; Alberto, D.; An, F. F.; An, Q.; An, Z. H.; Bai, J. Z.; Baldini, R.; Ban, Y.; Becker, J.; Berger, N.; Bertani, M.; Bian, J. M.; Boger, E.; Bondarenko, O.; Boyko, I.; Briere, R. A.; Bytev, V.; Cai, X.; Calcaterra, A. C.; Cao, G. F.; Chang, J. F.; Chelkov, G.; Chen, G.; Chen, H. S.; Chen, J. C.; Chen, M. L.; Chen, S. J.; Chen, Y.; Chen, Y. B.; Cheng, H. P.; Chu, Y. P.; Cronin-Hennessy, D.; Dai, H. L.; Dai, J. P.; Dedovich, D.; Deng, Z. Y.; Denysenko, I.; Destefanis, M.; Ding, Y.; Dong, L. Y.; Dong, M. Y.; Du, S. X.; Fang, J.; Fang, S. S.; Feng, C. Q.; Fu, C. D.; Fu, J. L.; Gao, Y.; Geng, C.; Götzen, K.*; Gong, W. X.; Greco, M.; Gu, M. H.; Gu, Y. T.; Guan, Y. H.; Guo, A. Q.; Guo, L. B.; Guo, Y. P.; Han, Y. L.; Hao, X. Q.; Harris, F. A.; He, K. L.; He, M.; He, Z. Y.; Heng, Y. K.; Hou, Z. L.; Hu, H. M.; Hu, J. F.; Hu, T.; Huang, B.; Huang, G. M.; Huang, J. S.; Huang, X. T.; Huang, Y. P.; Hussain, T.; Ji, C. S.; Ji, Q.; Ji, X. B.; Ji, X. L.; Jia, L. K.; Jiang, L. L.; Jiang, X. S.; Jiao, J. B.; Jiao, Z.; Jin, D. P.; Jin, S.; Jing, F. F.; Kalantar-Nayestanaki, N.; Kavatsyuk, M.; Kuehn, W.; Lai, W.; Lange, J. S.; Leung, J. K. C.; Li, C. H.; Li, C.; Li, C.; Li, D. M.; Li, F.; Li, G.; Li, H. B.; Li, J. C.; Li, K.; Li, L.; Li, N. B.; Li, Q. J.; Li, S. L.; Li, W. D.; Li, W. G.; Li, X. L.; Li, X. N.; Li, X. Q.; Li, X. R.; Li, Z. B.; Liang, H.; Liang, Y. F.; Liang, Y. T.; Liao, X. T.; Liu, B. J.; Liu, C. L.; Liu, C. X.; Liu, C. Y.; Liu, F. H.; Liu, F.; Liu, F.; Liu, H.; Liu, H. B.; Liu, H. H.; Liu, H. M.; Liu, H. W.; Liu, J. P.; Liu, K.; Liu, K.; Liu, K. Y.; Liu, Q.; Liu, S. B.; Liu, X.; Liu, X. H.; Liu, Y. B.; Liu, Y. W.; Liu, Y.; Liu, Z. A.; Liu, Z. Q.; Liu, Z. Q.; Loehner, H.; Lu, G. R.; Lu, H. J.; Lu, J. G.; Lu, Q. W.; Lu, X. R.; Lu, Y. P.; Luo, C. L.; Luo, M. X.; Luo, T.; Luo, X. L.; Lv, M.; Ma, C. L.; Ma, F. C.; Ma, H. L.; Ma, Q. M.; Ma, S.; Ma, T.; Ma, X.; Ma, X. Y.; Maggiora, M.; Malik, Q. A.; Mao, H.; Mao, Y. J.; Mao, Z. P.; Messchendorp, J. G.; Min, J.; Min, T. J.; Mitchell, R. E.; Mo, X. H.; Muchnoi, N. Y.; Nefedov, Y.; Nikolaev, I. B.; Ning, Z.; Olsen, S. L.; Ouyang, Q.; Pacetti, S.; Park, J. W.; Pelizaeus, M.; Peters, K.*; Ping, J. L.; Ping, R. G.; Poling, R.; Pun, C. S. J.; Qi, M.; Qian, S.; Qiao, C. F.; Qin, X. S.; Qiu, J. F.; Rashid, K. H.; Rong, G.; Ruan, X. D.; Sarantsev, A.; Schulze, J.; Shao, M.; Shen, C. P.; Shen, X. Y.; Sheng, H. Y.; Shepherd, M. R.; Song, X. Y.; Spataro, S.; Spruck, B.; Sun, D. H.; Sun, G. X.; Sun, J. F.; Sun, S. S.; Sun, X. D.; Sun, Y. J.; Sun, Y. Z.; Sun, Z. J.; Sun, Z. T.; Tang, C. J.; Tang, X.; Tian, H. L.; Toth, D.; Varner, G. S.; Wang, B.; Wang, B. Q.; Wang, K.; Wang, L. L.; Wang, L. S.; Wang, M.; Wang, P.; Wang, P. L.; Wang, Q.; Wang, Q. J.; Wang, S. G.; Wang, X. L.; Wang, Y. D.; Wang, Y. F.; Wang, Y. Q.; Wang, Z.; Wang, Z. G.; Wang, Z. Y.; Wei, D. H.; Wen, Q. G.; Wen, S. P.; Wiedner, U.; Wu, L. H.; Wu, N.; Wu, W.; Wu, Z.; Xiao, Z. J.; Xie, Y. G.; Xiu, Q. L.; Xu, G. F.; Xu, G. M.; Xu, H.; Xu, Q. J.; Xu, X. P.; Xu, Y.; Xu, Z. R.; Xu, Z. Z.; Xue, Z.; Yan, L.; Yan, W. B.; Yan, Y. H.; Yang, H. X.; Yang, T.; Yang, Y.; Yang, Y. X.; Ye, H.; Ye, M.; Ye, M. H.; Yu, B. X.; Yu, C. X.; Yu, S. P.; Yuan, C. Z.; Yuan, W. L.; Yuan, Y.; Zafar, A. A.; Zallo, A.; Zeng, Y.; Zhang, B. X.; Zhang, B. Y.; Zhang, C.; Zhang, C. C.; Zhang, D. H.; Zhang, H. H.; Zhang, H. Y.; Zhang, J.; Zhang, J. Q.; Zhang, J. W.; Zhang, J. Y.; Zhang, J. Z.; Zhang, L.; Zhang, S. H.; Zhang, T. R.; Zhang, X. J.; Zhang, X. Y.; Zhang, Y.; Zhang, Y. H.; Zhang, Y. S.; Zhang, Z. P.; Zhang, Z. Y.; Zhao, G.; Zhao, H. S.; Zhao, J. W.; Zhao, J. W.; Zhao, L.; Zhao, L.; Zhao, M. G.; Zhao, Q.; Zhao, S. J.; Zhao, T. C.; Zhao, X. H.; Zhao, Y. B.; Zhao, Z. G.; Zhao, Z. L.; Zhemchugov, A.; Zheng, B.; Zheng, J. P.; Zheng, Y. H.; Zheng, Z. P.; Zhong, B.; Zhong, J.; Zhong, L.; Zhou, L.; Zhou, X. K.; Zhou, X. R.; Zhu, C.; Zhu, K.; Zhu, K. J.; Zhu, S. H.; Zhu, X. L.; Zhu, X. W.; Zhu, Y. S.; Zhu, Z. A.; Zhuang, J.; Zou, B. S.; Zou, J. H.; Zuo, J. X.: **Higher-order multipole amplitude measurement in $\psi' \to \gamma\chi_{c2}$.** *Phys. Rev. D* **84**(9): 092006, 2011. DOI: 10.1103/PhysRevD.84.092006

010 Ablikim, M.; Achasov, M. N.; Alberto, D.; An, F. F.; An, Q.; An, Z. H.; Bai, J. Z.; Baldini, R.; Ban, Y.; Becker, J.; Berger, N.; Bertani, M.; Bian, J. M.; Boger, E.; Bondarenko, O.; Boyko, I.; Briere, R. A.; Bytev, V.; Cai, X.; Calcaterra, A. C.; Cao, G. F.; Chang, J. F.; Chelkov, G.; Chen, G.; Chen, H. S.; Chen, J. C.; Chen, M. L.; Chen, S. J.; Chen, Y.; Chen, Y. B.; Cheng, H. P.; Chu, Y. P.; Cronin-Hennessy, D.; Dai, H. L.; Dai, J. P.; Dedovich, D.; Deng, Z. Y.; Denysenko, I.; Destefanis, M.; Ding, Y.; Dong, L. Y.; Dong, M. Y.; Du, S. X.; Fang, J.; Fang, S. S.; Feng, C. Q.; Fu, C. D.; Fu, J. L.; Gao, Y.; Geng, C.; Götzen, K.*; Gong, W. X.; Greco, M.; Gu, M. H.; Gu, Y. T.; Guan, Y. H.; Guo, A. Q.; Guo, L. B.; Guo, Y. P.; Han, Y. L.; Hao, X. Q.; Harris, F. A.; He, K. L.; He, M.; He, Z. Y.; Heng, Y. K.; Hou, Z. L.; Hu, H. M.; Hu, J. F.; Hu, T.; Huang, B.; Huang, G. M.; Huang, J. S.; Huang, X. T.; Huang, Y. P.; Hussain, T.; Ji, C. S.; Ji, Q.; Ji, X. B.; Ji, X. L.; Jia, L. K.; Jiang, L. L.; Jiang, X. S.; Jiao, J. B.; Jiao, Z.; Jin, D. P.; Jin, S.; Jing, F. F.; Kalantar-Nayestanaki, N.; Kavatsyuk, M.; Kuehn, W.; Lai, W.; Lange, J. S.; Leung, J. K. C.; Li, C. H.; Li, C.; Li, C.; Li, D. M.; Li, F.; Li, G.; Li, H. B.; Li, J. C.; Li, K.; Li, L.; Li, N. B.; Li, Q. J.; Li, S. L.; Li, W. D.; Li, W. G.; Li, X. L.; Li, X. N.; Li, X. Q.; Li, X. R.; Li, Z. B.; Liang, H.; Liang, Y. F.; Liang, Y. T.; Liao, X. T.; Liu, B. J.; Liu, C. L.; Liu, C. X.; Liu, C. Y.; Liu, F. H.; Liu, F.; Liu, F.; Liu, H.; Liu, H. B.; Liu, H. H.; Liu, H. M.; Liu, H. W.; Liu, J. P.; Liu, K.; Liu, K.; Liu, K. Y.; Liu, Q.; Liu, S. B.; Liu, X.; Liu, X. H.; Liu, Y. B.; Liu, Y. W.; Liu, Y.; Liu, Z. A.; Liu, Z. Q.; Liu, Z. Q.; Loehner, H.; Lu, G. R.; Lu, H. J.; Lu, J. G.; Lu, Q. W.; Lu, X. R.; Lu, Y. P.; Luo, C. L.; Luo, M. X.; Luo, T.; Luo, X. L.; Lv, M.; Ma, C. L.; Ma, F. C.; Ma, H. L.; Ma, Q. M.; Ma, S.; Ma, T.; Ma, X.; Ma, X. Y.; Maggiora, M.; Malik, Q. A.; Mao, H.; Mao, Y. J.; Mao, Z. P.; Messchendorp, J. G.; Min, J.; Min, T. J.; Mitchell, R. E.; Mo, X. H.; Muchnoi, N. Y.; Nefedov, Y.; Nikolaev, I. B.; Ning, Z.; Olsen, S. L.; Ouyang, Q.; Pacetti, S.; Park, J. W.; Pelizaeus, M.; Peters, K.*; Ping, J. L.; Ping, R. G.; Poling, R.; Pun, C. S. J.; Qi, M.; Qian, S.; Qiao, C. F.; Qin,

X. S.; Qiu, J. F.; Rashid, K. H.; Rong, G.; Ruan, X. D.; Sarantsev, A.; Schulze, J.; Shao, M.; Shen, C. P.; Shen, X. Y.; Sheng, H. Y.; Shepherd, M. R.; Song, X. Y.; Spataro, S.; Spruck, B.; Sun, D. H.; Sun, G. X.; Sun, J. F.; Sun, S. S.; Sun, X. D.; Sun, Y. J.; Sun, Y. Z.; Sun, Z. J.; Sun, Z. T.; Tang, C. J.; Tang, X.; Tian, H. L.; Toth, D.; Varner, G. S.; Wang, B.; Wang, B. Q.; Wang, K.; Wang, L. L.; Wang, L. S.; Wang, M.; Wang, P.; Wang, P. L.; Wang, Q.; Wang, Q. J.; Wang, S. G.; Wang, X. L.; Wang, Y. D.; Wang, Y. F.; Wang, Y. Q.; Wang, Z.; Wang, Z. G.; Wang, Z. Y.; Wei, D. H.; Wen, Q. G.; Wen, S. P.; Wiedner, U.; Wu, L. H.; Wu, N.; Wu, W.; Wu, Z.; Xiao, Z. J.; Xie, Y. G.; Xiu, Q. L.; Xu, G. F.; Xu, G. M.; Xu, H.; Xu, Q. J.; Xu, X. P.; Xu, Y.; Xu, Z. R.; Xu, Z. Z.; Xue, Z.; Yan, L.; Yan, W. B.; Yan, Y. H.; Yang, H. X.; Yang, T.; Yang, Y.; Yang, Y. X.; Ye, H.; Ye, M.; Ye, M. H.; Yu, B. X.; Yu, C. X.; Yu, S. P.; Yuan, C. Z.; Yuan, W. L.; Yuan, Y.; Zafar, A. A.; Zallo, A.; Zeng, Y.; Zhang, B. X.; Zhang, B. Y.; Zhang, C.; Zhang, C. C.; Zhang, D. H.; Zhang, H. H.; Zhang, H. Y.; Zhang, J.; Zhang, J. Q.; Zhang, J. W.; Zhang, J. Y.; Zhang, J. Z.; Zhang, L.; Zhang, S. H.; Zhang, T. R.; Zhang, X. J.; Zhang, X. Y.; Zhang, Y.; Zhang, Y. H.; Zhang, Y. S.; Zhang, Z. P.; Zhang, Z. Y.; Zhao, G.; Zhao, H. S.; Zhao, J. W.; Zhao, J. W.; Zhao, L.; Zhao, L.; Zhao, M. G.; Zhao, Q.; Zhao, S. J.; Zhao, T. C.; Zhao, X. H.; Zhao, Y. B.; Zhao, Z. G.; Zhao, Z. L.; Zhemchugov, A.; Zheng, B.; Zheng, J. P.; Zheng, Y. H.; Zheng, Z. P.; Zhong, B.; Zhong, J.; Zhong, L.; Zhou, L.; Zhou, X. K.; Zhou, X. R.; Zhu, C.; Zhu, K.; Zhu, K. J.; Zhu, S. H.; Zhu, X. L.; Zhu, X. W.; Zhu, Y. S.; Zhu, Z. A.; Zhuang, J.; Zou, B. S.; Zou, J. H.; Zuo, J. X.: **Search for η_c' decays into vector meson pairs.** *Phys. Rev. D* **84**(9): 091102, 2011. DOI: 10.1103/PhysRevD.84.091102

011 Ablikim, M.; Achasov, M. N.; Alberto, D.; An, L.; An, Q.; An, Z. H.; Bai, J. Z.; Baldini, R.; Ban, Y.; Becker, J.; Berger, N.; Bertani, M.; Bian, J. M.; Bondarenko, O.; Boyko, I.; Briere, R. A.; Bytev, V.; Cai, X.; Cao, G. F.; Cao, X. X.; Chang, J. F.; Chelkov, G.; Chen, G.; Chen, H. S.; Chen, J. C.; Chen, M. L.; Chen, S. J.; Chen, Y.; Chen, Y. B.; Cheng, H. P.; Chu, Y. P.; Cronin-Hennessy, D.; Dai, H. L.; Dai, J. P.; Dedovich, D.; Deng, Z. Y.; Denysenko, I.; Destefanis, M.; Ding, Y.; Dong, L. Y.; Dong, M. Y.; Du, S. X.; Fan, R. R.; Fang, J.; Fang, S. S.; Feng, C. Q.; Fu, C. D.; Fu, J. L.; Gao, Y.; Geng, C.; Götzen, K.*; Gong, W. X.; Greco, M.; Grishin, S.; Gu, M. H.; Gu, Y. T.; Guan, Y. H.; Guo, A. Q.; Guo, L. B.; Guo, Y. P.; Hao, X. Q.; Harris, F. A.; He, K. L.; He, M.; He, Z. Y.; Heng, Y. K.; Hou, Z. L.; Hu, H. M.; Hu, J. F.; Hu, T.; Huang, B.; Huang, G. M.; Huang, J. S.; Huang, X. T.; Huang, Y. P.; Hussain, T.; Ji, C. S.; Ji, Q.; Ji, X. B.; Ji, X. L.; Jia, L. K.; Jiang, L. L.; Jiang, X. S.; Jiao, J. B.; Jiao, Z.; Jin, D. P.; Jin, S.; Jing, F. F.; Kalantar-Nayestanaki, N.; Kavatsyuk, M.; Komamiya, S.; Kuehn, W.; Lange, J. S.; Leung, J. K. C.; Li, C.; Li, C.; Li, D. M.; Li, F.; Li, G.; Li, H. B.; Li, J. C.; Li, L.; Li, N. B.; Li, Q. J.; Li, W. D.; Li, W. G.; Li, X. L.; Li, X. N.; Li, X. Q.; Li, X. R.; Li, Z. B.; Liang, H.; Liang, Y. F.; Liang, Y. T.; Liao, G. R.; Liao, X. T.; Liu, B. J.; Liu, B. J.; Liu, C. L.; Liu, C. X.; Liu, C. Y.; Liu, F. H.; Liu, F.; Liu, F.; Liu, G. C.; Liu, H.; Liu, H. B.; Liu, H. M.; Liu, H. W.; Liu, J. P.; Liu, K.; Liu, K.; Liu, K. Y.; Liu, Q.; Liu, S. B.; Liu, X.; Liu, X. H.; Liu, Y. B.; Liu, Y. W.; Liu, Y.; Liu, Z. A.; Liu, Z. Q.; Loehner, H.; Lu, G. R.; Lu, H. J.; Lu, J. G.; Lu, Q. W.; Lu, X. R.; Lu, Y. P.; Luo, C. L.; Luo, M. X.; Luo, T.; Luo, X. L.; Ma, C. L.; Ma, F. C.; Ma, H. L.; Ma, Q. M.; Ma, T.; Ma, X.; Ma, X. Y.; Maggiora, M.; Malik, Q. A.; Mao, H.; Mao, Y. J.; Mao, Z. P.; Messchendorp, J. G.; Min, J.; Mitchell, R. E.; Mo, X. H.; Muchnoi, N. Y.; Nefedov, Y.; Ning, Z.; Olsen, S. L.; Ouyang, Q.; Pacetti, S.; Pelizaeus, M.; Peters, K.*; Ping, J. L.; Ping, R. G.; Poling, R.; Pun, C. S. J.; Qi, M.; Qian, S.; Qiao, C. F.; Qin, X. S.; Qiu, J. F.; Rashid, K. H.; Rong, G.; Ruan, X. D.; Sarantsev, A.; Schulze, J.; Shao, M.; Shen, C. P.; Shen, X. Y.; Sheng, H. Y.; Shepherd, M. R.; Song, X. Y.; Sonoda, S.; Spataro, S.; Spruck, B.; Sun, D. H.; Sun, G. X.; Sun, J. F.; Sun, S. S.; Sun, X. D.; Sun, Y. J.; Sun, Y. Z.; Sun, Z. J.; Sun, Z. T.; Tang, C. J.; Tang, X.; Tang, X. F.; Tian, H. L.; Toth, D.; Varner, G. S.; Wan, X.; Wang, B. Q.; Wang, K.; Wang, L. L.; Wang, L. S.; Wang, M.; Wang, P.; Wang, P. L.; Wang, Q.; Wang, S. G.; Wang, X. L.; Wang, Y. D.; Wang, Y. F.; Wang, Y. Q.; Wang, Z.; Wang, Z. G.; Wang, Z. Y.; Wei, D. H.; Wen, Q. G.; Wen, S. P.; Wiedner, U.; Wu, L. H.; Wu, N.; Wu, W.; Wu, Z.; Xiao, Z. J.; Xie, Y. G.; Xu, G. F.; Xu, G. M.; Xu, H.; Xu, Y.; Xu, Z. R.; Xu, Z. Z.; Xue, Z.; Yan, L.; Yan, W. B.; Yan, Y. H.; Yang, H. X.; Yang, M.; Yang, T.; Yang, Y.; Yang, Y. X.; Ye, M.; Ye, M. H.; Yu, B. X.; Yu, C. X.; Yu, L.; Yuan, C. Z.; Yuan, W. L.; Yuan, Y.; Zafar, A. A.; Zallo, A.; Zeng, Y.; Zhang, B. X.; Zhang, B. Y.; Zhang, C. C.; Zhang, D. H.; Zhang, H. H.; Zhang, H. Y.; Zhang, J.; Zhang, J. W.; Zhang, J. Y.; Zhang, J. Z.; Zhang, L.; Zhang, S. H.; Zhang, T. R.; Zhang, X. J.; Zhang, X. Y.; Zhang, Y.; Zhang, Y. H.; Zhang, Z. P.; Zhang, Z. Y.; Zhao, G.; Zhao, H. S.; Zhao, J. W.; Zhao, J. W.; Zhao, L.; Zhao, L.; Zhao, M. G.; Zhao, Q.; Zhao, S. J.; Zhao, T. C.; Zhao, X. H.; Zhao, Y. B.; Zhao, Z. G.; Zhao, Z. L.; Zhemchugov, A.; Zheng, B.; Zheng, J. P.; Zheng, Y. H.; Zheng, Z. P.; Zhong, B.; Zhong, J.; Zhong, L.; Zhou, L.; Zhou, X. K.; Zhou, X. R.; Zhu, C.; Zhu, K.; Zhu, K. J.; Zhu, S. H.; Zhu, X. L.; Zhu, X. W.; Zhu, Y. S.; Zhu, Z. A.; Zhuang, J.; Zou, B. S.; Zou, J. H.; Zuo, J. X.; Zweber, P.: **Study of χ_{cJ} radiative decays into a vector meson.** *Phys. Rev. D* **83**(11): 112005, 2011. DOI: 10.1103/PhysRevD.83.112005

012 Ablikim, M.; Achasov, M. N.; Alberto, D.; An, L.; An, Q.; An, Z. H.; Bai, J. Z.; Baldini, R.; Ban, Y.; Becker, J.; Berger, N.; Bertani, M.; Bian, J. M.; Bondarenko, O.; Boyko, I.; Briere, R. A.; Bytev, V.; Cai, X.; Cao, G. F.; Cao, X. X.; Chang, J. F.; Chelkov, G.; Chen, G.; Chen, H. S.; Chen, J. C.; Chen, M. L.; Chen, S. J.; Chen, Y.; Chen, Y. B.; Cheng, H. P.; Chu, Y. P.; Cronin-Hennessy, D.; Dai, H. L.; Dai, J. P.; Dedovich, D.; Deng, Z. Y.; Denysenko, I.; Destefanis, M.; Ding, Y.; Dong, L. Y.; Dong, M. Y.; Du, S. X.; Fan, R. R.; Fang, J.; Fang, S. S.; Feng, C. Q.; Fu, C. D.; Fu, J. L.; Gao, Y.; Geng, C.; Götzen, K.*; Gong, W. X.; Greco, M.; Grishin, S.; Gu, M. H.; Gu, Y. T.; Guan, Y.

H.; Guo, A. Q.; Guo, L. B.; Guo, Y. P.; Hao, X. Q.; Harris, F. A.; He, K. L.; He, M.; He, Z. Y.; Heng, Y. K.; Hou, Z. L.; Hu, H. M.; Hu, J. F.; Hu, T.; Huang, B.; Huang, G. M.; Huang, J. S.; Huang, X. T.; Huang, Y. P.; Hussain, T.; Ji, C. S.; Ji, Q.; Ji, X. B.; Ji, X. L.; Jia, L. K.; Jiang, L. L.; Jiang, X. S.; Jiao, J. B.; Jiao, Z.; Jin, D. P.; Jin, S.; Jing, F. F.; Kalantar-Nayestanaki, N.; Kavatsyuk, M.; Komamiya, S.; Kuehn, W.; Lange, J. S.; Leung, J. K. C.; Li, C.; Li, C.; Li, D. M.; Li, F.; Li, G.; Li, H. B.; Li, J. C.; Li, L.; Li, N. B.; Li, Q. J.; Li, W. D.; Li, W. G.; Li, X. L.; Li, X. N.; Li, X. Q.; Li, X. R.; Li, Z. B.; Liang, H.; Liang, Y. F.; Liang, Y. T.; Liao, G. R.; Liao, X. T.; Liu, B. J.; Liu, B. J.; Liu, C. L.; Liu, C. X.; Liu, C. Y.; Liu, F. H.; Liu, F.; Liu, G. C.; Liu, H.; Liu, H. B.; Liu, H. M.; Liu, H. W.; Liu, J. P.; Liu, K.; Liu, K. Y.; Liu, Q.; Liu, S. B.; Liu, X.; Liu, X. H.; Liu, Y. B.; Liu, Y. W.; Liu, Y.; Liu, Z. A.; Liu, Z. Q.; Loehner, H.; Lu, G. R.; Lu, H. J.; Lu, J. G.; Lu, Q. W.; Lu, X. R.; Lu, Y. P.; Luo, C. L.; Luo, M. X.; Luo, T.; Luo, X. L.; Ma, C. L.; Ma, F. C.; Ma, H. L.; Ma, Q. M.; Ma, T.; Ma, X.; Ma, X. Y.; Maggiora, M.; Malik, Q. A.; Mao, H.; Mao, Y. J.; Mao, Z. P.; Messchendorp, J. G.; Min, J.; Mitchell, R. E.; Mo, X. H.; Muchnoi, N. Y.; Nefedov, Y.; Ning, Z.; Olsen, S. L.; Ouyang, Q.; Pacetti, S.; Pelizaeus, M.; Peters, K.*; Ping, J. L.; Ping, R. G.; Poling, R.; Pun, C. S. J.; Qi, M.; Qian, S.; Qiao, C. F.; Qin, X. S.; Qiu, J. F.; Rashid, K. H.; Rong, G.; Ruan, X. D.; Sarantsev, A.; Schulze, J.; Shao, M.; Shen, C. P.; Shen, X. Y.; Sheng, H. Y.; Shepherd, M. R.; Song, X. Y.; Sonoda, S.; Spataro, S.; Spruck, B.; Sun, D. H.; Sun, G. X.; Sun, J. F.; Sun, S. S.; Sun, X. D.; Sun, Y. J.; Sun, Y. Z.; Sun, Z. J.; Sun, Z. T.; Tang, C. J.; Tang, X.; Tang, X. F.; Tian, H. L.; Toth, D.; Varner, G. S.; Wan, X.; Wang, B. Q.; Wang, K.; Wang, L. L.; Wang, L. S.; Wang, M.; Wang, P.; Wang, P. L.; Wang, Q.; Wang, S. G.; Wang, X. L.; Wang, Y. D.; Wang, Y. F.; Wang, Y. Q.; Wang, Z.; Wang, Z. G.; Wang, Z. Y.; Wei, D. H.; Wen, Q. G.; Wen, S. P.; Wiedner, U.; Wu, L. H.; Wu, N.; Wu, W.; Wu, Z.; Xiao, Z. J.; Xie, Y. G.; Xu, G. F.; Xu, G. M.; Xu, H.; Xu, Y.; Xu, Z. R.; Xu, Z. Z.; Xue, Z.; Yan, L.; Yan, W. B.; Yan, Y. H.; Yang, H. X.; Yang, M.; Yang, T.; Yang, Y.; Yang, Y. X.; Ye, M.; Ye, M. H.; Yu, B. X.; Yu, C. X.; Yu, L.; Yuan, C. Z.; Yuan, W. L.; Yuan, Y.; Zafar, A. A.; Zallo, A.; Zeng, Y.; Zhang, B. X.; Zhang, B. Y.; Zhang, C. C.; Zhang, D. H.; Zhang, H. H.; Zhang, H. Y.; Zhang, J.; Zhang, J. W.; Zhang, J. Y.; Zhang, J. Z.; Zhang, L.; Zhang, S. H.; Zhang, T. R.; Zhang, X. J.; Zhang, X. Y.; Zhang, Y.; Zhang, Y. H.; Zhang, Z. P.; Zhang, Z. Y.; Zhao, G.; Zhao, H. S.; Zhao, J. W.; Zhao, J. W.; Zhao, L.; Zhao, L.; Zhao, M. G.; Zhao, Q.; Zhao, S. J.; Zhao, T. C.; Zhao, X. H.; Zhao, Y. B.; Zhao, Z. G.; Zhao, Z. L.; Zhemchugov, A.; Zheng, B.; Zheng, J. P.; Zheng, Y. H.; Zheng, Z. P.; Zhong, B.; Zhong, J.; Zhong, L.; Zhou, L.; Zhou, X. K.; Zhou, X. R.; Zhu, C.; Zhu, K.; Zhu, K. J.; Zhu, S. H.; Zhu, X. L.; Zhu, X. W.; Zhu, Y. S.; Zhu, Z. A.; Zhuang, J.; Zou, B. S.; Zou, J. H.; Zuo, J. X.; Zweber, P.: **Observation of χ_{cJ} decaying into the $p\bar{p}K^+K^-$ final state.** *Phys. Rev. D* **83**(11): 112009, 2011. DOI: 10.1103/PhysRevD.83.112009

013 Ablikim, M.; Achasov, M. N.; Alberto, D.; An, Q.; An, Z. H.; Bai, J. Z.; Baldini, R.; Ban, Y.; Becker, J.; Berger, N.; Bertani, M.; Bian, J. M.; Bondarenko, O.; Boyko, I.; Briere, R. A.; Bytev, V.; Cai, X.; Calcaterra, A. C.; Cao, G. F.; Cao, X. X.; Chang, J. F.; Chelkov, G.; Chen, G.; Chen, H. S.; Chen, J. C.; Chen, M. L.; Chen, S. J.; Chen, Y.; Chen, Y. B.; Cheng, H. P.; Chu, Y. P.; Cronin-Hennessy, D.; Dai, H. L.; Dai, J. P.; Dedovich, D.; Deng, Z. Y.; Denysenko, I.; Destefanis, M.; Ding, Y.; Dong, L. Y.; Dong, M. Y.; Du, S. X.; Fan, R. R.; Fang, J.; Fang, S. S.; Feng, C. Q.; Fu, C. D.; Fu, J. L.; Gao, Y.; Geng, C.; Götzen, K.*; Gong, W. X.; Greco, M.; Grishin, S.; Gu, M. H.; Gu, Y. T.; Guan, Y. H.; Guo, A. Q.; Guo, L. B.; Guo, Y. P.; Hao, X. Q.; Harris, F. A.; He, K. L.; He, M.; He, Z. Y.; Heng, Y. K.; Hou, Z. L.; Hu, H. M.; Hu, J. F.; Hu, T.; Huang, B.; Huang, G. M.; Huang, J. S.; Huang, X. T.; Huang, Y. P.; Hussain, T.; Ji, C. S.; Ji, Q.; Ji, X. B.; Ji, X. L.; Jia, L. K.; Jiang, L. L.; Jiang, X. S.; Jiao, J. B.; Jiao, Z.; Jin, D. P.; Jin, S.; Jing, F. F.; Kalantar-Nayestanaki, N.; Kavatsyuk, M.; Komamiya, S.; Kuehn, W.; Lange, J. S.; Leung, J. K. C.; Li, C.; Li, C.; Li, D. M.; Li, F.; Li, G.; Li, H. B.; Li, J. C.; Li, K.; Li, L.; Li, N. B.; Li, Q. J.; Li, W. D.; Li, W. G.; Li, X. L.; Li, X. N.; Li, X. Q.; Li, X. R.; Li, Z. B.; Liang, H.; Liang, Y. F.; Liang, Y. T.; Liao, X. T.; Liu, B. J.; Liu, B. J.; Liu, C. L.; Liu, C. X.; Liu, C. Y.; Liu, F. H.; Liu, F.; Liu, F.; Liu, G. C.; Liu, H.; Liu, H. B.; Liu, H. H.; Liu, H. M.; Liu, H. W.; Liu, J. P.; Liu, K.; Liu, K.; Liu, K. Y.; Liu, Q.; Liu, S. B.; Liu, X.; Liu, X. H.; Liu, Y. B.; Liu, Y. W.; Liu, Y.; Liu, Z. A.; Liu, Z. Q.; Loehner, H.; Lu, G. R.; Lu, H. J.; Lu, J. G.; Lu, Q. W.; Lu, X. R.; Lu, Y. P.; Luo, C. L.; Luo, M. X.; Luo, T.; Luo, X. L.; Ma, C. L.; Ma, F. C.; Ma, H. L.; Ma, Q. M.; Ma, T.; Ma, X.; Ma, X. Y.; Maggiora, M.; Malik, Q. A.; Mao, H.; Mao, Y. J.; Mao, Z. P.; Messchendorp, J. G.; Min, J.; Mitchell, R. E.; Mo, X. H.; Muchnoi, N. Y.; Nefedov, Y.; Nikolaev, I. B.; Ning, Z.; Olsen, S. L.; Ouyang, Q.; Pacetti, S.; Pelizaeus, M.; Peters, K.*; Ping, J. L.; Ping, R. G.; Poling, R.; Pun, C. S. J.; Qi, M.; Qian, S.; Qiao, C. F.; Qin, X. S.; Qiu, J. F.; Rashid, K. H.; Rong, G.; Ruan, X. D.; Sarantsev, A.; Schulze, J.; Shao, M.; Shen, C. P.; Shen, X. Y.; Sheng, H. Y.; Shepherd, M. R.; Song, X. Y.; Sonoda, S.; Spataro, S.; Spruck, B.; Sun, D. H.; Sun, G. X.; Sun, J. F.; Sun, S. S.; Sun, X. D.; Sun, Y. J.; Sun, Y. Z.; Sun, Z. J.; Sun, Z. T.; Tang, C. J.; Tang, X.; Tian, H. L.; Toth, D.; Varner, G. S.; Wan, X.; Wang, B. Q.; Wang, K.; Wang, L. L.; Wang, L. S.; Wang, M.; Wang, P.; Wang, P. L.; Wang, Q.; Wang, S. G.; Wang, X. L.; Wang, Y. D.; Wang, Y. F.; Wang, Y. Q.; Wang, Z.; Wang, Z. G.; Wang, Z. Y.; Wei, D. H.; Wen, Q. G.; Wen, S. P.; Wiedner, U.; Wu, L. H.; Wu, N.; Wu, W.; Wu, Z.; Xiao, Z. J.; Xie, Y. G.; Xu, G. F.; Xu, G. M.; Xu, H.; Xu, Q. J.; Xu, X. P.; Xu, Y.; Xu, Z. R.; Xu, Z. Z.; Xue, Z.; Yan, L.; Yan, W. B.; Yan, Y. H.; Yang, H. X.; Yang, M.; Yang, T.; Yang, Y.; Yang, Y. X.; Ye, M.; Ye, M. H.; Yu, B. X.; Yu, C. X.; Yu, L.; Yu, S. P. Y.; Yuan, C. Z.; Yuan, W. L.; Yuan, Y.; Zafar, A. A.; Zallo, A.; Zeng, Y.; Zhang, B. X.; Zhang, B. Y.; Zhang, C. C.; Zhang, D. H.; Zhang, H. H.; Zhang, H. Y.; Zhang, J.; Zhang, J. W.; Zhang, J. Y.; Zhang, J. Z.; Zhang, L.; Zhang, S. H.; Zhang,

T. R.; Zhang, X. J.; Zhang, X. Y.; Zhang, Y.; Zhang, Y. H.; Zhang, Z. P.; Zhang, Z. Y.; Zhao, G.; Zhao, H. S.; Zhao, J. W.; Zhao, J. W.; Zhao, L.; Zhao, L.; Zhao, M. G.; Zhao, Q.; Zhao, S. J.; Zhao, T. C.; Zhao, X. H.; Zhao, Y. B.; Zhao, Z. G.; Zhao, Z. L.; Zhemchugov, A.; Zheng, B.; Zheng, J. P.; Zheng, Y. H.; Zheng, Z. P.; Zhong, B.; Zhong, J.; Zhong, L.; Zhou, L.; Zhou, X. K.; Zhou, X. R.; Zhu, C.; Zhu, K.; Zhu, K. J.; Zhu, S. H.; Zhu, X. L.; Zhu, X. W.; Zhu, Y. S.; Zhu, Z. A.; Zhuang, J.; Zou, B. S.; Zou, J. H.; Zuo, J. X.: $\eta\pi^+\pi^-$ **Resonant Structure around 1.8 GeV/**c^2 **and** $\eta(1405)$ **in** $J/\psi \to \omega\eta\pi^+\pi^-$**.** *Phys. Rev. Lett.* **107**(18): 182001, 2011. DOI: 10.1103/PhysRevLett.107.182001

014 Ablikim, M.; Achasov, M. N.; Alberto, D.; An, Q.; An, Z. H.; Bai, J. Z.; Baldini, R.; Ban, Y.; Becker, J.; Berger, N.; Bertani, M.; Bian, J. M.; Bondarenko, O.; Boyko, I.; Briere, R. A.; Bytev, V.; Cai, X.; Calcaterra, A. C.; Cao, G. F.; Cao, X. X.; Chang, J. F.; Chelkov, G.; Chen, G.; Chen, H. S.; Chen, J. C.; Chen, M. L.; Chen, S. J.; Chen, Y.; Chen, Y. B.; Cheng, H. P.; Chu, Y. P.; Cronin-Hennessy, D.; Dai, H. L.; Dai, J. P.; Dedovich, D.; Deng, Z. Y.; Denysenko, I.; Destefanis, M.; Ding, Y.; Dong, L. Y.; Dong, M. Y.; Du, S. X.; Fan, R. R.; Fang, J.; Fang, S. S.; Feng, C. Q.; Fu, C. D.; Fu, J. L.; Gao, Y.; Geng, C.; Götzen, K.*; Gong, W. X.; Greco, M.; Grishin, S.; Gu, M. H.; Gu, Y. T.; Guan, Y. H.; Guo, A. Q.; Guo, L. B.; Guo, Y. P.; Hao, X. Q.; Harris, F. A.; He, K. L.; He, M.; He, Z. Y.; Heng, Y. K.; Hou, Z. L.; Hu, H. M.; Hu, J. F.; Hu, T.; Huang, B.; Huang, G. M.; Huang, J. S.; Huang, X. T.; Huang, Y. P.; Hussain, T.; Ji, C. S.; Ji, Q.; Ji, X. B.; Ji, X. L.; Jia, L. K.; Jiang, L. L.; Jiang, X. S.; Jiao, J. B.; Jiao, Z.; Jin, D. P.; Jin, S.; Jing, F. F.; Kalantar-Nayestanaki, N.; Kavatsyuk, M.; Komamiya, S.; Kuehn, W.; Lange, J. S.; Leung, J. K. C.; Li, C.; Li, C.; Li, D. M.; Li, F.; Li, G.; Li, H. B.; Li, J. C.; Li, L.; Li, N. B.; Li, Q. J.; Li, W. D.; Li, W. G.; Li, X. L.; Li, X. N.; Li, X. Q.; Li, X. R.; Li, Z. B.; Liang, H.; Liang, Y. F.; Liang, Y. T.; Liao, G. R.; Liao, X. T.; Liu, B. J.; Liu, B. J.; Liu, C. L.; Liu, C. X.; Liu, C. Y.; Liu, F. H.; Liu, F.; Liu, F.; Liu, G. C.; Liu, H.; Liu, H. B.; Liu, H. M.; Liu, H. W.; Liu, J. P.; Liu, K.; Liu, K.; Liu, K. Y.; Liu, Q.; Liu, S. B.; Liu, X.; Liu, X. H.; Liu, Y. B.; Liu, Y. W.; Liu, Y.; Liu, Z. A.; Liu, Z. Q.; Loehner, H.; Lu, G. R.; Lu, H. J.; Lu, J. G.; Lu, Q. W.; Lu, X. R.; Lu, Y. P.; Luo, C. L.; Luo, M. X.; Luo, T.; Luo, X. L.; Ma, C. L.; Ma, F. C.; Ma, H. L.; Ma, Q. M.; Ma, T.; Ma, X.; Ma, X. Y.; Maggiora, M.; Malik, Q. A.; Mao, H.; Mao, Y. J.; Mao, Z. P.; Messchendorp, J. G.; Min, J.; Mitchell, R. E.; Mo, X. H.; Muchnoi, N. Y.; Nefedov, Y.; Nikolaev, I. B.; Ning, Z.; Olsen, S. L.; Ouyang, Q.; Pacetti, S.; Pelizaeus, M.; Peters, K.*; Ping, J. L.; Ping, R. G.; Poling, R.; Pun, C. S. J.; Qi, M.; Qian, S.; Qiao, C. F.; Qin, X. S.; Qiu, J. F.; Rashid, K. H.; Rong, G.; Ruan, X. D.; Sarantsev, A.; Schulze, J.; Shao, M.; Shen, C. P.; Shen, X. Y.; Sheng, H. Y.; Shepherd, M. R.; Song, X. Y.; Sonoda, S.; Spataro, S.; Spruck, B.; Sun, D. H.; Sun, G. X.; Sun, J. F.; Sun, S. S.; Sun, X. D.; Sun, Y. J.; Sun, Y. Z.; Sun, Z. J.; Sun, Z. T.; Tang, C. J.; Tang, X.; Tang, X. F.; Tian, H. L.; Toth, D.; Varner, G. S.; Wan, X.; Wang, B. Q.; Wang, K.; Wang, L. L.; Wang, L. S.; Wang, M.; Wang, P.; Wang, P. L.; Wang, Q.; Wang, S. G.; Wang, X. L.; Wang, Y. D.; Wang, Y. F.; Wang, Y. Q.; Wang, Z.; Wang, Z. G.; Wang, Z. Y.; Wei, D. H.; Wen, Q. G.; Wen, S. P.; Wiedner, U.; Wu, L. H.; Wu, N.; Wu, W.; Wu, Z.; Xiao, Z. J.; Xie, Y. G.; Xu, G. F.; Xu, G. M.; Xu, H.; Xu, Y.; Xu, Z. R.; Xu, Z. Z.; Xue, Z.; Yan, L.; Yan, W. B.; Yan, Y. H.; Yang, H. X.; Yang, M.; Yang, T.; Yang, Y.; Yang, Y. X.; Ye, M.; Ye, M. H.; Yu, B. X.; Yu, C. X.; Yu, L.; Yu, S. P. Y.; Yuan, C. Z.; Yuan, W. L.; Yuan, Y.; Zafar, A. A.; Zallo, A.; Zeng, Y.; Zhang, B. X.; Zhang, B. Y.; Zhang, C. C.; Zhang, D. H.; Zhang, H. H.; Zhang, H. Y.; Zhang, J.; Zhang, J. W.; Zhang, J. Y.; Zhang, J. Z.; Zhang, L.; Zhang, S. H.; Zhang, T. R.; Zhang, X. J.; Zhang, X. Y.; Zhang, Y.; Zhang, Y. H.; Zhang, Z. P.; Zhang, Z. Y.; Zhao, G.; Zhao, H. S.; Zhao, J. W.; Zhao, J. W.; Zhao, L.; Zhao, L.; Zhao, M. G.; Zhao, Q.; Zhao, S. J.; Zhao, T. C.; Zhao, X. H.; Zhao, Y. B.; Zhao, Z. G.; Zhao, Z. L.; Zhemchugov, A.; Zheng, B.; Zheng, J. P.; Zheng, Y. H.; Zheng, Z. P.; Zhong, B.; Zhong, J.; Zhong, L.; Zhou, L.; Zhou, X. K.; Zhou, X. R.; Zhu, C.; Zhu, K.; Zhu, K. J.; Zhu, S. H.; Zhu, X. L.; Zhu, X. W.; Zhu, Y. S.; Zhu, Z. A.; Zhuang, J.; Zou, B. S.; Zou, J. H.; Zuo, J. X.: **Search for** CP **and** P **violating pseudoscalar decays into** $\pi\pi$**.** *Phys. Rev. D* **84**(3): 032006, 2011. DOI: 10.1103/PhysRevD.84.032006

015 Ablikim, M.; Achasov, M. N.; An, L.; An, Q.; An, Z. H.; Bai, J. Z.; Baldini, R.; Ban, Y.; Becker, J.; Berger, N.; Bertani, M.; Bian, J. M.; Bondarenko, O.; Boyko, I.; Briere, R. A.; Bytev, V.; Cai, X.; Cao, G. F.; Cao, X. X.; Chang, J. F.; Chelkov, G.; Chen, G.; Chen, H. S.; Chen, J. C.; Chen, M. L.; Chen, S. J.; Chen, Y.; Chen, Y. B.; Cheng, H. P.; Chu, Y. P.; Cronin-Hennessy, D.; Dai, H. L.; Dai, J. P.; Dedovich, D.; Deng, Z. Y.; Denysenko, I.; Destefanis, M.; Ding, Y.; Dong, L. Y.; Dong, M. Y.; Du, S. X.; Duan, M. Y.; Fan, R. R.; Fang, J.; Fang, S. S.; Feng, C. Q.; Fu, C. D.; Fu, J. L.; Gao, Y.; Geng, C.; Götzen, K.*; Gong, W. X.; Greco, M.; Grishin, S.; Gu, M. H.; Gu, Y. T.; Guan, Y. H.; Guo, A. Q.; Guo, L. B.; Guo, Y. P.; Hao, X. Q.; Harris, F. A.; He, K. L.; He, M.; He, Z. Y.; Heng, Y. K.; Hou, Z. L.; Hu, H. M.; Hu, J. F.; Hu, T.; Huang, B.; Huang, G. M.; Huang, J. S.; Huang, X. T.; Huang, Y. P.; Hussain, T.; Ji, C. S.; Ji, Q.; Ji, X. B.; Ji, X. L.; Jia, L. K.; Jiang, L. L.; Jiang, X. S.; Jiao, J. B.; Jiao, Z.; Jin, D. P.; Jin, S.; Jing, F. F.; Kavatsyuk, M.; Komamiya, S.; Kuehn, W.; Lange, J. S.; Leung, J. K. C.; Li, C.; Li, C.; Li, D. M.; Li, F.; Li, G.; Li, H. B.; Li, J. C.; Li, L.; Li, N. B.; Li, Q. J.; Li, W. D.; Li, W. G.; Li, X. L.; Li, X. N.; Li, X. Q.; Li, X. R.; Li, Z. B.; Liang, H.; Liang, Y. F.; Liang, Y. T.; Liao, G. R.; Liao, X. T.; Liu, B. J.; Liu, B. J.; Liu, C. L.; Liu, C. X.; Liu, C. Y.; Liu, F. H.; Liu, F.; Liu, F.; Liu, G. C.; Liu, H.; Liu, H. B.; Liu, H. M.; Liu, H. W.; Liu, J. P.; Liu, K.; Liu, K. Y.; Liu, Q.; Liu, S. B.; Liu, X.; Liu, X. H.; Liu, Y. B.; Liu, Y. W.; Liu, Y.; Liu, Z. A.; Liu, Z. Q.; Loehner, H.; Lu, G. R.; Lu, H. J.; Lu, J. G.; Lu, Q. W.; Lu, X. R.; Lu, Y. P.; Luo, C. L.; Luo, M. X.; Luo, T.; Luo, X. L.; Ma, C. L.; Ma, F. C.; Ma, H. L.; Ma, Q. M.; Ma, T.; Ma, X.; Ma,

X. Y.; Maggiora, M.; Malik, Q. A.; Mao, H.; Mao, Y. J.; Mao, Z. P.; Messchendorp, J. G.; Min, J.; Mitchell, R. E.; Mo, X. H.; Muchnoi, N. Y.; Nefedov, Y.; Ning, Z.; Olsen, S. L.; Ouyang, Q.; Pacetti, S.; Pelizaeus, M.; Peters, K.*; Ping, J. L.; Ping, R. G.; Poling, R.; Pun, C. S. J.; Qi, M.; Qian, S.; Qiao, C. F.; Qin, X. S.; Qiu, J. F.; Rashid, K. H.; Rong, G.; Ruan, X. D.; Sarantsev, A.; Schulze, J.; Shao, M.; Shen, C. P.; Shen, X. Y.; Sheng, H. Y.; Shepherd, M. R.; Song, X. Y.; Sonoda, S.; Spataro, S.; Spruck, B.; Sun, D. H.; Sun, G. X.; Sun, J. F.; Sun, S. S.; Sun, X. D.; Sun, Y. J.; Sun, Y. Z.; Sun, Z. J.; Sun, Z. T.; Tang, C. J.; Tang, X.; Tang, X. F.; Tian, H. L.; Toth, D.; Varner, G. S.; Wan, X.; Wang, B. Q.; Wang, K.; Wang, L. L.; Wang, L. S.; Wang, M.; Wang, P.; Wang, P. L.; Wang, Q.; Wang, S. G.; Wang, X. L.; Wang, Y. D.; Wang, Y. F.; Wang, Y. Q.; Wang, Z.; Wang, Z. G.; Wang, Z. Y.; Wei, D. H.; Wen, Q. G.; Wen, S. P.; Wiedner, U.; Wu, L. H.; Wu, N.; Wu, W.; Wu, Z.; Xiao, Z. J.; Xie, Y. G.; Xu, G. F.; Xu, G. M.; Xu, H.; Xu, Y.; Xu, Z. R.; Xu, Z. Z.; Xue, Z.; Yan, L.; Yan, W. B.; Yan, Y. H.; Yang, H. X.; Yang, M.; Yang, T.; Yang, Y.; Yang, Y. X.; Ye, M.; Ye, M. H.; Yu, B. X.; Yu, C. X.; Yu, L.; Yuan, C. Z.; Yuan, W. L.; Yuan, Y.; Zafar, A. A.; Zallo, A.; Zeng, Y.; Zhang, B. X.; Zhang, B. Y.; Zhang, C. C.; Zhang, D. H.; Zhang, H. H.; Zhang, H. Y.; Zhang, J.; Zhang, J. W.; Zhang, J. Y.; Zhang, J. Z.; Zhang, L.; Zhang, S. H.; Zhang, T. R.; Zhang, X. J.; Zhang, X. Y.; Zhang, Y.; Zhang, Y. H.; Zhang, Z. P.; Zhang, Z. Y.; Zhao, G.; Zhao, H. S.; Zhao, J. W.; Zhao, J. W.; Zhao, L.; Zhao, L.; Zhao, M. G.; Zhao, Q.; Zhao, S. J.; Zhao, T. C.; Zhao, X. H.; Zhao, Y. B.; Zhao, Z. G.; Zhao, Z. L.; Zhemchugov, A.; Zheng, B.; Zheng, J. P.; Zheng, Y. H.; Zheng, Z. P.; Zhong, B.; Zhong, J.; Zhong, L.; Zhou, L.; Zhou, X. K.; Zhou, X. R.; Zhu, C.; Zhu, K.; Zhu, K. J.; Zhu, S. H.; Zhu, X. L.; Zhu, X. W.; Zhu, Y. S.; Zhu, Z. A.; Zhuang, J.; Zou, B. S.; Zou, J. H.; Zuo, J. X.; Zweber, P.: **Measurement of the matrix element for the decay** $\eta' \to \eta\pi^+\pi^-$**.** *Phys. Rev. D* **83**(1): 012003, 2011. DOI: 10.1103/PhysRevD.83.012003

016 Ablikim, M.; Achasov, M. N.; An, L.; An, Q.; An, Z. H.; Bai, J. Z.; Baldini, R.; Ban, Y.; Becker, J.; Berger, N.; Bertani, M.; Bian, J. M.; Bondarenko, O.; Boyko, I.; Briere, R. A.; Bytev, V.; Cai, X.; Cao, G. F.; Cao, X. X.; Chang, J. F.; Chelkov, G.; Chen, G.; Chen, H. S.; Chen, J. C.; Chen, M. L.; Chen, S. J.; Chen, Y.; Chen, Y. B.; Cheng, H. P.; Chu, Y. P.; Cronin-Hennessy, D.; Dai, H. L.; Dai, J. P.; Dedovich, D.; Deng, Z. Y.; Denysenko, I.; Destefanis, M.; Ding, Y.; Dong, L. Y.; Dong, M. Y.; Du, S. X.; Duan, M. Y.; Fan, R. R.; Fang, J.; Fang, S. S.; Feng, C. Q.; Fu, C. D.; Fu, J. L.; Gao, Y.; Geng, C.; Götzen, K.*; Gong, W. X.; Greco, M.; Grishin, S.; Gu, M. H.; Gu, Y. T.; Guan, Y. H.; Guo, A. Q.; Guo, L. B.; Guo, Y. P.; Hao, X. Q.; Harris, F. A.; He, K. L.; He, M.; He, Z. Y.; Heng, Y. K.; Hou, Z. L.; Hu, H. M.; Hu, J. F.; Hu, T.; Huang, B.; Huang, G. M.; Huang, J. S.; Huang, X. T.; Huang, Y. P.; Hussain, T.; Ji, C. S.; Ji, Q.; Ji, X. B.; Ji, X. L.; Jia, L. K.; Jiang, L. L.; Jiang, X. S.; Jiao, J. B.; Jiao, Z.; Jin, D. P.; Jin, S.; Jing, F. F.; Kavatsyuk, M.; Komamiya, S.; Kuehn, W.; Lange, J. S.; Leung, J. K. C.; Li, C.; Li, C.; Li, D. M.; Li, F.; Li, G.; Li, H. B.; Li, J. C.; Li, L.; Li, N. B.; Li, Q. J.; Li, W. D.; Li, W. G.; Li, X. L.; Li, X. N.; Li, X. Q.; Li, X. R.; Li, Z. B.; Liang, H.; Liang, Y. F.; Liang, Y. T.; Liao, G. R.; Liao, X. T.; Liu, B. J.; Liu, B. J.; Liu, C. L.; Liu, C. X.; Liu, C. Y.; Liu, F. H.; Liu, F.; Liu, F.; Liu, G. C.; Liu, H.; Liu, H. B.; Liu, H. M.; Liu, H. W.; Liu, J. P.; Liu, K.; Liu, K. Y.; Liu, Q.; Liu, S. B.; Liu, X.; Liu, X. H.; Liu, Y. B.; Liu, Y. W.; Liu, Y.; Liu, Z. A.; Liu, Z. Q.; Loehner, H.; Lu, G. R.; Lu, H. J.; Lu, J. G.; Lu, Q. W.; Lu, X. R.; Lu, Y. P.; Luo, C. L.; Luo, M. X.; Luo, T.; Luo, X. L.; Ma, C. L.; Ma, F. C.; Ma, H. L.; Ma, Q. M.; Ma, T.; Ma, X.; Ma, X. Y.; Maggiora, M.; Malik, Q. A.; Mao, H.; Mao, Y. J.; Mao, Z. P.; Messchendorp, J. G.; Min, J.; Mitchell, R. E.; Mo, X. H.; Muchnoi, N. Y.; Nefedov, Y.; Ning, Z.; Olsen, S. L.; Ouyang, Q.; Pacetti, S.; Pelizaeus, M.; Peters, K.*; Ping, J. L.; Ping, R. G.; Poling, R.; Pun, C. S. J.; Qi, M.; Qian, S.; Qiao, C. F.; Qin, X. S.; Qiu, J. F.; Rashid, K. H.; Rong, G.; Ruan, X. D.; Sarantsev, A.; Schulze, J.; Shao, M.; Shen, C. P.; Shen, X. Y.; Sheng, H. Y.; Shepherd, M. R.; Song, X. Y.; Sonoda, S.; Spataro, S.; Spruck, B.; Sun, D. H.; Sun, G. X.; Sun, J. F.; Sun, S. S.; Sun, X. D.; Sun, Y. J.; Sun, Y. Z.; Sun, Z. J.; Sun, Z. T.; Tang, C. J.; Tang, X.; Tang, X. F.; Tian, H. L.; Toth, D.; Varner, G. S.; Wan, X.; Wang, B. Q.; Wang, K.; Wang, L. L.; Wang, L. S.; Wang, M.; Wang, P.; Wang, P. L.; Wang, Q.; Wang, S. G.; Wang, X. L.; Wang, Y. D.; Wang, Y. F.; Wang, Y. Q.; Wang, Z.; Wang, Z. G.; Wang, Z. Y.; Wei, D. H.; Wen, Q. G.; Wen, S. P.; Wiedner, U.; Wu, L. H.; Wu, N.; Wu, W.; Wu, Z.; Xiao, Z. J.; Xie, Y. G.; Xu, G. F.; Xu, G. M.; Xu, H.; Xu, Y.; Xu, Z. R.; Xu, Z. Z.; Xue, Z.; Yan, L.; Yan, W. B.; Yan, Y. H.; Yang, H. X.; Yang, M.; Yang, T.; Yang, Y.; Yang, Y. X.; Ye, M.; Ye, M. H.; Yu, B. X.; Yu, C. X.; Yu, L.; Yuan, C. Z.; Yuan, W. L.; Yuan, Y.; Zafar, A. A.; Zallo, A.; Zeng, Y.; Zhang, B. X.; Zhang, B. Y.; Zhang, C. C.; Zhang, D. H.; Zhang, H. H.; Zhang, H. Y.; Zhang, J.; Zhang, J. W.; Zhang, J. Y.; Zhang, J. Z.; Zhang, L.; Zhang, S. H.; Zhang, T. R.; Zhang, X. J.; Zhang, X. Y.; Zhang, Y.; Zhang, Y. H.; Zhang, Z. P.; Zhang, Z. Y.; Zhao, G.; Zhao, H. S.; Zhao, J. W.; Zhao, J. W.; Zhao, L.; Zhao, L.; Zhao, M. G.; Zhao, Q.; Zhao, S. J.; Zhao, T. C.; Zhao, X. H.; Zhao, Y. B.; Zhao, Z. G.; Zhao, Z. L.; Zhemchugov, A.; Zheng, B.; Zheng, J. P.; Zheng, Y. H.; Zheng, Z. P.; Zhong, B.; Zhong, J.; Zhong, L.; Zhou, L.; Zhou, X. K.; Zhou, X. R.; Zhu, C.; Zhu, K.; Zhu, K. J.; Zhu, S. H.; Zhu, X. L.; Zhu, X. W.; Zhu, Y. S.; Zhu, Z. A.; Zhuang, J.; Zou, B. S.; Zou, J. H.; Zuo, J. X.; Zweber, P.: **Measurement of the matrix element for the decay eta ' -¿ eta pi(+)pi(-).** *Phys. Rev. D* **83**(1): 012003, 2011. DOI: 10.1103/PhysRevD.83.012003

017 Ablikim, M.; Achasov, M. N.; An, L.; An, Q.; An, Z. H.; Bai, J. Z.; Baldini, R.; Ban, Y.; Becker, J.; Berger, N.; Bertani, M.; Bian, J. M.; Bondarenko, O.; Boyko, I.; Briere, R. A.; Bytev, V.; Cai, X.; Cao, G. F.; Cao, X. X.; Chang, J. F.; Chelkov, G.; Chen, G.; Chen, H. S.; Chen, J. C.; Chen, M. L.; Chen, S. J.; Chen, Y.; Chen, Y. B.; Cheng, H. P.; Chu, Y. P.; Cronin-Hennessy, D.; Dai, H. L.; Dai, J.

P.; Dedovich, D.; Deng, Z. Y.; Denysenko, I.; Destefanis, M.; Ding, Y.; Dong, L. Y.; Dong, M. Y.; Du, S. X.; Duan, M. Y.; Fan, R. R.; Fang, J.; Fang, S. S.; Feng, C. Q.; Fu, C. D.; Fu, J. L.; Gao, Y.; Geng, C.; Götzen, K.*; Gong, W. X.; Greco, M.; Grishin, S.; Gu, M. H.; Gu, Y. T.; Guan, Y. H.; Guo, A. Q.; Guo, L. B.; Guo, Y. P.; Hao, X. Q.; Harris, F. A.; He, K. L.; He, M.; He, Z. Y.; Heng, Y. K.; Hou, Z. L.; Hu, H. M.; Hu, J. F.; Hu, T.; Huang, B.; Huang, G. M.; Huang, J. S.; Huang, X. T.; Huang, Y. P.; Hussain, T.; Ji, C. S.; Ji, Q.; Ji, X. B.; Ji, X. L.; Jia, L. K.; Jiang, L. L.; Jiang, X. S.; Jiao, J. B.; Jiao, Z.; Jin, D. P.; Jin, S.; Jing, F. F.; Kavatsyuk, M.; Komamiya, S.; Kuehn, W.; Lange, J. S.; Leung, J. K. C.; Li, C.; Li, C.; Li, D. M.; Li, F.; Li, G.; Li, H. B.; Li, J. C.; Li, L.; Li, N. B.; Li, Q. J.; Li, W. D.; Li, W. G.; Li, X. L.; Li, X. N.; Li, X. Q.; Li, X. R.; Li, Z. B.; Liang, H.; Liang, Y. F.; Liang, Y. T.; Liao, G. R.; Liao, X. T.; Liu, B. J.; Liu, B. J.; Liu, C. L.; Liu, C. X.; Liu, C. Y.; Liu, F. H.; Liu, F.; Liu, F.; Liu, G. C.; Liu, H.; Liu, H. B.; Liu, H. M.; Liu, H. W.; Liu, J. P.; Liu, K.; Liu, K. Y.; Liu, Q.; Liu, S. B.; Liu, X.; Liu, X. H.; Liu, Y. B.; Liu, Y. W.; Liu, Y.; Liu, Z. A.; Liu, Z. Q.; Loehner, H.; Lu, G. R.; Lu, H. J.; Lu, J. G.; Lu, Q. W.; Lu, X. R.; Lu, Y. P.; Luo, C. L.; Luo, M. X.; Luo, T.; Luo, X. L.; Ma, C. L.; Ma, F. C.; Ma, H. L.; Ma, Q. M.; Ma, T.; Ma, X.; Ma, X. Y.; Maggiora, M.; Malik, Q. A.; Mao, H.; Mao, Y. J.; Mao, Z. P.; Messchendorp, J. G.; Min, J.; Mitchell, R. E.; Mo, X. H.; Muchnoi, N. Y.; Nefedov, Y.; Ning, Z.; Olsen, S. L.; Ouyang, Q.; Pacetti, S.; Pelizaeus, M.; Peters, K.*; Ping, J. L.; Ping, R. G.; Poling, R.; Pun, C. S. J.; Qi, M.; Qian, S.; Qiao, C. F.; Qin, X. S.; Qiu, J. F.; Rashid, K. H.; Rong, G.; Ruan, X. D.; Sarantsev, A.; Schulze, J.; Shao, M.; Shen, C. P.; Shen, X. Y.; Sheng, H. Y.; Shepherd, M. R.; Song, X. Y.; Sonoda, S.; Spataro, S.; Spruck, B.; Sun, D. H.; Sun, G. X.; Sun, J. F.; Sun, S. S.; Sun, X. D.; Sun, Y. J.; Sun, Y. Z.; Sun, Z. J.; Sun, Z. T.; Tang, C. J.; Tang, X.; Tang, X. F.; Tian, H. L.; Toth, D.; Varner, G. S.; Wan, X.; Wang, B. Q.; Wang, K.; Wang, L. L.; Wang, L. S.; Wang, M.; Wang, P.; Wang, P. L.; Wang, Q.; Wang, S. G.; Wang, X. L.; Wang, Y. D.; Wang, Y. F.; Wang, Y. Q.; Wang, Z.; Wang, Z. G.; Wang, Z. Y.; Wei, D. H.; Wen, Q. G.; Wen, S. P.; Wiedner, U.; Wu, L. H.; Wu, N.; Wu, W.; Wu, Z.; Xiao, Z. J.; Xie, Y. G.; Xu, G. F.; Xu, G. M.; Xu, H.; Xu, Y.; Xu, Z. R.; Xu, Z. Z.; Xue, Z.; Yan, L.; Yan, W. B.; Yan, Y. H.; Yang, H. X.; Yang, M.; Yang, T.; Yang, Y.; Yang, Y. X.; Ye, M.; Ye, M. H.; Yu, B. X.; Yu, C. X.; Yu, L.; Yuan, C. Z.; Yuan, W. L.; Yuan, Y.; Zafar, A. A.; Zallo, A.; Zeng, Y.; Zhang, B. X.; Zhang, B. Y.; Zhang, C. C.; Zhang, D. H.; Zhang, H. H.; Zhang, H. Y.; Zhang, J.; Zhang, J. W.; Zhang, J. Y.; Zhang, J. Z.; Zhang, L.; Zhang, S. H.; Zhang, T. R.; Zhang, X. J.; Zhang, X. Y.; Zhang, Y.; Zhang, Y. H.; Zhang, Z. P.; Zhang, Z. Y.; Zhao, G.; Zhao, H. S.; Zhao, J. W.; Zhao, J. W.; Zhao, L.; Zhao, L.; Zhao, M. G.; Zhao, Q.; Zhao, S. J.; Zhao, T. C.; Zhao, X. H.; Zhao, Y. B.; Zhao, Z. G.; Zhao, Z. L.; Zhemchugov, A.; Zheng, B.; Zheng, J. P.; Zheng, Y. H.; Zheng, Z. P.; Zhong, B.; Zhong, J.; Zhong, L.; Zhou, L.; Zhou, X. K.; Zhou, X. R.; Zhu, C.; Zhu, K.; Zhu, K. J.; Zhu, S. H.; Zhu, X. L.; Zhu, X. W.; Zhu, Y. S.; Zhu, Z. A.; Zhuang, J.; Zou, B. S.; Zou, J. H.; Zuo, J. X.; Zweber, P.: **Observation of chi(c1) Decays into Vector Meson Pairs phi phi, omega omega, and omega phi.** *Phys. Rev. Lett.* **107**(9): 092001, 2011. DOI: 10.1103/PhysRevLett.107.092001

018 Ablikim, M.; Achasov, M. N.; An, L.; An, Q.; An, Z. H.; Bai, J. Z.; Baldini, R.; Ban, Y.; Becker, J.; Berger, N.; Bertani, M.; Bian, J. M.; Boyko, I.; Briere, R. A.; Bytev, V.; Cai, X.; Cao, G. F.; Cao, X. X.; Chang, J. F.; Chelkov, G.; Chen, G.; Chen, H. S.; Chen, J. C.; Chen, M. L.; Chen, S. J.; Chen, Y.; Chen, Y. B.; Cheng, H. P.; Chu, Y. P.; Cronin-Hennessy, D.; Dai, H. L.; Dai, J. P.; Dedovich, D.; Deng, Z. Y.; Denysenko, I.; Destefanis, M.; Ding, Y.; Dong, L. Y.; Dong, M. Y.; Du, S. X.; Duan, M. Y.; Fan, R. R.; Fang, J.; Fang, S. S.; Feldbauer, F.; Feng, C. Q.; Fu, C. D.; Fu, J. L.; Gao, Y.; Geng, C.; Götzen, K.*; Gong, W. X.; Greco, M.; Grishin, S.; Gu, M. H.; Gu, Y. T.; Guan, Y. H.; Guo, A. Q.; Guo, L. B.; Guo, Y. P.; Hao, X. Q.; Harris, F. A.; He, K. L.; He, M.; He, Z. Y.; Heng, Y. K.; Hou, Z. L.; Hu, H. M.; Hu, J. F.; Hu, T.; Huang, B.; Huang, G. M.; Huang, J. S.; Huang, X. T.; Huang, Y. P.; Hussain, T.; Ji, C. S.; Ji, Q.; Ji, X. B.; Ji, X. L.; Jia, L. K.; Jiang, L. L.; Jiang, X. S.; Jiao, J. B.; Jiao, Z.; Jin, D. P.; Jin, S.; Jing, F. F.; Kavatsyuk, M.; Komamiya, S.; Kuehn, W.; Lange, J. S.; Leung, J. K. C.; Li, C.; Li, C.; Li, D. M.; Li, F.; Li, G.; Li, H. B.; Li, J. C.; Li, L.; Li, N. B.; Li, Q. J.; Li, W. D.; Li, W. G.; Li, X. L.; Li, X. N.; Li, X. Q.; Li, X. R.; Li, Z. B.; Liang, H.; Liang, Y. F.; Liang, Y. T.; Liao, G. R.; Liao, X. T.; Liu, B. J.; Liu, B. J.; Liu, C. L.; Liu, C. X.; Liu, C. Y.; Liu, F. H.; Liu, F.; Liu, F.; Liu, G. C.; Liu, H.; Liu, H. B.; Liu, H. M.; Liu, H. W.; Liu, J. P.; Liu, K.; Liu, K. Y.; Liu, Q.; Liu, S. B.; Liu, X.; Liu, X. H.; Liu, Y. B.; Liu, Y. W.; Liu, Y.; Liu, Z. A.; Liu, Z. Q.; Loehner, H.; Lu, G. R.; Lu, H. J.; Lu, J. G.; Lu, Q. W.; Lu, X. R.; Lu, Y. P.; Luo, C. L.; Luo, M. X.; Luo, T.; Luo, X. L.; Ma, C. L.; Ma, F. C.; Ma, H. L.; Ma, Q. M.; Ma, T.; Ma, X.; Ma, X. Y.; Maggiora, M.; Malik, Q. A.; Mao, H.; Mao, Y. J.; Mao, Z. P.; Messchendorp, J. G.; Min, J.; Mitchell, R. E.; Mo, X. H.; Motzko, C.; Muchnoi, N. Y.; Nefedov, Y.; Ning, Z.; Olsen, S. L.; Ouyang, Q.; Pacetti, S.; Pelizaeus, M.; Peters, K.*; Ping, J. L.; Ping, R. G.; Poling, R.; Pun, C. S. J.; Qi, M.; Qian, S.; Qiao, C. F.; Qin, X. S.; Qiu, J. F.; Rashid, K. H.; Rong, G.; Ruan, X. D.; Sarantsev, A.; Schulze, J.; Shao, M.; Shen, C. P.; Shen, X. Y.; Sheng, H. Y.; Shepherd, M. R.; Song, X. Y.; Sonoda, S.; Spataro, S.; Spruck, B.; Sun, D. H.; Sun, G. X.; Sun, J. F.; Sun, S. S.; Sun, X. D.; Sun, Y. J.; Sun, Y. Z.; Sun, Z. J.; Sun, Z. T.; Tang, C. J.; Tang, X.; Tang, X. F.; Tian, H. L.; Toth, D.; Varner, G. S.; Wan, X.; Wang, B. Q.; Wang, K.; Wang, L. L.; Wang, L. S.; Wang, M.; Wang, P.; Wang, P. L.; Wang, Q.; Wang, S. G.; Wang, X. L.; Wang, Y. D.; Wang, Y. F.; Wang, Y. Q.; Wang, Z.; Wang, Z. G.; Wang, Z. Y.; Wei, D. H.; Wen, S. P.; Wiedner, U.; Wu, L. H.; Wu, N.; Wu, W.; Wu, Z.; Xiao, Z. J.; Xie, Y. G.; Xu, G. F.; Xu, G. M.; Xu, H.; Xu, Y.; Xu, Z. R.; Xu, Z. Z.; Xue, Z.; Yan, L.; Yan, W. B.; Yan, Y. H.; Yang, H. X.; Yang, M.; Yang, T.; Yang, Y.; Yang, Y. X.; Ye, M.; Ye, M. H.; Yu, B. X.; Yu, C. X.; Yu, L.; Yuan, C. Z.; Yuan, W. L.; Yuan, Y.; Zafar, A. A.; Zallo, A.;

Zeng, Y.; Zhang, B. X.; Zhang, B. Y.; Zhang, C. C.; Zhang, D. H.; Zhang, H. H.; Zhang, H. Y.; Zhang, J.; Zhang, J. W.; Zhang, J. Y.; Zhang, J. Z.; Zhang, L.; Zhang, S. H.; Zhang, T. R.; Zhang, X. J.; Zhang, X. Y.; Zhang, Y.; Zhang, Y. H.; Zhang, Z. P.; Zhang, Z. Y.; Zhao, G.; Zhao, H. S.; Zhao, J. W.; Zhao, J. W.; Zhao, L.; Zhao, L.; Zhao, M. G.; Zhao, Q.; Zhao, S. J.; Zhao, T. C.; Zhao, X. H.; Zhao, Y. B.; Zhao, Z. G.; Zhao, Z. L.; Zhemchugov, A.; Zheng, B.; Zheng, J. P.; Zheng, Y. H.; Zheng, Z. P.; Zhong, B.; Zhong, J.; Zhong, L.; Zhou, L.; Zhou, X. K.; Zhou, X. R.; Zhu, C.; Zhu, K.; Zhu, K. J.; Zhu, S. H.; Zhu, X. L.; Zhu, X. W.; Zhu, Y. S.; Zhu, Z. A.; Zhuang, J.; Zou, B. S.; Zou, J. H.; Zuo, J. X.; Zweber, P.: **Confirmation of the $X(1835)$ and Observation of the Resonances $X(2120)$ and $X(2370)$ in $J/\psi \to \gamma\pi^+\pi^-\eta'$.** *Phys. Rev. Lett.* **106**(7): 072002, 2011. DOI: 10.1103/PhysRevLett.106.072002

019 Ablikim, M.; Achasov, M. N.; An, L.; An, Q.; An, Z. H.; Bai, J. Z.; Baldini, R.; Ban, Y.; Becker, J.; Berger, N.; Bertani, M.; Bian, J. M.; Boyko, I.; Briere, R. A.; Bytev, V.; Cai, X.; Cao, G. F.; Cao, X. X.; Chang, J. F.; Chelkov, G.; Chen, G.; Chen, H. S.; Chen, J. C.; Chen, M. L.; Chen, S. J.; Chen, Y.; Chen, Y. B.; Cheng, H. P.; Chu, Y. P.; Cronin-Hennessy, D.; Dai, H. L.; Dai, J. P.; Dedovich, D.; Deng, Z. Y.; Denysenko, I.; Destefanis, M.; Ding, Y.; Dong, L. Y.; Dong, M. Y.; Du, S. X.; Duan, M. Y.; Fan, R. R.; Fang, J.; Fang, S. S.; Feldbauer, F.; Feng, C. Q.; Fu, C. D.; Fu, J. L.; Gao, Y.; Geng, C.; Götzen, K.*; Gong, W. X.; Greco, M.; Grishin, S.; Gu, M. H.; Gu, Y. T.; Guan, Y. H.; Guo, A. Q.; Guo, L. B.; Guo, Y. P.; Hao, X. Q.; Harris, F. A.; He, K. L.; He, M.; He, Z. Y.; Heng, Y. K.; Hou, Z. L.; Hu, H. M.; Hu, J. F.; Hu, T.; Huang, B.; Huang, G. M.; Huang, J. S.; Huang, X. T.; Huang, Y. P.; Hussain, T.; Ji, C. S.; Ji, Q.; Ji, X. B.; Ji, X. L.; Jia, L. K.; Jiang, L. L.; Jiang, X. S.; Jiao, J. B.; Jiao, Z.; Jin, D. P.; Jin, S.; Jing, F. F.; Kavatsyuk, M.; Komamiya, S.; Kuehn, W.; Lange, J. S.; Leung, J. K. C.; Li, C.; Li, C.; Li, D. M.; Li, F.; Li, G.; Li, H. B.; Li, J. C.; Li, L.; Li, N. B.; Li, Q. J.; Li, W. D.; Li, W. G.; Li, X. L.; Li, X. N.; Li, X. Q.; Li, X. R.; Li, Z. B.; Liang, H.; Liang, Y. F.; Liang, Y. T.; Liao, G. R.; Liao, X. T.; Liu, B. J.; Liu, B. J.; Liu, C. L.; Liu, C. X.; Liu, C. Y.; Liu, F. H.; Liu, F.; Liu, F.; Liu, G. C.; Liu, H.; Liu, H. B.; Liu, H. M.; Liu, H. W.; Liu, J. P.; Liu, K.; Liu, K. Y.; Liu, Q.; Liu, S. B.; Liu, X.; Liu, X. H.; Liu, Y. B.; Liu, Y. W.; Liu, Y.; Liu, Z. A.; Liu, Z. Q.; Loehner, H.; Lu, G. R.; Lu, H. J.; Lu, J. G.; Lu, Q. W.; Lu, X. R.; Lu, Y. P.; Luo, C. L.; Luo, M. X.; Luo, T.; Luo, X. L.; Ma, C. L.; Ma, F. C.; Ma, H. L.; Ma, Q. M.; Ma, T.; Ma, X.; Ma, X. Y.; Maggiora, M.; Malik, Q. A.; Mao, H.; Mao, Y. J.; Mao, Z. P.; Messchendorp, J. G.; Min, J.; Mitchell, R. E.; Mo, X. H.; Motzko, C.; Muchnoi, N. Y.; Nefedov, Y.; Ning, Z.; Olsen, S. L.; Ouyang, Q.; Pacetti, S.; Pelizaeus, M.; Peters, K.*; Ping, J. L.; Ping, R. G.; Poling, R.; Pun, C. S. J.; Qi, M.; Qian, S.; Qiao, C. F.; Qin, X. S.; Qiu, J. F.; Rashid, K. H.; Rong, G.; Ruan, X. D.; Sarantsev, A.; Schulze, J.; Shao, M.; Shen, C. P.; Shen, X. Y.; Sheng, H. Y.; Shepherd, M. R.; Song, X. Y.; Sonoda, S.; Spataro, S.; Spruck, B.; Sun, D. H.; Sun, G. X.; Sun, J. F.; Sun, S. S.; Sun, X. D.; Sun, Y. J.; Sun, Y. Z.; Sun, Z. J.; Sun, Z. T.; Tang, C. J.; Tang, X.; Tang, X. F.; Tian, H. L.; Toth, D.; Varner, G. S.; Wan, X.; Wang, B. Q.; Wang, K.; Wang, L. L.; Wang, L. S.; Wang, M.; Wang, P.; Wang, P. L.; Wang, Q.; Wang, S. G.; Wang, X. L.; Wang, Y. D.; Wang, Y. F.; Wang, Y. Q.; Wang, Z.; Wang, Z. G.; Wang, Z. Y.; Wei, D. H.; Wen, S. P.; Wiedner, U.; Wu, L. H.; Wu, N.; Wu, W.; Wu, Z.; Xiao, Z. J.; Xie, Y. G.; Xu, G. F.; Xu, G. M.; Xu, H.; Xu, Y.; Xu, Z. R.; Xu, Z. Z.; Xue, Z.; Yan, L.; Yan, W. B.; Yan, Y. H.; Yang, H. X.; Yang, M.; Yang, T.; Yang, Y.; Yang, Y. X.; Ye, M.; Ye, M. H.; Yu, B. X.; Yu, C. X.; Yu, L.; Yuan, C. Z.; Yuan, W. L.; Yuan, Y.; Zafar, A. A.; Zallo, A.; Zeng, Y.; Zhang, B. X.; Zhang, B. Y.; Zhang, C. C.; Zhang, D. H.; Zhang, H. H.; Zhang, H. Y.; Zhang, J.; Zhang, J. W.; Zhang, J. Y.; Zhang, J. Z.; Zhang, L.; Zhang, S. H.; Zhang, T. R.; Zhang, X. J.; Zhang, X. Y.; Zhang, Y.; Zhang, Y. H.; Zhang, Z. P.; Zhang, Z. Y.; Zhao, G.; Zhao, H. S.; Zhao, J.; Zhao, J.; Zhao, L.; Zhao, L.; Zhao, M. G.; Zhao, Q.; Zhao, S. J.; Zhao, T. C.; Zhao, X. H.; Zhao, Y. B.; Zhao, Z. G.; Zhao, Z. L.; Zhemchugov, A.; Zheng, B.; Zheng, J. P.; Zheng, Y. H.; Zheng, Z. P.; Zhong, B.; Zhong, J.; Zhong, L.; Zhou, L.; Zhou, X. K.; Zhou, X. R.; Zhu, C.; Zhu, K.; Zhu, K. J.; Zhu, S. H.; Zhu, X. L.; Zhu, X. W.; Zhu, Y. S.; Zhu, Z. A.; Zhuang, J.; Zou, B. S.; Zou, J. H.; Zuo, J. X.; Zweber, P.: **First observation of the decays $\chi_{cJ} \to \pi^0\pi^0\pi^0\pi^0$.** *Phys. Rev. D* **83**(1): 012006, 2011. DOI: 10.1103/PhysRevD.83.012006

020 Ablikim, M.; Achasov, M. N.; An, L.; An, Q.; An, Z. H.; Bai, J. Z.; Baldini, R.; Ban, Y.; Becker, J.; Berger, N.; Bertani, M.; Bian, J. M.; Boyko, I.; Briere, R. A.; Bytev, V.; Cai, X.; Cao, G. F.; Cao, X. X.; Chang, J. F.; Chelkov, G.; Chen, G.; Chen, H. S.; Chen, J. C.; Chen, M. L.; Chen, S. J.; Chen, Y.; Chen, Y. B.; Cheng, H. P.; Chu, Y. P.; Cronin-Hennessy, D.; Dai, H. L.; Dai, J. P.; Dedovich, D.; Deng, Z. Y.; Denysenko, I.; Destefanis, M.; Ding, Y.; Dong, L. Y.; Dong, M. Y.; Du, S. X.; Duan, M. Y.; Fan, R. R.; Fang, J.; Fang, S. S.; Feng, C. Q.; Fu, C. D.; Fu, J. L.; Gao, Y.; Geng, C.; Götzen, K.*; Gong, W. X.; Greco, M.; Grishin, S.; Gu, M. H.; Gu, Y. T.; Guan, Y. H.; Guo, A. Q.; Guo, L. B.; Guo, Y. P.; Hao, X. Q.; Harris, F. A.; He, K. L.; He, M.; He, Z. Y.; Heng, Y. K.; Hou, Z. L.; Hu, H. M.; Hu, J. F.; Hu, T.; Huang, B.; Huang, G. M.; Huang, J. S.; Huang, X. T.; Huang, Y. P.; Hussain, T.; Ji, C. S.; Ji, Q.; Ji, X. B.; Ji, X. L.; Jia, L. K.; Jiang, L. L.; Jiang, X. S.; Jiao, J. B.; Jiao, Z.; Jin, D. P.; Jin, S.; Jing, F. F.; Kavatsyuk, M.; Komamiya, S.; Kuehn, W.; Lange, J. S.; Leung, J. K. C.; Li, C.; Li, C.; Li, D. M.; Li, F.; Li, G.; Li, H. B.; Li, J. C.; Li, L.; Li, N. B.; Li, Q. J.; Li, W. D.; Li, W. G.; Li, X. L.; Li, X. N.; Li, X. Q.; Li, X. R.; Li, Z. B.; Liang, H.; Liang, Y. F.; Liang, Y. T.; Liao, G. R.; Liao, X. T.; Liu, B. J.; Liu, B. J.; Liu, C. L.; Liu, C. X.; Liu, C. Y.; Liu, F. H.; Liu, F.; Liu, F.; Liu, G. C.; Liu, H.; Liu, H. B.; Liu, H. M.; Liu, H. W.; Liu, J. P.; Liu, K.; Liu, K. Y.; Liu, Q.; Liu, S. B.; Liu, X.; Liu, X. H.; Liu, Y. B.; Liu, Y. W.; Liu, Y.; Liu, Z. A.; Liu, Z. Q.; Loehner, H.; Lu, G. R.; Lu, H. J.; Lu, J. G.; Lu, Q. W.; Lu, X. R.; Lu, Y. P.; Luo, C. L.; Luo, M. X.; Luo, T.; Luo, X. L.; Ma, C.

L.; Ma, F. C.; Ma, H. L.; Ma, Q. M.; Ma, T.; Ma, X.; Ma, X. Y.; Maggiora, M.; Malik, Q. A.; Mao, H.; Mao, Y. J.; Mao, Z. P.; Messchendorp, J. G.; Min, J.; Mitchell, R. E.; Mo, X. H.; Muchnoi, N. Y.; Nefedov, Y.; Ning, Z.; Olsen, S. L.; Ouyang, Q.; Pacetti, S.; Pelizaeus, M.; Peters, K.*; Ping, J. L.; Ping, R. G.; Poling, R.; Pun, C. S. J.; Qi, M.; Qian, S.; Qiao, C. F.; Qin, X. S.; Qiu, J. F.; Rashid, K. H.; Rong, G.; Ruan, X. D.; Sarantsev, A.; Schulze, J.; Shao, M.; Shen, C. P.; Shen, X. Y.; Sheng, H. Y.; Shepherd, M. R.; Song, X. Y.; Sonoda, S.; Spataro, S.; Spruck, B.; Sun, D. H.; Sun, G. X.; Sun, J. F.; Sun, S. S.; Sun, X. D.; Sun, Y. J.; Sun, Y. Z.; Sun, Z. J.; Sun, Z. T.; Tang, C. J.; Tang, X.; Tang, X. F.; Tian, H. L.; Toth, D.; Varner, G. S.; Wan, X.; Wang, B. Q.; Wang, K.; Wang, L. L.; Wang, L. S.; Wang, M.; Wang, P.; Wang, P. L.; Wang, Q.; Wang, S. G.; Wang, X. L.; Wang, Y. D.; Wang, Y. F.; Wang, Y. Q.; Wang, Z.; Wang, Z. G.; Wang, Z. Y.; Wei, D. H.; Wen, S. P.; Wiedner, U.; Wu, L. H.; Wu, N.; Wu, W.; Wu, Z.; Xiao, Z. J.; Xie, Y. G.; Xu, G. F.; Xu, G. M.; Xu, H.; Xu, Y.; Xu, Z. R.; Xu, Z. Z.; Xue, Z.; Yan, L.; Yan, W. B.; Yan, Y. H.; Yang, H. X.; Yang, M.; Yang, T.; Yang, Y.; Yang, Y. X.; Ye, M.; Ye, M. H.; Yu, B. X.; Yu, C. X.; Yu, L.; Yuan, C. Z.; Yuan, W. L.; Yuan, Y.; Zafar, A. A.; Zallo, A.; Zeng, Y.; Zhang, B. X.; Zhang, B. Y.; Zhang, C. C.; Zhang, D. H.; Zhang, H. H.; Zhang, H. Y.; Zhang, J.; Zhang, J. W.; Zhang, J. Y.; Zhang, J. Z.; Zhang, L.; Zhang, S. H.; Zhang, T. R.; Zhang, X. J.; Zhang, X. Y.; Zhang, Y.; Zhang, Y. H.; Zhang, Z. P.; Zhang, Z. Y.; Zhao, G.; Zhao, H. S.; Zhao, J. W.; Zhao, J. W.; Zhao, L.; Zhao, L.; Zhao, M. G.; Zhao, Q.; Zhao, S. J.; Zhao, T. C.; Zhao, X. H.; Zhao, Y. B.; Zhao, Z. G.; Zhao, Z. L.; Zhemchugov, A.; Zheng, B.; Zheng, J. P.; Zheng, Y. H.; Zheng, Z. P.; Zhong, B.; Zhong, J.; Zhong, L.; Zhou, L.; Zhou, X. K.; Zhou, X. R.; Zhu, C.; Zhu, K.; Zhu, K. J.; Zhu, S. H.; Zhu, X. L.; Zhu, X. W.; Zhu, Y. S.; Zhu, Z. A.; Zhuang, J.; Zou, B. S.; Zou, J. H.; Zuo, J. X.; Zweber, P.: **Study of $a_0^0(980) - f_0(980)$ mixing.** *Phys. Rev. D* **83**(3): 032003, 2011. DOI: 10.1103/PhysRevD.83.032003

021 Achenbach, P.; Gayoso, C. A.; Bernauer, J. C.; Bohm, R.; Bosnar, D.; Debenjak, L.; Distler, M. O.; Esser, A.; Friscic, I.; de la Paz, M. G. R.; Hoffmann, J.; Makek, M.; Merkel, H.; Minami, S.*; Muller, U.; Nungesser, L.; Ott, W.*; Pochodzalla, J.; Potokar, M.; Rusanov, I.*; Saito, T. R.*; Majos, S. S.; Schlimme, B. S.; Sirca, S.; Voltz, S.; Weindel, K.; Weinriefer, M.: **A Large-Scale FPGA-Based Trigger and Dead-Time Free DAQ System for the KAOS Spectrometer at MAMI.** *IEEE Trans. Nucl. Sci.* **58**(4): 1677–1684, 2011. DOI: 10.1109/TNS.2011.2157523

022 Ackermann, D.*: **SUPERHEAVY ELEMENTS AT GSI - INVESTIGATING EXOTIC NUCLEAR MATTER.** *Acta Phys. Pol. B* **42**(3-4): 577–586, 2011. DOI: 10.5506/APhysPolB.42.577

023 Adachi, T.; Harakeh, M. N.; Kalantar-Nayestanaki, N.; Wortche, H. J.; Berg, G. P. A.; Simon, H.*; Koop, I. A.; Couder, M.; Fujiwara, M.: **Constant-gap spectrometer design for the electron/ion collider ELISe.** *Nucl. Instrum. Methods Phys. Res. Sect. A-Accel. Spectrom. Dect. Assoc. Equip.* **659**(1): 198–206, 2011. DOI: 10.1016/j.nima.2011.06.081

024 Adamczewski-Musch, J. *; Essel, H. G.*; Linev, S.*: **Online Object Monitoring With Go4 V4.4.** *IEEE Trans. Nucl. Sci.* **58**(4): 1477–1481, 2011. DOI: 10.1109/TNS.2011.2149541

025 Adamczewski-Musch, J.*; Essel, H. G.*; Linev, S.*: **The DABC Framework Interface to Readout Hardware.** *IEEE Trans. Nucl. Sci.* **58**(4): 1728–1732, 2011. DOI: 10.1109/TNS.2011.2158112

026 Adelberger, E. G.; Garcia, A.; Robertson, R. G. H.; Snover, K. A.; Balantekin, A. B.; Heeger, K.; Ramsey-Musolf, M. J.; Bemmerer, D.; Junghans, A.; Bertulani, C. A.; Chen, J. W.; Costantini, H.; Prati, P.; Couder, M.; Uberseder, E.; Wiescher, M.; Cyburt, R.; Davids, B.; Freedman, S. J.; Gai, M.; Gazit, D.; Gialanella, L.; Imbriani, G.; Greife, U.; Hass, M.; Haxton, W. C.; Itahashi, T.; Kubodera, K.; Langanke, K.*; Leitner, D.; Leitner, M.; Vetter, P.; Winslow, L.; Marcucci, L. E.; Motobayashi, T.; Mukhamedzhanov, A.; Tribble, R. E.; Nollett, K. M.; Nunes, F. M.; Park, T. S.; Parker, P. D.; Schiavilla, R.; Simpson, E. C.; Spitaleri, C.; Strieder, F.; Trautvetter, H. P.; Suemmerer, K.; Typel, S.*: **Solar fusion cross sections. II. The pp chain and CNO cycles.** *Rev. Mod. Phys.* **83**(1): 195–245, 2011. DOI: 10.1103/RevModPhys.83.195

027 Agakishiev, G.; Balanda, A.; Bannier, B.; Bassini, R.; Belver, D.; Belyaev, A. V.; Blanco, A.; Bohmer, M.; Boyard, J. L.; Cabanelas, P.; Castro, E.; Chernenko, S.; Christ, T.; Destefanis, M.; Diaz, J.; Dohrmann, F.; Dybczak, A.; Eberl, T.; Epple, E.; Fabbietti, L.; Fateev, O. V.; Finocchiaro, P.; Fonte, P.; Friese, J.; Frohlich, I.; Galatyuk, T.*; Garzon, J. A.; Gernhauser, R.; Gil, A.; Gilardi, C.; Golubeva, M.; Gonzalez-Diaz, D.*; Guber, F.; Gumberidze, M.*; Heilmann, M.; Heinz, T.*; Hennino, T.; Holzmann, R.0491; Huck, P.; Iori, I.; Ivashkin, A.; Jurkovic, M.; Kampfer, B.; Kanaki, K.; Karavicheva, T.; Kirschner, D.; Koenig, I.*; Koenig, W.*; Kolb, B. W.*; Kotte, R.; Krizek, F.; Krucken, R.; Kuhn, W.; Kugler, A.; Kurepin, A.; Lang, S.; Lange, J. S.; Lapidus, K.; Liu, T.; Lopes, L.; Lorenz, M.*; Maier, L.; Mangiarotti, A.; Markert, J.*; Metag, V.; Michalska, B.; Michel, J.*; Mishra, D.; Moriniere, E.; Mousa, J.; Muntz, C.*; Naumann, L.; Otwinowski, J.*; Pachmayer, Y. C.; Palka, M.; Parpottas, Y.; Pechenov, V.*; Pechenova, O.; Cavalcanti, T. P.; Pietraszko, J.*; Przygoda, W.; Ramstein, B.; Reshetin, A.; Roy-Stephan, M.; Rustamov, A.*; Sadovsky, A.; Sailer, B.; Salabura, P.*; Schmah, A.; Schwab, E.*; Siebenson, J.; Sobolev, Y. G.; Spataro, S.; Spruck, B.; Strobele, H.*; Stroth, J.*; Sturm, C.*; Tarantola, A.; Teilab, K.*; Tlusty, P.; Traxler, M.*; Trebacz, R.; Tsertos, H.; Wagner, V.; Weber, M.; Wendisch, C.; Wisniowski, M.; Wojcik, T.; Wustenfeld, J.*; Yurevich, S.*; Zanevsky, Y. V.; Zhou, P.;

Zumbruch, P.*: **pp and pi pi intensity interferometry in collisions of Ar+KCl at 1.76A GeV.** *Eur. Phys. J. A* **47**(5): 63, 2011. DOI: 10.1140/epja/i2011-11063-x

028 Agakishiev, G.; Balanda, A.; Bannier, B.; Bassini, R.; Belver, D.; Belyaev, A.; Blanco, A.; Bohmer, M.; Boyard, J. L.; Cabanelas, P.; Castro, E.; Chernenko, S.; Christ, T.; Destefanis, M.; Diaz, J.; Dohrmann, F.; Dybczak, A.; Eberl, T.; Epple, E.; Fabbietti, L.; Fateev, O.; Finocchiaro, P.; Fonte, P.; Friese, J.; Frohlich, I.; Galatyuk, T.*; Garzon, J. A.; Gernhauser, R.; Gil, A.; Gilardi, C.; Golubeva, M.; Gonzalez-Diaz, D.*; Guber, F.; Gumberidze, M.*; Heilmann, M.; Heinz, T.*; Hennino, T.; Holzmann, R.*; Huck, P.; Iori, I.; Ivashkin, A.; Jurkovic, M.; Kampfer, B.; Kanaki, K.; Karavicheva, T.; Kirschner, D.; Koenig, I.*; Koenig, W.*; Kolb, B. W.*; Kotte, R.; Krizek, F.; Krucken, R.; Kuhn, W.; Kugler, A.; Kurepin, A.; Lang, S.; Lange, J. S.; Lapidus, K.; Liu, T.; Lopes, L.; Lorenz, M.*; Maier, L.; Mangiarotti, A.; Markert, J.*; Metag, V.; Michalska, B.; Michel, J.*; Mishra, D.; Moriniere, E.; Mousa, J.; Muntz, C.*; Naumann, L.; Otwinowski, J.*; Pachmayer, Y. C.; Palka, M.; Parpottas, Y.; Pechenov, V.*; Pechenova, O.; Cavalcanti, T. P.; Pietraszko, J.*; Przygoda, W.; Ramstein, B.; Reshetin, A.; Roy-Stephan, M.; Rustamov, A.*; Sadovsky, A.; Sailer, B.; Salabura, P.*; Schmah, A.; Schwab, E.*; Siebenson, J.; Sobolev, Y. G.; Spataro, S.; Spruck, B.; Strobele, H.*; Stroth, J.*; Sturm, C.*; Tarantola, A.; Teilab, K.*; Tlusty, P.; Traxler, M.*; Trebacz, R.; Tsertos, H.; Wagner, V.; Weber, M.; Wendisch, C.; Wisniowski, M.; Wojcik, T.; Wustenfeld, J.*; Yurevich, S.*; Zanevsky, Y.; Zhou, P.; Zumbruch, P.*: **Hyperon production in Ar plus KCl collisions at 1.76A GeV.** *Eur. Phys. J. A* **47**(2): 21, 2011. DOI: 10.1140/epja/i2011-11021-8

029 Agakishiev, G.; Balanda, A.; Belver, D.; Belyaev, A.; Blanco, A.; Bohmer, M.; Boyard, J. L.; Cabanelas, P.; Castro, E.; Chernenko, S.; Christ, T.; Destefanis, M.; Dohrmann, F.; Dybczak, A.; Eberl, T.; Epple, E.; Fabbietti, L.; Fateev, O.; Finocchiaro, P.; Fonte, P.; Friese, J.; Frohlich, I.; Galatyuk, T.*; Garzon, J. A.; Gernhauser, R.; Gilardi, C.; Golubeva, M.; Gonzalez-Diaz, D.*; Guber, F.; Gumberidze, M.*; Heinz, T.*; Hennino, T.; Holzmann, R.*; Huck, P.; Iori, I.; Ivashkin, A.; Jurkovic, M.; Kampfer, B.; Kanaki, K.; Karavicheva, T.; Koenig, I.*; Koenig, W.*; Kolb, B. W.*; Kotte, R.; Krasa, A.; Krizek, F.; Krucken, R.; Kuc, H.; Kuhn, W.; Kugler, A.; Kurepin, A.; Lang, S.; Lange, J. S.; Lapidus, K.; Liu, T.; Lopes, L.; Lorenz, M.*; Maier, L.; Mangiarotti, A.; Markert, J.*; Metag, V.; Michalska, B.; Michel, J.*; Moriniere, E.; Mousa, J.; Muntz, C.*; Naumann, L.; Otwinowski, J.*; Pachmayer, Y. C.; Palka, M.; Pechenov, V.*; Pechenova, O.; Pietraszko, J.*; Przygoda, W.; Ramstein, B.; Reshetin, A.; Rustamov, A.*; Sadovsky, A.; Sailer, B.; Salabura, P.*; Schmah, A.; Schwab, E.*; Siebenson, J.; Sobolev, Y. G.; Spataro, S.; Spruck, B.; Strobele, H.; Stroth, J.*; Sturm, C.*; Tarantola, A.; Teilab, K.*; Tlusty, P.; Traxler, M.*; Trebacz, R.; Tsertos, H.; Wagner, V.; Weber, M.; Wendisch, C.; Wisniowski, M.; Wustenfeld, J.*; Yurevich, S.*; Zanevsky, Y.: **Dielectron production in Ar plus KCl collisions at 1.76A GeV.** *Phys. Rev. C* **84**(1): 014902, 2011. DOI: 10.1103/PhysRevC.84.014902

030 Aggarwal, M. M.; Ahammed, Z.; Angelis, A. L. S.; Antonenko, V.; Arefiev, V.; Astakhov, V.; Avdeitchikov, V.; Awes, T. C.; Baba, P. V. K. S.; Badyal, S. K.; Bathe, S.; Batiounia, B.; Bernier, T.; Bhalla, K. B.; Bhatia, V. S.; Blume, C.; Bucher, D.; BÃ$\frac{1}{4}$sching, H.; Carlen, L.; Chattopadhyay, S.; Decowski, M. P.; Delagrange, H.; Donni, P.; Majumdar, M. R. D.; El Chenawi, K.; Dubey, A. K.; Enosawa, K.; Fokin, S.; Frolov, V.; Ganti, M. S.; Garpman, S.; Gavrishchuk, O.; Geurts, F. J. M.; Ghosh, T. K.; Glasow, R.; Gupta, R.; Guskov, B.; Gustafsson, H. A.; Gutbrod, H. H.; Hrivnacova, I.; Ippolitov, M.; Kalechofsky, H.; Kamermans, R.; Karadjev, K.; Karpios, K.; Kolb, B. W.*; Kosarev, I.; Koutcheryaev, I.; Kugler, A.; Kulinich, P.; Kurata, M.; Lebedev, A.*; Liu, H.; Lohner, H.; Luquin, L.; Mahapatra, D. P.; Manko, V.; Martin, M.; Martinez, G.; Maximov, A.; Miake, Y.; Mishra, G. C.; Mohanty, B.; Mora, M. J.; Morrison, D.; Moukhanova, T.; Mukhopadhyay, D. S.; Naef, H.; Nandi, B. K.; Nayak, S. K.; Nayak, T. K.; Nianine, A.; Nikitine, V.; Nikolaev, S.; Nilsson, P.; Nishimura, S.; Nomokonov, P.; Nystrand, J.; Oskarsson, A.; Otterlund, I.; Pavliouk, S.; Peitzmann, T.; Peressounko, D.; Petracek, V.; Pinaud, W.; Plasil, F.; Purschke, M. L.; Rak, J.; Raniwala, R.; Raniwala, S.; Rao, N. K.; Retiere, F.; Reygers, K.; Roland, G.; Rosselet, L.; Roufanov, I.; Roy, C.; Rubio, J. M.; Sambyal, S. S.; Santo, R.; Sato, S.; Schlagheck, H.; Schmidt, H. R.*; Schutz, Y.; Shabratova, G.; Shah, T. H.; Sibiriak, I.; Siemiarczuk, T.; Silvermyr, D.; Sinha, B. C.; Slavine, N.; Soderstrom, K.; Sood, G.; Sorensen, S. P.; Stankus, P.; Stefanek, G.; Steinberg, P.; Stenlund, E.; Sumbera, M.; Svensson, T.; Tsvetkov, A.; Tykarski, L.; Pijll, E. C. V. D.; Eijndhoven, N. V.; Nieuwenhuizen, G. J. V.; Vinogradov, A.; Viyogi, Y. P.; Vodopianov, A.; Voros, S.; Wyslouch, B.; Young, G. R.: **Event-by-event charged-neutral fluctuations in Pb plus Pb collisions at 158 A GeV.** *Phys. Lett. B* **701**(3): 300–305, 2011. DOI: 10.1016/j.physletb.2011.06.003

031 Aguado, M. E. E.; Algora, A.; Rubio, B.; Bernabeu, J.; Nacher, E.; Tain, J. L.; Gadea, A.; Agramunt, J.; Burkard, K.*; Huller, W.*; Doring, J.; Kirchner, R.; Mukha, I. G.*; Plettner, C.; Roeckl, E.; Grawe, H.; Collatz, R.; Hellstrom, M.; Cano-Ott, D.; Karny, M.; Janas, Z.; Gierlik, M.; Plochocki, A.; Rykaczewski, K.; Batist, L.; Moroz, F.; Wittman, V.; Blazhev, A.; Valiente, J. J.; Espinoza, C.: **beta-decay study of (150)Er, (152)Yb, and (156)Yb: Candidates for a monoenergetic neutrino beam facility.** *Phys. Rev. C* **84**(3): 034304, 2011. DOI: 10.1103/PhysRevC.84.034304

032 Ahmed, G.; Bühler, P.; Cargnelli, M.; Hohler, R.; Marton, J.; Orth, H.*; Suzuki, K.: **Application of Geiger-mode photosensors in Cherenkov detectors.** *Nucl. Instrum. Methods Phys. Res. Sect. A-Accel. Spectrom. Dect. Assoc. Equip.* **639**(1): 107–110, 2011.

DOI: 10.1016/j.nima.2010.10.114

033 Al-Khateeb, A. M.; Boine-Frankenheim, O.*; Plotnikov, A.; Shim, S. Y.*; Hanichen, L.: **Longitudinal impedance of a step-in for a round beam at arbitrary beam energy.** *Nucl. Instrum. Methods Phys. Res. Sect. A-Accel. Spectrom. Dect. Assoc. Equip.* **626**: 1–7, 2011. DOI: 10.1016/j.nima.2010.09.026

034 Al-Turany, M.: **Optimization of HEP codes on GPUs.** *Eur. Phys. J. Plus* **126**(1): 1, 2011. DOI: 10.1140/epjp/i2011-11001-5

035 Algora, A.; Jordan, D.; Tain, J. L.; Rubio, B.; Agramunt, J.; Caballero, L.; Nacher, E.; Perez-Cerdan, A. B.; Molina, F.; Krasznahorkay, A.; Hunyadi, M. D.; Gulyas, J.; Vitez, A.; Csatlos, M.; Csige, L.; Aysto, J.; Penttila, H.; Rinta-Antila, S.; Moore, I.; Eronen, T.; Jokinen, A.; Nieminen, A.; Hakala, J.; Karvonen, P.; Kankainen, A.; Hager, U.; Sonoda, T.; Saastamoinen, A.; Rissanen, J.; Kessler, T.; Weber, C.; Ronkainen, J.; Rahaman, S.; Elomaa, V.; Burkard, K.*; Huller, W.*; Batist, L.; Gelletly, W.; Yoshida, T.; Nichols, A. L.; Sonzogni, A.; Perajarvi, K.: **Improvements on Decay Heat Summation Calculations by Means of Total Absorption Gamma-ray Spectroscopy Measurements.** *J. Korean Phys. Soc.* **59**(2): 1479–1482, 2011. DOI: 10.3938/jkps.59.1479

036 Andronic, A.*; Braun-Munzinger, P.*; Stachel, J.; Stoecker, H.*: **Production of light nuclei, hypernuclei and their antiparticles in relativistic nuclear collisions.** *Phys. Lett. B* **697**(3): 203–207, 2011. DOI: 10.1016/j.physletb.2011.01.053

037 Antalic, S.; Hesserger, F. P.; Ackermann, D.*; Heinz, S.*; Hofmann, S.*; Kalaninova, Z.; Kindler, B.*; Khuyagbaatar, J.; Kojouharov, I.*; Kuusiniemi, P.; Leino, M.; Lommel, B.*; Mann, R.; Nishio, K.; Saro, S.; Streicher, B.; Sulignano, B.; Venhart, M.: **Isomeric states in (253)No and (253)Fm.** *Eur. Phys. J. A* **47**(5): 62, 2011. DOI: 10.1140/epja/i2011-11062-y

038 Anticic, T.; Baatar, B.; Barna, D.; Bartke, J.; Beck, H.; Betev, L.; Bialkowska, H.; Blume, C.; Bogusz, M.; Boimska, B.; Book, J.; Botje, M.; Buncic, P.; Cetner, T.; Christakoglou, P.; Chung, P.; Chvala, O.; Cramer, J. G.; Eckardt, V.; Fodor, Z.; Foka, P.*; Friese, V.*; Gazdzicki, M.; Grebieszkow, K.; Höhne, C.*; Kadija, K.; Karev, A.; Kolesnikov, V. I.; Kollegger, T.; Kowalski, M.; Kresan, D.*; Laszlo, A.; Lacey, R.; van Leeuwen, M.; Mackowiak, M.; Makariev, M.; Malakhov, A. I.; Mateev, M.; Melkumov, G. L.; Mitrovski, M.; Mrowczynski, S.; Nicolic, V.; Palla, G.; Panagiotou, A. D.; Peryt, W.; Pluta, J.; Prindle, D.; Puhlhofer, F.; Renfordt, R.; Roland, C.; Roland, G.; Rybczynski, M.; Rybicki, A.; Sandoval, A.; Schmitz, N.; Schuster, T.; Seyboth, P.; Sikler, F.; Skrzypczak, E.; Slodkowski, M.; Stefanek, G.; Stock, R.; Strobele, H.; Susa, T.; Szuba, M.; Utvic, M.; Varga, D.; Vassiliou, M.; Veres, G. I.; Vesztergombi, G.; Vranic, D.*; Wlodarczyk, Z.; Wojtaszek-Szwarc, A.: **Energy dependence of kaon-to-proton ratio fluctuations in central Pb plus Pb collisions from root s(NN)=6.3 to 17.3 GeV.** *Phys. Rev. C* **83**(6): 061902, 2011. DOI: 10.1103/PhysRevC.83.061902

039 Anticic, T.; Baatar, B.; Barna, D.; Bartke, J.; Beck, H.; Betev, L.; Bialkowska, H.; Blume, C.; Bogusz, M.; Boimska, B.; Book, J.; Botje, M.; Buncic, P.; Cetner, T.; Christakoglou, P.; Chung, P.; Chvala, O.; Cramer, J. G.; Eckardt, V.; Fodor, Z.; Foka, P.*; Friese, V.*; Gazdzicki, M.; Grebieszkow, K.; Hohne, C.; Kadija, K.; Karev, A.; Kolesnikov, V. I.; Kowalski, M.; Kresan, D.*; Laszlo, A.; Lacey, R.; van Leeuwen, M.; Mackowiak, M.; Makariev, M.; Malakhov, A. I.; Mateev, M.; Melkumov, G. L.; Mitrovski, M.; Mrowczynski, S.; Nicolic, V.; Palla, G.; Panagiotou, A. D.; Peryt, W.; Pluta, J.; Prindle, D.; Puhlhofer, F.; Renfordt, R.; Roland, C.; Roland, G.; Rybczynski, M.; Rybicki, A.; Sandoval, A.; Schmitz, N.; Schuster, T.; Seyboth, P.; Sikler, F.; Skrzypczak, E.; Slodkowski, M.; Stefanek, G.; Stock, R.; Strobele, H.*; Susa, T.; Szuba, M.; Utvic, M.; Varga, D.; Vassiliou, M.; Veres, G. I.; Vesztergombi, G.; Vranic, D.; Wlodarczyk, Z.; Wojtaszek-Szwarc, A.: **Centrality dependence of proton and antiproton spectra in Pb plus Pb collisions at 40A GeV and 158A GeV measured at the CERN Super Proton Synchrotron.** *Phys. Rev. C* **83**(1): 014901, 2011. DOI: 10.1103/PhysRevC.83.014901

040 Anticic, T.; Baatar, B.; Barna, D.; Bartke, J.; Beck, H.; Betev, L.; Bialkowska, H.; Blume, C.; Bogusz, M.; Boimska, B.; Book, J.; Botje, M.; Buncic, P.; Cetner, T.; Christakoglou, P.; Chung, P.; Chvala, O.; Cramer, J. G.; Eckardt, V.; Fodor, Z.; Foka, P.*; Friese, V.*; Gazdzicki, M.; Grebieszkow, K.; Hohne, C.; Kadija, K.; Karev, A.; Kolesnikov, V. I.; Kowalski, M.; Kresan, D.*; Laszlo, A.; Lacey, R.; van Leeuwen, M.; Mackowiak, M.; Makariev, M.; Malakhov, A. I.; Mateev, M.; Melkumov, G. L.; Mitrovski, M.; Mrowczynski, S.; Nicolic, V.; Palla, G.; Panagiotou, A. D.; Peryt, W.; Pluta, J.; Prindle, D.; Puhlhofer, F.; Renfordt, R.; Roland, C.; Roland, G.; Rybczynski, M.; Rybicki, A.; Sandoval, A.; Schmitz, N.; Schuster, T.; Seyboth, P.; Sikler, F.; Skrzypczak, E.; Slodkowski, M.; Stefanek, G.; Stock, R.; Strobele, H.; Susa, T.; Szuba, M.; Utvic, M.; Varga, D.; Vassiliou, M.; Veres, G. I.; Vesztergombi, G.; Vranic, D.; Wlodarczyk, Z.; Wojtaszek-Szwarc, A.: **Proton-Lambda correlations in central Pb plus Pb collisions at root s(NN)=17.3 GeV.** *Phys. Rev. C* **83**(5): 054906, 2011. DOI: 10.1103/PhysRevC.83.054906

041 Anticic, T.; Baatar, B.; Barna, D.; Bartke, J.; Beck, H.; Betev, L.; Bialkowska, H.; Blume, C.; Bogusz, M.; Boimska, B.; Book, J.; Botje, M.; Buncic, P.; Cetner, T.; Christakoglou, P.; Chung, P.; Chvala, O.; Cramer, J. G.; Eckardt, V.; Fodor, Z.; Foka, P.; Friese, V.; Gazdzicki, M.; Grebieszkow, K.; Hohne, C.; Kadija, K.; Karev, A.; Kolesnikov, V. I.; Kowalski, M.; Kresan, D.; Laszlo, A.; Lacey, R.; van Leeuwen, M.; Mackowiak, M.; Makariev, M.; Malakhov, A. I.; Mateev, M.; Melkumov, G. L.; Mitro-

vski, M.; Mrowczynski, S.; Nicolic, V.; Palla, G.; Panagiotou, A. D.; Peryt, W.; Pluta, J.; Prindle, D.; P"uhlhofer, F.; Renfordt, R.; Roland, C.; Roland, G.; Rybczynski, M.; Rybicki, A.; Sandoval, A.; Schmitz, N.; Schuster, T.; Seyboth, P.; Sikler, F.; Skrzypczak, E.; Slodkowski, M.; Stefanek, G.; Stock, R.; Strobele, H.; Susa, T.; Szuba, M.; Utvic, M.; Varga, D.; Vassiliou, M.; Veres, G. I.; Vesztergombi, G.; Vranic, D.; Wlodarczyk, Z.; Wojtaszek-Szwarc, A.: **K*(892)(0) and (K)over-bar*(892)(0) production in central Pb plus Pb, Si plus Si, C plus C, and inelastic p plus p collisions at 158A GeV.** *Phys. Rev. C* **84**(6): 064909, 2011. DOI: 10.1103/PhysRevC.84.064909

042 Antonov, A. N.; Gaidarov, M. K.; Ivanov, M. V.; Kadrev, D. N.; Aiche, M.; Barreau, G.; Czajkowski, S.; Jurado, B.; Belier, G.; Chatillon, A.; Granier, T.; Taieb, J.; Dore, D.; Letourneau, A.; Ridikas, D.; Dupont, E.; Berthoumieux, E.; Panebianco, S.; Farget, F.; Schmitt, C.; Audouin, L.; Khan, E.; Tassan-Got, L.; Aumann, T.*; Beller, P.; Boretzky, K.*; Dolinskii, A.; Egelhof, P.*; Emling, H.; Franzke, B.; Geissel, H.*; Kelic-Heil, A.*; Kester, O.; Kurz, N.; Litvinov, Y.*, Y.; Munzenberg, G.; Nolden, F.; Schmidt, K. H.*; Scheidenberger, C.*; Simon, H.*; Steck, M.; Weick, H.*; Enders, J.; Pietralla, N.; Richter, A.; Schrieder, G.; Zilges, A.; Distler, M. O.; Merkel, H.; Muller, U.; Junghans, A. R.; Lenske, H.; Fujiwara, M.; Suda, T.; Kato, S.; Adachi, T.; Hamieh, S.; Harakeh, M. N.; Kalantar-Nayestanaki, N.; Wortche, H.; Berg, G. P. A.; Koop, I. A.; Logatchov, P. V.; Otboev, A. V.; Parkhomchuk, V. V.; Shatilov, D. N.; Shatunov, P. Y.; Shatunov, Y. M.; Shiyankov, S. V.; Shvartz, D. I.; Skrinsky, A. N.; Chulkov, L. V.; Danilin, B. V.; Korsheninnikov, A. A.; Kuzmin, E. A.; Ogloblin, A. A.; Volkov, V. A.; Grishkin, Y.; Lisin, V. P.; Mushkarenkov, A. N.; Nedorezov, V.; Polonski, A. L.; Rudnev, N. V.; Turinge, A. A.; Artukh, A.; Avdeichikov, V.; Ershov, S. N.; Fomichev, A.; Golovkov, M.; Gorshkov, A. V.; Grigorenko, L.; Klygin, S.; Krupko, S.; Meshkov, I. N.; Rodin, A.; Sereda, Y.; Seleznev, I.; Sidorchuk, S.; Syresin, E.; Stepantsov, S.; Ter-Akopian, G.; Teterev, Y.; Vorontsov, A. N.; Kamerdzhiev, S. P.; Litvinova, E. V.; Karataglidis, S.; Rodriguez, R. A.; Borge, M. J. G.; Ramirez, C. F.; Garrido, E.; Sarriguren, P.; Vignote, J. R.; Prieto, L. M. F.; Herraiz, J. L.; de Guerra, E. M.; Udias-Moinelo, J.; Soriano, J. E. A.; Rojo, A. M. L.; Caballero, J. A.; Johansson, H. T.; Jonson, B.; Nilsson, T.; Nyman, G.; Zhukov, M.; Golubev, P.; Rudolph, D.; Hencken, K.; Jourdan, J.; Krusche, B.; Rauscher, T.; Kiselev, D.; Trautmann, D.; Al-Khalili, J.; Catford, W.; Johnson, R.; Stevenson, P. D.; Barton, C.; Jenkins, D.; Lemmon, R.; Chartier, M.; Cullen, D.; Bertulani, C. A.; Heinz, A.: **The electron-ion scattering experiment ELISe at the International Facility for Antiproton and Ion Research (FAIR)-A conceptual design study.** *Nucl. Instrum. Methods Phys. Res. Sect. A-Accel. Spectrom. Dect. Assoc. Equip.* **637**(1): 60–76, 2011. DOI: 10.1016/j.nima.2010.12.246

043 Arcones, A.*; Martinez-Pinedo, G.*: **Dynamical r-process studies within the neutrino-driven wind scenario and its sensitivity to the nuclear physics input.** *Phys. Rev. C* **83**(4): 045809, 2011. DOI: 10.1103/PhysRevC.83.045809

044 Arcones, A.*; Montes, F.: **PRODUCTION OF LIGHT-ELEMENT PRIMARY PROCESS NUCLEI IN NEUTRINO-DRIVEN WINDS.** *Astrophys. J.* **731**(1): 5, 2011. DOI: 10.1088/0004-637X/731/1/5

045 Arsene, I.*; Bearden, I. G.; Beavis, D.; Bekele, S.; Besliu, C.; Budick, B.; Boggild, H.; Chasman, C.; Christensen, C. H.; Christiansen, P.; Dalsgaard, H. H.; Debbe, R.; Gaardhoje, J. J.; Hagel, K.; Ito, H.; Jipa, A.; Johnson, E. B.; Jorgensen, C. E.; Karabowicz, R.*; Katrynska, N.; Kim, E. J.; Larsen, T. M.; Lee, J. H.; Lovhoiden, G.; Majka, Z.; Murray, M.; Natowitz, J.; Nielsen, B. S.; Nygaard, C.; Pal, D.; Qviller, A.; Rami, F.; Ristea, C.; Ristea, O.; Rohrich, D.; Sanders, S. J.; Staszel, P.; Tveter, T. S.; Videbaek, F.; Wada, R.; Yang, H.; Yin, Z.; Zgura, S.: **Rapidity dependence of deuteron production in central Au plus Au collisions at root s(NN)=200 GeV.** *Phys. Rev. C* **83**(4): 044906, 2011. DOI: 10.1103/PhysRevC.83.044906

046 Audi, G.; Wang, M.; Wapstra, A. H.; Pfeiffer, B.*; Kondev, F. C.: **Atomic Mass Evaluation: the Mass Tables.** *J. Korean Phys. Soc.* **59**(2): 1318–1321, 2011. DOI: 10.3938/jkps.59.1318

047 Ayyad, Y.; Benlliure, J.; Casarejos, E.; Alvarez-Pol, H.; Paradela, C.; Perez-Loureiro, D.; Tarrio, D.; Bacquias, A.; Enqvist, T.; Fohr, V.; Kelic-Heil, A.*; Pleskac, R.; Boudard, A.; Kezzar, K.; Leray, S.: **Total Fission Cross Sections in Reactions p+(181)Ta Investigated in Inverse Kinematics at Relativistic Energies.** *J. Korean Phys. Soc.* **59**(2): 1852–1855, 2011. DOI: 10.3938/jkps.59.1852

048 Badalian, A. M.; Bakker, B. L. G.; Danilkin, I. V.*: **The hyperfine splittings in heavy-light mesons and quarkonia.** *Phys. Atom. Nuclei* **74**(4): 631–642, 2011. DOI: 10.1134/S1063778811040028

049 Balasi, K. G.; Ydrefors, E.; Kosmas, T. S.*: **Theoretical study of neutrino scattering off the stable even Mo isotopes at low and intermediate energies.** *Nucl. Phys. A* **868-69**: 82–98, 2011. DOI: 10.1016/j.nuclphysa.2011.08.003

050 Bayer, E. *; Traxler, M.*: **A High-Resolution (¡ 10 ps RMS) 48-Channel Time-to-Digital Converter (TDC) Implemented in a Field Programmable Gate Array (FPGA).** *IEEE Trans. Nucl. Sci.* **58**(4): 1547–1552, 2011. DOI: 10.1109/TNS.2011.2141684

051 Bazylev, S. N.; Davkov, K. I.; Gregor, I.; Haas, D.; Mouraviev, S. V.; Myalkovskiy, V. V.; Naumann, L.; Peshekhonov, V. D.; Rembser, C.; Rufanov, I. A.; Russakovich, N. A.; Senger, P.*; Shutov, A. V.; Slepnev, I. V.; Smirnov, S. Y.; Tikhomirov, V. O.; Zhukov, I. A.: **A prototype coordinate detector based on granulated thin-walled drift tubes.** *Nucl. Instrum. Methods Phys. Res.*

Sect. A-Accel. Spectrom. Dect. Assoc. Equip. **632**(1): 75–80, 2011. DOI: 10.1016/j.nima.2010.09.073

052 Benedikt, M.; Bechtold, A.; Borgnolutti, F.; Bouquerel, E.; Bozyk, L.*; Bruer, J.; Chance, A.; Delahaye, P.; Fabich, A.; Hancock, S.; Hansen, C.; Jensen, E.; Kallberg, A.; Kirk, M.*; Lachaize, A.; Lindroos, M.; Loiselet, M.; Magistris, M.; Mitrofanov, S.; Mueller, A. C.; Payet, J.; Podlech, H.; Puppel, P.*; Silari, M.; Simonsson, A.; Spiller, P.*; Stadlmann, J.*; Stora, T.; Tkatchenko, A.; Trovati, S.; Vlachoudis, V.; Wildner, E.: **Conceptual design report for a Beta-Beam facility.** *Eur. Phys. J. A* **47**(2): 24, 2011. DOI: 10.1140/epja/i2011-11024-5

053 Berg, G. P. A.; Adachi, T.; Harakeh, M. N.; Kalantar-Nayestanaki, N.; Wortche, H. J.; Simon, H.*; Koop, I. A.; Couder, M.; Fujiwara, M.: **A novel spectrometer for studying exotic nuclei with the electron/ion collider ELISe.** *Nucl. Instrum. Methods Phys. Res. Sect. A-Accel. Spectrom. Dect. Assoc. Equip.* **640**(1): 123–132, 2011. DOI: 10.1016/j.nima.2011.02.025

054 Bhang, H.; Ajimura, S.; Aoki, K.; Banu, A.; Fukuda, T.*; Hashimoto, O.; Hwang, J. I.; Kameoka, S.; Kang, B. H.; Kim, E.; Kim, J. H.; Maruta, T.; Miura, Y.; Miyake, Y.; Nagae, T.; Nakamura, M.; Nakamura, S. N.; Noumi, H.; Okada, S.; Okayasu, Y.; Outa, H.; Park, H.; Saha, P. K.; Sato, Y.; Sekimoto, M.; Takahashi, T.; Tamura, H.; Tanida, K.; Toyoda, A.; Tshoo, K.; Tsukada, K.; Watanabe, T.; Yim, H. J.: **The Weak Decay Widths of Lambda Hypernuclei.** *J. Korean Phys. Soc.* **59**(2): 1461–1466, 2011. DOI: 10.3938/jkps.59.1461

055 Blaizot, J. P.; Pawlowski, J. M.*; Reinosa, U.: **Exact renormalization group and Phi-derivable approximations.** *Phys. Lett. B* **696**(5): 523–528, 2011. DOI: 10.1016/j.physletb.2010.12.058

056 Boller, T.; Schady, P.; Heftrich, T.*: **XMM-NEWTON, SWIFT, AND ROSAT OBSERVATIONS OF LBQS 0102-2713.** *Astrophys. J. Lett.* **731**(1): L16, 2011. DOI: 10.1088/2041-8205/731/1/L16

057 Bonnet, J. A.; Fischer, C. S.*; Williams, R.: **Effects of anisotropy in QED(3) from Dyson-Schwinger equations in a box.** *Phys. Rev. B* **84**(2): 024520, 2011. DOI: 10.1103/PhysRevB.84.024520

058 Boutachkov, P.*; Gorska, M.*; Grawe, H.; Blazhev, A.; Braun, N.; Brock, T. S.; Liu, Z.; Singh, B. S. N.; Wadsworth, R.; Pietri, S.*; Domingo-Pardo, C.; Kojouharov, I.*; Caceres, L.; Engert, T.; Farinon, F.*; Gerl, J.*; Goel, N.; Grbosz, J.; Hoischen, R.; Kurz, N.; Nociforo, C.*; Prochazka, A.*; Schaffner, H.*; Steer, S. J.; Weick, H.*; Wollersheim, H. J.*; Faestermann, T.; Podolyak, Z.; Rudolph, D.; Atac, A.; Bettermann, L.; Eppinger, K.; Finke, F.; Geibel, K.; Gottardo, A.; Hinke, C.; Ilie, G.; Iwasaki, H.; Jolie, J.; Krucken, R.; Merchan, E.*; Nyberg, J.; Pfutzner, M.; Regan, P. H.; Reiter, P.; Rinta-Antila, S.; Scholl, C.; Soderstrom, P. A.; Warr, N.; Woods, P. J.; Nowacki, F.; Sieja, K.: **High-spin isomers in (96)Ag: Excitations across the Z=38 and Z=50, N=50 closed shells.** *Phys. Rev. C* **84**(4): 044311, 2011. DOI: 10.1103/PhysRevC.84.044311

059 Brambilla, N.; Eidelman, S.; Heltsley, B. K.; Vogt, R.; Bodwin, G. T.; Eichten, E.; Frawley, A. D.; Meyer, A. B.; Mitchell, R. E.; Papadimitriou, V.; Petreczky, P.; Petrov, A. A.; Robbe, P.; Vairo, A.; Andronic, A.; Arnaldi, R.; Artoisenet, P.; Bali, G.; Bertolin, A.; Bettoni, D.; Brodzicka, J.; Bruno, G. E.; Caldwell, A.; Catmore, J.; Chang, C. H.; Chao, K. T.; Chudakov, E.; Cortese, P.; Crochet, P.; Drutskoy, A.; Ellwanger, U.; Faccioli, P.; Mokhtar, A. G.; Tormo, X. G. I.; Hanhart, C.; Harris, F. A.; Kaplan, D. M.; Klein, S. R.; Kowalski, H.; Lansberg, J. P.; Levichev, E.; Lombardo, V.; Lourenco, C.; Maltoni, F.; Mocsy, A.; Mussa, R.; Navarra, F. S.; Negrini, M.; Nielsen, M.; Olsen, S. L.; Pakhlov, P.; Pakhlova, G.; Peters, K.*; Polosa, A. D.; Qian, W.; Qiu, J. W.; Rong, G.; Sanchis-Lozano, M. A.; Scomparin, E.; Senger, P.; Simon, F.; Stracka, S.; Sumino, Y.; Voloshin, M.; Weiss, C.; Wohri, H. K.; Yuan, C. Z.: **Heavy quarkonium: progress, puzzles, and opportunities.** *Eur. Phys. J. C* **71**(2): 1534, 2011. DOI: 10.1140/epjc/s10052-010-1534-9

060 Braun, J.; Haas, L. M.; Marhauser, F.; Pawlowski, J. M.*: **Phase Structure of Two-Flavor QCD at Finite Chemical Potential.** *Phys. Rev. Lett.* **106**(2): 022002, 2011. DOI: 10.1103/PhysRevLett.106.022002

061 Braun-Munzinger, P.*; Friman, B.*; Karsch, F.; Redlich, K.; Skokov, V.: **Net-proton probability distribution in heavy ion collisions.** *Phys. Rev. C* **84**(6): 064911, 2011. DOI: 10.1103/PhysRevC.84.064911

062 Buyukcizmeci, N.; Bulut, F.; Erdogan, M.; Imal, H.; Ogul, R.; Botvina, A. S.; Mishustin, I. N.; Trautmann, W.*: **INVESTIGATING THE ISOTOPIC EFFECTS IN NUCLEAR FRAGMENTATION.** *Acta Phys. Pol. B* **42**(3-4): 697–700, 2011. DOI: 10.5506/APhysPolB.42.697

063 Böhmer, F. V.; Angerer, H.; Doerheim, S.; Höppner, C.; Ketzer, B.; Konorov, I.; Neubert, S.; Paul, S.; Vandenbroucke, M.; Zhang, X.; Berger, M.; Cusanno, F.; Fabbietti, L.; Lalik, R.; Beck, R.; Kaiser, D.; Lang, M.; Schmitz, R.; Walther, D.; Winnebeck, A.; Zenke, F.; Arora, R.*; Averbeck, R.*; Hehner, J.*; Herrmann, N.; Kleipa, V.*; Kunkel, J.*; Leifels, Y.*; Mladen, K.*; Schmidt, C.*; Schwab, S.*; Soyk, D.*; Voss, B.*; Voss, J.*; Weinert, J. *; Zmeskal, J.: **A Continuously Running High-Rate GEM-TPC for PANDA.** *Nucl. Phys. B-Proc. Suppl.* **215**: 278–280, 2011. DOI: 10.1016/j.nuclphysbps.2011.04.030

064 Caamano, M.; Rejmund, F.; Schmidt, K. H.*: **Evidence for the predominant influence of the asymmetry degree of freedom on the even-odd structure in fission-fragment yields.** *J. Phys. G-Nucl. Part. Phys.* **38**(3): 035101, 2011. DOI: 10.1088/0954-3899/38/3/035101

065 Chakraborty, S.; Fischer, T.*; Mirizzi, A.; Saviano, N.; Tomas, R.: **Analysis of matter suppression in collective neutrino oscillations during the supernova accretion phase.** *Phys. Rev. D* **84**(2): 025002, 2011. DOI: 10.1103/PhysRevD.84.025002

066 Chakraborty, S.; Fischer, T.*; Mirizzi, A.; Saviano, N.; Tomas, R.: **No Collective Neutrino Flavor Conversions during the Supernova Accretion Phase.** *Phys. Rev. Lett.* **107**(15): 151101, 2011. DOI: 10.1103/PhysRevLett.107.151101

067 Cheng, M.; Datta, S.; Francis, A.; van der Heide, J.; Jung, C.; Kaczmarek, O.; Karsch, F.*; Laermann, E.; Mawhinney, R. D.; Miao, C.; Mukherjee, S.; Petreczky, P.; Rantaharju, J.; Schmidt, C.*; Soldner, W.: **Meson screening masses from lattice QCD with two light quarks and one strange quark.** *Eur. Phys. J. C* **71**(2): 1564, 2011. DOI: 10.1140/epjc/s10052-011-1564-y

068 Chetvertkova, V.*; Strasik, I.*; Belousov, A.*; Iwase, H.; Mokhov, N.; Mustafin, E.*; Latysheva, L.; Pavlovic, M.; Ratzinger, U.; Sobolevsky, N.: **Activation of aluminum by argon: Experimental study and simulations.** *Nucl. Instrum. Methods Phys. Res. Sect. B-Beam Interact. Mater. Atoms* **269**(12): 1336–1340, 2011. DOI: 10.1016/j.nimb.2011.03.017

069 Chiaveri, E.; Andriamonje, S.; Calviani, M.; Vlachoudis, V.; Brugger, M.; Cennini, P.; Cerutti, F.; Chin, M.; Ferrari, A.; Kadi, Y.; Lebbos, E.; Losito, R.; Guerrero, C.; Becares, V.; Cano-Ott, D.; Fernandez-Ordonez, M.; Gonzalez-Romero, E.; Martinez, T.; Mendoza, E.; Ovejero, M. C.; Berthoumieux, E.; Gunsing, F.; Andrzejewski, J.; Marganiec, J.*; Perkowski, J.; Audouin, L.; Berthier, B.; Tassan-Got, L.; Becvar, F.; Krticka, M.; Belloni, F.; Milazzo, P. M.; Calvino, F.; Hornillos, M. B. G.; Carrapico, C.; Cortes, G.; Goncalves, I. F.; Sarmento, R.; Vaz, P.; Colonna, N.; Marrone, S.; Meaze, M.; Tagliente, G.; Variale, V.; Cortes-Giraldo, M.; Lozano, M.; Praena, J.; Quesada, J. M.; Dillmann, I.*; Domingo-Pardo, C.; Heil, M.*; Plag, R.*; Reifarth, R.*; Duran, I.; Paradela, C.; Tarrio, D.; Ganesan, S.; Giubrone, G.; Tain, J. L.; Gramegna, F.; Mastinu, P. F.; Harrisopulos, S.; Ioannides, K.; Karadimos, D.; Jericha, E.; Leeb, H.; Weiss, C.; Kappeler, F.; Lederer, C.; Pavlik, A.; Wallner, A.; Massimi, C.; Vannini, C.; Mengoni, A.; Ventura, A.; Mosconi, M.; Nolte, R.; Rubbia, C.; Vlastou, R.; Vykydal, Z.: **Past, Present and Future of the n_TOF Facility at CERN.** *J. Korean Phys. Soc.* **59**(2): 1620–1623, 2011. DOI: 10.3938/jkps.59.1620

070 Ciobanu, M.*; Berdermann, E.*; Herrmann, N.; Hildenbrand, K. D.*; Kis, M.*; Koenig, W.*; Pietraszko, J.*; Pomorski, M.; Rebisz-Pomorska, M.; Schüttauf, A.*: **In-Beam Diamond Start Detectors.** *IEEE Trans. Nucl. Sci.* **58**(4): 2073–2083, 2011. DOI: 10.1109/TNS.2011.2160282

071 Clement, E.; De France, G.; Casandjian, J. M.; Gorgen, A.; Korten, W.; Bouchez, L.; Chatillon, A.; Hurstel, A.; Le Coz, Y.; Obertelli, A.; Theisen, C.; Wilson, J. N.; Delaroche, J. P.; Girod, M.; Goutte, H.; Peru, S.; Czosnyka, T.; Iwanicki, J.; Napiorkowski, P. J.; Srebrny, J.; Wrzosek-Lipska, K.; Zielinska, M.; Bree, N.; Stefanescu, I.; Van De Walle, J.; Andreoiu, C.; Butler, P. A.; Herzberg, R. D.; Jenkins, D. G.; Jones, G. D.; Petts, A.; Becker, F.; Gerl, J.*; Catford, W. N.; Timis, C. N.; Sletten, G.; Georgiev, G.; Ljungvall, J.: **EXPERIMENTAL MEASUREMENT OF THE DEFORMATION THROUGH THE ELECTROMAGNETIC PROBE: SHAPE COEXISTENCE IN EXOTIC KR AND SR ISOTOPES.** *Int. J. Mod. Phys. E-Nucl. Phys.* **20**(2): 415–421, 2011. DOI: 10.1142/S0218301311017806

072 Clemente, G.*; Ratzinger, U.; Podlech, H.; Groening, L.*; Brodhage, R.; Barth, W.*: **Development of room temperature crossbar-H-mode cavities for proton and ion acceleration in the low to medium beta range.** *Phys. Rev. Spec. Top.-Accel. Beams* **14**(11): 110101, 2011. DOI: 10.1103/PhysRevSTAB.14.110101

073 Cleymans, J.; Kabana, S.; Kraus, I.*; Oeschler, H.*; Redlich, K.; Sharma, N.: **Antimatter production in proton-proton and heavy-ion collisions at ultrarelativistic energies.** *Phys. Rev. C* **84**(5): 054916, 2011. DOI: 10.1103/PhysRevC.84.054916

074 Colonna, N.; Andriamonje, S.; Andrzejewski, J.; Audouin, L.; Barbagallo, M.; Becares, V.; Becvar, F.; Belloni, F.; Berthier, B.; Berthoumieux, E.; Brugger, M.; Calviani, M.; Calvino, F.; Cano-Ott, D.; Carrapico, C.; Cennini, P.; Cerutti, F.; Chiaveri, E.; Chin, M.; Cortes, G.; Cortes-Giraldo, M. A.; Diakaki, M.; Dillmann, I.*; Domingo-Pardo, C.; Duran, I.; Fernandez-Ordonez, M.; Ferrari, A.; Fraval, K.; Ganesan, S.; Giomataris, I.; Giubrone, G.; Gomez-Hornillos, M. B.; Goncalves, I. F.; Gonzalez-Romero, E.; Gramegna, F.; Guerrero, C.; Gunsing, F.; Harrisopulos, S.; Heil, M.*; Ioannides, K.; Jericha, E.; Kadi, Y.; Kappeler, F.; Karadimos, D.; Krticka, M.; Lebbos, E.; Lederer, C.; Leeb, H.; Losito, R.; Lozano, M.; Marganiec, J.; Marrone, S.; Martinez, T.; Massimi, C.; Mastinu, P. F.; Meaze, M.; Mendoza, E.; Mengoni, A.; Milazzo, P. M.; Mosconi, M.; Nolte, R.; Papaevangelou, T.; Paradela, C.; Pavlik, A.; Perkowski, J.; Plag, R.; Plompen, A.; Praena, J.; Quesada, J. M.; Rauscher, T.; Reifarth, R.*; Roman, F.; Rubbia, C.; Sarmento, R.; Tagliente, G.; Tain, J. L.; Tarrio, D.; Tassan-Got, L.; Tlustos, L.; Tsinganis, A.; Vannini, G.; Variale, V.; Vaz, P.; Ventura, A.; Vlachoudis, V.; Vlastou, R.; Vykydal, Z.; Wallner, A.; Weiss, C.: **Neutron measurements for advanced nuclear systems: The n_TOF project at CERN.** *Nucl. Instrum. Methods Phys. Res. Sect. B-Beam Interact. Mater. Atoms* **269**(24): 3251–3257, 2011. DOI: 10.1016/j.nimb.2011.04.014

075 Cowie, E. N.; Britting, A.; Clarkson, A.; Dodokhof, V. K.; Duren, M.; Dutta, D.; Eyrich, W.; Fohl, K.; Glazer, D. I.; Hayrapetyan, A.; Hoek, M.; Hohler, R.*; Kaiser, R.; Keri, T.; Koch, P.; Krock, B.; Lehmann, A.; Lehmann,

D.*; Lumsden, S.; Marton, J.; Merle, O.; Montgomery, R.; Peters, K.*; Reinicke, S.; Rosner, G.; Roy, B.; Schepers, G.*; Schmitt, L.*; Schwarz, C.*; Schwiening, J.*; Seitz, B.; Sfienti, C.; Suzuki, K.; Uhlig, F.; Vodopianov, A. S.; Watts, D. P.; Yu, W.: **A focussing disc DIRC for PANDA.** *Nucl. Instrum. Methods Phys. Res. Sect. A-Accel. Spectrom. Dect. Assoc. Equip.* **639**(1): 181–184, 2011. DOI: 10.1016/j.nima.2010.09.132

076 Düllmann, C. E.*: **Heavy element research at the recoil separator TASCA at GSI.** *Abstr. Pap. Am. Chem. Soc.* **241**: No Page ?

077 Düllmann, C. E.*: **Superheavy element studies with preseparated isotopes.** *Radiochim. Acta* **99**(7-8): 515–526, 2011. DOI: 10.1524/ract.2011.1852

078 Danchev, M.; Rainovski, G.; Pietralla, N.*; Gargano, A.; Covello, A.; Baktash, C.; Beene, J. R.; Bingham, C. R.; Galindo-Uribarri, A.; Gladnishki, K. A.; Gross, C. J.; Ponomarev, V. Y.; Radford, D. C.; Riedinger, L. L.; Scheck, M.; Stuchbery, A. E.; Wambach, J.*; Yu, C. H.; Zamfir, N. V.: **One-phonon isovector 2(1,MS)(+) state in the neutron-rich nucleus (132)Te.** *Phys. Rev. C* **84**(6): 061306, 2011. DOI: 10.1103/PhysRevC.84.061306

079 Danilkin, I. V.*; Gasparyan, A. M.; Lutz, M. F. M.*: **On causality, unitarity and perturbative expansions.** *Phys. Lett. B* **697**(2): 147–152, 2011. DOI: 10.1016/j.physletb.2011.01.036

080 Danilkin, I. V.; Gil, L. I. R.; Lutz, M. F. M.*: **Dynamical light vector mesons in low-energy scattering of Goldstone bosons.** *Phys. Lett. B* **703**(4): 504–509, 2011. DOI: 10.1016/j.physletb.2011.08.001

081 Daugas, J. M.; Matea, I.; Delaroche, J. P.; PfÃ$\frac{1}{4}$tzner, M.; Sawicka, M.; Becker, F.*; Belier, G.; Bingham, C. R.; Borcea, R.; Bouchez, E.; Buta, A.; Dragulescu, E.; Georgiev, G.; Giovinazzo, J.; Girod, M.; Grawe, H.*; Grzywacz, R.; Hammache, F.; Ibrahim, F.; Lewitowicz, M.; Libert, J.; Mayet, P.*; Meot, V.; Negoita, F.; Santos, F. D.; Perru, O.; Roig, O.; Rykaczewski, K.; Saint-Laurent, M. G.; Sauvestre, J. E.; Sorlin, O.; Stanoiu, M.*; Stefan, I.; Stodel, C.; Theisen, C.; Verney, D.; Zylicz, J.: **beta-decay measurements for N ¿ 40 Mn nuclei and inference of collectivity for neutron-rich Fe isotopes.** *Phys. Rev. C* **83**(5): 054312, 2011. DOI: 10.1103/PhysRevC.83.054312

082 Davkov, V. I.; Gregor, I.; Haas, D.; Mouraviev, S. V.; Myalkovskiy, V. V.; Naumann, L.; Peshekhonov, V. D.; Rembser, C.; Rufanov, I. A.; Russakovich, N. A.; Senger, P.*; Smirnov, S. Y.; Tikhomirov, V. O.: **Spatial resolution of thin-walled high-pressure drift tubes.** *Nucl. Instrum. Methods Phys. Res. Sect. A-Accel. Spectrom. Dect. Assoc. Equip.* **634**(1): 5–7, 2011. DOI: 10.1016/j.nima.2010.10.045

083 Dillmann, I.*; Litvinov, Y. A.*: **r-Process nucleosynthesis: Present status and future experiments at the FRS and ESR.** *Prog. Part. Nucl. Phys.* **66**(2): 358–362, 2011. DOI: 10.1016/j.ppnp.2011.01.034

084 Dolinskii, A.*; Knie, K.*; Dimopoulou, C.*; Gostishchev, V.*; Litvinov, S.*; Nolden, F.*; Steck, M.*: **Antiproton complex at the FAIR project.** *Nucl. Instrum. Methods Phys. Res. Sect. A-Accel. Spectrom. Dect. Assoc. Equip.* **629**(1): 16–24, 2011. DOI: 10.1016/j.nima.2010.11.037

085 Domingo-Pardo, C.; Goel, N.*; Engert, T.*; Gerl, J.*; Kojouharov, I.*; Schaffner, H.*; Didierjean, F.; Duchene, G.; Sigward, M. H.: **A novel gamma-ray imaging method for the pulse-shape characterization of position sensitive semiconductor radiation detectors.** *Nucl. Instrum. Methods Phys. Res. Sect. A-Accel. Spectrom. Dect. Assoc. Equip.* **643**(1): 79–88, 2011. DOI: 10.1016/j.nima.2011.04.021

086 Droese, C.*; Block, M.*; Dworschak, M.; Eliseev, S.; Ramirez, E. M.; Nesterenko, D.; Schweikhard, L.: **Investigation of the magnetic field fluctuation and implementation of a temperature and pressure stabilization at SHIPTRAP.** *Nucl. Instrum. Methods Phys. Res. Sect. A-Accel. Spectrom. Dect. Assoc. Equip.* **632**(1): 157–163, 2011. DOI: 10.1016/j.nima.2010.12.176

087 Dutta, D.: **Software development for the PANDA barrel DIRC.** *Nucl. Instrum. Methods Phys. Res. Sect. A-Accel. Spectrom. Dect. Assoc. Equip.* **639**(1): 264–266, 2011. DOI: 10.1016/j.nima.2010.10.080

088 Dvorak, J.*; Block, M.*; Düllmann, C. E.*; Heinz, S.*; Herzberg, R. D.; Schädel, M.*: **IRiS-Exploring new frontiers in neutron-rich isotopes of the heaviest elements with a new Inelastic Reaction Isotope Separator.** *Nucl. Instrum. Methods Phys. Res. Sect. A-Accel. Spectrom. Dect. Assoc. Equip.* **652**(1): 687–691, 2011. DOI: 10.1016/j.nima.2010.08.124

089 Dzhioev, A. A.; Vdovin, A. I.; Ponomarev, V. Y.; Wambach, J.*: **Thermal effects on neutrino-nucleus inelastic scattering in stellar environments.** *Phys. Atom. Nuclei* **74**(8): 1162–1170, 2011. DOI: 10.1134/S1063778811080059

090 Eichhorn, A.; Gies, H.; Pawlowski, J. M.*: **Gluon condensation and scaling exponents for the propagators in Yang-Mills theory.** *Phys. Rev. D* **83**(4): 045014, 2011. DOI: 10.1103/PhysRevD.83.045014

091 Elseviers, J.; Andreyev, A. N.; Antalic, S.; Barzakh, A.; Bree, N.; Cocolios, T. E.; Comas, V. F.*; Diriken, J.; Fedorov, D.; Fedosseyev, V. N.; Franchoo, S.; Heredia, J. A.*; Huyse, M.; Ivanov, O.; Koster, U.; Marsh, B. A.; Page, R. D.; Patronis, N.; Seliverstov, M.; Tsekhanovich, I.; Van den Bergh, P.; Van De Walle, J.; Van Duppen, P.; Venhart, M.; Vermote, S.; Veselsky, M.; Wagemans, C.: **Shape coexistence in (180)Hg studied through the beta**

decay of (180)Tl. *Phys. Rev. C* **84**(3): 034307, 2011. DOI: 10.1103/PhysRevC.84.034307

092 Elvers, M.; Pascu, S.; Ahmed, T.; Ahn, T.; Anagnostatou, V.; Cooper, N.; Deng, C.; Endres, J.; Goddard, P.; Heinz, A.*; Ilie, G.; Jiang, E.; Kuppersbusch, C.; Radeck, D.; Savran, D.*; Shenkov, N.; Werner, V.; Zilges, A.: **Investigation of octupole vibrational states in (150)Nd via inelastic proton scattering (p,p 'gamma).** *Phys. Rev. C* **84**(5): 054323, 2011. DOI: 10.1103/PhysRevC.84.054323

093 Eschke, J.*; Hohne, C.: **Results from first beam tests for the development of a RICH detector for CBM.** *Nucl. Instrum. Methods Phys. Res. Sect. A-Accel. Spectrom. Dect. Assoc. Equip.* **639**(1): 307–310, 2011. DOI: 10.1016/j.nima.2010.10.104

094 Even, J.; Ballof, J.; Bruchle, W.; Buda, R. A.; Düllmann, C. E.*; Eberhardt, K.; Gorshkov, A.; Gromm, E.; Hild, D.; Jäger, E.*; Khuyagbaatar, J.; Kratz, J. V.; Krier, J.*; Liebe, D.; Mendel, M.; Nayak, D.; Opel, K.; Omtvedt, J. P.; Reichert, P.; Runke, J.*; Sabelnikov, A.; Samadani, F.; Schädel, M.*; Schausten, B.*; Scheid, N.; Schimpf, E.; Semchenkov, A.; Thorle-Pospiech, P.; Toyoshima, A.; Turler, A.; Vilas, V. V.; Wiehl, N.; Wunderlich, T.; Yakushev, A.*: **The recoil transfer chamber-An interface to connect the physical preseparator TASCA with chemistry and counting setups.** *Nucl. Instrum. Methods Phys. Res. Sect. A-Accel. Spectrom. Dect. Assoc. Equip.* **638**(1): 157–164, 2011. DOI: 10.1016/j.nima.2011.02.053

095 Ewerz, C.; von Manteuffel, A.; Nachtmann, O.: **On the energy dependence of the dipole-proton cross section in deep inelastic scattering.** *J. High Energy Phys.* **1103**: 062, 2011. DOI: 10.1007/JHEP03(2011)062

096 Fabbietti, L; Angerer, H; Arora, R; Beck, R; Berger, M; Bühler, P; Cargnelli, M; Doerheim, S; Hehner, J; Herrmann, N; Hoppner, C; Kaiser, D; Ketzer, B; Mladen, K*; Kleipa, V*; Konorov, I; Kunkel, J*; Lalik, R; Lang, M; Leifels, Y*; Marton, J; Neubert, S; Paul, S; Schmitz, R; Schmidt, C*; Schwab, S*; Soyk, D*; Suzuki, K; Thoma, U; Vandenbroucke, M; Voss, B*; Voss, J*; Walther, D; Weinert, J; Winnebeckd, A; Zenke, F; Zhang, X; Zmeskal, J: **The PANDA GEM-based TPC prototype.** *Nucl. Instrum. Methods Phys. Res. Sect. A-Accel. Spectrom. Dect. Assoc. Equip.* **628**(1): 204–208, 2011. DOI: 10.1016/j.nima.2010.06.317

097 Feldmeier, H.*; Horiuchi, W.; Neff, T.*; Suzuki, Y.: **Universality of short-range nucleon-nucleon correlations.** *Phys. Rev. C* **84**(5): 054003, 2011. DOI: 10.1103/PhysRevC.84.054003

098 Filinov, V. S.; Bonitz, M.; Ivanov, Y. B.*; Skokov, V. V.; Levashov, P. R.; Fortov, V. E.: **Quantum Color Dynamic Simulations of the Strongly Coupled Quark-Gluon Plasma.** *Contrib. Plasma Phys.* **51**(4): 322–327, 2011. DOI: 10.1002/ctpp.201010125

099 Fischer, C. S.*; Goecke, T.; Williams, R.: **A fresh look at hadronic light-by-light scattering in the muon g-2 with the Dyson-Schwinger approach.** *Eur. Phys. J. A* **47**(2): 28, 2011. DOI: 10.1140/epja/i2011-11028-1

100 Fischer, C. S.*; Müller, J. A.: **Critical scaling at the QCD N(f)=2 chiral phase transition.** *Phys. Rev. D* **84**(5): 054013, 2011. DOI: 10.1103/PhysRevD.84.054013

101 Fischer, C. S.; Luecker, J.*; Mueller, J. A.: **Chiral and deconfinement phase transitions of two-flavour QCD at finite temperature and chemical potential.** *Phys. Lett. B* **702**(5): 438–441, 2011. DOI: 10.1016/j.physletb.2011.07.039

102 Fischer, E.*; Schnizer, P.*; Mierau, A.*; Wilfert, S.*; Bleile, A.*; Shcherbakov, P.; Schroder, C.*: **Design and Test Status of the Fast Ramped Superconducting SIS100 Dipole Magnet for FAIR.** *IEEE Trans. Appl. Supercond.* **21**(3): 1844–1848, 2011. DOI: 10.1109/TASC.2010.2091372

103 Fischer, T.; Sagert, I.; Pagliara, G.; Hempel, M.; Schaffner-Bielich, J.; Rauscher, T.; Thielemann, F. K.; Kappeli, R.; Martinez-Pinedo, G.*; Liebendorfer, M.: **CORE-COLLAPSE SUPERNOVA EXPLOSIONS TRIGGERED BY A QUARK-HADRON PHASE TRANSITION DURING THE EARLY POST-BOUNCE PHASE.** *Astrophys. J. Suppl. Ser.* **194**(2): 39, 2011. DOI: 10.1088/0067-0049/194/2/39

104 Fohr, V.; Bacquias, A.; Casarejos, E.; Enqvist, T.; Junghans, A. R.; Kelic-Heil, A.*; Kurtukian, T.; Lukic, S.; Perez-Loureiro, D.; Pleskac, R.; Ricciardi, M. V.*; Schmidt, K. H.*; Taieb, J.: **Experimental study of fragmentation products in the reactions (112)Sn+(112)Sn and (124)Sn+(124)Sn at 1A GeV.** *Phys. Rev. C* **84**(5): 054605, 2011. DOI: 10.1103/PhysRevC.84.054605

105 Fomichev, A. S.; Mukha, I. G.*; Stepantsov, S. V.; Grigorenko, L. V.; Litvinova, E. V.; Chudoba, V.; Egorova, I. A.; Golovkov, M. S.; Gorshkov, A. V.; Gorshkov, V. A.; Kaminski, G.; Krupko, S. A.; Parfenova, Y. L.; Sidorchuk, S. I.; Slepnev, R. S.; Ter-Akopian, G. M.; Wolski, R.; Zhukov, M. V.: **LIFETIME OF (26)S AND A LIMIT FOR ITS 2p DECAY ENERGY.** *Int. J. Mod. Phys. E-Nucl. Phys.* **20**(6): 1491–1508, 2011. DOI: 10.1142/S0218301311018216

106 Friman, B.*; Karsch, F.*; Redlich, K.*; Skokov, V.: **Fluctuations as probe of the QCD phase transition and freeze-out in heavy ion collisions at LHC and RHIC.** *Eur. Phys. J. C* **71**(7): 1694, 2011. DOI: 10.1140/epjc/s10052-011-1694-2

107 Gadea, A.; Farnea, E.; Valiente-Dobon, J. J.; Million, B.; Mengoni, D.; Bazzacco, D.; Recchia, F.; Dewald, A.; Pissulla, T.; Rother, W.; de Angelis, G.; Austin, A.; Aydin, S.; Badoer, S.; Bellato, M.; Benzoni, G.; Berti, L.; Beunard, R.; Birkenbach, B.; Bissiato, E.; Blasi, N.; Boiano,

C.; Bortolato, D.; Bracco, A.; Brambilla, S.; Bruyneel, B.; Calore, E.; Camera, F.; Capsoni, A.; Chavas, J.; Cocconi, P.; Coelli, S.; Colombo, A.; Conventi, D.; Costa, L.; Corradi, L.; Corsi, A.; Cortesi, A.; Crespi, F. C. L.; Dosme, N.; Eberth, J.; Fantinel, S.; Fanin, C.; Fioretto, E.; Fransen, C.; Giaz, A.; Gottardo, A.; Grave, X.; Grebosz, J.*; Griffiths, R.; Grodner, E.; Gulmini, M.; Habermann, T.*; He, C.; Hess, H.; Isocrate, R.; Jolie, J.; Jones, P.; Latina, A.; Legay, E.; Lenzi, S.; Leoni, S.; Lelli, F.; Lersch, D.; Lunardi, S.; Maron, G.; Menegazzo, R.; Michelagnoli, C.; Molini, P.; Montagnoli, G.; Montanari, D.; Moller, O.; Napoli, D. R.; Nicoletto, M.; Nicolini, R.; Ozille, M.; Pascovici, G.; Peghin, R.; Pignanelli, M.; Pucknell, V.; Pullia, A.; Ramina, L.; Rampazzo, G.; Rebeschini, M.; Reiter, P.; Riboldi, S.; Rigato, M.; Alvarez, C. R.; Rosso, D.; Salvato, G.; Strachan, J.; Sahin, E.; Scarlassara, F.; Simpson, J.; Stefanini, A. M.; Stezowski, O.; Tomasi, F.; Toniolo, N.; Triossi, A.; Turcato, M.; Ur, C. A.; Vandone, V.; Venturelli, R.; Veronese, F.; Veyssiere, C.; Viscione, E.; Wieland, O.; Wiens, A.; Zocca, F.; Zucchiatti, A.: **Conceptual design and infrastructure for the installation of the first AGATA sub-array at LNL.** *Nucl. Instrum. Methods Phys. Res. Sect. A-Accel. Spectrom. Dect. Assoc. Equip.* **654**(1): 88–96, 2011. DOI: 10.1016/j.nima.2011.06.004

108 Galatyuk, T.*; Das, S.: **Di-electron spectroscopy in CBM.** *Indian J. Phys.* **85**(1): 81–85, 2011. DOI: 10.1007/s12648-011-0022-x

109 Garzon, J. A.; Cabanelas, P.; Gonzalez-Diaz, D.*; Kurtukian, T.: **TimTrack: A new concept for the tracking of charged particles with timing detectors.** *Nucl. Instrum. Methods Phys. Res. Sect. A-Accel. Spectrom. Dect. Assoc. Equip.* **629**(1): 311–322, 2011. DOI: 10.1016/j.nima.2010.10.095

110 Gasparyan, A. M.*; Haidenbauer, J.; Hanhart, C.: **Extraction of Scattering Lengths from Production Reactions.** *J. Phys. Conf. Ser.* **295**: 012104, 2011. DOI: 10.1088/1742-6596/295/1/012104

111 Gasparyan, A. M.; Lutz, M. F. M.*; Pasquini, B.: **Compton scattering from chiral dynamics with unitarity and causality.** *Nucl. Phys. A* **866**(1): 79–92, 2011. DOI: 10.1016/j.nuclphysa.2011.07.005

112 Gates, J. M.; Düllmann, C. E.*; Schädel, M.*; Yakushev, A.*; Türler, A.; Eberhardt, K.; Kratz, J. V.; Ackermann, D.*; Andersson, L. L.*; Block, M.*; Bruchle, W.; Dvorak, J.*; Essel, H. G.; Ellison, P. A.; Even, J.; Forsberg, U.; Gellanki, J.; Gorshkov, A.; Graeger, R.; Gregorich, K. E.; Hartmann, W.; Herzberg, R. D.; Heßberger, F. P.*; Hild, D.; Hubner, A.; Jäger, E.*; Khuyagbaatar, J.; Kindler, B.; Krier, J.*; Kurz, N.; Lahiri, S.; Liebe, D.; Lommel, B.; Maiti, M.; Nitsche, H.; Omtvedt, J. P.; Parr, E.; Rudolph, D.; Runke, J.*; Schaffner, H.*; Schausten, B.*; Schimpf, E.; Semchenkov, A.; Steiner, J.; Thorle-Pospiech, P.; Uusitalo, J.; Wegrzecki, M.; Wiehl, N.: **First superheavy element experiments at the GSI recoil separator TASCA: The production and decay of element 114 in the (244)Pu((48)Ca,3-4n) reaction.** *Phys. Rev. C* **83**(5): 054618, 2011. DOI: 10.1103/PhysRevC.83.054618

113 Geithner, R.; Neubert, R.; Vodel, W.; Schwickert, M.*; Reeg, H.*; von Hahn, R.; Seidel, P.: **A Non-Destructive Beam Monitoring System Based on an LTS-SQUID.** *IEEE Trans. Appl. Supercond.* **21**(3): 444–447, 2011. DOI: 10.1109/TASC.2010.2089956

114 Giubrone, G.; Tain, J. L.; Lederer, C.; Pavlik, A.; Wallner, A.; Andriamonje, S.; Brugger, M.; Calviani, M.; Cerutti, F.; Chiaveri, E.; Ferrari, A.; Kadi, Y.; Lebbos, E.; Vlachoudis, V.; Andrzejewski, J.; Marganiec, J.*; Perkowski, J.; Audouin, L.; Berthier, B.; Tassan-Got, L.; Avrigeanu, V.; Mirea, M.; Becares, V.; Cano-Ott, D.; Fernandez-Ordonez, M.; Gonzalez-Romero, E.; Guerrero, C.; Martin-Fuertes, F.; Martinez, T.; Mendoza, E.; Pina, G.; Quinones, J.; Becvar, F.; Krticka, M.; Belloni, F.; Milazzo, P. M.; Berthoumieux, E.; Gunsing, F.; Calvino, F.; Cortes, G.; Gomez-Hornillos, M. B.; Carrapico, C.; Goncalves, I. F.; Sarmento, R.; Vaz, P.; Colonna, N.; Marrone, S.; Meaze, M. H.; Tagliente, G.; Variale, V.; Dillman, I.; Domingo-Pardo, C.; Heil, M.*; Duran, I.; Paradela, C.; Tarrio, D.; Ganesan, S.; Gramegna, F.; Mastinu, P. F.; Harrisopulos, S.; Ioannides, K.; Karadimos, D.; Jericha, E.; Leeb, H.; Weiss, C.; Kappeler, F.; Lozano, M.; Praena, J.; Quesada, J. M.; Massimi, C.; Vannini, G.; Mengoni, A.; Ventura, A.; Mosconi, M.; Nolte, R.; Vlastou, R.: **The Role of Fe and Ni for S-process Nucleosynthesis and Innovative Nuclear Technologies.** *J. Korean Phys. Soc.* **59**(2): 2106–2109, 2011. DOI: 10.3938/jkps.59.2106

115 Goecke, T.; Fischer, C. S.*; Williams, R.: **Hadronic light-by-light scattering in the muon g-2: A Dyson-Schwinger equation approach.** *Phys. Rev. D* **83**(9): 094006, 2011. DOI: 10.1103/PhysRevD.83.094006

116 Goecke, T.; Fischer, C. S.*; Williams, R.: **Leading-order calculation of hadronic contributions to the Muon g-2 using the Dyson-Schwinger approach.** *Phys. Lett. B* **704**(3): 211–217, 2011. DOI: 10.1016/j.physletb.2011.09.019

117 Goel, N.*; Domingo-Pardo, C.; Engert, T.; Gerl, J.*; Kojouharov, I.*; Schaffner, H.*: **Spatial calibration via imaging techniques of a novel scanning system for the pulse shape characterisation of position sensitive HPGe detectors.** *Nucl. Instrum. Methods Phys. Res. Sect. A-Accel. Spectrom. Dect. Assoc. Equip.* **652**(1): 591–594, 2011. DOI: 10.1016/j.nima.2011.01.146

118 Gonzalez-Diaz, D.*; Chen, H. S.; Wang, Y.: **Signal coupling and signal integrity in multi-strip resistive plate chambers used for timing applications.** *Nucl. Instrum. Methods Phys. Res. Sect. A-Accel. Spectrom. Dect. Assoc. Equip.* **648**(1): 52–72, 2011. DOI: 10.1016/j.nima.2011.05.039

119 Gorbunov, S.; Rohr, D.; Aamodt, K.; Alt, T.; Appelshauser, H.; Arend, A.; Bach, M.; Becker, B.; Bottger, S.; Breitner, T.; Busching, H.; Chattopadhyay, S.; Cleymans, J.; Cicalo, C.; Das, I.; Djuvsland, O.; Engel, H.; Erdal, H. A.; Fearick, R.; Haaland, O. S.; Hille, P. T.; Kalcher, S.; Kanaki, K.; Kebschull, U. W.; Kisel, I.*; Kretz, M.; Lara, C.; Lindal, S.; Lindenstruth, V. *; Masoodi, A. A.; Ovrebekk, G.; Panse, R.; Peschek, J.; Ploskon, M.; Pocheptsov, T.; Ram, D.; Rascanu, T.; Richter, M.; Rohrich, D.; Ronchetti, F.; Skaali, B.; Smorholm, O.; Stokkevag, C.; Steinbeck, T. M.; Szostak, A.; Thader, J.; Tveter, T.; Ullaland, K.; Vilakazi, Z.; Weis, R.; Yin, Z. B.; Zelnicek, P.: **ALICE HLT High Speed Tracking on GPU.** *IEEE Trans. Nucl. Sci.* **58**(4): 1845–1851, 2011. DOI: 10.1109/TNS.2011.2157702

120 Gostishchev, V.*; Dimopoulou, C.*; Dolinskii, A.*; Nolden, F.*; Steck, M.*; Smirnov, A.: **Comparison of measurements and simulations of internal target effects in the ESR storage ring.** *Nucl. Instrum. Methods Phys. Res. Sect. A-Accel. Spectrom. Dect. Assoc. Equip.* **641**(1): 12–18, 2011. DOI: 10.1016/j.nima.2011.03.047

121 Grigorenko, L. V.; Litvinova, E. V.*; Zhukov, M. V.: **RECENT ADVANCES IN THEORETICAL STUDIES OF 2p RADIOACTIVITY: NUCLEAR MANY-BODY STRUCTURE IN THREE-BODY MODEL.** *Acta Phys. Pol. B* **42**(3-4): 555–558, 2011. DOI: 10.5506/APhysPolB.42.555

122 Grigorenko, L. V.; Mukha, I. G.*; Scheidenberger, C.*; Zhukov, M. V.: **Two-neutron radioactivity and four-nucleon emission from exotic nuclei.** *Phys. Rev. C* **84**(2): 021303, 2011. DOI: 10.1103/PhysRevC.84.021303

123 Groening, L.*: **Concept for controlled transverse emittance transfer within a linac ion beam.** *Phys. Rev. Spec. Top.-Accel. Beams* **14**(6): 064201, 2011. DOI: 10.1103/PhysRevSTAB.14.064201

124 Gubler, P.*; Morita, K.; Oka, M. *: **Charmonium Spectra at Finite Temperature from QCD Sum Rules with the Maximum Entropy Method.** *Phys. Rev. Lett.* **107**(9): 092003, 2011. DOI: 10.1103/PhysRevLett.107.092003

125 Guerrero, C.; Becares, V.; Cano-Ott, D.; Fernandez-Ordonez, M.; Gonzalez-Romero, E.; Martin-Fuertes, F.; Martinez, T.; Mendoza, E.; Pina, G.; Quinones, J.; Vlachoudis, V.; Calviani, M.; Andriamonje, S.; Brugger, M.; Cerutti, F.; Chiaveri, E.; Ferrari, A.; Kadi, Y.; Lebbos, E.; Berthoumieux, E.; Gunsing, F.; Andrzejewski, J.; Marganiec, J.*; Perkowski, J.; Audouin, L.; Berthier, B.; Tassan-Got, L.; Avrigeanu, V.; Mirea, M.; Becvar, F.; Krticka, M.; Belloni, F.; Milazzo, P. M.; Calvino, F.; Cortes, G.; Gomez-Hornillos, M. B.; Carrapico, C.; Goncalves, I. F.; Sarmento, R.; Vaz, P.; Colonna, N.; Marrone, S.; Moinul, M.; Tagliente, G.; Variale, V.; Dillmann, I.*; Domingo-Pardo, C.; Heil, M.*; Duran, I.; Paradela, C.; Tarrio, D.; Ganesan, S.; Giubrone, G.; Tain, J. L.; Gramegna, F.; Mastinu, P. F.; Harrisopulos, S.; Ioannides, K.; Karadimos, D.; Jericha, E.; Leeb, H.; Weiss, C.; Kappeler, F.; Lederer, C.; Pavlik, A.; Wallner, A.; Lozano, M.; Praena, J.; Quesada, J. M.; Massimi, C.; Vannini, G.; Mengoni, A.; Ventura, A.; Mosconi, M.; Nolte, R.; Vlastou, R.: **Characterization of the New n_TOF Neutron Beam: Fluence, Profile and Resolution.** *J. Korean Phys. Soc.* **59**(2): 1624–1627, 2011. DOI: 10.3938/jkps.59.1624

126 Hadynska-Klek, K.; Napiorkowski, P. J.; Maj, A.; Azaiez, F.; Valiente-Dobon, J. J.; de Angelis, G.; Kumar, G. A.; Bazzacco, D.; Bednarczyk, P.; Bellato, M.; Benzoni, G.; Berti, L.; Bortolato, D.; Bruyneel, B.; Camera, F.; Ciemala, M.; Cocconi, P.; Colombo, A.; Corsi, A.; Crespi, F.; Czermak, A.; Dulny, B.; Farnea, E.; Fornal, B.; Franchoo, S.; Gadea, A.; Giaz, A.; Gottardo, A.; Grave, X.; Grebosz, J.*; Gulmini, M.; Hess, H.; Isocrate, R.; Jaworski, G.; Kicinska-Habior, M.; Kmiecik, M.; Kondratyev, N.; Korichi, A.; Korten, W.; Lehaut, G.; Lenzi, S.; Leoni, S.; Lunardi, S.; Maron, G.; Menegazzo, R.; Mengoni, D.; Merchan, E.*; Meczynski, W.; Michelagnoli, C.; Molini, P.; Napoli, D. R.; Nicolini, R.; Niikura, M.; Palacz, M.; Rampazzo, G.; Recchia, F.; Redon, N.; Reiter, P.; Rosso, D.; Sahin, E.; Srebrny, J.; Stefan, I.; Stezowski, O.; Styczen, J.; Toniolo, N.; Ur, C. A.; Vandone, V.; Wadsworth, B.; Wiens, A.; Wrzosek-Lipska, K.; Zielinska, M.; Zieblinski, M.: **REFINEMENT OF THE (42)Ca LEVEL SCHEME. PRELIMINARY RESULTS FROM THE FIRST AGATA DEMONSTRATOR EXPERIMENT.** *Acta Phys. Pol. B* **42**(3-4): 817–824, 2011. DOI: 10.5506/APhysPolB.42.817

127 Haettner, E.; Ackermann, D.*; Audi, G.; Blaum, K.; Block, M.*; Eliseev, S.; Fleckenstein, T.; Herfurth, F.; Heßberger, F. P.*; Hofmann, S.*; Ketelaer, J.; Ketter, J.; Kluge, H. J.; Marx, G.; Mazzocco, M.; Novikov, Y. N.; Plaß, W. R.*; Rahaman, S.; Rauscher, T.; Rodriguez, D.; Schatz, H.; Scheidenberger, C.*; Schweikhard, L.; Sun, B.; Thirolf, P. G.; Vorobjev, G.; Wang, M.; Weber, C.: **Mass Measurements of Very Neutron-Deficient Mo and Tc Isotopes and Their Impact on rp Process Nucleosynthesis.** *Phys. Rev. Lett.* **106**(12): 122501, 2011. DOI: 10.1103/PhysRevLett.106.122501

128 Haussler, W.; Boni, P.; Klein, M.; Schmidt, C. J.*; Schmidt, U.; Groitl, F.; Kindervater, J.: **Detection of high frequency intensity oscillations at RESEDA using the CASCADE detector.** *Rev. Sci. Instrum.* **82**(4): 045101, 2011. DOI: 10.1063/1.3571300

129 Hebeler, K.; Bogner, S. K.; Furnstahl, R. J.; Nogga, A.; Schwenk, A.*: **Improved nuclear matter calculations from chiral low-momentum interactions.** *Phys. Rev. C* **83**(3): 031301, 2011. DOI: 10.1103/PhysRevC.83.031301

130 Hempel, M.; Schaffner-Bielich, J.; Typel, S.*; Ropke, G.: **Light clusters in nuclear matter: Excluded volume**

versus quantum many-body approaches. *Phys. Rev. C* **84**(5): 055804, 2011. DOI: 10.1103/PhysRevC.84.055804

131 Herbst, T. K.; Pawlowski, J. M.*; Schaefer, B. J.: **The phase structure of the Polyakov-quark-meson model beyond mean field.** *Phys. Lett. B* **696**(1-2): 58–67, 2011. DOI: 10.1016/j.physletb.2010.12.003

132 Hofmann, S.*: **Synthesis of superheavy elements by cold fusion.** *Radiochim. Acta* **99**(7-8): 405–428, 2011. DOI: 10.1524/ract.2011.1854

133 Hohne, C.; Choi, K. E.; Dobyrn, V.; Durr, M.; Eschke, J.*; Evseev, V.; Kampert, K. H.; Kochenda, L.; Koczon, P.*; Kopfer, J.*; Kormin, E.; Kresan, D.*; Lebedev, S.*; Miftakhov, M.; Pauly, C.*; Oh, K.; Ososkov, G.; Poliakov, V.; Rautenberg, J.; Samsonov, V.; Son, C. W.; Tarasenkova, O.; Tolchin, V.; Vznuzdaev, E.; Yi, J.; Yoo, I. K.: **Development of a RICH detector for CBM: simulations and experimental tests.** *Nucl. Instrum. Methods Phys. Res. Sect. A-Accel. Spectrom. Dect. Assoc. Equip.* **639**(1): 294–297, 2011. DOI: 10.1016/j.nima.2010.10.062

134 Hoischen, R.; Pietri, S.*; Rudolph, D.; Prokopowicz, W.; Schaffner, H.*; Emde, S.; Golubev, P.; Wendt, A.; Kurz, N.; Wollersheim, H. J.*; Gerl, J.*: **Fast timing with plastic scintillators for in-beam heavy-ion spectroscopy.** *Nucl. Instrum. Methods Phys. Res. Sect. A-Accel. Spectrom. Dect. Assoc. Equip.* **654**(1): 354–360, 2011. DOI: 10.1016/j.nima.2011.07.013

135 Hoischen, R.; Rudolph, D.; Ma, H. L.; Montuenga, P.; Hellstrom, M.; Pietri, S.*; Podolyak, Z.; Regan, P. H.; Garnsworthy, A. B.; Steer, S. J.; Becker, F.; Bednarczyk, P.; Caceres, L.; Doornenbal, P.; Gerl, J.*; Gorska, M.*; Grebosz, J.*; Kojouharov, I.*; Kurz, N.; Prokopowicz, W.; Schaffner, H.*; Wollersheim, H. J.*; Andersson, L. L.*; Atanasova, L.; Balabanski, D. L.; Bentley, M. A.; Blazhev, A.; Brandau, C.; Brown, J. R.; Fahlander, C.; Johansson, E. K.; Jungclaus, A.: **Isomeric mirror states as probes for effective charges in the lower pf shell.** *J. Phys. G-Nucl. Part. Phys.* **38**(3): 035104, 2011. DOI: 10.1088/0954-3899/38/3/035104

136 Horiuchi, W.*; Suzuki, Y.; Baye, D.: **Strength Function in Continuum with a Square Integrable Basis.** *Few-Body Syst.* **50**(1-4): 455–458, 2011. DOI: 10.1007/s00601-010-0139-z

137 Horiuchi, W.*; Suzuki, Y.; Sato, T.: **ELECTROWEAK TRANSITIONS OF (4)He USING REALISTIC NUCLEAR INTERACTIONS.** *Int. J. Mod. Phys. E-Nucl. Phys.* **20**(4): 781–784, 2011. DOI: 10.1142/S0218301311018666

138 Horiuchi, W.; Feldmeier, H.*; Neff, T.*; Suzuki, Y.: **Universality of short-range correlations in light nuclei.** *J. Phys. Conf. Ser.* **321**: 012043, 2011. DOI: 10.1088/1742-6596/321/1/012043

139 Huther, L.*; Loens, H. P.; Martinez-Pinedo, G.*; Langanke, K.*: **s-process stellar enhancement factors obtained within the statistical model with parity-dependent level densities.** *Eur. Phys. J. A* **47**(1): 10, 2011. DOI: 10.1140/epja/i2011-11010-y

140 Isaak, J.; Savran, D.*; Fritzsche, M.; Galaviz, D.; Hartmann, T.; Kamerdzhiev, S.; Kelley, J. H.; Kwan, E.; Pietralla, N.; Romig, C.; Rusev, G.; Sonnabend, K.; Tonchev, A. P.; Tornow, W.; Zilges, A.: **Investigation of low-lying electric dipole strength in the semimagic nucleus (44)Ca.** *Phys. Rev. C* **83**(3): 034304, 2011. DOI: 10.1103/PhysRevC.83.034304

141 Ishii, Y.; Toyoshima, A.; Tsukada, K.; Asai, M.; Li, Z. J.; Nagame, Y.; Miyashita, S.; Mori, T.; Suganuma, H.; Haba, H.; Goto, S.; Kudo, H.; Akiyama, K.; Oura, Y.; Shinohara, A.; Schädel, M.*; Pershina, V.; Kratz, J. V.: **Fluorido Complex Formation of Element 104, Rutherfordium (Rf).** *Bull. Chem. Soc. Jpn.* **84**(9): 903–911, 2011. DOI: 10.1246/bcsj.20110126

142 Iwasa, N.; Weick, H.*; Geissel, H.*: **New features of the Monte-Carlo code MOCADI.** *Nucl. Instrum. Methods Phys. Res. Sect. B-Beam Interact. Mater. Atoms* **269**(8): 752–758, 2011. DOI: 10.1016/j.nimb.2011.02.007

143 Iwata, Y.*; Maruhn, J. A.: **Enhanced spin-current tensor contribution in collision dynamics.** *Phys. Rev. C* **84**(1): 014616, 2011. DOI: 10.1103/PhysRevC.84.014616

144 Iwata, Y.*; Maruhn, J. A.: **The spin-current tensor contribution in collision dynamics.** *J. Phys. Conf. Ser.* **295**: 012126, 2011. DOI: 10.1088/1742-6596/295/1/012126

145 Janik, R.; Prochazka, A.*; Sitar, B.; Strmen, P.; Szarka, I.; Geissel, H.*; Behr, K. H.*; Karagiannis, C.*; Nociforo, C.*; Weick, H.*; Winkler, M.*: **Time Projection Chambers with C-pads for heavy ion tracking.** *Nucl. Instrum. Methods Phys. Res. Sect. A-Accel. Spectrom. Dect. Assoc. Equip.* **640**(1): 54–57, 2011. DOI: 10.1016/j.nima.2011.02.052

146 Jansen, G. R.; Hjorth-Jensen, M.; Hagen, G.; Papenbrock, T.*: **Toward open-shell nuclei with coupled-cluster theory.** *Phys. Rev. C* **83**(5): 054306, 2011. DOI: 10.1103/PhysRevC.83.054306

147 Jungclaus, A.; Walker, J.; Leske, J.; Speidel, K. H.; Stuchbery, A. E.; East, M.; Boutachkov, P.*; Cederkall, J.; Doornenbal, P.; Egido, J. L.; Ekstrom, A.; Gerl, J.*; Gernhauser, R.; Goel, N.; Gorska, M.*; Kojouharov, I.*; Maier-Komor, P.; Modamio, V.; Naqvi, F.*; Pietralla, N.; Pietri, S.*; Prokopowicz, W.; Schaffner, H.*; Schwengner, R.; Wollersheim, H. J.*: **Evidence for reduced collectivity around the neutron mid-shell in the stable even-mass Sn isotopes from new lifetime measurements.** *Phys. Lett. B* **695**(1-4): 110–114, 2011. DOI: 10.1016/j.physletb.2010.11.012

148 Kaczmarek, O.; Karsch, F.*; Laermann, E.; Miao, C.; Mukherjee, S.; Petreczky, P.; Schmidt, C. Schmidt; Soeldner, W.; Unger, W.: **Phase boundary for the chiral transition in (2+1)-flavor QCD at small values of the chemical potential.** *Phys. Rev. D* **83**(1): 014504, 2011. DOI: 10.1103/PhysRevD.83.014504

149 Kalandarov, S. A.; Adamian, G. G.; Antonenko, N. V.; Scheid, W.; Heinz, S.*; Comas, V. F.*; Hofmann, S.*; Khuyagbaatar, J.; Ackermann, D.*; Heredia, J. A.*; Heßberger, F. P.*; Kindler, B.; Lommel, B.; Mann, R.: **Emission of clusters with Z ¿ 2 from excited actinide nuclei.** *Phys. Rev. C* **84**(5): 054607, 2011. DOI: 10.1103/PhysRevC.84.054607

150 Kanada-En'yo, Y.; Feldmeier, H.*; Suhara, T.: **Two-neutron correlations in microscopic wave functions of (6)He, (8)He, and (12)C.** *Phys. Rev. C* **84**(5): 054301, 2011. DOI: 10.1103/PhysRevC.84.054301

151 Kanungo, R.; Prochazka, A.*; Horiuchi, W.; Nociforo, C.*; Aumann, T.*; Boutin, D.; Cortina-Gil, D.; Davids, B.; Diakaki, M.; Farinon, F.*; Geissel, H.*; Gernhauser, R.; Gerl, J.*; Janik, R.; Jonson, B.; Kindler, B.; Knöbel, R.*; Krucken, R.; Lantz, M.; Lenske, H.; Litvinov, Y.; Lommel, B.; Mahata, K.; Maierbeck, P.; Musumarra, A.; Nilsson, T.; Perro, C.; Scheidenberger, C.*; Sitar, B.; Strmen, P.; Sun, B.; Suzuki, Y.; Szarka, I.; Tanihata, I.; Utsuno, Y.; Weick, H.*; Winkler, M.*: **Matter radii of (32-35)Mg.** *Phys. Rev. C* **83**(2): 021302, 2011. DOI: 10.1103/PhysRevC.83.021302

152 Kanungo, R.; Prochazka, A.; Uchida, M.; Horiuchi, W.; Hagen, G.; Papenbrock, T.; Nociforo, C.*; Aumann, T.*; Boutin, D.; Cortina-Gil, D.; Davids, B.; Diakaki, M.; Farinon, F.; Geissel, H.*; Gernh"auser, R.; Gerl, J.; Janik, R.; Jensen, O.; Jonson, B.; Kindler, B.0575; Knöbel, R.*; Krücken, R.; Lantz, M.; Lenske, H.; Litvinov, Y.; Lommel, B.*; Mahata, K.; Maierbeck, P.; Musumarra, A.; Nilsson, T.; Perro, C.; Scheidenberger, C.*; Sitar, B.; Strmen, P.; Sun, B.; Suzuki, Y.; Szarka, I.; Tanihata, I.; Weick, H.*; Winkler, M.*: **Exploring the anomaly in the interaction cross section and matter radius of (23)O.** *Phys. Rev. C* **84**(6): 061304, 2011. DOI: 10.1103/PhysRevC.84.061304

153 Kappeler, F.; Mengoni, A.; Mosconi, M.; Fujii, K.; Heil, M.*; Domingo-Pardo, C.: **Neutron Studies for Dating the Universe.** *J. Korean Phys. Soc.* **59**(2): 2094–2099, 2011. DOI: 10.3938/jkps.59.2094

154 Karsch, F.*; Redlich, K.: **Has T(c) been measured by heavy ion experiments?.** *Phys. Rev. D* **84**(5): 051504, 2011. DOI: 10.1103/PhysRevD.84.051504

155 Karsch, F.*; Schaefer, B. J.; Wagner, M.; Wambach, J.*: **Towards finite density QCD with Taylor expansions.** *Phys. Lett. B* **698**(3): 256–264, 2011. DOI: 10.1016/j.physletb.2011.03.013

156 Kavatsyuk, M.; Bremer, D.; Dormenev, V.; Drexler, P.; Eissner, T.; Erni, W.; Guliyev, E.; Hennino, T.; Krusche, B.; Lewandowski, B.*; Lohner, H.; Moritz, M.; Novotny, R. W.; Peters, K.*; Pouthas, J.; Rosier, P.; Steinacher, M.; Tambave, G.; Wilms, A.*: **Performance of the prototype of the electromagnetic calorimeter for PANDA.** *Nucl. Instrum. Methods Phys. Res. Sect. A-Accel. Spectrom. Dect. Assoc. Equip.* **648**(1): 77–91, 2011. DOI: 10.1016/j.nima.2011.06.044

157 Khvorostukhin, A. S.; Toneev, V. D.*; Voskresensky, D. N.*: **Relaxation time ansatz and shear and bulk viscosities of gluon matter.** *Phys. Rev. C* **84**(3): 035202, 2011. DOI: 10.1103/PhysRevC.84.035202

158 Khvorostukhin, A. S.; Toneev, V. D.*; Voskresensky, D. N.*: **Shear and bulk viscosities for pure glue matter.** *Phys. Rev. C* **83**(3): 035204, 2011. DOI: 10.1103/PhysRevC.83.035204

159 Khvorostukhin, A. S.; Toneev, V. D.*; Voskresensky, D. N.*: **Viscosity of hadron matter within relativistic mean-field-based model with scaled hadron masses and couplings.** *Phys. Atom. Nuclei* **74**(4): 650–658, 2011. DOI: 10.1134/S1063778811040089

160 Kindler, B.*; Lommel, B.*; Hübner, A.*; Hartmann, W.*; Steiner, J.*: **Targets for the electron-positron pair spectrometer HADES.** *Nucl. Instrum. Methods Phys. Res. Sect. A-Accel. Spectrom. Dect. Assoc. Equip.* **655**(1): 95–99, 2011. DOI: 10.1016/j.nima.2011.06.029

161 Kis, M.*; Ciobanu, M.*; Deppner, I.; Hildenbrand, K. D.*; Herrmann, N.; Kang, T. I.; Kim, Y. J.; Koczon, P. *; Leifels, Y. *; Marquardt, M.*; Petrovici, M.; Piasecki, K.; Ryu, M. S.; Schüttauf, A.*; Simion, V.; Weinert, J*; Zhang, X.*: **A Multi-strip Multi-gap RPC Barrel for Time-of-Flight Measurements.** *Nucl. Instrum. Methods Phys. Res. Sect. A-Accel. Spectrom. Dect. Assoc. Equip.* **646**(1): 27–34, 2011. DOI: 10.1016/j.nima.2011.02.076

162 Kiseev, O. A.; Aksouh, F.; Bleile, A.; Bochkarev, O. V.; Chulkov, L. V.; Cortina-Gil, D.; Dobrovolsky, A. V.; Egelhof, P.*; Geissel, H.*; Hellstrom, M.; Isaev, N. B.; Komkov, B. G.; Matos, M.; Moroz, F. V.; Munzenberg, G.; Mutterer, M.; Mylnikov, V. A.; Neumaier, S. R.; Pribora, V. N.; Seliverstov, D. M.; Sergueev, L. O.; Shrivastava, A.; Summerer, K.; Weick, H.*; Winkler, M.*; Yatsoura, V. I.: **A new experimental approach to investigate intermediate-energy proton elastic scattering and breakup reactions on exotic nuclei in inverse kinematics.** *Nucl. Instrum. Methods Phys. Res. Sect. A-Accel. Spectrom. Dect. Assoc. Equip.* **641**(1): 72–86, 2011. DOI: 10.1016/j.nima.2011.03.046

163 Kiseleva, A.; Bhaduri, P. P.; Chattopadhyay, S.; Dubey, A. K.; Ganti, M. S.; Ghosh, P.; Hoehne, C.; Senger, P.*; Vassiliev, I.*; Khanzadeev, A.; Kryshen, E.; Nikulin, V.; Samsonov, V.; Ryzhinskiy, M.: **Di-muon measurements with the CBM experiment at FAIR.** *Indian J. Phys.* **85**(1): 211–216, 2011. DOI: 10.1007/s12648-011-0043-5

164 Klein-Bosing, C.: **JET AND HIGH P(T) MEASUREMENTS WITH THE ALICE EXPERIMENT.** *Int. J. Mod. Phys. E-Nucl. Phys.* **20**(7): 1533–1538, 2011. DOI: 10.1142/S0218301311019829

165 Klingbeil, H.*; Laier, U.*; Ningel, K. P.*; Schäfer, S.*; Thielmann, C.*; Zipfel, B.*: **New digital low-level rf system for heavy-ion synchrotrons.** *Phys. Rev. Spec. Top.-Accel. Beams* **14**(10): 102802, 2011. DOI: 10.1103/PhysRevSTAB.14.102802

166 Knoll, J.*: **Suppression of back-to-back particle-antiparticle correlations in high-energy nuclear collisions.** *Phys. Rev. C* **83**(4): 044914, 2011. DOI: 10.1103/PhysRevC.83.044914

167 Kolomeitsev, E. E.; Voskresensky, D. N.*: **Spin excitonic and diffusive modes in superfluid Fermi liquids.** *Phys. Rev. C* **84**(6): 068801, 2011. DOI: 10.1103/PhysRevC.84.068801

168 Kuboki, T.; Ohtsubo, T.; Takechi, M.*; Hachiuma, I.; Namihira, K.; Suzuki, T.; Yamaguchi, T.; Ohkuma, Y.; Shimbara, Y.; Suzuki, S.; Watanabe, R.; Fukuda, M.; Mihara, M.; Nishimura, D.; Ishibashi, Y.; Ito, Y.; Moriguchi, T.; Nagae, D.; Ooishi, H.; Ogawa, K.; Ozawa, A.; Yasuda, Y.; Suzuki, H.; Sumikama, T.; Yoshinaga, K.; Geissel, H.*; Winkler, M.*; Izumikawa, T.; Momota, S.; Aoi, N.; Fukuda, N.; Inabe, N.; Kameda, D.; Kusaka, K.; Kubo, T.; Lantz, M.; Ohnishi, T.; Ohtake, M.; Suda, T.; Takeda, H.; Tanaka, K.; Yanagisawa, Y.; Yoshida, A.; Yoshida, K.: **MEASUREMENT OF INTERACTION CROSS-SECTIONS FOR NEUTRON-RICH Na ISOTOPES.** *Acta Phys. Pol. B* **42**(3-4): 765–768, 2011. DOI: 10.5506/APhysPolB.42.765

169 Kumar, R.; Doornenbal, P.; Jhingan, A.; Bhowmik, R. K.; Appannababu, S.; Bednarczyk, P.; Caceres, L.; Cederkall, J.; Ekstrom, A.; Garg, R.; Gerl, J.*; Gorska, M.*; Grawe, H.; Kaur, J.; Kojouharov, I.*; Mandal, S.; Mukherjee, S.; Muralithar, S.; Prokopowicz, W.; Singh, P. P.*; Reiter, P.; Schaffner, H.*; Sharma, A.; Singh, R. P.; Siwal, D.; Wollersheim, H. J.*: **ENHANCED 0(g.s.)(+) -¿ 2(1)(+) E2 TRANSITION STRENGTH IN (112,114)Sn.** *Acta Phys. Pol. B* **42**(3-4): 813–816, 2011. DOI: 10.5506/APhysPolB.42.813

170 Langanke, K.*; Martinez-Pinedo, G.*; Petermann, I.*; Thielemann, F. K.: **Nuclear quests for supernova dynamics and nucleosynthesis.** *Prog. Part. Nucl. Phys.* **66**(2): 319–328, 2011. DOI: 10.1016/j.ppnp.2011.01.027

171 Langer, C.*; Algora, A.; Couture, A.; Csatlos, M.; Gulyas, J.; Heil, M.*; Krasznahorkay, A.; O'Donnell, J. M.; Plag, R.*; Reifarth, R.*; Stuhl, L.; Sonnabend, K.; Tornyi, T.; Tovesson, F.: **Simulations and developments of the Low Energy Neutron detector Array LENA.** *Nucl. Instrum. Methods Phys. Res. Sect. A-Accel. Spectrom. Dect. Assoc. Equip.* **659**(1): 411–418, 2011. DOI: 10.1016/j.nima.2011.06.079

172 Leder, M.; Pawlowski, J. M.*; Reinhardt, H.; Weber, A.: **Hamiltonian flow in Coulomb gauge Yang-Mills theory.** *Phys. Rev. D* **83**(2): 025010, 2011. DOI: 10.1103/PhysRevD.83.025010

173 Lederer, C.; Colonna, N.; Domingo-Pardo, C.; Gunsing, F.; Kappeler, F.; Massimi, C.; Mengoni, A.; Wallner, A.; Abbondanno, U.; Aerts, G.; Alvarez, H.; Alvarez-Velarde, F.; Andriamonje, S.; Andrzejewski, J.; Assimakopoulos, P.; Audouin, L.; Badurek, G.; Barbagallo, M.; Baumann, P.; Becvar, F.; Belloni, F.; Berthoumieux, E.; Calviani, M.; Calvino, F.; Cano-Ott, D.; Capote, R.; Carrapico, C.; de Albornoz, A. C.; Cennini, P.; Chepel, V.; Chiaveri, E.; Cortes, G.; Couture, A.; Cox, J.; Dahlfors, M.; David, S.; Dillmann, I.*; Dolfini, R.; Dridi, W.; Duran, I.; Eleftheriadis, C.; Embid-Segura, M.; Ferrant, L.; Ferrari, A.; Ferreira-Marques, R.; Fitzpatrick, L.; Frais-Koelbl, H.; Fujii, K.; Furman, W.; Goncalves, I.; Gonzalez-Romero, E.; Goverdovski, A.; Gramegna, F.; Griesmayer, E.; Guerrero, C.; Haas, B.; Haight, R.; Heil, M.*; Herrera-Martinez, A.; Igashira, M.; Isaev, S.; Jericha, E.; Kadi, Y.; Karadimos, D.; Karamanis, D.; Kerveno, M.; Ketlerov, V.; Koehler, P.; Konovalov, V.; Kossionides, E.; Krticka, M.; Lampoudis, C.; Leeb, H.; Lindote, A.; Lopes, I.; Losito, R.; Lozano, M.; Lukic, S.; Marganiec, J.*; Marques, L.; Marrone, S.; Martinez, T.; Mastinu, P.; Mendoza, E.; Milazzo, P. M.; Moreau, C.; Mosconi, M.; Neves, F.; Oberhummer, H.; O'Brien, S.; Oshima, M.; Pancin, J.; Papachristodoulou, C.; Papadopoulos, C.; Paradela, C.; Patronis, N.; Pavlik, A.; Pavlopoulos, P.; Perrot, L.; Pigni, M. T.; Plag, R.*; Plompen, A.; Plukis, A.; Poch, A.; Praena, J.; Pretel, C.; Quesada, J.; Rauscher, T.; Reifarth, R.*; Rosetti, M.; Rubbia, C.; Rudolf, G.; Rullhusen, P.; Salgado, J.; Santos, C.; Sarchiapone, L.; Sarmento, R.; Savvidis, I.; Stephan, C.; Tagliente, G.; Tain, J. L.; Tarrio, D.; Tassan-Got, L.; Tavora, L.; Terlizzi, R.; Vannini, G.; Vaz, P.; Ventura, A.; Villamarin, D.; Vlachoudis, V.; Vlastou, R.; Voss, F.; Walter, S.; Wendler, H.; Wiescher, M.; Wisshak, K.: **(197)Au(n,gamma) cross section in the unresolved resonance region.** *Phys. Rev. C* **83**(3): 034608, 2011. DOI: 10.1103/PhysRevC.83.034608

174 Lehmann, A.; Britting, A.; Cowie, E.; Dodokhof, V. K.; Duren, M.; Dutta, D.; Eyrich, W.; Fohl, K.; Glazier, D. I.; Hayrapetyan, A.; Hoek, M.; Hohler, R.*; Kaiser, R.; Keri, T.; Koch, P.; Krock, B.; Lehmann, D.*; Marton, J.; Merle, O.; Montgomery, R.; Peters, K.*; Reinicke, S.; Rosner, G.; Roy, B.; Schepers, G.*; Schmitt, L.*; Schwarz, C.*; Schwiening, J.*; Seitz, B.; Sfientie, C.; Suzuki, K.; Uhlig, F.; Vodopianov, A. S.; Watts, D. P.; Yu, W.: **Systematic studies of micro-channel plate PMTs.** *Nucl. Instrum. Methods Phys. Res. Sect. A-Accel. Spectrom. Dect. Assoc. Equip.* **639**(1): 144–147, 2011. DOI: 10.1016/j.nima.2010.09.071

175 Li, Q. F.; Shen, C. W.; Guo, C. C.; Wang, Y. J.; Li, Z. X.; Lukasik, J.; Trautmann, W.*: **Nonequilibrium dynamics in heavy-ion collisions at low energies available**

at the GSI Schwerionen Synchrotron. *Phys. Rev. C* **83**(4): 044617, 2011. DOI: 10.1103/PhysRevC.83.044617

176 Litvinova, E. V.*; Afanasjev, A. V.: **Dynamics of nuclear single-particle structure in covariant theory of particle-vibration coupling: From light to superheavy nuclei.** *Phys. Rev. C* **84**(1): 014305, 2011. DOI: 10.1103/PhysRevC.84.014305

177 Lommel, B.*; Hartmann, W.*; Hübner, A.*; Kindler, B.*; Steiner, J.*: **Preparation of self-supporting nickel targets from (58)Ni, (60)Ni and (61)Ni.** *Nucl. Instrum. Methods Phys. Res. Sect. A-Accel. Spectrom. Dect. Assoc. Equip.* **655**(1): 44–46, 2011. DOI: 10.1016/j.nima.2011.06.017

178 Lutz, M. F. M.*; Samart, D.*; Semke, A.*: **Combined large-N(c) and heavy-quark operator analysis of two-body meson-baryon counterterms in the chiral Lagrangian with charmed mesons.** *Phys. Rev. D* **84**(9): 096015, 2011. DOI: 10.1103/PhysRevD.84.096015

179 Lutz, M. F. M.*; Semke, A.*: **Large-N(c) operator analysis of 2-body meson-baryon counterterms in the chiral Lagrangian.** *Phys. Rev. D* **83**(3): 034008, 2011. DOI: 10.1103/PhysRevD.83.034008

180 Mancusi, D.; Cugnon, J.; Boudard, A.; David, J. C.; Leray, S.; Charity, R. J.; Kelic-Heil, A.*; Ricciardi, M. V.*: **Multifragmentation in Reactions of 1-GeV Protons with Iron Nuclei.** *J. Korean Phys. Soc.* **59**(2): 943–946, 2011. DOI: 10.3938/jkps.59.943

181 Martinez-Pinedo, G.*; Ziebarth, B.; Fischer, T.; Langanke, K.*: **Effect of collective neutrino flavor oscillations on nu p-process nucleosynthesis.** *Eur. Phys. J. A* **47**(8): 98, 2011. DOI: 10.1140/epja/i2011-11098-y

182 Masciocchi, S.*: **Inclusive electron spectrum from heavy-flavour decays in proton-proton collisions at root s=7 TeV measured with ALICE at LHC.** *Nucl. Phys. A* **855**(1): 432–435, 2011. DOI: 10.1016/j.nuclphysa.2011.02.098

183 Matsuda, Y.; Sakaguchi, H.; Zenihiro, J.; Ishimoto, S.; Suzuki, S.; Otsu, H.; Ohnishi, T.; Takeda, H.; Ozeki, K.; Tanaka, K.; Terashima, S. *; Maeda, Y.; Kobayashi, T.; Koreeda, A.; Kamei, K.: **Large, thin solid hydrogen target using para-H(2).** *Nucl. Instrum. Methods Phys. Res. Sect. A-Accel. Spectrom. Dect. Assoc. Equip.* **643**(1): 6–10, 2011. DOI: 10.1016/j.nima.2011.04.017

184 Mendoza, E.; Becares, V.; Casado, A.; Cano-Ott, D.; Fernandez-Ordonez, M.; Gonzalez-Romero, E.; Guerrero, C.; Martinez, T.; Vidriales, J. J.; Andrzejewski, J.; Marganiec, J.*; Perkowski, J.; Audouin, L.; Berthier, B.; Tassan-Got, L.; Avrigeanu, V.; Mirea, M.; Becvar, F.; Krticka, M.; Belloni, F.; Milazzo, P. M.; Berthoumieux, E.; Gunsing, F.; Calvino, F.; Cortes, G.; Gomez-Hornillos, M. B.; Andriamonje, S.; Brugger, M.; Calviani, M.; Cerutti, F.; Chiaveri, E.; Ferrari, A.; Kadi, Y.; Lebbos, E.; Losito, H.; Vlachoudis, V.; Carrapico, C.; Goncalves, I. F.; Saarmento, H.; Vaz, P.; Colonna, N.; Marrone, S.; Moinul, M.; Tagliente, G.; Variale, V.; Dillmann, I.*; Domingo-Pardo, C.; Heil, M.*; Duran, I.; Paradela, C.; Tarrio, D.; Ganesan, S.; Giubrone, G.; Tain, J. L.; Gramegna, F.; Mastinu, P. F.; Harrisopulos, S.; Ioannides, K.; Karadimos, D.; Jericha, E.; Leeb, H.; Weiss, C.; Kappeler, F.; Lederer, C.; Pavlik, A.; Wallner, A.; Lozano, M.; Prena, J.; Quesada, J. M.; Massimi, C.; Vannini, G.; Mengoni, A.; Ventura, A.; Mosconi, M.; Nolte, R.; Vlastou, R.: **Improved Neutron Capture Cross Section Measurements with the n_TOF Total Absorption Calorimeter.** *J. Korean Phys. Soc.* **59**(2): 1813–1816, 2011. DOI: 10.3938/jkps.59.1813

185 Menendez, J.*; Gazit, D.; Schwenk, A.: **Chiral Two-Body Currents in Nuclei: Gamow-Teller Transitions and Neutrinoless Double-Beta Decay.** *Phys. Rev. Lett.* **107**(6): 062501, 2011. DOI: 10.1103/PhysRevLett.107.062501

186 Michel, J.*; Böhmer, M.; Fröhlich, I.; Korcyl, G.; Maier, L.; Palka, M.; Stroth, J.*; Traxler, M.*; Yurevich, S.*: **The HADES DAQ System: Trigger and Readout Board Network.** *IEEE Trans. Nucl. Sci.* **58**(4): 1745–1750, 2011. DOI: 10.1109/TNS.2011.2141150

187 Minami, S.*; Hoffmann, J.*; Kurz, N.*; Ott, W.*: **Design and Implementation of a Data Transfer Protocol Via Optical Fiber.** *IEEE Trans. Nucl. Sci.* **58**(4): 1816–1819, 2011. DOI: 10.1109/TNS.2011.2159808

188 Moeini, H.; Ilieva, S.*; Aksouh, F.; Boretzky, K.*; Chatillon, A.; Corsi, A.; Egelhof, P.*; Emling, H.*; Ickert, G.*; Jourdan, J.; Nayestanaki, N. K.; Kiselev, D.; Kiselev, O.*; Kozhuharov, C.*; Le Bleis, T.; Le, X. C.*; Litvinov, Yu. A.*; Mahata, K.; Meier, J. P.; Nolden, F.; Paschalis, S.; Popp, U.; Simon, H.*; Steck, M.*; Stöhlker, T. *; Weick, H.*; Werthmuller, D.; Zalite, A.: **First feasibility experiment for the EXL project with prototype detectors at the ESR storage ring.** *Nucl. Instrum. Methods Phys. Res. Sect. A-Accel. Spectrom. Dect. Assoc. Equip.* **634**(1): 77–84, 2011. DOI: 10.1016/j.nima.2011.01.036

189 Morales, A. I.; Benlliure, J.; Agramunt, J.; Algora, A.; Alkhomashi, N.; Alvarez-Pol, H.; Boutachkov, P.*; Bruce, A. M.; Caceres, L. S.; Casarejos, E.; Bacelar, A. M. D.; Doornenbal, P.; Dragosavac, D.; Farrelly, G.; Gadea, A.; Gelletly, W.; Gerl, J.*; Gorska, M.*; Grebosz, J.*; Kojouharov, I.*; Molina, F.; Perez-Loureiro, D.; Pietri, S.*; Podolyak, Z.; Regan, P. H.; Rubio, B.; Shaffner, H.; Steer, S. J.; Tashenov, S.; Verma, S.; Wollersheim, H. J.*: **Synthesis of N=127 isotones through (p,n) charge-exchange reactions induced by relativistic (208)Pb projectiles.** *Phys. Rev. C* **84**(1): 011601, 2011. DOI: 10.1103/PhysRevC.84.011601

190 Morita, K.*; Skokov, V.*; Friman, B.*; Redlich, K.: **Probing deconfinement in a chiral effective**

model with Polyakov loop at imaginary chemical potential. *Phys. Rev. D* **84**(7): 076009, 2011. DOI: 10.1103/PhysRevD.84.076009

191 Morita, K.; Skokov, V.; Friman, B.*; Redlich, K.: **Role of mesonic fluctuations in the Polyakov loop extended quark-meson model at imaginary chemical potential.** *Phys. Rev. D* **84**(7): 074020, 2011. DOI: 10.1103/PhysRevD.84.074020

192 Moukaddam, M.; Duchene, G.; Beaumel, D.; Burgunder, J.; Caceres, L.; Clement, E.; Curien, D.; Didierjean, F.; Fernandez, B.; Finck, C.; Flavigny, F.; Franchoo, S.; Gibelin, J.; Giron, S.; Gillibert, A.; Goasduff, A.; Grevy, S.; Guillot, J.; Haas, F.; Hammache, F.; Harakeh, M. N.; Kemper, K.; Lapoux, V.; Matea, Y.; Matta, A.; Nalpas, L.; Nowacki, F.; Obertelli, A.; Pancin, J.; Perrot, L.; Piot, J.; Pllumbi, E.; Raabe, R.; Scarpaci, J. A.; de Sereville, N.; Sieja, K.; Sorlin, O.; Stefan, I.; Stoedel, C.; Thomas, J. C.: **SEARCH FOR 2d(5/2) NEUTRON STATES IN (69)Ni.** *Acta Phys. Pol. B* **42**(3-4): 541–544, 2011. DOI: 10.5506/APhysPolB.42.541

193 Napolitani, P.; Schmidt, K. H.*; Tassan-Got, L.: **Inclusive selection of intermediate-mass-fragment formation modes in the spallation of (136)Xe.** *J. Phys. G-Nucl. Part. Phys.* **38**(11): 115006, 2011. DOI: 10.1088/0954-3899/38/11/115006

194 Naqvi, F.*; Boutachkov, P.*; Gorska, M.*; Gerl, J.*; Farinon, F.*; Gregor, E. T.*; Hadynska, K.; Jhingan, A.; Janik, R.; Kojouharov, I.*; Kondratyev, N. A.; Alvarez, M. A. G.; Mukha, I. G.*; Napiorkowski, P.; Nociforo, C.*; Pietak, D.; Prokopowicz, W.; Pietri, S.*; Prochazka, A.*; Schaffner, H.*; Strmen, P.; Weick, H.*; Wollersheim, H. J.*: **DEVELOPMENT OF SLOWED DOWN BEAMS AT THE FRAGMENT SEPARATOR FOR FAIR.** *Acta Phys. Pol. B* **42**(3-4): 725–728, 2011. DOI: 10.5506/APhysPolB.42.725

195 Neff, T.*: **Microscopic Calculation of the (3)He(alpha, gamma)(7)Be and (3)H(alpha, gamma)(7)Li Capture Cross Sections Using Realistic Interactions.** *Phys. Rev. Lett.* **106**(4): 042502, 2011. DOI: 10.1103/PhysRevLett.106.042502

196 Neff, T.*; Feldmeier, H.*; Langanke, K.*: **Microscopic calculation of the (3)He(alpha,gamma)(7)Be reaction rate using realistic interactions.** *J. Phys. Conf. Ser.* **321**: 012007, 2011. DOI: 10.1088/1742-6596/321/1/012007

197 Neff, T.*; Feldmeier, H.*; Langanke, K.*: **Towards microscopic ab initio calculations of astrophysical S-factors.** *Prog. Part. Nucl. Phys.* **66**(2): 341–345, 2011. DOI: 10.1016/j.ppnp.2011.01.031

198 Ogul, R.*; Botvina, A. S.; Atav, U.; Buyukcizmeci, N.; Mishustin, I. N.; Adrich, P.; Aumann, T.*; Bacri, C. O.; Barczyk, T.; Bassini, R.; Bianchin, S.*; Boiano, C.; Boudard, A.; Brzychczyk, J.; Chbihi, A.; Cibor, J.; Czech, B.; De Napoli, M.; Ducret, J. E.; Emling, H.*; Frankland, J. D.; Hellstrom, M.*; Henzlova, D.; Imme, G.; Iori, I.; Johansson, H.; Kezzar, K.; Lafriakh, A.; Le Fevre, A.*; Le Gentil, E.; Leifels, Y.*; Lühning, J.*; Lukasik, J.*; Lynch, W. G.; Lynen, U.*; Majka, Z.; Mocko, M.; Müller, W. F. J.*; Mykulyak, A.; Orth, H.*; Otte, A. N.; Palit, R.; Pawlowski, P.; Pullia, A.; Raciti, G.; Rapisarda, E.; Sann, H.*; Schwarz, C.*; Sfienti, C.*; Simon, H.*; Sümmerer, K.*; Trautmann, W.*; Tsang, M. B.; Verde, G.; Volant, C.; Wallace, M.; Weick, H.*; Wiechula, J.; Wieloch, A.; Zwieglinski, B.: **Isospin-dependent multifragmentation of relativistic projectiles.** *Phys. Rev. C* **83**(2): 024608, 2011. DOI: 10.1103/PhysRevC.83.024608

199 Paar, N.; Suzuki, T.; Honma, M.; Marketin, T. XXXX; Vretenar, D.: **Uncertainties in modeling low-energy neutrino-induced reactions on iron-group nuclei.** *Phys. Rev. C* **84**(4): 047305, 2011. DOI: 10.1103/PhysRevC.84.047305

200 Pangon, V.*; Nagy, S.; Polonyi, J.; Sailer, K.: **ONSET OF SYMMETRY BREAKING BY THE FUNCTIONAL RG METHOD.** *Int. J. Mod. Phys. A* **26**(7-8): 1327–1345, 2011. DOI: 10.1142/S0217751X11052839

201 Papenbrock, T.*: **Effective theory for deformed nuclei.** *Nucl. Phys. A* **852**(1): 36–60, 2011. DOI: 10.1016/j.nuclphysa.2010.12.013

202 Parascandolo, C.; Pierroutsakou, D.; Silvestri, R.; Agodi, C.; Alba, R.; Baran, V.; Boiano, A.; Colonna, M.; Coniglione, R.; De Filippo, E.; Del Zoppo, A.; Di Toro, M.; Emanuele, U.; Farinon, F.*; Guglielmetti, A.; Inglima, G.; La Commara, M.; Maiolino, C.; Martin, B.; Mazzocco, M.; Mazzocchi, C.; Molini, P.; Rizzo, C.; Romoli, M.; Sandoli, M.; Santonocito, D.; Signorini, C.; Soramel, F.; Trifiro, A.; Trimarchi, M.: **INVESTIGATION OF THE DYNAMICAL DIPOLE MODE IN THE (192)Pb MASS REGION.** *Acta Phys. Pol. B* **42**(3-4): 629–632, 2011. DOI: 10.5506/APhysPolB.42.629

203 Parfenova, A.*; Franchetti, G.*: **Experimental benchmarking of nonlinear tune response matrix with several controlled sextupolar errors.** *Nucl. Instrum. Methods Phys. Res. Sect. A-Accel. Spectrom. Dect. Assoc. Equip.* **646**(1): 7–11, 2011. DOI: 10.1016/j.nima.2011.03.051

204 Perez-Cerdan, A. B.; Rubio, B.; Gelletly, W.; Algora, A.; Agramunt, J.; Burkard, K.*; Huller, W.*; Nacher, E.; Sarriguren, P.; Caballero, L.; Molina, F.; Fraile, L. M.; Reillo, E.; Borge, M. J. G.; Dessagne, P.; Jungclaus, A.; Salsac, M. D.: **beta decay of (78)Sr.** *Phys. Rev. C* **84**(5): 054311, 2011. DOI: 10.1103/PhysRevC.84.054311

205 Perez-Loureiro, D.; Benlliure, J.; Alvarez-Pol, H.; Blank, B.; Casarejos, E.; Dragosavac, D.; Fohr, V.; Gascon, M.; Gawlikowicz, W.; Heinz, A.; Helariutta, K.; Kelic-Heil, A.*; Lukic, S.; Montes, F.; Pienkowski, L.; Schmidt,

K. H.*; Staniou, M.; Subotic, K.; Sümmerer, K. *; Taieb, J.; Trzcinska, A.: **Production of neutron-rich nuclei in fragmentation reactions of (132)Sn projectiles at relativistic energies.** *Phys. Lett. B* **703**(5): 552–556, 2011. DOI: 10.1016/j.physletb.2011.08.037

206 Pershina, V.*: **Relativistic electronic structure studies on the heaviest elements.** *Radiochim. Acta* **99**(7-8): 459–476, 2011. DOI: 10.1524/ract.2011.1855

207 Petris, M.; Petrovici, M.; Simion, V.; Bartos, D.; Caragheorgheopol, G.; Dohrmann, F.; Hildenbrand, K. D.*; Kämpfer, B.; Kotte, R.; Naumann, L.; Stach, D.; Williams, M. C. S.; Wüstenfeld, J.: **STRIP READOUT RPC BASED ON LOW RESISTIVITY GLASS ELECTRODES.** *Rom. J. Phys.* **56**(3-4): 349–358, 2011.

208 Pietri, S.*; Jungclaus, A.; Gorska, M.*; Grawe, H.; Pfutzner, M.; Caceres, L.; Detistov, P.; Lalkovski, S.; Modamio, V.; Podolyak, Z.; Regan, P. H.; Rudolph, D.; Walker, J.; Werner-Malento, E.; Bednarczyk, P.; Doornenbal, P.; Geissel, H.*; Gerl, J.*; Grebosz, J.*; Kojouharov, I.*; Kurz, N.; Prokopowicz, W.; Schaffner, H.*; Wollersheim, H. J.*; Andgren, K.; Benlliure, J.; Benzoni, G.; Bruce, A. M.; Casarejos, E.; Cederwall, B.; Crespi, F. C. L.; Hadinia, B.; Hellstrom, M.; Hoischen, R.; Ilie, G.; Khaplanov, A.; Kmiecik, M.; Kumar, R.; Maj, A.; Mandal, S.; Montes, F.; Myalski, S.; Simpson, G.; Steer, S. J.; Tashenov, S.; Wieland, O.: **First observation of the decay of a 15(-) seniority v=4 isomer in (128)Sn.** *Phys. Rev. C* **83**(4): 044328, 2011. DOI: 10.1103/PhysRevC.83.044328

209 Rapisarda, E.; Stefanescu, I.; Balabanski, D. L.; Bastin, B.; Blazhev, A.; Bree, N.; Danchev, M.; Bruyneel, B.; Davinson, T.; Delahaye, P.; Diriken, J.; Eberth, J.; Georgiev, G.; Fedorov, D.; Fedosseev, V. N.; Fiori, E.*; Franchoo, S.; Fransen, C.; Geibel, K.; Gladnishki, K.; Hadynska, K.; Hess, H.; Heyde, K.; Huyse, M.; Ivanov, O.; Iwanicki, J.; Jolie, J.; Kalkühler, M.; Kroll, T.; Krücken, R.; Koster, U.; Lo Bianco, G.; Lozeva, R.; Marsh, B. A.; Nardelli, S.; Nowacki, F.; Patronis, N.; Reiter, P.; Seidlitz, M.; Sieja, K.; Smirnova, N.; Srebrny, J.; Van de Walle, J.; Van Duppen, P.; Warr, N.; Wenander, F.; Wimmer, K.; Wrzosek, K.; Zemlyanoi, S.; Zielinska, M.: **Coulomb excitation of the 3(-) isomer in (70)Cu.** *Phys. Rev. C* **84**(6): 064323, 2011. DOI: 10.1103/PhysRevC.84.064323

210 Rauscher, T.; Mohr, P.; Dillmann, I.*; Plag, R.*: **OPPORTUNITIES TO CONSTRAIN ASTROPHYSICAL REACTION RATES FOR THE s-PROCESS VIA DETERMINATION OF THE GROUND-STATE CROSS-SECTIONS.** *Astrophys. J.* **738**(2): 143, 2011. DOI: 10.1088/0004-637X/738/2/143

211 Richter, M.; Aamodt, K.; Alt, T.; Appelshauser, H.; Arend, A.; Becker, B.; Bottger, S.; Breitner, T.; Busching, H.; Cicalo, C.; Chattopadhyay, S.; Cleymans, J.; Das, I.; Djuvsland, O.; Erdal, H.; Fearick, R.; Gorbunov, S.; Haaland, O. S.; Hille, P. T.; Kalcher, S.; Kanaki, K.; Kebschull, U.; Kisel, I.*; Kretz, M.; Lara, C.; Lindal, S.; Lindenstruth, V.*; Masoodi, A. A.; Ovrebekk, G.; Panse, R.; Peschek, J.; Ploskon, M.; Pocheptsov, T.; Rascanu, T.; Ronchetti, F.; Rohr, D.; Rohrich, D.; Skaali, B.; Steinbeck, T.; Szostak, A.; Thader, J.; Tveter, T. S.; Ullaland, K.; Vilakazi, Z.; Weis, R.; Zelnicek, P.: **Event Reconstruction Performance of the ALICE High Level Trigger p plus p for Collisions.** *IEEE Trans. Nucl. Sci.* **58**(4): 1706–1713, 2011. DOI: 10.1109/TNS.2011.2160093

212 Rodriguez, T. R.*; Egido, J. L.: **Configuration mixing description of the nucleus (44)S.** *Phys. Rev. C* **84**(5): 051307, 2011. DOI: 10.1103/PhysRevC.84.051307

213 Rodriguez, T. R.*; Egido, J. L.: **Multiple shape coexistence in the nucleus (80)Zr.** *Phys. Lett. B* **705**(3): 255–259, 2011. DOI: 10.1016/j.physletb.2011.10.003

214 Rodriguez, T. R.*; Martinez-Pinedo, G.*: **Neutrino less double beta decay studied with configuration mixing methods.** *Prog. Part. Nucl. Phys.* **66**(2): 436–440, 2011. DOI: 10.1016/j.ppnp.2011.01.047

215 Rodriguez-Tajes, C.; Cortina-Gil, D.; Alvarez-Pol, H.; Aumann, T.*; Benjamim, E.; Benlliure, J.; Borge, M. J. G.; Caamano, M.; Casarejos, E.; Chatillon, A.; Chulkov, L. V.; Eppinger, K.; Faestermann, T.; Gascon, M.; Geissel, H.*; Gernhauser, R.; Jonson, B.; Kanungo, R.; Krucken, R.; Kurtukian, T.; Larsson, K.; Maierbeck, P.; Nilsson, T.; Nociforo, C.*; Parfenova, Y.; Pascual-Izarra, C.; Perea, A.; Perez-Loureiro, D.; Prochazka, A.*; Schwertel, S.; Simon, H.*; Summerer, K.; Tengblad, O.; Weick, H.*; Winkler, M.*; Zhukov, M. V.: **Structure of (22)N and the N=14 subshell.** *Phys. Rev. C* **83**(6): 064313, 2011. DOI: 10.1103/PhysRevC.83.064313

216 Romita, R.*: **Status of the ALICE experiment and first results on heavy flavour production.** *Nucl. Phys. B-Proc. Suppl.* **210-11**: 15–20, 2011. DOI: 10.1016/j.nuclphysbps.2010.12.036

217 Russotto, P; Wu, PZ; Zoric, M; Chartier, M; Leifels, Y*; Lemmon, RC; Li, Q; Lukasik, J; Pagano, A; Pawlowski, P; Trautmann, W*: **Symmetry energy from elliptic flow in (197)Au+(197)Au.** *Phys. Lett. B* **697**(5): 471–476, 2011. DOI: 10.1016/j.physletb.2011.02.033

218 Rustamov, A.*; Agakishiev, G.; Balanda, A.; Belver, D.; Belyaev, A.; Blanco, A.; Bohmer, M.; Boyard, J. L.; Cabanelas, P.; Castro, E.; Chernenko, S.; Diaz, J.; Dybczak, A.; Epple, E.; Fabbietti, L.; Fateev, O.; Finocchiaro, P.; Fonte, P.; Friese, J.; Frohlich, I.; Galatyuk, T.*; Garzon, J. A.; Gil, A.; Golubeva, M.; Gonzalez-Diaz, D.*; Guber, F.; Gumberidze, M.*; Hennino, T.; Holzmann, R.*; Huck, P.; Ierusalimov, A.; Iori, I.; Ivashkin, A.; Jurkovic, M.; Kampfer, B.; Karavicheva, T.; Koenig, I.*; Koenig, W.*; Kolb, B. W.*; Kopp, A.; Korcyl, G.; Kornakov, G. K.; Kotte, R.; Kozuch, A.; Krasa, A.; Krizek, F.; Krucken, R.; Kuc, H.; Kuhn, W.; Kugler, A.; Kurepin, A.; Kurilkin, A.; Kurilkin, P.; Kahlitz, P.; Ladygin, V.; Lamas-Valverde,

J.; Lang, S.; Lapidus, K.; Liu, T.; Lopes, L.; Lorenz, M.*; Maier, L.; Mangiarotti, A.; Markert, J.*; Metag, V.; Michalska, B.; Michel, J.*; Muntz, C.*; Naumann, L.; Pachmayer, Y. C.; Palka, M.; Parpottas, Y.; Pechenov, V.*; Pechenova, O.; Pietraszko, J.*; Przygoda, W.; Ramstein, B.; Reshetin, A.; Roskoss, J.; Sadovsky, A.; Salabura, P.*; Schmah, A.; Siebenson, J.; Sobolev, Y. G.; Spataro, S.; Strobele, H.*; Stroth, J.*; Sturm, C.*; Tarantola, A.; Teilab, K.*; Tlusty, P.; Traxler, M.*; Trebacz, R.; Tsertos, H.; Vasiliev, T.; Wagner, V.; Weber, M.; Wustenfeld, J.*; Yurevich, S.*; Zanevsky, Y.: **DILEPTON PRODUCTION STUDIED WITH THE HADES SPECTROMETER.** *Int. J. Mod. Phys. A* **26**(3-4): 384–389, 2011. DOI: 10.1142/S0217751X11051706

219 Ryu, M. S.; Hong, B.; Kang, T. I.*: **FOPI Detector for Heavy-ion Collision Experiment at SIS/GSI.** *J. Korean Phys. Soc.* **59**(2): 1605–1608, 2011. DOI: 10.3938/jkps.59.1605

220 Sümmerer, K.: **High-energy break-up of (6)Li as a tool to study the Big-Bang nucleosynthesis reaction (2)H(alpha, gamma)(6)Li.** *Prog. Part. Nucl. Phys.* **66**(2): 298–302, 2011. DOI: 10.1016/j.ppnp.2011.01.024

221 Salvadori, M. C.; Teixeira, F. S.; Nikolaev, A.; Savkin, K. P.; Oks, E. M.; Spädtke, P.*; Yu, K. M.; Brown, I. G.: **Self-neutralized ion beam.** *J. Appl. Phys.* **110**(8): 083308, 2011. DOI: 10.1063/1.3638714

222 Sasano, M.; Perdikakis, G.; Zegers, R. G. T.; Austin, S. M.; Bazin, D.; Brown, B. A.; Caesar, C.*; Cole, A. L.; Deaven, J. M.; Ferrante, N.; Guess, C. J.; Hitt, G. W.; Meharchand, R.; Montes, F.; Palardy, J.; Prinke, A.; Riley, L. A.; Sakai, H.; Scott, M.; Stolz, A.; Valdez, L.; Yako, K.: **Gamow-Teller Transition Strengths from (56)Ni.** *Phys. Rev. Lett.* **107**(20): 202501, 2011. DOI: 10.1103/PhysRevLett.107.202501

223 Savran, D.*; Elvers, M.; Endres, J.; Fritzsche, M.; Löher, B.; Pietralla, N.; Ponomarev, V. Y.; Romig, C.; Schnorrenberger, L.; Sonnabend, K.; Zilges, A.: **Fragmentation and systematics of the pygmy dipole resonance in the stable N=82 isotones.** *Phys. Rev. C* **84**(2): 024326, 2011. DOI: 10.1103/PhysRevC.84.024326

224 Schnizer, P.*; Fischer, E.*; Kiesewetter, H. R.*; Mierau, A.*; Schnizer, B. ????: **Field Measurements on Curved Superconducting Magnets.** *IEEE Trans. Appl. Supercond.* **21**(3): 1799–1803, 2011. DOI: 10.1109/TASC.2010.2091390

225 Scholl, C.; Fujita, Y.; Adachi, T.; von Brentano, P.; Fujita, H.; Gorska, M.*; Hashimoto, H.; Hatanaka, K.; Matsubara, H.; Nakanishi, K.; Ohta, T.; Sakemi, Y.; Shimbara, Y.; Shimizu, Y.; Tameshige, Y.; Tamii, A.; Yosoi, M.; Zegers, R. G. T.: **High-resolution study of the (9)Be((3)He,t) (9)B reaction up to the (9)B triton threshold.** *Phys. Rev. C* **84**(1): 014308, 2011. DOI: 10.1103/PhysRevC.84.014308

226 Schwarz, C.*; Ahmed, G.; Britting, A.; Buhler, P.; Cowie, E.; Dodokhov, V. K.; Duren, M.; Dutta, D.; Eyrich, W.; Fohl, K.; Glazier, D. I.; Hayrapetyan, A.; Hoek, M.; Hohler, R.*; Lehmann, A.; Lehmann, D.*; Kaiser, R.; Keri, T.; Koch, P.; Krock, B.; Marton, J.; Merle, O.; Montgomery, R.; Peters, K.*; Reinicke, S.; Rosner, G.; Roy, B.; Schepers, G.*; Schmitt, L.*; Schwiening, J.*; Seitz, B.; Sfienti, C.; Suzuki, K.; Uhlig, F.; Vodopianov, A. S.; Watts, D. P.; Yu, W.: **Particle identification for the PANDA detector.** *Nucl. Instrum. Methods Phys. Res. Sect. A-Accel. Spectrom. Dect. Assoc. Equip.* **639**(1): 169–172, 2011. DOI: 10.1016/j.nima.2010.10.116

227 Schwiening, J.*: **The barrel DIRC detector for the PANDA experiment at FAIR.** *Nucl. Instrum. Methods Phys. Res. Sect. A-Accel. Spectrom. Dect. Assoc. Equip.* **639**(1): 315–318, 2011. DOI: 10.1016/j.nima.2010.10.061

228 Seidlitz, M.; Reiter, P.; Dewald, A.; Moller, O.; Bruyneel, B.; Christen, S.; Finke, F.; Fransen, C.; Gorska, M.*; Grawe, H.; Holler, A.; Ilie, G.; Kotthaus, T.; Kudejova, P.; Lenzi, S. M.; Mandal, S.; Melon, B.; Mucher, D.; Regis, J. M.; Saha, B.; von Brentano, P.; Wiens, A.; Zell, K. O.: **Precision lifetime measurements of the first 2(+) and 4(+) states in (56)Cr at the N=32 subshell closure.** *Phys. Rev. C* **84**(3): 034318, 2011. DOI: 10.1103/PhysRevC.84.034318

229 Seitz, B.; Bettoni, D.; Branford, D.; Britting, A.; Carassiti, V.; Cecchi, A.; Cowie, E.; Dodokhof, V. K.; Duren, M.; Eyrich, W.; Fohl, K.; Hayrapetyan, A.; Hill, G.; Hoek, M.; Hohler, R.*; Kaiser, R.; Keri, T.; Lehmann, A.; Lehmann, D.*; Marton, J.; Murray, M.; Montgomery, R. A.; Peters, K.*; Pizzoloto, C.; Rosner, G.; Schmitt, L.*; Schepers, G.*; Schwarz, C.*; Schwiening, J.*; Sfienti, C.; Suzuki, K.; Uhlig, F.; Vodopianov, A. S.; Watts, D.: **Development of DIRC counters for the PANDA experiment at FAIR.** *Nucl. Instrum. Methods Phys. Res. Sect. A-Accel. Spectrom. Dect. Assoc. Equip.* **628**(1): 304–308, 2011. DOI: 10.1016/j.nima.2010.06.341

230 Senger, P.*: **The Compressed Baryonic Matter experiment at FAIR.** *Nucl. Phys. A* **862-63**: 139–145, 2011. DOI: 10.1016/j.nuclphysa.2011.05.032

231 Serwane, F.*; Zurn, G.; Lompe, T.*; Ottenstein, T. B.*; Wenz, A. N.; Jochim, S.*: **Deterministic Preparation of a Tunable Few-Fermion System.** *Science* **332**(6027): 336–338, 2011. DOI: 10.1126/science.1201351

232 Sexty, D.; Gasenzer, T.*; Pawlowski, J.: **Real-time effective-action approach to the Anderson quantum dot.** *Phys. Rev. B* **83**(16): 165315, 2011. DOI: 10.1103/PhysRevB.83.165315

233 Singh, B. S. N.; Liu, Z.; Wadsworth, R.; Grawe, H.; Brock, T. S.; Boutachkov, P.*; Braun, N.; Blazhev, A.; Gorska, M.*; Pietri, S.*; Rudolph, D.; Domingo-Pardo, C.; Steer, S. J.; Atac, A.; Bettermann, L.; Cac-

eres, L.; Eppinger, K.; Engert, T.; Faestermann, T.; Farinon, F.*; Finke, F.; Geibel, K.; Gerl, J.*; Gernhauser, R.; Goel, N.; Gottardo, A.; Grebosz, J.*; Hinke, C.; Hoischen, R.; Ilie, G.; Iwasaki, H.; Jolie, J.; Kaskas, A.; Kojouharov, I.*; Krucken, R.; Kurz, N.; Merchan, E.*; Nociforo, C.*; Nyberg, J.; Pfutzner, M.; Prochazka, A.*; Podolyak, Z.; Regan, P. H.; Reiter, P.; Rinta-Antila, S.; Scholl, C.; Schaffner, H.*; Soderstrom, P. A.; Warr, N.; Weick, H.*; Wollersheim, H. J.*; Woods, P. J.; Nowacki, F.; Sieja, K.: **16(+) Spin-Gap Isomer in (96)Cd.** *Phys. Rev. Lett.* **107**(17): 172502, 2011. DOI: 10.1103/PhysRevLett.107.172502

234 Skokov, V.; Friman, B.; Redlich, K.*: **Quark number fluctuations in the Polyakov loop-extended quark-meson model at finite baryon density.** *Phys. Rev. C* **83**(5): 054904, 2011. DOI: 10.1103/PhysRevC.83.054904

235 Skokov, V.; Morita, K.; Friman, B.*: **Mapping the phase diagram of strongly interacting matter.** *Phys. Rev. D* **83**(7): 071502, 2011. DOI: 10.1103/PhysRevD.83.071502

236 Smponias, T.; Kosmas, T. S.*: **Modelling the equatorial emission in a microquasar.** *Mon. Not. Roy. Astron. Soc.* **412**(2): 1320–1330, 2011. DOI: 10.1111/j.1365-2966.2010.17989.x

237 Sobiczewski, A.; Rozmej, P.: **ESTIMATION OF THE INACCURACY OF CALCULATED MASSES AND FISSION-BARRIER HEIGHTS OF HEAVY NUCLEI.** *Int. J. Mod. Phys. E-Nucl. Phys.* **20**(2): 325–332, 2011. DOI: 10.1142/S0218301311017685

238 Soderstrom, P. A.; Recchia, F.; Nyberg, J.; Al-Adili, A.; Atac, A.; Aydin, S.; Bazzacco, D.; Bednarczyk, P.; Birkenbach, B.; Bortolato, D.; Boston, A. J.; Boston, H. C.; Bruyneel, B.; Bucurescu, D.; Calore, E.; Colosimo, S.; Crespi, F. C. L.; Dosme, N.; Eberth, J.; Farnea, E.; Filmer, F.; Gadea, A.; Gottardo, A.; Grave, X.; Grebosz, J.*; Griffiths, R.; Gulmini, M.; Habermann, T.*; Hess, H.; Jaworski, G.; Jones, P.; Joshi, P.; Judson, D. S.; Kempley, R.; Khaplanov, A.; Legay, E.; Lersch, D.; Ljungvall, J.; Lopez-Martens, A.; Meczynski, W.; Mengoni, D.; Michelagnoli, C.; Molini, P.; Napoli, D. R.; Orlandi, R.; Pascovici, G.; Pullia, A.; Reiter, P.; Sahin, E.; Smith, J. F.; Strachan, J.; Tonev, D.; Unsworth, C.; Ur, C. A.; Valiente-Dobon, J. J.; Veyssiere, C.; Wiens, A.: **Interaction position resolution simulations and in-beam measurements of the AGATA HPGe detectors.** *Nucl. Instrum. Methods Phys. Res. Sect. A-Accel. Spectrom. Dect. Assoc. Equip.* **638**(1): 96–109, 2011. DOI: 10.1016/j.nima.2011.02.089

239 Sonnabend, K.; Savran, D.*; Beller, J.; Bussing, M. A.; Constantinescu, A.; Elvers, M.; Endres, J.; Fritzsche, M.; Glorius, J.; Hasper, J.; Isaak, J.; Löher, B.; Mullner, S.; Pietralla, N.; Romig, C.; Sauerwein, A.; Schnorrenberger, L.; Walzlein, C.; Zilges, A.; Zweidinger, M.: **The Darmstadt High-Intensity Photon Setup (DHIPS) at the S-DALINAC.** *Nucl. Instrum. Methods Phys. Res. Sect. A-Accel. Spectrom. Dect. Assoc. Equip.* **640**(1): 6–12, 2011. DOI: 10.1016/j.nima.2011.02.107

240 Steer, S. J.; Podolyak, Z.; Pietri, S.*; Gorska, M.*; Grawe, H.; Maier, K. H.; Regan, P. H.; Rudolph, D.; Garnsworthy, A. B.; Hoischen, R.; Gerl, J.*; Wollersheim, H. J.*; Becker, F.; Bednarczyk, P.; Caceres, L.; Doornenbal, P.; Geissel, H.*; Grebosz, J.*; Kelic-Heil, A.*; Kojouharov, I.*; Kurz, N.; Montes, F.; Prokopwicz, W.; Saito, T.; Schaffner, H.*; Tashenov, S.; Heinz, A.; Pfutzner, M.; Kurtukian-Nieto, T.; Benzoni, G.; Jungclaus, A.; Balabanski, D. L.; Bowry, M.; Brandau, C.; Brown, A.; Bruce, A. M.; Catford, W. N.; Cullen, I. J.; Dombradi, Z.; Estevez, M. E.; Gelletly, W.; Ilie, G.; Jolie, J.; Jones, G. A.; Kmiecik, M.; Kondev, F. G.; Krucken, R.; Lalkovski, S.; Liu, Z.; Maj, A.; Myalski, S.; Schwertel, S.; Shizuma, T.; Walker, P. M.; Werner-Malento, E.; Wieland, O.: **Isomeric states observed in heavy neutron-rich nuclei populated in the fragmentation of a (208)Pb beam.** *Phys. Rev. C* **84**(4): 044313, 2011. DOI: 10.1103/PhysRevC.84.044313

241 Steinheimer, J.; Schramm, S.; Stöcker, H. *: **Hadronic SU(3) parity doublet model for dense matter and its extension to quarks and the strange equation of state.** *Phys. Rev. C* **84**(4): 045208, 2011. DOI: 10.1103/PhysRevC.84.045208

242 Steinheimer, J.; Schramm, S.; Stoecker, H.*: **An effective chiral hadron-quark equation of state.** *J. Phys. G-Nucl. Part. Phys.* **38**(3): 035001, 2011. DOI: 10.1088/0954-3899/38/3/035001

243 Stoecker, H.; Sturm, C.: **The FAIR start.** *Nucl. Phys. A* **855**(1): 506–509, 2011. DOI: 10.1016/j.nuclphysa.2011.02.117

244 Stoica, S.; Lutz, M. F. M.*; Scholten, O.: **Kinematical constraints in fermion-antifermion systems.** *Phys. Rev. D* **84**(12): 125001, 2011. DOI: 10.1103/PhysRevD.84.125001

245 Streicher, B.; Egelhof, P.*; Ilieva, S.*; Kalantar-Nayestanaki, N.; Kollmus, H.; Kroll, T.; Mutterer, M.; von Schmid, M.; Trager, M.: **Application of a double-sided silicon-strip detector as a differential pumping barrier for NESR experiments at FAIR.** *Nucl. Instrum. Methods Phys. Res. Sect. A-Accel. Spectrom. Dect. Assoc. Equip.* **654**(1): 604–607, 2011. DOI: 10.1016/j.nima.2011.06.075

246 StÃ¶cker, H.; Sturm, C.*: **The Facility for Antiproton and Ion Research FAIR Cosmic Matter in the Laboratory.** *Nucl. Phys. A* **862-63**: 92–97, 2011. DOI: 10.1016/j.nuclphysa.2011.05.025

247 Türler, A.; Eichler, R.; Gaggeler, H. W.; Yakushev, A.*; Düllmann, C. E.*; Schädel, M.*; Dmitriev, S. N.; Kratz, J. V.; Moody, K. J.; Nitsche, H.; Trautmann, N.: **Chemical experiments with element 114.** *Abstr. Pap. Am. Chem. Soc.* **241**: No Page ?

248 Tagliente, G.; Milazzo, P. M.; Fujii, K.; Abbondanno, U.; Aerts, G.; Alvarez, H.; Alvarez-Velarde, F.; Andriamonje, S.; Andrzejewski, J.; Audouin, L.; Badurek, G.; Baumann, P.; Becvar, F.; Belloni, F.; Berthoumieux, E.; Calvino, F.; Calviani, M.; Cano-Ott, D.; Capote, R.; Carrapico, C.; Cennini, P.; Chepel, V.; Chiaveri, E.; Colonna, N.; Cortes, G.; Couture, A.; Dahlfors, M.; David, S.; Dillmann, I.*; Domingo-Pardo, C.; Dridi, W.; Duran, I.; Eleftheriadis, C.; Embid-Segura, M.; Ferrari, A.; Ferreira-Marques, R.; Furman, W.; Goncalves, I.; Gonzalez-Romero, E.; Gramegna, F.; Guerrero, C.; Gunsing, F.; Haas, B.; Haight, R.; Heil, M.*; Herrera-Martinez, A.; Jericha, E.; Kappeler, F.; Kadi, Y.; Karadimos, D.; Karamanis, D.; Kerveno, M.; Kossionides, E.; Krticka, M.; Lamboudis, C.; Leeb, H.; Lindote, A.; Lopes, I.; Lukic, S.; Marganiec, J.*; Marrone, S.; Martinez, T.; Massimi, C.; Mastinu, P.; Mengoni, A.; Moreau, C.; Mosconi, M.; Neves, F.; Oberhummer, H.; O'Brien, S.; Pancin, J.; Papachristodoulou, C.; Papadopoulos, C.; Paradela, C.; Patronis, N.; Pavlik, A.; Pavlopoulos, P.; Perrot, L.; Pigni, M. T.; Plag, R.*; Plompen, A.; Plukis, A.; Poch, A.; Praena, J.; Pretel, C.; Quesada, J.; Reifarth, R.*; Rosetti, M.; Rubbia, C.; Rudolf, G.; Rullhusen, P.; Salgado, J.; Santos, C.; Sarchiapone, L.; Savvidis, I.; Stephan, C.; Tain, J. L.; Tassan-Got, L.; Tavora, L.; Terlizzi, R.; Vannini, G.; Vaz, P.; Ventura, A.; Villamarin, D.; Vincente, M. C.; Vlachoudis, V.; Vlastou, R.; Voss, F.; Walter, S.; Wiescher, M.; Wisshak, K.: **(96)Zr(n,gamma) measurement at the n_TOF facility at CERN.** *Phys. Rev. C* **84**(5): 055802, 2011. DOI: 10.1103/PhysRevC.84.055802

249 Tamii, A.; Poltoratska, I.; von Neumann-Cosel, P.; Fujita, Y.; Adachi, T.; Bertulani, C. A.; Carter, J.; Dozono, M.; Fujita, H.; Fujita, K.; Hatanaka, K.; Ishikawa, D.; Itoh, M.; Kawabata, T.; Kalmykov, Y.; Krumbholz, A. M.; Litvinova, E.; Matsubara, H.; Nakanishi, K.; Neveling, R.; Okamura, H.; Ong, H. J.; Ozel-Tashenov, B.; Ponomarev, V. Y.; Richter, A.; Rubio, B.; Sakaguchi, H.; Sakemi, Y.; Sasamoto, Y.; Shimbara, Y.; Shimizu, Y.; Smit, F. D.; Suzuki, T.; Tameshige, Y.; Wambach, J.; Yamada, R.; Yosoi, M.; Zenihiro, J.: **Complete Electric Dipole Response and the Neutron Skin in (208)Pb.** *Phys. Rev. Lett.* **107**(6): 062502, 2011. DOI: 10.1103/PhysRevLett.107.062502

250 Tandecki, M.; Beck, D.*; Beck, M.; Brand, H.*; Breitenfeldt, M.; De Leebeeck, V.; Friedag, P.; Herlert, A.; Kozlov, V.; Mader, J.; Roccia, S.; Soti, G.; Traykov, E.; Van Gorp, S.; Wauters, F.; Weinheimer, C.; Zakoucky, D.; Severijns, N.: **Computer controls for the WITCH experiment.** *Nucl. Instrum. Methods Phys. Res. Sect. A-Accel. Spectrom. Dect. Assoc. Equip.* **629**(1): 396–405, 2011. DOI: 10.1016/j.nima.2010.10.111

251 Tarrio, D.; Tassan-Got, L.; Audouin, L.; Berthier, B.; Duran, I.; Ferrant, L.; Isaev, S.; Le Naour, C.; Paradela, C.; Stephan, C.; Trubert, D.; Abbondanno, U.; Aerts, G.; Alvarez-Velarde, F.; Andriamonje, S.; Andrzejewski, J.; Assimakopoulos, P.; Badurek, G.; Baumann, P.; Becvar, F.; Belloni, F.; Berthoumieux, E.; Calvino, F.; Calviani, M.; Cano-Ott, D.; Capote, R.; Carrapico, C.; de Albornoz, A. C.; Cennini, P.; Chepel, V.; Chiaveri, E.; Colonna, N.; Cortes, G.; Couture, A.; Cox, J.; Dahlfors, M.; David, S.; Dillmann, I.*; Dolfini, R.; Domingo-Pardo, C.; Dridi, W.; Eleftheriadis, C.; Embid-Segura, M.; Ferrari, A.; Ferreira-Marques, R.; Fitzpatrick, L.; Frais-Koelbl, H.; Fujii, K.; Furman, W.; Goncalves, I.; Gonzalez-Romero, E.; Goverdovski, A.; Gramegna, F.; Griesmayer, E.; Guerrero, C.; Gunsing, F.; Haas, B.; Haight, R.; Heil, M.*; Herrera-Martinez, A.; Igashira, M.; Jericha, E.; Kadi, Y.; Kappeler, F.; Karadimos, D.; Karamanis, D.; Kerveno, M.; Ketlerov, V.; Koehler, P.; Konovalov, V.; Kossionides, E.; Krticka, M.; Lampoudis, C.; Leeb, H.; Lederer, C.; Lindote, A.; Lopes, I.; Losito, R.; Lozano, M.; Lukic, S.; Marganiec, J.*; Marques, L.; Marrone, S.; Martinez, T.; Massimi, C.; Mastinu, P.; Mendoza, E.; Mengoni, A.; Milazzo, P. M.; Moreau, C.; Mosconi, M.; Neves, F.; Oberhummer, H.; O'Brien, S.; Oshima, M.; Pancin, J.; Papachristodoulou, C.; Papadopoulos, C.; Patronis, N.; Pavlik, A.; Pavlopoulos, P.; Perrot, L.; Pigni, M. T.; Plag, R.*; Plompen, A.; Plukis, A.; Poch, A.; Praena, J.; Pretel, C.; Quesada, J.; Rauscher, T.; Reifarth, R.*; Rosetti, M.; Rubbia, C.; Rudolf, G.; Rullhusen, P.; Salgado, J.; Santos, C.; Sarchiapone, L.; Sarmento, R.; Savvidis, I.; Tagliente, G.; Tain, J. L.; Tavora, L.; Terlizzi, R.; Vannini, G.; Vaz, P.; Ventura, A.; Villamarin, D.; Vlachoudis, V.; Vlastou, R.; Voss, F.; Walter, S.; Wendler, H.; Wiescher, M.; Wisshak, K.: **Neutron-induced fission cross section of (nat)Pb and (209)Bi from threshold to 1 GeV: An improved parametrization.** *Phys. Rev. C* **83**(4): 044620, 2011. DOI: 10.1103/PhysRevC.83.044620

252 Thielemann, F. K.; Arcones, A.*; Kappeli, R.; Liebendorfer, M.; Rauscher, T.; Winteler, C.; Frohlich, C.; Dillmann, I.*; Fischer, T.; Martinez-Pinedo, G.*; Langanke, K.*; Farouqi, K.; Kratz, K. L.; Panov, I.; Korneev, I. K.: **What are the astrophysical sites for the r-process and the production of heavy elements?.** *Prog. Part. Nucl. Phys.* **66**(2): 346–353, 2011. DOI: 10.1016/j.ppnp.2011.01.032

253 Tsakstara, V.; Kosmas, T. S.*: **Analyzing astrophysical neutrino signals using realistic nuclear structure calculations and the convolution procedure.** *Phys. Rev. C* **84**(6): 064620, 2011. DOI: 10.1103/PhysRevC.84.064620

254 Tsakstara, V.; Kosmas, T. S.*: **Low-energy neutral-current neutrino scattering on (128,130)Te isotopes.** *Phys. Rev. C* **83**(5): 054612, 2011. DOI: 10.1103/PhysRevC.83.054612

255 Tsakstara, V.; Kosmas, T. S.; Sinatkas, J.: **Neutrino and anti-neutrino scattering off Zn isotopes with quasiparticle RPA calculations.** *Prog. Part. Nucl. Phys.* **66**(2): 430–435, 2011. DOI: 10.1016/j.ppnp.2011.01.046

256 Tsakstara, V.; Kosmas, T. S.; Wambach, J.*: **Studying**

low-energy astrophysical neutrinos with neutrino nucleus cross-section calculations and beta beam neutrino spectra. *Prog. Part. Nucl. Phys.* **66**(2): 424–429, 2011. DOI: 10.1016/j.ppnp.2011.01.045

257 Tsukiyama, K.; Bogner, S. K.; Schwenk, A.*: **In-Medium Similarity Renormalization Group For Nuclei.** *Phys. Rev. Lett.* **106**(22): 222502, 2011. DOI: 10.1103/PhysRevLett.106.222502

258 Tumino, A.; Spitaleri, C.; Mukhamedzhanov, A. M.; Typel, S.*; Aliotta, M.; Burjan, V.; del Santo, M. G.; Kiss, G. G.; Kroha, V.; Hons, Z.; La Cognata, M.; Lamia, L.; Mrazek, J.; Pizzone, R. G.; Piskor, S.; Rapisarda, G. G.; Romano, S.; Sergi, M. L.; Sparta, R.: **Low-energy d + d fusion reactions via the Trojan Horse Method (vol 700, pg 111, 2011).** *Phys. Lett. B* **705**(5): 546–546, 2011. DOI: 10.1016/j.physletb.2011.10.056

259 Tumino, A.; Spitaleri, C.; Mukhamedzhanov, A. M.; Typel, S.*; Aliotta, M.; Burjan, V.; del Santo, M. G.; Kiss, G. G.; Kroha, V.; Hons, Z.; La Cognata, M.; Lamia, L.; Mrazek, J.; Pizzone, R. G.; Piskor, S.; Rapisarda, G. G.; Romano, S.; Sergi, M. L.; Sparta, R.: **Low-energy d plus d fusion reactions via the Trojan Horse Method.** *Phys. Lett. B* **700**(2): 111–115, 2011. DOI: 10.1016/j.physletb.2011.05.001

260 Tumino, A.; Spitaleri, C.; Mukhamedzhanov, A.; Typel, S.*; Aliotta, M.; Burjan, V.; del Santo, M. G.; Kiss, G. G.; Kroha, V.; Hons, Z.; La Cognata, M.; Lamia, L.; Mrazek, J.; Pizzone, R. G.; Piskor, S.; Rapisarda, G. G.; Romano, S.; Sergi, M. L.; Sparta, R.: **Indirect Study of the (2)H(d,p)(3)H and (2)H(d,n)(3)He Reactions at Astrophysical Energies via the Trojan Horse Method.** *Few-Body Syst.* **50**(1-4): 323–325, 2011. DOI: 10.1007/s00601-010-0213-6

261 Vantournhout, K.*; Jachowicz, N.; Ryckebusch, J.: **Doubly periodic structure for the study of inhomogeneous bulk fermion matter with spatial localizations.** *Phys. Rev. C* **84**(3): 032801, 2011. DOI: 10.1103/PhysRevC.84.032801

262 Vantournhout, K.*; Neff, T.*; Feldmeier, H.*; Jachowicz, N.; Ryckebusch, J.: **Towards a quantal dynamical simulation of the neutron star's crust.** *Prog. Part. Nucl. Phys.* **66**(2): 271–275, 2011. DOI: 10.1016/j.ppnp.2011.01.019

263 Vaquero, N. L.; Rodriguez, T. R.*; Egido, J. L.: **On the impact of large amplitude pairing fluctuations on nuclear spectra.** *Phys. Lett. B* **704**(5): 520–526, 2011. DOI: 10.1016/j.physletb.2011.09.073

264 Vaquero, N. L.; Rodriguez, T. R.*; Egido, J. L.: **On the impact of large amplitude pairing fluctuations on nuclear spectra (vol 704, pg 520, 2011).** *Phys. Lett. B* **705**(5): 543–543, 2011. DOI: 10.1016/j.physletb.2011.10.019

265 Vascon, A.; Düllmann, C. E.*; Eberhardt, K.; Kindler, B.; Lommel, B.; Runke, J.*: **Toward large-area targets for "TRAKULA".** *Nucl. Instrum. Methods Phys. Res. Sect. A-Accel. Spectrom. Dect. Assoc. Equip.* **655**(1): 72–79, 2011. DOI: 10.1016/j.nima.2011.06.024

266 Venhart, M.; Heßberger, F. P.*; Ackermann, D.*; Antalic, S.; Gray-Jones, C.; Greenlees, P. T.; Heinz, S.*; Herzberg, R. D.; Hofmann, S.*; Ketelhut, S.; Kindler, B.; Kojouharov, I.*; Leino, M.; Lommel, B.; Mann, R.; Papadakis, P.; Rostron, D.; Rudolph, D.; Saro, S.; Sulignano, B.: **Decay study of (246)Fm at SHIP.** *Eur. Phys. J. A* **47**(2): 20, 2011. DOI: 10.1140/epja/i2011-11020-9

267 von Schmid, M.; Egelhof, P.*; Eremin, V.; Gernhäuser, R.; Kroll, T.; Mutterer, M.; Pietralla, N.; Streicher, B.; Weber, M.: **First application of pulse-shape analysis to silicon micro-strip detectors.** *Nucl. Instrum. Methods Phys. Res. Sect. A-Accel. Spectrom. Dect. Assoc. Equip.* **629**(1): 197–201, 2011. DOI: 10.1016/j.nima.2010.10.096

268 Voskresensky, D. N.*: **Hydrodynamics of resonances.** *Nucl. Phys. A* **849**(1): 120–146, 2011. DOI: 10.1016/j.nuclphysa.2010.11.007

269 Walker, J.; Jungclaus, A.; Leske, J.; Speidel, K. H.; Ekstrom, A.; Boutachkov, P.*; Cederkall, J.; Doornenbal, P.; Gerl, J.*; Gernhauser, R.; Goel, N.; Gorska, M.*; Kojouharov, I.*; Maier-Komor, P.; Modamio, V.; Naqvi, F.*; Pietralla, N.; Pietri, S.*; Prokopowicz, W.; Schaffner, H.*; Schwengner, R.; Wollersheim, H. J.*: **Magnetic moments of the first excited 2(+) states in the semi-magic (112,114,116,122,124)Sn isotopes.** *Phys. Rev. C* **84**(1): 014319, 2011. DOI: 10.1103/PhysRevC.84.014319

270 Walz, C.; Fujita, H.; Krugmann, A.; von Neumann-Cosel, P.; Pietralla, N.; Ponomarev, V. Y.; Scheikh-Obeid, A.; Wambach, J.*: **Origin of Low-Energy Quadrupole Collectivity in Vibrational Nuclei.** *Phys. Rev. Lett.* **106**(6): 062501, 2011. DOI: 10.1103/PhysRevLett.106.062501

271 Weinrich, U.*: **Recent advances for ion beam therapy accelerators using synchrotrons.** *Nucl. Instrum. Methods Phys. Res. Sect. B-Beam Interact. Mater. Atoms* **269**(24): 2879–2881, 2011. DOI: 10.1016/j.nimb.2011.04.045

272 Wollersheim, H. J.*: **RELATIVISTIC COULOMB EXCITATION: FROM RISING TO PreSPEC.** *Acta Phys. Pol. B* **42**(3-4): 705–716, 2011. DOI: 10.5506/APhysPolB.42.705

273 Yakorev, D.; Aumann, T.*; Bemmerer, D.; Boretzky, K.*; Caesar, C.*; Ciobanu, M.; Cowan, T.; Elekes, Z.; Elvers, M.; Diaz, D. G.; Hannaske, R.; Hehner, J.; Heil, M.*; Kempe, M.; Maroussov, V.; Nusair, O.; Simon, H.*; Sobiella, M.; Stach, D.; Wagner, A.; Zilges, A.: **Prototyping and tests for an MRPC-based time-of-flight detector for 1 GeV neutrons.** *Nucl. Instrum. Methods Phys. Res.*

Sect. A-Accel. Spectrom. Dect. Assoc. Equip. **654**(1): 79–87, 2011. DOI: 10.1016/j.nima.2011.05.031

274 Zhi, Q.; Langanke, K.*; Martinez-Pinedo, G.*; Nowacki, F.; Sieja, K.: **The (76)Se Gamow-Teller strength distribution and its importance for stellar electron capture rates.** *Nucl. Phys. A* **859**(1): 172–184, 2011. DOI: 10.1016/j.nuclphysa.2011.04.010

WoS publications to the programme 'Large-scale facilities for research with photons, neutrons and ions' published in 2011

T. Litvinova[1]
[1]GSI, Darmstadt, Germany

001 Afra, B.; Lang, M.; Rodriguez, M. D.; Zhang, J.; Giulian, R.; Kirby, N.; Ewing, R. C.; Trautmann, C.*; Toulemonde, M.; Kluth, P.: **Annealing kinetics of latent particle tracks in Durango apatite.** *Phys. Rev. B* **83**(6): 064116, 2011. DOI: 10.1103/PhysRevB.83.064116

002 Ali, M.*; Nasir, S.*; Nguyen, Q. H.*; Sahoo, J. K.; Tahir, M. N.; Tremel, W.; Ensinger, W.*: **Metal Ion Affinity-based Biomolecular Recognition and Conjugation inside Synthetic Polymer Nanopores Modified with Iron-Terpyridine Complexes.** *J. Am. Chem. Soc.* **133**(43): 17307–17314, 2011. DOI: 10.1021/ja205042t

003 Ali, M.*; Ramirez, P.; Tahir, M. N.; Mafe, S.; Siwy, Z.; Neumann, R.*; Tremel, W.; Ensinger, W.: **Biomolecular conjugation inside synthetic polymer nanopores via glycoprotein-lectin interactions.** *Nanoscale* **3**(4): 1894–1903, 2011. DOI: 10.1039/c1nr00003a

004 Ali, M.*; Tahir, M. N.; Siwy, Z.; Neumann, R.*; Tremel, W.; Ensinger, W.: **Hydrogen Peroxide Sensing with Horseradish Peroxidase-Modified Polymer Single Conical Nanochannels.** *Anal. Chem.* **83**(5): 1673–1680, 2011. DOI: 10.1021/ac102795a

005 Amaro, P.; Surzhykov, A.*; Parente, F.; Indelicato, P.; Santos, J. P.: **Calculation of two-photon decay rates of hydrogen-like ions by using B-polynomials.** *J. Phys. A-Math. Theor.* **44**(24): 245302, 2011. DOI: 10.1088/1751-8113/44/24/245302

006 Anicin, I. V.; Pejovic, V.; Pavicevic, M. K.; Amthauer, G.; Boev, B.; Bosch, F.*; Brüchle, W.*; Djurcic, Z.; Henning, W. F.; Faestermann, T.; Jelenkovic, R.; Niedermann, S.; Weiss, A.: **ON THE POSSIBILITY TO SIMULTANEOUSLY DETERMINE THE LONG-TERM AVERAGE FLUXES OF SOLAR pp-NEUTRINOS AND COSMIC RAY MUONS.** *Mod. Phys. Lett. A* **26**(17): 1267–1271, 2011. DOI: 10.1142/S0217732311035626

007 Artemyev, A. N.*; McConnell, S. R.*; Surzhykov, A.*; Najjari, B.; Voitkiv, A. B.: **Coulomb excitation of highly charged projectile ions in relativistic collisions with diatomic molecules.** *Phys. Rev. A* **84**(4): 042709, 2011. DOI: 10.1103/PhysRevA.84.042709

008 Aumayr, F.; Facsko, S.; El-Said, A. S.; Trautmann, C.*; Schleberger, M.: **Single ion induced surface nanostructures: a comparison between slow highly charged and swift heavy ions.** *J. Phys.-Condes. Matter* **23**(39): 393001, 2011. DOI: 10.1088/0953-8984/23/39/393001

009 Aurand, B.*; Kuschel, S.; Rodel, C.; Heyer, M.; Wunderlich, F.; Jackel, O.; Kaluza, M. C.; Paulus, G. G.; Kühl, T.*: **Creating circularly polarized light with a phase-shifting mirror.** *Opt. Express* **19**(18): 17151–17157, 2011.

010 Aurand, B.*; Seres, J.; Bagnoud, V.*; Ecker, B.*; Hochhaus, D. C.*; Neumayer, P.*; Seres, E.; Spielmann, C.; Zielbauer, B.*; Zimmer, D.*; Kuehl, T.*: **Laser driven X-ray parametric amplification in neutral gases-a new brilliant light source in the XUV.** *Nucl. Instrum. Methods Phys. Res. Sect. A-Accel. Spectrom. Dect. Assoc. Equip.* **653**(1): 130–133, 2011. DOI: 10.1016/j.nima.2010.12.208

011 Avgoulea, M.; Gangrsky, Y. P.; Marinova, K. P.; Zemlyanoi, S. G.; Fritzsche, S.*; Iablonskyi, D.; Barbieri, C.; Simpson, E. C.; Stevenson, P. D.; Billowes, J.; Campbell, P.; Cheal, B.; Tordoff, B.; Bissell, M. L.; Forest, D. H.; Gardner, M. D.; Tungate, G.; Huikari, J.; Nieminen, A.; Penttila, H.; Aysto, J.: **Nuclear charge radii and electromagnetic moments of radioactive scandium isotopes and isomers.** *J. Phys. G-Nucl. Part. Phys.* **38**(2): 025104, 2011. DOI: 10.1088/0954-3899/38/2/025104

012 Baake, O.; Seidl, T.*; Hossain, U. H.*; Delgado, A. O.*; Bender, M.*; Severin, D.*; Ensinger, W.: **An apparatus for in situ spectroscopy of radiation damage of polymers by bombardment with high-energy heavy ions.** *Rev. Sci. Instrum.* **82**(4): 045103, 2011. DOI: 10.1063/1.3571301

013 Beilmann, C.; Mokler, P. H.; Bernitt, S.; Keitel, C. H.; Ullrich, J.; Lopez-Urrutia, J. R. C.; Harman, Z.*: **Prominent Higher-Order Contributions to Electronic Recombination.** *Phys. Rev. Lett.* **107**(14): 143201, 2011. DOI: 10.1103/PhysRevLett.107.143201

014 Bernhardt, D.; Brandau, C.*; Harman, Z.*; Kozhuharov, C.*; Muller, A.; Scheid, W.; Schippers, S.; Schmidt, E. W.; Yu, D.; Artemyev, A. N.*; Tupitsyn, I. I.; Böhm, S.; Bosch, F.*; Currell, F. J.; Franzke, B.*; Gumberidze, A.*; Jacobi, J.; Mokler, P. H.; Nolden, F.*; Spillman, U.*; Stachura, Z.; Steck, M.*; Stöhlker, Th.*: **Breit interaction in dielectronic recombination of hydrogenlike uranium.** *Phys. Rev. A* **83**(2): 020701, 2011. DOI: 10.1103/PhysRevA.83.020701

015 Boehme, M.*; Voelklein, F.; Ensinger, W.: **Low cost chemical sensor device for supersensitive pentaerythritol tetranitrate (PETN) explosives detection based on titanium dioxide nanotubes.** *Sens. Actuator B-Chem.* **158**(1): 286–291, 2011. DOI: 10.1016/j.snb.2011.06.020

016 Bondarevskaya, A. A.; Labzowsky, L. N.; Prozorov, A. A.; Plunien, G.; Liesen, D.*; Bosch, F.*: **Linear polarization of x-ray photons in HFQ transitions of polarized He-like ions with application to the search for parity nonconservation effects.** *Phys. Scr.* **T144**: 014007, 2011. DOI: 10.1088/0031-8949/2011/T144/014007

017 Bondarevskaya, A.; Prozorov, A.; Labzowsky, L.; Plunien, G.; Liesen, D.*; Bosch, F.*: **Theory of the polarization of highly charged ions in storage rings: Production, preservation, observation and application to the search for a violation of the fundamental symmetries.** *Phys. Rep.-Rev. Sec. Phys. Lett.* **507**(1): 1–42, 2011. DOI: 10.1016/j.physrep.2011.06.001

018 Borowska, L.; Fritzsche, S.*; Kik, P. G.; Masunov, A. E.: **Near-field enhancement of infrared intensities for $f - f$ transitions in Er^{3+} ions close to the surface of silicon nanoparticles.** *J. Mol. Model.* **17**(3): 423–428, 2011. DOI: 10.1007/s00894-010-0708-6

019 Botermann, B.; Novotny, C.; Bing, D.; Geppert, C.*; Gwinner, G.; Hänsch, T. W.; Huber, G.; Karpuk, S.; Kühl, T.*; Nörtershäuser, W.; Reinhardt, S.; Saathoff, G.; Schwalm, D.; Stöhlker, T.*; Wolf, A.: **Preparatory measurements for a test of time dilation in the ESR.** *Can. J. Phys.* **89**(1): 85–93, 2011. DOI: 10.1139/P10-117

020 Brantov, A. V.; Bychenkov, V. Y.; Popov, K. I.; Fedosejevs, R.; Rozmus, W.; Schlegel, T.*: **Comparative analysis of laser-triggered proton generation from overdense and low-density targets.** *Nucl. Instrum. Methods Phys. Res. Sect. A-Accel. Spectrom. Dect. Assoc. Equip.* **653**(1): 62–65, 2011. DOI: 10.1016/j.nima.2011.01.112

021 Burris-Mog, T.; Harres, K.; Nürnberg, F.; Busold, S.; Bussmann, M.; Deppert, O.; Hoffmeister, G.; Joost, M.; Sobiella, M.; Tauschwitz, A.*; Zielbauer, B.*; Bagnoud, V.*; Herrmannsdoerfer, T.; Roth, M.; Cowan, T. E.: **Laser accelerated protons captured and transported by a pulse power solenoid.** *Phys. Rev. Spec. Top.-Accel. Beams* **14**(12): 121301, 2011. DOI: 10.1103/PhysRevSTAB.14.121301

022 Böhme, M.*; Ensinger, W.: **Fabrication of Zinc Oxide Nanotubes by Chemical Bath Deposition Using Ion Track-Etched Templates.** *IEEE Trans. Nanotechnol.* **10**(1): 63–69, 2011. DOI: 10.1109/TNANO.2010.2057443

023 Cocolios, T. E.; Dexters, W.; Seliverstov, M. D.; Andreyev, A. N.; Antalic, S.; Barzakh, A. E.; Bastin, B.; Büscher, J.; Darby, I. G.; Fedorov, D. V.; Fedosseyev, V. N.; Flanagan, K. T.; Franchoo, S.; Fritzsche, S.*; Huber, G.; Huyse, M.; Keupers, M.; Köster, U.; Kudryavtsev, Y.; Mane, E.; Marsh, B. A.; Molkanov, P. L.; Page, R. D.; Sjoedin, A. M.; Stefan, I.; Van de Walle, J.; Van Duppen, P.; Venhart, M.; Zemlyanoy, S. G.; Bender, M.; Heenen, P. H.: **Early Onset of Ground State Deformation in Neutron Deficient Polonium Isotopes.** *Phys. Rev. Lett.* **106**(5): 052503, 2011. DOI: 10.1103/PhysRevLett.106.052503

024 De Filippo, E.; Lanzano, G.; Amorini, F.; Geraci, E.; Grassi, L.; La Guidara, E.; Lombardo, I.; Politi, G.; Rizzo, F.; Russotto, P.; Volant, C.; Hagmann, S.*; Rothard, H.: **Slowing down of fast electrons as probe for charging and decharging dynamics of ion-irradiated insulators.** *Phys. Rev. A* **83**(6): 064901, 2011. DOI: 10.1103/PhysRevA.83.064901

025 Ditter, M.; Stork, H.; Schuster, B.*; Fujara, F.: **Combining one-dimensional stray-field micro-imaging with mechanical field-cycling NMR: A new spectrometer design.** *J. Magn. Reson.* **209**(1): 47–52, 2011. DOI: 10.1016/j.jmr.2010.12.009

026 Eibach, M.; Beyer, T.; Blaum, K.; Block, M.*; Eberhardt, K.; Herfurth, F.*; Ketelaer, J.; Nagy, S.*; Neidherr, D.*; Nörtershäuser, W.*; Smorra, C.: **First investigation of phase-shifted Ramsey excitation in Penning trap mass spectrometry.** *Int. J. Mass Spectrom.* **303**(1): 27–30, 2011. DOI: 10.1016/j.ijms.2010.12.006

027 El-Said, A. S.; Wilhelm, R. A.; Heller, R.; Facsko, S.; Trautmann, C.*; Aumayr, F.: **Surface nanostructuring of $SrTiO_3$ single crystals by slow highly charged ions and swift heavy ions.** *Nucl. Instrum. Methods Phys. Res. Sect. B-Beam Interact. Mater. Atoms* **269**(11): 1234–1237, 2011. DOI: 10.1016/j.nimb.2010.10.020

028 Eliseev, S.; Goncharov, M.; Blaum, K.; Block, M.*; Droese, C.*; Herfurth, F.*; Minaya Ramirez, E.*; Novikov, Y. N.; Schweikhard, L.; Shabaev, V. M.; Tupitsyn, I. I.; Zuber, K.; Zubova, N. A.: **Multiple-resonance phenomenon in neutrinoless double-electron capture.** *Phys. Rev. C* **84**(1): 012501, 2011. DOI: 10.1103/PhysRevC.84.012501

029 Eliseev, S.; Nesterenko, D.; Blaum, K.; Block, M.*; Droese, C.*; Herfurth, F.*; Minaya Ramirez, E.*; Novikov, Y. N.; Schweikhard, L.; Zuber, K.: **Q values for neutrinoless double-electron capture in ^{96}Ru, ^{162}Er, and ^{168}Yb.** *Phys. Rev. C* **83**(3): 038501, 2011. DOI: 10.1103/PhysRevC.83.038501

030 Eliseev, S.; Roux, C.; Blaum, K.; Block, M.*; Droese, C.*; Herfurth, F.*; Kluge, H. J.*; Krivoruchenko, M. I.; Novikov, Yu. N.; Minaya Ramirez, E.*; Schweikhard, L.; Shabaev, V. M.; Simkovic, F.; Tupitsyn, I. I.; Zuber, K.; Zubova, N. A.: **Resonant Enhancement of Neutrinoless Double-Electron Capture in ^{152}Gd.** *Phys. Rev. Lett.* **106**(5): 052504, 2011. DOI: 10.1103/PhysRevLett.106.052504

031 Eliseev, S.; Roux, C.; Blaum, K.; Block, M.*; Droese, C.*; Herfurth, F.*; Kretzschmar, M.;

Krivoruchenko, M. I.; Minaya Ramirez, E.*; Novikov, Y. N.; Schweikhard, L.; Shabaev, V. M.; Simkovic, F.; Tupitsyn, I. I.; Zuber, K.; Zubova, N. A.: **Octupolar-Excitation Penning-Trap Mass Spectrometry for Q-Value Measurement of Double-Electron Capture in ^{164}Er.** *Phys. Rev. Lett.* **107**(15): 152501, 2011. DOI: 10.1103/PhysRevLett.107.152501

032 Enculescu, M.; Neumann, R.*: **Luminescent Dye-Doped KAP Nanorods Obtained by Template Assisted Crystallization.** *J. Nanosci. Nanotechnol.* **11**(5): 3943–3948, 2011. DOI: 10.1166/jnn.2011.3832

033 Ferro, F.*; Artemyev, A.*; Surzhykov, A.*; Stöhlker, T.*: **Hyperfine interaction effects on the $(1s2p)^3P_1$-$(1s2s)^1S_0$ energy splitting in He-like ions for parity nonconservation studies.** *Can. J. Phys.* **89**(1): 73–77, 2011. DOI: 10.1139/P10-069

034 Ferro, F.*; Surzhykov, A.*; Stöhlker, T.*: **Hyperfine transitions in He-like ions as a tool for nuclear-spin-dependent parity-nonconservation studies.** *Phys. Rev. A* **83**(5): 052518, 2011. DOI: 10.1103/PhysRevA.83.052518

035 Fluerasu, D.; Bräuning-Demian, A.*; Dumitriu, D.: **MEASUREMENTS WITH HEAVY IONS ON POLYCRYSTALLINE CVD - DIAMOND.** *Rom. J. Phys.* **56**(1-2): 80–85, 2011.

036 Fratini, F.*; Tichy, M. C.; Jahrsetz, T.*; Buchleitner, A.; Fritzsche, S.*; Surzhykov, A.*: **Quantum correlations in the two-photon decay of few-electron ions.** *Phys. Rev. A* **83**(3): 032506, 2011. DOI: 10.1103/PhysRevA.83.032506

037 Fratini, F.*; Trotsenko, S.*; Tashenov, S.*; Stöhlker, T.*; Surzhykov, A.*: **Photon-photon polarization correlations as a tool for studying parity nonconservation in heliumlike uranium.** *Phys. Rev. A* **83**(5): 052505, 2011. DOI: 10.1103/PhysRevA.83.052505

038 Fritzsche, S.*; Grum-Grzhimailo, A. N.; Gryzlova, E. V.; Kabachnik, N. M.: **Sequential two-photon double ionization of the 4d shell in xenon.** *J. Phys. B-At. Mol. Opt. Phys.* **44**(17): 175602, 2011. DOI: 10.1088/0953-4075/44/17/175602

039 Fritzsche, S.*; Surzhykov, A.*; Stöhlker, Th.*: **X-ray emission from highly charged ions following dielectronic recombination: relativistic effects upon angular distributions and polarization.** *Phys. Scr.* **T144**: 014002, 2011. DOI: 10.1088/0031-8949/2011/T144/014002

040 Galow, B. J.; Salamin, Y. I.; Liseykina, T. V.; Harman, Z.*; Keitel, C. H.: **Dense Monoenergetic Proton Beams from Chirped Laser-Plasma Interaction.** *Phys. Rev. Lett.* **107**(18): 185002, 2011. DOI: 10.1103/PhysRevLett.107.185002

041 George, S.; Blaum, K.; Block, M.*; Breitenfeldt, M.; Dworschak, M.*; Herfurth, F.*; Herlert, A.; Kowalska, M.; Kretzschmar, M.; Minaya Ramirez, E.*; Neidherr, D.; Schwarz, S.; Schweikhard, L.: **Damping effects in Penning trap mass spectrometry.** *Int. J. Mass Spectrom.* **299**(2-3): 102–112, 2011. DOI: 10.1016/j.ijms.2010.09.030

042 Goncharov, M.; Blaum, K.; Block, M.*; Droese, C.*; Eliseev, S.; Herfurth, F.*; Minaya Ramirez, E.*; Novikov, Y. N.; Schweikhard, L.; Zuber, K.: **Probing the nuclides ^{102}Pd, ^{106}Cd, and ^{144}Sm for resonant neutrinoless double-electron capture.** *Phys. Rev. C* **84**(2): 028501, 2011. DOI: 10.1103/PhysRevC.84.028501

043 Gumberidze, A.; Fritzsche, S.*; Hagmann, S.*; Kozhuharov, C.*; Ma, X.; Steck, M.*; Surzhykov, A.*; Warczak, A.; Stöhlker, Th.*: **Magnetic-sublevel population and alignment for the excitation of H- and He-like uranium in relativistic collisions.** *Phys. Rev. A* **84**(4): 042710, 2011. DOI: 10.1103/PhysRevA.84.042710

044 Günther, M. M.; Sonnabend, K.; Brambrink, E.; Vogt, K.*; Bagnoud, V.*; Harres, K.; Roth, M.: **A novel nuclear pyrometry for the characterization of high-energy bremsstrahlung and electrons produced in relativistic laser-plasma interactions.** *Phys. Plasmas* **18**(8): 083102, 2011. DOI: 10.1063/1.3613923

045 Hahn, M.; Grieser, M.; Krantz, C.; Lestinsky, M.*; Müller, A.; Novotny, O.; Repnow, R.; Schippers, S.; Wolf, A.; Savin, D. W.: **STORAGE RING CROSS SECTION MEASUREMENTS FOR ELECTRON IMPACT IONIZATION OF Fe^{12+} FORMING Fe^{13+} AND Fe^{14+}.** *Astrophys. J.* **735**(2): 105, 2011. DOI: 10.1088/0004-637X/735/2/105

046 Harman, Z.*; Salamin, Y. I.; Galow, B. J.; Keitel, C. H.: **Optimizing direct intense-field laser acceleration of ions.** *Phys. Rev. A* **84**(5): 053814, 2011. DOI: 10.1103/PhysRevA.84.053814

047 Herfurth, F.*; Audi, G.; Beck, D.*; Blaum, K.*; Bollen, G.; Delahaye, P.; Dworschak, M.*; George, S.; Guenaut, C.; Kellerbauer, A.; Lunney, D.; Mukherjee, M.*; Rahaman, S.*; Schwarz, S.; Schweikhard, L.; Weber, C.*; Yazidjian, C.: **New mass data for the rp-process above $Z = 32$.** *Eur. Phys. J. A* **47**(6): 75, 2011. DOI: 10.1140/epja/i2011-11075-6

048 Heßling, T.*; Blazevic, A.*; Frank, A.; Kraus, D.; Roth, M.; Schaumann, G.; Schumacher, D.; Stöhlker, T.*; Hoffmann, D. H. H.: **Time- and spectrally resolved measurements of laser-driven hohlraum radiation.** *Phys. Rev. E* **84**(1): 016412, 2011. DOI: 10.1103/PhysRevE.84.016412

049 Jakubassa-Amundsen, D. H.; Surzhykov, A.*: **Polarization correlations in electron-nucleus bremsstrahlung: the short-wavelength limit.** *Eur. Phys. J. D* **62**(2): 177–184, 2011. DOI: 10.1140/epjd/e2011-20053-0

050 Katzenmeyer, A. M.; Leonard, F.; Talin, A. A.; Toimil-Molares, M. E.*; Cederberg, J. G.; Huang, J. Y.; Lensch-Falk, J. L.: **Observation of Space-Charge-Limited Transport in InAs Nanowires.** *IEEE Trans. Nanotechnol.* **10**(1): 92–95, 2011. DOI: 10.1109/TNANO.2010.2062198

051 Kellerbauer, A.; Canali, C.; Fischer, A.; Warring, U.; Fritzsche, S.*: **Isotope shift of the electric-dipole transition in Os(-).** *Phys. Rev. A* **84**(6): 062510, 2011. DOI: 10.1103/PhysRevA.84.062510

052 Kern, C.; Zürch, M.; Petschulat, J.; Pertsch, T.; Kley, B.; Käsebier, T.; Hübner, U.; Spielmann, C.: **Comparison of femtosecond laser-induced damage on unstructured vs. nano-structured Au-targets.** *Appl. Phys. A-Mater. Sci. Process.* **104**(1): 15–21, 2011. DOI: 10.1007/s00339-011-6449-2

053 Ketelaer, J.; Audi, G.; Beyer, T.; Blaum, K.; Block, M.*; Cakirli, R. B.; Casten, R. F.; Droese, C.*; Dworschak, M.; Eberhardt, K.; Eibach, M.; Herfurth, F.*; Minaya Ramirez, E.*; Nagy, S.*; Neidherr, D.; Nörtershäuser, W.*; Smorra, C.; Wang, M.: **Mass measurements on stable nuclides in the rare-earth region with the Penning-trap mass spectrometer TRIGA-TRAP.** *Phys. Rev. C* **84**(1): 014311, 2011. DOI: 10.1103/PhysRevC.84.014311

054 Krantz, C.; Blaum, K.; Grieser, M.; Litvinov, Yu. A.*; Repnow, R.; Wolf, A.: **Enhanced Schottky signals from electron-cooled, coasting beams in a heavy-ion storage ring.** *Nucl. Instrum. Methods Phys. Res. Sect. A-Accel. Spectrom. Dect. Assoc. Equip.* **629**(1): 1–5, 2011. DOI: 10.1016/j.nima.2010.12.034

055 Krauser, J.; Nix, A. K.; Gehrke, H. G.; Hofsäss, H.; Trautmann, C.*; Weidinger, A.: **Highly conductive ion tracks in tetrahedral amorphous carbon by irradiation with 30 MeV C_{60} projectiles.** *New J. Phys.* **13**: 083023, 2011. DOI: 10.1088/1367-2630/13/8/083023

056 Krieger, A.; Geppert, C.*; Catherall, R.; Hochschulz, F.; Krämer, J.; Neugart, R.; Rosendahl, S.; Schipper, J.; Siesling, E.; Weinheimer, C.; Yordanov, D. T.; Nörtershäuser, W.*: **Calibration of the ISOLDE acceleration voltage using a high-precision voltage divider and applying collinear fast beam laser spectroscopy.** *Nucl. Instrum. Methods Phys. Res. Sect. A-Accel. Spectrom. Dect. Assoc. Equip.* **632**(1): 23–31, 2011. DOI: 10.1016/j.nima.2010.12.145

057 Kugland, N. L.; Constantin, C. G.; Doppner, T.; Neumayer, P.*; Glenzer, S. H.; Niemann, C.: **Characterization of a spherically bent quartz crystal for K alpha x-ray imaging of laser plasmas using a focusing monochromator geometry.** *J. Instrum.* **6**: T03002, 2011. DOI: 10.1088/1748-0221/6/03/T03002

058 Kumar, A.; Trotsenko, S.*; Volotka, A. V.*; Banas, D.; Beyer, H. F.*; Bräuning, H.*; Fritzsche, S.*; Gumberidze, A.*; Hagmann, S.*; Hess, S.*; Kozhuharov, C.*; Reuschl, R.*; Spillmann, U.*; Trassinelli, M.; Weber, G.*; Stöhlker, Th.*: **Spectral distribution of the $2S \rightarrow 1S$ two-photon transition in atoms and few-electron ions.** *Pramana-J. Phys.* **76**(2): 331–337, 2011.

059 Kühnel, M.; Fernandez, J. M.; Tejeda, G.; Kalinin, A.; Montero, S.; Grisenti, R. E.*: **Time-Resolved Study of Crystallization in Deeply Cooled Liquid Parahydrogen.** *Phys. Rev. Lett.* **106**(24): 245301, 2011. DOI: 10.1103/PhysRevLett.106.245301

060 Lamperti, A.; Radnoczi, G.; Geszti, O.; Birjega, R.; Caricato, A. P.; Trautmann, C.*; Ossi, P. M.: **Structural changes in thin films of yttria-stabilized zirconia irradiated with uranium ions in the electronic stopping regime.** *J. Nucl. Mater.* **416**(1-2): 173–178, 2011. DOI: 10.1016/j.jnucmat.2010.12.032

061 Li, W. X.; Wang, L. M.; Lang, M. I.; Trautmann, C.*; Ewing, R. C.: **Thermal annealing mechanisms of latent fission tracks: Apatite vs. zircon.** *Earth Planet. Sci. Lett.* **302**(1-2): 227–235, 2011. DOI: 10.1016/j.epsl.2010.12.016

062 Linusson, P.; Fritzsche, S.*; Eland, J. H. D.; Hedin, L.; Karlsson, L.; Feifel, R.: **Double ionization of atomic cadmium.** *Phys. Rev. A* **83**(2): 023424, 2011. DOI: 10.1103/PhysRevA.83.023424

063 Litvinov, Y. A.*; Bosch, F.*: **Beta decay of highly charged ions.** *Rep. Prog. Phys.* **74**(1): 016301, 2011. DOI: 10.1088/0034-4885/74/1/016301

064 Litvinov, Y. A.*; Bosch, F.*; Kozhuharov, C.*; Ma, X. W.; Stöhlker, T.*; Winckler, N.*; Yamaguchi, T.: **At the borderline between atomic and nuclear physics: two-body beta-decay of highly charged ions.** *Phys. Scr.* **T144**: 014001, 2011. DOI: 10.1088/0031-8949/2011/T144/014001

065 Lu, F. Y.; Huang, M. B.; Lang, M.; Namavar, F.; Trautmann, C.*; Ewing, R. C.; Lian, J.: **Nanocrystalline ZrN behaviors under intensive radiation conditions.** *Abstr. Pap. Am. Chem. Soc.* **241**: 100-NUCL, 2011.

066 Mahner, E.; Evans, L.; Küchler, D.; Scrivens, R.; Bender, M.*; Kollmus, H.*; Severin, D.*; Wengenroth, M.*: **Heavy-ion induced desorption yields of cryogenic surfaces bombarded with 4.2 MeV/u lead ions.** *Phys. Rev. Spec. Top.-Accel. Beams* **14**(5): 050102, 2011. DOI: 10.1103/PhysRevSTAB.14.050102

067 Mahner, E.; Holzer, D.; Küchler, D.; Scrivens, R.; Pinto, P. C.; Vallgren, C. Y.; Bender, M.*: **Heavy-ion induced desorption yields of amorphous carbon films bombarded with 4.2 MeV/u lead ions.** *Phys. Rev. Spec. Top.-Accel. Beams* **14**(10): 101001, 2011. DOI: 10.1103/PhysRevSTAB.14.101001

068 Maiorova, A. V.; Shabaev, V. M.; Volotka, A. V.; Zaytsev, V. A.; Plunien, G.; Stöhlker, T.*: **Parity nonconservation effect in resonance recombination of polarized electrons with heavy hydrogen-like ions.** *J. Phys. B-At. Mol. Opt. Phys.* **44**(22): 225003, 2011. DOI: 10.1088/0953-4075/44/22/225003

069 Mane, E.; Cheal, B.; Billowes, J.; Bissell, M. L.; Blaum, K.; Charlwood, F. C.; Flanagan, K. T.; Forest, D. H.; Geppert, C.*; Kowalska, M.; Krieger, A.; Krämer, J.; Moore, I. D.; Neugart, R.; Neyens, G.; Nörtershäuser, W.*; Rajabali, M. M.; Sanchez, R.*; Schug, M.; Stroke, H. H.; Vingerhoets, P.; Yordanov, D. T.; Zakova, M.: **Ground-state spins and moments of ^{72,74,76,78}Ga nuclei.** *Phys. Rev. C* **84**(2): 024303, 2011. DOI: 10.1103/PhysRevC.84.024303

070 Maniks, J.; Manika, I.; Grants, R.; Zabels, R.; Schwartz, K.*; Sorokin, M.; Papaleo, R. M.: **Nanostructuring and hardening of LiF crystals irradiated with 3-15 MeV Au ions.** *Appl. Phys. A-Mater. Sci. Process.* **104**(4): 1121–1128, 2011. DOI: 10.1007/s00339-011-6387-z

071 Maniks, J.; Manika, I.; Zabels, R.; Grants, R.; Schwartz, K.*; Sorokin, M.: **Modification of the Structure and Nano-Mechanical Properties of LiF Crystals Under Irradiation with Swift Heavy Ions.** *Mater. Sci.-Medzg.* **17**(3): 223–228, 2011.

072 Matula, O.*; Fritzsche, S.*; Currell, F. J.; Surzhykov, A.*: **Angular correlations in radiative cascades following resonant electron capture by highly charged ions.** *Phys. Rev. A* **84**(5): 052723, 2011. DOI: 10.1103/PhysRevA.84.052723

073 McConnell, S. R.*; Artemyev, A. N.*; Surzhykov, A.*: **Alignment of atomic inner-shells following alpha-decay-induced ionization.** *J. Phys. B-At. Mol. Opt. Phys.* **44**(14): 145204, 2011. DOI: 10.1088/0953-4075/44/14/145204

074 Meftah, A.; Assmann, W.; Khalfaoui, N.; Stoquert, J. P.; Studer, F.; Toulemonde, M.; Trautmann, C.*; Voss, K. O.: **Electronic sputtering of $Gd_3Ga_5O_{12}$ and $Y_3Fe_5O_{12}$ garnets: Yield, stoichiometry and comparison to track formation.** *Nucl. Instrum. Methods Phys. Res. Sect. B-Beam Interact. Mater. Atoms* **269**(9): 955–958, 2011. DOI: 10.1016/j.nimb.2010.12.083

075 Mooser, A.; Blaum, K.; Kracke, H.; Kreim, S.; Quint, W.*; Rodegheri, C.; Ulmer, S.; Walz, J.: **Towards a direct measurement of the g-factor of a single isolated proton.** *Can. J. Phys.* **89**(1): 165–168, 2011. DOI: 10.1139/P10-070

076 Muench, F.; Oezaslan, M.; Seidl, T.*; Lauterbach, S.; Strasser, P.; Kleebe, H. J.; Ensinger, W.: **Multiple activation of ion track etched polycarbonate for the electroless synthesis of metal nanotubes.** *Appl. Phys. A-Mater. Sci. Process.* **105**(4): 847–854, 2011. DOI: 10.1007/s00339-011-6646-z

077 Nakano, Y.; Takano, Y.; Shindo, T.; Ikeda, T.; Kanai, Y.; Suda, S.; Azuma, T.; Bräuning, H.*; Bräuning-Demian, A.*; Stöhlker, Th.*; Dauvergne, D.; Yamazaki, Y.: **Observation of intrashell radiative decay of Li-like uranium ($2p_{3/2}$-$2s_{1/2}$) using silicon drift detectors.** *Phys. Scr.* **T144**: 014010, 2011. DOI: 10.1088/0031-8949/2011/T144/014010

078 Nolden, F.*; Hülsmann, P.*; Litvinov, Y. A.*; Moritz, P.*; Peschke, C.*; Petri, P.*; Sanjari, M. S.*; Steck, M.*; Weick, H.*; Wu, J. X.; Zang, Y. D.; Zhang, S. H.; Zhao, T. C.: **A fast and sensitive resonant Schottky pick-up for heavy ion storage rings.** *Nucl. Instrum. Methods Phys. Res. Sect. A-Accel. Spectrom. Dect. Assoc. Equip.* **659**(1): 69–77, 2011. DOI: 10.1016/j.nima.2011.06.058

079 Nowak, B.; Sexty, D.; Gasenzer, T.: **Superfluid turbulence: Nonthermal fixed point in an ultracold Bose gas.** *Phys. Rev. B* **84**(2): 020506, 2011. DOI: 10.1103/PhysRevB.84.020506

080 Nörtershäuser, W.*; Neff, T.*; Sanchez, R.; Sick, I.: **Charge radii and ground state structure of lithium isotopes: Experiment and theory reexamined.** *Phys. Rev. C* **84**(2): 024307, 2011. DOI: 10.1103/PhysRevC.84.024307

081 Nörtershäuser, W.*; Sanchez, R.*; Ewald, G.*; Dax, A.*; Behr, J.; Bricault, P.; Bushaw, B. A.; Dilling, J.; Dombsky, M.; Drake, G. W. F.; Götte, S.*; Kluge, H. J.*; Kühl, T.*; Lassen, J.; Levy, C. D. P.; Pachucki, K.; Pearson, M.; Puchalski, M.; Wojtaszek, A.*; Yan, Z. C.; Zimmermann, C.: **Isotope-shift measurements of stable and short-lived lithium isotopes for nuclear-charge-radii determination.** *Phys. Rev. A* **83**(1): 012516, 2011. DOI: 10.1103/PhysRevA.83.012516

082 Orlov, N. Y.; Denisov, O. B.; Rosmej, O. N.*; Schäfer, D.; Nisius, T.; Wilhein, T.; Zhidkov, N.; Kunin, A.; Suslov, N.; Pinegin, A.; Vatulin, V.; Zhao, Y.: **Theoretical and experimental studies of material radiative properties and their applications to laser and heavy ion inertial fusion.** *Laser Part. Beams* **29**(1): 69–80, 2011. DOI: 10.1017/S0263034610000777

083 Ovchinnikov, A. V.; Kostenko, O. F.; Chefonov, O. V.; Rosmej, O. N.*; Andreev, N. E.; Agranat, M. B.; Duan, J. L.; Liu, J.; Fortov, V. E.: **Characteristic X-rays generation under the action of femtosecond laser pulses on nano-structured targets.** *Laser Part. Beams* **29**(2): 249–254, 2011. DOI: 10.1017/S026303461100022X

084 Pachucki, K.; Yerokhin, V. A.*: **Fine structure of helium and light helium-like ions.** *Can. J. Phys.* **89**(1): 95–101, 2011. DOI: 10.1139/P10-050

085 Petridis, N.; Kalinin, A.; Popp, U.*; Gostishchev, V.*; Litvinov, Yu. A.*; Dimopoulou, C.*; Nolden, F.*; Steck,

M.*; Kozhuharov, C.*; Thorn, D. B.; Gumberidze, A.*; Trotsenko, S.*; Hagmann, S.*; Spillmann, U.*; Winters, D. F. A.*; Dörner, R.; Stöhlker, T.*; Grisenti, R. E.*: **Energy loss and cooling of relativistic highly charged uranium ions interacting with an internal hydrogen droplet target beam.** *Nucl. Instrum. Methods Phys. Res. Sect. A-Accel. Spectrom. Dect. Assoc. Equip.* **656**(1): 1–4, 2011. DOI: 10.1016/j.nima.2011.07.035

086 Pezzagna, S.; Rogalla, D.; Becker, H. W.; Jakobi, I.; Dolde, F.; Naydenov, B.; Wrachtrup, J.; Jelezko, F.; Trautmann, C.*; Meijer, J.: **Creation of colour centres in diamond by collimated ion-implantation through nanochannels in mica.** *Phys. Status Solidi A-Appl. Mat.* **208**(9): 2017–2022, 2011. DOI: 10.1002/pssa.201100455

087 Piriz, A. R.; Di Lucchio, L.; Prieto, G.; Tahir, N. A.*: **Vibration waveform effects on dynamic stabilization of ablative Rayleigh-Taylor instability.** *Phys. Plasmas* **18**(8): 082705, 2011. DOI: 10.1063/1.3622639

088 Piriz, A. R.; Piriz, S. A.; Tahir, N. A.*: **Dynamic stabilization of classical Rayleigh-Taylor instability.** *Phys. Plasmas* **18**(9): 092705, 2011. DOI: 10.1063/1.3633487

089 Postavaru, O.; Harman, Z.*; Keitel, C. H.: **High-Precision Metrology of Highly Charged Ions via Relativistic Resonance Fluorescence.** *Phys. Rev. Lett.* **106**(3): 033001, 2011. DOI: 10.1103/PhysRevLett.106.033001

090 Quinn, M. N.; Yuan, X. H.; Lin, X. X.; Carroll, D. C.; Tresca, O.; Gray, R. J.; Coury, M.; Li, C.; Li, Y. T.; Brenner, C. M.; Robinson, A. P. L.; Neely, D.; Zielbauer, B.*; Aurand, B.*; Fils, J.*; Kuehl, T.*; McKenna, P.: **Refluxing of fast electrons in solid targets irradiated by intense, picosecond laser pulses.** *Plasma Phys. Control. Fusion* **53**(2): 025007, 2011. DOI: 10.1088/0741-3335/53/2/025007

091 Rahman, M. S.*; Evangelou, E. K.*: **Dielectric Relaxation and Charge Trapping Characteristics Study in Germanium Based MOS Devices With HfO_2/Dy_2O_3 Gate Stacks.** *IEEE Trans. Electron Devices* **58**(10): 3549–3558, 2011. DOI: 10.1109/TED.2011.2162095

092 Rahman, M. S.*; Evangelou, E. K.; Dimoulas, A.; Mavrou, G.; Galata, S.: **Current instabilities in rare-earth oxides-HfO_2 gate stacks grown on germanium based metal-oxide-semiconductor devices due to Maxwell-Wagner instabilities and dielectrics relaxation.** *J. Vac. Sci. Technol. B* **29**(1): 01AB06, 2011. DOI: 10.1116/1.3532946

093 Rauber, M.*; Alber, I.*; Müller, S.*; Neumann, R.*; Picht, O.*; Roth, C.; Schokel, A.; Toimil-Molares, M. E.*; Ensinger, W.: **Highly-Ordered Supportless Three-Dimensional Nanowire Networks with Tunable Complexity and Interwire Connectivity for Device Integration.** *Nano Lett.* **11**(6): 2304–2310, 2011. DOI: 10.1021/nl2005516

094 Ray, C.; Bräuning-Demian, A.*; Bräuning, H.*; Chevallier, M.; Cohen, C.; Dauvergne, D.; L'Hoir, A.; Kozhuharov, C.*; Liesen, D.*; Mokler, P. H.; Poizat, J. C.; Stöhlker, T.*; Testa, E.; Toulemonde, M.: **Measurements of high energy loss rates of fast highly charged U ions channeled in thin silicon crystals.** *Phys. Rev. B* **84**(2): 024119, 2011. DOI: 10.1103/PhysRevB.84.024119

095 Regan, C.; Schlegel, T.*; Tikhonchuk, V. T.; Honrubia, J. J.; Feugeas, J.-L.; Nicolai, Ph.: **Cone-guided fast ignition with ponderomotively accelerated carbon ions.** *Plasma Phys. Control. Fusion* **53**(4): 045014, 2011. DOI: 10.1088/0741-3335/53/4/045014

096 Ros, D.; Cassou, K.; Cros, B.; Daboussi, S.; Demailly, J.; Guilbaud, A.; Kazamias, S.; Lagron, J. C.; Maynard, G.; Neveu, O.; Pittman, M.; Zielbauer, B.*; Zimmer, D.*; Kuhl, T.*; Lacombe, S.; Porcel, E.; du Penhoat, M. A.; Zeitoun, P.; Mourou, G.: **LASERIX: An open facility for developments of EUV and soft X-ray lasers and applications-Developments of XUV sources using high power laser facilities: ILE, ELI.** *Nucl. Instrum. Methods Phys. Res. Sect. A-Accel. Spectrom. Dect. Assoc. Equip.* **653**(1): 76–79, 2011. DOI: 10.1016/j.nima.2011.01.109

097 Rosmej, F.; Bennadji, K.*; Lisitsa, V. S.: **Effect of dense plasmas on exchange-energy shifts in highly charged ions: An alternative approach for arbitrary perturbation potentials.** *Phys. Rev. A* **84**(3): 032512, 2011. DOI: 10.1103/PhysRevA.84.032512

098 Rosmej, O. N.*; Bagnoud, V.*; Eisenbarth, U.*; Vatulin, V.; Zhidkov, N.; Suslov, N.; Kunin, A.; Pinegin, A.; Schafer, D.; Nisius, T.; Wilhein, T.; Rienecker, T.; Wiechula, J.; Jacoby, J.; Zhao, Y.; Vergunova, G.; Borisenko, N.; Orlov, N.: **Heating of low-density CHO-foam layers by means of soft X-rays.** *Nucl. Instrum. Methods Phys. Res. Sect. A-Accel. Spectrom. Dect. Assoc. Equip.* **653**(1): 52–57, 2011. DOI: 10.1016/j.nima.2011.01.167

099 Saathoff, G.; Reinhardt, S.; Holzwarth, R.; Hänsch, T. W.; Udem, T.; Bing, D.; Schwalm, D.; Wolf, A.; Karpuk, S.; Huber, G.; Novotny, C.*; Botermann, B.; Geppert, C.*; Nörtershäuser, W.*; Kühl, T.*; Stöhlker, T.*; Gwinner, G.: **Comment on: "Lorentz violation in high-energy ions" by Santosh Devasia.** *Eur. Phys. J. C* **71**(3): 1596, 2011. DOI: 10.1140/epjc/s10052-011-1596-3

100 Schippers, S.; Bernhardt, D.; Grieser, M.; Hahn, M.; Krantz, C.; Lestinsky, M.*; Novotny, O.; Repnow, R.; Savin, D. W.; Wolf, A.; Möller, A.: **Recombination of Au^{20+} at low electron-ion collision energies.** *Phys. Scr.* **T144**: 014039, 2011. DOI: 10.1088/0031-8949/2011/T144/014039

101 Schippers, S.; Bernhardt, D.; Müller, A.; Krantz, C.; Grieser, M.; Repnow, R.; Wolf, A.; Lestinsky, M.*; Hahn, M.; Novotny, O.; Savin, D. W.: **Dielectronic recombi-**

nation of xenonlike tungsten ions. *Phys. Rev. A* **83**(1): 012711, 2011. DOI: 10.1103/PhysRevA.83.012711

102 Sharma, L.*; Srivastava, R.; Stauffer, A. D.: **Excitation of the $5p^5 7p$ levels of xenon by electron impact.** *Eur. Phys. J. D* **62**(3): 399–403, 2011. DOI: 10.1140/epjd/e2011-10644-0

103 Sharma, L.*; Surzhykov, A.*; Srivastava, R.; Fritzsche, S.*: **Electron-impact excitation of singly charged metal ions.** *Phys. Rev. A* **83**(6): 062701, 2011. DOI: 10.1103/PhysRevA.83.062701

104 Shevelko, V. P.; Beigman, I. L.; Litsarev, M. S.; Tawara, H.; Tolstikhina, I. Y.; Weber, G.*: **Charge-changing processes in collisions of heavy many-electron ions with neutral atoms.** *Nucl. Instrum. Methods Phys. Res. Sect. B-Beam Interact. Mater. Atoms* **269**(12): 1455–1463, 2011. DOI: 10.1016/j.nimb.2011.03.024

105 Siegien-Iwaniuk, K.; Winckler, N.*; Bosch, F.*; Geissel, H.*; Litvinov, Y. A.*; Patyk, Z.: **Orbital electron capture of hydrogen- and helium-like ions.** *Phys. Rev. C* **84**(1): 014301, 2011. DOI: 10.1103/PhysRevC.84.014301

106 Siomau, M.; Fritzsche, S.*: **Quantum computing with mixed states.** *Eur. Phys. J. D* **62**(3): 449–456, 2011. DOI: 10.1140/epjd/e2011-20070-y

107 Stolterfoht, N.; Hellhammer, R.; Sulik, B.; Juhasz, Z.; Bayer, V.*; Trautmann, C.*; Bodewits, E.; Hoekstra, R.: **Evidence of blocking effects on 3-keV Ne^{7+} ions guided through nanocapillaries in polycarbonate.** *Phys. Rev. A* **83**(6): 062901, 2011. DOI: 10.1103/PhysRevA.83.062901

108 Sturm, S.; Wagner, A.; Schabinger, B.; Zatorski, J.; Harman, Z.*; Quint, W.*; Werth, G.; Keitel, C. H.; Blaum, K.: **g Factor of Hydrogenlike $^{28}Si^{13+}$.** *Phys. Rev. Lett.* **107**(2): 023002, 2011. DOI: 10.1103/PhysRevLett.107.023002

109 Surzhykov, A.*; Artemyev, A. N.*; Yerokhin, V. A.*: **Interelectronic interaction effects on the polarization of recombination photons.** *Phys. Rev. A* **83**(6): 062710, 2011. DOI: 10.1103/PhysRevA.83.062710

110 Surzhykov, A.*; Indelicato, P.; Santos, J. P.; Amaro, P.; Fritzsche, S.*: **Two-photon absorption of few-electron heavy ions.** *Phys. Rev. A* **84**(2): 022511, 2011. DOI: 10.1103/PhysRevA.84.022511

111 Tahir, N. A.*; Schmidt, R.; Shutov, A.; Lomonosov, I. V.; Gryaznov, V.; Piriz, A. R.; Deutsch, C.; Fortov, V. E.: **The Large Hadron Collider and the Super Proton Synchrotron at CERN as Tools to Generate Warm Dense Matter and Non-Ideal Plasmas.** *Contrib. Plasma Phys.* **51**(4): 299–308, 2011. DOI: 10.1002/ctpp.201010120

112 Tahir, N. A.*; Shutov, A.; Lomonosov, I. V.; Piriz, A. R.; Redmer, R.; Stöhlker, T.*; Geissel, H.*; Deutsch, C.; Fortov, V. E.: **High Energy Density Physics Studies at the Facility for Antiprotons and Ion Research: the HEDgeHOB Collaboration.** *Contrib. Plasma Phys.* **51**(4): 309–321, 2011. DOI: 10.1002/ctpp.201010117

113 Tahir, N. A.*; Shutov, A.; Zharkov, A. P.; Piriz, A. R.; Stöhlker, Th.*: **Generation of plane shocks using intense heavy ion beams: Application to Richtmyer-Meshkov instability growth studies.** *Phys. Plasmas* **18**(3): 032704, 2011. DOI: 10.1063/1.3561816

114 Tahir, N. A.*; Stöhlker, T.*; Shutov, A.; Lomonosov, I. V.; Fortov, V. E.; French, M.; Nettelmann, N.; Redmer, R.; Piriz, A. R.; Deutsch, C.: **Laboratory planetary physics using intense heavy ion beams at the Facility for Antiprotons and Ion Research at Darmstadt: the HEDgeHOB collaboration.** *Astrophys. Space Sci.* **336**(1): 61–65, 2011. DOI: 10.1007/s10509-011-0598-9

115 Tashenov, S.*: **Circular polarimetry with gamma-ray tracking detectors.** *Nucl. Instrum. Methods Phys. Res. Sect. A-Accel. Spectrom. Dect. Assoc. Equip.* **640**(1): 164–169, 2011. DOI: 10.1016/j.nima.2011.03.011

116 Tashenov, S.; Bäck, T.; Barday, R.; Cederwall, B.; Enders, J.; Khaplanov, A.; Poltoratska, Y.; Schässburger, K. U.; Surzhykov, A.*: **Measurement of the Correlation between Electron Spin and Photon Linear Polarization in Atomic-Field Bremsstrahlung.** *Phys. Rev. Lett.* **107**(17): 173201, 2011. DOI: 10.1103/PhysRevLett.107.173201

117 Thorn, D. B.*; Gumberidze, A.*; Trotsenko, S.*; Banas, D.; Beyer, H.*; Bostock, C. J.; Bray, I.; Chen, W.*; DuBois, R.; Fontes, C. J.; Fritzsche, S.*; Fursa, D. V.; Grisenti, R.*; Geyer, S.*; Hagmann, S.*; Hess, S.*; Hegewald, M.*; Kozhuharov, C.*; Märtin, R.*; Orban, I.; Petridis, N.*; Reuschl, R.*; Simon, A.; Spillmann, U.*; Surzhykov, A.*; Trassinelli, M.*; Weber, G.*; Winters, D. F. A.*; Winters, N.*; Zhang, H. L.; Stöhlker, Th.*: **Polarization and anisotropic emission of K-shell radiation from heavy few electron ions.** *Can. J. Phys.* **89**(5): 513–519, 2011. DOI: 10.1139/P11-033

118 Titze, J.; Schöffler, M. S.; Kim, H. K.; Trinter, F.; Waitz, M.; Voigtsberger, J.; Neumann, N.; Ulrich, B.; Kreidi, K.*; Wallauer, R.; Odenweller, M.; Havermeier, T.; Schössler, S.; Meckel, M.; Foucar, L.; Jahnke, T.; Czasch, A.; Schmidt, L. P. H.; Jagutzki, O.; Grisenti, R. E.; Schmidt-Böcking, H.; Lüdde, H. J.; Dörner, R.: **Ionization Dynamics of Helium Dimers in Fast Collisions with He^{++}.** *Phys. Rev. Lett.* **106**(3): 033201, 2011. DOI: 10.1103/PhysRevLett.106.033201

119 Trassinelli, M.; Kumar, A.; Beyer, H. F.*; Indelicato, P.; Märtin, R.*; Reuschl, R.; Kozhedub, Y. S.; Brandau, C.*; Bräuning, H.*; Geyer, S.*; Gumberidze, A.; Hess, S.*; Jagodzinski, P.; Kozhuharov, C.*; Liesen, D.*; Spillmann, U.*; Trotsenko, S.*; Weber, G.*; Winters, D. F. A.*; Stöhlker, Th.*: **Differential energy**

measurement between He- and Li-like uranium intra-shell transitions. *Phys. Scr.* **T144**: 014003, 2011. DOI: 10.1088/0031-8949/2011/T144/014003

120 Tresca, O.; Carroll, D. C.; Yuan, X. H.; Aurand, B.*; Bagnoud, V.*; Brenner, C. M.; Coury, M.; Fils, J.*; Gray, R. J.; Kühl, T.*; Li, C.; Li, Y. T.; Lin, X. X.; Quinn, M. N.; Evans, R. G.; Zielbauer, B.*; Roth, M.; Neely, D.; McKenna, P.: **Controlling the properties of ultraintense laser-proton sources using transverse refluxing of hot electrons in shaped mass-limited targets.** *Plasma Phys. Control. Fusion* **53**(10): 105008, 2011. DOI: 10.1088/0741-3335/53/10/105008

121 Tu, X. L.; Wang, M.; Litvinov, Yu. A.*; Zhang, Y. H.; Xu, H. S.; Sun, Z. Y.; Audi, G.; Blaum, K.; Du, C. M.; Huang, W. X.; Hu, Z. G.; Geng, P.; Jin, S. L.; Liu, L. X.; Liu, Y.; Mei, B.; Mao, R. S.; Ma, X. W.; Suzuki, H.; Shuai, P.; Sun, Y.; Tang, S. W.; Wang, J. S.; Wang, S. T.; Xiao, G. Q.; Xu, X.; Xia, J. W.; Yang, J. C.; Ye, R. P.; Yamaguchi, T.; Yan, X. L.; Yuan, Y. J.; Yamaguchi, Y.; Zang, Y. D.; Zhao, H. W.; Zhao, T. C.; Zhang, X. Y.; Zhou, X. H.; Zhan, W. L.: **Precision isochronous mass measurements at the storage ring CSRe in Lanzhou.** *Nucl. Instrum. Methods Phys. Res. Sect. A-Accel. Spectrom. Dect. Assoc. Equip.* **654**(1): 213–218, 2011. DOI: 10.1016/j.nima.2011.07.018

122 Tu, X. L.; Xu, H. S.; Wang, M.; Zhang, Y. H.; Litvinov, Y. A.*; Sun, Y.; Schatz, H.; Zhou, X. H.; Yuan, Y. J.; Xia, J. W.; Audi, G.; Blaum, K.; Du, C. M.; Geng, P.; Hu, Z. G.; Huang, W. X.; Jin, S. L.; Liu, L. X.; Liu, Y.; Ma, X.; Mao, R. S.; Mei, B.; Shuai, P.; Sun, Z. Y.; Suzuki, H.; Tang, S. W.; Wang, J. S.; Wang, S. T.; Xiao, G. Q.; Xu, X.; Yamaguchi, T.; Yamaguchi, Y.; Yan, X. L.; Yang, J. C.; Ye, R. P.; Zang, Y. D.; Zhao, H. W.; Zhao, T. C.; Zhang, X. Y.; Zhan, W. L.: **Direct Mass Measurements of Short-Lived $A = 2Z - 1$ Nuclides ^{63}Ge, ^{65}As, ^{67}Se, and ^{71}Kr and their Impact on Nucleosynthesis in the rp Process.** *Phys. Rev. Lett.* **106**(11): 112501, 2011. DOI: 10.1103/PhysRevLett.106.112501

123 Ulmer, S.; Rodegheri, C. C.; Blaum, K.; Kracke, H.; Mooser, A.; Quint, W.*; Walz, J.: **Observation of Spin Flips with a Single Trapped Proton.** *Phys. Rev. Lett.* **106**(25): 253001, 2011. DOI: 10.1103/PhysRevLett.106.253001

124 Verhoef, A. J.; Mitrofanov, A. V.; Nguyen, X. T.; Krikunova, M.; Fritzsche, S.*; Kabachnik, N. M.; Drescher, M.; Baltuska, A.: **Time-and-energy resolved measurement of the cascaded Auger decay in krypton.** *Laser Phys.* **21**(7): 1270–1274, 2011. DOI: 10.1134/S1054660X11130263

125 Verhoef, A. J.; Mitrofanov, A. V.; Nguyen, X. T.; Krikunova, M.; Fritzsche, S.*; Kabachnik, N. M.; Drescher, M.; Baltuska, A.: **Time-and-energy-resolved measurement of Auger cascades following Kr 3d excitation by attosecond pulses.** *New J. Phys.* **13**: 113003, 2011. DOI: 10.1088/1367-2630/13/11/113003

126 Verma, P.*; Mokler, P. H.; Bräuning-Demian, A.*; Kozhuharov, C.*; Bräuning, H.*; Anton, J.; Fricke, B.; Bosch, F.*; Hagmann, S.*; Liesen, D.*; Stachura, Z.; Wahab, M. A.: **Inner-shell couplings in transiently formed superheavy quasimolecules.** *Phys. Scr.* **T144**: 014032, 2011. DOI: 10.1088/0031-8949/2011/T144/014032

127 Vingerhoets, P.; Flanagan, K. T.; Billowes, J.; Bissell, M. L.; Blaum, K.; Cheal, B.; De Rydt, M.; Forest, D. H.; Geppert, C.; Honma, M.; Kowalska, M.; Krämer, J.; Kreim, K.; Krieger, A.; Neugart, R.; Neyens, G.; Nörtershäuser, W.*; Papuga, J.; Procter, T. J.; Rajabali, M. M.; Sanchez, R.*; Stroke, H. H.; Yordanov, D. T.: **Magnetic and quadrupole moments of neutron deficient $^{58-62}$Cu isotopes.** *Phys. Lett. B* **703**(1): 34–39, 2011. DOI: 10.1016/j.physletb.2011.07.050

128 Voitkiv, A. B.; Najjari, B.; Fischer, D.; Artemyev, A. N.*; Surzhykov, A.*: **Young-Type Interference in Projectile-Electron Loss in Energetic Ion-Molecule Collisions.** *Phys. Rev. Lett.* **106**(23): 233202, 2011. DOI: 10.1103/PhysRevLett.106.233202

129 Volotka, A. V.*; Surzhykov, A.*; Shabaev, V. M.; Plunien, G.: **Interelectronic-interaction effects on the two-photon decay rates of heavy He-like ions.** *Phys. Rev. A* **83**(6): 06250, 2011. DOI: 10.1103/PhysRevA.83.062508

130 von Lindenfels, D.*; Brantjes, N. P. M.*; Birkl, G.; Quint, W.*; Shabaev, V. M.; Vogel, M.: **Bound electron g-factor measurement by double-resonance spectroscopy on a fine-structure transition.** *Can. J. Phys.* **89**(1): 79–84, 2011. DOI: 10.1139/P10-071

131 Wang, X.; Schneider, K.; Kelkar, A.; Schulz, M.; Najjari, B.; Voitkiv, A.; Gundmundsson, M.; Grieser, M.; Krantz, C.; Lestinsky, M.*; Wolf, A.; Hagmann, S.*; Moshammer, R.; Ullrich, J.; Fischer, D.: **Mutual projectile and target ionization in 1-MeV/amu N^{4+} and N^{5+} + He collisions.** *Phys. Rev. A* **84**(2): 022707, 2011. DOI: 10.1103/PhysRevA.84.022707

132 Weber, G.*; Bräuning, H.*; Märtin, R.*; Spillmann, U.*; Stöhlker, Th.*: **Monte Carlo simulations for the characterization of position-sensitive x-ray detectors dedicated to Compton polarimetry.** *Phys. Scr.* **T144**: 014034, 2011. DOI: 10.1088/0031-8949/2011/T144/014034

133 Weikusat, C.; Glasmacher, U. A.; Schuster, B.; Trautmann, C.*; Miletich, R.; Neumann, R.*: **Raman study of apatite amorphised with swift heavy ions under various irradiation conditions.** *Phys. Chem. Miner.* **38**(4): 293–303, 2011. DOI: 10.1007/s00269-010-0403-2

134 Winters, D. F. A.*; Kühl, T.*; Schneider, D. H.; Indelicato, P.; Reuschl, R.; Schuch, R.; Lindroth, E.; Stöhlker, Th.*: **Laser spectroscopy of the $(1s^2 2s2p)\ ^3P_0$-$^3P_1$ level splitting in Be-like krypton.** *Phys. Scr.* **T144**: 014013, 2011. DOI: 10.1088/0031-8949/2011/T144/014013

135 Yerokhin, V. A.*; Surzhykov, A.*: **Relativistic theory of the double photoionization of helium-like atoms.** *Phys. Rev. A* **84**(3): 0327, 2011. DOI: 10.1103/PhysRevA.84.032703

136 Yerokhin, V. A.; Pachucki, K.; Harman, Z.*; Keitel, C. H.: **QED Theory of the Nuclear Magnetic Shielding in Hydrogenlike Ions.** *Phys. Rev. Lett.* **107**(4): 043004, 2011. DOI: 10.1103/PhysRevLett.107.043004

137 Yuan, X. H.; Carroll, D. C.; Coury, M.; Gray, R. J.; Brenner, C. M.; Lin, X. X.; Li, Y. T.; Quinn, M. N.; Tresca, O.; Zielbauer, B.*; Neely, D.; McKenna, P.: **Spatially resolved X-ray spectroscopy using a flat HOPG crystal.** *Nucl. Instrum. Methods Phys. Res. Sect. A-Accel. Spectrom. Dect. Assoc. Equip.* **653**(1): 145–149, 2011. DOI: 10.1016/j.nima.2010.12.147

138 Zang, Y. D.; Wu, J. X.; Zhao, T. C.; Zhang, S. H.; Mao, R. S.; Xu, H. S.; Sun, Z. Y.; Ma, X. W.; Tu, X. L.; Xiao, G. Q.; Nolden, F.*; Hülsmann, P.*; Litvinov, Y. A.*; Peschke, C.*; Petri, P.*; Sanjari, M. S.*; Steck, M.*: **Simulation and measurement of the resonant Schottky pickup.** *Chin. Phys. C* **35**(12): 1124–1129, 2011. DOI: 10.1088/1674-1137/35/12/008

139 Zhang, W.; Chen, W.*; Qiu, M. L.; Fu, Y. Q.; Hutton, R.; Zou, Y.: **A high-precision high-voltage divider applied to electron beam energy measurements.** *Phys. Scr.* **T144**: 014063, 2011. DOI: 10.1088/0031-8949/2011/T144/014063

WoS publications to the programme 'Health' in the field 'Cancer research' published in 2011

C. Kausch[1]
[1]GSI, Darmstadt, Germany

001 Averbeck, N. B.*; Durante, M.*: **Protein Acetylation Within the Cellular Response to Radiation.** *J. Cell. Physiol.* **226**(4): 962–967, 2011. DOI: 10.1002/jcp.22466

002 Bert, C.*; Durante, M.*: **Motion in radiotherapy: particle therapy.** *Phys. Med. Biol.* **56**(16): R113–R114, 2011. DOI: 10.1088/0031-9155/56/16/R01

003 Bill, V.; Arenz, A.; Seay, U.; Rudolph, S.; Fournier, C.*; Taucher-Scholz, G.*; Hanze, J.; Rose, F.; Engenhart-Cabillic, R.; Kamlah, F.: **Expression of HIF-1 dependent Gene in human Lung adenocarcinoma (A549) Cells and their behavior by Photon and Particle radiation.** *Strahlenther. Onkol.* **187**: 65–65, 2011.

004 Bischoff, B.; Arenz, A.; Eberle, F.; Savai, R.; Fournier, C.*; Taucher-Scholz, G.*; Engenhart-Cabillic, R.; Kamlah, F.: **Radiotherapeutic Characterization of murine Lewis-Lung Carcinoma (LLC1) Cells by Photon and Particle Radiation.** *Strahlenther. Onkol.* **187**: 64–65, 2011.

005 De Lellis, G.; Buontempo, S.; Di Capua, F.; Di Crescenzo, A.; Migliozzi, P.; Petukhov, Y.; Pistillo, C.; Russo, A.; Strolin, P.; Tioukov, V.; Durante, M.*; Furusawa, Y.; Toshito, T.; Yasuda, N.; Ariga, A.; Naganawa, N.: **Measurement of the fragmentation of Carbon nuclei used in hadron-therapy.** *Nucl. Phys. A* **853**(1): 124–134, 2011. DOI: 10.1016/j.nuclphysa.2011.01.019

006 De Micco, V.; Arena, C.; Pignalosa, D.*; Durante, M.*: **Effects of sparsely and densely ionizing radiation on plants.** *Radiat. Environ. Biophys.* **50**(1): 1–19, 2011. DOI: 10.1007/s00411-010-0343-8

007 Di Fino, L.; Casolino, M.; De Santis, C.; Larosa, M.; La Tessa, C.*; Narici, L.; Picozza, P.; Zaconte, V.: **Heavy-Ion Anisotropy Measured by ALTEA in the International Space Station.** *Radiat. Res.* **176**(3): 397–406, 2011. DOI: 10.1667/RR2179.1

008 Du, G. H.; Fischer, B. E.*; Voss, K. O.*: **Live cell calcium imaging at the single ion hit facility of GSI.** *Nucl. Instrum. Methods Phys. Res. Sect. B-Beam Interact. Mater. Atoms* **269**(20): 2312–2316, 2011. DOI: 10.1016/j.nimb.2011.02.016

009 Durante, M.*: **Human embryo stem cells and DNA repair.** *Aging-US* **3**(6): 564–564, 2011.

010 Durante, M.*; Cucinotta, F. A.: **Physical basis of radiation protection in space travel.** *Rev. Mod. Phys.* **83**(4): 1245–1281, 2011. DOI: 10.1103/RevModPhys.83.1245

011 Durante, M.*; Friedl, A. A.: **New challenges in radiobiology research with microbeams.** *Radiat. Environ. Biophys.* **50**(3): 335–338, 2011. DOI: 10.1007/s00411-011-0373-x

012 Durgaryan, A.; Sommer, S.: **Chromosome imaging: fluorescence in situ hybridisation (FISH) in human peripheral blood lymphocytes.** *Eur. Biophys. J. Biophys. Lett.* **40**: 125–125, 2011.

013 Faethe, C.; Goetze, K.; Scholz, M.*; Tauther-Scholz, G.*; Mueller-Klieser, W.: **Change of the Migration Behavior of Tumor Cells and Influence of EGFR mediated Signaling Cascade after Heavy Ion Irradiation in vitro.** *Strahlenther. Onkol.* **187**: 63–63, 2011.

014 Gatei, M.; Jakob, B.*; Chen, P.; Kijas, A. W.; Becherel, O. J.; Gueven, N.; Birrell, G.; Lee, J. H.; Paull, T. T.; Lerenthal, Y.; Fazry, S.; Taucher-Scholz, G.*; Kalb, R.; Schindler, D.; Waltes, R.; Dork, T.; Lavin, M. F.: **ATM Protein-dependent Phosphorylation of Rad50 Protein Regulates DNA Repair and Cell Cycle Control.** *J. Biol. Chem.* **286**(36): 31542–31556, 2011. DOI: 10.1074/jbc.M111.258152

015 Gemmel, A.; Rietzel, E.; Kraft, G.*; Durante, M.*; Bert, C.*: **Calculation and experimental verification of the RBE-weighted dose for scanned ion beams in the presence of target motion.** *Phys. Med. Biol.* **56**(23): 7337–7351, 2011. DOI: 10.1088/0031-9155/56/23/001

016 Hofmann, I.*; Meyer-ter-Vehn, J.; Yan, X. Q.; Orzhekhovskaya, A.*; Yaramyshev, S.*: **Collection and focusing of laser accelerated ion beams for therapy applications.** *Phys. Rev. Spec. Top.-Accel. Beams* **14**(3): 031304, 2011. DOI: 10.1103/PhysRevSTAB.14.031304

017 Jakob, B.*; Splinter, J.; Conrad, S.; Voss, K. O.*; Zink, D.; Durante, M.*; Lobrich, M.; Taucher-Scholz, G.*: **DNA double-strand breaks in heterochromatin elicit fast repair protein recruitment, histone H2AX phosphorylation and relocation to euchromatin.** *Nucleic Acids Res.* **39**(15): 6489–6499, 2011. DOI: 10.1093/nar/gkr230

018 Kamlah, F.; Hanze, J.; Arenz, A.; Seay, U.; Hasan, D.; Juricko, J.; Bischoff, B.; Gottschald, O. R.; Fournier, C.*;

Taucher-Scholz, G.*; Scholz, M.*; Seeger, W.; Engenhart-Cabillic, R.; Rose, F.: **COMPARISON OF THE EFFECTS OF CARBON ION AND PHOTON IRRADIATION ON THE ANGIOGENIC RESPONSE IN HUMAN LUNG ADENOCARCINOMA CELLS.** *Int. J. Radiat. Oncol. Biol. Phys.* **80**(5): 1541–1549, 2011. DOI: 10.1016/j.ijrobp.2011.03.033

019 Kamlah, F.; Hanze, J.; Seay, U.; Arenz, A.; Juricko, J.; Hasan, D.; Bischoff, B.; Gottschald, O. R.; Fournier, C.*; Taucher-Scholz, G.*; Scholz, M.*; Engenhart-Cabillic, R.: **Photon Irradiation of human Adenocarcinoma of the Lung (A549) induced in Contrast to Irradiation with Carbon Ions the Induction of Angiogenesis by Stem Cell Factor (SCF).** *Strahlenther. Onkol.* **187**: 64–64, 2011.

020 Kozlov, S. V.; Graham, M. E.; Jakob, B.*; Tobias, F.*; Kijas, A. W.; Tanuji, M.; Chen, P. L.; Robinson, P. J.; Taucher-Scholz, G.*; Suzuki, K.; So, S. R.; Chen, D. V.; Lavin, M. F.: **Autophosphorylation and ATM Activation ADDITIONAL SITES ADD TO THE COMPLEXITY.** *J. Biol. Chem.* **286**(11): 9107–9119, 2011. DOI: 10.1074/jbc.M110.204065

021 Lee, R.; Nasonova, E.; Hartel, C.*; Durante, M.*; Ritter, S.*: **Chromosome aberration measurements in mitotic and G(2)-PCC lymphocytes at the standard sampling time of 48 h underestimate the effectiveness of high-LET particles.** *Radiat. Environ. Biophys.* **50**(3): 371–381, 2011. DOI: 10.1007/s00411-011-0360-2

022 Luumlchtenborg, R.*; Saito, N.*; Durante, M.*; Bert, C.*: **Experimental verification of a real-time compensation functionality for dose changes due to target motion in scanned particle therapy.** *Med. Phys.* **38**(10): 5448–5458, 2011. DOI: 10.1118/1.3633891

023 Maalouf, M.; Durante, M.*; Foray, N.: **Biological Effects of Space Radiation on Human Cells: History, Advances and Outcomes.** *J. Radiat. Res.* **52**(2): 126–146, 2011. DOI: 10.1269/jrr.10128

024 Newhauser, W. D.; Durante, M.*: **Assessing the risk of second malignancies after modern radiotherapy.** *Nat. Rev. Cancer* **11**(6): 438–448, 2011. DOI: 10.1038/nrc3069

025 Pignalosa, D.*; Durante, M.*: **CELLULAR EFFECTS OF ENERGETIC HEAVY IONS: FROM DNA BREAKS TO CHROMOSOMAL REARRANGEMENTS.** *Radiat. Prot. Dosim.* **143**(2-4): 391–393, 2011. DOI: 10.1093/rpd/ncq514

026 Schlampp, I.; Karger, C. P.; Jakel, O.; Scholz, M.*; Didinger, B.; Nikoghosyan, A.; Hoess, A.; Kramer, M.*; Edler, L.; Debus, J.; Schulz-Ertner, D.: **TEMPORAL LOBE REACTIONS AFTER RADIOTHERAPY WITH CARBON IONS: INCIDENCE AND ESTIMATION OF THE RELATIVE BIOLOGICAL EFFECTIVENESS BY THE LOCAL EFFECT MODEL.** *Int. J. Radiat. Oncol. Biol. Phys.* **80**(3): 815–823, 2011. DOI: 10.1016/j.ijrobp.2010.03.001

027 Shibata, A.; Conrad, S.; Birraux, J.; Geuting, V.; Barton, O.; Ismail, A.; Kakarougkas, A.; Meek, K.; Taucher-Scholz, G.*; Lobrich, M.; Jeggo, P. A.: **Factors determining DNA double-strand break repair pathway choice in G2 phase.** *Embo J.* **30**(6): 1079–1092, 2011. DOI: 10.1038/emboj.2011.27

028 Wiesenfeld, L.; Scifoni, E.*; Faure, A.; Roueff, E.: **Collisional excitation of doubly deuterated ammonia ND(2)H by para-H(2).** *Mon. Not. Roy. Astron. Soc.* **413**(1): 509–513, 2011. DOI: 10.1111/j.1365-2966.2010.18151.x

Doctoral theses 2011 in the research field hadrons and nuclei supported by GSI

K. Götzen, M.V. Ricciardi, and C. Sturm

GSI, Darmstadt, Germany

Hadron Physics

Roland Hohler: Prototyp-Radiatoren eines Barrel-DIRC für das PANDA-Experiment (Goethe Universität Frankfurt, Nov. 2011).

Daisuke Nakajima: Hypernuclear Spectroscopy with Heavy Ion Induced Reaction (Tokyo University, May 2011)

Jerome Boucher: Feasibility studies of the *pbar p* → $\pi^0 e^+ e^-$ electromagnetic channel at PANDA (Johannes Gutenberg Universität Mainz & Université de Paris Sud, Dec. 2011)

Nuclear Reactions

Saúl Beceiro Novo: Coulomb Dissociation of ^{27}P at 498 *A* MeV: an indirect measurement of the astrophysical ^{26}Si(p,γ) reaction (Universidad de Santiago de Compostela, November 2011).

Johnatan T. Taylor: Proton Induced Quasi-free Scattering with Inverse Kinematics (University of Liverpool, September 2011).

Felix Wamers: Quasi-Free-Scattering and One-Proton-Removal Reactions with the Proton-Dripline Nucleus ^{17}Ne at Relativistic Beam Energies (Technische Universität Darmstadt, May 2011).

Nuclear Structure

Fabio Farinon: Unambiguous Identification and Investigation of Uranium Projectile Fragments and Discovery of 63 New Neutron-rich Isotopes in the Element Range 61<Z<78 at the FRS (Justus-Liebig-Universität Gießen, October 2011).

Emma K. Haettner: A novel radio frequency quadrupole system for SHIPTRAP and new mass measurements of rp nuclides (Justus-Liebig-Universität Gießen, October 2011).

Natalia Kuzminchuk: Performance Studies and Improvements of a Time-of-Flight Detector for Isochronous Mass Measurements at the FRS-ESR Facility (Justus-Liebig-Universität Gießen, October 2011).

Andrej Prochaska: Nuclear Structure Studies via Precise Momentum Measurements (Justus-Liebig-Universität Gießen, May 2011).

Gamma Spectroscopy

Namita Goel: Spatial characterisation of a 36-fold segmented AGATA detector via a novel scanning system (Technische Universität Darmstadt, Juni 2011)

Robert Hoischen: An isomer study of the nucleus 54Ni preparations, simulations, and first results (Lund University, February 2011)

Farheen Naqvi: Probing the collectivity in neutron-rich Cd isotopes via gamma-ray spectroscopy (Universität zu Köln, May 2011)

Super Heavy Elements

Julia Even: Developments for transactinide chemistry experiments behind the gas-filled separator TASCA (Johannes Gutenberg-Universität Mainz, December 2011)

NQM/CBM

Christina Dritsa: Design of a microvertex detector for CBM(JWG Universität Frankfurt, December 2011)

Andrey Lebedev: Algorithms and Software for Track Reconstruction in the Transition Radiation Detector and Muon System of the CBM Experiment (University Dubna, January 2011)

Semen Lebedev: Algorithms and Software for Cherenkov Ring Reconstruction and Electron Identification in the RICH detector of the CBM Experiment (University Dubna, March 2011)

Samir Amar-Youcef: Development of the MVD Demonstrator (JWG Universität Frankfurt, September 2011)

Christoph Schrader: A Prototype MVD Read-Out-Syste (JWG Universität Frankfurt, June 2011)

Selim Sedikki: Design Studies for the MVD SIS 100 Read-Out (JWG Universität Frankfurt, October 2011)

NQM/HADES

Khaled Teilab: Exclusive Omega Production in p+p Collisions at 3.5 GeV (JWG Universität Frankfurt, August 2011)

Accelerator

Sabrina Appel: Simulation und Messung longitudinaler Raumladungseffekte in intensiven Ionenstrahlen im SIS18 Synchrotron (TU Darmstadt, May 2011)

Wafa Daga: Linear coupling with space charge (JWG Universität Frankfurt, September 2011)

Oleskii Gorda: Field interference of Magnets and its Influence on Beam Dynamics in Storage Rings (JWG Universität Frankfurt, May 2011)

Eiko Gütlich: Abbildungseigenschaften von Szintillatoren für Schwerionenstrahlen und diesbezügliche Modellrechnungen (TU Darmstadt, July 2011)

Angela Saa Hernandez, Design and optimization of the Lattice of the Superconducting Synchrotron SIS 300 for slow extraction (JWG Universität Frankfurt, July 2011)

Tripti Shekhar Mohite, Beam Loading Effect and Adiabatic Capture in SIS-18 at GSI (TU Darmstadt, January 2011)

Doctoral theses 2011 (PNI) supported by GSI

Atomic Physics

Stefan Ulmer: First Observation of Spin Flips with a Single Proton Stored in a Cryogenic Penning Trap (Univ. Heidelberg, July 2011)

Märtin Renate: Röntgenpolarimetrie angewandt zur Untersuchung der Bremsstrahlung spinpolarisierter Elektronen (Univ. Heidelberg, Oct. 2011)

Filippo Fratini: Polarization and correlation phenomena in the two-photon absorption and decay of heavy ions (Univ. Heidelberg, Dec. 2011)

Birgit Schabinger: Ein Experiment zur Bestimmung des g-Faktors des gebundenen Elektrons in wasserstoff- lithiumähnlichen mittelschweren Ionen (Univ. Mainz, May 2011)

Felix Laux: Entwicklung von kapazitiven Positions-, Strom- und Schottkysignal-Messsystemen für den kryogenen Speicherring CSR (Univ. Heidelberg, July 2011)

Schuh Marcel: Study of Higher Order Modes in Superconducting Accelerating Structures for Linac Applications (Univ. Heidelberg, Jun 2011)

Plasma Physics

Johannes Ling: Entwicklung, Aufbau und Test eines kontaktfreien Messverfahrens zur Bestimmung der elektrischen Leitfähigkeit dichter Plasmen (TUD, Feb. 2011)

Muhammad Imran: Study of Heavy Ion Beam Interaction with High Energy Laser Produced Plasmas (TUD, Feb. 2011)

Alexander Hug: Thermodynamische Eigenschaften von schwerionengeheizten hochschmelzenden Metallen (TUD, May 2011)

Marc Günther: Untersuchung relativistischer Laserplasmen mittels nukleardiagnostischer Verfahren (TUD, Jan. 2011)

Alexander Frank: Energieverlust und Umladung von schweren Ionen in lasererzeugten Plasmen (TUD, Nov. 2011)

Materials Research

Beatrice Schuster: Oxide ceramics under extreme pressure and radiation conditions (TUD, July 2011)

Markus Rauber: Controlled Synthesis of Nanowire Assemblies by Ion-Track Template Electrodeposition (TUD, Dec. 2011)

Elena Matei: Fabrication of semiconducting nanowires (Univ. of Bucharest, 2011)

Doctoral theses 2011 (Health) supported by GSI

C. Kausch

[1]GSI, Darmstadt

Robert Lüchtenborg: Real-time dose compensation methods for scanned ion beam therapy of moving tumors (TU Darmstadt, FB Physik, Dezember, 2011)

Peter Steidl: Gating for scanned ion-beam therapy Durante (TU Darmstadt, FB Physik Dezember 2011)

Robert Kaderka: Out-of-field dose measurements in radiotherapy: Dosismessungen außerhalb des Zielvolumens in der Strahlentherapie (TU Darmstadt, FB Physik Juli, 2011)

Frenzel Monika: Mitochondrial ageing in rat brain areas and human fibroblasts (TU Darmstadt, FB Chemie, 2011)

Sebastian Zahnreich: Untersuchungen zur genetischen Stabilität von normalen humanen Fibroblasten nach Einwirkung von dicht-ionisierender Strahlung (TU Darmstadt, FB Physik Februar, 2011)

Daniela Kraft: Strahlenantwort von hämatopoetischen Stammzellen nach Bestrahlung mit hochergetischen schweren Ionen (Universitäte Frankfurt, FB Pharmazie, Juni 2011)

Experiments performed at the GSI accelerators in 2011

Compiled by Andreas Tauschwitz, beam time coordinator 2011

In all tables 1 shift represents 8 hours of beam delivered to an experiment including necessary accelerator tuning time.

Exp	Short title	Spokesperson	Area	Ion	Shifts main	Shifts parasitic
U224	X-ray projectile and target radiation	Rosmej	Z6	^{50}Ti		3
U239	Towards element 117	Düllman	X8	^{40}Ar, ^{48}Ti	22	
U245	Electron-capture delayed fission in the lead region	Andreyev	Y7	^{60}Ni	13	
U258	Synthesis of New Elements at TASCA	Düllmann	X8	^{50}Ti	131	
U261	X-ray Fingerprinting of Z=115 Decay Chains	Rudolph	X8	^{48}Ca	18	
U264	Investigation of rare isotopes with SHIPTRAP	Block	Y7	^{48}Ca, ^{50}Ti	20	21
U265	Energy loss in indirectly heated dense plasma	Roth	Z6	^{48}Ca		24
U266	Investigation of low Z foams as plasma targets	Rosmej	Z6	^{50}Ti		12
U267	Study of superheavy elements using ^{248}Cm targets	Hofmann	Y7	^{54}Cr	105	
UBIO	Biology Experiments at UNILAC	Friedrich / Voss	X0, X6	C, Au, Cr, Sn	12	43
UMAT	Material Science Proposals at the UNILAC	Severin / Voss	X0, UU, M	Au, Xe	79	71

E064	Light-ion induced reactions in storage rings	Chartier	ESR	^{40}Ar	6	
E074	Radiative Double Electron Capture	Warczak	ESR	^{54}Cr	6	
E075	HITRAP commissioning	Herfurth	HI TRAP	Xe, ^{54}Cr, ^{14}N	37	
E079	Isotope shift in dielectronic rec. of L-shell ions	Brandau	ESR	U	17	
E082	Single-Ion spectroscopy of two-body beta-decays	Litvinov	ESR	^{152}Sm	16	
E083	Laser spectroscopy of lithium-like bismuth	Nörtershäuser	ESR	Bi	21	
E087	Breakout from the hot CNO cycles in X-ray bursters	Woods	ESR	^{22}Ne	4	
E090	Bremsstrahlung during Electron Transfer to Continuum	Hagmann	ESR	Bi	9	
E092	Radiative transitions into bare heavy ions	Tashenov	ESR	U	20	
E101	Electron-impact excitation of K-shell transitions	Thorn	ESR	Bi	2	
E103	Quasi-Molecular Radiation: Impact Parameter Studies	Gumberidze	ESR	Bi	9	
E111	Measurement of Breit interaction in Be-like U-ions	Trotsenko	ESR	U	10	

Exp	Short title	Spokesperson	Area	Ion	Shifts main	Shifts parasitic
S323	Beta-decay of very neutron-rich Rh, Pd, Ag nuclei	Montes	FRS	U, Bi	11	8
S338	Strangeness in heavy ion collisions	Herrmann	HTB	^{14}N	1	
S339	Pion-induced In-medium Production of Strangeness	Hartmann	HTB	^{14}N	42	
S358	Nuclear spatial structure of neutron-rich B and C	Khanzadeev	FRS-HTC	^{22}Ne	30	
S362	Test of the GEM-TPC prototype for PANDA	Ketzer	HTB	^{22}Ne		12
S364	Proton and neutron radial distributions	Benlliure	HFS	^{112}Sn, ^{124}Sn	15	
S370	Investigation of excited states in He-like uranium	Reuschl	HTA	U	8	
S371	Nuclear reactions for medical and space applications	Cuttone	HTC	C	32	
S375	Recoiling through ferromagnetic hosts	Jungclaus	HFS	^{54}Cr		8
S377	Neutron-deficient sd-shell nuclei	Reiter	HFS	^{36}Ar, ^{54}Cr	12	12
S378	Characterization of the H_2-target at PRESPEC	Obertelli	HFS	^{54}Cr		8
S386	DIRCs for the PANDA detector	Schwarz	HTD	^{14}N		16
S390	Test of the AIDA Detector System for DESPEC	Liu	HTD	Bi		6
S391	PRESPEC Commissioning Request	Bentley	HFS	^{54}Cr		8
S394	Symmetry Energy at Supra-Saturation Densities	Lemmon	HTC	Au, Ru, Zr	37	12
S395	Determination of proton radii and neutron skin	Kanungo	HFS	^{22}Ne, ^{40}Ar	20	
S398	Electrical Conductivity of WDM	Udrea	HHT			18
S402	Cryogenic Ion Catcher for SIS100	Bozyk	HHT	Bi, Au, Ta	4	14
S405	^{64}Ni(p,n) reaction in inverse kinematics	Reifarth	HTC	^{152}Sm	16	
S407	Investigation of baryon rich dense nuclear matter	Salabura	HAD	Au	11	12
S408	Constraining the symmetry energy of the EoS	Krasznahorkay	FRS-HTC	^{124}Sn	12	
S410	Measurement of beta-delayed neutrons	Domingo-Pardo	FRS	U	16	
S411	Cryogenic Stopping Cell for the Super-FRS	Dendooven	FRS	U	11	
S415	R&D on advanced detection techniques	Taieb	HTD	U, ^{124}Sn		19
S419	Commissioning of HISPEC/DESPEC detectors	Algora	FRS	U		3
S420	Activation of FAIR relevant construction materials	Chetvertkova	HHD	U, ^{14}N	2	8
S423	Radiation hardness of FAIR insulating materials	Seidl	HTA, X0	U, ^{54}Cr	2	3
SBIO	Biology Experiments at SIS	Scholz	HTA, HTM	C	12,5	
STHE	Therapy Studies: Physics and Technology	Bert	HTM		16	
STUN	Beam Tuning for Bio- and Therapy Experiments	Scholz/Bert	HTM		14	
SMAT	Materials research at SIS	Trautmann / Schuster	HTA	Bi, Au	14	

Cross references to experimental proposal numbers, GSI F&E projects and main universities contracts

Experimental proposal numbers

10-IBER-13: CANCER-80
50WB0929: CANCER-74
AO10IBER1: CANCER-78
AOIBER10: CANCER-85
BIO05002: CANCER-17
BIO-05-003: CANCER-13, CANCER-14, CANCER-15, CANCER-16, CANCER-20, CANCER-25, CANCER-27, CANCER-72,
BIO-05-009: CANCER-02, CANCER-03, CANCER-04, CANCER-05, CANCER-06, CANCER-08, CANCER-10, CANCER-11, CANCER-12
BIO-05-011: CANCER-29
CBM: PHN-NQM-CBM-28
E000: PNI-AP-25
E048: PHN-NUSTAR-FRS-15, PHN-NUSTAR-FRS-16
E062: PHN-NUSTAR-NR-23
E064: PHN-NUSTAR-NR-08
E067: PNI-AP-03
E083: PNI-AP-01
E084: PHN-NUSTAR-FRS-19, PHN-NUSTAR-FRS-21
E090: PNI-AP-15
E103: PNI-AP-09
IBER-16: CANCER-81, CANCER-83
IBER2 ESA: CANCER-07
P035: PNI-PP-21
P036: PNI-PP-05
P041: PNI-PP-04
P045: PNI-PP-18
PANDA: PHN-HSD-PANDA-12, PHN-HSD-PANDA-13, PHN-HSD-PANDA-14
PT-05-002: CANCER-57, CANCER-58, CANCER-63
PT16: CANCER-49, CANCER-50
S130: PHN-NQM-CBM-32, PHN-NQM-CBM-33
S200: PHN-NQM-HADES-05
S287: PHN-NUSTAR-NR-21
S295: PHN-NUSTAR-NR-15
S296: PHN-NUSTAR-NR-18
S306: PHN-NUSTAR-NR-20
S318: PHN-NUSTAR-NR-17
S323: PHN-NUSTAR-FRS-03, PHN-NUSTAR-FRS-05
S325: PHN-NQM-FOPI-01, PHN-NQM-FOPI-02
S333: PHN-NQM-HADES-08, PHN-NQM-HADES-14, PHN-NQM-HADES-15
S339: PHN-NQM-FOPI-05, PHN-NQM-FOPI-06, PHN-NQM-FOPI-07
S341: PHN-NUSTAR-FRS-09
S349: PHN-NQM-FOPI-03, PHN-NQM-FOPI-04
S369: PHN-NUSTAR-FRS-11
S370: PNI-AP-06
S371: CANCER-66, CANCER-67, CANCER-68, CANCER-69, CANCER-70
S377: PHN-NUSTAR-FRS-10
S378: PHN-NUSTAR-FRS-13
S389: PHN-NUSTAR-FRS-07
S393: PHN-NUSTAR-NR-12, PHN-NUSTAR-NR-13, PHN-NUSTAR-NR-14
S394: PHN-NQM-FOPI-11, PHN-NQM-FOPI-12
S395: PHN-NUSTAR-FRS-08
S402: PHN-ACC-RD-29
S405: PHN-NUSTAR-NR-22
S410: PHN-NUSTAR-FRS-04, PHN-NUSTAR-FRS-05
S411: PHN-NUSTAR-FRS-24, PHN-NUSTAR-FRS-26
S8355: CANCER-75
U14: PHN-ACC-RD-58
U182: PHN-NUSTAR-SHE-12
U200: PHN-NUSTAR-SHE-06
U207: PHN-NUSTAR-SHE-15
U225: PHN-NUSTAR-SHE-05
U249: PHN-IS-DL-05
U249: PHN-IS-DL-06
U250: PHN-NUSTAR-SHE-04
U252: PNI-PP-08
U255: PHN-NUSTAR-FRS-23
U258: PHN-NUSTAR-SHE-02
U258: PHN-NUSTAR-SHE-08, PHN-NUSTAR-SHE-13
U261: PHN-NUSTAR-SHE-03
U264: PHN-NUSTAR-SHE-07, PHN-NUSTAR-SHE-09
U266: PNI-PP-07, PNI-PP-15, PNI-PP-16, PNI-PP-17
U267: PHN-NUSTAR-SHE-01, PHN-NUSTAR-SHE-16
U270: PNI-MR-13
U271: PNI-MR-14, PNI-MR-15, PNI-MR-16, PNI-MR-21
U274: PNI-PP-11
UMAT: PNI-MR-09

GSI E&E projects

BOWIED1012+27: PHN-HSD-PANDA-12, PHN-HSD-PANDA-13, PHN-HSD-PANDA-14
DDPLUN1012+21: PNI-AP-27, PNI-AP-28, PNI-AP-30, PNI-AP-34,
DDWEBE1012+24: PNI-MR-12
DDZSCH1012+30: PNI-AP-19
EILIAK+9: CANCER-74
EREYRI1012+3: PHN-HSD-PANDA-06
GFMARX1012+18: PHN-NUSTAR-SHE-07
HDENSS+2: PNI-AP-21
HDHERR+8: PHN-NQM-CBM-31, PHN-NQM-CBM-35, PHN-NQM-CBM-36, PHN-NQM-FOPI-01, PHN-NQM-FOPI-02
KJOLIE1012+10: PHN-NUSTAR-FRS-05, PHN-NUSTAR-FRS-11, PHN-NUSTAR-FRS-30
LMTHIR1012+23: PHN-NUSTAR-SHE-18

MSKHOU1012+13: PHN-HSD-PANDA-01
MSWESS1012+26: PHN-NQM-CBM-22, PHN-NQM-CBM-25, PHN-NQM-CBM-28
TMFABI1012+4: PHN-NQM-FOPI-03, PHN-NQM-FOPI-09, PHN-NQM-HADES-14
TMKRUE1013+20: PHN-HSD-PANDA-04, PHN-HSD-PANDA-05, PHN-NQM-FOPI-10
TMPAUL1012+14: PHN-IS-DL-01, PHN-NUSTAR-NR-08, PHN-NUSTAR-NR-09, PHN-NUSTAR-NR-14, PHN-NUSTAR-NR-16, PHN-NUSTAR-NR-20
TMWEIS1012+25: PHN-NQM-T-HQ-02
WKAMPE1011+11: PHN-NQM-CBM-23
WMUELL1012+16: PNI-MR-34
WOKEID1012+12: PHN-IS-EE-08

Main universities co-operations contracts

Darmstadt
CANCER-01, CANCER-04, CANCER-05, CANCER-24, CANCER-26, CANCER-34, CANCER-46, CANCER-52, CANCER-56, CANCER-58, CANCER-60, CANCER-63, CANCER-64, CANCER-75, CANCER-76, CANCER-81, CANCER-82, CANCER-84, PHN-ACC-RD-16, PHN-ACC-RD-19, PHN-ACC-RD-20, PHN-ACC-RD-21, PHN-ACC-RD-26, PHN-ACC-RD-29, PHN-ACC-RD-32, PHN-ACC-RD-33, PHN-ACC-RD-37, PHN-ACC-RD-41, PHN-ACC-RD-51, PHN-ACC-RD-52, PHN-ACC-RD-53, PHN-ACC-RD-59, PHN-ACC-SP-07, PHN-IS-IT-13, PHN-NQM-CBM-51, PHN-NQM-CBM-52, PHN-NQM-CBM-53, PHN-NQM-CBM-56, HN-NUSTAR-FRS-09, PHN-NUSTAR-FRS-23, PHN-NUSTAR-FRS-28, PHN-NUSTAR-NR-01, PHN-NUSTAR-NR-03, PHN-NUSTAR-NR-12, PHN-NUSTAR-NR-14, PHN-NUSTAR-NR-17,PHN-NUSTAR-NR-18, PHN-NUSTAR-NR-19, PHN-NUSTAR-NR-21, PHN-NUSTAR-SHE-15, PHN-NUSTAR-T-03, PHN-NUSTAR-T-04, PHN-NUSTAR-T-05, PHN-NUSTAR-T-08, PHN-NUSTAR-T-10, PHN-NUSTAR-T-13, PNI-ACC-07, PNI-ACC-10, PNI-AP-18, PNI-MR-02, PNI-MR-17, PNI-MR-18, PNI-MR-19, NI-MR-20, PNI-PP-05, PNI-PP-08, PNI-PP-09, PNI-PP-11, PNI-PP-18, PNI-PP-25, PNI-PP-28, PNI-PP-31

Frankfurt
PHN-ACC-RD-07, PHN-ACC-RD-08, PHN-ACC-RD-09, PHN-ACC-RD-10, PHN-ACC-RD-11, PHN-ACC-RD-23, PHN-ACC-RD-25, PHN-ACC-RD-50, PHN-ACC-RD-58, PHN-IS-DL-04, PHN-IS-EE-06, PHN-IS-IT-08, PHN-NQM-ALICE-03, PHN-NQM-ALICE-04, PHN-NQM-ALICE-06, PHN-NQM-ALICE-07, PHN-NQM-ALICE-08, PHN-NQM-ALICE-09, PHN-NQM-ALICE-10, PHN-NQM-ALICE-12, PHN-NQM-CBM-03, PHN-NQM-CBM-04, PHN-NQM-CBM-05, PHN-NQM-CBM-06, PHN-NQM-CBM-08, PHN-NQM-CBM-09, PHN-NQM-CBM-10, PHN-NQM-CBM-11, PHN-NQM-CBM-26, PHN-NQM-CBM-38, PHN-NQM-CBM-39, PHN-NQM-CBM-40, PHN-NQM-CBM-41, PHN-NQM-CBM-44, PHN-NQM-CBM-45, PHN-NQM-CBM-46, PHN-NQM-CBM-47, PHN-NQM-CBM-49, PHN-NQM-CBM-50, PHN-NQM-CBM-54, PHN-NQM-CBM-55, PHN-NQM-HADES-01, PHN-NQM-HADES-03, PHN-NQM-HADES-04, PHN-NQM-HADES-05, PHN-NQM-HADES-07, PHN-NQM-HADES-11, PHN-NQM-HADES-12, PHN-NQM-HADES-13, PHN-NQM-T-HQ-01, PHN-NQM-T-SI-01, PHN-NUSTAR-FRS-07, PHN-NUSTAR-NR-06, PHN-NUSTAR-NR-13, PHN-NUSTAR-NR-15, PHN-NUSTAR-NR-22, PHN-NUSTAR-NR-23, PHN-NUSTAR-NR-26, PHN-NUSTAR-NR-27, PHN-NUSTAR-T-11, PNI-ACC-06, PNI-ACC-11, PNI-ACC-12, PNI-AP-09, PNI-AP-10, PNI-AP-15, PNI-AP-26, PNI-PP-04, PNI-PP-07, PNI-PP-10, PNI-PP-12, PNI-PP-13, PNI-PP-14, PNI-PP-15, PNI-PP-16, PNI-PP-17, PNI-PP-26, PNI-PP-27, PNI-PP-32

Gießen
PHN-HSD-PANDA-10, PHN-NQM-CBM-48, PHN-NQM-T-SI-02, PHN-NQM-T-SI-03, PHN-NQM-T-SI-04, PHN-NUSTAR-FRS-01, PHN-NUSTAR-FRS-03, PHN-NUSTAR-FRS-04, PHN-NUSTAR-FRS-05, PHN-NUSTAR-FRS-19, PHN-NUSTAR-FRS-20, PHN-NUSTAR-FRS-21, PHN-NUSTAR-FRS-24, PHN-NUSTAR-FRS-25, PHN-NUSTAR-FRS-26

Heidelberg
CANCER-55, PHN-IS-EE-08, PHN-NQM-ALICE-11, PHN-NQM-CBM-31, PHN-NQM-CBM-32, PHN-NQM-CBM-33, PHN-NQM-CBM-35, PHN-NQM-CBM-36, PHN-NQM-FOPI-01, PHN-NQM-FOPI-02, PNI-AP-14, PNI-AP-21, PNI-AP-23, PNI-AP-25, PNI-AP-29, PNI-AP-31, PNI-AP-32, PNI-AP-33, PNI-MR-23

Statutory organs and scientific advisory committees of GSI (2011)

Compiled by K. Füssel

Supervisory Board/Aufsichtsrat:

Dr. B. Vierkorn-Rudolf [chair],
Bundeministerium für Bildung und Forschung, Bonn/Berlin (Germany),
as representative of the Federal Republic of Germany

Ministerialrätin O. Keppler,
Bundesministerium für Bildung und Forschung, Bonn/Berlin (Germany),
as representative of the Federal Republic of Germany

Ministerialdirigent Dr. R. Bernhardt,
Hessisches Ministerium für Wissenschaft und Kunst, Wiesbaden (Germany),
as representative of the State of Hesse in Germany

Prof. Dr. K.-H. Kampert
Bergische Universität Wuppertal (Germany),
as representative of the Scientific Council of GSI

Scientific Directorate/Wissenschaftliches Direktorium WD:

Prof. Dr. H. Stöcker, P. Hassenbach (since September 1, 2011)
Dr. H. Eickhoff, Prof. Dr. K. Langanke

Divisions/Bereiche:

Accelerator: O. *Kester*
Finances / Controlling / admin. Organisations: *N.N.*
Personnel and Legal Services: *A. Lambert*
Research: *K. Langanke*
Technical Infrastructure: *B. Schönfelder*

Research Areas/Forschungsschwerpunkte:

APPA / PNI + Health: T. *Stöhlker*
CBM / NQM: J. *Stroth*
NuSTAR / ENNA: C. *Scheidenberger*
PANDA / HSD: K. *Peters*
IT: V. *Lindenstruth*

Research Divisions/Forschungsabteilungen:

ALICE: *P. Braun-Munzinger/ S. Mascciochi (since October 1, 2011)*
Atomic Physics: *T. Stöhlker*
Biophysics: *M. Durante*
CBM: *P. Senger*
Core-IT: *K. Miers (since October 1, 2011)*
FOPI: *Y. Leifels*
FRS/SFRS: *H. Geissel*
Gamma-Spectroscopy: *J. Gerl / N. Pietralla*
HADES: *J. Stroth*
Hadron Physics I: *K. Peters*
Hadron Physics II: *F. Maas*

High Performance Computing: *W. Schön*
Materials Research: *C. Trautmann*
Nuclear Reactions: *T. Aumann*
Plasma Physics and PHELIX: *T. Stöhlker (provisional)*
Scientific Computing: P. *Malzacher*
SHE-Chemistry: *C. E. Düllmann*
SHE-Physics: *F.-P. Hessberger*
Theory: *H. Feldmeier, C. Greiner, F. Karsch, J. Wambach*

Scientific Council/Wissenschaftlicher Rat WR:
http://www.gsi.de/informationen/users/EAC/wr/

K.-H. Kampert [chair], Bergische Universität Wuppertal (Germany);
D. von Harrach [vice chair], Johannes-Gutenberg-Universität Mainz (Germany);
A. Bracco, University of Milano (Italy); *P. Chomaz*, Irfu/SPP, Gif-sur-Yvette (France); *R. Hayano*, University of Tokyo (Japan); *R. Heuer*, European Organization of Nuclear Research, CERN, Geneva (Switzerland); *B. Jacak*, Stony Brook University, Stony Brook, New York (USA); *S. Myers*, CERN AB, Geneva (Switzerland); *T. Roser*, BNL, Upton (USA); *R. Sauerbrey*, Forschungszentrum Rossendorf, Dresden (Germany); *D. Vernhet*, Université Paris (France); *M. C. Wiescher*, University of Notre Dame, Notre Dame, Indiana (USA).
Secretary: K.-D. Groß

Scientific Committee/Wissenschaftlicher Ausschuss WA:
http://www-w2k.gsi.de/wa/scientific_committee.htm

H. Simon [chair]*; Y. Leifels* [vice chair]*; D. Ackermann; E. Badura; J. Heuser; B. Lommel; M. Lutz; P. Malzacher; M. Reich-Sprenger; C. Schmidt; L. Schmitt; M. Scholz; G. Schreiber; J. Stadlmann; M. Steck; C. Trautmann; H. Weick; U. Weinrich; A. Bräuning-Demian* (guest)*; H. Kreiser* (guest).

Scientific Advisory Committees of GSI

GSI General Program Advisory Committee G-PAC:
http://www.gsi.de/informationen/users/EAC/ea/

P. Giubellino[chair], INFN Turin, Turin (Italy);
B. Blank, CEN Bordeaux-Gradignan, Gradignan (France); *Y. Blumenfeld*, CERN, Geneva (Switzerland); *W. Catford*, University of Physics, Guilford (UK); *R. Hoekstra*, KVI Groningen, Groningen (The Netherlands); *S. Leupold*, Uppsala University, Uppsala (Sweden); *N. Pietralla*, Technische Universität Darmstadt, Darmstadt (Germany); *H. Schatz*, Michigan State University, East Leasing (USA); *R. Schuch*, Stockholm University, Stockholm (Sweden); *A. Türler*, Paul Scherer Institut, Villigen (Switzerland); *M. Wada*, RIKEN, Saitama (Japan); *M. Weidemüller*, Ruprecht-Karls-Universität Heidelberg, Heidelberg (Germany).

GSI Phelix and Plasmaphysics Program Advisory Committee (PPAC):
http://www.gsi.de/informationen/users/EAC/ppac/

D. Schneider [chair], LLNL-PAT/NIF, Livermore, California (USA);
S. Jacquemot, LULI, Ecole Polytechnique, Palaiseau (France); *B. G. Logan*, LBL, Berkeley, California (USA); *G. Maynard*, CNRS, Orsay (France); *O. Willi*, Heinrich Heine Universität Düsseldorf, Düsseldorf (Germany).

GSI Biophysics & Radio-Biology Program Advisory Committee (Bio-PAC):

http://www.gsi.de/informationen/users/EAC/bio-pac/

G. Reitz [chair], Deutsches Zentrum für Luft- und Raumfahrt (DLR), Cologne (Germany); *F. A. Cucinotta*, NASA Johnson Space Center, Houston, Texas (USA); D. *Goodhead*, Emeritus Director of the Med. Res. Council Rad. and Genome Stability Unit, Oxford (United Kingdom); *T. Haberer*, HIT Betriebs GmbH am Universitätsklinikum Heidelberg, Heidelberg (Germany); *A. Kronenberg*, Lawrence Berkeley National Laboratory, Berkeley, California (USA); *L. Sabatier*, Institute of Cell. & Mol. Radiation Biology, Fonteney-aux-Roses (France).

GSI Materials Research Program Advisory Committee (Mat-PAC):

http://www.gsi.de/informationen/users/EAC/mat-pac/

P. Apel, JINR, Dubna (Russia); *S. Bouffard*, CEA-CNRS-ENSICAEN, Caen (France); *K. Hjort*, University of Uppsala, Uppsala (Sweden); *W. Wesch*, Friedrich-Schiller-Universität Jena, Jena (Germany).

Program Advisory Committee for FAIR-Related Beam Time Proposals (F-PAC):

J. Stadlmann [chair], GSI; L. Schmitt, GSI; W. Müller, GSI; C. Trautmann, GSI; H. Weick, GSI.

GSI Users' Group Executive Committee (UEC):

http://www.gsi.de/forschung/usersgroup/index.html

Nuclear Structure:
T. Faestermann (Germany); M. Pfutzner (Poland); D. Cortina (Spain); A. Jungclaus (Spain); P. Regan [past chair], (UK)
Nuclear Collision:
P. Salabura (Poland); T. Matulewicz (Poland); Nicole Bastid (France)
Atomic Physics:
D. Dauvergne (France); A. Mueller (Germany)
Plasma Physics:
J. Jacoby (Germany); T. Kühl (Germany)
Heavy Elements:
J. Kratz (Germany); A. Türler (Germany)
Theory:
W. Cassing (Germany)
Biophysics:
M. Löbrich (Germany)
Materials Research:
W. Ensinger [chair], (Germany)
Students:
B. Schuster (Germany)

Scientific Coordination:

Dr. K.-D. Groß

Organigramm

GSI Helmholtzzentrum für Schwerionenforschung GmbH

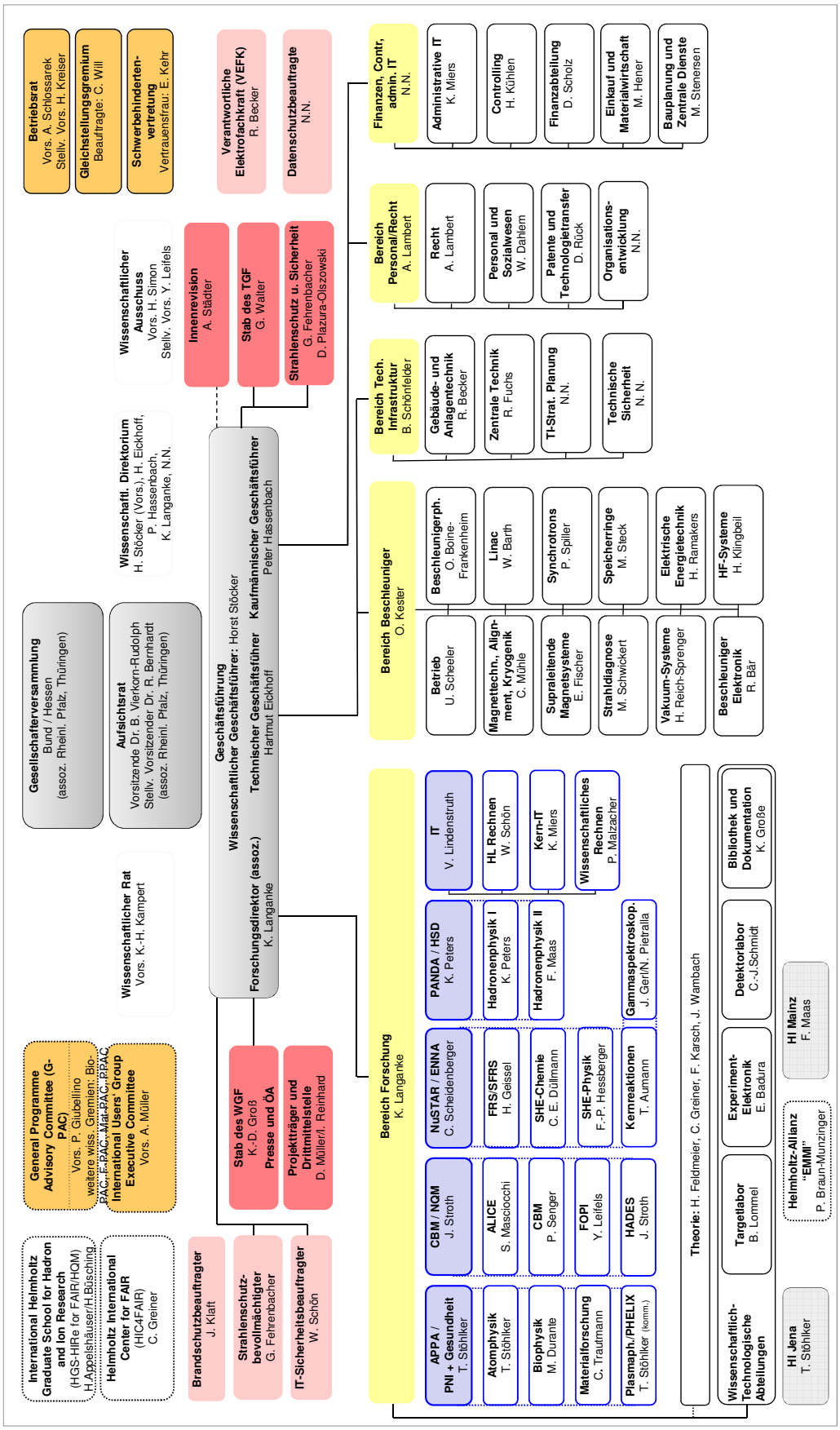

Stand: Dezember 2011.
Dieses Organigramm wurde am 14.7.2011 vom Aufsichtsrat der GSI verabschiedet und in Details im Dezember 2011 angepasst.

List of Authors